Fourth Computational Aeroacoustics (CAA) Workshop on Benchmark Problems

The NASA STI Program Office . . . in Profile

Since its founding, NASA has been dedicated to the advancement of aeronautics and space science. The NASA Scientific and Technical Information (STI) Program Office plays a key part in helping NASA maintain this important role.

The NASA STI Program Office is operated by Langley Research Center, the Lead Center for NASA's scientific and technical information. The NASA STI Program Office provides access to the NASA STI Database, the largest collection of aeronautical and space science STI in the world. The Program Office is also NASA's institutional mechanism for disseminating the results of its research and development activities. These results are published by NASA in the NASA STI Report Series, which includes the following report types:

- TECHNICAL PUBLICATION. Reports of completed research or a major significant phase of research that present the results of NASA programs and include extensive data or theoretical analysis. Includes compilations of significant scientific and technical data and information deemed to be of continuing reference value. NASA's counterpart of peer-reviewed formal professional papers but has less stringent limitations on manuscript length and extent of graphic presentations.

- TECHNICAL MEMORANDUM. Scientific and technical findings that are preliminary or of specialized interest, e.g., quick release reports, working papers, and bibliographies that contain minimal annotation. Does not contain extensive analysis.

- CONTRACTOR REPORT. Scientific and technical findings by NASA-sponsored contractors and grantees.

- CONFERENCE PUBLICATION. Collected papers from scientific and technical conferences, symposia, seminars, or other meetings sponsored or cosponsored by NASA.

- SPECIAL PUBLICATION. Scientific, technical, or historical information from NASA programs, projects, and missions, often concerned with subjects having substantial public interest.

- TECHNICAL TRANSLATION. English-language translations of foreign scientific and technical material pertinent to NASA's mission.

Specialized services that complement the STI Program Office's diverse offerings include creating custom thesauri, building customized databases, organizing and publishing research results . . . even providing videos.

For more information about the NASA STI Program Office, see the following:

- Access the NASA STI Program Home Page at *http://www.sti.nasa.gov*

- E-mail your question via the Internet to help@sti.nasa.gov

- Fax your question to the NASA Access Help Desk at 301–621–0134

- Telephone the NASA Access Help Desk at 301–621–0390

- Write to:
  NASA Access Help Desk
  NASA Center for AeroSpace Information
  7121 Standard Drive
  Hanover, MD 21076

Fourth Computational Aeroacoustics (CAA) Workshop on Benchmark Problems

Proceedings of a conference held at the Ohio Aerospace Institute
and cosponsored by the Ohio Aerospace Institute,
AeroAcoustics Research Consortium, and NASA Glenn Research Center
Brook Park, Ohio
October 20–22, 2003

National Aeronautics and
Space Administration

Glenn Research Center

September 2004

Available from

Preface

This publication contains the proceedings of the Fourth Computational Aeroacoustics (CAA) Workshop on Benchmark Problems. In this workshop, as in previous workshops, the problems were devised to gauge the technological advancement of computational techniques to calculate all aspects of sound generation and propagation in air directly from the fundamental governing equations. A variety of benchmark problems have been previously solved ranging from simple geometries with idealized acoustic conditions to test the accuracy and effectiveness of computational algorithms and numerical boundary conditions; to sound radiation from a duct; to gust interaction with a cascade of airfoils; to the sound generated by a separating, turbulent viscous flow. By solving these and similar problems, workshop participants have shown the technical progress from the basic challenges to accurate CAA calculations to the solution of CAA problems of increasing complexity and difficulty.

The fourth CAA workshop emphasized the application of CAA methods to the solution of realistic problems. The workshop was held at the Ohio Aerospace Institute in Cleveland, Ohio, on October 20 to 22, 2003. At that time, workshop participants presented their solutions to problems in one or more of five categories. Their solutions are presented in this proceedings along with the comparisons of their solutions to the benchmark solutions or experimental data. The five categories for the benchmark problems were as follows:

Category 1—Basic Methods. The numerical computation of sound is affected by, among other issues, the choice of grid used and by the boundary conditions. The first of three problems involves the issue of aliasing where spatial resolution errors affect the computation of sound. Second, the interface condition problem involves computing the propagation of sound through a surface of discontinuity. The third problem considers the long-term stability and accuracy of boundary treatments.

Category 2—Complex Geometry. The ability to compute the sound in the presence of complex geometric surfaces is important in practical applications of CAA. In this problem, complexity is achieved by multiple placements of simple circular cylinders.

Category 3—Sound Generation by Interacting With a Gust. The practical application of CAA for computing noise generated by turbomachinery involves the modeling of the noise source mechanism as a vortical gust interacting with an airfoil. The two problems in this category involve a single, thick airfoil and a cascade of realistic stator vanes. Unlike the thick airfoil problem, the cascade problem has no analytic solution. Its benchmark solution is itself numerically derived.

Category 4—Sound Transmission and Radiation. The first problem in this category is to compute the sound transmitted through a turbulent shear layer without triggering a possible instability wave that may form part of the solution. The second problem involves computing the interaction of a given sound source with a computed laminar shear flow. The solution to this problem is numerical with the initial benchmark solution computed by Barone and Lele.

Category 5—Sound Generation in Viscous Problems. Sound is generated under certain conditions by a viscous flow as the flow passes an object or a cavity. In the first problem, an aeolian tone is generated as the flow passes two nearby circular cylinders. Tones are generated in the second problem when the flow passes over a cavity. In both problems, experimental data are provided for comparison to computed solutions.

These proceedings are available on CD–ROM in the portable document format or PDF. In addition, the CD–ROM contains information related to all five categories of the benchmark problems including the numerical results from the calculations of the analytical and numerical solutions and the experimental data. See the README file in the CD–ROM directory entitled "caawksp4data" for further details.

Milo D. Dahl, NASA Glenn Research Center

Organizing Committee
Milo Dahl, NASA Glenn Research Center
Edmane Envia, NASA Glenn Research Center
Dennis Huff, NASA Glenn Research Center
Christopher Tam, Florida State University

Scientific Committee
The benchmark problems were proposed and
decided on by the following:

Professor Christophe Bailly, Ecole Centrale de Lyon, France
Professor Tim Colonius, California Institute of Technology
Dr. Milo Dahl, NASA Glenn Research Center
Dr. Jan Delfs, DLR, Germany
Dr. Edmane Envia, NASA Glenn Research Center
Professor Jonathan Freund, University of Illinois at Urbana-Champaign
Professor Thomas Hagstrom, The University of New Mexico
Dr. Brenda Henderson, NASA Langley Research Center
Professor Charles Hirch, Vrije Universiteit Brussel, Belgium
Professor Fang Hu, Old Dominion University
Dennis Huff, NASA Glenn Research Center
Professor Osamu Inoue, Tohoku University, Japan
Professor Soogab Lee, Seoul National University, Korea
Professor Sanjiva Lele, Stanford University
Dr. David Lockard, NASA Langley Research Center
Professor Reda Mankbadi, Embry-Riddle Aeronautical University
Dr. Eric Manoha, ONERA, France
Professor Philip Morris, The Pennsylvania State University
Professor Wei Shyy, University of Florida
Dr. Kenji Takeda, University of Southampton, United Kingdom
Professor Christopher Tam, Florida State University
Professor Frank Thiele, Technische Universite Berlin, Germany
Dr. Miguel Visbal, Air Force Research Laboratory, Wright-Patterson Air Force Base (WPAFB)

Table of Contents

Benchmark Problems

PROBLEM 1—ALIASING

Compute the solution of the convective wave equation

$$\frac{\partial u}{\partial t} + \frac{\partial u}{\partial x} = 0$$

on a uniform mesh with Δx=1 and the following initial condition,

$$t=0\ ,\qquad u = [2 + \cos(\alpha x)]\exp[-(\ln 2)(x/10)^2]$$

Consider two cases

(i) $\alpha = 1.7$

(ii) $\alpha = 4.6$

Results to be reported are the spatial distributions of u at t=400 and t=800.

Note : If computation is done by methods other than finite difference, an equivalent mesh size of Δx=1 should be used.

Contributed by Christopher Tam, email tam@math.fsu.edu

PROBLEM 2—INTERFACE TRANSMISSION
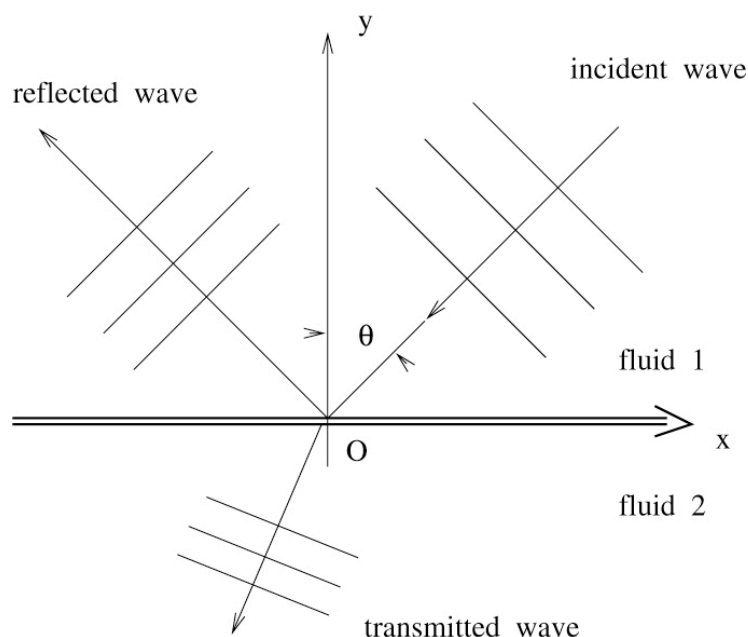
This problem is intended to test the discrete formulation and computation of sound transmitted through a surface of discontinuity. Here the surface of discontinuity is formed by the interface of two fluids with different densities and sound speeds as shown in the figure. An incident acoustic wave at an angle of incidence θ impinges on the interface. Part of the wave is transmitted and part of it is reflected. For computation purpose, we will use the following length, velocity, time, pressure and density scales. Subscripts 1 and 2 indicate fluid 1 and 2.

length scale $= L$

velocity scale $= a_1$ (sound speed in region 1)

time scale $= \dfrac{L}{a_1}$

density scale $= \bar{\rho}_1$ (density of fluid in region 1)

pressure scale $= \bar{\rho}_1 a_1^2$

$$\alpha = \frac{\rho_2}{\rho_1}, \qquad \lambda = \frac{\gamma_2}{\gamma_1}$$

The governing equations for small amplitude disturbances in fluid 1 are

$$\frac{\partial \rho_1}{\partial t} + \left(\frac{\partial u_1}{\partial x} + \frac{\partial v_1}{\partial y} \right) = 0$$

$$\frac{\partial u_1}{\partial t} = -\frac{\partial p_1}{\partial x}$$

$$\frac{\partial v_1}{\partial t} = -\frac{\partial p_1}{\partial y}$$

$$\frac{\partial p_1}{\partial t} + \left(\frac{\partial u_1}{\partial x} + \frac{\partial v_1}{\partial y} \right) = 0$$

The governing equations for small amplitude disturbances in fluid 2 are,

$$\frac{\partial \rho_2}{\partial t} + \alpha \left(\frac{\partial u_2}{\partial x} + \frac{\partial v_2}{\partial y} \right) = 0$$

$$\alpha \frac{\partial u_2}{\partial t} = -\frac{\partial p_2}{\partial x}$$

$$\alpha \frac{\partial v_2}{\partial t} = -\frac{\partial p_2}{\partial y}$$

$$\frac{\partial p_2}{\partial t} + \lambda \left(\frac{\partial u_2}{\partial x} + \frac{\partial v_2}{\partial y} \right) = 0$$

The dynamic and kinematic boundary conditions at the fluid interface are,

$$p_1 = p_2, \qquad v_1 = v_2$$

Now consider a plane wave at an incident angle θ and frequency ω given below

$$\begin{bmatrix} p_1 \\ u_1 \\ v_1 \\ \rho_1 \end{bmatrix}_{\text{incidence wave}} = \text{Re} \begin{bmatrix} 1 \\ -\sin\theta \\ -\cos\theta \\ 1 \end{bmatrix} e^{-i\omega(\sin\theta x + \cos\theta y + t)}$$

(Re = real part of.) Determine the intensity and direction of the transmitted and reflected waves for the two cases with $\theta = 20°$ and $65°$. The frequency and other parameters are $\omega = 0.7$, $\alpha = 0.694$ and $\lambda = 1$. Plot contours of p at intervals of 0.25 at the beginning of a cycle.

PROBLEM 3—ACCURACY OF BOUNDARY TREATMENTS

Proposer: Tom Hagstrom

Goal: Detailed study of the accuracy of boundary treatments with a range of incidence angles including shear and a sonic point.

Part 1: Uniform Flow We take the two-dimensional linearized Euler equations in dimensionless form, first assuming a uniform base flow:

$$\frac{\partial \rho}{\partial t} + (U \cdot \nabla)\rho + \nabla \cdot u = 0, \tag{1}$$

$$\frac{\partial u}{\partial t} + (U \cdot \nabla)u + \nabla p = 0, \tag{2}$$

$$\frac{\partial p}{\partial t} + (U \cdot \nabla)p + \nabla \cdot u = 0. \tag{3}$$

The base flow is given by:

$$U_1 = 0.3, \quad U_2 = 0.4, \tag{4}$$

and initial conditions, $\rho(x_1, x_2, 0)$, $u_j(x_1, x_2, 0)$ and $p(x_1, x_2, 0)$ are provided which lead to propagating sound, vorticity and entropy waves. The initial conditions are supported in $x_1 \in (-2, 2)$; that is

$$\rho(x_1, x_2, 0), u_j(x_1, x_2, 0), p(x_1, x_2, 0) = 0, \quad |x_1| \geq 2. \tag{5}$$

We take the computational domain to be:

$$(x_1, x_2) \in (-2, 2) \times (0, 1), \tag{6}$$

with periodic boundary conditions in x_2. That is we have the periodic boundary conditions:

$$\rho(x_1, 1, t) = \rho(x_1, 0, t), \quad u_j(x_1, 1, t) = u_j(x_1, 0, t), \quad p(x_1, 1, t) = p(x_1, 0, t). \tag{7}$$

The solvers can use their favorite radiation boundary conditions or absorbing layers at the inflow and outflow boundaries, $x_1 = \pm 2$.

The configuration of the problem is shown in Figure 1.

The problem is to solve up to $t = 64$, reporting relative L^2 errors measured on a uniform 129×33 mesh. The initial data and solution are 1-periodic in x_2 and will be provided on a uniform 513×129 mesh. (People who wish to use a finer mesh can interpolate. We have found that the data on a 257×65 mesh is accurate enough to generate numerical solutions with $7 - 8$ digits of accuracy.) Full details on obtaining the initial and solution data and reporting results is given below.

We note that the difficulty of the problem, from the point of view of boundary conditions, is that for late times sound waves incident on the boundary are produced by far away image sources, and thus the angles of incidence become more and more glancing.

Part 2: Subsonic Couette Flow

For the second part we make the base flow subsonic Couette flow:

$$U_1 = Mx_2, \quad M = 0.9, \quad U_2 = 0, \tag{8}$$

with the periodicity conditions replaced by the wall condition:

$$u_2 = 0, \quad x_2 = 0, 1. \tag{9}$$
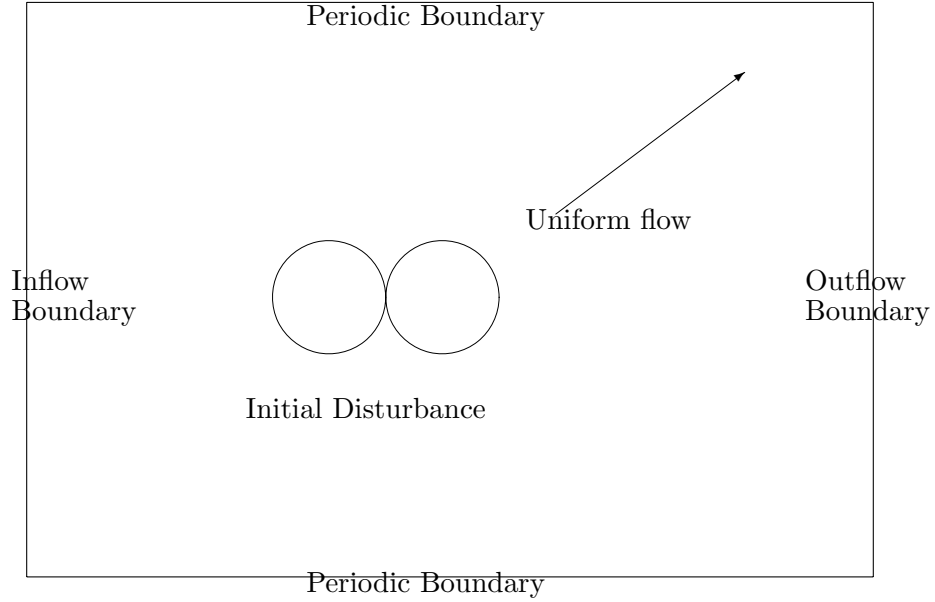
Figure 1: Computational Domain for Problem 1

Thus the governing equations are:

$$\frac{\partial \rho}{\partial t} + M x_2 \frac{\partial \rho}{\partial x_1} + \nabla \cdot u = 0, \tag{10}$$

$$\frac{\partial u}{\partial t} + M x_2 \frac{\partial u}{\partial x_1} + (M u_2 \ \ 0)^T + \nabla p = 0, \tag{11}$$

$$\frac{\partial p}{\partial t} + M x_2 \frac{\partial p}{\partial x_1} + \nabla \cdot u = 0. \tag{12}$$

Again the solver may choose any method for specifying boundary conditions at inflow and outflow, $x_2 = \pm 2$. The domain configuration for Problems 2 and 3 is represented in Figure 2.

Part 3: Transonic Couette Flow

The third example is the same as the second except that we use (8) with:

$$M = 1.2. \tag{13}$$

We note that the new features introduced in Problems 2 and 3 are the presence of shear and a sonic point at the inflow and outflow boundaries.
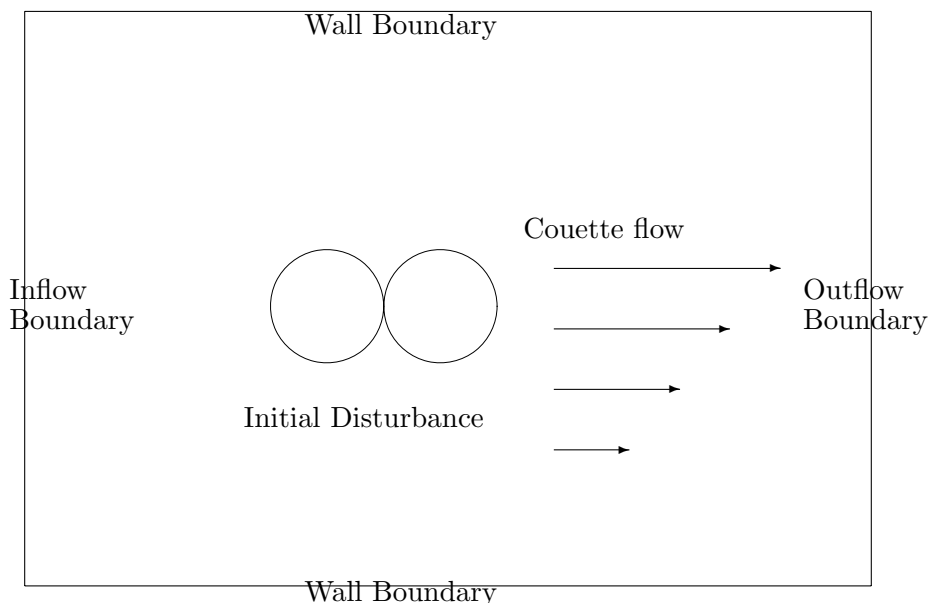
Figure 2: Computational Domain for Problems 2 and 3

DETAILED PROCEDURES

Initial and solution data can be obtained from the URL:

http://www.math.unm.edu/˜ hagstrom/CAAWorkshop

Each line of each file contains 8 numbers:

$$i_1 \quad i_2 \quad x_1 \quad x_2 \quad u_1 \quad u_2 \quad p \quad \rho;$$

the first two are integer indices associated with a data point, the second two are the double precision coordinates of the data point, and the last four are the double precision values of the fields. Each file is identified by the subproblem: Pr1,Pr2,Pr3, and the time: t00,t01,t02,t04,...,t64. Thus the file Pr1.t00 contains the initial data for Problem 1 on the grid:

$$(x_{1,i_1}, x_{2,i_2}), \quad x_{1,i_1} = -2 + (i_1 - 1)/128, \quad x_{2,i_2} = (i_2 - 1)/128. \tag{14}$$

Here $1 \le i_1 \le 513$ and $1 \le i_2 \le 129$. Similarly, the file Pr3.t24 contains the solution of Problem 3 at $t = 24$ on the coarser grid:

$$(x_{1,i_1}, x_{2,i_2}), \quad x_{1,i_1} = -2 + (i_1 - 1)/32, \quad x_{2,i_2} = (i_2 - 1)/32, \tag{15}$$

$$1 \le i_1 \le 129, \quad 1 \le i_2 \le 33. \tag{16}$$

The times are:

$$t_1 = 1, \quad t_2 = 2, \quad t_k = 4(k - 2), \quad k = 3, \ldots 18. \tag{17}$$

As the files are large and numerous, you may prefer to download the tarred versions, which are: Pr1.tgz, Pr2.tgz and Pr3.tgz.

You may use **any mesh you like** for solving the problem, interpolating between your mesh and the one on which I have given the data. Information which you should include in describing your solution is:

(i.) The discretization method used.

(ii.) The grid and time step.

(iii.) The detailed treatment of the artificial inflow and outflow boundaries, including the number of grid points used in any absorbing layers, absorption profiles, boundary condition orders, etc.

(iv.) Relative l_2 error data for all four fields at each of the eighteen time stations, t_k, computed on the 129×33 mesh. Precisely:

$$e_\rho(t_k) = \frac{\left(\sum_{i_1=1}^{129} \sum_{i_2=1}^{33} \left(\rho_{\text{exact}}(x_{1,i_1}, x_{2,i_2}, t_k) - \rho_{\text{comp}}(x_{1,i_1}, x_{2,i_2}, t_k)\right)^2\right)^{1/2}}{\left(\sum_{i_1=1}^{129} \sum_{i_2=1}^{33} \rho_{\text{exact}}^2(x_{1,i_1}, x_{2,i_2}, t_k)\right)^{1/2}}, \qquad (18)$$

$$e_{u_1}(t_k) = \frac{\left(\sum_{i_1=1}^{129} \sum_{i_2=1}^{33} \left(u_{1,\text{exact}}(x_{1,i_1}, x_{2,i_2}, t_k) - u_{1,\text{comp}}(x_{1,i_1}, x_{2,i_2}, t_k)\right)^2\right)^{1/2}}{\left(\sum_{i_1=1}^{129} \sum_{i_2=1}^{33} u_{1,\text{exact}}^2(x_{1,i_1}, x_{2,i_2}, t_k)\right)^{1/2}}, \qquad (19)$$

$$e_{u_2}(t_k) = \frac{\left(\sum_{i_1=1}^{129} \sum_{i_2=1}^{33} \left(u_{2,\text{exact}}(x_{1,i_1}, x_{2,i_2}, t_k) - u_{2,\text{comp}}(x_{1,i_1}, x_{2,i_2}, t_k)\right)^2\right)^{1/2}}{\left(\sum_{i_1=1}^{129} \sum_{i_2=1}^{33} u_{2,\text{exact}}^2(x_{1,i_1}, x_{2,i_2}, t_k)\right)^{1/2}}, \qquad (20)$$

$$e_p(t_k) = \frac{\left(\sum_{i_1=1}^{129} \sum_{i_2=1}^{33} \left(p_{\text{exact}}(x_{1,i_1}, x_{2,i_2}, t_k) - p_{\text{comp}}(x_{1,i_1}, x_{2,i_2}, t_k)\right)^2\right)^{1/2}}{\left(\sum_{i_1=1}^{129} \sum_{i_2=1}^{33} p_{\text{exact}}^2(x_{1,i_1}, x_{2,i_2}, t_k)\right)^{1/2}}. \qquad (21)$$

Recall that the times are $t_1 = 1$, $t_2 = 2$, $t_k = 4(k-2)$, $k = 3, \ldots, 18$.

Solutions as well as any questions concerning the problem should be emailed to me at:

hagstrom@math.unm.edu.

At the URL mentioned above there is also a README file with additional information and contour plots of the solution fields at each time. PLEASE DO NOT HESITATE TO CONTACT ME IF YOU HAVE ANY QUESTIONS OR DIFFICULTIES.

Happy solving!

Multi-Geometry Scattering Problem

The problem considered here is the scattering of sound generated by a spatially distributed, axisymmetric, acoustic source from multiple rigid circular cylinders. This case provides a stringent test of the ability of high-order CAA codes to handle increasingly complex geometries. It also serves to examine the performance of well-established low-order CFD codes, developed for complex geometries, when applied to the simulation of aeroacoustic phenomena. In addition, this problem provides a demonstration of numerical robustness, long-time stability and suitability of far-field radiation treatments in the presence of multiple scattering bodies.

The acoustic scattering problem is governed by the linearized Euler equations, which may be written in two spatial dimensions as

$$\frac{\partial \rho}{\partial t} + \frac{\partial u}{\partial x} + \frac{\partial v}{\partial y} = 0 \tag{1}$$

$$\frac{\partial u}{\partial t} + \frac{\partial p}{\partial x} = 0 \tag{2}$$

$$\frac{\partial v}{\partial t} + \frac{\partial p}{\partial y} = 0 \tag{3}$$

$$\frac{\partial p}{\partial t} + \frac{\partial u}{\partial x} + \frac{\partial v}{\partial y} = S \tag{4}$$

The flow variables in the above expressions are fluctuating quantities and have been non-dimensionalized by the following scales:

length scale	=	diameter of largest circular cylinder, D_{max}
velocity scale	=	ambient speed of sound, c_∞
time scale	=	$\frac{D_{max}}{c_\infty}$
density scale	=	ambient gas density, ρ_∞
pressure scale	=	$\rho_\infty c_\infty^2$

The time-dependent acoustic source term on the right-hand side of the energy equation is assumed axisymmetric and is written in the source-centered coordinate system as

$$S = \exp\left[-\ln 2 * \left\{\frac{x_S^2 + y_S^2}{b^2}\right\}\right] \sin(\omega t) \tag{5}$$

where $\omega = 8\pi$ and $b = 0.2$

Case 1

The first case, shown in Fig. 1, consists of two cylinders of unequal diameters $(D_1 = 1.0, D_2 = 0.5)$, with a co-linearly located source equidistant from the center of each cylinder. In the (x_S, y_S)-coordinate system centered on the source, the location of the cylinders are given by $L_1 = (-4, 0), L_2 = (4, 0)$.
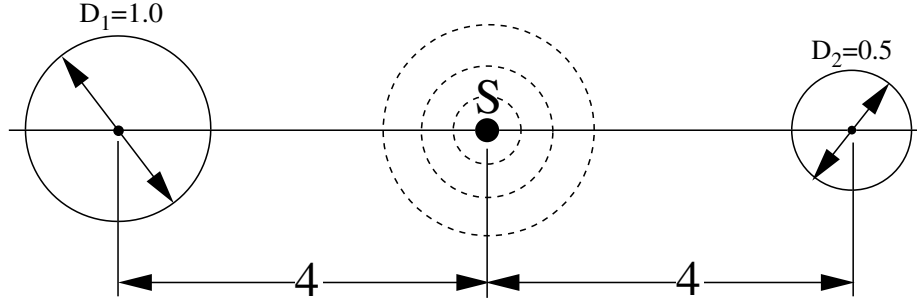
Figure 1: Geometry for acoustic scattering Case 1

Compute the time-averaged pressure $< p^2 >$ along the surface of both cylinders. Compute $< p^2 >$ along the centerline between the two cylinders, to the left of the leftmost cylinder and to the right of the rightmost cylinder, for $-9 \leq x_S \leq 9$. Provide details on both the spatial and temporal discretizations employed. This includes: (a) the total number of grid points or elements used, (b) the typical mesh spacing in the near field in terms of points per wave, (c) the farfield boundary location, (d) the number of time steps per period of the source, and (e) the total number of time steps used to achieved a fully time-asymptotic solution.

Case 2

The second case, shown in Fig. 2, consists of three cylinders with diameters $D_1 = 1.0$ and $D_2 = D_3 = 0.75$. The locations of the cylinders with respect to the source are given by $L_1 = (-3, 0), L_2 = (3, 4), L_3 = (3, -4)$.

Compute the time-averaged pressure $< p^2 >$ along the surface of cylinders 1 and 2. Compute $< p^2 >$ along the centerline, to the right and left of cylinder 1, for $-8 \leq x_S \leq 8$. Provide details on both the spatial and temporal discretizations employed as specified above for Case 1.
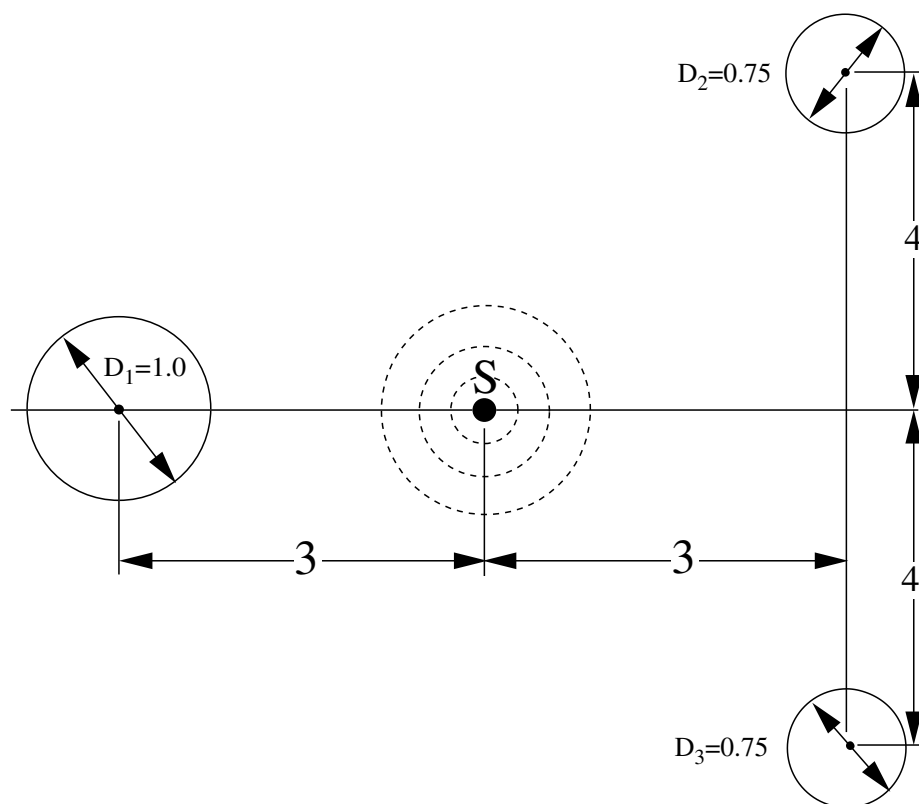
Figure 2: Geometry for acoustic scattering Case 2

Contributed by Miguel Visbal, email: visbal@vaa.wpafb.af.mil

SOUND GENERATION BY INTERACTING WITH A GUST

PROBLEM 1—SINGLE AIRFOIL GUST RESPONSE

James R. Scott

NASA Glenn Research Center

The purpose of this problem is to test the ability of a CFD/CAA code to accurately predict the unsteady aerodynamic and aeroacoustic response of a single airfoil to a two-dimensional, periodic vortical gust.

Consider the airfoil configuration shown in Figure 1. The airfoil has chord length c and angle of attack α. The upstream velocity is

$$\vec{U} = U_\infty \vec{\mathrm{i}} + \vec{a} \cos[\vec{k} \cdot (\vec{x} - \vec{\mathrm{i}} U_\infty t)] \tag{1}$$

where $\vec{x} = (x_1, x_2)$ denotes the spatial coordinates, $\vec{a} = (a_1, a_2)$ is the gust amplitude vector with $a_1 = -\epsilon U_\infty k_2/|\vec{k}|$, $a_2 = \epsilon U_\infty k_1/|\vec{k}|$, $\vec{k}$ is the wave number vector, and ϵ is a small parameter satisfying $\epsilon \ll 1$.

The governing equations are the 2-D Euler equations

$$\frac{\partial \rho}{\partial t} + \frac{\partial}{\partial x}(\rho\, u) + \frac{\partial}{\partial y}(\rho\, v) = 0 \tag{2}$$

$$\frac{\partial}{\partial t}(\rho u) + \frac{\partial}{\partial x}(\rho\, u^2 + p) + \frac{\partial}{\partial y}(\rho\, u\, v) = 0 \tag{3}$$

$$\frac{\partial}{\partial t}(\rho v) + \frac{\partial}{\partial x}(\rho\, u\, v) + \frac{\partial}{\partial y}(\rho\, v^2 + p) = 0 \tag{4}$$

$$\frac{\partial E_t}{\partial t} + \frac{\partial}{\partial x}[(E_t + p)\, u] + \frac{\partial}{\partial y}[(E_t + p)\, v] = 0 \tag{5}$$

where ρ, u, v, p and E_t denote the fluid density, velocity, pressure, and internal energy per unit volume.

Since the gust amplitude $\vec{a}$ satisfies $|\vec{a}| \ll U_\infty$, one can alternatively solve the linearized unsteady Euler equations

$$\frac{D_0 \rho'}{Dt} + \rho' \vec{\nabla} \cdot \vec{U}_0 + \vec{\nabla} \cdot (\rho_0 \vec{u}) = 0 \tag{6}$$

$$\rho_0\left(\frac{D_0 \vec{u}}{Dt} + \vec{u} \cdot \vec{\nabla}\vec{U}_0\right) + \rho' \vec{U}_0 \cdot \vec{\nabla}\vec{U}_0 = -\vec{\nabla}p' \tag{7}$$

$$\frac{D_0 s'}{Dt} = 0, \tag{8}$$

where $\frac{D_0}{Dt} = \frac{\partial}{\partial t} + \vec{U}_0 \cdot \vec{\nabla}$ is the material derivative associated with the mean flow, $\vec{u} = (u', v')$, primed quantities are the unknown perturbation variables, and "0" subscripts denote steady mean flow quantities which must be independently solved for and are assumed to be known.

Nondimensionalize the Euler equations as follows:

x_1, x_2	by	$\frac{c}{2}$
$\vec{U} = (u, v)$	by	U_∞
c_0 (sound speed)	by	U_∞
ρ	by	ρ_∞
p	by	$\rho_\infty U_\infty^2$
T	by	T_∞
t	by	$\frac{c}{2U_\infty}$
$\omega = k_1 U_\infty$	by	$\frac{2U_\infty}{c}$
k_1, k_2	by	$\frac{2}{c}$

If solving the linearized unsteady Euler equations, nondimensionalize the mean flow variables as above, and the perturbation variables as follows:

$\vec{u} = (u', v')$	by	U_∞
ρ'	by	ρ_∞
p'	by	$\rho_\infty U_\infty^2$
T'	by	T_∞
$\vec{a}$	by	U_∞

For the following two cases, solve the gust response problem for a Joukowski airfoil in a two-dimensional gust with $k_2 = k_1$ for reduced frequencies $k_1 = 0.1$, 1.0, and 2.0. The nondimensional upstream velocity is $\vec{U} = \vec{i} + \epsilon \vec{a} \cos(\vec{k} \cdot \vec{x} - k_1 t)$, where $\vec{a} = (a_1, a_2) = (-\frac{\sqrt{2}}{2}, \frac{\sqrt{2}}{2})$. Take $\epsilon = .02$.

For Case 1, the airfoil has a 12% thickness ratio, free stream Mach number $M_\infty = 0.5$, angle of attack $\alpha = 0^o$, and a camber ratio of zero.

For Case 2, change α to 2° and the camber ratio to .02.

The airfoil geometries can be generated as follows. Set

$$\zeta_1 = r_0 e^{i\theta} + \zeta_{0'} \tag{9}$$

where

$$\zeta_{0'} = -\epsilon_1 + i \epsilon_2 \tag{10}$$

is a complex constant. Letting $z = x + iy$ denote the airfoil coordinates in the complex z plane, the transformation

$$z = \left(\zeta_1 + \frac{d^2}{\zeta_1}\right) e^{-i\alpha} \tag{11}$$

transforms the ζ_1 circle defined by equation (9) into the desired airfoil shape.

For Case 1, use $r_0 = 0.54632753$, $\epsilon_1 = 0.05062004$, $\epsilon_2 = 0$, $d^2 = 0.24572591$, $\alpha = 0$. Discretize the ζ_1 circle in θ, starting from 0 and going to 2π, and then apply equation (11) to get the airfoil coordinates. The values $\theta = 0$ and $\theta = 2\pi$ map into the trailing edge point.

For Case 2, use $r_0 = 0.54676443$, $\epsilon_1 = 0.05062004$, $\epsilon_2 = 0.02185310$, $d^2 = 0.24572591$, $\alpha = 0.034906585$. Discretize the ζ_1 circle in θ, starting from $\theta = -\beta$ and going to $\theta = 2\pi - \beta$, where $\beta = 0.039978687$, and then apply equation (11) to get the airfoil coordinates. The values $\theta = -\beta$ and $\theta = 2\pi - \beta$, map into the trailing edge point.

The above procedure for generating the airfoil geometries will generate a Joukowski airfoil of chord length 2, situated very nearly between $x = -1$ and $x = 1$. The airfoil geometries are shown in Figure 2.

For both Case 1 and Case 2, march the discrete equations in time until the solution becomes periodic. On the airfoil surface, calculate the RMS pressure $\sqrt{\overline{(p')^2}}$. In the far field, calculate the intensity $\overline{(p')^2}$ at the following three locations: (i) on a circle of radius $R = 2$ (one chord length) centered about the airfoil center; (ii) on a circle of radius $R = 4$ (two chord lengths); (iii) on a circle of radius $R = 8$ (four chord lengths).

State whether the solution is from the Euler equations or linearized Euler equations. Also state the grid dimensions for each calculation, the number of complete periods computed, the CPU time per period, and the type of machine the calculations were run on.

email: James.R.Scott@nasa.gov

Problem Author: James R. Scott

Problem Submitted By: Milo D. Dahl
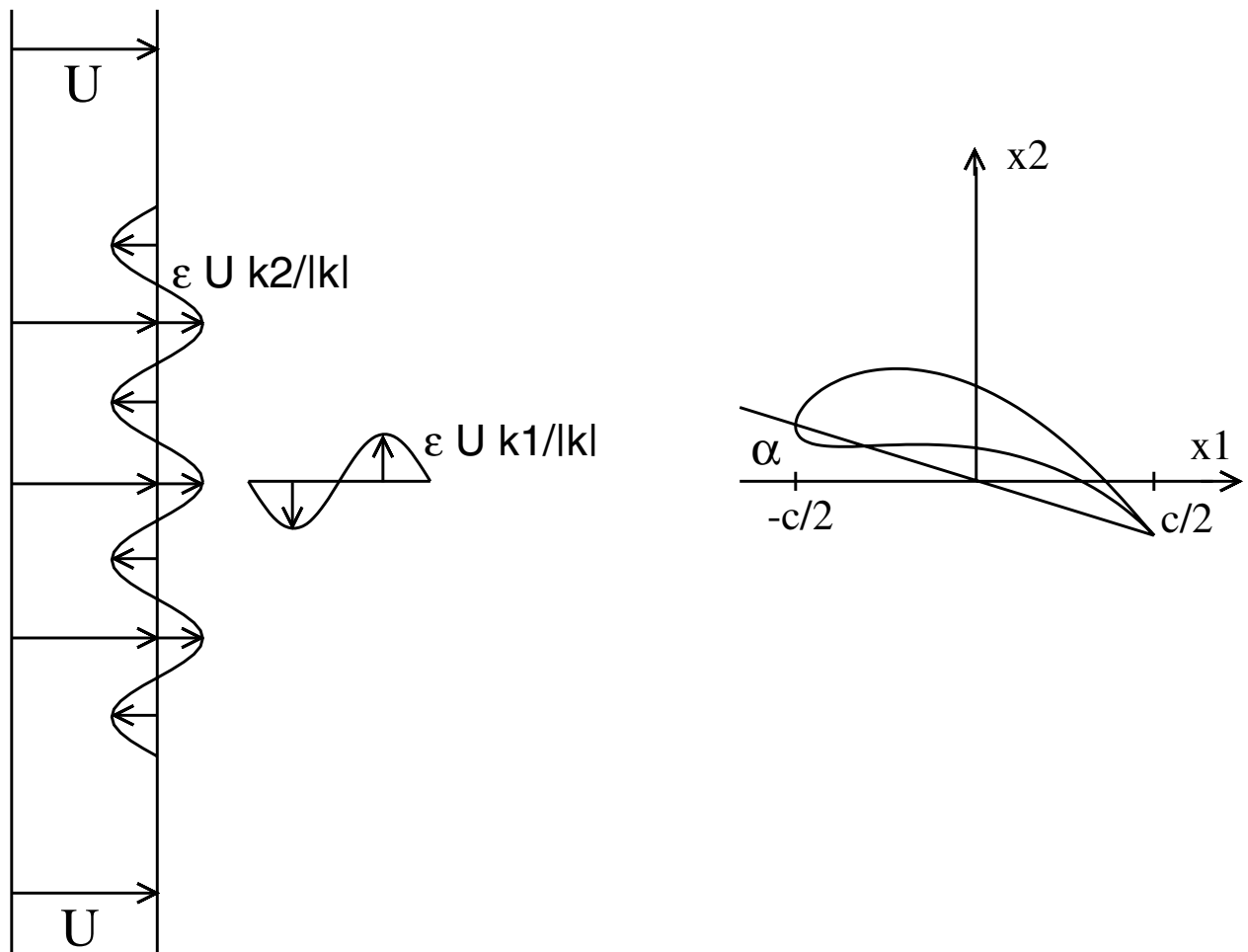
Figure 1   Airfoil in a two-dimensional, periodic gust.
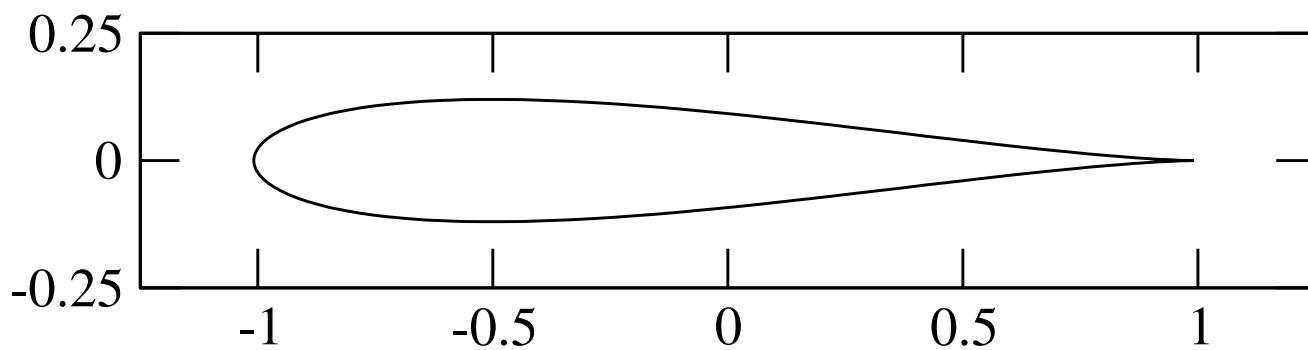
Figure 2a   Airfoil geometry for Case 1.
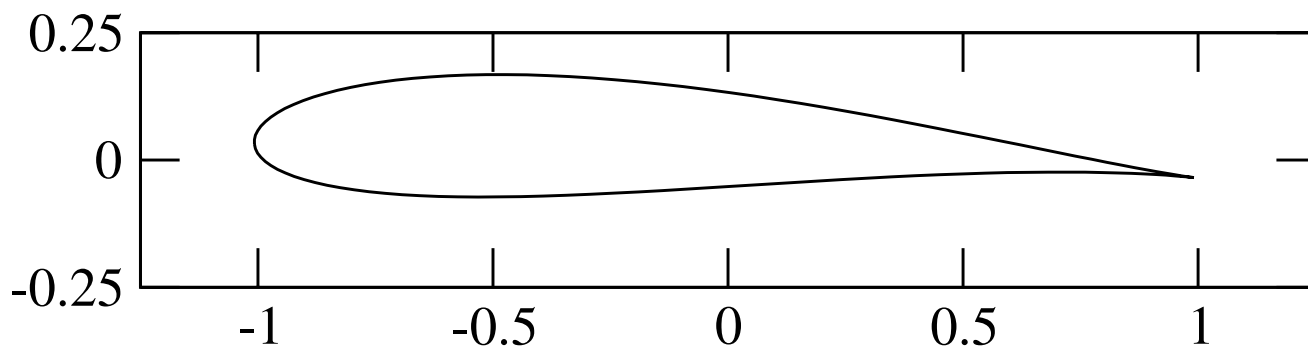
Figure 2b   Airfoil geometry for Case 2.

SOUND GENERATION BY INTERACTING WITH A GUST

PROBLEM 2—CASCADE-GUST INTERACTION

Geometry

The two-dimensional geometry, shown in Fig. 1, is the unrolled section of a realistic three-dimensional fan outlet guide vane stator. The cascade has a gap-to-chord ratio of $d/c = 2/3$ with the inflow and outflow planes located at $x_{\mp} = \mp 3/2c$. The airfoil definition is given in the accompanying ASCII file and reproduced at the end of this note.
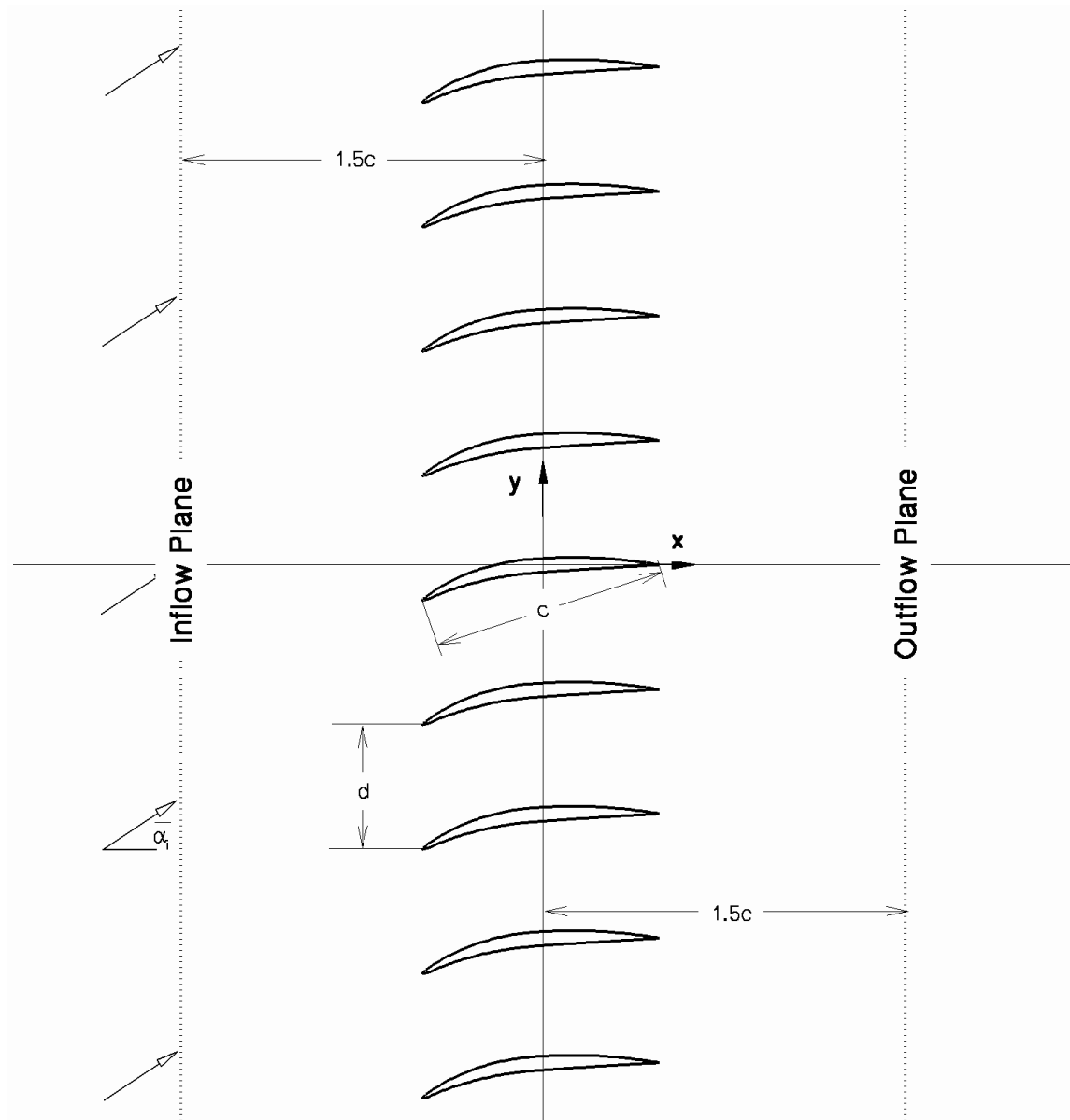
Fig. 1 - Stator Cascade Geometry

Inflow/Outflow Conditions and Gust Input

The mean (i.e., time-averaged) inflow/outflow conditions are:

$$\text{inflow conditions:} \quad \begin{cases} \overline{P}_i = 1 \\ \overline{T}_i = 1 \\ \overline{a}_i = 36° \end{cases}, \qquad \text{outflow condition:} \quad \overline{p}_o / \overline{P}_i = 0.92$$

where $\overline{P}_i$ and $\overline{T}_i$ are the normalized inflow plane mean stagnation pressure and mean stagnation temperature. $\overline{a}_i$ is the mean flow angle and $\overline{p}_o$ the normalized outflow plane mean static pressure. Assume the flow to be inviscid and isentropic throughout the domain and that the reference conditions used for normalization are $P_{\text{ref}} = 2116.8 \text{ lb}_f /\text{ft}^2$, $T_{\text{ref}} = 519 °\text{R}$.

The inflow gust (produced, say, by the wake of an upstream blade row) is given, <u>at the inflow plane</u>, by

$$\vec{u}'_g(y, t) = \left\{ a_1 \cos\left(k_y y - wt\right) + a_2 \cos\left(2\left(k_y y - wt\right)\right) + a_3 \cos\left(3\left(k_y y - wt\right)\right) \right\} \hat{e}_b$$

$$r'_g(y, t) = 0, \qquad p'_g(y, t) = 0$$

$$\hat{e}_b = \cos(b)\hat{e}_x - \sin(b)\hat{e}_y, \qquad b = 44°$$

$$w = 3p/4, \qquad k_y = 11p/9, \qquad \begin{cases} a_1 = 5 \times 10^{-3} \\ a_2 = 3 \times 10^{-3} \\ a_3 = 7 \times 10^{-4} \end{cases}$$

where w is the fundamental reduced frequency[1], k_y is the transverse wavenumber[2], and a_i's are the gust harmonic amplitudes[3].

---

[1] Frequency is normalized by the chord divided by the ambient speed of sound.
[2] Wavenumber is normalized by the vane chord.
[3] Gust harmonic amplitudes are normalized by the ambient speed of sound.

Requirements

Solve the time-dependent <u>inviscid</u> flow equations for this geometry subject to the specified inflow/outflow mean conditions and the fluctuating inflow velocity distortion.

(1)   Compute the unsteady solution until periodicity in pressure is achieved by showing that at least two successive periods are identical[4]. Periodicity must be achieved on both the airfoil surface and the inflow/outflow boundaries.

(2)   Once periodicity is achieved, compute the pressure frequency spectra on the reference airfoil on both the upper and lower surfaces at $x = (-0.25c,\ 0.00,\ +0.25c)$, on the inflow boundary at $(x, y) = \{(-1.5c,\ -0.3c),(-1.5c,\ 0.0),(-1.5c,\ 0.3c)\}$, and on the outflow boundary at $(x, y) = \{(1.5c,\ -0.3c),(1.5c,\ 0.0),(1.5c,\ 0.3c)\}$. Express the spectral results in dB using the standard definition $20\ \log\left(p_{\text{r.m.s.}} / p_{\text{ref.}}\right)$, where $p_{\text{ref.}} = 20\ m\text{Pa}$.

(3)   Extract the harmonic pressure distributions on the inflow and outflow boundaries (i.e., on $x = \mp 1.5c$ lines) at the fundamental frequency w and apply a Fourier transform in y direction to identify the spatial (i.e., mode order) structure of the pressure perturbations. Express the result in dB for each mode order. Repeat the process for the frequencies $2w$ and $3w$.

Note: The benchmark solution to this problem will be computed using a frequency-domain linearized Euler code called LINFLUX which has been extensively tested at United Technology Research Center and NASA Glenn Research Center.

Contributed by Ed Envia, <u>Edmane.Envia-1@nasa.gov</u>.

---

[4] The maximum difference between the spectra of two successive periods must be less than 1% at any of the three input frequencies.

Airfoil Section Data[5]

Suction Side		Pressure Side	
x	*y*	*x*	*y*
-0.5000000	-0.1901280	-0.5000000	-0.1901280
-0.5002920	-0.1894140	-0.4993730	-0.1905700
-0.5002540	-0.1884780	-0.4984500	-0.1907420
-0.4999420	-0.1873940	-0.4973270	-0.1906820
-0.4994300	-0.1862410	-0.4960960	-0.1904450
-0.4984710	-0.1845490	-0.4942390	-0.1899110
-0.4961960	-0.1812740	-0.4905490	-0.1884920
-0.4915950	-0.1757120	-0.4840870	-0.1854640
-0.4836860	-0.1674000	-0.4741110	-0.1801880
-0.4716500	-0.1560880	-0.4599970	-0.1722870
-0.4550310	-0.1414710	-0.4410590	-0.1619740
-0.4443170	-0.1324970	-0.4290580	-0.1557100
-0.4334350	-0.1237260	-0.4169740	-0.1496080
-0.4201140	-0.1134380	-0.4024270	-0.1425270
-0.4065630	-0.1034570	-0.3877700	-0.1356790
-0.3959670	-0.0959786	-0.3764920	-0.1306010
-0.3852400	-0.0886887	-0.3651540	-0.1256600
-0.3743860	-0.0815891	-0.3537570	-0.1208550
-0.3621360	-0.0738989	-0.3410850	-0.1156980
-0.3497360	-0.0664518	-0.3283470	-0.1107070
-0.3371910	-0.0592516	-0.3155440	-0.1058820
-0.3234920	-0.0517603	-0.3017670	-0.1009010
-0.3096350	-0.0445642	-0.2879220	-0.0961104
-0.2956260	-0.0376667	-0.2740120	-0.0915107
-0.2845230	-0.0324608	-0.2631260	-0.0880571
-0.2733330	-0.0274428	-0.2522040	-0.0847192
-0.2620600	-0.0226143	-0.2412460	-0.0814972
-0.2507070	-0.0179772	-0.2302560	-0.0783912
-0.2390860	-0.0134608	-0.2191170	-0.0753706
-0.2273890	-0.0091454	-0.2079460	-0.0724691
-0.2156200	-0.0050325	-0.1967460	-0.0696870
-0.2037810	-0.0011236	-0.1855160	-0.0670250
-0.1918560	0.0025865	-0.1742920	-0.0644907
-0.1798690	0.0060908	-0.1630430	-0.0620746
-0.1678230	0.0093899	-0.1517680	-0.0597753
-0.1557230	0.0124843	-0.1404710	-0.0575911
-0.1435580	0.0153764	-0.1291750	-0.0555260
-0.1313440	0.0180566	-0.1178570	-0.0535799
-0.1190850	0.0205178	-0.1065200	-0.0517589
-0.1067840	0.0227529	-0.0951624	-0.0500690
-0.0944786	0.0247549	-0.0837561	-0.0485073

---

[5] These coordinates are normalized by the vane chord.

−0.0821404	0.0265503	−0.0723342	−0.0470608
−0.0697762	0.0281647	−0.0609005	−0.0457072
−0.0573926	0.0296234	−0.0494585	−0.0444238
−0.0436985	0.0310812	−0.0361405	−0.0429933
−0.0299907	0.0323960	−0.0228173	−0.0416151
−0.0162715	0.0335834	−0.0094903	−0.0402770
−0.0025430	0.0346593	0.0038395	−0.0389665
0.0111930	0.0356362	0.0171762	−0.0376738
0.0249356	0.0365136	0.0305150	−0.0364027
0.0386844	0.0372880	0.0438564	−0.0351594
0.0524387	0.0379556	0.0572009	−0.0339503
0.0661944	0.0385130	0.0705583	−0.0327780
0.0799541	0.0389579	0.0839183	−0.0316348
0.0937171	0.0392878	0.0972799	−0.0305095
0.1074820	0.0395006	0.1106420	−0.0293905
0.1212460	0.0395944	0.1240260	−0.0282670
0.1350090	0.0395694	0.1374110	−0.0271416
0.1487720	0.0394264	0.1507950	−0.0260174
0.1625330	0.0391659	0.1641800	−0.0248975
0.1759700	0.0387987	0.1772820	−0.0238079
0.1894040	0.0383201	0.1903840	−0.0227245
0.2028330	0.0377299	0.2034870	−0.0216466
0.2162570	0.0370281	0.2165910	−0.0205733
0.2287510	0.0362742	0.2288210	−0.0195753
0.2412380	0.0354237	0.2410520	−0.0185808
0.2537190	0.0344771	0.2532830	−0.0175899
0.2661920	0.0334347	0.2655140	−0.0166029
0.2809030	0.0320815	0.2799840	−0.0154403
0.2956010	0.0305956	0.2944550	−0.0142832
0.3102850	0.0289773	0.3089260	−0.0131318
0.3225580	0.0275219	0.3210570	−0.0121710
0.3348200	0.0259744	0.3331870	−0.0112142
0.3470710	0.0243354	0.3453180	−0.0102617
0.3614500	0.0222929	0.3596040	−0.0091454
0.3758110	0.0201246	0.3738900	−0.0080337
0.3965670	0.0167648	0.3945990	−0.0064307
0.4101550	0.0144220	0.4081910	−0.0053863
0.4180750	0.0130020	0.4161300	−0.0047777
0.4253860	0.0116572	0.4234920	−0.0042149
0.4306480	0.0106702	0.4290990	−0.0037887
0.4434420	0.0081752	0.4422550	−0.0027922
0.4562150	0.0055715	0.4554110	−0.0017987
0.4689730	0.0028954	0.4685680	−0.0008073
0.4817240	0.0001831	0.4817240	0.0001831

SOUND TRANSMISSION AND RADIATION

PROBLEM 1—RADIATION AND REFRACTION OF SOUND WAVES THROUGH A TWO-DIMENSIONAL SHEAR LAYER

The propagation of sound in a turbulent shear flow can be described by a solution of the linearized Euler equations. The base flow is assumed to be the long-time average of the turbulent flow field. Viscous and nonlinear effects enter the problem through their influence in determining the base flow. However, the linearized Euler equations not only provide a solution for sound propagation, they also admit unstable solutions and instability waves can be triggered. In the complete physical problem, these instabilities contribute to the turbulence and are limited and modified by nonlinear and viscous effects. In that sense they are non-physical solutions, if the actual problem to be solved is for sound propagation in a turbulent sheared flow. It should be remembered that the inhomogeneous linearized Euler equations only represent a mathematical model of part of the complete physical problem.

The purpose of this benchmark problem is to find ways to suppress the non-physical instabilities but to retain that part of the solution associated with the sound propagation.

The problem to be solved is very similar to the Category 5 problem at the Third Computational Aeroacoustics Workshop on Benchmark Problems: "Generation and Radiation of Acoustic Waves From a 2D Shear Layer." The operating conditions have been changed and, in the present problem, **the required solution should only consist of the acoustic part of the solution: not the instability wave that is generated**. The problem consists of an energy source inside a two-dimensional jet that generates an acoustic wave that is refracted as it moves through the jet shear layer. The benchmark problem requires the solution of the two-dimensional linearized Euler equations to calculate the fluctuations associated with only the sound radiation and refraction through the jet. The locations of the required output data and its format are given below. The numerical solutions will be evaluated by comparison with an exact analytical solution.

The linearized Euler equation for a parallel jet can be written as

$$L\left(\frac{\partial}{\partial \boldsymbol{x}}, \frac{\partial}{\partial t}, \boldsymbol{x}\right) \boldsymbol{U}(\boldsymbol{x}, t) = \boldsymbol{S}(\boldsymbol{x}) \cos(\omega_o t), \tag{1}$$

where

$$
L = \begin{bmatrix} \boxdot & \bar{\rho}(y)\frac{\partial}{\partial x} & \frac{\partial \bar{\rho}(y)}{\partial y} + \bar{\rho}(y)\frac{\partial}{\partial y} & 0 \\ 0 & \boxdot & \frac{\partial \bar{u}(y)}{\partial y} & \frac{1}{\bar{\rho}(y)}\frac{\partial}{\partial x} \\ 0 & 0 & \boxdot & \frac{1}{\bar{\rho}(y)}\frac{\partial}{\partial y} \\ 0 & \gamma \bar{p}\frac{\partial}{\partial x} & \gamma \bar{p}\frac{\partial}{\partial y} & \boxdot \end{bmatrix}, \quad \boldsymbol{U} = \left\{ \begin{array}{c} \rho \\ u \\ v \\ p \end{array} \right\}, \quad \boldsymbol{S} = \left\{ \begin{array}{c} 0 \\ 0 \\ 0 \\ \Lambda(\boldsymbol{x}) \end{array} \right\}, \quad (2)
$$

$$
\boxdot = \tfrac{\partial}{\partial t} + \bar{u}(y)\tfrac{\partial}{\partial x} \quad , \quad \Lambda(\boldsymbol{x}) = A \exp[-(B_x x^2 + B_y y^2)]
$$

The mean flow variables are denoted by an overbar and are given by

$$
\bar{u}(y) = \left\{ \begin{array}{ll} u_j \exp[-(\ln 2)(y/b - h/b)^2] & y \geq h \\ u_j & 0 \leq y \leq h \end{array} \right. \tag{3}
$$

$$
\frac{1}{\bar{\rho}(y)} = -\frac{1}{2}\frac{\gamma-1}{\gamma\bar{p}}(\bar{u}(y) - u_j)\bar{u}(y) + \frac{1}{\rho_j}\frac{\bar{u}(y)}{u_j} + \frac{1}{\rho_\infty}\frac{u_j - \bar{u}(y)}{u_j} \tag{4}
$$

$$
\bar{p} = \text{constant} = 103330 \text{ m}^{-1} \text{ kg s}^{-2} \tag{5}
$$

The parameters for the problem are given in the Table. $M_j = u_j/a_j$, $a_j = (\gamma R T_j)^{1/2}$.

M_j	T_j K	T_∞ K	R m²s⁻²K⁻¹	γ	h m	b m	A kgm⁻¹s⁻³	B_x m⁻²	B_y m⁻²
0.756	600	300	287.0	1.4	0.0	1.3	0.001	0.04 ln(2)	0.32 ln(2)

The source frequency $\omega_o = 76$ rad/s. Note that this source frequency generates an instability wave that can overwhelm the acoustic solution. Therefore, the numerical scheme must filter out the instability wave.

The physical domain Ω is a rectangle with dimensions $\Omega = [-50, 150] \times [0, 50]$. A symmetry boundary condition should be used along the x-axis.

Calculate p at the start of a cycle and $\bar{p^2}$ along:

1. $y = 15$, $\quad -50 \leq x \leq 150$

2. $y = 50$, $\quad -50 \leq x \leq 150$

3. $x = 100$, $\quad 5 \leq y \leq 50$

Output data in ASCII text format with three columns: x, y, and p or $\bar{p^2}$. Specify the grid layout, memory used, CPU time, and the computational scheme (including the boundary conditions) used for the numerical simulation.

Contributed by Philip J. Morris and Anurag Agarwal, email: pjm@psu.edu

PROBLEM 2—TRAILING EDGE NOISE PROBLEM

Consider a two-dimensional, compressible mixing layer flow formed by a splitter plate with a blunt trailing edge. The lower stream has free stream Mach number $M_1 = 0.6$ with a boundary layer momentum thickness θ_1^* at $x^* = x_1^*$, while the upper stream has free stream Mach number $M_2 = 0.1$ with momentum thickness $\theta_2^* = \theta_1^*$ at $x^* = x_1^*$. The splitter plate has width $w^* = 2\theta_1^*$ with a shape consisting of a flat plate section capped by a super-ellipse at the trailing edge. With all lengths nondimensionalized by θ_1^*, the definition of the splitter plate surface is:

$$\left(\frac{2y}{w}\right)^2 + \left(1 + \frac{x}{\mathrm{AR}}\right)^m = 1 \quad , \qquad -AR \le x \le 0 \tag{1}$$

$$y = \pm\frac{w}{2} \quad , \qquad x < -AR \tag{2}$$

with aspect ratio $\mathrm{AR} = 2.5$ and order $m = 6$. The Reynolds number based on the lower free stream properties is $Re_{\theta_1^*} = \frac{\rho_1^* u_1^* \theta_1^*}{\mu_1^*} = 250$, and the Prandtl number is $Pr = 0.7$. The governing equations are the two-dimensional Navier-Stokes equations:

$$\frac{\partial \mathbf{U}}{\partial t} + \frac{\partial \mathbf{F}}{\partial x} + \frac{\partial \mathbf{G}}{\partial y} = \frac{\partial \mathbf{V}_x}{\partial x} + \frac{\partial \mathbf{V}_y}{\partial y} \tag{3a}$$

$$\mathbf{U} = \begin{bmatrix} \rho \\ \rho u \\ \rho v \\ \rho E \end{bmatrix} \quad \mathbf{F} = \begin{bmatrix} \rho u \\ \rho u^2 + p \\ \rho uv \\ u(p + \rho E) \end{bmatrix} \quad \mathbf{G} = \begin{bmatrix} \rho v \\ \rho uv \\ \rho v^2 + p \\ v(p + \rho E) \end{bmatrix} \tag{3b}$$

$$\mathbf{V}_x = \frac{M_1}{Re_{\theta_1^*}} \begin{bmatrix} 0 \\ \tau_{xx} \\ \tau_{xy} \\ u\tau_{xx} + v\tau_{xy} - \frac{1}{Pr}q_x \end{bmatrix} \quad \mathbf{V}_y = \frac{M_1}{Re_{\theta_1^*}} \begin{bmatrix} 0 \\ \tau_{xy} \\ \tau_{yy} \\ u\tau_{xy} + v\tau_{yy} - \frac{1}{Pr}q_y \end{bmatrix} \tag{3c}$$

$$E = \frac{1}{\gamma}T + \frac{1}{2}\left(u^2 + v^2\right) \tag{3d}$$

where ρ is the density, u, v are the velocity components, p is the pressure, T is the temperature, E is the total energy per unit mass, τ is the viscous stress tensor, q is the heat flux vector, and $\gamma = \frac{C_p}{C_v} = 1.4$ is the ratio of specific heats. All variables are non-dimensionalized using reference length θ_1^* and the following lower free stream dimensional quantities: speed of sound $c_1^* = \sqrt{(\gamma - 1)C_v T^*}$, time θ_1^*/c_1^*, density ρ_1^*, pressure $\rho_1^* c_1^{*^2}$, temperature $(\gamma - 1)T_1^*$, and viscosity μ_1^*. The following constitutive relations close the system

$$p = \frac{\gamma - 1}{\gamma}\rho T \tag{4a}$$

$$q_x = -k\frac{\partial T}{\partial x} \qquad q_y = -k\frac{\partial T}{\partial y} \tag{4b}$$

$$\tau_{xx} = \mu\left(\frac{4}{3}\frac{\partial u}{\partial x} - \frac{2}{3}\frac{\partial v}{\partial y}\right) \quad \tau_{xy} = \mu\left(\frac{\partial u}{\partial y} + \frac{\partial v}{\partial x}\right) \quad \tau_{yy} = \frac{4}{3}\frac{\partial v}{\partial y} - \frac{2}{3}\frac{\partial u}{\partial x} \tag{4c}$$

$$\mu = k = ([\gamma - 1]T)^{0.7} \tag{4d}$$

Steady State Solution

First find a steady, laminar solution to (3) for the given geometry and flow conditions. The rectangular solution domain is given by $-50 \le x \le 100$, $-100 \le y \le 100$, with the trailing edge of the splitter plate at the origin. The flow state at the inflow boundary at $x_1 = -50$ is approximated above and below the plate by

solutions to the compressible boundary layer equations with zero pressure gradient. Free stream conditions above the plate are $T_2 = T_1$ and $\rho_2 = \rho_1$. Boundary conditions on the plate surface are the no slip condition $u = v = 0$ and the isothermal condition $T_{wall} = T_1$. The steady solution is denoted $\bar{\mathbf{U}} = [\bar{\rho} \;\; \bar{\rho}\bar{u} \;\; \bar{\rho}\bar{v} \;\; \bar{\rho}\bar{E}]^T$. Plot streamwise velocity profiles of $\bar{u}(y)$ at $x = 5$, $x = 40$, and $x = 75$, so that mean mixing layer solutions may be compared.

Problem 1

Once the steady solution is obtained, solve the initial value problem of a pressure pulse superimposed on the steady flow, with initial condition

$$\mathbf{U}(x,y,0) = \bar{\mathbf{U}}(x,y) + 0.05 \begin{bmatrix} 0 \\ 0 \\ 0 \\ \frac{f(x,y)}{\gamma-1} \end{bmatrix}, \qquad f(x,y) = e^{-\ln 2\left(\left[\frac{x+20}{4}\right]^2 + \left[\frac{y+20}{4}\right]^2\right)} \tag{5}$$

where $\bar{\mathbf{U}}$ is the steady solution. The unsteady calculation is performed on the same domain as the steady calculation over the time period $0 \le t \le 1200$. Give the disturbance pressure $p' = p - \bar{p}$ along the line $y = -3$ at times $t = 200, 400, \ldots, 1200$. Give the data at 401 points equally spaced along the interval $-50 \le x \le 150$. Also give the disturbance pressure time history for $0 \le t \le 1200$ at $(x,y) = (-30,1)$ and at $(x,y) = (50,50)$. Give data in time increments of $\Delta t = 0.5$. Each data set should contain t, x, y, p' and be saved in `FORMAT(4(1X,E15.6))`.

Problem 2

Solve the initial value problem where a "vortex" is initiated upstream of the trailing edge below the splitter plate. The initial condition is given by:

$$\begin{bmatrix} \rho \\ u \\ v \\ p \end{bmatrix}(x,y,0) = \begin{bmatrix} \bar{\rho} \\ \bar{u} \\ \bar{v} \\ \bar{p} \end{bmatrix}(x,y) + \begin{bmatrix} \left(1 - \frac{\gamma-1}{2}M_v^2\exp\left(1 - \left[\frac{r}{\sigma}\right]^2\right)\right)^{\frac{1}{\gamma-1}} - 1 \\ -M_v(y-y_0)\exp\left(\frac{1-\left[\frac{r}{\sigma}\right]^2}{2}\right) \\ M_v(x-x_0)\exp\left(\frac{1-\left[\frac{r}{\sigma}\right]^2}{2}\right) \\ \frac{1}{\gamma}\left(\left[1 - \frac{\gamma-1}{2}M_v^2\exp\left(1 - \left[\frac{r}{\sigma}\right]^2\right)\right]^{\frac{\gamma}{\gamma-1}} - 1\right) \end{bmatrix} \tag{6}$$

where $(x_0,y_0) = (-35,-8)$, $M_v = 0.1$, $\sigma = 1$, and $r = \sqrt{(x-x_0)^2 + (y-y_0)^2}$. Find the solution for $0 \le t \le 1200$, and give the same data as for Problem 1.
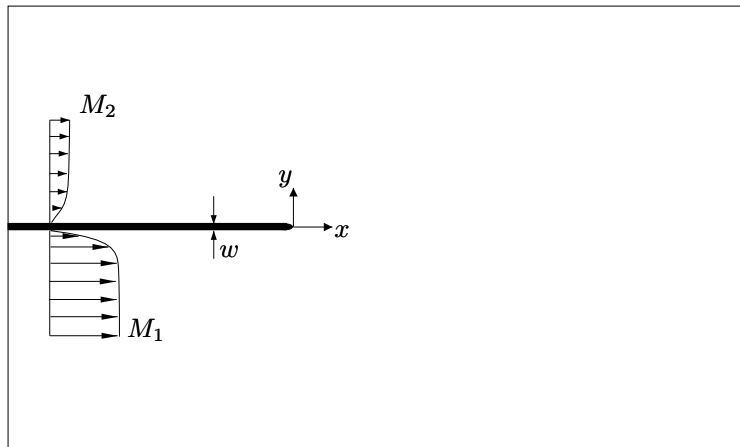
$x = x_1$

Contributed by Sanjiva Lele and Matt Barone, email: `lele@stanford.edu`.

SOUND GENERATION IN VISCOUS PROBLEMS

PROBLEM 1—AEOLIAN TONE GENERATION FROM TWO CYLINDERS

Aeolian tones, sound generation by flow over cylinders, are relevant to airframe and power plant noise (heat exchanger, power transmission lines and chimneys). The purpose of this problem is to test the ability of a CFD/CAA code to accurately predict sound generation by viscous flows and sound propagation through interactions between acoustic wave & solid wall and between acoustic waves & shear layers.

Consider the cylinder configuration shown in Figure 1. The Reynolds number $Re_\infty = 1.58 \times 10^4$ based on inflow velocity $U_\infty = 24.5$ m/s and cylinder diameter D = 0.955 cm are imposed on the computation. It is known that the streets of regularly spaced vortices exist with laminar cores over the range of Reynolds numbers from 65 to approximately 400. The range of Reynolds numbers above which vortices with turbulent cores are shed periodically extends to approximately 2×10^5. The governing equations are the 2-D Navier-Stokes Equations. We are interested in the acoustic waves emitted from unit span.

1) Calculate the Strouhal No. of vortex shedding from two cylinders.

2) In the far field, calculate the intensity $\overline{(p')^2}$ on the circle $x^2+y^2 = (100D)^2$ at $\Delta\theta = 3°$, θ measured from the x-axis.

3) In the near field, compute the intensity $\overline{(p')^2}$ on the circle $x^2+y^2 = (10D)^2$ at $\Delta\theta = 1°$, θ measured from the x-axis.
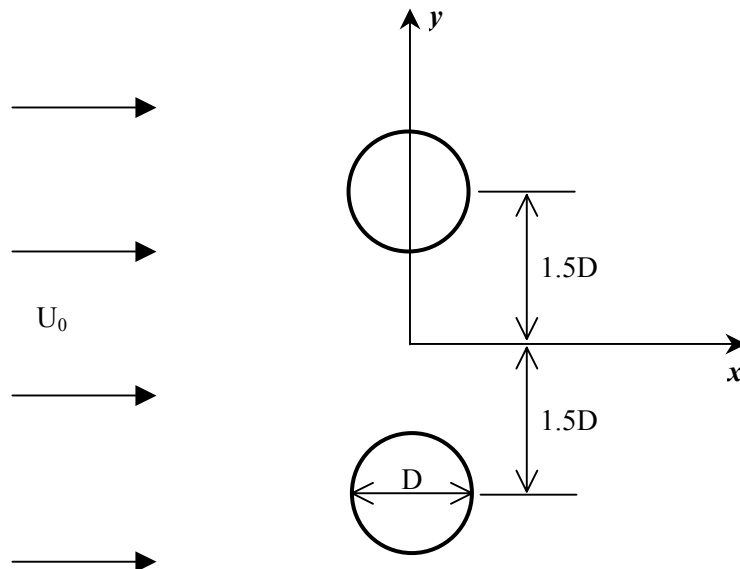
Figure 1

Contributed by Professor Soogab Lee : Email: solee@plaza.snu.ac.kr

PROBLEM 2—SOUND GENERATION BY FLOW OVER A CAVITY

Air flows over the cavity shown below with a mean approach flow velocity of 50 m/s. The boundary layer that develops over the flat plate is turbulent with a thickness of 14 mm at the entrance to the cavity. Calculate the power spectra at the center of each cavity wall and the center of the cavity floor. Experimental data will be available for comparison.
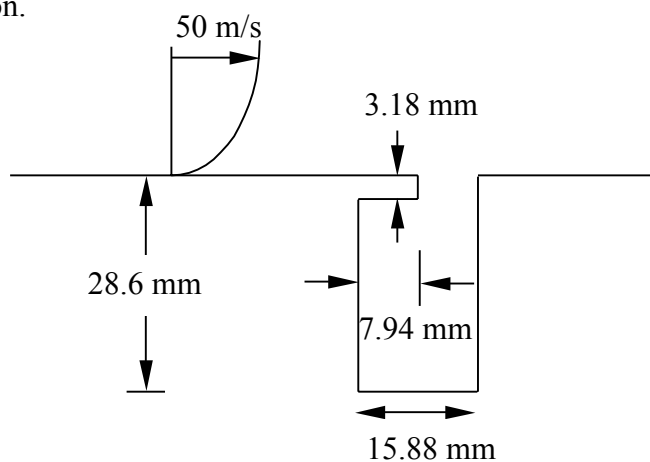
Contributed by Brenda Henderson, email : b.s.henderson@larc.nasa.gov

Analytical Solutions

ALIASING PROBLEM: CATEGORY 1, PROBLEM 1
ANALYTICAL SOLUTION

Christopher K.W. Tam
Department of Mathematics
Florida State University
Tallahassee, FL 32306-4510, USA
`tam@math.fsu.edu`

The exact analytical solution of the convective wave equation,

$$\frac{\partial u}{\partial t} + \frac{\partial u}{\partial x} = 0 \tag{1}$$

satisfying initial condition $t = 0$

$$u = (2 + \cos \alpha x) \exp\left[-(\ln 2)\left(\frac{x}{10}\right)^2\right] \tag{2}$$

is

$$u(x,t) = [2 + \cos \alpha(x-t)] \exp\left[-(\ln 2)\left(\frac{x-t}{10}\right)^2\right] \tag{3}$$

However, for $\Delta x = 1$ and $\alpha = 4.6 > \pi$ (case (b)) (3) is not the exact computational solution. Because α is larger than π, the solution is subjected to aliasing. In solving the above initial value problem, the computer code has, first, to sample the initial condition (2). For $\alpha > \pi$; i.e., waves with wavelength less than two mesh spacing, which is the Nyquist limit, the sampled initial condition is aliased into a wave with wavenumber $(\alpha - 2\pi)$. Thus the exact computational solution for case (b) is

$$u(x,t) = [2 + \cos[(2\pi - \alpha)(x-t)]] \exp\left[-(\ln 2)\left(\frac{x-t}{10}\right)^2\right] \tag{4}$$

To understand the origin of aliasing, let us assume that the mesh size is Δx and that the initial condition at $t = 0$ is

$$u = f(x) = e^{-(\ln 2)\left(\frac{x}{b}\right)^2 + i\alpha_0 x} \tag{5}$$

where $\alpha_0 \Delta x$ is larger than π but less than 2π so that the initial data represents ultra short waves located outside the fundamental resolved wavenumber range of $-\pi \le \alpha \Delta x \le \pi$. Note that the real part of (5) is the oscillatory part of (4). Let ℓ (integer) be the index of the mesh points. On the mesh we have,

$$x = \ell \Delta x$$

and the initial condition (5) is

$$f(\ell) = e^{-(\ln 2)\left(\frac{\ell\Delta x}{b}\right)^2 + i\alpha_0 \Delta x \ell}. \tag{6}$$

Since $\alpha \Delta x > \pi$, we may write

$$\alpha_0 \Delta x = \pi + \delta. \tag{7}$$

But $e^{i\alpha_0 \Delta x \ell} = e^{i[2\pi + (\delta - \pi)]\ell} = e^{i(\delta - \pi)\ell}$. Therefore initial condition (6) becomes, on the mesh

$$f(\ell) = e^{-(\ln 2)\left(\frac{\ell \Delta x}{b}\right)^2 + i(\delta - \pi)\ell}. \tag{8}$$

In terms of continuous variable x, the initial condition is

$$f(x) = e^{-(\ln 2)\left(\frac{x}{b}\right)^2 + i\left(\frac{\delta - \pi}{\Delta x}\right)x}. \tag{9}$$

The oscillatory part of (9) represents a wave with wave number

$$\alpha = \frac{\delta - \pi}{\Delta x} = \left(\alpha_0 - \frac{2\pi}{\Delta x}\right).$$

Now the aliased wave lies within the resolved wave number range.

INTERFACE TRANSMISSION PROBLEM: CATEGORY 1, PROBLEM 2
ANALYTICAL SOLUTION

Christopher K.W. Tam
Department of Mathematics
Florida State University
Tallahassee, FL 32306-4510, USA
`tam@math.fsu.edu`

The incident wave is given as

$$\begin{bmatrix} u_1 \\ v_1 \\ p_1 \end{bmatrix}_{\text{incident}} = \text{Re}\left\{ \begin{bmatrix} -\sin\theta \\ -\cos\theta \\ 1 \end{bmatrix} e^{-i\omega(\sin\theta x + \cos\theta y + t)} \right\}. \tag{1}$$

This is a solution of the governing equations in fluid 1.

$$\frac{\partial u_1}{\partial t} = -\frac{\partial p_1}{\partial x}$$

$$\frac{\partial v_1}{\partial t} = -\frac{\partial p_1}{\partial y} \tag{2}$$

$$\frac{\partial p_1}{\partial t} + \left(\frac{\partial u_1}{\partial x} + \frac{\partial v_1}{\partial y} \right) = 0$$

The reflected wave must have the same x and t dependence as the incident wave. It is easy to find that the appropriate outgoing reflected wave solution of (2) is,

$$\begin{bmatrix} u_1 \\ v_1 \\ p_1 \end{bmatrix}_{\text{reflected}} = Re\left\{ R \begin{bmatrix} -\sin\theta \\ \cos\theta \\ 1 \end{bmatrix} e^{-i\omega(\sin\theta x - \cos\theta y + t)} \right\}. \tag{3}$$

where R is the unknown amplitude.

The transmitted wave satisfies the governing equations in the region occupied by fluid 2. The governing equations are,

$$\alpha \frac{\partial u_2}{\partial t} = -\frac{\partial p_2}{\partial x}$$

$$\alpha \frac{\partial v_2}{\partial t} = -\frac{\partial p_2}{\partial y} \tag{4}$$

$$\frac{\partial p_2}{\partial t} + \lambda \left(\frac{\partial u_2}{\partial x} + \frac{\partial v_2}{\partial y} \right) = 0$$

The transmitted wave must also have the same x and t dependence as the incident wave. Thus, let

$$\begin{bmatrix} u_1 \\ v_1 \\ p_1 \end{bmatrix}_{\text{transmitted}} = \text{Re}\left\{ \begin{bmatrix} \hat{u}(y) \\ \hat{v}(y) \\ \hat{p}(y) \end{bmatrix} e^{-i\omega(\sin\theta x + t)} \right\}. \tag{5}$$

Substitution of (5) into (4), it is easy to find upon eliminating $\hat{u}$ and $\hat{v}$ a single equation for $\hat{p}$

$$\frac{d^2\hat{p}}{dy^2} + \omega^2\left(\alpha - \sin^2\theta\right)\hat{p} = 0 \tag{6}$$

The outgoing wave solution is,

$$\hat{p} = e^{-i\omega\left(\alpha - \sin^2\theta\right)^{1/2} y} \tag{7}$$

On finding $\hat{u}$ and $\hat{v}$ from the governing equations, it is straightforward to determine that the transmitted wave is,

$$\begin{bmatrix} u_2 \\ v_2 \\ p_2 \end{bmatrix}_{\text{transmitted}} = \text{Re}\left\{ T \begin{bmatrix} -\sin\theta/\alpha \\ -\left(\alpha - \sin^2\theta\right)^{1/2}/\alpha \\ 1 \end{bmatrix} e^{-i\omega\left[\sin\theta x + \left(\alpha - \sin^2\theta\right)^{1/2} y + t\right]} \right\}. \tag{8}$$

where T is the unknown wave amplitude.

The wave amplitudes of the reflected and transmitted waves are found by imposing the dynamic and kinematic boundary conditions at the fluid interface, namely,

$$p_1 = p_2, \qquad v_1 = v_2 \tag{9}$$

(9) leads to the following relations

$$1 + R = T \tag{10}$$

$$-\cos\theta + R\cos\theta = -\frac{T}{\alpha}\left(\alpha - \sin^2\theta\right)^{1/2} \tag{11}$$

On solving (10) and (11) for T and R, it is found

$$T = \frac{2\cos\theta}{\cos\theta + \dfrac{1}{\alpha}\left(\alpha - \sin^2\theta\right)^{1/2}} \tag{12}$$

$$R = T - 1 \tag{13}$$

Of interest to the present problem is when the incident angle is large so that $\sin^2\theta > \alpha$. In this case, T is no longer real suggesting that there is no transmitted wave or the incident wave is totally reflected at the interface. This is true for $\alpha = 0.694$ and $\theta = 65°$, which is one of the cases prescribed in this benchmark problem.

Exact Solutions to Category 1 Problem 3

Thomas Hagstrom[1] **and Igor Nazarov**
Dept. of Mathematics and Statistics
The University of New Mexico, Albuquerque, NM 87131
email: hagstrom@math.unm.edu, FAX: (505) 277-5505.

The goal of this problem was to provide a detailed study of the accuracy of boundary treatments with a range of incidence angles including shear and a sonic point.

There are three parts. In each we solve the linearized Euler equations on a prescibed domain: $(-2, 2) \times (0, 1)$ with initial conditions consisting of a pressure dipole, entropy and vorticity disturbances. Here $x_1 = \pm 2$ are the artificial boundaries, the speed of sound is scaled to 1, and we solve up to $t = 64$.

PART 1

For part 1 the base flow is a uniform subsonic flow skew to the boundaries:

$$U_1 = 0.3, \quad U_2 = 0.4. \tag{1}$$

In addition, periodic boundary conditions are prescribed x_2.

The exact solution is given by the following formulas:

$$p = P(x_1 - U_1 t, x_2 - U_2 t, t), \quad \rho = D(x_1 - U_1 t, x_2 - U_2 t, t),$$
$$u = U(x_1 - U_1 t, x_2 - U_2 t, t), \quad v = V(x_1 - U_1 t, x_2 - U_2 t, t),$$

where

$$P(x_1, x_2, t) = \sum_{i=1}^{2} B_i \sum_{k=-\infty}^{\infty} \int_{-\infty}^{t-r_{ik}} \frac{e^{-\mu_i (s - \tau_i)^2}}{\sqrt{(t-s)^2 - r_{ik}^2}} ds,$$

$$D(x_1, x_2, t) = P(x_1, x_2, t) + S \sum_{k=-\infty}^{\infty} e^{-\mu_S r_{Sk}^2},$$

$$U(x_1, x_2, t) = - \int_0^t \frac{\partial P}{\partial x_1} (x_1, x_2, s) ds + U_0(x_1, x_2),$$

$$V(x_1, x_2, t) = - \int_0^t \frac{\partial P}{\partial x_2} (x_1, x_2, s) ds + V_0(x_1, x_2),$$

$$U_0(x_1, x_2) = f_1(x_1) \int_{-2}^{2} \frac{\partial P}{\partial t} (z, x_2, 0) dz - \int_{-2}^{x_1} \frac{\partial P}{\partial t} (z, x_2, 0) dz,$$

$$V_0(x_1, x_2) = -f_1'(x_1) \int_0^{x_2} \int_{-2}^{2} \frac{\partial P}{\partial t} (z, w, 0) dz dw.$$

and

$$r_{ik}^2 = (x_1 - x_{1,i})^2 + (x_2 - x_{2,ik})^2,$$

$$r_{Sk}^2 = (x_1 - x_{1,S})^2 + (x_2 - x_{2,Sk})^2,$$

$$f_1(x_1) = \begin{cases} 0, & x_1 < -1.9 \\ 1 - e^{-((x_1+1.9)/2.5)^8}, & |x_1| \le 1.9 \\ 1, & x_1 > 1.9. \end{cases}$$

The parameters B_i, μ_i, $x_{1,i}$, $x_{2,ik}$, S, μ_S, $x_{1,S}$, $x_{2,Sk}$ are chosen so that, to a high degree of accuracy (11 digits), the initial data is supported on $(-2, 2)$ and the boundary conditions are satisfied. The integrals are evaluated using a combination of Gaussian quadrature and endpoint corrected trapezoid rules, again to high accuracy. The infinite sums are truncated after the point where their contributions are below machine precision. We also note that the jump in f_1 is approximately 4×10^{-13}.

Precisely we chose a dipole-like initial configuration for the pressure pulse:

$$\tau_1 = \tau_2 = -.95, \quad \mu_1 = \mu_2 = 30, \quad B_2 = -B_1 = 1,$$

$$x_{1,1} = -x_{1,2} = 0.1, \quad x_{2,10} = x_{2,20} = 1/2.$$

and for the entropy pulse:

$$\mu_S = 12, \quad S = 1, \quad x_{1,S} = 0, \quad x_{2,S0} = 1/2.$$

To guarantee periodicity we have:

$$x_{2,ik}, x_{2,Sk} = \frac{1}{2} + k, \quad -\infty < k < \infty.$$

We note that similar solutions have been used to test boundary conditions for the linearized Euler equations in [2] and for the scalar wave equation in [1].

PARTS 2 AND 3

In part 2 the base flow is given by the subsonic Couette flow:

$$U_1 = Mx_2, \quad M = 0.9, \quad U_2 = 0, \tag{2}$$

and in part 3 by the transonic Couette flow:

$$U_1 = Mx_2, \quad M = 1.2, \quad U_2 = 0. \tag{3}$$

For these problems we replace the periodic boundary conditions by the wall boundary condition, $v = 0$. The initial conditions are defined by the same functions and parameters as part 1 except that the image source locations $x_{2,ik}$ are determined to guarantee compatibility with the wall conditions. For $k \ge 0$:

$$x_{2,i,k+1} = 2 - x_{2,i,-k}, \quad x_{2,i,-(k+1)} = -x_{2,ik},$$

$$x_{2,S,k+1} = 2 - x_{2,S,-k}, \quad x_{2,S,-(k+1)} = -x_{2,Sk}.$$

In this case we don't have a code which evaluates an exact solution. Instead we use a well-resolved numerical solution on a sufficiently long domain to eliminate the influence of the boundaries. Tha basic numerical scheme is identical to the one we used to solve these and other benchmark problems, and is described in more detail elsewhere in the proceedings. In time we use a standard 4th order Runge-Kutta method with time step $dt = 1/2000$: $128,000$ steps for the entire solution. Space derivatives are calculated using an 8th order difference scheme on a square grid with an extra point near the boundaries (added for stability). Thus the mesh in the domain $[-L, L] \times [0, 1]$ has $(nx + 3) * (ny + 3)$ points ($nx = 128 * 2 * L$, $ny = 128$; $h_x = h_y = 1/128$)

The length of the domain is chosen so that reflection from the left and right boundaries causing possible errors would not come before time $t = 64.0$

$$\frac{L-2}{M+1} + (L-2) > 64.0$$

Hence, $L = 44$ for Problem 2 ($M = .9$), and $L = 47$ for Problem 3 ($M = 1.2$). We note that this required $385,120$ points in the transonic case. We have not fully assessed the accuracy of this solution, but preliminary comparisons with coarser mesh solutions suggests that it is accurate to more than three digits.

References

[1] B. Alpert, L. Greengard, and T. Hagstrom. Nonreflecting boundary conditions for the time-dependent wave equation. *J. Comput. Phys.*, 180:270–296, 2002.

[2] T. Hagstrom and J. Goodrich. Accurate radiation boundary conditions for the linearized Euler equations in Cartesian domains. *SIAM J. Sci. Comput.*, 24:770–795, 2002.

ACOUSTIC SCATTERING FROM MULTIPLE CIRCULAR CYLINDERS: CATEGORY 2, PROBLEMS 1 AND 2, ANALYTIC SOLUTION

Scott E. Sherer
Computational Sciences Center of Excellence
Air Vehicles Directorate, Air Force Research Laboratory
2210 Eighth Street
Wright-Patterson AFB, OH 45433-7510

INTRODUCTION

The main goal of this benchmark problem set is to assess the ability of computational algorithms to simulate the aeroacoustic phenomenon of linear scattering with increasingly complex geometries. These algorithms may include advanced high-order methods being extended to handle complex grid topologies, or mature structured and unstructured approaches developed for intricate geometries that are either low-order or are being adapted to incorporate high-order algorithms. For the problems considered here, the complex geometry does not arise from the shape of the bodies, which are simple circular cylinders, but by the presence of multiple bodies in the computational domain. This problem also provides a test of numerical robustness, long-time stability, and suitability of far-field radiation boundary conditions for more realistic problems. The solution presented here is discussed in more detail in Ref. 1, which is an extension of the single-scattering solution of Ref. 2. These references should be consulted for more detail on the solution methodology.

ANALYTIC SOLUTION

Because of the small amplitudes of the acoustic waves, linear scattering is assumed. The governing equations are given by the linearized Euler equations

$$\frac{\partial \rho}{\partial t} + \frac{\partial u}{\partial x} + \frac{\partial v}{\partial y} = 0 \tag{1}$$

$$\frac{\partial u}{\partial t} + \frac{\partial p}{\partial x} = 0 \tag{2}$$

$$\frac{\partial v}{\partial t} + \frac{\partial p}{\partial y} = 0 \tag{3}$$

$$\frac{\partial p}{\partial t} + \frac{\partial u}{\partial x} + \frac{\partial v}{\partial y} = S \tag{4}$$

The term on the right-hand side of the energy equation (Eq. 4) represents the spatially-distributed, time-periodic, acoustic source present in the domain, and is specified in the problem statement as

$$S = \exp\left[\frac{-\ln 2\left(x^2 + y^2\right)}{b^2}\right]\sin(\omega t) \tag{5}$$

where $b = 0.2, \omega = 8\pi$.

Decoupling the pressure from the velocity components in Eqs. 2 through 4 above and assuming a time-periodic pressure distribution results in the governing partial differential equation for the spatially varying pressure field $\tilde{p}$ to be given by the nonhomogeneous Helmholtz equation,

$$\nabla^2 \tilde{p} + \omega^2 \tilde{p} = -i\omega \exp\left[\frac{-\ln 2\left(x^2 + y^2\right)}{b^2}\right] \tag{6}$$

Because of the linear nature of the problem, the principle of superposition can be used to write the spatially varying pressure field as the sum of the incident pressure and the scattered field from each of the M cylinders in the collection,

$$\tilde{p} = p^{inc} + \sum_{i=1}^{M} p_i^s \qquad (7)$$

The scattered fields then each independently satisfy the homogeneous Helmholtz equation

$$\nabla^2 p_i^s + \omega^2 p_i^s = 0 \qquad i = 1, 2, \ldots M \qquad (8)$$

and the incident field satisfies the nonhomogeneous Helmholtz equation,

$$\nabla^2 p^{inc} + \omega^2 p^{inc} = -i\omega \exp\left[-\ln 2 \frac{R^2}{b^2}\right] \qquad (9)$$

where $R^2 = x^2 + y^2$ is the distance from the center of the source to some point in the domain. The rigid-body boundary condition $\vec{v} \cdot \vec{n} = 0$, applicable on the surface of each cylinder, may also be expressed in terms of pressure and decomposed using Eq. 7 to yield the set of equations

$$\sum_{i=1}^{M} \frac{\partial p_i^s}{\partial r_j}\bigg|_{r_j = a_j} = -\frac{\partial p^{inc}}{\partial r_j}\bigg|_{r_j = a_j} \qquad j = 1, 2, \ldots M \qquad (10)$$

where r_j is the radial distance from the center of each cylinder and a_j is the radius of each cylinder.

The incident pressure distribution was found by Morris (Ref. 2) using a Hankel transform method to solve Eq. 9, and may be expressed in the polar coordinate system of the axisymmetric source given in Eq. 5 as

$$p^{inc}(R) = \frac{i\omega b^2}{2\ln 2} \int_0^\infty \frac{s J_0(sR)}{(s^2 - \omega^2)} \exp\left[-\frac{b^2 s^2}{4\ln 2}\right] ds \qquad (11)$$

To find the scattered pressure distribution, Equation 8 may be solved through a straightforward separation of variables technique for each of the cylinders. Written in the local (r_i, θ_i)-coordinate system, the scattered field generated by cylinder i is given by

$$p_i^s(r_i, \theta_i) = A_{0i} H_0(\omega r_i) + \sum_{n=1}^\infty H_n(\omega r_i)[A_{ni}\cos(n\theta_i) + B_{ni}\sin(n\theta_i)] \quad i = 1, 2, \ldots M \qquad (12)$$

where H_n is the Hankel function of the first kind of order n, and A_{ni} and B_{ni} are unknown coefficients.

The unknown scattering coefficients in Eq. 12 may be found through the application of the M boundary conditions given in Eq. 10. This is done by first applying a generalized form of Graf's addition theorem (Ref. 3), which allows for the incident field of Eq. 11 and the scattered fields of Eq. 12 to be written in terms of the local coordinate system of cylinder j. The transformed equations are then differentiated with respect to r_j and the M boundary conditions of Eq. 10 are applied. The resulting expressions consist of infinite summations on both sides of the equalities, with each term possessing a factor of $\cos(m\theta_j)$ or $\sin(m\theta_j)$ arising from the addition theorem (m is the dummy summation index variable). Equating like factors across the equality on a term-by-term basis and truncating the infinite series at some finite value N results in a system of $M \cdot (2N+1)$ equations for the equal number of unknown scattering coefficients. This linear system of equations may be written as

$$\tilde{Z}\vec{x} = \vec{b} \qquad (13)$$

where the matrix $\tilde{Z}$ may be written in terms of M^2 submatrices of dimension $(2N+1) \times (2N+1)$ as

$$\tilde{Z} = \begin{bmatrix} Z_{11} & Z_{12} & \cdots & Z_{1M} \\ Z_{21} & Z_{22} & \cdots & Z_{2M} \\ \vdots & \vdots & \ddots & \vdots \\ Z_{M1} & Z_{M2} & \cdots & Z_{MM} \end{bmatrix} \qquad (14)$$

The off-diagonal submatrices $Z_{ij} (i \neq j)$ may be further broken down by submatrix as

$$Z_{ij} = \begin{bmatrix} C_{ij}^+ & S_{ij}^+ \\ S_{ij}^- & -C_{ij}^- \end{bmatrix} \qquad (i \neq j) \qquad (15)$$

The mth-row, n^{th}-column elements of these submatrices are given by

$$\left[(C, S)_{ij}^\pm \right]_{mn} = \frac{\varepsilon_m}{2} \mathcal{K}_{jimn}^{(c,s)\pm} \qquad (16)$$

where

$$\mathcal{K}_{ijmn}^{(c,s)\pm} = (-1)^m K_{ijmn}^{(c,s)+}{}' \pm K_{ijmn}^{(c,s)-}{}' \qquad (17)$$

and

$$K_{ijmn}^{(c,s)\pm}{}' = \frac{\omega}{2} H_{m\pm n}(\omega D_{ij}) \left[J_{m-1}(\omega a_j) - J_{m+1}(\omega a_j) \right] \cdot \begin{cases} \cos\left[(n \pm m)\psi_{ij} \right] \\ \sin\left[(n \pm m)\psi_{ij} \right] \end{cases} \qquad (18)$$

and

$$\varepsilon_m = \begin{cases} 1 & \text{if } m = 0 \\ 2 & \text{if } m \geq 1 \end{cases} \qquad (19)$$

In Eq. 18, D_{ij} and ψ_{ij} are the polar coordinates of the center of cylinder j in the local coordinate system of cylinder i. The submatrices Z_{jj} on the diagonal of Eq. 14 are themselves diagonal matrices of the form

$$Z_{jj} = \begin{bmatrix} H'_{0j} & & & & & & \\ & \ddots & & & & 0 & \\ & & H'_{Nj} & & & & \\ & & & H'_{1j} & & & \\ & 0 & & & \ddots & & \\ & & & & & & H'_{Nj} \end{bmatrix} \qquad (20)$$

where

$$H'_{nj} = \frac{\omega}{2} \left[H_{n-1}(ka_j) - H_{n+1}(ka_j) \right] \qquad (21)$$

The solution and right-hand side vectors are expressed as

$$\vec{x} = \begin{bmatrix} \vec{X}_1 \\ \vec{X}_2 \\ \vdots \\ \vec{X}_M \end{bmatrix} \quad \to \quad \vec{X}_i = \begin{bmatrix} A_{0i} \\ A_{1i} \\ \vdots \\ A_{Mi} \\ B_{1i} \\ B_{2i} \\ \vdots \\ B_{Mi} \end{bmatrix} \tag{22}$$

and

$$\vec{b} = \begin{bmatrix} \vec{B}_1 \\ \vec{B}_2 \\ \vdots \\ \vec{B}_M \end{bmatrix} \quad \to \quad \vec{B}_i = \begin{bmatrix} I'^c_{0i} \\ I'^c_{1i} \\ \vdots \\ I'^c_{Mi} \\ I'^s_{1i} \\ I'^s_{2i} \\ \vdots \\ I'^s_{Mi} \end{bmatrix} \tag{23}$$

where

$$I'^{(c,s)}_{mj} = -\frac{i\omega b^2}{2\ln 2}\frac{\varepsilon}{2}(-1)^m \int_0^\infty \frac{s^2 J_m(sL_j)[J_{m-1}(sa_j) - J_{m+1}(sa_j)]}{(s^2 - \omega^2)} \exp\left[\frac{-b^2 s^2}{4\ln 2}\right] ds \cdot \begin{cases} \cos(m\alpha_j) \\ \sin(m\alpha_j) \end{cases} \tag{24}$$

and (L_j, α_j) gives the location of the center of cylinder j in the local coordinate system centered on the source.

Solving Eq. 13 for the unknown coefficients allows the individual scattered fields to be found from Eq. 12, while the incident field is found from Eq. 11. Determination of the both the scattered fields (through Eq. 24) and the incident field require the evaluation of an indefinite integral expression. Since closed-form solutions for these integrals have yet to be found, they are evaluated numerically using the technique of Morris (Ref. 2). In this approach, the variable of integration s is replaced by a new variable τ such that

$$s = \tau - i\gamma \exp\left[-\beta(\tau - \omega)^2\right] \tag{25}$$

where $\gamma = \omega/10$ and $\beta = -\ln(1 \times 10^{-10}/\gamma)/\omega^2$. The new path of integration is thus deformed below the real axis around the pole at $s = \omega$, allowing the integration to be performed using standard numerical techniques. Both the numerical integration and solution of the linear system of equations is done using the computer software package *Mathematica* (Ref. 4), which allows for the accuracy of the numerical integration and the potential ill-conditioning of the linear system to be controlled.

The analytic root-mean squared pressure distribution on the surfaces of the cylinders and along the centerline for both benchmark problems are plotted in Figs. 1 through 4. Files containing this data in numerical form are available by contacting the author, as well as the *Mathematica* notebook used to generate these results. This notebook may be easily modified for other cylinder configurations or source parameters to provide additional test cases for comparison.

REFERENCES

1. Sherer, S.E.: "Scattering of sound from a spatially distributed source by multiple circular cylinders"; *J. Acoust Soc. Am.*, vol. 115, no. 2, 2004, pp. 488-496.
2. Morris, P.J.: "The scattering of sound from a spatially distributed symmetric cylindrical source by a circular cylinder", *J. Acoust. Soc. Am.*, vol. 97, no. 5, 1995, pp. 2651-2656.
3. Abramowitz, M. and Stegen, I.A.: *Handbook of Mathematical Functions with Formulas, Graphs and Mathematical Tables*; Dover Publishers, Inc., 5th Edition, 1968.
4. Wolfram, S.: *The Mathematica Book;* Cambridge University Press, New York, 1999.

Figure 1. Analytic root-mean-squared pressure on surface of cylinders for two-cylinder benchmark problem

Figure 2. Analytic root-mean-squared pressure on centerline of domain for two-cylinder benchmark problem
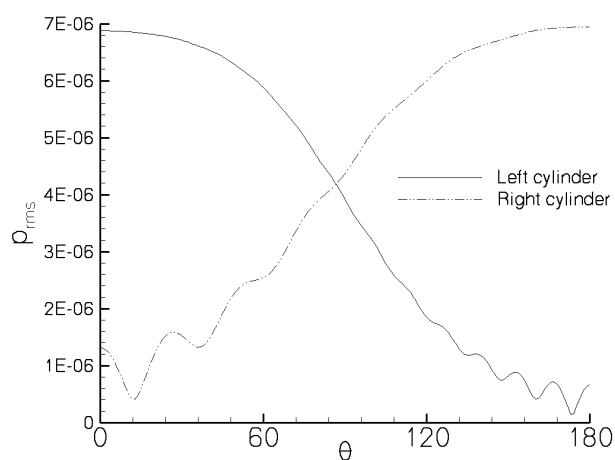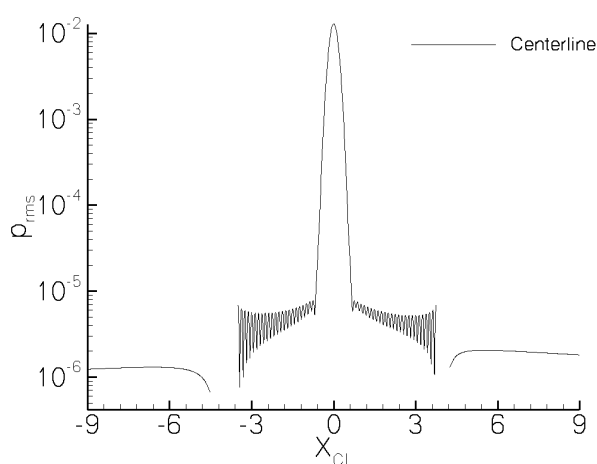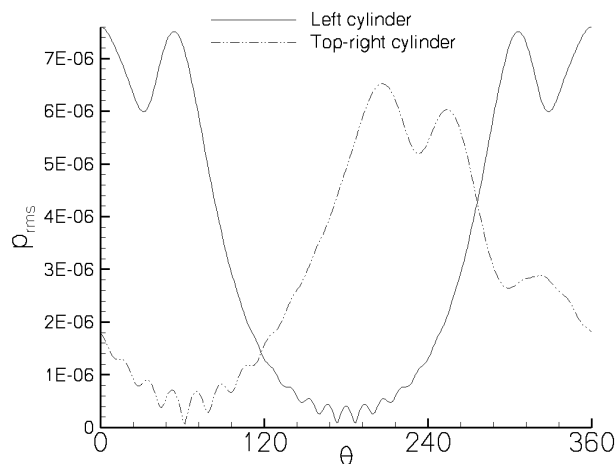

Figure 3. Analytic root-mean-squared pressure on surface of cylinders for three-cylinder benchmark problem
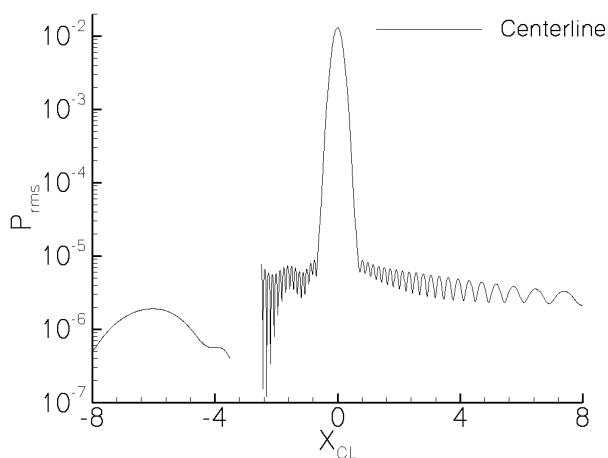
Figure 4. Analytic root-mean-squared pressure on centerline of domain for three-cylinder benchmark problem

SINGLE AIRFOIL GUST RESPONSE PROBLEM

James R. Scott
National Aeronautics and Space Administration
Glenn Research Center
Cleveland, Ohio 44135

The solution to this problem can be obtained by solving the linearized unsteady Euler equations. Let the unsteady flow field be given by

$$\vec{U}(\vec{x},t) = \vec{U}_0(\vec{x}) + \vec{u}(\vec{x},t) \tag{1}$$

$$p(\vec{x},t) = p_0(\vec{x}) + p'(\vec{x},t) \tag{2}$$

$$\rho(\vec{x},t) = \rho_0(\vec{x}) + \rho'(\vec{x},t) \tag{3}$$

$$s(\vec{x},t) = s_0 + s'(\vec{x},t) \tag{4}$$

where the entropy s_0 is constant, and $\vec{u}$, p', ρ', and s' are the unsteady perturbation velocity, pressure, density and entropy, respectively. Zero subscripts denote mean flow quantities which are assumed to be known.

Substituting (1) – (4) into the nonlinear Euler equations and neglecting products of small quantities, one obtains the linearized equations

$$\frac{D_0 \rho'}{Dt} + \rho' \vec{\nabla} \cdot \vec{U}_0 + \vec{\nabla} \cdot (\rho_0 \vec{u}) \; = \; 0 \tag{5}$$

$$\rho_0 \left(\frac{D_0 \vec{u}}{Dt} + \vec{u} \cdot \vec{\nabla} \vec{U}_0 \right) + \rho' \vec{U}_0 \cdot \vec{\nabla} \vec{U}_0 \; = \; -\vec{\nabla} p' \tag{6}$$

$$\frac{D_0 s'}{Dt} \; = \; 0, \tag{7}$$

where $\frac{D_0}{Dt} = \frac{\partial}{\partial t} + \vec{U}_0 \cdot \vec{\nabla}$ is the convective derivative associated with the mean flow.

If the mean velocity $\vec{U}_0$ can be expressed as the gradient of a potential Φ_0, then equations (5) - (7) can be reduced to a single, non-constant coefficient, inhomogeneous convective wave equation (refs. 1,2)

$$\frac{D_0}{Dt} \left(\frac{1}{c_0{}^2} \frac{D_0 \phi}{Dt} \right) - \frac{1}{\rho_0} \vec{\nabla} \cdot (\rho_0 \vec{\nabla} \phi) \; = \; \frac{1}{\rho_0} \vec{\nabla} \cdot (\rho_0 \vec{u}^{(R)}), \tag{8}$$

where the unsteady velocity is decomposed into a known vortical component $\vec{u}^{(R)}$ and an unknown potential component $\vec{\nabla} \phi$,

$$\vec{u}(\vec{x},t) \; = \; \vec{u}^{(R)} + \vec{\nabla} \phi. \tag{9}$$

The unsteady pressure is given by

$$p' \; = \; -\rho_0(\vec{x}) \frac{D_0 \phi}{Dt}. \tag{10}$$

An unsteady aerodynamic code, called GUST3D (ref. 3), has been developed to solve equation (8) for flows with periodic vortical disturbances. The code uses a frequency-domain approach with second-order central differences and a pressure radiation condition in the far field. GUST3D requires as input certain mean flow quantities which are calculated separately by a potential flow solver. This solver calculates the

mean flow using a Gothert's Rule approximation (ref. 3). On the airfoil surface, it uses the solution calculated by the potential code FLO36 (ref. 4). Figures 1-2 show the mean pressure along the airfoil surface for the two airfoil geometries.

In Figures 3 - 8, we present the RMS pressure on the airfoil surface. Each figure shows three GUST3D solutions (calculated on grids with different far-field boundary locations). Three solutions are shown to provide some indication of the numerical uncertainty in the results.

Figures 9 - 13 present the acoustic intensity. We again show three solutions per case. Note that no results are presented for the $k_1 = k_2 = 2.0$ loaded airfoil case, as an acceptable solution could not be obtained.

A few comments need to be made about the results shown.

First, since the last Workshop, the GUST3D code has been substantially upgraded. This includes implementing a more accurate far-field boundary condition (ref. 5) and developing improved gridding capabilities. This is the reason for any differences that may exist between the present results and results from the last Workshop.

Second, the intensity results on the circle $R = 4C$ were obtained using a Kirchoff method (ref. 6). The Kirchoff surface was the circle $R = 2C$.

Finally, the GUST3D code is most accurate for low reduced frequencies. A new domain decomposition approach (ref. 7) has been developed to improve accuracy. Both the single domain and domain decomposition approaches were used in generating the present results.

REFERENCES

1. M.E. Goldstein, "Unsteady vortical and entropic distortions of potential flows round arbitrary obstacles," *J. Fluid Mech.,* vol. 89, 1978, pp. 433-468.

2. H.M. Atassi and J. Grzedzinski, "Unsteady disturbances of streaming motions around bodies," *J. Fluid Mech.,* vol. 209, 1989, pp. 385-403.

3. J.R. Scott and H.M. Atassi, "A Finite-Difference, Frequency-Domain Numerical Scheme for the Solution of the Gust Response Problem," *J. Comp. Phys.*, vol. 119, 1995, pp. 75-93.

4. A. Jameson and D.A. Caughey, "A Finite Volume Method for Transonic Potential Flow Calculations," *Proceedings of the AIAA 3rd Computational Fluid Dynamics Conference*, Williamsburg, Virginia, 1979, p. 122.

5. J.R. Scott, K.L. Kreider, and J.A. Heminger, "Evaluation of Radiation Boundary Conditions for the Gust Response Problem," Accepted for publication in *AIAA Journal*.

6. S.I. Hariharan, J.R. Scott and K.L. Kreider, "A Potential-Theoretic Method for Far-Field Sound Radiation Calculations," *J. Comp. Phys.*, vol. 164, 2000, pp. 143-164.

7. J.R. Scott, H.M. Atassi, and R.F. Susan-Resiga, "A New Domain Decomposition Approach for the Gust Response Problem," AIAA Paper 2003-0883, Jan., 2003.
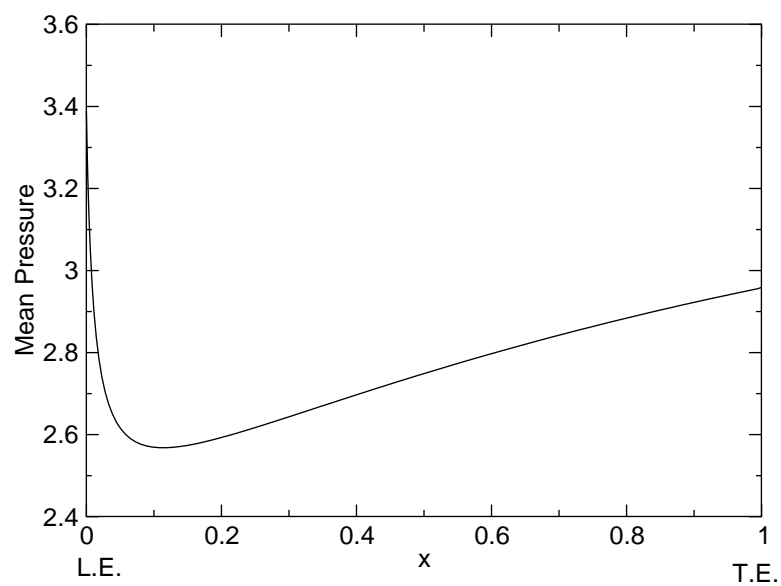
Figure 1   Mean pressure on airfoil surface - Case 1.
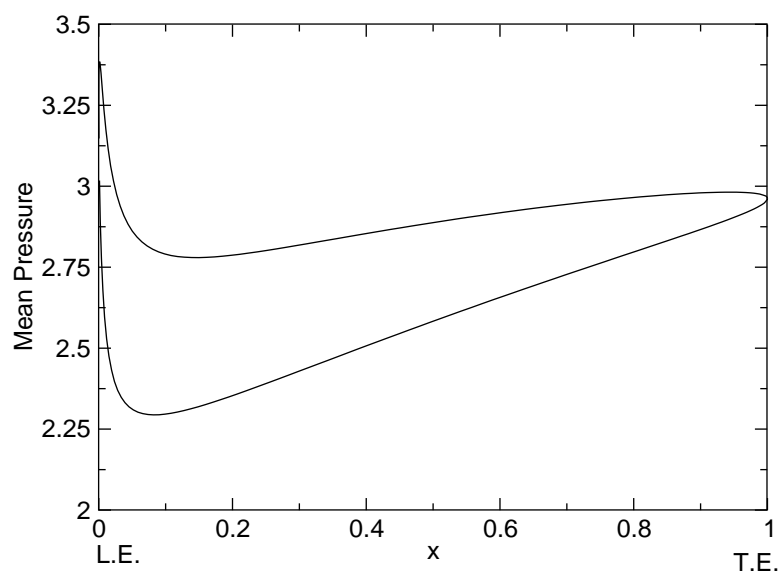
Figure 2   Mean pressure on airfoil surface - Case 2.
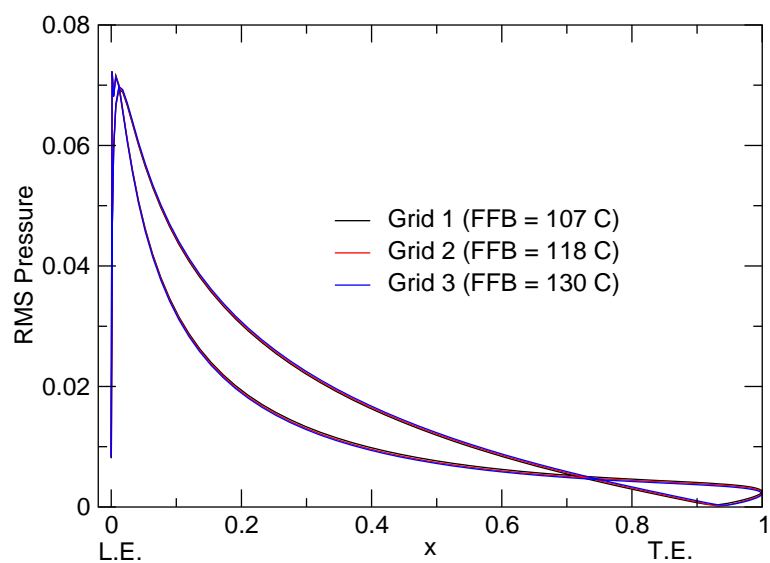
Figure 3   RMS pressure on airfoil surface, Case 1, k1=k2=0.1
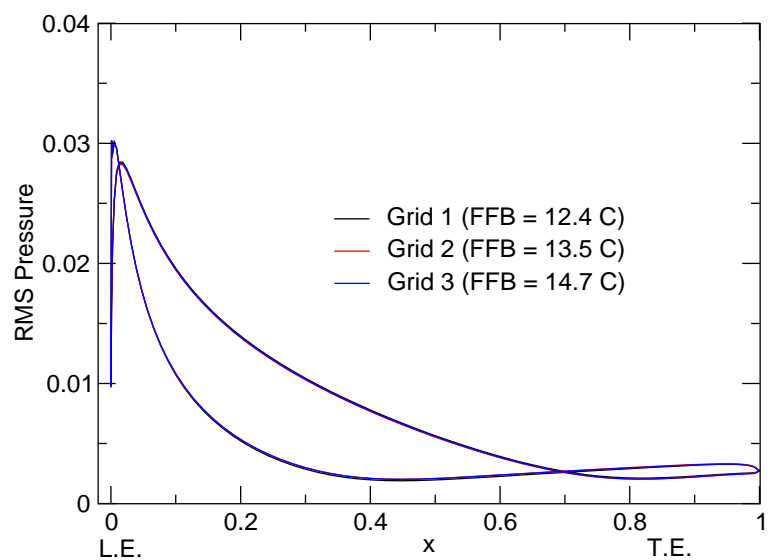
Figure 4   RMS pressure on airfoil surface, Case 1, k1=k2=1.0
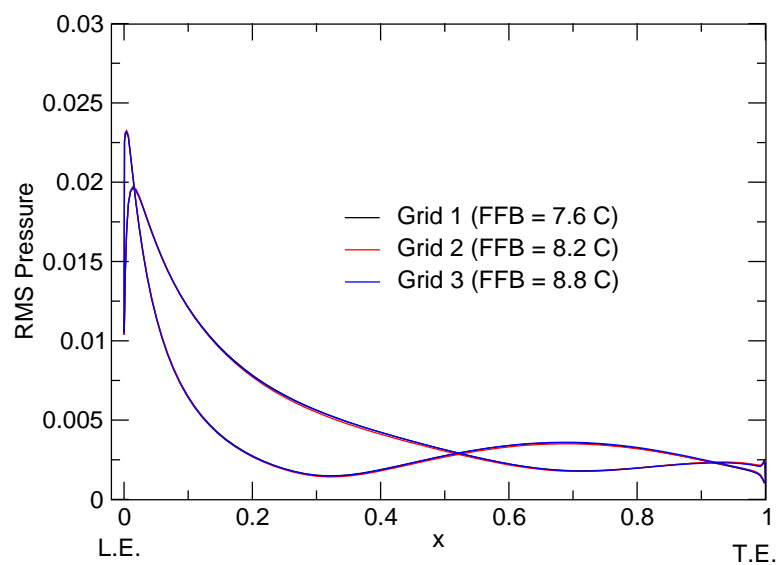
Figure 5   RMS pressure on airfoil surface, Case 1, k1=k2=2.0
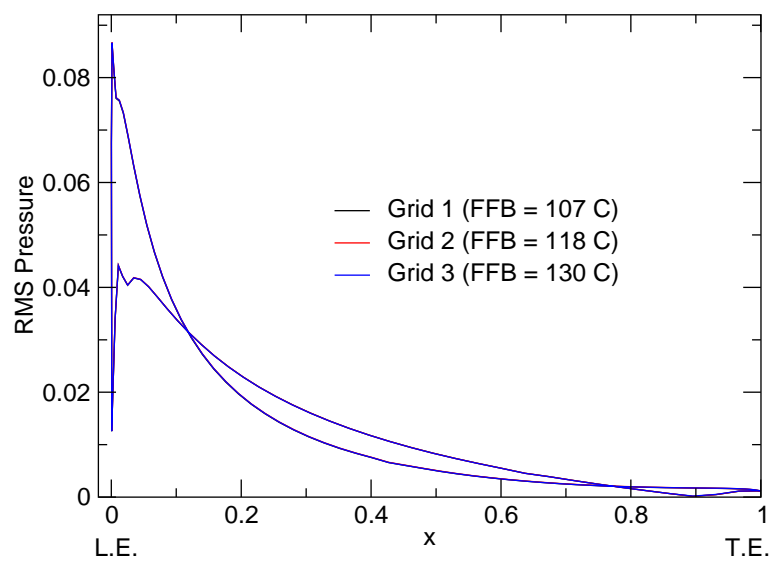
Figure 6   RMS pressure on airfoil surface, Case 2, k1=k2=0.1
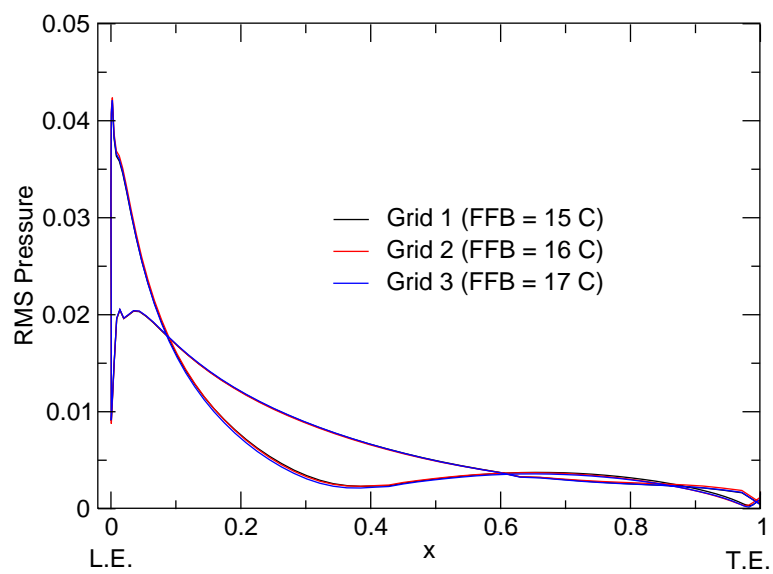
Figure 7   RMS pressure on airfoil surface, Case 2, k1=k2=1.0
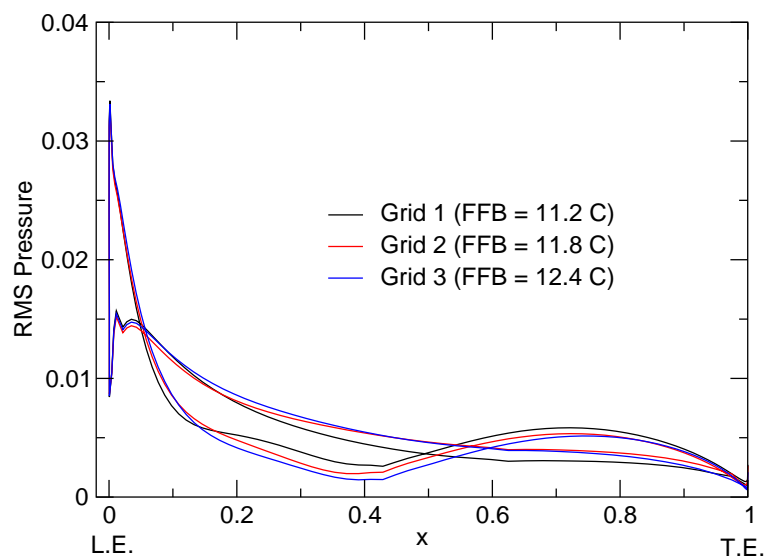
Figure 8   RMS pressure on airfoil surface, Case 2, k1=k2=2.0
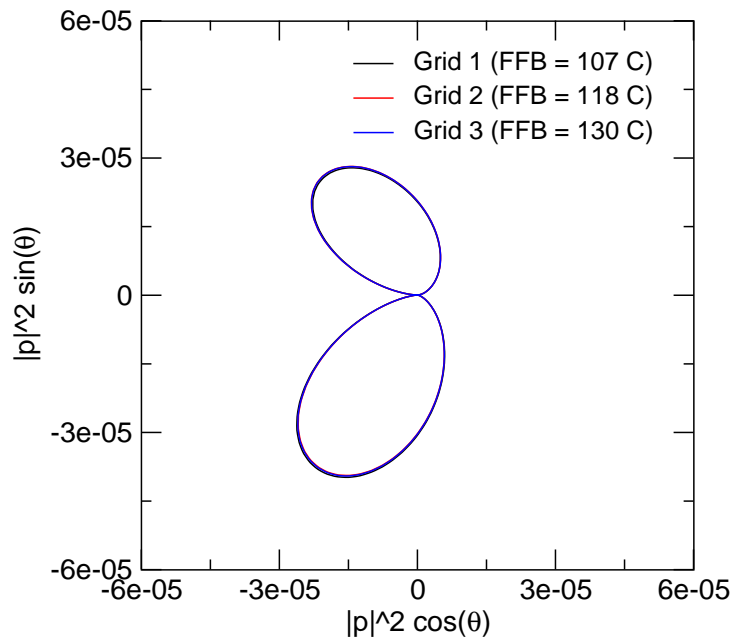
Figure 9.a   Acoustic intensity on circle R = 1 C,
Case 1, k1 = k2 = 0.1.
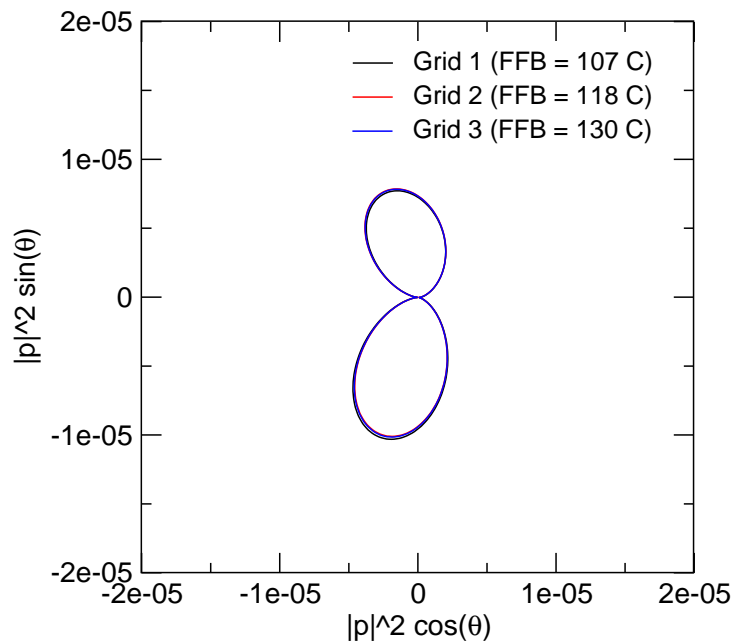
Figure 9.b   Acoustic intensity on circle R = 2 C,
Case 1, k1 = k2 = 0.1.
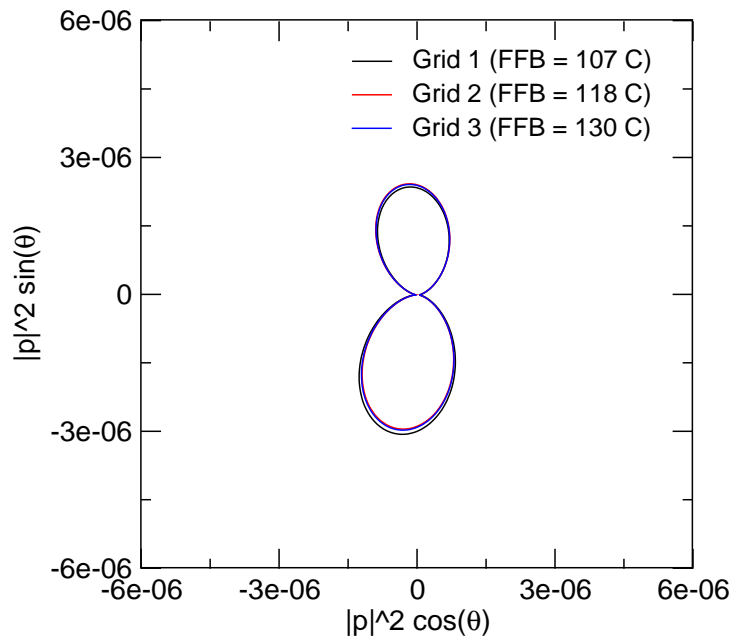
Figure 9.c   Acoustic intensity on circle R = 4 C,
Case 1, k1 = k2 = 0.1.
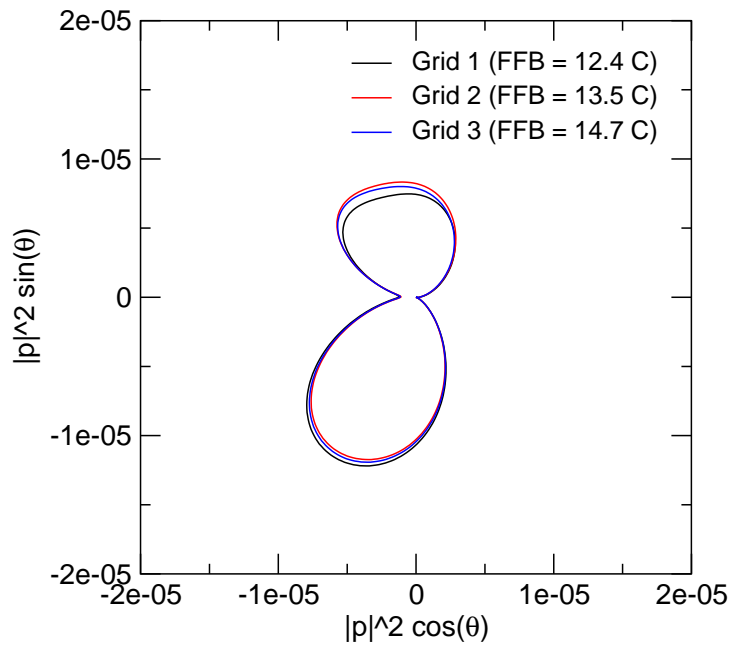
Figure 10.a   Acoustic intensity on circle R = 1 C,
Case 1, k1 = k2 = 1.0.
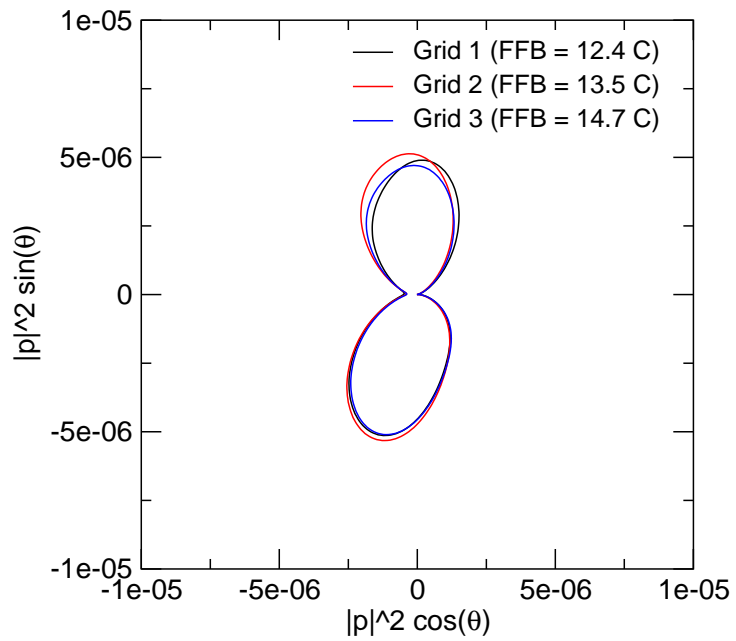
Figure 10.b   Acoustic intensity on circle R = 2 C,
Case 1, k1 = k2 = 1.0.
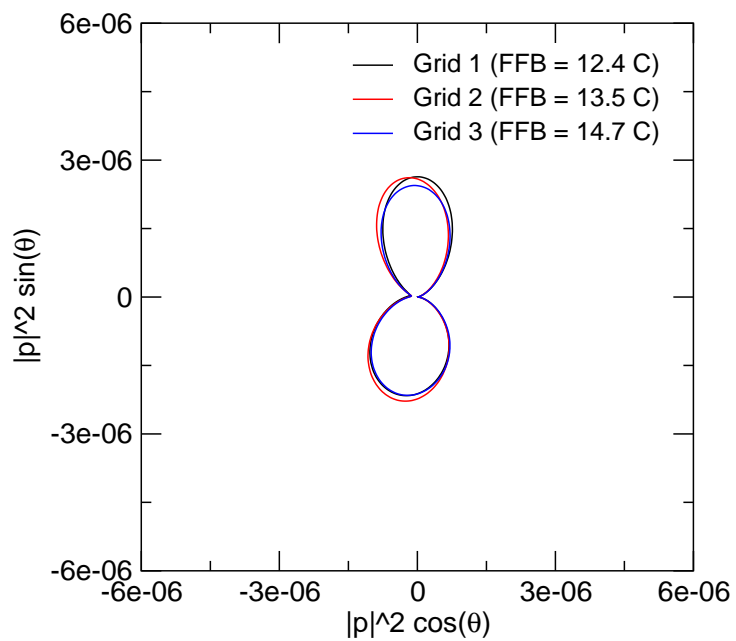
Figure 10.c   Acoustic intensity on circle R = 4 C,
Case 1, k1 = k2 = 1.0.
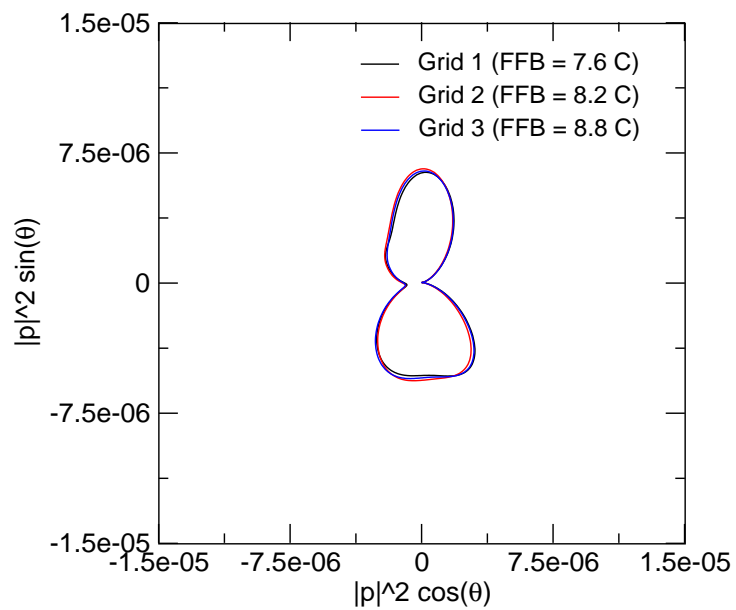
Figure 11.a   Acoustic intensity on circle R = 1 C,
Case 1, k1 = k2 = 2.0.
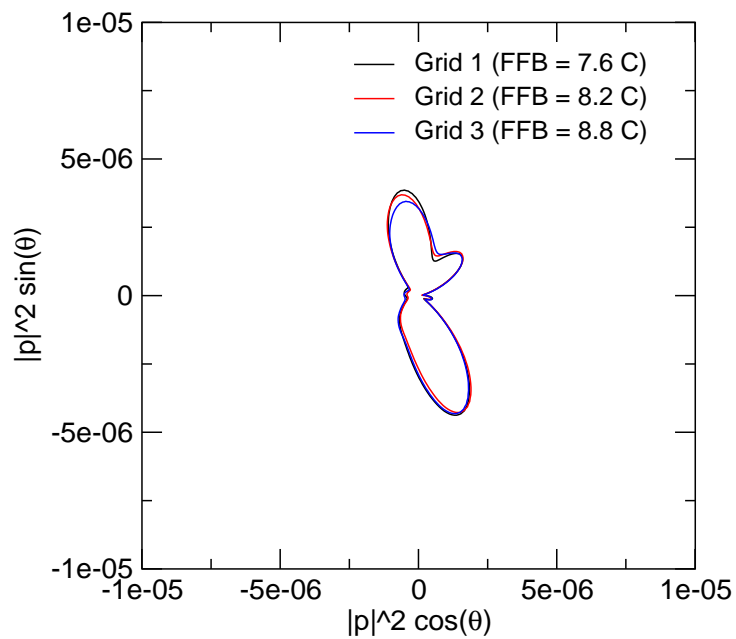
Figure 11.b   Acoustic intensity on circle R = 2 C,
Case 1, k1 = k2 = 2.0.
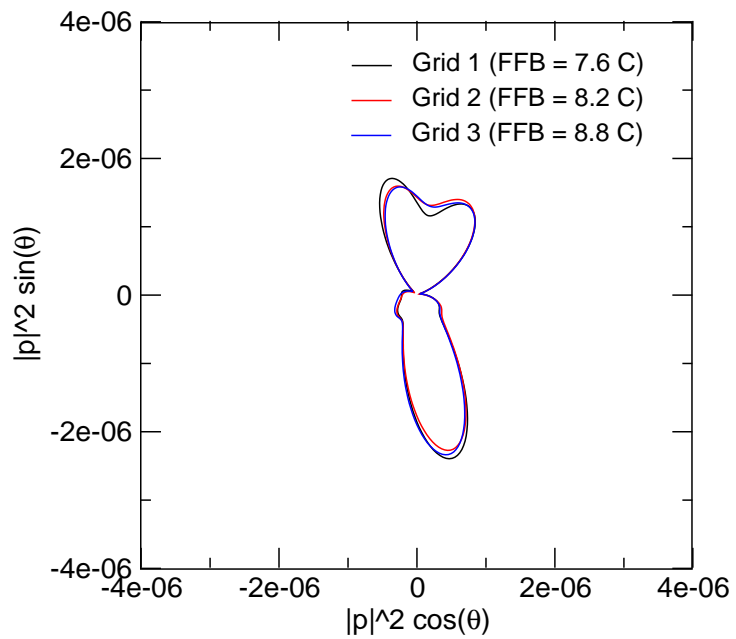
Figure 11.c   Acoustic intensity on circle R = 4 C,
Case 1, k1 = k2 = 2.0.
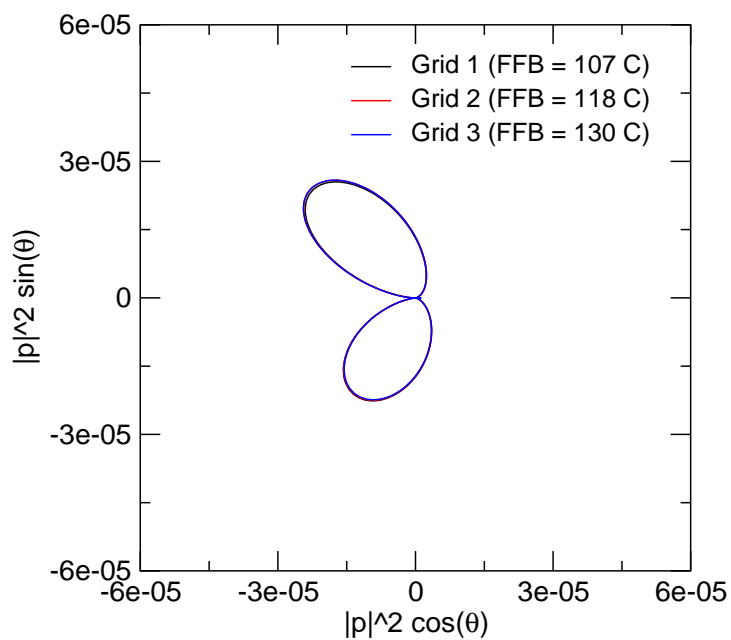
Figure 12.a   Acoustic intensity on circle R = 1 C,
Case 2, k1 = k2 = 0.1.
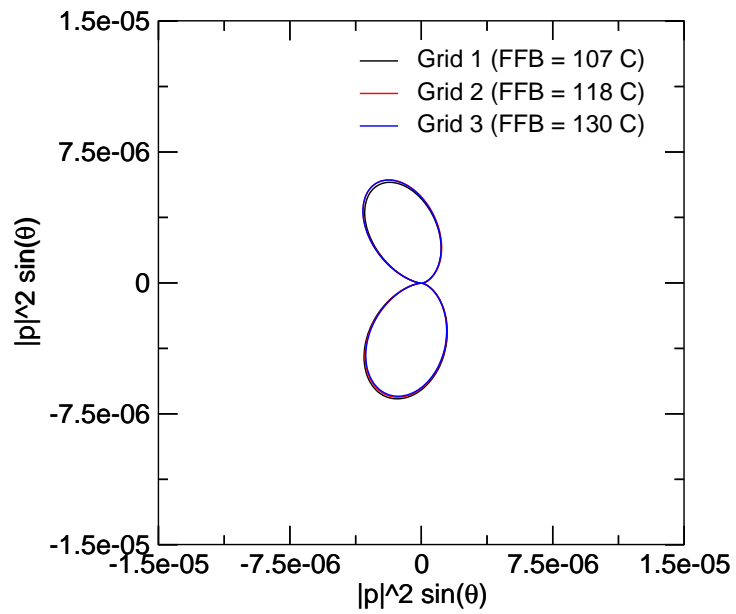
Figure 12.b Acoustic intensity on circle R = 2 C, Case 2, k1 = k2 = 0.1.
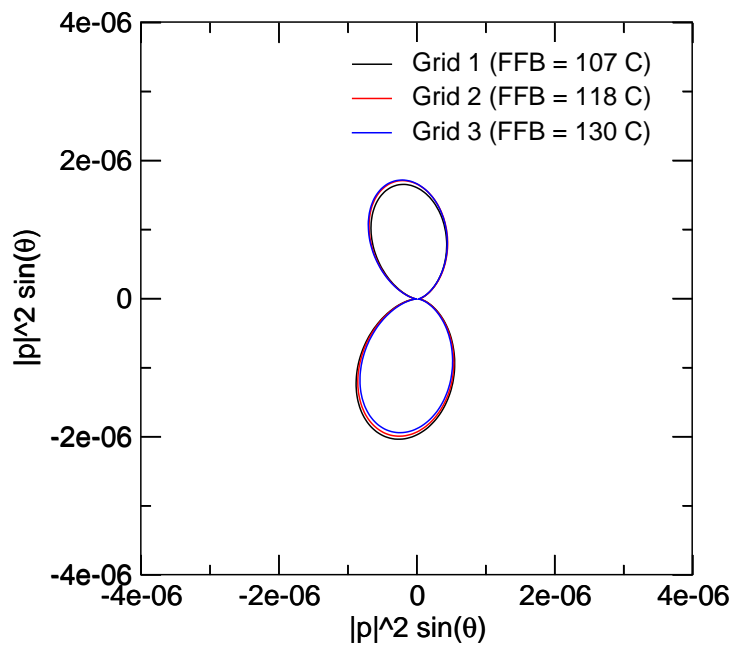
Figure 12.c Acoustic intensity on circle R = 4 C, Case 2, k1 = k2 = 0.1.
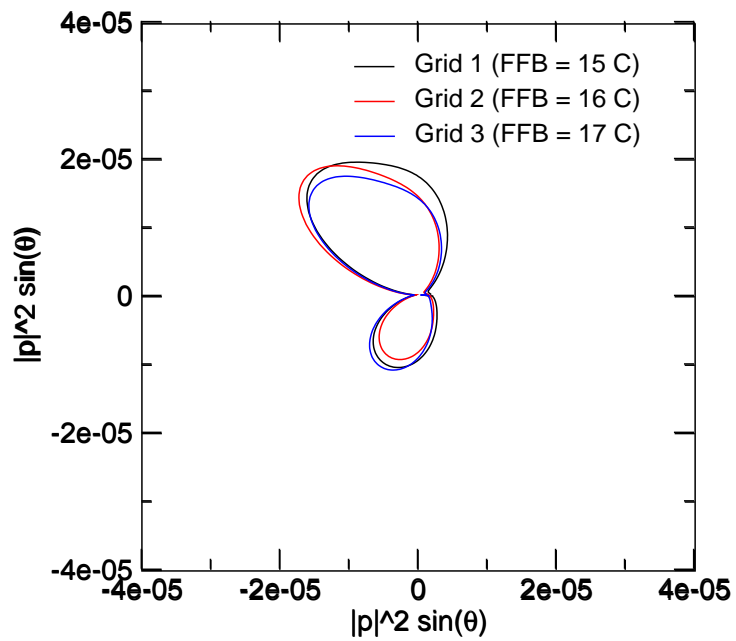
Figure 13.a   Acoustic intensity on circle R = 1 C,
Case 2, k1 = k2 = 1.0.
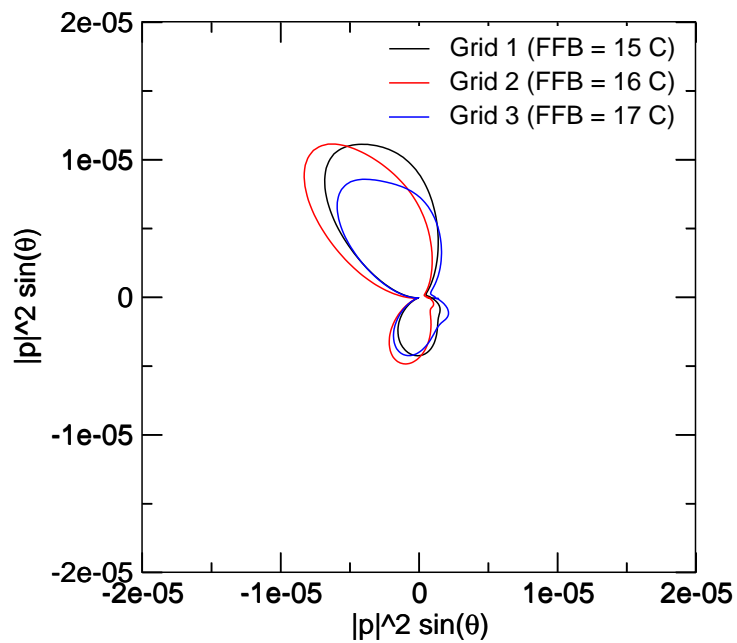
Figure 13.b   Acoustic intensity on circle R = 2 C,
Case 2, k1 = k2 = 1.0.
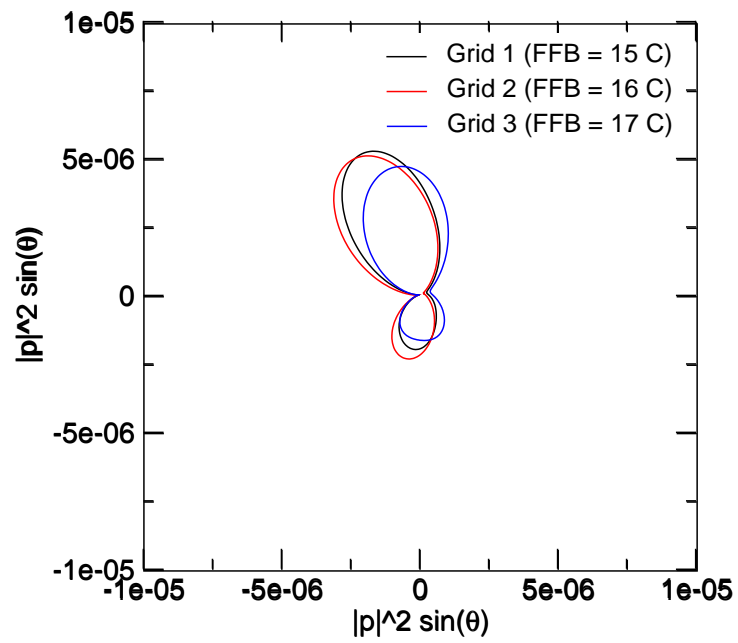
Figure 13.c   Acoustic intensity on circle R = 4 C,
Case 2, k1 = k2 = 1.0.

BENCHMARK SOLUTION FOR
THE CATEGORY 3—PROBLEM 2: CASCADE–GUST INTERACTION

Edmane Envia
National Aeronautics and Space Administration
Glenn Research Center
Cleveland, Ohio 44135

ABSTRACT

The benchmark solution for the cascade-gust interaction problem is computed using a linearized Euler code called LINFLUX. The inherently three-dimensional code is run in the thin-annulus limit to compute the two-dimensional cascade response. The calculations are carried out in the frequency-domain and the unsteady response at each of the gust's three frequency component is computed. The results are presented on modal basis for pressure perturbations (i.e., acoustic modes) as well as velocity perturbations (i.e., convected gust modes) at each frequency.

INTRODUCTION

The periodic impingement of the wakes of a rotor on a downstream stator is one of the principal sources of turbomachinery noise and a significant contributor to the overall noise produced by modern aircraft engines. As such, this source has been the focus of many analytical modeling efforts over the years, but with the recent emergence of computational aeroacoustics (CAA) as a viable alternative, the emphasis has now shifted away from analytical approaches to purely numerical ones. Naturally, as in the other aeroacoustic problems of engineering interest, the success of CAA is predicated on the availability of efficient computational algorithms and robust boundary conditions. In theory, a candidate algorithm must be able to handle the generation and propagation of sound waves in the presence of complex geometries, and through non-uniform media, with no dispersion or dissipation; the boundary conditions must be able to handle the passage of the unsteady disturbances through the boundaries of the computational domain with no reflection; and both of these requirements must be satisfied at frequencies of engineering interest. The usefulness of CAA is, therefore, greatly dependent on the extent to which all of these conditions are met, and its practicality is dependent on the resource requirements (hardware and CPU time) that must be expended to achieve reasonably accurate solutions for design and analysis purposes. The proposed two-dimensional benchmark problem was designed to address principally the question of usefulness. The issue of practicality is best addressed using a three-dimensional benchmark problem, which is postponed until the next workshop.

BENCHMARK SOLUTION

The solution for the benchmark problem was obtained using a code called LINFLUX which is based on a linearized frequency-domain method for solving the three-dimensional inviscid unsteady flow equations. The method has been extensively documented and validated using two- and three-dimensional test cases (see refs.1 through 4) and so will not be covered here. LINFLUX is actually part of a collection of codes which also includes a grid generation package called TIGER, a steady nonlinear inviscid flow solver called TURBO, and a set of processing routines for generating the harmonic content of the incident disturbance (i.e., acoustic, vortical and entropic). The information obtained from all three codes is used to run LINFLUX, which calculates the acoustic response produced by the incident disturbances on the blade row at specified harmonics of the rotor-stator blade passing frequency.

Computational grid

Since LINFLUX cannot be easily modified to run in two-dimensional mode, the cascade geometry was "wrapped" around an annulus with a mean radius of $\bar{R} \approx 5.7c$ and a hub-to-tip radius ratio of 0.996 (see Figure 1a). The result is a blade row that is, strictly speaking, three-dimensional, but owing to its extremely small spanwise extent (only ~2.3% of the vane chord) would result in solutions that are effectively two-dimensional in nature

depending only on the axial and tangential coordinates (see Figure 1b). Since the solution is computed in the frequency-domain, only one passage of the blade row is needed when appropriate periodicity conditions are enforced (see Figure 1c). To ensure sufficient resolution of the mean flow details and the response to the highest frequency gust (i.e., reduced frequency of $9\pi/4$), a grid with 301×81×7 points in the axial, tangential and radial directions was created. The grid is packed near the airfoil boundaries and also in the vicinity of the leading edge (see Figure 1d).
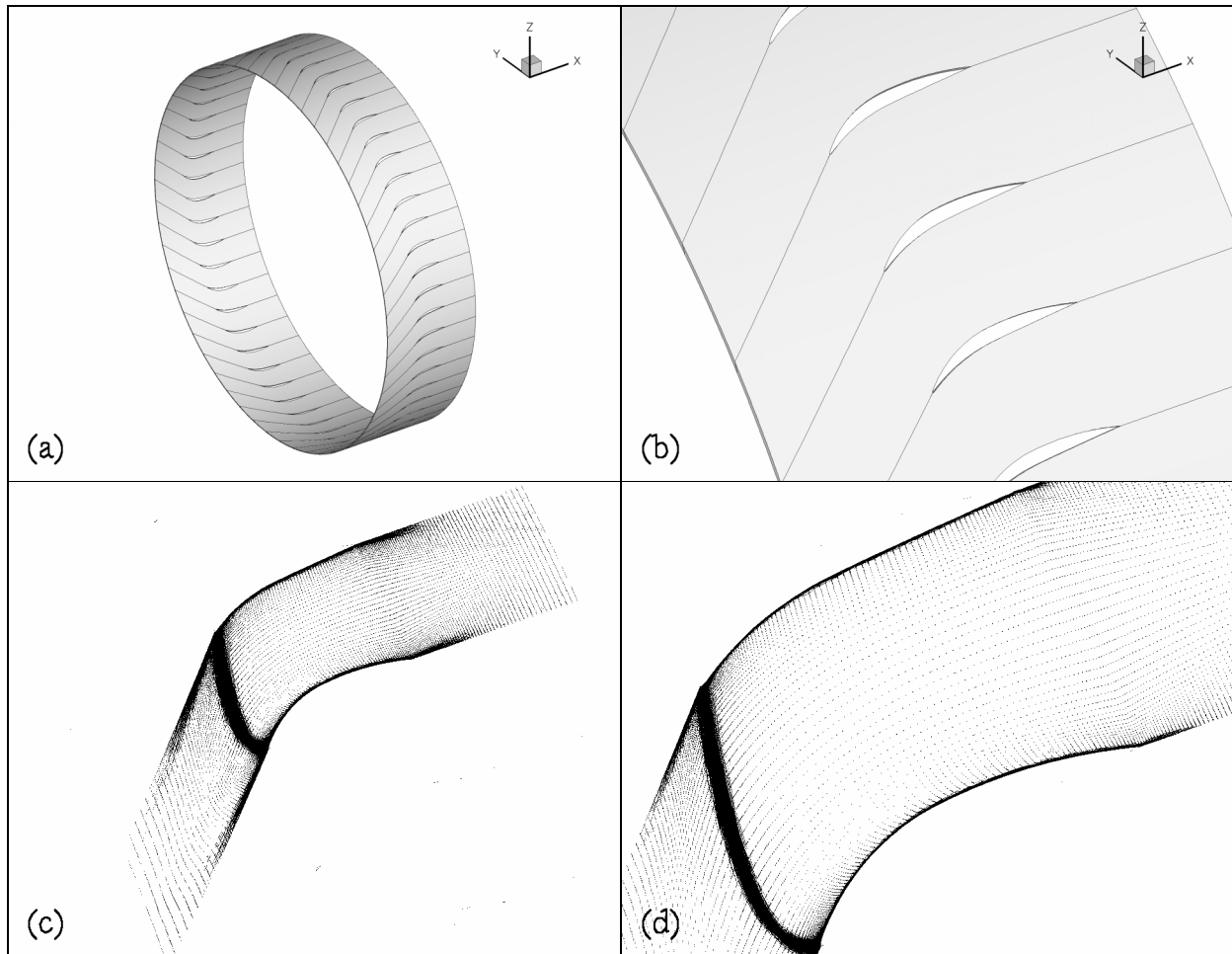
Figure 1. Three-dimensional thin annulus representation of the two-dimensional geometry of the benchmark problem (a). Hub-to-tip radius ratio is 0.996 (b) resulting in a solution that is effectively independent of the radial coordinate. The passage grid, which has 301×81×7 points in the axial, tangential and radial directions, is shown for the radial grid index = 4 (c). The grid is packed near the airfoil surfaces and in the vicinity of the leading edge (d).

Steady flow solution

The steady flow needed as input to LINFLUX was computed using the nonlinear Euler code called TURBO (see ref. 5) on the grid discussed in the previous section. The computation was run to convergence as indicated on the left side of Figure 2. The graph shows the convergence history of the error (residual) as a function of the iteration count. The residual was reduced by five orders of magnitude after 25,000 iterations, but the iteration process was continued a further 10,000 steps to ensure convergence of all relevant flow parameters. On the right, the resulting Mach number distribution after 35,000 iterations is shown.

For the purposes of the presentation, the $x-\theta$ plane corresponding to the radial grid index = 4 is unrolled and both the geometry and solution are duplicated. In this two-dimensional representation, x denotes the horizontal

coordinate, and $y = r\theta$ denotes the vertical coordinate. Clearly the steady flow is uniform along the y-direction at the inflow and outflow planes ($x = \mp 1.5c$) except for the presence of a thin wake downstream of the vane trailing edge produced as a result of numerical dissipation. The flow over the vane itself behaves as expected with steady loading evident in the form of low Mach number values (corresponding to high pressure values) on the pressure side and high Mach number values (corresponding to low pressure values) on the suction side of the vane.

Representative averaged flow quantities at the inflow and outflow planes obtained using TURBO are shown in Table 1. It should be noted that the inflow plane flow angle is an input in TURBO. Using the isentropic flow relations, the stagnation pressure and temperature at the inflow and outflow planes can be readily computed and found to be equal to 1.00000 satisfying the other requirements specified in the benchmark problem.
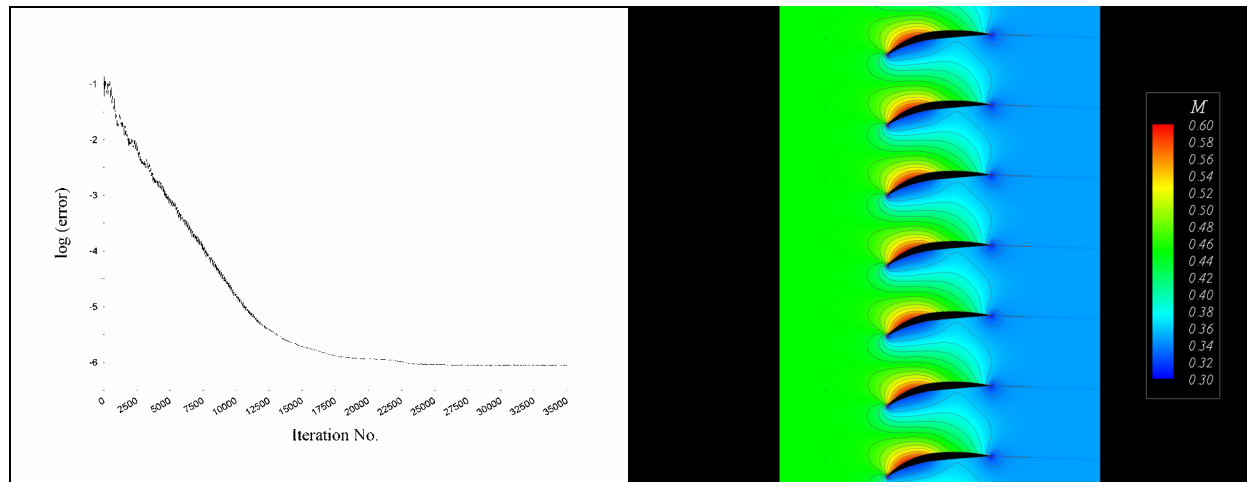
Figure 2. Steady flow obtained using the TURBO code. Convergence history over 35,000 iterations is shown on the left and the resulting Mach number distribution is shown on the right. There is evidence of slight numerical dissipation in the form of a thin wake downstream of the vane trailing edge.

	Mach No.	Static Pressure	Static Temperature	Flow Angle (deg.)
Inflow Plane	0.44958	0.87049	0.96115	36.00*
Outflow Plane	0.34704	0.92000	0.97648	1.71

Table 1. Steady flow quantities at the inflow and outflow planes of the computational domain after 35,000 iterations. The flow variables are normalized by the standard conditions; pressure = 2116.2 lbf/ft^2, temperature = 519 ^{o}R, and the speed of sound = 1116.8 ft/s.

Unsteady flow solution

Using the steady background flow described in the previous section and the gust harmonic content given in benchmark problem, LINFLUX was executed to calculate the harmonics of the unsteady response produced as a result of the impingement of the gust on the cascade. For each harmonic component of the gust (i.e., $n = 1$ to 3), the code was run until the residual level had reached the round-off error region. This required almost 20,000 iterations for the first harmonic, little over 33,000 iterations for the second harmonic, and nearly 12,000 iterations for the third harmonic. In every case, the size of the residual was reduced by at least six orders of magnitude.

Samples from the unsteady response are shown in Figure 3, 4 and 5. As before, the $x - \theta$ plane corresponding to the radial grid index = 4 is unrolled and duplicated. This time, however, the harmonic solution (for each n) is shifted by $\exp(ijn\sigma)$ for the jth passage, where $\sigma = 2\pi B/V$ is the so-called inter-blade phase angle and i is the square root of -1. The quantity B/V denotes the relationship between the gust and cascade periods in the y-direction which, using

the information supplied in the benchmark problem can be readily shown to equal 22/54 over a 2π period. It is convenient to interpret B and V as the blade and vane counts for the annulus problem. Then, in view of the Tyler-Sofrin rule, $m = nB - kV$ (where k is an integer), the modal structure of the response can be interpreted. The computed unsteady field includes both acoustic and convective modes. The acoustic modes, which correspond to $k = 0$, $k = 1$ or both, propagate at the speed of sound relative to the medium in both directions. The convective modes always correspond to $k = 0$ and travel at the speed of the background flow (i.e., are convected by it). The pressure field is comprised of acoustic modes only, while the velocity field includes both acoustic and convective modes, but tends to be dominated by the latter. The dominant acoustic modes produced in response to each gust frequency are listed in Table 2. The computed response is evanescent (i.e., cut-off) at the primary frequency, a deliberate design feature of the benchmark problem. The conversion from the 3D mode orders to the 2D wavenumbers is through the relation $k_y^{(a)} = m / \overline{R}$ where the superscript (a) denotes the acoustic wavenumber.

Frequency	Annulus Mode Order (3D)	Mode Wavenumber (2D)	Mode Type
ω	$m = +22$	$\hat{k}_y^{(a)} = +3.84$	Evanescent
	$m = -32$	$\hat{k}_y^{(a)} = -5.59$	Evanescent
	$m = +22$	$\hat{k}_y^{(c)} = +3.84$	Convected
2ω	$m = -10$	$\hat{k}_y^{(a)} = -1.75$	Propagating
	$m = +44$	$\hat{k}_y^{(c)} = +7.68$	Convected
3ω	$m = +12$	$\hat{k}_y^{(a)} = +2.09$	Propagating
	$m = -42$	$\hat{k}_y^{(a)} = -7.33$	Propagating
	$m = +66$	$\hat{k}_y^{(c)} = +11.52$	Convected

Table 2. The dominant unsteady response modes in the annulus and their two-dimensional transverse wavenumber equivalents. The 2D wavenumbers are normalized by the vane chord. The acoustic response at the primary frequency is cut-off. The convected mode wavenumbers (denoted by the superscript (c)) are multiples of the input gust wavenumber 11π/9.

In Figure 3 the response to the incident gust corresponding to the primary frequency $\omega = 3\pi / 4$ is shown. The real part of pressure perturbation is shown on the left, and the real part of the axial component of velocity perturbation is shown on the right. The pressure and velocity perturbations are normalized by the inflow plane static pressure and steady velocity which can be obtained from Table 1. The pressure response, which is cut-off at this frequency, is dominated by two evanescent acoustic modes $m = +22$ and $m = -32$. The perturbation velocity field is dominated by the convected gust and thus is mainly comprised of $m = +22$ convected mode. The incident gust is distorted as it passes through the cascade. Note that the axial velocity perturbations are essentially out of phase downstream of the vane leading edge, and there is a jump in axial velocity across the wake sheet downstream of the trailing edge. It should be noted that the jump is not an artifact of the numerical dissipation discussed earlier, but a feature of the physical problem.
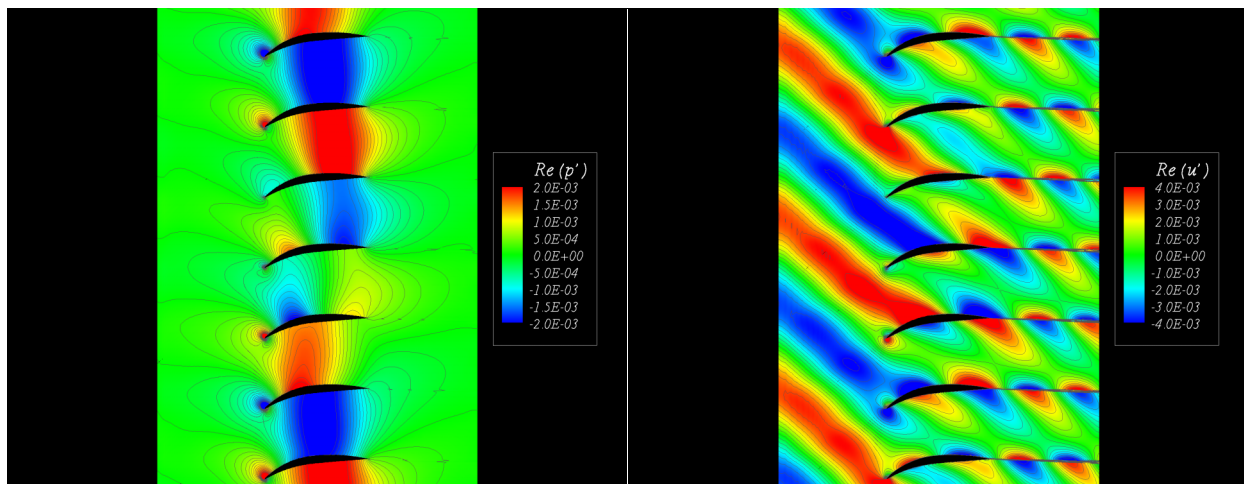
Figure 3. The computed response due to the gust at the primary frequency (i.e., $\omega = 3\pi/4$). Real part of the pressure perturbation is shown on the left and real part of the axial velocity perturbation is shown on the right. The pressure response is cut-off at this frequency and includes two evanescent acoustic modes $m = +22$ and $m = -32$. The perturbation axial velocity field is dominated by the convected gust and is mainly comprised of $m = +22$ convective mode.

Figure 4 shows the corresponding plots for the calculated response at twice the primary frequency. The pressure field at this frequency is due to a single propagating acoustic mode $m = -10$ with the wave fronts clearly evident away from the cascade especially at the exit plane. The axial velocity field is dominated by the convective mode $m = +44$ exhibiting twice as many wave fronts as that in Figure 1. Note the change in scale for both the pressure and velocity plots.

Finally, Figure 5 shows the calculated response at three times the primary frequency. The pressure field at this frequency is comprised of two propagating acoustic modes $m = +12$ and $m = -42$. The axial velocity field at this frequency is due to the convective mode $m = +66$ exhibiting three times as many wave fronts as that in Figure 1. Note the change in scale for both the pressure and velocity plots. The pressure wave fronts are not as clearly discernable as in Figure 4 due to interference between two contributing acoustic modes.
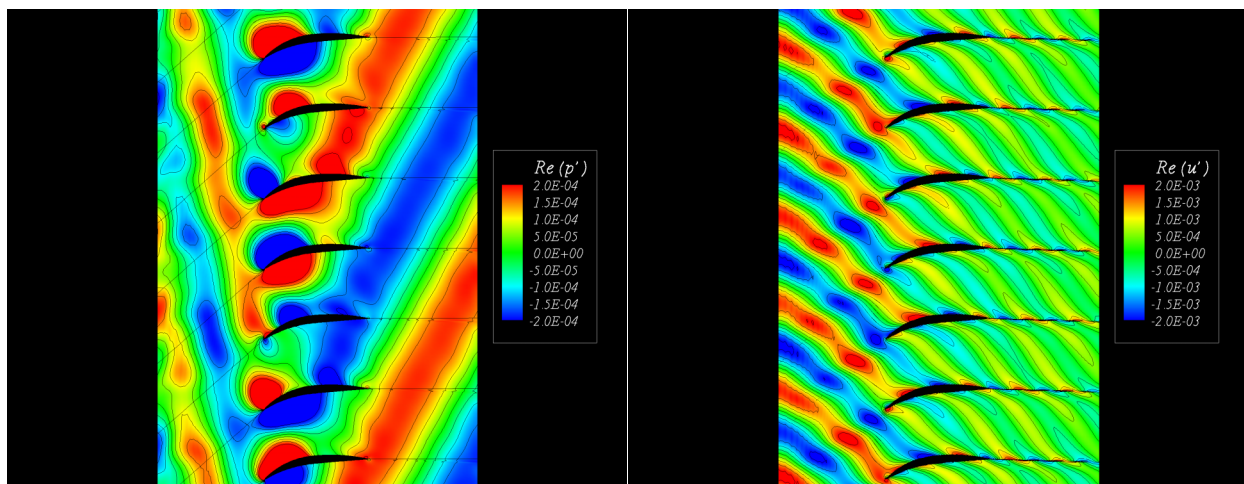
Figure 4. The computed response due to the gust at the twice the primary frequency. The pressure field is entirely comprised of the propagating (i.e., cut-on) acoustic mode $m = -10$. The axial velocity perturbation is due to the $m = +44$ convective mode.
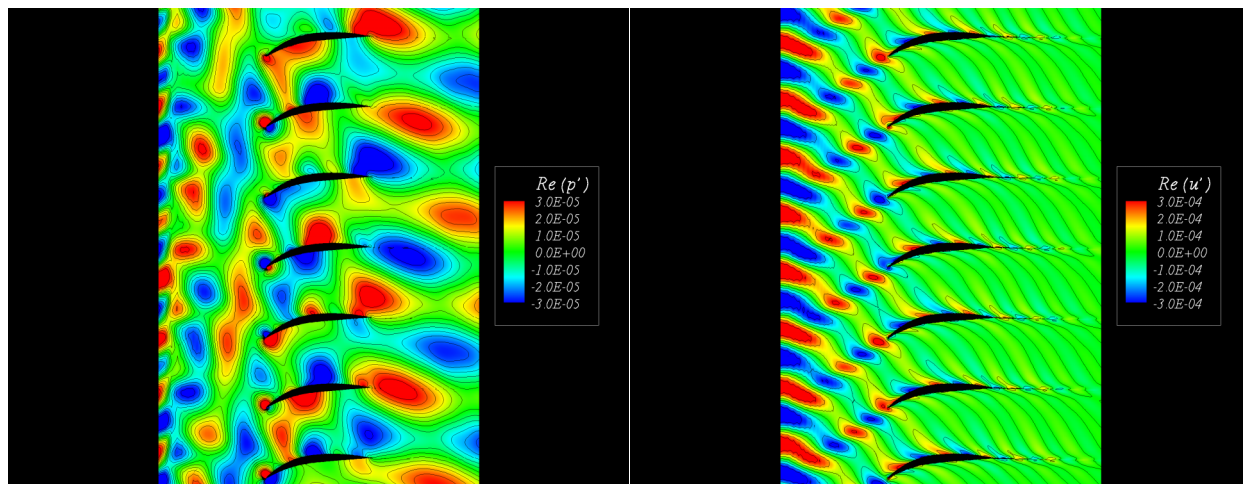
Figure 5. The computed response due to the gust at three times the primary frequency. The pressure response is comprised of two propagating acoustic modes _m_ = +12 and _m_ = -42. The axial velocity perturbation field is due to the _m_ = +66 convective mode.

Computed spectra and mode information

In Tables 3 through 5 pressure levels for select locations in the domain are listed per requirements of the benchmark problem. All levels are expressed in dB using the standard definition of sound pressure level (SPL) given by $20 \log_{10}(p_{\mathrm{rms}} / p_{\mathrm{ref}})$ where $p_{\mathrm{ref}} = 20 \, \mu\mathrm{Pa}$. The complete solution package, including both steady and unsteady parts of the flow, is supplied on the workshop proceedings CD.

Frequency	Suction Side SPL (dB)			Pressure Side SPL (dB)		
	_x/c_ = –0.25	_x/c_ = 0.00	_x/c_ = +0.25	_x/c_ = –0.25	_x/c_ = 0.00	_x/c_ = +0.25
ω	140.7	140.6	141.2	138.0	141.5	140.5
2ω	128.3	118.4	121.0	128.6	121.4	119.5
3ω	104.1	107.5	92.8	104.5	103.0	97.6

Table 3. Acoustic pressure spectrum on the vane.

Frequency	Inflow Plane SPL (dB)			Outflow Plane SPL (dB)		
	_y/c_ = –0.30	_y/c_ = 0.00	_y/c_ = +0.30	_y/c_ = –0.30	_y/c_ = 0.00	_y/c_ = +0.30
ω	111.9	106.6	110.9	109.5	107.8	107.2
2ω	113.2	119.3	116.2	119.6	119.4	119.3
3ω	105.6	105.4	103.7	99.7	98.4	101.5

Table 4. Acoustic pressure spectrum at the inflow and outflow planes.

Frequency	Dominant Acoustic Pressure Modes	Inflow Plane SPL (dB)	Outflow Plane SPL (dB)
ω	$m = +22$	101.3	108.4
	$m = -32$	113.0	83.8
2ω	$m = -10$	116.8	119.2
3ω	$m = +12$	97.6	95.6
	$m = -42$	88.1	98.0

Table 5. Acoustic pressure modal amplitudes at the inflow and outflow planes.

REFERENCES

1. Montgomery, M.D. and Verdon, J.M.: A 3D Linearized Unsteady Euler Analysis for Turbomachinery Blade Rows, Part 1: Aerodynamic and Numerical Formulations; Part 2: Unsteady Aerodynamic Response Predictions. Published in Unsteady Aerodynamics and Aeroelasticity of Turbomachines, T.H. Fransson (ed.), pp. 427-464, Kluwer, Dordrecht, Netherlands, 1998.
2. Verdon, J.M.: Linearized Unsteady Aerodynamic Analysis of the Acoustic Response of Wake/Blade-Row Interaction. NASA/CR–2001-210713, 2001.
3. Prasad, D. and Verdon, J.M.: A Three-Dimensional Linearized Euler Analysis of Classical Wake/Stator Interactions: Validation and Unsteady Response Predictions. International Journal of Aeroacoustics, vol. 1 no. 2, 2002.
4. Envia, E.: Application of a Linearized Euler Analysis to Fan Noise Prediction. Presented at Fan-Gust Workshop, Institute of Sound and Vibration Research, University of Southampton, U.K., 2002. (http://www.isvr.soton.ac.uk/FDAG/fangust/)
5. Janus, J.M.; Horstman, H.Z.; and Whitfield, D.L.: Unsteady Flowfield Simulations of Ducted Propfan Configurations. AIAA Paper 92-0521, 1992.

ANALYTICAL SOLUTION: CATEGORY 4

Philip J. Morris and Anurag Agarwal
Department of Aerospace Engineering
The Pennsylvania State University
University Park, PA 16802, USA

INTRODUCTION

The propagation of sound waves through non-uniform fluid flows can be described by the linearized Euler equations. However, the linearized Euler equations also support instability wave solutions. For parallel mean flows, these are unstable eigensolutions that, for a jet, are the Kelvin-Helmholtz instability waves. These instability waves can completely overwhelm the acoustic-wave solution. Thus, in order to characterize the properties of the acoustic waves alone, it is important to filter out the unwanted instability waves. The objective of this benchmark problem is to develop a numerical scheme that captures only the acoustic wave solution of the linearized Euler equations.

ANALYTICAL SOLUTION

In this problem, a time-harmonic source is embedded in a two-dimensional parallel jet. The linearized Euler equations are solved in the frequency domain after assuming a time-harmonic response to factor out the time dependent terms. The ensuing time-independent equations can be reduced to a single third-order partial differential equation. The third-order differential operator is the well known Lilley wave operator. The first step in the solution procedure is to apply a Fourier transform in the streamwise (x) direction. This reduces the Lilley operator to the compressible Rayleigh operator, which is a second-order ordinary differential operator. The final solution is obtained after integrating the Rayeligh equation in the cross-stream direction (y), and applying the inverse Fourier transform in x. The inverse Fourier transform is obtained by the Method of Steepest Descent. The analytical solution procedure is described in detail in reference 1.

REFERENCES

1. A. Agarwal, P. J. Morris, and R. Mani: Calculation of Sound Propagation in Nonuniform Flows: Suppression of Instability Waves. AIAA J., vol. 41, no. 12, Dec. 2003.

Experimental Results

CATEGORY 5: SOUND GENERATION IN VISCOUS PROBLEMS

PROBLEM 2: SOUND GENERATION BY FLOW OVER A CAVITY

Brenda S. Henderson
NASA Langley Research Center, Hampton, VA 23681-2199, Brenda.S.Henderson@nasa.gov

ABSTRACT

The discrete frequency sound produced by the flow of air at low subsonic speeds over a deep cavity was investigated. A long aspect ratio rectangular cavity with a leading edge overhang that cut off ½ of the cavity opening was placed flush with the top surface of a wind tunnel. The approach flow velocity was maintained at 50 m/s for the benchmark problem although results are also presented for other conditions.   Boundary layer measurements conducted with a single element hotwire anemometer indicated that the boundary layer thickness just upstream of the cavity was equal to 17 mm. Sound pressure level measurements were made at three locations in the cavity: the center of the leading edge wall, the center of the cavity floor, and the center of the trailing edge wall. Three discrete tones were measured at all three locations with corresponding Strouhal numbers (based on cavity opening length and approach flow velocity) equal to 0.24, 0.26, and 0.41. The amplitudes of each tone were approximately equal at each measurement location in the cavity. Measurements made at other approach flow conditions indicated that the approach flow velocity and the boundary layer thickness affected the frequency characteristics of the discrete tones.

INTRODUCTION

The production of discrete frequency sound by the flow of air over a cavity occurs at low subsonic approach flow speeds for many automotive applications such as those associated with car door gaps and sunroofs, and at high subsonic or supersonic approach flow speeds for many aeronautical applications. The flow is often characterized by complex oscillations of the shear layer, the production of discrete tones as well as broadband noise, and wave motion (longitudinal or transverse) within the cavity. The flow and acoustic phenomena are often broadly categorized by the cavity length (l) to depth (D) ratio, with values of l/D below one indicating deep cavities and values of l/D greater than one indicating shallow cavities (refs. 1 and 2). Experiments have shown (ref. 3) that the shear layer oscillations associated with shallow and deep cavities are fundamentally different. The cavity wave motion may also be significantly different for these two cases with longitudinal waves occurring for deep cavities and transverse waves occurring for shallow cavities. While the resulting discrete frequencies produced by shallow cavities are often well described by Rossiter's equation (ref. 4), the frequencies produced by deep cavities may significantly deviate from the values predicted by this early model. Helmholtz type resonances have also been observed for some cavity geometries.

The broad range of flow and geometric parameters affecting the production of cavity tones makes the development of general flow and sound production models somewhat difficult. Experimental investigations have shown (ref. 5) that the amplitude and frequency of discrete tones are affected by the type of boundary layer (laminar or turbulent) and the boundary layer thickness. The type of boundary layer also affects the appropriate scaling parameters relating the boundary layer thickness and the Strouhal number of the discrete tones. The many parameters governing the cavity mouth geometry can also have a significant impact on the resulting acoustic production and flow field characteristics (refs. 6 and 7).

The cavity problem chosen for the 4th Computational Aeroacoustics Workshop on Benchmark Problems is one somewhat resembling the door gap of an automobile although slightly larger dimensions have been used for experimental purposes. The approach flow is at low subsonic speeds but well above that associated with an automobile. The purpose of the higher velocity is to ensure that a strong acoustic resonance is produced by the numerical models and in the experiments. The geometry of the cavity mouth is similar to that of the door gap and also introduces additional complication to the problem that may result in multiple types of flow resonances.

BENCHMARK PROBLEM STATEMENT

Air flows over the cavity shown below with a mean approach flow velocity of 50 m/s. The boundary layer that develops over the flat plate is turbulent with a thickness of 14 mm at the entrance to the cavity. Calculate the power spectra at the center of each cavity wall and the center of the cavity floor.
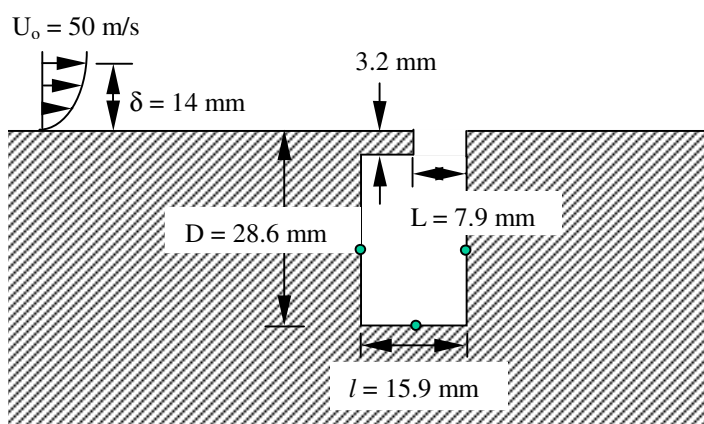
Figure 1. The cavity geometry used for the benchmark problem. The microphone measurement locations are indicated by a ● .

EXPERIMENTS

The experiments were conducted in the 0.46 m x 0. 46 m test section of the recirculating wind tunnel at Kettering University. The tunnel was equipped with silencers before and after the fan.

The Plexiglas cavity shown in Fig. 2 was placed along the upper surface of the wind tunnel and spanned the entire tunnel cross section. End caps were placed at the outer edges of the cavity so that only the cavity mouth remained open to the flow. Condenser microphones, 6.35 mm in diameter, were mounted in the center of the cavity leading edge wall, the center of the cavity trailing edge wall, and the center of the cavity floor at a single cavity cross-section. The resulting power spectra were obtained with an 8 Hz bandwidth FFT.

Boundary layer measurements were made with a single element hot wire anemometer traversed vertically near the wind tunnel top surface at different axial locations in the test section. A continuous test section surface (no cavity present) was used during the boundary layer studies. Although the benchmark problem statement called for a boundary layer thickness of 14 mm, the boundary layer studies indicated that the thickness of the boundary layer at a location corresponding to the cavity entrance was 17 mm when the approach flow velocity was 50 m/s. Additional acoustic measurements were made for a second axial position in the test section 65 cm upstream of the original cavity location. The boundary layer was thinner in this region of the test section. Measurements made at the second location served to determine the sensitivity of the acoustic radiation to changes in the boundary layer thickness.

(a)

(b)
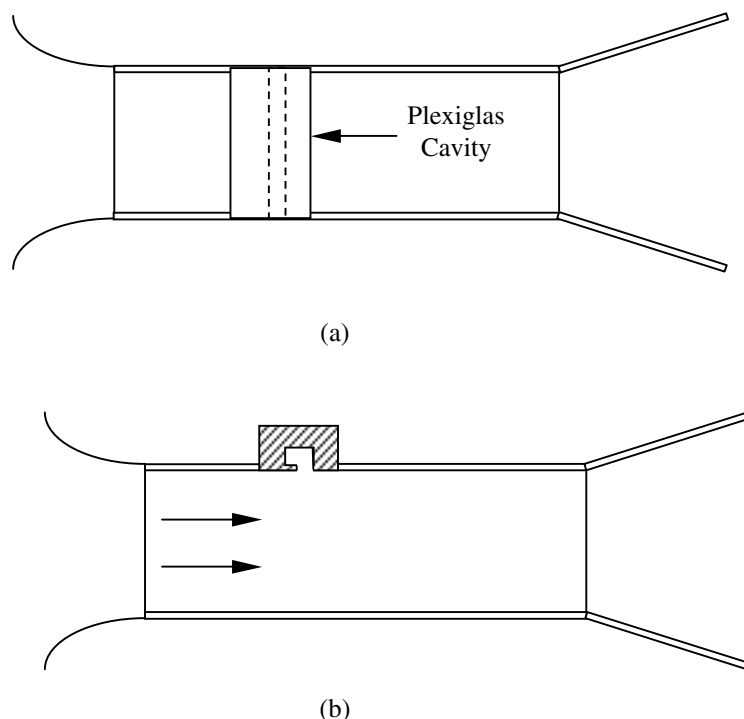
Figure 2. Schematics of the wind tunnel test section with the cavity showing (a) the top view and (b) the side view.

RESULTS

The results for the benchmark problem as well as results for the same cavity with different approach flow conditions will be presented in the following two sections. The additional results are intended to further clarify the sensitivity of the resulting acoustic radiation to changes in the approach flow.

Benchmark problem

The power spectra obtained from the cavity measurements are shown in Fig. 3. The corresponding locations of the microphones are also indicated on the plot. Three discrete peaks with frequencies equal to 1504 Hz, 1624 Hz, and 2616 Hz are observed in the spectra. The corresponding Strouhal numbers are 0.24, 0.26, and 0.41, respectively, where the Strouhal number is given by $\dfrac{fL}{U_o}$. The sound pressure levels of the discrete peaks are approximately equal at each location in the cavity cross-section.

It is not possible to determine the nature of the flow resonance associated with each discrete tone in Fig. 3 from the spectral data. However, it is possible to perform some rough calculations and compare with other published data to determine the likely type of resonance associated with the three peaks. If a cavity mode (longitudinal) coupled with the shear layer oscillations in the cavity mouth, the first cavity mode would result in a resonant wavelength equal to four times the cavity dimension, D, or a resonance frequency of 3016 Hz. The second mode would result in a resonance frequency of 1508 Hz, a value remarkably close to that of the lowest discrete frequency in Fig. 3. The second peak in the spectrum, 1624 Hz, produces a Strouhal number consistent with that measured by De Metz and Farabee (ref. 5) for cylindrical deep cavities with approach flow velocities similar to those used in the present investigation. In the experiments of De Metz and Farabee, the tone was attributed to the second cavity resonance mode although phase measurements within the cavity were not made in the experiments. It is possible that the tone at 1624 Hz is associated with a longitudinal cavity resonance for an effective depth less than 28.6 mm. The

reduction in effective cavity depth could be due to the complicated cavity mouth geometry and the complicated shear layer oscillations in this region of the flow.

The tone at 2616 Hz is most likely associated with an edgetone type resonance. The feedback criterion applied to the cavity (refs. 8 and 9) is given by

$$\frac{N+p}{f} = \int \frac{dL}{u_{con}} + \frac{L}{c},$$

where N is an integer, p is a fraction accounting for the delay between a particular phase of the flow disturbance and the resulting acoustic wave (equal to ¼ for the edgetone), u_{con} is the convection velocity of the shear layer disturbances, and c is the speed of sound. The above equation assumes that the sound is produced at the trailing edge of the cavity. The first term on the right hand side of the equation accounts for the travel time of the shear layer disturbances while the second term accounts for the propagation time of the acoustic wave from the sound source to the leading edge of the cavity. Since the acoustic wavelengths are large compared to L, the second term may be neglected. Assuming that N is equal to one and a value of ¼ is used for p, the resulting calculated acoustic frequency is equal to 2610 Hz when a convection velocity of $0.33U_o$ is used for the shear layer disturbances. The value for the convection velocity was obtained from the measurements of De Metz and Farabee. The calculated value is quite close to the measured frequency of the third discrete peak in the spectra of Fig. 3.

Although Helmholtz type resonance has been observed in many cavity flows, calculations for the cavity geometry used in the benchmark problem indicate that frequencies close to 1000 Hz would be observed in the spectrum for this type of resonance. All of the measured discrete frequencies are all well above this value. Additionally, if the cavity displayed three-dimensional affects, it would be possible to obtain wavelengths on the order of the width of the wind tunnel test section (0.46 m). All of the measured discrete frequencies in the spectra correspond to wavelengths much shorter than this dimension. It is, therefore, unlikely that either of these types of resonances were present in the flow. However, additional measurements are necessary to determine the exact origin of each tone in the spectra.
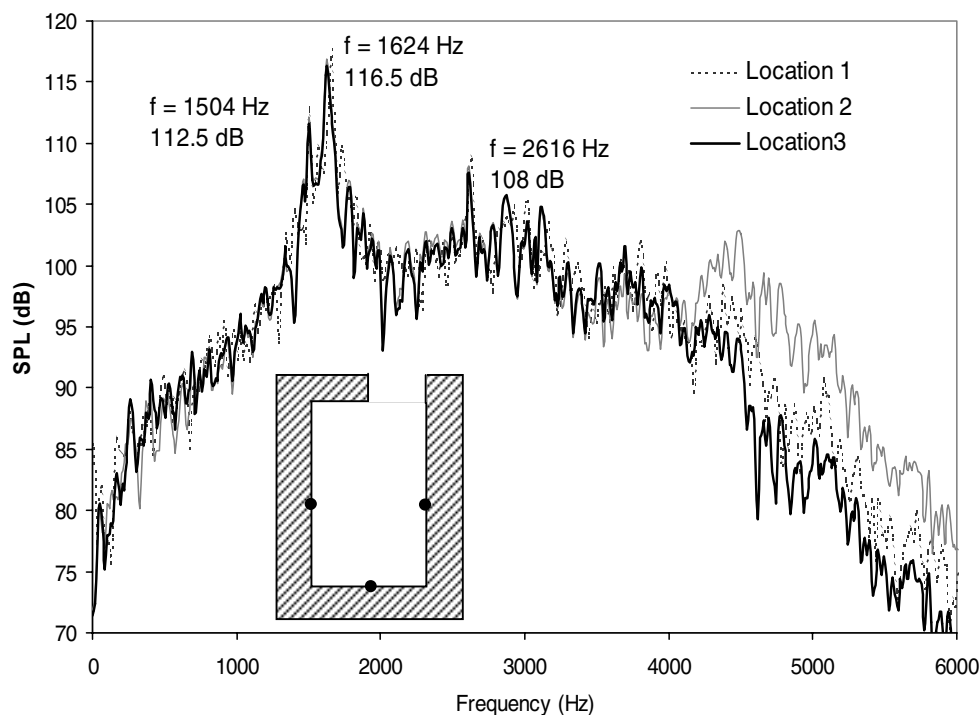
Figure 3. The power spectra obtained at the three microphone locations indicated in the figure.

Results at other approach conditions

Cavity sound pressure level measurements were made for other approach flow velocities with the cavity located at the same axial location in the test section as that used in the benchmark problem. Although sound pressure level measurements were made at the three microphone locations indicated in Fig. 1, results will only be presented for one microphone location since similar spectra were obtained at all three locations. The power spectra shown in Figs. 4 (a) and (b) were obtained for approach flow velocities equal to 45 m/s and 60 m/s, respectively. By comparing Figs. 3, 4 (a), and 4 (b), it can be seen that multiple discrete peaks are observed in the spectra obtained with approach flow velocities between 45 and 50 m/s, while and a single dominant peak is present in the spectrum obtained at an approach flow velocity of 60 m/s. When a single discrete peak is present, the sound pressure level of the tone is much higher than that associated with the dominant peak of the spectra when multiple tones occur. This result would indicate that the energy is divided among the resonant modes when multiple tones are produced. This could have implications for computational results that do not properly reproduce all of the resonance modes observed in the experiments.

(a)

(b)
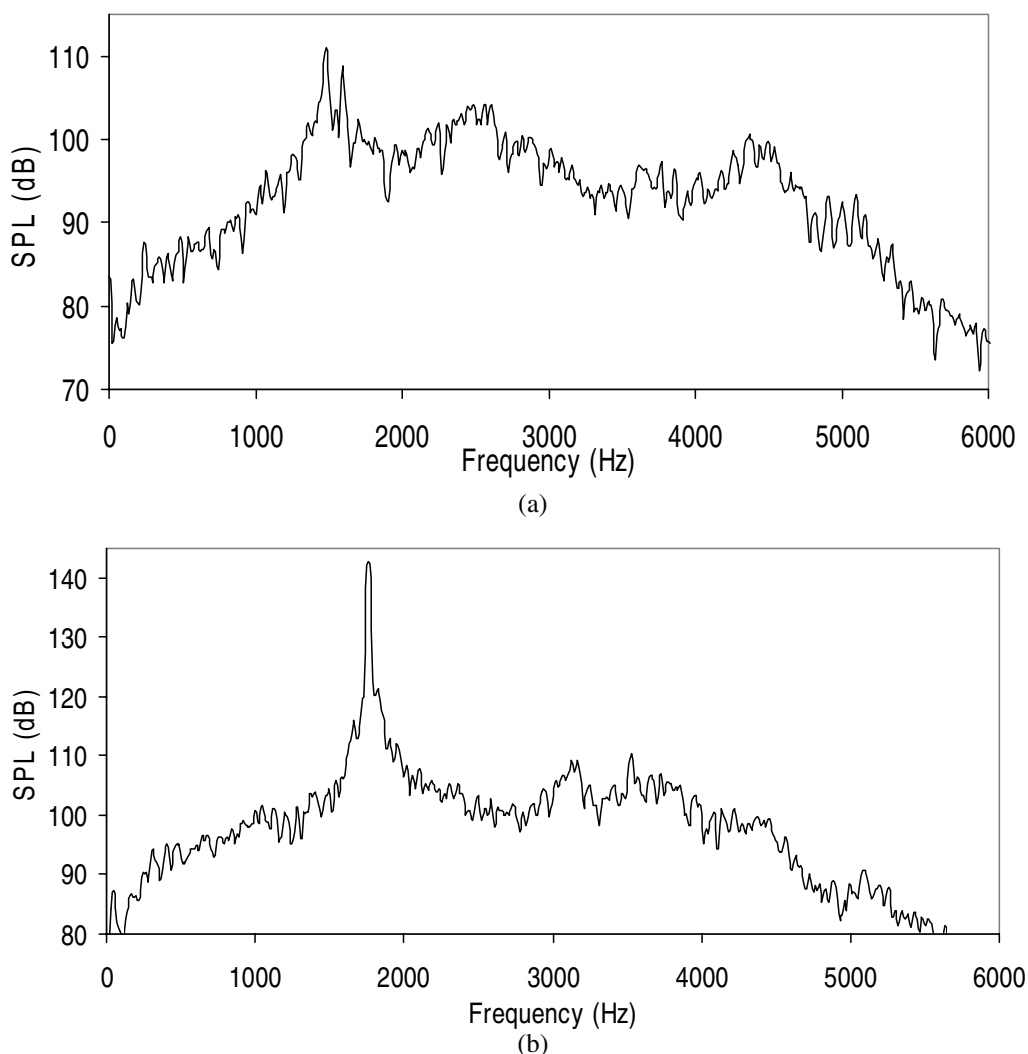
Figure 4. The power spectrum obtained in the cavity for approach flow velocities equal to (a) 45 m/s and (b) 60 m/s.

The power spectrum in Fig. 5 was obtained when the cavity was moved 65 cm upstream in the test section from the location used in the benchmark problem. At this location in the tunnel, the boundary layer was thinner than 17 mm. The multiple peaks in the spectra of Fig. 3 are no longer present for the thinner boundary layer although the approach velocity is equal to 50 m/s for both cases. Additionally, the peak sound pressure level in Fig. 5 is greater than the peak sound pressure level in Fig. 3 indicating that boundary layer thickness affects both the frequency characteristics and the amplitude of the dominant peak in the spectrum. De Metz and Farabee (ref. 5) found that the Strouhal number for the dominant tone was affected by the normalized boundary layer thickness where the length of the cavity mouth was used for the normalization. The results are consistent with the present experiments which indicate that the Strouhal number increases with decreasing boundary layer thickness. The sensitivity of cavity tones to boundary layer changes could have a significant impact on numerical models used to represent this type of flow.
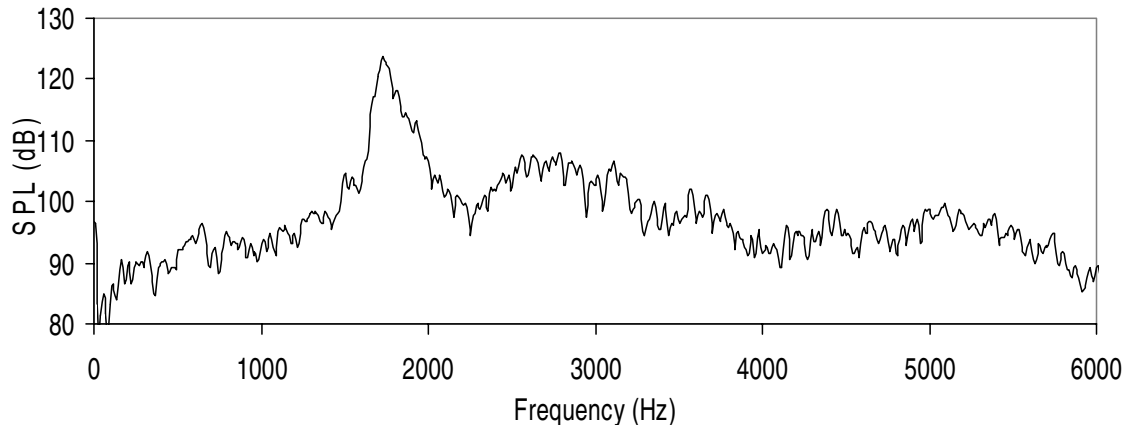
Figure 5. The power spectrum obtained in the cavity for an approach flow with a thin boundary layer and a velocity equal 50 m/s.

DISCUSSION AND RELEVANT CONSIDERATIONS FOR COMPUTATIONAL COMPARISONS

The intent of benchmark problems is to provide a means to test the ability of numerical schemes to properly predict flow fields and acoustic radiation. As the flow fields become more complicated, experimental data may be the only results available for comparison. However, it is important to understand the experiments and the sensitivity of the flow field to changes that may occur during the experiment investigation. In many cases, the numerical problem may be far more "perfect" than the real world experiment. In other cases, the models used in the numerical schemes may lead to significant numerical errors that cause the results to deviate significantly from that observed in experiments. Emphasis should be placed on the ability of the numerical scheme to predict trends observed in experiments.

The ability to properly represent the boundary layer in the experiments and the numerical models was perhaps the most difficult problem faced in this benchmark problem. Any small experimental error in the boundary layer thickness measurement could easily be on the order of a significant fraction of the cavity mouth dimension due to the small value of L. Additionally, the introduction of the cavity to the test cell could result in small imperfections that lead to a thicker boundary layer than that measured for the test section without the cavity. The ability to properly represent the boundary layer in a numerical scheme also presents a problem for this type of flow. Experiments have shown that the tonal characteristics associated with cavities introduced in flows with laminar boundary layers are significantly different from those associated with cavities introduced in flows with turbulent boundary layers. It is only reasonable to expect that calculated frequency characteristics will also be affect by numerical turbulence and boundary layer models.

For this type of flow, it may be sufficient to have a numerical scheme that predicts trends observed in the experimental data. Since it is often difficult to obtain exact experimental values across facilities, it may be unrealistic to expect an exact comparison between experimental data and numerical results. In the present experiments, the peak sound pressure levels were quite similar at all three locations in the cavity for a given approach flow condition. As the approach flow velocity increased, multiple tones disappeared and a single discrete

peak was present in the acoustic data. If multiple tones were present in the spectra associated with a thick boundary layer, thinning the boundary layer tended to lead to a single discrete peak. The Strouhal numbers for the dominant peak were between 0.26 and 0.27 for all flow conditions investigated. When the approach flow velocity was equal to 50 m/s, the measured peak sound pressure level was between 116 dB and 123 dB. Perhaps a successful numerical scheme is one that that successfully predicts the data trends noted above. A final test of the scheme should involve comparing the computed flow field data to that measured by techniques such as particle image velocimetry.

REFERENCES

1. Rockwell, D.; and Naudasher, E.: Self-sustaining oscillations of flow past cavities, Transactions of ASME, 100, 1978, pp. 152 – 165.
2. Blake, W.: Mechanics of Flow-Induced Sound and Vibration, Academic Press, New York, NY, 1986, pp. 138 – 149.
3. Forestier, N.; Jacquin, L.; and Geoffroy, P.: The mixing layer over a deep cavity at high-subsonic speed, J. Fluid Mech., 475, 2003, pp 101 - 145.
4. Rossiter, J. E..: Wind-tunnel experiments on the flow over rectangular cavities at subsonic and transonic speeds, ARC R & M No. 3438, 1966.
5. De Metz F. C.; and Farabee, T. M.: Laminar and turbulent shear flow induced cavity resonances, AIAA-P-77-1293, 1977.
6. Dequand, S; Luo, X.; Willems, J.; and Hirschberg, A.: Helmholtz-like resonator self-sustained oscillations, Part 1: acoustical measurements and analytical models, AIAA J., 41, 2003, pp. 408 –415.
7. Dequand, S., et al.: Helmholtz-like resonantor self-sustained oscillations, part 2: detailed flow measurements and numerical simulations, AIAA J., 41, 2003, 416 – 423.
8. Powell, A.: On edge tones and associated phenomena, Acustica, 3, 1953, pp. 233 – 243.
9. Powell, A.: On the edgetone, J. Acoust. Soc. Am., 34, 1961, pp. 902 – 906.

Contributions of Workshop Participants

CASCADE-GUST-INTERACTION PROBLEM ANALYSIS BASED ON LINEAR CFD CALCULATIONS

Antonio G. Escribano, Adolfo Serrano, and Carlos Vasco
Industria de Turbo Propulsores, S.A., 28830, Madrid, Spain

ABSTRACT

A two-dimensional (2–D) cascade-gust-interaction problem, known as the Fourth Computational Aeroacoustics (CAA) Workshop on Benchmark Problems, Category 3, Problem 2 (ref. 1), is solved using a frequency domain unstructured Euler solver. The numerical scheme uses a second-order central spatial discretization, and the integration in time is done using a fifth-stage Runge-Kutta scheme. Two-dimensional nonreflective boundary conditions are used at the computational domain inlet and outlet. Unsteady results for three different harmonics are provided, and a mesh sensitivity analysis is carried out to determine the grid resolution required in the solver for this type of calculation.

The code, known as Mu^2s^2T-L, has been developed at Industria de Turbo Propulsores, SA (ITP), and is used in production to compute turbomachinery unsteady flows due to either vibrating blades or vortical/potential gust interactions between adjacent bladerows. The Mu^2s^2T-L solver has been extensively validated against several 2–D semi-analytical methods (ref. 2) where the fan/turbine blade geometries are replaced by flat plates. In this work, Mu^2s^2T-L code's ability to deal with complex geometries like a fan blade is tested, and its results are compared with the benchmark solution in a companion paper (ref. 1).

INTRODUCTION

Airfoil-wake interaction is one of the major sources of noise in aircraft engines. It is certainly the most important in turbines, and in certain operating conditions, like approach, it is the dominant source in fan noise. This noise source is still a phenomenon not fully understood and difficult to simulate with numerical tools. The great demand for quieter technology, imposed by the actual noise legislation, is pushing industry to improve the accuracy of current noise-prediction tools and to understand the physical mechanisms involved in noise-generation processes.

SOLVER DESCRIPTION

In Mu^2s^2T-L, unsteady results are computed as small linear perturbations of the mean steady flow. First, a nonlinear solver, known as Mu^2s^2T, is used to get the mean steady flow. Then, the linear solver is used to compute the unsteady perturbations in the frequency domain.

Both solvers, Mu^2s^2T and Mu^2s^2T-L, are Euler/Navier-Stokes hybrid unstructured and edge-based solvers that are based on the same principles. The numerical scheme uses a second-order central spatial discretization with a blend of second- and fourth-order artificial viscosity terms, with the standard scalar formulation based upon that of Jameson et al. (ref. 3). Time integration uses a fifth-stage Runge-Kutta scheme. The analytically exact 2–D nonreflecting boundary conditions based on Giles (ref. 4) are used at the inlet/outlet domain to prevent spurious reflections.

Two-dimensional hybrid unstructured grids are used in the calculations, and they are generated using an in-house mesh generator that fills the computational domain with triangles using a Delaunay approach (ref. 5).

Several acceleration techniques are used in the calculations; the multigrid technique being the most effective. In particular, in Euler calculations, a computational time speed up factor of about 10 times is achieved.

The Mu^2s^2T-L ability to cope both aeroelastic and aeroacoustic problems has been extensively tested and its capability to reproduce analytical results in simple geometries, like flat plates, and in complex geometries, like turbine blades, is demonstrated in reference 2.

PROBLEM DESCRIPTION

To properly define a 2–D gust-interaction problem, three set of data are required:

Geometry: The geometry definition is given in the ASCII file (ref. 1). Figure 1 shows the airfoil shape along with the inflow/outflow plane locations. A single passage computational domain (fig. 1) is used in the calculations for both the steady flow calculation, where the flow is considered periodic at every passage, and for the unsteady linear calculations, where a constant phase difference between adjacent airfoils is considered.

Boundary conditions for the mean steady calculations: As unsteady noise levels will be presented in decibels, physical magnitudes, rather than dimensionless magnitudes, are required to set up the required mean flow pressure level.

The ones used in the calculations are

$$P_{0\ inlet} = 101353\ Pa \qquad\qquad P_{exit} = 93244.7\ Pa$$
$$T_{0\ inlet} = 288.3\ K \qquad\qquad \gamma = 1.4$$
$$\alpha_{inlet} = 36° \qquad\qquad C_p = 1008\ Jul/KgK$$

where $P_{0\ inlet}$ inlet is the total pressure, $T_{0\ inlet}$ is the inlet total temperature, α_{inlet} is the inlet flow angle, P_{exit} is the exit static pressure, C_p is the specific heat at constant pressure, and γ is the specific heat ratio.
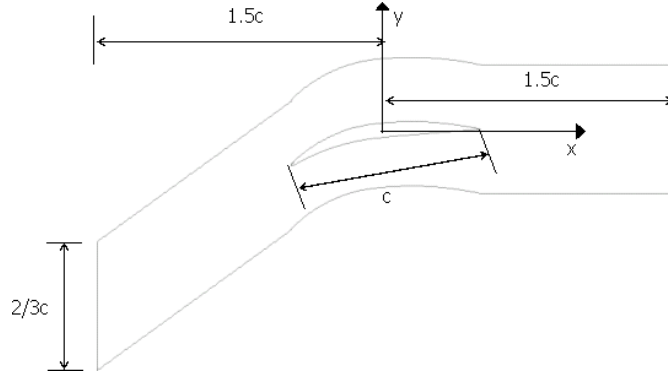
Figure 1.—Geometry and calculation domain.

Boundary conditions for the unsteady linear runs: In gust-blade interaction, the parameters required to define the linear calculations are the ones that define incoming vorticity wave at the inlet plane. These are

$$\vec{u}'_g = \left\{ a_1 \cos\left(k_{y,g}\, y - \omega t\right) + a_2 \cos\left(2\left(k_{y,g}\, y - \omega t\right)\right) + a_3 \cos\left(3\left(k_{y,g}\, y - \omega t\right)\right) \right\}\vec{e}_\beta \qquad [1]$$

$$\vec{e}_\beta = \cos\beta\,\vec{e}_x - \sin\beta\,\vec{e}_y \qquad [2]$$

where $\omega = n \cdot 3\pi/4$ is the reduced frequency normalized by the airfoil chord divided by the inlet speed of sound (n is the harmonic number), $k_{y,g} = n \cdot 11\pi/9$ is the transverse wave number normalized by the airfoil chord, and the gust amplitudes normalized by the inlet speed of sound are $a_1 = 5 \cdot 10^{-03}$, $a_2 = 3 \cdot 10^{-03}$ and $a_3 = 7 \cdot 10^{-04}$, for the first, second, and third harmonic, respectively.

It is important to note that as pressure and density fluctuations cannot exist in pure 2–D vorticity waves, the wake propagation angle β is fixed once the reduced frequency and the transverse wave number are specified. For the conditions given above, the wake propagation angle turns out to be $\beta = 44°$.

STEADY RESULTS

Steady results are presented in figure 2 where the Mach number distribution on the airfoil surface is shown. The Mach number spike around the leading edge region in figure 2 indicates that for the conditions defined above, the airfoil is facing positive incidence. Higher grid densities around this area are required to properly capture these local mean-flow gradients.
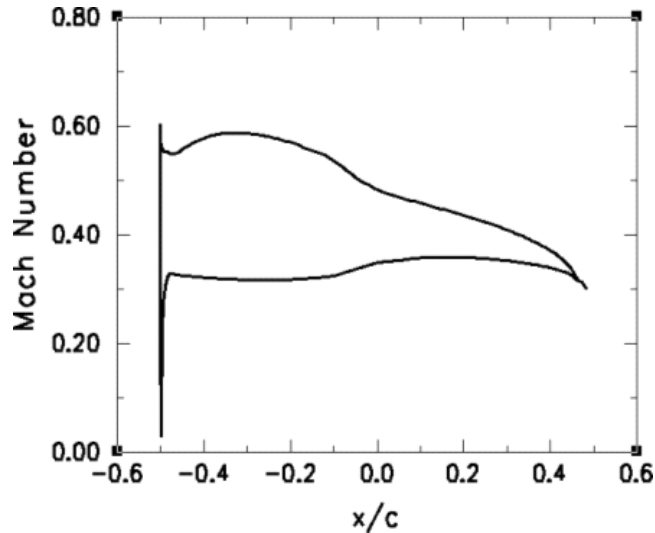
Figure 2.—Mach number distribution on the airfoil number.

UNSTEADY RESULTS

Unsteady pressure amplitude (rms in decibels) on the airfoil surface and in the upstream and downstream regions are presented in this section. Figure 3 shows the unsteady pressure distribution on the airfoil for the three harmonics considered. As the harmonic number increases, the incoming vorticity wave amplitude is decreased and the reduced frequency is increased, and as a consequence, the unsteady pressure levels on the airfoil surface decrease from the first to the third harmonic.
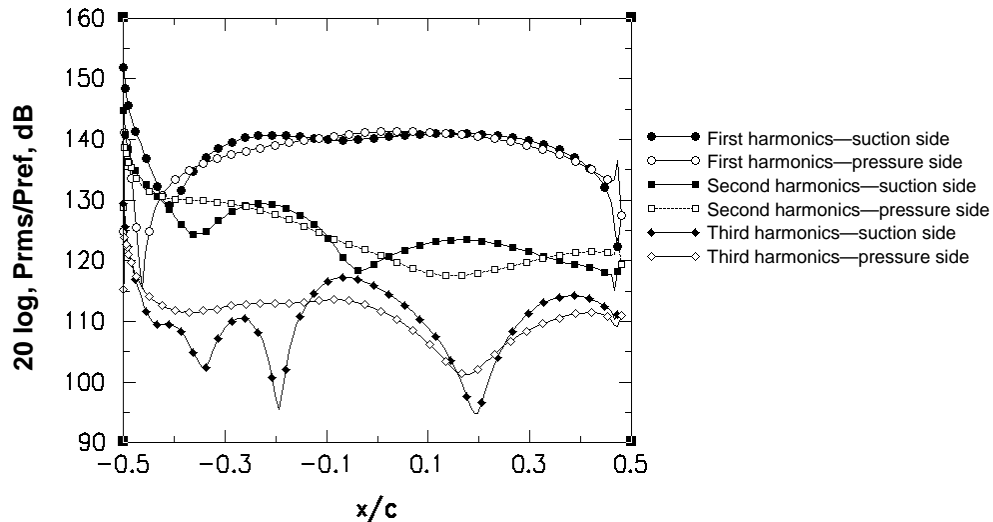
Figure 3.—Unsteady pressure distribution over the vane for the three harmonics.

Figure 4 shows the acoustic field radiated upstream and downstream by means of the unsteady pressure distribution at the inflow and outflow planes. It can be seen that despite being the first harmonic, the one with higher unsteady pressure levels on the airfoil, the second harmonic is the one with the higher noise levels at the inflow/outflow planes.
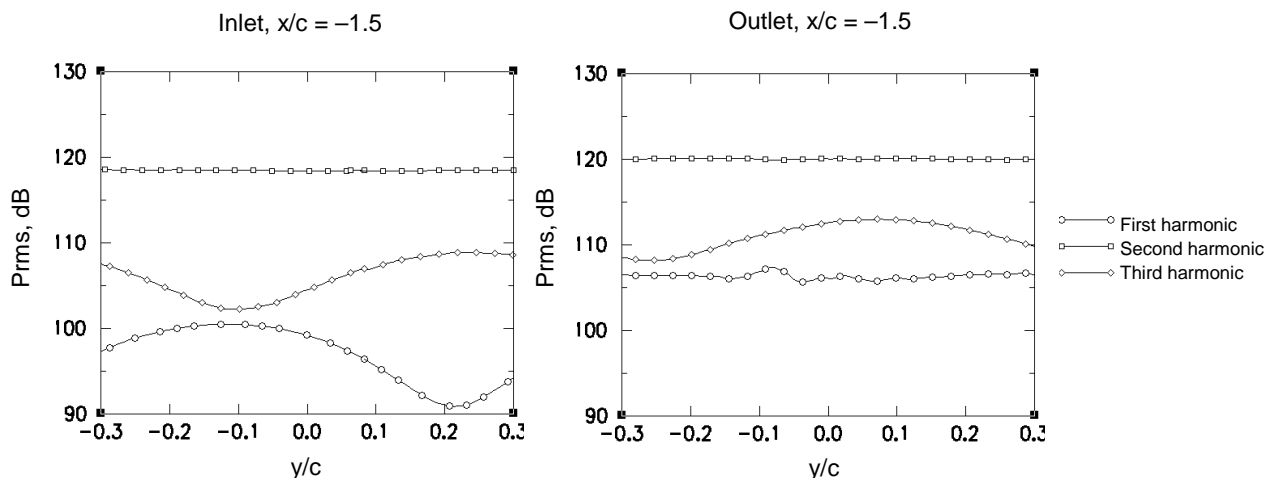
Figure 4.—Unsteady pressure distributions at the inlet/outlet calculation domain for the three harmonics.

This can be easily explained when the unsteady pressure field in the upstream and downstream gaps is analyzed in terms of acoustic modes. According to Tyler and Sofrin (ref. 6) the upstream and downstream acoustic propagation can only take place in certain transverse wave numbers (acoustic modes) given by the following expression:

$$k_y = nk_{y,g} - k\frac{2\pi}{d/c} \qquad [3]$$

where the transverse wave numbers are normalized by the airfoil chord, n is the harmonic number, d/c is the pitch-to-chord ratio, and k is any integer. Depending on its wave number, reduced frequency, and mean-flow Mach number, the different acoustic modes will propagate (cut-on modes) or decay (cut-off modes) in the upstream and downstream gaps. Table 1 lists the different acoustic modes that contain most of the acoustic pressure for the three harmonic calculations and its cut-on/cut-off condition. Higher-order harmonics content very little acoustic pressure and they are not considered. Unsteady pressure amplitudes smaller than 0.2 Pa (80 dB) at domain inlet/outlet are not considered.

From table 1, all the acoustic modes corresponding to the first harmonic calculation are in cut-off condition, the second harmonic has one cut-on mode, and the third harmonic has two different cut-on propagating modes. Therefore, the acoustic modes corresponding to the second and third harmonics (listed in table 1) will keep their amplitude from the leading edge (or trailing edge) to the inlet (or outlet) domain, while the acoustic mode amplitudes corresponding to the first harmonic will decay away from the airfoil. For this reason, the first harmonic calculation inflow/outflow pressure amplitudes are lower than the ones in the second and third runs, despite having higher unsteady pressure levels on the airfoil (fig. 3).

Tyler and Sofrin acoustic modes		k_y	Upstream	Downstream
n	k			
1	0	3.84	Cut-off	Cut-off
1	1	−5.59	Cut-off	Cut-off
2	1	−1.75	Cut-on	Cut-on
3	1	2.09	Cut-on	Cut-on
3	2	−7.33	Cut-on	Cut-on

Table 1. —Tyler and Sofrin acoustic modes and its cut-on/cut-off condition.

Figure 5 shows the propagation of the different acoustic modes along the gaps for the three harmonic calculations. As expected, cut-on modes (corresponding to the second and third harmonics) have a constant

amplitude in the gaps away from the leading- and trailing-edge. In the leading and trailing edge regions, the lack of uniformity in the steady mean flow leads to nonuniform cut-on mode amplitudes. Cut-off mode pressure amplitudes should decay exponentially within the gaps (linearly in a logarithmic scale, dB), and this is demonstrated in figure 5 (top).

Figure 5 also shows that the nonreflecting boundary conditions work properly in these calculations as there are no spurious reflections at the inflow and outflow planes.

Figure. 5—Acoustic modes propagation at the upstream and downstream gaps.

Finally, in the benchmark problem definition (ref. 1) the unsteady pressure amplitude (rms in decibels) was requested at certain locations to enable code-to-code comparison, these values are listed in table 2.

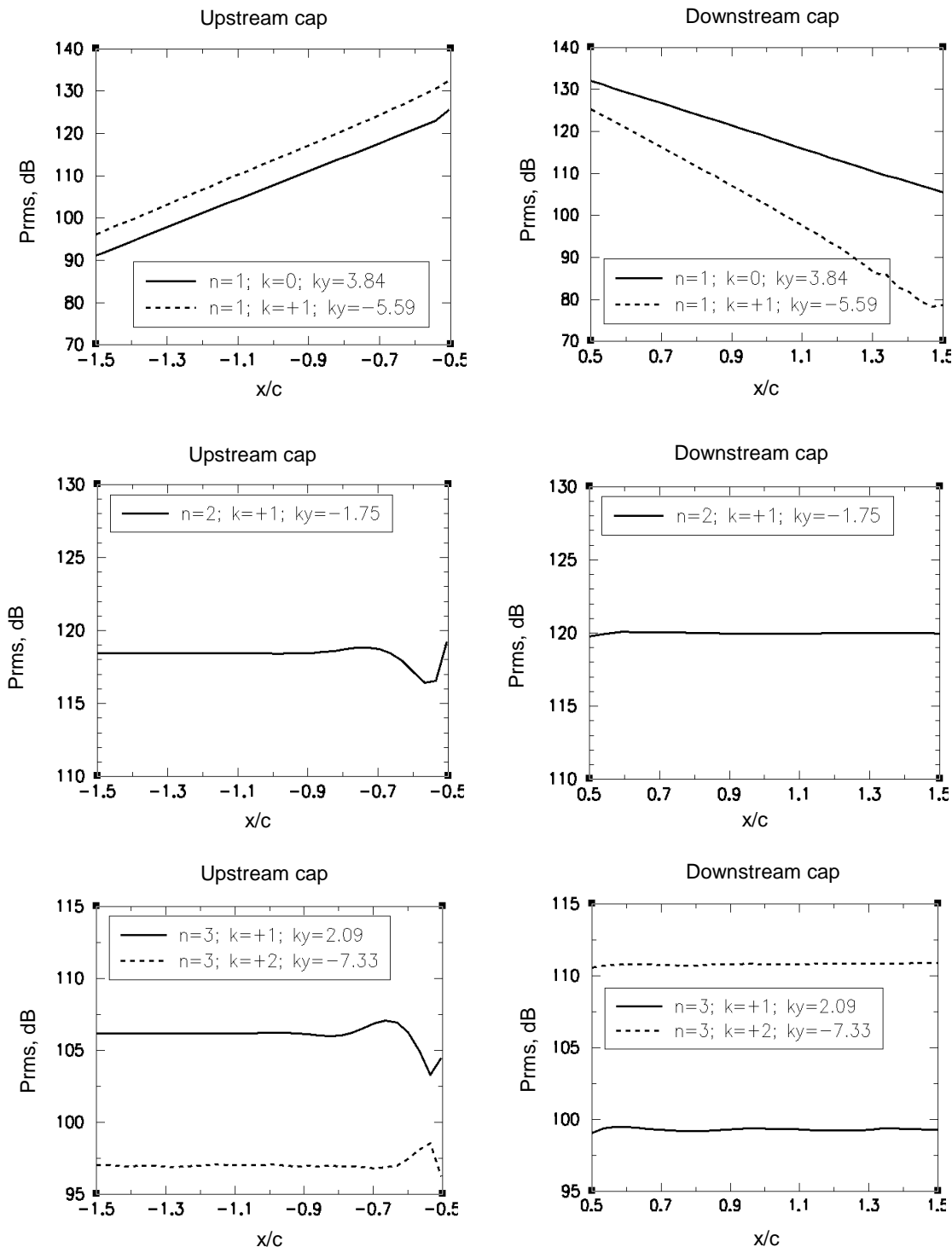| x/c = −0.25	First harmonic	Second harmonic	Third harmonic	x/c = 0	First harmonic	Second harmonic	Third harmonic	x/c = 0.25	First harmonic	Second harmonic	Third harmonic
Pressure side	138.2	128.8	112.9	Pressure side	141.2	121.0	111.9	Pressure side	139.8	118.9	106.1
Suction side	140.4	129.2	109.8	Suction Side	140.3	119.7	115.6	Suction side	140.5	122.6	106.3

y/c = −0.3	First harmonic	Second harmonic	Third harmonic	y/c = 0	First harmonic	Second harmonic	Third harmonic	y/c = 0.3	First harmonic	Second harmonic	Third harmonic
x/c = −1.5	97.3	118.5	107.5	x/c = −1.5	99.2	118.4	104.5	x/c = −1.5	94.3	118.5	108.6
x.c = 1.5	106.5	120.0	108.6	x/c = 1.5	106.1	120.0	112.6	x/c = 1.5	106.6	120.0	109.8

Tyler and Sofrin acoustic modes		k_y	Pressure amplitude (dB) x/c = −1.5	Pressure amplitude (dB) x/c = 1.5
n	k			
1	0	3.84	91.1	106.4
1	1	−5.59	96.0	79.5
2	1	−1.75	118.4	120.0
3	1	2.09	106.1	99.3
3	2	−7.33	97.0	110.9

Table 2.—Pressure amplitudes on the airfoil surface (top), pressure amplitude on the inflow/outflow boundaries (middle), and acoustic mode amplitudes on the inflow/outflow boundaries (bottom).

GRID SELECTION CRITERIA AND MESH SENSITIVITY ANALYSIS

As mentioned before, to get the unsteady results for the three different harmonics, we need to perform four different runs, one to get the steady flow (nonlinear solver), and one for each harmonic of the wake (linear solver). Let us discuss the grid requirements for each of these calculations. For the steady flow calculation, the strongest gradients are usually around the leading and trailing edge regions and therefore the main grid requirement will be to have a sufficient grid point concentration around these areas. This is illustrated in figure 6 (left). On the other hand, for the linear calculations, the unsteady flow made of acoustic and vorticity waves has a uniform distribution all over the computational domain, and the preferred grid will be a constant density, like the one shown in figure 6 (middle). To meet both requirements, both type of calculations (steady nonlinear and unsteady linear) are run on the same grid. An example of this type of grid is shown in figure 6 (right).

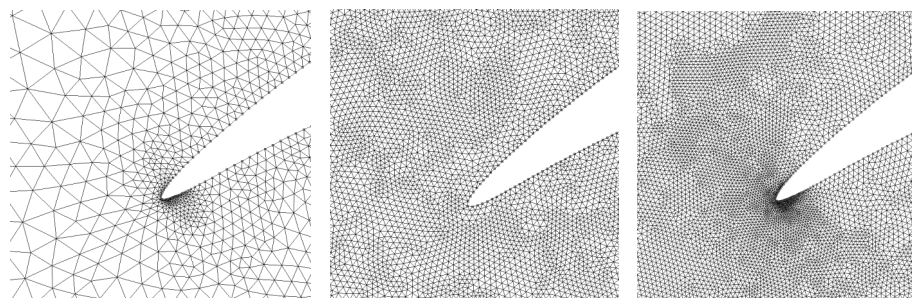**Figure 6.—Different grid point distribution types.**

Unstructured grids are always difficult to define as the grid point locations depend on the algorithm used to generate the triangles. For this reason, we will just define the mean grid density (away from the leading and trailing edge regions. More grid selection criteria for these types of problems are given in reference 7. The requirement to

select the mean grid density will be to have a sufficient number of points per wavelength to solve the smallest wavelength of interest in the problem. The wavelengths of interest can be easily calculated and are shown in table 3. It can be seen that for each harmonic, the smallest wavelength, and therefore the most restrictive, is always the one that corresponds to the vorticity waves.

Harmonic number n	Vorticity wave		Tyler and Sofrin acoustic modes		
	$\lambda_{y,g}$	$\lambda_{x,g}$	k	λ_y	λ_x
1	1.636	1.694	0	1.636	−8.273
			1	−11.250	−2.925
2	0.818	0.847	1	−3.600	1.320
3	0.545	0.565	1	3.000	1.038
			2	−0.857	1.548

Table 3.—Wavelengths of interest (normalized with the airfoil chord).

As the vorticity wave determines the grid resolution, we will focus on the loss of amplitude of the vorticity wave as a function of the number of grid points per vorticity wavelength, illustrated in figure 6. On the left-hand side of figure 7, the loss of vorticity wave amplitude per vorticity wavelength is shown for different grid densities. Note that every point in this plot corresponds to a computation in a different grid, i.e., for every number of points per wavelength (axial location in fig. 7), we show results for three different harmonics, and as the second harmonic vorticity wavelength is half the first harmonic (the third harmonic is three times smaller), the grid density for the second harmonic calculation is about four times larger than the first harmonic calculation (nine times larger for the third harmonic run). Figure 7 (left) shows that when the number of points per wavelength is too small, like 20, the loss of vorticity amplitude can go up to 10 percent. For a number of points per wavelength of 40 and larger, the loss of amplitude is smaller than 1 percent, which is considered acceptable. Figure 7 (right) shows the loss of vorticity amplitude in the inlet gap (approximately 1.5, 3, and 4.5 axial wavelengths for the first, second, and third harmonics, respectively), and therefore, cumulative losses of vorticity amplitude per wavelength are shown in this figure. The grid density selection criteria is chosen to have a cumulative loss of vorticity amplitude less than 1 percent in the inlet gap, therefore, the grid densities chosen are 40 points per wavelength for the first harmonic run and 120 points for the second and third harmonic calculations. With this criteria the total number of grid nodes are about 9000, 90 000, and 360 000 for the first, second, and third harmonics, respectively.
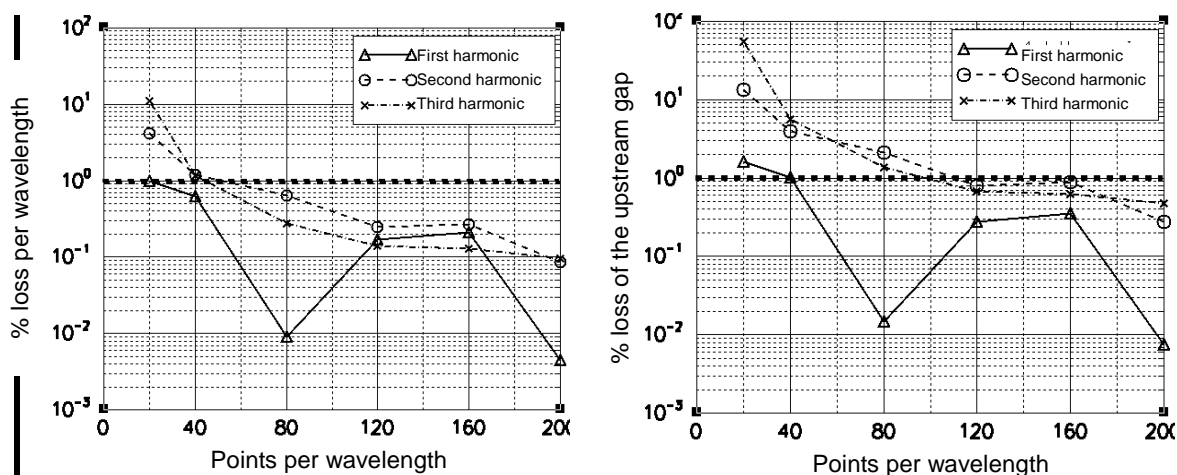

Figure 7.—Loss-of-vorticity amplitude versus number of points per wavelength.

Finally, figure 8 shows the propagation of the cut-on acoustic mode n = 2, k = 1, in the upstream and downstream gaps for different grid densities. It can be clearly observed how grid convergence is achieved from 120 points per wavelength.
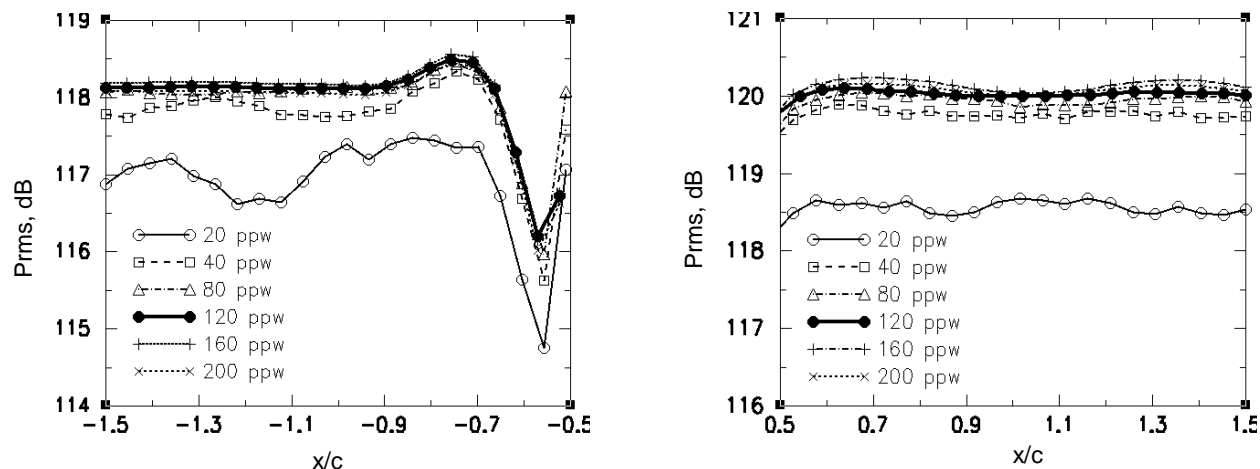
Figure 8.—Acoustic mode propagation in the upstream and downstream gaps with different grid densities (second harmonic).

CONCLUSIONS

A two-dimensional cascade-gust interaction problem (ref. 1) has been solved using a frequency domain linearized solver, used in production at ITP, known as Mu^2s^2T-L. Two-dimensional nonreflective boundary conditions are used in the calculations and its capability to deal with these types of problems is demonstrated by the absence of spurious reflections in the solution. Unsteady results show coherence on a global basis, i.e., cut-on acoustic modes keep their amplitude in upstream and downstream gaps, cut-off mode decay ratios are in concordance with the analytical values. In terms of absolute values, the author of the benchmark problem compares Mu^2s^2T-L results, and results submitted by other authors, against the benchmark solution in a companion paper. The benchmark solution is the one given by a frequency-domain linearized Euler code, known as LINFLUX, was extensively tested at United Technology Research Center and NASA Glenn Research Center.

Finally, a mesh sensitivity analysis is carried out showing grid selection criteria to obtain accurate results for each harmonic calculation, and proving that once the appropriate grid resolution is achieved, unsteady linear results do not depend on the selected grid.

REFERENCES

1. Envia, E: Fourth CAA Workshop on Benchmark Problems. Category 3—Sound Generation by Interacting With a Gust, Problem 2—Cascade-Gust Interaction, 2003.
2. Corral, R., et al.: Validation of a Linear Multigrid Accelerated Unstructured Navier-Stokes Solver for the Computation of Turbine Blades on Hybrid Grids. AIAA Paper 2003–3326–2003.
3. Jameson, A.; Schmidt, W.; and Turkel, E.: Numerical Solution of the Euler Equations by Finite Volume Technique using Runge-Kutta Time Stepping Schemes. AIAA Paper 81–1259–1981.
4. Giles, M.B.: Non-Reflecting Boundary Conditions for Euler Equation Calculations. AIAA J. vol. 28, no. 12, 1990, pp. 2050–2057, 1990.
5. Corral, R.; and Fernández-Castañeda, J.: Surface Mesh Generation by Means of Steiner Triangulations. AIAA J. vol. 39, no. 1, 2001, pp. 176–180.
6. Tyler, J.M.; and Sofrin, T.G.: Axial Flow Compressor Noise Studies. SAE Transactions, vol. 70, 1962, pp. 309–332.
7. Escribano, A.G.; Serrano, A.; and De la Calzada, P.: Investigation on Numerical and Geometry Modelling Effects on the CFD Simulation of Interaction Noise in LP Turbines. 5th European Conference on Turbomachinery, Fluid Dynamics and Thermodynamics, 2003.

CATEGORY 3: SOUND GENERATION BY INTERACTING WITH A GUST
PROBLEM 2: CASCADE-GUST INTERACTION

M. Nallasamy
QSS Group, Inc.
NASA Glenn Research Center
Cleveland, Ohio 44135
e-mail: nallasamy@grc.nasa.gov

R. Hixon
University of Toledo
Toledo, Ohio 43606

S.D. Sawyer
University of Akron
Akron, Ohio 44325

R. W. Dyson
Acoustics Branch
NASA Glenn Research Center
Cleveland Ohio 44135

ABSTRACT

The cascade – gust interaction problem is solved employing a time-domain approach. Nonlinear time dependent Euler equations are solved using higher order spatial differencing and time marching techniques. The solutions indicate the generation and propagation of expected mode orders for the given configuration and flow conditions. The blade passing frequency (BPF) is cutoff for this cascade while higher harmonic, 2BPF and 3BPF, modes are cuton.

INTRODUCTION

The category 3, problem 2 of the 4th CAA workshop is concerned with the noise resulting from acoustic response of a 2-D cascade to an incident gust. The interaction of the gust with the cascade produces an unsteady loading on the airfoil surface. The unsteady loading on the airfoil generates acoustic modes that propagate upstream and downstream of the cascade. The problem is illustrated in Figure 1. The velocity triangle at the inflow shows the gust (representing the wake from the rotor blades) in the direction of relative flow velocity (W_∞) at an angle β to the x-axis. The direction of tangential velocity (Ωr) is in the positive y-direction as indicated resulting in the axial velocity (V_∞) making an angle α to the x-axis. The mean flow vector plot (Figure 2a) shows the axial velocity making an angle α = 36° at the inflow plane. (At the outflow plane, it was found that the flow makes a small angle (~ -1.5°) to the x-axis. At the inflow, the gust makes an angle β as shown in Figure 2b.

A time domain analysis is employed to study the gust-cascade interaction problem. In this approach, the full nonlinear Euler equations are solved using a higher order accurate time marching scheme. The time marching scheme in general requires significantly larger computational time compared to a linearized Euler analysis. The advantage of a time domain analysis is that from a single solution for multi-frequency excitation, responses at all harmonics of interest may be extracted.

GOVERNING EQUATIONS

The full nonlinear time dependent Euler equations governing the 2-D cascade flow are solved using a time marching technique. In Cartesian coordinates these equations are written as:

$$\frac{\partial Q}{\partial t} + \frac{\partial E}{\partial x} + \frac{\partial F}{\partial y} = 0 \qquad (1)$$

where,
$$Q = \begin{bmatrix} \rho \\ \rho u \\ \rho v \\ E \end{bmatrix} \qquad E = \begin{bmatrix} \rho u \\ \rho u^2 + p \\ \rho u v \\ u(E + p) \end{bmatrix} \qquad F = \begin{bmatrix} \rho v \\ \rho u v \\ \rho v^2 + p \\ v(E + p) \end{bmatrix}$$

and $\quad p = (\gamma - 1)\{E - \dfrac{1}{2}\rho(u^2 + v^2)\}$ (2)

These equations are cast in generalized curvilinear coordinates employing the chain rule formulation as:

$$\frac{\partial Q}{\partial \tau} + \frac{\partial \xi \partial E}{\partial x \partial \xi} + \frac{\partial \eta \partial E}{\partial x \partial \eta} + \frac{\partial \xi \partial F}{\partial y \partial \xi} + \frac{\partial \eta \partial F}{\partial y \partial \eta} = 0 \quad (3)$$

SOLUTION TECHNIQUE

The nonlinear time dependent Euler equations are solved employing a parallel computational aeroacoustic code described in [1, 2]. The spatial derivatives of equation 3 are approximated using a prefactored 6th order compact scheme [3]. The time marching uses a 2N storage fourth order nonlinear extension of Hu's 5-6 Low Dissipation and Dispersion Runge-Kutta (LDDRK) scheme [4,5]. An explicit 10th order constant coefficient dissipation model [6] is used for damping unresolved waves. To satisfy the specified mean flow boundary conditions the method described in [7] is employed. At the inflow and outflow planes the nonreflecting boundary conditions described in [8] are implemented in the code. On the airfoil surface, the time derivative of the velocity normal to the wall is set to zero.

COMPUTATIONAL DOMAIN AND NUMERICAL SOLUTION

The grid used in the computations has eight grid blocks per passage with 9,506 grid points. Care is taken to increase the grid resolution in the leading edge, trailing edge, and wake regions. In this grid the minimum number of grid points in the axial direction is 123 and in the lateral direction is 43 and the grid is sufficient to produce the resolutions required for the excitation frequencies considered. From the description of the gust in the problem, to be able to specify periodic boundary conditions in the y direction, the flow through 27 passages are solved in the present solution procedure. With the specified gust amplitudes, the solution is run till periodicity in pressure is achieved on the inflow, outflow boundaries and on the airfoil surface. The solution has to be run for over 200 periods to obtain a reasonably converged solution. To obtain a change in circumferential mode order levels within one percent between successive periods, the solution had to be run up to 235 periods. Once the periodic solution is established, the solution is processed to obtain the acoustic response at blade passing frequency (BPF) tone, 2nd and 3rd harmonics and circumferential mode orders.

JOINT TEMPORAL – SPATIAL TRANSFORM

The cascade unsteady flow solution as a function time is known over a specified period. The acoustic pressure response is not only harmonic in time, but also periodic in the tangential direction, y. From the known acoustic pressure p as a function of (x, y, t), the acoustic mode amplitude P as a function of (x, m, n) where m is the circumferential mode order and n is the harmonic order [9]:

$$P(x, m, n) = \frac{2}{NN_{\Delta t}} \sum_{l=0}^{N-1} \sum_{j=0}^{N_{\Delta t}-1} p(x, y_l, t_j) e^{-2\pi i n j / N_{\Delta t}} e^{-2\pi i m l / N}$$

where, Δt – time between samples, $N_{\Delta t}$ is the number of samples over interval T, frequency f = n/T, and n = 0, 1, 2, ….$(N_{\Delta t}-1)/2$ is the harmonic number. N – number of points in the tangential direction. m – spatial (circumferential) mode order, -N/2 < m < (N/2 – 1).

RESULTS

Unsteady Loading and Harmonics

The gust incident on the cascade sets up unsteady loading on the airfoil surfaces and the unsteady forces generate noise that propagate upstream of the leading edge of the airfoil and downstream of the trailing edge of the

airfoil. From the converged periodic solution the steady mean pressure on the airfoil as well as the periodic variation of minimum and maximum pressures that occur in a period are shown in Figure 3. The harmonic contents of the unsteady loading are shown in Figure 4. The first harmonic loading is large and expected to produce acoustic modes of higher amplitude. But the cascade configuration results in a BPF mode that is cutoff or decays exponentially upstream and downstream as will be shown below. The loading in higher harmonics are much smaller and produce propagating acoustic modes.

Sound Pressure Levels in Three Harmonics

The unsteady loading generates acoustic modes and their levels in decibels are the required computational results of this benchmark problem. The circumferential mode orders in BPF are -16 and 11, in 2BPF it is -5, and in 3BPF the modes are 6 and -21. A plus mode rotates in the direction of the rotor blade (wake) and a minus sign indicates mode rotation in the direction opposite to that of the rotor. The sound pressure levels of the modes at the inflow and outflow planes are shown in Figure 5. The mode -5 of the 2nd harmonic dominates and the level at the outflow is about 1.1 dB higher than at the inflow. Of the two modes in 3BPF, mode 6 dominates the inflow while mode -21 dominates in the outflow. In the cutoff BPF, mode -16 shows higher than mode 11 in the while the reverse is true at the outflow.

Temporal Transforms, Spatial Transforms, and Mode Amplitudes

The BPF mode amplitudes as a function of axial distance x in the inflow and outflow regions are shown in Figure 6. The rotor-stator interaction mode, -16, and the rotor locked mode, 11, are decaying as expected and in the inflow region mode -16 dominates and in the outflow region mode 11 has higher amplitudes. The temporal transform shown in Figure 7, the real part of unsteady pressure clearly shows the dominating modes in the inflow and outflow regions. The spatial transform showing the circumferential mode orders as a function of x shows the two decaying modes.

The well cuton propagating mode (-5) amplitudes in the inflow and outflow regions are shown in Figure 8 for 2BPF. The amplitude is nearly constant along x in both regions. The temporal transform (Figure 9) shows the mode, -5, clearly in the inflow and outflow regions. The spatial transform shows the propagating mode -5 for which the amplitude variation along x is shown in Figure 8.

At the third harmonic, two modes are propagating. In the inflow, modes m=6 and m=-21 are both well cuton and propagates as indicated by constant amplitude along x in Figure 10. In the outflow, m=6 is well cuton while m = -21 is very close to cutoff, but both modes propagate as indicated in the figure. A temporal transform (Figure 11) shows the mode m=6, the dominant mode in the inflow region while m = -21 is observed in the outflow region. In the inflow, the two modes whose amplitudes are very close and are interacting produce a wavy pattern seen in the Figure. The spatial transform shows again the two modes existing through the region along x.

CONCLUSIONS

A time domain approach was employed to study the gust-cascade problem. The results show that the present time marching method produces the expected acoustic modes and their propagation/decay of characteristics. Further analysis is needed to understand the linear/nonlinear behavior of the acoustic response with excitation amplitude level.

ACKNOWLEDGEMENTS

REFERENCES

1. Hixon, R, Nallasamy, M. and Sawyer, S.S, "Parallelization strategy for an explicit computational aeroacoustic code," AIAA Paper 2002-2583, 2002.
2. Nallasamy, M., et al., "A Time domain Analysis of gust – cascade interaction noise," AIAA Paper 2003-3134, 2003.
3. Hixon, R, "Nonlinear comparison of high-order and optimized finite-difference schemes," Journal of Computational Fluid Dynamics, Vol. 13, pp. 257-277, 2000.
4. Hu, F.Q., Hussaini, M.Y. and Manthey, J., "Low-Dissipation and dispersion Runge-Kutta schemes for computational acoustics," Journal of Computational physics, Vol. 124, pp. 121-133, 1996
5. Stanescu, D. and Habashi, W.G., "2N-Storage low dissipation and dispersion Runge-Kutta schemes for computational acoustics," Journal of Computational Physics, Vol. 143, pp. 674-681, 1998.
6. Kennedy, C.A. and Carpenter, M.H., "Several new numerical methods for compressible shear layer simulations," Applied Num. Math., Vol. 4, 1994, pp. 397 – 433.
7. Hixon, R., et al., "Mean flow boundary conditions for computational aeroacoustics," AIAA Paper 2003-3299, 2003.
8. Giles, M., "Nonreflecting boundary gust problem using a higher order compact conditions for Euler equation calculations," AIAA Journal, Vol. 28, pp. 2050-2058, 1990.
9. Sawyer, S, et al., "Computational aeroacoustic prediction of discrete frequency noise generated by rotor-stator interaction," AIAA Paper 2003-3268, 2003.
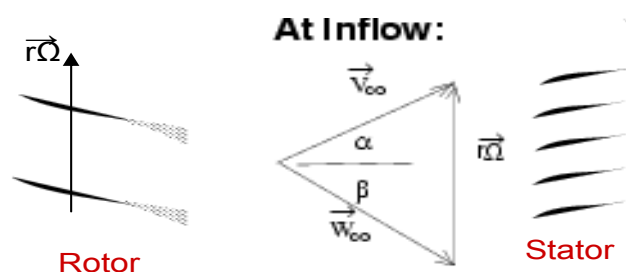
Figure 1 Gust-Cascade problem
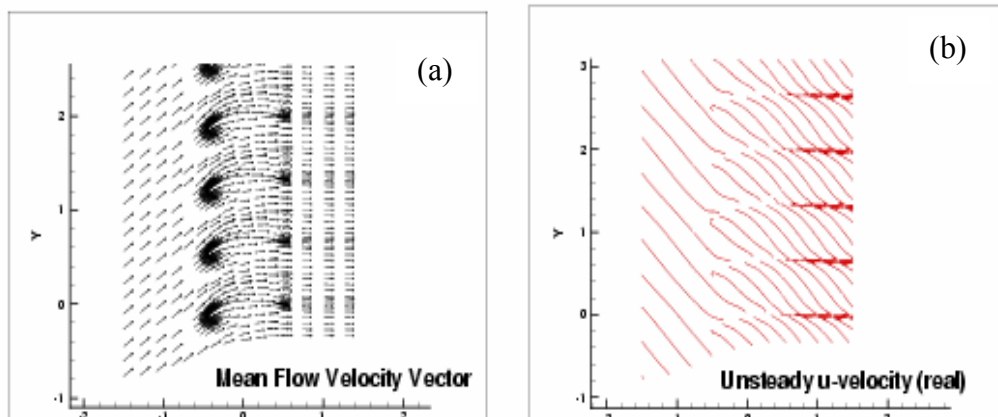
Figure 2 Mean flow and gust definitions
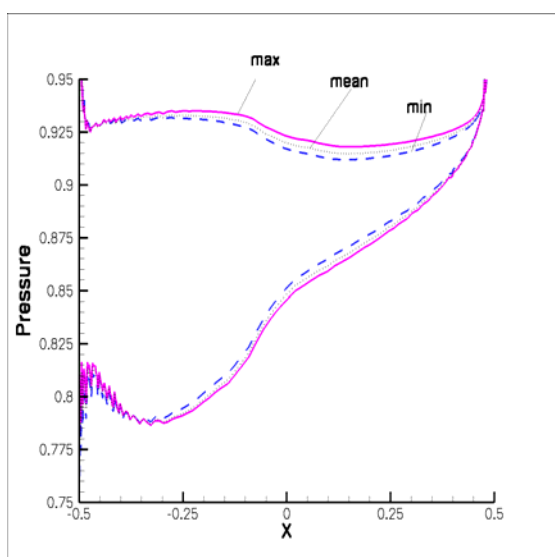
Figure 3 Unsteady airfoil surface pressure
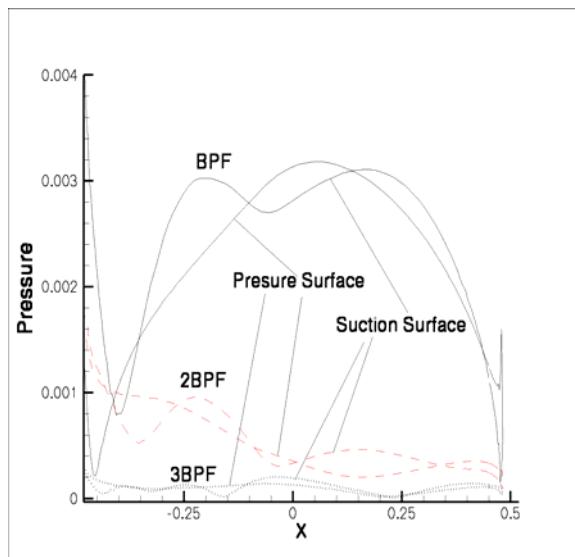
Figure 4 Airfoil surface pressure harmonics
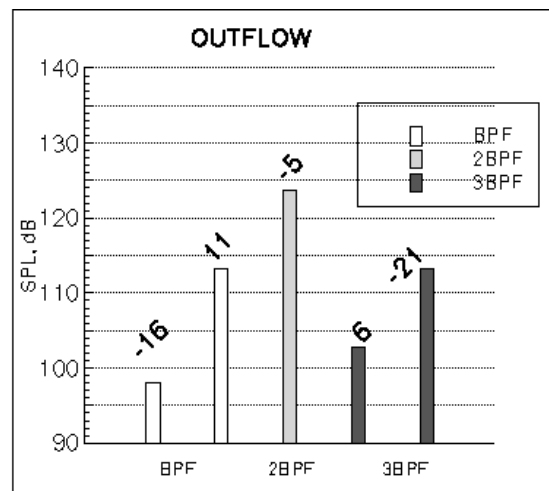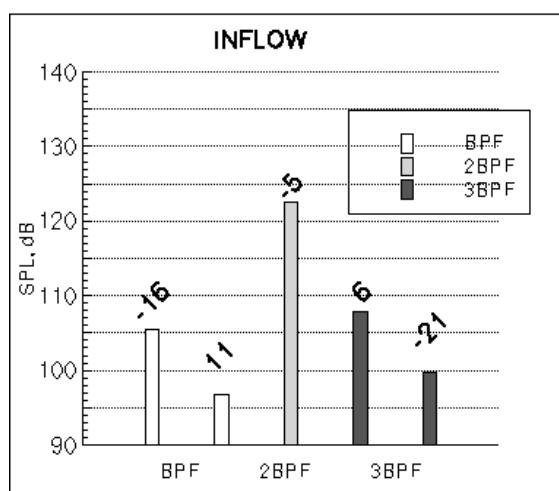
Figure 5 Sound Pressure levels in three harmonics
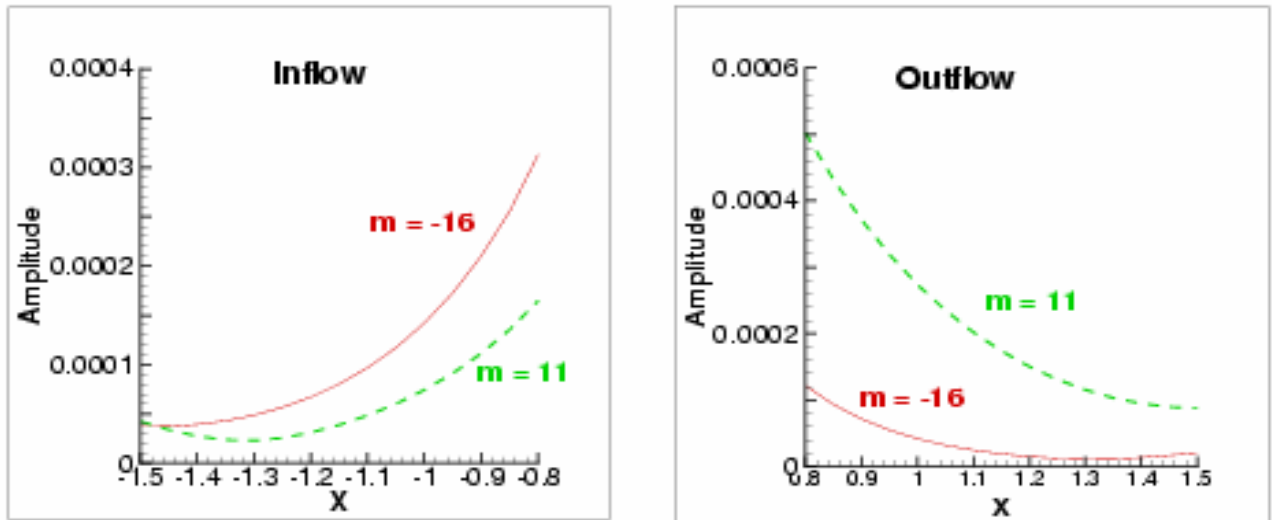
Figure 6 Acoustic Response at BPF
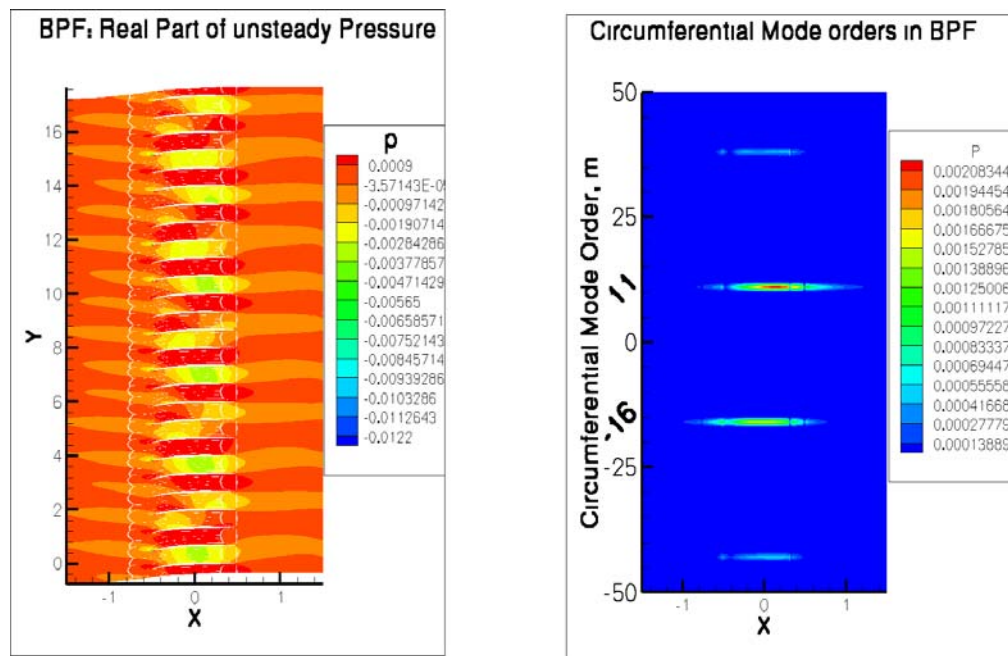
Figure 7   Temporal and Spatial transforms for BPF
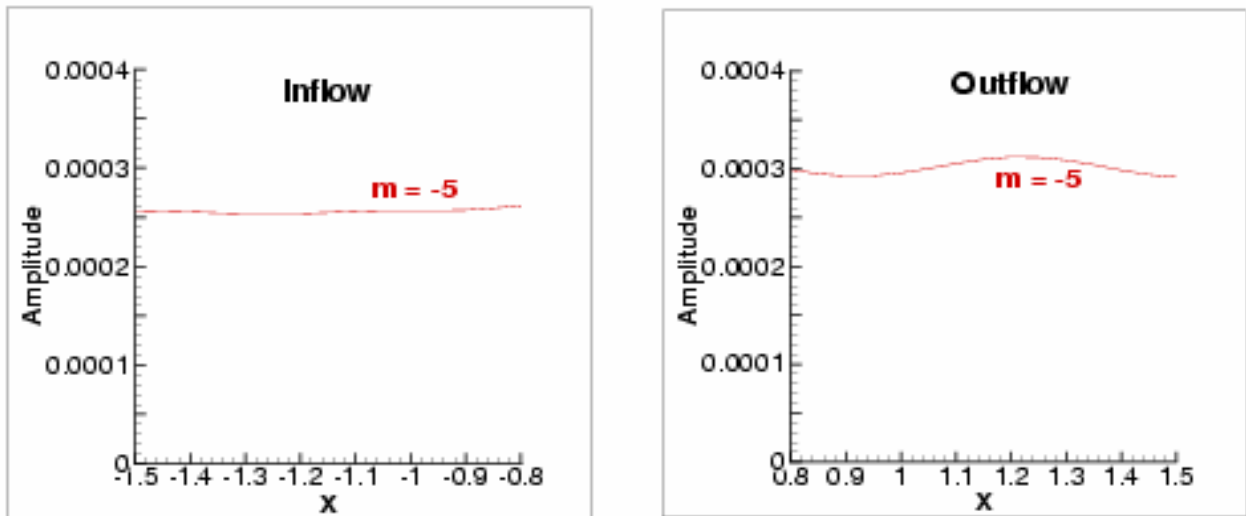
Figure 8 Acoustic Response at 2BPF
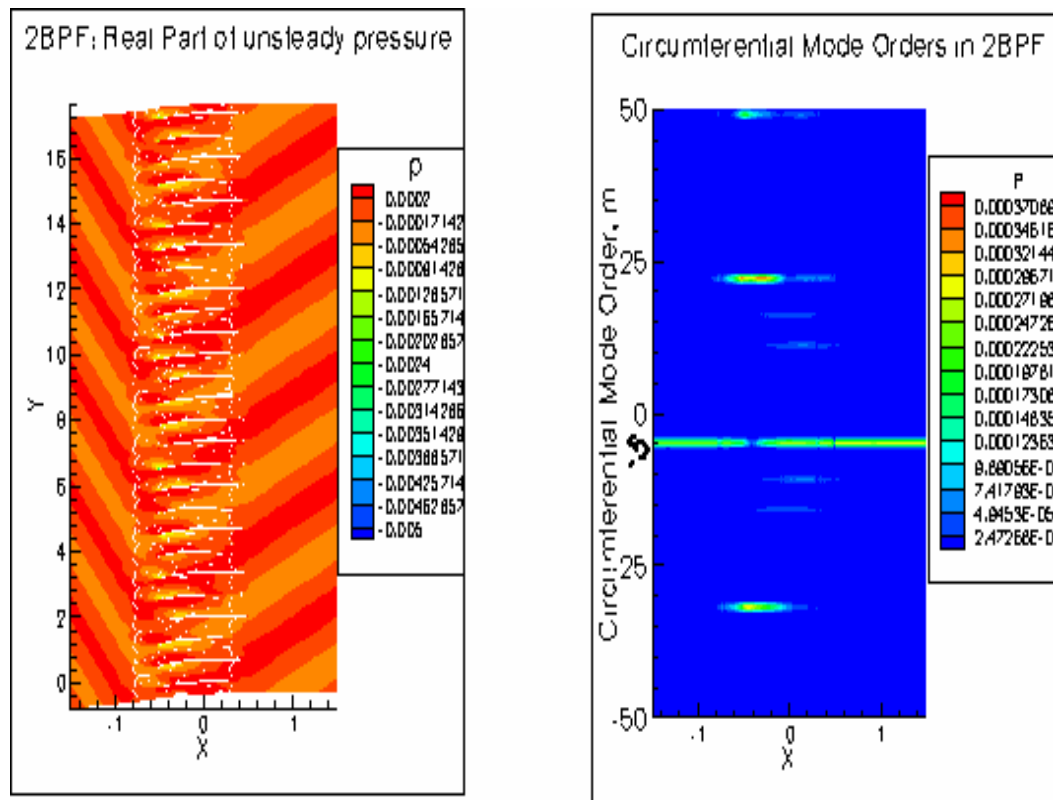
Figure 9 Temporal and Spatial Transforms for 2BPF
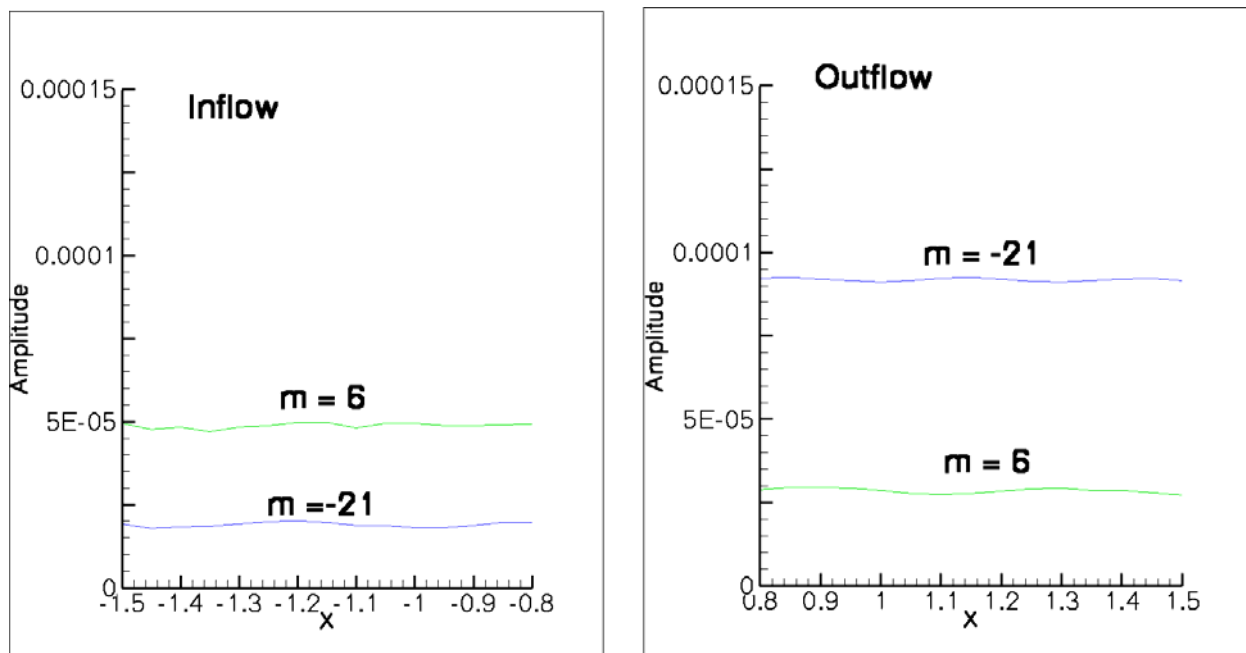
Figure 10 Acoustic Response at 3BPF
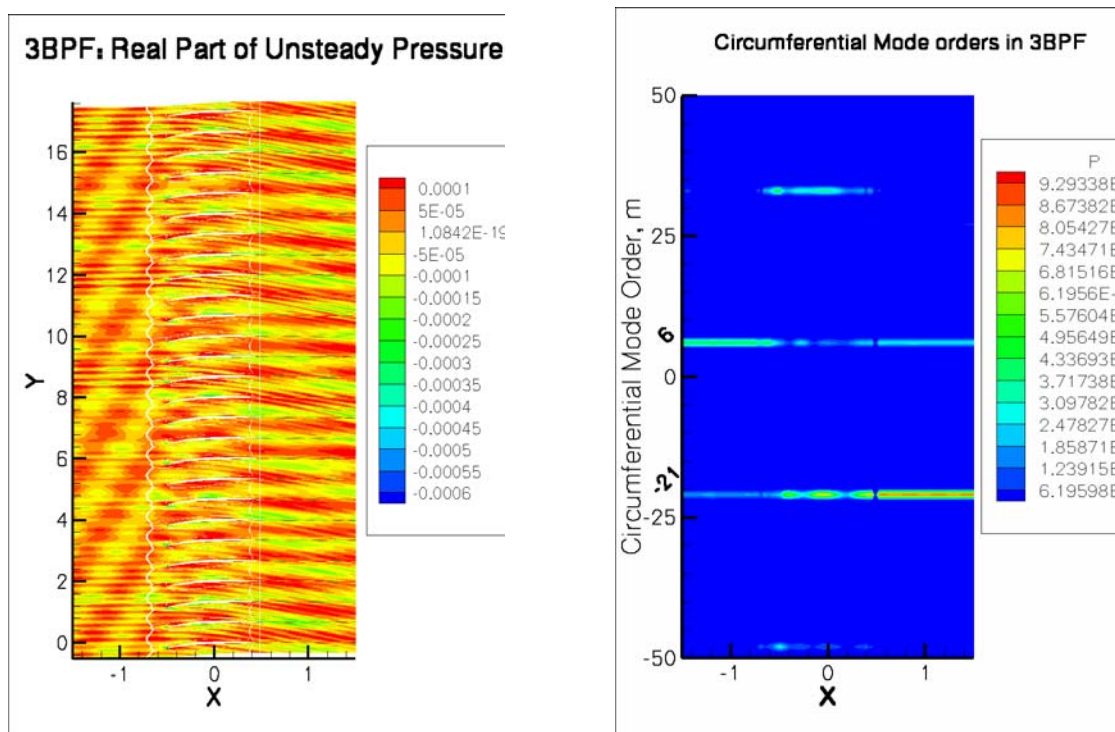
Figure 11 Temporal and spatial transform for 3BPF

LINEAR UNSTEADY CFD ANALYSIS OF THE CASCADE-GUST INTERACTION PROBLEM

John Coupland
Rolls-Royce plc
PO Box 31
Derby
United Kingdom
DE24 8BJ

E-mail : john.coupland@rolls-royce.com
Tel : +44-1332-249541
Fax : +44-1332-245672

ABSTRACT

A linearised unsteady Navier-Stokes code, HYDLIN, is used to provide the results for the cascade-gust interaction test problem. The HYDLIN approach is based on linearistion of the unsteady flow about the cascade mean flow generated by the steady non-linear flow solution from the HYDRA CFD code. The test problem solutions for the workshop have been run using a multiblock quadrilateral mesh of around 48K nodes, using boundary conditions as defined in the test problem specification. The physical aspects of the cascade-gust interaction and the waves generated by the interaction are studied using the linear unsteady CFD results.

INTRODUCTION

Cascade-gust interaction forms a fundamental part of the noise generation process in turbomachinery. 3D Computational Fluid Dynamics (CFD) codes are being used in industry to analyse tone noise generation in the Fan/Bypass OGV system and the LP turbine stages of aero-engines. The 2D cascade-gust interaction test problem of the CAA4 Workshop provides a relevant test of these methods being used for tone noise generation due to wake-blade interaction.

The method used here is a 3D viscous CFD code, HYDRA, developed by Giles et al at the University of Oxford, UK, and by Rolls-Royce plc (refs 1 and 2). The full non-linear compressible CFD code uses a second-order edge based discretisation on unstructured hybrid grids. For Navier-Stokes solutions a Spalart-Allmaras turbulence model (ref 3) is employed. A 5 step Runge-Kutta algorithm, with multi-grid acceleration, is used to converge the numerical solution. A linear unsteady version of the code, HYDLIN, is used at Rolls-Royce to provide 3D viscous unsteady solutions for the analysis of wake-blade interaction problems for aeromechanical and aeroacoustic investigations.

LINEAR UNSTEADY CFD

The linear unsteady method is based on a full linearisation of the Navier-Stokes equation and Spalart-Allmaras turbulence model at a specific temporal frequency.

$$q(\underline{x},t) = \overline{q}(\underline{x}) + \hat{q}(\underline{x})e^{i\omega t}$$

The unsteady problem is solved in the frequency domain for the complex amplitudes, $\hat{q}(\underline{x})$, of the solution vector, U. A pseudo-time derivative is introduced into the linear equations to enable the same numerical methods adopted for the non-linear CFD code to be used to converge the linear unsteady solution.

For the workshop cascade-gust test problem the HYDRA and HYDLIN codes are used in the inviscid formulation and in a true 2D mode. For these inviscid calculations no explicit steady or unsteady Kutta condition is enforced at the cascade trailing edge. For the test problem steady flow solution the flow leaves the trailing edge cusp symmetrically at the blade angle and so the Kutta condition is essentially satisfied.

Boundary conditions are specified for the test problem in accordance with the definition provided. For the linear unsteady solution a 2D non-reflecting condition is imposed based on wavesplitting of the unsteady

solution into incoming and outgoing waves. The unsteady perturbations are then adjusted iteratively to impose just outgoing waves at the inlet and the exit of the domain, in addition to the imposed incoming vortical wave at the inlet that forms the incident gust. The wavesplitting is based on the waves present in a uniform circumferential mean flow which is formed from the circumferential average of the non-linear mean flow HYDRA solution. For this 2D test problem these waves can be determined analytically, (ref 4). The same wavesplitting procedure is adopted to post-process the unsteady solution in terms of the acoustic, vortical and entropy waves present in the unsteady flow.

For the cascade-gust test problem the incoming gust fundamental wave is characterised by the circumferential wave number,

$$k_{y,gust} = 3.84$$

where the unsteady wave perturbations vary as

$$dq \sim e^{i\omega t - ik_x x - ik_y y}$$

The waves generated by the interaction of the incoming gust with the cascade will be determined by

$$k_y = k_{y,gust} - k\frac{2\pi}{P}$$

where P is the cascade pitch and k is any integer. For the first, second and third harmonics of the incoming gust the lowest circumferential wave numbers of the interaction waves are given in Tables 1(a) to 1(c), where n is the incoming harmonic number. The test problem is equivalent to a rotor-stator interaction in a turbomachine where the number of rotors is 11 and the number of stators is 27. The tables also include the equivalent order, m, of the generated circumferential modes, where in 3D

$$dq \sim e^{i\omega t - ik_x x - im\theta}$$

For the first harmonic, n=1, all the waves are decaying (cut-off). For the second harmonic, n=2, only the interaction mode corresponding to k=1 is propagating (cut-on), other waves are cut-off. For the third harmonic, n=3, the two interaction modes corresponding to k=1 and k=2 are cut-on.

n	k	m	ky
1	-2	65	22.69
1	-1	38	13.26
1	0	11	3.84
1	1	-16	-5.59
1	2	-43	-15.01

(a)

n	k	m	ky
2	-2	76	26.53
2	-1	49	17.10
2	0	22	7.68
2	1	-5	-1.75
2	2	-32	-11.17

(b)

n	k	m	ky
3	-2	87	30.37
3	-1	60	20.94
3	0	33	11.52
3	1	6	2.09
3	2	-21	-7.33

(c)

Table 1 : Circumferential wave numbers of interaction modes
(a) 1st harmonic n=1 (b) 2nd harmonic n=2 (c) 3rd harmonic n=3

The procedure followed to do the cascade-gust test problem linear unsteady calculations is –

- generate an acceptable mesh for accurate unsteady calculations up to the 3rd harmonic

- use the non-linear code HYDRA to solve for the cascade mean flow subject to the required boundary conditions

- for each incoming harmonic (1st, 2nd and 3rd) solve the linear unsteady code HYDLIN using the test case incoming gust definition

- post-process the linear unsteady results to determine the amplitudes of the propagating and decaying waves upstream and downstream of the cascade

CALCULATION MESH

The unstructured mesh used for the test problem calculations has a multi-block arrangement, with a C-mesh of quadrilateral cells around the blade and 3 H-meshes arranged above and below the C-mesh and in the inlet flow region. The mesh density was chosen to give acceptable propagation of the propagating waves using the linear HYDLIN code, based on earlier tests of the capability of the code on simpler wave propagation test problems.

The resulting total number of nodes for the mesh is 47731. The full mesh is illustrated in Figures 1 and 2. The detailed figures of the blade leading edge and trailing edge mesh illustrate the fine resolution still required for these inviscid calculations.
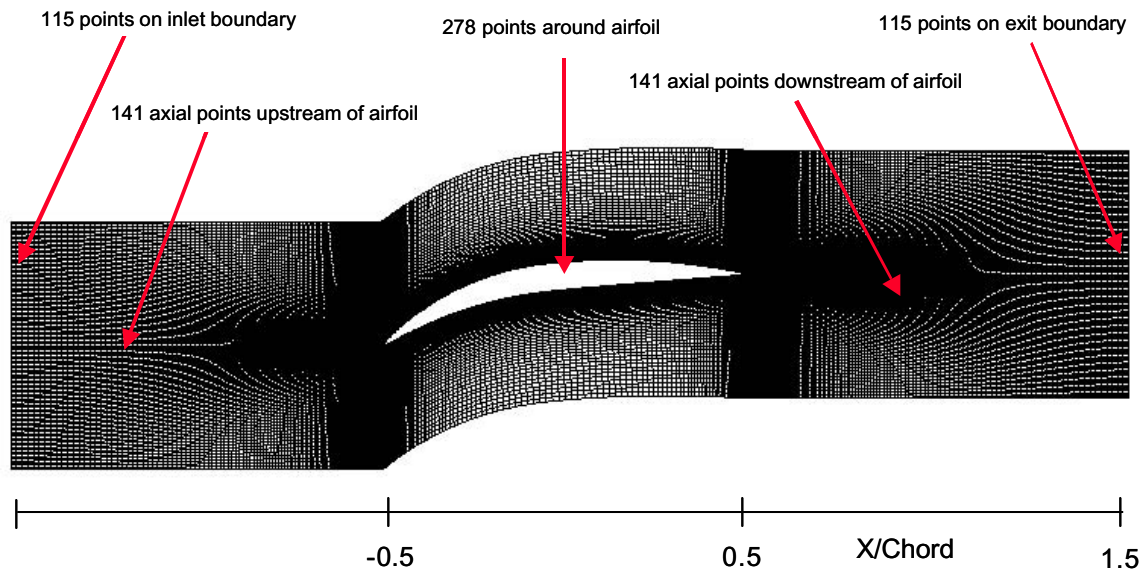
Figure 1 : Cascade Mesh used for Linear Unsteady CFD Calculations
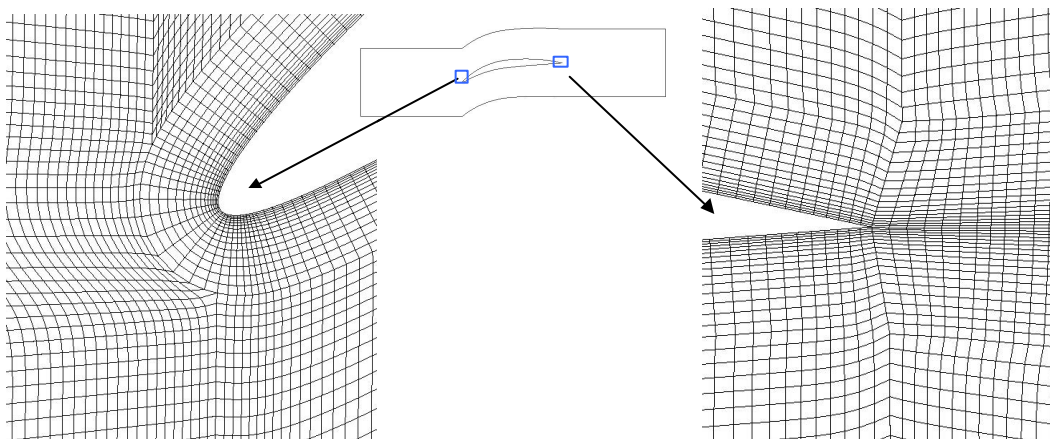
Figure 2 : Cascade Leading Edge and Trailing Edge Mesh

The mesh used gave a minimum of 30 points per wavelength for the upstream or downstream propagating waves at the 3rd harmonic. At the lower harmonics the spatial resolution of the waves was of course much greater. Some studies were conducted with a coarser mesh with around 14400 nodes, with approximately half the resolution of the datum mesh in both the axial and circumferential directions. The results on the coarser mesh were within 0.2dB of the unsteady blade surface pressure or the dominant wave amplitudes for the 1st harmonic, within 0.5dB for the 2nd harmonic and within 1.5dB for the 3rd harmonic. These results give a good level of confidence in the low mesh dependence of the results presented below for the datum mesh.

RESULTS

The non-linear mean flow solution for the cascade was obtained for the required inlet flow angle of 36 deg and a pressure ratio (exit static pressure to inlet total pressure) of 0.92. The non-linear HYDRA solution was run for 200 multi-grid iterations, using 4 levels of multi-grid, and this gave a convergence level greater than 4 orders of magnitude reduction of the rms (root mean square) residual. The run time for the mean flow calculation was just under 2 hours on a Sun Ultra 30 (512 MB RAM) desktop workstation, and required 69MB of memory. The resulting inlet Mach number was 0.448 and the exit flow angle was –1.6 deg.

The steady and unsteady flow results are presented below, where appropriate, in dimensional form. The parameters provided in the non-dimensional test case specification have been scaled to achieve an inlet total pressure of 101362 Pa and an inlet total temperature of 288.333 K.

Figure 3 shows the static pressure over the cascade blade passage. Figure 4 shows the blade surface pressure distribution plotted as the surface isentropic Mach number. Note the larger Mach number spike on the pressure surface side at the blade leading edge, indicating that the blade is operating at negative incidence. The trailing edge Mach number is also smooth on both surfaces of the blade.
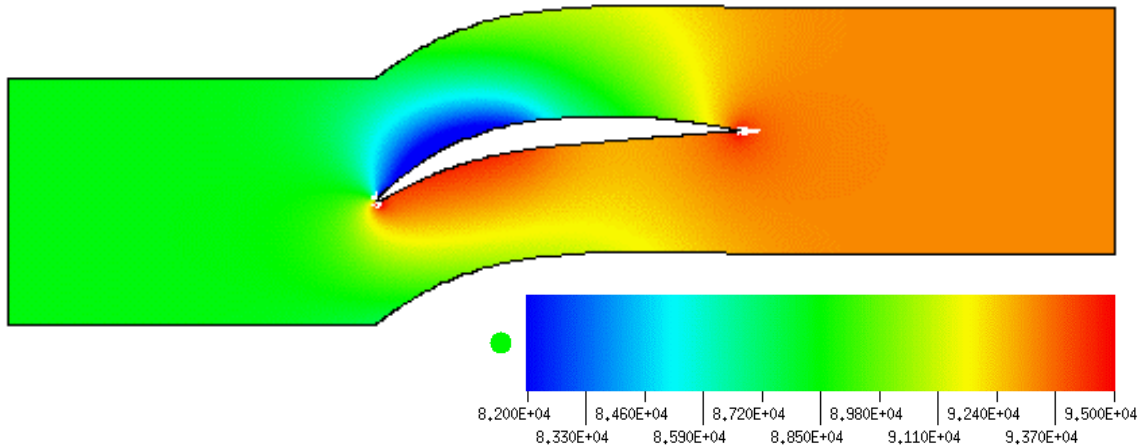
Figure 3 : Steady Mean Flow - Cascade Blade Static Pressure (Pa)
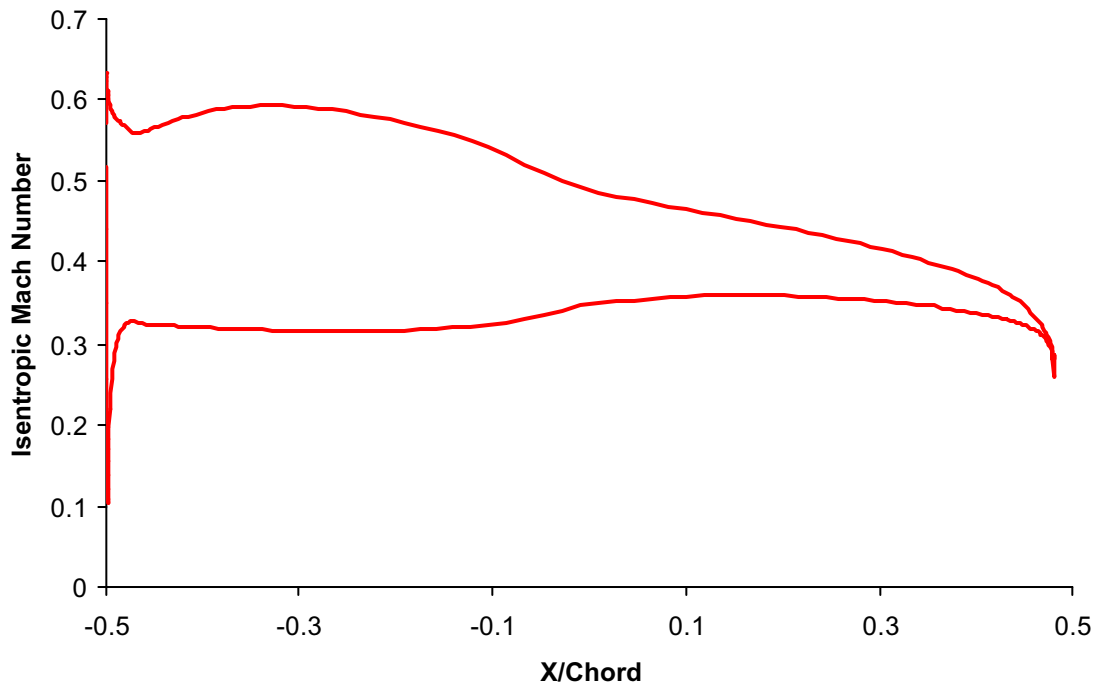
Figure 4 : Steady Mean Flow - Blade Surface Isentropic Mach Number Distribution

The linear unsteady solution for each incoming gust harmonic was obtained using the HYDLIN code using the gust amplitudes as provided in the test case specification. The relative level of the circumferential velocity and axial velocity perturbations (defined $\tan(\beta)$) in the incoming gust was prescribed using an angle, β, of 45 deg. This gives a gust definition consistent with a pure 2D vortical wave for the circumferentially averaged

mean flow at the cascade inlet plane. For each incoming harmonic the inter-blade phase angle appropriate to the incoming circumferential wave number was applied at the cascade periodic boundaries.

Each linear unsteady calculation was run for 1000 multi-grid iterations, using 4 levels of multi-grid, to give a convergence level greater than 5 orders of magnitude reduction of the rms residual. The run time for each linear unsteady flow calculation was around 6 hours on a Sun Ultra 30 (512 MB RAM) desktop workstation, and required 117MB of memory (roughly twice the steady calculation because of the use of complex variables).

Figure 5 shows the predicted amplitude of the unsteady blade surface pressure for each of the 3 incoming harmonics. The results are plotted as SPL (dB) where

$$SPL = 20\log\left(\frac{\hat{p}}{2*10^{-5}\sqrt{2}}\right)$$

where $\hat{p}$ is the amplitude of the harmonic pressure signal in Pa and the $\sqrt{2}$ is there to convert the amplitude to an rms pressure. The observed axial variation of the unsteady pressure amplitude on both the suction and pressure surfaces of the blade is a result of the interference of upstream and downstream propagating waves within the blade passage. The variation in the level of the different harmonics is partly a result of the differing level of the incoming gust amplitude for each harmonic provided in the test problem specification. Relative to the 1st harmonic the incoming gust for the 2nd harmonic was 4.4 dB lower and the incoming gust for the 3rd harmonic was 17.1 dB lower. Even allowing for this it is evident that the blade surface response reduces with the higher harmonics.
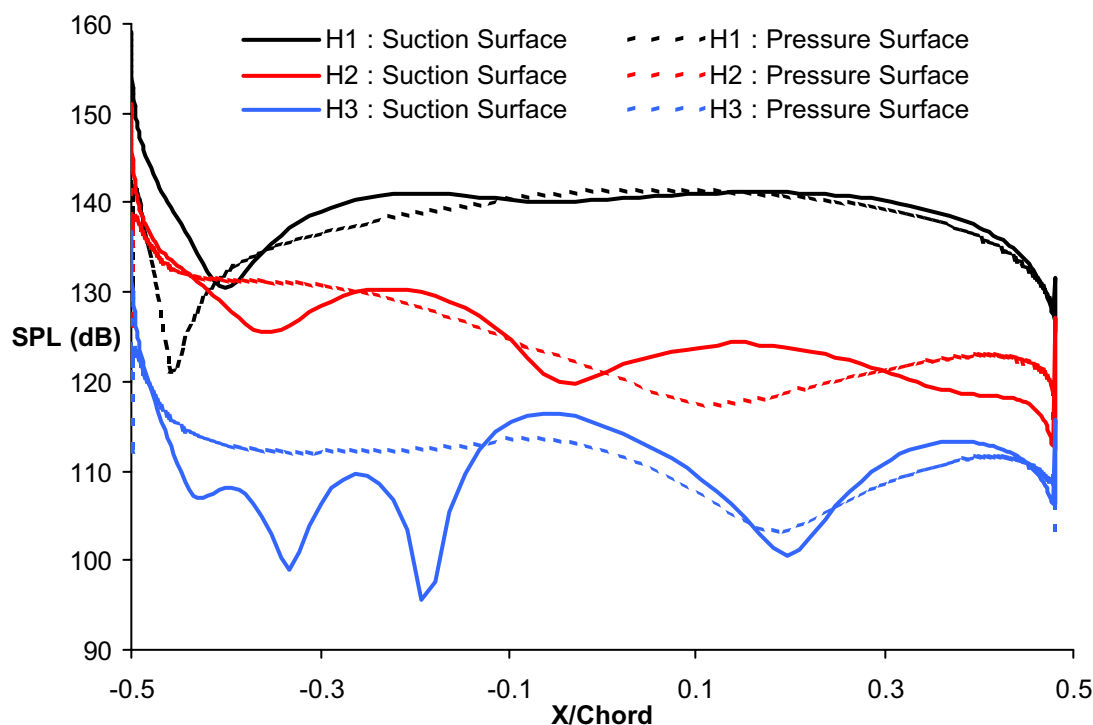
Figure 5 : Unsteady Flow : Blade Surface Unsteady Pressure Amplitude as SPL (dB) for the 1st harmonic (H1), 2nd harmonic (H2) and 3rd harmonic (H3)

Figure 6 illustrates the linear unsteady solution for the 1st harmonic as plots of the instantaneous axial velocity and pressure perturbations at a point in the temporal cycle of the linear solution. Figure 7 shows the amplitudes in SPL (dB) of the unsteady pressure, both upstream and downstream of the airfoil, in each of the circumferential wave numbers highlighted on Table 1. Figures 8 and 9, and then Figures 10 and 11, display the equivalent results for the 2nd and 3rd harmonics respectively.
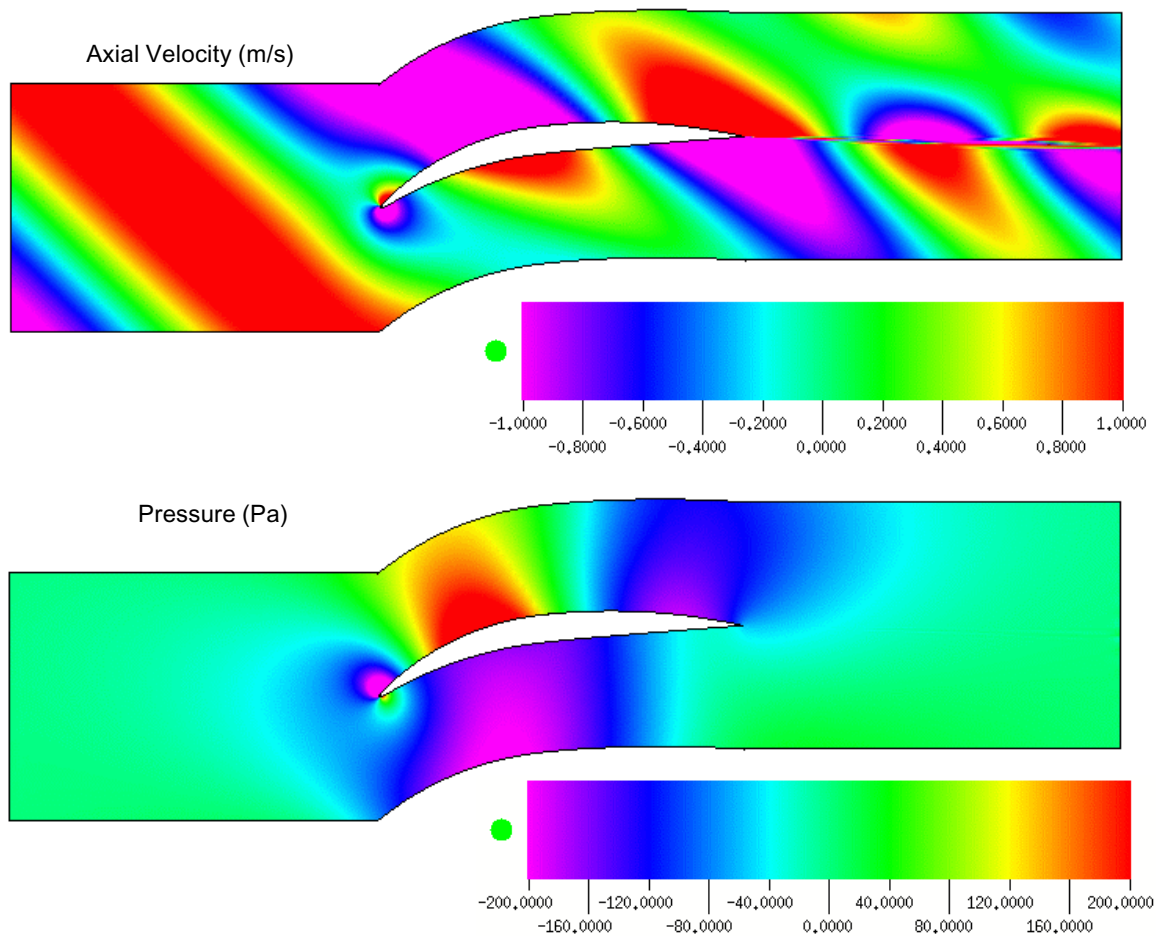
Figure 6 : 1st Harmonic Instantaneous Linear Unsteady Flow Solution
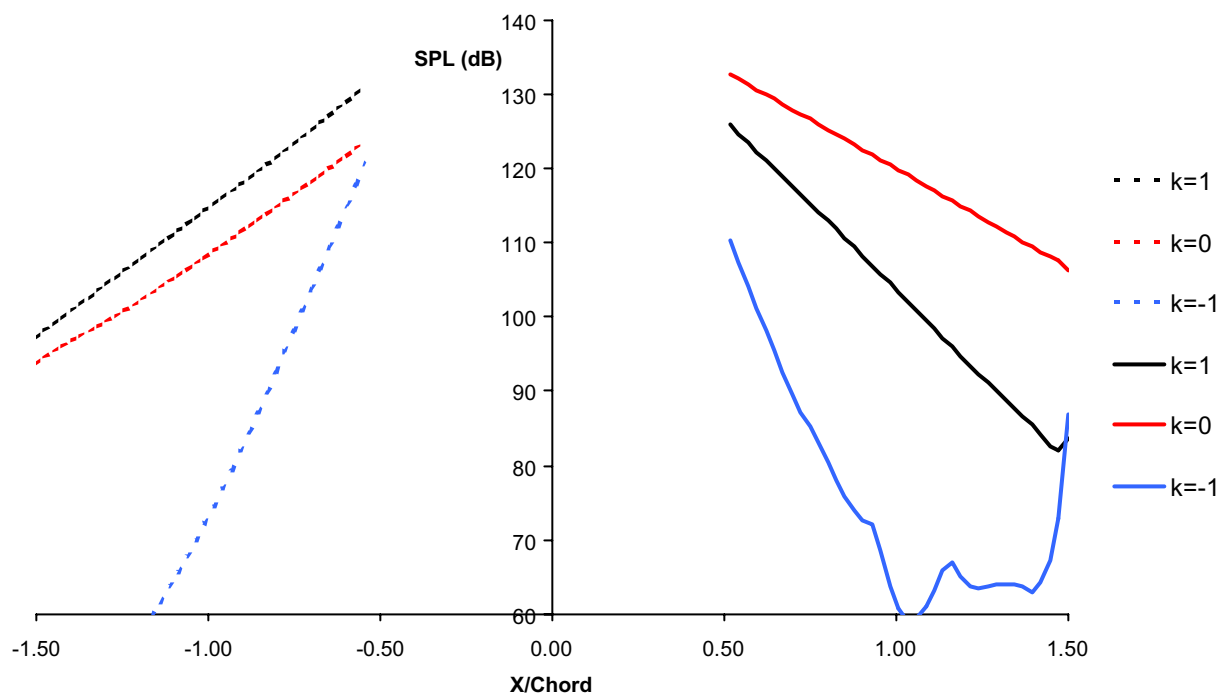
Figure 7 : 1st Harmonic Pressure Amplitude in Circumferential Wave Numbers k=-1 to k=1
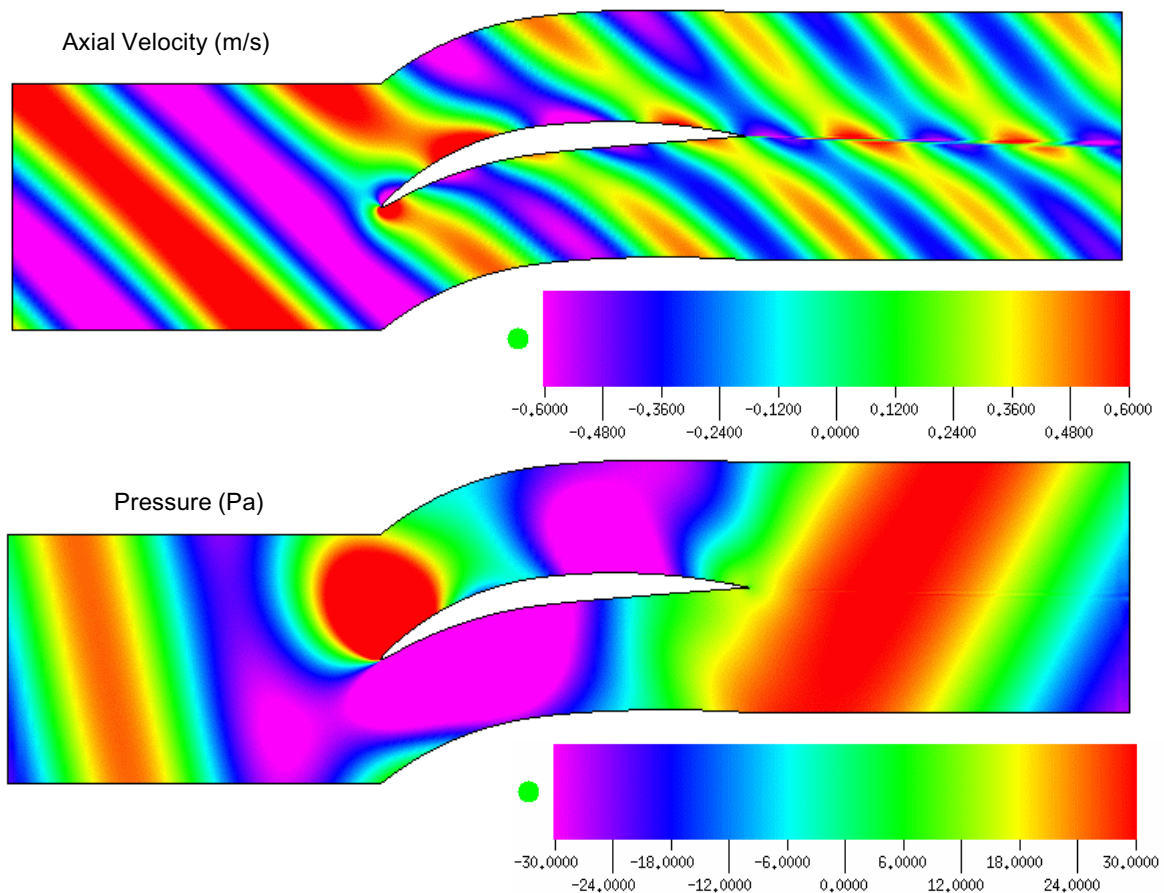
Figure 8 : 2nd Harmonic Instantaneous Linear Unsteady Flow Solution
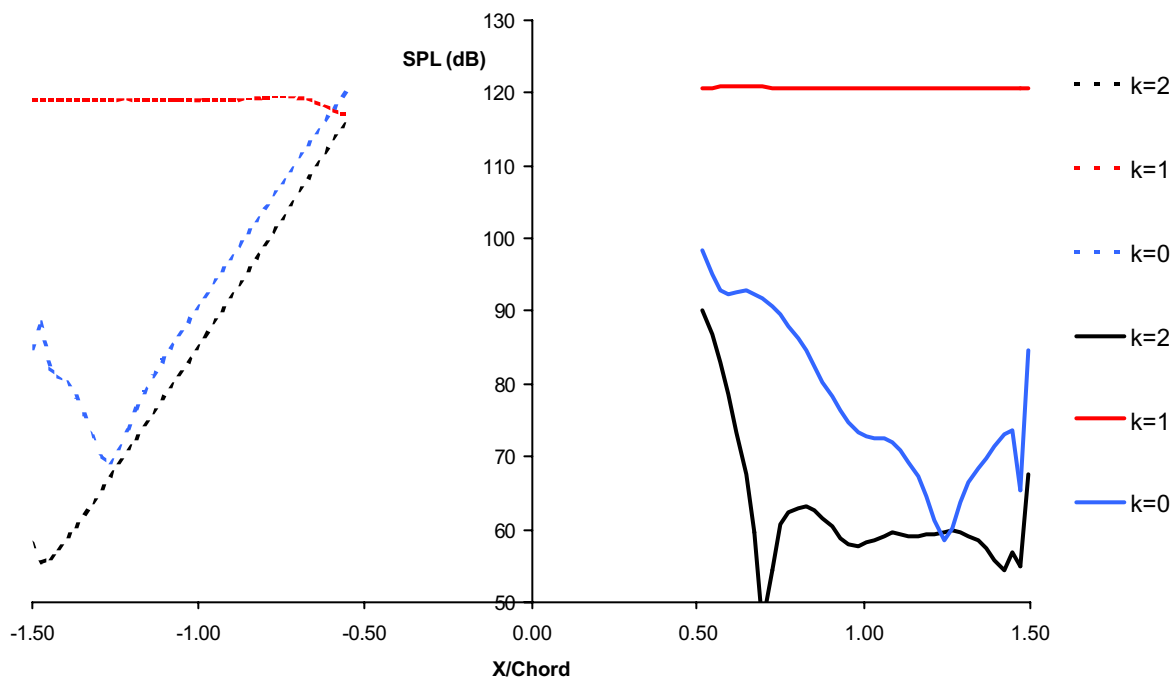
Figure 9 : 2nd Harmonic Pressure Amplitude in Circumferential Wave Numbers k=0 to 2
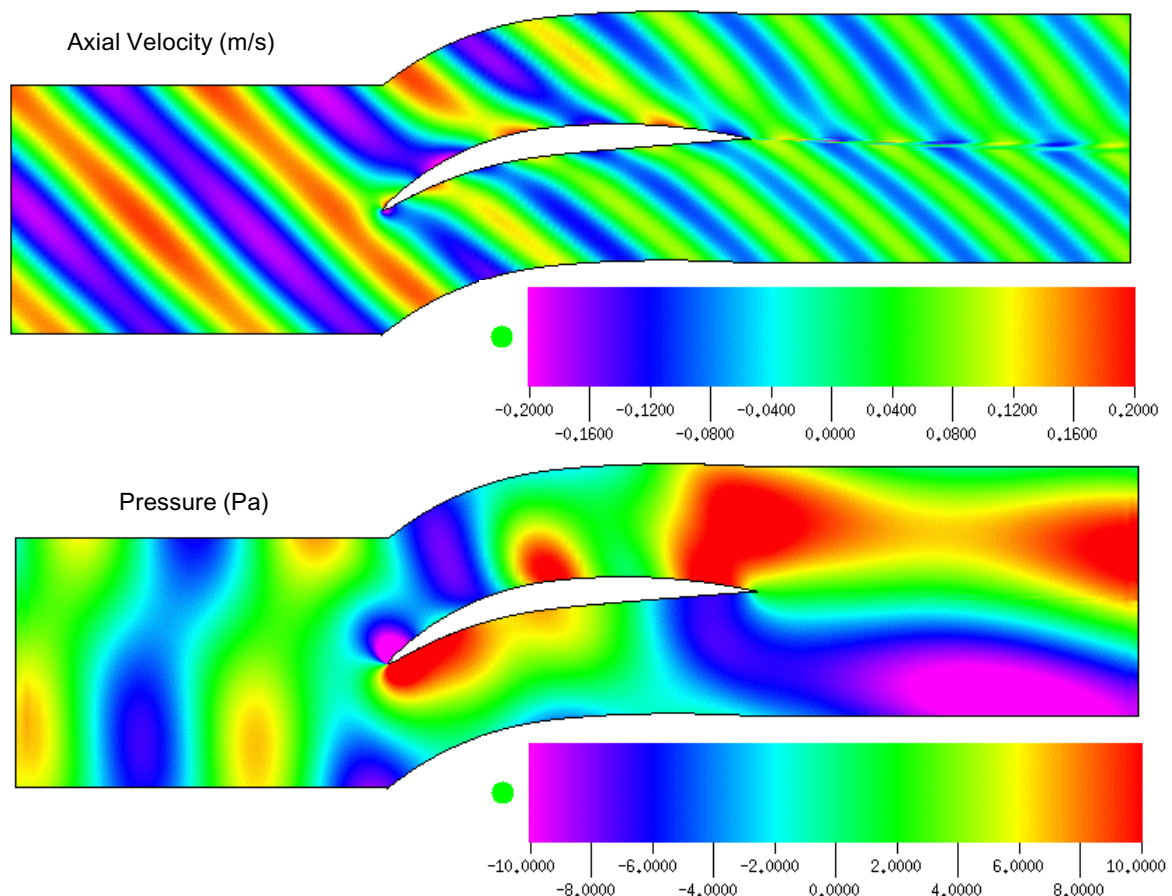
Figure 10 : 3rd Harmonic Instantaneous Linear Unsteady Flow Solution
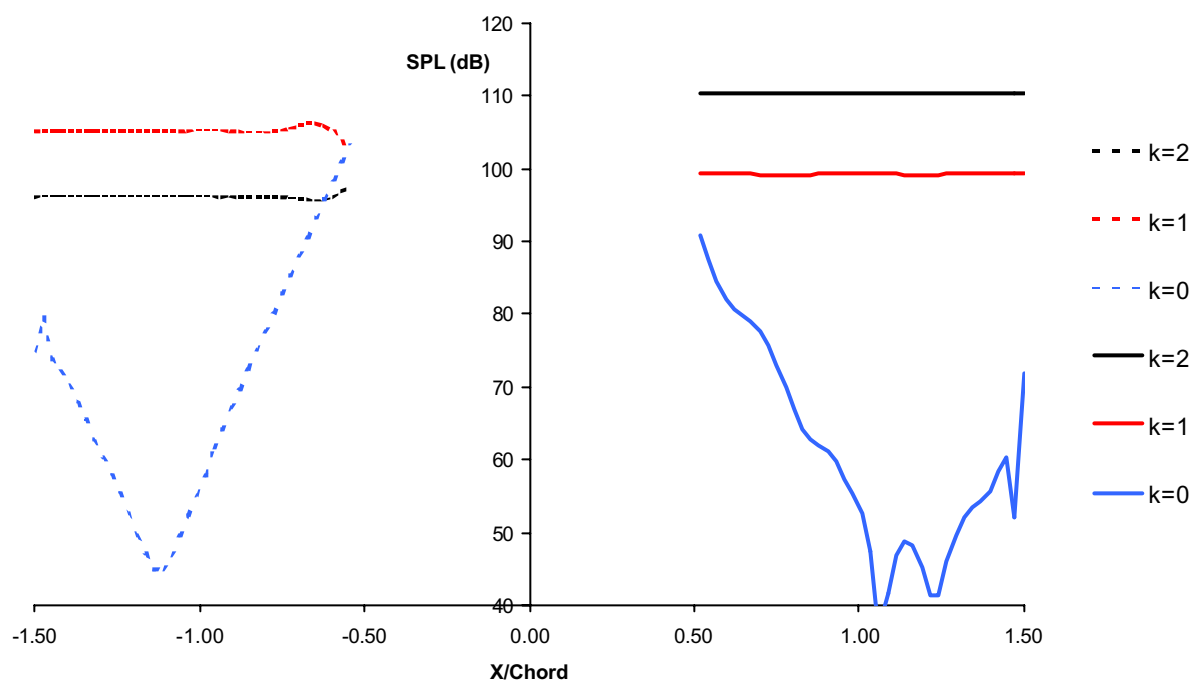
Figure 11 : 3rd Harmonic Pressure Amplitude in Circumferential Wave Numbers k=0 to k=2

For the 1st harmonic all of the acoustic waves are expected to be cut-off (decaying). From Figure 7 it is clear that the acoustic waves generated by the cascade-gust interaction decay away from the blade. The acoustic waves are expected to decay exponentially in the axial direction as evident by the linear decay of the logarithmic SPL. The unsteady field is dominated by the circumferential modes k=1 and k=0, which correspond to the lowest circumferential wave numbers (see Table 1) and hence lowest axial decay rate. Circumferential mode k=1 has a much larger wave number and decay rate as evident on Figure 7, though because of the increase in SPL near the outlet boundary there must still be a problem with reflection of this mode at the boundary.

The axial velocity perturbation on Figure 6 clearly illustrates the incoming gust (vortical wave) upstream of the blade. The velocity component in the acoustic waves is much smaller than the incoming gust for this harmonic. Downstream of the blade the vortex sheet expected in these inviscid calculations is well captured in this numerical CFD analysis. The fluctuating lift on the blade due to the incoming gust will lead to unsteady vorticity shed at the blade trailing edge. The vortex sheet is maintained well with distance downstream of the blade though there is some mixing due to the limited numerical dissipation implicit in the HYDLIN scheme. The pressure perturbation on Figure 6 shows the high response in the blade passage, as also shown on the blade surface on Figure 5, and the decaying pressure away from the blade.

For the 2nd harmonic Figure 9 shows that we now have one propagating acoustic wave in circumferential order k=1, which has the lowest circumferential wave number as shown on Table 1. The other modes are cut-off though there is clearly still a problem with reflection at the inlet and outlet boundaries for these cut-off modes. The constant level of the cut-on mode indicates that the signal is dominated by the wave propagating away from the blade and that there is little reflection of this mode at the boundary. Also there is little numerical dissipation of the mode on the grid used from the 2nd order numerical scheme in HYDLIN. The variation of the apparent pressure in mode k=1 just upstream of the blade (-0.75 < X/chord < -0.5) is due to the circumferential non-uniformity of the mean flow in this region. The single propagating wave is very clear on the unsteady pressure of Figure 8. The axial velocity perturbation on Figure 8 again shows the persistence of the vortex sheet downstream of the blade.

For the 3rd harmonic there are now two propagating waves, corresponding to k=1 and k=2 of Table 1. Again there is little dissipation of the waves due to the numerical scheme. The pressure perturbation on Figure 10 shows now the circumferential and axial interference of these two propagating waves. Downstream of the blade the dominant wave is the mode k=2, which actually has the larger circumferential wave number, whilst upstream of the blade the dominant mode is k=1. Note that k=1 has a positive circumferential wave number, from Table 1, and accordingly is "spinning" in the same direction as the incoming gust vortical wave (which is towards the top of the page on Figure 10), whilst mode k=2 has a negative circumferential wave number and is "spinning" opposite the incoming vortical wave.

SUMMARY AND CONCLUSIONS

A linear unsteady CFD approach has been used to analyse the cascade-gust interaction test problem with incoming gusts in the 1st, 2nd and 3rd harmonics. A fine 2D multi-block structured mesh has been used with around 48K nodes for the single blade passage. Even when extended to 3D such a fine mesh resolution remains a practical approach with today's computing resources for a linear unsteady CFD approach to wake-blade interaction.

The linear CFD analysis has demonstrated the key physics of the cascade-gust interaction and predicted the levels of the acoustic waves propagating upstream and downstream of the blade generated by the interaction.

REFERENCES

1. Moinier, P., "Algorithm Developments for an Unstructured Viscous Flow Solver", Ph.D. Dissertation, Oxford University, 1999
2. Campobasso, M.S. and Giles, M.B., "Effects of Flow Instabilities on the Linear Analysis of Turbomachinery Aeroelasticity", Jnl of Propulsion and Power, vol. 19, no. 2, March-April 2003, 250-259.
3. Spalart, P.R. and Allmaras, S.R., "A one-equation turbulence model for aerodynamic flows", AIAA-92-0439, 30th Aerospace Sciences Meeting and Exhibit, January 1992
4. Giles, M.B. "Non-reflecting boundary conditions for the Euler equations", CFDL Report 88-1, MIT Dept. of Aero. and Astro., 1988

SIMULATION OF CASCADE – GUST INTERACTION BY USING GRID-OPTIMIZED DISPERSION-RELATION-PRESERVING METHODS

Jonghoon Bin[†] , Cheolung Cheong[‡] and Soogab Lee[*]
School of Mechanical and Aerospace Engineering
Seoul National University
Seoul 151-742, Korea

ABSTRACT

Prediction and reduction of unsteady turbomachinery noise is the main issues for reducing overall acoustic emission for subsonic vehicles with high bypass ratio engines. This paper presents a numerical analysis of cascade/gust interaction using a time-marching solution of the unsteady, nonlinear Euler equations of which the spatial derivatives and the time integration are computed by using Grid-Optimized Dispersion-Relations-Preserving (GODRP) schemes and 3rd-other optimized Adams-Bashforth method, respectively. The incoming periodic gusts are specified through the subsonic nonreflecting boundary condition with care. Comparison of results for a flat-plate cascade with results using analytic theory demonstrates this method's capability to accurately predict unsteady response of periodic gust. Application of these methods and results for benchmark problem 2 of Category 3 are implemented.

INTRODUCTION

At subsonic flow, one of the primary sources of turbomachinery noise corresponds to unsteady loading on turbomachinery blades. The various mechanisms contributing to such unsteady loading on blades include inflow distortion, rotor-stator interaction and the interaction of vortices or unsteady disturbances with the fan or the stator. Especially, the gust-cascade interaction can be taken as representing the interaction of inflow disturbances with the fan or the interaction of the fan wakes and the stator. In the simplest gust-cascade model, the blades are considered as two-dimensional flat-plate cascades stacked in the spanwise direction in 2nd CAA Workshop. The inflow distortions or the fan wakes are given by periodic vortical gusts convected with the steady mean flow. The interaction of the gust with the blades produces unsteady pressure distribution on the surfaces of blades. If the unsteady surface pressure is coupled to the propagation duct modes inside the duct, the radiated inlet and exhaust sound can be obtained.

In the present decade, considerable progress in computational aeroacoustics (CAA) has been achieved. The unsteady governing equations are discretized and solved for time-dependent flow variables, which includes the mean flow and the flow or acoustic disturbances. High-order schemes are required for discretization to reduce dissipation and dispersion errors. The numerical solver used here is a Grid-Optimized Dispersion-Relation-Preserving (GODRP) scheme (ref. 1) which is developed to overcome the adverse effects of structured curvilinear grids on the dispersion and dissipation characteristics of numerical schemes where the mapping or transformation of equations introduce an inhomogeneous medium in the computation area, which inhomogeniety can adversely impact on the wave propagation properties, so-called the dispersion and dissipation, which are two major sources of error associated with numerical schemes in computational aeroacoustics (ref. 2). In addition, high-order schemes support the formation of spurious modes at the boundaries of the computational domain. Careful attention for unsteady boundary treatment is needed to produce the physically correct disturbance field. Therefore, accurate nonreflecting boundary conditions are necessary for computational aeroacoustics, especially internal problem such as turbomachinery noise. Furthermore, periodic vortical gusts at a inflow region require a periodicity upon lower/upper periodic lines. Considerable progress has been made in treating boundary conditions in computational

---

[†] Ph. D. Candidate, mrbin@snu.ac.kr
[‡] BK21 Post Doctor, accu99@snu.ac.kr
[*] Professor, solee@plaza.snu.ac.kr; Address: BD 301-1303, Seoul National University, Seoul 151-742, Korea

domain (refs. 3 to 8). None of these single passage methods has been shown to be able to obtain a solution to problems with more than one unsteady disturbance and there exist some ambiguity whether these approaches might ensure periodicities or non-linearity with only a single passage except the time efficiencies. In the present work, direct periodic multi-passage approach to two-dimensional unsteady Euler calculations using subsonic nonreflecting boundary condition by Kim & Lee (ref. 10) has been used. The developed solver enables a multi-passage solution of unsteady acoustic response in blade rows under multiple disturbances with arbitrary inter-blade phase angles.

The methodology of numerical method together with the governing equations and numerical boundary treatment will be discussed in Section 2. In Section 3, code validation is presented in case of 2-D flat-pate cascade problem in 2nd CAA Workshop and a numerical calculation of a blade row under single or multiple disturbances will be presented.

METHODOLOGY

1. Governing Equations and Solution Methods

To improve the computation of unsteady aerodynamics, a time-linearized analysis method is mainly used. The linearized Euler analysis to produce well the response to the acoustic or vortical waves is shown in many previous studies assuming that the gust is to be a small harmonic perturbation of the uniform steady flow. However, in the time-linearized approach, nonlinear effects cannot be assessed when the amplitude of excitation is no longer in the linear range. And so, nonlinear Euler equations governing the 2-D cascade flow are solved to cover the linear and nonlinear response to periodic gust excitation with high-order CAA method in the present investigation.

$$\frac{\partial}{\partial t}\begin{bmatrix} \rho \\ \rho u \\ \rho v \\ E \end{bmatrix} + \frac{\partial}{\partial x}\begin{bmatrix} \rho u \\ \rho u^2 + p \\ \rho uv \\ u(E+p) \end{bmatrix} + \frac{\partial}{\partial y}\begin{bmatrix} \rho v \\ \rho uv \\ \rho v^2 + p \\ v(E+p) \end{bmatrix} = 0 \tag{1}$$

The pressure is related to the density, velocities by the following equation that assume a perfect gas with a constant specific heat ratio.

$$p = (\gamma - 1)\left[E - \tfrac{1}{2}\rho(u^2 + v^2)\right] \tag{2}$$

The above time dependent Euler equations governing the 2-D cascade flow are discretized in space using Grid-Optimized Dispersion-Relation-Preserving (GODRP) schemes (ref. 1) together with second order artificial damping to damp out numerical oscillations and fourth order dissipation to suppress high-frequency modes and to allow the numerical scheme to converge to a steady state. Temporal integration of the discretized equations is carried out using the third order explicit Adams-Bashforth method (ref. 9). In this problem, the grid used was a H-hype curvilinear grid with 193×46 in each block, which computational mesh is built up from a non-uniform grid highly clustered near the walls. For the calculation, two-multi blocks are used for steady mean flow calculation and 27 blocks are used for unsteady gust-cascade interaction simulation.

2. Boundary Condition Formulation

Because the computational domain is usually finite, boundary conditions must be imposed at the edge of the grid. These boundary conditions can generate undesirable spurious fluctuations. Therefore, accurate nonreflecting boundary conditions are necessary for computational aeroacoustics, especially internal problem such as turbomachinery noise. The duct acoustic modes are dispersive, i.e., different frequency duct modes propagate at different speeds. This dispersive behavior of the duct modes practically eliminates the possibility of the existence of a simple asymptotic solution that can be used for developing suitable numerical boundary conditions. For the construction of steady-state and unsteady nonreflecting boundary conditions for the Euler equations, the normal flux derivative term is linearized and decomposed into one-dimensional characteristics. Subsonic nonreflecting boundary conditions are applied in steady-state and unsteady cases. When a periodic vortical gust enters the inflow plane, the

gust terms are added in characteristic variables. On the surfaces, the slip-wall boundary condition is applied. The contents in detail are introduced.

Solid Wall Boundary Conditions

Solid wall is mainly implemented by setting equal to zero the mass flux through the solid wall faces. Many methods have been developed and are useful for treating wall boundaries. Some of the more recent work in this area has been implemented by Tam & Dong (ref. 11) and by Chung & Morris (ref. 12). Tam & Dong developed wall boundary conditions with their Dispersion Relation Preserving (DRP) scheme and this method minimizes the number of required ghost values. An analysis of these conditions shows that they are capable of numerically simulating the presence of a solid wall without introducing significant errors associated with spurious numerical wave generation and numerical boundary layers. Chung & Morris have been developed a method for introducing a solid wall into the computational domain that is quite simple to implement. Their approach, Impedance Mismatch Method(IMM), is based on the concept that a solid wall can be modeled by an acoustic medium with an impedance that is much higher that that of the fluid. It is, however, not clear how this approach would be applied to problem with flow. Therefore, the wall conditions implemented here are based on the approach by Tam & Dong.

To set the normal pressure derivative to zero, a ghost point was used inside the wall for only the normal pressure derivative.

$$
(\eta_x \xi_x + \xi_x \eta_y) p_\xi + (\eta_x^2 + \eta_y^2) p_\eta
$$

$$
= \rho(\frac{\partial \eta_t}{\partial t} + u \frac{\partial \eta_x}{\partial t} + v \frac{\partial \eta_y}{\partial t}) - \rho(\xi_t + \xi_x u + \xi_y v)(\eta_x u_\xi + \eta_y v_\xi)
$$

(3)

At the leading and trailing edge of the cascade, i.e., grid singularities, the wall condition is set on both the upper and lower surfaces and then the result is averaged in singular points.

Periodic Boundary Conditions

For steady flows and unsteady flows, the periodic boundary condition is applied to upper and lower periodic lines assuming that the flows on one periodic boundary are exactly the same as the flow at the corresponding point on the other periodic boundary at the same time.

$$
U(x, y, t) = U(x, y + P, t)
$$

(4)

where P is periodic length. Generally speaking, there are many examples in solutions in which periodic terms produce solutions with a sub-harmonic component, whose period, P, is a multiple of the original period. In example of vortex shedding from a cascade, imposition of spatially periodic boundary conditions forces the solution to exhibit
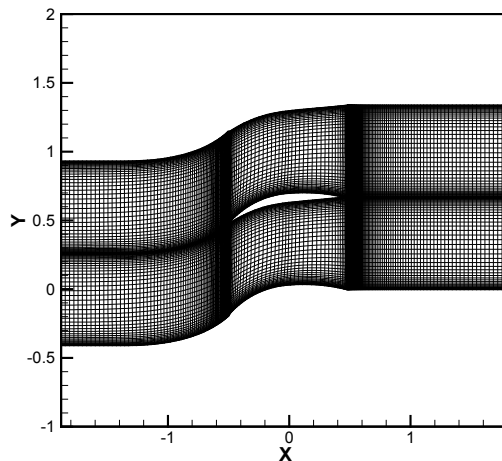

Figure 1. Computational grids for steady and unsteady calculation

synchronous shedding, in which each cascade sheds vortices of alternating sign, with one cascade shedding a vortex of positive sign at the same time, but shed vortices of alternating sign, with one blade shedding a vortex of positive sign at the same time that its two neighbors shed vortices of negative sign. And so, to ensure general solutions of stead mean flow, a computational domain spanning two cascade passages is adopted and implemented in this case.

On the contrary to steady case, unsteady simulations require more careful treatments in use of periodic conditions. This benchmark problem must consist of at least 27 passages in an unstaggered cascade for periodicity of incoming periodic gusts. In this problem, a periodic vortical gust is convected in a mean flow computed in previous steady flow calculation. This problem is to be solved with the full Euler equations.

Inflow/Outflow Boundary Conditions

The computational domain consists of twin or multiple passages with a blade being at the center of each passage domain. For the steady mean flow, stagnation pressure, stagnation temperature and flow angles are specified at the inlet while static pressure is specified at the stage exit, and local nonreflecting boundary conditions are used. And then 2-D nonreflecting boundary conditions are adopted at both inlet and exit far-filed boundaries for the harmonic perturbations as incoming gusts. The inflow and outflow boundary conditions are implemented using subsonic nonreflecting boundary conditions by Kim & Lee (ref. 11). These boundary conditions are based on the local one-dimensional characteristics in the direction normal to the inflow and outflow boundary. The physical boundary conditions are imposed to the characteristic convection terms using the local one-dimensional inviscid relations. For a two-dimensional subsonic flow, three characteristic waves, L_1, L_2 and L_3 are entering the computational domain while L_4 is leaving it at the speed of (u-c). When a periodic vortical gust enters the inflow plane, the gust terms are added in characteristic variables.

For the velocity perturbation like a periodic gust, the incoming waves are given by following relations.

$$L_2 = K_{in}\frac{\tilde{V} - \tilde{V}_\infty}{2} = K_{in}\frac{-\tilde{\xi}_x(v - v_\infty) + \tilde{\xi}_y(u - u_\infty)}{2} - (-\tilde{\xi}_x\varepsilon_y + \tilde{\xi}_y\varepsilon_x)\omega\cos(\omega t)$$

$$L_3 = K_{in}\left[(\tilde{U} - \tilde{U}_\infty) + \frac{p - p_\infty}{\rho c}\right] = K_{in}\left[\tilde{\xi}_x(u - u_\infty) + \tilde{\xi}_y(v - v_\infty) + \frac{p - p_\infty}{\rho c}\right] - 2(\tilde{\xi}_x\varepsilon_x + \tilde{\xi}_y\varepsilon_y)\omega\cos(\omega t)$$

$$where, K_{in} = \sigma_{in}(1 - M_{max}^2)\frac{c}{l}, (\tilde{\xi}_x, \tilde{\xi}_y) = (\frac{\xi_x}{\sqrt{\xi_x^2 + \xi_y^2}}, \frac{\xi_y}{\sqrt{\xi_x^2 + \xi_y^2}})$$

(5)

L_1 is determined by the quasi-isentropic condition and L_4 is computed from interior domain information.

At the outflow boundary, only one characteristic is corrected. This is to set the amplitude of incoming wave as

$$L_4 = K_{out}\left[\frac{p - p_\infty}{\rho c}\right]$$

$$K_{out} = \sigma_{out}(1 - M_{max}^2)\frac{c}{l}, \sigma_{out} = 0.25$$

(6)

The time derivatives of the flow variables are then determined by

$$\frac{\partial \rho}{\partial t} + L_1 + \frac{\rho}{2c}(L_3 + L_4) = 0$$

$$\frac{\partial u}{\partial t} + \frac{1}{2}(L_3 - L_4) = 0$$

$$\frac{\partial v}{\partial t} + L_2 = 0$$

$$\frac{\partial p}{\partial t} + \frac{\rho c}{2}(L_3 + L_4) = 0$$

(7)

Values obtained for the wave amplitude variation will be approximate and then applied in inflow and outflow boundary region with three rows of boundary points.

NUMERICAL RESULTS

Steady Mean Flow Results

Figure 2 shows converged flow results in steady-state. From numerical results, we get inflow Mach number is 0.4365, outflow mach number is 0.3497 and inflow angle is 36.0. By CFL requirements of minimum grid cell and selection of explicit time integration, it took considerable iteration time to reach the flow in steady-state about order of 5.
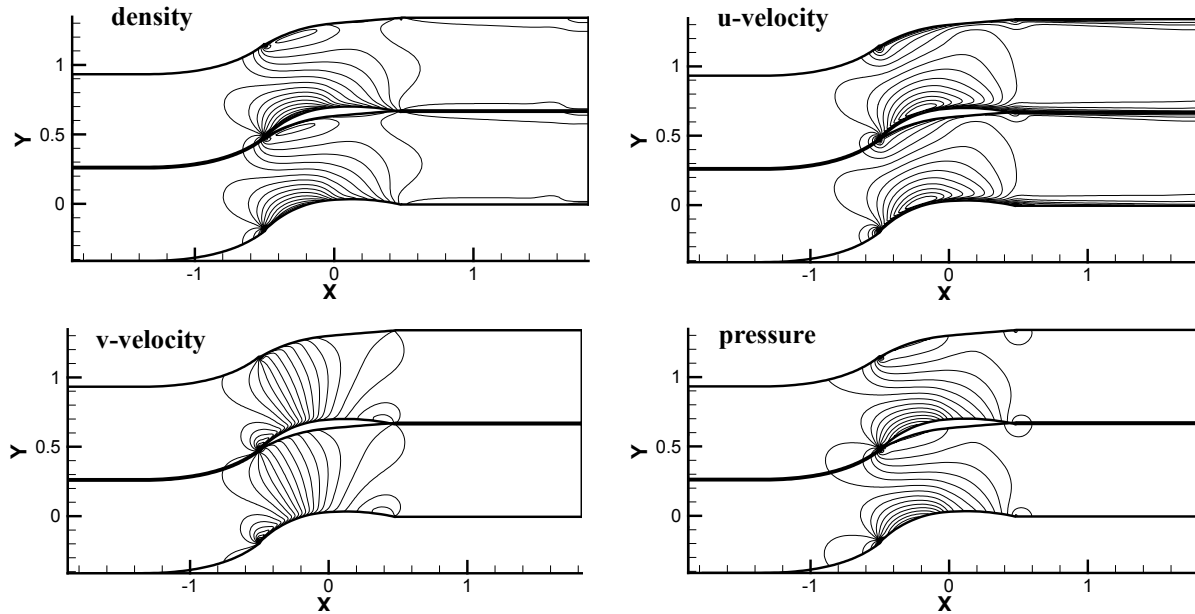
Figure 2. Steady mean values computed with the CAA

Table 1. Steady Solution of blade row.

	Inflow region	Outflow region
Mach No	0.4365	0.3497
Pressure	0.876	0.920
Flow angle	36.0°	-0.82°

The mean flow past cascade rows was computed. This method provide efficient resolution of the mean flow features near the leading and trailing edge of cascade airfoil as well as slightly thin vortex sheet generations near the trailing edge.

Code Validation for Unsteady Flow Simulation

Flat-Plate Cascade: the 2nd Benchmark Problem

To validate the current Euler solver, unsteady simulation involved a benchmark problem in Category 3 from the 2nd Workshop on Benchmark Problems in Computational Aeroacoustics (ref. 13) is performed. This problem involves noise generation due to the vortical gust by an unstaggered flat-plate cascade. The mean flow and vortical gusts are defined as follows:

$$M_\infty = 0.5, \quad u_{gust} = (A\beta/\alpha)\cos(\alpha x + \beta y - \omega t), \quad v_{gust} = A\cos(\alpha x + \beta y - \omega t), \tag{8}$$

where $A = 0.01, \ \alpha = \beta = \omega = 5\pi/2$

For the periodicity, the computational domain is given as $-2 \le x \le 3, \ 0 \le y \le 4$. The grid for all calculations had a uniform spacing of $\Delta x = \Delta y = 0.02$ and the time step used was $\Delta t = 0.0002$.
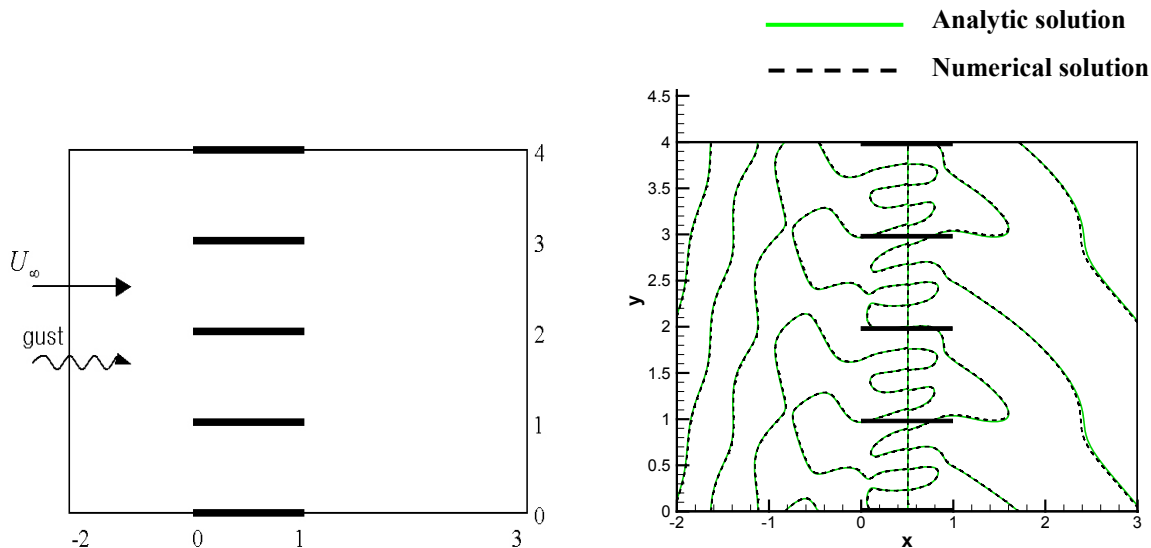
Figure 3. Schematic of flat-plate cascade simulation

This figure shows zero pressure contours between the analytic and numerical solutions at time =20. At the outflow region, there is a little error due to the outflow boundary conditions.

Sound Generation by Interacting with a Gust

The acoustic waves generated by the interaction between a gust and cascade can propagate or exponentially decay in the duct upstream and downstream of cascade rows. In particular, the propagation or decay of acoustic waves can be predicted assuming that the vortical gusts and the acoustic pressure are relatively small on a steady mean flow. As mentioned above, this benchmark problem must consist of at least 27 passages in an unstaggered cascade for periodicity. In this problem, a periodic vortical gust is convected in a mean flow computed in previous steady flow calculation. This problem is to be solved with the full Euler equations. The grid used in this calculation is H-type grid with 27 passages stacked in the spanwise direction, which can provide accurate flow resolutions and gust response. Each passage has the number of grid points in the axial direction of 193 and in the lateral direction of 46. Thus total 239706 grid points with 8878 points per passages are used in steady and unsteady computations. The numerical computations are continued until periodicity in pressure is achieved by showing that at least two successive periods are identical on the inflow/outflow boundaries and on the airfoil surfaces. The solution is to be run about computation time of 40 with the time interval of 7.0×10^{-5}.

Figure 4 and 5 illustrate time history at given inflow and outflow points in case of the fundamental frequency and harmonic frequency. In this figure, vortical gust enters the computational domain well. However, there exists a little variation of pressure history at outflow region because this solution is not fully converged due to the restriction of computation time to meet the publication day of 4th CAA Workshop proceedings. In previous study (ref. 14), it is insisted that the solution is to be run about 200 periods in order to get accurate acoustic signals without spurious wave reflection on the inflow/outflow boundary. Periodic constant acoustic waves propagate downstream but spurious reflected perturbations are generated at the outflow plane and propagate upstream. Finally these undesired disturbances contaminate the interior computation results. Particularly, reflections from the inflow/outflow boundary interacting with the cascade and initiating a nonphysical feedback loop may result in instability or non-periodicity. However, as the unsteady computation is repeated with high order GODRP scheme and careful boundary treatment, periodicity in pressure is achieved. We are restarting the numerical computation until periodicity in pressure is achieved.

(-1.5c, -0.3c)　　　　　　(-1.5c, 0.0c)　　　　　　(-1.5c, 0.3c)

(1.5c, -0.3c)　　　　　　(1.5c, 0.3c)
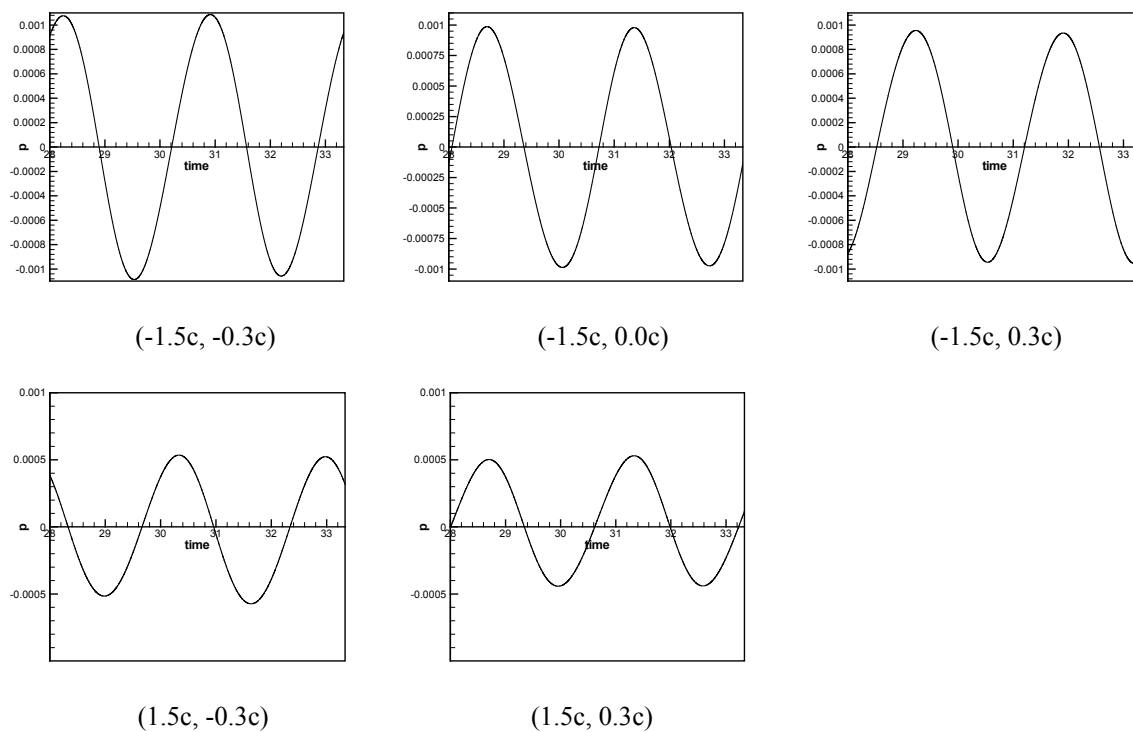
Figure 4. Pressure waveforms for 1ˢᵗ harmonic excitation

(-1.5c, -0.3c)　　　　　　(-1.5c, 0.0c)　　　　　　(-1.5c, 0.3c)
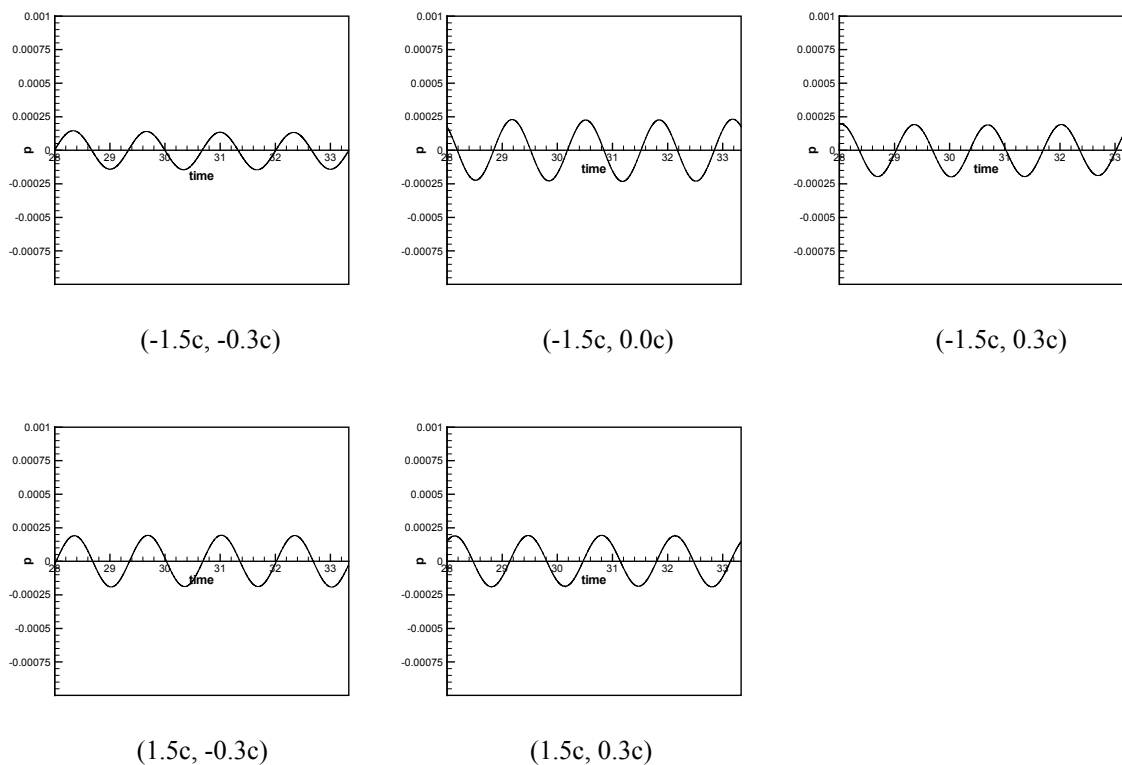
(1.5c, -0.3c)　　　　　　(1.5c, 0.3c)

Figure 5. Pressure waveforms for 2ⁿᵈ harmonic excitation

Table 2 shows the computed acoustic pressure level (SPL) at given points. In the computational domain with the fundamental reduced frequency $\omega = 3\pi / 4$ and the transverse wavenumber $k_y = 11\pi / 9$, the non-dimensional acoustic pressure level at inflow region is much larger than that at outflow region. This is due to the propagation or decay of acoustic mode in a duct.

Table 2. Non-dimensional sound pressure level(SPL) with $p_{ref} = 20 \mu Pa$.

position	Inflow region			Outflow region	
	(-1.5c, -0.3c)	(-1.5c, 0.0c)	(-1.5c, 0.3c)	(1.5c, -0.3c)	(1.5c, 0.3c)
1st harmonic	131.72	130.91	130.58	125.68	124.58
2nd harmonic	114.06	118.26	116.82	116.71	116.64

CONCLUDING REMARKS

A new nonlinear harmonic method with the GODRP scheme and nonreflecting boundary conditions has been developed for aeroacoustic analysis of unsteady multi-stage turbo-machinery noise. The present nonlinear harmonic method can be efficient noise prediction tools to get accurate solutions to realistic noise prediction problems. In particular, the reasonable prediction of turbo-machinery noise will play an important role in aerodynamic and aeroacoustic design process.

REFERENCES

1. Cheong, C.; and Lee, S.: Grid-optimized dispersion-relation-preserving schemes on general geometries for computational aeroacoustics. *J. Comput. Phys.* **174**, 2001, 248-276.
2. Tam, C. K. W.: Computational Aeroacoustics: Issues and Methods. *AIAA J.* **33**,1995, pp. 1788-1796.
3. Kaji, S.; and Okazaki, T.: Generation of Sound by Rotor-Stator Interaction, Journal of Sound and Vibration **13**(3), 1970, pp. 281-307.
4. Namba, M.: Three-Dimensional Analysis of Blade Force and Sound Generation for an Annular Cascade in Distorted Flows, Journal of Sound and Vibration **50**(4), 1997, pp. 479-508.
5. Atassi, H.; Fang, J.; and Hardy, B.: Sound Radiated from a Loaded Cascade in Nonuniform Transonic Flow. AIAA Paper 95-0166, Jan. 1995.
6. Mankbadi, R. R.: Computational Aero-Acoustics in Propulsion System, Journal of Propulsion and Power **15**(4), 1999, pp. 504-512.
7. Giles, M.: Nonreflecting Boundary Conditions for Euler Equation Calculations. *AIAA J* **12**, 1990, pp. 250-2058.
8. Hixon, R.; Shih, S.-H.; and Mankbadi, R. R.: Evaluation of Boundary Conditions for the Gust-Cascade Problem. Journal of Propulsion and Power **16**, 2000, pp. 72-78.
9. Tam, C.K.W.; and Webb, J.C.: Dispersion-Relation-Preserving Schemes for Computational Acoustics. *J. Comput. Phys.* **107**, 1993, pp. 262-281.
10. Kim, J.W.; and Lee, D. J.: Generalized Formulation and Application of Characteristic Boundary Conditions. AIAA/CEAS-98-2222, 1998.
11. Tam, C.K.W.;and Dong, Z.: Wall boundary conditions for high order finite difference schemes in computational aeroacoustics. *Theor. Comput. Fluid Dyn.* **6**, 1994, pp.303-322.
12. Chung. C.; and Morris. P. J.: Acoustic scattering from two- and three- dimensional bodies. *CEAS/AIAA Paper* 95-008, 1995.
13. Tam, C.K.W.; and Hardin, J.C.: *Second computational aeroacoustics workshop on benchmark problems.* NASA CP 3352, 1997.
14. Nallasamy, M.; et al.: A Time Domain Analysis of Gust-Cascade interaction Noise, AIAA-2003-3134, Jul. 2003.

COMPUTATION OF A SINGLE AIRFOIL GUST RESPONSE AND GUST-CASCADE INTERACTION USING THE CE/SE METHOD

Xiao-Yen Wang[*],   **Ananda Himansu**

Taitech Inc., NASA Glenn Research Center, Cleveland, OH 44135

*email: xiao-yen.wang@grc.nasa.gov

Sin-Chung Chang   and   **Philip C.E. Jorgenson**

NASA Glenn Research Center, Cleveland, OH 44135

ABSTRACT

The problems 1 and 2 in Category 3 are solved using the space-time conservation element and solution element (CE/SE) method. Problem 1 concerns the acoustic field generated by the interaction of a convected harmonic vortical gust with a single isolated airfoil. Problem 2 models rotor-stator interaction in a 2D cascade. Both problems involve complex geometries and flow physics including vortex shedding and acoustic radiation. An unstructured triangular mesh is used to solve both problems. For problem 2, the Giles approach is incorporated with the CE/SE method to handle non-equal pitches of the rotor and stator. Numerical solution of both near and far fields of problem 1 are presented and compared with a frequency-domain solver GUST3D and a time-domain high-order Discontinuous Spectra Element Method (DSEM) solutions. For problem 2, numerical solutions on the blade surface, inlet and outlet planes are presented.

1. INTRODUCTION

The method of space-time conservation element and solution element (abbreviated as the CE/SE method) is a finite volume method with second-order accuracy in both space and time. The flux conservation is enforced in both space and time instead of space only. It has low numerical dissipation and dispersion errors. It uses simple non-reflecting boundary conditions and is compatible with unstructured meshes. It is simple, flexible, and generate reasonably accurate solutions. The CE/SE method has been successfully applied to solve numerous practical problems, especially aeroacoustic problems. Details of the numerical algorithm based on the CE/SE method are referred to [1-4]. Applications of the CE/SE method to Computational AeroAcoustic (CAA) problems are referred to [5-10].

2. CATEGORY 3: PROBLEM 1

Consider a Joukowski airfoil in a two-dimensional gust. The geometry of the Joukowski airfoil and mean flow conditions can be found in [11]. The incoming gust has velocity fluctuations described as follows:

$$u' \stackrel{\text{def}}{=} -(v_g \, k_y/|\mathbf{k}|) \cos(k_x x + k_y y - \omega t) \tag{1}$$

$$v' \stackrel{\text{def}}{=} (v_g \, k_x/|\mathbf{k}|) \cos(k_x x + k_y y - \omega t) \tag{2}$$

and

$$\rho' \stackrel{\text{def}}{=} 0 \quad \text{and} \quad p' \stackrel{\text{def}}{=} 0 \tag{3}$$

where (i) $v_g = 0.02$, and $k_x = k_y = 0.1, 1.0, 3.0$, (ii) $|\mathbf{k}|$ is the absolute value of $\mathbf{k} = (k_x, k_y)$, i.e.,

$$|\mathbf{k}| \stackrel{\text{def}}{=} \sqrt{k_x^2 + k_y^2} \tag{4}$$

and (iii)

$$\omega = \overline{u}_\infty k_x \tag{5}$$

with $\overline{u}_\infty$ being the mean x-velocity at infinity.

The solution procedure and initial and boundary conditions used in solving this problem are referred to [9] and will not repeated here due to limited space. A 2D parallel CE/SE nonlinear Euler solver is used

in the computation. The parallelization of the CE/SE code is referred to [12]. In the following, numerical results will be presented for both symmetric and cambered airfoils at three gust frequencies.

2.1 Numerical Results of Problem 3.1

In the following subsections, the RMS pressure on the airfoil surface, and the sound intensity at one and four chord lengths from the origin, are presented in the following for all cases to examine both the near and far field solutions. In all figures, the numerical solution of the acoustic pressure non-dimensionalized by v_g is plotted.

2.1.1 Symmetric Airfoil

The symmetric Joukowski airfoil of 12% thickness is analyzed to show the geometrical capability of the CE/SE method. As shown in Fig. 1, the airfoil is surrounded by an unstructured mesh (Fig. 1(a)) which, in turn, is embedded in a triangulated structured mesh (Fig. 1(b)). The unstructured mesh is generated using the code TRUMPET [13]. The mean pressure on the airfoil surface is plotted in Fig. 2 and compared with the potential code FLO36 solutions. The corresponding acoustic solutions are shown in Figs. 3–5 for the three frequencies. A reasonable agreement between CE/SE and GUST3D solutions is observed for $k_x = k_y = 0.1$ and 1.0, while there are discrepancies at $k_x = k_y = 3.0$. However, the CE/SE solutions agree well with the DSEM solution at the far field for $k_x = k_y = 3.0$(Fig. 5(c)).

As an example, a computational domain of $-23 \leq x, y \leq 23$ is used for $k_x = k_y = 3.0$. An unstructured mesh with 7392 triangles is used in the region of $-2 \leq x, y \leq 2$ while a uniform triangulated structured mesh formed from 420000 triangles is used in the rest of the computational domain. On the airfoil surface, there are 168 cells. The RMS pressure solution converges by $t = 10T$ (14000 marching steps). The computation takes 1.5 hours wall-clock-time using 16 CPUs on a SGI Origin 2000 system with 400 MHz MIPS R12000 processors.

2.1.2 Cambered Airfoil

The airfoil considered here has the same thickness as the symmetric airfoil but with a camber ratio of 0.02 and an angle of attack of 2°. The steady lift is no longer zero and the flow field is more complex. A larger computational domain is necessary. As an example, a computational domain of $-40 \leq x, y \leq 40$ is used for the case $k_x = k_y = 1.0$. Among the 643744 triangular cells that fill the entire computational domain, 5344 cells are contained in the region of $-2 \leq x, y \leq 2$ (see Fig. 6). There are 168 points on the airfoil surface. The numerical results are obtained assuming $\Delta t = T/1050$.

The computed mean pressure on the airfoil surface is plotted in Fig. 7 with the FLO36 solution, showing that the CE/SE pressure solution on the upper surface is slightly under-predicted. For the two frequencies $k_x = k_y = 0.1$ and 1.0, the unsteady solutions are plotted in Figs. 8–9, respectively. The CE/SE solutions are very close to the GUST3D solution at $k_x = k_y = 0.1$. However larger discrepancies are observed at $k_x = k_y = 1.0$. The CE/SE solution gives reasonably good agreement with the DSEM solution at $k_x = k_y = 1.0$.

The domain size study is performed for the cambered airfoil at $k_x = k_y = 1.0$. The near field solutions, including the RMS pressure on the airfoil surface and the sound intensity at one chord length, obtained in a smaller domain of $-23 \leq x, y \leq 23$, are identical to the solution presented above. The sound intensity at four chord lengths is slightly different from the presented solution. The non-reflecting boundary condition has some reflections that are generated at the far-field boundary, which is also observed in the RMS pressure contour plot. However the reflection is generally less than 5% of the maximum value of the acoustic field and has little effect on the accuracy of the numerical solutions.

Grid refinement study is not performed because the mesh used in the computation is fine enough to capture both the acoustic waves and the gust. About 30–40 mesh points per wave length are necessary for the CE/SE method since it is 2nd order accurate. In the current computation, about 40 mesh points per wave length are used.

3. CATEGORY 3: PROBLEM 2

Consider the rotor-stator interaction problem. The wake generated by the rotor blade at the upstream of the stator is described as follows:

$$u'_g = \sum_{n=1}^{3} a_n \cos[n(k_y y - \omega t)] \cos \beta \tag{6}$$

$$v'_g = -u'_g \tan \beta \tag{7}$$

where $k_y = 11\pi/9, \omega = 3\pi/4, \beta = 44°, a_1 = 5\text{x}10^{-3}, a_2 = 3\text{x}10^{-3}$, and $a_3 = 7\text{x}10^{-4}$. And $n = 1, 2, 3$ corresponds to the rotor blade passing frequency (BPF) and its harmonics. Assume the pitches of the rotor and stator be P_r and P_s. Then $P_r = 2\pi/k_y = 18/11$, while $P_s = 2/3$ is given. The ratio of the rotor and stator pitches, $P_r/P_s(=27/11)$, is not unity. In order to impose the periodic boundary condition in the y- direction, 27 passages of the stator vane has to be used in the computation, which is very expensive. An approach to treat non-equal pitches was developed by Giles in [14] for the analysis of rotor/stator interaction. The same approach is adopted in the space-time CE/SE method in this work. In the following, the Giles approach and its validation will be described briefly, which is followed by the numerical results of the benchmark problem.

3.1 Non-equal Pitch Treatment and its Validations

Consider the 2D nonlinear Euler equations described as follows:

$$\frac{\partial u_m}{\partial t} + \frac{\partial f_m}{\partial x} + \frac{\partial g_m}{\partial y} = 0, \quad m = 1, 2, 3, 4 \tag{8}$$

Here

$$u_1 = \rho, \quad u_2 = \rho u, \quad u_3 = \rho v, \quad u_4 = E_t \tag{9}$$

$$f_1 = \rho u, \; f_2 = \rho u^2 + p, \; f_3 = \rho uv, \; f_4 = (E_t + p)u \tag{10}$$

$$g_1 = \rho v, \; g_2 = \rho uv, \; g_3 = \rho v^2 + p, \; g_4 = (E_t + p)v \tag{11}$$

with $E_t = p/(\gamma - 1) + \rho(u^2 + v^2)/2$. By introducing the coordinate transformation:

$$x' = x, \quad y' = y, \quad t' = t - \lambda y \tag{12}$$

where $\lambda = \frac{P_s - P_r}{V P_s}$ with V being the rotor wheel speed, the 2D Euler equations become

$$\frac{\partial(u_m - \lambda g_m)}{\partial t'} + \frac{\partial f_m}{\partial x'} + \frac{\partial g_m}{\partial y'} = 0 \tag{13}$$

Thus the conservation state variables have changed from u_m to $u_m - \lambda g_m$. The numerical scheme for Eq. (13) can be constructed based on the CE/SE method. The time-marching is performed in the x'-y'-t' coordinate. Note that at a constant t', the physical time t is not necessarily the same for different y locations. The periodic boundary condition:

$$u_m(x', y', t') = u_m(x', y' + P_s, t') \tag{14}$$

is imposed at the upper and lower boundaries in the y direction of the computational domain.

The problem 2 in Category 3 of the 2nd CAA Workshop is used here to validate the Giles approach with the CE/SE method. Details of this benchmark problem are referred to [7]. Numerical results obtained by using 4 passages and single passage are presented in Figs. 10–13. When 4 passages are used, the original Euler equations are solved, while the Giles approach is used when the single passage is used in the computation. In this problem, $P_s = 1.0, P_r = 0.8, V = 1.0$, then $\lambda = 0.2$. In Fig. 10, the acoustic pressure contour at one time instance is plotted in the 4 passages to show the wave pattern. In Fig. 11, the acoustic pressure on the upper surface of the flat-plate blade at $y = 0$ is plotted for both solutions obtained by using 4 passages and single passage, showing a good agreement except a slight difference near the leading edge. The RMS pressure at the inlet and outlet planes obtained using 4 passages is plotted in Fig. 12 with the analytical solution, while the corresponding solution obtained using single passage is plotted in Fig. 13, showing slightly better agreement with the analytical solution because of less numerical reflections from the open inlet and outlet boundaries.

3.2 Numerical Results of Problem 3.2

In the current benchmark problem, $P_r = 18/11, P_s = 2/3$, and $V = 27/44$. Due to the numerical stability restriction [14], two passages of the stator vane are used in the computation. Then $\lambda = -10/27$. A mixed triangulated structured and unstructured triangular mesh is used. Approximately 48k triangles exist in the region of $-1.5 \leq x \leq 1.5$ and 300 points define each blade surface. On the blade surface, the slip condition is imposed, i.e., the normal velocity is set to be zero. At the inlet plane, the total pressure, total temperature, and flow angle are specified. The velocity fluctuation (gust) is also imposed. At the outlet, the back pressure is specified, others are extrapolated from neighboring interior points. In the time-marching, the mean flow variables at both the inlet and outlet planes are computed at every time period, T. At the upper and lower boundaries of the computational domain, the periodic boundary condition is imposed. The time step $\Delta t = T/6200$ is used. For one run, it takes around 100T to reach the time periodic state. A Fast Fourier Transform(FFT) analysis in time is performed based on the time-domain solutions to examine the sound pressure level at different BPF ($n = 1, 2, 3$). And a joint FFT analysis in time and spatial y- direction is performed to investigate the sound pressure level as a function of rotor harmonic n, spatial mode order m, and axial location x [15].

The steady-state pressure contour is plotted in Fig. 14. The mean pressure distribution on the blade surface is compared with the Turbo code solution in Fig. 15, showing a good agreement. The sound pressure level versus the rotor harmonic n at the six designated positions on the blade surface, three locations at inlet plane, and three locations at the outlet plane are plotted in Figs. 16 and 17, respectively. It can be seen that the acoustic response exists only at the excitation frequencies ($n = 1, 2, 3$). On the blade surface, the acoustic wave at $n = 1$ is dominant, while at the inlet and outlet planes, the sound pressure level at $n = 2$ becomes the largest. In Fig. 18, the distribution of sound pressure level at different spatial modes along the x- direction is plotted for $n = 1, 2, 3$, respectively. It shows that the spatial modes $m = -32$ and 22 at $n = 1$ exponentially decay, and the spatial modes $m = 10$ at $n = 2$, $m = -42$ and 12 at $n = 3$ propagate both upstream and downstream. Some oscillations are observed in Fig. 18(c), which needs to be investigated further. For $n = 1, 2, 3$, the distribution of sound pressure level on the blade surface, inlet and outlet planes are also plotted in Fig. 19, respectively, to provide a more complete picture of the sound pressure level distribution.

4. CONCLUSIONS

The problems 1 and 2 in Category 3 have been solved using the space-time (CE/SE) method. Numerical results of both problems have been presented. For problem 1, the CE/SE solutions are compared with GUST3D and DSEM solutions. A fairly good agreement between CE/SE and GUST3D solutions at lower frequencies is achieved. There are some discrepancies between CE/SE and GUST3D solution for higher frequencies. However, the CE/SE solution is in good agreement with the DSEM solution for these higher frequencies. For problem 2, no direct comparison between CE/SE and other solutions is made. The CE/SE solutions are similar to the results presented in [15] and agree with the prediction based on the linearized theory [16].

ACKNOWLEDGMENTS

References

[1] S.C. Chang, "The Method of Space-Time Conservation Element and Solution Element – A New Approach for Solving the Navier-Stokes and Euler Equations," *J. Comput. Phys.*, **119,** pp. 295-324, (1995).

[2] S.C. Chang, X.Y. Wang, and C.Y. Chow, "The Space-Time Conservation Element and Solution Element Method – A New High-Resolution and Genuinely Multidimensional Paradigm for Solving Conservation Laws," *J. Comput. Phys.*, **156**, pp. 89–136, (1999).

[3] X.Y. Wang and S.C. Chang, "A 2D Non-splitting Unstructured-triangular-mesh Euler Solver based on the Method of Space-Time Conservation Element and Solution Element," Vol. 8, No. 2, pp. 326-340, 1999, *Computational Fluid Dynamics JOURNAL.*

[4] X.Y. Wang and S.C. Chang, "A 3D Non-splitting Structured/Unstructured Euler Solver based on the Method of Space-Time Conservation Element and Solution Element," AIAA Paper 98-3278, Norfolk, Virginia, June, 1998.

[5] C.Y. Loh, S.C. Chang, J.R. Scott and S.T. Yu, "The Space-Time Conservation Element Method – A New Numerical Scheme for Computational Aeroacoustics," AIAA Paper 96-0276, January 15-18, 1996, Reno, NV.

[6] C.Y. Loh, L.S. Hultgren and S.C. Chang, "Waves Computations in Compressible Flow Using the Space-Time Conservation Element and Solution Element method," *AIAA Journal*, Vol.39, No.5, pp. 794–801, May 2001.

[7] X.Y. Wang, C.Y. Chow and S.C. Chang, "Numerical Simulation of Gust Generated Aeroacoustics in a Cascade Using the Space-Time Conservation Element and Solution Element Method," AIAA Paper 98-0178, January 12-15, 1998, Reno, NV.

[8] X.Y. Wang, S.C. Chang, and P. Jorgenson, "Prediction of Sound Waves Propagating through a Nozzle without/with a Shock Wave Using the Space-Time CE/SE Method," AIAA 2000-0222, Reno, NV, January, 2000.

[9] X.Y. Wang, S.C. Chang, A. Himansu, and P. Jorgenson, "Gust Acoustic Response of a Single Airfoil Using the Space-time Method," AIAA 2002-0801, Reno, NV, January, 2002.

[10] X.Y. Wang, A. Himansu, P. Jorgenson, and S.C. Chang, "Gust Acoustic Response of a Swept Rectilinear Cascade Using the Space-Time CE/SE Method," FEDSM 2001-18134, in *Proceedings of FEDSM'01 2001 Fluids Engineering Summer Meeting*, May 29–June 1, 2001.

[11] The Announcement of the Fourth Computational Aeroacoustics (CAA) Workshop on Benchmark Problems, August, 2003.

[12] A. Himansu, P. Jorgenson, X.Y. Wang and S.C. Chang, "Parallel CE/SE Computations via Domain Decomposition," in *Proceedings of 1st International Conference of Computational Fluid Dynamics*, Kyoto, June, 2000.

[13] P.C.E. Jorgenson and R.H. Pletcher, "An Implicit Numerical Scheme for the Simulation of Internal Viscous Flows on Unstructured Grids," AIAA-94-0306, January 1994.

[14] M. B. Giles, "Generalized Conservation Cells for Finite Volume Calculations," AIAA-87-1118, July, 1987.

[15] S. Sawyer, M. Nallasamy, R. Hixon, R.W. Dyson, L.D. Koch, "Computational Aeroacoustic Prediction of Discrete-Frequency Noise Generated by a Rotor-Stator Interaction," AIAA-2003-3268, May 12–14, 2003.

[16] S.N. Smith, "Discrete Frequency Sound Generation in Axial Flow Turbomachines," Aeronautical Research Council Reports and Memorandum, No. 3709, 1973.
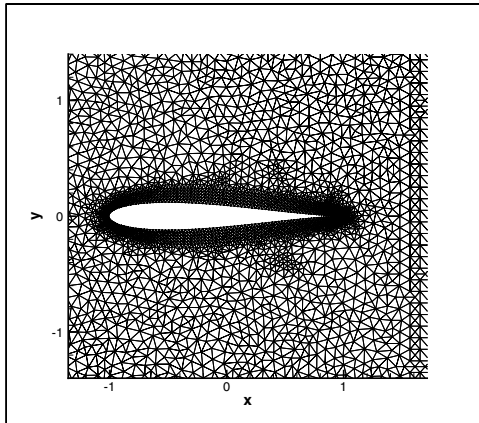
(a)
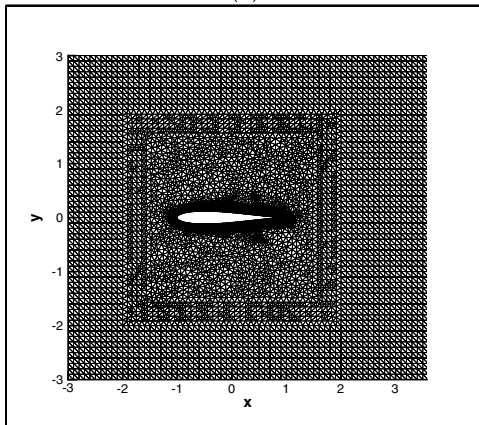
(b)

Figure 1: Structured/Unstructured mesh used for the symmetric airfoil calculation.

Figure 2: Mean pressure distribution on the airfoil surface for the symmetric airfoil.

(a) RMS pressure on the airfoil surface.

(b) Sound intensity at one chord length.

(c) Sound intensity at four chord lengths.

Figure 3: CE/SE solutions for the symmetric airfoil case assuming $k_x = k_y = 0.1$.

(a) RMS pressure on the airfoil surface.
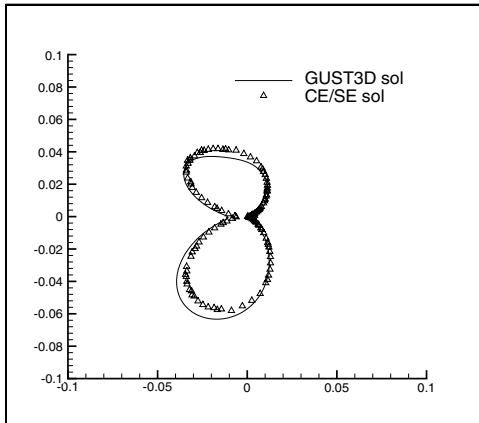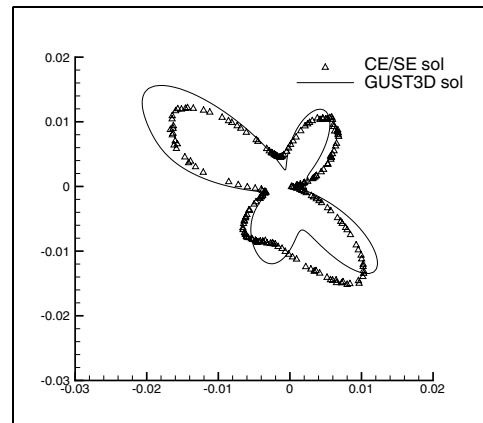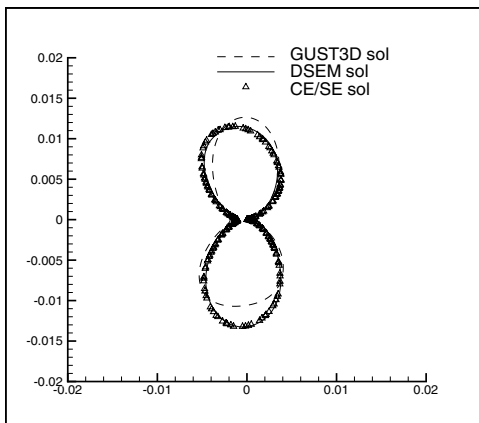
(b) Sound intensity at one chord length.
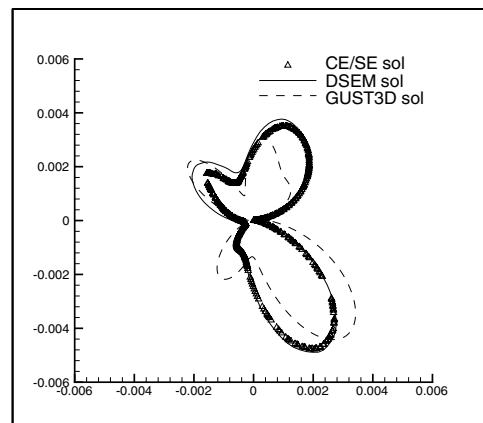
(c) Sound intensity at four chord lengths.

Figure 4: CE/SE solutions for the symmetric airfoil case assuming $k_x = k_y = 1.0$.

(a) RMS pressure on the airfoil surface.

(b) Sound intensity at one chord length.

(c) Sound intensity at four chord lengths.

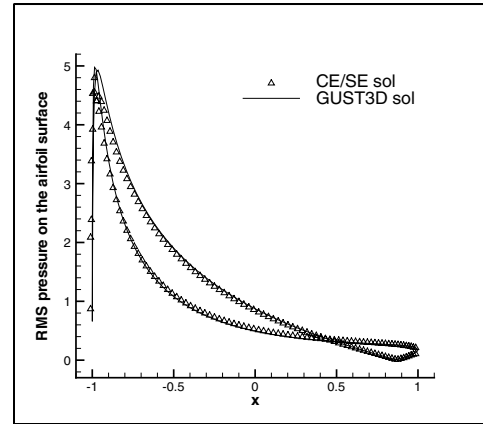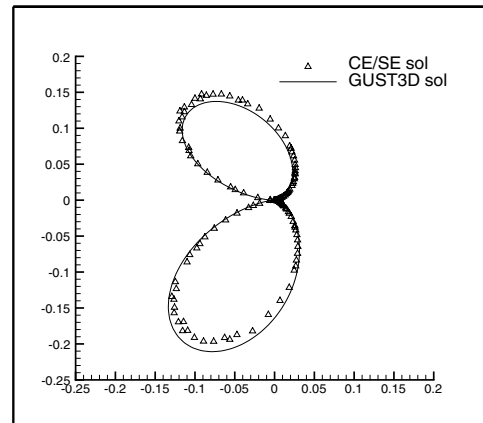Figure 5: CE/SE solutions for the symmetric airfoil case assuming $k_x = k_y = 3.0$.
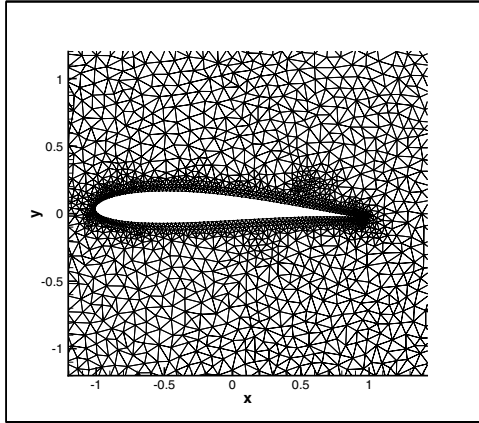
(a)
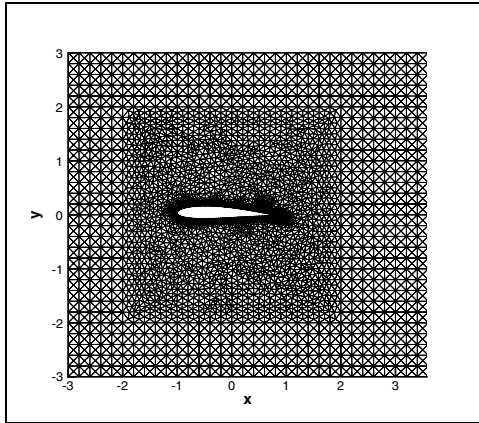
(b)

Figure 6: Structured/Unstructured mesh used in the cambered airfoil calculation.
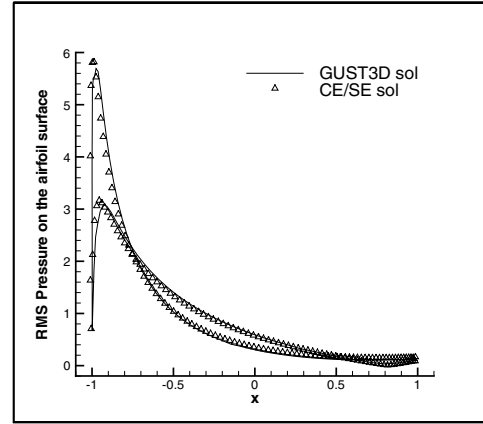
(a) RMS pressure on the airfoil surface.
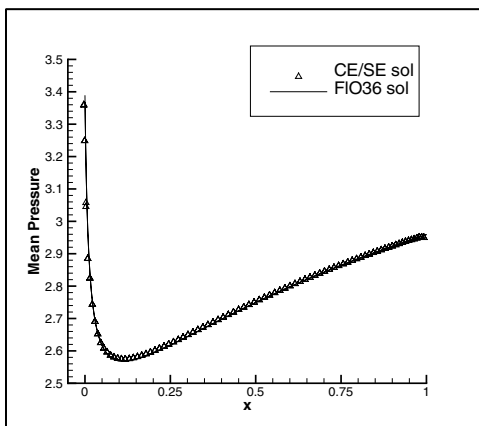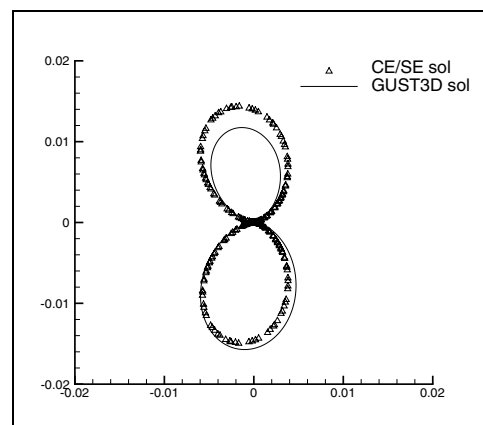

(b) Sound intensity at one chord length.
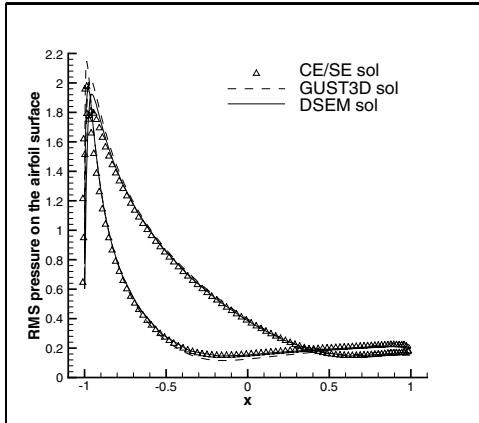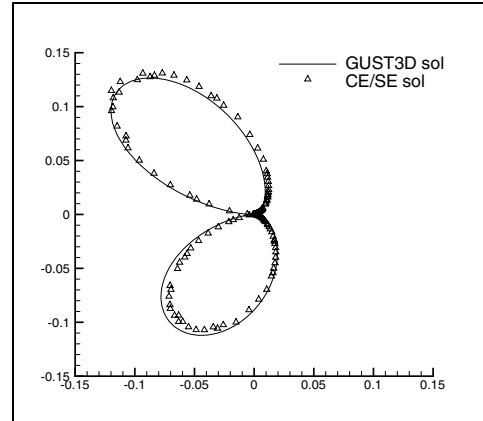

(c) Sound intensity at four chord lengths.
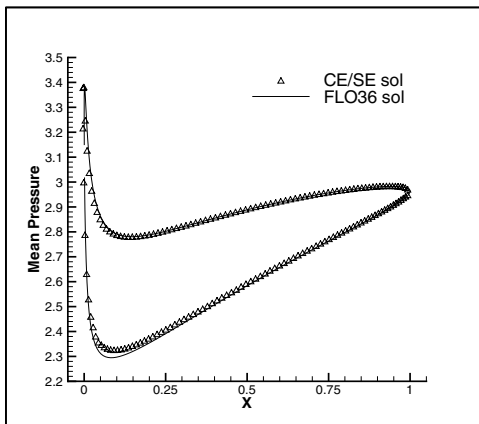
Figure 7: Mean pressure distribution on the airfoil surface for the cambered airfoil.
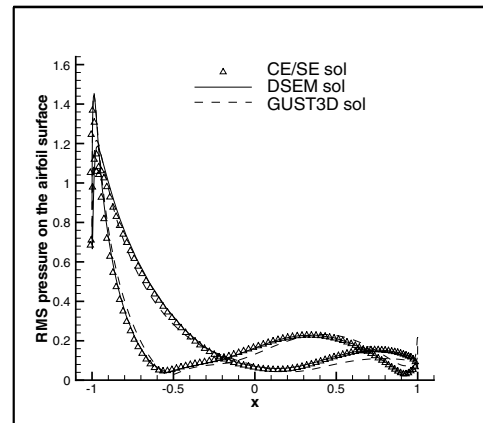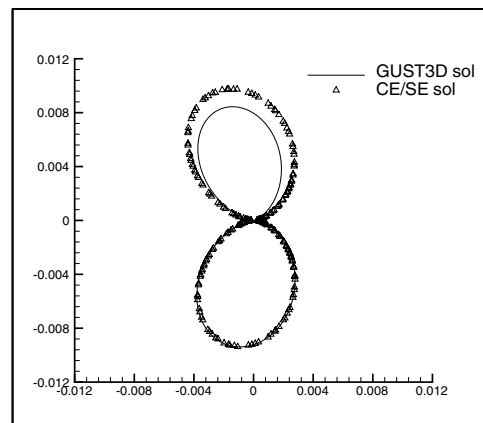
Figure 8: CE/SE solutions for the cambered airfoil case assuming $k_x = k_y = 0.1$.
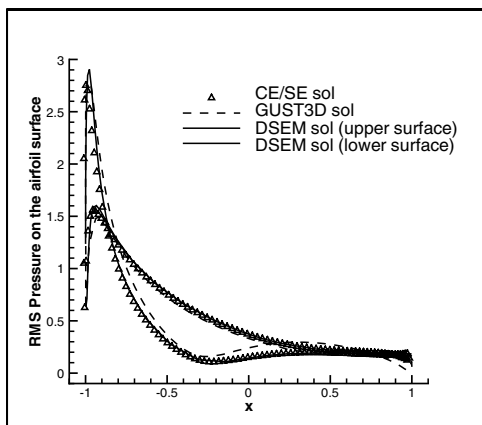
(a) RMS pressure on the airfoil surface.
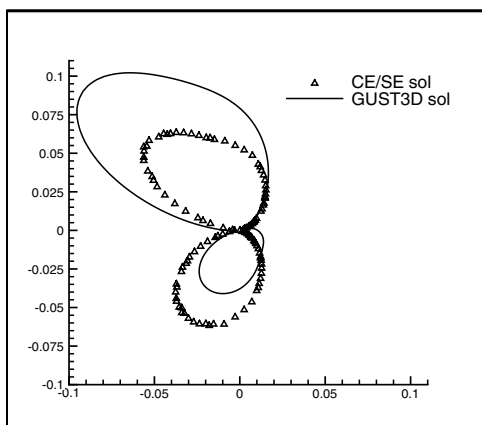
(b) Sound intensity at one chord length.
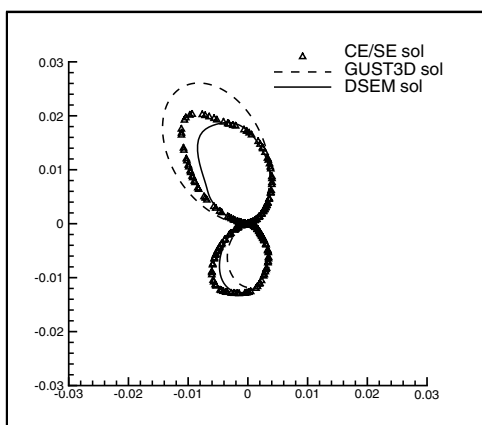
(c) Sound intensity at four chord lengths.

Figure 9: CE/SE solutions for the cambered airfoil case assuming $k_x = k_y = 1.0$.
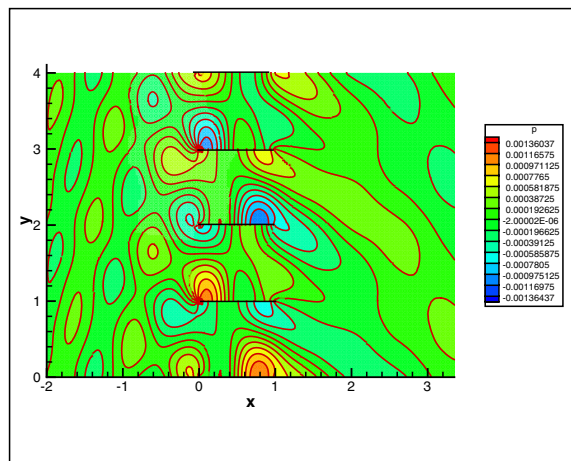
Figure 10: Acoustic pressure contour at one time instance.
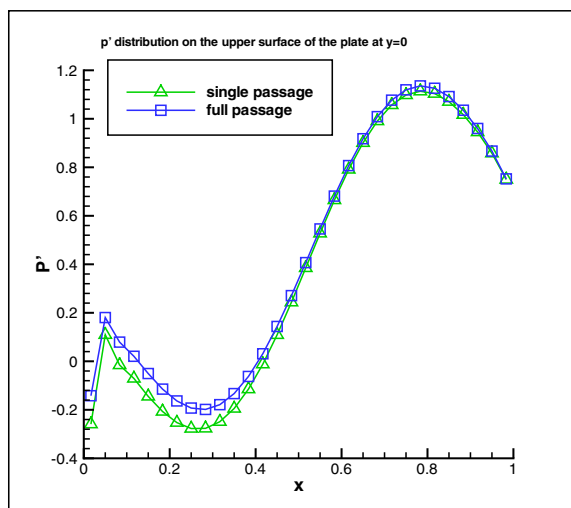
Figure 11: Acoustic pressure distribution on the upper surface of the flat plate located at $y = 0$.
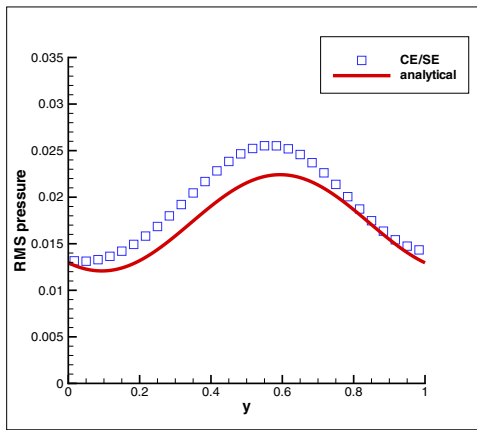
(a) inlet
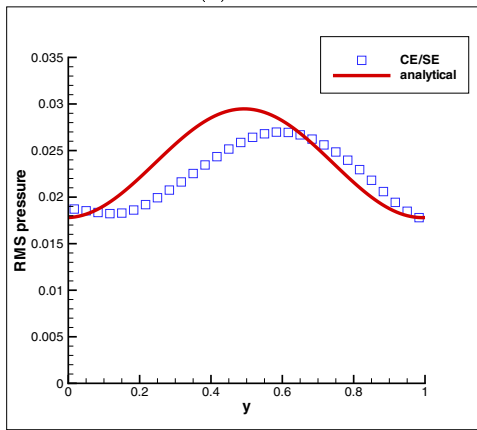
(b) outlet

Figure 12: RMS pressure at the inlet and outlet planes obtained using 4 passages.
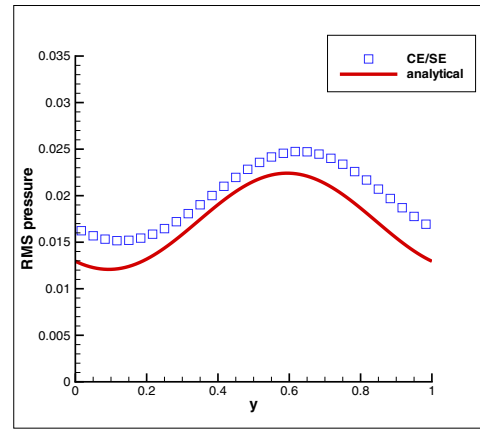
(a) inlet
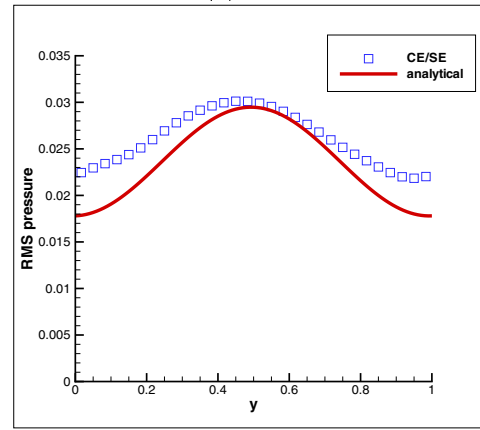
(b) outlet

Figure 13: RMS pressure at the inlet and outlet planes obtained using single passage.
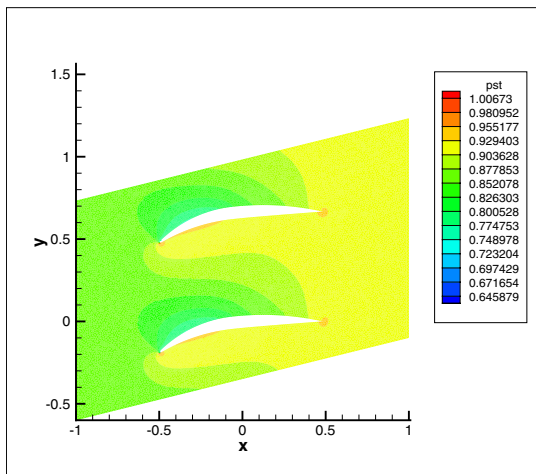
Figure 14: Numerical solution of the mean pressure contours.
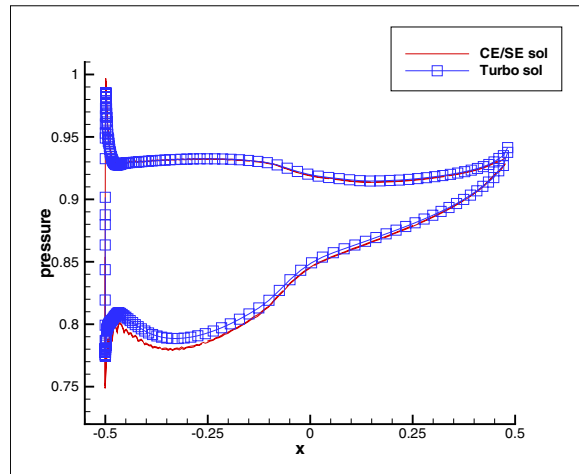
Figure 15: Mean pressure distribution on the blade surface compared with Turbo solution.
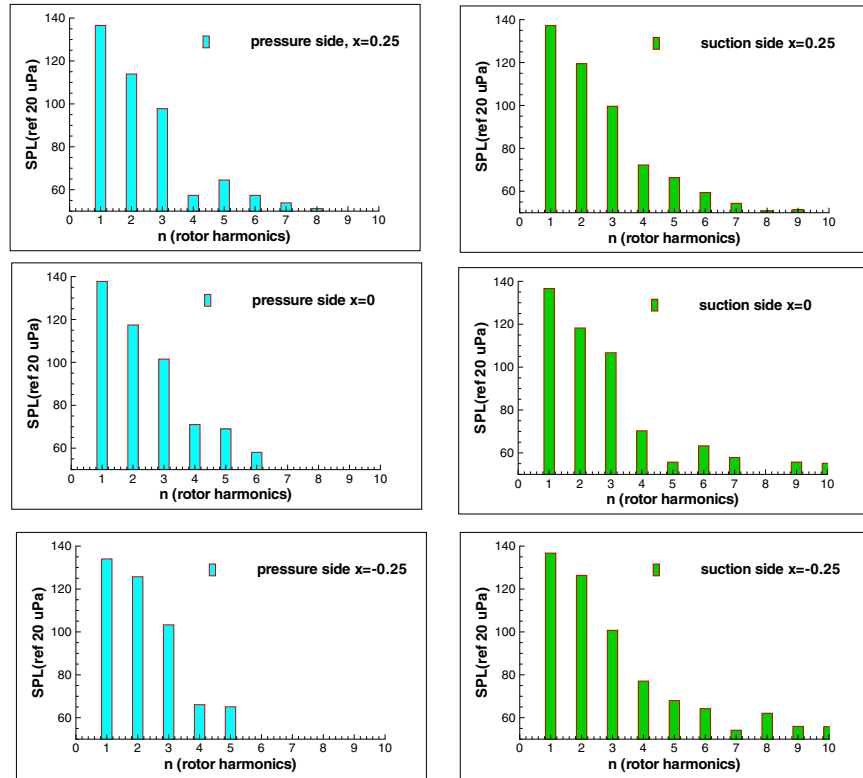
Figure 16: Sound pressure level at six different locations on the blade surface at $n = 1, 2, 3$.
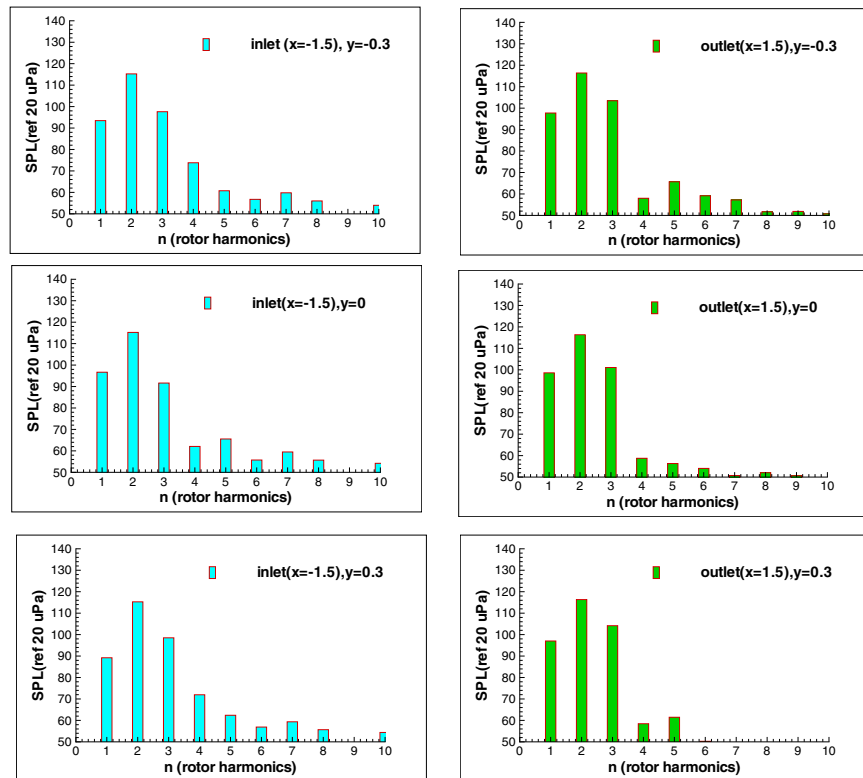
Figure 17: Sound pressure level at three different locations at inlet/outlet planes at $n = 1, 2, 3$.

(a) n=1

(b) n=2

(c) n=3
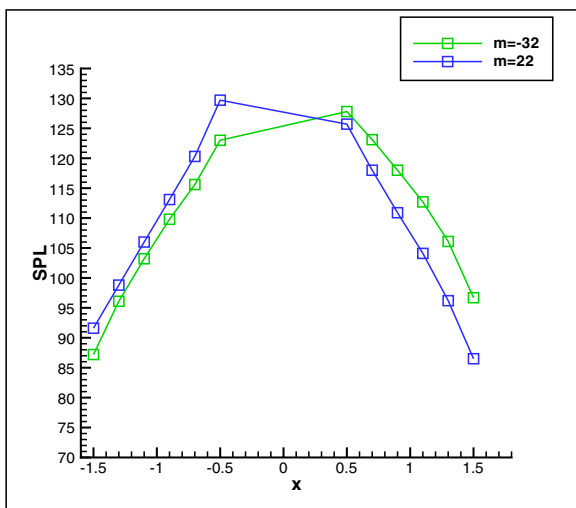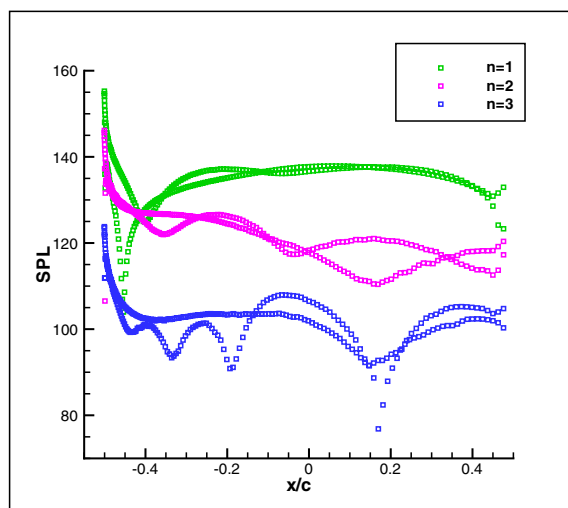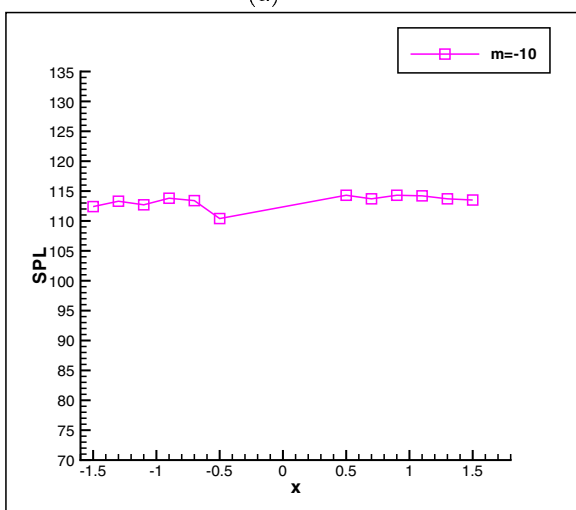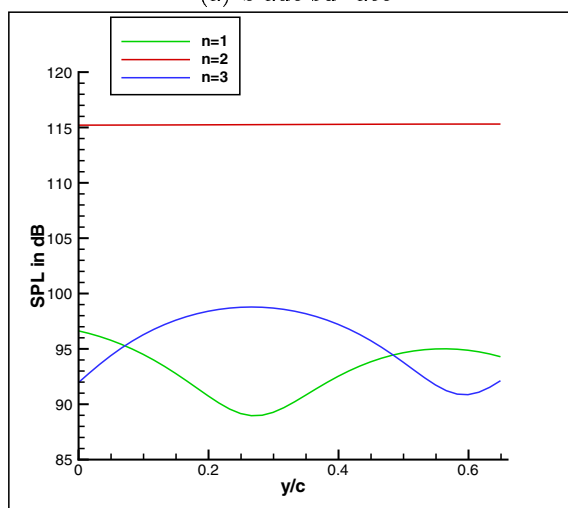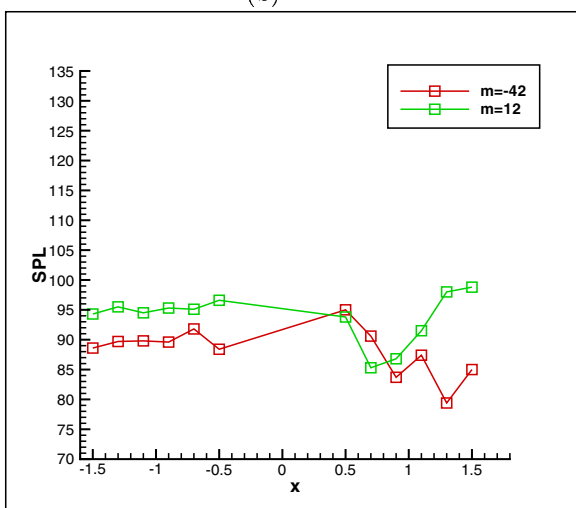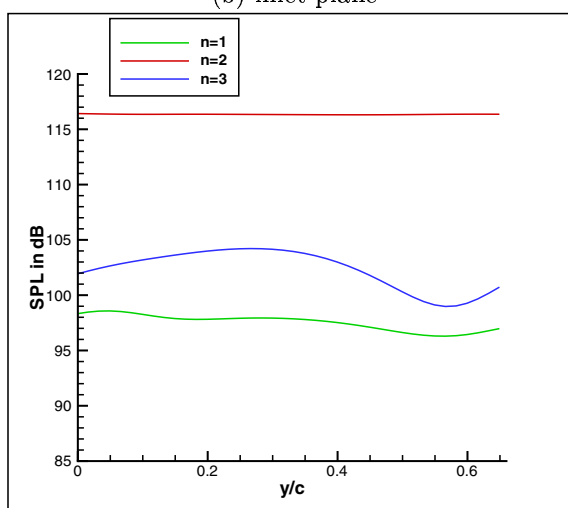
Figure 18: The distribution of sound pressure level along the cascade for different spatial modes (m) at $n = 1, 2, 3$.

(a) blade surface

(b) inlet plane

(c) outlet plane

Figure 19: Sound pressure level distribution on the blade surface and at the inlet/outlet planes for $n = 1, 2, 3$.

SOLUTION OF CATEGORY 3, PROBLEM 2, USING THE SPACE-TIME MAPPING ANALYSIS (STMA) METHOD*

Ray Hixon
Hixon Technologies, LLC
22187 Sandy Lane
Fairview Park, OH 44126
Phone: (440) 979-1783
email: rhixon@wideopenwest.com

ABSTRACT

The Space-Time Mapping Analysis (STMA) approach is used to solve the Category 3 Problem 2 benchmark problem. This benchmark is a realistic problem of multifrequency vortical gusts interacting with a row of stationary cascade blades. The STMA approach is designed to solve highly complex nonlinear unsteady flows in an efficient, straightforward way, and is uniquely suited for the distributed-processor parallel machines that are becoming widely available. Results are shown for a 'proof-of-concept' calculation, illustrating the ability of the STMA method to accurately predict the mean and unsteady nonlinear flows encountered in a realistic problem.

INTRODUCTION

The goal of Computational Aeroacoustics is to accurately solve unsteady flow and noise problems. To accomplish this, high-accuracy spatial derivatives are combined with a high-accuracy temporal integration method. For a nonlinear unsteady flow, explicit time marching methods such as Adams-Bashforth (e.g., ref. 1) or Runge-Kutta (e.g., refs. 2 and 3) are used to obtain accurate solutions with the least number of time steps.

In a time marching method, the time evolution of the flow is computed by marching the flow solution from one time level to the next time level. At each time level, the spatial derivatives of the governing equations are used to determine the time rate of change of the flow at that time. Every time the spatial derivatives are calculated, the entire flow must lie on a single plane in the time direction. Thus, the flow solution must be 'synchronized' at each time level to allow the spatial derivatives to be calculated before the flow at the next time level can be obtained.

In an explicit time marching method, the allowable time step size is proportional to the CFL number, which is a measure of the physical time taken by the fastest wave to propagate through the smallest cell in the grid. Thus, in an explicit time marching scheme with a single time step, a single time scale based on the CFL number is used to evolve the solution globally, regardless of whether the scale is appropriate or necessary everywhere in the flow. For flow problems with a single length and time scale, explicit time marching can be very efficient. However, in most realistic flow problems of interest, there is a wide range of length and time scales in the flow.

Even in flow problems with a single time scale, the mean flow may have sharp gradients that require closely spaced grid points in order to obtain an accurate numerical solution. Due to the CFL constraints, these small grid cells reduce the allowable time step for an explicit method to a value well below the time step needed to resolve the actual time scales of the unsteadiness in the flow. An implicit time marching method can remove the CFL restrictions, allowing larger time steps to be used; however, implicit time marching methods are generally low-order, requiring care to obtain an accurate unsteady solution.

In order to gain more flexibility, Tam et al. (ref. 1) have developed and demonstrated a multi-time-stepping explicit Adams-Bashforth method; in this approach, each grid block marches at an integer multiple of the minimum time step in the total grid. This method can substantially reduce the amount of CPU work required to solve a realistic flow problem. However, the multi-time-stepping approach effectively decomposes the calculation into a set of smaller calculations, with one calculation for each group of blocks using a given multiple of the minimum time step. When using a multi-time-stepping method, each of these calculations must be properly synchronized with the others to retain time accuracy.

The synchronization requirements of time marching methods can limit their effectiveness on large-scale distributed-memory parallel computers. In a distributed-memory parallel computer cluster, the flow calculation is decomposed into smaller domains, each of which is assigned to a processor in the cluster. To perform the spatial derivatives required for time marching, each processor requires data from other processors in the cluster. This data is communicated between the processors by messages passed between the processors. Thus, before a spatial

---

* The STMA method and its applications are the subject of a U.S. Patent application.

derivative can be calculated, the appropriate messages must be passed. Until these messages arrive, the calculation cannot continue.

In a dedicated high-performance parallel supercomputer, there is a high-performance communication network connecting all processors. This results in a minimum amount of idle time for the processors and the best parallel performance. Such computers are costly, and this limits their availability for the majority of researchers and engineers.

Low-cost parallel computer clusters are becoming widely available for large-scale computations. Generally, these clusters have relatively low-performance communication networks (loosely-coupled) between the processors. For such computers, the parallel performance of highly synchronized codes diminishes rapidly as more processors are used, due to the relative increase in processor idle time while messages are passed.

In order to efficiently solve complex unsteady flow problems on large-scale, loosely-coupled parallel computer clusters, it is necessary to reduce or remove the synchronization requirements of current algorithms. The Space-Time Mapping Analysis method of Hixon (ref. 4) accomplishes this goal by replacing the time marching methods with an iterative solution procedure to obtain the solution of an unsteady flow in a space-time volume. If the total space-time volume of a unsteady flow problem is too large, it may be decomposed into a series of smaller space-time volumes and 'marched' in a coarse-grain fashion.

Previously, the STMA method has been validated on earlier CAA benchmark problems (ref. 4), and has been tested by Golubev and Rodhe (ref. 5) for nonlinear flow calculations. This work continues the validation of the STMA method for realistic engineering problems.

GOVERNING EQUATIONS AND NUMERICAL METHOD

The equations solved in this work are the nonlinear 2D Euler equations, given in Cartesian coordinates as:

$$Q_t + E_x + F_y = 0 \tag{1}$$

In the STMA approach, a curvilinear transformation is used for all three dimensions of the problem (space and time combined):

$$\begin{aligned} \xi &= \xi(x, y, t) \\ \eta &= \eta(x, y, t) \\ \tau &= \tau(x, y, t) \end{aligned} \tag{2}$$

Using this transformation, the Euler equations become:

$$\left\{ \tau_t \frac{Q}{J} + \tau_x \frac{E}{J} + \tau_y \frac{F}{J} \right\}_\tau + \left\{ \xi_t \frac{Q}{J} + \xi_x \frac{E}{J} + \xi_y \frac{F}{J} \right\}_\xi + \left\{ \eta_t \frac{Q}{J} + \eta_x \frac{E}{J} + \eta_y \frac{F}{J} \right\}_\eta = 0 \tag{3}$$

Unlike the conventional time-marching equations, this transformed equation does not have a dedicated coordinate in the time direction. Instead, the time direction is treated identically to the spatial directions; in fact, the STMA method uses the same high accuracy differencing method is all three directions. Because of this, the solution procedure is iterative.

This curvilinear transformation has several advantages compared to time marching. First, since the equations are transformed in space-time, grid points may be clustered to resolve small regions of rapid change, without requiring high temporal resolution where it is not needed. Second, since the solution procedure is iterative, the high-performance convergence accelerators developed for steady-flow CFD solvers can be applied to unsteady flow solutions. Third, the iterative procedure can be much more efficient on large-scale parallel computers than time marching methods are, due to the lack of strict synchronization requirements (i.e., the iterative procedure can continue without the latest results from other processors).

In this work, the transformed equations given in Eq. (3) are solved using a Runge-Kutta iterative method described by Jameson et al. (ref. 6). The derivatives are evaluated using the high-accuracy DRP scheme of Tam and Webb (ref. 7). To provide damping for unresolved high-wavenumber disturbances, a constant-coefficient 10th order explicit artificial dissipation from Kennedy and Carpenter (ref. 8) is used in all three directions.

This solution method can be accelerated by adding implicit residual smoothing, local iteration stepping, a multigrid method, and preconditioning. For this 'proof of concept' calculation, however, no convergence

acceleration techniques were used. While this resulted in an excessive CPU time for convergence, it also showed the capability of the method to obtain the correct solution.

The code used for this work was the Mapping Analysis Research Code 1 (MARC1.14) of H2 Advanced Concepts, Inc. (ref. 9). This code uses the STMA method to solve the 2D unsteady nonlinear Euler equations on a curvilinear structured multiblock grid. The computation was performed on a 2.4 GHz Intel Pentium 4 with 768 MB of RAM.

COMPUTATIONAL GRID AND BOUNDARY CONDITIONS

The benchmark problem solved was Category 3 Problem 2. In this problem, a multifrequency vortical gust impinges on a loaded cascade. The inflow and outflow boundaries are located one chord length upstream and downstream of the cascade. The cascade has a gap-to-chord ratio of 2/3.

The mean flow conditions for this problem are:

$$(\bar{p}_0)_{inflow} = 1.0$$
$$(\bar{T}_0)_{inflow} = 1.0$$
$$(\bar{\alpha})_{inflow} = 36.0^\circ \tag{4}$$
$$\left(\frac{(\bar{p})_{outflow}}{(\bar{p}_0)_{inflow}} \right) = 0.92$$

The vortical gust is specified at the inflow boundary as:

$$\rho'_{gust} = 0$$

$$u'_{gust} = (\cos\beta) \left(\begin{array}{l} a_1 \cos(k_y y - \omega t) \\ + a_2 \cos(2(k_y y - \omega t)) \\ + a_3 \cos(3(k_y y - \omega t)) \end{array} \right) \tag{5}$$

$$v'_{gust} = -(\sin\beta) \left(\begin{array}{l} a_1 \cos(k_y y - \omega t) \\ + a_2 \cos(2(k_y y - \omega t)) \\ + a_3 \cos(3(k_y y - \omega t)) \end{array} \right)$$

$$p'_{gust} = 0$$

where:

$$\beta = 50^\circ$$
$$k_y = \frac{11\pi}{9}$$
$$\omega = \frac{3\pi}{4} \tag{6}$$
$$a_1 = 0.005$$
$$a_2 = 0.003$$
$$a_3 = 0.0007$$

Figure 1 shows one grid plane in space-time. The computational domain extends from one chord length upstream of the cascade to one chord length downstream of the cascade. The grid is periodic in both the y-direction and the t-direction. In the y-direction, the grid covers one passage, and in the t-direction the grid covers one period of the gust fundamental frequency. The grid consisted of 33 space-time planes stacked along the time direction, with each plane having 9506 grid points; the total grid consisted of 313,698 grid points divided into eight grid blocks.

The grid was generated using the GridPro/az3000 grid generator from Program Development Corporation (ref. 10). In order for high-accuracy methods to perform to their potential, a smooth, well-behaved grid is necessary. Previous testing has shown that GridPro produces a very smooth grid about complex geometries, particularly performing well near grid singularities. The grid used several 3-way and 5-way grid singularities.

Due to the cascade and gust geometry, a time-marching code would require 27 passages in the domain in order to avoid using a phase-lagged boundary condition. In those 27 passages, there are 11 wavelengths of the gust fundamental frequency. To allow only one passage to be calculated, the 33 space-time planes are oriented to impose the proper phase shift between the upper and lower boundaries of the grid. Note that the 33 space-time planes result in 11 time points per wavelength of the highest-frequency gust. Such a coarse gird spacing in the time direction is possible due to the high-accuracy differencing method employed.

It is important to note that, even though the grid appears to impose a particular periodicity on the solution due to the space-time shifts at the boundaries, the solution is still nonlinear, and is not constrained to reject solutions with different frequencies. Thus, even with these grid constraints, this problem is still a valid test of the STMA solution methodology.

The inflow and outflow boundary conditions used in this calculation are very similar to those used by time-marching codes (e.g., ref. 11) for this type of flow problem, with some modifications due to the iterative solution method used in the STMA approach. The inflow boundary condition is divided into three parts, each of which have separate boundary conditions:

1. Instantaneous nonreflecting boundary condition (Giles (ref. 12)).
2. User-specified incoming disturbances (gust).
3. Mean-flow boundary conditions (Hixon et al. MFBC (ref. 13)).

The outflow boundary condition is similarly specified, with only the nonreflecting and mean flow boundary conditions.

COMPUTED RESULTS

The MARC1.14 code was run until the residual had decreased approximately four orders of magnitude. The results given are not converged to machine precision; although it would be theoretically possible to achieve this level of convergence, the code would require an excessive amount of CPU time due to the lack of residual smoothing and other convergence acceleration techniques. In the future, these calculations will be repeated using convergence accelerators to gauge their effectiveness.

Figure 2 shows the results for the mean values of the conserved variables on the blade surface, compared to the reference solution. The STMA approach is getting very good agreement, with very little loss. The apparent disagreement near the leading edge of the cascade is due to an inaccuracy in the projection of the 3D annulus used for the reference solution to a 2D plane, resulting in a reduced chord length for the reference solution.

Figures 3-5 show the amplitude of the unsteady pressure distribution on the blade surface obtained by the STMA method. These results indicate that most of the noise radiation is from the leading edge, as expected.

Table 1 gives the pressure frequency spectra at the requested locations, and Table 2 gives the sound pressure levels at the inflow and outflow in terms of the mode order. The STMA calculation correctly identified the cut-on and cut-off modes for each gust frequency, with the possible exception of the 3xBPF, m=-21 mode at the outflow. This mode is very close to cut-on, and slight differences in the nonlinear solution may cause this mode to be cut-off.

CONCLUSIONS

In this work, Category 3 Problem 2 was solved using the Space-Time Mapping Analysis (STMA) method. This problem consisted of a realistic nonlinear flow about a loaded 2D cascade, with a multifrequency gust impinging on the cascade. The solution to this problem requires the mean flow to be correctly calculated, as well as a range of cut-off and cut-on modes to be accurately captured. It was thought that this problem would serve as a stringent validation test for the STMA method, revealing any problems in the methodology.

The results obtained by the STMA approach showed the ability of the solver to accurately compute unsteady nonlinear flows about complex geometries. The boundary conditions worked very well, and the high-accuracy

derivatives used in the temporal direction allowed a very coarse grid to be used. This calculation, which represents the 'worst-case' convergence rate for the STMA method, indicates that the convergence rate can be accelerated greatly, making this fully nonlinear approach much faster than the equivalent time-marching methods.

Table 1. Pressure Spectra at Reference Locations.

Location	BPF	2 x BPF	3 x BPF
Inflow, y = -0.3	109.2 dB	121.7 dB	109.2 dB
Inflow, y = 0.0	90.2 dB	120.6 dB	93.4 dB
Inflow, y = 0.3	108.7 dB	121.8 dB	109.3 dB
Outflow, y = -0.3	109.4 dB	122.4 dB	99.9 dB
Outflow, y = 0.0	112.0 dB	122.8 dB	105.5 dB
Outflow, y = 0.3	110.6 dB	122.6 dB	104.4 dB
Lower Airfoil, x = -0.25	139.9 dB	132.5 dB	114.1 dB
Upper Airfoil, x = -0.25	142.8 dB	133.0 dB	116.5 dB
Lower Airfoil, x = 0.0	143.8 dB	124.7 dB	116.8 dB
Upper Airfoil, x = 0.0	142.6 dB	125.4 dB	119.7 dB
Lower Airfoil, x = 0.25	142.6 dB	122.4 dB	102.2 dB
Upper Airfoil, x = 0.25	143.2 dB	125.5 dB	97.1 dB

Table 2. Sound Pressure Levels by Mode at Inflow and Outflow Boundaries.

Frequency	Mode	Inflow	Outflow
BPF	+11	104 dB (cut off)	110.6 dB (cut off)
	-16	103.9 dB (cut off)	86.4 dB (cut off)
2 x BPF	-5	121.2 dB (cut on)	123.2 dB (cut on)
3 x BPF	+6	104.7 dB (cut on)	101.7 dB (cut on)
	-21	100.8 dB (cut on)	102.9 dB (cut off)

ACKNOWLEDGEMENTS

REFERENCES

1. Shen, H. and Tam, C. K. W.: Numerical Simulation of the Generation of Axisymmetric Mode Jet Screech Tones. AIAA J., Vol. 36, No. 10, 1998, pp. 1801-1807.
2. Hu., F. Q., Hussaini, M. Y., and Manthey, J. L.: 'Low-Dissipation and Low-Dispersion Runge-Kutta Schemes for Computational Acoustics', J. Comp. Phys., Vol. 124, No. 1, 1996, pp. 177-191.
3. Stanescu, D. and Habashi, W. G., 2N Storage Low Dissipation and Dispersion Runge-Kutta Schemes for Computational Acoustics. J. Comp. Phys., Vol. 143, 1998, pp. 674-681.
4. Hixon, R.: Space-Time Mapping Analysis for the Accurate Calculation of Complex Unsteady Flows. AIAA Paper AIAA-2003-3205, Hilton Head, SC, May 2003.
5. Golubev, V. V. and Rodhe, A.: Application of Space-Time Mapping Analysis Method to Unsteady Nonlinear Gust-Airfoil Interaction Problem. AIAA Paper AIAA-2003-3693, Orlando, FL, July 2003.
6. Jameson, A., Schmidt, W., and Turkel, E.: Numerical Solutions of the Euler Equations by Finite-Volume Methods Using Runge-Kutta Time-Stepping Schemes. AIAA Paper AIAA-81-1259, June 1981.
7. Tam, C. K. W. and Webb, J. C.: Dispersion-Relation-Preserving Scheme for Computational Acoustics. J. Comp. Phys., Vol. 107, 1993, pp. 262-281.

8. Kennedy, C. A. and Carpenter, M. H.: Several New Numerical Methods for Compressible Shear-Layer Simulations. Appl. Num. Math., Vol. 14, 1994, pp. 397-433.

9. MARC1.14, ©2002 by H2 Advanced Concepts, Inc., Fairview Park, OH.

10. GridPro/az3000, Program Development Corporation, White Plains, NY.

11. Nallasamy, M., Hixon, R., Sawyer, S., Dyson, R., and Koch, L.: A Time-Domain Analysis of Gust-Cascade Interaction Noise. AIAA Paper AIAA-2003-3134, Hilton Head, SC, May 2003.

12. Giles, M. B.: Nonreflecting Boundary Conditions for Euler Equation Calculations. AIAA J., Vol. 28, No. 12, 1990, pp. 2050-2058.

13. Hixon, R., Nallasamy, M., Sawyer, S., and Dyson, R.: Unsteady Validation of a Mean Flow Boundary Conditions for Computational Aeroacoustics. AIAA Paper AIAA-2004-0521, Reno, NV, January 2004.

FIGURES
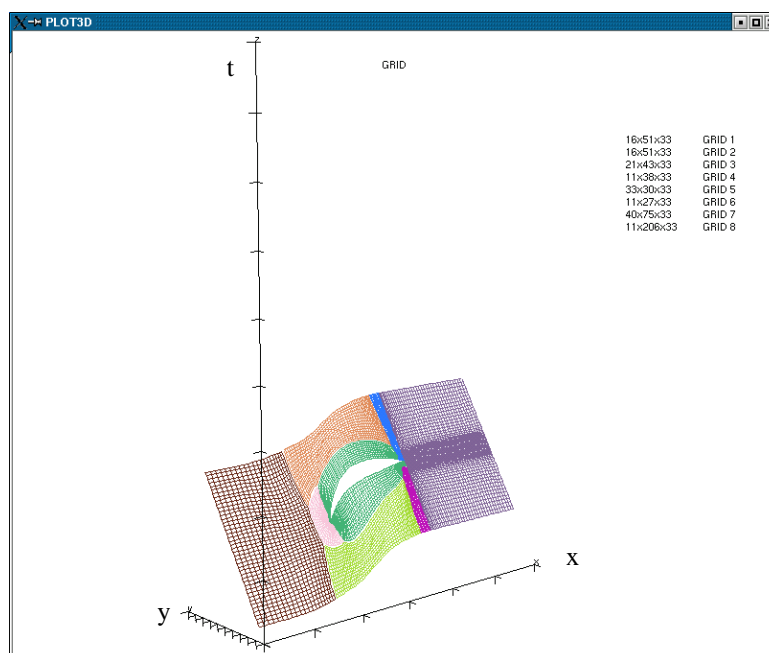
Figure 1: Space-time grid plane used by STMA method, illustrating the inclination in space-time.
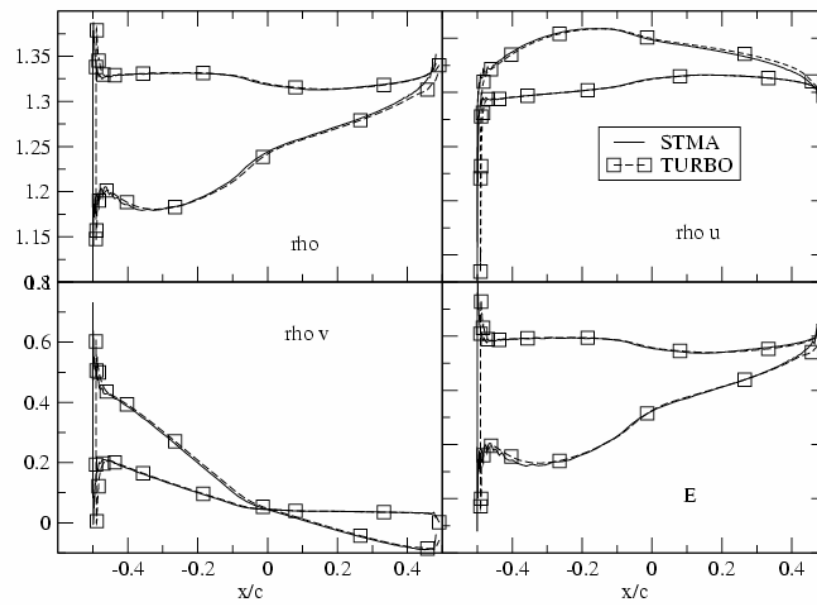
Figure 2: Comparison of mean flow distribution on blade surface.
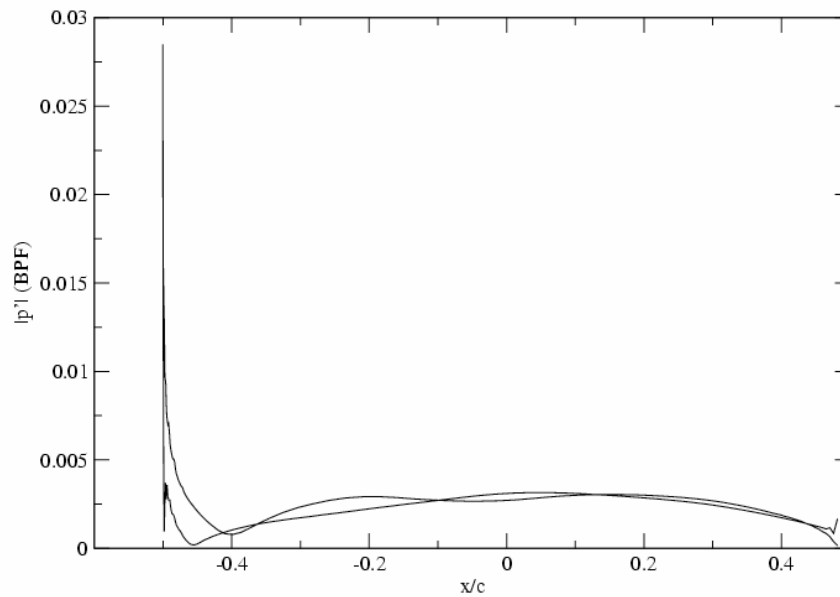
Figure 3: Unsteady pressure distribution on blade surface for BPF
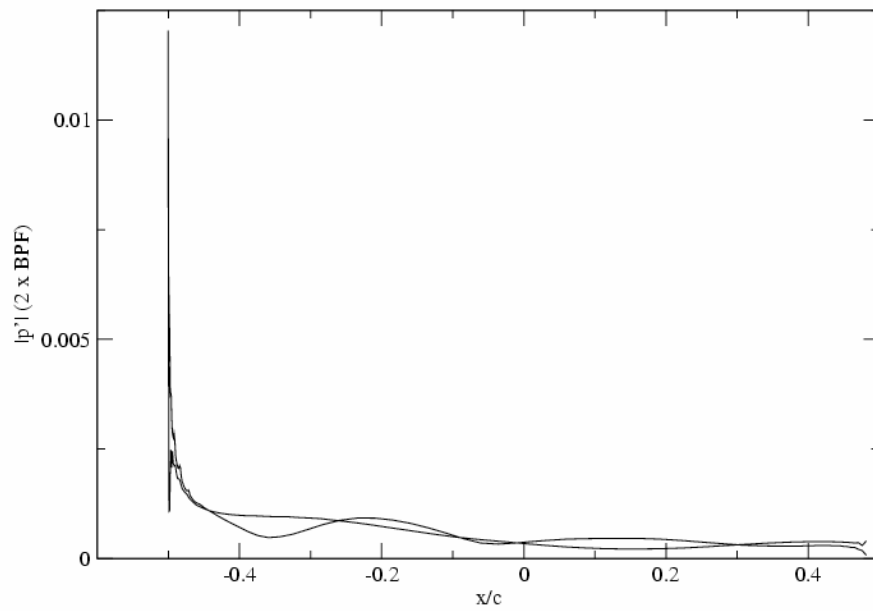
Figure 4: Unsteady pressure distribution on blade surface for 2 x BPF
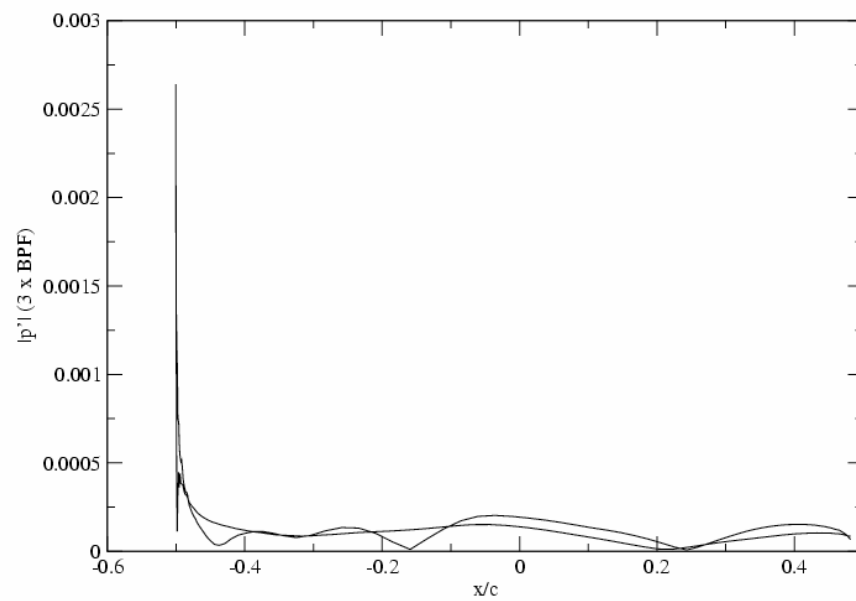
Figure 5: Unsteady pressure distribution on blade surface for 3 x BPF

SPACE-TIME MAPPING ANALYSIS OF AIRFOIL RESPONSE TO IMPINGING GUST

Vladimir V. Golubev and Reda R. Mankbadi
Embry-Riddle Aeronautical University
600 S. Clyde Morris Blvd, Daytona Beach, FL 32118, USA

ABSTRACT

A new numerical approach first presented in Ref. [1], is applied to the nonlinear analysis of the unsteady gust-airfoil interaction problem (Problem 1 in Category 3). The Space-Time Mapping Analysis (STMA) method has been developed to effectively treat any two- or three-dimensional unsteady problems as a steady-state one in the three- or four-dimensional space. Such approach essentially paves the way for extending high-accuracy discretization schemes developed in Computational Aeroacoustics (CAA) for spatial derivatives, to the time derivative, thus achieving highly time-accurate computations with absolute stability. It appears to provide additional flexibility of clustering space-time grid in regions of rapid solution changes, and is well-suited for the distributed-memory parallel processing. The numerical formulation used in the current study employs a high-order discretization scheme to achieve time-accurate predictions of both unsteady aerodynamic and aeroacoustic airfoil responses.

INTRODUCTION

The traditional prediction methods employed in the field of Computational Aeroacoustics (CAA) are capable of retaining the nonlinear character of the equations while accurately capturing the propagating waves. The CAA codes have been developed to accurately capture transient flow behavior by combining a high-accuracy spatial differencing scheme with an optimized time-marching method. Thus, they treat any unsteady problem as being a transient problem that requires high time accuracy throughout the calculation process. On the other hand, the gust-airfoil interaction problem is an example of a periodic problem, where the exact transient solution starting from the initial conditions may not be of interest. Instead, the long-term periodic solution is usually the desired output, with the excessive accuracy of the transient calculations being redundant. In the STMA approach proposed recently by Hixon in Ref. [1], the unsteady marching problem in two spatial dimensions is transformed into a steady-state iterative problem in three dimensions. At the same time, the highly convergent iterative methods from classical CFD can be applied, increasing accuracy (by using better time derivatives), reducing CPU time (because of less grid points in space-time as well as improved iterative methods), and increasing the parallel performance of the codes (through larger block volumes on each processor and reduced synchronization needs during the iterative process).

In application to the unsteady gust-airfoil interaction problem, the periodic nature of the flow can be further used to minimize the computational time and effort required to solve the test cases. In particular, the mesh is designed to cover one period of the vortical gust in the time direction, with a periodic boundary condition applied at the time inflow and time outflow boundaries. Thus, the computed solution is driven directly to the final long-time periodic solution of interest, rather than expending effort in accurately resolving the initial transient solution.

GOVERNING EQUATIONS

The unsteady, inviscid analysis of the gust-airfoil interaction problem is based on the numerical solution to the nonlinear Euler equations,

$$\frac{\partial Q}{\partial t} + \frac{\partial E}{\partial x} + \frac{\partial F}{\partial y} = 0, \qquad (1)$$

where Q is the solution vector, E and F are the flux vectors,

$$Q = \begin{bmatrix} \rho \\ \rho u \\ \rho v \\ e \end{bmatrix}, \quad E = \begin{bmatrix} \rho u \\ \rho u^2 + p \\ \rho uv \\ u(e + p) \end{bmatrix}, \quad F = \begin{bmatrix} \rho v \\ \rho uv \\ \rho v^2 + p \\ v(e + p) \end{bmatrix} \quad (2)$$

Unsteady pressure can be immediately recovered from the solution vector,

$$p = (\gamma - 1)\left(e - \frac{1}{2}\rho(u^2 + v^2) \right) \quad (3)$$

Furthermore, for complex geometries, recasting the equations in the generalized curvilinear coordinates,

$$\xi = \xi(x, y)$$
$$\eta = \eta(x, y)$$

results in Euler equations written as

$$Q_t + \xi_x E_\xi + \eta_x E_\eta + \xi_y F_\xi + \eta_y F_\eta = 0 \quad (4)$$

which are conventionally solved by a time marching procedure.

In the STMA process, the governing equations written in Cartesian (x,y,t) coordinates are transformed into curvilinear coordinates (ξ,η,τ) that are *all* functions of space and time,

$$\xi = \xi(x,y,t)$$
$$\eta = \eta(x,y,t) \quad (5)$$
$$\tau = \tau(x,y,t)$$

In this development, it is important to note that τ is a function of x, y, and t; thus τ is not, in general, a time-like variable. From (1), the following governing equation is then obtained in the strong conservation form:

$$\left(\tau_t \frac{Q}{J} + \tau_x \frac{E}{J} + \tau_y \frac{F}{J} \right)_\tau +$$
$$\left(\xi_t \frac{Q}{J} + \xi_x \frac{E}{J} + \xi_y \frac{F}{J} \right)_\xi + \quad (6)$$
$$\left(\eta_t \frac{Q}{J} + \eta_x \frac{E}{J} + \eta_y \frac{F}{J} \right)_\eta = 0$$

Since there is no time-like variable in the STMA approach, the time-marching procedure cannot be used. Instead, an iterative method is used to solve Eq. (6). In application to the unsteady gust-airfoil interaction problem, the periodic nature of the flow may be used to minimize the computational time and effort required to solve the test cases. For instance, the mesh is designed to cover one period of the vortical gust in the time direction (more periods would be required, e.g., for the nonlinear response study; see Ref. [2] for details), with a periodic boundary condition applied at the time inflow and time outflow boundaries. Thus, the computed solution is driven directly to the final long-time periodic solution of interest, rather than expending effort in accurately resolving the initial transient solution.

The H2 Advanced Concepts, Inc., Mapping Analysis Research Code 1 (MARC1) [3] was applied to solve the STMA equations. The solver employed the 7-point 4th order Dispersion Relation Preserving (DRP) scheme by Tam and Web [4], with the 10th order artificial dissipation [5] added in all coordinate directions. In general, a time-like term may be added to the equation, and the third-order Runge-Kutta scheme of Jameson et al. [6] can be used in

combination with implicit residual smoothing and local time stepping to accelerate convergence. For the test cases presented, however, a single iterative step was used with no implicit residual smoothing. Computations for the cases with two lower gust frequencies were run on a mesh $N_x*N_y*N_t=433*125*17$. On a singe-processor 2.8 GHz Linux PC station, a single case run was taking up to a week to fully converge (with approximately 25,000 iterations). The case with the high gust frequency was run on a 605*240*17 grid, and thus took longer to converge. Even with the latter finer mesh, the high-frequency gust appeared not to be well resolved in the far field region, which contributed to some inaccuracy in the acoustic directivity prediction in the far field as observed below.

FLOW INITIALIZATION

According to the formulation of the benchmark problem, the two-dimensional vortical gust is initiated with the following distribution of perturbation velocity,

$$u_{gust} = -\left(\frac{\varepsilon\beta M}{\sqrt{\alpha^2 + \beta^2}}\right)\cos(\alpha x + \beta y - \omega t)$$

$$v_{gust} = -\left(\frac{\varepsilon\alpha M}{\sqrt{\alpha^2 + \beta^2}}\right)\cos(\alpha x + \beta y - \omega t)$$

(7)

where ε is the gust intensity relative to the mean flow, α and β are the gust wave numbers, and ω is the imposed gust frequency. The mean flow is defined far upstream from the airfoil as:

$$\bar{\rho} = 1$$
$$\bar{u} = M$$
$$\bar{v} = 0$$
$$\bar{p} = \frac{1}{\gamma}(\bar{\rho}^\gamma)$$

(8)

where M is the Mach number, and $\gamma=1.4$. . In all computations, the Mach number is fixed at $M=0.5$, and the gust intensity is $\varepsilon=0.02$. The two-dimensional gust is considered with $\alpha = 2k, \beta = 2k, \omega = 2kM$ in (7), where k is the reduced frequency of the gust non-dimensionalized by the airfoil half-chord and the upstream mean flow velocity. The computations were conducted for k=0.1, 1.0 and 2.0. The present study focused on one case corresponding to a loaded, 12%-thick, 2%-cambered Joukowski airfoil at a two-degree angle of attack.

Figure 1 provides illustration of the computational domain, along with contours of the conservative variable ρv from the solution vector Q in Eq. (1), for the gust reduced frequency k=1.0. Note that the *(x,y)* planes correspond to slices of the computational domain at each instant of time (with the airfoil in the middle of the planes). The *(x,y)* plane grid was generated as a single block using the GridPro commercial software [7]. In Figure 1, the additional time coordinate points in the z-direction. The translucent contour plot thus shows gust evolution both in space and time.

At the beginning of the pseudo-time marching iterative convergence process, the flow is initialized throughout the physical domain with the gust perturbation superimposed on the mean flow. At the inflow boundary of each *(x,y)* plane, the standard acoustic radiation condition is applied to the outgoing perturbation, defined, e.g., for X-component of flow velocity as $u_{BC} = u_{boundary} - \bar{u} - u_{gust}$. At the outflow boundary of each *(x,y)* plane, Tam and Webb's [4] condition is applied.

RESULTS

Along the surface of the airfoil, the aerodynamic response contains both the mean (due to the airfoil camber and angle of attack) and the unsteady perturbation (due to the incident gust) pressure components. The results for the mean pressure distribution on the suction and pressure sides are compared in Figure 2 with computations from FLO36 mean flow solver.
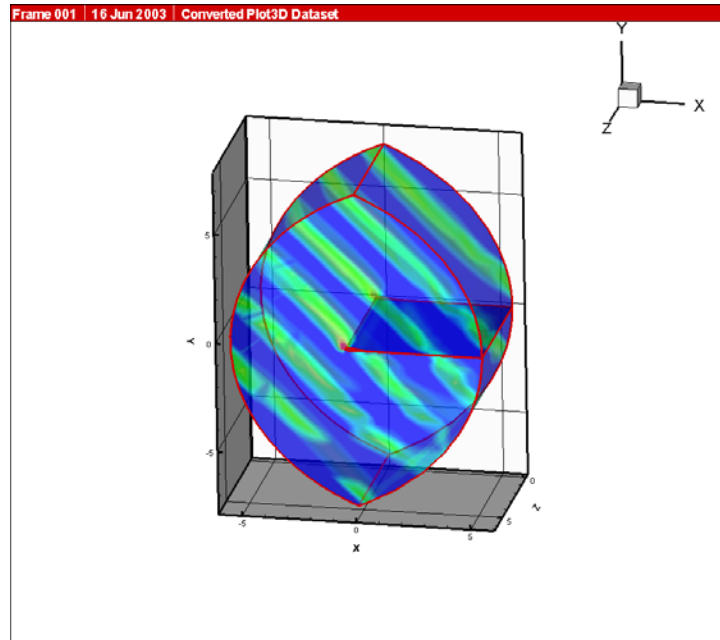
Figure 1: Computational (x,y,t) domain with instantaneous ρv –component of gust, k=1.0.
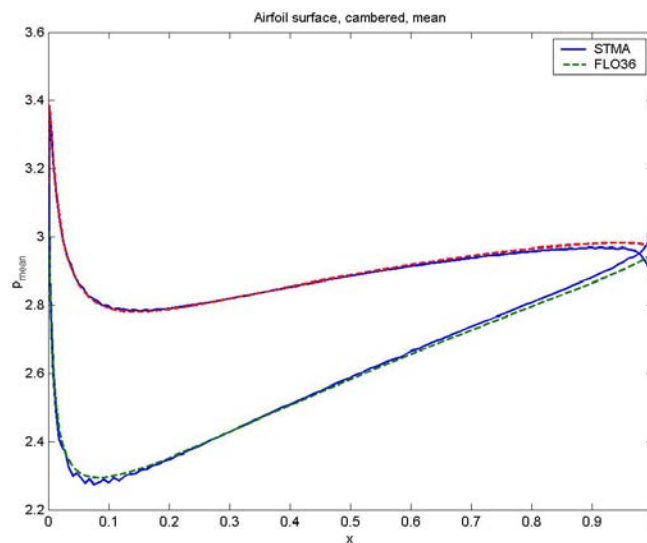
Figure 2: Mean pressure on the airfoil suction and pressure sides: comparison of FLO36 solution with STMA prediction.

The corresponding plots for the predicted unsteady RMS airfoil surface pressure are provided in Figure 3, for the gust reduced frequencies k=0.1, 1.0 and 2.0.

Finally, the directivity plots for the non-dimensional acoustic intensities are shown in Figures 4, 5 and 6, for distances R/c= 1, 2 and 4 from the airfoil centerpoint, respectively.
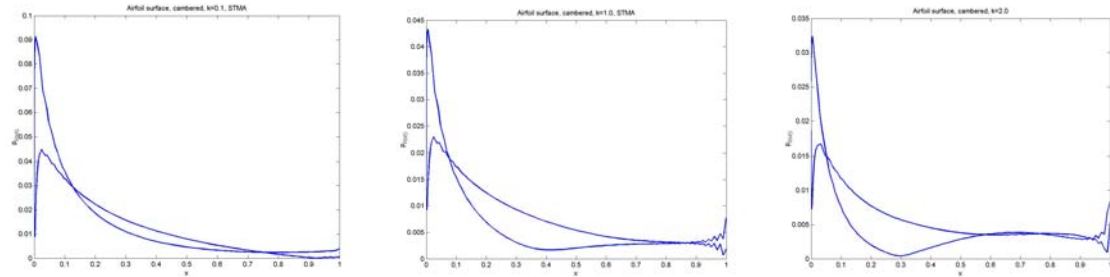
Figure 3. Unsteady RMS pressure on airfoil upper and lower surfaces. Left to right: k=0.1, 1.0, 2.0.
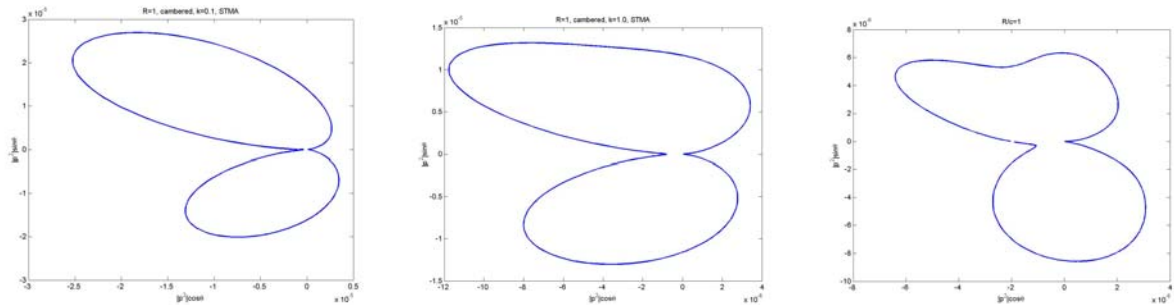
Figure 4. Directivity of |p'²| for RMS unsteady pressure at R/c=1. Left to right: k=0.1, 1.0, 2.0.
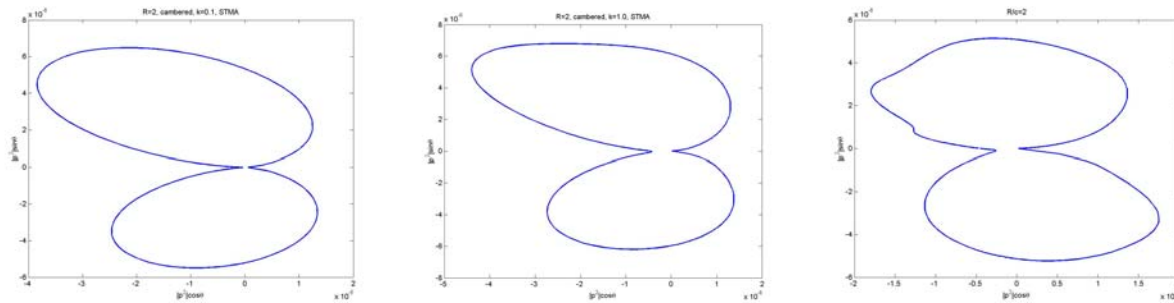
Figure 5. Directivity of |p'²| for RMS unsteady pressure at R/c=2. Left to right: k=0.1, 1.0, 2.0.
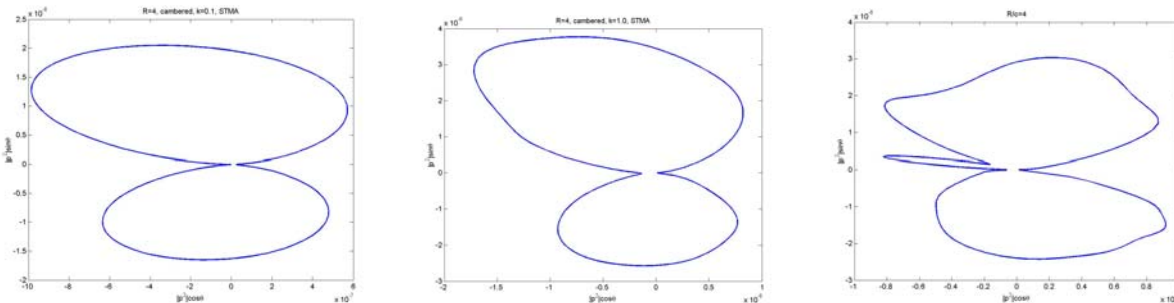
Figure 6. Directivity of |p'²| for RMS unsteady pressure at R/c=4. Left to right: k=0.1, 1.0, 2.0.

REFERENCES

1. Hixon, R., "Space-Time Mapping Analysis for the Accurate Calculation of Complex Unsteady Flows," AIAA Paper 2003-3205, May 2003.
2. Golubev, V.V. and Rohde, A., "Application of Space-Time Mapping Analysis Method to Unsteady Nonlinear Gust-Airfoil Interaction Problem," AIAA Paper 2003-3693, 2003.
3. MARC1.11, ©2002 by H2 Advanced Concepts, Inc. Fairview Park, OH.
4. Tam, C. K. W. and Webb, J. C., "Dispersion-Relation-Preserving Finite-Difference Schemes for Computational Acoustics," Journal of Computational Physics, Vol. 107, 1993, pp. 262-281.
5. Kennedy, C. A. and Carpenter, M. H., "Several New Numerical Methods for Compressible Shear-Layer Simulations," Applied Numerical Mathematics, Vol. 14, 1994, pp. 397-433.
6. Jameson, A., Schmidt, W., and Turkel, E., "Numerical Solutions of the Euler Equations by Finite-Volume Methods Using Runge-Kutta Time-Stepping Schemes," AIAA Paper AIAA-81-1259, June 1981.
7. GridPro™, Program Development Corporation, White Plains, NY.

SIMULATION OF AIRFOIL RESPONSE TO IMPINGING GUST USING HIGH-ORDER PREFACTORED COMPACT CODE

Vladimir V. Golubev and Reda R. Mankbadi
Embry-Riddle Aeronautical University
600 S. Clyde Morris Blvd, Daytona Beach, FL 32118, USA

Ray Hixon
University of Toledo, Toledo, OH 43606, USA

ABSTRACT

Unsteady aerodynamic and acoustic responses of symmetric and loaded Joukowski airfoils to an impinging 2D vortical gust (Problem 1 in Category 3) are predicted using a nonlinear high-order prefactored compact code. The analysis is based on obtaining finite-difference solutions to the nonlinear Euler equations in the generalized curvilinear coordinates. The numerical formulation uses the low-storage 4th order 5-6 Low Dispersion and Dissipation Runge-Kutta scheme for explicit time marching, and prefactored 6th order compact scheme and explicit boundary stencils for spatial derivatives. A 10th order explicit filter is used at every stage of the Runge-Kutta solver to provide dissipation. C-grid 2D topologies are generated using GridPro software, with the mesh extending at least 10 chords away from the airfoil surface in each direction. The reported results were obtained through scalar and parallel implementations on the Beowulf-type PC Linux cluster.

FORMULATION

The analysis of nonlinear inviscid gust-airfoil interaction is based on the numerical solution to the nonlinear Euler equations which can be written in two-dimensional Cartesian coordinates as

$$\frac{\partial Q}{\partial t} + \frac{\partial E}{\partial x} + \frac{\partial F}{\partial y} = 0, \tag{1}$$

where Q is the solution vector, and E and F are the flux vectors,

$$Q = \begin{bmatrix} \rho \\ \rho u \\ \rho v \\ e \end{bmatrix}, \quad E = \begin{bmatrix} \rho u \\ \rho u^2 + p \\ \rho uv \\ u(e+p) \end{bmatrix}, \quad F = \begin{bmatrix} \rho v \\ \rho uv \\ \rho v^2 + p \\ v(e+p) \end{bmatrix} \tag{2}$$

Unsteady pressure is recovered from

$$p = (\gamma - 1)\left(e - \frac{1}{2}\rho(u^2 + v^2) \right) \tag{3}$$

Since the gust response is investigated for the complex-shaped airfoil geometry, it requires recasting the equations in generalized curvilinear coordinates, with the chain-rule curvilinear Euler equations written as

$$\frac{\partial Q}{\partial t} + \frac{\partial \xi}{\partial x}\frac{\partial E}{\partial \xi} + \frac{\partial \eta}{\partial x}\frac{\partial E}{\partial \eta} + \frac{\partial \xi}{\partial y}\frac{\partial F}{\partial \xi} + \frac{\partial \eta}{\partial y}\frac{\partial F}{\partial \eta} = 0 \tag{4}$$

The numerical formulation employs the low-storage 4th order 5-6 Low Dispersion and Dissipation Runge-Kutta scheme [1] for time marching, and the prefactored 6th order compact scheme and explicit boundary stencils for spatial derivatives [2]. Most of results reported below were obtained from an early version of the BASS code [3] and employed the 10th artificial dissipation. A few results were obtained from an older prefactored code [4, 5] that used the 10th order explicit filtering at every stage of the Runge-Kutta solver to provide dissipation.

For the analysis of the benchmark gust-airfoil interaction problem, a C-grid 2D topology is used to generate grids for both cases of symmetric and cambered 12% thick Joukowski airfoil, with the grid extending at least 10 chords away from the surface in each direction. All the meshes are generated as single blocks the by GridPro commercial software [6] using algebraic clustering around the airfoil in the normal direction ($\Delta n=0.01$) and near the trailing edge ($\Delta x=0.01$), with the stretching ratio of 1.05 used to expand to the far field. Some oscillations and loss of accuracy are observed in numerical results near the trailing edge due to the singularity treatment in the grid topology. A careful clustering of grid points near the trailing edge helps to keep these effects localized, with minimal impact on the overall solution.

The computational codes employed in the analysis are written in Fortran 90 and use the MPI library for parallelization. Results from the most recent version of the code are obtained from scalar runs on a single Dell GX260 2.8GHz/2GB Intel4 Linux station. Numerical solutions from the previous version of the code were obtained through parallel implementation on the Beowulf-type Linux Athlon cluster consisting of eight dual-processor 1.4GHz/1GB AMD nodes. Figure 1 illustrates the computational domain partitioned into 16 blocks corresponding to the number of processors. The domain decomposition is done by a special routine to provide adequate load balance between processors.
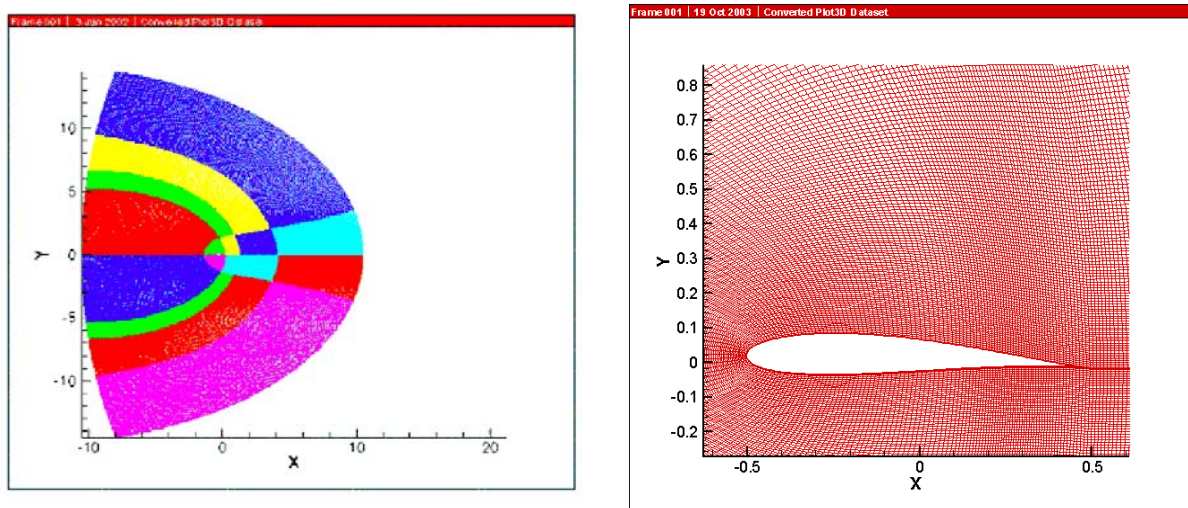
Figure 1. Left: grid-partitioned computational domain. Right: grid details near cambered airfoil surface.

FLOW INITIALIZATION

According to the formulation of the benchmark problem, the vortical gust harmonic is initially imposed on the mean flow with the following distribution:

$$u_{gust} = -\left(\frac{\varepsilon \beta M}{\sqrt{\alpha^2 + \beta^2}} \right) \cos(\alpha x + \beta y - \omega t)$$

$$v_{gust} = -\left(\frac{\varepsilon \alpha M}{\sqrt{\alpha^2 + \beta^2}} \right) \cos(\alpha x + \beta y - \omega t)$$

$$(5)$$

where ε is the gust intensity relative to the mean flow, α and β are the gust wave numbers in the x and y directions, and ω is the imposed gust frequency.

The mean flow is defined far upstream from the airfoil as:

$$\bar{\rho} = 1$$
$$\bar{u} = M$$
$$\bar{v} = 0 \qquad\qquad (6)$$
$$\bar{p} = \frac{1}{\gamma}(\bar{\rho}^{\gamma})$$

where M is the upstream mean flow Mach number, and γ=1.4. In all computations, the Mach number is fixed at M=0.5, and the gust intensity is ε=0.02. The two-dimensional gust is considered with $\alpha = 2k, \beta = 2k, \omega = 2kM$ in (5), where k is the reduced frequency of the gust non-dimensionalized by the airfoil half-chord and the upstream mean flow velocity. The computations are conducted for k=0.1, 1.0 and 2.0. Finally, two configurations for the airfoil geometry are considered: (i) Unloaded symmetric 12%-thick Joukowski airfoil (no angle of attack), and (ii) Loaded 12%-thick 2%-cambered Joukowski airfoil at a two-degree angle of attack.

At the beginning of the time marching procedure, the flow is initialized throughout the physical domain with the gust perturbation superimposed on the mean flow. At the inflow boundary, the standard acoustic radiation condition given is applied to the outgoing perturbation and defined, e.g., for X-component of flow velocity as $u_{BC} = u_{boundary} - \bar{u} - u_{gust}$. At the outflow boundary, Tam and Webb's [7] condition is applied.

RESULTS

Results for the benchmark cases were obtained from simulations time-marched over periods sufficient to achieve converged, time-accurate solutions. In terms of the non-dimensional time (normalized by the airfoil half-chord and the speed of sound), the values between 360 and 450 were found necessary for the more slowly converging loaded airfoil simulations to accurately resolve the mean flowfield and the acoustic field. More time iterations were required for the lowest gust frequency case in order to march through an adequate number of longer periods. To quantify the computational effort in parallel simulations, a 16-hour numerical run was required to march to the non-dimensional time value of 360, which corresponded to 70,000 iterations on the 600x240 cambered-airfoil case grid using sixteen processors (i.e., approximately 15 CPU min per oscillation period). On a single node, the computational effort went as high as 250 CPU min per oscillation period.

Figure 2 shows contours of the Y-component of the flow velocity for all three frequencies in the unloaded (symmetric) airfoil case. For k=2.0, the grid density appears barely sufficient to resolve the gust perturbation near the upper and lower corners of the domain, which manifested itself in the form of slightly smeared contours and affected the accuracy of acoustics resolution in those zones.
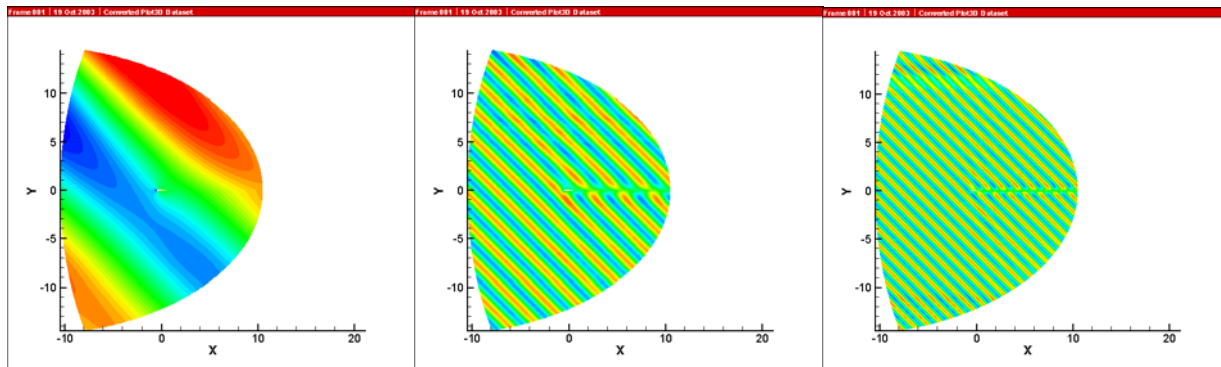
Figure 2. Instantaneous velocity, Y-component, symmetric airfoil case. From left to right: k=0.1, 1.0, 2.0.

Calculated mean pressure on the upper and lower airfoil surfaces is shown in Figure 3, in comparison with FLO36 solver results. The localized effect of the trailing-edge grid singularity is more pronounced in the cambered airfoil case.
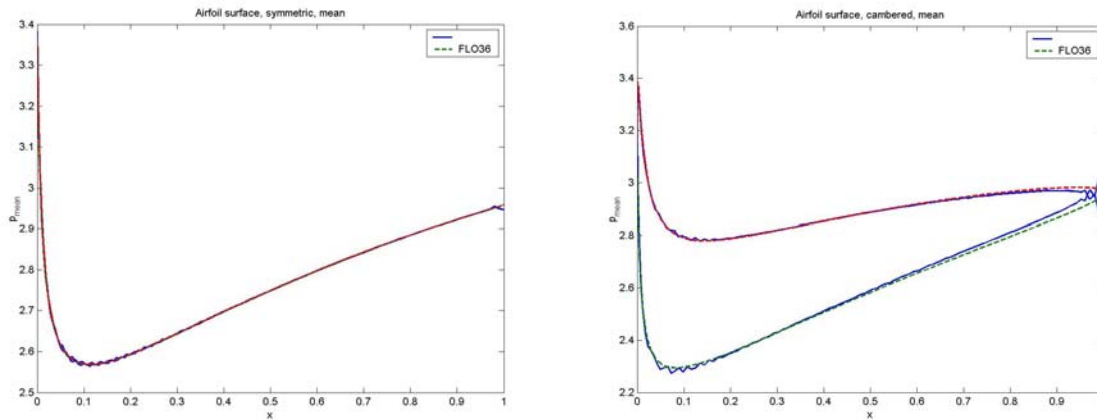
Figure 3. Mean airfoil surface pressure. Left: symmetric airfoil. Right: cambered airfoil.

The corresponding predicted unsteady RMS airfoil surface pressures are provided for reduced gust frequencies k=1.0 and 2.0, for the symmetric airfoil in Figure 4, and for the cambered airfoil in Figure 5.
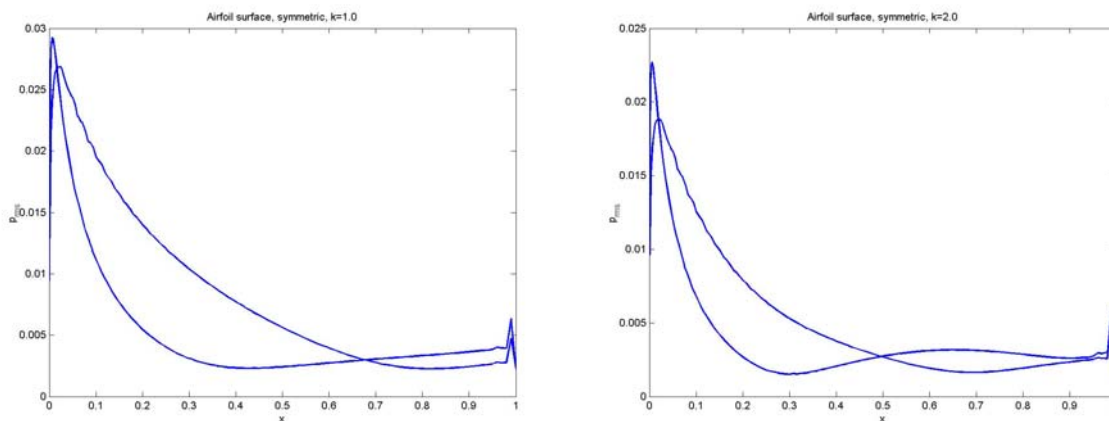
Figure 4. Unsteady RMS pressure on airfoil surface, symmetric airfoil. Left: k=1.0. Right: k=2.0.
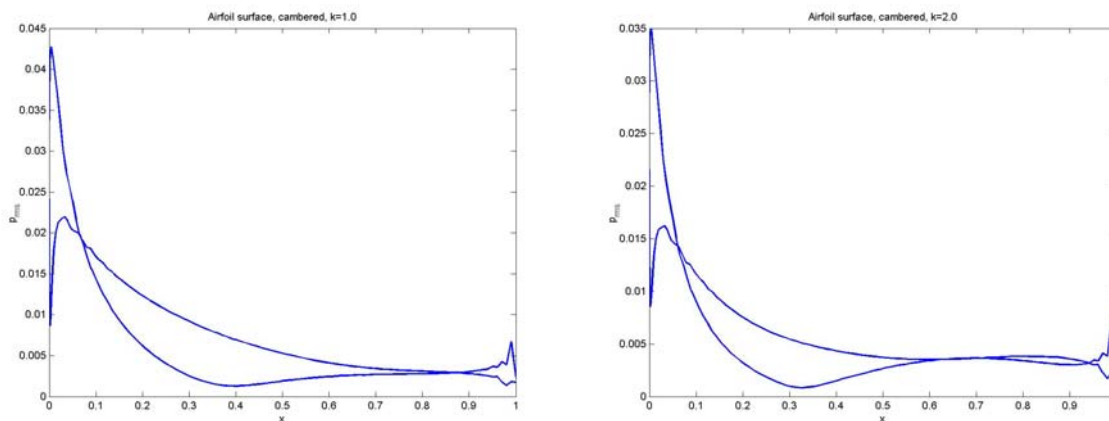
Figure 5. Unsteady RMS pressure on airfoil surface, cambered airfoil. Left: k=1.0. Right: k=2.0.

Finally, the directivity plots for the non-dimensional acoustic intensities predicted for the symmetric airfoil cases with gust reduced frequencies k=0.1, 1.0 and 2.0, are shown in Figures 6, 7 and 8 for distances R/c= 1, 2 and 4 from the airfoil centerpoint, respectively. Similar plots for the cambered airfoil cases are provided in Figures 9, 10 and 11. At R/c=2, only the results predicted for k=1.0 and 2.0 are shown in Figures 7 and 10. In the case of the cambered airfoil, the results calculated for k=2.0 appear to have suffered significantly from the above-mentioned poor gust resolution in the corner regions of the domain, and thus are not shown in Figure 11.
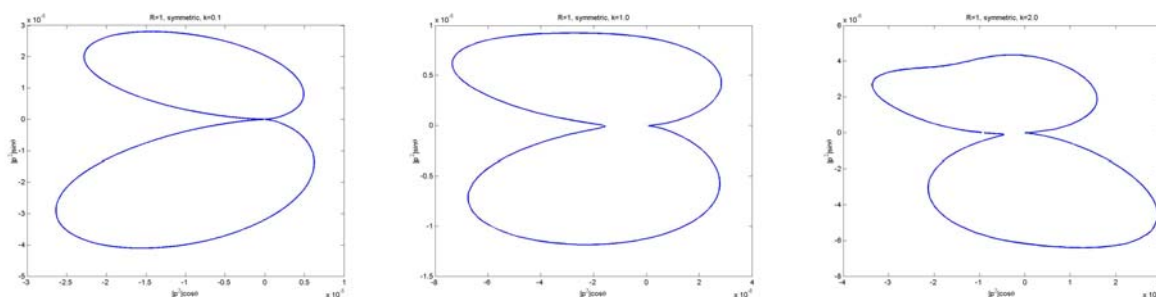
Figure 6. Directivity of $|p'^2|$ for RMS unsteady pressure at R/c=1, symmetric airfoil. Left to right: k=0.1, 1.0, 2.0.
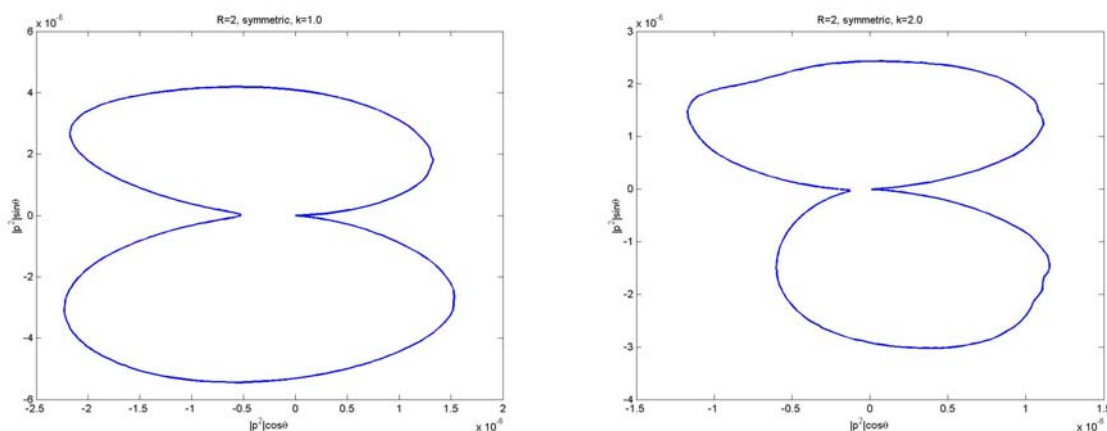
Figure 7. Directivity of $|p'^2|$ for RMS unsteady pressure at R/c=2, symmetric airfoil. Left to right: k=1.0, 2.0.
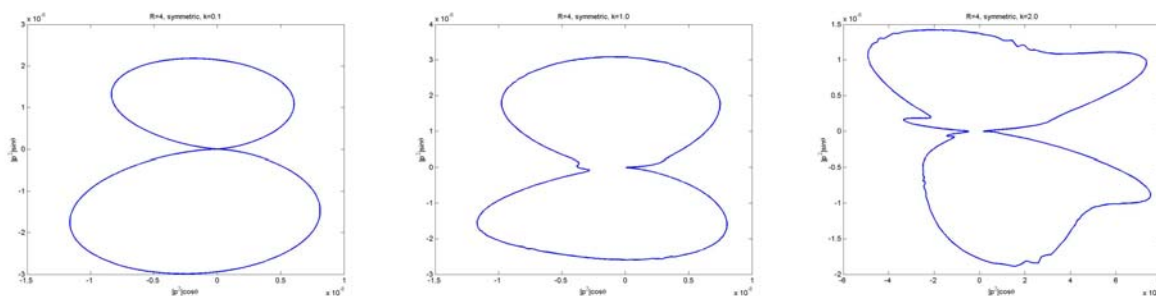
Figure 8. Directivity of $|p'^2|$ for RMS unsteady pressure at R/c=4, symmetric airfoil. Left to right: k=0.1, 1.0, 2.0.
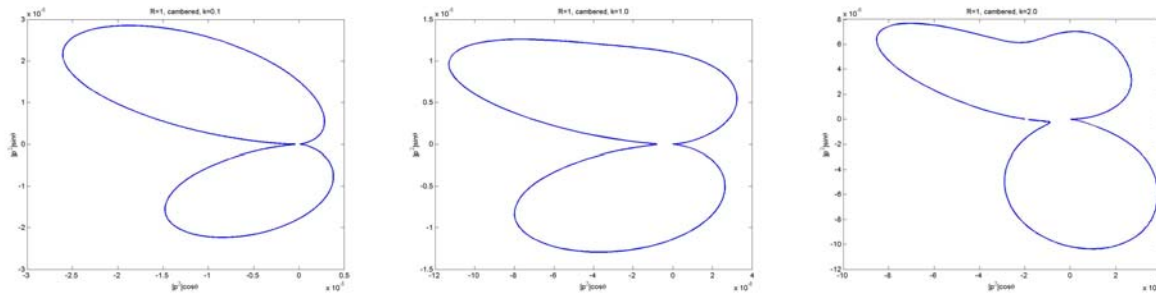
Figure 9. Directivity of $|p'^2|$ for RMS unsteady pressure at R/c=1, cambered airfoil. Left to right: k=0.1, 1.0, 2.0.
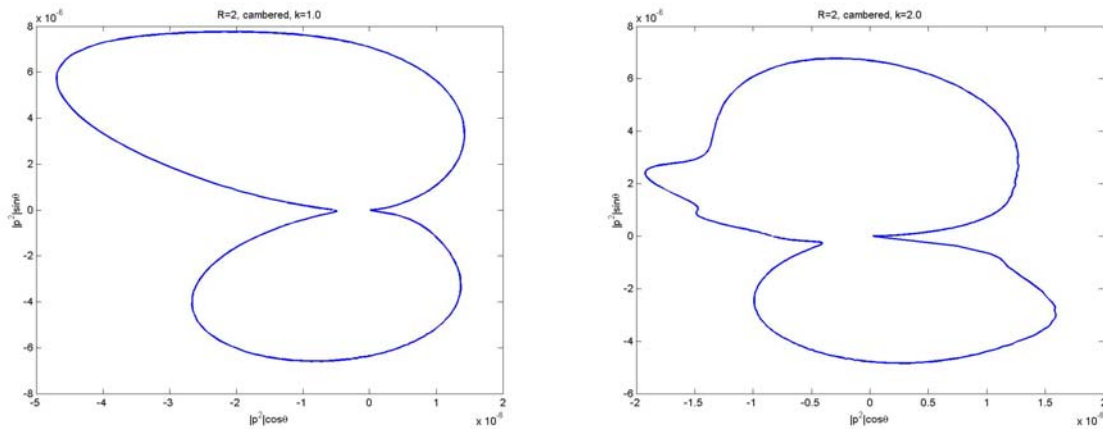
Figure 10. Directivity of $|p'^2|$ for RMS unsteady pressure at R/c=2, cambered airfoil. Left to right: k=1.0, 2.0.
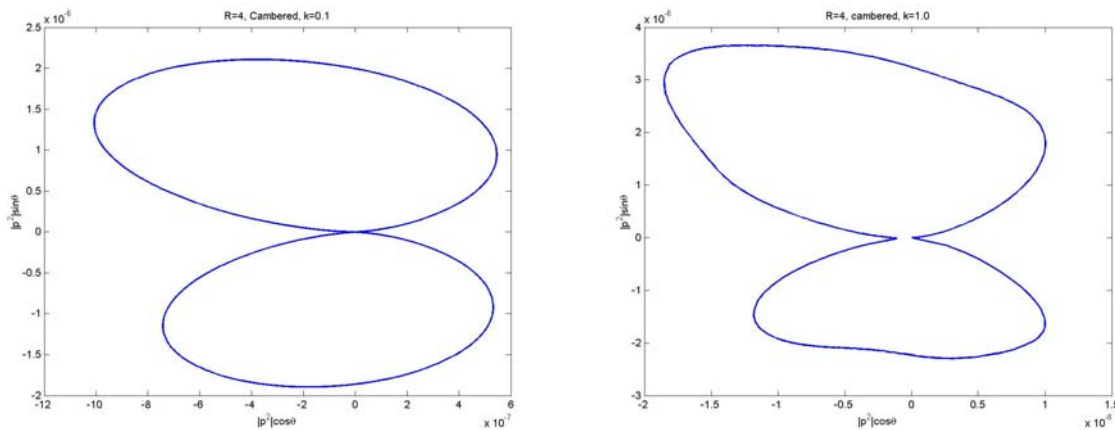
Figure 11. Directivity of $|p'^2|$ for RMS unsteady pressure at R/c=4, cambered airfoil. Left to right: k=0.1, 1.0.

REFERENCES

1. Stanescu, D. and Habashi, W.G., "2N-Storage Low Dissipation and Dispersion Runge-Kutta Schemes for Computational Acoustics," Journal of Computational Physics, Vol.143, pp.674-681, 1998.
2. Hixon, R., "A New Class of Compact Schemes," AIAA Paper 98-0367, Reno, NV, January 1998.
3. Hixon, R., Nallasamy, M. and Sawyer, S.S., "Parallelization Strategy for an Explicit Computational Aeroacoustic Code," AIAA Paper 2002-2583, 2002.

4. Hixon, R., Shih, S.-H., Mankbadi, R.R., and Scott, J.R., "Time Domain Solution of the Airfoil Gust Problem Using a High-Order Compact Scheme," AIAA Paper 98-3241, Cleveland, OH, 1998.

5. Crivellini, A., Golubev, V.V., Mankbadi, R.R., Scott, J.R., Hixon, R. and Povinelli, L.A., "Nonlinear Analysis of Airfoil High-Intesnity Gust Response Using a High-Order Prefactored Compact Code," AIAA Paper 2002-2535, 2002.

6. GridPro™, Program Development Corporation, White Plains, NY.

7. Tam, C.K.W. and Webb, J.C., "Dispersion-Relation-Preserving Finite Difference Schemes for Computational Acoustics," Journal of Computational Physics, Vol. 107, pp.262-281, 1993

RADIATION AND REFRACTION OF SOUND WAVES THROUGH

A TWO-DIMENSIONAL SHEAR LAYER

Christophe Bailly & Christophe Bogey

Laboratoire de Mécanique des Fluides et d'Acoustique
UMR CNRS 5509 & Ecole Centrale de Lyon
36 avenue Guy de Collongue, 69134 Ecully, France
http://acoustique.ec-lyon.fr

INTRODUCTION

As a starting point, we consider the linearized Euler equations which govern sound propagation in a steady mean flow $(\bar{\rho}, \bar{\mathbf{u}}, \bar{p})$ where ρ, $\mathbf{u} = (u, v)$ and p denote the density, the velocity and the pressure respectively. Using Cartesian coordinates $\mathbf{x} = (x, y)$, these equations read

$$
\begin{cases}
\dfrac{\partial \rho'}{\partial t} + \nabla \cdot (\rho' \bar{\mathbf{u}} + \bar{\rho} \mathbf{u}') = 0 \\[2mm]
\dfrac{\partial (\bar{\rho} \mathbf{u}')}{\partial t} + \nabla \cdot (\bar{\rho} \bar{\mathbf{u}} \mathbf{u}') + \nabla p' + (\bar{\rho} \mathbf{u}' + \rho' \bar{\mathbf{u}}) \cdot \nabla \bar{\mathbf{u}} = 0 \\[2mm]
\dfrac{\partial p'}{\partial t} + \nabla \cdot [p' \bar{\mathbf{u}} + \gamma \bar{p} \mathbf{u}'] + (\gamma - 1) [p' \nabla \cdot \bar{\mathbf{u}} - \mathbf{u}' \cdot \nabla \bar{p}] = \Lambda
\end{cases}
\tag{1}
$$

where γ is the specific heat ratio, r the gas constant, T the temperature, for a perfect gas $p = \rho r T$, and $f = \bar{f} + f'$ for any variable f. In the present work, these equations are solved in the following form

$$
\frac{\partial \mathbf{U}}{\partial t} + \frac{\partial \mathbf{E}}{\partial x} + \frac{\partial \mathbf{F}}{\partial y} + \mathbf{H} = \mathbf{S}
\tag{2}
$$

where the vectors $\mathbf{U}$, $\mathbf{E}$, $\mathbf{F}$ and $\mathbf{H}$ are given by

$$
\mathbf{U} = \begin{pmatrix} \rho' \\ \bar{\rho} u' \\ \bar{\rho} v' \\ p' \end{pmatrix}
\quad
\mathbf{E} = \begin{pmatrix} \rho' \bar{u} + \bar{\rho} u' \\ \bar{u} \bar{\rho} u' + p' \\ \bar{u} \bar{\rho} v' \\ \bar{u} p' + \gamma \bar{p} u' \end{pmatrix}
\quad
\mathbf{F} = \begin{pmatrix} \bar{\rho} v' \\ 0 \\ p' \\ \gamma \bar{p} v' \end{pmatrix}
\quad
\mathbf{H} = \begin{pmatrix} 0 \\ \bar{\rho} v' \dfrac{d\bar{u}}{dy} \\ 0 \\ 0 \end{pmatrix}
$$

for a parallel base flow $\bar{u}(y)$, $\bar{\rho}(y)$, $\bar{v} = 0$ and $\bar{p} = p_\infty = $ constant. A Gaussian function is taken for the unidirectional sheared mean flow

$$
\frac{\bar{u}}{u_j} = \exp \left(-\log(2) \left(\frac{y}{b} \right)^2 \right)
\tag{3}
$$

and the density profile is deduced from the Crocco-Busemann relation

$$
\frac{\rho_j}{\bar{\rho}} = \frac{T_\infty}{T_j} - \left(\frac{T_\infty}{T_j} - 1 \right) \frac{\bar{u}}{u_j} + \frac{\gamma - 1}{2} \mathrm{M}_j^2 \frac{\bar{u}}{u_j} \left(1 - \frac{\bar{u}}{u_j} \right)
$$

where the variables with subscript j are defined at the jet axis. The time-harmonic acoustic source term $\mathbf{S}^T = (0, 0, 0, \Lambda)$ is given by $\Lambda = S(x, y) \cos(\omega_0 t)$ with $S = A e^{-\alpha_x x^2 - \alpha_y y^2}$. For the numerical resolution, the equations are made dimensionless by using:

$$
\tilde{\mathbf{x}} = \frac{\mathbf{x}}{b} \qquad \tilde{u} = \frac{u}{u_j} \qquad \tilde{\rho} = \frac{\rho}{\rho_j} \qquad \tilde{t} = \frac{t}{b/u_j} \qquad \tilde{p} = \frac{p}{\rho_j u_j^2}
$$

The parameters of the problem are $M_j = 0.756$, $T_j = 600$ K, $T_\infty = 300$ K, $\gamma = 1.4$, $r = 287$ m^2.s^{-2}.K^{-1}, $b = 1.3$, $\alpha_x = 0.04 \log(2)$ m^{-2}, $\alpha_y = 0.32 \log(2)$ m^{-2}, $A = 10^{-3}$ kg.m^{-1}.s^{-3} and $\omega_0 = 76$ rad.s^{-1}. The mean pressure is $\bar{p} = 103330$ kg.m^{-1}.s^{-2}. A Strouhal number based on the jet exit velocity and an estimation of the jet diameter $2b$ can be defined as St$= f_0\, 2b/u_j = \tilde{\omega}_0/\pi \simeq 0.085$ where $\tilde{\omega}_0 = \omega_0 b/u_j$.

In the present simulations a dimensionless amplitude $\tilde{A}_0 = 10^{-3}$ has been used rather than $\tilde{A} = A \times b/(\rho_j u_j^2)$. As a consequence dimensional pressure of the test case is obtained by multiplying $\tilde{p}$ by a factor $b/u_j \simeq 3.5 \times 10^{-3}$ since the problem is linear.

SIMPLIFIED LINEARIZED EULER'S EQUATIONS

The linearized Euler equations (1) govern the propagation of small acoustical disturbances through a steady mean flow in taking into account all the mean flow effects such as refraction and convection of the sound by the mean flow. However, spatially growing instability waves are also solutions of these equations. The fluctuating velocity and density can be eliminated by differentiating (1) for a parallel mean flow and the resulting equation for the pressure reads

$$\bar{D}^3 p' - \bar{c}^2 \left(\bar{D}\nabla^2 p' - \frac{1}{\bar{\rho}}\frac{d\bar{\rho}}{dy}\bar{D}\frac{\partial p'}{\partial y} - 2\frac{d\bar{u}}{dy}\frac{\partial^2 p'}{\partial x \partial y} \right) = \bar{D}^2 \Lambda \tag{4}$$

where $\bar{D} = \partial/\partial t + \bar{u}\partial/\partial x$ is the convective derivative. Equation (4) can be seen as a wave equation, but represents also the generalization of the Rayleigh equation for a compressible perturbation. Figure 1 shows the spatial growth rate and the phase velocity as a function of the frequency of the Kelvin-Helmholtz instability wave obtained by seeking solutions of the homogeneous equation in the form $p'(\mathbf{x}, t) = \hat{p}(y) \exp(ikx - \omega t)$ where $k = k_r + ik_i$ is the complex wave number. The wave number corresponding to the angular frequency $\tilde{\omega}_0$ of the acoustic forcing is found to be $\tilde{k}_H \simeq 0.53883 - i0.04906$.

The objective of the present problem is to compute only the acoustic part of the solution, and not the associated instability wave. The authors have developed an acoustic analogy based on the Linearized Euler Equation (LEE) with an *ad hoc* source term reducing to Lilley's analogy for a parallel mean flow.[3] In order to prevent the development of instability waves which can overwhelm the radiated acoustic field and thus prohibit the use of the hybrid approach, a simplified formulation of LEE has been proposed. This simplified formulation is obtained in removing arbitrarily the term $d\bar{u}/dy$ in the vector $\mathbf{H}$. As a result, the equation for the pressure reads now

$$\bar{D}^3 p' - \bar{c}^2 \left(\bar{D}\nabla^2 p' - \frac{1}{\bar{\rho}}\frac{d\bar{\rho}}{dy}\bar{D}\frac{\partial p'}{\partial y} - \frac{d\bar{u}}{dy}\frac{\partial^2 p'}{\partial x \partial y} \right) = \bar{D}^2 \Lambda \tag{5}$$

The only difference between equations (4) and (5) is the factor 2 in the velocity gradient term. The consequences for the description of the acoustic propagation are not easy to describe. Note however that this approximation is not the usual high-frequency approximation of (4), namely the ray-tracing equations, as given by Candel[6] for instance. Note also that this formulation has been successfully applied to the noise generated by an isothermal mixing layer,[3] where vortex pairings produce a relatively low-frequency sound field.

NUMERICAL METHOD

LEE (2) are solved with the Sprint-2d solver developed for aeroacoustic applications.[2,3] The numerical algorithm has been updated with numerical schemes optimized in the wave-number space ensuring accuracy
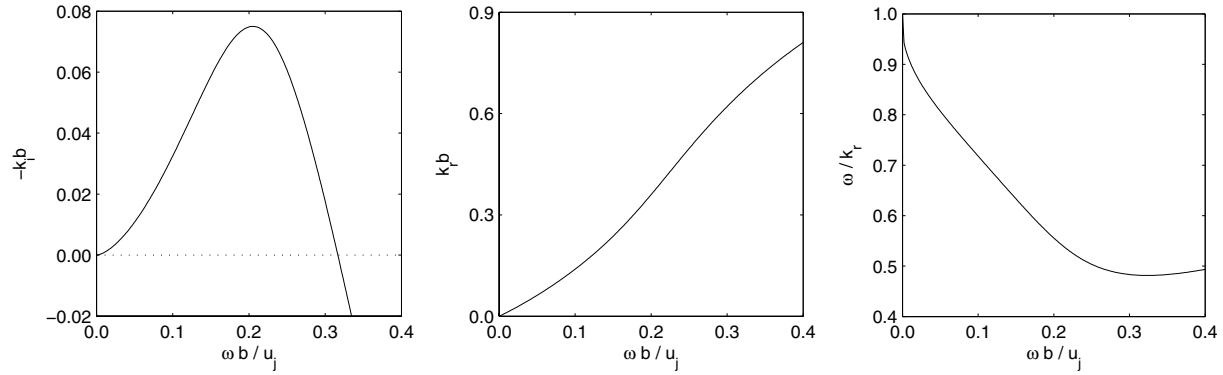
Figure 1: Spatial growth rate $-k_i b$, real wave number $k_r b$ and phase velocity $v_\varphi/u_j = \omega/k_r$ as a function of the frequency $\omega b/u_j$. The compressible Rayleigh equation is solved using a 4th-order Runge-Kutta shooting method and the integration path is deformed in the complex plane to avoid the critical point.

up to five points per wavelength. A 11-point-stencil finite-difference scheme and a 6-step low storage Runge-Kutta algorithm are used for the spatial derivation and time integration.[5] Grid-to-grid oscillations are removing by filtering the unknow vector using a highly selective filter on 11 points. The radiation boundary conditions of Tam & Webb are implemented on the three last points of the computational domain and a small buffer zone is added at the inflow boundary condition to prevent the possible generation of instability waves by the outgoing acoustic field.[4] A symmetry boundary condition is applied along the line $x = 0$.

After preliminary calculations, two grids of different size have been adopted and are presented in the paper. The first one is a regular grid of 601×301 points with $\Delta \tilde{x} = 0.4/b$ and $\Delta \tilde{y} = 0.25/b$. The whole computational domain is $-63 \leq \tilde{x} \leq 175$ and $0 \leq \tilde{y} \leq 74$. The domain of the second grid is similar but the step size in the two directions is divided by 2 yielding a grid of 1201×601 points. Thus there are 10 points in the mean shear flow with the finest grid. The time of the simulation corresponds to 18 periods of the source with a CFL number of 0.9 and the average is calculated at the last period to obtain the root mean square pressure. The computations are performed on a Nec-Sx5 with a CPU time per time iteration and by mesh point of around 3.8×10^{-7} s. Using a Dec α server 1280 GS MARVEL (EV7, 1.15 GHz) the CPU time per time iteration and by mesh point is 6.3×10^{-6} s.

RESULTS AND DISCUSSION

Numerical results obtained with the simplified formulation of LEE associated to wave equation (5) are presented in figures 2 to 5. Figure 2 shows the pressure at the start of a cycle along the two lines $\tilde{y} = 15$ and $\tilde{y} = 50$. No appreciable difference has been observed between the two grids which emphasizes the good accuracy of the optimized schemes. Figure 3 displays the pressure along the line $\tilde{x} = 100$. Time evolution and root mean square pressure profiles are reported in figures 4 and 5.

The simplified wave equation (5) prevents the development of instability waves as observed and discussed in early works.[3] But only an approximate high frequency acoustic field is obtained, not appropriate for the low frequency source of the test case corresponding to a Strouhal number St < 0.1. The pressure field obtained with the simplified formulation of LEE is shown in figure 6. A ray-tracing has been superimposed to show that the wave equation (5) associated to the simplified LEE is not a full high-frequency approximation. As expected the comparison with the analytical solution in figure 7 also displays some significant differences especially in the shadow zone for $\tilde{x} > 50$.
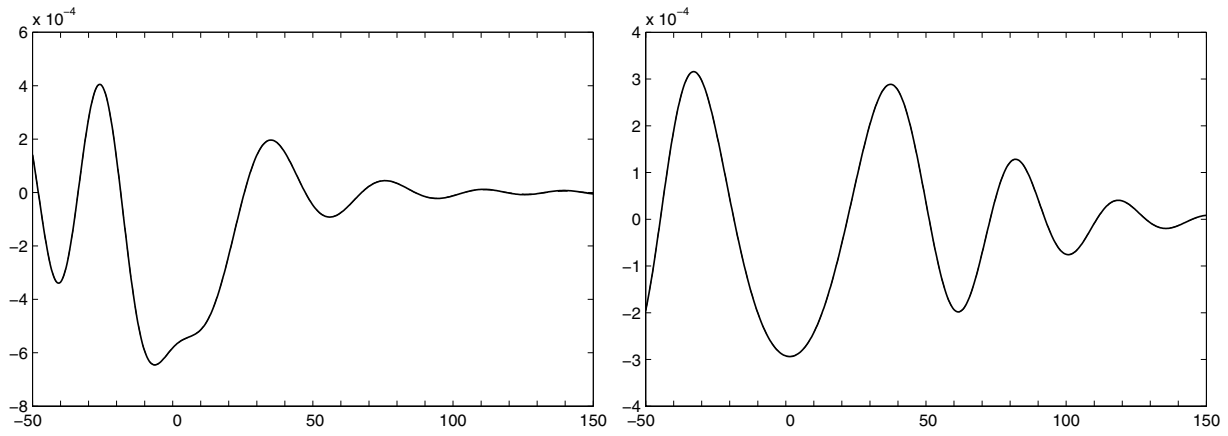
Figure 2: Pressure $\tilde{p}'$ at the start of a cycle along the line $\tilde{y} = 15$ (left) and the line $\tilde{y} = 50$ (right): ——— coarse grid   – – – fine grid.
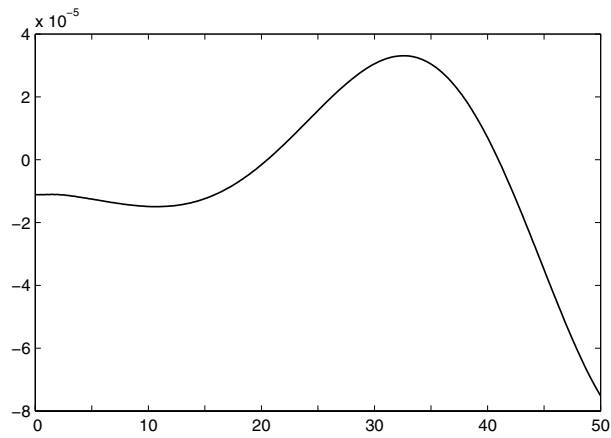
Figure 3: Pressure $\tilde{p}'$ at the start of a cycle along the line $\tilde{x} = 100$.
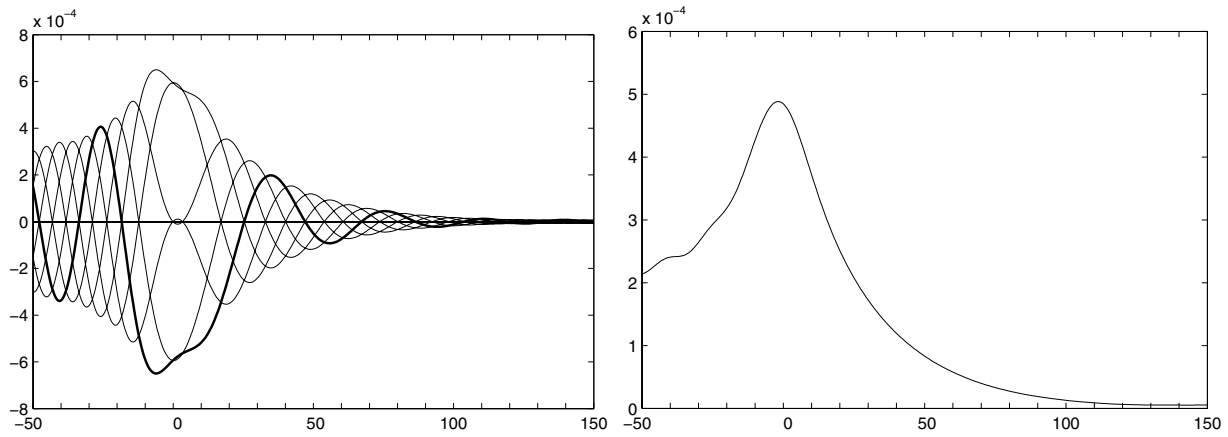
Figure 4: Time history of the pressure $\tilde{p}'$ and root mean square pressure $\tilde{p}_{rms}$ along the line $\tilde{x} = 15$.
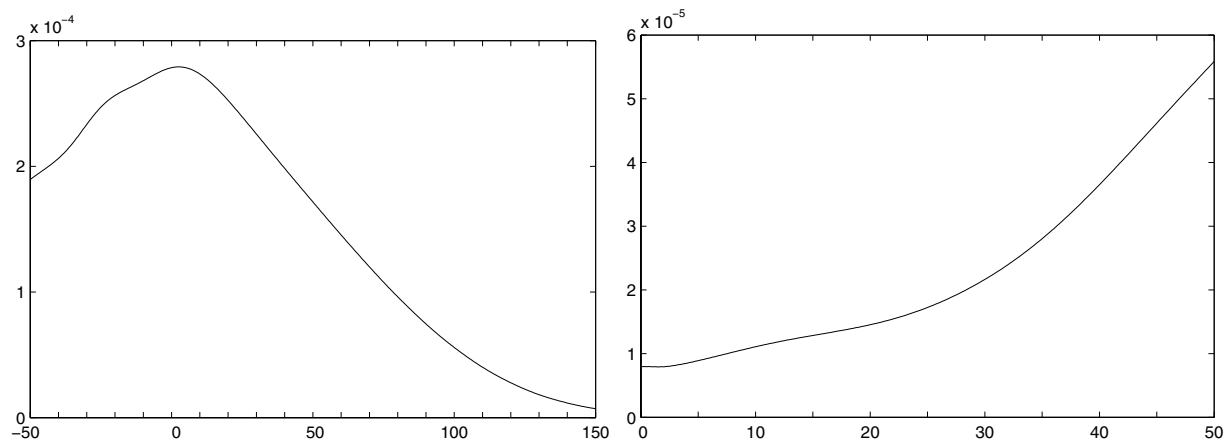
Figure 5: Root mean square pressure $\tilde{p}_{rms}$ along the line $\tilde{y} = 50$ (left) and along the line $\tilde{x} = 100$ (right).
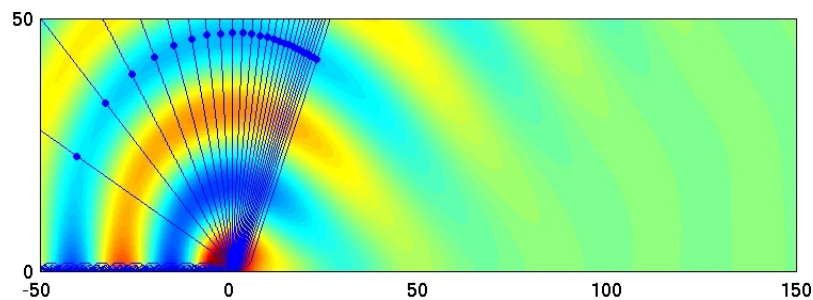
Figure 6: Pressure field $\tilde{p}'$ at the start of a cycle and ray-tracing from the source: 32 rays are plotted from $0 \leq \theta \leq \pi$.
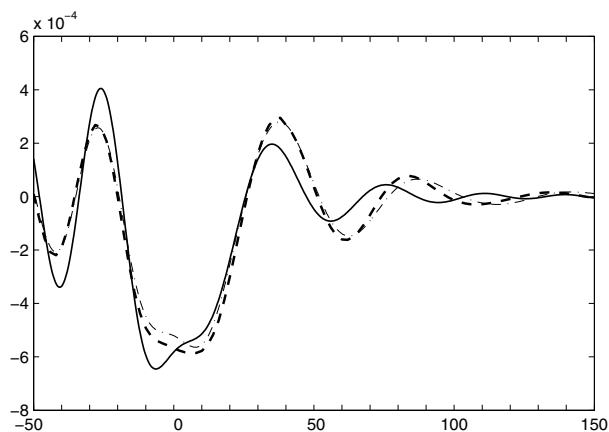
Figure 7: Pressure $\tilde{p}'$ at the start of a cycle along the line $\tilde{y} = 15$: $- - -$ analytical solution,[1] $\longrightarrow$ simplified formulation of LEE associated to wave equation (5), $-\cdot-\cdot-$ LEE (2) + source term (6).

Finally, Eschricht, Thiele and their coauthors[7] have presented during the workshop a new formulation to remove the instability wave in the time domain. LEE (2) are solved forced by following source term in the right hand side

$$\mathbf{S}^T = \left(0, S_x = \frac{\partial \bar{v}}{\partial x}\, u', S_y = \frac{\partial \bar{u}}{\partial y}\, v', \Lambda\right) \tag{6}$$

with $S_x \equiv 0$ for the workshop test case. The corresponding wave equation writes as

$$\bar{D}^3 p' - \bar{c}^2 \left(\bar{D}\nabla^2 p' - \frac{1}{\bar{\rho}}\frac{d\bar{\rho}}{dy}\bar{D}\frac{\partial p'}{\partial y} - 2\frac{d\bar{u}}{dy}\frac{\partial^2 p'}{\partial x \partial y}\right) = \bar{D}^2 \Lambda - \gamma\bar{p}\bar{D}\left(\frac{\partial S_x}{\partial x} + \frac{\partial S_y}{\partial y}\right) + 2\gamma\bar{p}\frac{d\bar{u}}{dy}\frac{\partial S_y}{\partial x} \tag{7}$$

The computed pressure thus obtained is reported in figure 7. The solution compares better with the analytical one than the solution based on the simplified LEE.

REFERENCES

[1] AGARWAL, A., MORRIS, P.J. & MANI, R., 2003, The calculation of sound propagation in nonuniform flows: suppression of instability waves, AIAA Paper 2003-0878, *41st Aerospace Sciences Meeting and Exhibit*.

[2] BAILLY, C. & JUVÉ, D., 2000, Numerical solution of acoustic propagation problems using linearized Euler equations, *AIAA Journal*, **38**(1), 22-29

[3] BOGEY, C., BAILLY, C. & JUVÉ, D., 2002, Computation of flow noise using source terms in linearized Euler's equations, *AIAA Journal*, **40**(2), 235-243.

[4] BOGEY, C. & BAILLY, C., 2002, Three-dimensional non-reflective boundary conditions for acoustic simulations : far field formulation and validation test cases, *Acta Acustica*, **88**(4), 463-471

[5] BOGEY, C. & BAILLY, C., 2002, A family of low dispersive and low dissipative schemes for Large Eddy Simulation and for sound propagation, accepted in the *Journal of Computational Physics*. See also AIAA Paper 2002-2509.

[6] CANDEL, S.M., 1977, Numerical solution of conservation equations arising in linear wave theory: application to aeroacoustics, *J. Fluid Mech.*, **83**(3), 465-493

[7] ESCHRICHT, D., THIELE, F. *et al.*, 2003, contribution in the present 4th CAA workshop proceedings.

RADIATION AND REFRACTION OF SOUND WAVES THROUGH A 2-D SHEAR LAYER: NUMERICAL SOLUTION

Anurag Agarwal and Philip J. Morris
Department of Aerospace Engineering
The Pennsylvania State University
University Park, PA 16802, USA

INTRODUCTION

Acoustic propagation in sheared mean flows can be calculated using the linearized Euler equations (LEE). However the LEE also support instabilities. These instabilities are nonphysical since, in the real flow problem, they are suppressed by nonlinear effects. In fact, they constitute the fundamental driving mechanism in their nonlinear form, for turbulent free shear flows. These instabilities can overwhelm the acoustic solution thus complicating the prediction of mean flow/acoustic interaction effects. In this paper, a numerical solution for sound propagation through a 2-D shear layer is presented that suppresses the LEE instabilities. The solution is obtained using a direct frequency domain solver. A frequency domain buffer-zone is used to implement the boundary conditions. The numerical solution avoids the instability-wave solution and accurately captures the acoustic-wave solution. The rationale for the success of this technique is described in reference 1. The numerical algorithm is straightforward and is presented in this paper along with the results.

GOVERNING EQUATIONS

The governing equations are the LEE that can be written in the following component form:

$$L\left(\frac{\partial}{\partial \boldsymbol{x}},\frac{\partial}{\partial t},\boldsymbol{x}\right)\boldsymbol{U}(\boldsymbol{x},t) = \boldsymbol{S}(\boldsymbol{x})\cos(\omega_o t), \tag{1}$$

where

$$L = \begin{bmatrix} \boxdot & \bar{\rho}(y)\frac{\partial}{\partial x} & \frac{d\bar{\rho}(y)}{dy}+\bar{\rho}(y)\frac{\partial}{\partial y} & 0 \\ 0 & \boxdot & \frac{d\bar{u}(y)}{dy} & \frac{1}{\bar{\rho}(y)}\frac{\partial}{\partial x} \\ 0 & 0 & \boxdot & \frac{1}{\bar{\rho}(y)}\frac{\partial}{\partial y} \\ 0 & \gamma\bar{p}\frac{\partial}{\partial x} & \gamma\bar{p}\frac{\partial}{\partial y} & \boxdot \end{bmatrix},$$

$$\boldsymbol{U} = \left\{ \begin{array}{c} \rho \\ u \\ v \\ p \end{array} \right\}, \boldsymbol{S} = \left\{ \begin{array}{c} 0 \\ 0 \\ 0 \\ \Lambda(\boldsymbol{x}) \end{array} \right\}, \tag{2}$$

$\boxdot = \partial/\partial t + \bar{u}(y)\partial/\partial x$, $\Lambda(\boldsymbol{x})$ is the source term, the mean flow variables are denoted by an overbar, and ω_o is the source frequency that excites an instability wave.

Equations (1) can be solved in the space-time domain by an explicit time-marching scheme. It is found that the solution provided by this technique is contaminated with the instability wave. The instability waves can be suppressed if the governing equations are solved in the frequency domain after assuming a time-harmonic response.

Since the source is time-harmonic and the coefficients of the LEE are independent of time, the response can be assumed to be time-harmonic. That is,

$$\boldsymbol{U}(\boldsymbol{x},t) = \boldsymbol{U}(\boldsymbol{x};\omega)e^{-i\omega_o t}, \tag{3}$$

if the source term in Eq. (1) is made complex. Then the governing equation for the response is given by

$$L\left(\frac{\partial}{\partial \boldsymbol{x}},\frac{\partial}{\partial t},\boldsymbol{x}\right)\boldsymbol{U}(\boldsymbol{x},t) = \boldsymbol{S}(\boldsymbol{x})\exp[-i\omega_o t], \tag{4}$$

with the understanding that the physical response is given by the real part of the solution. After the substitution of Eq. (3) into Eq. (4), replacing the time derivative terms $\partial/\partial t \to -i\omega_o$, and factoring out the $\exp[-i\omega_o t]$ term from both

sides of the resulting equation, the resulting system of equations can be manipulated to eliminate all the dependent variables in favor of the perturbation pressure p. This results in the following partial differential equation

$$\left[D^3 - \bar{c}^2(y) \left\{ D\nabla^2 - \frac{1}{\bar{\rho}(y)} \frac{d\bar{\rho}(y)}{dy} D \frac{\partial}{\partial y} - 2 \frac{d\bar{u}(y)}{dy} \frac{\partial^2}{\partial x \partial y} \right\} \right] p = D^2 \Lambda(\boldsymbol{x}) \tag{5}$$

where $D = (-i\omega_o + \bar{u}\partial/\partial x)$, and $\nabla^2 = \partial^2/\partial x^2 + \partial^2/\partial y^2$. The operator on p in Eq. (5) is also known as Lilley's wave operator (ref. 2). This equation is solved here in space by a direct frequency-domain solver. Note that the present technique is also applicable to the linearized Euler equations in their component form. The component equations have been reduced to a single equation only for simplicity.

Space-time solution

The LEE are solved here in the space-time domain by an explicit finite-difference scheme. A fourth-order Dispersion-Relation-Preserving scheme is used for spatial discretization and a fourth-order Runge-Kutta scheme is used for time integration (see reference 3 for the numerical implementation details and boundary treatment). The given source frequency excites an instability wave. This is accurately captured by the space-time solver as can be seen in Fig. (1) that compares the numerical solution on the line $y = 15$ with the analytical solution. The solution exhibits a growing spatial instability. The numerical and analytical solutions agree well.

Figure 1: Comparison of the analytical solution ($\diamond$) along the sideline $y = 15$ with numerical solution (—) obtained by a space-time solver.

Assumed time-harmonic response

To obtain the assumed time-harmonic response, Eq. (5) is solved in space as a boundary-value problem. The computational domain is the interval $[x_{\min}, x_{\max}] \times [y_{\min}, y_{\max}] = [-250, 225] \times [0, 100]$. A symmetry boundary condition is applied along the line $y = 0$. The left and top boundaries must absorb the outgoing acoustic wave. The right boundary must absorb the acoustic, vorticity and entropy waves that are generated by the source. A buffer domain treatment is used to allow for a clean passage of the outgoing waves (no reflection). The basic step in the application of this boundary condition involves surrounding the physical domain of interest by a buffer domain in which the waves are forced to decay exponentially away from the source, so that at the outer edge of the buffer domain the waves have decayed to a negligible value.

The exponential decay in the buffer domain is achieved by replacing the assumed frequency of the response (ω_o) by a complex frequency of the form

$$\beta(\boldsymbol{x}) = \omega_o + i\sigma(\boldsymbol{x}) \tag{6}$$

where $\sigma(\boldsymbol{x})$ is zero within the physical domain and takes on real positive values for outgoing waves in the buffer domain. Numerical experiments performed on different benchmark problems reveal that the length of the buffer domain must be at least two wavelengths of the outgoing wave.

The damping function, σ, must be chosen so that its slope is zero at the edge of the physical domain and its value rises gradually to a maximum at the domain's outer edge. For the present calculations, the damping function is chosen

to be an exponential function. For a one-dimensional problem, the damping function takes the form

$$\sigma(x) = \mu\omega_o \frac{1 - \exp[\kappa x_b(x)^2]}{1 - \exp[\kappa]} \tag{7}$$

where x_b is a buffer domain coordinate that is 0 at the beginning of the buffer domain and 1 at the end and has a linear variation in between. μ and κ are constants with values of 2 and 4 respectively. For a 2-D domain the damping function is shaped like an inverted 'table-cloth'.

The computational domain is discretized by a grid that is clustered around $y = 0$ to capture the sharp gradients within the shear layer. The grid is also clustered around $x = 0$, so that it can be stretched out to a reasonable distance upstream and downstream of the source location while providing a better resolution near the source. The required grid layout is obtained by mapping the physical domain into a computational domain by the coordinate transformations (from reference 4):

$$\xi = A + \frac{1}{\chi} \sinh^{-1} \left[\left(\frac{x}{D} - 1 \right) \sinh(\chi A) \right] \tag{8}$$

$$\eta = 1 - \frac{\log\left[(\mu + 2 - y/y_{\max})/(\mu - 1 + y/y_{\max})\right]}{\log[(\mu + 1)/(\mu - 1)]}, \tag{9}$$

where

$$A = \frac{1}{2\chi} \log\left[\frac{1 + (\exp[\chi] - 1)(D/L)}{1 + (\exp[-\chi] - 1)(D/L)} \right] \tag{10}$$

The computational domain (ξ, η) consists of uniformly spaced grid points. Then the pre-image of ξ and η describes the grid layout in the physical domain. The parameters used for the present simulation are: $\chi = 5.0$, $\mu = 1.01$, $D = -x_{\min}$, and $L = x_{\max} - x_{\min}$. A total of $N_x \times N_y = 440 \times 300$ grid points are used. The buffer domain is 70 units deep along the left, top, and right boundaries.

Equation (5) is solved using a finite difference method. The spatial derivatives are approximated by second-order, central-difference formulas. After application of the Dirichlet boundary conditions, the finite-difference equations can be written in the following matrix form

$$S \cdot p = l \tag{11}$$

There are a total of $N_x \times N_y$ grid points resulting in $N_x \times N_y$ unknowns $p_{i,j}$ that are approximations of the actual function $p(x, y)$ at the grid points (i, j). These unknowns can be put in a one-dimensional sequence to obtain a vector form $p = [p_0, p_1, \ldots, p_{N_x N_y - 1}]^T$, where $p_k = p_{i,j}$ for $k = i + jN_x$. S is a sparse matrix that is banded with left and right bandwidths of $N_x + 1$, and l is the right-hand side (known) or load vector. Further details of the matrix set-up can be found in reference 5.

The matrix S is inverted by a direct matrix inversion method (for example LU decomposition). The resulting solution for pressure is found to be free of instabilities, as expected. Figure (2) shows a comparison between the numerical and the analytical solution for the acoustic waves along the line $y = 15$. Calculations with a coarser grid, $N_x \times N_y = 325 \times 300$ showed a small discrepancy with the analytical solution in the vicinity of $x = 0$. This error has been eliminated with the present, higher resolution grid.

CONCLUSIONS

The instability-wave solution to the linearized Euler equation can be suppressed by using a frequency-domain solver. The resulting solution captures the acoustic waves accurately. The frequency-domain solution is obtained by a direct matrix inversion. This makes the method computationally more efficient compared to time-domain solvers. For the present problem, the frequency-domain solver recorded a computational time of 57 minutes, whereas the time-domain solver reached a time-periodic state after approximately 100 hours. However, direct matrix inversions are very costly in that they require large amounts of memory. For the present problem, the frequency domain solver used 2.6 GB of memory. The memory problem can be alleviated by the use of parallel matrix-inversion solvers.

For most practical aeroacoustic problems, the frequency spectrum of noise has a broad band. Thus, it may be argued that a frequency-domain solver is inappropriate since it can only solve for a single frequency at a time. However, a broadband signal can be divided into discrete frequencies. With a parallel matrix-inversion solver the solution for each frequency can be obtained in just a few minutes. In fact, the total time required for obtaining solutions for the frequencies of interest would be comparable to that required for a single time-domain solution. Thus frequency-domain solvers should be useful for both tonal and broadband noise predictions.
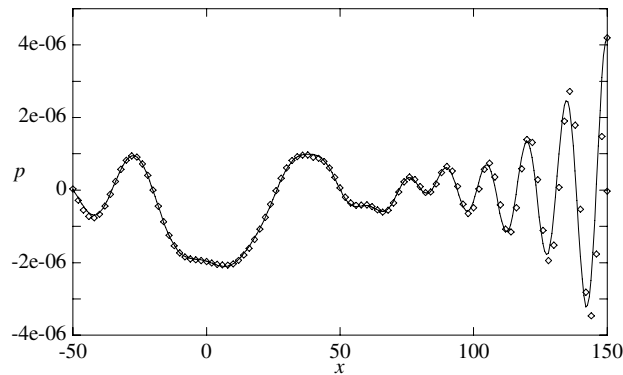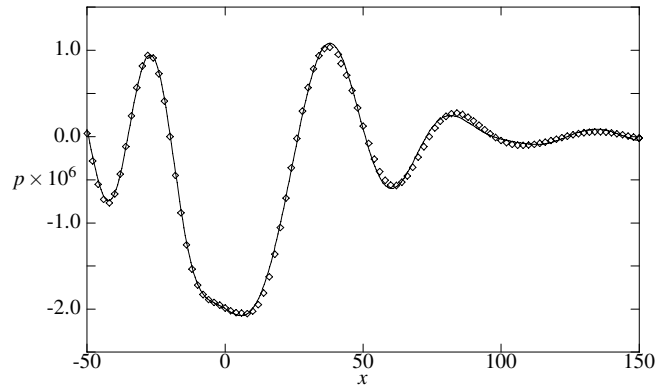
Figure 2: Comparison of the analytical solution (⋄) along the sideline $y = 15$ with numerical solution (—) obtained by a direct, frequency-domain solver.

REFERENCES

1. A. Agarwal, P. J. Morris, and R. Mani: Calculation of Sound Propagation in Nonuniform Flows: Suppression of Instability Waves. AIAA J., vol. 41, no. 12, Dec. 2003.

2. G. M. Lilley: The Generation and Radiation of Supersonic Jet Noise. Vol IV – Theory of Turbulence Generated Jet Noise, Noise Radiation from Upstream Sources and Combustion Noise., Tech. Rep. TR-72-53, United States Air Force Aero Propulsion Laboratory, (Available from Defence Technical Information Center as AD 749 139.), 1972.

3. A. Agarwal and P. J. Morris: Generation and Radiation of Acoustic Waves from a 2-D Shear Layer, in Third Computational Aeroacoustics (CAA) Workshop on Benchmark Problems, NASA Glenn Research Center, Aug. 2000, NASA CP 2000-209790, 309–314.

4. K. A. Hoffmann and S. T. Chiang: Computational Fluid Dynamics for Engineers, Engineering Education System, chap. 9, 1989.

5. W. Press, B. Flannery, S. Teukolsky, et al.: Numerical Recipes in C, Cambridge University Press, chap. 19, 1988.

Numerical Computation of the Radiation and Refraction of Sound Waves Through a Two-Dimensional Shear Layer

X. D. Li,   J. H. Gao,   D. Eschricht[†]   and   F. Thiele[†]

School of Jet Propulsion,
Beijing University of Aeronautics & Astronautics
Xueyuan Road 37, 100083, Beijing, PRC
and
[†]Hermann-Foettinger-Institute of Fluid Mechanics, Berlin University of Technology
Strasse des 17. Juni 135, D-10623, Berlin, Germany

Abstract

The linearized Euler equations are numerically solved to compute the radiation and refraction of sound waves through a two-dimensional shear layer. The dispersion-relation-preserving (DRP) scheme is employed for spatial discretization and the low dispersion and low dissipation Runge-Kutta (LDDRK) algorithm is used for time integration. The linearized Euler equations do not only provide a solution for sound propagation, but also admit unstable solutions and instability waves can thereby be triggered. These have to be suppressed numerically. The main objective of this research is to accurately capture the sound radiation and refraction through the shear layer while simultaneously suppressing the instability waves. To realize this aim, two methods are proposed in this paper. The first is to employ a multi-size mesh coupled with a spatial filter, while the second involves the introduction of a source filter into the linearized Euler equations. Numerical test results are presented to demonstrate the feasibility of the two proposed techniques.

Physical Problem

The propagation of sound in a turbulent shear flow can be described by a solution of the linearized Euler equations. However, in addition to providing a solution for sound propagation, the linearized Euler equations also admit unstable solutions and instability waves can sometimes be triggered. The purpose of the benchmark problem is to find ways to suppress the non-physical instabilities while retaining that part of the solution associated with the sound propagation.

The linearized Euler equations for a parallel jet are written as

$$L(\frac{\partial}{\partial \mathbf{x}}, \frac{\partial}{\partial t}, \mathbf{x})\mathbf{U}(\mathbf{x}, \mathbf{t}) = \mathbf{S}(\mathbf{x})\cos(\omega_0 \mathbf{t}) \tag{1}$$

where

$$L = \begin{bmatrix} \boxdot & \bar{\rho}(y)\frac{\partial}{\partial x} & \frac{\partial \bar{\rho}(y)}{\partial y} + \bar{\rho}(y)\frac{\partial}{\partial y} & 0 \\ 0 & \boxdot & \frac{\partial \bar{u}(y)}{\partial y} & \frac{1}{\bar{\rho}(y)}\frac{\partial}{\partial x} \\ 0 & 0 & \boxdot & \frac{1}{\bar{\rho}(y)}\frac{\partial}{\partial x} \\ 0 & \gamma\bar{p}\frac{\partial}{\partial x} & \gamma\bar{p}\frac{\partial}{\partial x} & \boxdot \end{bmatrix}, \mathbf{U} = \left\{ \begin{array}{c} \rho \\ u \\ v \\ p \end{array} \right\}, \mathbf{S} = \left\{ \begin{array}{c} 0 \\ 0 \\ 0 \\ \Lambda(x) \end{array} \right\}$$

$$\boxdot = \frac{\partial}{\partial t} + \bar{u}(y)\frac{\partial}{\partial x}, \Lambda(x) = A\exp[-(B_x x^2 + B_y y^2)]$$

The mean flow variables are denoted by an overbar and are given by

$$\bar{u}(y) = \left\{ \begin{array}{ll} u_j \exp[-(\ln 2)(y/b - h/b)^2] & y \geq h \\ u_j & 0 \leq y \leq h \end{array} \right.$$

$$\frac{1}{\bar{\rho}(y)} = -\frac{1}{2}\frac{\gamma-1}{\gamma\bar{p}}(\bar{u}(y) - u_j)\bar{u}(y) + \frac{1}{\rho_j}\frac{\bar{u}(y)}{u_j} + \frac{1}{\rho_\infty}\frac{u_j - \bar{u}(y)}{u_j}$$

$$\bar{p} = constant = 103330 \, m^{-1}kgs^{-2}$$

The parameters for the problem are give in table 1. $M_j = u_j/a_j$, $a_j = (\gamma R T_j)^{1/2}$, and the source frequency $\omega_0 = 76 \, rad/s$.

Table 1: The parameters of the benchmark problem

M_j	T_j K	T_∞ K	R $m^2s^{-2}K^{-1}$	γ	h m	b m	A $kgm^{-1}s^{-3}$	B_x m^{-2}	B_y m^{-2}
0.756	600	300	287.0	1.4	0.0	1.3	0.001	$0.04\ln(2)$	$0.32\ln(2)$

Numerical Methods

General Numerical Algorithm

Numerical discretization schemes and far-field boundary conditions are the key elements of a computational aeroacoustics (CAA) approach. Following our previous work at the third CAA workshop [4], the 7-point Dispersion-Relation-Preserving (DRP) scheme ($\eta = 1.1$)[1] is used for spatial discretization and the 4/6-stage Low-Dissipation and Low-Dispersion Runge-Kutta (LDDRK) scheme [2] is explored for time integration. The artifical selective damping [3]is adopted as a background damping to eliminate short wavelength spurious waves.

As sketched in fig. 1, Tam & Webb's radiation boundary conditions [1] are applied at the inflow boundary and outer boundary regions where the local mean flow Mach number $M_a \le 0.001$. At the downstream boundary region where $M_a \ge 0.001$, the outflow boundary conditions by Tam & Webb [1] are implemented. Symmetric boundary condition is applied at $y = 0$. The implemented boundary conditions performed very well for the benchmark problem of category 5 at the third CAA workshop [4].
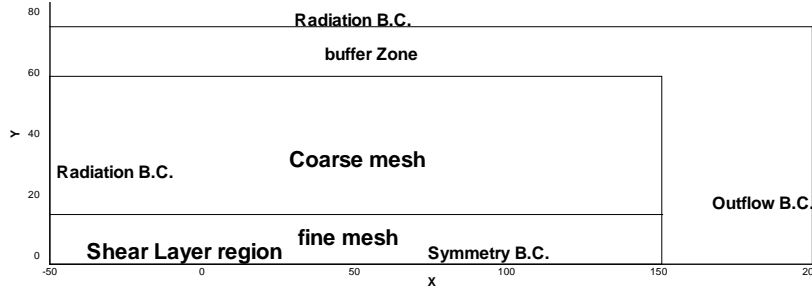
Figure 1: Schematic diagram of the computational domain and boundary conditions

Techniques for Suppressing Instability Waves

Two techniques are proposed to suppress instability waves generated in the shear layer. One is to introduce a spatial filter and the other is to introduce a source filter term into the governing equations. Detailed information is described below.

Spatial Filter

A low-pass 6th-order and an 8th-order explicit spatial filter are utilized to filter out the instability wave excited in the shear layer. The filters are distributed differently in different regions through the introduction of a coefficient α to control the filter effect. With this filter coefficient the spatial filter is written as

$$\bar{f}_i = (1 - \alpha)f_i + \alpha \sum_{j=-N}^{N} d_j f_{i+j} \qquad (2)$$

where the filter effect reaches its maximum value when $\alpha = 1$, and becomes inactive when $\alpha = 0$. In the present simulation, $\alpha = 1$ is applied across the entire shear layer region. However, a very small coefficient is introduced in the outer field in order to filter out grid oscillations, and increase the numerical stability.

Source Filter

The instability waves are generated in the shear layer, and are essentially associated with the gradients of the non-uniform mean flows. If the vorticity waves in the shear layer are removed, the instability waves should not be trigged. Therefore, a source filter term is introduced to the linearized Euler equations to suppress the instability waves in numerical computations. The governing equations with the introduced source filter term are finally written as:

$$L(\frac{\partial}{\partial \mathbf{x}}, \frac{\partial}{\partial t}, \mathbf{x})\mathbf{U}(\mathbf{x}, \mathbf{t}) = \mathbf{S}(\mathbf{x}, \mathbf{t}) + \mathbf{S_f}(\mathbf{x}) \qquad (3)$$

where $\mathbf{S_f} = (\mathbf{0}, \frac{\partial \bar{\mathbf{v}}}{\partial \mathbf{x}}\mathbf{u}', \frac{\partial \bar{\mathbf{u}}}{\partial \mathbf{y}}\mathbf{v}', \mathbf{0})^{\mathbf{T}}$.

For uniform mean flow, the introduced source filter will vanish automatically. It is only effective for non-uniform mean flow regions.

Grid

In all the test cases listed in table 2, the grid sizes shown are used in the shear layer region ($0 \leq y \leq 10$) only, while a coarse grid ($\Delta x = 0.5, \Delta y = 0.5$) is used in the remaining region except the buffer zone. A high-order polynomial interpolation method is implemented between the coarse and the fine grid. For the purpose of minimizing the reflection at the boundary region, a very coarse grid is used near the boundary as a buffer zone.

Table 2: Mesh and Numerical Test Cases

Numerical Test Cases	Grid Size across the Shear Layer
Coarse Grid without Spatial Filter(CG)	$\Delta x = 0.5, \Delta y = 0.5$
Coarse Grid with Spatial Filter(CGSPF)	$\Delta x = 0.5, \Delta y = 0.5$
Fine Grid with Spatial Filter(FGSPF)	$\Delta x = 0.5, \Delta y = 0.25$
Fine Grid with Source Filter(FGSOF)	$\Delta x = 0.5, \Delta y = 0.25$
Coarse Grid with Source Filter(CGSOF)	$\Delta x = 0.5, \Delta y = 0.5$

Numerical Results and Discussion

For the coarse grid without spatial filter numerical test case, figure 2 presents the instantaneous pressure contours at $t = 12T$ and p' along $y = 15$, where T is one period of the acoustic wave. It can be observed that the instability waves can not be removed from the coarse grid without the introduction of the spatial filter. Figure 3 gives the instantaneous pressure contours at $t = 21T$ and p' along $y = 15$ of coarse grid with spatial filter numerical test case. The results clearly show that the instability waves were suppressed successfully with the spatial filter technique on a coarse grid. To show the effects of grid, figure 4 shows the results of a fine grid with spatial filter test case. It is shown that the instability waves can not be filtered out on the fine mesh even with the spatial filter switched on. Thus, an effective way to suppress instability waves is the introduction of a spatial filter and to calculate on a coarse grid. Here, the problem of choosing a grid coarse enough for stable calculations but still fine enough to resolve the propagating waves arises. This may not not always be possible.

To illustrate the feasibility of the proposed source filtering technique, two numerical test results are presented. Figures 5 and 6 show the numerical test results calculated on a fine and coarse grid, respectively. It can be observed
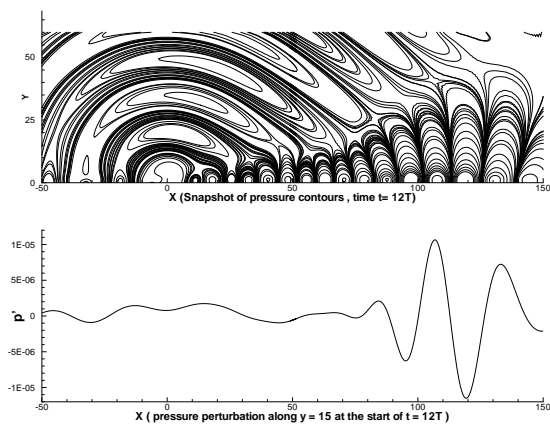
Figure 2: Coarse gird without spatial filter
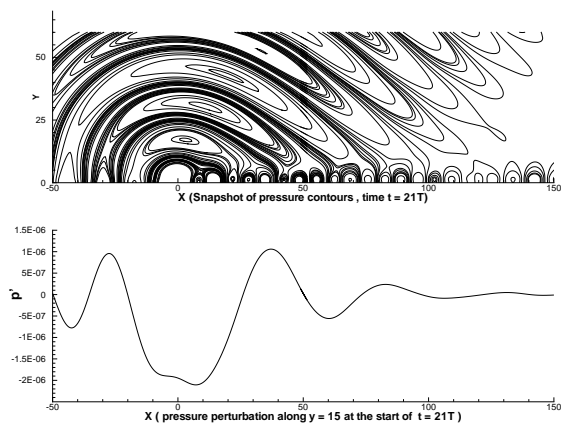
Figure 3: Coarse grid with spatial filter
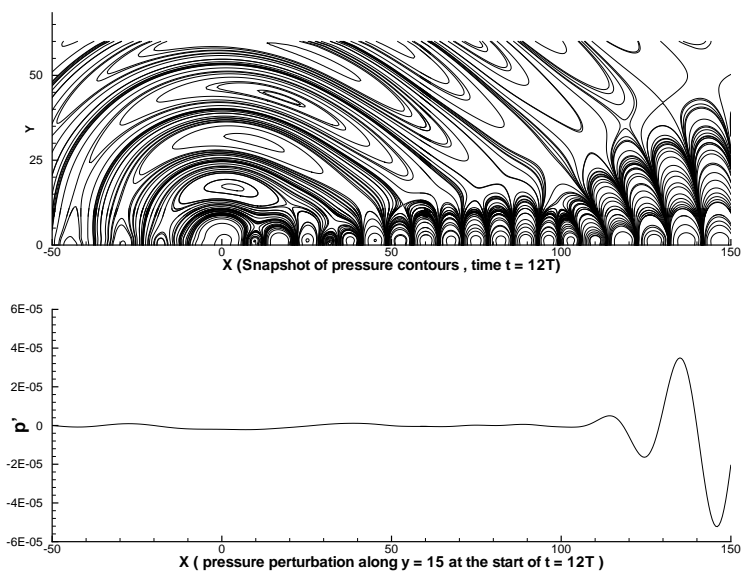
Figure 4: Fine grid with spatial filter
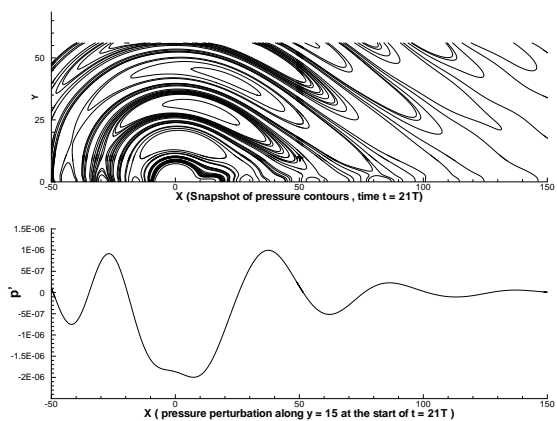
Figure 5: Fine grid with source filter
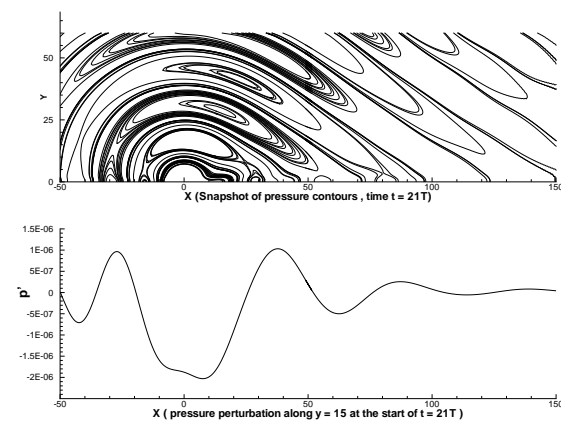
Figure 6: Coarse grid with source filter

that the sound pressures downstream of the sound source are controlled within a limited range, and that almost no amplified instability wave has been excited. It should also be noted that the proposed source filter technique performed in a very stable manner for both test cases.

The pressure perturbation p' at the start of a cycle along $(x = 100, 5 \leq y \leq 50)$, $(y = 15, -50 \leq x \leq 150)$ and $(y = 50, -50 \leq x \leq 150)$ of the three successful numerical test cases and the analytical results are shown in figures 7 and 8, respectively. The numerical results using the spatial filter technique agree very well with the analytical data, however, some differences can be observed between the results using the source filter technique and the analytical results. The mean square pressure $\bar{p}'^2$ along $(x = 100, 5 \leq y \leq 50)$, $(y = 15, -50 \leq x \leq 150)$ and $(y = 50, -50 \leq x \leq 150)$ are shown in figures 9 and 10, respectively. In each figure there are three lines corresponding to the three successful numerical test cases (coarse gird with spatial filter, fine grid with source filter and coarse grid with source filter). The numerical results using the source filter technique agree well with each other. However, some differences can still be observed between the results from the spatial filter and the source filter technique.
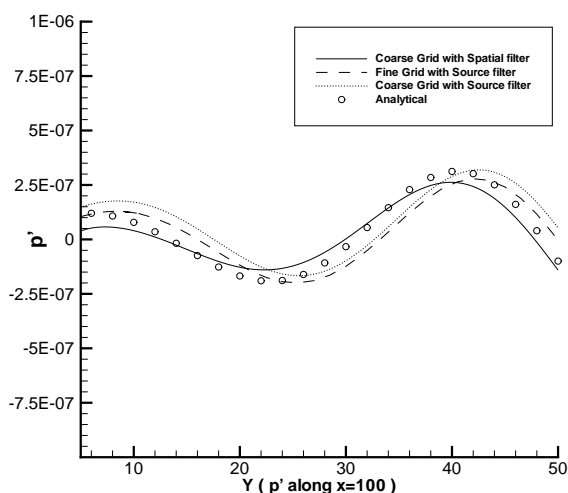
Figure 7: Pressure perturbation at the start of a cycle along $x = 100$
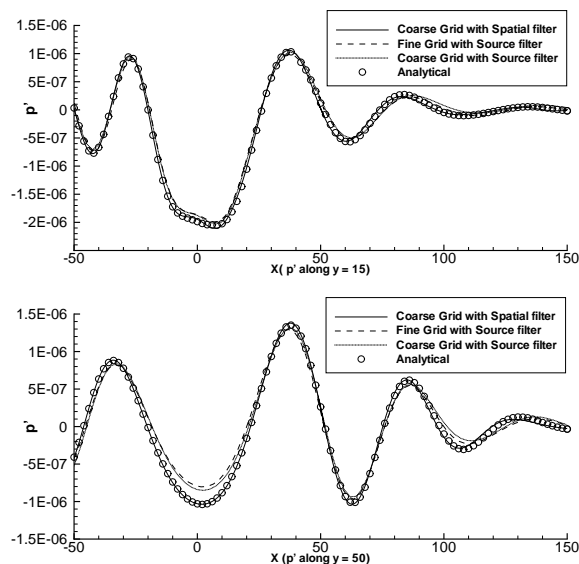
Figure 8: Pressure perturbation at the start of a cycle along $y = 15$ and $y = 50$
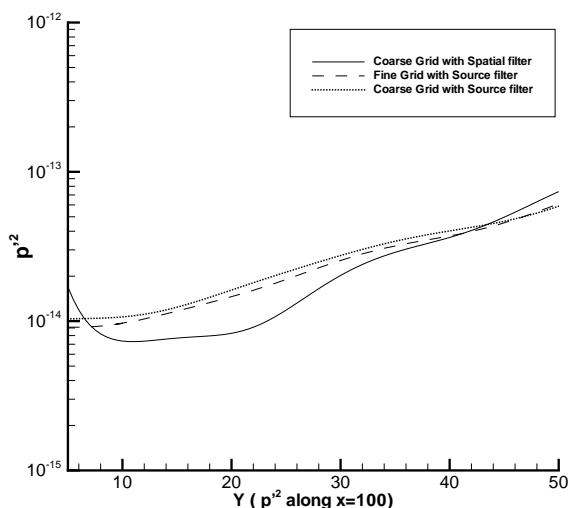
Figure 9: $\bar{p}'^2$ along $x = 100$
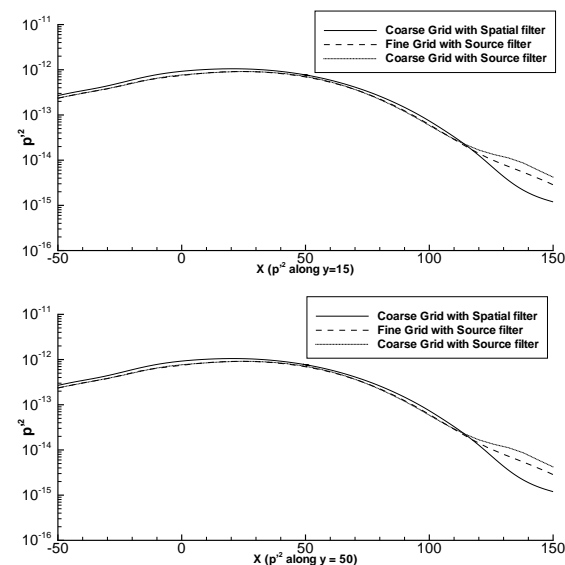
Figure 10: $\bar{p}'^2$ along $y = 15$ and $y = 50$

Table 3 gives a summary of main parameters of the three successful numerical test cases (CGSPF, FGSOF and CGSOF), the type and number of computers used, the total number of grid points, the time step size, the total time steps, the CPU time on each PC, the total CPU time and the parallel efficiency.

Table 3: A summary of main parameters in the successful calculations

Main Parameters	CGSPF	FGSOF	CGSOF
Computer used	P IV 2.4GHz RAM 512MB	$2 \times$ P IV 2.4GHz RAM $2 \times$ 512MB	P IV 2.4GHz RAM 512MB
Memory used	34MB	$2 \times$ 40MB	34MB
Total number of grid points	66092	152528	66092
Time step size	0.030688	0.030688	0.030688
Total time steps	48000	31000	48000
CPU Time on each PC(s)	24519	17883	24519
Total CPU Time(s)	24519	35766	24519
Parallel Efficiency	99%	90%	99%

Conclusion

A 2D CAA procedure is proposed to predict the sound wave radiation and refraction through a 2D shear layer. The 2D Linearized Euler equations are discretized by the optimized DRP and LDDRK schemes for space and time respectively. Two techniques are proposed to suppress excited instability waves. One is to use a blend spatial filter and a coarse grid. The other is to add a source filter in the governing equations. Numerical results show that the spatial filtering technique can only work on a coarse grid, and agree very well with the analytical results. The proposed source filtering technique is robust and generally applicable, and can remove the instability waves for both coarse and fine grids. However, small differences can be observed between the numerical results and the analytical solutions. This requires further study for improvement.

Acknowledgement

References

1. Tam, C. K. W. and Webb, C., "Dispersion-Relation-Preserving Finite Difference Schemes for Computational Aeroacoustics," *Journal of Computational Physics,* Vol. 107, August 1993, pp. 262–281.

2. Hu, F. Q., Hussani, M. Y., and Manthey, J. L., "Low-dissipation and Low-dispersion Runge-Kutta Schemes for Computational Acoustics," *Journal of Computational Physics,* Vol. 124, No. 1, 1996, pp. 177–191.

3. Tam, C. K. W., Webb, J. C., and Dong, T. Z., "A Study of the Short Wave Components in Computational Acoustics," *Journal of Computational Acoustics,* Vol. 1, 1993, pp. 1–30.

4. Li, X. D., Thiele, F., "Numerical Computation of the Generation and Radiation of Acoustic Waves from a 2-D Shear Layer," NASA CP-2000-209790, 2000, pp. 323-329.

5. Hu, F. Q. "On Perfectly Matched Layer As An Absorbing Boundary Condition," AIAA Paper 96-1664, 1996

RADIATION AND REFRACTION OF SOUND WAVES THROUGH A TWO-DIMENSIONAL SHEAR LAYER

Shi Zheng[*], Steve A. E. Miller[¶], Mei Zhuang[§]
Department of Mechanical Engineering
Michigan State University, East Lansing, MI 48823
Tel: (517)353-9450 Fax: (517)353-1750 Email: zhuangm@egr.msu.edu

ABSTRACT

This report presents solutions to Problem 1 of Category 4 in the 4th CAA Workshop on Benchmark Problems. The problem is numerically solved on a clustered orthogonal grid using a high-order optimized upwind Dispersion-Relation-Preserving scheme. The Perfectly-Matched-Layer (PML) boundary condition in unsplit physical variables is applied to ensure minimum numerical reflections. The numerical results by solving the linearized Euler equations are the total solution, being the superposition of the acoustic wave solution and the instability wave solution. In order to get the instability wave solution, a source term of the same excitation frequency is effectively placed upstream of the region of interest. Such a source term produces a stronger instability wave of the same excitation frequency but a weaker acoustic wave in the region of interest and thus the total solution in this region can well approximate a pure instability wave. The acoustic wave solution, which is desired in the problem, is then successfully achieved by subtracting the instability wave solution from the total solution. The benchmark problem is also analytically solved to an accuracy sufficient to evaluate the numerical solutions.

1. INTRODUCTION

In this paper, we demonstrate an approach of separating the instability waves and the acoustic waves by solving Problem 1 of Category 4 in the 4th CAA Workshop on Benchmark (ref. 1). The formulation of the problem is given in the next section. In section 3, analysis is made to show the existence of the instability wave induced by the acoustic source and the analytical solution is also presented. In section 4, our numerical methodology is described and our approach of numerically separating the instability waves and the acoustic waves is demonstrated. The numerical results are shown in comparison with the analytical solutions. In section 5 are our conclusions.

2. FORMULATION OF THE PROBLEM

The problem is symmetric about the x-axis. Figure 1 shows the domain of interest in $-50 \leq x \leq 150$ and $0 \leq y \leq 50$, with an acoustic source centered at $x = 0$ and $y = 0$. The mean flow is parallel to the x-axis and the mean flow velocities, density and pressure are given by

$$
\begin{cases}
\bar{u}(y) = \begin{cases} u_j \exp\left[-(\ln 2)(y/b - h/b)^2\right] & y \geq h \\ u_j & 0 \leq y \leq h \end{cases} \\
\bar{v} \equiv 0 \\
\dfrac{1}{\bar{\rho}(y)} = -\dfrac{1}{2}\dfrac{\gamma-1}{\gamma\bar{p}}(\bar{u}(y) - u_j)\bar{u}(y) + \dfrac{1}{\rho_j}\dfrac{\bar{u}(y)}{u_j} + \dfrac{1}{\rho_\infty}\dfrac{u_j - \bar{u}(y)}{u_j} \\
\bar{p} = \text{constant} = 103330 \text{ m}^{-1} \text{ kg s}^{-2}
\end{cases}
\tag{1}
$$

The governing equations are the two-dimensional linearized Euler equations (LEE) for a parallel mean flow in the x-direction.

$$
\left(\frac{\partial}{\partial t} + A\frac{\partial}{\partial x} + B\frac{\partial}{\partial y}\right)\mathbf{U} + D\frac{\partial \bar{\mathbf{U}}}{\partial y} = \mathbf{S}
\tag{2}
$$

where

---

[*] Graduate research assistant
[¶] Undergraduate summer research intern
[§] Associate Professor

$$\mathbf{U} = \begin{bmatrix} \rho \\ u \\ v \\ p \end{bmatrix}, A = \begin{bmatrix} \bar{u} & \bar{\rho} & 0 & 0 \\ 0 & \bar{u} & 0 & 1/\bar{\rho} \\ 0 & 0 & \bar{u} & 0 \\ 0 & \gamma\bar{p} & 0 & \bar{u} \end{bmatrix}, B = \begin{bmatrix} 0 & 0 & \bar{\rho} & 0 \\ 0 & 0 & 0 & 0 \\ 0 & 0 & 0 & 1/\bar{\rho} \\ 0 & 0 & \gamma\bar{p} & 0 \end{bmatrix}, \bar{\mathbf{U}} = \begin{bmatrix} \bar{\rho} \\ \bar{u} \\ \bar{v} \\ \bar{p} \end{bmatrix}, D = \begin{bmatrix} v & 0 & 0 & 0 \\ 0 & v & 0 & 0 \\ 0 & 0 & 0 & 0 \\ 0 & 0 & 0 & 0 \end{bmatrix},$$

$$\mathbf{S} = \begin{bmatrix} 0 \\ 0 \\ 0 \\ A\exp\left[-\left(B_x x^2 + B_y y^2\right)\right]\cos(\omega_o t) \end{bmatrix}$$

The non-homogeneous term $\mathbf{S}$ on the right hand side of equation (2) acts as the source term.
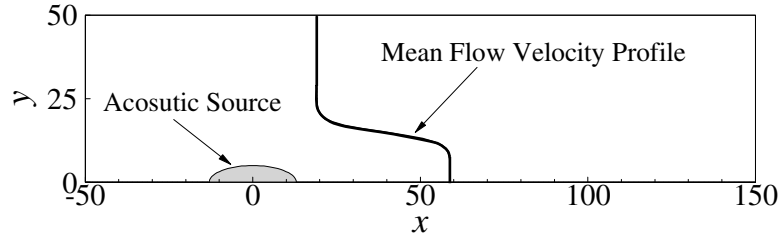
Figure 1. The domain of interest with an acoustic source centered at $x = 0$ and $y = 0$ and the schematic mean flow velocity profile.

The parameters for the problem are given in Table 1, where $M_j = u_j/a_j$ and $a_j = \sqrt{\gamma R T_j}$.

Table 1. The parameters used in the problem.

M_j	T_j (K)	T_∞ (K)	R (m^{2}s^{-2}K^{-1})	γ	h (m)	b (m)	A (Kg m^{-1} s^{-3})	B_x (m^{-2})	B_y (m^{-2})	ω_o (rad s^{-1})
0.756	600	300	287.0	1.4	0.0	1.3	0.001	0.04ln(2)	0.32ln(2)	76

As we will see in the next section, the acoustic source at excitation frequency $\omega_o = 76$ rad/s will trigger a wave that grows along the x-direction and co-exists with the acoustic wave radiated from the acoustic source. Such a growing wave, termed as an instability wave, can overwhelm the acoustic wave solution where it is strong. Therefore, it is the requirement of the benchmark problem that the instability wave be "filtered out" to get the acoustic wave.

3. INSTABILITY WAVE AND ANALYTICAL SOLUTION

Instability wave
Assuming that the flow variables have a time- and space-dependence of the following form

$$\begin{cases} \rho = \Phi(y)e^{i(kx-\omega t)} \\ u = U(y)e^{i(kx-\omega t)} \\ v = V(y)e^{i(kx-\omega t)} \\ p = P(y)e^{i(kx-\omega t)} \end{cases} \tag{3}$$

where k is the wavenumber in the x-direction, we can get the characteristic equation of the homogeneous LEE

$$\frac{d}{dy}\left(\frac{1}{\bar{\rho}(\omega - k\bar{u})^2}\frac{dP}{dy}\right) + \left(\frac{1}{\gamma\bar{p}} - \frac{k^2}{\bar{\rho}(\omega - k\bar{u})^2}\right)P = 0 \tag{4}$$

which is an ordinary differential equation (ODE) with only one unknown function $P(y)$.

The boundary condition at $y = 0$ is given by the symmetry condition

$$\frac{dP}{dy} = 0, \; y = 0 \tag{5}$$

In the far field, the medium is uniform, effectively free of acoustic source and without mean flow. Therefore, for a wavenumber k and an excitation frequency ω, the wave solution to equation (4) in that region must be in a form of $C \exp(i\beta y)$, where C is an arbitrary constant, $\beta = \sqrt{(\omega/a_\infty)^2 - k^2}$ and a_∞ is the sound speed in the far field. Note that a positive sign has been chosen for β such that the wave is outgoing at $y \to \infty$. When an equivalent form is used to get rid of the constant C, the boundary condition at $y \to \infty$ is

$$\frac{dP}{dy} = i\beta P, \; y \to \infty \tag{6}$$

The ODE (4) with its two boundary conditions (5) and (6) has a solution only for a certain wavenumber, or characteristic wavenumber, $k = \alpha$ for a given excitation frequency ω. Numerical procedures are implemented to find such an $\alpha - \omega$ relationship and the result is shown in Figure (2). At the excitation frequency given in the problem, $\omega = 76$ rad/s, the corresponding characteristic wavenumber is $\alpha = 0.4145 - 0.0377i$ (1/m), whose imaginary part is negative and thus the form assumed in equation (3) indicates a wave growing in the positive x-direction. Such a spatially amplifying wave is termed as an instability wave in this paper.
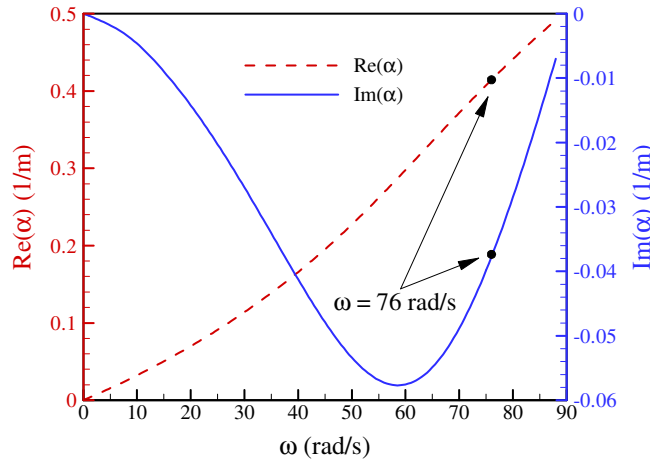
Figure 2. The characteristic wavenumber α for a given excitation frequency ω.

The above analysis shows that the instability wave is intrinsic to the homogenous system under the mean flow and boundary conditions given in section 2. It, therefore, exists in any non-homogeneous system that is obtained by adding acoustic source terms to the homogeneous system, as long as the homogenous system is linear. The non-homogenous term acts both as a source radiating acoustic waves to the surroundings and as a trigger to the instability wave.

Analytical solution to the acoustic wave

The analytical solution to such a problem has been derived by Dahl in a non-dimensional form by means of Fourier Transform and Green's functions (ref. 2). The solutions to the instability wave and the acoustic wave are obtained separately. Here we present only the derived formula for the acoustic pressure in a dimensional form.

$$p_a(k,y) = -\frac{iA^*M_j^2}{2\pi}\sqrt{\frac{\pi}{B'}}\int_{-\infty}^{\infty} e^{-k^2/4B'}\left[\zeta_1(k,y)\int_y^\infty \frac{\overline{\rho}(y_0)(\omega - \overline{u}(y_0)k)}{\Delta(k,y_0)} e^{-B'y_0^2}\zeta_2(k,y_0)dy_0 \right.$$
$$\left. +\zeta_2(k,y)\int_0^y \frac{\overline{\rho}(y_0)(\omega - \overline{u}(y_0)k)}{\Delta(k,y_0)} e^{-B'y_0^2}\zeta_1(k,y_0)dy_0 \right]dk \tag{7}$$

where $\zeta_1(k,y)$ ($\zeta_2(k,y)$) is the solution to the initial-value problem of the characteristic equation (3) only with the boundary condition at $y = 0$ ($y = \infty$) for a given wavenumber k; $\Delta(k,y)$ is the Wronskian of $\zeta_1(k,y)$ and $\zeta_2(k,y)$ with respect to y, defined as

$$\Delta(k, y) = \zeta_1(k, y) \frac{\partial \zeta_2(k, y)}{\partial y} - \zeta_2(k, y) \frac{\partial \zeta_1(k, y)}{\partial y} \qquad (8)$$

Note that even $\zeta_1(k, y)$ and $\zeta_2(k, y)$, and thus their Wronskian, are not analytically obtainable for a general parallel mean flow condition. They, along with the integrals in equation (7) are numerically evaluated and the numerical result of the acoustic pressure will be compared with that of the numerical solution.

4. NUMERICAL SOLUTION

Numerical schemes

The problem is also numerically solved using a fourth-order seven-point-stencil optimized upwind Dispersion-Relation-Preserving scheme (ref. 3). The spatial coefficients for both the interior and the boundary points are the same as those listed in reference 3 while the temporal coefficients are from reference 4. The accuracy of this scheme has been demonstrated in reference 3.

One the left, right and upper boundaries, a radiation or absorbing boundary condition is to be applied to allow waves to leave the computational domain with minimum numerical reflections. In our problem, this requirement on such a boundary condition is made specially challenging due to two factors. One is the existence of the shear layer and the sharp change in its profile. The other is the exponentially amplifying effect of the instability wave, as has been seen in section 3. A weak wave generated by the numerical reflections could grow in the amplifying direction into one that is strong enough to contaminate the solution and the amplified wave will cause another reflected wave when hitting on the boundaries. We found that the Perfectly-Matched-Layer (PML) boundary condition in unsplit physical variables (ref. 5) can meet the requirement very satisfactorily. At the outer boundaries of the PML regions, a characteristics-based boundary condition is applied to terminate the computational domain. Note that a numerical implementation of the PML boundary condition in unsplit physical variables has not seen reported in a non-uniform mean flow condition, as in the current problem.

At the lower boundary of the domain of interest, a symmetry boundary condition is applied. A ghost point is introduced right below each of the node at the lower boundary in implementing the condition $\partial p/\partial y = 0$ at $y = 0$.

The domain of interest is uniformly discretized in the x-direction with grid spacing $\Delta x = 1.5 \text{ m}$. In the y-direction, a clustered grid is used for a locally refined resolution of the shear layer and the source region. The grid density is specified as a function of the physical coordinate,

$$\left(\frac{dy}{d\xi}\right)_j = 1 - 0.6 \exp[-(\ln 2) \, y_j^2 / 50] \qquad (9)$$

where ξ is the transformed coordinate in the computational domain and j is the node index in the y-direction. Determined by equation (9), the size of the grid in the y-direction ranges from $\Delta y = 0.4 \text{ m}$ in the shear layer and the source region to $\Delta y = 1 \text{ m}$ in the far field. Shown in Figure 3 are the sizes and numbers of grid spacings used for the domain of interest and the PML region.
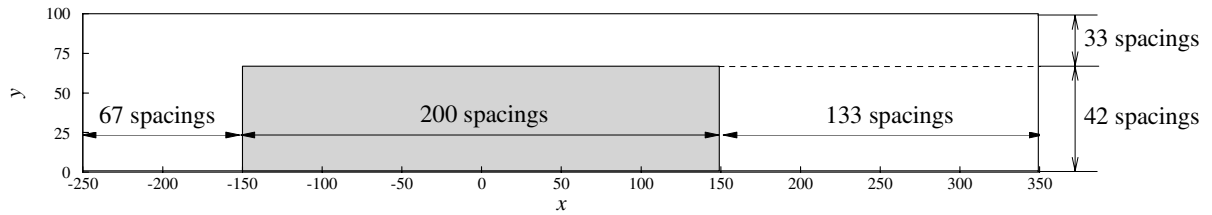
Figure 3. The whole computational domain with the PML region and the distribution of the grid spacings.

The time step is set to $\Delta t = 2.0668372 \times 10^{-5} s$, or a 4000th the period of the acoustic source at $\omega_0 = 76 \text{ rad/s}$. A very periodic solution is reached after 200 periods, or 800,000 time steps. The CPU time and memory usage are about 7.5 hours and 10 MB on a computer with an Athlon XP 1800+ CPU at 1533MHz, 512MB physical memory and a compiler of DIGITAL Visual Fortran, version 6.0.A.

Shown in Figure 4 is the numerical solution for acoustic pressure p at the start of a period on the whole computational domain. The region outside the long-dashed-line rectangle is the PML region and the region confined by the short-dashed line is the domain of interest. We can see that the solution very distinctly consists of the acoustic waves radiated by the acoustic source centered at the origin and the instability wave growing along the x-direction.

Little reflection is observed at the interface of the interior and the PML region and both of the acoustic wave and the instability wave are absorbed very neatly in the PML region. In contrast to the analytical solution, where the instability wave and the acoustic wave are obtained separately, the numerical solution always gives the total solution, i.e., the sum of the two wave solutions. Therefore, we need to subtract the instability wave solution from the total solution to get the acoustic wave solution.
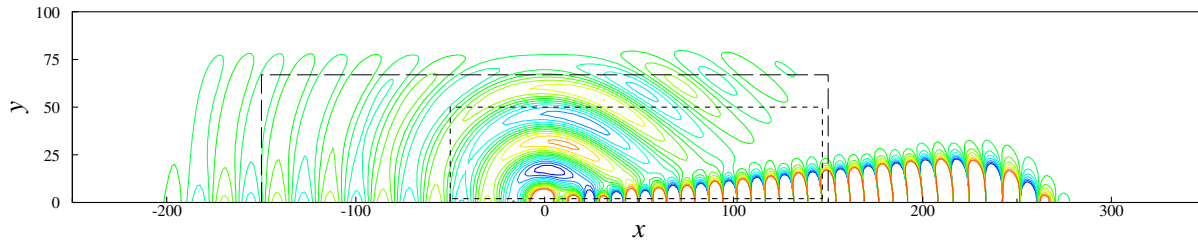
Figure 4. The acoustic pressure for the total solution at the start of a period in the whole computational domain of $-250 \le x \le 350$ and $0 \le y \le 100$. Outside the region confined by the long-dashed line is the PML region; the region confined by the short-dashed line is the domain of interest.

Separation of the instability and acoustic waves

In order to get the instability wave solution, a source term of the same excitation frequency is effectively placed upstream of the region of interest ($-50 \le x \le 150$ and $0 \le y \le 50$). Such a source term produces a stronger instability wave but a weaker acoustic wave in the region of interest and thus the total solution in this region can well approximate a pure instability wave. We use a dipole as such a source since the acoustic wave that it produces tends to be more local to the source. The numerical solution in such a configuration is calculated with the same numerical schemes on the same grid and is assumed to be a pure instability wave in the domain of interest. Since the instability wave is an eigen-solution of the homogeneous LEE, the instability waves in the two numerical solutions differ with a complex constant, or two real constants, corresponding to the phase and the amplitude. Thus we adjusted the phase and the amplitude of the "pure" instability wave to those of the total solution based on a grid point at $x = 147$ m and $y = 0$ m. We then get the acoustic wave solution by subtracting the adjusted instability wave solution for the total solution. Figures 5 (a), (b) and (c) show the acoustic pressure field at the start of a period in the region of interest for the total solution, the (adjusted) instability wave solution, and the acoustic wave solution respectively. Figures 6 (a), (b) and (c) show the pressure at the start of a period along the lines of $-50 \le x \le 150$ at $y = 15$, $-50 \le x \le 150$ at $y = 50$ and $5 \le y \le 50$ at $x = 100$, as compared with the analytical solution calculated in section 2. The agreements between the numerical solutions and the analytical solutions are excellent.

5. CONCLUSIONS AND DISCUSSIONS

In this paper, we demonstrate a numerical method to calculate and separate the acoustic wave and the instability wave in a two-dimensional shear layer. The method is entirely based on the time domain calculations and is verified by the analytical solution to the same problem. To exploit the advantage of time-domain methods, it is desirable to extend the current method to the cases of multi-frequency and broadband sound sources.

6. REFERENCES

1. Morris, Phillip J.; Agarwal, Anurag: "Radiation and Refraction of Sound Waves through a Two-Dimensional Shear Layer," the Fourth Computational Aeroacoustics Workshop on Benchmark Problems, Cleveland, Ohio, October, 2003.
2. Dahl, Milo D.: "Solution to the Category 5 Problem: Generation and Radiation of Acoustic Waves from a 2D Shear Layer," *Proceedings of the Third Computational Aeroacoustics Workshop on Benchmark Problems*, Cleveland, Ohio, November, 1999, NASA/CP-2000-209790, August, 2000, pp. 87-92.
3. Zhuang, M.; Chen, R. F.: "Applications of High-Order Optimized Upwind Schemes for Computational Aeroacoustics," *AIAA Journal*, Vol. 40, No. 2, 2002, pp. 443-449.
4. Tam, C. K. W.; Webb, J. C.: "Dispersion-Relation-Preserving Finite Difference Schemes for Computational Acoustics," *Journal of Computational Physics*, Vol. 107, No. 2, 1993, pp. 262-281.

5. Hu, F. Q.: "A Stable, Perfectly Matched Layer for Linearized Euler Equations in Unsplit Physical Variables," *Journal of Computational Physics*, Vol. 173, 2001, pp. 455-480.

(a)

(b)

(c)
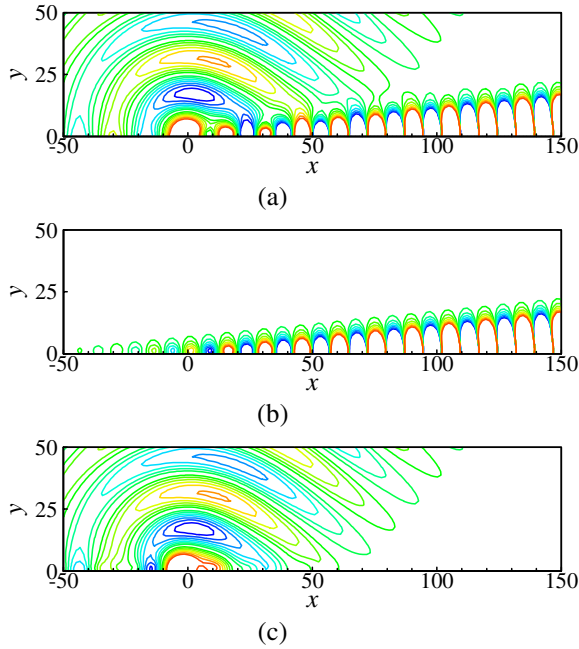
Figure 5. The acoustic pressure at the start of a cycle in the domain of interest. (a) the total solution; (b) the (adjusted) instability wave solution; (c) the acoustic wave solution.
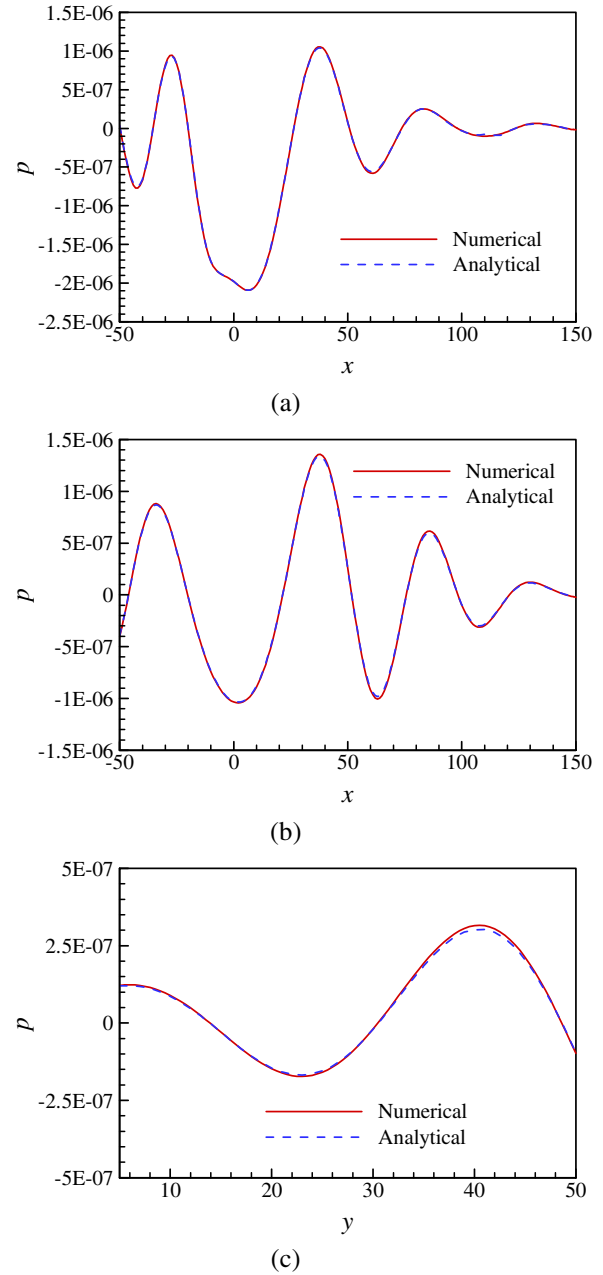

(a)

(b)

(c)

Figure 6. The acoustic pressure at the start of a cycle as compared with the analytical solution along the lines of (a) $-50 \leq x \leq 150$ at $y = 15$, (b) $-50 \leq x \leq 150$ at $y = 50$, and (c) $5 \leq y \leq 50$ at $x = 100$.

TRAILING EDGE NOISE BENCHMARK PROBLEM: HIGH FIDELITY FINITE DIFFERENCE SOLUTIONS

Matthew F. Barone

Senior Member of Technical Staff, Sandia National Laboratories
Aerosciences and Compressible Fluid Mechanics Dept.,
P.O. Box 5800, Albuquerque, NM, 87185-0825

Sanjiva K. Lele

Professor, Stanford University
Dept. of Aeronautics and Astronautics, Stanford, CA 94305-4035

ABSTRACT

Solutions to Category 4, Problem 2 of the Fourth CAA Workshop on Benchmark Problems are obtained using a high order overset grid finite difference scheme. Emphasis is placed on solution quality, including checks of grid and time step convergence, so that the present solutions may be viewed as "benchmark quality." Grid convergence of the steady mixing layer solution required for this problem is assessed using the grid convergence index defined by Roach (1998). All solutions, both steady and unsteady, are shown to be temporally and spatially converged on the finest grid considered. The vortex passage problem is found to produce a large initial acoustic transient with high frequency content, which appears to be the most difficult acoustic feature to capture accurately. Both the acoustic pulse problem and the vortex passage problem excite nonlinear shear layer vortices, which lead to late-time hydrodynamic oscillations of the pressure at the near-field acoustic observervation point.

INTRODUCTION

As numerical methods for computational aeroacoustics (CAA) mature, the set of benchmark problems by which their performance is measured should necessarily grow to include more "real-world" test problems. The Category 4, Problem 2 benchmark problem of the present workshop falls in this category and tests several important capabilities of CAA methods: 1) non-trivial problem geometry, 2) non-reflective outflow boundary conditions with mean shear, 3) acoustic refraction by a mean flow and reflection from solid surfaces, and 4) solution robustness in the presence of inexact initial conditions. These are all common issues which are present in most aeroacoustic applications of engineering interest.

Although this benchmark problem provides a good test of these capabilities, it suffers from a lack of an exact solution or experimental data for comparison with numerical solutions. It is the goal of the present work to provide high fidelity, benchmark quality solutions for comparison with numerical solutions. The benchmark solutions should contain negligible numerical error as measured by spatial and temporal convergence tests. They should also be free of boundary condition errors, which are often the most pernicious source of error in CAA applications. The objective, then, is to produce such benchmark quality solutions with a fairly well-established numerical technique, emphasizing solution accuracy and reliability over computational efficiency. Future researchers will then have a realistic test problem for their numerical techniques and a database of high quality solutions with which to compare their results.

PROBLEM SETUP AND NUMERICAL METHOD

A schematic of the computational domain is shown in Figure 1. The thin splitter plate separates two streams of different velocity. The trailing edge of the splitter plate terminates at $x = 0$ with a rounded edge shape. The high order overset grid technique described in reference [1] is used to discretize the region near the plate with a curvilinear grid and away from the plate with a Cartesian grid (see Figure 2). This scheme uses sixth order Padè finite differences (ref. [2]) and fourth order Hermite inter-grid interpolation (ref. [3]). As shown in Figure 1, the solution domain is surrounded by a damping sponge zone. The outflow sponge is augmented by addition of artificial
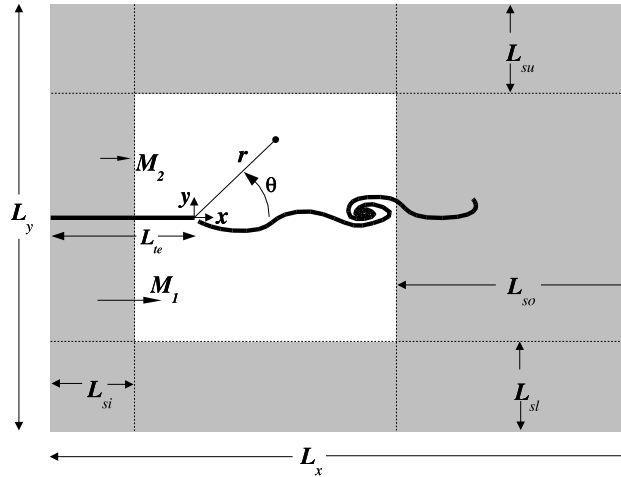
Figure 1: Schematic of the computational domain. The solution domain is unshaded and is surrounded by the sponge zones, which are shaded grey. This figure is not to scale.

convection terms which raise the effective convection Mach number to $M_b = 1.1$ at the edge of the computational domain; the combination of the damping sponge with the convective buffer zone treatment is described in reference [4]. One dimensional characteristic boundary conditions are applied at the outer edges of each of the sponge zones. The upper and lower sponges have length $L_{su} = L_{sl} = 75$ and maximum strength of $\sigma = 0.05$. The steady solutions were obtained with the upper and lower sponges turned off to avoid mean streamline distortion and allow entrainment flow to enter the domain. The inflow sponge has a length of $L_{si} = 25$ and a maximum strength of $\sigma = 1.0$, while the outflow sponge has a length of $L_{so} = 225$ and a maximum strength of $\sigma = 0.1$. Cubic ramping functions are applied for smooth variation of the sponge strength from zero at the beginning of the boundary zone to the maximum value at the edge of the computational domain. The length of the outflow sponge is required to be relatively long for this problem to ensure minimal reflection of acoustic energy as shear layer vortices convect out of the solution domain.

Solutions were obtained on three different grids, defined in Table 1. The medium grid solutions were found to be nearly converged for both unsteady calculations, so temporal convergence was investigated on the medium grid with two distinct time steps. The unsteady solutions were advanced in time with the standard fourth order Runge Kutta integration scheme, while the steady solutions were relaxed to a time-independent state using a first order Runge Kutta algorithm described briefly in the next section. More detail on all aspects of the numerical scheme may be found in reference [1].

Table 1: Grid sizes and time steps used for each problem.

Grid	Cartesian	Overset	Time Step
Coarse	432x256	32x224	0.025
Medium	640x384	48x320	0.025, 0.0125
Fine	960x576	64x480	0.025

RESULTS AND DISCUSSION

Steady State Solutions

A time independent base flow solution was computed using the same spatial discretization appplied to the unsteady calculations, but with a modified time-advancement scheme designed to accelerate convergence to a steady solution. The modified time marching scheme consists of a five stage Runge Kutta algorithm with explicit residual averaging. The rather long (in the streamwise direction) outflow sponge region effectively dampens spurious boundary reflection feedback, preventing the flow from sustaining an oscillatory state within the computational domain. In other words, the feedback from the boundary reflection error is less than the gain of the unstable shear layer, which supports
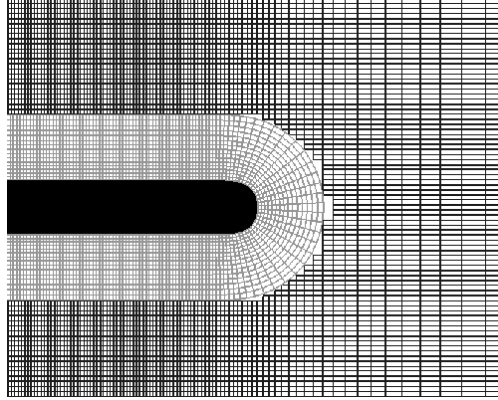
Figure 2: **Near-edge grid schematic showing the overset curvilinear grid surrounding the flat plate and the Cartesian grid away from the plate.**

exponentially growing small disturbances. The flow is therefore able to achieve a damped state, ultimately relaxing to a steady solution. Figure 3(a) shows the history of the maximum norm of the residual R for the coarse grid calculation. The residual is a measure of iterative convergence. The steady solutions were considered iteratively converged when the residual dropped at least seven orders of magnitude from its initial value.

Figure 3(b) shows streamwise velocity profiles for the steady solution obtained on the fine grid. Results for the coarse and medium grids are indistinguishable from those of the fine grid when plotted in the same fashion. This suggests that spatial convergence of the mean velocity profiles was obtained, and this is reinforced quantitatively by examining the grid convergence index (GCI). Defining the solution on the medium grid as U_{g2} and the fine grid solution as U_{g1}, the GCI (ref. [5]) is given by

$$\text{GCI} = 3\frac{|\varepsilon|}{r^p - 1}, \tag{1}$$

where p is the spatial convergence order of the numerical scheme, r is the ratio of the grid spacing on the medium grid to that on the fine grid, and $\varepsilon = (U_{g2} - U_{g1})/U_1$. The value U_1 is a reference quantity to ensure proper scaling, and is taken to be equal to the free stream velocity of the "fast" stream. Figures 4(a) and 4(b) give the GCI calculated from the streamwise velocity profiles as a percentage at three streamwise locations, assuming either fourth order or sixth order accuracy. Recall that the formal order of accuracy of the finite difference scheme is six while the overset grid interpolation scheme is fourth order. The very small values of the GCI indicate a well-converged solution has been obtained even considering the case of fourth order convergence.

Problem 1: Acoustic Pulse

The first initial value problem to be solved is the scattering of an acoustic pulse which originates near the trailing edge within a compact region of over-pressure. The pulse expands in an initially cylindrical manner before interacting with the trailing edge. It then scatters into a reflected component, a transmitted component, and a diffracted component which is centered about the trailing edge. In addition, a Kelvin-Helmholtz instability wave packet is excited within the shear layer. The instability wave grows exponentially in the downstream direction before nonlinear processes lead to the formation of a train of vortices which convect downstream.

Figure 5 shows the computed pressure disturbance distribution within the shear layer at $y = -3$ for $t = 200$ and for $t = 1000$. The medium and fine grid solutions are nearly identical for both solution times, indicating that spatial convergence has been achieved. The coarse grid solution shows appreciable dissipative error and some dispersion of the instability wave packet. Figure 6(a) gives the acoustic signal recorded at $(x,y) = (50,50)$ for the entire duration of the computation. The coherent pressure pulse event is noted beginning at about $t = 80$, followed at a later time by a low frequency pressure drop which occurs at about $t = 600$. The pressure drop also appears in Problem 2 and is explained in the discussion of that problem below. Figure 6(b) gives a resolved picture of the pulse event, which is seen to be captured well by all three grids.

The effect of time step for the medium grid is shown in Figure 7. The solution within the shear layer at $t = 200$ and the acoustic signal recorded at $(x,y) = (50,50)$ are independent of the time step chosen, indicating the solutions are also temporally converged.
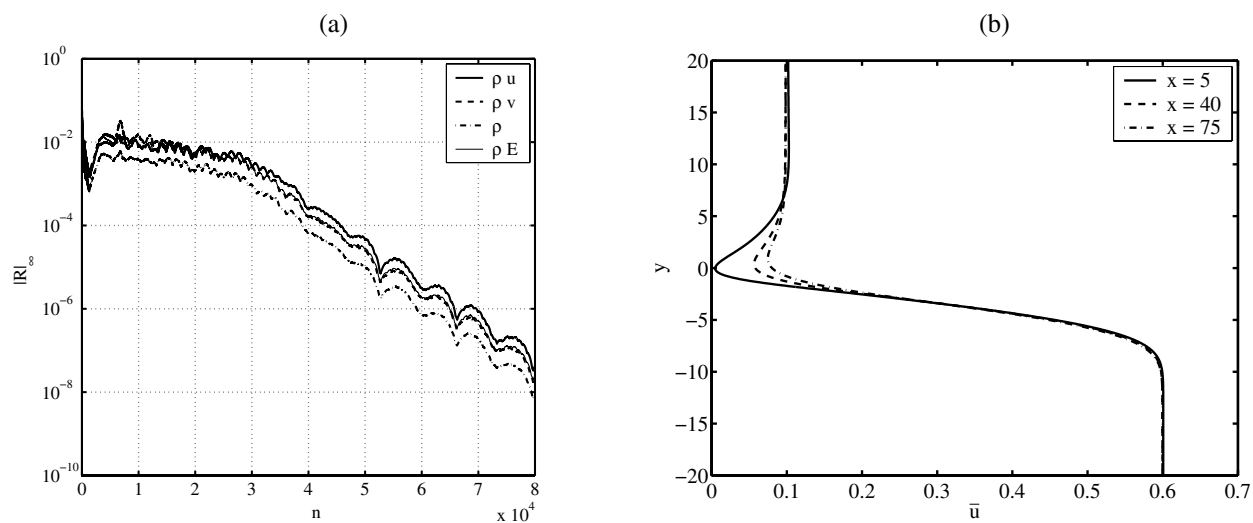
Figure 3: (a) Residual norm history for the coarse grid steady state calculation. (b) Steady state streamwise velocity profiles from the fine grid solution at three locations downstream of the trailing edge.
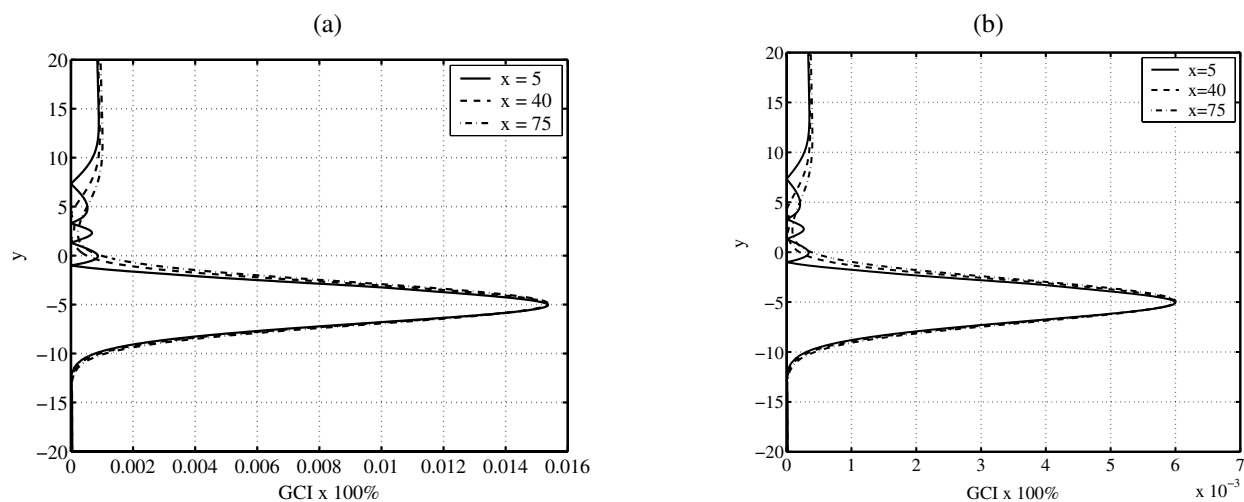
Figure 4: Grid convergence index profiles based on the streamwise velocity at three downstream locations, assuming (a) fourth order spatial accuracy and (b) sixth order spatial accuracy.
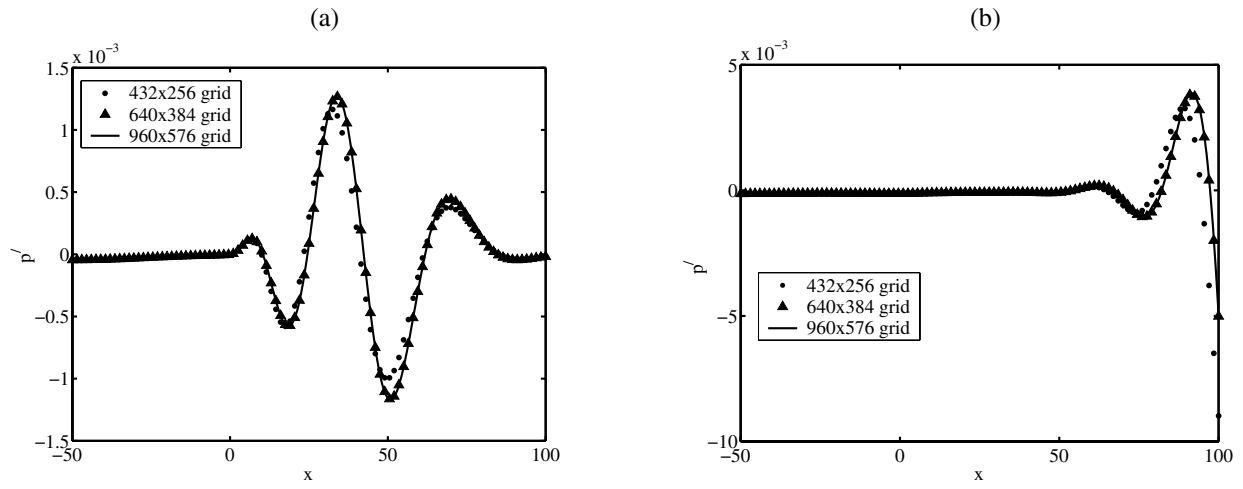
Figure 5: Pressure disturbance along the line y = −3 at (a) t = 200, (b) t = 1000 for Problem 1.

Figure 6: Time history of the pressure disturbance signal at $(x, y) = (50, 50)$ for Problem 1. (a) Complete fine grid solution time history. (b) Grid dependence of the acoustic pulse behavior.
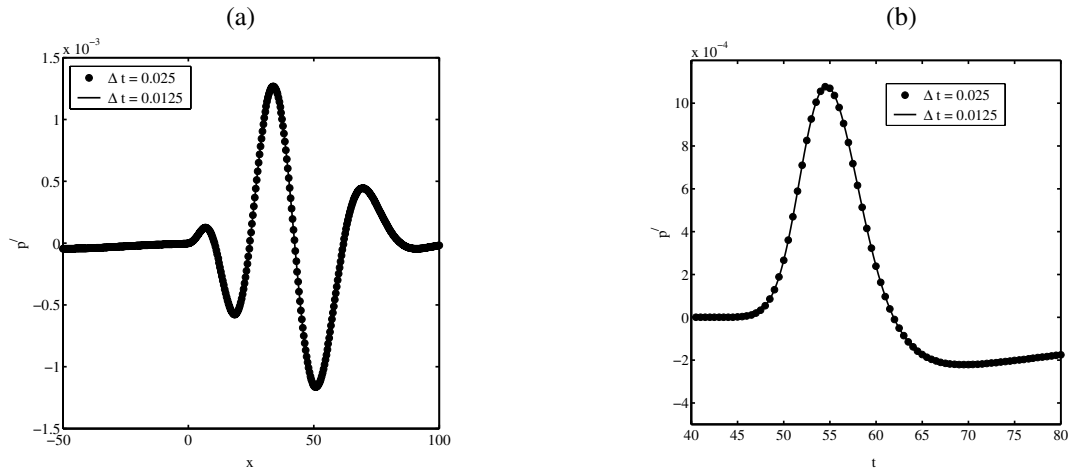
Figure 7: Dependence of the Problem 1 medium grid solution on time step. (a) Pressure disturbance distribution at t = 200. (b) Acoustic pulse signal at (x, y) = (50, 50).

Problem 2: Vortex Passage

The second problem describes the response of the trailing edge flow to the passage of a vortex past the edge. The initial condition is only an approximate solution to the governing equations and therefore excites an initial transient as the vortex "adjusts" to the surrounding flow. The transient includes an initial acoustic pulse which exhibits similar properties to the pulse described in Problem 1. As the vortex convects past the trailing edge it excites both a weak acoustic wave and an instability wave. The vortex-induced acoustic wave trails the initial transient acoustic wave by a short distance, while the instability wave grows within the downstream shear layer and saturates as in Problem 1.

Figure 8 shows the computed pressure disturbance within the shear layer at $y = -3$ for the vortex passage problem. The coarse grid relative error is somewhat larger than the coarse grid error for the acoustic pulse problem, suggesting that the near-edge scattering behavior is not captured as well for the vortex problem. However, the medium and fine grid solutions are nearly identical, again demonstrating grid convergence. The transient acoustic signal at $(x, y) = (50, 50)$ is plotted in Figure 9. The initial transient pulse contains relatively high frequency oscillations and is not well-resolved by the coarse grid solution. The coarse and medium grid solutions also show wiggles in the trailing-edge scattered pulse which are likely due to numerical dispersion of the initial transient wave. These wiggles are very small for the fine grid solution, and the overall good agreement between the medium and fine grid solutions suggests that the fine grid solution is nearly converged (spatially).

Figure 9(a) shows that the low frequency pressure drop observed in Problem 1 is again seen in Problem 2. Figure 10(a) shows the signals from both problems plotted on the same scale, demonstrating similarity in the pressure drop for the two cases. The pressure drop evidently scales with the amplitude of the nonlinear shear layer vortices and not with the acoustic pulse amplitude. Solution animations reveal that the pressure drop is induced by the vortices upon roll-up and is hydrodynamic in nature. The low frequency pressure drop makes it difficult to estimate outflow boundary condition reflection error at this location, but an estimate of the reflection error from the side boundaries can be deduced from Figure 10(b). A close-up view of the recorded pressure signal for Problem 1 reveals small amplitude pressure oscillations. Solution animations reveal these oscillations to be reflection error from the initial acoustic pulse impacting the lower boundary. This source of boundary error is associated with an estimated reflection boundary reflection coefficent of about 0.5%.

Figure 11 shows the medium grid solution to Problem 2 using two different choices for time step. The agreement between the solutions is very good, confirming temporal convergence for this problem.

ACKNOWLEDGEMENTS

(a)

(b)
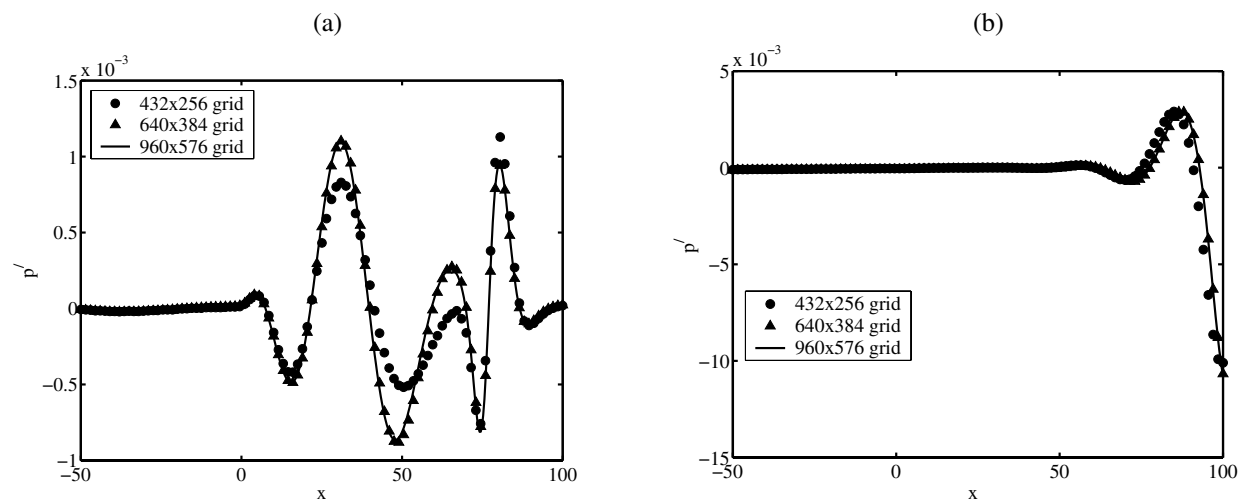
Figure 8: Pressure disturbance along the line y = −3 at (a) t = 200, (b) t = 1000 for Problem 2.
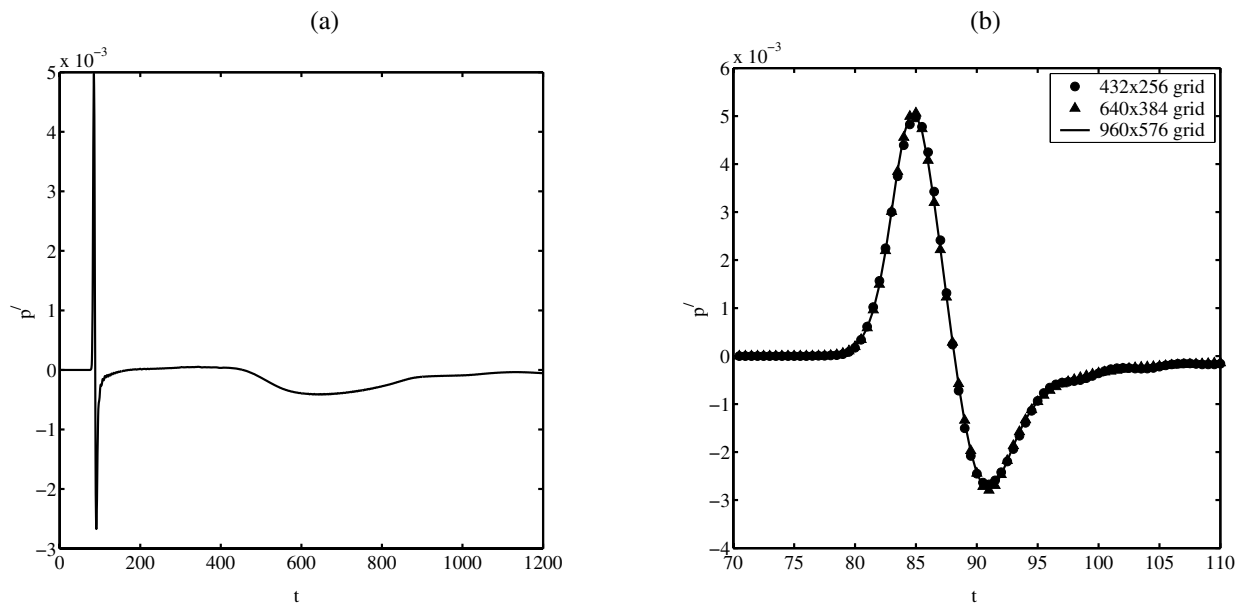
(a)

(b)
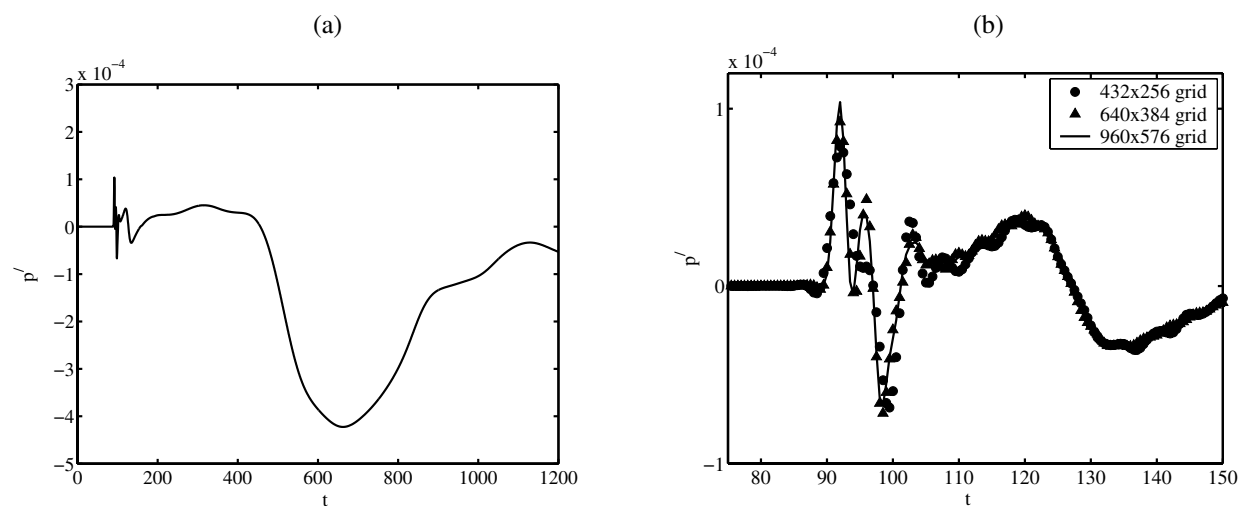
Figure 9: Time history of the pressure disturbance signal at $(x, y) = (50, 50)$ for Problem 2. (a) Complete fine grid solution time history. (b) Grid dependence of the acoustic pulse behavior.

REFERENCES

[1] M.F. Barone. *Receptivity of Compressible Mixing Layers*. PhD thesis, Department of Aeronautics and Astronautics, Stanford University, May 2003.

[2] S. K. Lele. Compact finite difference schemes with spectral-like resolution. *Journal of Computational Physics*, 103(1):16–42, 1992.

[3] J. W. Delfs. An overlapped grid technique for high resolution CAA schemes for complex geometries. AIAA Paper 2001-2199, 2001.

[4] J.B. Freund. Proposed inflow/outflow boundary condition for direct computation of aerodynamic sound. *AIAA Journal*, 35(4):740–742, 1997.

[5] P. J. Roach. *Verification and Validation in Computational Science and Engineering*, pages 114–117. Hermosa Publishers, Albuquerque, NM, 1998.
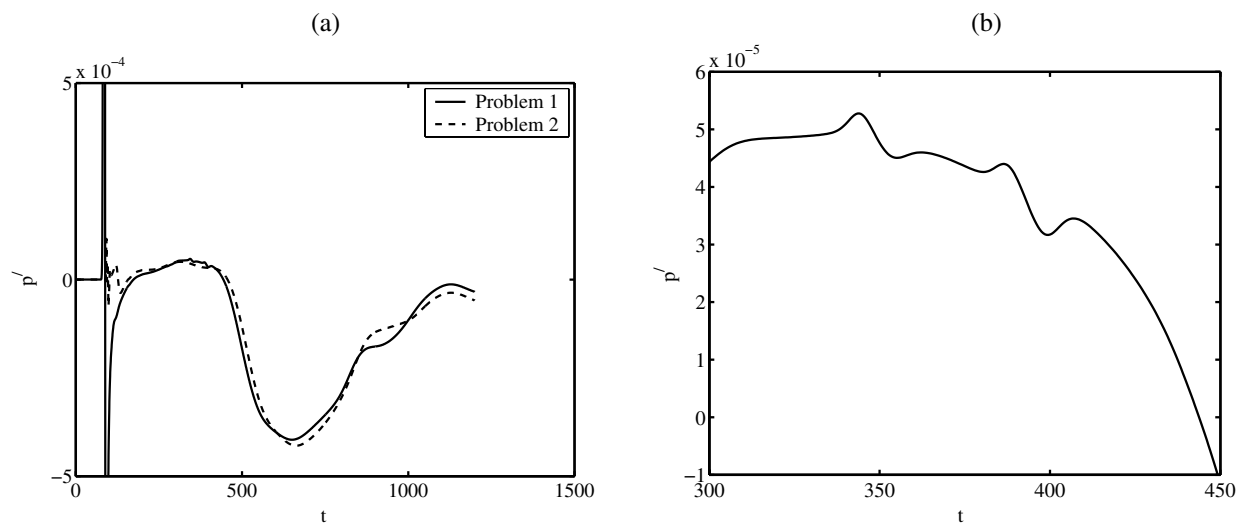
Figure 10: (a) Comparison of the pressure disturbance signals at $(x, y) = (50, 50)$ for Problems 1 and 2. (b) Close-up view of wiggles in the solution due to boundary reflection error.
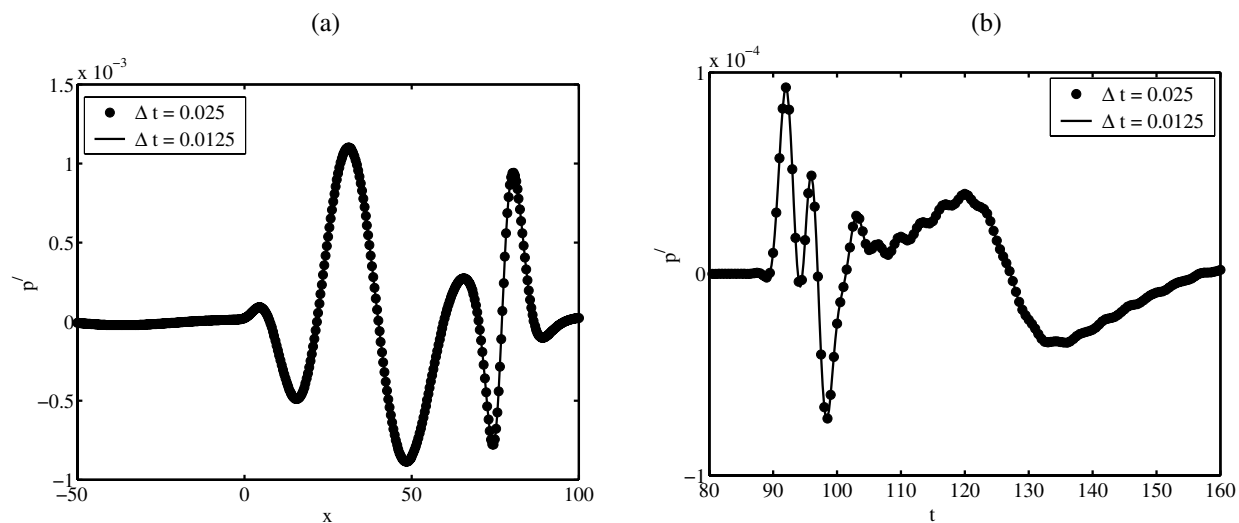
Figure 11: Dependence of the Problem 2 medium grid solution on time step. (a) Pressure disturbance distribution at $t = 200$. (b) Acoustic pulse signal at $(x, y) = (50, 50)$.

SIMULATION OF TRAILING EDGE SCATTERING BY USING ACOUSTIC/VISCOUS SPLITTING METHODS WITH OVERSET GRID TECHNIQUES

Yonghwan Park[*], Jonghoon Bin[*], Cheolung Cheong[#] and Soogab Lee[†]
School of Mechanical and Aerospace Engineering
Seoul National University
Seoul 151-742, Korea

ABSTRACT

Receptivity of steady shear flows is the main issues for analysis overall acoustic scattering for airfoil trailing edge and near-nozzle lip. This paper focuses on the development of accurate and robust numerical methods to accompany high-order computational aeroacoustics algorithms towards the simulation of trailing edge scattering problem in Category 4 and on the analysis of the generation mechanism of the instability wave by the interaction of trailing edge, shear layer and initial disturbance. The numerical methods is based on Grid-Optimized Dispersion-Relations-Preserving (GODRP) schemes developed with grid-optimization algorithm to make finite difference equations possess the same dispersion relations as the corresponding partial differential equations on general geometries. Acoustic/viscous splitting techniques, based on flow noise solvers using acoustic governing equations such as simplified linearized Euler equations and full linearized Euler equations, are utilized to solve the receptivity by the interactions of trailing edge, shear layer and initial disturbance. The numerical analysis consists of two steps. First, steady mean flow is determined by solution of the compressible Navier-Stokes equation using Roe's scheme for spatial discretization and local time stepping for time discretization. Then, unsteady trailing edge scattering phenomena are simulated with the CAA solvers. Through the comparison of acoustic simulations, it will be shown that mean flow gradient terms play a crucial role in triggering the instability wave

1. INTRODUCTION

At subsonic flow, one of the primary sources of trailing edge noise corresponds to receptivity, excitation of shear layer. The various mechanisms contributing to such receptivity on trailing edge include the interaction between vortices, shear layer, and unsteady disturbances. Especially, in the receptivity process, shear layer instability waves are generated (ref. 1). These waves excite shear layer and produce sound. The noise generated by these phenomena has become an important issue for the design of engine, nozzle and airfoil trailing edge.

In the present decade, considerable progress in computational aeroacoustics (CAA) has been achieved. The unsteady governing equations are discretized and solved for time-dependent flow variables, which includes the mean flow and the flow or acoustic disturbances. High-order schemes are required for discretization to reduce dissipation and dispersion errors. Recently, Grid-Optimized Dispersion-Relation-Preserving (GODRP) scheme (ref. 2) have been developed with the grid-optimization algorithm to make the finite difference equations possess the same dispersion relations as the corresponding partial differential equations and, at the same time, optimized dissipation characteristics at the given grids that are the non-uniform Cartesian or curvilinear grids. In this work, the GODRP schemes are utilized to solve this complex geometry problem with curvilinear grids on a guarantee of local and, thus resultant global dispersion-relation-preserving properties. In addition, high-order schemes support the formation of spurious modes at the boundaries of the computational domain. Careful attention for unsteady boundary treatment is needed to produce the physically correct disturbance field. Therefore, accurate nonreflecting boundary conditions are necessary for computational aeroacoustics. The sponge zone technique by Baily & Bogey

---

[*] Ph. D. Candidate, qwer1104@snu.ac.kr
[*] Ph. D. Candidate, mrbin@snu.ac.kr
[#] BK21 Post Doctor, accu99@snu.ac.kr
[†] Professor, solee@plaza.snu.ac.kr, Bldg. 301-1303, Seoul National University, Seoul 151-742, Korea

(ref. 3) is used with the nonreflecting boundary condition of Tam & Dong(ref. 4) as the inflow/outflow boundary conditions.

Acoustic/viscous splitting technique is utilized for the analysis of the receptivity phenomena. These methods are based on the concept of variable decomposition in the governing equations into a source component and an acoustic one, which leads to two separate sets of equations governing viscous flow field and acoustic disturbance field, respectively. This approach is based on the assumption that the wave propagation is essentially inviscid in nature and sound perturbations are so small that their contribution to the convection velocity of the flow is negligible in most cases. The most important advantage of the decomposition method is that algorithms are used that best suited to each solver: traditional CFD algorithms for the viscous flow and CAA algorithms for the acoustic perturbations.

It is very difficult to construct a single body-fitted mesh for thin plate which gives the proper resolution to both the near source region and far acoustic field. This difficulty is overcome by the use of a multi-scale overset grid technique, where body-fitted meshes are applied only near the plate and Cartesian background mesh is applied elsewhere.

Problem statement will be briefly demonstrated in Section 2. The numerical methods together with the governing equations and numerical boundary treatment will be discussed in Section 3, which is followed by numerical results and discussion will be provided in Section 4.

2. PROBLEM STATEMENT

This benchmark problem consists of a two-dimensional compressible mixing layer flow formed by a splitter plate with blunt trailing edge. First, a steady laminar mixing layer solution is determined by 2D compressible laminar Navier-Stokes equation.

$$\frac{\partial U}{\partial t} + \frac{\partial F}{\partial x} + \frac{\partial G}{\partial y} = \frac{\partial V_x}{\partial x} + \frac{\partial V_y}{\partial y}$$
(1)

where $U = \begin{pmatrix} \rho \\ \rho u \\ \rho v \\ \rho E \end{pmatrix}$, $F = \begin{pmatrix} \rho u \\ \rho u^2 + p \\ \rho u v \\ u(p + \rho E) \end{pmatrix}$, $G = \begin{pmatrix} \rho v \\ \rho u v \\ \rho v^2 + p \\ v(p + \rho E) \end{pmatrix}$, $V_x = \frac{M_1}{\mathrm{Re}_{\theta 1}} \begin{pmatrix} 0 \\ \tau_{xx} \\ \tau_{xy} \\ u\tau_{xx} + v\tau_{xy} - q_x/\mathrm{Pr} \end{pmatrix}$, and $V_y = \frac{M_1}{\mathrm{Re}_{\theta 1}} \begin{pmatrix} 0 \\ \tau_{xy} \\ \tau_{yy} \\ u\tau_{xy} + v\tau_{yy} - q_y/\mathrm{Pr} \end{pmatrix}$.

The lower stream has free stream Mach number $M_1 = 0.6$ with a boundary layer momentum thickness θ_1 while the upper stream has free stream Mach number $M_2 = 0.1$ with momentum thickness $\theta_2 = \theta_1$ and plate width is $2\theta_1$. Initial pressure pulse and acoustic/vortical disturbance ares imposed in a steady state mean flow. Finally, initial value problems are solved for each case. The initiated pressure pulse and acoustic/vortical disturbances are defined as follows:

ⓐ *Initial value problem of a pressure pulse:*   ⓑ *Initial value problem of a initiated vortical disturbance:*

$$\begin{pmatrix} \rho \\ \rho u \\ \rho v \\ pE \end{pmatrix} = \begin{pmatrix} \rho_0 \\ \rho_0 u_0 \\ \rho_0 v_0 \\ \rho_0 E_0 \end{pmatrix} + \begin{pmatrix} 0 \\ 0 \\ 0 \\ 0.05/\gamma \cdot \exp(-\ln(2) \cdot (((x+20)/4)^2 + ((y+20)/4)^2)) \end{pmatrix}$$

$$\begin{pmatrix} \rho \\ u \\ v \\ p \end{pmatrix} = \begin{pmatrix} \rho_0 \\ u_0 \\ v_0 \\ p_0 \end{pmatrix} + \begin{pmatrix} (1 - (\gamma-1)/2 \cdot M_v^2 \exp(1-(\gamma/\sigma)^2))^{1/(\gamma-1)} - 1 \\ -M_v(y-y_0)\exp((1-(\gamma/\sigma)^2)/2) \\ M_v(x-x_0)\exp((1-(\gamma/\sigma)^2)/2) \\ ((1-(\gamma-1)/2 \cdot M_v^2 \exp(1-(\gamma/\sigma)^2))^{\gamma/(\gamma-1)} - 1)/\gamma \end{pmatrix}$$

where $x_0 = -35$, $y_0 = -8$, $\gamma = 1.4$ $M_v = 0.1$, $\sigma = 1$ and $r = \sqrt{(x+35)^2 + (y+8)^2}$)

3. NUMERICAL METHODS

3.1. Solution Algorithm and Numerical Schemes

The wave propagation itself is hardly affected by viscosity and contribution of sound perturbations to the convection velocity of flow is negligible. Furthermore, nonlinear terms are generally small. Therefore, sound propagation is essentially described by linearized Euler equation.

$$\frac{\partial U}{\partial t} + \frac{\partial E}{\partial x} + \frac{\partial F}{\partial y} + H = S \tag{2}$$

where $\mathbf{U} = \begin{pmatrix} \rho' \\ \rho u' \\ \rho v' \\ p' \end{pmatrix}$, $\mathbf{E} = \begin{pmatrix} \rho' u_0 + \rho_0 u' \\ u_0 \rho_0 u' + p' \\ u_0 \rho_0 v' \\ u_0 p' + \gamma p_0 u' \end{pmatrix}$, $\mathbf{F} = \begin{pmatrix} \rho' v_0 + \rho_0 v' \\ v_0 \rho_0 u' \\ v_0 \rho_0 v' + p' \\ v_0 p' + \gamma p_0 v' \end{pmatrix}$, and $\mathbf{H} = \begin{pmatrix} 0 \\ (\rho_0 u' + \rho' u_0)\partial u_0/\partial x + (\rho_0 v' + \rho' v_0)\partial u_0/\partial y \\ (\rho_0 u' + \rho' u_0)\partial v_0/\partial x + (\rho_0 v' + \rho' v_0)\partial v_0/\partial y \\ (\gamma-1)(p' \nabla \cdot v_0 - u' \partial p_0/\partial x - v' \partial p_0/\partial y) \end{pmatrix}$.

Here, **U** is the unknown vector, **E** and **F** are the linear flux vectors and the vector **H** consists of mean flow gradient terms, which are equal to zero when mean flow is uniform. The vector **S** represents possible unsteady sources in the flow. For the efficient description of later numerical results, some terms are defined such that Full Linearized Euler Equation (FLEE) represents Eq. (2) and Simplified Linearized Euler Equations (SLEE) is defined as without **H**. The SLEE is proposed by Bogey et al. (ref. 5) to suppress the instability waves in shear layer problem. In section 4, the results of FLEE will be compared with results of SLEE.

In present problem, Hybrid method (CFD for the base mean flow + CAA for acoustic scattering) is utilized. The solution procedure for trailing edge scattering problem has two parts. First, a steady mean flow solution to governing equation (1) is determined by 2D compressible laminar Navier-Stokes solution. Then acoustic simulations are carried out with the linearized Euler equation with the prescribed base flow and initial disturbances. The time dependent Euler equations (2) are discretized in space using the GODRP scheme (ref. 2) together with selective artificial damping (ref. 6) to damp out numerical oscillations and fourth order dissipation to suppress high-frequency modes. Temporal integration of the discretized equations is carried out using the third order explicit Adams-Bashford method (ref. 6). In this problem, the used grid was a H-hype rectangular grid with 601×401 in the background block and 266×45 in body-fitted block, which computational mesh is built up from a non-uniform grid clustered around the shear layer.

3.2. Boundary Condition Formulation

Because the computational domain is usually finite, boundary conditions must be imposed at the edge of the grid. These boundary conditions can generate undesirable spurious fluctuations. Therefore, accurate nonreflecting boundary conditions are necessary for computational aeroacoustics. On the surfaces, the slip boundary condition is enforced by the ghost point method. The contents in detail are introduced.

Solid Wall Boundary Conditions

Solid wall boundary (Fig. 1 ⑤) is mainly implemented by setting normal gradient of pressure at the solid wall faces equal to zero. Many methods have been developed and are useful for treating wall boundaries. Some of the more recent work in this area has been implemented by Tam & Dong (ref. 7). Tam & Dong developed wall boundary conditions with their Dispersion Relation Preserving (DRP) scheme and this method minimizes the number of required ghost values. An analysis of these conditions shows that they are capable of numerically simulating the presence of a solid wall without introducing significant errors associated with spurious numerical wave generation and numerical boundary layers. Therefore, the wall conditions implemented here are based on the approach by Tam & Dong. To set the normal pressure derivative to zero, a ghost point was used inside the wall for only the normal pressure derivative. Following equation is derived from momentum equations and setting the normal velocity at wall to zero.

$$\frac{\partial p'}{\partial n} = -\frac{1}{(\eta_x^2 + \eta_y^2)}[(\eta_x \xi_x + \eta_y \xi_y)\frac{\partial p'}{\partial \xi} + \eta_x^2 \frac{\partial}{\partial \eta}(u_0 \rho_0 u') + \eta_y^2 \frac{\partial}{\partial \eta}(v_0 \rho_0 v')$$
$$+ \eta_x \eta_y (\frac{\partial}{\partial \eta}(v_0 \rho_0 u') + \frac{\partial}{\partial \eta}(u_0 \rho_0 v'))] \tag{3}$$

Inflow/Outflow Boundary Conditions & Sponge zone

The formulation of precise boundary condition is important for acoustic computation. Spurious waves generated when fluctuations leave the boundary region must be minimized. In present problem, the nonreflecting boundary condition of Tam & Dong (ref. 7) is implemented. When only acoustic fluctuation reach the boundary (for inflow and lateral boundary, Fig. 1 ①, ②, ③), the radiation boundary conditions are applied. Outflow boundary conditions (Fig. 1 ④) are also necessary when fluctuations quantities (ρ', u', v', p') reach the boundary (outflow boundary).

When strong vortical wave reaches the outflow boundary, this vortical wave causes an acoustic wave reflection at the outflow boundary. This spurious wave contaminates computational domain solution. For the minimization of a spurious wave, the decrease of vortical wave strength is needed at

Figure. 1 Computation domain and applied boundary conditions
①,②,③: Radiation boundary condition
④   : Outflow boundary condition
⑤   : Wall boundary condition
⑥   : Sponge zone & grid stretching
⑦   : Interpolation Region

the vicinity of outflow boundary. A sponge zone (Fig. 1 ⑥) with grid stretching is then built to dissipate aerodynamic fluctuation before their reaching the outflow boundary. Larger size of sponge zone generates the smaller reflection of spurious wave. However, large size of sponge zone requires large computational domain and computational time, the selection of suitable size is important. In present problem, the sponge zone implemented by Baily & Bogey (ref. 7) is used.

4. NUMERICAL RESULTS AND DISCUSSIONS

4.1 Steady Mean Flow Results

Steady mean flow is determined by 2D Navier-Stokes Equation using Roe's scheme (ref. 8) for spatial discretization and local time stepping for time discretization to further accelerate convergence to steady state. to further accelerate convergence to steady state. Free stream conditions above the plate are $T_1=T_2$ and $\rho_1=\rho_2$. Wall boundary conditions are the no slip condition and the isothermal condition. Nonreflecting boundary condition is used at the outflow boundary.

Fig. 2 shows mean flow streamwise velocity profiles at the several lines for the mixing layer which develops downstream of the plate. Near the edge, a small wake component exists due to the co-flow stream. As the mixing layer develops downstream, the wake ingredient almost disappears and the profile becomes similar to a single inflection point shear layer. The flow profiles change rather quickly near the plate edge. Then the flow settles into a slowly growing, mildly non-parallel shear layer in further downstream.
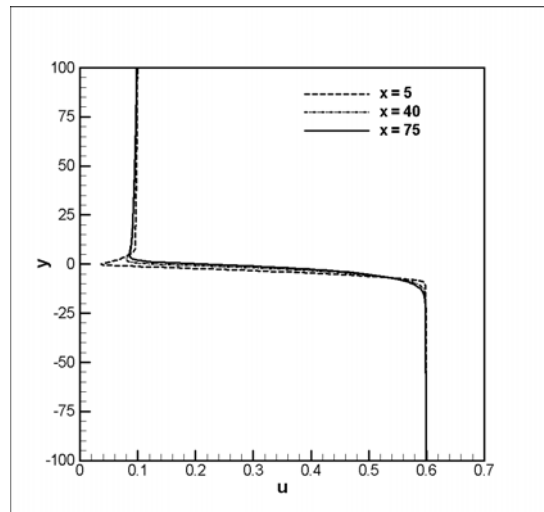
Figure. 2 Mean flow streamwise velocities profile

4.2 Acoustic Results

Overset Grids
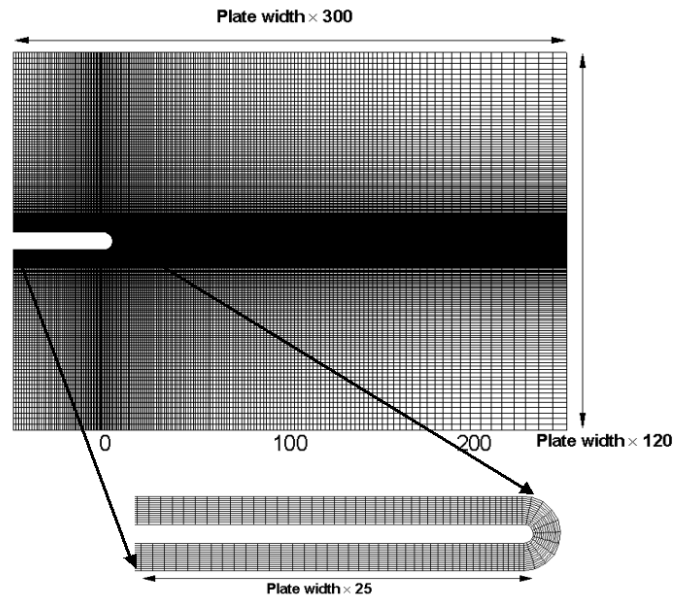
Figure. 3 Overset grids for the acoustic simulations

Construction of a single body-fitted mesh for a rounded trailing edge is very difficult. Furthermore, when the mesh is irregular or highly distorted, the numerical solutions in finite difference methods are degraded. These difficulties are overcome by the use of an overset grid technique. To retain the accuracy of the numerical schemes, high-order interpolation scheme (Fig.1 ⑦) is required for information exchange between two grid structures. In present problem, Bin's interpolation algorithm (ref. 9) is utilized.

Sound Generation by Interacting with Vortical Disturbance and Edge
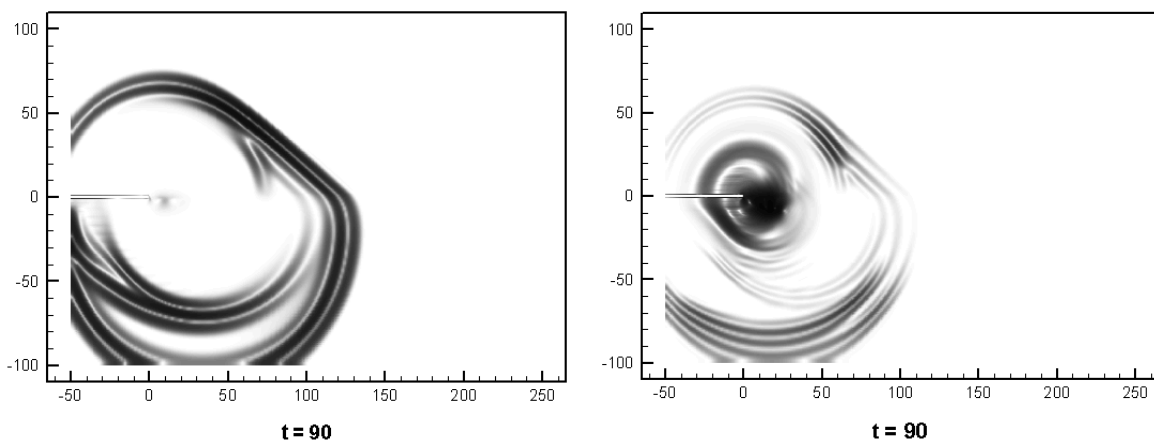
t = 90

The response to pressure pulse ⓐ

t = 90

The response to vortical disturbance ⓑ

Figure. 4 Comparison of instantaneous pressure fluctuations at time = 90

Figure 4 shows the pressure distributions for the cases ⓐ and ⓑ at t = 90 by using the FLEE. When vortical disturbance is imposed on the steady mean flow, acoustic wave is generated by the interaction of the trailing edge and vorticity wave, of which phenomena cannot found in case a where only pressure pulse is imposed. However, instability waves are generated to start to flow downstream for both of cases.

Instability Waves

The amplitude of instability wave increases exponentially along streamwise (x-axis) and time. This instability waves flow to downstream with mean flow velocity, interacting with shear flow. These instability waves, which have strong strength, can cause a spurious wave reflection at the outflow boundary. So accurate outflow boundary condition and suitable size of sponge zone are required. Instability waves will go out of the computational domain at approximately t = 1400. Fig. 5 show the pressure distributions along *y = -3* at *t = 200, 400, 600,.....1200* for initial value problem ⓑ.
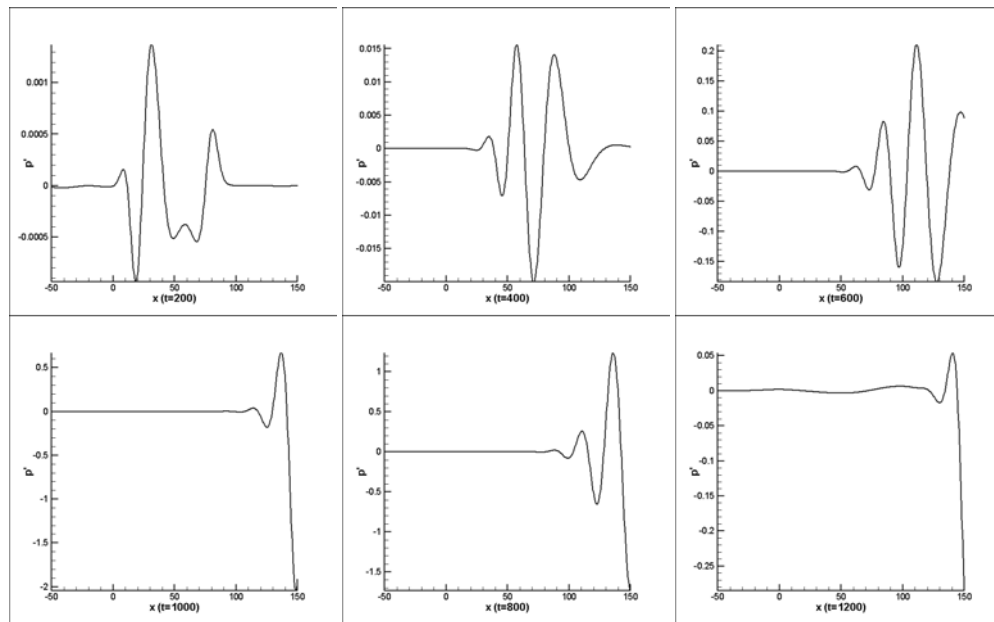
Figure. 5 Instantaneous pressure fluctuations along y = -3 at each time.
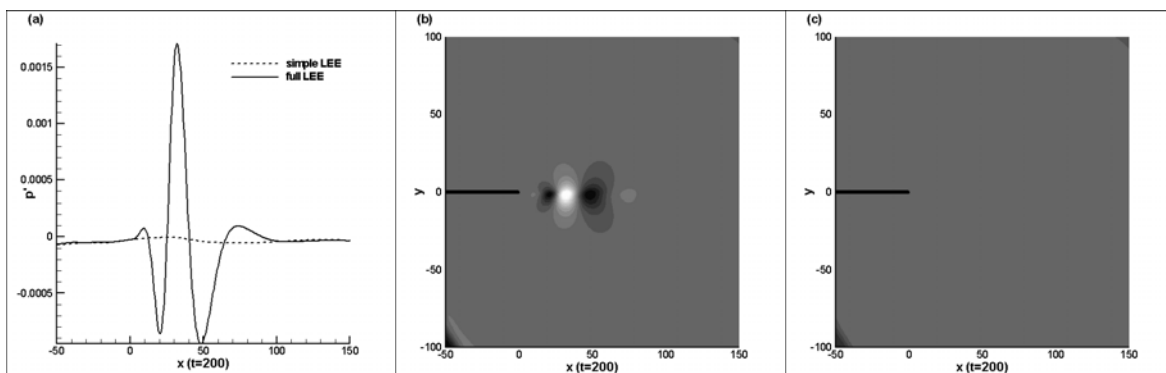
Figure. 6 Comparison of full LEE and simple LEE to pressure pulse ⓐ at t=200
(a) Instantaneous pressure fluctuation along y=-3 to full LEE and simple LEE
(b) Pressure fluctuation contour to full LEE at t=200, 15level from -0.001(black) to 0.0015(white)
(c) Pressure fluctuation contour to simple LEE at t=200, 15level from -0.001(black) to 0.0015(white)

However, it is found that the instability waves are not generated by using the SLEE for both of cases. Fig. 6 shows the comparison of the numerical results using the SLEE and the FLEE. From this figure, it is found that the

acoustic simulation using the SLEE does not generate the instability wave which exist in the results using the FLEE. The SLEE is proposed by Bogey et al. to prevent the exponential development of linear instability waves excited by source terms introduced into FLEE, through the mean shear $\partial \bar{u}_1/\partial x_2$ in the vector H. However, this instability waves are unphysical wave. But, Baron (ref. 10) shows that the same instability waves are generated by using the full Navier-Stokes equations. This means that instability wave in this benchmark problem is physical wave. From this, the mean flow gradient terms, especially the mean shear $\partial \bar{u}_1/\partial x_2$ in H, seem to play a crucial role in the instability wave generation through the interactions of the initial disturbance and the trailing edge.

Time history of the instantaneous pressure fluctuation
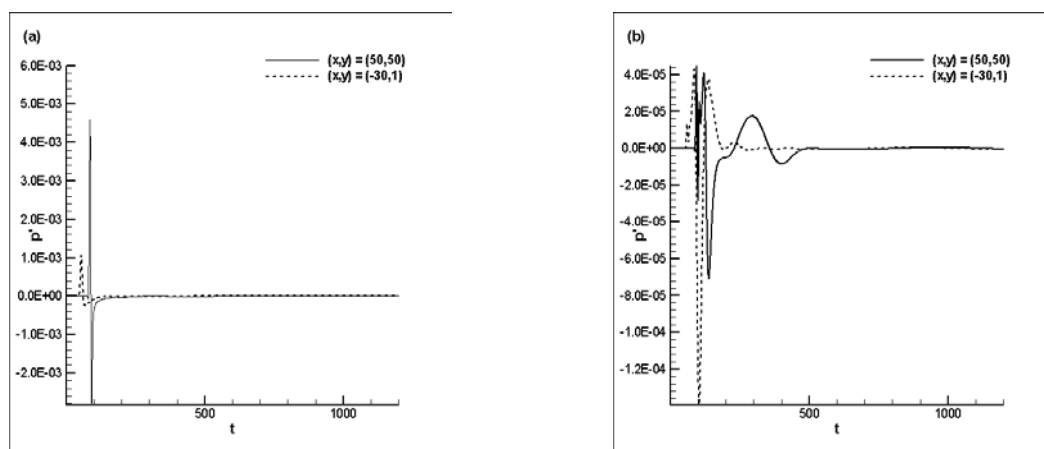
**Figure. 7 Time history of the instantaneous pressure fluctuation from the FLEE
(a) The response to pressure pulse ⓐ and (b) The response to vortical disturbance ⓑ**

Fig. 7 shows the time histories of pressure at the locations (-30,1) and (50, 50) for both of cases. Initial disturbance and diffracted waves are found for both of cases. However, the instabilities cannot be found in these locations. This result is also different from that of Baron et al. (please, refer to the solution comparison paper of Category 4, problem 2). It is found in our numerical simulations that the instability waves don't pass through the location (50,50) but the same thing cannot be said for that of Baron et al.. At this moment, this difference in the zone affected by the instability wave is difficult to interpret, and only one conjecture can be proposed. Baron et al. use the full Navier-Stokes equations while we use the LEE. Different terms of the governing equations, such as the nonlinear interactions and viscous terms, may affect the zone affected by the instability wave.

CONCLUSIONS

Category 4, problem 2 is solved by using the acoustic/viscous splitting techniques of which acoustic solver is governed by the LEE. CAA solver is based on the GODRP schemes to guarantee the dispersion-relation-preserving properties of the numerical scheme on the curvilinear grids. The overset grid technique is also applied to resolve complex geometries. Trailing edge scattering problem is tackled by using the FLEE and the SLEE. Through the comparison of both numerical results, it is found that the mean shear term $\partial \bar{u}_1/\partial x_2$ plays a crucial role in generating the instabilities wave in the trailing edge scattering phenomena.

Future work will be aimed at the acoustic simulation using the full Navier-Stokes Eq. and its extension to 3-dimesional engine nacelle geometries.

REFERENCES

1. Barone, M. F. and Lele, S. K.: A numerical technique for trailing edge acoustic scattering problems. *J. AIAA* , 2002-0226, 2002
2. Cheong, C. and Lee, S.: Grid-optimized dispersion-relation-preserving schemes on general geometries for computational aeroacoustics. *J. Comput. Phys.* **174**, 148 (2001)
3. Christophe Bogey.; Christophe Bailly.: Three-dimensional non-reflective boundary conditions for acoustic simulations: far field formulation and validation test cases. *ACTA ACUSTICA UNITED WITH ACUSTICA*, vol. 88, 2002
4. Tam, C.K.W.; and Dong. Z.: Radiation and Outflow Boundary Conditions for Direct Computation of Acoustic and Flow Disturbances in a Nonuniform Mean Flow. *Journal of computational Acoustics*, Vol. 4, No. 11, 1996
5. Bogey, C.; Bailly, C.; and Juve, D.: Computation of Flow Noise Using Source Terms in Linearized Euler's Equations. *J. AIAA* 40(2), 2002, pp. 235-243.
6. Tam, C.K.W.; and Webb, J.C.: Dispersion-Relation-Preserving Schemes for Computational Acoustics. *J. Comput. Phys.* **107**, 1993, pp. 262-281.
7. Tam, C.K.W.; and Dong. Z.: Wall boundary conditions for high order finite difference schemes in computational aeroacoustics. *Theor. Comput. Fluid Dyn.* **6**, 1994, pp.303-322.
8. Roe, P.L.: Approximate Riemann Solvers, Parameter Vectors and Difference Schemes. J. Comput. Phys. 43, 1981, pp. 357-372.
9. Bin, J.; Cheong, C.; and Lee, S.: Optimized Boundary Treatment for Curved Walls for High-order Computational Aeroacoustics Schemes. *J. AIAA* (In print)
10. Baron, M.F.: Receptivity of Compressible Mixing Layers, Ph. D Thesis, Stanford University, May 2003.

NUMERICAL SOLUTIONS TO THE FOURTH AND SECOND COMPUTATIONAL AEROACOUSTICS (CAA) WORKSHOP BENCHMARK PROBLEMS

Wen H. Lin and Roy H. Loh

Rocketdyne Propulsion & Power
The Boeing Company
6633 Canoga Avenue
Canoga Park, CA 91309-7922
wen-hwang.lin@boeing.com
(818) 586-1593; (818)586-0588 (fax)

ABSTRACT

This paper presents computational fluid dynamics (CFD) solutions to problems concerning sound generation by viscous flows. Two of CAA Workshop benchmark problems have been studied in this paper and they are Problem 2 of Category 5 of the fourth CAA Workshop benchmark problems and Category 4 of the second CAA Workshop benchmark problems. The former solution is to study aerodynamic sound generated by a viscous airflow over a rectangular cavity, and the latter solution is to study Aeolian tones created by a viscous airflow over a circular cylinder. Both solutions were computed by a Navier-Stokes flow solver TIDAL (Time Iterative Density/pressure based Algorithm) developed at Boeing Rocketdyne Division. The numerical algorithm of TIDAL used in this study is based on a dual-time stepping scheme for temporal discretization and a third-order finite-volume scheme for spatial discretization. The aims of this study are (1) to apply TIDAL to solve aero/acoustic problems of sound generation by viscous flows, and (2) to validate the computed solutions with the experimental data of benchmark problems for certifying TIDAL for future aero/acoustic computations of noise sources.

1. INTRODUCTION

Flow-generated sound accompanies the operations of most devices in our daily life. Accurate determination of sound pressure level (SPL) is vital for us to understand the physics of noise generation, control, and reduction in relation to designing a quiet device, machinery, and vehicle. Currently, an analytic solution to a problem of flow-generated sound is formidable because the governing equations, and initial and boundary conditions are so complicated. In most cases, experimental or numerical schemes are used to obtain the desired SPL for a flow-induced noise problem. In this paper we present two time-dependent CFD solutions to study sound generation in the viscous flows of the CAA benchmark problems mentioned above.

2. GOVERNING EQUATIONS

Acoustic wave motion in a flow field is considered as a small perturbation to the flow. The total field of the reference flow and acoustic perturbations satisfies the equations of continuity, momentum, energy, and state. For a viscous compressible fluid the two-dimensional governing equations written in a flux vector form with a pre-condition matrix are

$$D_p \frac{\partial Q_p}{\partial \tau} + \frac{\partial Q_c}{\partial t} + \frac{\partial E}{\partial \xi} + \frac{\partial F}{\partial \eta} = 0, \tag{1}$$

where $Q_p = \{p, u, v, h\}$, $Q_c = \{\rho, \rho u, \rho v, \rho e\}$, D_p is a pre-condition matrix, τ and t are respectively pseudo and real time, p, u, v, and h are pressure, velocity components, and enthalpy, ρ and e are density and internal energy, E and F are flux vectors of mass, momentum, and energy.

At the $(n+1)^{th}$ physical-time and $(s+1)^{th}$ iterative-time levels, we can write the above equations in a semi-discrete form with a temporal accuracy parameter θ $(0 \le \theta < 1)$ as

$$D_p \left(\frac{\partial Q_p}{\partial \tau} \right)^{s+1} + (1+\theta) \left(\frac{\partial Q_c}{\partial t} \right)^{n+1} - \theta \left(\frac{\partial Q_c}{\partial t} \right)^{n} + \left(\frac{\partial E}{\partial \xi} \right)^{n+1} + \left(\frac{\partial F}{\partial \eta} \right)^{n+1} = 0$$

Defining $D_c = \left(\dfrac{\partial Q_c}{\partial Q_p} \right)^{s}$, we then have

$$D_p \frac{(Q_p)^{s+1} - (Q_p)^{s}}{\Delta \tau} + (1+\theta) D_c \frac{(Q_p)^{s+1} - (Q_p)^{s}}{\Delta t} + \left(\frac{\partial E}{\partial \xi} \right)^{n+1} + \left(\frac{\partial F}{\partial \eta} \right)^{n+1}$$

$$= -(1+\theta) \frac{(Q_c)^{s} - (Q_c)^{n}}{\Delta t} + \theta \frac{(Q_c)^{n} - (Q_c)^{n-1}}{\Delta t} \tag{2}$$

Now putting $D \equiv D_p + D_c \dfrac{(1+\theta)\Delta \tau}{\Delta t}$, we have

$$D \frac{(Q_p)^{s+1} - (Q_p)^{s}}{\Delta \tau} + A \frac{\partial Q_p}{\partial \xi} + B \frac{\partial Q_p}{\partial \eta}$$

$$= -(1+\theta) \frac{(Q_c)^{s} - (Q_c)^{n}}{\Delta t} + \theta \frac{(Q_c)^{n} - (Q_c)^{n-1}}{\Delta t} - \left(\frac{\partial E}{\partial \xi} \right)^{s} - \left(\frac{\partial F}{\partial \eta} \right)^{s} \tag{3}$$

where transformation matrices *A* and *B* are defined as

$$A \equiv \left(\frac{\partial E}{\partial Q_p} \right)^{s} = \left(\frac{\partial E}{\partial Q_c} \frac{\partial Q_c}{\partial Q_p} \right)^{s}, \quad B \equiv \left(\frac{\partial F}{\partial Q_p} \right)^{s} = \left(\frac{\partial F}{\partial Q_c} \frac{\partial Q_c}{\partial Q_p} \right)^{s}$$

Equation (3) is the two-dimensional dual-time stepping equation used to design the numerical algorithm in TIDAL to compute time-dependent flows and their fluctuating quantities. Detail of the numerical algorithm was discussed in Ref. 1 and therefore omitted in this study.

Acoustic quantities are considered as the fluctuating part of the total flow field, which is assumed to be time-stationary. That is, every flow variable can be written as the sum of a mean part and a purely fluctuating part as described in Ref. 2:

$$G(x_i, t) \equiv \overline{G}(x_i) + G'(x_i, t) \tag{4}$$

$$\overline{G}(x_i) \equiv \frac{1}{2\tau} \int_{-\tau}^{\tau} G(x_i, t)\, dt$$

$$\int_{-\tau}^{\tau} G'(x_i, t)\, dt = 0$$

where $i = 1, 2, 3$, and *G* is any variable in Q_p or Q_c. In this study, we solved Equation (3) numerically and applied Equation (4) to extract the acoustic quantities. We also employed a zero-equation turbulence model in Equation (3) to compute the unsteady flows at the specific Reynolds numbers of the two-benchmark problems. The effect of grid spacing was not particularly pursued for each problem; however, the combination of grid size (Δx or Δy) and time step size Δt was checked to satisfy the condition $c\Delta t/\Delta x \leq 1$, $c\Delta t/\Delta x \leq 1$, where *c* is the speed of sound, to ensure stable solutions. The time step size was selected to cover all possible frequencies up to 10 KHz. Detail of the time step size is discussed in the following numerical results of each problem. All spectra of sound pressures were computed by the digital Fourier transformation of time series of $G'(x_i, t)$ for fixed spatial points x_i.

3. CATEGORY 5 OF THE FOURTH CAA WORKSHOP BENCHMARK PROBLEMS

3.1 **Problem** 2

This problem is to study aerodynamic sound generation by a turbulent airflow over a moderately deep rectangular cavity (i. e., cavity width/cavity depth = 0.3124). Figure 1 shows the geometry and computational grid for simulating this cavity flow. The dimension of the cavity tongue is 7.94 mm long and 3.18 mm thick. The computational domain extends 87 cavity-mouth widths upstream and downstream of the cavity and 25 cavity-mouth widths vertically to cover all possible sound fields radiated from the cavity. The inflow at the far left boundary was set as uniform with a velocity magnitude of 50 m/s in the horizontal direction. The distance of 87 cavity-mouth widths upstream of the cavity leading edge was chosen to ensure that the turbulent boundary-layer thickness at the entrance of the cavity was approximately 14 mm based on the theory of turbulent flow on a flat plate.

Figures 2 and 3 show the detailed flow fields around and in the cavity. As seen in Figure 2, the cavity mouth and cavity are full of vortices, which are created when the incoming turbulent flow separates at the leading edge of the cavity. These vortices oscillate in the cavity; especially between the leading and trailing edges of the cavity, and create acoustic wave radiation. The acoustic waves propagate upstream, interact with the incoming turbulent flow, and cause flow separation at the leading edge of the cavity, which in turn creates a new vortex moving downstream and bouncing back at the trailing edge of the cavity. Therefore, a self-sustaining feedback loop of flow oscillations and acoustic waves forms. Figure 3 shows the wavy motion in the cavity, around the cavity mouth, and behind the trailing edge of the cavity.

Figure 4 shows a time series of pressure fluctuations at the centers of the left, right, and bottom walls of the cavity. From this figure, one can see that harmonic behaviors are established in the cavity oscillations. To capture the detail of these oscillations, we used a time step of one microsecond (i. e., 10^{-6} sec) to compute the fluctuating flow field. The detailed frequency contents of the time series were computed by a digital fast Fourier analysis. Figures 5-7 show the computed Fourier spectra of sound pressures with the measured sound pressure spectra of Henderson (ref. 3). The tonal frequencies and amplitudes of computed spectra agree well with those of experimental spectra. However, the magnitude of computed spectra in between two peaks are less than that of measured spectra. That is, the computed magnitude of broadband pressure fluctuations, which are due mostly to turbulence, does not compare well with the measured one. This is explainable because of the fact that the discrete harmonic is due to vortex shedding and the broadband acoustic waves are caused by turbulence. In our CFD simulation of the cavity flow the turbulence model used is a zero-order Reynolds-averaged model, which cannot resolve fully an unsteady turbulent flow. On the other hand, a turbulence model does not influence much the vortex shedding.

4. CATEGORY 4 OF THE SECOND CAA WORKSHOP BENCHMARK PROBLEM

This problem is to simulate airframe or automobile noise generated by a viscous airflow. The representative solid object used for the airframe or automobile in this study is a two-dimensional circular cylinder immersed in a uniform airflow of Mach 0.2. Figure 8 shows the two-dimensional computational grid for a viscous flow over the circular cylinder. The diameter of the cylinder is 1.9cm, and the radius of the circular domain used in the calculation is 42 times the diameter of the cylinder. In order to capture the detail of the wake flow behind the cylinder, we clustered the grid spacing behind the cylinder more than in other areas. The Reynolds number based on the cylinder diameter and free-stream velocity is 90,000. At this Reynolds number the wake flow is turbulent but the boundary layer on the forward portion of the cylinder still remains laminar; therefore, it is legitimate to use a zero-equation turbulence model to compute the flow field around the cylinder.

Figures 9 and 10 show the general features of entire flow around the cylinder. In Figure 9 the instantaneous Mach number contours show a wavy layer of discrete vortices moving downstream in the wake of the cylinder. Near the cylinder the wave pattern is sharper than in the far downstream because of turbulent diffusion process occurring in the region. The train of discrete vortices can be also seen in the contours of instantaneous vorticity shown in Figure 10. The arrangement of vortices is similar to that observed in the Karman vortex street (ref. 4); that is, the spatial formation of vortices is unsymmetrical. The positions of vortices change with respect to time; in fact, these vortices oscillate and radiate sound waves into the flow. To capture the detail of the motion of these vortices, we used a time step of five microseconds (i., e. 5×10^{-6} sec) to compute the unsteady flow field around the cylinder.

Figure 11 presents a time series of pressure fluctuations at the point of $r/D = 35$ and $\theta = 90^{\circ}$, where r is the radial co-ordinate from the cylinder center and θ is the angle between the horizontal axis and r, and D is the cylinder diameter. This figure reveals the harmonic behavior of pressure fluctuations, which relates to sound pressure radiated. The frequency content of this time series, computed by a digital fast Fourier transformation, is presented in Figure 12 with the measured sound pressure spectra of Ref. 5. The computed spectrum of sound pressure compares

well with the measured sound pressure spectrum of Mach 0.25 both in frequency and dB level. The measured frequency of vortex shedding is around 692.31 Hz at Mach 0.2 and 882.35 Hz at Mach 0.25. The computed frequency of the dominant mode of vortex shedding is 870.69 Hz. The discrepancy is probably due to turbulence modeling because we used Reynolds-averaged Navier-Stokes (RANA) equations to compute the entire flow fields including the boundary layer flow around the cylinder. The true unsteadiness in the turbulent wake flow may not be simulated correctly. Figure 13 plots the computed spectra of sound pressures at $r/D = 35$ and $\theta = 60^{o}$, 90°, 120°. All three spectra look alike and they all have a dominant peak frequency at 870.69 Hz.

SUMMARY

In general, the computed tonal frequencies of flow-generated sound obtained from the two unsteady CFD solutions agree reasonably well with the corresponding experimental frequencies. However, the RANS turbulence model used in the algorithm cannot predict the right frequencies and amplitudes of SPL in a turbulent flow.

ACKNOWLEDGEMENTS

REFERENCES

1. Loh, H. T., Smith-Kent, R., Perkins, F., and Chwalowski, P.: Evaluation of Aft Skirt Length Effects on Rocket Motor Base Heat, Using Computational Fluid Dynamics, *AIAA* Paper 96-2645.

2. Doak, P. E.: Fluctuating Total Enthalpy as the Basic Generated Acoustic Field. *Theoret. and Comput. Fluid Dynamics*, vol. 10 (1-4), 1998, pp. 115-133.

3. Henderson, B.: Problem 2 of Category 5 – Sound Generation by Viscous Flows. Private Communication.

4. Karman, Th. V.: Flussigkeits und Luftwiderstand. *Physik. Z.* 13, 49, 1911; also, Abernathy, F. H., and Kronauer, R. E.: The Formation of Vortex Streets, *J. Fluid Mech.* 13 Part 1, May 1962, pp 1-20.

5. Revell, J. D., Prydz, R. A., and Hays, A. P.: Experimental Study of Airframe Noise verse Drag Relationship for Circular Cylinder, Lockheed Report 28074, February 25 1977 (NASA Contract NAS1-14403).
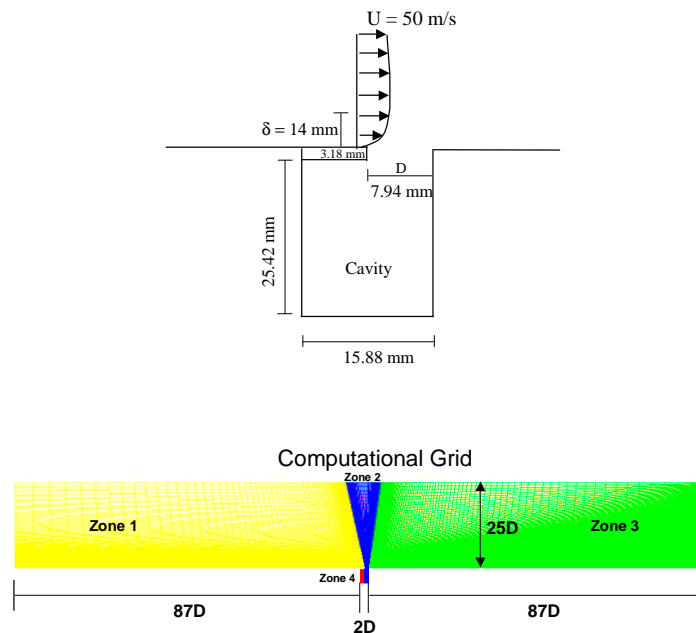
Figure 1. Geometry and computational grid of cavity flow
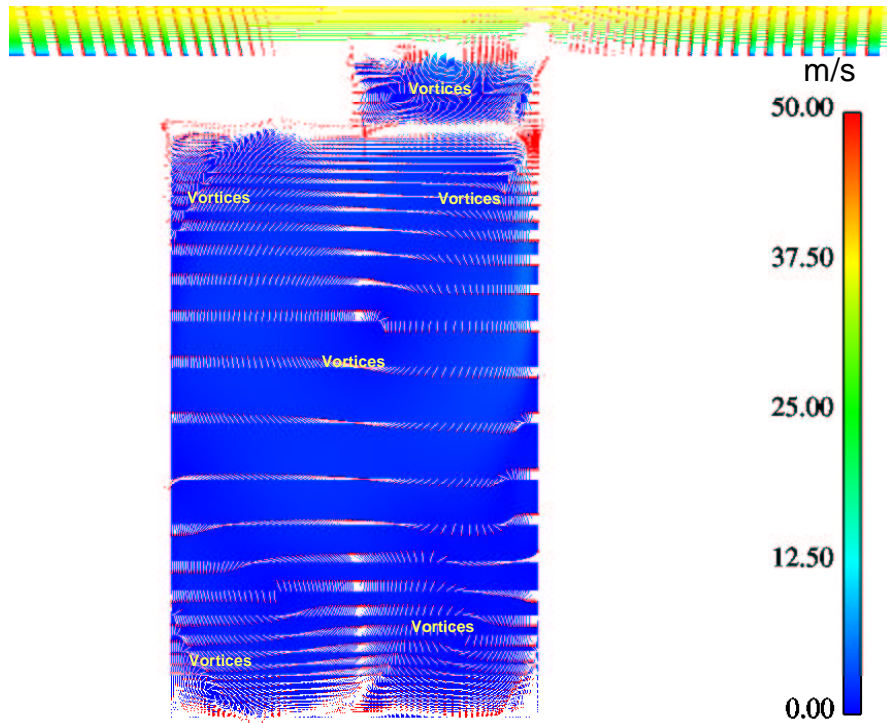
Figure 2. Instantaneous velocity vectors show strongly vortical motion in the cavity
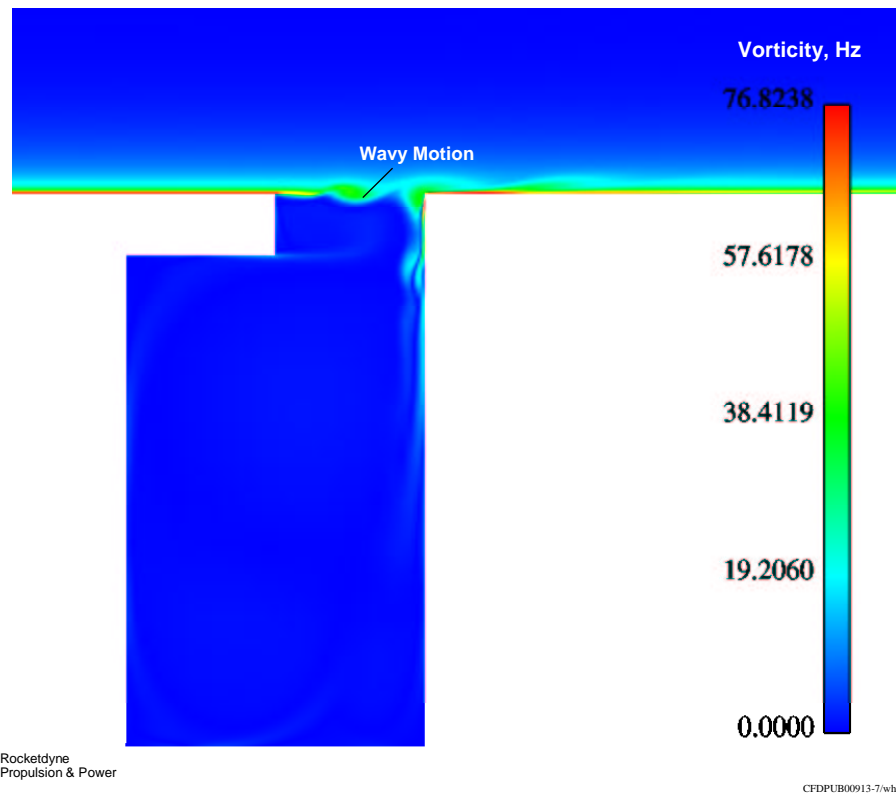
Figure 3. Instantaneous vorticity field shows wavy motion around the cavity mouth and its trailing edge
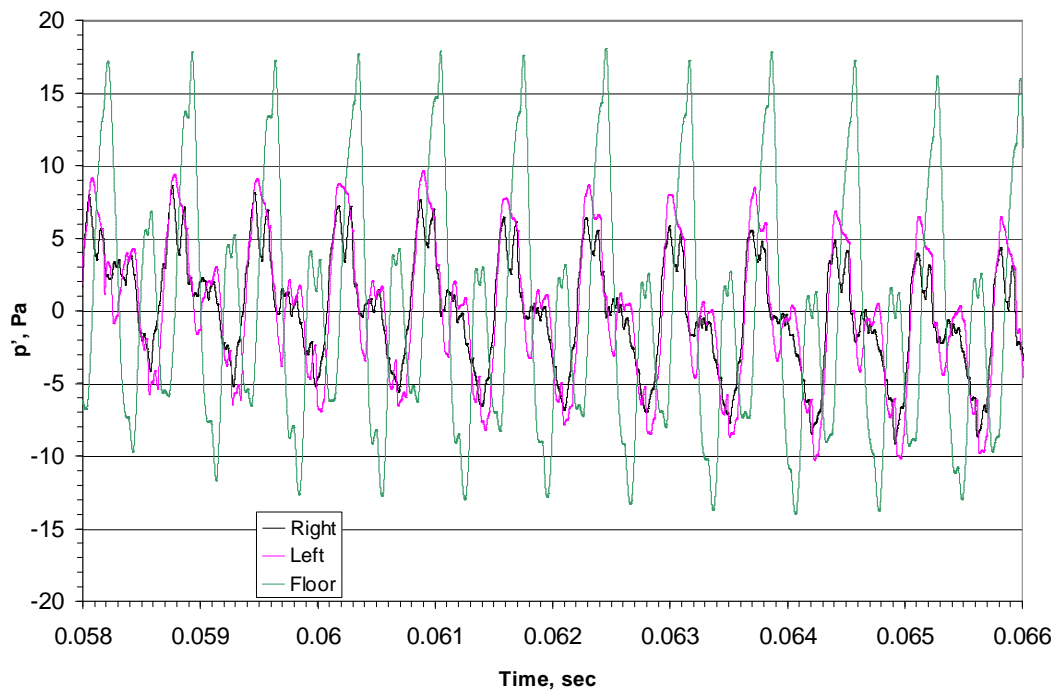
Figure 4. Time series of pressure fluctuations at the centers of the cavity floor, left and right walls
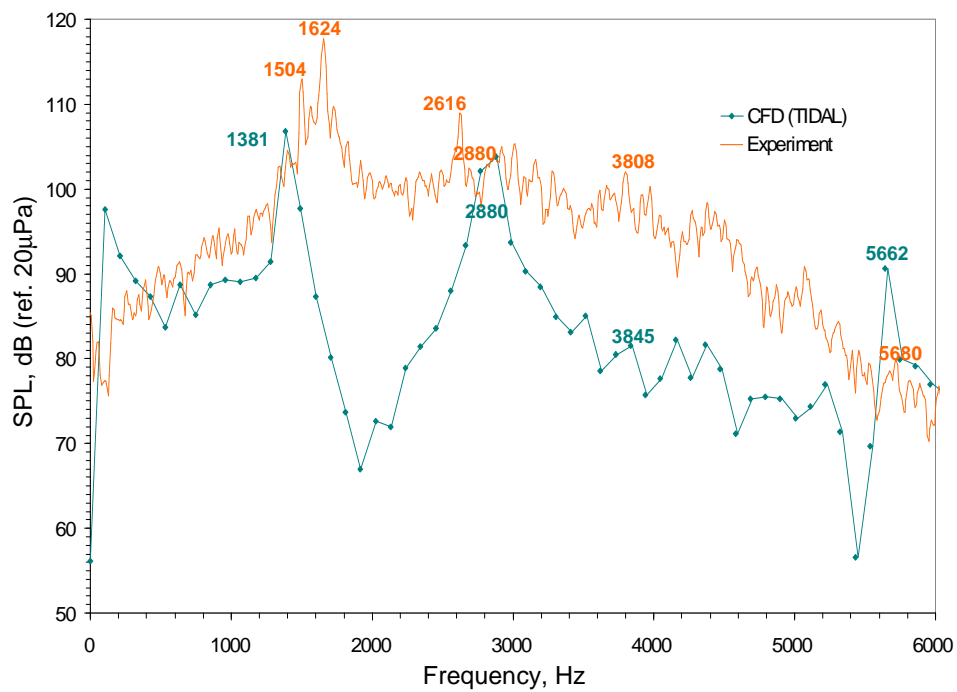
Figure 5. Comparison of sound pressure spectra at the center of the cavity left wall
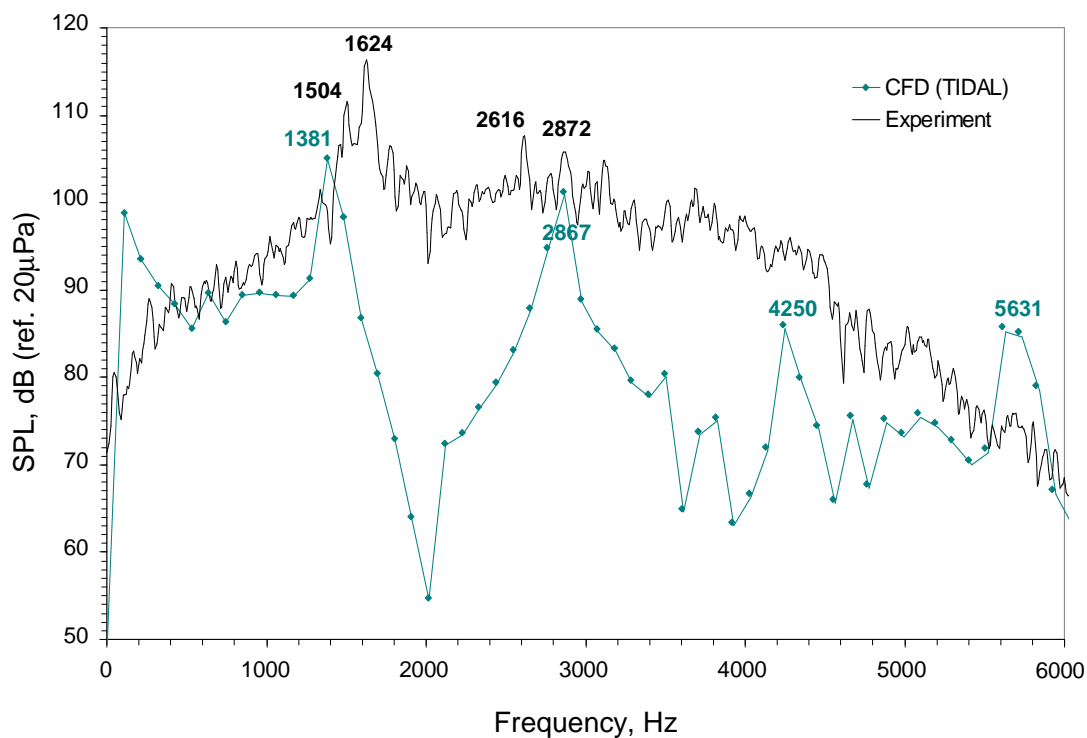
Figure 6. Comparison of sound pressure spectra at the center of the cavity right wall
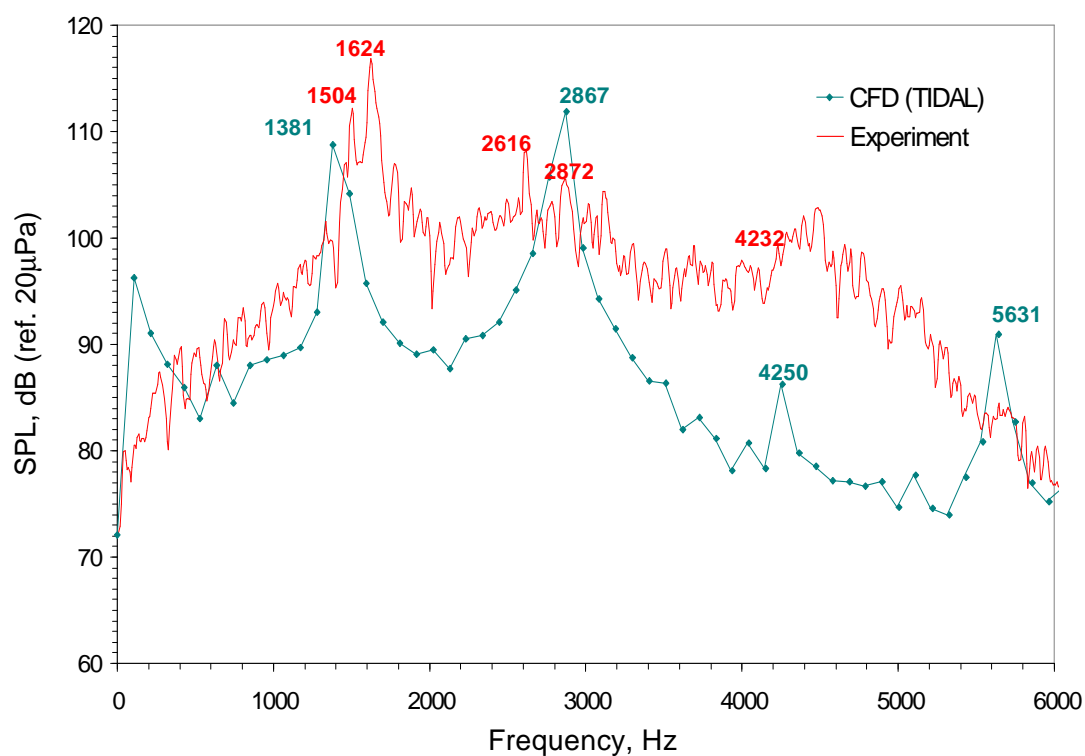
Figure 7. Comparison of sound pressure spectra at the center of the cavity floor
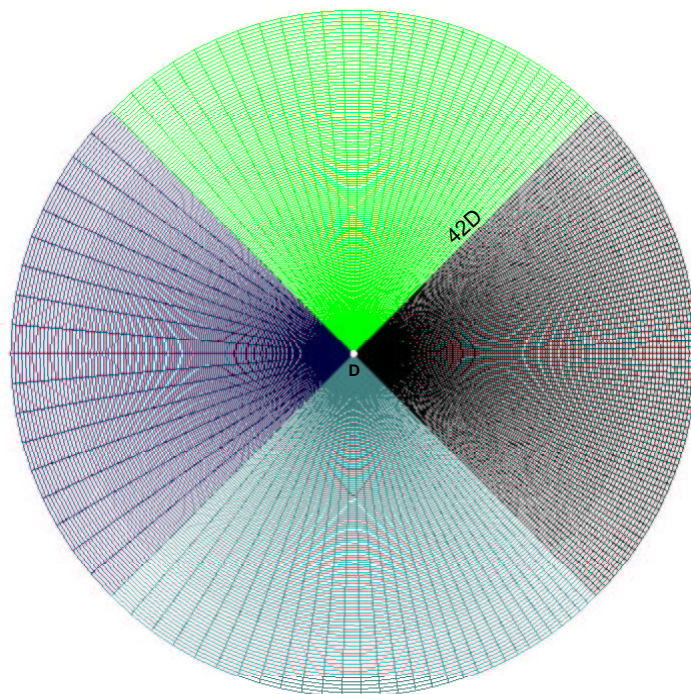
Figure 8. Computational grid for flow passing a circular cylinder
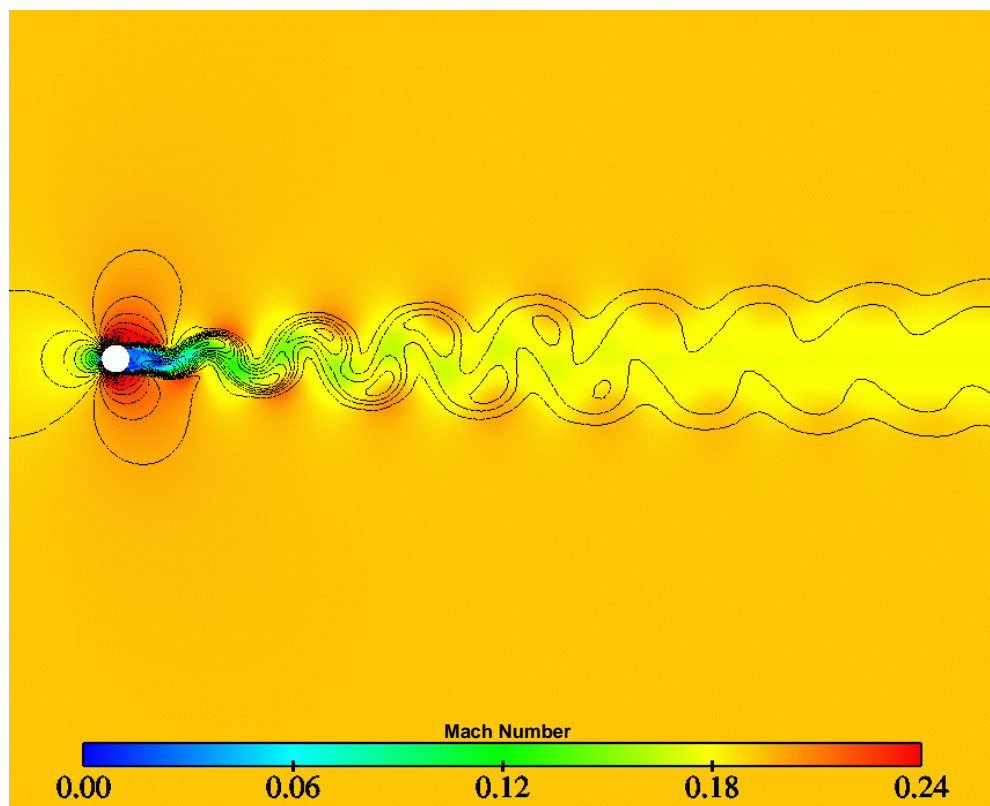
Figure 9. Instantaneous Mach number contours show wavy motion of vortices behind the cylinder
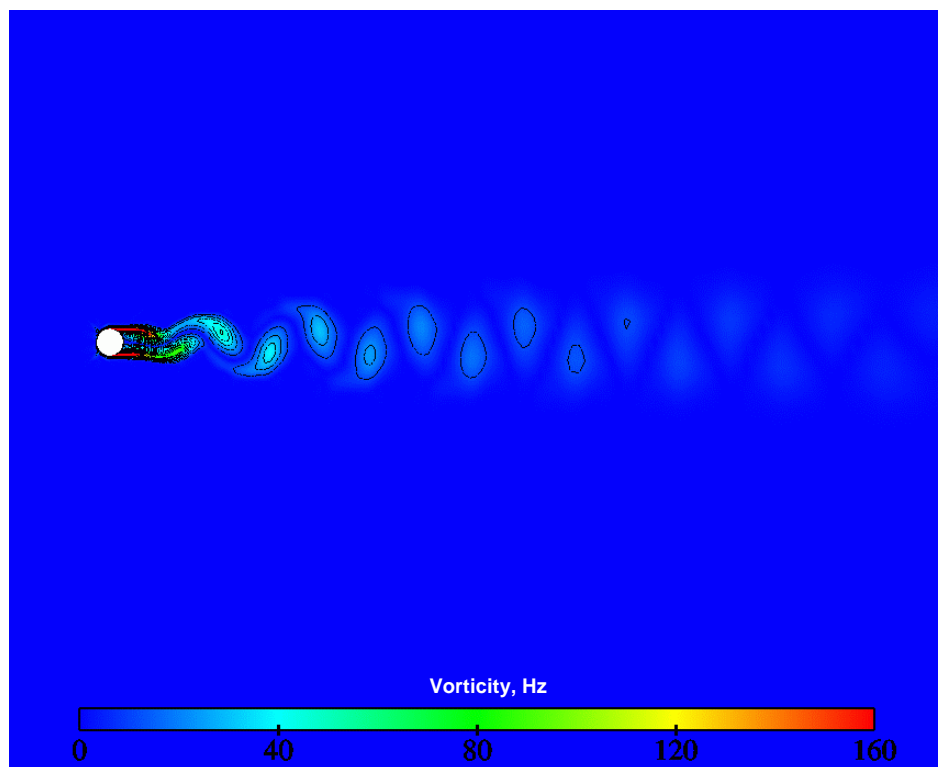
Figure 10. Instantaneous vorticity contours show discrete vortex behind the cylinder
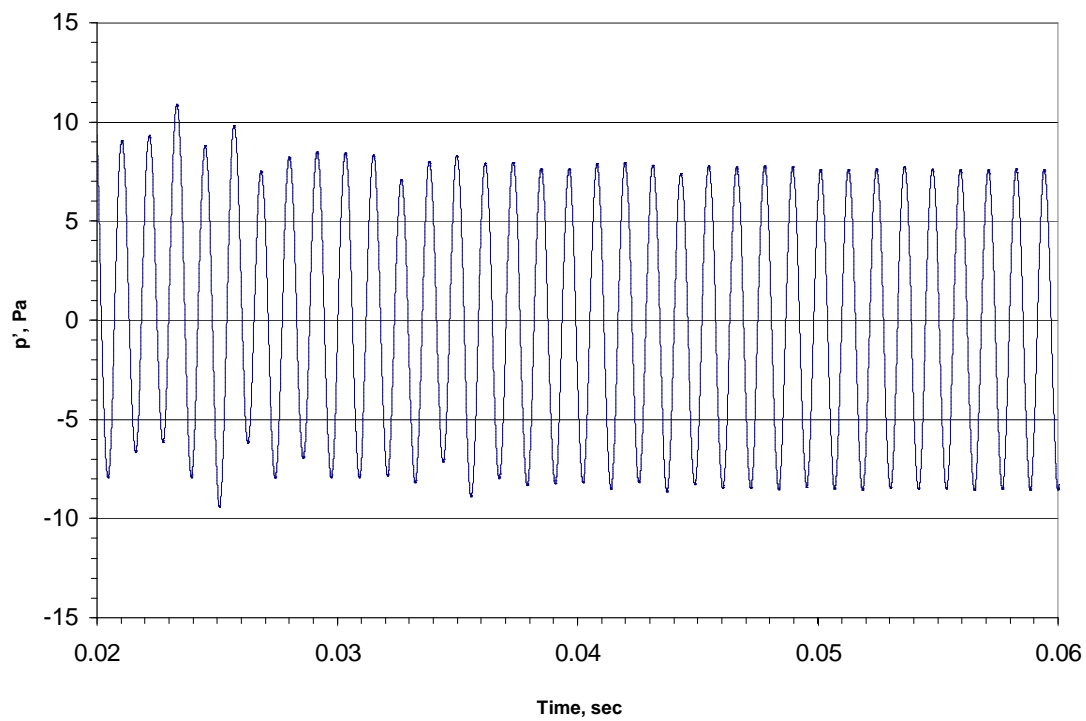
Figure 11. Time series of sound pressures at r/D = 35 and $\theta = 90^{o}$
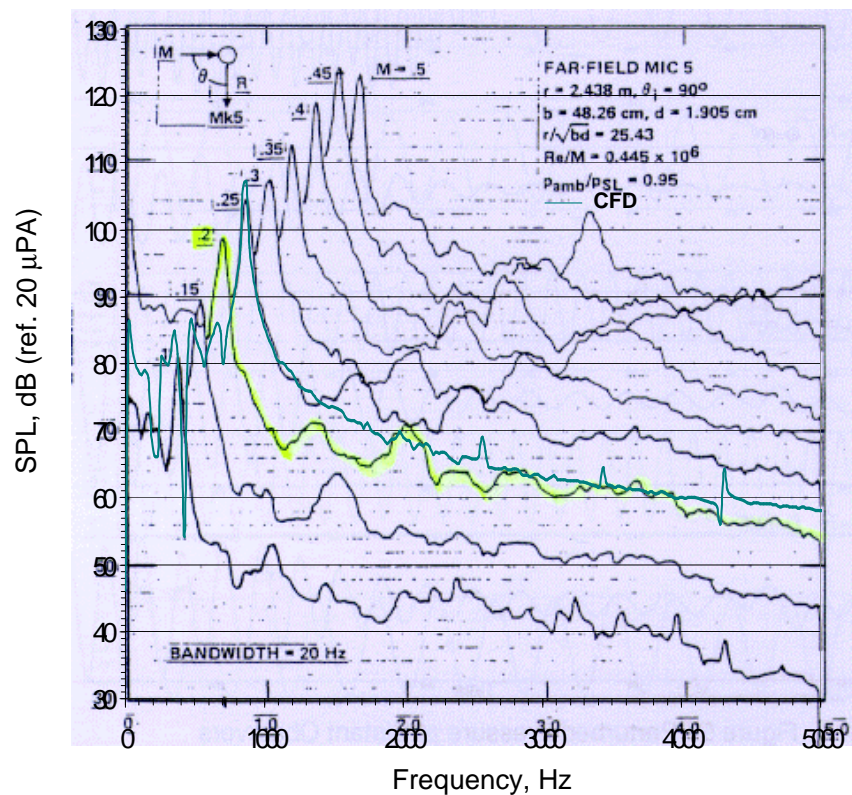
Figure 12. Comparison of sound pressure spectra at r/D = 35 and θ = 90°
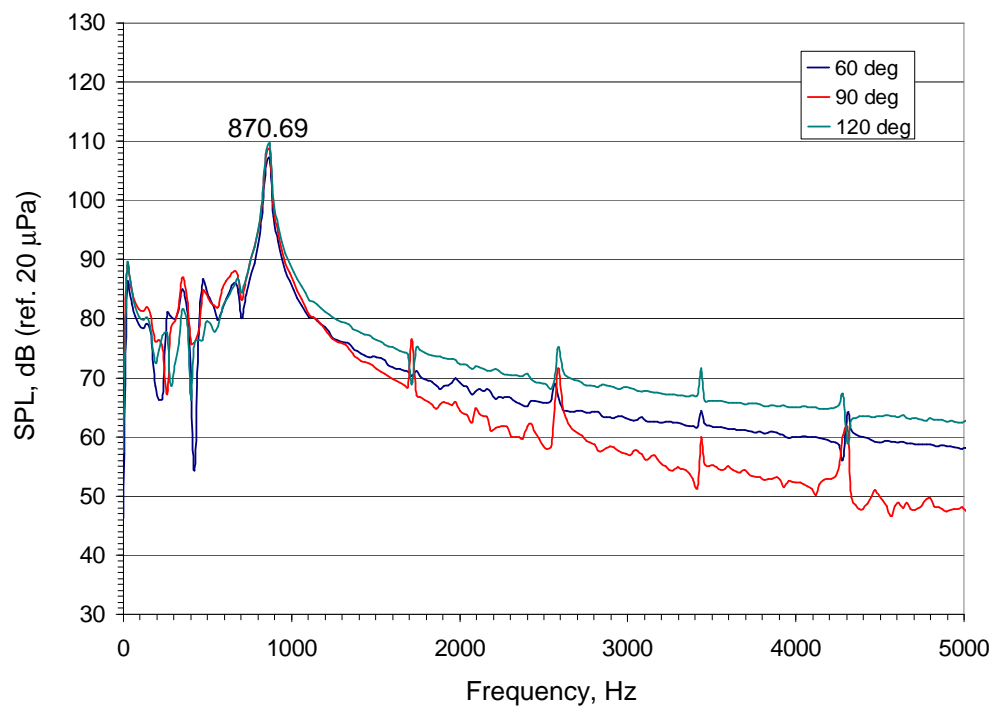
Figure 13. Comparison of computed spectra of sound pressures at r/D = 35 and θ = 60°, 90°, 120°

SPECTRAL ANALYSIS FOR AIR FLOW OVER A CAVITY

Z. Zhang, R. Barron* and C.-F. An
Fluid Dynamics Research Institute
University of Windsor
Windsor, ON, Canada N9B 3P4

ABSTRACT

A procedure has been developed to perform spectral analysis for air flow over a cavity. The air flow is simulated numerically using the commercial CFD software Fluent and the pressure fluctuations are acoustically post-processing using FFT in the mathematical tool Matlab. A parametric study is undertaken that illustrates the importance of achieving a stable and accurate CFD solution in order to obtain reliable noise predictions. Simulation results are compared to experimental data presented at the Computational Aeroacoustics Workshop.

INTRODUCTION

Air flowing over a cavity may cause pressure fluctuation and noise radiation, which is of great concern in industries such as aeronautical and automotive (refs. 1 to 3). In fact, one source of aerodynamic noise of a road vehicle comes from the opening of a window or sunroof, which can be considered as flow over a cavity. The self-sustaining oscillations of flow over a cavity can be categorized into three groups (ref. 4): fluid-dynamic, fluid-resonant and fluid-elastic. Fluid-dynamic oscillations are excited by the amplification of an unstable cavity shear layer, and enhanced by a feedback mechanism. Fluid-resonant oscillations are strongly coupled with the resonant wave at the cavity. Fluid-elastic oscillations are coupled with the motion or vibration of a solid boundary.

Due to the technical importance, flow over a deep cavity with a lip at the cavity entrance was selected as one of the benchmark problems in the Third Computational Aeroacoustics (CAA) Workshop in 1999. In that workshop, Henderson (ref. 5) provided experimental data for a particular cavity. Some participants (refs. 6 to 9) presented their computational results and compared with the data. A similar problem was selected as a new benchmark in the Fourth Computational Aeroacoustics (CAA) Workshop in 2003. The present paper includes results that the authors presented at this workshop and additional results based on more recent simulations.

In this paper, we present the results of our computation for the prediction of peak frequencies and sound pressure levels in a cavity, and discuss the effects of parameters used in the process of spectral analysis.

PROBLEM DESCRIPTION AND SOLUTION METHODOLOGY

Problem description

The geometry of the cavity for the benchmark problem is shown in Fig.1. The turbulent flow over the cavity has a mean velocity of 50 m/s. In the experimental setup, the thickness of the boundary layer developed over the flat plate is 0.14m at the entrance of the cavity. The objective is to calculate the power spectra at the center of each cavity wall and the center of the cavity floor and to compare the computational results with the experimental data.

Solution methodology

The computational domain includes the cavity and a rectangle above it, as shown in Fig. 1. The rectangle is 0.3m high and 0.3m downstream from the trailing edge of the cavity. For the purpose of investigating the effect of boundary layer thickness, upstream lengths of 0.3m, 0.5m and 0.682m are considered. The lower edge of the rectangle coincides with the upper edge of the cavity. Since the geometry of the computational domain is rectangular and all boundaries are parallel to the coordinate axes, a non-uniform Cartesian grid system is utilized. Generally, a uniform mesh is used in the cavity neck area where the noise source is located. Then, the grid is smoothly enlarged from the cavity neck outwards towards all far boundaries of the rectangle and clustered near the walls within the cavity. In order to investigate the effect of mesh size, several grid number distributions are also chosen, as listed in Table 1. In this table, each column depicts a case of mesh size arrangement and the capital letters in the first column represent the segments of the boundaries in Fig. 1.

---

*   Corresponding author: address as above, email: az3@uwindsor.ca; fax: (519) 971-3667;
    phone: (519) 253-3000,x2110

The flow velocity on the left side of the rectangle (inlet boundary) is uniform and equal to 50 m/s. The right side of the computational domain is set to be a pressure-outlet boundary (p=0). The top boundary of the rectangle is set to be either a frictionless wall (symmetry boundary) or a pressure-outlet boundary. The rest of the boundaries are no-slip solid walls. The rectangle and the cavity are connected through the cavity neck.

In the simulation of the cavity flow, unsteady compressible Reynolds Averaged Navier-Stokes equations are solved using the commercial CFD software, Fluent (ref. 10). To capture the high frequency fluctuating features of the cavity flow, a second order implicit scheme is used for time marching and a second order upwind scheme is used for the convection terms in the momentum, energy and turbulence equations. Ideal gas is selected as the air model to consider density change along with pressure fluctuations. Both RNG k-ε and one-equation turbulence models are considered in this study.

All computations are started from a uniform initial flow field of 50m/s. Relaxation factors for various parameters are adjusted as required to get convergence. The residual of the pressure equation is found to be the most critical residual for convergence. In our simulations the residual of the pressure equation is set at 10^{-5} to 10^{-4} depending on the particular case.

In most cases, the time step is set to be 1×10^{-5}sec. This time step provides sufficient accuracy and stability to capture high frequency signals (over 1 kHz). To study the effect of time step, other time steps from 1×10^{-6} to 1×10^{-3} sec were also employed in the computation. To reach the prescribed residual of the pressure equation, about 20 - 30 sub-iterations are carried out in each time step. This is especially important during the first thousand time steps.

The computation is performed step-by-step until a stably fluctuating pressure signal at a given location is obtained. During the computation, the pressure signals at three points in the cavity, the centers of the two sidewalls and the center of the cavity floor, are monitored.

The recorded signals are then acoustically post-processed using the mathematical tool Matlab that has an option of Fast Fourier Transform (FFT). Using Matlab, a special procedure has been designed and used for acoustic post-processing, as shown in the plots in Fig. 2. Figure 2(a) shows a typical noise signal, i.e. a time history of pressure fluctuation. After application of the FFT, the signal is converted from the format of time history to the format of power density expressed in terms of frequency, as shown in Fig. 2(b). Then, the amplitude of the signal can be calculated and expressed as a function of frequency, as shown in Fig. 2(c). Finally, the sound pressure level (SPL) is calculated from SPL = $10\text{Log}_{10}(P/P_{ref})^2$, where P is the amplitude of the signal and $P_{ref} = 2x10^{-5}$ Pa, as shown in Fig. 2(d).

RESULTS AND DISCUSSION

Comparison with experimental data and other simulations

The measurements for the benchmark problem provided by Henderson in the 3rd CAA workshop are chosen for comparison, since the geometry and operating condition are quite close to the current study.

Figure 3 shows the comparison of SPL-frequency spectra between the computational results and the experimental data for both thin and thick boundary layers considered by Henderson (ref. 5). Here, three cases from our computations are included. This figure demonstrates that: (1) the spectral patterns of our results are quite similar to the experimental data. The frequencies of the first peaks for all cases are around 1.9kHz with the deviation of about 50Hz; (2) the SPL of the first peak is also very close to one another with the deviation of about 5-10dB; (3) the spectra obtained from our computations show a harmonic pattern. The frequency of the second peak is almost twice the frequency of the first peak. In turn, the frequency of the third peak is about three times the frequency of the first peak, etc. This demonstrates the resonant characteristics of the flow over a cavity. However, the experimental results seem to have only three harmonics, including two smeared high frequency peaks; (4) all peaks in the spectral curves from our computations are very sharp. This means that the computational results have low background noise, whereas the experimental spectrum appears to contain more background noise.

Figure 4 shows the peak frequency and SPL from our computational results for Grid 3, i.e., 30×30 cells in the neck area, using time steps 5×10^{-6} and 1×10^{-5} sec, two turbulence models and different boundary layer thicknesses at the entrance of the cavity. In addition, some computed peak frequency and SPL from other researchers (refs. 6 to 9) are included to compare with the experimental data. This figure indicates that our models can predict at least the first two peak frequencies and SPL quite well. The detailed differences between our simulations are discussed below.

Parameter study for flow over a cavity

Certain parameters have significant influence on the spectral characteristics of the flow over a cavity, especially time step and mesh size. Therefore, special attention has been paid to both time step and mesh size in this study.

Effect of time step

In general, a large time step ($\Delta t \geq 5\times10^{-5}$ sec) tends to activate and enhance the low frequency components and reduce or smear the high frequency components of the fluctuation. As a matter of fact, in the early stage of our study, where $\Delta t \geq 5\times10^{-5}$ sec was used, only the low frequency peak was captured, as shown in Table 2. Moreover, an increase in time step may cause further decrease in peak frequency. On the other hand, although a decrease in time step may give a better signal to involve high frequency components, very small time steps may cause difficulty with convergence and high computational cost. From our experience, a time step in the range $\Delta t = 5\times10^{-6}$ to 2×10^{-5} sec is an appropriate choice for this problem. Therefore, most of the computations in this study were performed at a time step $\Delta t = 1\times10^{-5}$ sec.

Effect of mesh size

Using an upstream length $l_f = 300$ mm and $\Delta t = 1\times10^{-5}$ sec, the computed values of peak frequency and SPL for various mesh size, represented by the grid number in the cavity neck, are listed in Table 3. Computations were also carried out for a fine mesh of 100×100 grids in the cavity neck area, but convergent results could not be achieved. It can be seen from this table that the high frequency first peak can be captured even for the coarsest mesh, 15×15, with a small time step $\Delta t = 1\times10^{-5}$ sec. However, the predicted frequency of the first peak on this coarse mesh may not be accurate enough. Discarding the results of the 15×15 mesh, we can see from the table that refining mesh size leads to a lower first peak frequency, but seems to have very little effect on the SPL.

Effect of boundary layer thickness

In the computations, the upstream length l_f, from inlet to the leading edge of the cavity neck, is adjusted to establish boundary layer thickness δ_f at the leading edge of the cavity neck. This thickness is measured in the plot of velocity magnitude contour. If the number of the contour curves from the bottom to the top of the rectangle is set to be 100, the location of the 99th contour curve at the leading edge of the cavity gives boundary layer thickness. Therefore, δ_f can be measured from this plot. In Table 4, three upstream lengths $l_f = 300$, 500 and 682mm are used, and two conditions at the top boundary, symmetry (frictionless wall) and pressure-outlet, are applied to each of the three upstream lengths to give six different boundary layer thickness, as listed in the table. These thicknesses represent their actual values in the flow. However, the boundary layer thickness for a flow over a flat plate should be thicker than that for the flow over a cavity. For example, the boundary layer thickness for a plate at 682mm from the leading edge is about 14mm. This value is higher than the 12.5mm indicated on the bottom line of Table 4.

In order to reduce computational time for this study, and based on the results presented in Table 3, a coarse mesh of 20×20 in the cavity neck is used, the time step is $\Delta t = 1\times10^{-5}$ sec and the RNG k-ε turbulence model is invoked. From Table 4 we can see that as the boundary layer thickness at the entrance of the cavity neck increases, the frequency at the first peak usually decreases, but the SPL of the first peak remains almost constant. It appears that both the symmetry and pressure-outlet boundary conditions are adequate when the boundary layer is thin. However, as the boundary layer thickens, the symmetry condition becomes less reliable. Convergence could not be obtained for the 12mm thick boundary layer with the symmetry condition on the top boundary.

Comparison of spectra at different locations in the cavity

As shown in Fig. 5, the spectra at different locations (center of the floor, center of the front wall and center of the rear wall) are quite close to one another. The peak frequencies are the same for all the locations. However, the SPL at the cavity floor is higher than that on the two sides of the cavity. This indicates that the air near the cavity floor has the strongest pressure fluctuations.

CONCLUSION

In this paper, a procedure has been established and implemented to perform spectral analysis for air flow over a cavity. The air flow is simulated numerically by solving transient flow using the commercial CFD software Fluent and the pressure fluctuations are acoustically post-processing using FFT in the mathematical tool Matlab.

The computational results for the spectra of pressure fluctuations are obtained at three locations in the cavity, centers of the cavity walls and center of the cavity floor. The numerical predictions compare favorably with the corresponding experimental data provided by Henderson at the 3rd CAA Workshop.

The computed frequency at the first peaks in the spectral curves, for various combinations of computational parameters, are close to one another and to the experimental data within the range of about 50Hz. The computed SPL of the first peaks are also close to the experimental data with a deviation of 5-10dB.

A parametric study demonstrates that time step is the most crucial factor that has a strong influence on the computational convergence and solution accuracy, especially on the capture of the high frequency components of pressure fluctuations. It also shows that mesh size is another important parameter in the spectral analysis. Boundary layer thickness has some effect on the frequency at the first peak but not much effect on the SPL in the spectrum of pressure fluctuations. Two tested turbulence models show little difference in this study.

It is readily apparent that the reliability of the noise predictions is heavily dependent on the accuracy of the underlying CFD simulations. The procedure still needs to be fine-tuned in order to improve its convergence behavior, solution accuracy and computational efficiency.

REFERENCES

1. Block, P.J.W.: Noise response of cavities of varying dimensions at subsonic speed, NASA TN D-8351, 1976.
2. George, A.G.: Automobile aeroacoustics, AIAA-89-1067, 1989.
3. Mongean, L.; Bezenek, J.; and Danforth, R.: Pressure fluctuations in a flow-excited door gap cavity model, SAE Paper 971923, 1997.
4. Rockwell, D.; and Naudascher, E.: Review - Self-sustaining oscillations of flow past cavities, J. Fluids Eng., Vol. 100, 1978, 152-165.
5. Henderson, B.: Automobile noise involving feedback-sound generation by low speed cavity flows, NASA/CP-2000-209790, 2000, 95-100.
6. Moon, Y.J., et al.: Aeroacoustic computations of the unsteady flows over a rectangular cavity with a lip, NASA/CP-2000-209790, 2000, 347-353.
7. Aschcroft, G.B.; Takeda, K.; and Zhang, X.: Computations of self-induced oscillatory flow in an automobile door cavity, NASA/CP-2000-209790, 2000, 355-361.
8. Shieh, C.M.; and Morris, P.J.: A parallel numerical simulation of automobile noise involving feedback, NASA/CP-2000-209790, 2000, 363-370.
9. Kurbatskii, K.K.; and Tam, C.K.W.: Direct numerical simulation of automobile cavity tones, NASA/CP-2000-209790, 2000, 371-383.
10. Fluent User's Manual, version 6.0, Fluent Inc., Lebanon, NH, USA, 2001.
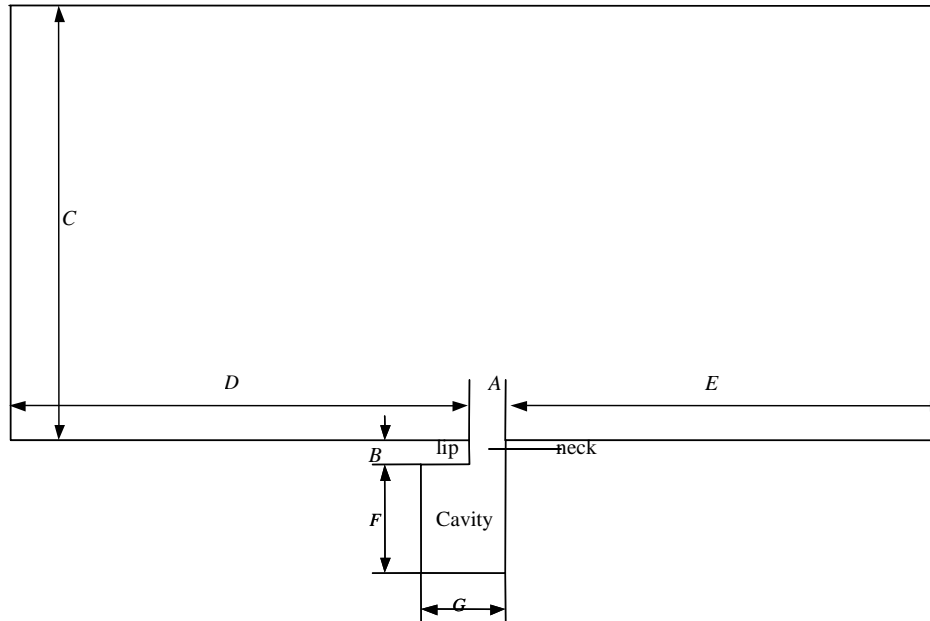
Figure 1. Cavity geometry and computational domain

Table 1. Grid number in various cases

	Grid 1	Grid 2	Grid 3	Grid 4
A	15	20	30	60
B	15	20	30	60
C	40	60	90	150
D	30	40	60	120
E	30	40	60	120
F	30	40	60	120
G	30	40	60	120
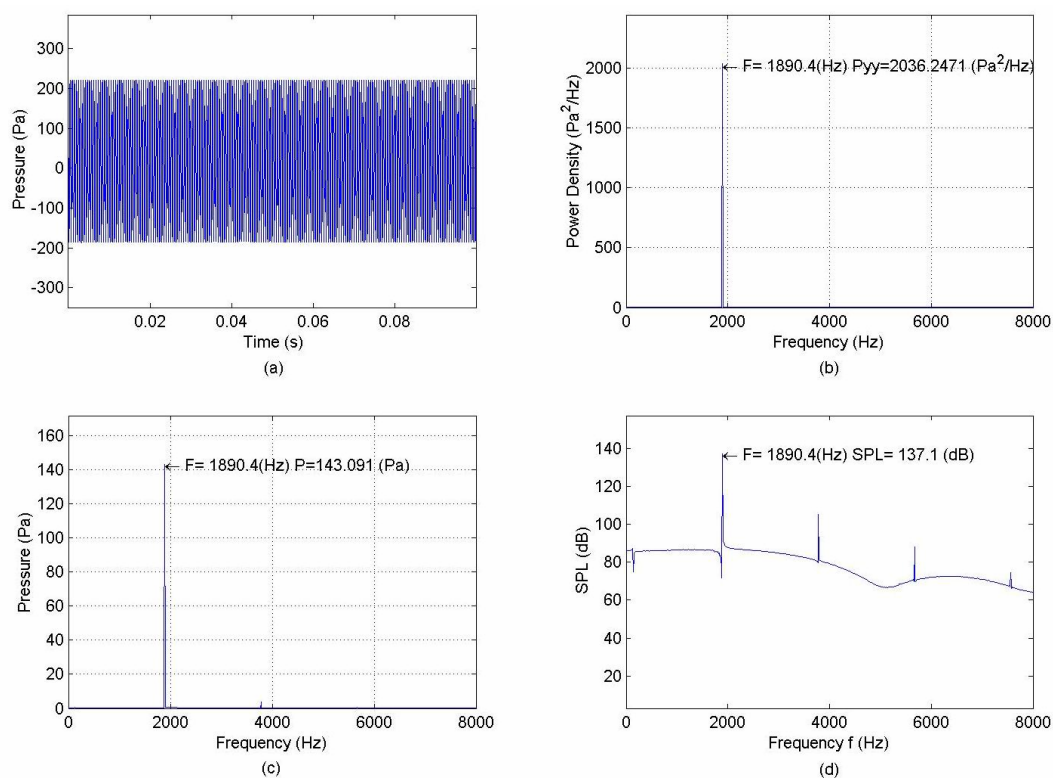
Figure 2. Fast Fourier Transform (FFT) for a sample signal
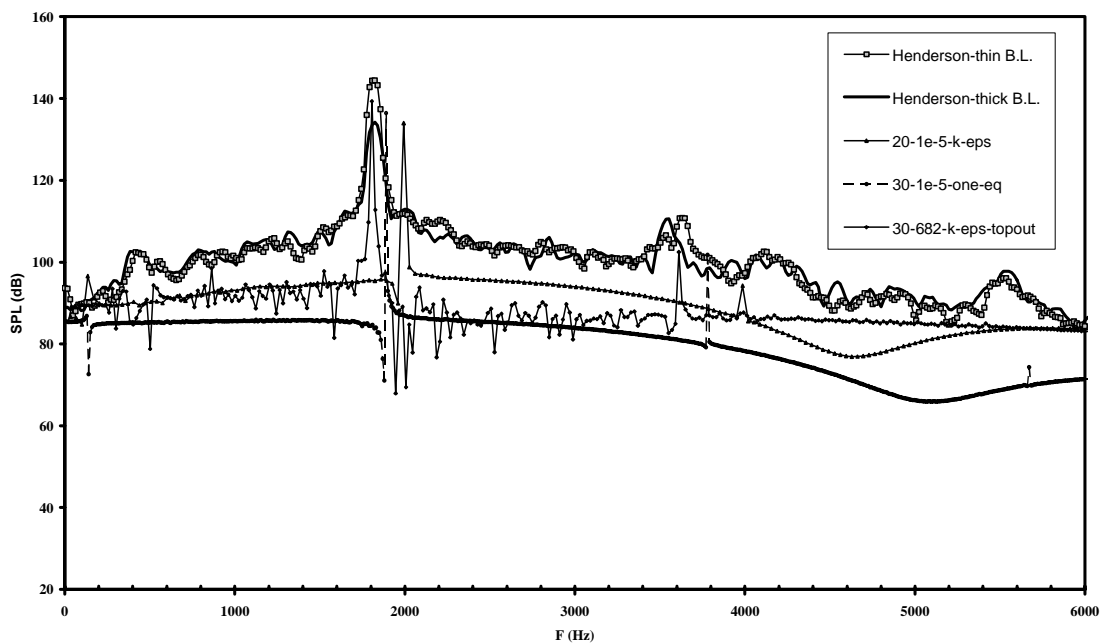
Figure 3. Comparison of spectra between computational and experimental data provided by Henderson in 3ʳᵈ CAA Workshop (ref. 5)
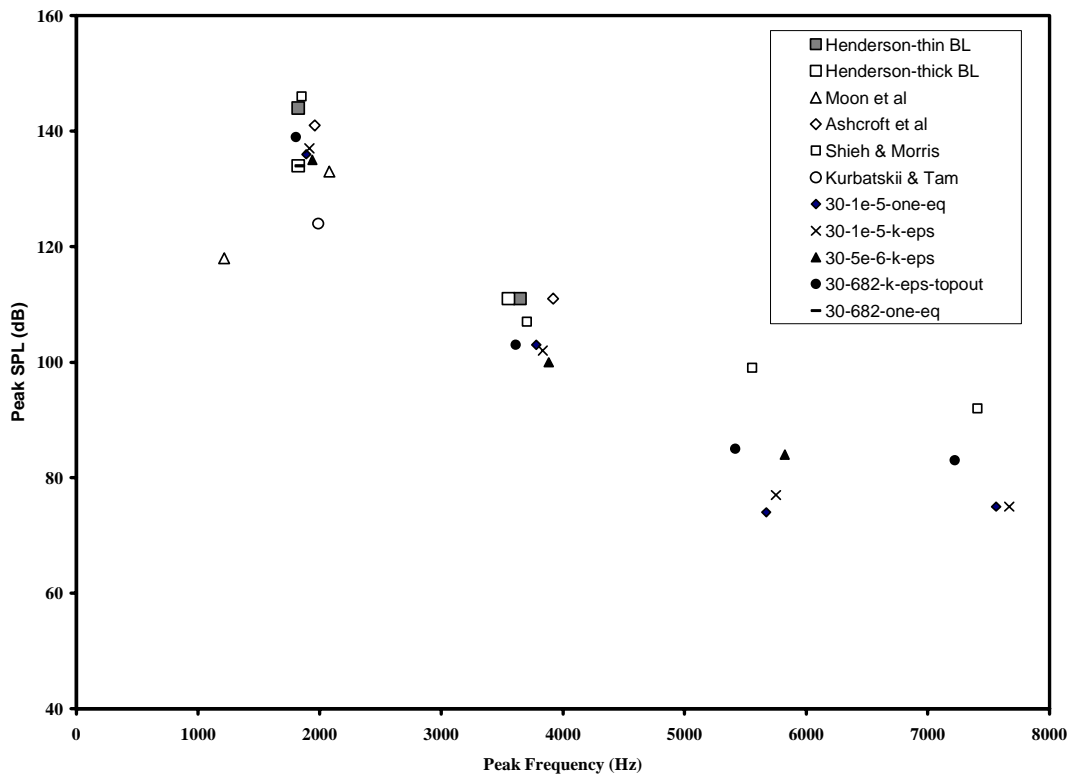
Figure 4. Comparison of peak frequency and SPL

Table 2. Peak frequency and SPL for various mesh size and time step

Mesh	Δt (sec)	F (Hz)	SPL (dB)
10×10	5×10^{-5}	125.2	110.1
	1×10^{-4}	104.7	105.5
	2×10^{-4}	83.6	79.3
15×15	2×10^{-5}	129.1	109.2
	5×10^{-5}	120.0	100.7
	2×10^{-4}	88.9	93.4
	5×10^{-4}	62.6	94.1
	1×10^{-3}	45.3	90.3
20×20	2×10^{-5}	125.0	110.0
	5×10^{-5}	112.4	102.1
	1×10^{-4}	98.5	95.4
30×30	5×10^{-5}	84.7	119.6
	1×10^{-4}	67.7	121.3

Table 3. Effect of mesh size on first peak frequency and SPL (l_f = 300mm, Δt =1×10⁻⁵ sec)

	F (k-ε)	F (one-eq)	SPL (k-ε)	SPL (one-eq)
15×15	1963.5	/	127.9	/
20×20	1993.0	1974.8	135.0	137.0
30×30	1917.7	1890.4	138.2	137.1
60×60	1897.4	1915.3	131.6	136.0

Table 4. Effect of boundary layer thickness (20×20 mesh, Δt =1×10⁻⁵ sec)

l_f (mm)	Top B.C.	δ_f (mm)	F_{peak} (Hz)	SPL_{peak} (dB)
300	Symmetry	7.0	1974.8	137.0
300	Pressure-outlet	7.5	2004.0	126.0
500	Symmetry	10.0	1938.8	124.7
500	Pressure-outlet	10.5	1935.7	126.1
682	Symmetry	12.0	Not available	
682	Pressure-outlet	12.5	1882.6	126.3

Figure 5. Comparison of spectra at different locations in the cavity

COMPUTATION OF AEOLIAN TONE NOISE FROM TWIN CYLINDERS BY USING GRID-OPTIMIZED DISPERSION-RELATION-PRESERVING SCHEMES WITH IMMERSED SURFACE DIPOLE MODEL

Cheolung Cheong[*], Jewook Ryu[#], and Soogab Lee[†]

School of Mechanical and Aerospace Engineering
Seoul National University
Seoul 151-742, Korea

ABSTRACT

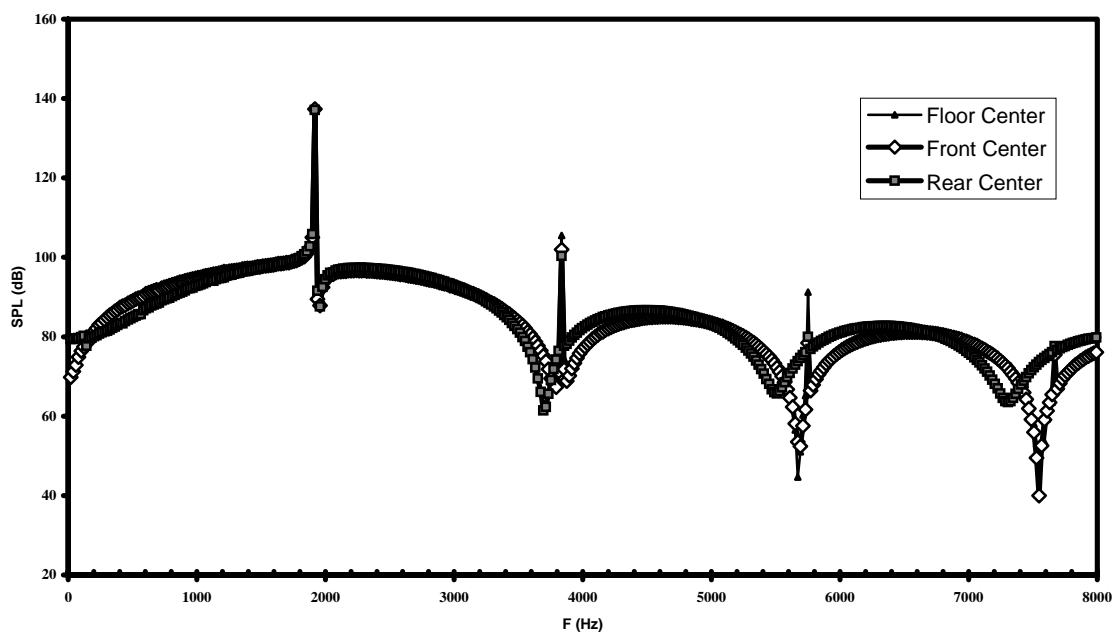Grid-Optimized Dispersion-Relation-Preserving (GODRP) schemes are used for the computation of category 5, problem 1 in 4th CAA Workshop. Tam's DRP scheme is implemented only on a uniform Cartesian grid while practical problems in aeroacoustics are seldom confined to uniform Cartesian geometry, with the associated computational grids usually being non-uniform or curvilinear. The GODRP schemes have been developed with grid-optimization algorithm to make finite difference equations possess the same dispersion relations as the corresponding partial differential equations on general geometries. Acoustic/viscous splitting techniques with immersed surface dipole model (ISDM) are utilized to solve the sound generation and propagation in viscous, low-Mach number flows for which direct computation of the aerodynamic noise remains difficult because of the large computing resources, the expensive cost and physical/numerical issues inherent in CAA. The ISDM is recently developed for the efficient computation of aerodynamic noise generation and propagation in low Mach number flows in which dipole source, originating from unsteady pressure fluctuation on a solid surface, is known to be more efficient than quadrupole sources. The multi-scale overset grid technique is also applied to resolve the complex geometries. Through the illustrative application to the benchmark problem, it will be shown that the current methods can broaden the application area of computational aeroacoustic techniques to practical aeroacoustic phenomena, enhancing both the speed and accuracy of the computation.

INTRODUCTION

Aeolian tones from flow over cylinders are relevant to airframe and power plant noise (tubular heat exchanger, power transmission lines and chimneys). The purpose of this benchmark problem is to test the ability of a CFD/CAA code to accurately and effectively predict sound generation by viscous flows over a blunt body and sound propagation through interactions with solid wall and moving flows.

Numerical dissipation and numerical dispersion are the two primary sources of error associated with computational schemes. Recent reviews of computational aeroacoustics by Tam (ref. 1) and Wells et al. (ref. 2) have discussed various numerical schemes currently popular in CAA. These include many compact and non-compact optimized schemes such as the family of high-order compact differencing schemes (refs. 3 to 5) and DRP scheme (ref. 6). They are all centered non-dissipative schemes, a property that is desirable for linear wave propagation. However, the DRP scheme has been more favored due to its simple and robust algorithm. The DRP scheme is implemented by using a symmetric finite difference stencil on a uniform Cartesian Grids. In this environment, the classic DRP schemes minimize numerical dispersion errors while producing essentially no dissipation errors. However, practical problems in aeroacoustics are seldom confined to uniform Cartesian geometry, with the associated computational grids usually being non-uniform or curvilinear. GODRP schemes (ref. 7) have been developed with the grid-optimization algorithm to make the finite difference equations possess the same dispersion relations as the corresponding partial differential equations and, at the same time, optimized dissipation characteristics at the given grids that are the non-uniform Cartesian or curvilinear grids. In this work, the GODRP schemes are utilized to solve this complex geometry problem with curvilinear grids on a guarantee of local and, thus resultant global dispersion-relation-preserving properties.

---

[*] BK21 Post Doctor, accu99@snu.ac.kr
[#] Ph. D. Candidate, jwryu1@snu.ac.kr
[†] Professor, solee@plaza.snu.ac.kr, Bldg. 301-1303, Seoul National University, Seoul 151-742, Korea

For many industrial problems originating from aerodynamic noise, computational aeroacoustics (CAA) technique, reliable and easy to apply, would be of great value to engineers and manufacturers. Recent and spectacular achievements in the understanding of aerodynamic noise generation mechanism are based on the CAA technique using the direct calculation of the acoustic field by solving the unsteady compressible Navier-Stokes equations. Most of them are related to jet noise phenomena, on which the direct numerical simulations (ref. 8) are carried out, providing directly an acoustic far field conformable to measurements. However, direct computation of the aerodynamic noise radiated by a subsonic flow remains difficult because of the large computing resources, the expensive cost and physical/numerical issues (ref. 1) inherent in CAA. These difficulties lead to alternative methods, so-called hybrid methods. These methods are based on the concept of variable decomposition in the governing equations into a source component and an acoustic one, which leads to two separate sets of equations governing viscous flow field and acoustic disturbance field, respectively. This approach is based on the assumption that the wave propagation is essentially inviscid in nature and sound perturbations are so small that their contribution to the convection velocity of the flow is negligible in most cases. The most important advantage of the decomposition method is that algorithms are used that best suited to each solver: traditional CFD algorithms for the viscous flow and CAA algorithms for the acoustic perturbations. These separate solvers accommodate the disparate length scales (i.e., acoustic and convective) associated with low Mach number aeroacoustics. The convective length scales are resolved on a hydrodynamic grid, while the acoustic length scales are resolved on a separate acoustic grid. Immersed surface dipole model (ISDM, ref. 9) are recently developed for the efficient computation of aerodynamic noise generation and propagation in low Mach number flows in which dipole source, originating from unsteady pressure fluctuation on a solid surface, is known to be more efficient than quadrupole sources. In this work, ISDM combined with the acoustic/viscous splitting method is utilized for this low-Mach number aeroacoustic problem.

It is very difficult to construct a single body-fitted mesh for twin cylinders which gives the proper resolution to both the near source region and far acoustic field. The complex geometries and large disparate length scales are overcome by the use of a multi-scale overset grid technique, where body-fitted meshes are applied only near the cylinders and multi-scale Cartesian background mesh is applied elsewhere.

In Section 2, fundamental formulations for the acoustic disturbance are given. The model of immersed surface dipole source terms forcing the disturbance equations is presented. Incompressible Navier-Stokes equations and turbulence model for viscous flow are also given. In Section 3, numerical methods for the acoustic and flow solvers are described. General numerical method modeling the surface dipole source terms is also given. In Section 4, Aeolian tone from the cross flow past twin-cylinders are investigated with the prescribed methods. Detailed discussion on the numerical results is presented. Final section is devoted to the concluding remarks.

FUNDAMENTAL EQUATIONS

The wave generation process is generally believed to be hardly affected by viscosity. We therefore begin with the unsteady Euler equations

$$\frac{\partial \rho}{\partial t} + \frac{\partial}{\partial x_j}\rho v_j = 0, \quad \frac{\partial}{\partial t}\rho v_i + \frac{\partial}{\partial x_j}\rho v_i v_j + \frac{\partial p}{\partial x_i} = 0 \quad \text{and} \quad \frac{\partial}{\partial t}\rho e_0 + \frac{\partial}{\partial x_j}\rho h_0 v_j = 0 \cdot \tag{1}$$

where $e_0 \equiv e + 1/2 \cdot v^2$ denotes the stagnation total energy (e = total energy) and $h_0 \equiv h + 1/2 \cdot v^2$ represents the stagnation total enthalpy (h = the enthalpy). The energy conservation equation of (1) can be transformed to an equation for the pressure p by using the relation $(\partial e / \partial p)_s = p / \rho^2 c^2$.

$$\frac{\partial p}{\partial t} + v_j \frac{\partial p}{\partial x_j} + \gamma p \frac{\partial v_j}{\partial x_j} = 0 \tag{2}$$

Where γ designates the ratio of specific heats, and is taken as $\gamma = 1.4$ for air. This equation (2) will be used instead of the energy equation because pressure is a quantity of great interest to acoustic problems.
The dependent variables can be divided into their base flow components and into their residual components such that $\rho = \bar{\rho} + \rho'$, $p = \bar{p} + p'$ and $v_i = \bar{v}_i + v_i'$. By inserting these decomposed variables to Eqs. (1) and (2) and then, by subtracting the resultant equations from the viscous flow equations satisfied by the base flow components, governing equations for the residual components can be obtained. It is evident that different choice of the base flow variables leads to the different forms of acoustic governing equations (ref. 10).

If the base flow is a steady mean flow, the 2-D governing equations for the residual components are written as the following form (ref. 11).

$$\frac{\partial \mathbf{U}}{\partial t} + \frac{\partial \mathbf{E}}{\partial x} + \frac{\partial \mathbf{F}}{\partial y} + \frac{\partial \mathbf{E}_{nl}}{\partial x} + \frac{\partial \mathbf{F}_{nl}}{\partial y} + \mathbf{H} = \mathbf{S} \tag{3}$$

where $\mathbf{U}$ is the unknown vector, $\mathbf{E}$ and $\mathbf{F}$ are the linear flux vectors, $\mathbf{E}_{nl}$ and $\mathbf{F}_{nl}$ are the nonlinear flux vectors, and the vector $\mathbf{H}$ consists of mean flow gradient terms, which are equal to zero when mean flow is uniform. The vector $\mathbf{S}$ represents possible unsteady sources in the flow.

Assuming isentropic flows, noise generation is provided by source terms in the momentum equation of Eq. (3). In present method, the source terms are modeled with the immersed surface dipoles (ref. 9) of magnitude corresponding to the hydrodynamic unsteady pressure fluctuations on a solid surface.
First, let's introduce a function f(x,t) where f is negative within the control surface, positive within the surrounding fluid and f also satisfies the equations $|\nabla f| = 1$. Also, define a Heaviside function H(x), by

$$H(x) = \begin{cases} 1 & for \quad x > 0 \\ 0 & for \quad x < 0 \end{cases}. \tag{4}$$

Then H(f) vanishes within the control surface and is equal to unity in the region exterior to the surface. Gradient of given fluctuating pressure in a solid body can be recast into the following form,

$$\nabla \left(P \cdot H(f) \right) = H(f)\nabla P + P\nabla H(f) = H(f)\nabla P + P\nabla f \delta(f) \tag{5}$$

where $P(\mathbf{x},t) = p(\mathbf{x},t) - p_0(\mathbf{x})$ and $p_0(\mathbf{x}) = \lim_{T \to \infty} \frac{1}{T}\int_{-T}^{T} p(\mathbf{x},t)dt$

Then, in computation domain,

$$\nabla \left(P \cdot H(f) \right) = P\nabla f \delta(f). \tag{6}$$

Figure 1. Schematic diagram of the procedure for the immersed surface dipole modeling

Then, the vector $\mathbf{S}$ is written as

$$\mathbf{S} = \begin{bmatrix} 0 & S_1 & S_2 & 0 \end{bmatrix}^T = \begin{bmatrix} 0 & P\delta(f)\nabla f_1 & P\delta(f)\nabla f_2 & 0 \end{bmatrix}^T \tag{7}$$

Data provided by incompressible or compressible simulations can be used to estimate S_i. The compressible simulations, however, must be used with special caution. In the compressible case, the acoustic field is included in the source terms, through density and fluctuating velocity. Although these acoustic components are very small compared to hydrodynamic fluctuations, they decay very slowly. Hence, their contribution might have a considerable influence on the predicted acoustic pressure magnitudes. The philosophy of covering a body surface with immersed surface dipole models (ISDM) is schematically described in Fig. 1.

Present approach is focused on low Mach number flows. Thus the 2-D incompressible Reynolds-Averaged Navier-Stokes (RANS) equations are used as the governing equations for viscous flow. Eddy viscosity ν_t is modeled from the low Reynolds number κ– ε turbulence model by Chen et al. (ref. 12).

NUMERICAL METHODS

The Cartesian coordinates employed in equation (3) are inconvenient for complex geometries. The spatial derivatives expressed as functions of coordinates (x, y) may be recast as functions of curvilinear coordinates (ξ, η) by a general transformation. Then, Eq. (3) in a physical domain is expressed by the coordinate variables in a computational domain.

$$\frac{\partial \mathbf{U}^*}{\partial t} + \frac{\partial \mathbf{E}^*}{\partial \xi} + \frac{\partial \mathbf{F}^*}{\partial \eta} + \frac{\partial \mathbf{E}^*_{nl}}{\partial \xi} + \frac{\partial \mathbf{F}^*_{nl}}{\partial \eta} + \mathbf{H} = \mathbf{S} \tag{8}$$
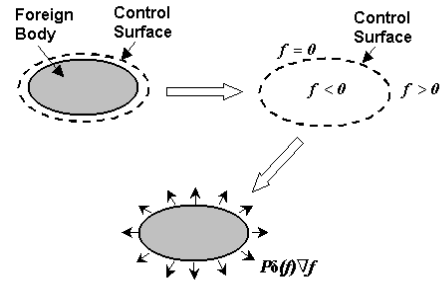
where $\mathbf{U}^* = \dfrac{\mathbf{U}}{J}$, $\mathbf{E}^* = \dfrac{1}{J}\left(\xi_x\mathbf{E} + \xi_y\mathbf{F}\right)$, $\mathbf{F}^* = \dfrac{1}{J}\left(\eta_x\mathbf{E} + \eta_y\mathbf{F}\right)$, $\mathbf{E}^*_{nl} = \dfrac{1}{J}\left(\xi_x\mathbf{E}_{nl} + \xi_y\mathbf{F}_{nl}\right)$, and $\mathbf{F}^*_{nl} = \dfrac{1}{J}\left(\eta_x\mathbf{E}_{nl} + \eta_y\mathbf{F}_{nl}\right)$.

Here, $J = \left(x_\xi y_\eta - x_\eta y_\xi\right)^{-1}$.

All the variables are nondimensionalized with the following scales: D (diameter of a cylinder) for the length scale, c_∞ for the velocity scale, D/c_∞ for the time scale, ρ_∞ for the density scale and $\rho_\infty c_\infty^2$ for the pressure scale, where c_∞ is the ambient speed of sound. The 7-point stencil, Grid-Optimized Dispersion-Relation-Preserving (GODRP) Scheme of Cheong & Lee (ref. 7) is utilized for the spatial flux derivatives of Eq. (8). Tam & Webb (ref. 6) have shown that if a given numerical scheme and the governing equations have the same dispersion relations, the numerical and exact solutions will have the same wave propagation characteristics and wave speeds. The GODRP schemes have been developed with the grid-optimization algorithm to make the finite difference equations possess the same dispersion relations as the corresponding partial differential equations on general geometries. Eq. (8) is discretized in space by the GODRP scheme as

$$\frac{\partial \mathbf{U}_{i,j}}{\partial t} = -\sum_{l=-3}^{l=3}\left[a_{\xi l \; (i,j)}\left(\mathbf{E}^*_{i+l,j} + \mathbf{E}^*_{nli+l,j}\right) + a_{\eta l \; (i,j)}\left(\mathbf{F}^*_{i,j+l} + \mathbf{F}^*_{nli,j+l}\right)\right] - \mathbf{H}_{i,j} + \mathbf{S}_{i,j} \tag{9}$$

where $a_{\xi l(i,j)}$ and $a_{\eta l(i,j)}$ are the lth optimized coefficients of the GODRP finite difference scheme at the (i, j) points along the ξ- and η- direction, respectively. The coefficients is chosen by requiring that the numerical wave number vectors of the finite difference scheme be a close approximation to the exact wave number of the corresponding partial differential equations. For more detailed description on the GODRP scheme, refer to ref. 7. In some cases it is necessary to remove spurious numerical oscillations due to non-linearities or mismatches with the boundary conditions or the initial conditions. These short waves can be filtered by an artificial selective damping proposed by Tam & Shen (ref. 13). Time integration is performed with the low-dissipation and low-dispersion Runge-Kutta schemes by Hu et al. (ref. 14) for their minimized dissipation and dispersion errors for wave propagation. Across the outflow boundaries of the computational domain, flow of information is associated with acoustic waves, vorticity waves and entropy waves. At these boundaries there is only one incoming characteristic, and only the pressure perturbation satisfies the convected wave equation. Therefore, B_1 operator of Bayliss and Turkel (ref. 15) is also used here, but for the pressure perturbation only. The other boundary conditions are formed by the linearized momentum equations and the equation of conservation of the acoustic speed, as adapted from Tam and Webb (ref. 6). For a high-order finite difference scheme the order of the difference equations is higher than that of the Euler equations. Thus the zero normal velocity boundary condition is insufficient for defining a unique solution. Extraneous numerical conditions must be imposed. Ghost value of pressure (ref. 16) is used as the extraneous boundary condition.

The very act of discretization causes many numerical artifacts. Modeling of the delta function in the analytic expression for immersed surface dipole sources is required for a discrete numerical simulation. The delta function is modeled as

$$\delta(\mathbf{x}) \cong \left(\ln 2 / \pi\sigma^2\right)^{\frac{n}{2}} \exp(-\ln 2 \cdot \mathbf{x}^2 / \sigma^2), \tag{10}$$

where n ($= 1$ or 2 or 3) denotes the dimension of delta function. Both sides of the equations satisfy the following space integral equation if $n = 2$.

$$\int_{-\infty}^{\infty}\int_{-\infty}^{\infty}\delta(\mathbf{x})dx_1 dx_2 = \int_{-\infty}^{\infty}\int_{-\infty}^{\infty}\left(\ln 2 / \pi\sigma^2\right)\exp(-\ln 2 \cdot \mathbf{x}^2 / \sigma^2)dx_1 dx_2 = 1 \tag{11}$$

Although Eq. (11) guarantees the conservation of total energy of the delta function, i.e., the acoustic sources, there is still difference in the distribution of source. It is evident that, as the value of σ is decreased, modeling Eq. (10) becomes more close approximation for the delta function. Combining (7) and (10), immersed surface dipole model is numerically expressed as

$$S_i(\mathbf{x}, t) = P(\mathbf{x}, t) \cdot \left(\ln 2 / \pi\sigma^2\right)\exp(-\ln 2 \cdot f(\mathbf{x}, t)^2 / \sigma^2)\nabla f_i(\mathbf{x}, t) \tag{12}$$

In real applications where a solid body exists, Eq. (12) needs to be slightly changed because the solid body replaces the some portion of the immersed surface dipole sources and thus, Eq. (11) can not be satisfied in a fluid region. Therefore, correction factor, C is multiplied to Eq. (12) as follows

$$S_i(\mathbf{x},t) = P(\mathbf{x},t) \cdot C \cdot \left(\ln 2 / \pi\sigma^2\right) \exp(-\ln 2 \cdot \mathrm{f}(\mathbf{x},t)^2 / \sigma^2) \nabla \mathrm{f}_i(\mathbf{x},t) \tag{13}$$

where $C = 1 / \left(\int\limits_{-\infty}^{\infty}\int\limits_{-\infty}^{\infty} \left(\ln 2 / \pi\sigma^2\right)\exp(-\ln 2 \cdot \mathbf{x}^2 / \sigma^2)dx_1 dx_2 - \int_B \left(\ln 2 / \pi\sigma^2\right)\exp(-\ln 2 \cdot \mathbf{x}^2 / \sigma^2)dx_1 dx_2 \right)$ and B denotes the region that the solid body occupies.

The numerical method used for viscous flow simulation is based on the unstructured grid finite volume method, which has been described in detail by Kang et al. (ref. 17). The scheme has extended the unstructured grid Navier-Stokes procedure for incompressible flows developed by Thomadakis et al. (ref. 18) to allow collocated storage of all variables. Since Thomadakis et al. used a staggered-grid formulation, pressure is stored at the centroid of a cell while velocity components are stored at grid points. However, the scheme has modified this procedure to employ collocated storage (non-staggered) in order to obviate the difficulties and disadvantages of implementing a non-collocated (staggered) mesh within the unstructured methodology. The algebraic pressure equation is derived by substituting the discretized momentum equations into the continuity equation (ref. 19). The process of deriving the pressure equation is almost the same as one used for a structured grid method. The scheme uses the Quadratic Upstream Interpolation for Convective Kinematics (QUICK) scheme for the convective terms and the second order Euler backward difference for time derivatives to keep second order accuracy spatially and temporally. All other spatial derivatives are approximated by the central difference schemes.

NUMERICAL RESULTS

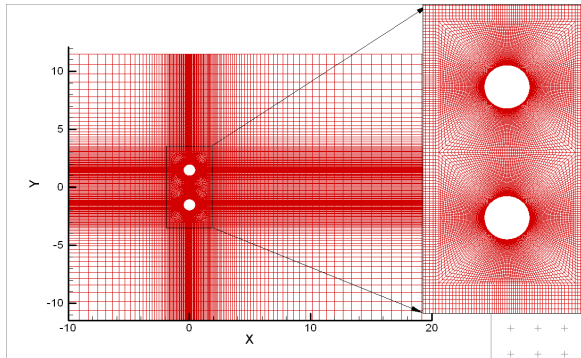### 1. Numerical Results for Viscous Flow Simulations

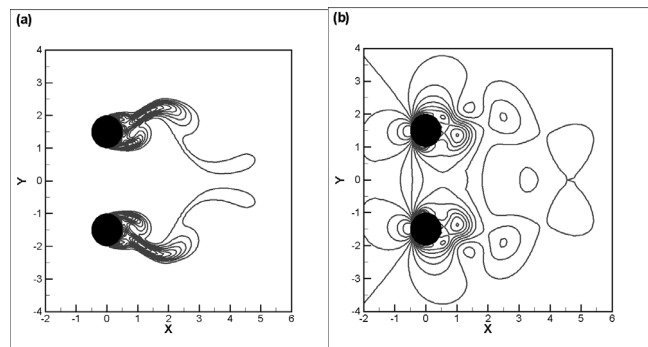Figure 2. The mesh for the viscous flow simulation

Figure 3. Instantaneous, non-dimensional (a) *k, 10 levels from 0.1 to 1.0* and (b) Pressure contours, 13 levels from –0.8 to 0.4

The flow calculations are carried out on a mesh with approximately 41,103 points in the computational domain. Pictures of the mesh and its close-up are shown in Fig.2. The mesh for viscous flow simulation consists of two types of grids: Inner mesh is the multiply connected grid and outer one is the Cartesian grid. Initially, random disturbances are imposed on a uniform velocity to quickly generate vortex shedding. The computational time step is fixed to be $\Delta t = 0.01/(D/u_\infty)$. Fig. 3 shows the iso-contours of turbulence kinetic energy and pressure at certain time instant. It is evident that Anti-phase lift and In-phase drag forces exerted on the cylinder surface fluctuate in time due to the periodic shedding of vortices. The frequency or period of vortex shedding can be estimated by evaluating those of the oscillating lift or drag coefficient. Time-dependent

Figure 4. Time dependent signals of C_l and C_d

signals of lift and drag coefficients are presented in Fig. 4, where the lift and drag coefficients. As the computation

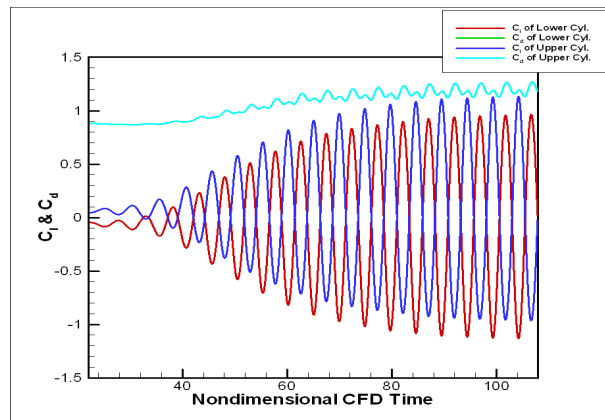begins with an initial condition that is given by the flow solutions, vortex shedding does not occur for a considerable time. However, after the first shedding happens, the flow goes through a transient state to arrive to the state of periodic shedding of vortices. Lift and drag coefficients show a sinusoidal variation corresponding to a Strouhal number of 0.2 and 0.4, respectively. This value is in good agreement with the experimental measurement (ref. 20).

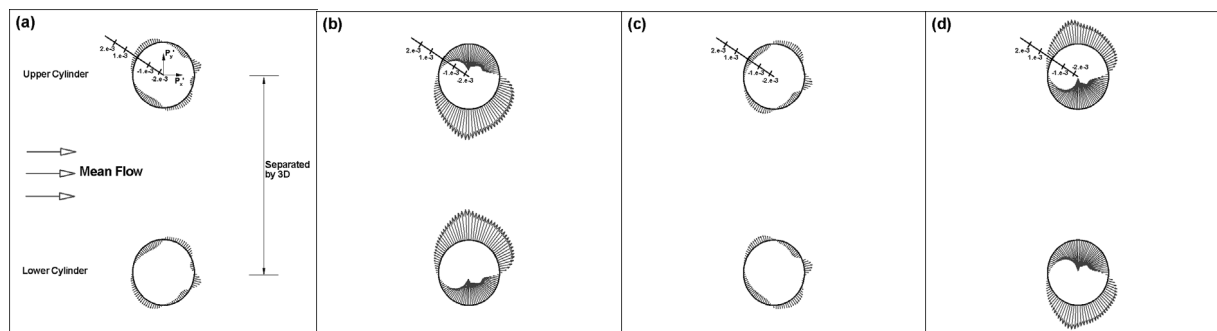## 2. Numerical Results of CAA Solver

Figure 5. A sequence of simultaneous surface fluctuating pressure ($P = p - p_0$) at (a) one quarter of a cycle, (b) a half cycle, (c) three quarters of a cycle, (d) the beginning of a cycle.

Hydrodynamic unsteady data provided by the previously calculated viscous flow simulation using incompressible RANS are now used to build up the source terms of Eq. (7). They are recorded every iteration during one period on solid surfaces for dipole sources. Non-dimensional period T_f of the flow simulation equals 4.9 with $\Delta t_f = 0.01$, i.e. 490 data points. Unsteady hydrodynamic pressures corresponding to dipole sources are stored on the cylinder surfaces consisting of 101 grid points, respectively. Physical time is non-dimensionalized by D/U_∞ in the viscous flow simulation and by D/C_∞ in the acoustic simulation. Different time-scale of the acoustic simulation from the viscous flow simulation
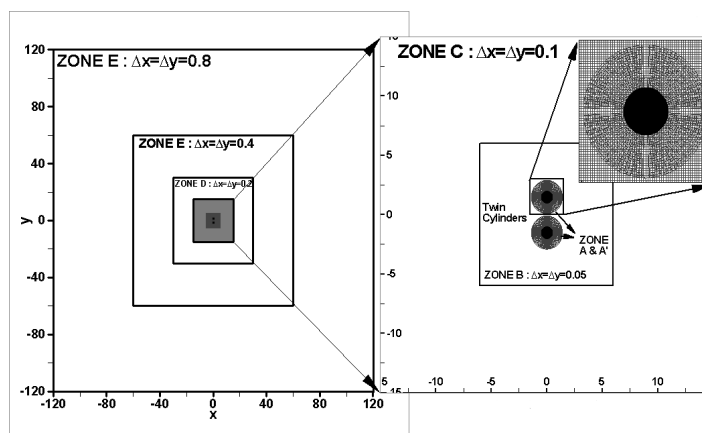

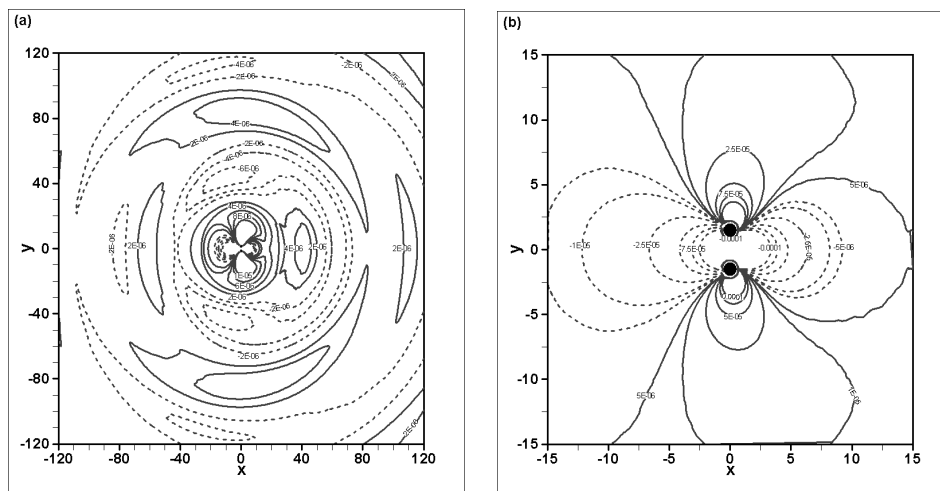**Figure 6. Multi-scale overset grid for the acoustic simulation**

Figure 7. Instantaneous fluctuating pressure distribution at T = 180 (a) over whole field and (b) at near field

leads to the different non-dimension period $T_a = 68.08$ and numerical time step $\Delta t_a = 0.02$, i.e. *3404* data points. Furthermore, full computation domain of the computational aeroacoustics covers the far-field reaching to *120D* in this computation, i.e. acoustic field as well as the near-field, i.e. source field. Thus raw data of the viscous flow are transformed into those of the acoustic grid and time by interpolation in space and time. Figures 5 shows the fluctuating pressure *P* on the cylinder surface at one quarter of a cycle, at a half cycle, at three quarters of a cycle and at the beginning of a cycle, respectively. It is also observed that the fluctuating pressures show symmetric patterns. Fluctuating pressure data are utilized as input data to the immersed surface dipole model. The acoustic calculations are performed on a multi-scale overset mesh where body-fitted meshes are applied only near the cylinders and multi-scale Cartesian background meshes are applied elsewhere in the domains (see Fig. 6). Interpolation algorithm of Bin et al. (ref. 21) is used for the information exchange between the meshes. In this paper, acoustic calculations are executed without mean flow, i.e. with only the modeled source terms because of the shortage of the allowed paper length. .

In Fig. 7, fluctuating pressure field obtained from the simulation using the ISDM in ambient condition is plotted at non-dimensional time $T = 180$. As expected, the acoustic waves from lift and drag dipoles are mainly propagated in the direction normal and parallel to the mean velocity, respectively. Fig. 8 shows the pressure waveform along the y-axis ($y < 0$) at various times. These waveforms conform to the 2-dimensional wave propagation characteristics, i.e. decaying proportional to $r^{-0.5}$. The directivity patterns of the current simulation using the ISDM without mean flow, measured at $r = 10D$ and $r = 100D$ are shown in Fig. 9. The amplitudes of the fluctuating pressures from the lift and drag dipole sources are comparable for each other at $r = 10D$ while acoustic waves from the lift dipoles are more strength that those from the drag dipoles at $r = 100D$. Nevertheless, due to anti-phase of the lift dipoles of twin cylinders, the amplitude of acoustic wave in the direction normal to the mean-flow is reduced compared with that from single cylinder.
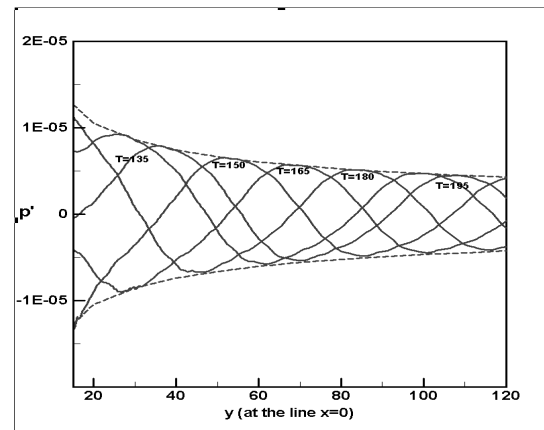

Figure 8. pressure distribution along the y-axis : ⸻ numerical results, − − − decay lines correspond to $a/r^{0.5}$ where *a* is the value of pressure at $y = 100$ in the lines of $T = 135$.
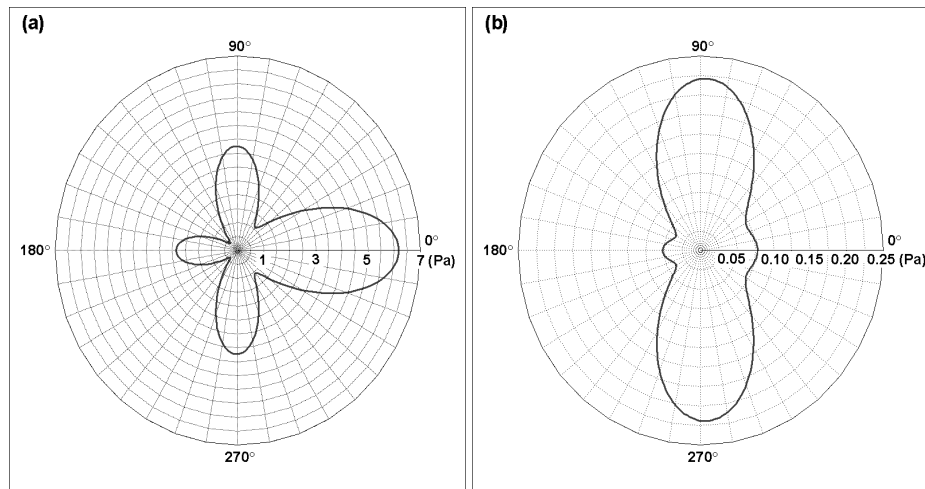

Figure 9. Directivity patterns of the mean square value of the fluctuating pressure (a)at $r = 10D$ and (b) at $r = 100D$

CONCLUDING REMARKS

The Grid-Optimized Dispersion-Relation-Preserving (GODRP) schemes are used for the computation of category 5, problem 1 in 4th CAA Workshop. The GODRP schemes have been developed with the grid-optimization algorithm to make the finite difference equations possess the same dispersion relations as the corresponding partial differential equations on general geometries. Acoustic/viscous splitting techniques with immersed surface dipole

model (ISDM) are utilized to solve the sound generation and propagation in viscous, low-Mach number flows for which direct computation of the aerodynamic noise remains difficult because of the large computing resources, the expensive cost and physical/numerical issues inherent in CAA. ISDM is recently developed for the efficient computation of aerodynamic noise generation and propagation in low Mach number flows in which dipole source, originating from unsteady pressure fluctuation on a solid surface, is known to be more efficient than quadrupole sources. The multi-scale overset grids technique is also applied to resolve the complex geometries. Through the illustrative application to the benchmark problem, it is shown that the current methods can broaden the application area of computational aeroacoustic techniques to practical aeroacoustic phenomena, enhancing both the speed and accuracy of the computation.

REFERENCES

1. Tam, C. K. W.: Computational Aeroacoustics: Issues and Methods. *AIAA J.* **33**,1995, pp. 1788-1796.
2. Wells, V.L.; and Renaut, R.A.: Computing Aerodynamically Generated Noise. *Annual Review of Fluid Mechanics* **29**, 1997, pp. 161-199.
3. Kim, J.W.; and Lee, D. J.: Optimized Compact Finite Difference Schemes with Maximum Resolution. *AIAA J.* **34**, 1996, pp. 887-893.
4. Deng, X.; and Zhang, H.: Developing High-order Weighted Compact Nonlinear Schemes. *J. Comput. Phys.* **165**, 2000, pp. 1-23.
5. Lele, S.K.: Compact Finite Difference Schemes with Spectral-Like Resolution. *J. Comput. Phys.* **103**, 1992. pp. 16-42.
6. Tam, C.K.W.; and Webb, J.C.: Dispersion-Relation-Preserving Schemes for Computational Acoustics. *J. Comput. Phys.* **107**, 1993, pp. 262-281.
7. Cheong, C.; and Lee, S.: Grid-optimized dispersion-relation-preserving schemes on general geometries for computational aeroacoustics. *J. Comput. Phys.* **174**, 2001, 248-276.
8. Freund, J. B.: Acoustic Sources in a Turbulent Jet: A Direct Numerical Simulation Study. Journal of Fluid Mechanics **438,** 2001, 277-305.
9. Ryu, J.; Cheong, C.; and Lee, S.: Efficient Computation of Flow Noise Generation and Propagation Using Immersed Surface Dipole Model Combined with Hybrid Methods. Journal of Sound and Vibration (In print)
10. Goldstein, M.E.; A unified approach to some recent developments in jet noise theory. International Journal of aeroacoustics **1**, 2002, pp.1-16.
11. Bogey, C.; Bailly, C.; and Juve D.: Computation of flow noise using source terms in linearized Euler's equations. AIAA J., 40, 2002, pp. 235-243.
12. Chen, K. Y.: Prediction of Channel and Boundary Layer Flows with a Low Reynolds Number Turbulence Model. *AIAA J.* 20, 1982, pp. 33-38,
13. Tam, C.K.W.; and Shen, H.: Direct computation on nonlinear acoustic pulses using high-order finite difference schemes. AIAA paper 93-4325, 1993.
14. Hu, F.Q.; Hussaini, M.Y.; and Manthey, J.L.: Low-dissipation and low-dispersion Runge-Kutta schemes for computational aeroacoustics. *J. Comput. Phys.* **124**, 1996, pp. 177-191.
15. Bayliss, A.; and Turkel, E.: Far field boundary conditions for compressible flow. *J. Comput. Phys.* **48**, 1982, pp. 182-199.
16. Tam, C.K.W.; and Dong, Z.: Wall boundary conditions for high-order finite difference schemes for computational aeroacoustics. *Theor. Comput. Fluid Dyn.* **8,** 1994, pp. 303-322.
17. Kang, D.J.; Bae, S.S.; and Joo, S.W.: An Unstructured FVM for the Numerical Prediction of Incompressible Viscous Flows. *Transactions of the KSME* **22,** 1998, pp. 1410-1421.
18. Thomadakis, M.; and Leschziner, M. A.: Pressure Correction Method for the Solution of Incompressible Viscous Flows on Unstructured Grids. *Int. J. Nume. Method in Fluids* **22**, 1996, pp. 581-600.
19. Hobson, G. V.; and Lakshiminarayana, B.: Prediction of Cascade Performance Using an Incompressible Navier-Stokes Technique. *J. Turbomachinery* **113**, 1991, pp. 561-572.
20. Kiya, M., et al.: Vortex Shedding From Two Circular Cylinders in Staggered Arrangement. Transactions of the ASME **102**, 1980, pp. 166-173.
21. Bin, J.; Cheong, C.; and Lee, S.; Optimized Boundary Treatment for Curved Walls for High-order Computational Aeroacoustics Schemes, *AIAA J.* (In print)

Computation of Tone Noises Generated in Viscous Flows

Ching Y. Loh
Taitech Inc.
Cleveland, Ohio 44135
Email: Ching.Y.Loh@grc.nasa.gov

Philip C.E. Jorgenson
National Aeronautics and Space Administration
Glenn Research Center at Lewis Field
Cleveland, Ohio 44135
Email: Jorgenson@nasa.gov

Abstract

Three benchmark problems from the current and previous CAA workshops involving tone noise generated in viscous flows are investigated using the CE/SE finite volume method. The CE/SE method is first briefly reviewed. Then, the benchmark problems, namely, flow past a single cylinder (CAA Workshop II problem), flow past twin cylinders (from the current CAA Workshop IV, Category 5, Problem 1) and flow past a deep cavity with overhang (CAA Workshop III problem) are investigated. Generally good results are obtained in comparison with the experimental data.

1 Introduction

The space-time conservation element and solution element (CE/SE) method [1,2] is a recently developed numerical method for solving conservation laws. Despite its formal second order accuracy in both space and time, it possesses low dispersion errors and low dissipation. The method may be categorized as a finite volume method, where the conservation element (CE) is equivalent to a finite control volume (cell) and the solution element (SE) can be understood as the space-time cell interface. The CE/SE scheme features:

1. conservation in both space and time—integral form of the governing equations is solved;
2. accurate (space-time) surface flux calculation;
3. conservative variables and their gradients are considered as unknowns—leads to improved accuracy using a compact cell stencil;
4. simple but effective non-reflecting boundary conditions (NRBC);
5. MILES (monotonically integrated large eddy simulation) type scheme [12, 13], the finite volume cell average process works as a spatial filter and the weighted average (van Albada) limiter plays a role somewhat like a subgrid scale (SGS) model;
6. naturally adapted to unstructured grids, relatively effortless implementation of computation—no numerical fix or parameter choice is needed;
7. robust enough to cover a wide spectrum of compressible flow—from weak linear acoustic waves to shocks—and appropriate for both CFD and CAA.

In this paper, the two-dimensional unstructured Navier-Stokes/Euler CE/SE solver is briefly described in §2. Based on this scheme, numerical investigations of the benchmark problems are presented consequently in §3, §4 and §5, with comparisons to experimental data.

2 The Two-Dimensional CE/SE Navier-Stokes/Euler Scheme
2.1 *Conservation form of the unsteady Euler equations*

Consider a dimensionless conservation form of the unsteady Euler equations for a perfect gas. Let ρ, u, v, p, and γ be the density, streamwise velocity component, transverse velocity component, static pressure, and constant specific heat ratio, respectively. The two-dimensional Euler equations then can be written in the following vector form:

$$\mathbf{U}_t + \mathbf{F}_x + \mathbf{G}_y = \mathbf{0}, \tag{1}$$

where x, y, and t are the streamwise, transverse, and time coordinates, respectively. The conservative flow variable vector $\mathbf{U}$ is given by

$$\mathbf{U} = \begin{pmatrix} U_1 \\ U_2 \\ U_3 \\ U_4 \end{pmatrix} = \begin{pmatrix} \rho \\ \rho u \\ \rho v \\ \rho e \end{pmatrix}, \quad e = p/\rho(\gamma - 1) + (u^2 + v^2)/2, \tag{2}$$

and the flux vectors $\mathbf{F}$ and $\mathbf{G}$ (including viscous fluxes) can be written in terms of $\mathbf{U}$. By considering (x, y, t) as coordinates of a three-dimensional Euclidean space E_3 and using the Gauss divergence theorem, it follows that Eq. (1) is equivalent to the following integral equation:

$$\oint_{S(V)} \mathbf{H}_m \cdot \mathrm{d}\mathbf{S} = \mathbf{0}, \qquad m = 1, 2, 3, 4, \tag{3}$$

where $S(V)$ is the surface around a volume V in E_3 and $\mathbf{H}_m = (F_m, G_m, U_m)$, $m = 1, 2, 3, 4$.
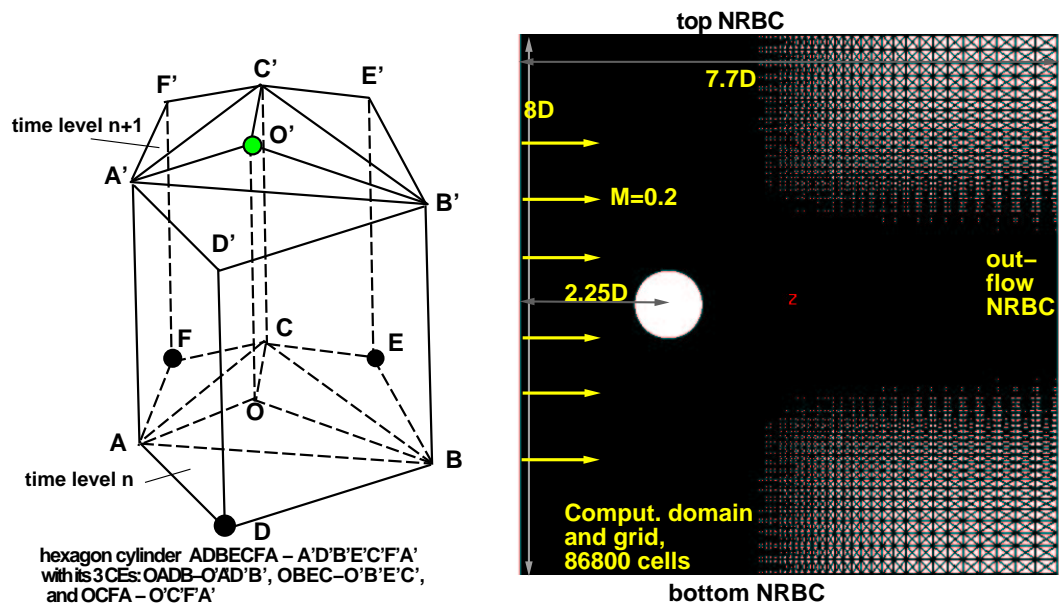
2.2 *Conservative updating*

In any explicit time-marching scheme, flow data at neighboring nodes at the previous time step are used to update flow data at the current node to the present time level. In most finite volume schemes a computational cell (e.g., the triangular cylinder with base $\triangle ABC$ in Fig. 1, left plot) is used as a control volume (CV). The first step is to determine the fluxes on its surfaces (e.g., $ABB'A'$ in Fig. 1, left plot). In the CE/SE algorithm, where not only the conservative flow variables, $\mathbf{U}$, but also their spatial derivatives are considered as unknowns (12 scalar unknowns in total), the CV is extended to a hexagon cylinder, with all the neighboring cell centers (D, E, F) included as vertices (Fig. 1, left plot). All of the surfaces (SEs) of the new composite CV, except the top surface (hexagon), are now associated with one of the three neighboring cell centers (D, E, F), where $\mathbf{U}$, $\mathbf{U_x}$, and $\mathbf{U_y}$ are known (at time step n). The advantage is that no extrapolation through the CV interior is needed in determining the fluxes. Furthermore, in order to achieve high resolution, flow data are computed by Taylor expansion from D to the centroids of the quadrilateral surfaces $ADD'A'$, $DBB'D'$ and $ADBO$, etc., *along* their surface planes. Compared to other updating techniques, conservative updating is truly multi-dimensional. It avoids the uncertainty of dimensional-splitting and extrapolation, and hence yields better accuracy.

2.3 *Evaluation of spatial gradients*

Applying Eq. (3) to the composite CV in Fig. 1 (left plot) directly yields $\mathbf{U^{n+1}}$ at the centroid of the top hexagon. Note that this location, in general, does not coincide with the triangle center O'. Furthermore, there are three hexagon cylinder composite CVs that partially overlap the current one. Because of this, three sets of derivatives, $\mathbf{U_x^{(i)}}$, $\mathbf{U_y^{(i)}}$, $i = 1, 2, 3$, can be constructed. The final values of the spatial derivatives at the current centroid, as well as at O', are obtained by applying the extended van Albada limiter (weighted average) to these, i.e.,

$$\mathbf{U_x^{n+1}} = \frac{\Sigma \mathbf{U_x^{(i)}} \phi_\mathbf{i}}{\Sigma \phi_\mathbf{i}}, \quad \mathbf{U_y^{n+1}} = \frac{\Sigma \mathbf{U_y^{(i)}} \phi_\mathbf{i}}{\Sigma \phi_\mathbf{i}},$$

where $\phi_i = \tau_i^{-1}$ if $\tau_i \neq 0$ and $\phi_i = 0$ otherwise; and $\tau_i = [(\mathbf{U_x^{(i)}})^\mathbf{2} + (\mathbf{U_y^{(i)}})^\mathbf{2}]^\alpha$, with α being any positive real index number. Finally, having determined $\mathbf{U_x^{n+1}}$ and $\mathbf{U_y^{n+1}}$, the solution $\mathbf{U^{n+1}}$ may now be transferred to the triangle center O'.

Figure 1. Left plot: CE/SE unstructured grid; three CEs and the hexagon cylinder CV in E_3; Right plot: Geometry of the computational domain and unstructured grid, $-2.2D \leqslant x \leqslant 5.5D$, $-4D \leqslant y \leqslant 4D$ for the one cylinder aeolian noise problem; seven exponentially stretched rectangular cells (as sponge zones) at the top and bottom are not shown.

2.4 *Non-reflecting boundary conditions (NRBCs)*

In the CE/SE scheme, NRBCs are constructed based on the first principle of plane wave propagation [3 , 5]. There are various variants of the NRBCs [5-8], the following are the NRBCs employed in the present paper. For a grid node (j, n) lying at the outer border of the domain, where j is the grid node index number and n the time step, the Type I NRBC requires that

$$(\mathbf{U_x})_\mathbf{j}^\mathbf{n} = (\mathbf{U_y})_\mathbf{j}^\mathbf{n} = \mathbf{0},$$

while $\mathbf{U_j^n}$ is kept fixed at the initially given steady boundary value. At the outflow boundary, where there are substantial gradients in the radial direction, the Type II NRBC requires that

$$(\mathbf{U_x})_\mathbf{j}^\mathbf{n} = \mathbf{0}, \quad \mathbf{U_j^n} = \mathbf{U_{j'}^n} \quad (\mathbf{U_y})_\mathbf{j}^\mathbf{n} = (\mathbf{U_y})_\mathbf{j'}^\mathbf{n}.$$

where j' is the nearest interior node. As will be observed later, generally, these NRBCs are robust enough to allow a near field computation without disturbing or distorting the flow and acoustic fields.

3 Aeolian Noise from a Single Cylinder (CAA Workshop II)

The current section and the two consequent sections are devoted to the numerical solution of the three benchmark problems. In this section, numerical results for the aeolian noise of a single cylinder [4] are presented and compared to their respective experimental data [9].

Consider a Mach number, M, of 0.2 uniform flow past a two-dimensional circular cylinder with a diameter, D, of $1.9cm$. Many researchers employ large computational domains comparable to the wavelength of the tone noises. In the present work, a relatively small near field computational domain is chosen. The domain size is only a fraction of the wave-length of the tone noise. The Fourier data sampling point is placed at a location beyond the reach of hydrodynamic waves (or vortex street) such that only aeroacoustic data is obtained.

Figure 1 (right plot) shows a sketch of the computational domain and the triangulated grid. The grid is obtained by dividing a rectangular cell into 4 triangles. By so doing, the advantage is that the cell size, which is important in aeroacoustics computation, is well-controlled. The diameter of the circular cylinder, the ambient speed of sound, and the ambient flow density are chosen as the scales for length, velocity, and density respectively. Although the grid
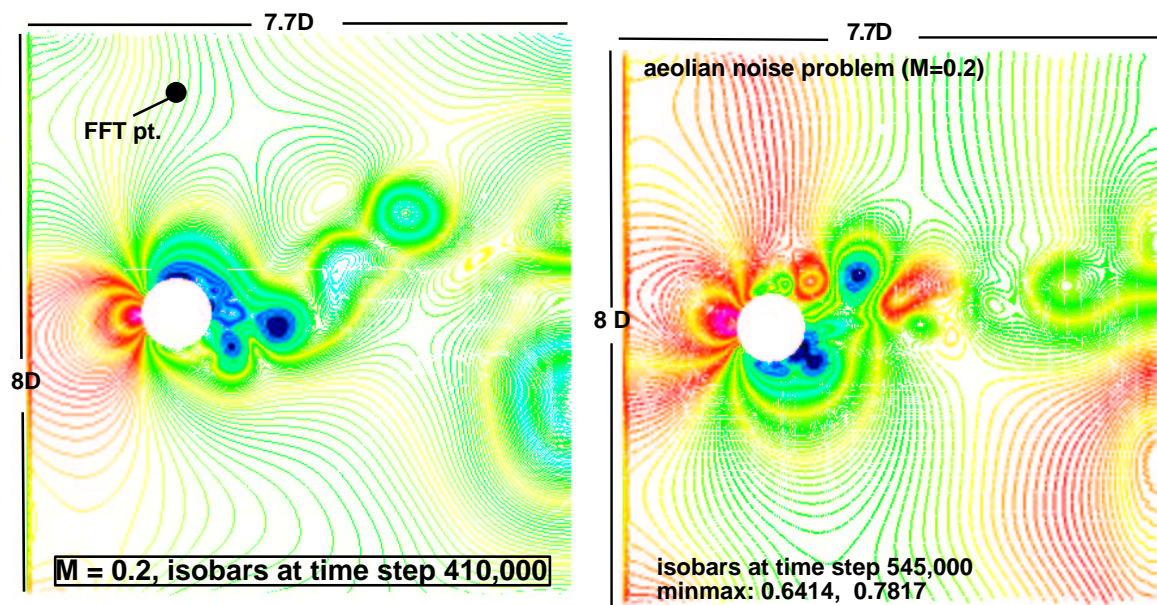
Figure 2.   Instantaneous isobars.

size is the smallest at the cylinder wall, it is not fine enough to resolve the details in the boundary layers. Still, good aeroacoustic data is collected. Even if the boundary layer is well resolved with a much refined grid (at a higher CPU cost), the boundary layer details will still be lost after flow separation and vortex roll-up, so they contribute very little to large scale turbulence and aeroacoustics.

3.1   *Initial conditions*

The entire flow field is initialized at ambient conditions, *i.e.*,

$$\rho_0 = 1.0, \quad u_0 = 0, \quad v_0 = 0, \quad p_0 = 1/\gamma,$$

All spatial derivatives are set to zero.

3.2   *Boundary conditions*

At the inflow boundary, the flow variables are specified as a uniform flow with a Mach number of 0.2:

$$\rho_i = 1.0, \quad u_i = 0.2, \quad v_i = 0, \quad p_i = 1/\gamma,$$

and their spatial derivatives are set to zero. Note that these inlet conditions also play a role as absorbing boundary conditions in the CE/SE scheme(Type I NRBC). At the surface of the circular cylinder, the no-slip wall condition is applied. The upper and lower boundaries are specified as Type I NRBCs. A Type II NRBC is applied at the outflow boundary.

3.3   *The unsteady flow and the vortex street*

In order to have a reasonable time series sampling size for FFT (fast Fourier transform) analysis, with a non-dimensional time step size of 0.005, over a half million time steps are run. Figure 2 shows the isobars at time step 410,000 and 545,000. The unsteadiness and the Karman vortex street in the wake are clearly illustrated. A point located at $(0D, 3.25D)$ is selected for recording the time series. At this location, there is no direct influence from the Karman vortex street. Figure 3 (left plot) depicts the result of the FFT, i.e., the sound pressure level (SPL) vs. frequency at this selected location. The SPL in dB is relative to the level of 20 μPa.
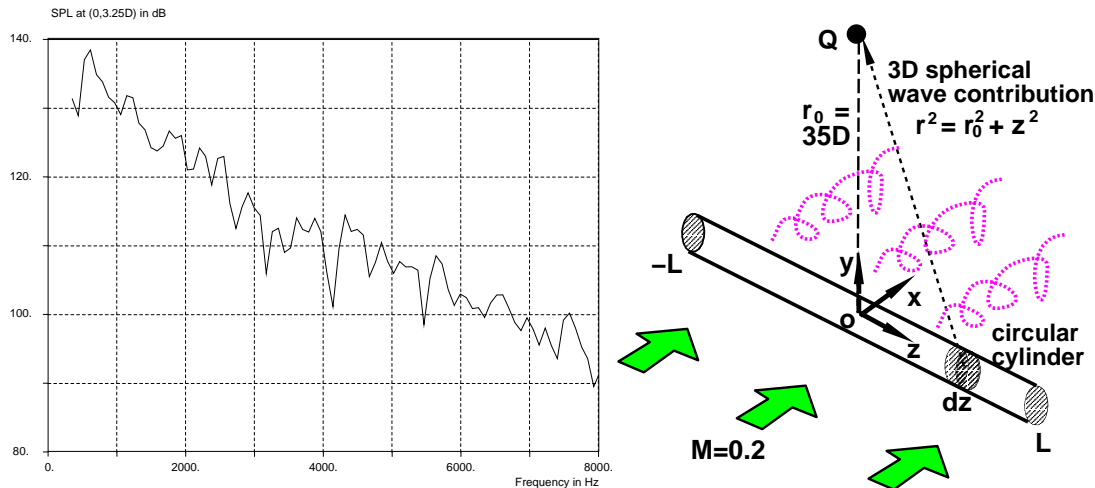
Figure 3. Left plot: Sound pressure level for Re=90,000 at (0, 3.25D), the highest peak corresponds to 617 Hz and 138 dB; Right plot: Estimate SPL at 35D, 90°.

3.4 *Tone noise frequency*

At a Reynolds number, Re, of 90,000 the highest peak of SPL in the plot corresponds to a computed frequency of 617 Hz (with a 3dB 'bandwidth' or binwidth of 88 Hz), which is quite close to the experimental one of 643 Hz [9] at this flow condition. A numerical experiment with a "very high" Reynolds number is also tested. The computed frequency is 652 Hz, which is slightly higher but still within a 4% range of the experimental value of 643 Hz. The phenomenon that the frequency (or Strouhal number) does not significantly change near this range of Re is justified by experimental observation (see Schlichting [10]) and also agrees with the observation of Townsend [11] that the large scale turbulence only weakly depends on the Reynolds number. The term "very high" used here is a synonym of turning off the viscous terms in the scheme. As a result of the numerical damping in the scheme, viscous effects still exist.

3.5 *Sound pressure level of the tone noise*

There is no direct comparison of the sound pressure level (SPL) to the experimental data which is of a three-dimensional nature and measured at a location $35D$ away from the circular cylinder center [9]. However, after some approximation and simple analysis from first principles, an estimated SPL for three-dimensional flow SPL at $r_0 = 35D$ at a point 90° to the flow direction can be obtained, Fig. 3, (right plot).

From the two-dimensional computation, at the point $(0D, 3.25D)$ (see the 'FFT point' in Fig. 2, left plot), an SPL of 138 dB is obtained. If the noise source is regarded to be a simple one and is located approximately at the circular cylinder centerline, for 2-D flow, the SPL attenuation is inversely proportional to r^2, where r is the distance from the source to the measuring point. Therefore, at the point Q $(0, 35D)$ the SPL is estimated to be:

$$SPL_{2d} = 138 - 20log(35D/3.25D) = 117.9dB.$$

This result is obtained under the two-dimensional assumption that the circular cylinder is infinitely long.

According to the experiment [9], a cylinder of length $10D$ is used. The point Q is assumed to be at the mid-plane normal to the cylinder centerline (the z direction), the cylinder rod ranges from $z = -5D$ to $z = 5D$. For a truly three-dimensional flow, let $p(z)$ be the r.m.s. pressure contribution from a line segment dz at z (coordinates along the cylinder centerline) to Q. Then

$$p(z) = \frac{r_0^2}{r_0^2 + z^2}p_0, \quad p_0 = p(0).$$

Table 1. **SPL of aeolian tone noise at 90° angle**

r (distance)	Experiment [9]	CE/SE numerical
3.25D		138 dB
35D	111 dB	110.4 dB (estimated)

Generally, let L be the half length of the cylinder, the square of the total sound pressure at Q is

$$p_L{}^2 = \int_{-L}^{L} p_0^2 \frac{dz}{[1 + (z/r_0)^2]^2} = r_0 p_0^2 [\alpha_0 + 0.5sin(2\alpha_0)],$$

where $\alpha_0 = tan^{-1}(L/r_0)$. Let $L = 5D$ and $L = \infty$ respectively and the ratio

$$R = \frac{p_{5D}^2}{p_\infty^2} = 0.1794612$$

Therefore, the sound pressure level at Q is estimated as:

$$SPL_{3d} = SPL_{2d} + 10logR = 110.4dB$$

Table 1 compares the numerical SPLs at these two locations at an angle of 90° with the available experimental data. Recall that the basic computation is two-dimensional, while the experimental data is for a circular cylinder of finite length in three-dimensional space. The agreement in this case is excellent.

4 Aeolian noise from twin cylinders (CAA Workshop IV)

Consider a uniform flow with a Mach number of 0.0714 (corresponding to the free stream velocity $24.5m/s$) past a pair of side-by-side two-dimensional circular cylinders with diameters, D, of $0.955cm$ and located $3D$ apart (center to center). A large computational domain is chosen in order to study the development of the vortex streets in the wake. The domain ranges $-12D \leqslant x \leqslant 30D$ and $-12D \leqslant y \leqslant 12D$ and has about 684000 unstructured triangular cells. The origin $(0,0)$ corresponds to the mid-point between the two cylinder centers. Instead of using a triangulated structured grid as in the previous problem, a truly unstructured triangular grid generated by Gridgen is used. Figure 4 (left plot) illustrates the grid around one of the cylinders. The purpose here is to find out how well a truly unstructured grid performs. The domain is decomposed into 8-12 subdomains using METIS and MPI is used to run the code on a parallel PC cluster.

After the Workshop, the same problem is run using another grid with smaller domain size $-3D \leqslant x \leqslant 5.5D$, $-6.5D \leqslant y \leqslant 6.5D$ and about 130,000 triangular cells are employed. Though the domain is much smaller, triangular cells are refined and relatively uniform around the wake area of the twin cylinders, rendering better aeroacoustic resolution.

The diameter of the circular cylinders, the ambient speed of sound ($a_0 = 343m/s$), and the ambient flow density are chosen as the scales for length, velocity, and density respectively. The initial and boundary conditions are almost identical to the previous problem except the free stream Mach number is smaller ($M = 0.0714$).

4.1 *Development of the vortex streets in the wakes*

Figures 4-6 illustrate respectively the snapshots of isobars, Mach number, and vorticity contours at time step 1.1 million. Near the twin cylinders, the contours exhibit symmetry with respect to the horizontal center line. This implies that the noise source is of the 'dipole' type. Around $20D$ downstream of the twin cylinders, the flow becomes highly asymmetrical, and vortex pairing occurs. However, since turbulence should have been fully developed in reality at this location, it is not clear that they represent true physics or just numerical artifacts due to the two-dimensional computation.

It should also be noted that at the workshop presentation, we presented the time-averaged p'^2, which is the true time averaged p'^2 which include the hydrodynamic waves in the vortex streets. It should *not* be interpreted or compared to the acoustic time averaged p'^2 from the acoustic models.
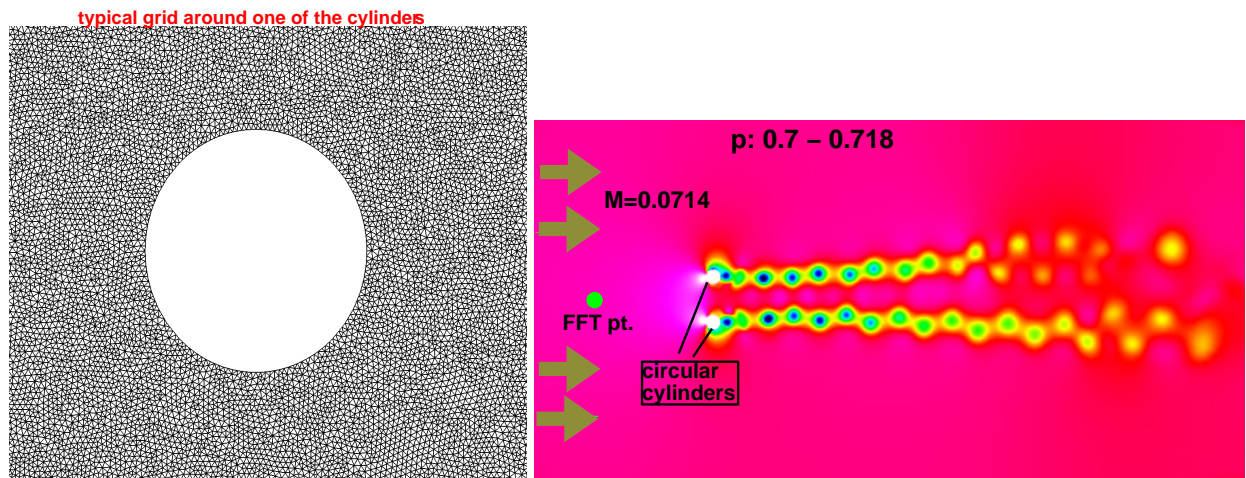
Figure 4. Left plot: Unstructured triangular grid around one of the cylinders; Right plot: Instantaneous isobars at time step 1,100,000.
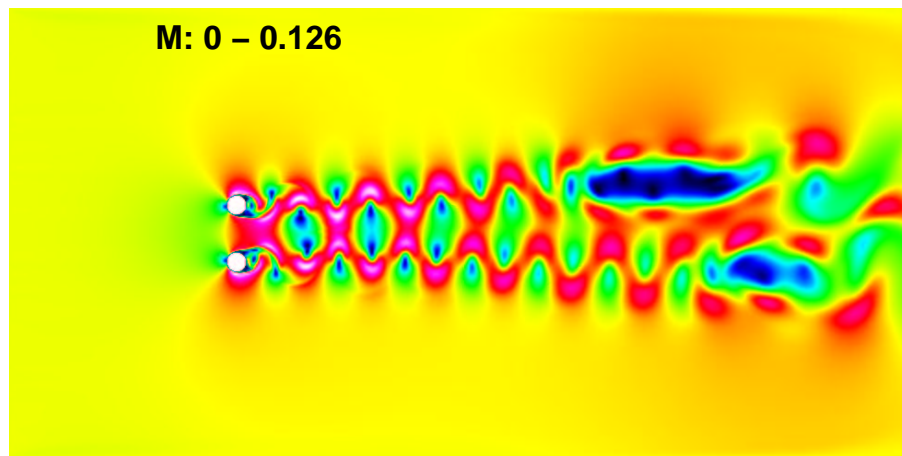

Figure 5. Instantaneous Mach No. at time step 1,100,000.

4.2 *Tone noise frequency and SPL*

Figure 7 depicts the result of the FFT, i.e., the sound pressure level (SPL) vs. frequency at a selected location $(0, 3.5D)$ for the second grid with a small domain. Again the SPL is relative to the level of 20 μPa. At a Reynolds number of 15800, the highest averaged peak of SPL in the plots corresponds to a computed Strouhal number, St, of 0.21 (with a 3dB 'bandwidth' or binwidth of 220 Hz), which is quite close to the experimental value $St = 0.205$. Figure 8 shows a plot of SPL vs. frequency for the larger domain (the first grid) but with unevenly distributed cells. The highest peak of SPL in the plot corresponds to a computed Strouhal number of 0.237 (with a 3dB 'bandwidth' or binwidth of 47 Hz), which is still reasonable, but less accurate than the the case with the second grid. Table 2 summarizes the comparison of experimental and numerical Strouhal number results. This shows that for an aeroacoustics computation, one should be cautious in choosing an unstructured grid.

5 Low-speed tone noise of a cavity with overhang (CAA Workshop III)

Cavity tone noises arise from an aeroacoustic feedback loop between the two edges of the cavity opening. At low subsonic Mach numbers (typically around or below Mach number of 0.1), or in the presence of a deep cavity, the noise due to flow-resonant phenomena occurs as well.

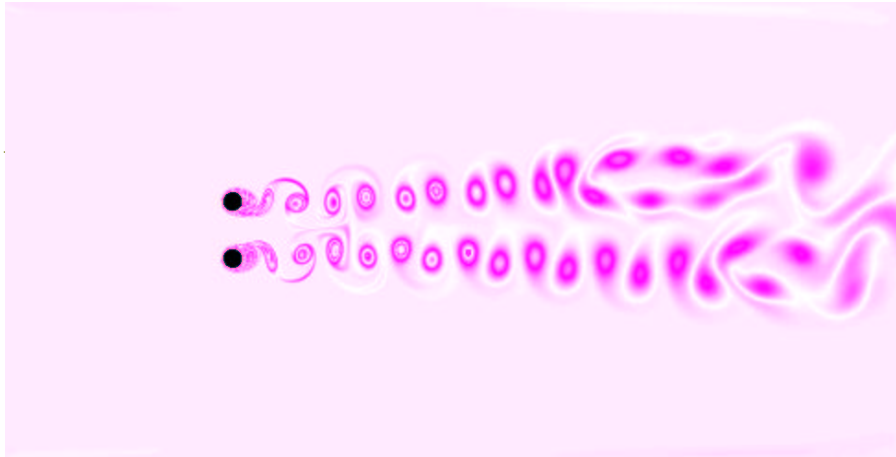In the present section, for low speed flows with Mach number as low as 0.08, a cavity with an overhang at the

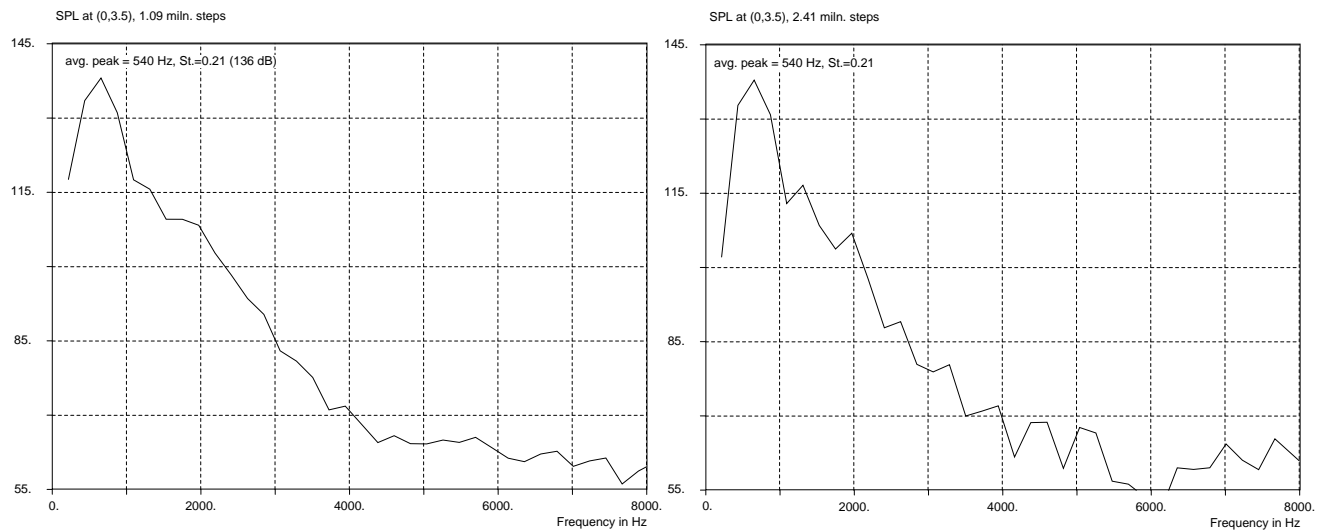Figure 6.   Vortex streets at time step 1,100,000.

Figure 7.   SPL vs. frequency at (0,3.5) for the small grid; Left plot: at time step 1,100,000; Right plot: at time step 2,400,000

Table 2.   **Tone noise frequency (Strouhal No. St) vs. Re**

Re	experimental	computational (1st grid)	computational (2nd grid)
1130		St.=0.237	
15800	St. = 0.205		St. = 0.21

opening (Fig. 9) is investigated. This is a prototype of the automobile door gap noise problem [14].

Figure 9 illustrates the geometric configuration and the actual dimensions of the cavity in the noise problem. Due to the presence of the overhang tongue, the two oscillation modes, namely, the fluid dynamic oscillation related to aeroacoustic feedback, and the Helmholtz fluid resonance in the cavity may emerge at the same time and compete with each other.
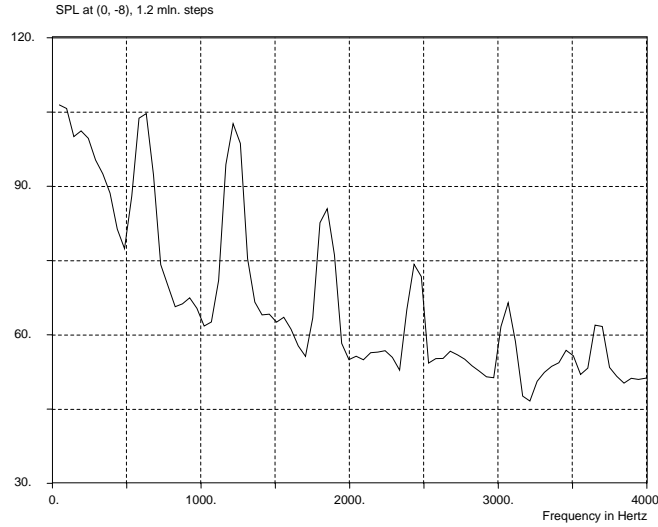
Figure 8.   SPL vs. frequency at (0, -8) for the large domain.
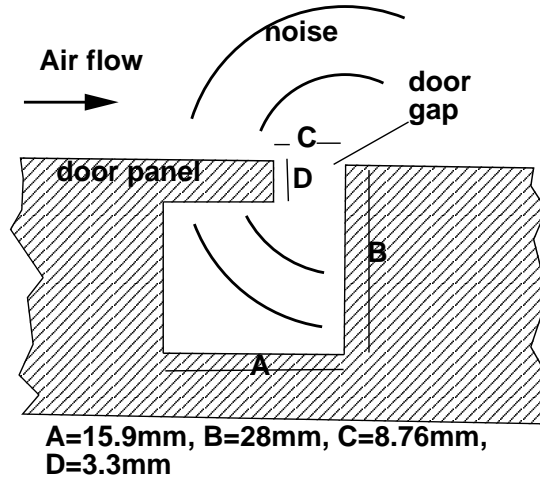
Figure 9.   Auto-door gap noise problem and the cavity dimensions.

Here, C is the length of the cavity opening. The dimension 2C is chosen as the length scale. The speed of sound ($343\ m/s$) and density of the ambient flow are the scales for velocity and density, respectively. In the current computation, there are about 85300 triangulated cells in the computational domain. The domain ranges $-1 \leqslant x \leqslant 2.1$ and $0 \leqslant y \leqslant 3.2$. The triangles are actually obtained by dividing a rectangular structured mesh cell into four pieces. The rectangular cell keeps a uniform size of $\Delta x = 0.00625$ and $\Delta y = 0.00625$ around the area of the opening and the interior of the cavity, but stretches near the outer boundaries. A nondimensional time step size of 0.0025 and a weighted average (van Albada limiter) index $\alpha = 0$ is employed in the CE/SE scheme.

5.1   *Initial and boundary conditions*

The flow field is initialized to the ambient conditions:

$$\rho_0 = 1.0, \quad u_0 = 0, \quad v_0 = 0, \quad p_0 = 1/\gamma,$$

All spatial derivatives are set to zero.
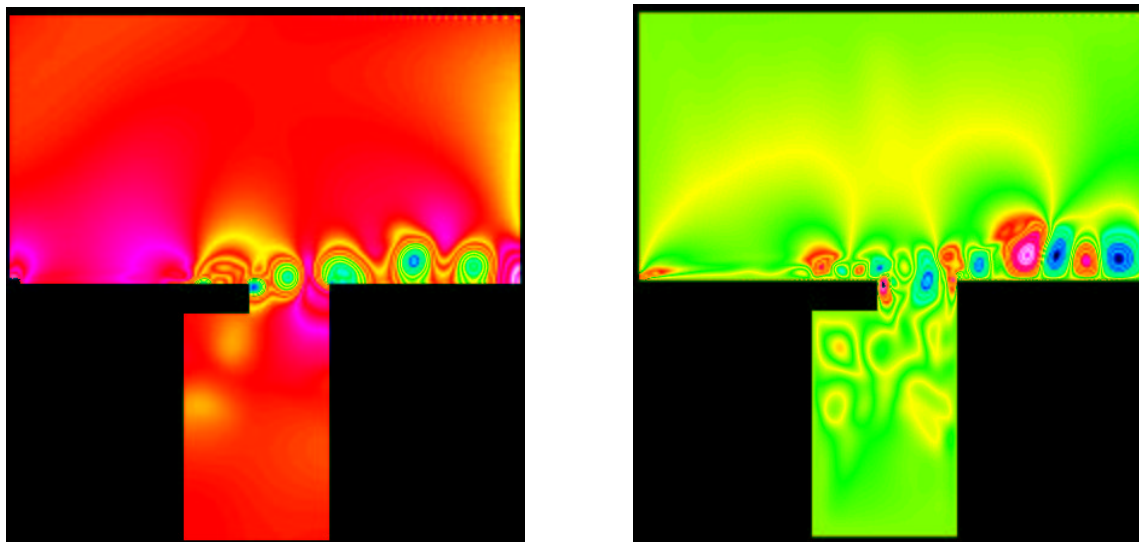
Figure 10. Left plot: Instantaneous isobars and Right plot: Instantaneous v- velocity contours at time step 740,000. Note that the color contrast is exaggerated here to highlight the flow features.

At the inflow boundary, the flow variables are specified as the uniform 'plug' flow:

$$\rho_i = 1.0, \quad u_i = M, \quad v_i = 0, \quad p_i = 1/\gamma,$$

and their spatial derivatives are set to zero. The Mach numbers range from 0.0788 to 0.147, corresponding respectively to flow speeds of $26.8\ m/s$ and $50\ m/s$. When a consistency test is conducted in §5.4, a prescribed profile is imposed to the u-velocity at the inlet boundary.

The no-slip wall boundary condition is applied to all the solid walls of the cavity body. The boundary condition at the domain top is the same as that specified at the inflow, which also acts as a Type I NRBC. At the outflow boundary, The Type II NRBC is imposed.

5.2 *Numerical results*

In this section, numerical results for the low speed cavity noises are presented and compared to their respective experimental data. As designed in the experiment, all the data are obtained at a location at the center of the inner left vertical wall of the cavity.

As mentioned earlier, for the overhung cavity considered here, there are two major modes for the tone noises: the fluid dynamic tone noise due to the feedback loop around the cavity opening, and the fluid-resonant tone noises due to the Helmholtz resonance of the cavity. In addition, there could exist other tone noise modes of uncertain origins or broadband noises, making the phenomena rather complicated. For the MILES approach, Fureby [13] points out that the numerical result is relatively insensitive to the subgrid scale model used in large eddy simulation (LES) but more dependent on the grid sizes. Generally, a finer grid yields more details in the acoustic field and higher SPL. It is important to choose a grid fine enough and an appropriate weighted average index number α.

In the following, numerical results corresponding to flow speeds of 50 m/s and 26.8 m/s are presented and compared to the respective experimental data [14]. For the case with flow speed of 50 m/s, several consitency tests for the numerical work are also conducted. All the SPLs are presented in dB based on their magnitudes against the standard $20\mu Pa$.

5.3 *Noise at flow speed of 50 m/s*

Figure 10 illustrates the isobars (left plot) and v-velocity (right plot) contours at time step 740,000 with time step size of 0.0025. The unsteadiness and the large scale turbulence or instability waves are clearly displayed. It is

SPL in dB

145.0

130.0

115.0

100.0

0.   1200.   2400.   3600.   4800.
Hz

SPL in dB, coarse grid

150.

120.

90.

60.

1875 Hz 2080 Hz

3960 Hz

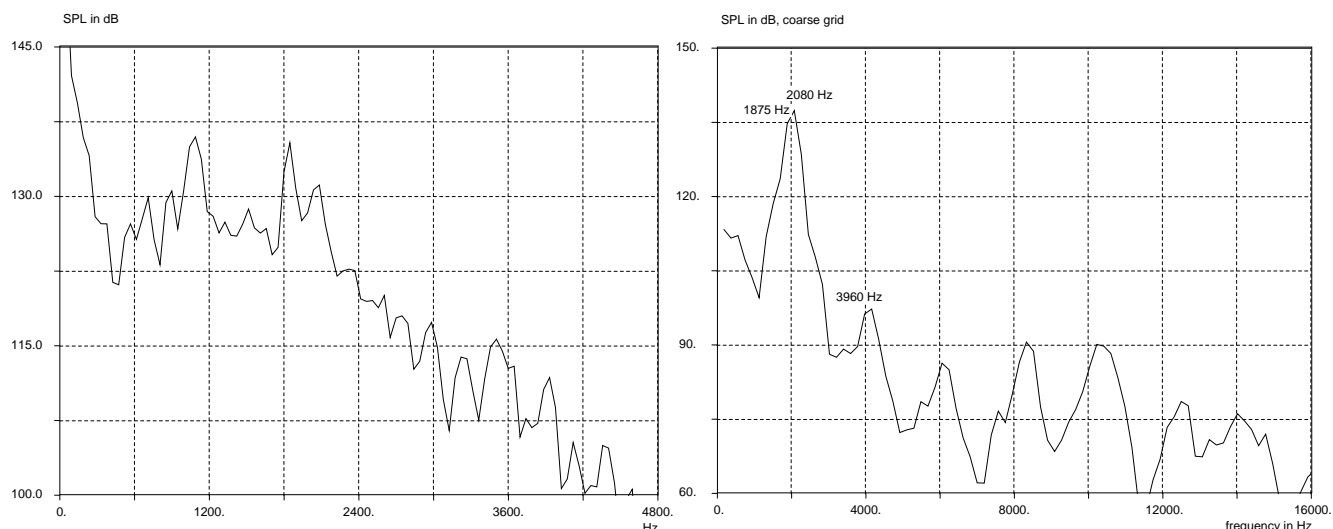0.   4000.   8000.   12000.   16000.
frequency in Hz

Figure 11.   Left plot: Sound pressure level (SPL) vs. frequency at a low speed of 50 m/s; Right plot: SPL vs. frequency at flow speed of 50 m/s with a coarse grid.

Table 3.   **Comparison of experimental and computed tone noises at 50 m/s**

Exp. Freq. Hz	Exp. SPL dB	Comput. Freq. Hz	Comput. SPL dB	Compt. Freq. Hz lrg. domain	Comput. SPL dB lrg. domain	Noise origin ? - unknown
930	103	1075	135	1062	131	?
1340	107	1326	127	1398	130	?
1824	134	1837	135	1860	129.6	feedback
2016	113	2062	130	2094	119	resonance
2848	106	2962	116	2808	111	?
3552	111	3513	115	3396	106	?

interesting to observe that the onset of the instability waves (vortices) does not occur right at the lip of the overhung tongue of the cavity, as expected for feedback oscillation, but occurs somewhat upstream. Evidently, the onset is triggered by the oscillation of cavity resonance. At the upper cavity surface around the overhung tongue, the turbulent boundary layer is disrupted and dominated by the large scale turbulence (vortices).

With a laminar uniform 'plug' flow at the inflow boundary, due to the no-slip wall boundary condition, a pulsating boundary layer is naturally formed, developed, and becomes turbulent near the overhung tongue of the cavity. No specific boundary layer thickness is given at the inlet. Table 3 provides a comparison of the experimental and computed data.

From Table 3, it is observed that for the fluid-dynamic feedback tone, the numerical results agree very well with the experimental data, 1837 Hz. vs. 1824 Hz and 135 dB vs. 134 dB. in SPL, with a binwidth (or bandwidth) of 47 Hz. The error in frequency or SPL is less than 1%, although Henderson stated that experimentally, when multiple tones occur in the spectrum, the preferred or dominant mode often changes randomly. This can result in a change of 3 dB or more in the peak sound pressure level [14]. For the Helmholtz cavity resonance, the frequencies are 2062 Hz vs. 2012 Hz with 2% error, while the error in SPL is larger. In addition, multiple tone peaks with lower SPL described

Table 4. **Comparison of experimental and computed tone noises at 50 m/s, with coarse grid**

Exp. Freq. Hz	Exp. SPL dB	Comput. Freq. Hz	Comput. SPL dB	Compt. Freq. Hz coarse grid	Comput. SPL dB coarse grid	Noise origin ? - unknown
930	103	1075	135	–	–	?
1340	107	1326	127	–	–	?
1824	134	1837	135	1875	134.8	feedback
2016	113	2062	130	2080	137	resonance
2848	106	2962	116	–	–	?
3552	111	3513	115	3960	98	?

by Henderson [14] as tones of unknown origins are also captured and fairly simulated.

Some of these tone peaks of unknown origins in Fig. 11 (left plot) and Table 3 at the low frequency end seem to be subharmonics, e.g. 1075 Hz vs. 2062 Hz. Subharmonics are often generated through vortex pairing; the excessively strong subharmonic spikes could be due to the two-dimensional simulation of a three-dimensional flow. Such spikes are absent when a coarse grid is used (Fig. 11, right plot).

5.4 *Consistency tests*

The same cavity noise problem is also tested with different grid size and computational domain to ensure that consistent and reasonable numerical results are obtained. As mentioned above, we are trying to simulate the large scale turbulence. As the grid is refined, more details of the turbulence emerge, as is experienced with many LES computations. In contrast to a deterministic flow computation problem, grid independence may *not* be tested in a rigorous way for the present noise problem due to the presence of two competing dominant modes. However, to a certain extent in a statistical way, some general agreements on frequencies may still be available for different grids. Several other consistency tests such as running with a larger computational domain and longer time, as well as imposing a specified boundary layer thickness are also conducted in the following subsections. The case presented in §5.3 will be referred to as the 'standard case' when making comparisons.

5.4.1 *Test with a coarse grid*   This cavity noise problem at flow speed 50 m/s was calculated with a coarser grid for grid independence test. Similarly, a nonuniform rectangular grid is used before it is triangulated. Although in the refined grid area Δx =0.00625 is about the same, $\Delta y = 0.0114$ is almost twice as large in the cavity opening area compared to the grid used in the standard case. Still, good agreement with experimental data and the standard case simulation is obtained. As shown in Fig. 11 (right plot), the two shoulder points of the highest spike correspond to 1875 Hz, 134.8 dB and 2080 Hz, 137 dB. Since the binwidth (or bandwidth) is about 190 Hz in this case, it is not clear that they represent the fluid dynamic feedback oscillation or the fluid resonance mode, or both and form a broad peak. However, in terms of frequency and SPL (sound pressure level), they are in good agreement with the experimental data of 1824 Hz and 134 dB (fluid dynamic feedback) and the computed data of 1837 Hz and 135 dB with the standard case (Table 4). The grid independence is thus somehow justified.

From Fig. 11 (right plot) and Table 4, it is observed that with a coarser grid, the dominant mode frequencies match the experimental ones quite well but the SPLs are lower. The tone peaks of unknown origins (broadband noises) are muffled, but persistent higher harmonics are generated.

5.4.2 *Test on a larger computational domain with longer run time*   In the CAA Workshop III Proceedings, several authors pointed out that the locations of the boundaries or the sizes of the computational domain have considerable effects on the noise frequencies and SPLs. In order to find out if the same phenomenon occurs with
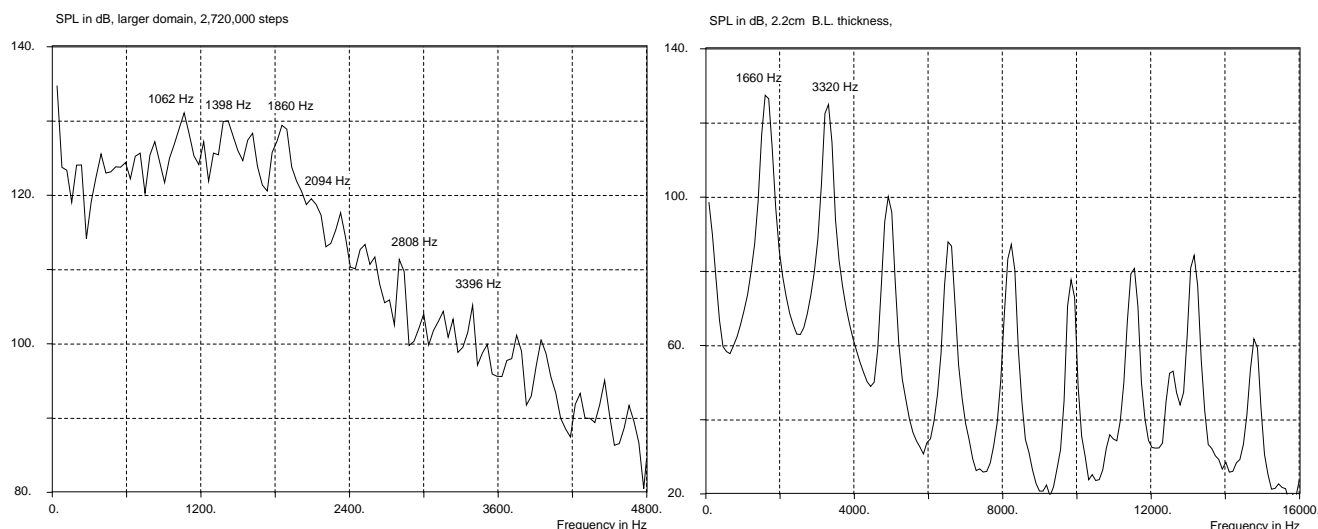
Figure 12.   Left plot: SPL vs. frequency at 50 m/s with larger domain and 2,720,000 marching steps; Right plot: SPL vs. frequency at 50 m/s, with 2.2cm thick boundary layer imposed.

the present scheme, the problem is also run with a larger domain ($-2.8 \leqslant x \leqslant 4$, $0 \leqslant y \leqslant 4$), which is about 3-times larger than the grid in the standard case. The grid size in this problem is about the same as in the standard case in the critical area, i.e. the cavity interior and around the opening, but stretches faster towards the inlet, outflow and top boundaries. With a time step size of 0.003, about 2.72 million steps are run in attempt to find out the long term behavior of the simulation. The numerical results are presented in Fig. 12 (left plot). Comparisons to the experimental data and the standard case are provided in Table 3. Generally speaking, for the dominant oscillation modes, the aeroacoustic feedback and flow resonance, the error is about 2% which is quite acceptable, despite their lower SPLs as expected due to the coarser grid size. The overall performance is quite similar to the standard case in that the subharmonic-like high SPL tones appear at the low frequency portion of the spectrum, possibly due to the two-dimensional simulation for a three-dimensional flow.

It is now demonstrated that at least for the present simulation, the size of the computational domain (i.e., locations of the boundaries) and the long run time have little influence on the major numerical results, i.e., frequencies and SPLs.

5.4.3 *Tests with artificially imposed boundary layer thickness*   In all the above numerical simulations, a simple uniform plug flow is imposed at the inlet boundary. The unsteady boundary layer develops due to the no-slip wall condition. On the other hand, it was suggested in the CAA Workshop III problem sheet that a prescribed boundary layer thickness may be used. Here, the idea is tested with the CE/SE scheme.

In this subsection, prescribed u-velocity profiles are imposed at the inlet boundary to mimic the turbulent boundary layers. Given a boundary thickness, δ, the formal u-velocity profile at the inlet boundary is specified as:

$$u = U_0(y/\delta)^{1/7}.$$

In the following two test cases, the same computational domain and grid used in the standard case are employed. In the first case, a thick turbulent boundary layer of $2.2\ cm$ is imposed at the inlet. After 1.4 million time steps are completed, the spectrum at the assigned point on the cavity vertical wall is depicted in Fig. 12 (right plot). The prominent peaks correspond to 1660 Hz, 127 dB and 3320 Hz, 125 dB. The second peak appears to be the first harmonic of the first peak. Note that the spectrum exhibits ample high frequency harmonics of a single tone, which implies numerically that there exists a highly nonlinear wave. The pattern is quite different from that seen in the experiment [14]. In the second case, the imposed boundary layer thickness at the inlet is reduced to $1.2\ cm$. Figure 13 (left plot) illustrates the spectrum after 1.4 million time steps. A slightly larger time step size (0.003) is used. Here, the prominent peaks correspond to 1824 Hz, 121 dB and 3642 Hz, 124 dB. It is also noted that in Fig. 13 (left plot), to the right of the peak
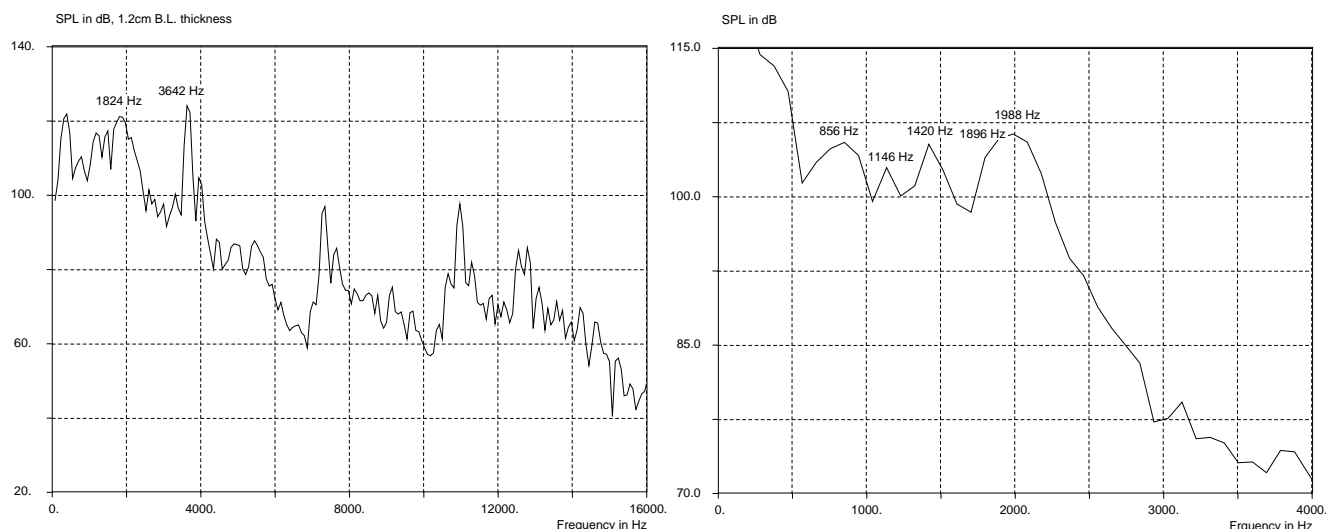
Figure 13. Left plot: SPL vs. frequency at 50 m/s, with 1.2 cm thick artificial boundary layer at inlet; Right plot: SPL vs. frequency at a low speed of 26.8 m/s.

Table 5. **Comparison of experimental and computed tone noises at 26.8 m/s**

Exp. Freq. Hz	Exp. SPL dB	Comput. Freq. Hz	Comput. SPL dB	Noise origin ? - unknown
928	97	856	105	?
1168	99	1146	103	feedback
1380	95	1420	105	?
1890	103	1896	105	?
1984	101	1988	106	resonance

at 1824 Hz, there appears a smaller peak at about 2020 Hz, which may correspond to the flow resonance frequency of 2016 Hz. In terms of frequency, the results are exceedingly good, almost agreeing exactly with the experimental data for 'thin' boundary layer [14]. There is no surprise since the boundary layer thickness of $1.2cm$ matches the experiment exactly. However, in terms of SPL, the numerical values are still low probably due to insufficient grid resolution. In addition, high SPL unwanted peaks appear at the low frequency end of the spectrum possibly due to the two-dimensional simulation.

The numerical experiments show that the prescribed boundary layer thickness has considerable effect on the spectrum and SPL. Without any knowledge or hint about the boundary layer, an arbitrarily prescribed boundary layer thickness may not work well; and it is probably best to let the flow develop its own.

5.5 *Noise at flow speed of 26.8 m/s*

Numerical experiments are also conducted for a lower flow speed of 26.8 m/s given the same cavity geometry. Table 5 lists a comparison of the experimental and computed data. As in the standard case, uniform plug flow is imposed at the inlet boundary.

From Table 5, it is observed that for the fluid-dynamic feedback tone, the numerical results agree very well with

the experimental data, 1146 Hz. vs. 1168 Hz and 103 dB vs. 99 dB in SPL, with a binwidth (or bandwidth) of 95 Hz. The error in frequency or SPL is about $3 - 4\%$. For the cavity resonance, the frequencies are 1988 Hz vs. 1984 Hz with 0.2% error, and the SPLs are respectively 106 dB and 101 dB. There are also other noise tones of unknown origin. The errors in frequencies and SPLs with these computed tones are larger. Similar to the standard case, their SPL are relatively high, possibly due to the two-dimensional simulation of a three-dimensional flow. From Fig. 13 (right plot), there is probably another tone of unknown origin - the one at 1896 Hz. Its frequency is so close to the resonance frequency 1988 Hz and the binwidth is 95 Hz, that it becomes difficult to distinguish the two frequencies. The two frequency spikes coalesce into a single broad peak. According to the experimental observation of Henderson [14], well defined discrete frequencies do not appear consistently until the flow velocity reaches 35 m/s. Based on this argument, the numerical results for the lower flow speed are indeed in very good agreement with the experiments.

6   Concluding Remarks

In this paper, a MILES type numerical approach - the CE/SE scheme, is adopted to simulate the tone noises arising from large scale turbulence generated in viscous flows. No explicit turbulence or subgrid models or acoustic models are used.

For the three benchmark CAA Workshop problems considered in this paper, generally good results are obtained and compare favorably to the experimental data. However, a two-dimensional simulation of a three-dimensional flow may generate some excessively strong subharmonics towards the lower end of the spectrum. Particularly for the cavity noise problem, as there are two dominant oscillation modes - aeroacoustic feedback and flow resonance competing with each other, accompanied by some tones of unknown origins, or broadband noise, it is important to select carefully the grid size and other parameters in the computations.

In the MILES type approach, we attempt to simulate only the large scale turbulence, which is believed to be the tone noise generating source. The smaller scale turbulence (higher frequencies and wave numbers) are practically ignored without an explicit subgrid scale model, since we are interested primarily in the aeroacoustic data. The CE/SE method is a scheme for solving conservation laws. When the divergence theorem (2) is applied to find the cell average, it also plays a role as a filter (such as the one used in LES approach). High frequency and high wave number disturbances are filtered out and aliasing errors are unlikely to occur. As pointed out by Fureby [13], choosing the parameters or limiters in the MILES approach, is somewhat equivalent to choosing a subgrid scale model in the conventional LES approach. The choice is not straightforward in the presence of complicated flows.

Acknowledgements

References

[1] Chang, S.-C., Wang, X.-Y. and Chow, C.-Y., "The Space-Time Conservation Element and Solution Element Method—A New High Resolution and Genuinely Multidimensional Paradigm for Solving Conservation Laws," J. Comp. Phys. vol. 159, pp. 89-136 (1999).

[2] Wang, X.-Y. and Chang S.-C., " A 2-D Non-splitting Unstructured Triangular Mesh Euler Solver Based on the Space-Time Conservation Element and Solution Element Method" C.F.D. J. vol. 8, pp309-325 (1999).

[3] Loh, C. Y., "On a Nonreflecting Boundary Condition for Hyperbolic Conservation Laws" AIAA Paper 2003-3975 (2003).

[4] Loh, C. Y., "Near Field Trailing Edge Tone Noise Computation" AIAA Paper 2003-0365 (2003).

[5] Loh, C. Y., Hultgren, L. S. and Chang S.-C., "Computing Waves in Compressible Flow Using the Space-Time Conservation Element Solution Element Method," AIAA J., Vol. 39, pp. 794-801 (2001).

[6] Loh, C. Y., Hultgren, L. S., and Jorgenson, P. C. E., 'Near Field Screech Noise Computation for an Underexpanded Supersonic Jet by the CE/SE Method', AIAA Paper 2001-2252, (2001).

[7] Loh, C. Y. and Zaman, K.B.M.Q., " Numerical Investigation of Transonic Resonance with a Convergent-Divergent Nozzle", AIAA J., Vol. 40, No. 12, pp. 2393-2401 (2002).

[8] Loh, C. Y., Himansu, A., and Hultgren, L.S., "A 3-D Navier-Stokes Solver with Unstructured Hexahedral grid for Computations of Near Field jet Screech Noise" AIAA Paper 2003-3207 (2003).

[9] C.K.W.Tam, J.C.Hardin, Eds., "Second Computational Aeroacoustics (CAA) Workshop on Benchmark problems", NASA CP-3352, June,1997.

[10] H.Schlichting, 'Boundary-Layer Theory', McGraw Hill, 1979.

[11] A.A.Townsend, 'The Structure of turbulent Shear Flow', 2nd edition, Cambridge University Press, 1976.

[12] J.P.Boris, F.F.Grinstein,E.S.Oran, and R.J.Kolbe, "New Insights into Large Eddy Simulation", Fluid Dynamics Research, vol.10, No.4-6, pp.199-227, 1992.

[13] C.Fureby and F.F.Grinstein, "Monotonically Integrated Large Eddy Simulation of Shear Flow", AIAA J. , vol.37, No.5, pp.544-556, 1999.

[14] B. Henderson, "Category 6, Automobile Noise Involving Feedback-Sound generation by Low Speed Cavity Flows", in "Third Computational Aeroacoustics (CAA) Workshop on Benchmark problems", NASA CP-2000-209790, August, 2000.

[15] Loh, C. Y., Chang, Sin-C., Wang, X.-Y. and Jorgenson, P. C. E., "Gap Noise Computation by the CE/SE Method" ASME paper, FEDSM-2001-18136.

Category 5 : Sound Generation in Viscous Problems
Problem 1 : Aeolian Tone Generation From Two Cylinders

R. Guénanff, E. Manoha, M.Terracol, and S. Redonnet
CFD and Aeroacoustics Department
ONERA, BP 72, 92322 Châtillon Cedex, France
eric.manoha@onera.fr

ABSTRACT

This paper addresses the Problem 1 (Aeolian Tone Generation from Two Cylinders) in Category 5 (Sound Generation in Viscous Problems), contributed by Professor Soogab Lee (solee@plaza.snu.ac.kr) at the 4th CAA Workshop held at the Ohio Aerospace Institute in Cleveland (OH), on October 20-22 2003. The problem is the simulation of the aeolian noise generated by the unsteady flow around a pair of cylinders in staggered arrangement. In the proposed solution, the Navier-Stokes equations are solved on a multi-domain conformal grid using a finite difference method with splitted mean flow / perturbation variables (Non Linear Disturbance Equation). The nearfield unsteady flow and the farfield acoustic field are obtained in a single computation.

INTRODUCTION

The numerical simulation of the aerodynamic noise generated by the unsteady flow around solid objects is a complex problem because it involves structures with scales and amplitudes that range over several orders of magnitude : turbulent scales near the solid body surfaces and in the wake are very small and intense, whereas radiated acoustic waves have large wavelengths and small amplitude. This is why such problems are generally solved using hybrid methods in which the nearfield turbulent flow and the farfield noise are computed separately, using the most adequate sets of equations with the most economic discretization strategy (Ref. 1).

However, Direct Numerical Simulation of the complete problem (turbulent near field and radiated sound) remains an interesting possibility in certain simple cases, at least to provide comparison to less straightforward techniques.

PROBLEM

The aim of the problem is to test the ability of CFD/CAA codes to accurately predict sound generation by viscous flows and sound propagation through interactions between acoustic wave and solid wall and between acoustic waves and shear layers.

The cylinder configuration is shown in Figure 1. The Reynolds number based on inflow velocity $U_\infty = 24.5$ m/s and the cylinder diameter $D = 0.955$ cm is $Re_\infty = 15800$, in a range where vortices with turbulent cores are shed periodically. The problem requires to compute the Strouhal number of vortex shedding from the two cylinders, and the directivity diagram of the RMS pressure fluctuation in the near field ($r = 10D$ or 9.55 cm) and in the far field ($r = 100D$ or 95.5 cm).
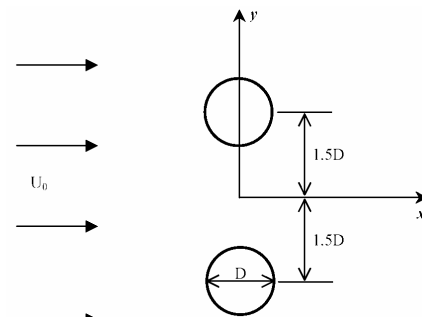
Figure 1 : : Geometry

GRID

According to available experimental data (Ref. 2) the Strouhal number of such aeolian problem depends (i) on the Reynolds number and (ii) on the parameter d/D in which d denotes the center-to-center distance between the cylinders. In this case $d/D = 3$ and the expected Strouhal number is about 0.2, which means an acoustic wavelength of about $70D$. Consequently the grid design result from a compromise between contradictory requirements. At the vicinity of the cylinders surfaces, very small cells are required to solve the small structures which develop in the boundary layers the vortices emitted in the wakes. On the contrary, the low-frequency acoustic radiation in the far-

field only requires a sufficient number of cells per acoustic wavelength. These requirements lead to a mesh with a significant radial stretching.
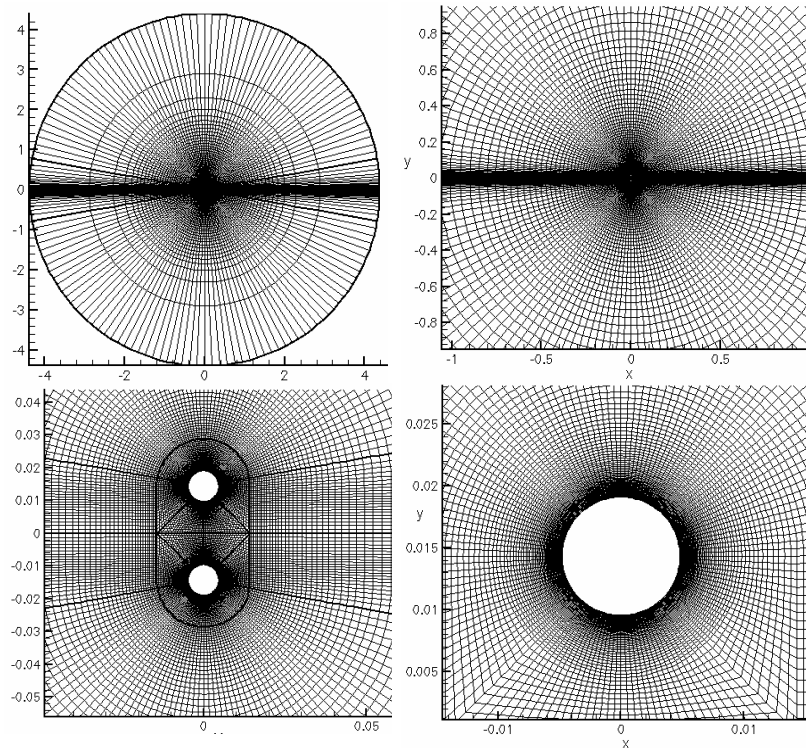

Figure 2 : Grid

Figure 2 shows several views of the grid. It is symmetrical with respect to the $y = 0$ axis. The mesh is composed of 16 domains and has a total of 45792 points. This number of points has been reduced to a minimum value with the objective of performing 3D computation in the next future, with the same grid replicated in the z direction.

The grid extends up to 400 D in the radial direction with a total of 183 points : the smallest cell is at the cylinder wall ($\Delta r = 0.0005$ or $\Delta r^+ = 1$ in wall units), then the cylinder boundary layer is meshed with 50 points with a radial stretching of 5 %. Then an "acoustic" zone is meshed with 108 points with a radial stretching of 6 %, up to $r = 100D$ where the radial cell size is about $\lambda/8$, where λ denotes the expected acoustic wavelength. Finally, a non-reflecting zone extends from $r = 100D$ up to $r = 400D$, with a strong radial stretching of 20 %. In the azimuthal direction along the cylinder, the mesh is composed of 144 points.

NUMERICAL PROCEDURE

ONERA's code *sAbrinA* (Solver for Aeroacoustics of BRoadband INteractions from Aerodynamics) is a multi-block, structured, multi-purpose code solving Euler or Navier Stokes steady/unsteady equations using various numerical procedures. Cell-centered finite volume and finite difference methods are available. Specific spatial high order schemes and filters are implemented for acoustic simulations (ref. 3). The code can handle complete variables or splitted (mean flow / perturbation) variables.

In the present case the Navier Stokes equations are solved in two steps. Firstly a RANS computation provides the viscous mean flow. Then the time perturbations over this initial state are computed separately using a finite difference method (Non Linear Disturbance Equations) (Ref. 4). The flux is split in two parts. The Eulerian flux is discretized with a sixth-order centered scheme and the viscous flux with a second-order centered scheme. The time discretization is based on a 3rd order Runge-Kutta scheme. The time step is $\Delta t = 10^{-8}$ s (or a maximum CFL number of 0.8 in the cylinder boundary layer), which means that each period of the vortex shedding is simulated over

about 200,000 time steps. The computation was performed over 1,600,000 iterations, or a total duration of 0.016 s, which means the transit of flow over about 40 cylinder diameters.

A perfect reflection condition (mirror) is applied on both cylinders surface. Non-reflecting characteristic boundary conditions are applied on all other boundaries. The results were stored every other 2000 time steps, which means a data sampling frequency of 50 kHz.

AERODYNAMIC RESULTS

The aeolian noise generated by the cylinders can be considered as the sum of (i) a dipolar noise generated by the surface load fluctuations on the cylinders, and (ii) a quadrupolar noise generated by turbulent vortices in the boundary layers and in the wakes. In most aeroacoustic configurations in which solid surfaces are involved, the dipolar noise is known to be dominant.

For the present combination of (i) the Reynolds number $Re_\infty = 15800$ and (ii) the geometrical ratio $d/D = 3$, experimental data (Ref. 2) predict that the vortex shedding is symmetrical with respect to the horizontal axis $y = 0$. The consequence is that the loads on both cylinders should also be symmetrical, and that a computation on a half grid using a symmetry condition imposed along the $y = 0$ axis should provide a reliable aeroacoustic result. However, such symmetry condition is probably unrelevant for the fine scale turbulent field around the cylinder and in the wake, which is certainly decorrelated from one cylinder to another. The consequence is that an imposed symmetry condition probably reinforces the quadrupolar noise in a proportion which is difficult to estimate.

Actually, a preliminary computation has been performed on the upper half-domain. Suspect strong fluctuating pressure levels were observed downstream the cylinders. In order to avoid any possible overestimation of the pressure field, a second computation was done on the whole grid of Figure 2, which results are presented below. For the conveniency of the presentation, only the results in the y > 0 half-space are shown.

Figure 3 compares the isocontours of the mean flow pressure field from the initial RANS computation and from time averaging the NLDE results at every other grid point. These fields are not identical because the NLDE variables have the capability to fluctuate about a non-zero value. In the present case, the time-averaged NLDE data displays cylinder wakes which deviate towards the $y = 0$ axis.
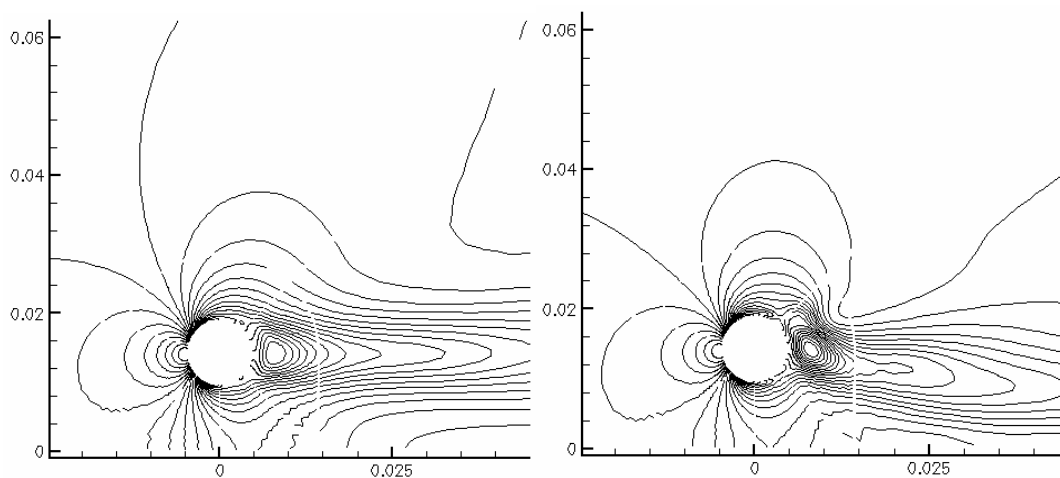
Figure 3 : Isocontours of mean flow pressure
Left : RANS– Right : time-averaged NLDE

Figure 4 (left) shows the time oscillations, over the whole duration of the computation, of the lift and drag coefficients of the upper cylinder, generated by the shedding of alternated vortices in the cylinder's wake. As expected, the lift amplitude is much larger than the drag. The lift oscillations are almost a perfect sine function, which confirms the dipolar character of each cylinder considered as an individual noise source. The time period of the drag fluctuations allows to estimate a vortex shedding frequency about $f = 540$ Hz or a Strouhal number of $St = 0.21$.

The right side of Figure 4 shows the distribution of the pressure coefficient C_p along the upper and lower sides of the upper cylinder, either from RANS or from time-averaged NLDE.
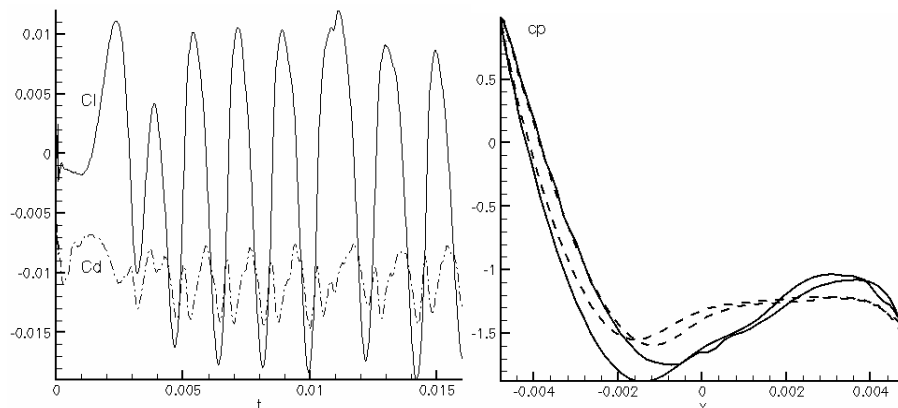
Figure 4 : <u>Left</u> : time evolution of lift (solid line) and drag (dashed line) of the upper cylinder. <u>Right</u> : C_p distribution on both sides of the upper cylinder, from RANS (dashed line) and from time-averaged NLDE (solid line).

ACOUSTIC RESULTS

Figure 5 compares the unsteady pressure fluctuations observed (i) at the surface of the upper cylinder ($\theta = 90°$) and (ii) in the acoustic far field ($r = 25D$, $\theta = 90°$). The power spectral densities of these signals are given on the same figure, confirming a dominant component at about $f = 540$ Hz or a Strouhal number of $St = 0.21$.
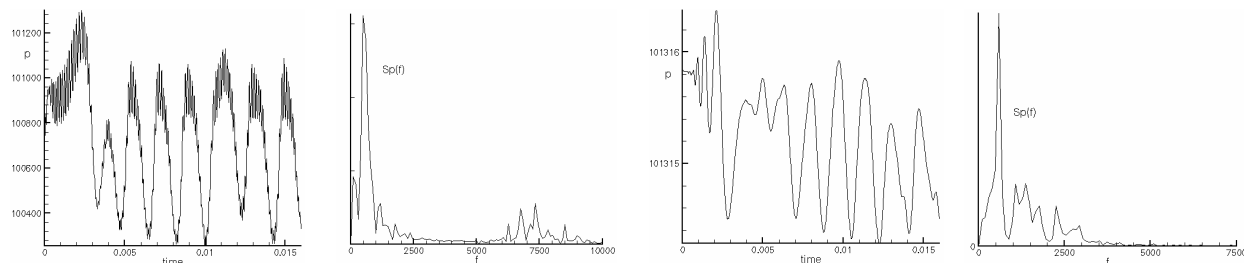
Figure 5 : Unsteady pressure in the nearfield unsteady flow (left) and in the acoustic far field (right). Time fluctuations (left) and spectral densities (right).
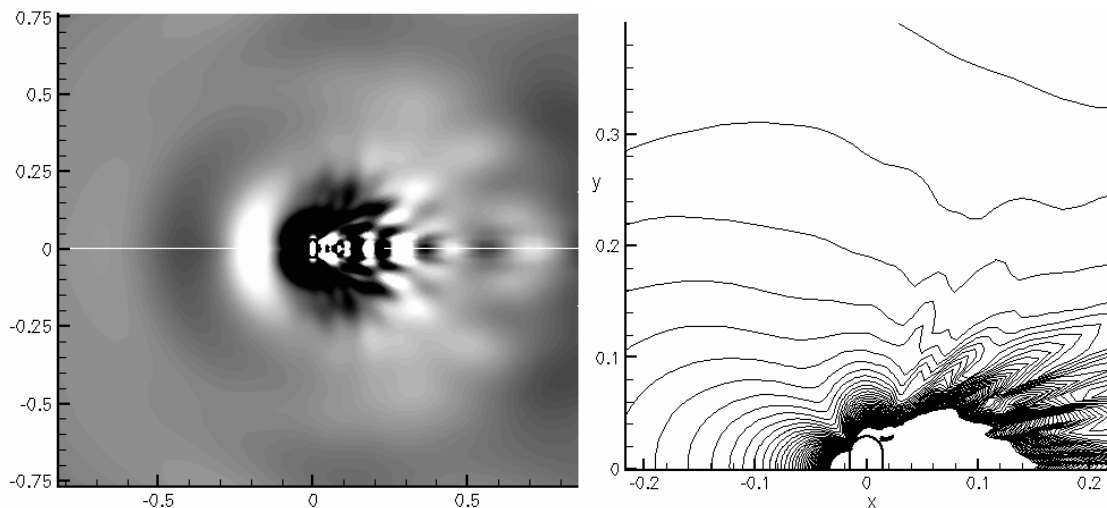
Figure 6 : Left : instantaneous pressure (acoustic) fluctuations up r = 80D
Right : isocontours of RMS pressure fluctuations up to r = 20D

The left side of Figure 6 shows the instantaneous pattern of the pressure fluctuations over the whole acoustic domain up to $r = 80D$. The grey scale range is adjusted to display the acoustic waves which propagate radially with small amplitude and large wavelength. The right side of the Figure 6 shows isocontours of the RMS pressure fluctuations up to $r = 20D$. Both diagrams suggest that acoustic directivity will be difficult to evaluate downstream the cylinders and close to them, since the "hydrodynamic" pressure fluctuations in the wake have much higher levels. This is illustrated on Figure 7, which displays the directivity diagrams of the RMS pressure fluctuations at r = 5D, 10D and 100D. The levels are in Pascals. At $r = 5D$ and $r = 10D$ the fluctuations downstream the cylinders are mostly hydrodynamic and mask the acoustic fluctuations. At $r = 100D$, the levels are still significant in the cylinders wake. Consequently, a comparison of these results with other computations using hybrid aeroacoustic method, for example the Ffowcs Williams-Hawkings integration based on the surface pressure fluctuation, should only account for the data corresponding to directions $-\pi \leq |\theta| \leq \theta_{min}(r)$ in which $\theta_{min}(r)$ is about $\pi/2$ at $r = 5D$ and $\pi/4$ at $r = 100D$. However, it should be underlined that these results would be directly comparable to experimental data.

| $r = 5D$ | $r = 10D$ | $r = 100D$ |
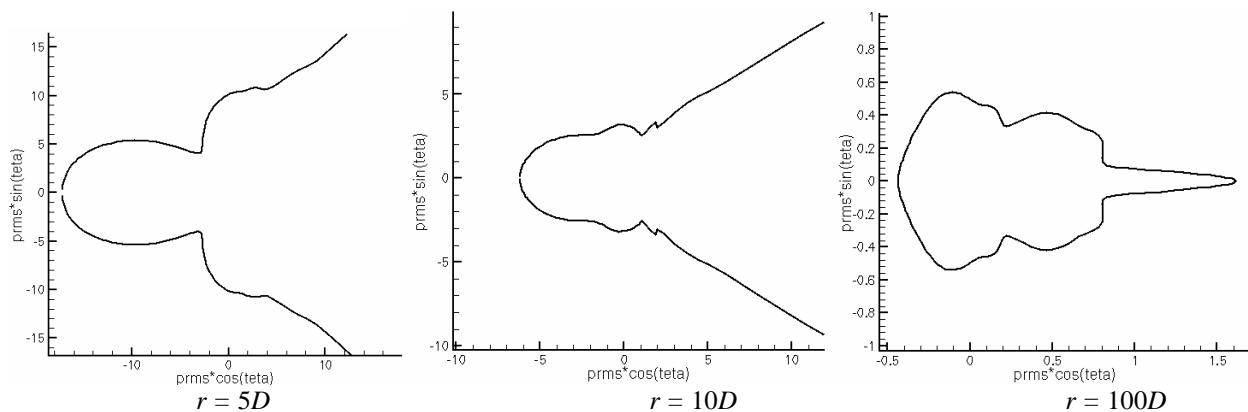
Figure. 7 : Directivity diagrams of the RMS pressure fluctuations at r = 5D, 10D and 100D (levels in Pascals).

CONCLUSIONS

The Category 5 (Sound Generation in Viscous Problems) – Problem 1 (Aeolian Tone Generation from Two Cylinders) of the 4th CAA Workshop is the simulation of the aeolian tone generated by the unsteady flow around a pair of cylinders in staggered arrangement. The proposed solution was obtained by solving the Navier-Stokes equations on a multi-domain conformal grid using a finite difference method with splitted mean flow / perturbation variables (Non Linear Disturbance Equation). The nearfield unsteady flow and the farfield acoustic field are obtained in a single computation : one consequence is that the directivities of the RMS pressure include the hydrodynamic field and the acoustic field. Acoustic waves are dominant in the x < 0 half-space, but hydrodynamic fluctuation are dominant downstream in an angular sector which becomes narrower at larger distance from the cylinders.

REFERENCES

1. Manoha E., Herrero C., Sagaut P. and Redonnet S. *"Numerical prediction of airfoil aerodynamic noise"*, AIAA paper 2002-2573, 8th AIAA/CEAS Aeroacoustics Conference, Breckenridge, USA, 17-19 May, 2002.

2. Kiya M., Arie M., Tamura H. and Mori H., *"Vortex Shedding From Two Circular Cylinders in Staggered Arrangement"*, Transactions of the ASME, Vol. 102, pp.166-173, June, 1980.

3. Guénanff R., Sagaut P., Manoha E., Terracol M. and Lewandowski R. *"Theoretical aspects of a multidomain high-order method for CAA"*. AIAA paper 2003-3117, 9th AIAA/CEAS Aeroacoustics Conference, Hilton Head, USA, 12-14 May, 2003.

4. Terracol M., Labourasse E., Manoha E. and Sagaut P. *"Simulation of the 3D unsteady flow in a slat cove noise prediction"*, AIAA paper 2003-3254, 9th AIAA/CEAS Aeroacoustics Conference, Hilton Head, USA, 12-14 May, 2003.

A HYBRID APPROACH TO TANDEM CYLINDER NOISE

David P. Lockard[*]

NASA Langley Research Center, Hampton, VA 23681-2199, U.S.A.

ABSTRACT

Aeolian tone generation from tandem cylinders is predicted using a hybrid approach. A standard computational fluid dynamics (CFD) code is used to compute the unsteady flow around the cylinders, and the acoustics are calculated using the acoustic analogy. The CFD code is nominally second order in space and time and includes several turbulence models, but the SST $k - \omega$ model is used for most of the calculations. Significant variation is observed between laminar and turbulent cases, and with changes in the turbulence model. A two-dimensional implementation of the Ffowcs Williams-Hawkings (FW-H) equation is used to predict the far-field noise.

INTRODUCTION

The process of generating a structured mesh for realistic configurations with the smoothness required for high-accuracy schemes is a time-consuming and difficult process. Furthermore, high-order schemes often lack the robustness of standard low-order computational fluid dynamics (CFD) codes. Although higher-order methods have the potential to produce improved solutions in less time, the advantages are difficult to realize for certain classes of problems, such as cylinder shedding.

To resolve the shedding from tandem cylinders with a structured grid requires a multiblock capability. In addition, the grid must be highly clustered in the vicinity of the cylinders to resolve the boundary layers and separated regions. The small grid spacing places stringent requirements on the time step unless an implicit time-stepping algorithm is employed. Furthermore, the flow is typically turbulent requiring some sort of model. These capabilities are typically available in standard CFD codes, although their accuracy can be questionable for fully unsteady flows. However, if the grid and time step are chosen appropriately, good near field solutions can be obtained. The accuracy of the turbulence model for unsteady flows is an area of research, but standard models appear to perform reasonably for low-frequency phenomena such as cylinder shedding. In addition, unsteady turbulence modeling is an important issue for all algorithms, regardless of their accuracy.

The present work attempts to resolve the near field around tandem cylinders using a standard CFD code. The computations are strictly two-dimensional. The Mach and Reynolds numbers are 0.714 and 15,800, respectively, and the cylinder diameter is 0.955cm. Computing the solution all the way to far-field observers would be prohibitively expenseive, so an acoustic analogy is used to predict the far-field noise. Unsteady CFD data on surfaces around the cylinders is used as input into a two-dimensional implementation of the Ffowcs Williams-Hawkings equation to determine the noise at desired observer locations. In the next section, the numerical methods are discussed. The results, timing information, and some conclusions are presented subsequently.

NUMERICAL METHOD

CFD Code

The CFD calculation employs the code CFL3D,[1,2] developed at NASA Langley Research Center to solve the three-dimensional, time-dependent, thin-layer Reynolds-Averaged Navier-Stokes (RANS) equations. The code employs third-ordering differencing of the convective terms, and is second-order for the viscous terms. The finite-volume formulation employs Roe's flux difference splitting to determine the flux at cell interfaces. For time accurate cases, a dual time strategy is employed. A second-order backward difference is used to discretize the temporal derivatives. A psuedo-time term is then added to allow the steady-state machinery to be employed to converge to the solution at the next time step. Local time-stepping and multigrid and used to accelerate the convergence. Twenty-five subiterations are used to converge each time step. For the current problem, test cases were run with ten to fifty subiterations, and the solutions were nearly identical for twenty-five subiterations and above.

---

[*]Aerospace Technologist

CFL3D has a large suite of turbulence models, but only three are investigated in this work. In addition, the code was run in a fully laminar mode. Cases employing the Spalart-Allmaras[3] turbulence model eventually supressed all unsteadiness if the code was run long enough. The SST k-ω model[4] of Menter is much less dissipative and is used for most of the runs. An Explicit Algebraic Stress (EASM) Model of Gatski[5] is also utilized to examine the effect of a higher-order closure model. When a turbulence model was used, the entire flowfield was assumed to be turbulent. No attempt was made to simulate transition.

FW-H Solver

The Ffowcs Williams and Hawkings[6] (FW-H) equation is an exact rearrangement of the continuity and Navier-Stokes equations. The time histories of all the flow variables are needed, but no spatial derivatives are explicitly required. The solution to the FW-H equation requires a surface and a volume integral, but the solution is often well approximated by the surface integral alone. The FW-H method has typically been applied by having the integration surface coincide with the surfaces of solid bodies, but the method is still applicable when the surface is off the body and permeable. Lockard[7] developed an efficient, two-dimensional formulation given by

$$
H(f)c_o^2\rho'(\mathbf{y},\omega) = -\oint_{f=0} F_i(\boldsymbol{\xi},\omega)\frac{\partial G(\mathbf{y};\boldsymbol{\xi})}{\partial \xi_i}\,dl - \oint_{f=0} i\omega Q(\boldsymbol{\xi},\omega)G(\mathbf{y};\boldsymbol{\xi})\,dl
$$
$$
- \int_{f>0} T_{ij}(\boldsymbol{\xi},\omega)H(f)\frac{\partial^2 G(\mathbf{y};\boldsymbol{\xi})}{\partial \xi_i \partial \xi_j}\,d\boldsymbol{\xi}. \tag{1}
$$

where

$$
F_i = \left(p\delta_{ij} + \rho(u_i - U_i)(u_j + U_j) + \rho_o U_i U_j\right)\frac{\partial f}{\partial y_j} \quad \text{and}
$$
$$
Q = \left(\rho(u_i + U_i) - \rho_o U_i\right)\frac{\partial f}{\partial y_i}. \tag{2}
$$

The contribution of the Lighthill stress tensor, T_{ij}, is known as the quadrupole term. The dipole term F_i involves an unsteady force, and Q gives rise to a monopole-type contribution that can be thought of as an unsteady mass addition. The function $f = 0$ defines the surface outside of which the solution is desired. The total density and pressure are given by ρ and p, respectively. The fluid velocities are u_i, while the v_i represent the velocities of the surface f. The Kronecker delta, δ_{ij}, is unity for $i = j$ and zero otherwise. A prime is used to denote a perturbation quantity relative to the free-stream conditions denoted by the subscript o. The Cartesian coordinates and time are x_i and t, respectively. The usual convention involves a quiescent ambient state with f prescribed as a function of time so that it always surrounds a moving source region of interest. $H(f)$ is the Heaviside function which is unity for $f > 0$ and zero for $f < 0$. The derivative of the Heaviside function $H'(f) = \delta(f)$ is the Dirac delta function, which is zero for $f \neq 0$, but yields a finite value when integrated over a region including $f = 0$. Although the equation is written in Cartesian tensor notation, by interpreting the indices to run only over 1 and 2 it can be thought of as being in two dimensions.

RESULTS

The baseline grid for the CFD computations contains 206479 grid points in 15 blocks. Figure 1(a) shows the grid with the block boundaries in light grey. All of the block interfaces are one-to-one. The cylinder diameter D=0.955cm. The normal spacing on the cylinder walls is 4.4e-4 cylinder diameters. The normal grid spacing was varied until there were minimal changes in the solution. The amplitude of the oscillations is strongly dependent on the grid spacing near the walls, but the shedding frequency is relatively insensitive.

Superimposed on the grid as white lines in Figure 1 are the surfaces used to sample data from the CFD computation for use in the FWH solver. Unsteady data was recorded on the cylinder surfaces, and on two nearly rectangular boxes around the cylinders. The penetrable surfaces are referred to as the inner and far porous surfaces.

Figure 1(b) shows the directivity results from a grid refinement study between the baseline grid and one refined by a factor of two in all directions. The pressure in the figure is nondimensionalized by $\rho_\infty c_\infty^2$. The observers are located 100 diameters from a point between the two cylinders. Although there is some variation between the results, the patterns

are similar and the peak noise radiation is nearly identical. The Strouhal number of the shedding changed from 0.222 to 0.224 between the baseline and fine grids. A detailed analysis of the fine grid results shows most differences are a result of resolving additional instabilities in the shear layers formed between the cylinders and the shedding vortices. These instabilities are somewhat artificial beacuse of the two-dimensional nature of the calculations. In fully three-dimensional simulations, the variation in the spanwise direction tends to significantly reduce the shear layer instabilities. Therefore, all subsequent cases utilize the baseline grid.

(a) Grid	(b) Directivities at R=100D
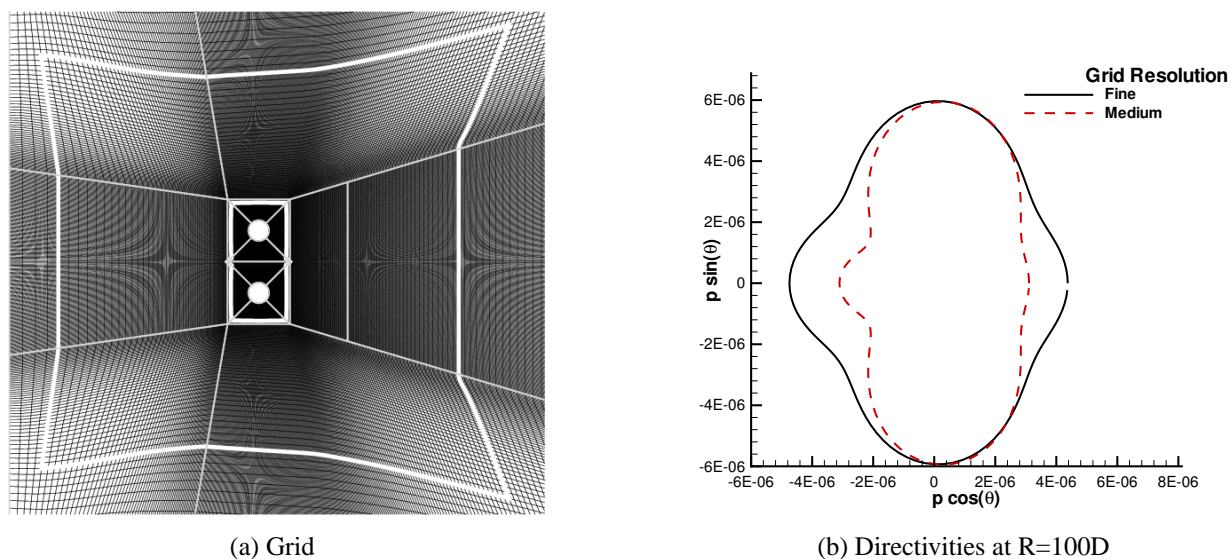
Figure 1: Baseline grid with block interfaces in grey and FWH surfaces in white and directivity comparison for grid refinement.

The near field pressure and vorticity fields for the k-ω turbulence model and laminar flow cases are shown in Figures 2 and 3. The vortex streets behind the cylinders is evident. The resolution within a few diameters of the cylinders is sufficient to maintain the vortices, but the grid coarsens significantly downstream smearing and dissipating the vortices. A comparison of the turbulent and laminar cases reveals considerably more randomness and scales for the laminar flow. The laminar results are highly grid dependent and are not believed to be indicative of the real flow. Because the grid resolution is very high in the vicinity of the cylinders, instabilities grow rapidly for this two-dimensional flow and overwhelm the solution. As the grid is refined, smaller scale instabilities develop. With a turbulence model, there is additional dissipation which suppresses most of these instabilities and synchronized shedding from the cylinders is observed. The lift and drag coefficients on the lower cylinder as a function of time for the laminar and turbulent cases are presented in Figure 4. Although there are some similarities, there is more randomness for the laminar case. A longer time record reveals much more irregularity. From the lift and drag curves, one would expect a dipole-type directivity for the resulting noise. Figure 5(a) does show considerably more noise normal to the flow direction for the laminar flow case, but the turbulent cases predict significant noise radiation in the upstream and downstream directions. Presumably, the synchonized shedding from the tandem cylinders in the turbulent cases causes the potential field to oscillate in a regular fashion resulting in the time-varying pressure fields in the streamwise direction. Both the EASM and SST k-ω turbulence models predict synchonized shedding, although the amplitude of the noise radiation is somewhat different. Table 1 gives the Strouhal numbers of the shedding for the different turbulence models.

Table 1: Strouhal numbers for different turbulence models.

Model	Strouhal Number
Laminar	0.206
EASM	0.249
SST k-ω	0.222

Three time steps where used to run calculations with the SST k-ω turbulence model to investigate the effect of time resolution. Twenty-five pseudo-time subiterations where run per time step to insure converge at each time step. Figure 5(b) shows that the results for the two smaller time steps are nearly identical, and only a small variation is observed with the largest time step. The Strouhal number varied from 0.220 to 0.223 as the time step was decreased. The time step is nondimensionalized by c_∞/D. All of the results presented in this paper where run with the smallest time step except for the grid refinement which was run with the intermediate value.

(a) Pressure

(b) Vorticity
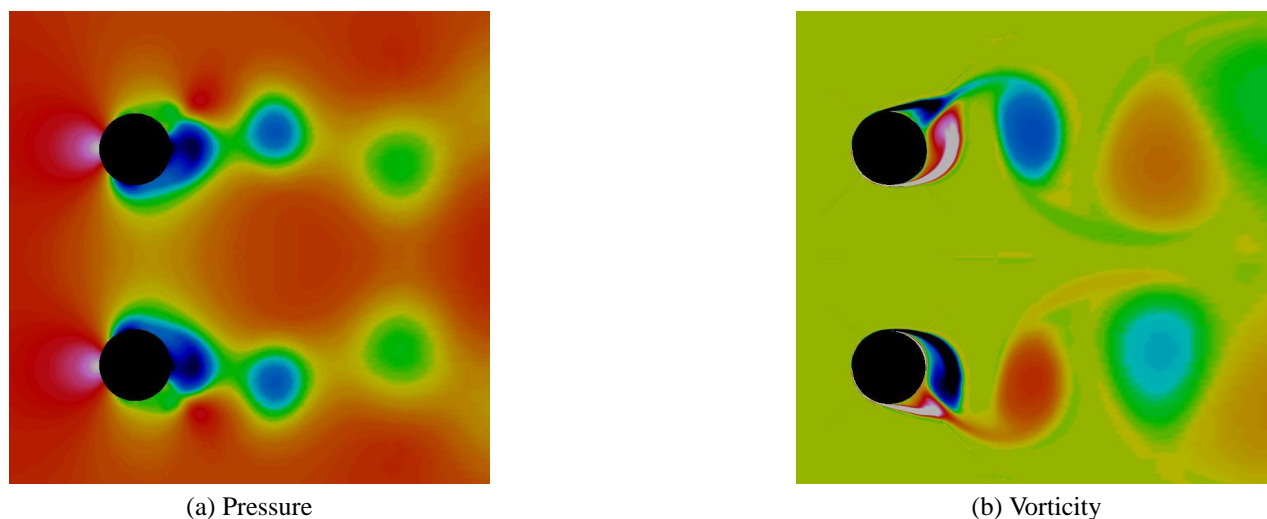
Figure 2: Instantaneous results for the SST k-ω turbulence model.

(a) Pressure

(b) Vorticity
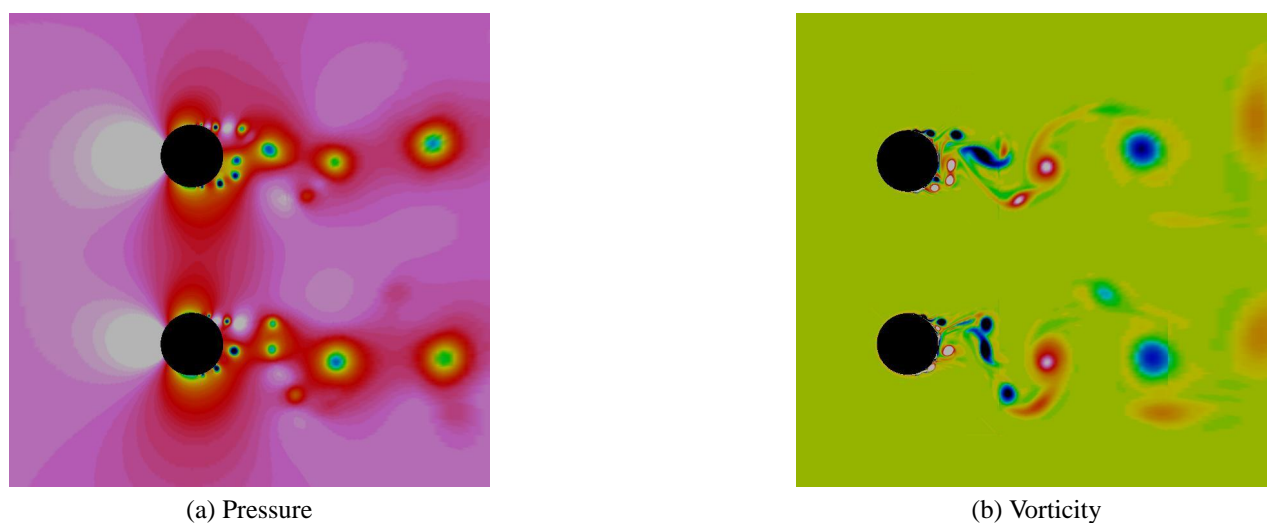
Figure 3: Instantaneous results for laminar flow.

The influence of the location of the Ffowcs Williams-Hawkings surface is examined in Figure 6. The results for observers at a radius of ten are shown in Figure 6(a), and for a radius of 100 in Figure 6(b). The observer location must be outside of the surface, but the far porous surface is beyond R=10, so no results are presented for the outer surface in Figure 6(a). The pressure fluctuation levels in the streamwise direction are considerably higher at R=10 compared with R=100 indicating that it is primarily a near field effect. The dominant noise radiation is normal to the flow at R=100, although there is still significant noise radiation upstream. For both observer distances, the agreement for different FWH surfaces is reasonable, and it is quite good for R=100.

The FWH equation only requires the pressure for impenetrable surfaces, but all the flow variables are needed otherwise. The advantage of a penetrable surface is that all quadrupole effects within the surface are included. Quadrupole

(a) SST k-ω

(b) Laminar
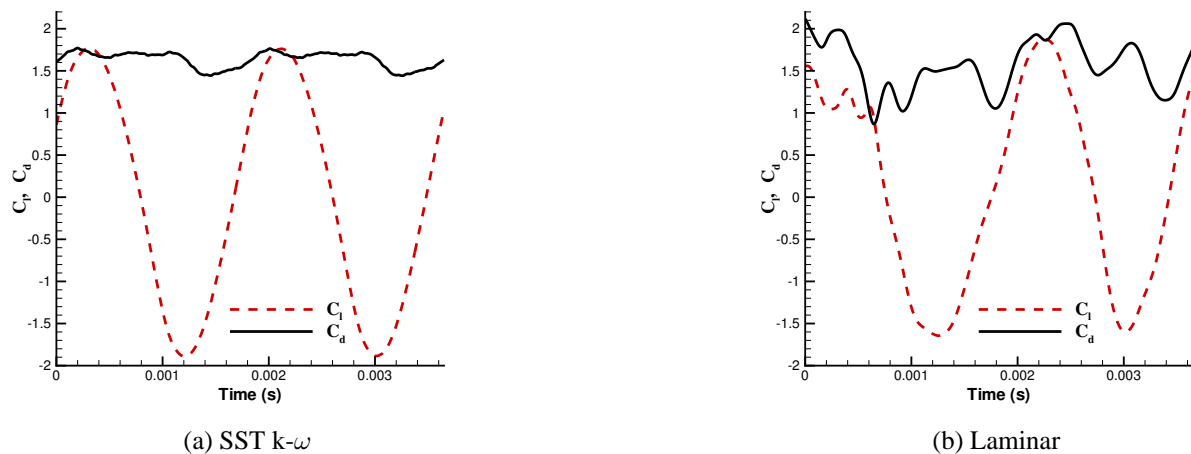
Figure 4: c_l and c_d results.

(a) Effect of turbulence model

(b) Time step refinement
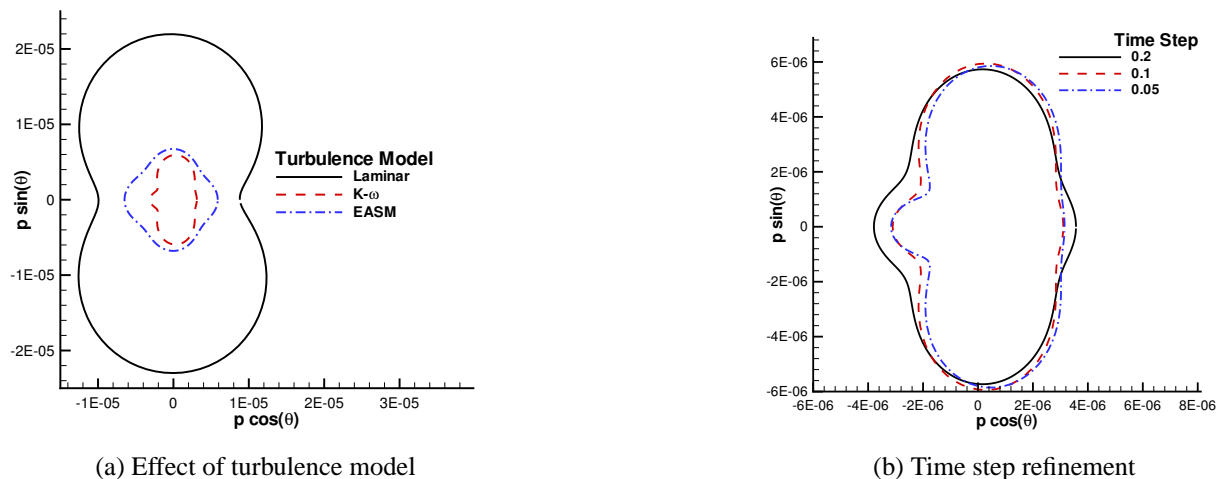
Figure 5: Time step study and influence of turbulence model for an observer at R=100

effects include nonlinear propagation, reflection, and refraction. For cylinder shedding, the noise tends to be at low frequencies where reflection and refraction by shear layers and unsteady flow structures tends to be minimal. Therefore, the results with the penetrable and impenetrable surfaces are not expected to differ significantly as Figure 6 demonstrates. An additional source of error for penetrable surfaces occurs when wakes pass through and generate erroneous noise because the volume integral for the quadrupole is not included. When a vortex is partially within the surface, the contribution from the surface terms should be canceled by the volume integration. However, the errors are typically much smaller than the real noise emanating from the cylinders. Another potential source of errors with penetrable surfaces is the accuracy of the input data. When the surface is far from the noise generation region, any errors in the propagation of the acoustic signal and flowfield by the CFD code will result in errors in the FWH computation. For the current problem, the wavelength is so long that it is unlikely that propagation errors are significant.

RESOURCES

A Beowulf cluster of 2.53 GHz Intel Pentium IV computers was used to run the CFD calculations. Total memory usage was approximately 500 MB for the baseline grid of 206479 points. Turbulent cases were run approximately 300 CPU hours to wash out all transients and obtain a nearly periodic state. Sampling was performed at a cost of 30 CPU hours/period. The laminar case was run considerably longer because of the randomness in the shedding. The FWH

(a) R=10   (b) R=100
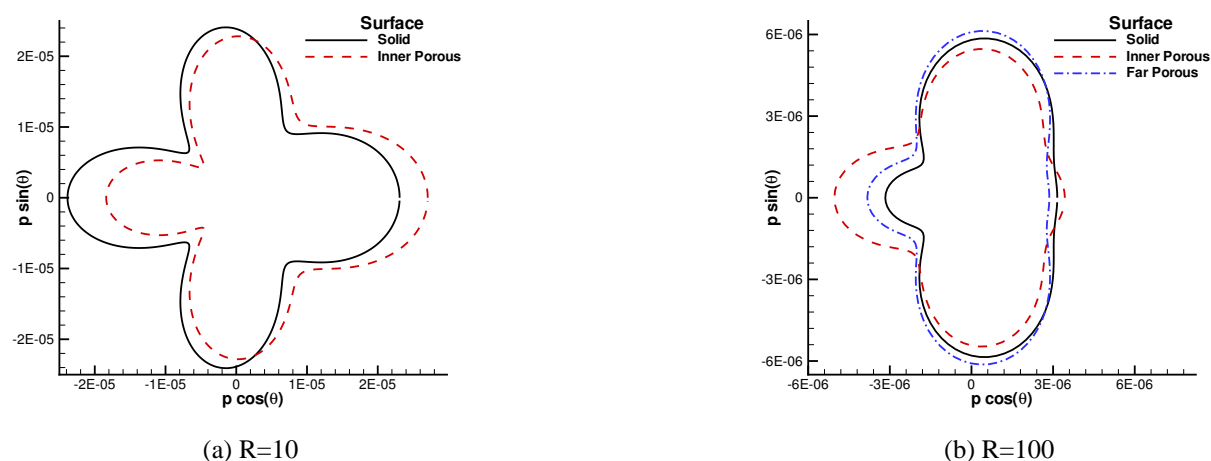
Figure 6: Directivities for k-ω turbulence model.

solver required only a few minutes to calculate the noise at 360 observer locations.

CONCLUSIONS

The hybrid coupling of a low-order CFD code with a FWH solver appears to be well suited to predicting the noise from tandem cylinders. The The multiblock capability of the CFD code allowed a grid to be generated with minimal difficulty, and the robustness of the code permitted the solutions to be computed without any special treatment. The greatest source of error appears to be in the turbulence model. Although standard turbulence models perform reasonably well for low-frequency phenomena, the choice of turbulence model clearly affected the solution. Furthermore, the low Reynolds number of the the current case probably results in a transitional flow around the cylinder which was not taken into account in the current calculations.

REFERENCES

[1] Rumsey, C.; Biedron, R.; and Thomas, J.: CFL3D: Its History and Some Recent Applications. NASA TM 1997-112861, May 1997. Presented at the Godonov's Method for Gas Dynamics Symposium, Ann Arbor, MI.

[2] Krist, S. L.; Biedron, R. T.; and Rumsey, C.: *CFL3D User's Manual (Version 5)*. NASA Langley Research Center, Aerodynamic and Acoustic Methods Branch, 1997.

[3] Spalart, P.; and Allmaras, S.: A One-Equation Turbulence Model for Aerodynamic Flows. *La Recherche Aerospatiale*, vol. 1, no. 1, 1994, pp. 5–21.

[4] Menter, F.; and Rumsey, C.: Assessment of Two-Equation Turbulence Models for Transonic Flows. AIAA-94-2343, 1994.

[5] Rumsey, C.; and Gatski, T.: Summary of EASM Turbulence Models in CFL3D With Validation Test Cases. NASA TM 2003-212431, June 2003.

[6] Ffowcs Williams, J. E.; and Hawkings, D. L.: Sound generation by turbulence and surfaces in arbitrary motion. *Philosophical Transactions of the Royal Society of London A*, vol. 342, 1969, pp. 264–321.

[7] Lockard, D. P.: An Efficient, Two-Dimensional Implementation of the Ffowcs Williams and Hawkings Equation. *Journal of Sound and Vibration*, vol. 229, no. 4, 2000, pp. 897–911.

SIMULATION OF MULTIGEOMETRY SCATTERING PROBLEMS AND THE RADIATION AND REFRACTION OF ACOUSTIC WAVES THROUGH A SHEAR LAYER WITH INSTABILITY WAVES SUPPRESSED

R. Ewert, J. Yin, and J.W. Delfs
DLR
Institute of Aerodynamics and Flow Technology, Technical Acoustics
Lilienthalplatz 7, 38108 Braunschweig, Germany

ABSTRACT

The scattering of harmonic acoustic waves at multiple rigid cylinders is simulated applying a Chimera technique and a body-fitted grid approach. The Chimera technique uses a Cartesian background mesh in conjunction with body-fitted O-grids in the immediate vicinity of the solid surfaces to resolve the geometry. The body-fitted grid approach applies a multiblock topology with O-grids wrapping the cylinders while an H-type topology is used away from the cylinders that converges against a Cartesian mesh in the far field. Both grid approaches are compared using a similar far-field resolution of about seven points per wavelength. The refraction of acoustic waves in an unstable jet is simulated using a modification of the linearized Euler equations that can be proven to be stable for arbitrary mean flow fields. The simulations confirm the modified perturbation equations to suppress the excitation of unstable modes. The wave operator encoded in the perturbation equations is known to be exact for irrotational mean flows, that is, in the high-frequency limit of the Strouhal number based on frequency f and mean-flow vorticity ω_0 tending to infinity: $St = f/\omega_0 \to \infty$. It is shown that even for a Strouhal numbers of $O(1)$, the modified acoustic perturbation equations resolve mean flow refraction and scattering effects accurately. For the jet, larger differences to the reference solution appear, in particular, downstream of the harmonic source position due to the small Strouhal number $St = f/\omega_0 \approx 10^{-2}$ in the jet shear layer.

INTRODUCTION

The category 2 problem of the Fourth Computational Acoustics (CAA) Workshop on Benchmark Problems is designed to test the capability of CAA methods to resolve complex geometry problems. In this work the acoustic computations have been carried out with a finite difference scheme based on the Dispersion-Relation-Preserving (DRP) scheme of Tam and Webb on structured mesh types. To resolve complex geometries there are three different approaches based on structured meshes.

Since the DRP scheme has the best acoustic resolution quality on a Cartesian grid, in the first approach proposed by Kurbatskii and Tam (ref. 1) an arbitrarily curved surface is completely resolved with a pure Cartesian grid. In this method the curved surfaces cut the Cartesian grid lines such that the two connected vertices are split into one point inside the computational domain and one beneath the surface. The latter ghost point is used in the differencing scheme and is appropriately loaded such that the surface boundary condition is fulfilled in certain control points on the surface. In the Kurbastkii and Tam approach the determination of the ghost point values yield a coupled problem that demands the solution of a linear equation system for all the ghost points of one continuous surface at each time step. The pure Cartesian methods have difficulty properly simulating problems with nonvanishing mean flows including the propagation of nonacoustic modes. (See, e.g., Yin et al. (ref. 2) for the application of the Kurbatskii and Tam boundary treatment to simulate vortex/airfoil interaction.)

The second grid approach uses additional Chimera or overset grids in conjunction with a Cartesian background mesh. The additional body-fitted grids resolve the complex geometry with an O- or C-topology, where in 2D (two dimensional), one curvilinear coordinate direction runs tangential to the boundary and the other runs normal to the

surface. The coupling between the different grid types is accomplished via an overlap region of background and surface meshes, where three points of the seven-point DRP stencil are determined from the other grid values such that in the interior computational domain, central DRP stencils always are applied. The data exchange between the overset grids demands some kind of interpolation from one grid to the other and vice versa. Since the body-fitted surface grids are better suited to resolve mean flows including boundary layers around the geometry, the Chimera grid approach combines the advantage of an optimal Cartesian grid in the far field with a better capability to resolve mean-flow effects close to a surface.

The third structured grid method adopts the well-known CFD approach of curvilinear multiblock grids for acoustic simulations. The combination of geometries that are meshed with O- or C-type grids with H-type grids to resolve the remaining computational domain, yields an optimal acoustic Cartesian grid in the far field. However, grid singularities will appear for such topologies. The influence of grid singularities on the accuracy of the computational scheme will be addressed in the next section. Subsequently, the computation of problem 2, cases 1 and 2, with a Chimera grid approach based on a 5- by 5-point Lagrangian interpolation and a body-fitted approach that includes multiple five-way singularities, is discussed.

In the last section, category 4, problem 1, the scattering of acoustic waves in an unstable jet, is treated with acoustic perturbation equations. In Ewert and Schröder (ref. 3), an acoustic analogy based on a system of linear acoustic perturbation equations was proposed. The homogeneous left-hand side equation system is equivalent to a convective wave equation that is exactly valid for irrotational mean flows. However, it is shown in the last section that the homogeneous acoustic equation system is able to resolve mean-flow scattering and refraction effects even for sufficiently mild levels of mean vorticity. Since mean-flow convection and refraction effects are resolved by the extended wave operator on the left-hand side, unlike the right-hand side sources of the acoustic analogy of Lighthill (ref. 4), the new acoustic analogy sources exclude these effects and the spatial extension of the non-zero source is reduced and more confined to the main acoustic source region. Therefore, an initial unsteady flow simulation also would have to resolve a smaller domain to describe the sources completely. The convective wave operator encoded in the acoustic perturbation equations can be proven to be stable for arbitrary mean flow fields. This is an important feature if the equations system is excited with additional sources in a hybrid acoustic analogy approach, since for globally unstable mean flows, otherwise unstable perturbation equations yield diverging computations. The acoustic perturbation equations are applied to simulate the scattering of the sound waves of a harmonic monopole source inside an unstable hot jet, using just the harmonic source on the right-hand side with all other nonzero analogy sources neglected.

NUMERICAL METHODS

Linearized Acoustic Equations

The computations of the category 2 problems are based on the linearized Euler equations (LEE) without mean flow. For the category 4, case 1 problem, a modified linear perturbation equation system is used that follows from the LEE and suppresses vortical eigenmodes. The spatial discretization of all linear perturbation equation systems is accomplished with the fourth-order dispersion-relation-preserving (DRP) scheme of Tam and Webb (ref. 5). The spatial derivatives are computed, for example, on a one-dimensional Cartesian grid with a central seven-point stencil

$$\left(\frac{\partial f}{\partial x}\right)_l \approx \frac{1}{\Delta x} \sum_{j=-3}^{3} a_j f_{l+j} \tag{1}$$

where optimized coefficients a_j minimize the difference between the physical and numerical dispersion relations over a chosen range of wavelengths and frequencies. For the use on curvilinear multidimensional grids, equation (1) is extended to spatial derivatives for the coordinate direction j via

$$\left(\frac{\partial f}{\partial x_j}\right) = \left(\frac{\partial f}{\partial \xi_i}\right)\left(\frac{\partial \xi_i}{\partial x_j}\right) \qquad (2)$$

where the terms with similar indices are summed over all spatial directions. In computational space the derivatives with respect to a curvilinear direction ξ_i are computed with equation (1) considering $\Delta \xi_i \equiv 1$. The metric terms are computed consistently with the DRP scheme too. At far-field boundaries the asymptotic radiation and outflow boundary condition of Tam and Webb (ref. 5) is used. The solid wall boundary condition is implemented based on a ghost point beneath the surface that yields the proper surface wall normal pressure gradient. To suppress high-frequency spurious waves, artificial selective damping, according to Tam and Dong (ref. 6) has been used which reads for a curvilinear mesh in 2D

$$\vec{S}_{l,m} = -\frac{1}{\Delta x_{,1} \mathrm{Re}_\Delta} \sum_j d_j \vec{U}^n_{l+j,m} - \frac{1}{\Delta x_{,2} \mathrm{Re}_\Delta} \sum_i d_i \vec{U}^n_{l,m+i}, \ \Delta x_{,i} = \sqrt{\left(\frac{\partial x_1}{\partial \xi_i}\right)^2 + \left(\frac{\partial x_2}{\partial \xi_i}\right)^2} \qquad (3)$$

A constant background value of the mesh Reynolds number $\mathrm{Re}_\Delta \approx 0.05$ with a slight increase close to boundaries has been chosen. In order to support fourth-order accuracy using the damping terms from the fourth-order central filtering coefficients of Vasilyev w_i (ref. 7), complementary damping coefficients have been computed and applied the following rule

$$d_0 = 1 - w_0, \ d_i = -w_i, \ i = \pm 1...\pm 3$$

The coefficients $d_0 = 0.3125, d_{\pm 1} = -0.234375, d_{\pm 2} = 0.09375,$ and $d_{\pm 3} = -0.015625$ closely match those derived by Tam and Dong for the parameter $\theta = 0.3\pi$ (ref. 6). The time integration is carried out with a fourth-order Runge Kutta method.

CAA Chimera Methodology

The Chimera methodology used in this present paper is based on the works described in (refs. 8 to 10). In general, three major steps are required in assembling a Chimera grid from a set of structured component grids. The first step called hole cutting involves detecting all the hole points outside the computation domain. In this step, the hole points which will not be updated during the computation are first determined according to boundary points of the other component grid. The second step is to classify the remainder of the grid points as either discretization, or interpolation points. The discretization points are those that can construct seven-point CAA DRP stencils in all coordinates. The rest of the points consist of interpolation points. The number of interpolation points depends on both the interpolation and space discretization stencils and should be kept minimal for efficiency reasons. Figure 1 (left) demonstrates where the interpolation points and hole area are located for the configuration of overlapped Cartesian grid and O-grid, when a 5- by 5-interpolation stencil (fifth-order interpolation) and 7 points DRP stencils are used. After the interpolation points are determined, the final step is to establish the correct interpolation coefficients. The function values on the interpolation points are updated by interpolation from neighboring component grids at each time step. In the present paper, the interpolations are carried out directly in physical domain if component grids are Cartesian grids or in the computational domain if body-fitted grids are involved. Therefore, a two-dimensional Lagrange interpolation scheme is implemented. The interpolation of at least one order higher than the order of the discretization scheme is required (ref. 8). Figure 1 (right) gives an example of the interpolation error dependency on both grid size (Δx) and width of the interpolation stencils (IW). The interpolation error based on a static test was numerically estimated on an overlapped Cartesian grid and O-grid. The maximum grid size for the O-grid is the same as the Cartesian grid size Δx. By imposing a known test function $f(x, y) = \sin(2 \cdot (x + y))$ on the grid points, the values on the interpolation points were obtained using the above interpolation schemes. The RMS errors, with respect to the exact solution for all interpolation points, are determined. The curves in figure (1) (right) show

strong grid dependency for small interpolation stencil size (i.e., IW = 3,4). For small grid size such as $\Delta x = 0.1$, the errors are almost independent on IW. For moving-grid simulation, all above mentioned three steps are repeated at each time step.

Singular Point Treatment

Care must be taken if high-order finite difference schemes are applied on curvilinear multiblock meshes, since the grid singularities that typically arise in grid topologies yield grid discontinuities that can deteriorate the order and accuracy of the computational scheme. In order to numerically study the behavior of singularities, figure 2 shows a grid setup that involves two three-way and two five-way singularities. The grid is globally smoothed using an elliptic grid smoother. The resulting gridlines are continuous across the block boundaries, which are marked by thick lines in figure 2. Typically for elliptic grid smoothers, three-way singularities appear to be attractive with the grid spacing decreasing close to the singularity, whereas the five-way singularities are repulsive with the grid spacing increasing. This is an important feature since five-way singularities on grids that exploit the resolution limit of the numerical scheme might cause a poor local resolution. In conjunction with a reduced accuracy close to the singularity, massive spurious waves are generated and the complete solution deteriorates unacceptably. The absolute accuracy and the order of accuracy are evaluated closely following the approach outlined in Hixon et al. (ref. 11). A constant mean flow field $M_x = 0.5$ is used from left to right and at the left inflow boundary plane vorticity waves are excited that convect through the computational domain. The analytical solution of the vorticity waves is

$$p', \rho' = 0, \quad u'(x,y,t) = 0, \quad v'(x,y,t) = \widehat{v}\sin\left(kM_x t - kx\right) \tag{4}$$

In equation (4), k is the wavenumber based on the vorticity wave wavelength. The unsteady flow quantities are sampled for four receiving points closely downstream of the singularities.
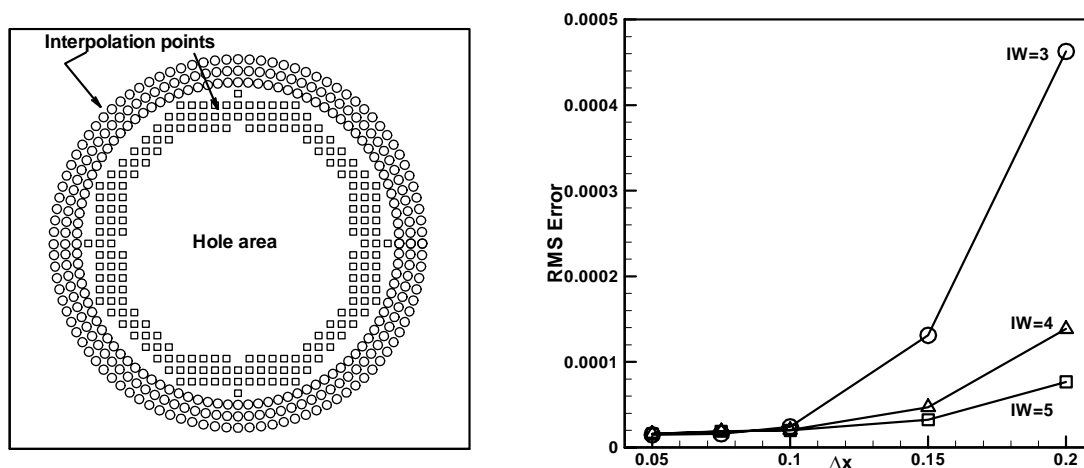
Figure 1.—Distribution of interpolation points and hole area for configuration of overlapped Cartesian grid and O-grid (left) and RMS error dependency on different width of stencils IW (right).

The dissipative error in the receiving points is determined from the known analytical solution. A grid convergence study can be performed either by keeping the wavelength constant while decreasing the grid spacing or by increasing the wavelength for constant grid resolution, respectively. Figure 3 (left) shows the error versus wavenumber in a double logarithmic plot. For the smaller wavenumbers, the plotted perturbation quantities show a straight line convergence property. The slope of the curves of the perturbation quantities are plotted together with the slopes of first-, second-, and third-order convergence. An order of accuracy less than second order and close to first order is apparent. This behavior is also evidenced in the right side of figure 3 which depicts the slopes of the perturbation curves from the left diagram. Figure 4 shows the error convergence for the three-way singularity.

Figure 4 (left) shows a decrease of the absolute error of about one order of magnitude compared to figure 3 (left), which is probably due to the smaller grid spacing in the vicinity of the three-way singularity (see fig. 2). The order of accuracy, however, is again evidenced to be clearly reduced close to the singularity and to be close to order one. The convergence properties close to singularities are juxtaposed in figure 5 to the solution obtained on a Cartesian reference grid with about the same grid resolution as the grid of figure 2. Figure 5 confirms the absolute error to be clearly smaller on the Cartesian reference grid. Furthermore, a higher order of accuracy is obtained. From figure 5 the order of accuracy can be identified to be close to three, hence slightly below the theoretical expectation of four. The reduced order might be caused by the back action of the boundary conditions. The conclusion can be drawn that grid singularities in conjunction with high-order finite difference schemes reduce the order and the accuracy of the computational scheme locally and need to have a higher local grid resolution which can not necessarily be accomplished with elliptic grid smoothers.
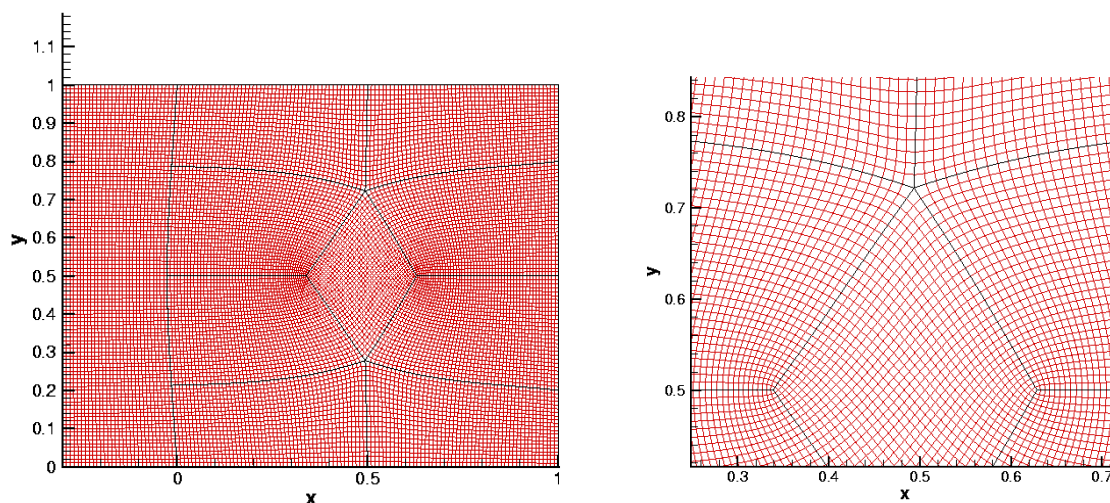
Figure 2.—Computational grid with two three-way and two five-way singularities.
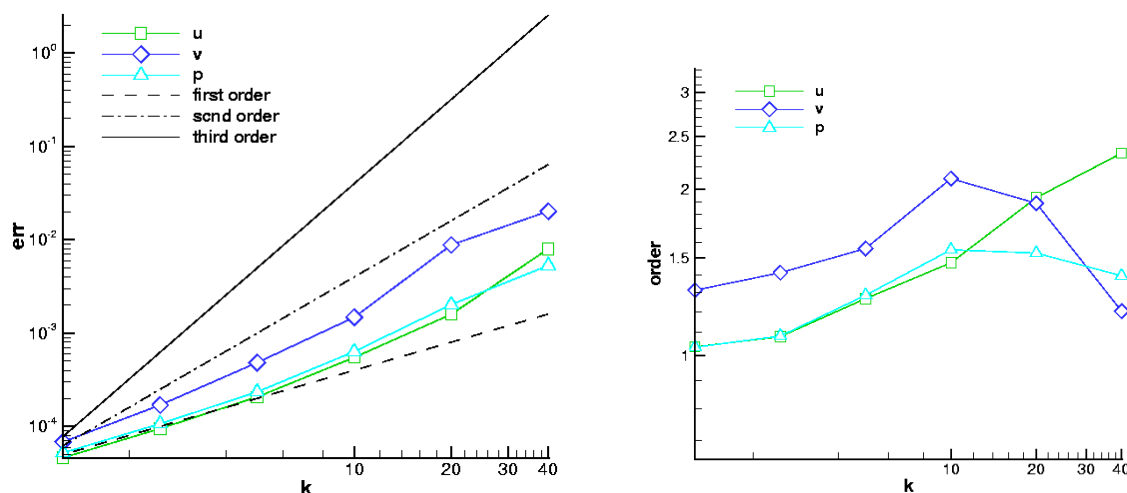
Figure 3.—Error dependence on wavenumber (left) and order of accuracy (right) for the five-way singularity.

COMPLEX GEOMETRY SIMULATIONS

The meshes of the Chimera and body-fitted grid approaches are chosen for the category 2 problems to have a similar far-field resolution of about seven points per wavelength, i.e., close to the effective resolution limit of the DRP scheme. A total number of 36 blocks with 1.27×10^5 grid points is used to resolve the geometry of case 1 with the body-fitted grid, where the grid extends from –10 to 10 and –3 to 3 in x- and y-direction, respectively. The Chimera grid of case 1 employs 1.4×10^5 points and extends from –10 to 10 and –4 to 4, respectively. For case 2, about 42 blocks are used for the curvilinear multiblock topology with a total of 2.17×10^5 points.
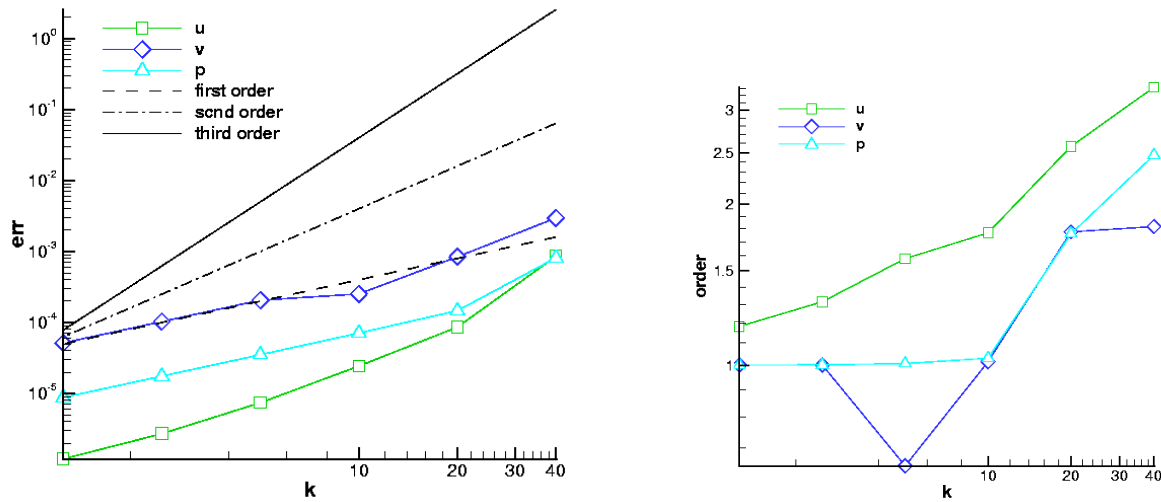
Figure 4.—Error dependence on wavenumber (left) and order of accuracy (right) for the three-way singularity.
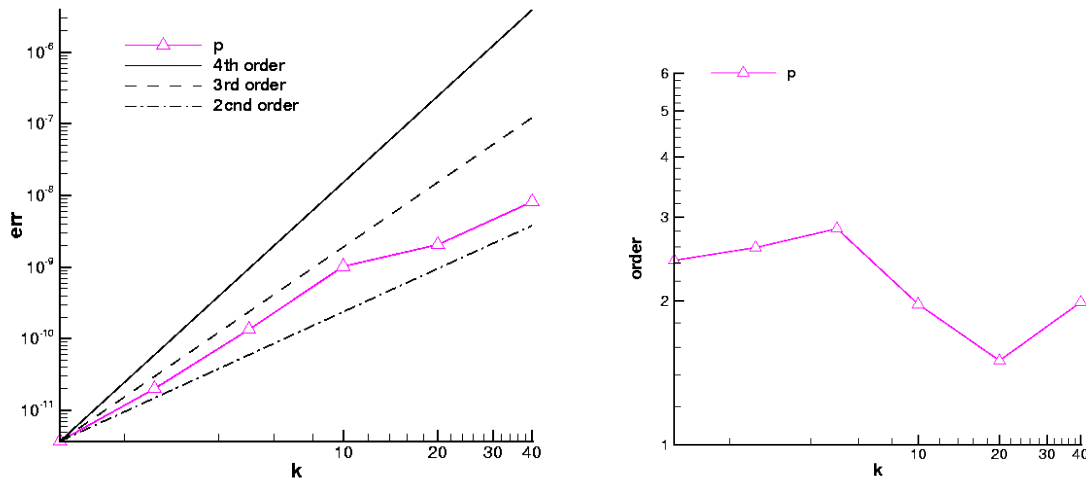
Figure 5.—Error dependence on wavenumber (left) and order of accuracy (right) for a Cartesian reference grid solution.

Figure 6 depicts the topology of the mesh. Figure 7 shows a closeup view of the meshed cylinder for both grid strategies. Only five-way singularities appear in both body-fitted grids. In order to avoid grid spacings too large and too close to the singularities, in addition to the elliptic grid smoothing, the shape and the resolution of the grid in the vicinity of the singularity is analytically prescribed and blended with the elliptically smoothed grid such that the grid spacings close to the singularity are exactly determined (see fig. 7). For both category 2 cases, a harmonic energy source is placed in the origin of the computational grids, that is,

$$S = \exp\left[-\ln(2) \cdot \left\{\frac{x_s^2 + y_s^2}{b^2}\right\}\right] \cdot \sin(\omega t) \qquad (5)$$

with $x_s = 0$, $y_s = 0$, $\omega = 8\pi$, and $b = 0.2$. Figure 8 shows a snapshot of the perturbation pressure fields of case 1 for the Chimera and the body-fitted grid. A very good qualitative agreement is apparent. In figure 9 the root mean square (RMS) pressure distributions on the cylinder surfaces and the mean square pressure (MS) distribution along the centerline $y = 0$ are compared for case 1. All pressure distributions show only a small difference between the Chimera and the body-fitted grid solutions. In this case the maximal peak pressure on the cylinder surfaces is slightly smaller for the BFG computation. Figures 10 and 11 give a snapshot of the pressure field and the pressure distributions for case 2. Again, very good agreement between the body-fitted grid and the Chimera approach is obtained. Note that for case 2 the pressure distributions of the Chimera solution on the smaller cylinder surfaces are slightly smaller compared to the body-fitted grid solution, although the incident waves of the harmonic source are passing through singularities that lie on the connecting lines between source and cylinders 2 and 3, respectively.
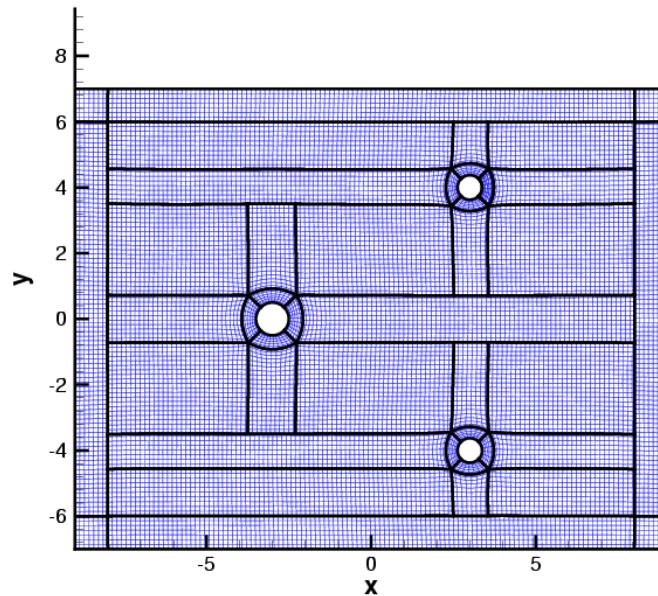
Figure 6.—Body-fitted multiblock grid for the category 2, case 2 problem.
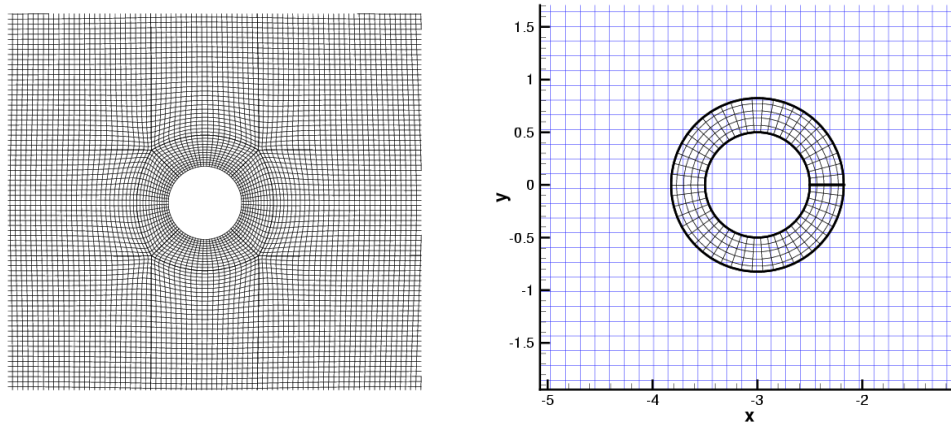
Figure 7.—Grid topology close to the cylinder for the body-fitted approach (left) and the surface and background grids of the Chimera approach (right, every other grid line shown).
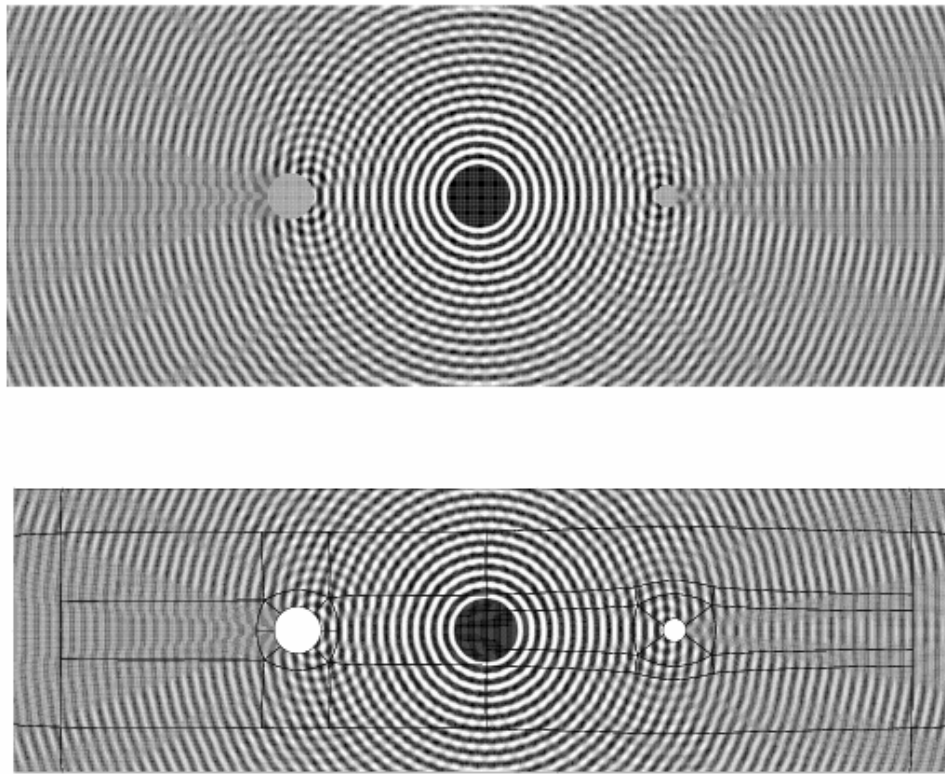
Figure 8.—Pressure plots for case 1, Chimera grid (top) and body-fitted grid (bottom).
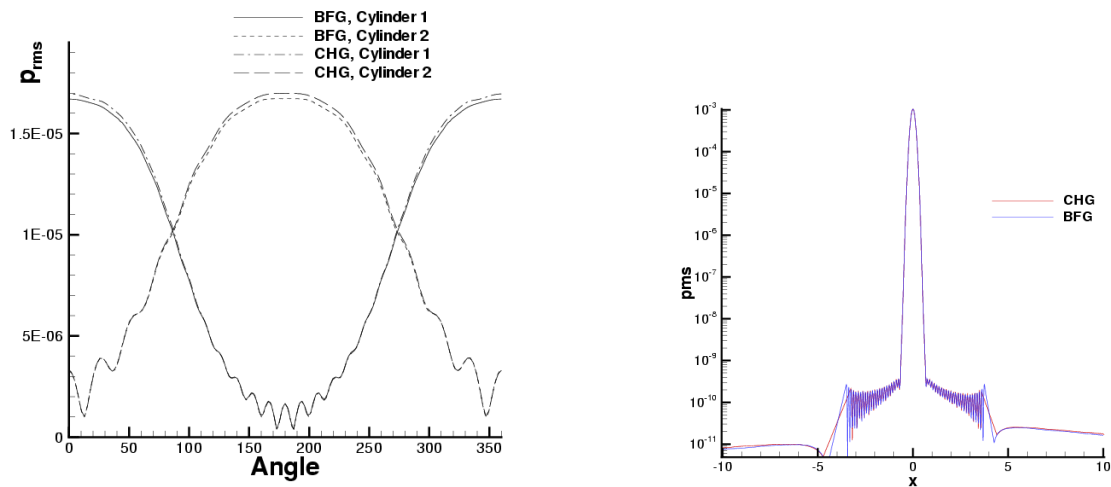
Figure 9.—RMS pressure distribution on the cylinder surfaces (left) and MS pressure distribution along the centerline y = 0 for case 1 (right). BFG is body-fitted grid, CHG is Chimera Grid.
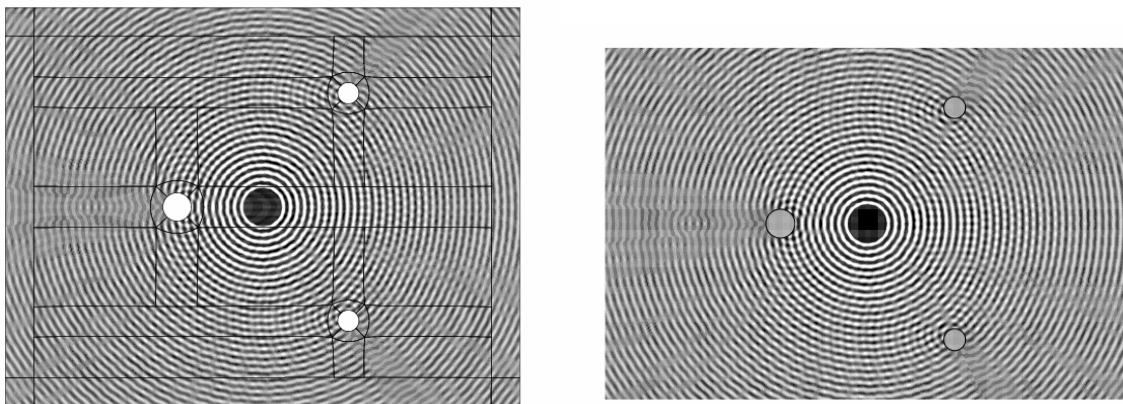
Figure 10.—Pressure plots for case 2, body-fitted grid (left) and Chimera (right).
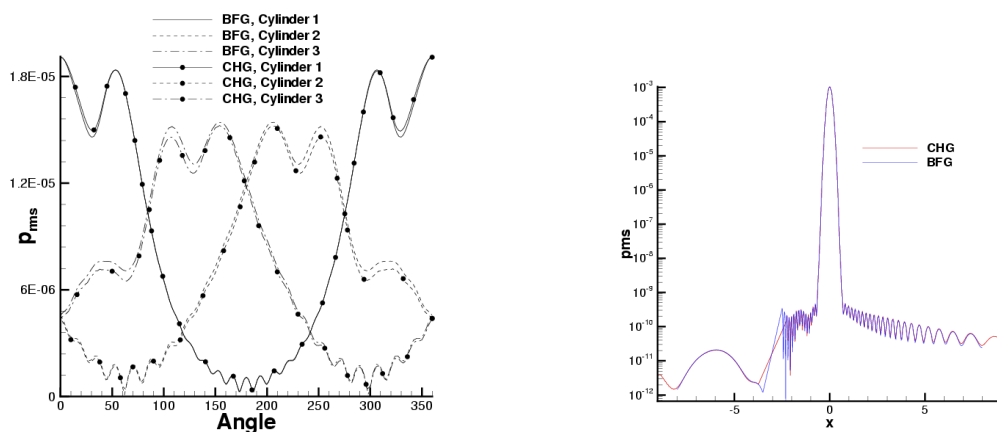
Figure 11.—RMS pressure distribution on the cylinder surfaces (left) and MS pressure distribution along the centerline y = 0 for case 2 (right). BFG is body-fitted grid, CHG is Chimera Grid.

REFRACTION OF SOUND WAVES IN AN UNSTABLE JET

Category 4, problem 1 considers the propagation of acoustic waves due to an energy source inside a two-dimensional hot jet. Due to the jet profile and chosen source frequencies the LEEs not only describe sound propagation but also the growth of convective instability waves. The required solution should only consist of the acoustic part of the solution with the onset of the instability wave suppressed. To suppress the instability waves, modifications of the LEE are used that were proposed in (ref. 3). The linear acoustic perturbation equations (APE) read

$$\frac{\partial p'}{\partial t} + c_0^2 \nabla \cdot \left(\rho_0 \vec{u}' + \vec{u}_0 \frac{p'}{c_0^2} \right) = q_p$$

$$\frac{\partial \vec{u}'}{\partial t} + \nabla \left(\vec{u}_0 \cdot \vec{u}' \right) + \nabla \left(\frac{p'}{\rho_0} \right) = \vec{q}_m$$

(6)

The right-hand side sources q_P, $\vec{q}_m$ follow by rewriting the Navier-Stokes equations in nonlinear disturbance form such that the left-hand side agrees with equation (6). That way an acoustic analogy is obtained, which is based on the acoustic wave operator encoded in the left-hand side equation system. The major source contribution for vortex sound is the Lamb vector $L = (\omega \times u)'$ (ref. 3). The perturbation velocity $\vec{u}'$ can be expressed through an acoustic potential $\nabla \varphi$ and a remaining part $\vec{u}^r$, where the decomposition is uniquely defined by demanding the former component to be related to the complete pressure fluctuations via

$$p' = -\rho_0 \frac{D_0 \varphi}{Dt}. \tag{7}$$

Note that $\vec{u}^r$ is not solenoidal but in general also contains an irrotational part. Introducing the velocity decomposition into the system (eq. (6)) with the right-hand side momentum source dropped yields an equivalent equation system for $\varphi, \vec{u}'$

$$L\varphi = \left[\frac{D_0}{Dt}\left(\frac{1}{c_0^2} \frac{D_0}{Dt} \right) - \frac{1}{\rho_0} \nabla \cdot (\rho_0 \nabla) \right] \varphi = \frac{1}{\rho_0} \nabla \cdot (\rho_0 \vec{u}^r) - \frac{q_P}{\rho_0 c_0^2} \tag{8a}$$

$$\frac{\partial \vec{u}^r}{\partial t} + \nabla (\vec{u}_0 \cdot \vec{u}^r) = \vec{0} \tag{8b}$$

The operator L in equation (8a) is a convective wave operator, hence φ can be related to acoustic fluctuations, while equation (8b) for $\vec{u}^r$ governs the evolution of all vortical components. The convective wave operator L was first used by Goldstein (ref. 12) and agrees with that of the approximate wave equation of Pierce (ref. 13). Möhring proved that the acoustic wave operator L is stable for arbitrary mean flow fields (ref. 14). The wave operator is exact for irrotational, hence isentropic, mean flows. Based on the above decomposition the LEE can be rewritten with the inclusion of an energy source q

$$L\varphi = \left[\frac{D_0}{Dt}\left(\frac{1}{c_0^2} \frac{D_0}{Dt} \right) - \frac{1}{\rho_0} \nabla \cdot (\rho_0 \nabla) \right] \varphi = \frac{1}{\rho_0} \nabla \cdot (\rho_0 \vec{u}^r) - \frac{1}{c_p} \frac{D_0 s'}{Dt} - \frac{q}{\rho_0 c_0^2} \tag{9a}$$

$$\frac{\partial \vec{u}^r}{\partial t} + (\vec{u}_0 \cdot \nabla) \vec{u}^r + (\vec{u}^r \cdot \nabla) \vec{u}_0 = -(\omega_0 \times \nabla \varphi) + T \nabla s_0 - s' \nabla T \tag{9b}$$

Besides the generic energy source q, entropy and temperature fluctuations appear on the right-hand side of the wave equation that have to be prescribed properly for an exact solution. Furthermore, the acoustic mode is coupled with the nonacoustic mode in a mean flow with vorticity, even if the generic source q excites initially only pure acoustic waves. Since the wave operator in equation (9a) is stable, a growing instability wave is described by equation (9b). The related equation (8b) is modified and stable, since taking the curl of it yields $\partial \omega^r / \partial t = 0$, that is, no vorticity is generated and vorticity levels remain constant. If q_P in equation (8a) is equivalent to q in equation (9a), a simplified form of system (eqs. (9a) and (9b)) is solved, where the instability mode is suppressed, but entropy sources and the coupling of the vortical fluctuations with the acoustic potential are neglected. Since the acoustic wave operator with all analogy sources neglected is strictly valid only for irrotational mean flows, the occurrence of mean vorticity will cause errors. In order to quantify these errors, a Strouhal number based on mean-vorticity ω_0 and frequency f of the acoustic waves can be introduced $St = f / \omega_0$. The irrotational limit is defined by the Strouhal number tending to infinity, that is, $St = f / \omega_0 \to \infty$.

In order to assess the errors caused by applying the acoustic perturbation equations without analogy sources in mean flows with vorticity, a harmonic source q in a shear-flow according to figure 12 was considered. The mean vorticity is about $\omega_0 \cong \Delta u / \delta_\omega$. Figure 13 shows a comparison of instantaneous pressure levels for an LEE and an APE simulation for $St = 7.96$. Figure 14 depicts perturbation pressure levels for a line $y = 70$ for Strouhal numbers $St = 7.96$ and $St = 1.59$. For the larger Strouhal number both LEE and APE curves match very well. For the smaller number some small deviations in the pressure curves occur. However, it is remarkable that the acoustic wave-operator that is exactly valid for Strouhal numbers tending to infinity resolves still refraction effects properly for values of the order $O(1)$. Figure 15 shows the scattering of acoustic waves of a harmonic monopole at an airfoil in a viscous mean flow at $M = 0.088$ and $Re = 8 \times 10^5$. Compared are LEE and APE simulations and a LEE simulation without mean flow. Interestingly, even a very small $M = 0.088$ mean flow clearly affects the directivity. The LEE and APE simulations match very well, hence, the latter is capable of resolving the mean-flow effects for mean flows with sufficient mild levels of vorticity.

The jet problem has been computed using a 441 by 331 mesh in the x- and y-direction, respectively. The mesh was clustered in vertical direction such that about 20 grid points were lying inside the jet. For the jet problem it is to be noted that the Strouhal number based on the mean vorticity is of the order of $St = 5 \times 10^{-2}$. Figure 16 shows a comparison of the pressure fields for the unstable LEE simulation and the APE simulation. It is evident that in the APE simulation no instability waves are excited. Figure 17 compares the pressure distributions along a line $y = 50$. Upstream of the heat source at $x = 0$, the pressure curves of the LEE and the APE simulation match quite closely. However, downstream of the source greater differences occur. These are probably due to the acoustic-mean-induced vorticity that again generates secondary acoustic waves that are completely missing in the APE simulation. It can be concluded that due to the small Strouhal number, larger deviations between the LEE and the APE solutions occur. Instability waves are effectively suppressed by the APE system.
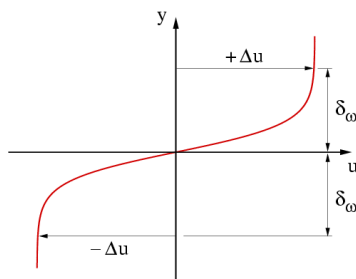
Figure 12.—Tanh-shear flow with mean vorticity ω_0.
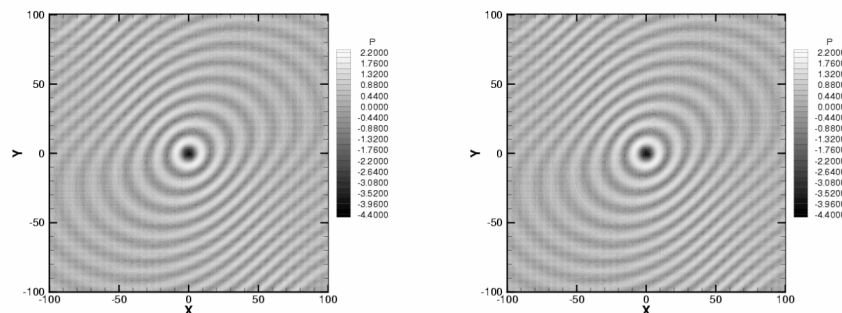
Figure 13.—Influence of mean-flow shear on refraction, pressure snapshot applying LEE (left) and APE (right), harmonic source with St = f/ω_0 = 7.96.
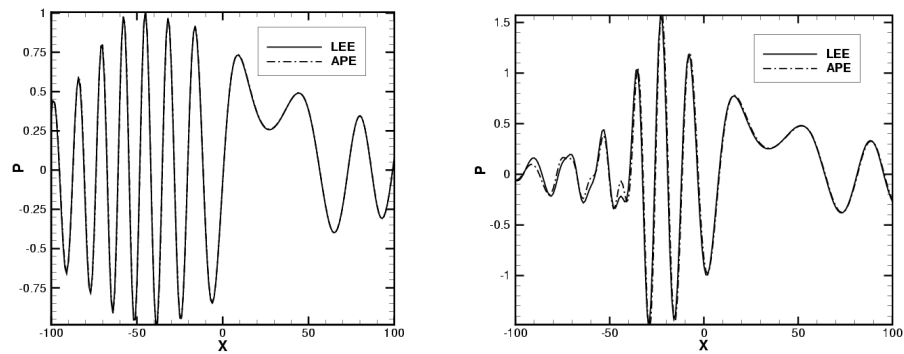
Figure 14.—Influence of mean-flow shear on refraction, cut along y = 70 for St = f/ω_0 = 7.96 (left), St = f/ω_0 = 1.59 (right).
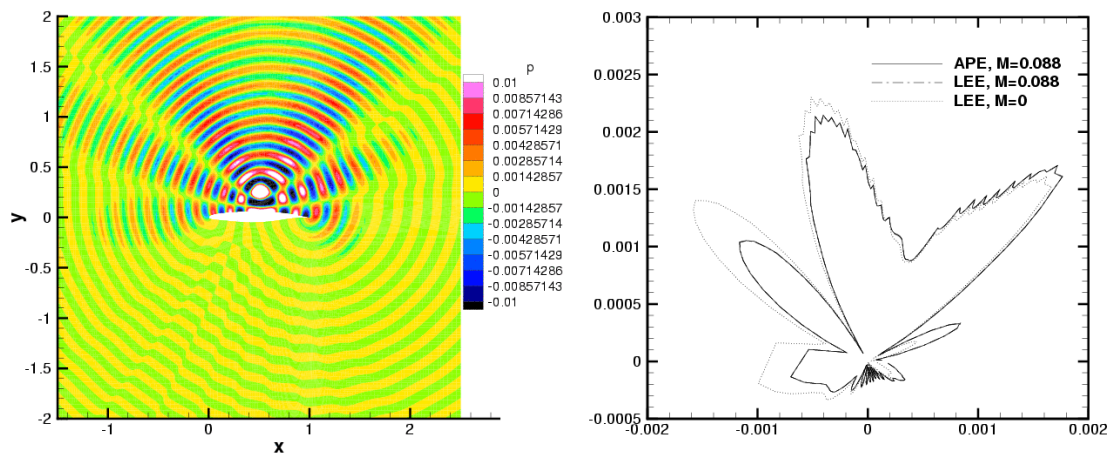
Figure 15.—Scattering of acoustic waves at an airfoil in a viscous M = 0.088 mean flow.
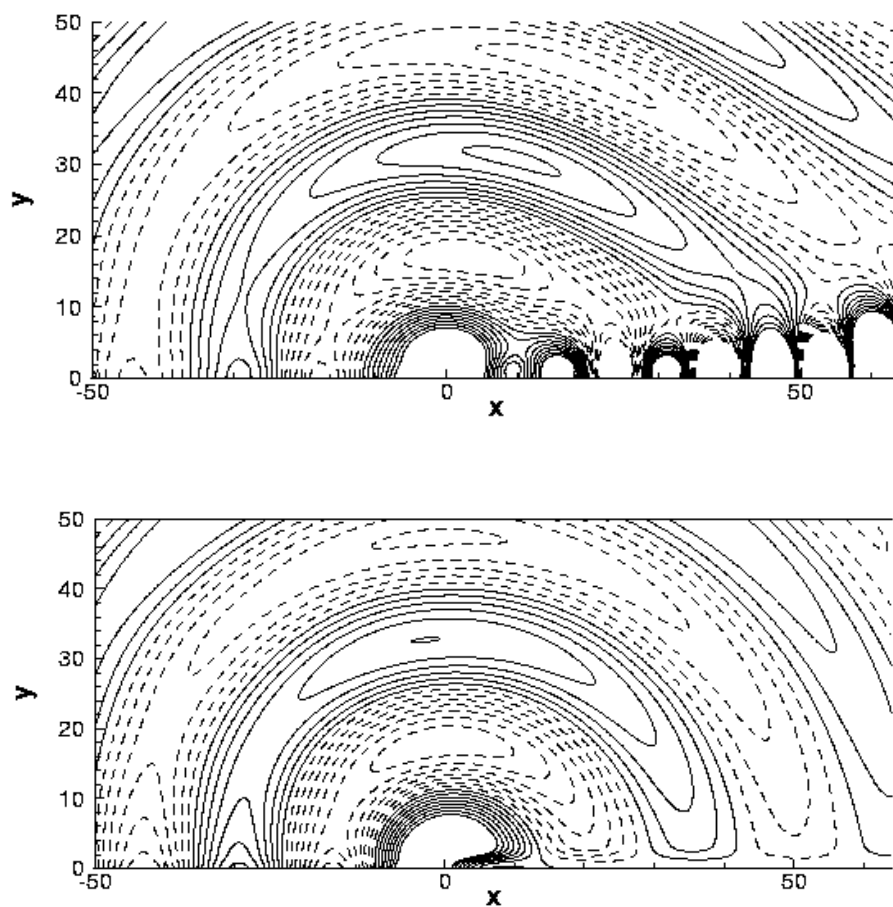
Figure 16.—Unstable LEE (top) and stable APE (bottom) simulation.
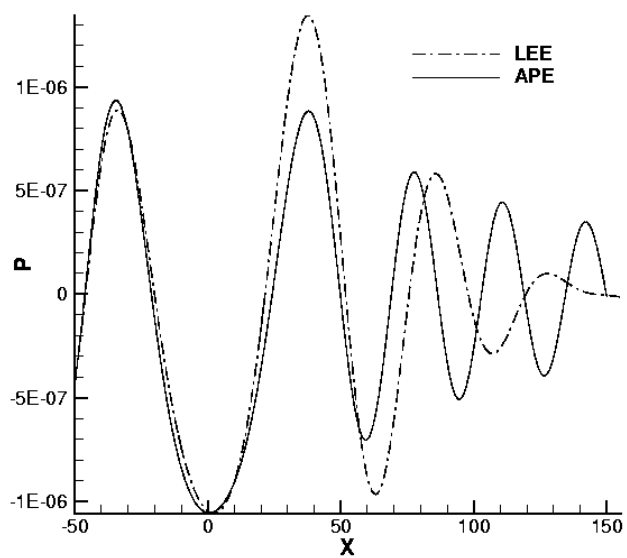
Figure 17.—Pressure distribution along y = 50.

REFERENCES

1. K. Kurbatskii and C.K.W. Tam: Cartesian Boundary Treatment of Curved Walls for High-Order Computational Aeroacoustics Schemes. AIAA J., vol. 35, 1997, pp. 133–140.
2. J. Yin, et al.: Prediction of Noise from Interaction of Vorticity With Airfoils Using CAA. 7th International Congress On Sound and Vibration, 2000, Garmisch Partenkirchen, Germany.
3. R. Ewert and W. Schröder: Acoustic Perturbation Equations Based on Flow Decomposition Via Source Filtering. J. Comput. Phys., vol. 188, 2003, pp. 365–398.
4. M.J. Lighthill: On Sound Generated Aerodynamically: I. General Theory. Proc. R. Soc. London Ser. A, vol. 211, 1952, pp. 654-687.
5. C.K.W. Tam and J.C. Webb: Dispersion-Relation-Preserving Finite Difference Scheme for Computational Acoustics. J. Comput. Phys., vol. 107, 1993, pp. 262–281.
6. C.K.W. Tam and Z. Dong: Wall Boundary Conditions for High-Order Finite-Difference Schemes in Computational Aeroacoustics. Theoret. Comput. Fluid Dynamics, vol. 6, 1994, pp. 303–322.
7. O. Vasilyev: A General Class of Commutative Filters for LES in Complex Geometries. J. Comput. Phys., vol. 146, 1998, pp. 82–104.
8. G. Chesshire and W.D. Henshaw: Composite Overlapping Meshes for the Solution of Partial Differential Equations, J. Comput. Phys., vol. 90, 1990, pp. 1–64.
9. J.W. Delfs: An Overlapping Grid Technique for the Use of High Resolution Schemes of Computational Aeroacoustics at Complex Geometries. AIAA Paper 2001–2199, 2001.
10. J. Yin and J.W. Delfs: Sound Generation from Gust-Airfoil Interaction Using CAA-Chimera Method. AIAA Paper 2001–2136, 2001.
11. R. Hixon, and M. Nallasamy, et al.: Effect of Grid Singularities on the Solution Accuracy of a CAA Code. AIAA Paper 2003–879, 2003.
12. M. Goldstein: Unsteady Vortical and Entropic Disturbances of Potential Flows Round Arbitrary Obstacles. J. Fluid Mech., vol. 891, 1978, pp. 433–468.
13. A. Pierce: Wave Equation for Sound in Fluids With Unsteady Inhomogeneous Flow. J. Acoustical Society of America, vol. 87, 1990, pp. 2292–2299.
14. W. Möhring: Modelling Low Mach Number Noise. Mechanics of Sound Generation in Flows, E.-A. Müller, ed., Springer, 1979.

HIGH-ORDER OVERSET-GRID SIMULATIONS OF ACOUSTIC SCATTERING FROM MULTIPLE CYLINDERS

Scott E. Sherer and Miguel R. Visbal
Computational Sciences Center of Excellence
Air Vehicles Directorate, Air Force Research Laboratory
2210 Eighth Street
Wright-Patterson AFB, OH 45433-7510

ABSTRACT

A parallel, overset-grid method based on high-order spatial and temporal algorithms is used to solve the multiple-body acoustic scattering problems associated with Category 2 of the Fourth Computational Aeroacoustics Workshop on Benchmark Problems. The solution methodology is based on a spatially high-order compact finite-difference algorithm coupled with high-order, low-pass spatial filtering. Various parametric studies are performed to evaluate the accuracy of the computational algorithm.

INTRODUCTION

Due to its stringent accuracy requirements, high-order and/or optimized methods are generally preferred for computational simulations of aeroacoustic phenomena (see Refs. 1, 2, 3 for various examples). These methods can reduce the numerical error for a given grid resolution, or conversely decrease the number of grid points necessary to maintain a particular error level, when compared to lower-order methods. However, very large grids may still be necessary, even when using such high-order methods, in order to resolve all important scales over a large computational domain. Also, the ability to handle geometrically complex problems has been identified as a key item in the continued maturation of the field (Ref. 4). In an attempt to address these concerns, a general, high-order CFD code has been parallelized and extended to general, overset-grid topologies to allow for larger and more complex structured grid topologies to be employed.

In the present work, this code is used to simulate the scattering of acoustic waves by multiple circular cylinders. The specific cases examined here are specified in Category 2 of the Fourth Computational Aeroacoustics (CAA) Workshop on Benchmark Problems. Computed results are compared to the analytic solutions, and accuracy of the results is evaluated. The following sections of this paper present the governing equations, the spatial and temporal algorithms being employed to solve them, and the results obtained for the two benchmark problems under consideration.

NUMERICAL APPROACH

Governing Equations

As the code used to perform these computations is a general, three-dimensional, fluid dynamics code, the full (non-linear), 3D Euler equations provide the governing set of equations, even though the third dimension is degenerate in this case. Applying a three-dimensional, curvilinear coordinate transformation between physical and computational space, the Euler equations may be written in computational coordinates as

$$\frac{\partial}{\partial t}\left(\frac{\vec{Q}}{J}\right) + \frac{\partial \hat{F}}{\partial \xi} + \frac{\partial \hat{G}}{\partial \eta} + \frac{\partial \hat{H}}{\partial \zeta} = \frac{\vec{S}}{J} \tag{1}$$

where J is the Jacobian of the coordinate transformation, and the solution vector as a function of the fluid density ρ, the velocity components u, v, w, and the total energy E is given by

$$\vec{Q} = \begin{bmatrix} \rho \\ \rho u \\ \rho v \\ \rho w \\ \rho E \end{bmatrix} \tag{2}$$

The inviscid flux vectors are defined by

$$\hat{F} = \frac{1}{J} \begin{bmatrix} \rho U \\ \rho u U + \xi_x p \\ \rho v U + \xi_y p \\ \rho w U + \xi_z p \\ (\rho E + p) U \end{bmatrix} \qquad \hat{G} = \frac{1}{J} \begin{bmatrix} \rho V \\ \rho u V + \eta_x p \\ \rho v V + \eta_y p \\ \rho w V + \eta_z p \\ (\rho E + p) V \end{bmatrix} \qquad \hat{H} = \frac{1}{J} \begin{bmatrix} \rho W \\ \rho u W + \zeta_x p \\ \rho v W + \zeta_y p \\ \rho w W + \zeta_z p \\ (\rho E + p) W \end{bmatrix} \tag{3}$$

where p is the fluid static pressure, $(\xi, \eta, \zeta)_{x,y,z}$ are the grid transformation metrics, and the contravariant velocity components are defined as

$$U = \xi_x u + \xi_y v + \xi_z w$$

$$V = \eta_x u + \eta_y v + \eta_z w \tag{4}$$

$$W = \zeta_x u + \zeta_y v + \zeta_z w$$

The total energy is given as a function of the fluid temperature T as

$$E = \frac{T}{(\gamma - 1)M_\infty^2} + \frac{1}{2}\left(u^2 + v^2 + w^2\right) \tag{5}$$

where γ is the ratio of specific heats. The perfect gas law, $p = \rho R T$, is also assumed, where R is the specific gas constant. The source term on the right-hand side of Eq. 1 applies to the energy equation only, and is specified by the benchmark problem statement as

$$S = \exp\left[-25\ln 2\left(x^2 + y^2\right)\right]\sin(8\pi t) \tag{6}$$

A cubic ramping function is added to the above equation to gradually introduce the source into the computational domain over some finite amount of time at the beginning of the computation.

Spatial Differencing

The code used to perform the calculations described here is a version of the FDL3DI code (Ref. 5), developed by researchers in the Computational Sciences Center of Excellence of the Air Force Research Laboratory's Air Vehicles Directorate. The numerical algorithm that forms the core of this code is a high-order finite-difference approach based on compact formulations (Ref. 6). On the interior of the computational domain, the spatial derivatives required by Eq. 1 are found at the node points in computational space through application of the general formula

$$\Gamma\phi'_{i-1} + \phi'_i + \Gamma\phi'_{i+1} = \frac{b}{4}\left(\phi_{i+2} - \phi_{i-2}\right) + \frac{a}{2}\left(\phi_{i+1} - \phi_{i-1}\right) \tag{7}$$

The coefficients $\Gamma, a,$ and b determine the spatial order-of-accuracy of the method as well as whether the derivatives are computed implicitly or explicitly. Two interior algorithms were employed in this work; a compact (implicit) sixth-order method denoted by $C6$ where $\Gamma = 1/3, a = 14/9, b = 1/9$ and an explicit fourth-order scheme denoted by $E4$ where $\Gamma = 0.0, a = 4/3, b = -1/3$. Both of these methods have identical five-point stencils. Additional details on the numerical differencing algorithm may be found in Refs. 5 and 7.

On or at one point away from a computational boundary, the centered formulation of Eq. 7 cannot be applied. In this case, high-order one-sided difference formulas that maintain the tridiagonal form of Eq. 7 are used. These formulas are given in Ref. 5.

Spatial Filtering

Because the algorithms generated by Eq. 7 are centered, they are non-dissipative and thus susceptible to the growth of numerical instabilities. For this reason, implicit, Padé-type, low-pass filters of up to 10th-order are employed to remove spurious, non-physical, high-frequency waves. These filters are given by the general equation

$$\alpha_f \hat{\phi}_{i-1} + \hat{\phi}_i + \alpha_f \hat{\phi}_{i+1} = \sum_{n=0}^{N} \frac{a_n}{2} \left(\phi_{i+n} + \phi_{i-n} \right) \tag{8}$$

where the filter coefficient α_f is a free parameter satisfying $-0.5 < \alpha_f \leq 0.5$ that controls the spectral response of the filter (Ref. 7). The values of a_n for even orders-of-accuracy up to 10th-order are tabulated as a function of the filter coefficient in Ref. 8. These interior filters are non-dispersive, do not amplify any waves, and result in the complete annihilation of the odd-even mode.

A $2N^{th}$-order centered filter as represented by Eq. 8 requires a $2N+1$ point stencil, and thus can not be applied near computational boundaries. In these regions, high-order one-sided filters are employed to maintain solution quality. These one-sided filters do result in the amplification of some waves, although this amplification occurs at higher values wavenumbers that typically have less energy content. Also these amplified waves occur at wavenumbers that are strongly filtered by the interior filters as they propagate away from the boundary. If necessary, the peak amplification can also be controlled through the adjustment of the filter coefficient in the boundary regions. The formulations for the high-order, one-sided boundary filters are given in Ref. 8 as well as further discussion on their application.

Temporal Integration

The classic, explicit, 4th-order accurate Runge-Kutta method is employed to advance the solution in time. Defining a residual using Eq. 1 as

$$\frac{\partial \vec{Q}}{\partial t} = R(\vec{Q}) = -J \left(\frac{\partial \hat{F}}{\partial \xi} + \frac{\partial \hat{G}}{\partial \eta} + \frac{\partial \hat{H}}{\partial \zeta} - \frac{\vec{S}}{J} \right) \tag{9}$$

the method integrates from time step n at time t_0 to time step $n+1$ at time $t_0 + \Delta t$ through a four-stage approach given by

$$k_0 = \Delta t\, R(\vec{Q}_0) \qquad\qquad k_1 = \Delta t\, R(\vec{Q}_1)$$

$$k_2 = \Delta t\, R(\vec{Q}_2) \qquad\qquad k_3 = \Delta t\, R(\vec{Q}_3) \tag{10}$$

$$\vec{Q}^{n+1} = \vec{Q} + \frac{1}{6} \left(k_0 + 2k_1 + 2k_2 + k_3 \right)$$

where $\vec{Q}_0 = \vec{Q}(x, y, z, t_0), \vec{Q}_1 = \vec{Q}_0 + k_0/2, \vec{Q}_2 = \vec{Q}_1 + k_1/2, \vec{Q}_3 = \vec{Q}_2 + k_2/2$. The method is implemented in low-storage form (Ref. 9).

Overset Grid Approach

As mentioned in the Introduction, an overset-grid approach (Refs. 10 and 11) has been incorporated into FDL3DI in order to address more geometrically complex problems as well as provide a means for parallel processing via domain decomposition. The first step in this approach is to generate overset, structured grids based on the physical nature of the problem. These grids could arise from the geometry of the problem as well as the need to resolve certain flow features at particular locations in the domain. Once this overset grid system is generated, the individual grids are decomposed into overlapping blocks for parallel processing, with each block assigned to a unique processor. Between two blocks decomposed from a single grid, the overlap consists of five coincident points, with a two-point fringe that exchanges data via direct-injection (see Fig. 1). This technique has been shown to reproduce the single-domain results for a variety of problems (Refs. 8 and 12).

In the overlap regions between different grids, the points are in general non-coincident as shown in Fig. 2. In these regions, a high-order Lagrangian interpolation procedure (Ref. 13) with a two-point fringe is used to provide grid communication. For both types of overlap regions, the connectivity between grids/blocks is determined using the PEGASUS Version 5 software (Ref. 14), a well-established code in the overset grid community. The

interpolation offsets and coefficients provided by PEGASUS, however, are only 2nd-order accurate. Thus a preprocessing code named BELLERO (after Bellerophone from Greek mythology, the tamer of Pegasus and heroic vanquisher of the monster Chimaera) was written to take the connectivity data provided by PEGASUS and extend it to arbitrarily high orders (Ref 15).

The idea of having one grid cut a "hole" in another grid adds more flexibility to the overset-grid approach. This concept is implemented here by having BELLERO identify the boundaries of any holes cut in grids by PEGASUS, which are treated by the flow solver as computational boundaries. One-sided differencing and filtering formulas are inserted into the implicit algorithm near the holes, while the hole points themselves are decoupled from the rest of the implicit algorithm.

More details on the overset grid approach, both as a parallelization technique as well as to handle geometric complexity, can be found in References 12, 13, and 16.

Boundary Conditions

Because both Problems 1 and 2 exhibit symmetry about the horizontal axis, only one-half of the domain was utilized in the computations. Standard symmetry conditions with 4th-order extrapolations were employed to find the flow variables along the centerline axis. At the solid surfaces, the physical velocity components are found from the contravariant velocity components by setting V at the surface equal to zero and extrapolating for U on the surface using a 4th-order formulation. The pressure and density at the wall are also found by using 4th-order extrapolations.

At the far-field boundaries, the energy transfer and annihilation (ETA) technique (Refs. 1 and 17) is employed. This technique exploits the characteristics of low-pass spatial filter by creating a buffer region of rapid grid stretching outside the resolved region of the grid. Energy that is reflected back into the resolved region by the grid stretching is in the high-frequency modes and is removed by the filter. The filter also dissipates the energy that is transmitted across the interface through the diminished resolution of the grid. At the outer boundary, simple extrapolation conditions are then employed. While this approach does add to the number of grid points in the computation, the fact that it uses an existing element of the solution algorithm (the filter) and does not require any additional equations to be solved makes it an attractive approach for aeroacoustic problems.

NUMERICAL RESULTS

Unless otherwise indicated, all solutions presented here were found using the $C6$ spatial differencing algorithm with 10th-order interior filtering ($C6F10$) and a filter coefficient of 0.45. Minimum 8th-order one-sided filters were used at grid points that were five points or less from a computational boundary, and 4th-order interpolation was employed at all interpolation boundaries. The solutions were advanced with a time step of 0.002 (125 time steps per source period) for a total of 20,000 time steps, with mean values computed over the last 2,000 time steps. While this time step was chosen to ensure time-step independence, no effort was made here to evaluate the effect of time step on the solution quality. Figure 3 shows a typical computational domain and decomposed blocks used for the three-cylinder configuration, with two body-fitted grids and a background Cartesian grid containing both resolved and stretched ETA regions. No attempt was made here to investigate the size of the background grid or the number of grid points used in the ETA region, and the values selected as shown in Fig. 3 are very conservative.

A summary of all of the cases presented here is given in Table 1. This table lists for each grid examined its resolution, number of grid points in one of the three two-dimensional planes used in the simulation, the number of processors the case was run on, the number of CPU-hours per processor required to generate the solutions, and the breakdown of grid points in the various elements of the overall grid topology (well-resolved background grid, body-fitted grids, ETA region and the amount of overhead arising from the domain decomposition process).

Two-Cylinder Scattering (Category 2 Problem 1)

Figure 4 shows the computed mean-squared fluctuating pressure field over the entire resolved portion of the computational domain. In Figs. 5 and 6, the RMS of the fluctuating pressure is plotted on the surface of the cylinders and along the centerline for the grid resolutions of 7 points-per-wave (PPW), 8 PPW and 12 PPW. The consistent improvement in the results with respect to the analytic solution is visible as the resolution is increased.

Table 1. Summary of cases examined

Case	Grid	2D Grid Points	Grid point breakdown by %				Number of Processors	CPUhr/ processor
			Resolved background	Body-fitted	ETA region	Decomp overhead		
2CYL	7 PPW	2.14e5	73.7	2.7	15.4	8.1	21	2.38
	8 PPW	2.72e5	75.6	2.1	13.8	8.6	26	2.87
	12 PPW	5.68e5	81.3	2.0	9.7	6.9	31	5.56
3CYL	8 PPW	2.77e5	74.1	3.4	13.5	9.0	26	2.87
	12 PPW	5.80e5	79.6	3.7	9.5	7.1	34	5.63

E4F8 results required 2.63 CPUhr/proc for the 8 PPW grid and 5.15 CPUhr/proc for the 12 PPW grid.

Figure 7 shows the RMS pressure on the cylinders computed using a compact 6th-order algorithm as well as with a standard 4th-order algorithm. The compact solver is seen to produce more accurate results on the 8 PPW grid than the explicit method does using the 12 PPW grid, and given the data in Table 1, in about half the time. Figure 8 examines the impact of the minimum order boundary filter employed at points adjacent to the computational boundaries with the 8 PPW grid. While the 2nd-order boundary filter clearly produces unsatisfactory results, the higher-order boundary filters match the analytic solution much better, with the accuracy improving as the order is increased. For all of the cases examined here, numerical stability was maintained without having to increase the filter coefficient in the near-boundary region. Figure 9 examines the impact of the order of accuracy of the interpolation method on the results obtained on the cylinder surfaces and in the left-most shadow region. While the 2nd-order interpolation produces reasonable results, those obtained with the higher-order interpolation better match the analytic results. The higher-order interpolation resulted in a much smoother transition between the body-fitted and background grids in the shadow region, while the result obtained with the 2nd-order method exhibits a substantial jump in this region. Although not shown, the 12 PPW grid produced less difference between computed and analytic solution with 2nd-order interpolation and a smoother transition across grids in the shadow region, while the results obtained with the 2nd-order interpolation on the 7 PPW grid exhibited poorer agreement between computed and analytic solutions and a larger jump between grids. A slight decrease in accuracy is seen when going from 4th-order to 6th-order interpolation, which is attributed to the more one-sided stencils in the higher-order method due to the minimum amount of overlap used between body-fitted and background grids.

Three-Cylinder Scattering (Category 2 Problem 2)
In Figure 10, the computed mean-squared fluctuating pressure field is plotted over the resolved portion of the grid for the three-cylinder case. For this case, only eight and twelve PPW grids were used, and the computed RMS fluctuating pressures on the cylinder surfaces and centerline obtained on these grids are shown in Figs. 11 and 12. Again, excellent results were obtained with both grids, with the 12 PPW grid being nearly indistinguishable from the analytic solution. Although not shown here, the computed solutions behaved in a similar manner as the two-cylinder results when the order of accuracy of the interpolation was varied, with the 2nd-order method generating reasonable results, but the higher-order accurate interpolation producing better agreement with the analytic solution and a smoother transition across the grids in the shadow region. A sample time history taken at a point located approximately midway between the left and top-right cylinder is shown in Fig. 13, demonstrating the ramping up of the source at the onset of the calculation, the transient waves bouncing between cylinders, and the eventual evolution of the time-periodic solution. Finally, Fig. 14 shows an instantaneous snapshot of the fluctuating pressure field after the solution has reached its time-periodic state. The interference pattern formed by the incident and scattered fields and the damping of the acoustic waves as they leave the resolved region of the background grid due to the ETA technique may be clearly observed.

CONCLUSIONS

A parallel, high-order, overset grid solver was successfully employed on the Category 2 problems of scattering from multiple circular cylinders. This approach allows for more complex geometric problems to be examined with the high-order algorithm as well as providing a means for more efficient use of resources through the ability to cluster grid points in regions of the domain that may require more resolution. The algorithm was shown to produce good results using grid resolutions as low as 7 points per wave (PPW), with excellent agreement between computed and analytic results observed at a resolution of 8 PPW. The accuracy of the computed solution was demonstrated to consistently increase as the grids were resolved. Based on the results obtained by varying the minimum-order boundary filter and the order-of-accuracy of the interpolation method, high-order boundary filters and interpolation methods are necessary to fully realize the benefits of the high-order algorithm.

ACKNOWLEDGMENTS

REFERENCES

1. Visbal, M.R. and Gaitonde, D.V.: "Very High-Order Spatially Implicit Schemes for Computational Acoustics on Curvilinear Meshes"; *J. Comput. Acoust.*, vol. 9, no. 4, 2001, pp. 1259-1286.
2. Casper, J. and Meadows, K.R.: "Using High-Order Accurate Essentially Nonoscillatory Schemes for Aeroacoustic Applications", *AIAA Journal*, vol. 34, no. 2, Feb. 1996, pp. 244-250.
3. Zhuang, M. and Chen, R.: "Optimized Upwind Dispersion-Relation-Preserving Finite Difference Scheme for Computational Aeroacoustics", *AIAA Journal*, vol. 33, no. 2, Feb. 1995, pp. 237-245.
4. *Third Computational Aeroacoustics Workshop on Benchmark Problems*, NASA/CP-2000-209790, Aug. 2000.
5. Gaitonde, D.V. and Visbal, M.R.: "High-Order Schemes for Navier-Stokes Equations: Algorithm and Implementation into FDL3DI", Technical Report AFRL-VA-WP-TR-1998-3060, Air Vehicles Directorate, Air Force Research Laboratory, Aug. 1998.
6. Lele, S.K.: "Compact Finite Difference Schemes with Spectral-like Resolution", *J. Comput. Phys.*, vol. 103, no. 1, 1992, pp. 16-42.
7. Visbal, M.R. and Gaitonde, D.V.: "High-Order-Accurate Methods for Complex Unsteady Subsonic Flows", *AIAA Journal*, vol. 37, no. 10, Oct. 1999, pp. 1231-1239.
8. Gaitonde, D.V. and Visbal, M.R.: "Padé-Type Higher-Order Boundary Filters for the Navier-Stokes Equations", *AIAA Journal*, vol. 38, no. 11, Nov. 2000, pp. 2103-2112.
9. Fyfe, D.: "Economical Evaluation of Runge-Kutta Formulae", *Math. Comp.*, vol. 20, 1966, pp. 392-398.
10. Benek, J., Steger, J., and Dougherty, F.: "A Flexible Grid Embedding Technique with Applications to the Euler Equations", AIAA Paper 83-1944, 1983.
11. Benek, J., Buning, P. and Steger, J.: "A 3-D Chimera Grid Embedding Technique", AIAA Paper 85-1523, 1985.
12. Morgan, P.E., Visbal, M.R., and Rizzetta, D.P.: "A Parallel High-Order Flow Solver for LES and DNS", AIAA Paper 2002-3123, 2002.
13. Sherer, S.E. and Visbal, M.R.: "Computational Study of Acoustic Scattering from Multiple Bodies Using a High-Order Overset Grid Approach", AIAA Paper 2003-3203, 2003.
14. Suhs, N.E., Rogers, S.E., and Dietz, W.E.: "PEGASUS 5: An Automated Pre-processor for Overset-Grid CFD", AIAA Paper 2002-3186, 2002.
15. Sherer, S.E.: *Investigation of High-Order and Optimized Interpolation Methods with Implementation in a High-Order Overset Grid CFD Code,* Ph.D. Thesis, The Ohio State University, 2002.
16. Sherer, S.E.: "Further Analysis of High-Order Overset Grid Method with Applications", AIAA Paper 2003-3839, 2003.
17. Edgar, N. and Visbal, M.R.: "A General Buffer Zone-type Non-Reflecting Boundary Condition for Computational Aeroacoustics", AIAA Paper 2003-3300, 2003.
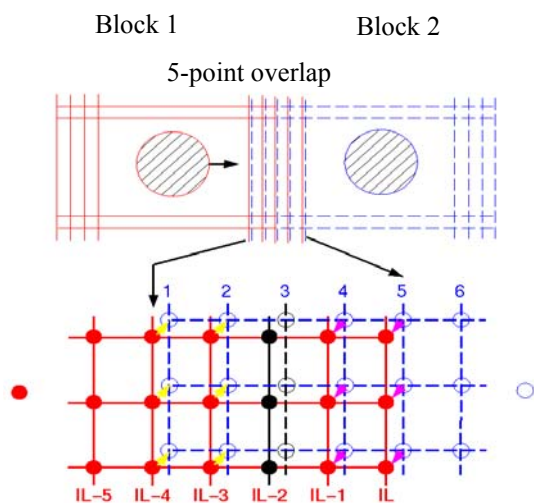
Figure 1. Overlap region between blocks decomposed from same grid; coincident grid points
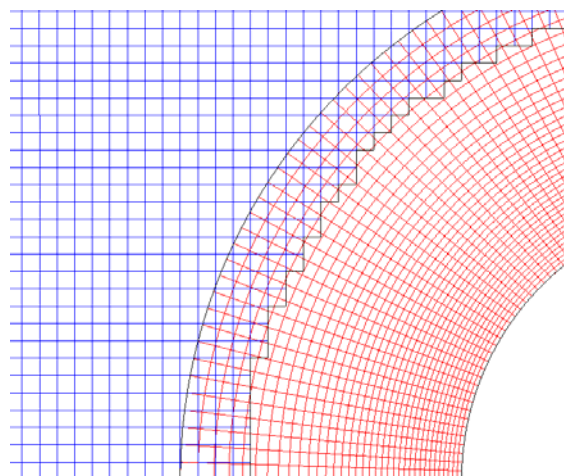
Figure 2. Overlap region between different grids; non-coincident grid points
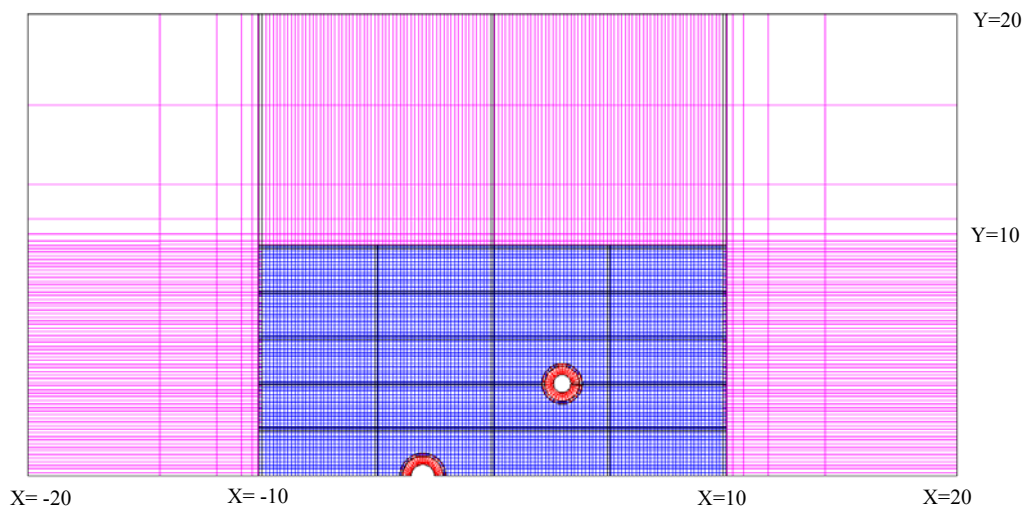
Figure 3. Sample topology for three-cylinder problem showing body-fitted and background grids and decomposed blocks (every fifth grid line shown).
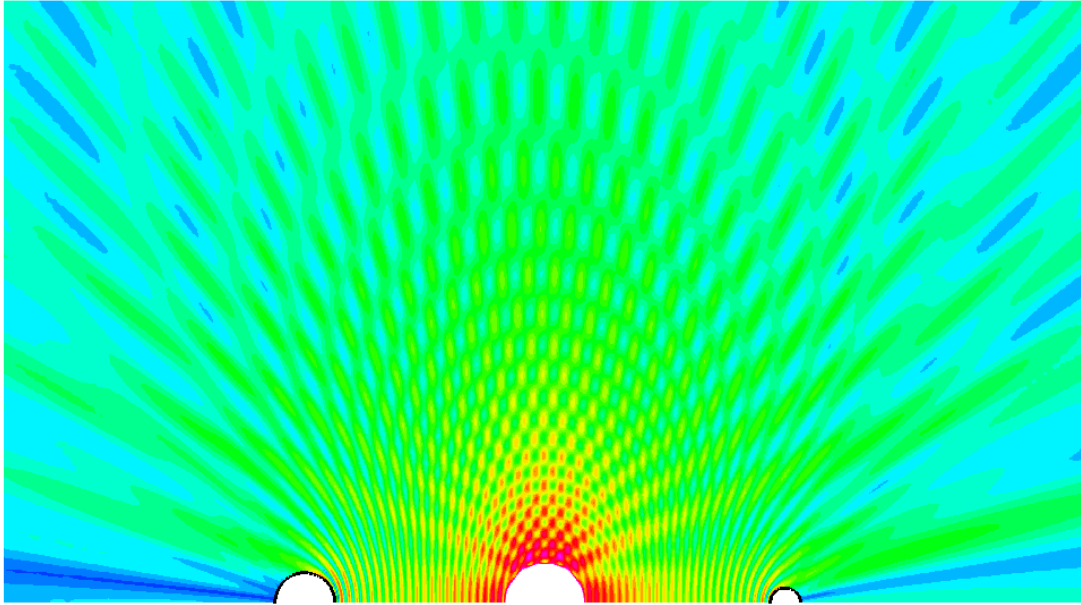
Figure 4. Mean-squared fluctuating pressure contours for two-cylinder configuration on resolved portion of domain.
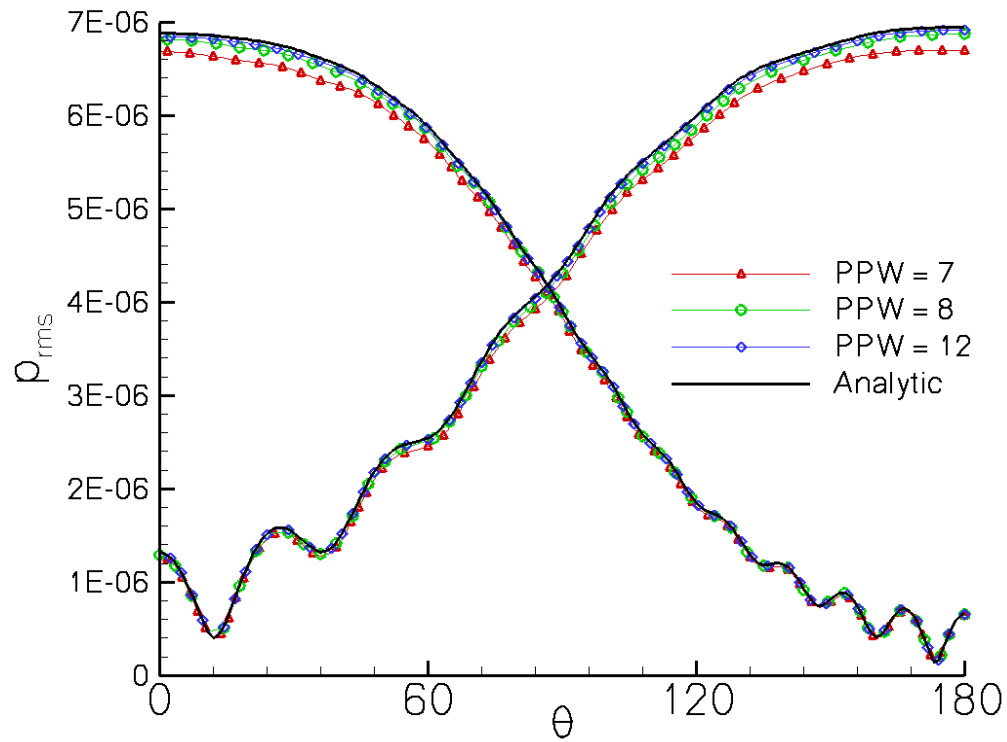
Figure 5. Variation of RMS fluctuating pressure with grid resolution on surface of cylinders; two-cylinder configuration.
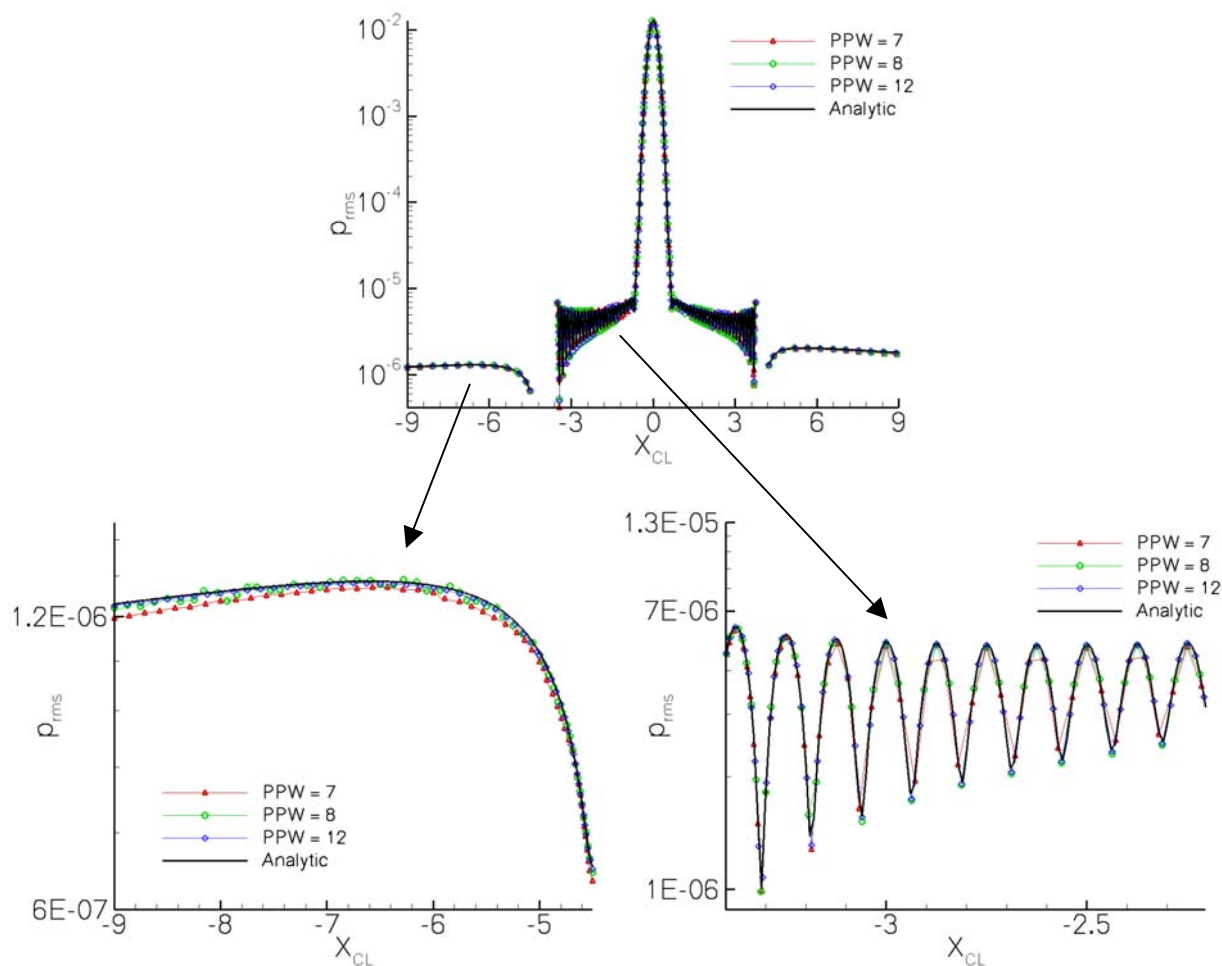
Figure 6. Variation of RMS fluctuating pressure with grid resolution on domain centerline; two-cylinder configuration.
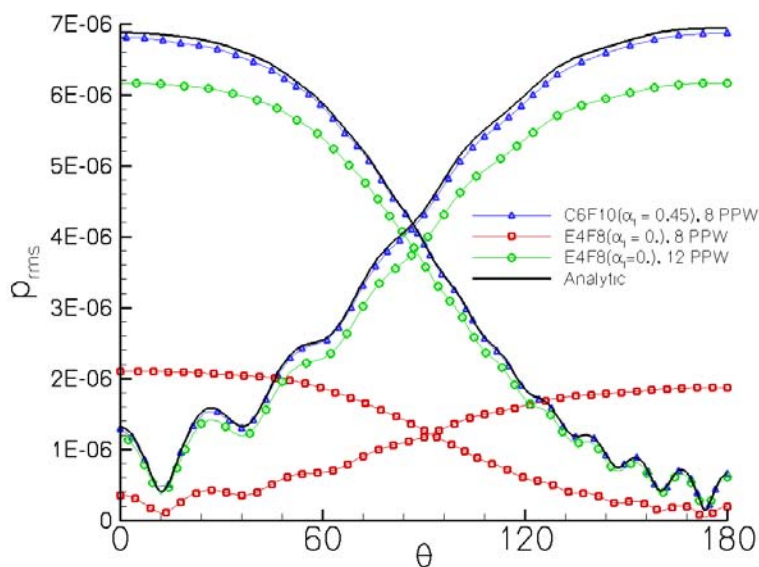
Figure 7. Comparison of RMS fluctuating pressure on cylinder surfaces between compact (C6F10) and standard explicit (E4F8) algorithms; two-cylinder configuration.
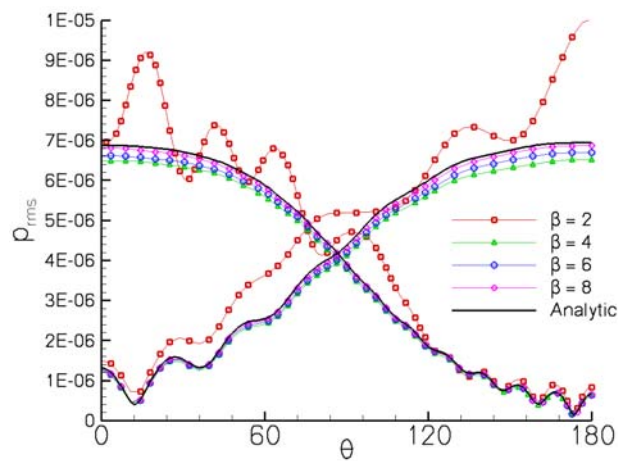
Figure 8. RMS fluctuating pressure profiles on cylinder surfaces for various boundary filter orders of accuracy; two-cylinder configuration.
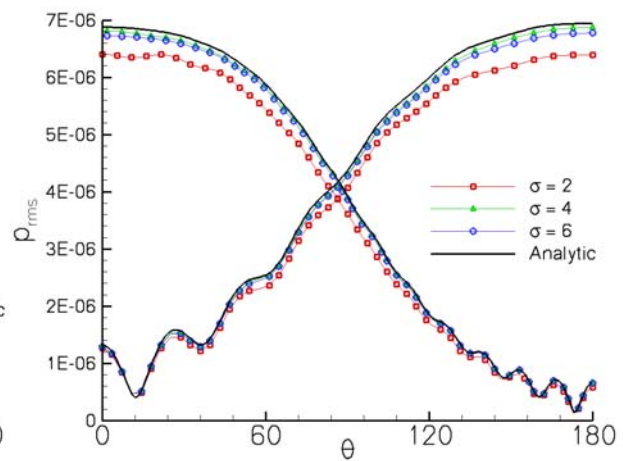
Figure 9. RMS fluctuating pressure profiles on cylinder surfaces for various interpolation orders of accuracy; two-cylinder configuration.
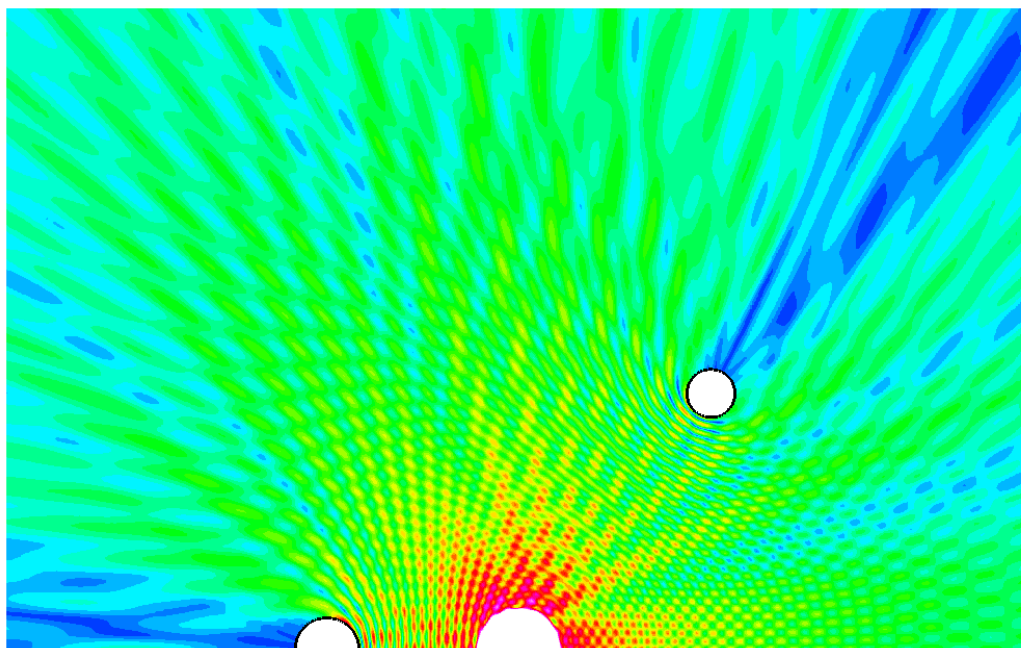
Figure 10. Mean-squared fluctuating pressure contours for three-cylinder configuration on resolved portion of domain.
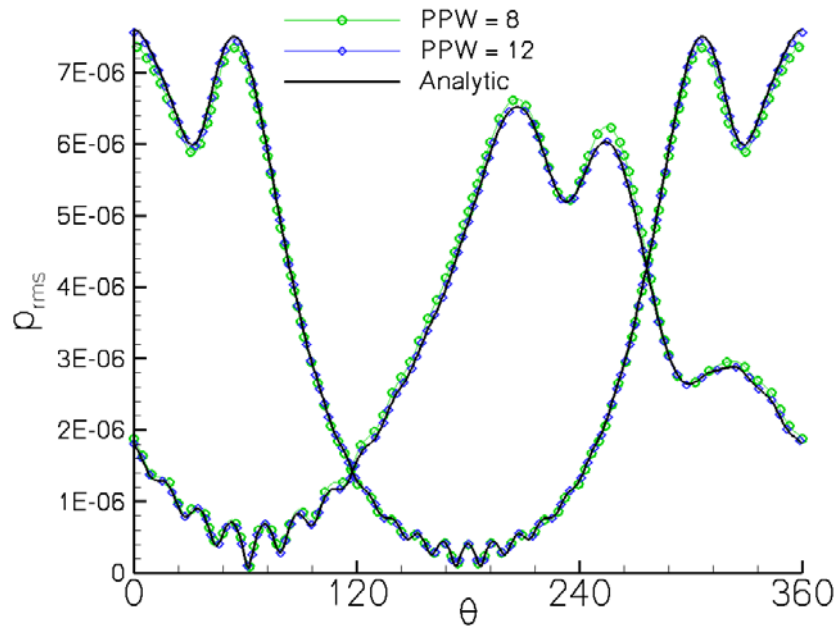
Figure 11. Variation of RMS fluctuating pressure with grid resolution on surface of cylinders; three-cylinder configuration.
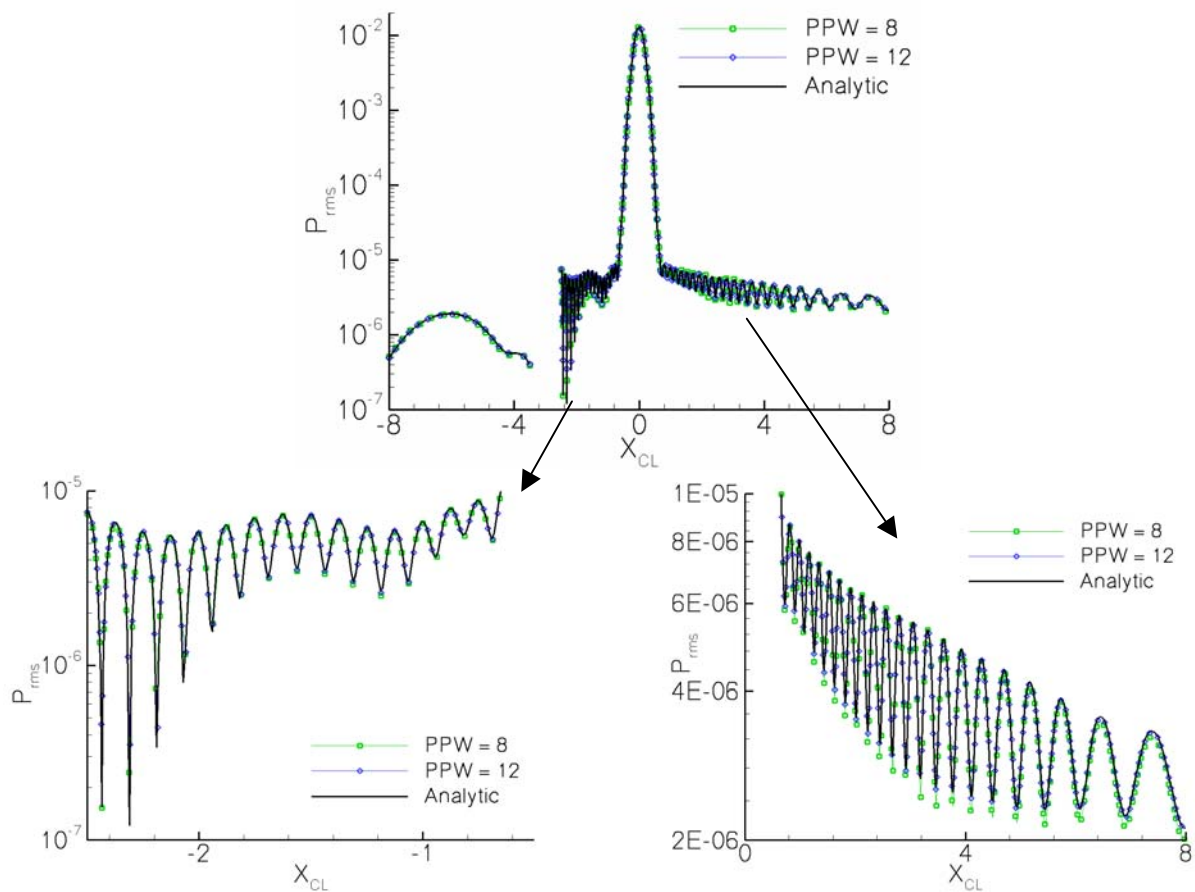
Figure 12. Variation of RMS fluctuating pressure with grid resolution on domain centerline; three-cylinder configuration.
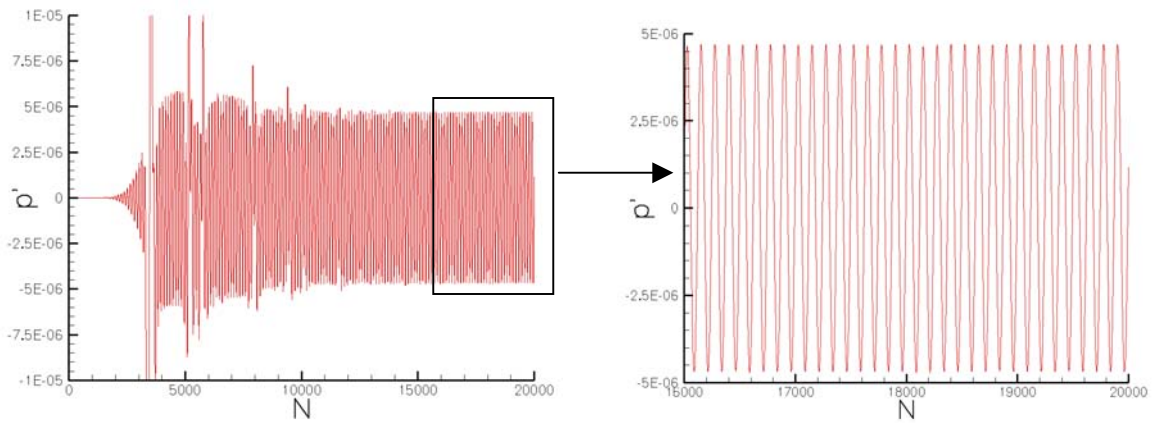
Figure 13. Typical point fluctuating pressure time history for three-cylinder configuration showing ramping up of source, initial transients, and evolution to time-periodic state.
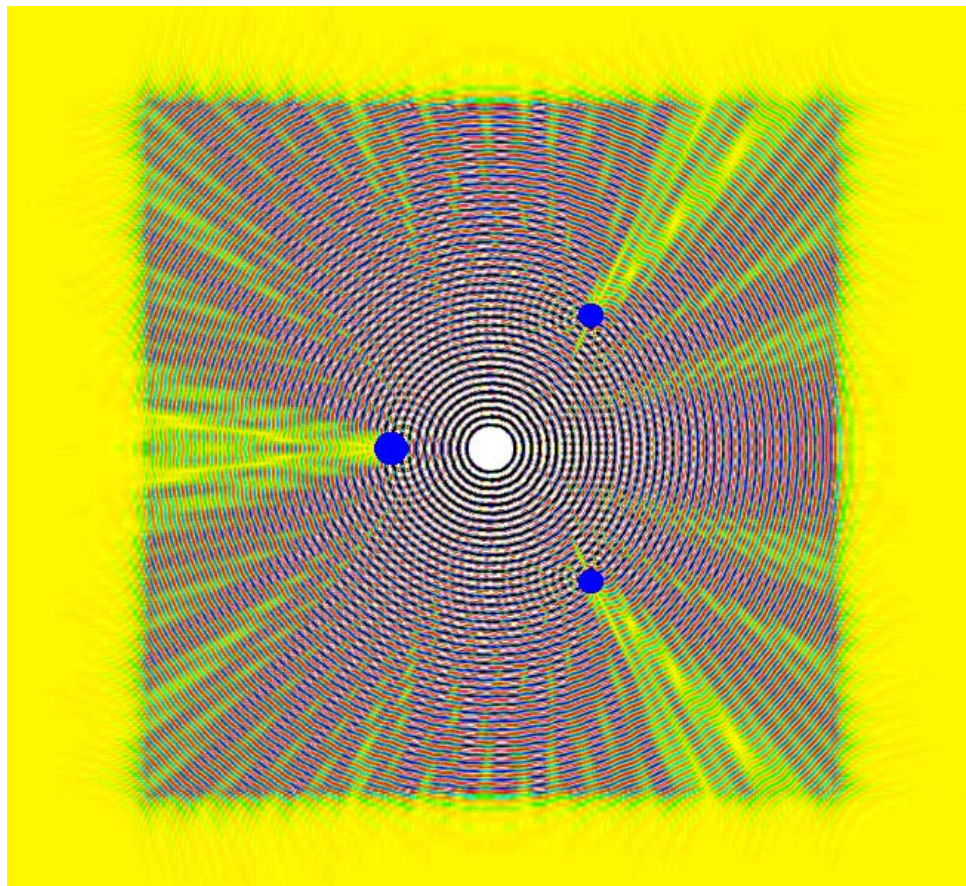
Figure 14. Instantaneous total fluctuating pressure field for three-cylinder configuration once solution has reached time-periodic state.

CHARACTERISTIC INTERFACE CONDITIONS FOR MULTIBLOCK HIGH-ORDER CAA IN COMPLEX GEOMETRY

Jae Wook Kim* and Duck Joo Lee†

Department of Aerospace Engineering, Korea Advanced Institute of Science and Technology

373-1 Guseong, Yuseong, Daejeon 305-701, Republic of Korea

*Research Professor; jwk@kaist.ac.kr

†Professor; djlee@kaist.ac.kr

ABSTRACT

A structured grid with an embedded body usually has a certain point where an abrupt change in the slope of grid line exists. The grid metrics are discontinuous at such a point because of the discrepancy between the left- and the right-hand limits of the gradients. This leads to grid singularity. It may cause serious numerical oscillations especially when high-order finite difference schemes are applied to solving conservation-form governing equations in generalized coordinates. In this paper, this problem is handled by decomposing the computational domain into blocks along the singular lines and imposing interface conditions at the block interfaces for communication between the blocks. A set of high-order finite difference schemes is used in each block: central differences on the interior nodes and one-sided differences on the near-interface nodes. The differencing stencils do not cross the block interfaces and each block is isolated without the singularity, which results in no oscillations. For communication between the isolated blocks, the interface conditions are derived from the characteristic relations of the compressible Euler or Navier-Stokes equations. The proposed interface conditions are applied to solutions of the computational aeroacoustics (CAA) benchmark problem in complex geometry.

1. INTRODUCTION

Structured grids have been widely used for computational fluid dynamics (CFD) performed by a variety of finite difference schemes (FDSs). The quality of grid generation has a great effect on the accuracy of numerical solutions. Many algorithms for the generation of structured grids have been published that are reviewed and summarized by Fletcher (Ref. 1), Hoffmann et al. (Ref. 2) and Anderson et al. (Ref. 3). Such algorithms are designed to provide sufficiently fine grid systems for a general computational domain surrounded by arbitrary boundaries with complex bodies. However, most grids have a singularity problem even when the body configuration is relatively simple. The grid singularity exists where an abrupt change in the slope of a grid line appears. The grid metrics are discontinuous at the singular point because of the discrepancy between the left- and the right-hand limits of the gradients. This means that the grid metrics are not unique at the point. The discontinuity of the grid metrics is an issue to be discussed both mathematically and numerically. Some attempts to use a whole Cartesian grid for avoiding this kind of problem are proposed recently by Kurbatskii and Tam (Ref. 4), and Dyson and Goodrich (Ref. 5). These new approaches wait to be further tested and validated through more applications.

In conventional CFD, for simplifying the calculation, the grid metrics at the singular points are often approximated to single values by an averaging the left- and the right-hand limits. This certainly incurs numerical errors in geometric point of view. In addition, the grid singularity increases the complexity, especially when it comes to discretization, i.e. numerical differentiation. It acts like a standing shock in the transformed flux variables and spurious oscillations can be generated as the numerical differentiation is carried out near the singular points. Well-established CFD solvers have produced accurate solutions with stable low-order FDSs and artificial dissipation that can suppress the errors. Meanwhile, high-order FDSs devoted to high resolution in unsteady aerodynamics and aeroacoustics can easily yield spurious results because of their high sensitivity to the grid quality. It becomes more serious when the

high-order FDS is based on the central differences rather than the upwind differences. To this time, the applications of the high-order central FDSs are limited to quite simple structured grids without singular points (Refs. 4 and 5).

In the present work, the grid singularity is avoided by a multi-block computing technique with suitable interface conditions for CAA. The computational domain is decomposed into blocks along the singular grid lines, where the left and the right blocks have the left- and right-hand limits of the grid metrics, respectively. High-order FDSs are used in each block, which employs central differences on the interior nodes and one-sided differences on the near-interface nodes. The differencing stencils do not cross the block interfaces. As a consequence, each block is isolated from the grid singularity and no spurious oscillations are generated in the numerical differentiation. The next step is imposing interface conditions at the block interfaces for correct physical communication between the isolated blocks. The interface conditions are derived from the characteristic relations of the compressible Euler or Navier-Stokes equations. The characteristic waves calculated in one block are interchanged or replaced by those in the next block at the interface according to their directions.

2. GOVERNING EQUATIONS

The governing equations are the unsteady compressible Euler or Navier-Stokes equations. The flux vector form of the equations, transformed to the computational domain, may be expressed in generalized coordinates as,

$$\partial \hat{\mathbf{Q}}/\partial t + \partial \hat{\mathbf{E}}/\partial \xi + \partial \hat{\mathbf{F}}/\partial \eta + \partial \hat{\mathbf{G}}/\partial \zeta = \hat{\mathbf{S}}_V \tag{1}$$

where '^' represents the transformed properties. The vectors of the conservative variables and the Euler fluxes in the generalized coordinates can be represented as

$$\hat{\mathbf{Q}} = \mathbf{Q}/J , \ \hat{\mathbf{E}} = (\xi_x \mathbf{E} + \xi_y \mathbf{F} + \xi_z \mathbf{G})/J , \ \hat{\mathbf{F}} = (\eta_x \mathbf{E} + \eta_y \mathbf{F} + \eta_z \mathbf{G})/J , \ \hat{\mathbf{G}} = (\zeta_x \mathbf{E} + \zeta_y \mathbf{F} + \zeta_z \mathbf{G})/J \tag{2}$$

and $\hat{\mathbf{S}}_V$ is a source term that consists of the viscous flux derivatives for the Navier-Stokes equations, but is zero for the Euler equations. All the components of $\hat{\mathbf{S}}_V$ are fully described in the textbooks (Refs. 1 to 3). The vectors of the conservative variables and the Euler fluxes in Cartesian coordinates are given by

$$\mathbf{Q} = (\rho , \ \rho u , \ \rho v , \ \rho w , \ \rho e_t)^T , \ \ \mathbf{E} = (\rho u , \ \rho u^2 + p , \ \rho vu , \ \rho wu , \ (\rho e_t + p)u)^T$$

$$\mathbf{F} = (\rho v , \ \rho uv , \ \rho v^2 + p , \ \rho wv , \ (\rho e_t + p)v)^T , \ \ \mathbf{G} = (\rho w , \ \rho uw , \ \rho vw , \ \rho w^2 + p , \ (\rho e_t + p)w)^T$$

where the total energy per unit mass is defined as $e_t = p/[(\gamma - 1)\rho] + (u^2 + v^2 + w^2)/2$ and $\gamma = c_p/c_v$ is the ratio of specific heats. For air, $\gamma = 1.4$, and this value is used in the present computation.

3. NUMERICAL ALGORITHMS

The main scheme is a pentadiagonal type of central compact FDS (Ref. 6). It is a generalization of the seven-point stencil Padé scheme, and is used on the interior nodes. It can be expressed as

$$\beta f'_{i-2} + \alpha f'_{i-1} + f'_i + \alpha f'_{i+1} + \beta f'_{i+2} = \sum_{m=1}^{3} a_m (f_{i+m} - f_{i-m})/h \tag{3}$$

where f_i is an objective function for the flux variables and f'_i is its space derivative at the *i*-th node. The grid spacing h is a constant independent of the index *i* in the computational domain where all the grid points are equally spaced. Equation (3) can be solved by inverting a pentadiagonal matrix. The matrix must be completed at the boundaries. Therefore, non-central or one-sided formulations other than Eq. (3) are needed on the boundary and the near-boundary nodes (Ref. 7). These may be represented as

$$f'_0 + \alpha_{0,1} f'_1 + \beta_{0,2} f'_2 = \sum_{m=0,m\neq 0}^{3} a_{0,m} (f_m - f_0)/h \ \text{ for } \ i = 0 \ \text{ (boundary node)}, \tag{4}$$

$$\alpha_{1,0} f'_0 + f'_1 + \alpha_{1,2} f'_2 + \beta_{1,3} f'_3 = \sum_{m=0,m\neq 1}^{4} a_{1,m} (f_m - f_1)/h \ \text{ for } \ i = 1 , \tag{5}$$

$$\beta_{2,0} f_0' + \alpha_{2,1} f_1' + f_2' + \alpha_{2,3} f_3' + \beta_{2,4} f_4' = \sum_{m=0, m \neq 2}^{5} a_{2,m}(f_m - f_2)/h \quad \text{for} \quad i = 2 \,. \tag{6}$$

The coefficients in Eqs. (3)-(6) were optimized, as described in Refs. 6 and 7, to achieve maximum resolution characteristics with fourth-order accuracy (second-order in Eq. (4) for numerical stability). A fourth-order four-stage Runge-Kutta scheme is used for marching the solutions in time.

High-order FDSs in space and time resolve a wider range of wavenumber or frequency than low-order schemes. However, even the present schemes do not resolve the highest wavenumber or frequency range effectively. An adaptive nonlinear artificial dissipation model (Ref. 8) is used to remove the unwanted numerical oscillations that may develop from the unresolved range. The artificial dissipation model is implemented only at the last (fourth) stage of the Runge-Kutta scheme in order to minimize computational costs. The boundary conditions for a time-dependent problem should be physically correct and numerically well posed. Generalized characteristic boundary conditions (Ref. 9) are used as the time-dependent boundary conditions in the present computation. Non-reflecting inflow/outflow and the inviscid/viscous wall conditions are imposed at the boundaries of the computational domain and the body surfaces respectively.

4. DECOMPOSITION OF COMPUTATIONAL DOMAIN

Usually, as mentioned in Section 2, most computational domains with bodies have particular points where grid lines are abruptly bent owing to the body configurations or the grid types. Figure 1 illustrates a simple example of a structured grid with a wedge-type body. The circles in Fig. 1 represent the particular points at which sudden slope changes of the grid lines occur. Obviously, the left- and the right-hand limits of the grid metrics disagree with each other at these points. The discontinuity of the grid metrics leads to a singularity problem.
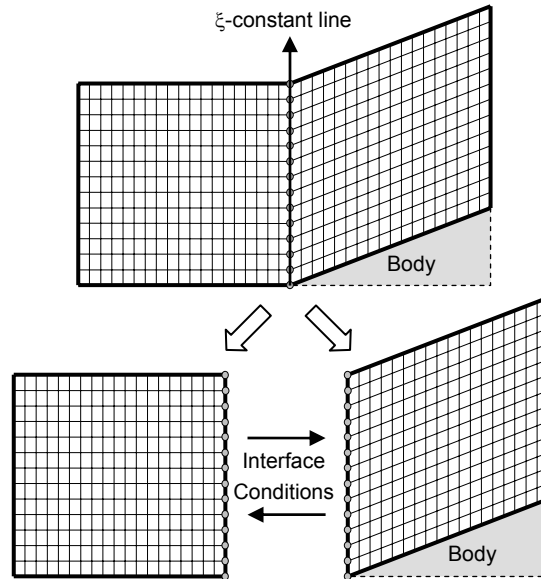
Figure 1. Illustration of decomposing a computational domain into virtual blocks

As a treatment for avoiding the grid singularity, the present paper suggests decomposing the domain into two blocks along the singular line as illustrated in Fig. 1. The singular points form a line interface in two dimensions and a surface interface in three dimensions. After the decomposition, each singular point is divided into two virtual points with different values of the grid metrics although they are essentially at the same location. The left- and the right-hand limits of the grid metrics are allocated at the singular points of the left and right blocks, respectively. All the flux derivatives in Eq. (1) are then evaluated independently in each block by using Eqs. (3)-(6). The differencing stencils do not cross the block interface. Therefore, the high-order FDSs avoid the discontinuity that would be an ori-

gin of spurious oscillations. In this way, the singularity problem vanishes in the numerical differentiation. However, this kind of decomposition leaves the blocks isolated without communication. The next step is imposing appropriate interface conditions for the exact communication between the blocks. This is presented in Section 5.

Before moving on to the next section, it should be remarked that the grid singularity is expressed mathematically as $\nabla \xi^L \neq \nabla \xi^R$ ($\xi_x^L \neq \xi_x^R$ or $\xi_y^L \neq \xi_y^R$ or $\xi_z^L \neq \xi_z^R$) at the interface if the interface is represented by a ξ-constant line or surface. The superscripts 'L' and 'R' mean the left- and the right-hand limits, respectively. However, one should realize that the gradient vectors if normalized by their own magnitudes are exactly the same because their directions are equal. The gradient vector $\nabla \xi$ analytically means a vector perpendicular to the ξ-constant line or surface, i.e. the interface. Therefore, the normalized gradient vectors (unit vectors) on the left and the right side of the interface coincide with each other, which is expressed as $\nabla \xi^L / |\nabla \xi^L| = \nabla \xi^R / |\nabla \xi^R|$. If the normalized gradient vector (unit vector) is defined as

$$\nabla \widetilde{\xi} \equiv \nabla \xi / |\nabla \xi| \tag{7}$$

then, from the above equation, following equation is satisfied at the interface:

$$(\widetilde{\xi}_x^L \, , \, \widetilde{\xi}_y^L \, , \, \widetilde{\xi}_z^L) = (\widetilde{\xi}_x^R \, , \, \widetilde{\xi}_y^R \, , \, \widetilde{\xi}_z^R) \, . \tag{8}$$

Equation (7) plays an important role for deriving the interface conditions as described in the next section.

5. CHARACTERISTIC INTERFACE CONDITIONS

This section presents the block interface conditions for correct physical communication between the blocks that are as yet isolated. They are derived from the characteristic relations that are obtained by transforming the governing equations into quasi-linear wave equations. An advantage of using the characteristic relations is that the flow properties can be classified into the physical wave modes. Characteristic relations have been used extensively for the boundary conditions in many publications during the past two decades (Ref. 9). In the present work, they are used for the interface conditions. The derivation of the interface conditions includes no assumption or simplification, which means the interface conditions are mathematically exact. The detailed procedure is explained in the following subsections.

5-1. Transformation to Characteristic Form

The starting point of the analysis in the derivation of the interface conditions is Eq. (1). Equation (1) can be transformed into a characteristic form in the direction normal to the interface where ξ keeps a constant value. The transformed characteristic equation is a quasi-linear wave equation with a source term. The resulting equation can be expressed as

$$\partial \mathbf{R} / \partial t + \underline{\boldsymbol{\lambda}} \, \partial \mathbf{R} / \partial \xi = \mathbf{S}_C \tag{9}$$

where the underline indicates a matrix. Equation (9) is derived using the following two identities in relation with Eq. (2):

$$\delta \mathbf{R} = \underline{\mathbf{P}}^{-1} \delta \mathbf{Q} \quad \text{and} \quad \underline{\boldsymbol{\lambda}} \, \partial \mathbf{R} / \partial \xi = \underline{\mathbf{P}}^{-1} (\xi_x \, \partial \mathbf{E} / \partial \xi + \xi_y \, \partial \mathbf{F} / \partial \xi + \xi_z \, \partial \mathbf{G} / \partial \xi) \, .$$

The source term in Eq. (9) is derived from Eq. (1), as given by

$$\mathbf{S}_C = J \underline{\mathbf{P}}^{-1} \{ \hat{\mathbf{S}}_V - [\mathbf{E} \, \partial (\xi_x / J) / \partial \xi + \mathbf{F} \, \partial (\xi_y / J) / \partial \xi + \mathbf{G} \, \partial (\xi_z / J) / \partial \xi + \partial \hat{\mathbf{F}} / \partial \eta + \partial \hat{\mathbf{G}} / \partial \zeta] \} \, .$$

The characteristic differential variables and the corresponding convection speeds are represented as

$$\delta \mathbf{R} = (\delta \rho - \delta p / c^2 \, , \, \delta \widetilde{W} \, , \, \delta \widetilde{V} \, , \, \delta p / (\rho c) + \delta \widetilde{U} \, , \, \delta p / (\rho c) - \delta \widetilde{U})^T \, , \tag{10}$$

$$\underline{\boldsymbol{\lambda}} \, (\text{diagonal}) = (U \, , \, U \, , \, U \, , \, U + c \sqrt{\xi_x^2 + \xi_y^2 + \xi_z^2} \, , \, U - c \sqrt{\xi_x^2 + \xi_y^2 + \xi_z^2})^T$$

where the tilde indicates a quantity normalized by $|\nabla \xi|$ as represented in Eq. (7), and c is the speed of sound. The

contravariant (normal) velocity and its differential are given by

$$U = \xi_x u + \xi_y v + \xi_z w , \ \delta\widetilde{U} = \widetilde{\xi}_x \delta u + \widetilde{\xi}_y \delta v + \widetilde{\xi}_z \delta w$$

while the velocity differentials in the parallel direction are expressed as

$$\delta\widetilde{V} = -\widetilde{\xi}_x \delta v + \widetilde{\xi}_y \delta u , \ \delta\widetilde{W} = \widetilde{\xi}_x \delta w - \widetilde{\xi}_z \delta u .$$

The matrix $\underline{\mathbf{P}}^{-1}$ that transforms the conservative variables into the characteristic variables and its inverse matrix $\underline{\mathbf{P}}$ can diagonalize the flux-Jacobian matrices in the direction normal to the interface and the resulting diagonal terms become the convection speeds of the characteristics. The diagonalizing procedure is described precisely in Refs. 10 and 11. The transformation matrices and its constituting variables are represented in the references.

Equation (9) represents the physical (entropy, vorticity and acoustic) waves with different convection speeds in the direction normal to the interface. An advantage of using the characteristic equation is that the incoming and the outgoing waves can be classified easily by the signs of their convection speeds. An incoming wave calculated within an isolated block is inaccurate because the information outside the block is not used for calculating the convection term in Eq. (9). Therefore, the incoming waves of one block should be compensated by the outgoing waves of the other adjacent block through the strict interface conditions. These conditions are presented in the following subsection.

5-2. Characteristic Interface Conditions

A crucial interface condition is matching the primitive variables on the left and the right side of the interface, i.e. $(\rho^L, \mathbf{v}^L, p^L) = (\rho^R, \mathbf{v}^R, p^R)$. This condition should be satisfied regardless of time. Therefore, their time derivatives should be matched at the interface, which means $\partial_t(\rho^L, \mathbf{v}^L, p^L) = \partial_t(\rho^R, \mathbf{v}^R, p^R)$. As a result, from Eqs. (8) and (10), it can be concluded that the time derivatives of the characteristic variables should be also matched:

$$\partial\mathbf{R}^L / \partial t = \partial\mathbf{R}^R / \partial t . \tag{11}$$

In the mean time, if one defines another expression for the convection term in Eq. (9) as $\mathbf{L} = \underline{\boldsymbol{\lambda}} \, \partial\mathbf{R}/\partial\xi$, then, Eq. (11) is represented by the convection and the source term through Eq. (9) as

$$\mathbf{L}^L - \mathbf{S}_C^L = \mathbf{L}^R - \mathbf{S}_C^R . \tag{12}$$

Equation (12) describes the interface condition in terms of the space derivatives rather than the time derivatives in Eq. (11), and it is further used for communicating physical information through the interface.

A conventional technique dealing with the characteristic equation is compensating the convection term. Either the left- or the right-hand convection term should be corrected by the other one according to Eq. (12). As mentioned above, the decision of which should be chosen is based upon the sign of the convection speed, and the incoming convection term is to be corrected while the outgoing term is maintained. The positive sign represents the outgoing wave from the left block and the incoming wave to the right block. On the contrary, the negative sign represents the incoming wave to the left block and the outgoing wave from the right block. This kind of analysis is for realistic communication between the blocks. In this course, the interface conditions can be summarized as follows:

$$\begin{cases} L_m^L = L_m^R - S_{Cm}^R + S_{Cm}^L & \text{if} \ \ \lambda_m^L / \left|\lambda_m^L\right| = \lambda_m^R / \left|\lambda_m^R\right| \le 0 \\ L_m^R = L_m^L - S_{Cm}^L + S_{Cm}^R & \text{if} \ \ \lambda_m^L / \left|\lambda_m^L\right| = \lambda_m^R / \left|\lambda_m^R\right| \ge 0 \end{cases} \tag{13}$$

where the subscript 'm' represents the components of a vector ($m = 1, \cdots, 5$). Equation (13) is the final form of the characteristic interface conditions. The last process to be presented is the equations of identity relating the characteristic convection term and the flux derivative term.

5-3. Implementation Procedure

For practical application to actual computations, the detailed procedure for implementing the characteristic interface conditions is summarized by the following steps:

1) All the flux derivatives in Eq. (1) are evaluated by the high-order FDSs given by Eqs. (3)-(6) in each isolated block including the interface points. The normal-flux derivative $\partial \hat{\mathbf{E}}/\partial \xi$ on the interface is used as an initial guess to be corrected next.

2) The initial guess of the characteristic convection term on the interface is then evaluated by the following identity: $\mathbf{L} = J \underline{\mathbf{P}}^{-1} \{ \partial \hat{\mathbf{E}}/\partial \xi - [\mathbf{E} \partial(\xi_x/J)/\partial \xi + \mathbf{F} \partial(\xi_y/J)/\partial \xi + \mathbf{G} \partial(\xi_z/J)/\partial \xi] \}$.

3) The characteristic convection term on each side of the interface is then corrected by imposing the interface conditions given by Eq. (13). The new corrected characteristic convection term is then represented by $\mathbf{L}^*$.

4) The normal-flux derivative term is then recalculated by the corrected characteristic convection term using the following identity: $(\partial \hat{\mathbf{E}}/\partial \xi)^* = \underline{\mathbf{P}} \mathbf{L}^* / J + [\mathbf{E} \partial(\xi_x/J)/\partial \xi + \mathbf{F} \partial(\xi_y/J)/\partial \xi + \mathbf{G} \partial(\xi_z/J)/\partial \xi]$. The new corrected normal-flux derivative term with the asterisk is then returned to Eq. (1) for integrating the solutions in time.

5) Finally, after the time integration of solutions, the primitive variables on the interface need to be refined by averaging the left- and the right-hand values: $(\rho^L, \mathbf{v}^L, p^L)^* = (\rho^R, \mathbf{v}^R, p^R)^* = (\rho^L + \rho^R, \mathbf{v}^L + \mathbf{v}^R, p^L + p^R)/2$, where the asterisk denotes the refined values. This last adjustment is necessary because a certain level of round-off errors exists in the numerical integration, which, otherwise, has no meaning in the mathematical sense.

This procedure is iterated in every stage of the time marching steps. In this course, the exact matching condition on the interface and the physical communication between the blocks can be accomplished and accurate numerical solutions can be guaranteed. Numerical implementation is simple and straightforward in that it just needs some additional operations only on the interface points using ready-made matrices.

6. APPLICATION TO BENCHMARK PROBLEM

In this section, the proposed interface conditions are applied to the benchmark problem of Case 1 in Category 2. The full nonlinear equation (1) in two dimensions with acoustic source term is solved, instead of the linearized equation provided by the committee. The acoustic source term added in the right-hand side of Eq. (1) is expressed as

$$\hat{\mathbf{S}}_A = (\dot{m}, \dot{m}u, \dot{m}v, \dot{m}e_t)/J \quad \text{where} \quad \dot{m} = (\varepsilon \rho_\infty c_\infty / D_{\max}) \exp\left[-(\ln 2)(x_s^2 + y_s^2)/b^2\right] \sin(\omega t).$$

The entire computational domain is decomposed into 10 blocks due to the multi-body configuration as shown in Fig. 2. The structured grid system in H topology set up for this problem is represented in Fig. 3. The total number of grid meshes used is 176,640. The typical mesh spacing is given by 10 points per wave in average. The far-field locations are at $x/D = \pm 11$ and $y/D = \pm 5$, respectively, and an absorbing layer with thickness of $2D$ is surrounding the computational domain. The time step size is determined by CFL condition with maximum Courant number of 1.0, which gives 57 time steps to calculate one period of the source. The total number of time steps used to achieve a fully time-asymptotic solution is 20,000 in this particular problem.
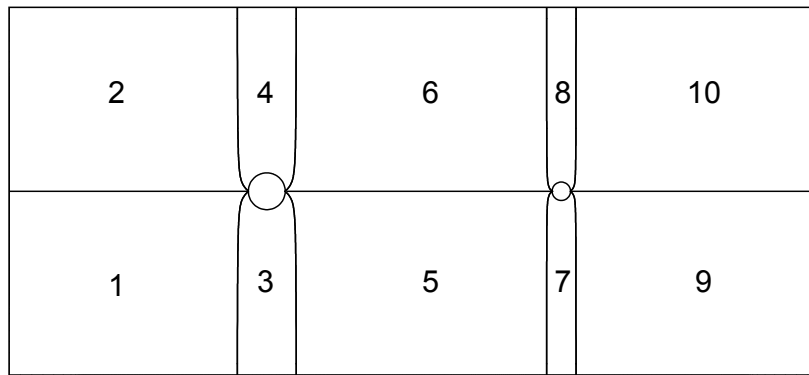
Figure 2. Computational domain decomposed into 10 blocks around two circular cylinders
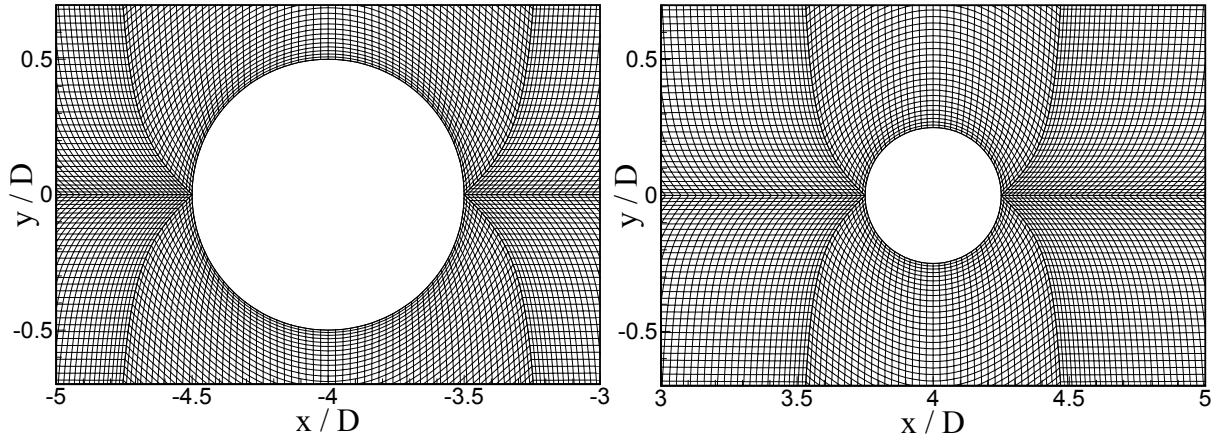
Figure 3. H-topology grid system in zoomed view of: a) left cylinder and b) right cylinder

Actually, imposing symmetric boundary conditions on the centerline, it is not necessary to use the lower blocks 1, 3, 5, 7 and 9. However, the present work is intended to test the proposed interface conditions also in the η-direction between the lower and the upper blocks as well as in the ξ-direction. In Fig. 2, it seems that the treatment of the leading and trailing edges is somehow complicated because four blocks meet at those locations. In this case, there are four virtual points to be evaluated simultaneously at the leading and trailing edges. At the leading edge of the left cylinder, for instance, the interface conditions are implemented for the $\partial \hat{\mathbf{E}}/\partial \xi$ terms between blocks 1 and 3 as well as blocks 2 and 4. The interface conditions are also implemented for the $\partial \hat{\mathbf{F}}/\partial \eta$ terms between blocks 1 and 2. Meanwhile, the $\partial \hat{\mathbf{F}}/\partial \eta$ terms of blocks 3 and 4 are calculated by the wall boundary conditions for simulating the leading edge. The same procedure applies at the trailing edge and at the right cylinder.

An instantaneous pressure contour plot in the time-asymptotic stage is shown in Fig. 4. The interference between the propagating and reflecting waves is shown in the inner region. The scattered acoustic fields are clearly visualized without spurious oscillations near the block interfaces. The root-mean-squared (RMS) pressure plots along the centerline and the cylinder surfaces are given in Fig. 5. It is shown that the present solution agrees well with the analytic solution except some over estimation at the "bright" side of the cylinder surfaces in the direction to the source. The overshoots are supposed to come from the one-sided differences near the block interfaces. They can be alleviated by increase of artificial dissipation level in that region, which is not applied in this paper for testing the proposed interface conditions only.
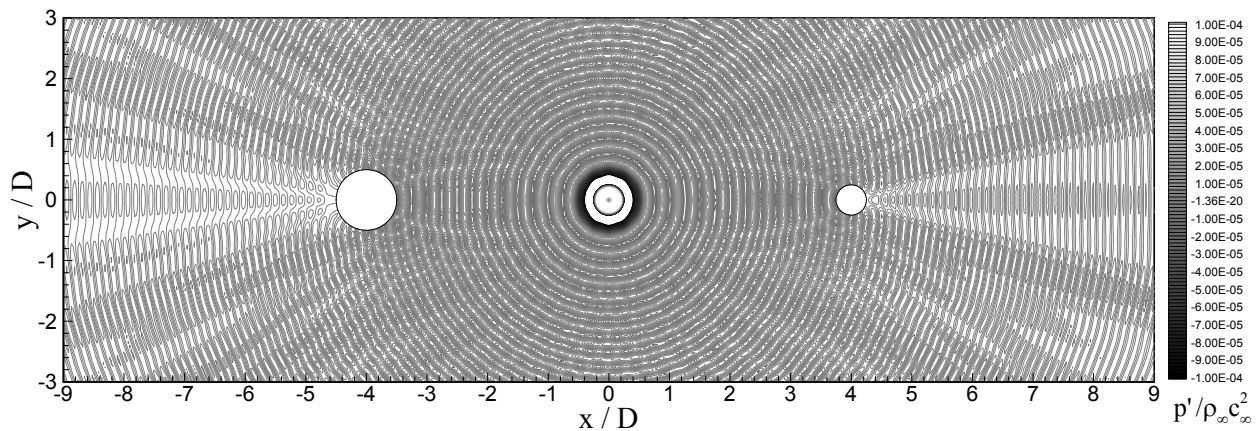
Figure 4. Instantaneous pressure contour plot in time-asymptotic stage
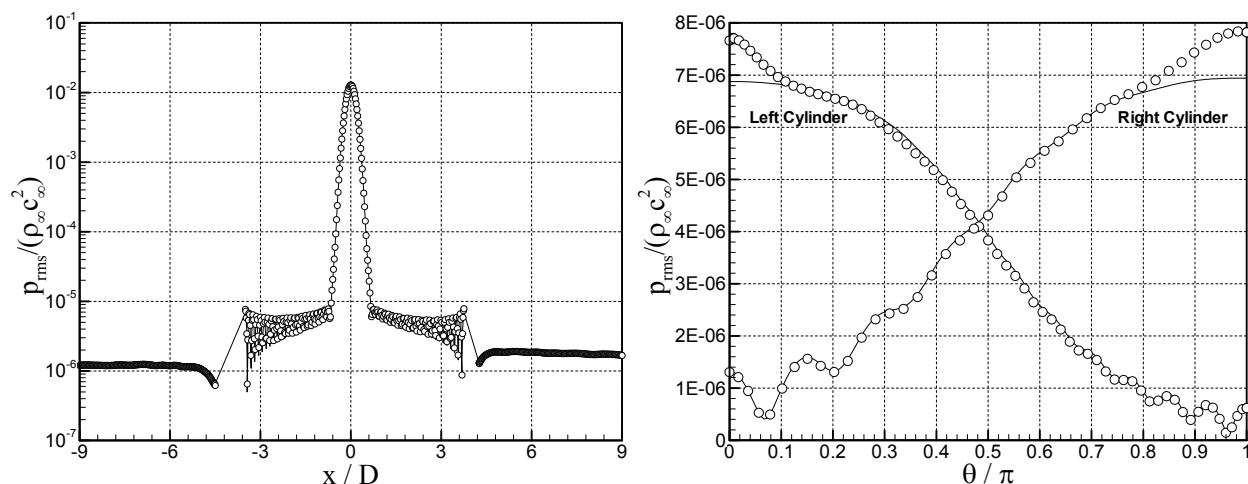
Figure 5. RMS pressure plots along the centerline (left) and the cylinder walls (right): ○, numerical; and —, analytic solution

7. CONCLUDING REMARKS

An accurate solution of the CAA benchmark problem in complex geometry is successfully accomplished on singular structured grids. Decomposing a computational domain into two virtual blocks along singular grid points and employing non-central or one-sided FDSs not crossing the block interfaces results in no spurious numerical oscillation that would have been generated by central FDSs across the singularity. The proposed interface conditions enable the correct physical communication between the blocks that are disconnected by the virtual decomposition. The mathematical exactness and the numerical accuracy of the proposed interface conditions have been validated. Further tests are desirable for verifying the generality of the present methodology in future studies.

REFERENCES

1. Fletcher C. A. J., *Computational Techniques for Fluid Dynamics*, 2nd ed., Vol. 2, Springer-Verlag, New York, 1991, pp. 47-127.

2. Hoffmann K. A. and Chiang S. T., *Computational Fluid Dynamics for Engineers*, 1st ed., Vol. 1, Engineering Education System, Wichita, 1993, pp. 344-411.

3. Anderson D. A., Tannehill J. C. and Pletcher R. H., *Computational Fluid Mechanics and Heat Transfer*, 2nd ed., Taylor & Francis, Washington DC, 1997, pp. 679-714.

4. Kurbatskii K. A. and Tam C. K. W., "Cartesian Boundary Treatment of Curved Walls for High-Order Computational Aeroacoustics Schemes," *AIAA Journal*, Vol. 35, No. 1, 1997, pp. 133-140.

5. Dyson R. W. and Goodrich J. W., "Automated Approach to Very High-Order Aeroacoustic Computations," *AIAA Journal*, Vol. 39, No. 3, 2001, pp. 396-406.

6. Kim J. W. and Lee D. J., "Optimized Compact Finite Difference Schemes with Maximum Resolution," *AIAA Journal*, Vol. 34, No. 5, 1996, pp. 887-893.

7. Kim J. W. and Lee D. J., "Implementation of Boundary Conditions for Optimized High-Order Compact Schemes," *Journal of Computational Acoustics,* Vol. 5, No. 2, 1997, pp. 177-191.

8. Kim J. W. and Lee D. J., "Adaptive Nonlinear Artificial Dissipation Model for Computational Aeroacoustics," *AIAA Journal*, Vol. 39, No. 5, 2001, pp. 810-818.

9. Kim J. W. and Lee D. J., "Generalized Characteristic Boundary Conditions for Computational Aeroacoustics," *AIAA Journal*, Vol. 38, No. 11, 2000, pp. 2040-2049.

10. Warming R. F., Beam R. M. and Hyett B. J., "Diagonalization and Simultaneous Symmetrization of Gas-Dynamic Matrices," *Mathematics of Computation*, Vol. 29, No. 132, 1975, pp. 1037-1045.

11. Hirsch C., *Numerical Computation of Internal and External Flows*, 1st ed., Vol. 2, John Wiley & Sons, New York, 1992, pp. 132-223.

CATEGORY 2: COMPLEX GEOMETRY

E. Manoha, S. Redonnet, R. Guenanff, and M. Terracol
CFD and Aeroacoustics Department
ONERA, BP 72, 92322 Châtillon Cedex, France

ABSTRACT

This paper addresses the Category 2 - Complex Geometry problem, contributed by Pr. Miguel Visbal (visbal@vaa.wpabf.af.mil) at the 4th CAA Workshop held at the Ohio Aerospace Institute in Cleveland (OH), on October 20–22, 2003. The problem is the simulation of the scattering, from multiple rigid circular cylinders, of sound generated by a spatially distributed, axisymmetric, acoustic source, by solving the two-dimensional linearized Euler equations. In the proposed solution, the full conservative Euler equations are solved on multi-domain conformal grids associating body-fitted grids near solid walls and quasi-cartesian grids elsewhere. The solutions are favorably compared to the analytical data provided by the contributor of the problem.

INTRODUCTION

The numerical simulation of acoustic propagation on complex non-uniform mean flows requires the solution of discretized (linearized or not) Euler equations using high-order non-dispersive spatial schemes. One straightforward strategy to reach this goal is to use high order finite difference schemes on multi-domain structured grids. The main drawback of this process is that building such grids may become tricky when complex geometry are concerned. The given problem provides a stringent test of the ability of high-order CAA codes to handle complex geometries. It provides a demonstration of numerical robustness, long-time stability, and suitability of far-field radiation treatments in the presence of multiple scattering bodies.

PROBLEM

The acoustic scattering problem is governed by the two-dimensional linearized Euler equations in non-conservative form:

$$\begin{cases} \dfrac{\partial \rho}{\partial t} + \dfrac{\partial u}{\partial x} + \dfrac{\partial v}{\partial y} = 0 \\[2mm] \dfrac{\partial u}{\partial t} + \dfrac{\partial p}{\partial x} = 0 \\[2mm] \dfrac{\partial v}{\partial t} + \dfrac{\partial p}{\partial y} = 0 \\[2mm] \dfrac{\partial p}{\partial t} + \dfrac{\partial u}{\partial x} + \dfrac{\partial v}{\partial y} = S \end{cases} \tag{1}$$

in which the flow variables are fluctuating quantities and have been non-dimensionalized by the following scales:

Length scale	:	diameter of the largest cylinder $D_1 = 1.0$
Velocity scale	:	the ambient speed of sound c_∞
Density scale	:	ambient gas density ρ_∞

The time-dependent acoustic source term S on the right-hand side of the energy equation is assumed axisymmetric and is written in the source-centered coordinates system as:

$$S(r,t) = \exp\left[-\ln 2\left(r^2/b^2\right)\right]\sin(\omega t) \tag{2}$$

where r denotes the distance to the source, ω the normalized pulsation $\omega = 8\pi$ and b the source half-width $b = 0.2$.

Figure 1 shows the geometries of Case 1 and Case 2. The problem requires to compute the time averaged pressure fluctuations along (i) the surface of both cylinders and (ii) the line passing through the center of Cylinder #1 and the source.
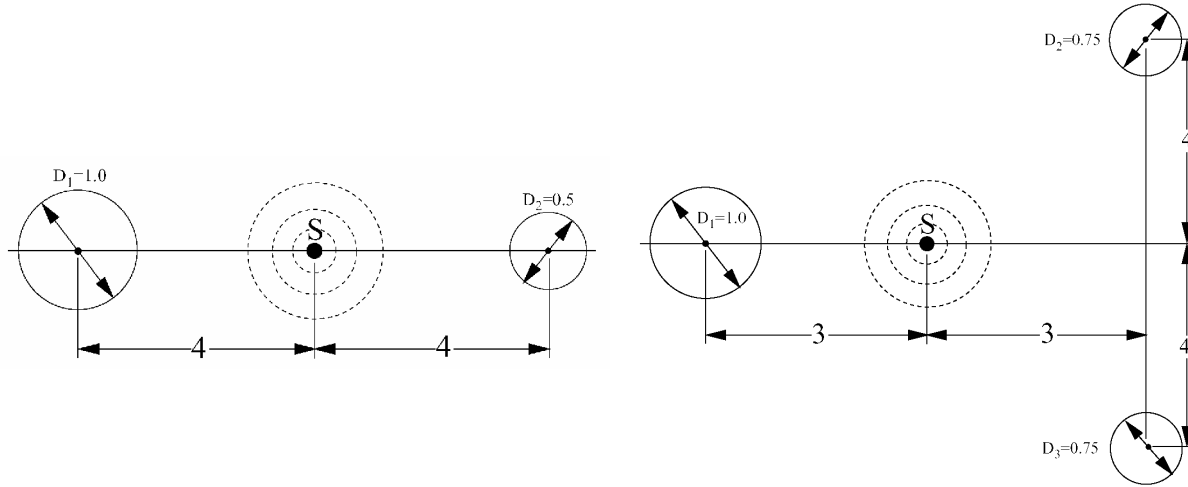
Figure 1 : Geometry for acoustic scattering problem. Case 1 (left side), Case 2 (right side).

NUMERICAL PROCEDURE

Both cases are solved by using ONERA's code *sAbrinA* (Solver for Aeroacoustics of BRoadband INteractions from Aerodynamics). This multi-block, structured, multi-purpose code solves Euler or Navier Stokes steady/unsteady equations using various numerical procedures. Cell-centered finite volume and finite difference methods are available. Specific spatial high order schemes and filters are implemented for acoustic simulations. The code can handle complete variables or splitted (mean flow / perturbation) variables (Refs. 1, 2).

For the present problem, the full (non-linearized) two-dimensional Euler equations are solved in their conservative form.

$$\frac{\partial \mathbf{u}}{\partial t} + \frac{\partial \mathbf{F_x}}{\partial x} + \frac{\partial \mathbf{F_y}}{\partial y} = \mathbf{S} \tag{3}$$

where $\mathbf{u}$, $\mathbf{F_x}$ and $\mathbf{F_y}$ denote the solution vector and the flux vectors of the perturbed problem. In the present case, where the flow is at rest, they are linked to the normalized, fluctuating non conservative variables (ρ, u, v, p) of (Eq. 1) by :

$$\mathbf{u} = \begin{pmatrix} \rho \\ (1+\rho)u \\ (1+\rho)v \\ \frac{1}{2}(1+\rho)(u^2+v^2)+\frac{p}{\gamma-1} \end{pmatrix} \quad \mathbf{F_x} = \begin{pmatrix} (1+\rho)u \\ (1+\rho)u^2+p \\ (1+\rho)uv \\ \left[\frac{1}{2}(1+\rho)(u^2+v^2)+\frac{\gamma p}{\gamma-1}\right]u \end{pmatrix} \quad \mathbf{F_y} = \begin{pmatrix} (1+\rho)v \\ (1+\rho)uv \\ (1+\rho)v^2+p \\ \left[\frac{1}{2}(1+\rho)(u^2+v^2)+\frac{\gamma p}{\gamma-1}\right]v \end{pmatrix} \tag{4}$$

The non conservative source term S in (Eq. 1) assumes that pressure is the only excited variable. For the present solution, assuming that the source is isentropic (*pressure source term = density source term* $\times c_\infty^2$), the conservative source vector $\mathbf{S}$ in (Eq. 3) should read :

$$\mathbf{S} = \left(S, 0, 0, \frac{S}{\gamma-1} \right) \tag{5}$$

However, it has been found that solving (Eq. 3) with this source term (Eq. 5) provided results which differed from the analytical solution by a factor $1/(\gamma-1)$, so the computations presented in this paper where actually done by using the source term $\mathbf{S}' = (\gamma-1)\mathbf{S}$. It should be noted that zeroing the density source term do not

significantly change the result (which means assuming $\mathbf{S} = (0, 0, 0, S)$, as it is done in (Ref. 3) in which analogue scattering problems are solved by using Euler equations in conservative form).

Equations (Eq. 4) are solved using spatial finite difference, 6th order scheme and filter and temporal RK3 scheme (Refs 4, 5). The normalized parameters of the problem are :

Right cylinder diameter	: $D_1 = 1.0$	Pulsation	: $\omega = 8\pi$
Left cylinder diameter	: $D_2 = 0.5$ for Case 1	Frequency	: $f = 4$
	: $D_2 = D_3 = 0.75$ for Case 2	Time period :	: $T = 0.25$
Sound velocity	: $c_\infty = 1.$	Acoustic wavelength :	: $\lambda = 0.25$ or $D/4$
Ambient density	: $\rho_\infty = 1.$		

The source compactness ratio b/λ is near unity ($b/\lambda = 0.8$), which means that the source is not compact and radiates acoustic waves with very small amplitudes, except a short initial transient in which a large wave front is emitted during the first cycles of the source. In order to allow this transient wave to leave the domain without generating spurious reflections, the source is ramped up over the first 16 periods using a square sine function $r(t)$:

$$r(t) = \begin{cases} \sin^2\left(\dfrac{\pi}{2}\dfrac{t}{16T}\right) & for\ t < 16T \\ 1.0 & for\ t \geq 16T \end{cases} \quad (6)$$

SOLUTIONS

The main features of the multi-domain structured grids built for Case 1 and Case 2 geometries are summarized in the following table. Cylinders are meshed using a body-fitted curvilinear grid, while other zones are cartesian-like grids. An exponential stretching covering 8 grid rows is applied on all external boundaries. The maximum resolution is about 12 points per acoustic wavelength. Figure 2 shows the structure of both grids and details of grids near the cylinders.

Case	Zones	Domain limits	Stretched zone	Cell number
1	10	$-9 < x < 9$ and $0 < y < 4$	$9 < abs(x) < 11$ and $4 < y < 6$	163,462
2	8	$-8 < x < 8$ and $0 < y < 6$	$8 < abs(x) < 10$ and $6 < y < 8$	250,045

It should be noted that the conformal mapping process (ghost points) at boundaries between adjacent zones assumes that grid lines connecting to the boundary are normal to it. Consequently, significant error can be generated whenever grid line direction is not continuous through a boundary, which is the case at several locations in the present grid.

A symmetry condition is imposed along the x axis. A perfect reflection condition (mirror) is applied on both cylinders surface. Non-reflecting characteristic boundary conditions are applied on all other boundaries, along with the exponential stretching described above. Computations are done with a time step set to $\Delta t = 0.01$ or $T/25$.

The initial wave front reaches the left and right boundaries of the domain after 1000 time steps or 40 source periods, but then multiple reflections occur on the cylinder surfaces and an additional 3000 iterations (120 source periods) are performed to ensure a stationary pressure field. Figures 3 shows the density contour pattern in the whole domain at this date ($t = 160T$) for both cases. The vanishing levels in the stretched zone demonstrate the efficacity of the non-reflecting boundary condition based on characteristics applied at the external border : at this time the initial transient has traveled over a normalized distance of 40 from the source location. Figure 4 shows details of this instantaneous density field for both cases.

Then the RMS pressure field is computed from data stored at each time step during one source period (25 time steps). This RMS pressure computation process has been repeated several times along the whole computation (at $t = 80T$, $t = 120T$ and $t = 160T$) without noticeable change. The following results are for $t = 160T$. Figure 5 shows the RMS pressure pattern in the whole domain.
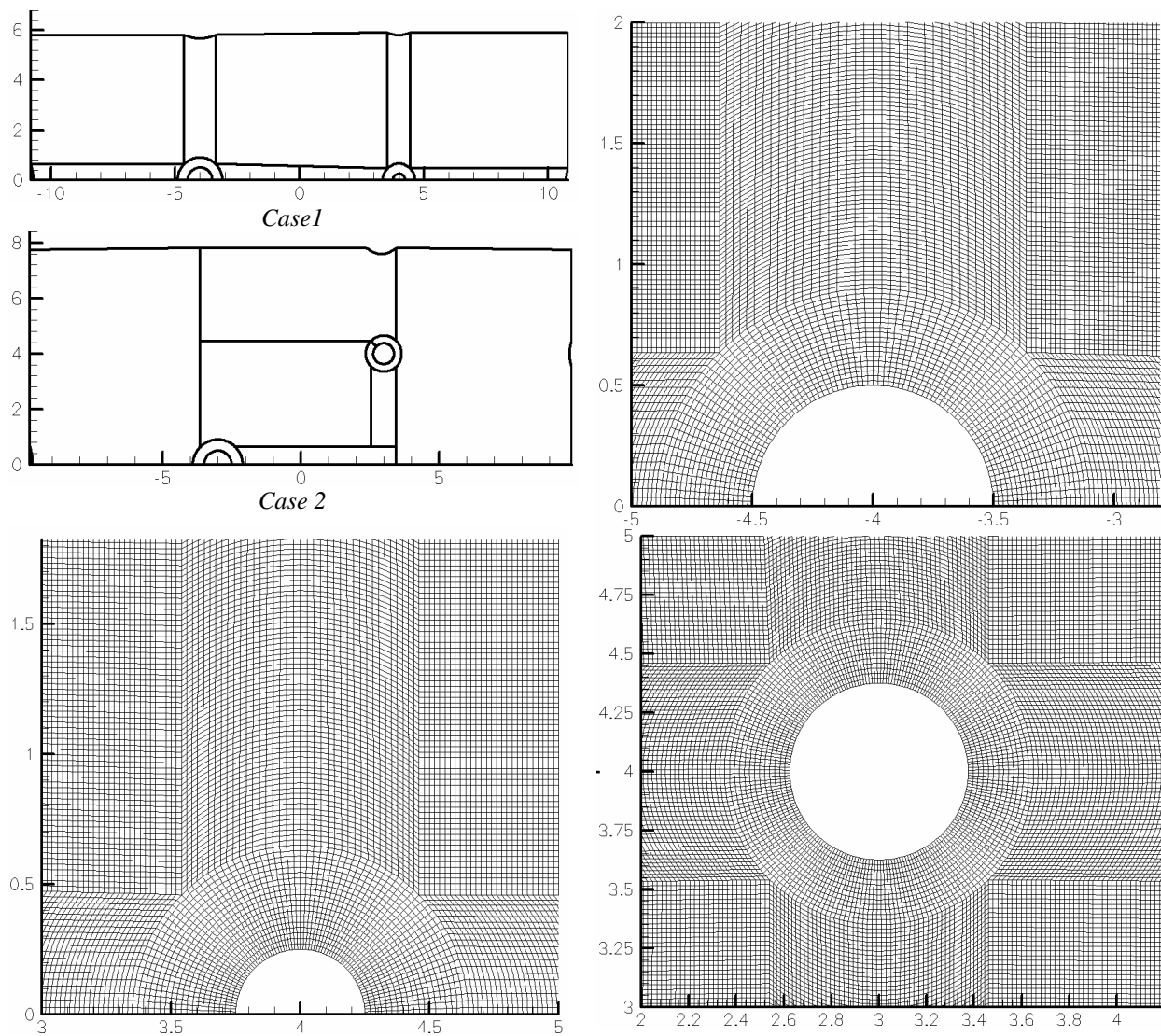
Figure 2 : Multiblock structure.
Grid details near cylinders.
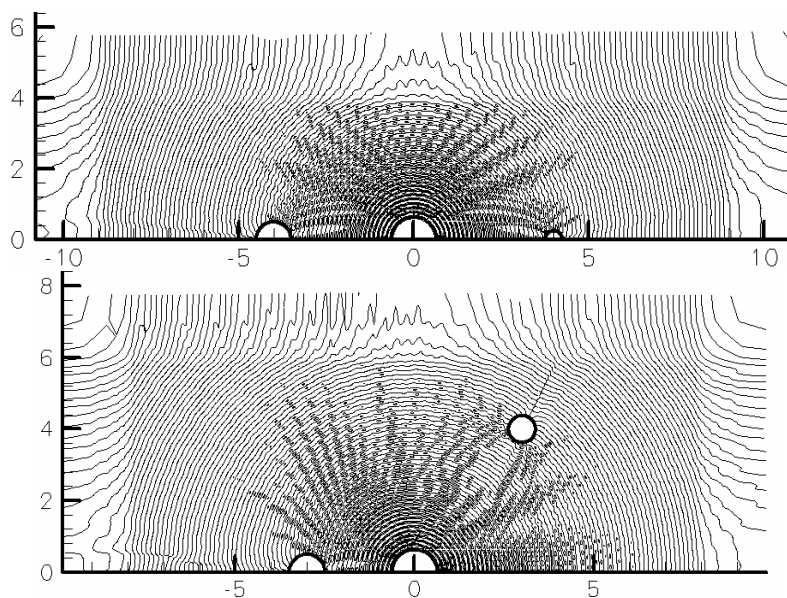
Figure 3 : Instantaneous density
pattern at t = 160T (15 contour levels
in the range ± 3.10⁻⁵)
Top : Case 1 – Bottom : Case 2
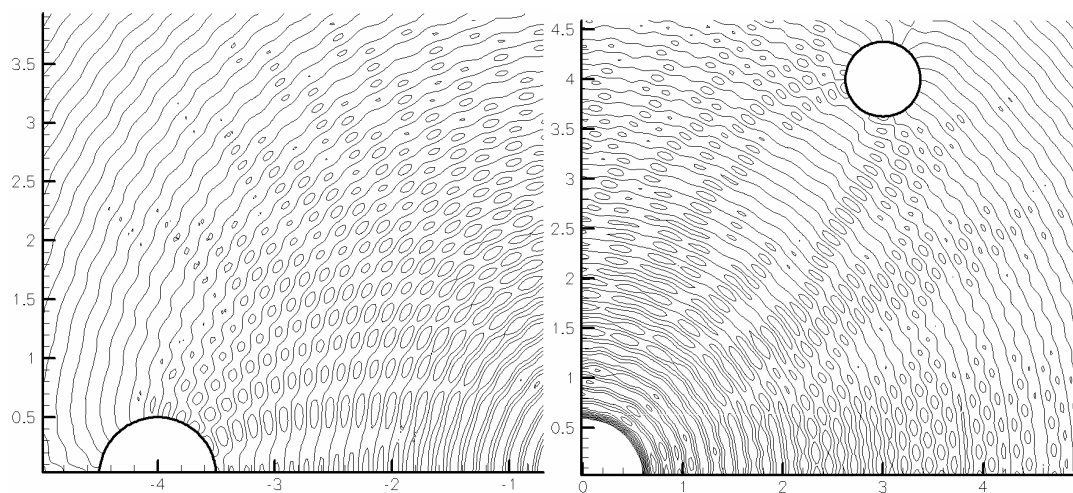
Figure 4 : Same as Figure 3. Details for Case 1 (left) and Case 2 (right).
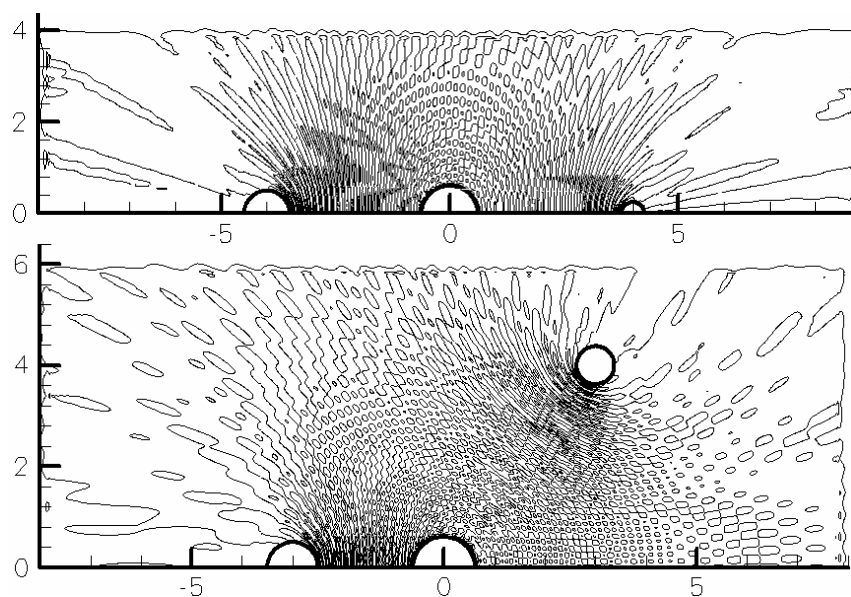
Figure 5 : RMS pressure pattern - (20 contour levels in the range [0., 2.5 10⁻⁵])
Top : Case 1
Bottom : Case 2
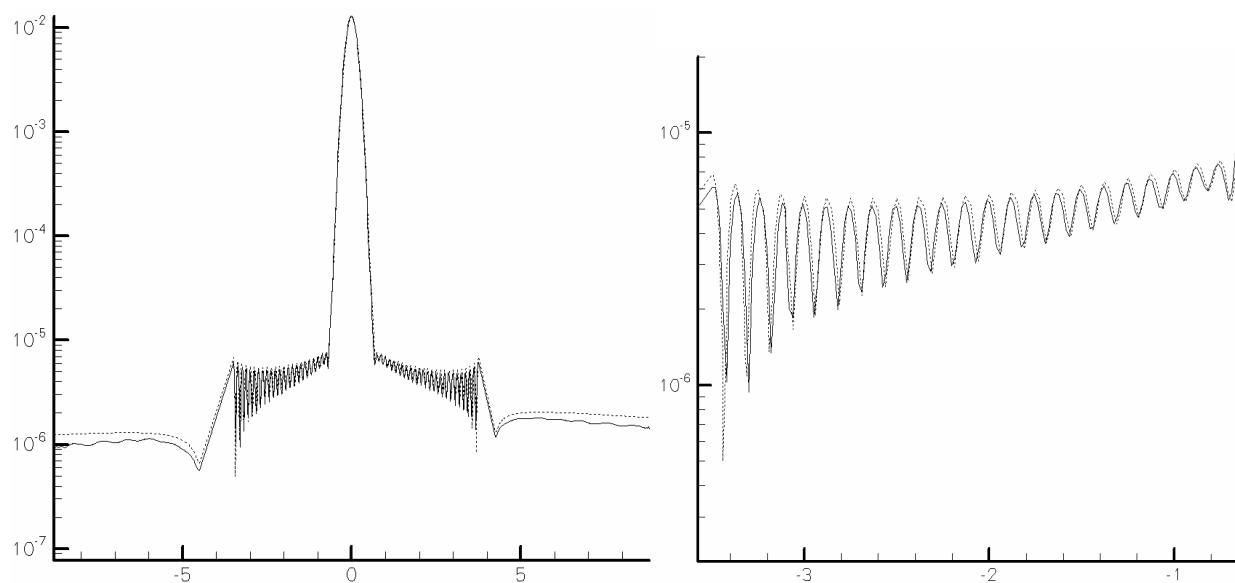
Figure. 6 : Case 1 - RMS pressure along the y = 0 axis (Euler : solid line, analytical : dashed line)
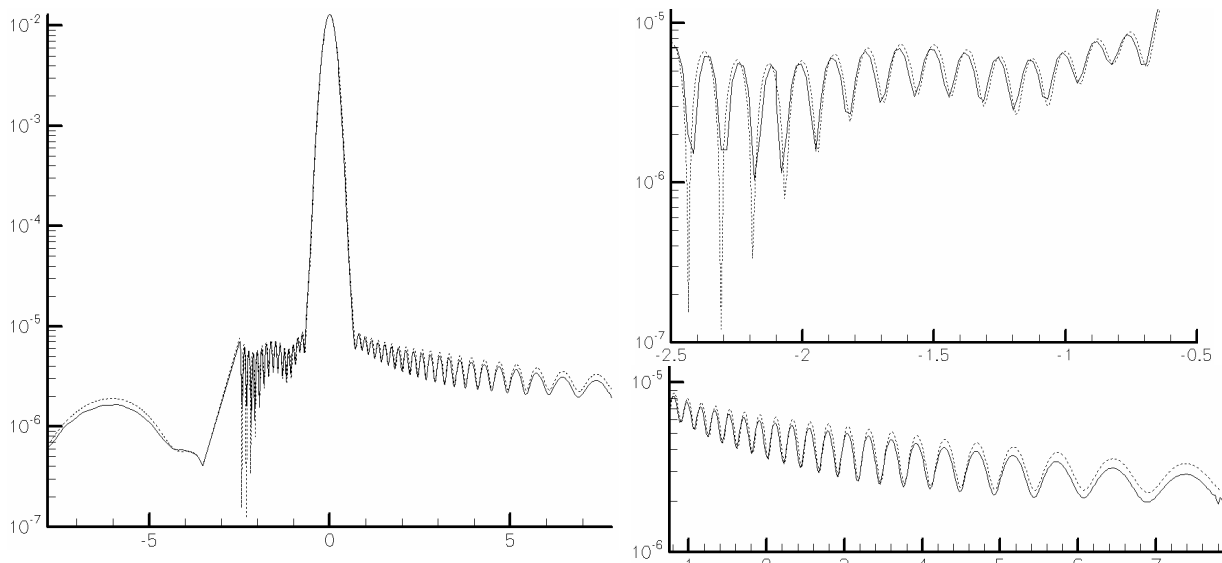
Figure. 7 : Case 2 - RMS pressure along the y = 0 axis (Euler : solid line, analytical: dashed line)
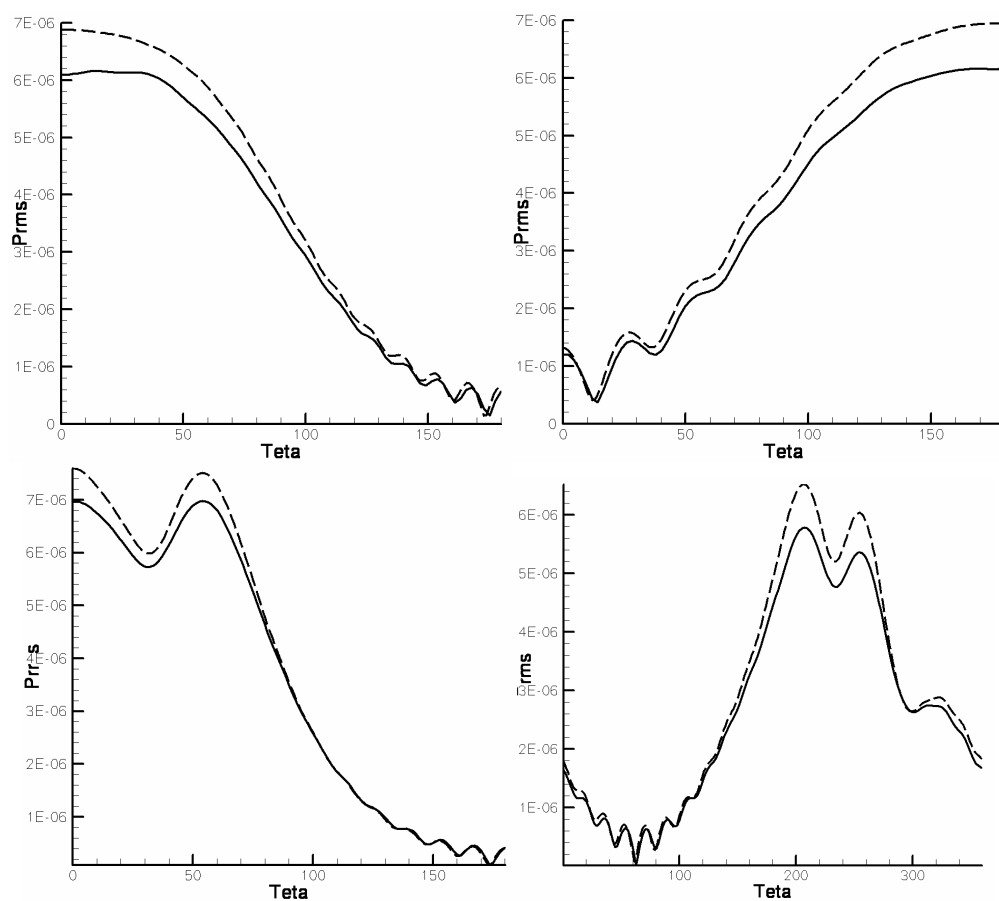
Figure 8 : RMS pressure along the surface of both cylinders
Top : Case 1 -_ Bottom : Case 2
Left : Cylinder #1 - Right :Cylinder #2
(Euler : solid line, analytical : dashed line)

Figures 6 and 7 show the RMS pressure along the axis ($y = 0$), compared to the analytical solution provided by Pr. Visbal. The computed solutions present levels slightly smaller than the analytical result. It has been checked that this results were already obtained at $t = 80T$, so it is not a convergence problem. At first sight, the most probable hypothesis to explain this deficit is the problem of conformal mapping between blocks with grid lines having non-continuous directions, which certainly produces a distortion of wavefronts. The exact influence of this problem has not been investigated further at the moment.

Finally, Figure 8 displays the RMS pressure along the surface of cylinders. For both cylinders of Case 1 (and for Cylinder #1 of Case 2), $\theta = 0°$ corresponds to the right part of the cylinders, $\theta = 180°$ corresponds to the left part. For Cylinder #2 of Case 2, $\theta = 0°$ is east, $\theta = 90°$ is north, $\theta = 180°$ is west and $\theta = 270°$ is south. The deficit of the Euler solution with respect to the analytical solution is observed again.

CONCLUSIONS

The Category 2 - Complex Geometry problem of the 4th CAA Workshop is the simulation of the scattering, from multiple rigid circular cylinders, of sound generated by a spatially distributed, axisymmetric, acoustic source. A numerical solution is proposed, obtained by solving the two-dimensional full conservative Euler equations in a perturbation form, using high order finite difference spatial schemes and filters. These equations are solved on structured multi-domain conformal grids associating body-fitted grids near solid walls and quasi-cartesian grids elsewhere. This grid strategy is very convenient for handling complex geometries with structured codes, but the conformal mapping at boundaries between blocks requires a specific treatment to account for unavoidable discontinuities of the grid line direction through the boundaries between adjacent blocks.

REFERENCES

1. Manoha E., Herrero C., Sagaut P. and Redonnet S. *"Numerical prediction of airfoil aerodynamic noise"*, AIAA paper 2002-2573, 8th AIAA/CEAS Aeroacoustics Conference, Breckenridge, USA, 17-19 May, 2002.

2. Terracol M., Labourasse E., Manoha E. and Sagaut P. *"Simulation of the 3D unsteady flow in a slat cove noise prediction"*, AIAA paper 2003-3254, 9th AIAA/CEAS Aeroacoustics Conference, Hilton Head, USA, 12-14 May, 2003.

3. Sherer S.E. and Visbal M.R., "*Computational Study of Acoustic Scattering from Multiple Bodies Using a High-Order Overset Grid Approach*", AIAA Paper 2003-3203, 9th AIAA/CEAS Aeroacoustics Conference, Hilton Head, USA, 12-14 May, 2003.

4. Redonnet S., Manoha, E. and Sagaut P. *"Numerical Simulation of Propagation of Small Perturbations interacting with Flows and Solid Bodies"*, AIAA Paper n° 2001-2223, 7th CEAS/AIAA Aeroacoustics Conference, Maastricht, The Netherlands, 28-30 May, 2001.

5. Guenanff R., Sagaut P., Manoha E., Terracol M., Lewandowski R. *"Theoretical aspects of a multidomain high-order method for CAA"*, AIAA paper 2003-3117, 9th AIAA/CEAS Aeroacoustics Conference, Hilton Head, USA, 12-14 May, 2003.

Numerical study on propagation and scattering of sound by two cylinders

Alex Povitsky

Department of Mechanical Engineering, University of Akron, Akron, OH, 44325-3903 USA,
E-mail: povitsky@uakron.edu, phone: 330-972-2685, fax: 330-972-6027

Tinghui Zheng and **Georgios H. Vatistas**

Department of Mechanical and Industrial Engineering, Concordia University, Montreal, Quebec, Canada

ABSTRACT

The propagation and scattering of sound by two rigid circular cylinders generated by a spatially distributed axisymmetric periodic acoustic source in the still air are simulated numerically using high-order compact spatial approximation of finite differences and high-order Runge-Kutta time integration. To solve the linearized Euler equations describing the wave propagation, the bipolar curvilinear coordinate system has been used in conservative and non-conservative variants. For bipolar curvilinear coordinate system, lines of the grid coincide with cylinders' envelopes for both cylinders. Use of bipolar coordinate system allows to solve the problem in frame of a single-block finite difference methodology. The details of implementation of artificial boundary conditions are discussed for this transformation of coordinates. This study shows numerical robustness and long-time stability of high-order finite-difference compact computations in bipolar coordinates. The results on the fine 600x600 grid coincide well with the analytical solution. The main advantages of the proposed approach are a straightforward coordinate transformation of available single-block finite-difference code in Cartesian or polar coordinates and reasonable processor time.

INTRODUCTION

The problem of airframe noise (non-propulsive noise of aircraft in flight) is the most prominent in the landing phase of flight where engines do not operate at full thrust. The relatively high noise levels generated by aircraft during descent are environmentally unacceptable to the general public. In particular, the deployment of the undercarriage gear (wheels, axles, struts, shafts) along with the high-lift devices such as trailing-edge flaps and leading-edge slats appears to be the major source of airframe noise. Achievements in reducing the engine noise have led to an increased awareness of landing gear noise and as a consequence, prompted computational studies of aeroacoustics of the landing gear, an area that did not receive much attention of the researchers in the past. The noise impact of tiltrotor, particularly during descent and ascent from airports, has been identified as a barrier for civil tiltrotor acceptance. With the anticipated demand for integration into the civil transport arena, the noise sources of tiltrotor aircraft must be well understood, modeled, and predicted. The high noise levels in tiltrotor descent flight operations are mainly caused by an impulsive noise-generating mechanism known as blade-vortex interaction (BVI) that results from the close proximity between a tiltrotor's main rotor blades and the vortices generated by them during the descent flight (refs 1,2).

In our recent study (ref. 3), the effect of vortex velocity profile on the amplitude and directivity of sound wave generated by the distorting vortex in a non-uniform sub-sonic flow has been studied by numerical modeling using fourth-order compact schemes. Taylor vortex with localized core and zero total circulation and gradually decaying Vatistas vortex with non-zero total circulation are adopted as examples of two different types of vortices. Our geometry was limited to a flow about single 2-D body with rectangular or round cross-section. The purpose of the present effort is to investigate the stringent test of the ability of our high-order CAA codes to handle increasingly complex geometries; it also provides a demonstration of numerical robustness, long-time stability in the presence of multiple scattering bodies.

The advantages of single-block finite-difference approach over multi-block or finite-element approaches are the absence of stability limitations of sub-domain interface boundaries, the small number of arithmetic operations per grid point characteristic for finite-difference compact schemes, and structural simplicity of the code. The main disadvantage of the single-block finite-difference codes is the difficulty to adhere to curvilinear boundary of rigid bodies to ensure reflecting boundary conditions.

The bipolar coordinate system exactly matches the two-body geometry, and gives a way to simulate acoustic feedback effect on flow separation at the surface of upstream body, vortex shedding and sound distribution. For the 3-D two-sphere case, the bipolar system could be replaced by the 3-D bi-spherical system (refs 4 and 5). In certain cases, bipolar coordinates can be extended to other arbitrary curvilinear two-body systems by an appropriate coordinate transformation.

METHODOLOGY

Bipolar coordinate system

The bipolar system is defined by

$$
\begin{aligned}
x &= \frac{a \sinh \eta}{\cosh \eta - \cos \zeta} \\
y &= \frac{a \sin \zeta}{\cosh \eta - \cos \zeta}
\end{aligned}
\tag{1}
$$

where the curves of constant ξ, η are circles in xy plane, $0 < \xi < 2\pi$ (see Fig. 1b). The coefficient a and the range of η can be analytically derived using given radius of two cylinders and the distance between them. In the considered case $-2.771608 < \eta < 3.461818$ and $a = 3.980439$. Numerical grid in bipolar coordinates is shown in Fig. 1b.

The scale factors to transform from Cartesian coordinate system to the bipolar coordinate system are

$$
\begin{aligned}
h_\zeta &= \frac{a}{\cosh \eta - \cos \zeta} \\
h_\eta &= \frac{a}{\cosh \eta - \cos \zeta}
\end{aligned}
\tag{2}
$$

The Euler equations in terms of small disturbances in this bipolar system are given as follows:

$$
\begin{aligned}
\frac{\partial p}{\partial t} &= -\frac{1}{h_\zeta h_\eta}\left(\frac{\partial(h_\eta u)}{\partial \zeta} - \frac{\partial(h_\zeta v)}{\partial \eta} \right) \\
\frac{\partial u}{\partial t} &= -\frac{\partial p}{\partial \zeta}\frac{1}{h_\zeta} \\
\frac{\partial v}{\partial t} &= -\frac{\partial p}{\partial \eta}\frac{1}{h_\eta}
\end{aligned}
\tag{3}
$$

Numerical method

In this study, the forth-order central-difference compact schemes are employed (ref. 7). These schemes require relatively few points per wavelength to ensure dispersion preserving, have low dispersion and dissipation errors, compact three-point stencil, and are frequently used for aeroacoustic computations (refs. 10, 11):

$$
\frac{1}{4}U'_{i-1} + U'_i + \frac{1}{4}U'_{i+1} = \frac{3}{4\Delta x}\left(U_{i+1} - U_{i-1}\right) ,
\tag{4}
$$

where U denotes disturbance components, $U = u, v, p$, U' is the spatial derivative of U in either of directions; and Δx is the grid step in the corresponding direction.

At the boundary of computational domain, a third-order scheme biased toward the interior nodes is used (ref. 9):

$$U_1' + 2U_2' = \frac{1}{\Delta x}\left(-\frac{5}{2}U_1 + 2U_2 + \frac{3}{2}U_3\right)$$

$$U_n' + 2U_{n-1}' = \frac{1}{\Delta x}\left(-\frac{5}{2}U_n + 2U_{n-1} + \frac{3}{2}U_{n-2}\right)$$

(5)

Explicit fourth-order Runge-Kutta time advancement, which is proposed by Williamson (ref. 9) and implemented by Wilson et al. (ref. 8), gives low amplitude and phase errors of traveling wave solutions;

$$H^M = S_x \frac{\partial U^M}{\partial x} + S_y \frac{\partial U^M}{\partial y} + a^M H^{M-1},$$

$$U^{M+1} = U^M + b^{M+1}\Delta t H^M,$$

(6)

where $M = 1,\ldots, 5$ is the particular stage number; and the coefficients a^M and b^M are given in ref. 9.

In the current study, conservative scheme which exactly satisfy the continuity equations and non-conservative scheme which satisfy the continuity equations only when very fine mesh used.

For conservative Eq. (3), the Runge-Kutta time marching is given by:

$$H^M = -\frac{1}{h_\zeta h_\eta}\left(\frac{\partial(h_\eta u)^M}{\partial \xi} + \frac{\partial(h_\xi v)^M}{\partial \eta}\right) + a^M H^{M-1},$$

$$U^{M+1} = U^M + b^{M+1}\Delta t H^M,$$

(7)

where the spatial derivatives $\dfrac{\partial(h_\eta u)}{\partial \zeta}$ and $\dfrac{\partial(h_\zeta v)}{\partial \eta}$ are computed by compact scheme (4).

For non-conservative variant of Eq. (3), the time marching is as follows:

$$H^M = -\frac{1}{h_\zeta h_\eta}\left(u^M \frac{\partial(h_\eta)^M}{\partial \xi} + v^M \frac{\partial(h_\xi)^M}{\partial \eta}\right) - \frac{1}{h_\zeta}\frac{\partial u^M}{\partial \xi} - \frac{1}{h_\eta}\frac{\partial v^M}{\partial \eta} + a^M H^{M-1},$$

$$U^{M+1} = U^M + b^{M+1}\Delta t H^M,$$

(8)

where the spatial derivatives $\dfrac{\partial u}{\partial \zeta}$ and $\dfrac{\partial v}{\partial \eta}$ are computed by compact scheme (4)

Boundary conditions

At the solid surface, reflection boundary conditions $dp/dn = 0, dv/dn = 0$ are used for pressure disturbance and for the tangential component of velocity, whereas the normal to the rigid surface component of velocity is set equal to zero. Discretization of spatial derivatives in the direction perpendicular to a rigid boundary is computed by one-sided finite differences (5).

For bipolar coordinate system, $\xi = 0$ and $\xi = 2\pi$ correspond to the centerline. Periodical boundary condition are used for the disturbance components, i.e. $U_{\xi=0} = U_{\xi=2\pi}$, where $U = u, v, p$. Discretization of the spatial derivatives at the centerline is given by second-order one-sided finite differences.

At the outer boundary, artificial boundary conditions (ABC) should be set-up to eliminate reflections of acoustic energy back into the computational domain. Perfect matched layer at the artificial boundary proposed by Hu (Refs. 12 and 13) and is implemented in Cartesian coordinates for two square cylinders. The PML is described as follows

$$\frac{\partial \vec{u}}{\partial t} + A\frac{\partial \vec{u}}{\partial x} + B\frac{\partial \vec{u}}{\partial y} + \sigma_y A\frac{\partial \vec{q}}{\partial x} + \sigma_x B\frac{\partial \vec{q}}{\partial y} + \left(\sigma_x + \sigma_y\right)\vec{u} + \sigma_x \sigma_y \vec{q} = 0$$

$$\frac{\partial \vec{q}}{\partial t} = \vec{u}$$

(9)

$$\sigma_x = \sigma_m \left|\frac{x - x_l}{D}\right|^\beta, \quad \sigma_y = \sigma_m \left|\frac{y - x_l}{D}\right|^\beta,$$

where x_l or y_l denotes the location where the PML starts, and D is the width of the PML. To compute σ, the relations $\sigma_m \Delta x = 2$, where Δx is the grid size, and $\beta = 2$ are used for all computations.

In the present study, simple damping term in near-boundary layer (so-called sponge layer) was employed in bipolar coordinates as a simplified alternative to perfect matched layer technique. Waves incident on this layer are damped and reflections into the computational domain are minimized.

$$\frac{\partial \vec{u}}{\partial t} + A\frac{\partial \vec{u}}{\partial x} + B\frac{\partial \vec{u}}{\partial y} + \sigma\vec{u} = 0,$$

(10)

where the non-zero damping term $\sigma = 1.2$ is taken for $r \geq 6$, where r is the distance to the source center.

RESULTS and DISCUSSION

In this study, the PC Dell-4550 equipped with Pentium (R)4 processors with 2.53GHz and 1.00GB of RAM is used and Microsoft Visual C++ 6.0 is taken as a compiler for the C++ code.

For preliminary evaluation of the code accuracy and reliability, the Cartesian coordinate system was employed for two infinite cylinders with square cross-section. For the Cartesian coordinate system, the choice of the grid step was defined by the source frequency on one side and accuracy of numerical presentation of dispersion-preserving relation (DPR) on the other side. For 1% discrepancy between numerical and analytical values of DPR, 5.6 grid points per wavelength are needed (ref. 7). The perimeter average root mean square pressures with respect to time are compared between two square cylinders and two round cylinders in Figs. 2 and 3. Geometric simplification of two square cylinders can roughly predict the transient period of wave propagation. However, more acoustic energy is trapped between two square cylinders and the convergence to periodical solution is slower for square cylinders.

For two round cylinders, two mesh grid levels denoted as the coarse mesh 300×300 and the fine mesh 600×600 are taken in the consideration. The computations run up to $t = 42$ in physical time. The CPU elapsed time on the above-mentioned computer system was 1.5 hour for the coarse mesh and 14 hours for the fine mesh. The size of the coarse mesh step was chosen from the dispersion-relation-preserving consideration as 5.6 grid points per wavelength on the bipolar grid. Unfortunately, the solution in the coarse mesh is different from the analytical solution for both conservative and non-conservative variants (see Fig 4.). On the contrary, the fine mesh produces the solution comparable to analytical for both conservative and non-conservative version (see Fig. 5). Comparison with analytical solution is presented in Figs. 6 and 7 for right and left cylinders, respectively.

The developed computational method based on bipolar coordinates shows a very good agreement with the analytical results while fine meshes are employed. Conservative and non-conservative schemes alike are capable of accurate prediction of the sound directivity.

REFERENCES

1. M. Gervais, "Tiltrotor Blade-Vortex Interaction(BVI) Noise Control Through Non-unique Longitudinal Force Trim", Presented at the Southeast Regional Competition of the American Helicopter Socity", College Park, Maryland, January 2001

2. R.D.JanakiRam and H.Kham, "Prediction and Validation of Helicopter Descent Flyover Noise," Presented at the American Helicopter Society 56th Annual Forum, Virginia Beach, VA, May 2000

3. A. Povitsky, T. Zheng, and G. Vatistas, Effect of Vortex Profile on Sound Generation in a Non-uniform Flow, accepted to Mathematics & Computers in Simulation (Special Issue on Wave Propagation), short version in Proceedings of ICCSA-2003, Lecture Notes in Computer Science 2668, pp. 826-837, 2003.

4. Lockwood, E. H, Bipolar Coordinates, in A Book of Curves. Cambridge, England: Cambridge University Press, 1967, pp. 186-190.

5. Arfken, G., Mathematical Methods for Physicists, 2nd ed. Orlando, FL: Academic Press, pp. 115-117, 1970.

6. Djambazov, G.S., Lai, C.H., and Koulis A.P., "Efficient Computation of Aerodynamic Noise", Contemporary Mathematics, Vol. 218, pp 500-506, 1998

7. Lele, S.K., "Compact Finite Difference Scheme with Spectral Like Resolution," Journal of Computational Physics 103. 16-42, 1992

8. R.V.Wilson, A.O. Demuren, and M.Carpenter. "High-order compact schemes for numerical simulation of incompressible flows," ICASE Report No. 98-13,1998

9. J.Williamson, "Low storage Runge-Kutta Schemes," Journal of Computational Pysicas, 35, 48(1980)

10. A. Povitsky, "Acoustics of a stagnation flow near a rigid wall, " Physics of fluids, Vol. 12, Number 10, 2000, pp. 2595-2608

11. A. Povitsky, "Numerical Study of Wave Propagation in a Nonuniform Compressible Flow", Physics of Fluids, Vol.14,No. 8,2002,pp.2657-2672

12. F. Q. Hu, "On Absorbing Boundary Conditions for Linearized Euler Equations by a Perfectly Matched Layer", Journal of Computational Phyics 129, 201-219 (1996)

13. F. Q. Hu, " A Stable, Perfectly Matched Layer for Linearized Euler Equations in Unsplit Physical Variables", Journal of Computational Physics 173,455-480, 2001
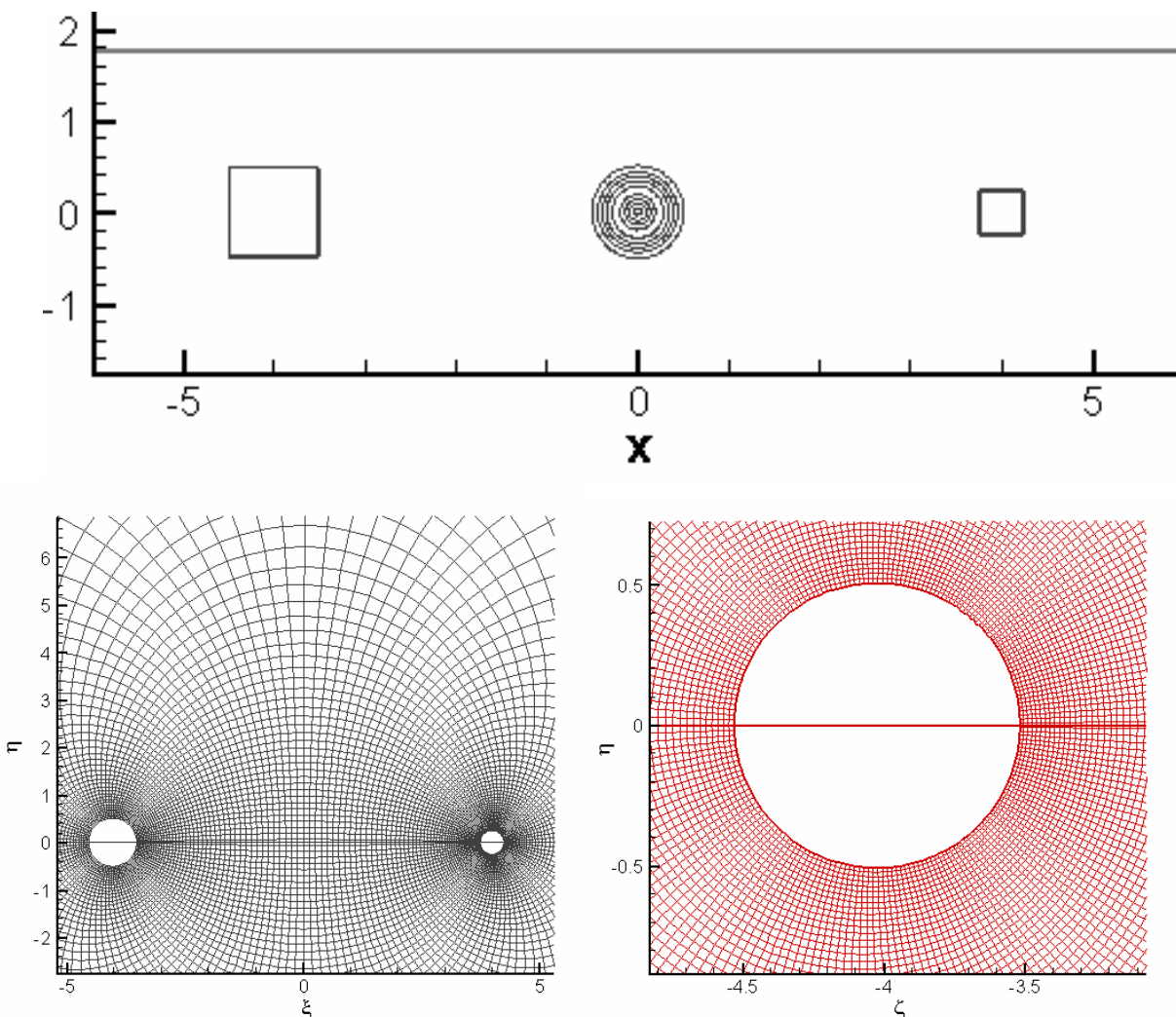
Figure 1. Computational domain and numerical grid: (a) Cartesian coordinates and (b) bipolar coordinates

a

b
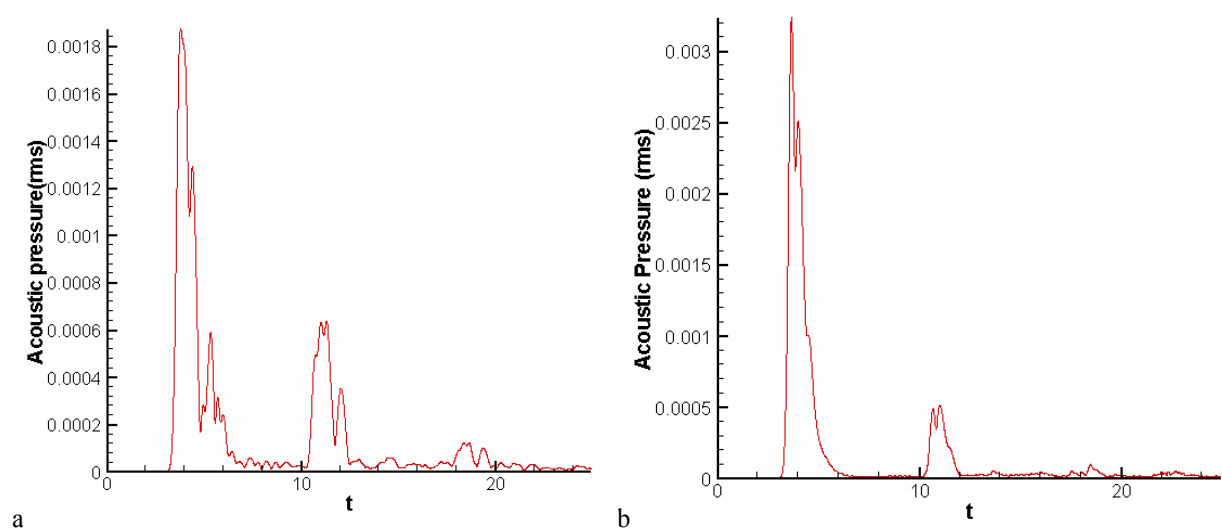
Figure 2. **Perimeter-averaged RMS for the right cylinder (a) Cartesian coordinates and (b) bipolar coordinates**

a

b
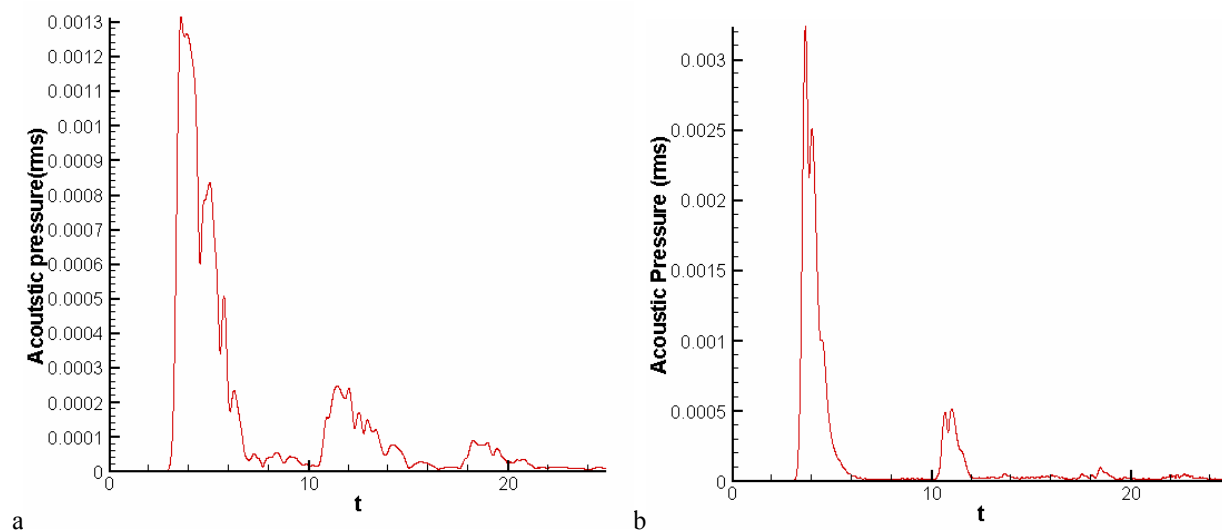
Figure 3. Perimeter-averaged RMS for the left cylinder: (a) Cartesian coordinates and (b) bipolar coordinates
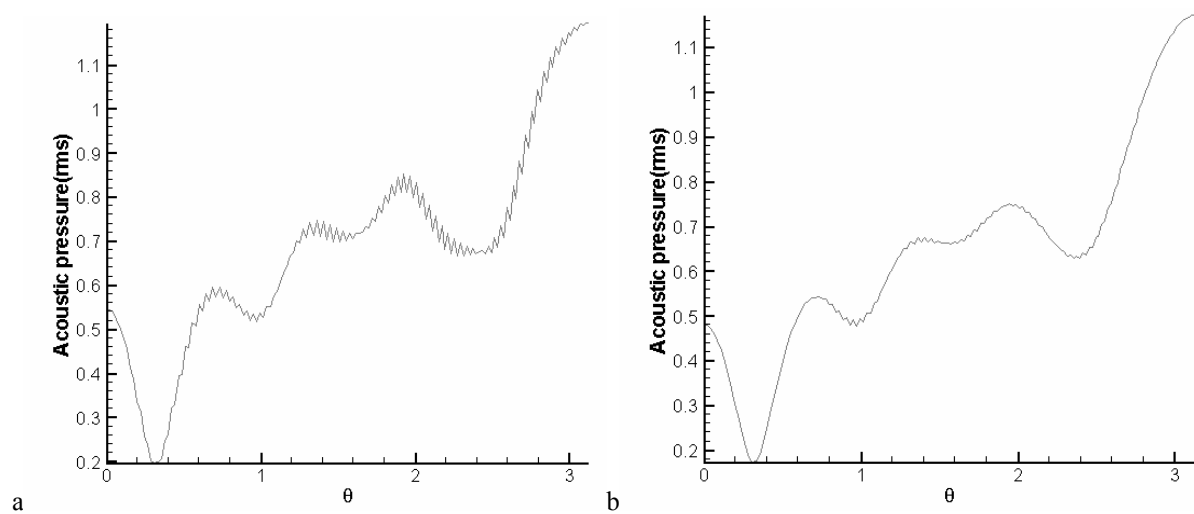
Figure 4. RMS for the right cylinder computed on the coarse mesh (300×300): **(a) conservative scheme and (b) non-conservative scheme**
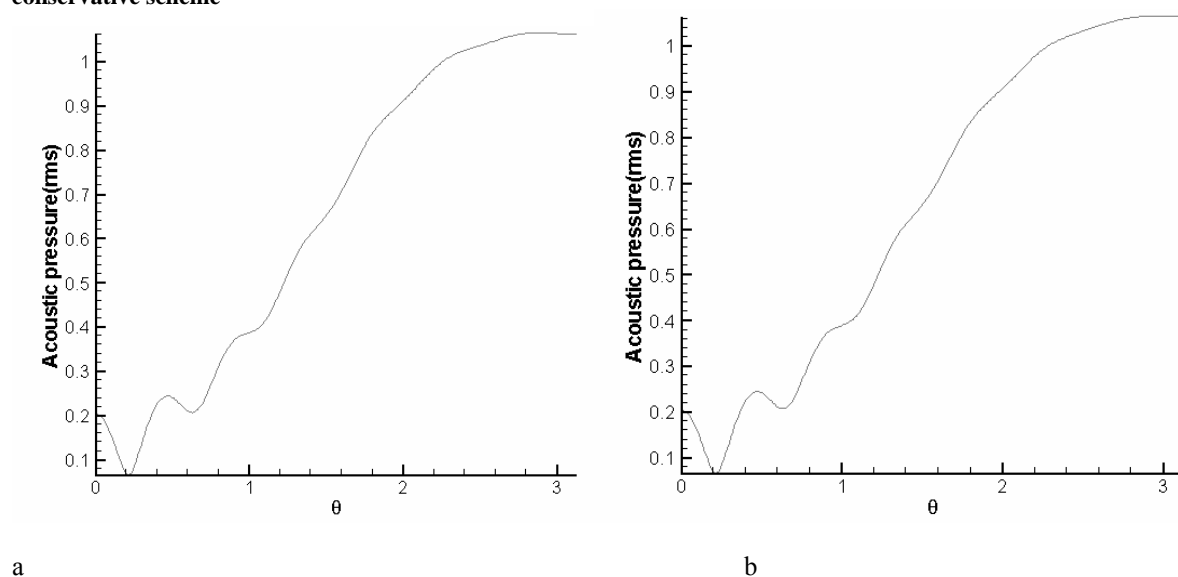
Figure 5. RMS for the right cylinder for fine mesh (600×600) **in bipolar coordinates: (a) conservative scheme and (b) non-conservative scheme**
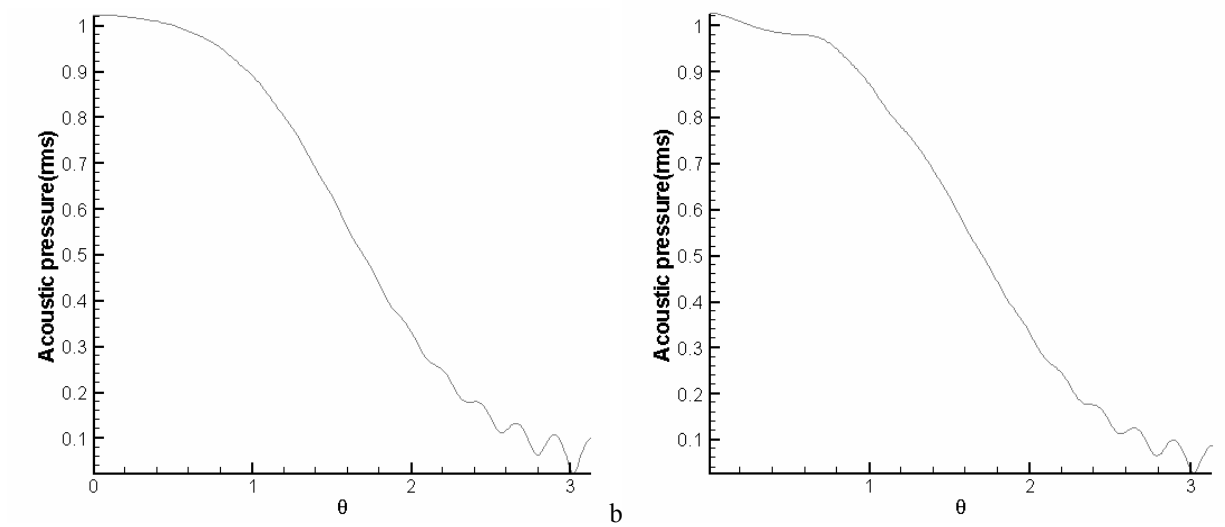
Figure 6. RMS for the left cylinder (a) analytical solution and (b) numerical solution on the (600×600) **grid**
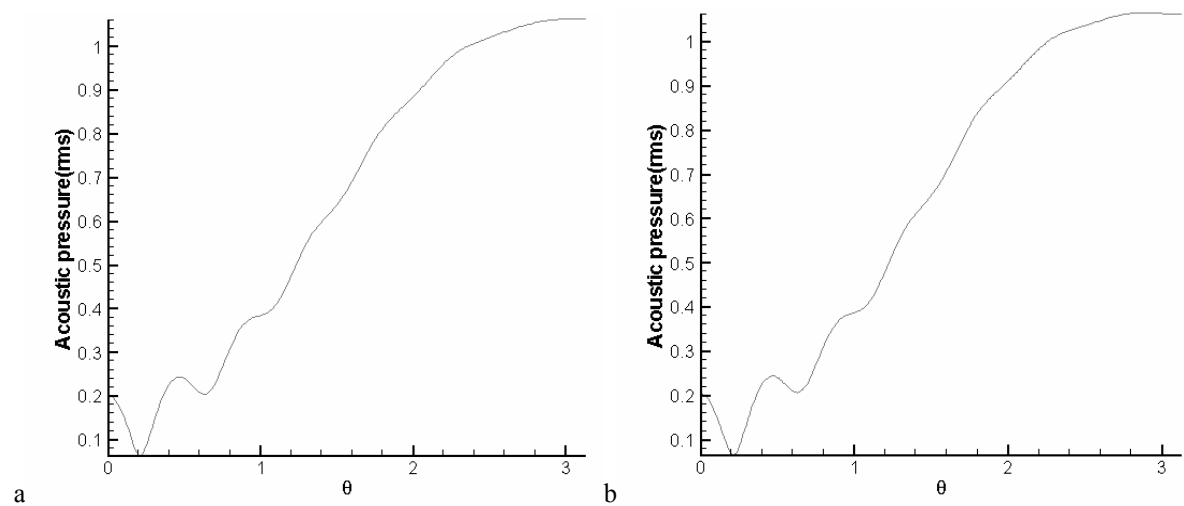
Figure 7. RMS for the right cylinder: (a) analytical solution and (b) numerical solution on the (600×600) **grid**

FREQUENCY DOMAIN CALCULATIONS OF ACOUSTIC PROPAGATION

David P. Lockard[*]

NASA Langley Research Center, Hampton, VA 23681-2199, U.S.A.

ABSTRACT

Two complex geometry problems are solved using the linearized Euler equations. The impedance mismatch method[1] is used to impose the solid surfaces without the need to use a body-fitted grid. The problem is solved in the frequency domain to avoid long run times. Although the harmonic assumption eliminates all time dependence, a pseudo-time term is added to allow conventional iterative methods to be employed. A Jameson[2] type, Runge-Kutta scheme is used to advance the solution in pseudo time. The spatial operator is based on a seven-point, sixth-order finite difference. Constant coefficient, sixth-derivative artificial dissipation is used throughout the domain. A buffer zone technique employing a complex frequency[3] to damp all waves near the boundaries is used to minimize reflections. The results show that the method is capable of capturing the salient features of the scattering, but an excessive number of grid points are required to resolve the phenomena in the vicinity of the solid bodies because the wavelength of the acoustics is relatively short compared with the size of the bodies. Smoothly transitioning into the immersed boundary condition alleviates the difficulties, but a fine mesh is still required.

INTRODUCTION

Problems involving complex geometries are commonplace in real world applications. Although considerable advances have been made in unstructured, multiblock, and overset grid methods, many of the algorithms that can take advantage of these capabilities do not have sufficient accuracy for acoustic problems. Even for high-accuracy methods with these capabilities, generating the grid is non-trivial, especially in three-dimensions. For acoustic problems involving only scattering, Chung and Morris[1] introduced an alternative that allows a Cartesian mesh to be used for arbitrarily complex geometries. All that is required to simulate solid surfaces is to change the density in the regions occupied by the bodies. Although very simple to apply, there are some numerical and resolution issues that will be illustrated in the example problems.

Another difficulty in most acoustic problems is the excessive run time required to wash out initial transients and obtain a periodic steady-state. For linearized problems that are truly periodic, the time dependence can be factored out and the equations solved using algorithms used to accelerate solutions to a steady-state.[4] Unfortunately, there are difficulties in applying standard acceleration algorithms to the resulting complex equations. Furthermore, for problems with broad frequency content, it is likely to be much more efficient to solve the problem in the time domain with a single computation. However, there are some classes of problems where only the behavior of a few important frequencies are needed.

This paper proceeds by describing a numerical method for solving the harmonic form of the linearized Euler equations and an implementation of the impedance mismatch method for simulating solid bodies. Example problems with two and three cylinders and a periodic source are solved to investigate the merits and disadvantages of the approaches. Some conclusions are made on the efficiency of the method as well as possible extensions.

NUMERICAL METHOD

The linearized Euler equations for a constant mean flow can be written in the form

$$\frac{\partial \rho}{\partial t} + \frac{\partial (\rho_o u)}{\partial x} + \frac{\partial (\rho_o v)}{\partial y} = 0, \quad \frac{\partial p}{\partial t} + \frac{\partial (\gamma P_o u)}{\partial x} + \frac{\partial (\gamma P_o v)}{\partial y} = S,$$

$$\frac{\partial u}{\partial t} + \frac{\partial (p/\rho_o)}{\partial x} = 0, \quad \frac{\partial v}{\partial t} + \frac{\partial (p/\rho_o)}{\partial y} = 0. \tag{1}$$

The subscript o represents mean quantities which are assumed constant. The mean speed of sound and density are used

---

[*]Aerospace Technologist

as reference quantities. The ratio of specific heats is denoted by γ. The source term is given by

$$S = \exp\left[-\ln(2)\frac{x^2 + y^2}{0.04}\right]\sin(8\pi t) \tag{2}$$

Equations 1 can be placed in the semi-discrete, compact form

$$\frac{\partial \mathbf{Q}}{\partial t} = -\left[\mathcal{F}(\mathbf{Q}) - \mathcal{D}(\mathbf{Q})\right]. \tag{3}$$

Here, $\mathcal{F}$ represents the discrete form of all the spatial derivatives and the source term S appearing in equations 1. A seven point, sixth-order operator is used for all spatial derivatives. $\mathcal{D}$ denotes sixth-derivative, constant coefficient, artificial dissipation. If we assume that all variables have a temporal time dependence of the form $\exp(-i\omega t)$, equation 3 becomes

$$-i\omega\mathbf{Q}\exp(-i\omega t) = -\left[\mathcal{F}(\mathbf{Q}) - \mathcal{D}(\mathbf{Q})\right]\exp(-i\omega t). \tag{4}$$

Equation 4 can be solved directly, or an iterative technique can be employed. Direct inversion is the most computationally efficient approach, but the memory requirement can be excessive. Research is ongoing into parallel versions of sparse matrix solvers that may make direct inversion feasible for large problems. However, In the current implementation, the equations are solved iteratively by adding a pseudo-time yielding

$$\frac{\partial \mathbf{Q}}{\partial \tau} = -\left[\mathcal{F}(\mathbf{Q}) - \mathcal{D}(\mathbf{Q}) - i\omega\mathbf{Q}\right] = -\mathcal{R}(\mathbf{Q}). \tag{5}$$

Equation 5 is advanced using a Jameson[2] type, five-stage, Runge-Kutta scheme of the form

$$
\begin{aligned}
\mathbf{Q}^{(0)} &= \mathbf{Q}^n, \\
\mathbf{Q}^{(s)} &= \mathbf{Q}^n - \frac{\alpha_s \Delta t}{1 + \alpha_s \omega \Delta t}\left[\mathcal{F}(\mathbf{Q}^{(s-1)}) - \mathcal{D}(\mathbf{Q}^{(0)}) - i\omega\mathbf{Q}^{(s-1)}\right], \\
\mathbf{Q}^{n+1} &= \mathbf{Q}^{(s_{max})}
\end{aligned}
\tag{6}
$$

where n is the iteration counter and $s = 1...5$ indicates the stage. The values of α_s are $[1/4, 1/6, 3/8, 1/2, 1]$. It should be noted that the stability characteristics of the scheme are considerably different in the complex plane, and the coefficients used in the Runge-Kutta scheme have been modified appropriately. To accelerate convergence, local time-stepping and implicit residual smoothing[5] are employed. Multigrid acceleration is generally less effective with complex equations, and is not appropriate for immersed boundary conditions because the effective location of the boundary varies with the mesh level.

Boundary Conditions

The impedance mismatch method[1] is used to impose solid bodies within the flow. All that is required is to set the mean density and pressure to 1/30 of their normal values when within solid bodies. Although one would normally expect that using a higher density within solid bodies would yield the desired solution, this problem is difficult to solve numerically because spatial derivatives of the acoustic variables must balance the discontinuities in the mean quantities. Instead, one can cast the governing equations in the form of 1 where the mean quantities are within the spatial derivatives producing smooth fluxes across the solid interfaces. The correct reflected wave is produced, but the solutions within solid bodies are fictitious.

The specified problems are symmetric about $y = 0$, so symmetry is applied using a reflection condition. All other boundaries employ a buffer domain technique[3] to minimize reflections. The frequency in equation 6 is made complex in the buffer so that waves are damped. The buffer is four wavelengths thick, and the complex component of the frequency varies as $\omega_i = 2\omega_r(1 - \exp(2d^2))/(1 - \exp(2))$ where d varies from unity at the start of the buffer and is zero at the outer boundary.

RESULTS

Scattering from Two Cylinders

Instantaneous pressure contours for the problem with two cylinders is presented in figure 1. In all cases, a uniform, Cartesian grid is used for the calculations. The grid extended 25 cylinder diameters in the x direction and 8 diameters in

the y direction. The reference cylinder at (-4,0) has a diameter of unity, whereas the cylinder at (4,0) has a diameter of 0.5. Because the impedance mismatch condition is used to simulate the solid cylinders, there is still a solution within the cylinders. However, the values are meaningless. The figure illustrates the complex radiation pattern that results because of the interaction of the scattered fields from the two cylinders and the direct radiation from the source. The lack of contours near the maximum y boundary in figure 1 reveals that the buffer zone boundary condition is damping out the waves. The damped region is not observed in the x direction because the plot has been truncated in that direction.
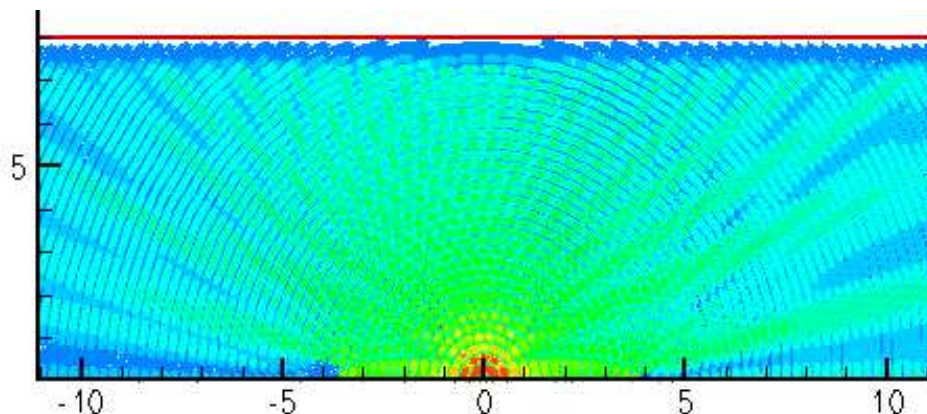
Figure 1: Instantaneous pressure contours for two cylinder problem.

Figure 2 shows averaged p^2 results along the centerline $y = 0$. From figure 2(a), it it can be seen that there are some differences between the 15 and 30 points-per-wavelength (PPW) solutions. The PPW are measure along a grid line, so there is less resolution along the diagonal. Figure 2(b) concentrates on the region around the cylinder at (-4,0). The symbols represent the analytic solution. Clearly, neither computational solution is in good agreement with the analytic solution in the vicinity of the cylinder. The amplitude of the oscillations on the side of the cylinder closest to the source ($x > -3.5$) are too low, whereas they appear too high in the shadow region ($x < -4.5$).
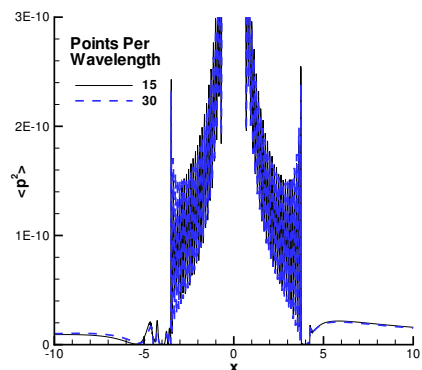
(a) Global view
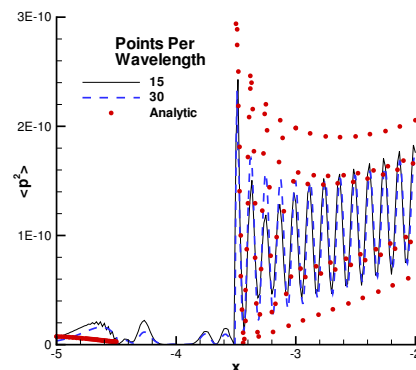
(b) Close-up

Figure 2: Averaged p^2 results along $y = 0$ for two cylinder problem.

The numerical algorithm can resolve acoustic wave propagation with considerably less than 15 PPW, so the errors are clearly associated with the representation of the cylinders. The actual location of the solid body is somewhat ambiguous with the impedance mismatch method because it occurs between grid lines. Therefore, the boundary changes as the grid is refined. In the current problem, the acoustic wavelength is considerably smaller than the diameter of the cylinders which exacerbates the problem. In addition, although the fluxes are continuous across the interface, the solution variables themselves are not. Hence, there is a difficulty in applying artificial dissipation in this region. This produces numerical oscillations which can contaminate the solution. Furthermore, the solution in the vicinity of the solid bodies is often less accurate than in the far-field. All of these issues contribute to the errors seen in figure 2.

One way to alleviate the numerical errors is to smooth the transition to the lower density within solid bodies. Figure 3(a) compares the density variation in the vicinity of the cylinder using the standard method which abruptly transitions across one grid cell (like a Heaviside function) with that of a $1/2(1 + \cos)$ function that transitions over seven points. The results near the cylinder in figure 3(b) shows that the solution with the smooth transition is in considerably better agreement with the analytic solution than the one employing a Heaviside function transition. However, the method of smoothly varying the density only works well when the distance covered by the transition region is small compared to the acoustic wavelength. Furthermore, it can be difficult to determine in which direction to apply the smooth transition for a general body. Nonetheless, it can produce considerably better results as seen in figure 4 which presents the pressure results on the cylinder surfaces. Because no grid points are actually on the cylinder surfaces, values were interpolated to the surface locations. Considering that the exact location of the surface is ambiguous, the results are reasonably good.

(a) Transition Function   (b) Solution near cylinder
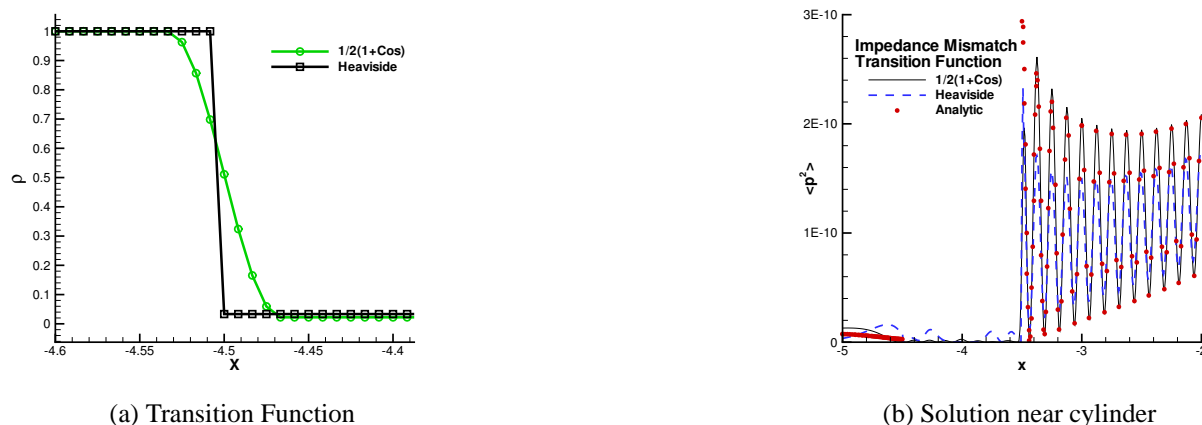
Figure 3: Transition function effect on averaged p^2 results along $y = 0$ for two cylinder problem. The grid has 30 PPW.

(a) Cylinder at $(-4, 0)$ (b) Cylinder at $(4, 0)$
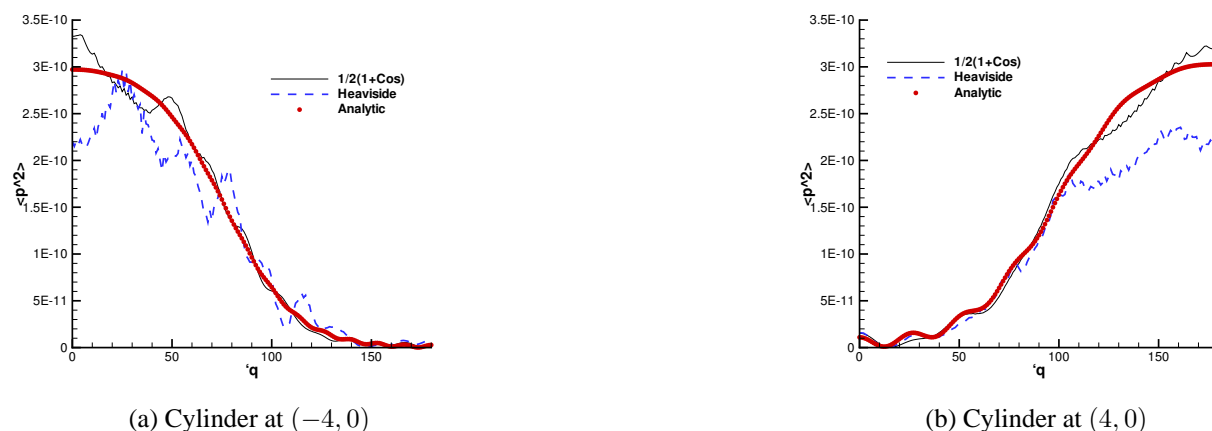
Figure 4: Averaged p^2 results on cylinder surfaces for two cylinder problem.

Scattering from Three Cylinders

Instantaneous pressure contours for the problem with three cylinders are presented in figure 5. The grid extended 23 cylinder diameters in the x direction and 12 diameters in the y direction. The reference cylinder at (-3,0) has a diameter of unity, whereas the cylinders at (3,4) and (3,-4) have diameters of 0.75. Considerably more interference is observable compared with the two cylinder solution shown in figure 1.

Figure 6 shows averaged p^2 results along the centerline $y = 0$. Although there are some differences between the solutions with 15 and 30 PPW, they are not as significant as for the two cylinder problem. The close-up view of a solution with a smooth density transition in figure 6(b) does show better agreement with the analytic solution, but it is
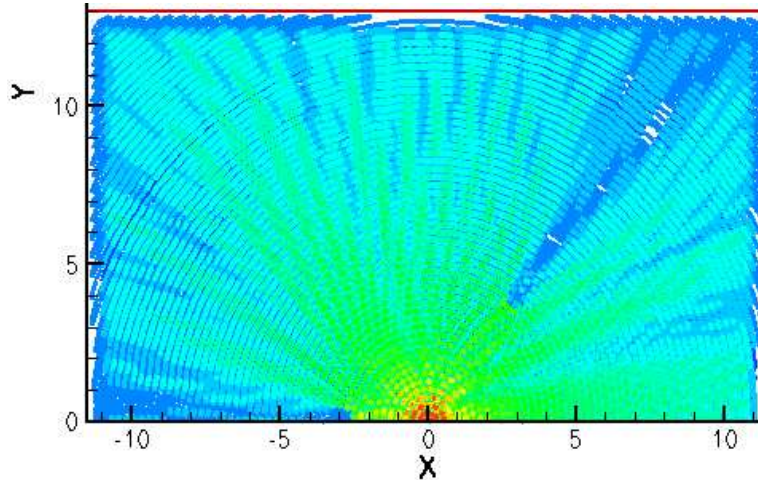
Figure 5: Instantaneous pressure contours for three cylinder problem.

only marginally better than the standard solution with a Heaviside type variation. The orientation and size of the smaller cylinders relative to the larger one may make the effect of secondary reflections less of an issue along the line $y = 0$.

(a) Global view

(b) Close-up, 30 PPW
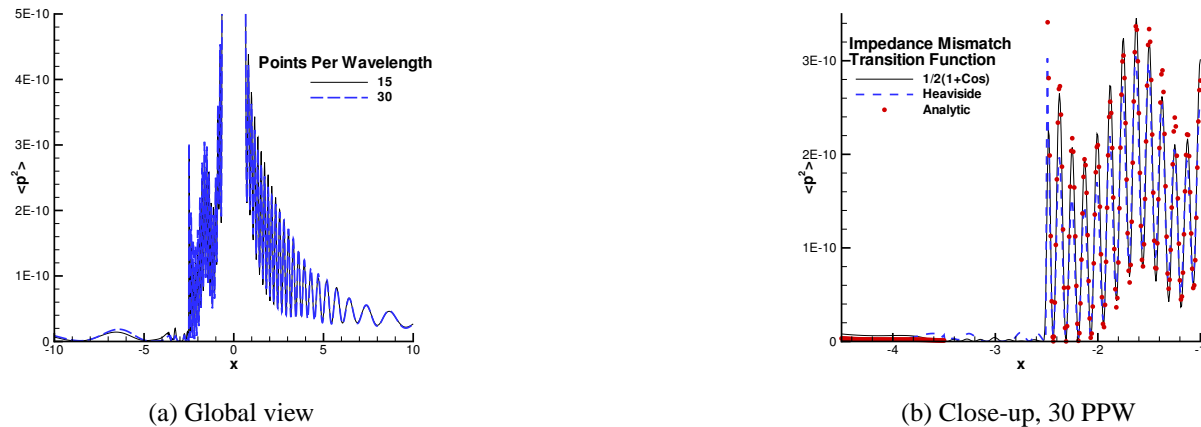
Figure 6: Averaged p^2 results along $y = 0$ for three cylinder problem.

Surface pressure comparisons are presented in figure 7. The solution on the larger cylinder (figure 7(a)) for the case with the smooth density transition does agree better with the analytic solution, but the solution on the smaller cylinder (figure 7(b)) is considerably more wavy than the solution using the standard method. It is unclear why the solution with the smooth density transition exhibits such waviness. Overall, the solutions for the three-cylinder case seem reasonable, although the grids are still excessively fine in order to resolve the regions around the cylinders.

RESOURCES

The CFL number for the calculations was 2.5. Three million grid points and 6241 iterations were used for the two cylinder problem, and 3.8 million points and 6998 iterations for the three-cylinder problem. The residual was forced to drop to 1e-10 in all cases. However, the solution doesn't vary significantly once the residual drops by several orders of magnitude. Hence, one could decrease the number of iterations by a factor of two and obtain the same basic solution.

A Beowulf cluster of 2.53 GHz Intel Pentium IV computers was used to run the calculations. The two cylinder problem took 16 hours on 36 processors, and the three cylinder problem took 25 hours on the same number of processors. The code used the Message Passing Interface (MPI) to perform communication over a standard Ethernet interconnect. The parallel efficiency is known to be quite low because of a communications bottleneck.
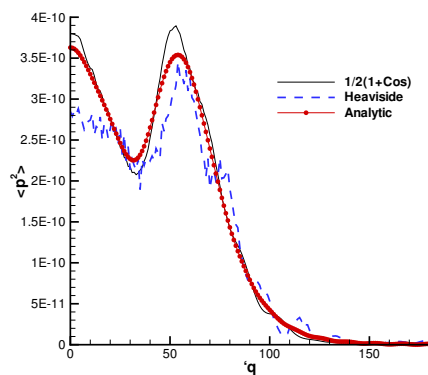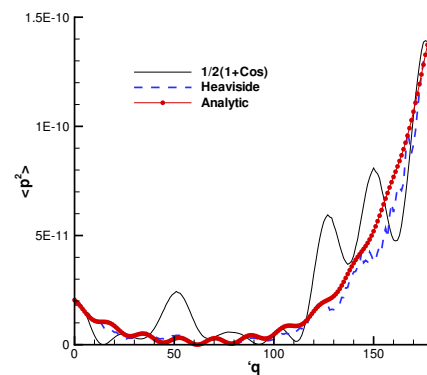
(a) Cylinder at $(-3, 0)$ (b) Cylinder at $(3, 4)$

Figure 7: Averaged p^2 results on cylinder surfaces for three cylinder problem. The grid has 30 PPW.

CONCLUSIONS

The performance of the method used in this work is rather disappointing, although the time to generate the grid and make coding changes were almost negligible. The need to have relatively high resolution in the vicinity of solid boundaries necessitated a very fine mesh everywhere because of the aim of using a simple Cartesian grid. The relatively short wavelength of the acoustics relative to the scattering bodies exacerbated the problem. Furthermore, solving the equations in the frequency domain only resulted in a minor improvement in efficiency. Since the grid was uniform, local time stepping was irrelevant. Implicit residual smoothing did allow a slightly larger time step to be used, but the improvement was probably less than a factor of 3. A different iterative technique employing some sort of implicitness may perform better. However, efficient direct solvers with minimal memory requirements hold the most promise. Furthermore, the impedance mismatch method does not appear to be the best choice for problems where detailed information near the scattering bodies is needed. This is especially true for high-frequency phenomena. If only far-field data for lower frequencies is needed, it has already been demonstrated to be useful. However, a finite-element formulation or a multiblock method may prove more useful in general.

REFERENCES

[1] Chung, C.; and Morris, P. J.: A new boundary treatment for two- and three-dimensional acoustic scattering problems. AIAA-95-008, 1995. Presented at the 1st AIAA/CEAS Aeroacoustics Conference.

[2] Jameson, A.; Schmidt, W.; and Turkel, E.: Numerical solution of the Euler equations by finite-volume methods using Runge-Kutta time-stepping schemes. AIAA-81-1259, Presented at the 14th AIAA Fluid and Plasma Dyanmics Conference, Palo Alto, CA, June 23-25, 1981.

[3] Agarwal, A.; and Morris, P. J.: The calculation of sound propagation in nonuniform flows: supporession of instability waves. AIAA-03-878, Presented at the 41st AIAA Aerospace Sciences Meeting & Exhibit, Reno, NV, 2003.

[4] Agarwäl, R. K.; and Huh, K. S.: Acoustic radiation due to gust-airfoil interaction in a compressible flow. CEAS/AIAA Paper-96-1755, 1996. Presented at the 2nd AIAA/CEAS Aeroacoustics Conference, State College, PA, May 6-8.

[5] Hirsch, C.: *Numerical Computation of Internal and External Flows, Volume 2*. John-Wiley and Sons, 1990.

THE APPLICATION OF "EMBEDDED SOLID" APPROACHES TO COMPUTATIONAL AEROACOUSTIC PROBLEMS WITH COMPLEX GEOMETRIES

Yih-Pin Liew, Said Boluriaan, and Philip J. Morris
Department of Aerospace Engineering
The Pennsylvania State University
University Park, Pennsylvania 16802, USA

INTRODUCTION

A number of practical problems in aeroacoustics involve the interaction of acoustic fields and bodies with complex geometries. Numerical simulations of these problems require special treatments of curved boundaries, sharp edges, and moving or deformable objects. A body fitted grid can sometimes be used to transform the physical domain to a computational domain with a Cartesian uniformly distributed grid but this is difficult in general. An unstructured grid can also be used together with either finite element or finite volume schemes. Such schemes usually suffer from the fact that they are mostly low-order and the acoustic waves have to propagate through irregular elements. Both approaches introduce numerical dissipation and dispersion that are not physical.

In an alternative approach, sometimes called the 'embedded solid' approach, a rectangular uniformly distributed Cartesian grid is used in the entire physical domain and the effect of solid objects is simulated by changing the fluid density or by applying a fictitious body force. For example, Chung and Morris (ref. 1), in the Impedance Mismatch Method (IMM), replaced the solid object by a fluid of lower density. In the Brinkman Penalization method (ref. 2), originally developed for flow simulation in porous media, a body force proportional to the local fluid velocity is used to simulate the solid object. A modification to this approach is the virtual surface method (ref. 3), in which the desired body force is calculated through an iterative feedback loop. Forcing the fluid velocity to be zero inside the body can also mimic the presence of a solid. In addition, raising the pressure within the body can be used to obtain reflection characteristics similar to those of a solid body.

The present paper uses the Category 2 workshop problems to investigate the accuracy and field of applicability of the embedded solid approach in computational aeroacoustics problems with complex geometries. The Brinkman Penalization method and an extension to it, which is under development by the authors, are examined.

GOVERNING EQUATIONS

Formulations
As the primary interest of the authors in this technique is in shockwave structure interaction, the nonlinear Euler equations are used. For simplicity, the formulation is shown using the non-dimensional nonlinear Euler equations in one dimension. They can be written as:

$$\frac{\partial}{\partial t}(\rho) + \frac{\partial}{\partial x}(\rho u) = 0 \qquad\qquad 1$$

$$\frac{\partial}{\partial t}(\rho u) + \frac{\partial}{\partial x}\left(\rho u^2 + P\right) = 0 \qquad\qquad 2$$

$$\frac{\partial}{\partial t}\left(\frac{P}{\gamma-1} + \frac{1}{2}\rho u^2\right) + \frac{\partial}{\partial x}\left[u\left(\frac{P}{\gamma-1} + \frac{1}{2}\rho u^2 + P\right)\right] = S \qquad\qquad 3$$

The equations have been non-dimensionalized with respect to a length scale L and the speed of sound and density in the undisturbed medium, a_0 and ρ_0 respectively.

Brinkman Penalization Method

The original Brinkman Penalization Method, described in detail in reference **2,** was developed for incompressible flows. In the original method, the 'embedded solid' region is represented by a source term that is included only in the momentum equations. This source term acts to cancel any inflow of momentum into the solid region, resulting in a no flow condition in the 'solid' or a reduced flow speed for a porous medium. The modified momentum equation is,

$$\frac{\partial}{\partial t}(u) + \frac{\partial}{\partial x}\left(\frac{P}{\rho}\right) = -\frac{1}{\varepsilon}\chi_0 u \qquad 4$$

Here ε is the penalization coefficient and the smaller its value the more impermeable is the solid. χ_0 is a Heaviside function that marks the location of the 'solid'.

For compressible flows, the following extensions have been implemented. The Brinkman source term, instead of being applied just to the velocity, is applied to the momentum. Also, the source term, multiplied by the instantaneous velocity, is now present in the energy equation. This accounts for the work done bringing the fluid to rest. The momentum and energy equations become,

$$\frac{\partial}{\partial t}(\rho u) + \frac{\partial}{\partial x}\left(\rho u^2 + P\right) = -\frac{1}{\varepsilon}\chi_0(\rho u) \qquad 5$$

$$\frac{\partial}{\partial t}\left(\frac{P}{\gamma-1} + \frac{1}{2}\rho u^2\right) + \frac{\partial}{\partial x}\left[u\left(\frac{P}{\gamma-1} + \frac{1}{2}\rho u^2 + P\right)\right] = S - \frac{C}{\varepsilon}\chi_0\left(\rho u^2\right) \qquad 6$$

C is a coefficient that has been introduced to control the energy source in Equation **6**. In the present calculations, $C = 1.0e^{-1}$ and $\varepsilon = 2.0e^{-4}$.

NUMERICAL SCHEME

The benchmark problem is solved in the space-time domain using an explicit finite-difference scheme. The third-order accurate Dispersion-Relation-Preserving (DRP) scheme, developed by Lockard et al. (ref. 4), is used for spatial discretization and a fourth-order Runge-Kutta (RK) scheme is used for time integration.

The spatial derivatives are calculated using a 3rd order accurate DRP scheme. For example,

$$\frac{\partial}{\partial x}(F_l) \approx \frac{1}{\Delta x}\sum_{i=-3}^{3} a_i F_{l+i} \qquad 7$$

where the coefficients a_i are given by Lockard et al. (ref. 4)

Since the DRP scheme is a higher order central difference method, Gibb's oscillations are expected to be observed in the vicinity of a discontinuity. To minimize these spurious oscillations in the solution the selective artificial dissipation scheme developed by Tam and Shen (ref. 5) is used to damp out these short wavelength spurious oscillations. The artificial dissipation terms are constructed in the following form,

$$D_{i,l} = -\frac{1}{(\Delta x)^2}\sum_{j=-3}^{3} c_j Q_{i,l+j} \quad . \qquad 8$$

where the coefficients c_j are given by Tam and Shen (ref. 5).

Then the system of equations becomes

$$\frac{\partial}{\partial t}(Q_i) + \frac{\partial}{\partial x}(F_i) = D_i \qquad\qquad 9$$

To solve the Brinkman equations, a semi-implicit scheme is used in the RK stages. Instead of using the previous time step's variable as part of the source term, this is now solved implicitly. For example, the solution of Equation *5* is obtained from,

$$Q_2^n\left(1 + \Delta t \frac{1}{\varepsilon} \chi_0\right) = Q_2^{n-1} - \Delta t \frac{\partial}{\partial x}(F_2) \qquad\qquad 10$$

Since the solution of the energy equation, Equation 6, requires the use of the momentum flux, a temporary value of the momentum flux is stored. For the calculation of the flux terms, F_i, direct calculation from the solution variables is used instead of the primary variables u, v and P, in an effort to minimize round off errors. The formulation for the calculation of the flux terms in terms of the solution variables is given by,

$$F_1 = Q_2 \qquad\qquad 11$$

$$F_2 = \frac{Q_2^2}{Q_1} + (\gamma - 1)\left(Q_3 - \frac{1}{2}\frac{Q_2^2}{Q_1}\right) \qquad\qquad 12$$

$$F_3 = \frac{Q_2}{Q_1}\left[Q_3 + (\gamma - 1)\left(Q_3 - \frac{1}{2}\frac{Q_2^2}{Q_1}\right)\right] \qquad\qquad 13$$

A sixth order filter, obtained by Taylor series expansion, is applied to the solution after each time step to smooth out the strong Gibbs oscillations near the surface of the bodies.

RESULTS

As the governing equations being used are the nonlinear Euler equations, the amplitude of the source term, A, as specified in the problem definition, should be much smaller than unity. To ensure that the simulation is in the linear range, A is chosen to be 0.01 in the source term, given by,

$$S = A\exp\left[-\ln 2 \times \left\{\frac{x_s^2 + y_s^2}{b^2}\right\}\right]\sin(\omega t) \qquad\qquad 14$$

The results are then multiplied by a factor 100 to correspond to the same scale as the problem definition.

Case 1

The computational domain is a uniform grid that stretches from –10.0 to 10.0 in the x direction and –2.5 to 2.5 in the y direction with 200 grid points per unit length and a CFL number of 0.25. The computation is performed on a Beowulf cluster using five dual processors nodes. Domain decomposition is used as the parallelization method. To

Penalization coefficient is gradually switched on after the initial pulse has passed through the location of the cylinder. Approximately forty time units are needed to achieve a periodic steady state. A simple buffer domain, of the general type introduced by Wasistho et al. (ref. 6) is used. In the present case a simple hyperbolic tangent function is used to weight the solution in the buffer zone. To ensure the absorption the waves, this buffer domain occupies one length unit in all directions from the boundary.

Figures 1 and 2 shows the root mean square (rms) pressure on the centerline and Figures 3 and 4 shows the rms pressure on the surfaces of cylinders 1 and 2 respectively. The analytical solution is shown for comparison. Since there is not necessarily a grid point on the cylinder surfaces and also due to Gibbs oscillations near the surfaces, the values shown in Figures 3 and 4 are taken from grid points 2Δ to 2.8Δ from the cylinder surface. This results in some small scatter. The pressure in the shadow zone of both cylinders is slightly over estimated. However, given the approximate nature of the technique used for the specification of the boundaries, the overall agreement is remarkably good.

Case 2

The computational domain for this case has the same grid density as for case 1 but with a larger domain that stretches from -9.0 to 9.0 in the x direction and -6.0 to 6.0 in the y direction. In this case, thirty time units are needed to reach a periodic steady state. The computation is performed using 8 dual processors nodes.

Figures 5 and 6 show the rms pressure on the centerline and Figures 7 and 8 shows the rms pressure on the surfaces of cylinders 1 and 2 respectively. The pressure in the shadow zone of both cylinders is slightly over estimated as with the previous case. However the overall agreement with the analytic solution is still remarkably good.

CONCLUSIONS

The Brinkman Penalization method, as demonstrated for this benchmark problem, correctly predicts the pressure distribution; the only small inconsistency is the pressure distribution in the shadow zone of the cylinders. The present code uses a completely uniform grid and is very inefficient in terms of computational cost. A version that uses a generalized coordinate system is under development. Then the grid need only be clustered in the vicinity of the body surface. In general, in spite of the simplicity of the technique for the specification of the boundaries, the method has been demonstrated to be very effective. The authors are presently using this approach to study shock structure interactions.

REFERENCES

1. Chung, C.; and Morris, P. J.: Acoustic Scattering from Two- and Three-Dimensional Bodies. J. Computational Acoustics, vol. 6, no. 3, 1988, pp. 357-375.
2. Brinkman, H. C.: A Calculation of the Viscous Force Exerted by a Flowing Fluid on a Dense Swarm of Particles. Applied Scientific Research, A1: 81-86, 1947.
3. Goldstein, D.; Handler, H.; and Sirovich, L.: Modeling a No-Slip Boundary with an External Force Field. J. of Computational Physics, vol. 105, no. 2, 1995, pp. 354-366.
4. Lockard, D. P.; Brentner, K. S.; and Atkins, H. L.: High Accuracy Algorithms for Computational Aeroacoustics. AIAA paper 94-0460, 1994.
5. Tam, C. K. W.; and Shen, H.: Direct Computation of Nonlinear Acoustic Pulses using High-Order Finite Difference Schemes. AIAA paper 93-4325, 1993.
6. Wasistho, B.; Geurts, B.J.; and Kuerten, J.G.M.: Simulation Techniques for Spatially Evolving Instabilities in Compressible Flow over a Flat Plate. Computers & Fluids, vol. 26, no. 7, pp 713-739, 1997.
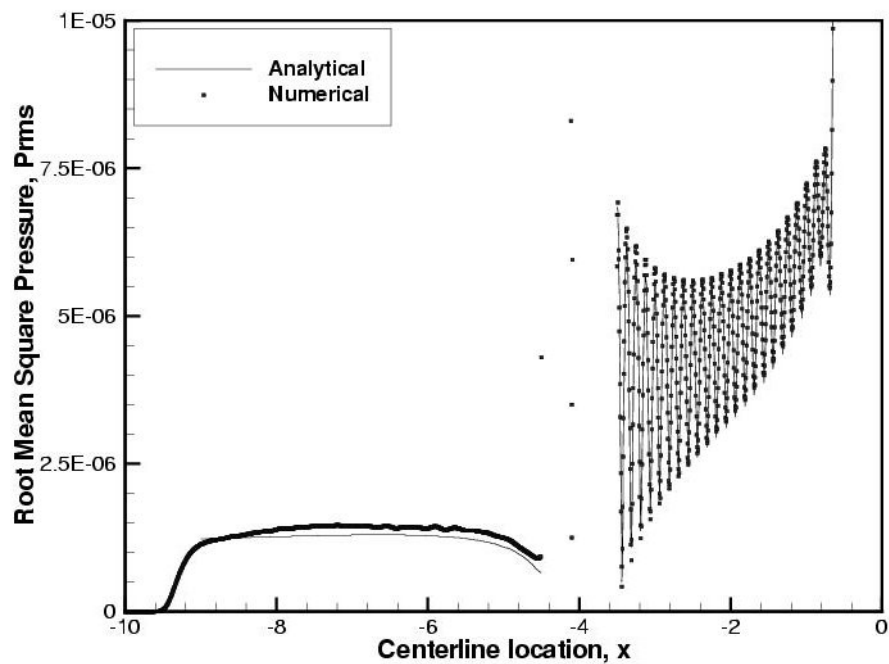
Figure 1. Case 1, centerline P_{rms} distribution for x = -8 to x = 0
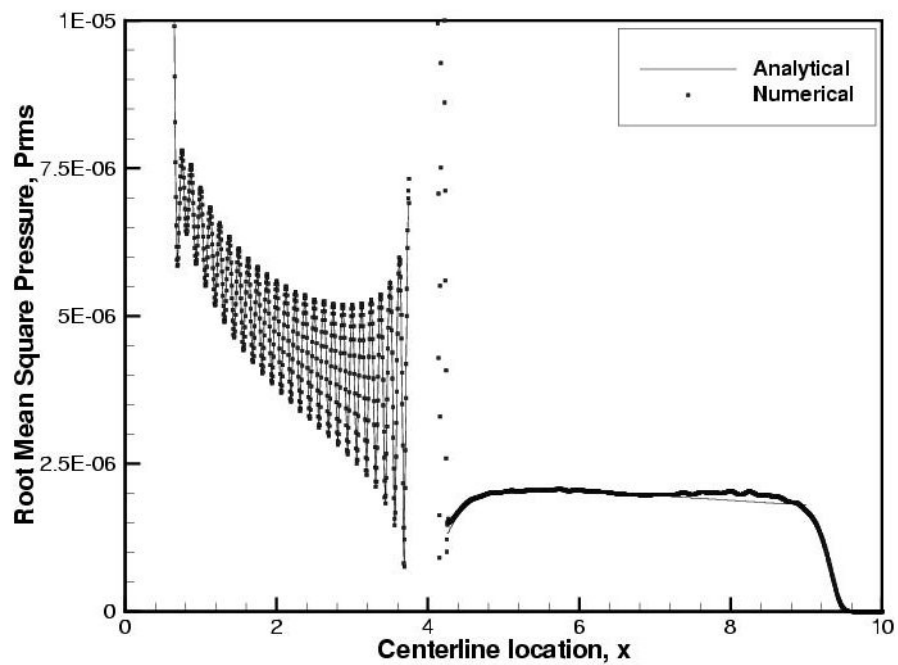
Figure 2. Case 1, centerline P_{rms} distribution for x = 0 to x = 8
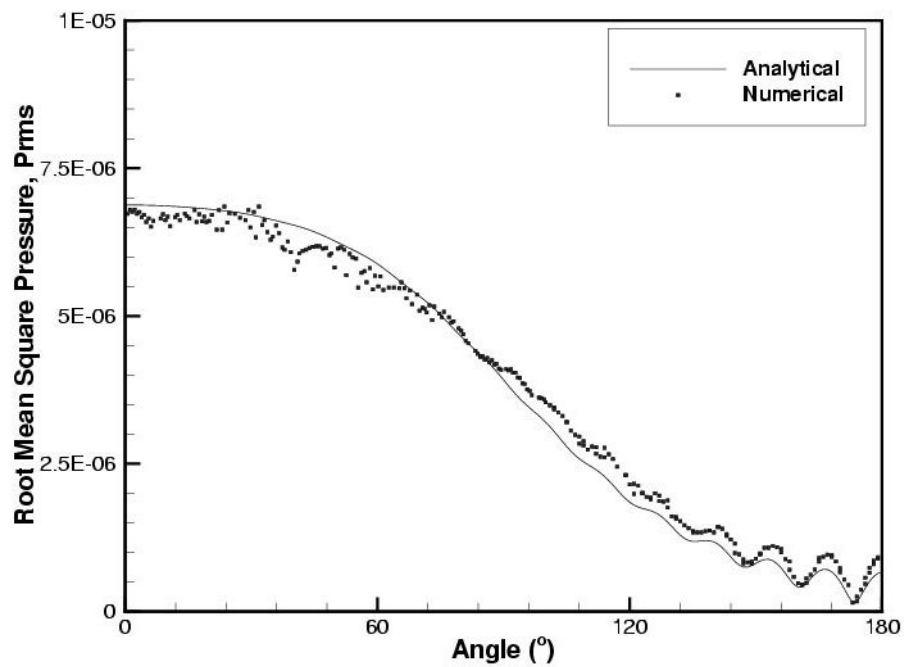
Figure 3. Case 1, P_{rms} distribution on surface of cylinder 1
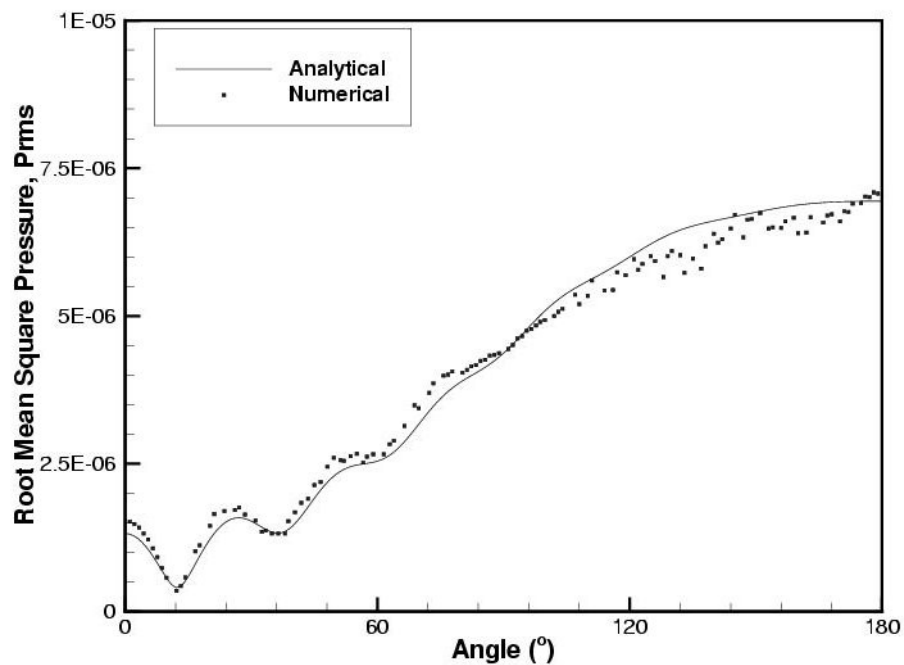
Figure 4. Case 1, P_{rms} distribution on surface of cylinder 2
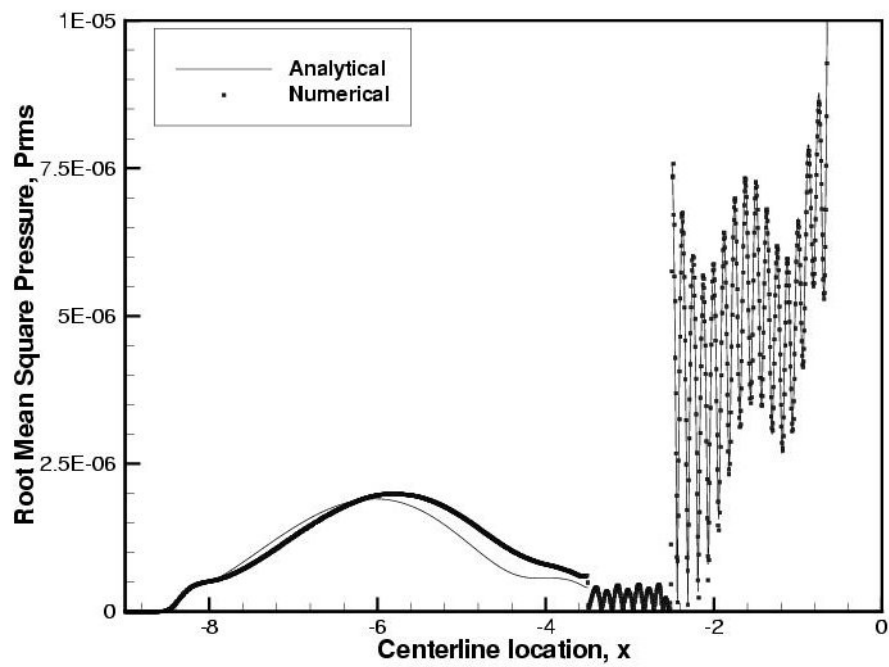
Figure 5. Case 2, centerline P_{rms} distribution for x = -8 to x = 0
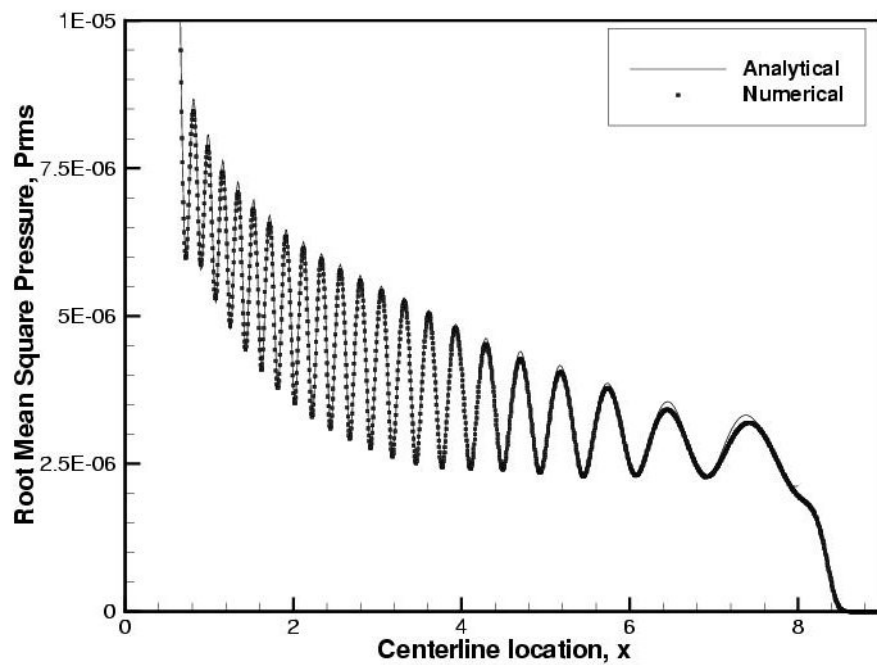
Figure 6. Case 2, centerline P_{rms} distribution for x = 0 to x = 8
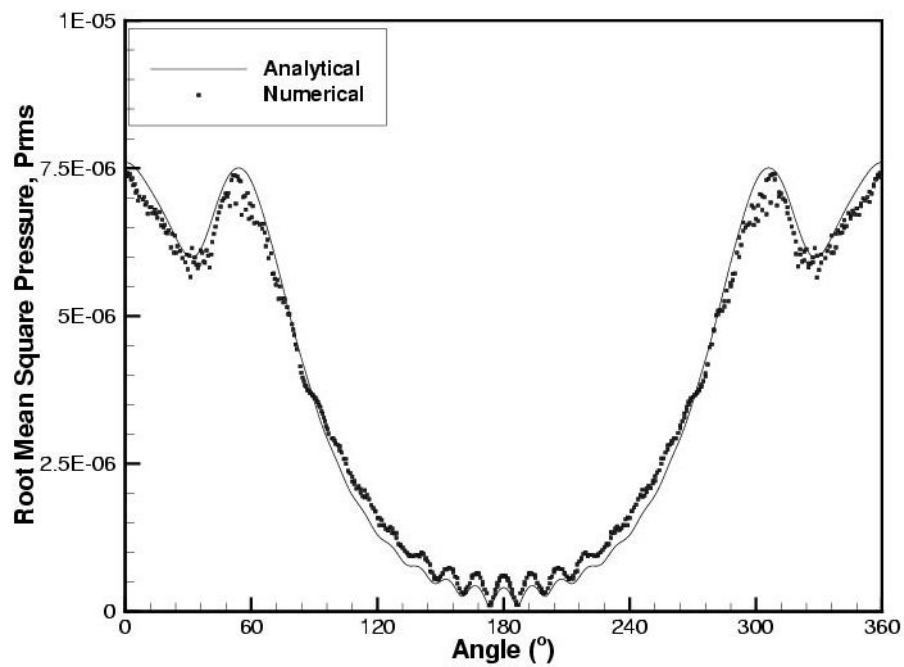
Figure 7. Case 2, P_{rms} distribution on surface of cylinder 1
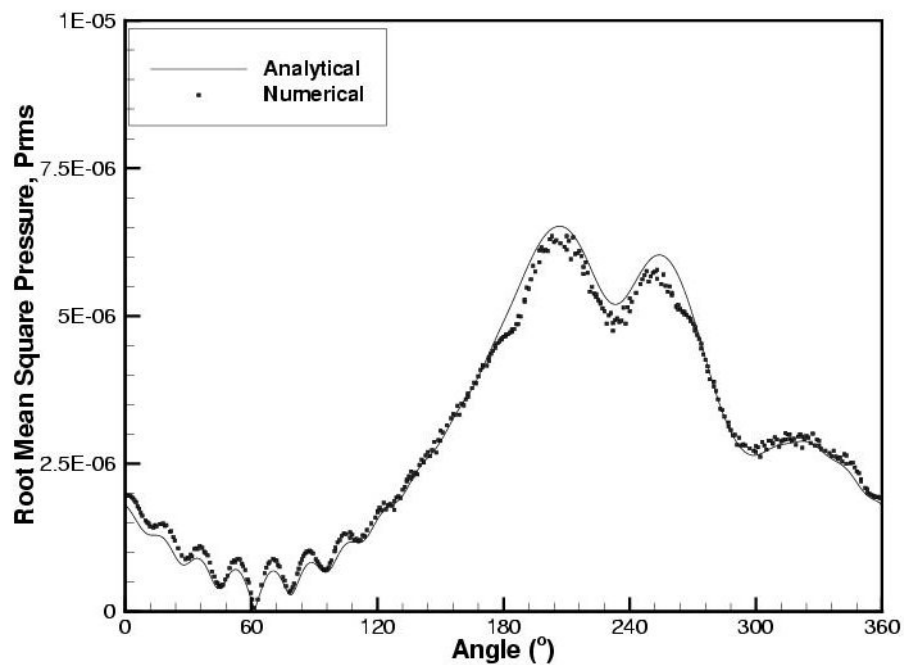
Figure 8. Case 2, P_{rms} distribution on surface of cylinder 2

HIGH ORDER SPECTRAL VOLUME METHOD
FOR CATEGORY 1, PROBLEM 1 AND CATEGORY 2 PROBLEMS

Z.J. Wang
2555 Engineering Building, Michigan State University
East Lansing, MI 48824, U.S.A.

ABSTRACT

A recently developed high-order finite volume (FV) method named the spectral volume (SV) method is employed to solve two categories of problems of the Fourth Computational Aeroacoustics (CAA) Workshop on Benchmark Problems: Problem 1 in Category 1 (C1P1) and Category 2 (C2) problems. In the SV method, a simplex grid element or cell is named a spectral volume, which is further partitioned into subcells called control volumes (CVs). The cell-averaged solutions on the CVs are the unknowns or degrees-of-freedom (DOFs). The DOFs are used to build high-order polynomials in the SV, which generate high-order updates for the unknowns. Therefore the resultant SV schemes are not optimized for any particular range of wave frequencies. In order to make a fair comparison with the finite difference method, the total number of DOFs is determined based on the requirement of an average 1 DOF per unit length for C1P1. SV schemes of as high as 100th order of accuracy are tested on C1P1. It was found that SV schemes of very high order are necessary for waves at 3.7 PPW (points per wave), and SV schemes showed a dissipative behavior for waves with less than 2 PPW. For C2 problems, a 4th order SV scheme was employed, and the numerical solutions agree well with the analytical solutions.

INTRODUCTION

A new high-order finite volume (FV) method named the spectral volume (SV) method has been developed recently for hyperbolic conservations laws, and successfully demonstrated for both scalar and system conservation laws in refs. 1-4. The SV method is a Godunov-type finite volume method (refs. 5 and 6), which has been under development for over three decades, and has become the-state-of-the-art for the numerical solution of hyperbolic conservation laws. The SV method is also related to the discontinuous Galerkin (DG) method in refs. 7 and 8. For a review of the literature on the Godunov-type FV and DG methods, refer to ref. 1, and the references therein. Like all Godunov-type finite volume method, the SV method has two key components. One is data reconstruction, and the other is the (approximate) Riemann solver, such as the Roe approximate Riemann solver in ref. 9. What distinguishes the SV method from the k-exact finite volume method (ref. 10) is in the data reconstruction. Instead of using a (large) stencil of neighboring cells to perform a high-order polynomial reconstruction, the unstructured grid cell - called a spectral volume - is partitioned into a "structured" set of sub-cells called control volumes (CVs), and cell-averages on these sub-cells are then the degrees-of-freedom (DOFs). These DOFs are used to reconstruct a high-order polynomial inside the macro-element, i.e., the SV. If all the spectral volumes are partitioned in a geometrically similar manner, the expression for the reconstruction in terms of the DOFs is universal for any simplex regardless of their shapes. This is because all simplex can be mapped into a standard simplex using a linear transformation. After the reconstruction step, the DOFs are updated to high-order accuracy using the usual finite volume method. Numerical tests with conservation laws in both 1D and 2D have verified that the SV method is indeed highly accurate, conservative, and geometrically flexible (refs. 1-4).

In this study, the SV method is evaluated for two categories of problems in the Fourth Computational Aeroacoustics (CAA) Workshop on Benchmark Problems. As pointed out by Tam in ref. 11, acoustic waves have their own characteristics which make their computation unique and challenging. Acoustic waves are inherently unsteady. Their amplitudes are several orders smaller than the magnitudes of the mean flow and their frequencies are generally very high and broad ranging. Computational methods with *high order accuracy* are required to capture the acoustic portion of the solution. The SV method has been developed to achieve high-order accuracy for unstructured grids capable of handling complex configurations in a very flexible manner.

The paper is organized as follows. In the next section, the basic formulation of the SV method is reviewed. In Section 3, solutions for the benchmark problems are presented. Conclusions are summarized in Section 4.

SPECTRAL (FINITE) VOLUME METHOD

Governing Equations

The governing equation for C1P1 is the linear wave equation with unit wave speed, i.e.,

$$\frac{\partial Q}{\partial t} + \frac{\partial Q}{\partial x} = 0 . \tag{1}$$

The governing equation for C2 problems is the unsteady linearized Euler equations with a time dependent source term in the energy equation. In the present study, the non-linear Euler equations are employed, which can be expressed as

$$\frac{\partial Q}{\partial t} + \frac{\partial E}{\partial x} + \frac{\partial F}{\partial y} = S , \tag{2a}$$

where Q is the vector of conserved variables, E and F are the inviscid flux vectors in x and y directions respectively:

$$Q = \begin{Bmatrix} \rho \\ \rho u \\ \rho v \\ E \end{Bmatrix}, \quad E = \begin{Bmatrix} \rho u \\ \rho u^2 + p \\ \rho uv \\ u(E+p) \end{Bmatrix}, \quad F = \begin{Bmatrix} \rho v \\ \rho uv \\ \rho v^2 + p \\ v(E+p) \end{Bmatrix}, \quad S = \begin{Bmatrix} 0 \\ 0 \\ 0 \\ e^{-\ln 2 \frac{x^2+y^2}{0.2^2}} \sin(\omega t) \end{Bmatrix}. \tag{2b}$$

In (2b) ρ is the density, u and v are the velocity components in x and y directions, p is the pressure, and E is the total energy. The pressure is related to the total energy by

$$E = \frac{p}{\gamma - 1} + \frac{1}{2}\rho(u^2 + v^2) , \tag{2c}$$

with a constant ratio of specific heats γ. The Euler equations (2) are hyperbolic since the Jacobian matrix of the flux vector in direction $\boldsymbol{n} = (n_x, n_y)$

$$B = n_x \frac{\partial E}{\partial Q} + n_y \frac{\partial F}{\partial Q} \tag{3}$$

has all real eigenvalues and a complete set of eigenvectors. In fact, B has 4 real eigenvalues $\lambda_{1,2} = v_n$, $\lambda_3 = v_n + c$, $\lambda_4 = v_n - c$, and a complete set of (right column) eigenvectors $\{r_1, r_2, r_3, r_4\}$, where $v_n = un_x + vn_y$ and c is the speed of sound. Let R be the matrix composed of these right eigenvectors, then the Jacobian matrix B can be diagonalized as

$$R^{-1}BR = \Lambda , \tag{4}$$

where Λ is the diagonal matrix containing the eigenvalues, i.e., $\Lambda = diag(v_n, v_n, v_n + c, v_n - c)$.

In the following presentation, both the 1D and 2D numerical algorithms are treated in the same manner. We therefore recast the governing equations uniformly as

$$\frac{\partial Q}{\partial t} + \nabla \bullet \mathbf{f} = S , \tag{5}$$

where $\mathbf{f} = (Q)$ in 1D and $\mathbf{f} = (E, F)$ in 2D, and S is the source vector.

Numerical Method

Assume that the equations (5) are solved in the computational domain Ω subject to proper initial and boundary conditions. The domain is discretized into N non-overlapping simplex elements (i.e. line segments in 1D, and triangular elements in 2D) called spectral volumes (SVs)

$$\Omega = \bigcup_{i=1}^{N} S_i . \tag{6}$$

In order to support a degree k polynomial reconstruction within each SV, the SV is further partitioned into m subcells, with m given by

$$m = \begin{cases} k+1 & 1D \\ (k+1)(k+2)/2 & 2D \end{cases}.$$ (7)

Note that m is also the dimension of P^k, the space of polynomials of degree at most k. It has been found in earlier studies that the proper partitioning of a SV into CVs is critical to the accuracy and stability of the method. In 1D, the partition using the Gauss-Lobatto points defined over [-1, 1], i.e.,

$$x_{i,j+1/2} = -\cos\left(\frac{j\pi}{m}\right), \qquad j = 0, \cdots, m,$$ (8)

gives accurate and convergent results. In 2D, many candidate partitions are evaluated in ref. 2. It was found that the partitions for various k shown in Figure 1 perform satisfactorily. Denote the *j-th* CV of S_i by $C_{i,j}$. The cell-averaged conservative variable Q at time t in control volume $C_{i,j}$ is defined as

$$\overline{Q}_{i,j}(t) = \frac{\int_{C_{i,j}} Q(\mathbf{r},t)dV}{V_{i,j}}$$ (9)

where $V_{i,j}$ is the volume of $C_{i,j}$. In the SV method, the degrees-of-freedom (DOFs) or unknowns are the cell-averaged conservative variable Q at the subcells, or the CVs. Given the DOFs $\{\overline{Q}_{i,j}\}$, a polynomial $p_i \in P^k$ can be reconstructed such that it is a *(k+1)-th* order accurate approximation to the solution Q inside S_i:

$$p_i(\mathbf{r}) = Q(\mathbf{r}) + O(h^{k+1}), \quad \mathbf{r} \in S_i,$$ (10)

where h is the maximum edge length. This reconstruction can be solved analytically by satisfying the following conditions:

$$\frac{\int_{C_{i,j}} p_i(\mathbf{r})dV}{V_{i,j}} = \overline{Q}_{i,j}, \; j = 1, \dots, m.$$ (11)

The reconstruction can be more conveniently expressed as

$$p_i(\mathbf{r}) = \sum_{j=1}^{m} L_j(\mathbf{r})\overline{Q}_{i,j},$$ (12)

where $L_j(\mathbf{r}) \in P^k$ are the "shape" functions which satisfy

$$\frac{\int_{C_{i,j}} L_m(\mathbf{r})dV}{V_{i,j}} = \delta_{jm}.$$ (13)

The shape functions can be computed analytically using commercial software capable of performing symbolic manipulations. The shape function formulas are given in ref. 1 and ref. 4 for 1D and 2D reconstructions. The high-order reconstruction is then used to generate high-order updates for the DOFs using the usual FV method. Integrating (5) in $C_{i,j}$, we obtain the following integral equation for the DOFs

$$\frac{d\overline{Q}_{i,j}}{dt} + \frac{1}{V_{i,j}} \sum_{r=1}^{K} \int_{A_r} (\mathbf{f} \bullet \mathbf{n})dA = \frac{1}{V_{i,j}} \int_{C_{i,j}} SdV,$$ (14)

where K is the number of faces in $C_{i,j}$, and A_r represents the *r*-th face of $C_{i,j}$. The surface and volume integrals on each face are performed with Gauss quadrature formulas which are exact for degree k polynomials, i.e.

$$\int_{A_r} (\mathbf{f} \bullet \mathbf{n})dA \approx \sum_{q=1}^{J} w_{rq}\mathbf{f}(Q(\mathbf{r}_{rq})) \bullet \mathbf{n}_r A_r,$$ (15)

$$\int_{C_{i,j}} SdA \approx \sum_{q=1}^{M} w_q S(\mathbf{r}_q)V_{i,j},$$ (16)

where J and M are the number of quadrature points for surface and volume integrals respectively, w_{rq} and w_q are the Gauss quadrature weights, $\mathbf{r}_{rq}$ and $\mathbf{r}_q$ are the Gauss quadrature points. With the SV-wise polynomial reconstructions,

no continuity is required at the interfaces of the SVs. Therefore, the state variables are discontinuous across the *SV* boundaries. The flux vectors at the quadrature points $\mathbf{f}(Q(\mathbf{r}_{rq}))$ are not uniquely defined because two different solutions exist on the left and right sides of the interface. The saving grace for this difficulty is the well-known approximate Riemann solvers used in the Godunov-type finite volume method, i.e.,

$$\mathbf{f}(Q(\mathbf{r}_{rq}))\bullet \mathbf{n}_r \approx \hat{f}(Q_L(\mathbf{r}_{rq}),Q_R(\mathbf{r}_{rq}),\mathbf{n}_r), \tag{17}$$

where Q_L and Q_R are the vector of conserved variables just to the left and right of the interface. It is the Riemann solver which introduces the "upwinding", and dissipation into the SV method such that the SV method is not only high-order accurate, but also stable. In this paper, we employ the Roe approximate Riemann solver in ref. 9. The Roe flux can be computed from

$$\hat{f}(Q_L,Q_R,\mathbf{n}) = \frac{1}{2}\Big[f_n(Q_L) + f_n(Q_R) - \big|\overline{B}\big|(Q_R - Q_L)\Big], \tag{18}$$

where $\big|\overline{B}\big|$ is the dissipation matrix given by

$$\big|\overline{B}\big| = R\big|\overline{\Lambda}\big|R^{-1}. \tag{19}$$

Here $\big|\overline{\Lambda}\big|$ is the diagonal matrix composed of the absolute values of the eigenvalues of the Jacobian matrix evaluated at the so-called Roe-averages.

Finally substituting (15-17) into (14), we obtain the following semi-discrete SV scheme

$$\frac{d\overline{Q}_{i,j}}{dt} + \frac{1}{V_{i,j}}\sum_{r=1}^{K}\sum_{q=1}^{J}w_{rq}\hat{f}(Q_L(\mathbf{r}_{rq}),Q_R(\mathbf{r}_{rq}),\mathbf{n}_r)A_r = \sum_{q=1}^{M}w_q S(\mathbf{r}_q). \tag{20}$$

Time Integration

For time integration, we use the third-order TVD Runge-Kutta scheme from ref. 12. We first rewrite (21) in a concise ODE form

$$\frac{d\overline{Q}}{dt} = R_h(\overline{Q}). \tag{21}$$

Then the third-order TVD Runge-Kutta scheme can be expressed as:

$$\overline{Q}^{(1)} = \overline{Q}^n + \Delta t R_h(\overline{Q}^n);$$

$$\overline{Q}^{(2)} = \frac{3}{4}\overline{Q}^n + \frac{1}{4}[\overline{Q}^{(1)} + \Delta t R_h(\overline{Q}^{(1)})]; \tag{22}$$

$$\overline{Q}^{n+1} = \frac{1}{3}\overline{Q}^n + \frac{2}{3}[\overline{Q}^{(2)} + \Delta t R_h(\overline{Q}^{(2)})].$$

Other aspects of the method such as boundary conditions are included in refs. 1-4. No special boundary conditions are implemented for the CAA problems presented in this paper. For example, the combined use of a buffer zone, grid coarsening and a characteristic boundary condition serves as the far field non-reflection boundary condition.

NUMERICAL RESULTS

Category 1 Problem 1

The governing equation is the scalar wave equation with unit wave speed, i.e.,

$$\frac{\partial u}{\partial t} + \frac{\partial u}{\partial x} = 0.$$

with the following initial condition,

$$u_0 = [2 + \cos(\alpha x)]\exp\left[-(\ln 2)\left(\frac{x}{10}\right)^2\right], \text{ at } t = 0.$$

Two different frequencies $\alpha = 1.7$ and $\alpha = 4.6$ are considered. In the SV method, we employ an equivalent 1 DOF for each $\Delta x = 1$. At this grid resolution, the high frequency wave embedded in the initial condition only has about 3.7 and 1.9 points-per-wave (PPW). It is therefore a challenge for any numerical scheme to adequately resolve the high frequency wave. Several very high-order SV schemes were employed in the simulation. The time integration

was carried out using a four-stage fourth-order Runge-Kutta scheme. A constant time step of 0.125 was used for all cases. Taking a smaller time step gave essentially the same solution. The solutions at t = 400 and 800 for α = 1.7 are displayed in Figures 2 and 3. Note that very high-order SV schemes are required to resolve the wave. Even a 20th order SV scheme produced highly dissipated waves at t = 400 and 800. It is a no surprise that the 100th order SV scheme gave the best results. The solutions for α = 4.6 at t = 400 and 800 are shown in Figures 4 and 5. At this resolution, all the schemes showed a dissipative behavior and were stable.

Category 2 Problem 1 – Two Cylinder Wave Diffraction Problem

The scattering of a periodic acoustic source from two circular cylinders is considered. The acoustic source used in this case has a transient term expressed in the following form

$$S = e^{-\ln 2 \frac{x^2 + y^2}{0.2^2}} \sin(\omega t) f(t)$$

$$f(t) = \min\left(1, \left(\frac{t}{t_0}\right)^3\right).$$

The following parameters are chosen in the present study: $\varpi = 8\pi$, $t_0 = 4$. Since the configuration is symmetric, only the upper half of the physical domain is used in the computation. The computational mesh is displayed in Figure 6. The entire computational domain extends to r = 15. The grid within r = 9 is nearly uniform with a mesh size = 0.06. Since each triangle is further partitioned into 10 subcells, the grid has an equivalent points-per-wave (PPW) of about 13 (sqrt(10)*0.25/0.06). The mesh is coarsened from r = 9 to r = 15 with an expansion factor of 1.1 to serve as the buffer zone. A constant time step of 0.002 was used in the computation with a total of 20,000 time steps. The 4th order SV scheme was employed in the computation. The rms pressure is computed in the last 2000 time steps. The computed pressure field at a certain time is shown in Figure 7. Note that the outgoing waves are significantly damped in the buffer zone without visible reflections. The computed rms pressure along the center line is compared with the analytical solution from ref. 13 in Figure 8. The rms pressure on the two cylinder surfaces is also compared with the analytical solution in Figure 9. Note that the agreement between the computation and analytical solutions is good with the current grid resolution.

Category 2 Problem 2 – Three Cylinder Wave Diffraction Problem

The computational mesh is displayed in Figure 10. Again the mesh has an inner zone inside r = 9, and an outer buffer zone from r = 9 to r = 14. The inner zone has a grid size of 0.06. The mesh is coarsened from r = 9 to r = 14 with an expansion factor of 1.1 to serve as the buffer zone. A constant time step of 0.002 was used in the computation with a total of 20,000 time steps. The 4th order SV scheme was employed in the computation. The rms pressure is computed in the last 2000 time steps. The computed pressure field is shown in Figure 11. The computed rms pressure along the center line is compared with the analytical solution in Figure 12. The rms pressure on the two cylinder surfaces is also compared with the analytical solution in Figure 13. Note that there is good agreement between the computation and analytical solutions.

4. CONCLUSIONS

The SV method has been tested on two categories of benchmark problems in the Fourth Computational Aeroacoustics (CAA) Workshop on Benchmark Problems: Problem 1 in Category 1 (C1P1) and Category 2 (C2) problems. For C1P1, it is shown that very high order SV schemes are needed to resolve waves at 3.7 PPW. For waves with less than 2 PPW, the SV schemes all showed a dissipative behavior, damping all unresolved waves in the process. For the Category 2 problems, the 4th SV scheme was capable of producing reasonable results with a grid resolution of about 13 PPW. The advantage of the SV method lies in its capability of handling complex geometries in a very flexible manner. The problems can all be set up in minutes.

ACKNOWLEDGEMENTS

REFERENCES

1. Wang, Z.J.: Spectral (Finite) Volume Method for Conservation Laws on Unstructured Grids: Basic Formulation, *J. Computational Physics*, Vol. 178, pp. 210-251, 2002.
2. Wang, Z.J. and Liu, Y.: Spectral (Finite) Volume Method for Conservation Laws on Unstructured Grids II: Extension to Two-Dimensional Scalar Equation*, J. Computational Physics,* Vol. 179, pp. 665-697, 2002.
3. Wang Z.J. and Liu, Y.: Spectral (Finite) Volume Method for Conservation Laws on Unstructured Grids III: Extension to One-Dimensional Systems, *Journal of Scientific Computing*, Vol. 20, No. 1, pp. 137-157, 2004.
4. Wang, Z.J., Zhang, L. and Liu, Y.: Spectral (Finite) Volume Method for Conservation Laws on Unstructured Grids IV: Extension to Two-Dimensional Euler Equations, to appear in, *J. Computational Physics*.
5. Godunov, S.K.: A finite-difference method for the numerical computation of discontinuous solutions of the equations of fluid dynamics, *Mat. Sb.* **47**, 271, 1959.
6. Van Leer, B.: Towards the ultimate conservative difference scheme V. a second order sequel to Godunov's method, *J. Comput. Phys*. **32,** 101-136 (1979).
7. Cockburn, B., Hou S. and Shu, C.-W.: TVB Runge-Kutta local projection discontinuous Galerkin finite element method for conservation laws IV: the multidimensional case, *Mathematics of Computation* **54**, 545-581 (1990).
8. Bassi, F. and Rebay, S.: High-order accurate discontinuous finite element solution of the 2D Euler equations, *J. Comput. Phys*. **138**, 251-285 (1997).
9. Roe, P.L.: Approximate Riemann solvers, parameter vectors, and difference schemes, *J. Comput. Phys.* **43** 357-372 (1981).
10. Barth, T.J. and Frederickson, P.O.: High-order solution of the Euler equations on unstructured grids using quadratic reconstruction, AIAA Paper No. 90-0013, 1990.
11. Tam, C.K.W.: Computational Aeroacoustics: Issues and Methods, AIAA Journal, Vol. 33, No. 10, Oct. 1995, pp. 1788-1796.
12. Shu, C.-W.: Total-Variation-Diminishing time discretizations, *SIAM Journal on Scientific and Statistical Computing* **9**, 1073-1084 (1988).
13. Sherer, S. and Visbal, M.: Computational study of acoustic scattering from multiple bodies using a high-order overset grid approach, AIAA Paper No. 2003-3203.
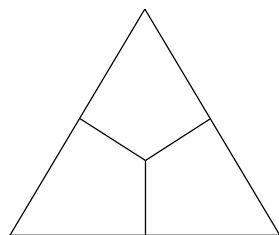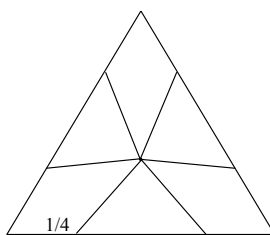
(a) Linear SV **(b) Quadratic SV** **(c) Cubic SV**
Figure 1. Spectral volumes of various degrees
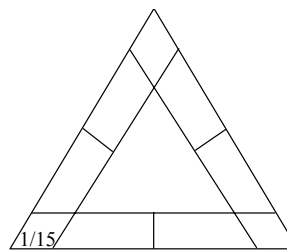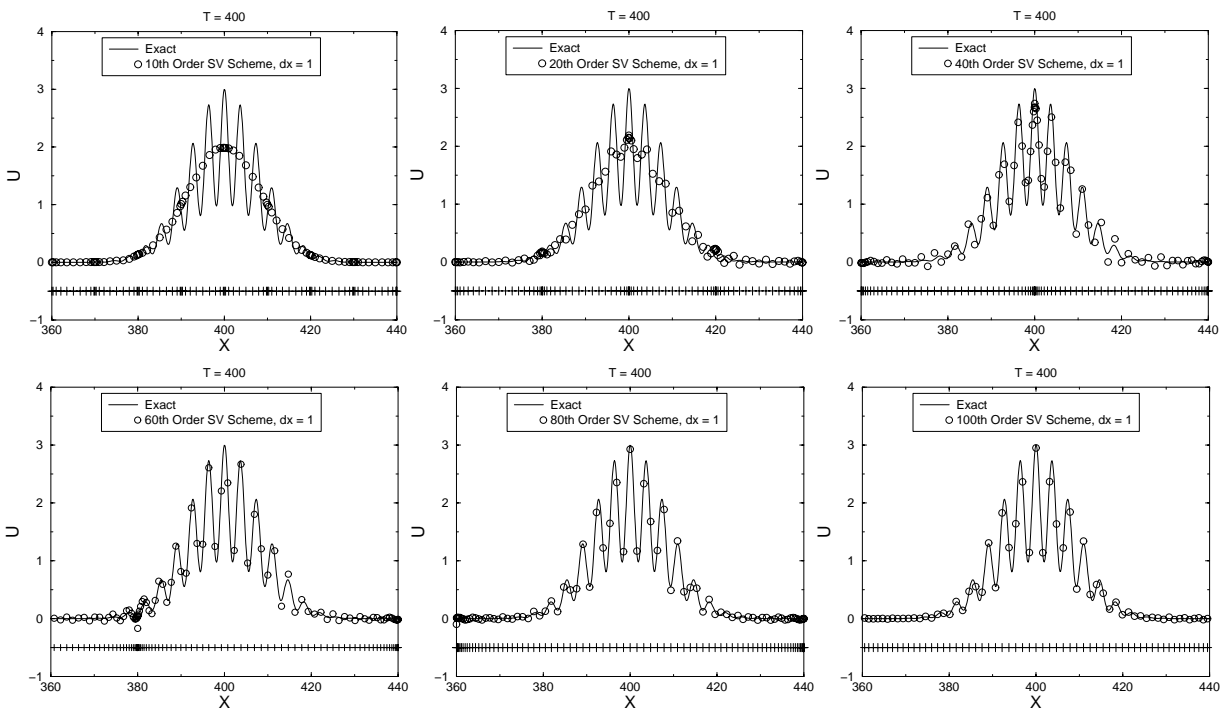
Figure 2. Comparison of numerical and exact solutions at t = 400 (α = 1.7).
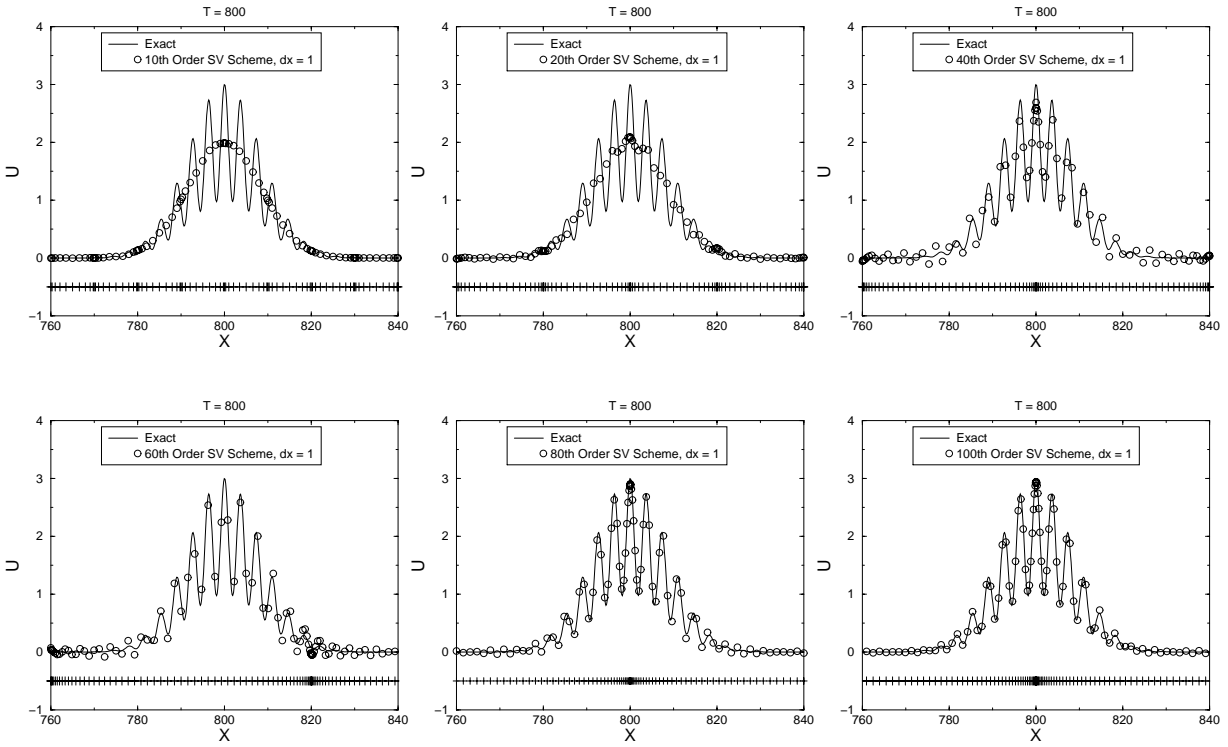
Figure 3. Comparison of numerical and exact solutions at t = 800 (α = 1.7).
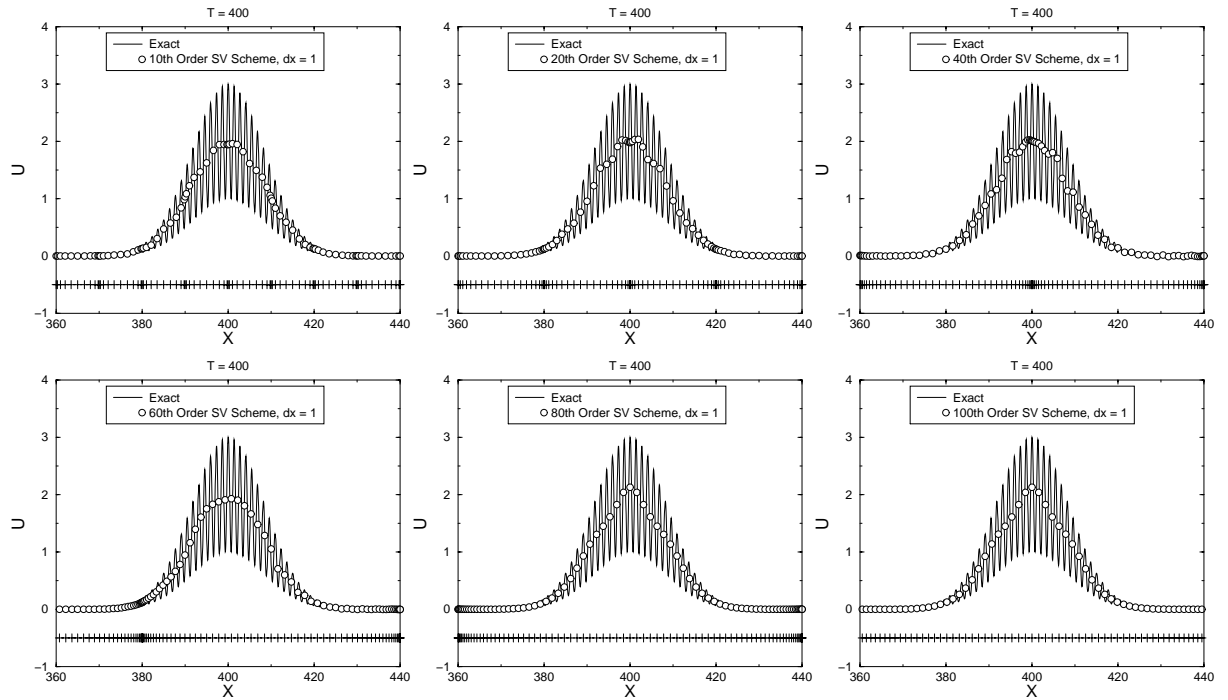
Figure 4. Comparison of numerical and exact solutions at t = 400 (α = 4.6).
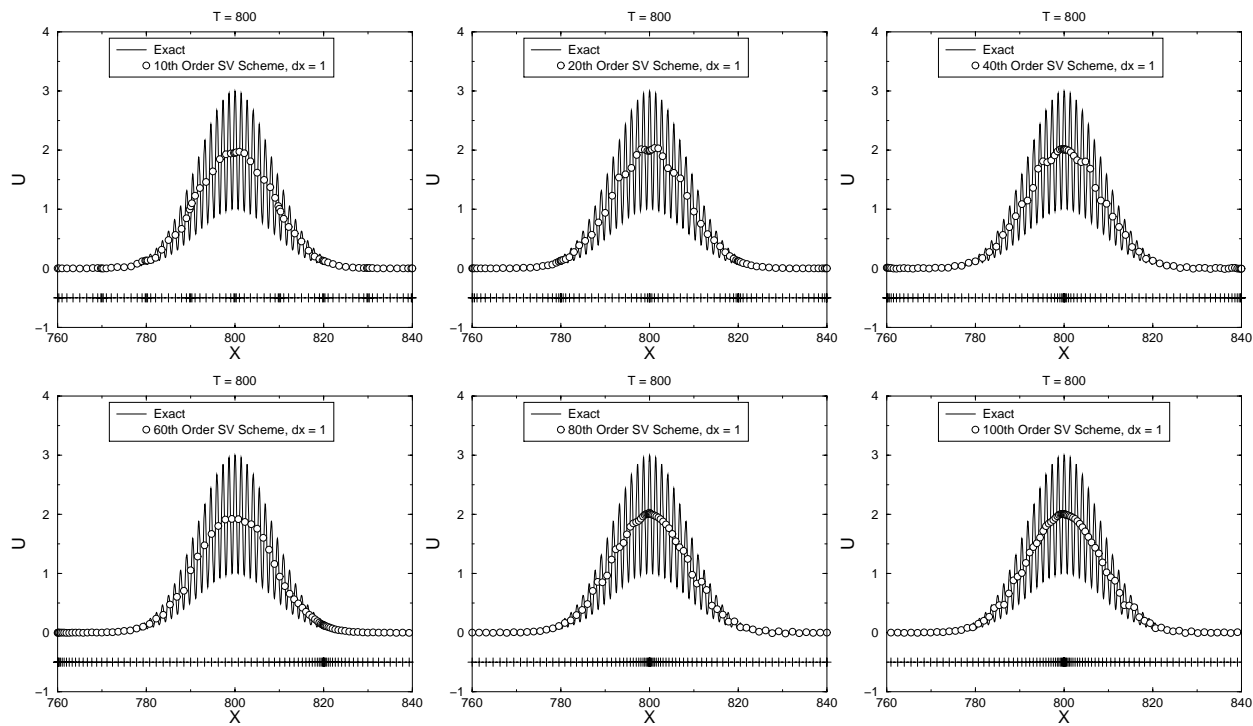
Figure 5. Comparison of numerical and exact solutions at t = 800 (α = 4.6).
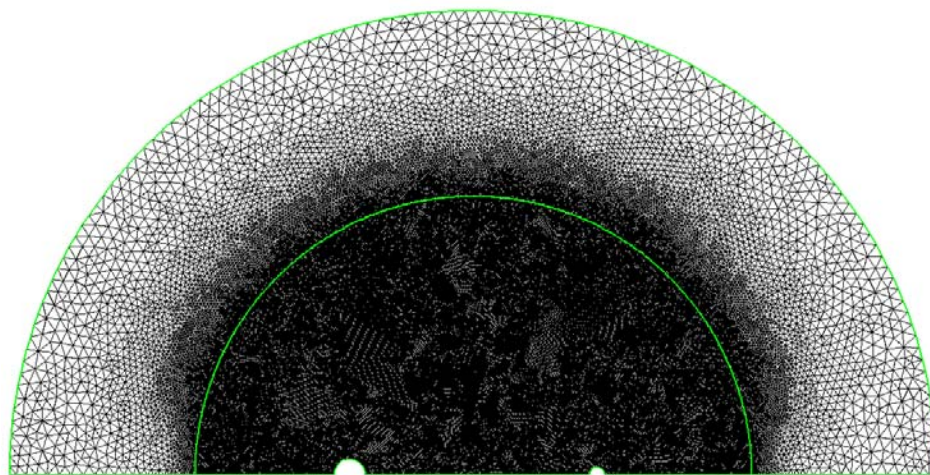
Figure 6. Computational grid for the two-cylinder diffraction problem
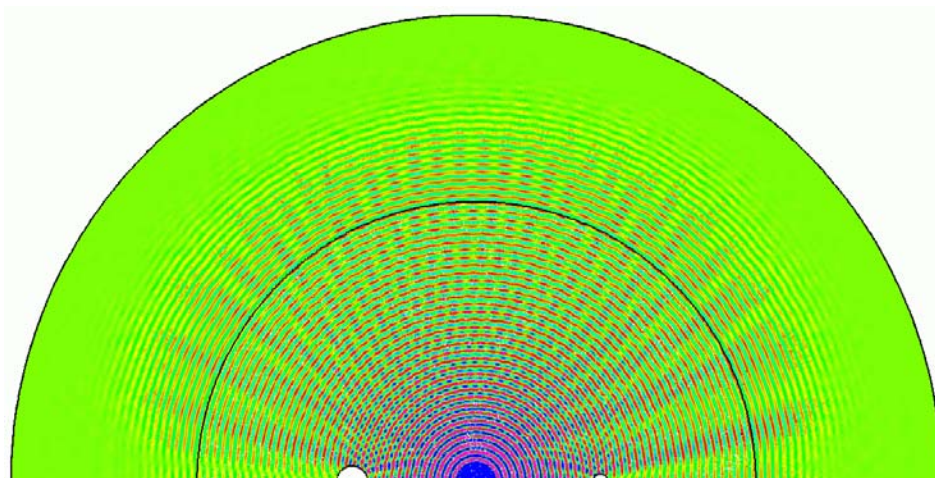
Figure 7. Pressure distribution computed with the 4th order SV scheme
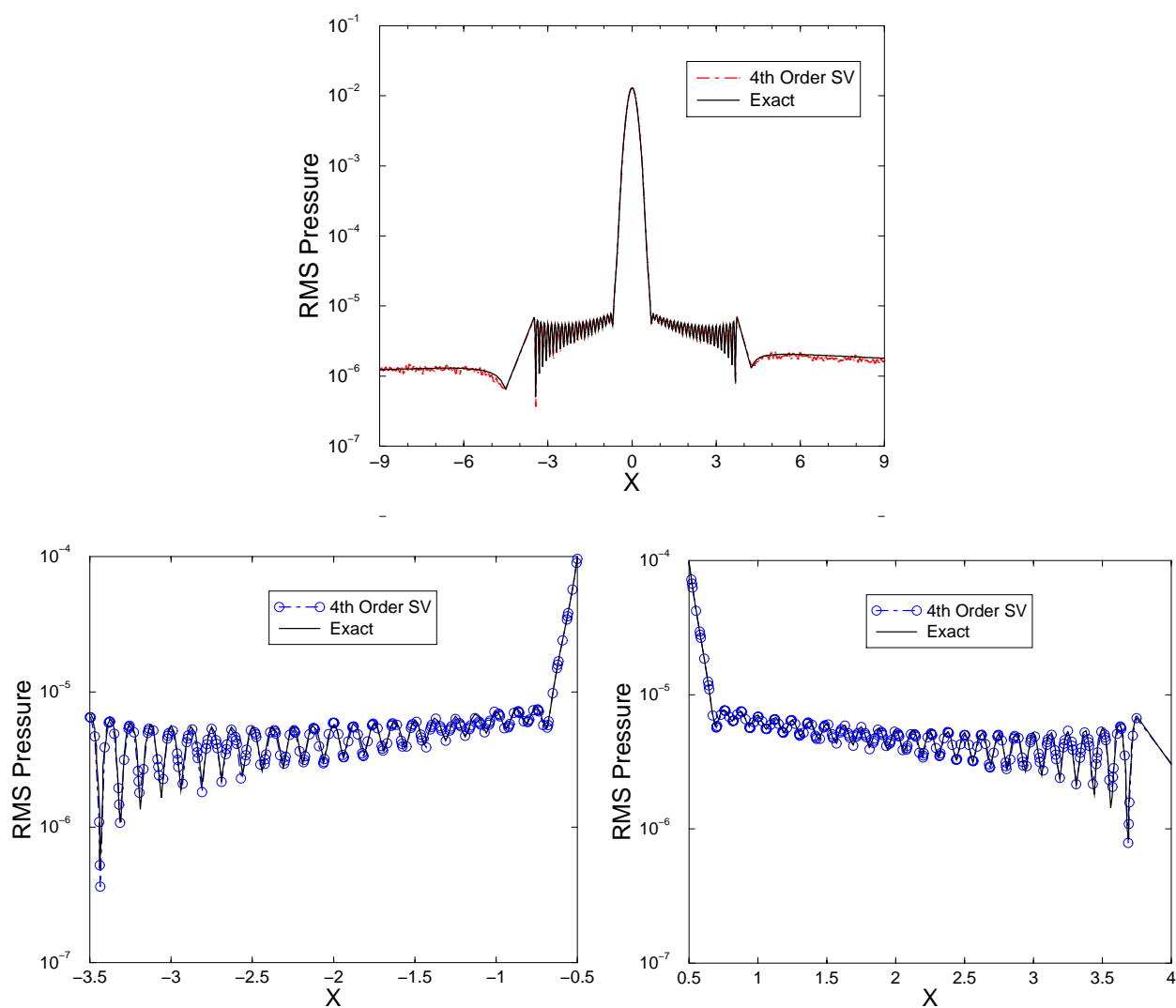
Figure 8. Comparison of the computational and analytical RMS pressure along the center line

(a) Left cylinder　　　　　　　　　　**(b) Right cylinder**
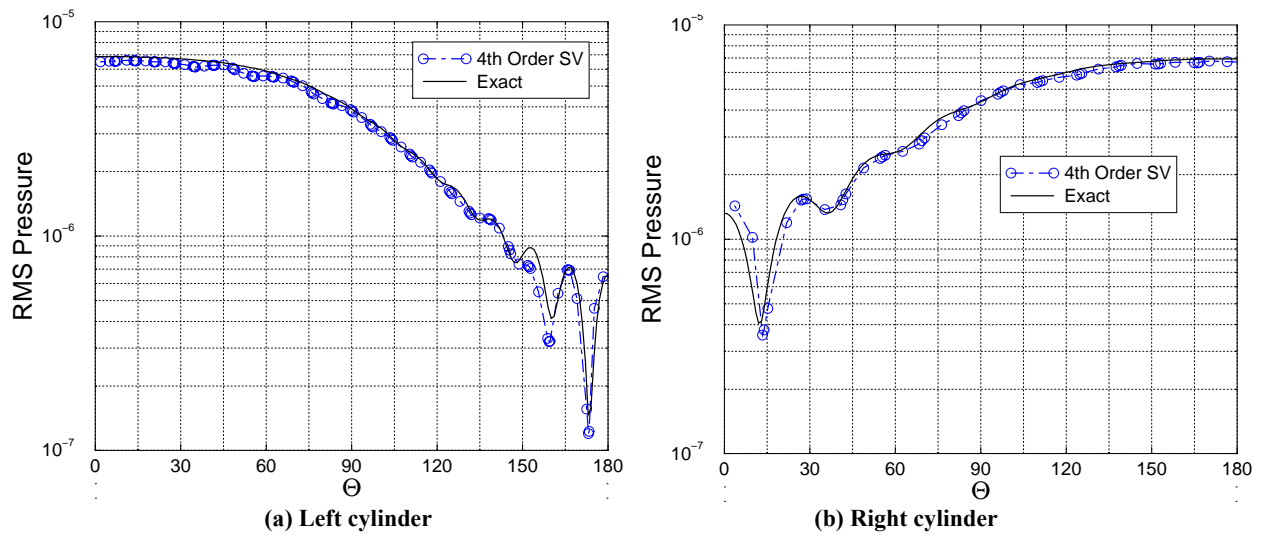
Figure 9. Comparison of the computational and analytical RMS pressure along the two cylinders
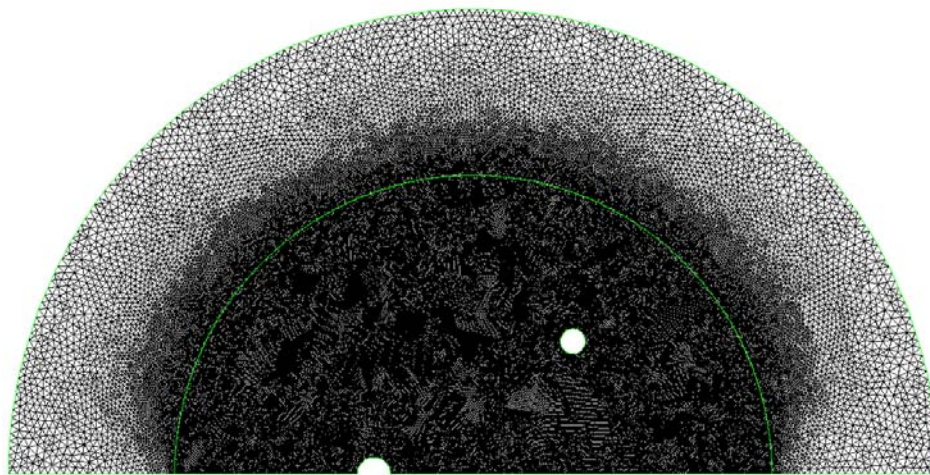
Figure 10. Computational grid for the three-cylinder diffraction problem

Figure 11. Pressure distribution computed with the 4th order SV scheme
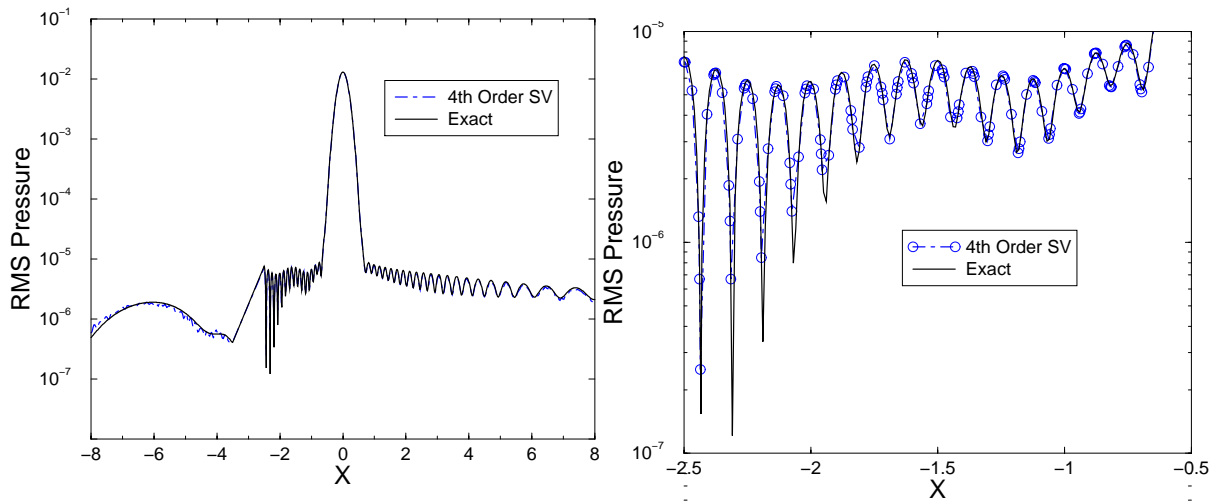
Figure 12. Comparison of the computational and analytical RMS pressure along the center line
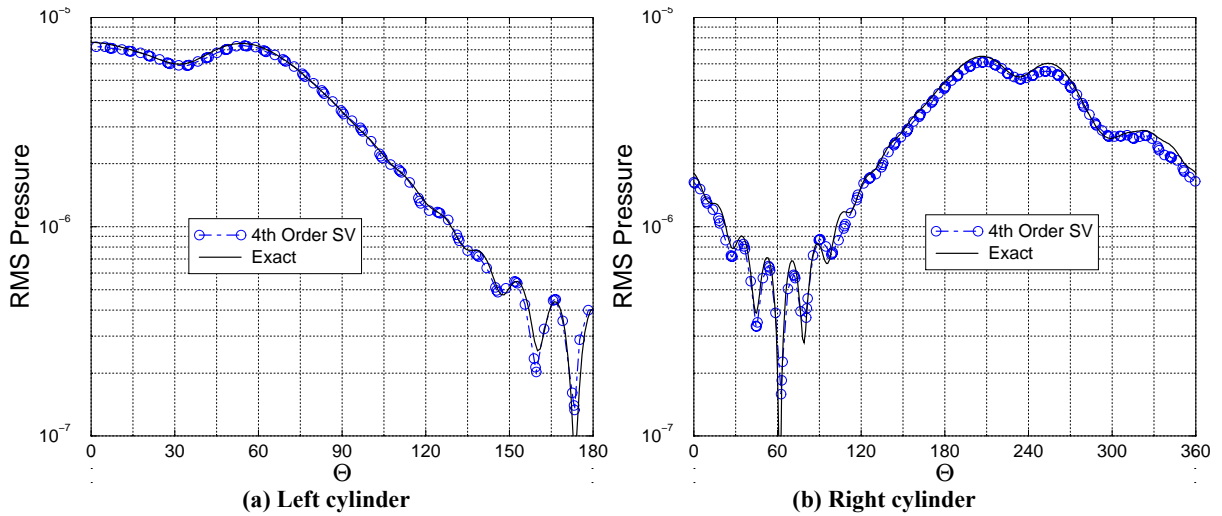
(a) Left cylinder
(b) Right cylinder
Figure 13. Comparison of the computational and analytical RMS pressure along the two cylinders

ACCURACY OF SUPERGRID BOUNDARY CONDITIONS FOR INCIDENT DISTURBANCES WITH A RANGE OF INCIDENCE ANGLES IN UNIFORM AND SHEARED FLOWS

Tim Colonius

California Institute of Technology, Pasadena, CA 91125; colonius@caltech.edu

ABSTRACT

We examine the accuracy of supergrid boundary conditions (BC) [6] for problems involving vortical, entropic, and acoustic waves propagating at a range of incidence angles in uniform and sheared flows (Benchmark Problem Category 1, Problem 3). For uniform flow, we compare the accuracy with high-order-accurate Fourier/Laplace BC [15]. Such BC can be extended to arbitrarily order of accuracy, but lead to large errors and instabilities in the presence of shear. The supergrid boundary condition is a buffer layer technique wherein the equations of motion are modified in a region near the boundary in order to attenuate disturbances. The modified equations are developed by analogy with subgrid-scale turbulence models, except that the role of small and large scales is interchanged. For uniform flow, both methods studied can give arbitrarily small errors, but the Fourier/Laplace BC are much more efficient than the supergrid BC. However, the supergrid BC produces similar results in the presence of shear as well as in cases involving sonic points. For the benchmark problem, relatively large buffers were needed to achieve acceptably small errors. The cause of the inefficiency is the incidence of faint, repeated reflections from distant image sources from the initial condition. In cases where such waves are not an important feature (many relevant CAA problems), the supergrid BC produces good results with relatively small buffers.

INTRODUCTION

Artificial BC for compressible flow, and specifically the linearized Euler equations, have been developed for many years. For linear disturbances to a uniform basic flow, a variety of adequate techniques have been developed and tested. The reader is referred to several reviews [8, 17, 9, 4] for detailed derivations and performance comparisons. The techniques may be broadly classified into (a) techniques that are based on Fourier/Laplace decomposition of the solution at the artificial boundary, (b) techniques that are based on asymptotic solutions for large distance from any source of waves, and (c) buffer layer methods where the equations of motion are modified to absorb outgoing waves.

The Fourier/Laplace techniques include local BC based on rational function approximations (Padé) to the non-local exact nonreflecting BC. For these BC stability has been analyzed in both the continuous [15, 11] and discrete [15] cases. Such BC may be computed to arbitrarily high accuracy. The additional computational cost of the BC is low, requiring $n + 1$ "ghost points" at any artificial boundary in order to achieve nth-order accuracy. The specific technique of Rowley and Colonius [15] is used to solve Part 1 of the present benchmark problem below.

Buffer layer techniques include the so-called Perfectly Matched Layer (PML) [3, 12, 1, 2, 13, 10]. Like the Fourier/Laplace conditions, well-posed PML techniques can be developed for which arbitrarily good accuracy can be obtained by taking progressively larger buffer regions. The computational cost of PML is relatively high compared to Fourier/Laplace conditions; in tests involving propagation of a cylindrical acoustic pulse, Colonius and Ran [6] show that a buffer width of 30 grid points was required to match the accuracy of the Fourier/Laplace BC with $n = 2$ (and hence 3 ghost points).

As discussed in Colonius [4], few BC developed for the uniform flow case are suitable for non-uniform (e.g. sheared) flows, or indeed the general nonlinear case. Only the lowest-order Fourier/Laplace conditions (which are equivalent to one-dimensional characteristics) may be appropriately generalized to nonuniform flows; higher-order conditions and PML have been found to lead to instabilities. An exception is Hagstrom's [10] formulation of PML specifically accounting for shear; his application of this latter technique to the present benchmark problem may be found elsewhere in this volume.

On the other hand, a variety of simple buffer layers have been developed for nonuniform and/or nonlinear flow (see the review [4]). These primarily rely on ad hoc (yet effective) ways to dissipate outgoing waves before they interact with an artificial boundary. Because the disturbance amplitudes are vastly reduced, relatively crude (usually one-dimensional characteristic) BC can then be employed. Some specific techniques commonly used in CAA are grid stretching and filtering [5] and the combination of damping and artificially acceleration of disturbances to supersonic speed [7]. Like PML, all the ad hoc buffer models require several tunable parameters and blending functions that have only been optimized by trial and error.

We have recently proposed a buffer layer technique that exploits an analogy between sub-grid scale turbulence modeling and the imposition of artificial BC [6]. The turbulence modeling problem deals with scales that are too small to be represented on the discrete mesh, the artificial BC with scales that are too large. The model exploits this connection by developing windowing techniques that are the large scale analog of the filtering of small scales. The model is dubbed the supergrid model by analogy with LES subgrid models. The model has only two *tunable* parameters. One of these parameters, s, controls how rapidly the window function is applied. The range of appropriate values is small ($2 < s < 4$), and results have shown little sensitivity to the value of s within this range. In what follows we take $s = 4$. The second more important parameter is the extent (in either physical dimensions or computational nodes) of the buffer region. As with PML, the extent of the buffer controls the accuracy–with the obvious penalty of more computational work for larger buffers. Another interesting feature of the supergrid model is that it allows the infinite domain to be computed using periodic BC with Fourier spectral methods. In the present paper, we apply the supergrid model to the CAA benchmark problem described below.

THE BENCHMARK PROBLEM

Category 1, Problem 3 of the 4th Computational Aeroacoustics Workshop on Benchmark Problems highlights the accuracy and long time behavior of nonreflecting BC for problems involving linear propagation of vortical, entropic, and acoustic waves in uniform and sheared flows. The exact solutions exhibit a wide range of incidence angles to the artificial boundaries. In each case, the computational domain is defined by $(x_1, x_2) \in (-2, 2) \times (0, 1)$, with nonreflecting boundaries at $x_1 = \pm 2$. In the first part, the transverse boundaries are taken as periodic, while in the second and third parts the periodic BC are replaced by inviscid walls. The specified initial condition gives rise to vortical, entropic, and acoustic disturbances with a variety of length scales (compactly supported on the domain) and involves acoustic waves that are incident on the boundary over the full range of angles from normal to glancing. Additional complications are (i) the presence of shear in Parts 2 and 3, and (ii) the presence of a sonic point in the base flow in Part 3.

NUMERICAL METHOD

The reader is referred to the problem description for Category 1, Problem 3 that appears elsewhere in this volume. The linearized equations, geometry, and initial conditions are discussed there. Implementations issues for the supergrid and Fourier/Laplace BC are discussed in [6] and [15], respectively. For the benchmark problems, we used different combinations of spatial discretization schemes depending on which artificial BC were chosen and the particular problem setup for Parts 1, 2 and 3. The various combinations and other parameters associated with the numerical solutions are presented in Table 1. When the supergrid BC are used for the nonreflecting boundaries, and when the transverse boundaries are periodic, then a periodic Fourier pseudo-spectral discretization is used. Compact sixth-order finite difference scheme [14] is used in all other cases. In all cases, the equations are integrated in time with the fourth-order Runge-Kutta scheme, using a time step consistent with a CFL number of 0.7.

RESULTS

The numerical solutions were compared against the exact solutions provided by Tom Hagstrom (see the discussion elsewhere in this volume). For Part 1, the exact solution could be found analytically, and was evaluated on the numerical mesh; for Parts 2 and 3, a numerical solution on a fine mesh on a much longer domain was used for comparison. In both cases, the specified metric to evaluate the performance of the BC was the L2 error in the solution on a discrete mesh of size 129 x 33 evaluated at the discrete times

	Part 1	**Part 2**	**Part 3**
	Supergrid BC		
Discretization in x	Fouier/pseudo-spectral	Fouier/pseudo-spectral	Fouier/pseudo-spectral
Discretization in y	Fourier/pseudo-spectral	6th-order compact finite difference	6th-order compact finite difference
N_x x N_y	128 x 32	512 x 33	512 x 33
Supergrid parameter, s	4	4	4
Buffer sizes used (in number of grid points / physical length)	16 / ½ 32 / 1 64 / 2 128 / 4	128 / 1 256 / 2 768 / 6	128 / 1 256 / 2
	Fourier/Laplace BC		
Discretization in x	6th-order compact finite difference	---	---
Discretization in y	Fourier/pseudo-spectral	---	---
Nx x Ny	128 x 32	---	---
Order of Pade rational function approx. in BC	(0,0),(4,4), and (8,8)	---	---

Table 1: Features of the numerical solution and BC used for Parts 1, 2, and 3.

$t = 1, 2, 4, 8, 12, \cdots, 64$. Time is normalized by the computational domain size in the normal direction and the speed of sound. Since the computational domain extends to ± 2 in the direction in which nonreflecting BC are applied, a normalized time of 4 corresponds roughly with the residence time of an acoustic wave in the domain. The error at each time was normalized by the L2 norm of the solution at the same time. The error was tabulated individually for all flow variables: density, ρ, velocities u_1 and u_2, and pressure, p. For brevity, we examine here only the errors in the u_1 velocity. The other quantities displayed error levels consistent with u_1 in all cases and at all times.

In Figure 1, errors for Part 1 are presented. Because the base flow for Part 1 is uniform, high-order-accurate Fourier/Laplace BC can be used. We compare these to the more general supergrid BC. For reference, the error for a one-dimensional characteristic BC (e.g. a linearized Thompson BC[16]) is also shown. This provides a reasonable reference since it is commonly used in practical compressible flow and CAA computations. At very early times, the error level for characteristic BC becomes unacceptably high, reaching 10% by about $t = 4$. Using the higher-order Fourier/Laplace BC vastly reduces the error at relatively short times. For example the highest-order BC used (the (8,8) Padé rational function approximation) gives less than 1% error until $t = 8$. However, the error at $t = 64$ reaches about 50% by $t = 64$. Still higher-order conditions could be used to reduce these errors, but achieving significantly smaller errrors at long time will require *very* high-order schemes to be used.
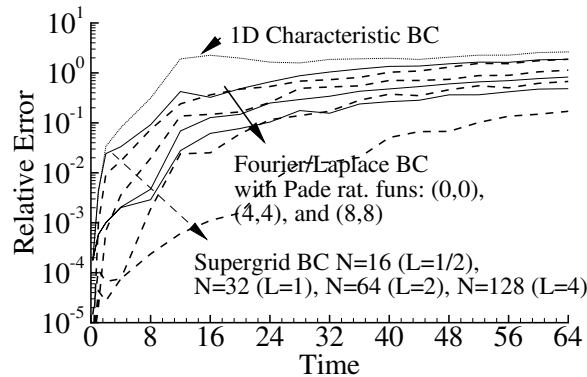
Figure 1: L2 error relative to the instantaneous L2 norm of the solution with different BC for Part 1. Fourier/Laplace BC (———); Supergrid BC (– – – –); 1D characteristic BC (········).

The supergrid model performs well provided that sufficiently large buffers are used. A buffer size of 64 grid points is required to (roughly) match the performance of the (4,4) Padé BC, and a buffer of size 128 is required to keep the error less than 10% until $t = 64$. Clearly, for disturbances to uniform states the high-order Fourier/Laplace BC are a much better choice than the supergrid BC. However, as noted above, the Fourier/Laplace BC cannot be used in nonuniform flows (or in nonlinear computations).

As mentioned above, the present benchmark problems provide a very stringent test of the efficacy of the BC. There are repeated reflections of the initial conditions from the transverse, periodic boundaries. For long times, these waves are produced by far away image sources and the angles of incidence to the nonreflecting boundary becomes nearly glancing; BC typically perform most poorly in that case. The amplitude of the outgoing acoustic waves decays slowly like $t^{-1/2}$. Errors made at earlier times can swamp the computation at later times.

In many problems of practical relevance to CAA, long-time errors associated with distant image sources will not be an issue. Such problems would include external flows with turbulence and sound generation, such as turbulent jets. For internal flow problems (such as in turbomachinery), *there are* repeated internal reflections that are somewhat analogous to the present benchmark problem. But in those flows one typically also has continuous generation of acoustic and vortical disturbances within the domain. In that case the amplitude of the outgoing acoustic waves is more nearly constant in time. Thus for typical CAA problems, an equally useful metric with which to assess the accuracy of the BC is the error at each time normalized by the L2 norm of the initial condition. This then gives the relative error for the reflection of the initial (and strongest) disturbances. In Figure 2, we display the error in this way, and note that for even the 16 point supergrid buffer, the error is less than 0.5%.

In Parts 2 and 3 of the benchmark problem, we add a uniform shear to the base flow, and replace the transverse periodic BC with wall BC. The streamwise velocity varies linearly from 0 to $M = 0.9$ for Part 2, and from 0 to $M = 1.2$ for Part 3. As discussed above, we can no longer apply the Fourier/Laplace BC that were used in the uniform flow case. Moreover, in Part 3, we have a sonic point along the nonreflecting boundary. This is traditionally a difficult feature to accommodate in nonreflecting BC, since at the point the number of characteristics entering the computational domain changes.

In Figure 3, we present the results using the supergrid BC for Parts 2 and 3. The error is once again normalized by the L2 norm of the instantaneous solution. Several issues regarding the results should be noted. First of all, the buffer sizes are significantly larger (in terms of numbers of grid points) compared to Part 1. However, the number of grid points within the physical point of the computational domain is much larger in these cases. In both cases, it was found that 512 points were required over $-2 < x_1 < 2$ in order to hold the discretization error associated with the numerical method well below the error associated with the BC. The required resolution can be attributed to the presence of a strong mean shear. The shear causes deformation of the vortical, entropic, and acoustic disturbances. In particular, convecting disturbances are
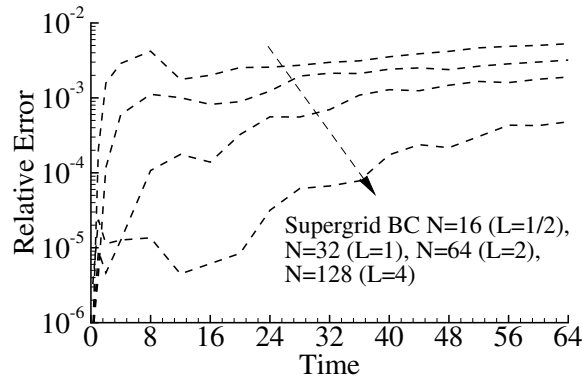
Figure 2: L2 error relative to the initial L2 norm of the solution for the supergrid BC, Part 1.
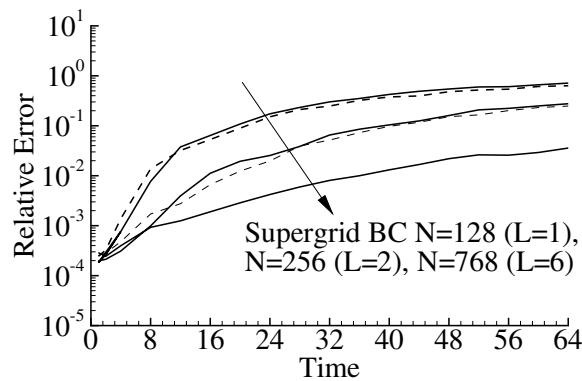
Figure 3: L2 error relative to the instantaneous L2 norm of the solution for the supergrid BC, Parts 2 and 3.

stretched into very thin sheets at an angle to the grid. The extent of the buffer regions, when compared in physical length units, are in fact comparable to those used in Part 1.

In both cases, the supergrid model yields stable results with errors comparable to those of Part 1. Apparently neither shear nor the presence of a sonic point have any significant impact on the accuracy of the BC. As in Part 1, very large buffers are needed to control the error at long times when incident waves produced by distant image sources impinge on the boundaries. The same caveat applies here–if one is interested in the largest reflection error produced by acoustic waves or vortical fluctuations of more nearly constant energy, than much smaller buffers yield acceptable results.

CONCLUSIONS

Regarding the particular benchmark problem studied here, the supergrid BC produced mixed results. Very large buffers were needed to reduce the error to acceptable levels for long times. On the other hand, the BC were robust, and yielded stable solutions regardless of the presence of nonuniform flow (shear) or sonic points along the boundary.

The present benchmark problem is a stringent test of the accuracy of nonreflecting BC. We argued that in most practical problems relevant to CAA, long time errors associated with faint, glancing acoustic waves produced by distant image sources would not be an important feature of the solution. In that case, one would be satisfied with sufficiently small reflection errors from incident waves (vortical, entropic or acoustic) that have nearly constant amplitude with time, and which are not dominated by disturbances glancing the

nonreflecting boundary. From this point of view, the results from the supergrid BC, even with relatively small buffers, are encouraging. Results from a previous study of the supergrid model [6] are also consistent with the present findings. It should be stressed that the supergrid BC is not based on any linearization of the equations near the computational boundary and can be used effectively in nonlinear computations.

REFERENCES

[1] S. Abarbanel and D. Gottlieb. A mathematical analysis of the PML method. *J. Comput. Phys.*, 134:357–363, 1997.

[2] S. Abarbanel, D. Gottlieb, and J. S. Hesthaven. Well-posed perfectly matched layers for advective acoustics. *J. Comput. Phys.*, 154(2):266–283, 1999.

[3] J. P. Berenger. A perfectly matched layer for the absorption of electromagnetic waves. *J. Comput. Phys.*, 114:185–200, 1994.

[4] T. Colonius. Modeling artificial boundary conditions for compressible flow. *To appear, Ann. Rev. Fluid Mech.*, 36, 2004.

[5] T. Colonius, S. K. Lele, and P. Moin. Boundary conditions for direct computation of aerodynamic sound generation. *AIAA J.*, 31(9):1574–1582, 1993.

[6] T. Colonius and H. Ran. A super-grid-scale model for simulating compressible flow on unbounded domains. *J. Comput. Phys.*, 182(1):191–212, 2002.

[7] J. B. Freund. Proposed inflow/outflow boundary condition for direct computation of aerodynamic sound. *AIAA J.*, 35(4):740–742, 1997.

[8] D. Givoli. Non-reflecting boundary conditions. *J. Comput. Phys.*, 94(1):1–29, 1991.

[9] T. Hagstrom. Radiation boundary conditions for the numerical simulation of waves. *Acta Numerica*, 8:47–106, 1999.

[10] T. Hagstrom. New results on absorbing layers and radiation boundary conditions. In M. Ainsworth, D. Duncan, P. Davies, and P. Martin, editors, *Computational Methods in Wave Propagation in Direct Scattering*. Springer, 2003. In press.

[11] T. Hagstrom and J. Goodrich. Accurate radiation boundary conditions for the linearized Euler equations in Cartesian domains. *SIAM J. Sci. Comput.*, 24(3):770–795, 2002.

[12] F. Q. Hu. On absorbing boundary conditions for linearized euler equations by a perfectly matched layer. *J. Comput. Phys.*, 129(1):201–219, 1996.

[13] F. Q. Hu. A stable, perfectly matched layer for linearized Euler equations in unsplit physical variables. *J. Comput. Phys.*, 173:455–480, 2001.

[14] S. K. Lele. Compact finite-difference schemes with spectral-like resolution. *J. Comput. Phys.*, 103(1):16–42, 1992.

[15] C. W. Rowley and T. Colonius. Discretely nonreflecting bounary conditions for linear hyperbolic systems. *J. Comput. Phys.*, 157:500–538, 2000.

[16] K. W. Thompson. Time-dependent boundary conditions for hyperbolic systems. *J. Comput. Phys.*, 68:1–24, 1987.

[17] S. V. Tsynkov. Numerical solution of problems on unbounded domains. A review. *Appl. Numer. Math*, 27(4):465–532, 1998.

CATEGORY 1 BENCHMARK SOLUTIONS USING FDL2DI

Nathan B. Edgar
Arkansas State University
College of Engineering
P.O. Box 1740
State University, AR 72467 USA
bedgar@astate.edu

Miguel R. Visbal
Air Force Research Laboratory
AFRL/VAAC, 2210 Eighth Street
Wright-Patterson AFB, OH 45458-7521 USA

ABSTRACT

Solutions to selected Category 1 methodology benchmark problems are investigated using computational techniques implemented into FDL2DI, a general purpose CFD code developed by the Air Force Research Laboratory's Computational Science branch. The code utilizes sixth-order compact difference operators for spatial discretization and a low-storage implementation of the classical fourth-order Runge-Kutta technique for temporal integration. An implicit high-order filter is available for the removal of high frequency signal content that may be unresolved by the computational grid or spurious wave content that may be generated in regions of sharp gradients, such as wall boundaries. The filter also plays a critical role in implementation of non-reflecting boundary conditions, which uses grid-stretching to transfer energy of the outgoing wave content into increasingly higher wavenumber spectrum, and then annihilating the poorly resolved wave content via the low pass filter. Solutions to the aliasing and y-periodic non-reflecting boundary condition problems of Category 1 are presented.

INTRODUCTION

The fidelity requirements of numerical techniques required for the successful numerical solution to the equations describing the propagation of acoustic signals are well documented [refs. 1-3]. For practical purposes, this generally requires the use of high-order spatial discretization schemes [refs. 4-5] and temporal integration techniques that have minimal effect on the resolution characteristics of the spatial scheme [refs. 6-7]. The lack of a viscous damping effect in the describing equations, the linearized Euler equations, means that any spurious high-frequency errors generated within the physical domain due to numerical boundary treatment will propagate quickly throughout the domain of interest, corrupting the solution. Therefore, a filtering or damping mechanism to remove poorly resolved wave content is seen as beneficial to the overall numerical algorithm [refs. 8-9].

In this work, a general purpose CFD code, FDL2DI, developed by the Air Force Research Laboratory's Computational Science branch will be used to solve Problem 1, aliasing, and Problem 3, non-reflecting boundary conditions, of Category 1 methodology problems. The code utilizes sixth-order compact finite difference stencils, a low-storage implementation of the classic fourth-order Runge-Kutta algorithm for temporal integration, and an implicit, high-order low-pass filter is available for removal of poorly resolved wave content [ref. 10].

CATEGORY 1, PROBLEM 1, ALIASING

Solution of the 1-D convective wave equation is sought with the following prescribed initial condition:

$$\frac{\partial u}{\partial t} + c\frac{\partial u}{\partial x} = 0 \qquad (1.a)$$

Initial condition:

$$u(x, t = 0) = [2 + \cos(\alpha x)] \exp\left(\frac{-\ln(2)x^2}{100}\right)$$ (1.b)

where, u is the wave amplitude and c is the wave speed of the signal. In the initial condition specification, the wavenumber, α, controls the high-frequency spatial component of the signal and is related to the wavelength, λ, by the relationship:

$$\alpha = \frac{2\pi}{\lambda}$$

The problem specification requests the numerical solution for wavenumber values of:

Case 1:　　　　$\alpha = 1.7$, $\lambda = 3.696$

Case 2:　　　　$\alpha = 4.6$, $\lambda = 1.366$

The use of a unit grid is specified, and the spatial distributions at t = 400 and t = 800 are requested.

Aliasing of Initial Condition on Unit Grid Mesh

The representation of the initial conditions for Case 1 and Case 2 are shown in Figure 1 for a unit grid as specified in the problem statement. Note that the high-frequency wavenumber component, $\alpha = 4.6$, is beyond the resolvable frequency spectrum ($-\pi < \alpha\Delta x < \pi$) and has folded back into the low-frequency spectrum at an apparent wavenumber of $\alpha = -1.6832$, due to the mesh coarseness.
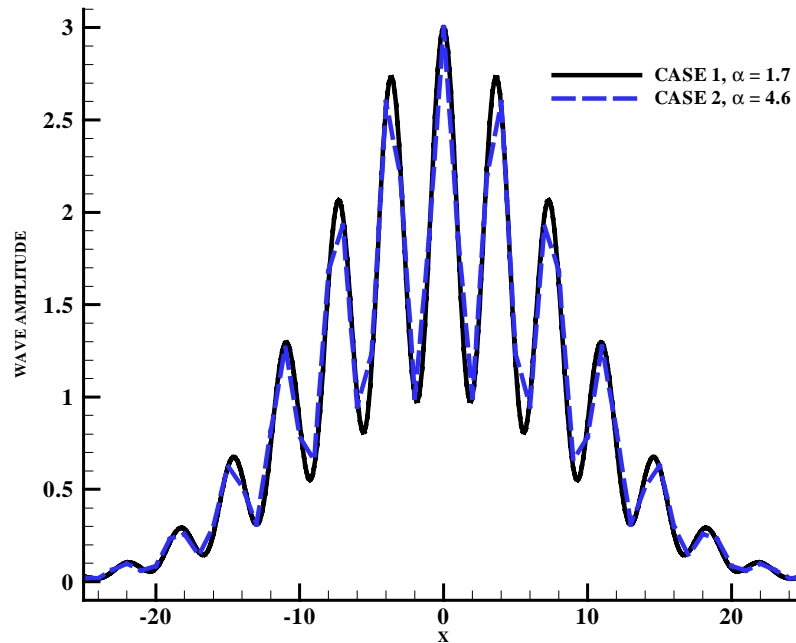
Figure 1. Initial condition comparison of Case 1 and Case 2 on unit grid.

Propagation characteristics of compact difference operator

The spatial discretization of equation (1.a) is attained using compact difference schemes of the following form:

$$\alpha_s u'_{i-1} + u'_i + \alpha_s u'_{i+1} = \frac{a}{2\Delta x}(u_{i+1} - u_{i-1}) + \frac{b}{4\Delta x}(u_{i+2} - u_{i-2})$$ (2)

where α_s, a, and b are constants, and Δx is the grid spacing between consecutive nodes. Derivatives are denoted by the prime designation, and the subscripts represent relative placement in the finite difference grid, with respect to node i.

The relationships between the constants are traditionally determined by manipulating the coefficients of like-ordered terms of the Taylor series expansion developed for each primary variable and its derivative. The constants are then manipulated to nullify the desired coefficients, yielding a remainder term that determines the order of the differencing scheme.

Fourier analysis of the difference operator leads to the expression for the modified (numerical) wavenumber:

$$k'(k) = \frac{\frac{b}{2}\sin(2k) + a\sin(k)}{2\alpha_s \cos(k) + 1}$$ (3)

While traditional representation of the dispersion characteristics is useful in evaluating the resolution of a given difference operator, it is the combined effect of the temporal integration scheme on the difference operation that is most meaningful.

By using Fourier analysis, the effect of the fourth-order Runge-Kutta method (RK-4) on the tridiagonal sixth-order compact scheme (C6) can be investigated. Following the technique developed by reference 11, and similar implementation by other researchers [refs. 12-13], a combined stability analysis for the linear convection equation and periodic boundary conditions is presented. General treatments for boundary conditions other than periodic must be treated on a case-by-case basis via matrix analysis.

Following the nomenclature advocated in reference 12, the amplification factors for the respective steps of the RK-4 integration scheme may be written as:

$$G_4(k) = 1 + Z + \beta_2 Z^2 + \beta_3 Z^3 + \beta_4 Z^4$$ (4)

where, the respective β values are:

$$\beta_2 = 1/4, \ \beta_3 = 1/3, \ \beta_4 = 1/2$$

The variable, Z, represents the Fourier symbol of the convective term after applying the compact difference operator and k is the wavenumber. In the present work, the specific form of Z is given by:

$$Z = -ik'(k)CFL$$ (5)

where k' is the numerical wavenumber predicted by the specific form of the difference operator and CFL is the Courant-Freidrichs-Lewy number defined as:

$$CFL = \frac{c\Delta t}{\Delta x}$$

The expression for the amplification factor (equation 4) can now be used to show the dependence of the RK-4 method, and thus the CFL dependence, on the resolution characteristics of the difference operator. Writing the amplification factor in polar form, the magnitude represents the dissipation characteristics,

while the exponential parameter represents the numerical wavenumber. The error in signal propagation speed can be analyzed by numerically differentiating the relationship between the numerical wavenumber and the actual wavenumber to obtain the group velocity. Any deviation from the exact value, c = 1, denotes a spurious group velocity of the signal. The group velocity error may be calculated as:

$$E_{GV} = 1 - \frac{dk'}{dk} \qquad (6)$$

Figure 2 shows a plot of the group velocity error for the sixth-order compact difference operator and the RK-4 integration scheme for a CFL number of 0.25. The figure shows that to propagate a signal 100 mesh spaces without appreciable error (phase error less than one grid point), it must be resolved with at least 4.8 points-per-wavelength (ppw) while 8 ppw would be needed to propagate the signal 1000 mesh spaces. For this wavenumber range, there is very little dissipation of the signal and the dominant error is dispersion.

Again, it should be noted that this analysis is valid only for propagation of a signal with periodic boundary conditions, and that a general treatment of boundary conditions is more difficult to analyze. But this does give a 'best case' scenario for the propagation characteristics of a particular difference operator and temporal integration scheme.
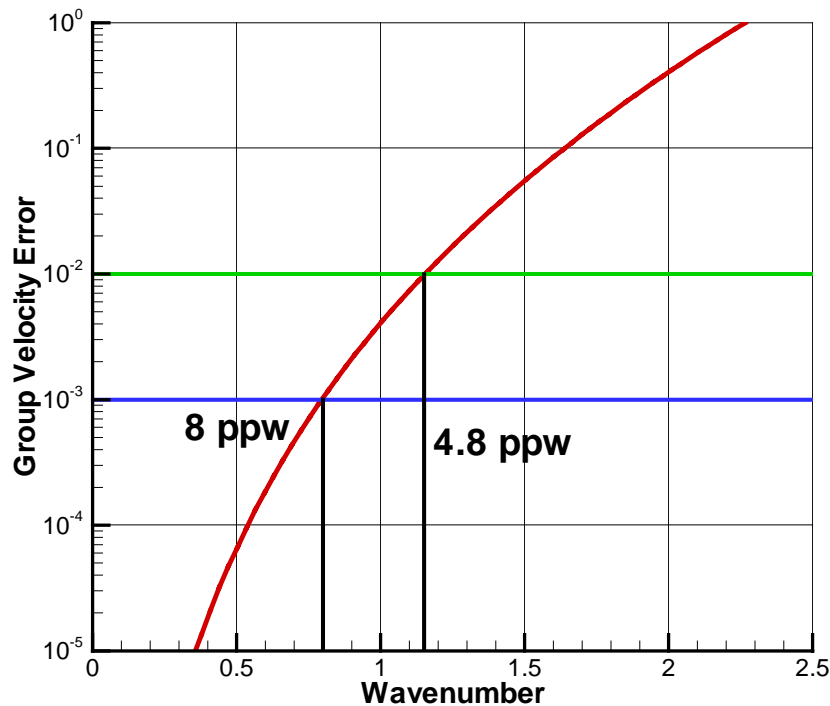
Figure 2. Effect of temporal integration scheme on group velocity error. Sixth-order compact difference operator and fourth-order Runge-Kutta integration with CFL of 0.25.

Numerical results

Based on the specified unit grid spacing, the high-frequency wave content specified in equation (1.b) is resolved using only 3.696 and 1.366 points-per-wavelength for Case 1 and Case 2, respectively. Since the apparent wavenumber for Case 2 is virtually the same as Case 1, the corresponding wavenumber for both cases is 1.7. From Figure 2, we see that C6 should propagate this high frequency content at a group velocity of 0.873, giving a peak location of 349.2 at t = 400 and 698.4 at t = 800. This is indeed the case as shown in Figures 3 and 4.

Note that because of aliasing, both spatial frequency cases behave exactly the same. Indeed, since the unit grid resolves the signal in Case 2 with less than two points per wavelength the only way to properly propagate that signal is to use either a finer mesh or to use a discretization scheme that incorporates multiple degrees-of-freedom at a single node (e.g. Hermitian-type schemes). For consistency, it may be more useful to report degrees-of-freedom-per-wavelength.
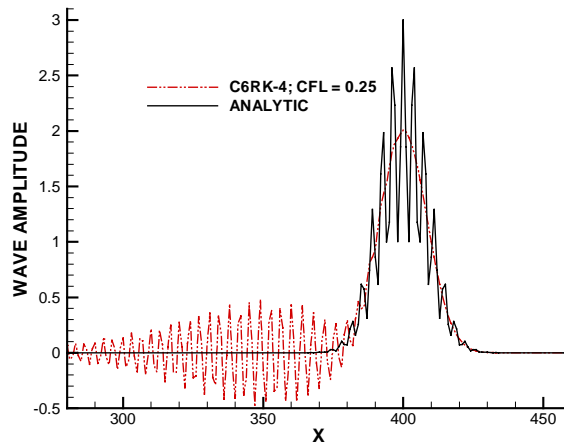
Figure 3. Numerical solution for Cases 1 and 2 at t = 400.
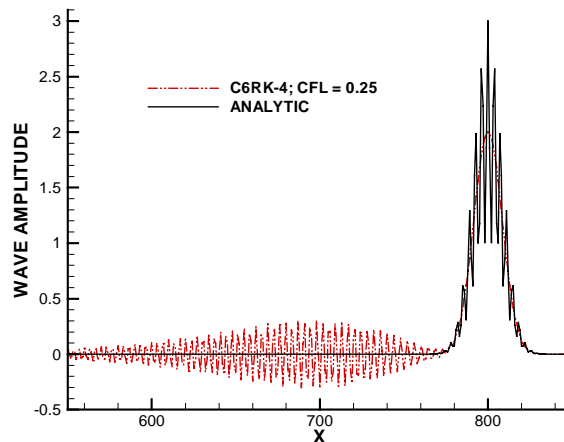
Figure 4. Numerical solution for Cases 1 and 2 at t = 800.

Since neither of the signals can be properly propagated the required number of mesh spacings when using the sixth-order compact difference operator on this particular grid, the high wavenumber content should be considered poorly resolved. The use of a tenth-order low-pass implicit filter will be used to remove this poorly resolved frequency content from the numerical solution leaving only the Gaussian pulse. Given a typical solution vector, ϕ, the filtered values, $\bar{\phi}$, on the interior are obtained via the high-order implicit filter shown below:

$$\alpha_f \bar{\phi}_{i-1} + \bar{\phi}_i + \alpha_f \bar{\phi}_{i+1} = \sum_{n=0}^{N} \frac{a_n}{2} (\phi_{i+n} - \phi_{i-n}) \tag{7}$$

where α_f controls the dissipative mechanism and frequency cutoff of the filter. Full implementation details of the filter may be found in reference 13.

It should be noted that even though only a single application of the filter is required for the present case, it will nevertheless be used at each Runge-Kutta stage to show that repeated application of the filter has no discernible effect on the well resolved portion of the signal. The frequency response of the filter is shown in Figure 5 for various values of the parameter α_f, and the filtered solutions at times 400 and 800 are shown in Figures 6 and 7, respectively.
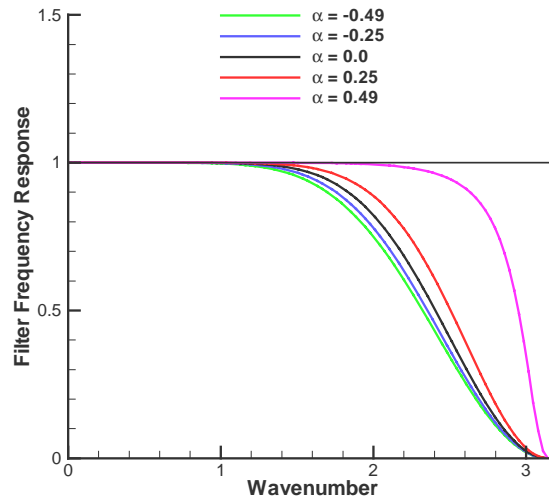
Figure 5. Frequency response of implicit filter
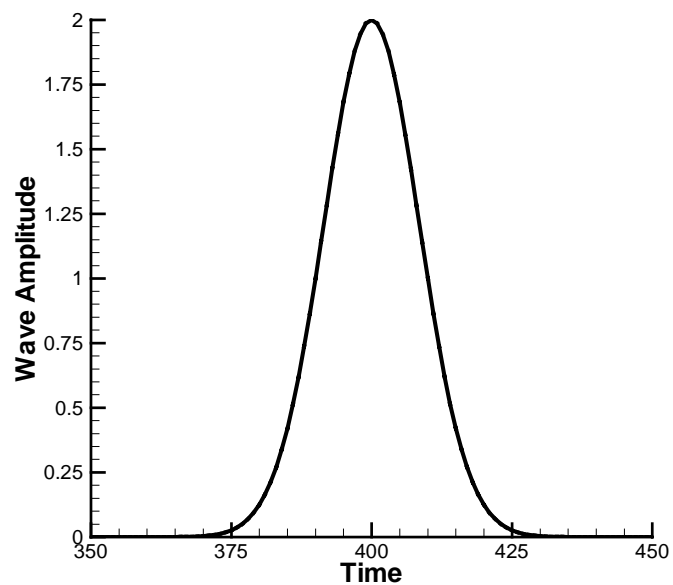
Figure 6. Filtered numerical solution at t = 400.
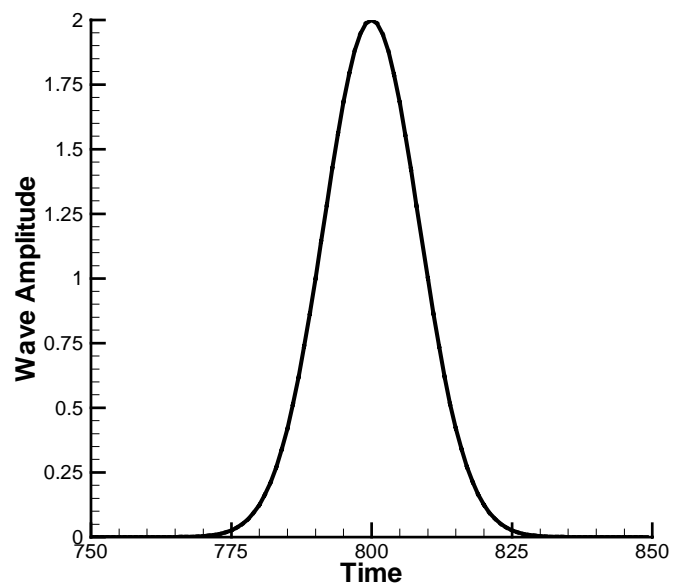
Figure 7. Filtered numerical solution at t = 800.

CATEGORY 1, PROBLEM 3: Non-Reflecting Boundary Conditions

To test the accuracy of non-reflecting boundary conditions, initial acoustic, vortical, and entropy waves are convected by a uniform mean flow. The computational domain spans $-2 < x < 2$, and is y-periodic over $0 < y < 1$. The problem specifies the solution of perturbation quantities at $t = 1, 2, 4(k-2); k = 3,\ldots 18$. The relative L_2 errors are requested at 129x33 specific points.

Case 1

The two-dimensional linearized Euler equations in dimensionless form, assuming a uniform mean flow are given as:

$$\frac{\partial \overline{U}}{\partial t} + \frac{\partial \overline{E}}{\partial x} + \frac{\partial \overline{F}}{\partial y} = 0$$

where;

$$\overline{U} = \begin{Bmatrix} \rho \\ u \\ v \\ p \end{Bmatrix}, \quad \overline{E} = \begin{Bmatrix} M_x \rho + u \\ M_x u + p \\ M_x v \\ M_x p + u \end{Bmatrix}, \quad \overline{F} = \begin{Bmatrix} M_y \rho + v \\ M_x v \\ M_y v + p \\ M_y p + v \end{Bmatrix}$$

The equations are recast via a generalized coordinate transformation from the physical space (x,y) into the computational space (ξ, η):

$$\frac{\partial U}{\partial t} + \frac{\partial E}{\partial \xi} + \frac{\partial F}{\partial \eta} = 0$$

The variables in computational space; **U**, **E**, and **F** are related to the dependent variables in physical space by:

$$U = \frac{\overline{U}}{J} \quad E = \frac{\left[\xi_x \overline{E} + \xi_y \overline{F}\right]}{J} \quad F = \frac{\left[\eta_x \overline{E} + \eta_y \overline{F}\right]}{J}$$

J is the Jacobian of transformation for the coordinate mapping while ξ_x, ξ_y, η_x, and η_y are the grid metrics and are related as follows:

$$J = \left| \xi_x \eta_y - \xi_y \eta_x \right|$$

The initial conditions are shown in Figure 8 in contour format.

Non-reflective boundary condition via grid-stretching and filtering

Grid-stretching in conjunction with an applied dissipation mechanism is used here as non-reflecting boundary condition. This method has been proposed and successfully used previously for viscous flow and acoustics (refs. 14-16). Out-going wave content is deposited into increasingly higher wavenumber modes by expanding the grid spacing, and then removing the poorly resolved wave content by use of filtering or damping. In the present work, this particular mechanism is deemed energy transfer and annihilation (ETA). One beneficial aspect of this boundary condition treatment is that the describing equations are not modified in any way. The non-reflecting quality is achieved by manipulating the grid point spacing.

To construct the non-reflecting region, additional node points are added to the outlet region much like any other buffer zone technique. The grid stretching strategy employed here consists of being able to smoothly dissipate the smallest structures that can be resolved by the grid in the particular domain of interest, while also being able to remove the larger wave structures. To accomplish this, an exponential grid-stretching parameter was defined as:

$$x_{i+1} = x_i + (e^{\gamma K}) \Delta x_{CD} \tag{8}$$

In the equation above, K is a node number counter of the grid points inside the ETA region, γ is the user defined stretching parameter, and Δx_{CD} is the uniform grid spacing within the domain of interest. The boundary condition used to truncate the difference stencil at the outside edges of the ETA regions is a simple one-point extrapolation (e.g. $\rho(x_1) = \rho(x_2)$ and $\rho(x_N) = \rho(x_{N-1})$). Higher-order Neumann-type conditions were investigated, but the simple one-point method works equally well. The success of the method depends most strongly on smoothly stretching the grid in the ETA region, and not the truncation of the difference stencil at the outermost edges.

For solution of Case 1, the y-periodic problem, the domain of interest was modeled using a uniform grid with $\Delta x = \Delta y = 1/64$ and a CFL number of 0.2 is used in the temporal integration. The non-reflecting boundary conditions are implemented at $x = \pm 2$, using an initial uniform transition region of 15 points followed by a region of 55 points (K = 70) smoothly stretched via the exponential stretching function with γ = 0.08. A tenth-order implicit filter is used throughout the computational domain, with degradation in order-of-accuracy from tenth-, to eighth-, to sixth-order as the filter is truncated at the computational boundary. The filter parameter used is α_f of 0.4 in both the domain of interest and the non-reflecting ETA regions.

The requested relative L_2 error for each primary variable is shown in Figure 9. Some increase in the magnitude of this error can be attributed to the fact the true solution is beginning to diminish in magnitude at later times. These errors decrease significantly if calculated with respect to the initial conditions. Figure 10 shows a comparison of the pressure contours at t = 64. As shown, the solution agreement is very good, with no sign of reflection apparent in the contour plot.
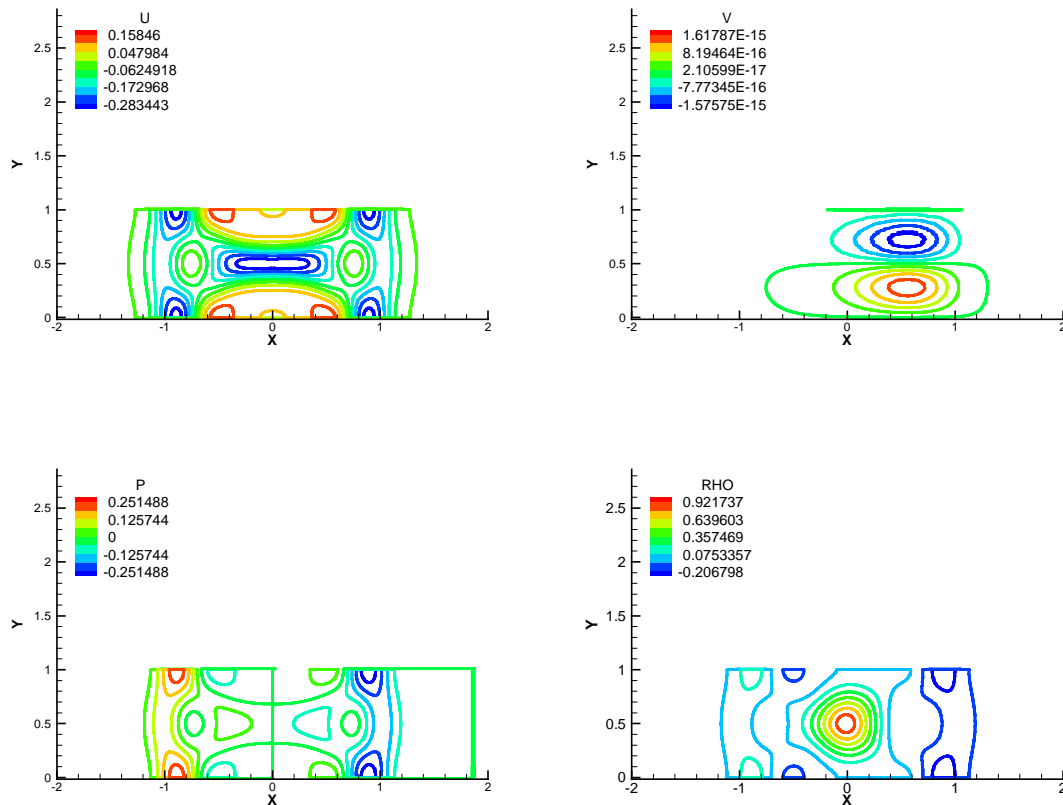
Figure 8. Contour plot of initial conditions. U-Velocity (top left), V-Velocity (top right), Pressure (bottom left) and Density (bottom right).
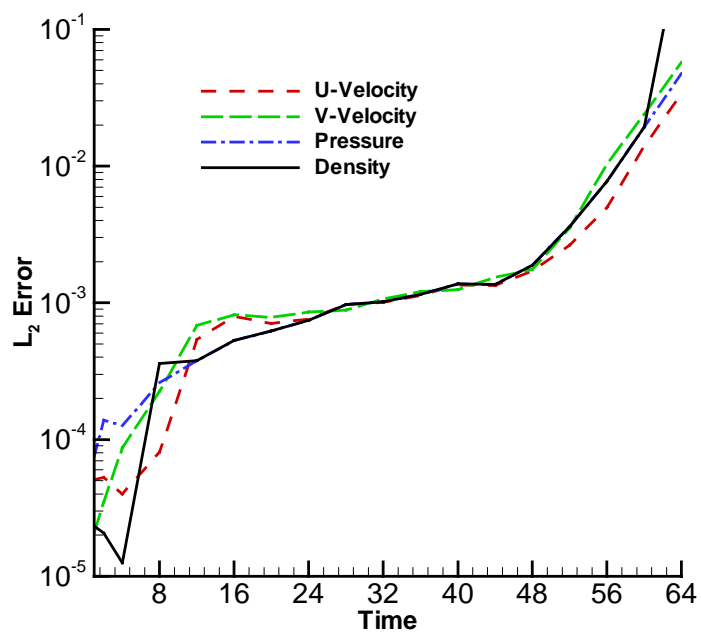
Figure 9. Relative L_2 errors for y-periodic non-reflecting boundary condition problem.
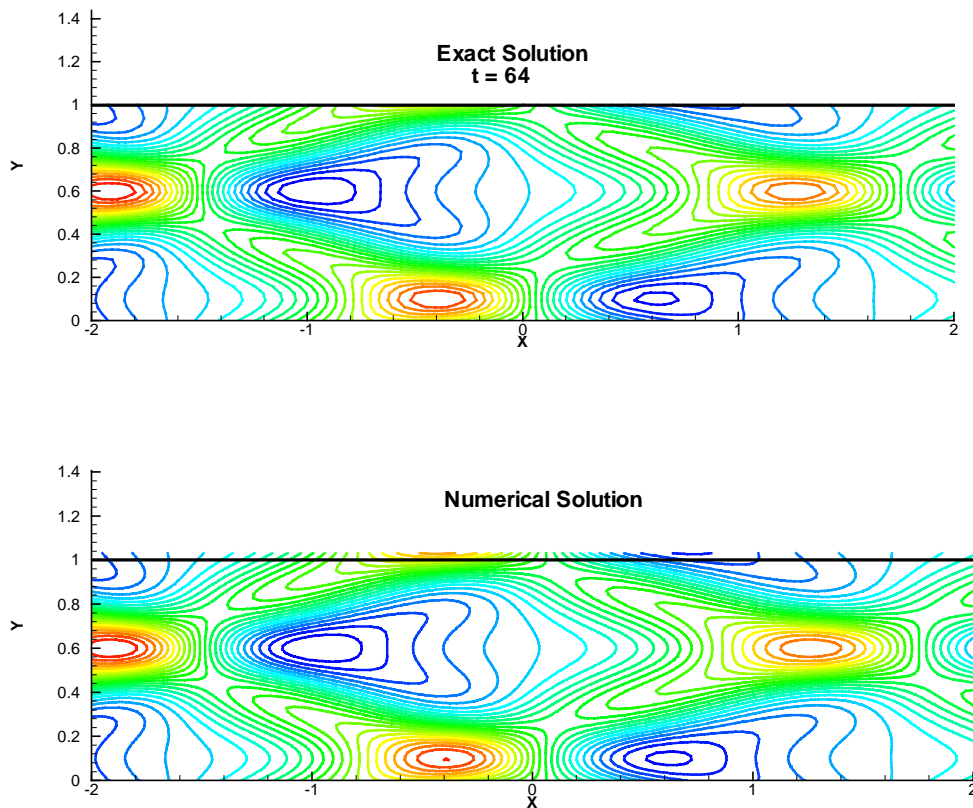
Figure 10. Comparison of analytic and numerical solutions for pressure at t = 64.

CONCLUSIONS

Problems 1 and 3 of Category 1 have been solved using FDL2DI. The use of the energy transfer and annihilation (ETA) treatment as a non-reflecting boundary condition is easily extensible to problems in CFD and CEM as well as acoustics. The treatment is predicated on efficient dissipation of out-going wave content by smoothly stretching the grid and removing unresolved waves by an implicit filter. Extension to a more sophisticated treatment may be possible by monitoring the wave amplitudes at the outermost edges of the ETA regions and either adaptively adding more grid nodes or using a more dissipative filter in selective areas.

ACKNOWLEDGEMENT

REFERENCES

1. Tam, C.K.W., "Computational Aeroacoustics: Issues and Methods", AIAA Journal, Vol. 35, No. 10, 1995.
2. Lele, S.K., "Computational Aeroacoustics: A Review", AIAA Paper 97-0018, 1997.
3. Visbal, M.R. and Gaitonde, D.V., "Very High-Order Spatially Implicit Schemes for Computational Acoustics on Curvilinear Meshes", Journal of Computational Acoustics, Vol. 9, No. 4, 2001, pp. 1259-1286.
4. Lele, S.K., "Compact Finite Difference Schemes with Spectral-like Resolution", Journal of Computational Physics, 103, 1992, pp.16-42.
5. Tam, Christopher K. W. and Webb, Jay C. "Dispersion-Relation-Preserving Finite Difference Schemes for Computational Acoustics" Journal of Comp. Physics Vol. 107, 1993, pp 262-261.
6. Hu, F. Q., Hussaini, M.Y., and Manthey, J. L., "Low-Dissipation and Low-Dispersion Runge-Kutta Schemes for Computational Acoustics" Journal of Comp. Physics Vol. 124, pp 177-191, 1996.
7. Fyfe, D., "Economical Evaluation of Runge-Kutta Formulae", Mathematics of Computation, Vol. 20, 1966, pp. 392-398.
8. Tam, C.K.W. and Shen, H., "Direct Computation of Nonlinear Acoustic Pulses Using High Order Finite Difference Schemes", AIAA Paper 93-4325, 15th AIAA Aeroacoustics Conference, Long Beach, CA, Oct. 25-27, 1993.
9. Bogey, C. and Bailly, C., "A Family of Low Dispersive and Low Dissipative Explicit Schemes for Computing Aerodynamic Noise", AIAA Paper 2002-2509, 2002.
10. Gaitonde, D.V. and Visbal, M.R., "High-Order Schemes for Navier-Stokes Equations: Algorithm and Implementation into FDL3DI", Technical Report AFRL-VA-WP-TR-1998-3060, Air Vehicles Directorate, Air Force Research Laboratory, August 1998.
11. Jameson, A. and Baker, T.J., "Solution of the Euler Equations for Complex Configurations", AIAA Paper 83-1929, 1983, pp. 293-302.
12. Yu, S., Hsieh, K., and Tsai, Y., "Simulating Waves in Flows by Runge-Kutta and Compact Difference Schemes", AIAA Journal, Vol. 22, No. 3, 1995.
13. Colonius, T., "Numerically Nonreflecting Boundary and Interface Conditions for Compressible Flow and Aeroacoustic Computations", AIAA Journal, Vol. 33, No. 7, 1997.
14. Rizzetta, D.P., Visbal, M.R., and Gaitonde, D.V., "Large-Eddy Simulation of Supersonic Compression-Ramp Flow by High-Order Method", AIAA Journal, Vol. 39, No. 12, 2001, pp. 2283-2292.
15. Colonius, T. Lele, S.K., and Moin, P., "Boundary Conditions for Direct Computation of Aerodynamic Sound Generation", AIAA Journal, Vol. 31, No. 9, 1993, pp. 1574-1582.
16. Visbal, M.R. and Gaitonde, D.V., "Very High-Order Spatially Implicit Schemes for Computational Acoustics on Curvilinear Meshes", Journal of Computational Acoustics, Vol. 9, No. 4, 2001, pp. 1259-1286.

SOLUTION OF AEROACOUSTIC BENCHMARK PROBLEMS BY DISCONTINUOUS GALERKIN METHOD AND PERFECTLY MATCHED LAYER FOR NONUNIFORM MEAN FLOWS

Fang Q. Hu

Department of Mathematics and Statistics, Old Dominion University
Norfolk, Virginia 23529
fhu@odu.edu

ABSTRACT

Numerical solutions of Problems 1 and 3 in Category 1 are presented. For Problem 1, the one-dimensional wave equation is solved by the discontinuous Galerkin method. Numerical dispersion and dissipation errors of the discontinuous Galerkin method are discussed and compared with finite difference schemes. For Problem 3, Perfectly Match Layer (PML) for the linearized Euler equations with a non-uniform mean flow is presented. The stable absorbing boundary condition is constructed based on a dispersive wave analysis of the normal modes of the Couette flow. Numerical results show excellent agreement with the exact solution. Solutions for both the subsonic and transonic Couette flow problems are presented.

ALIASING ERRORS

We solve the one-dimensional wave equation

$$\frac{\partial u}{\partial t} + \frac{\partial u}{\partial x} = 0 \tag{1}$$

with initial condition

$$u_0(x) = [2 + \cos(\alpha x)]e^{-(\ln 2)(x/10)^2}. \tag{2}$$

The value of α for the two cases specified in the problem is 1.7 and 4.6 respectively.

We first note that the Fourier transform of the initial condition (2) is

$$\hat{u}_0(k) = \frac{1}{2\pi}\int_{-\infty}^{\infty} u_0(x)e^{ikx}dx = \frac{10}{\sqrt{\pi \ln 2}}e^{-25k^2/\ln 2} + \frac{5}{2\sqrt{\pi \ln 2}}\left[e^{-25(k+\alpha)^2/\ln 2} + e^{-25(k-\alpha)^2/\ln 2}\right].$$

The Fourier transform is plotted in Figure 1. As we can see that, for the first case of $\alpha = 1.7$, the numerical scheme is required to resolve accurately waves of as short a wavelength as three grid points (i.e., $k\Delta x \approx 2$, with gird spacing $\Delta x = 1$). Although the resolution of a scheme generally improves as the order (or the number of stencil points) of the scheme increases, it may still require a scheme of an extraordinarily high order to satisfy the resolution requirement of this problem. This may not always be practical since the increase in the order of the scheme will increase the cost of computation as well.

On the other hand, Figure 1 clearly shows that there are two distinct parts in the initial condition, namely a smooth mean profile ($|k| \leq 0.5$) and a highly oscillatory part ($1.5 \leq |k| \leq 2$). In this paper, we will not try to resolve the high oscillations under the specified grid, but rather the objective of our computation will be to preserve the mean profile accurately while at the same time eliminate the high-frequency oscillations. The numerical scheme to be used is the 4th-order discontinuous Galerkin (DG) scheme. We will illustrate that the discontinuous Galerkin method has a much better wave propagation properties than finite difference schemes of the same order and the built-in dissipation mechanism of the DG scheme can effectively damp out the high frequency oscillations[15, 12].
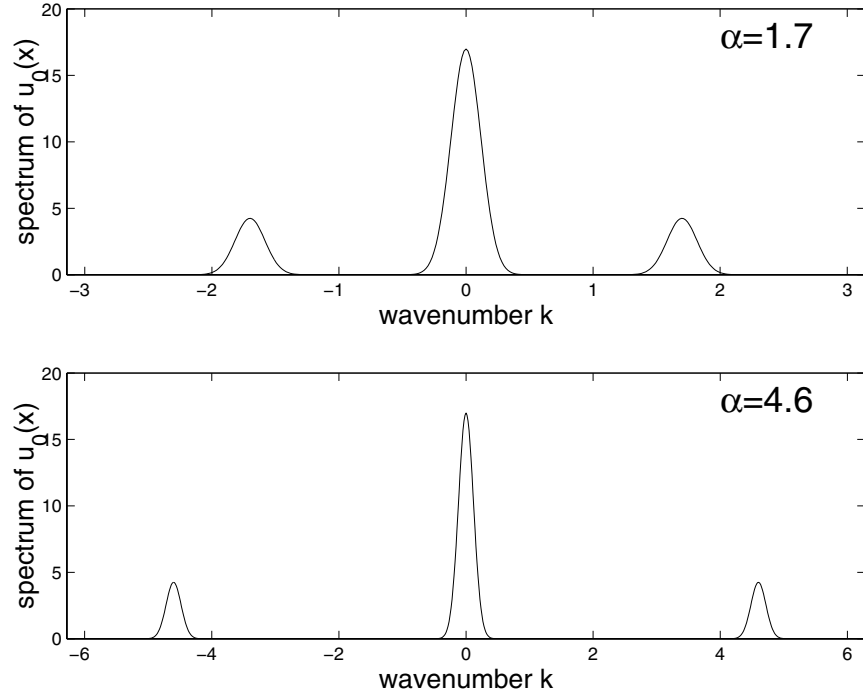
Figure 1: Fourier transform of the initial condition.

Discontinuous Galerkin method

Discontinuous Galerkin method is a finite element method that uses discontinuous basis functions[1, 3]. For the current problem, a computational domain of $[-56, 960]$ is divided into 254 elements with a length of 4 for each element. Since the solution in each element will be represented by a polynomial of order 3(with four coefficients), the total number of degrees of freedom is equivalent to that of an explicit finite difference scheme using $\Delta x = 1$.

In each element $[x_n, x_{n+1}]$, where

$$x_n = -56 + 4n, \quad n = 0, 1, ..., 253,$$

the solution is approximated by an expansion in basis polynomials,

$$u_n(x,t) = \sum_{\ell=0}^{p} c_\ell^n(t)\phi_\ell(x). \tag{3}$$

In (3), $\phi_\ell(x)$ is the basis function and $c_\ell^n(t)$ is the expansion coefficient. In this paper, Legendre polynomials are used for $\phi_\ell(x)$ and $p = 3$.

A weak formulation of the wave equation (1) is

$$\int_{x_n}^{x_{n+1}} \frac{\partial u}{\partial t} v dx + \left[uv \right]_{x_n}^{x_{n+1}} - \int_{x_n}^{x_{n+1}} u \frac{\partial v}{\partial x} dx = 0 \tag{4}$$

where v is the test function[1, 3]. By substituting (3) into (4) and choosing the test function to be the basis functions, we get a system of semi-discrete equations as follows[1, 12],
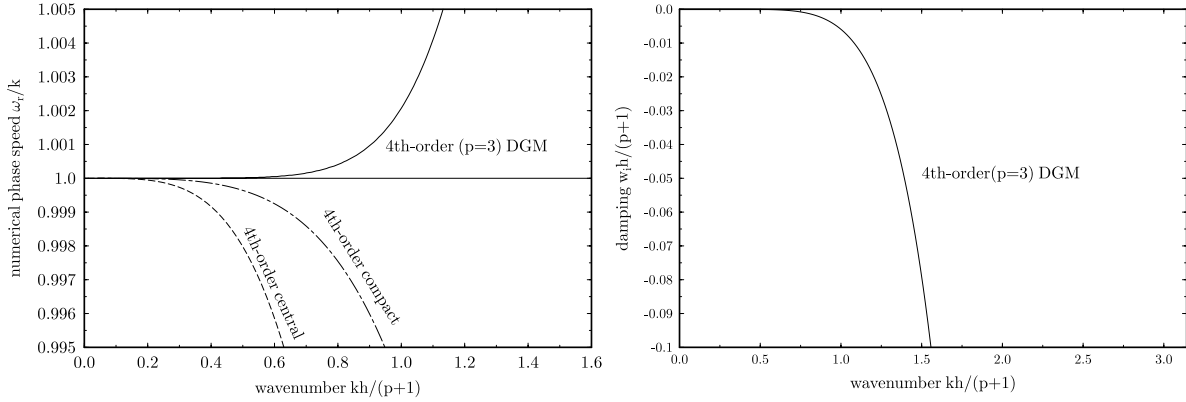
Figure 2: Left: numerical phase speed of the fourth-order DG and central difference schemes, compared using the wavenumber scaled by the degree of freedom; h is the element length and p is the order of basis polynomial in DG. Right: damping error of DG scheme.

$$\sum_{\ell=0}^{p} \frac{dc_{\ell}^n}{dt} \int_{x_n}^{x_{n+1}} \phi_{\ell}(x)\phi_m(x)dx + u^n(x_{n+1})\phi_m(x_{n+1}) - u^{n-1}(x_n)\phi_m(x_n) - \sum_{\ell=0}^{p} c_{\ell}^n \int_{x_n}^{x_{n+1}} \phi_{\ell} \frac{d\phi_m}{dx}dx = 0$$

(5)

for $m = 0, 1, ..., p$.

This is a system of ordinary differential equations for the expansion coefficients $c_{\ell}^n(t)$. It is solved numerically by the optimized low-dissipation and low-dispersion Runge-Kutta scheme (LDDRK[14]). In particular, the optimized 5- and 6-stage combined scheme (LDDRK 5-6) is used. This scheme is formally fourth-order and has been optimized to have larger accuracy and stability limits than single-stage optimized schemes.

The discontinuous Galerkin method does not require a uniform mesh and works naturally with unstructured grids in two and three space dimensions. Unlike the continuous finite element method, there is no global matrix to be inverted which make the method highly efficient for parallel computing.

Recent Fourier analysis of the semi-discrete equation (5) shows that DG schemes are super-accurate for wave propagations[12, 13]. That is, for a scheme using polynomials of order p, the numerical dispersion relation of the semi-discrete equation is accurate to order $2p+2$. For example, for the 4th-order DG scheme (employing third order polynomials) used in the present problem, the numerical phase speed is actually accurate to the 8th-order. In Figure 2 (left), we plot the phase speed of the 4th-order DG scheme as well as that of 4th-order explicit central and compact finite difference schemes, where the horizontal axis has been scaled to keep the degrees of freedom the same for a fair comparison. Clearly, the DG scheme preserves the phase speed much better than the finite difference schemes of the same order.

Due to upwinding at element interfaces, the DG scheme also has a built-in dissipation for high frequency waves[15, 12]. Figure 2 (right) shows the numerical damping rate of the 4ht-order DG scheme. The damping rate is also 8th-order accurate, i.e., proportional to $(kh)^{2p+2}$.

Numerical results

The numerical solution is initialized by a projection of the initial condition (2) onto the basis functions. Specifically, the initial state for element $[x_n, x_{n+1}]$ is obtained by
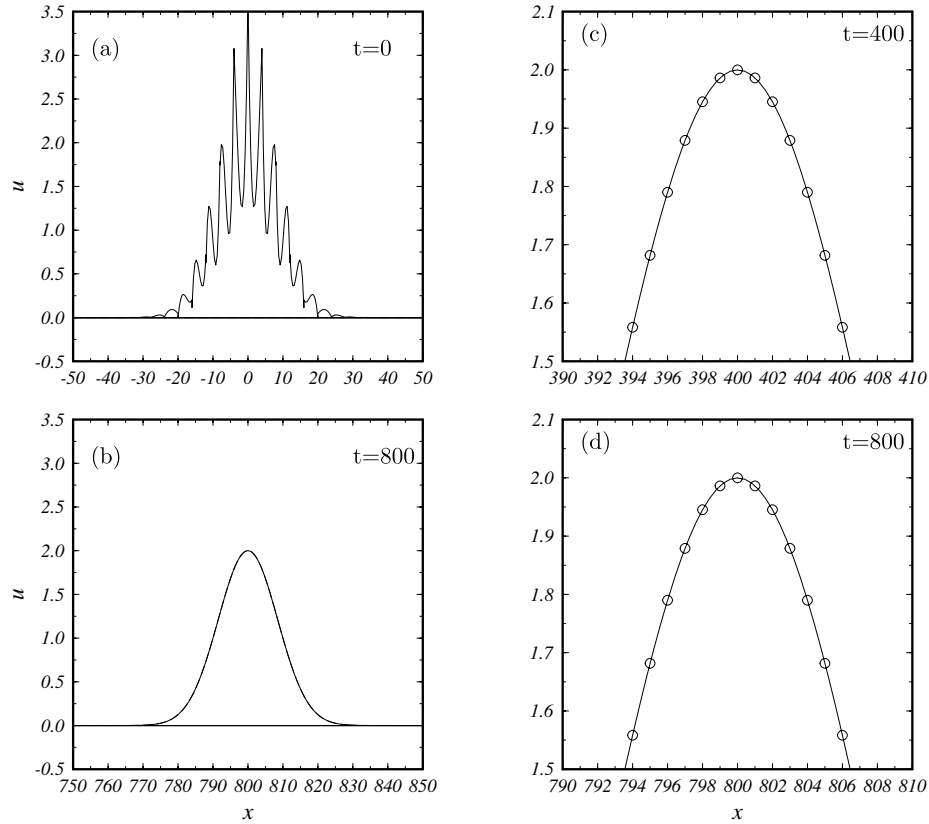
Figure 3: Numerical results of case I, $\alpha = 1.7$. (a) initial condition by projection process (7); (b) numerical solution at $t = 800$; (c) and (d) comparison with exact solution (without the oscillation part) at $t = 400$ and 800 respectively.

$$u_n(x,0) = \sum_{\ell=0}^{p} c_\ell^n(0)\phi_\ell(x) \tag{6}$$

where $c_\ell^n(0)$ is computed by the requirement that

$$\int_{x_n}^{x_{n+1}} u_0(x)\phi_m(x)dx = \sum_{\ell=0}^{p} c_\ell^n(0) \int_{x_n}^{x_{n+1}} \phi_\ell(x)\phi_m(x)dx \tag{7}$$

for $m = 0, 1, ..., p$. The integral on the left hand side of (7) is carried out by a 20-point Gaussian quadrature rule and the integral on the right hand side is evaluated exactly.

Case I, $\alpha = 1.7$

Figure 3(a) shows the projected initial condition. Since the DG scheme does not enforce continuity at element interfaces, discontinuities at element boundaries are expected when the function is not well resolved, which is the case for the highly oscillatory part of the initial condition. Figure 3(b) shows the solution at time $t = 800$. The high frequency oscillations are effectively damped out and a smooth mean solution is seen. In Figures 3(c) and 3(d), we plot the numerical solution with the exact solution (without the oscillation part, in circles), at $t = 400$ and 800 respectively. Clearly, the DG scheme preserves the mean Gaussian profile very well and the built-in dissipation affects only the unresolved high wavenumbers.
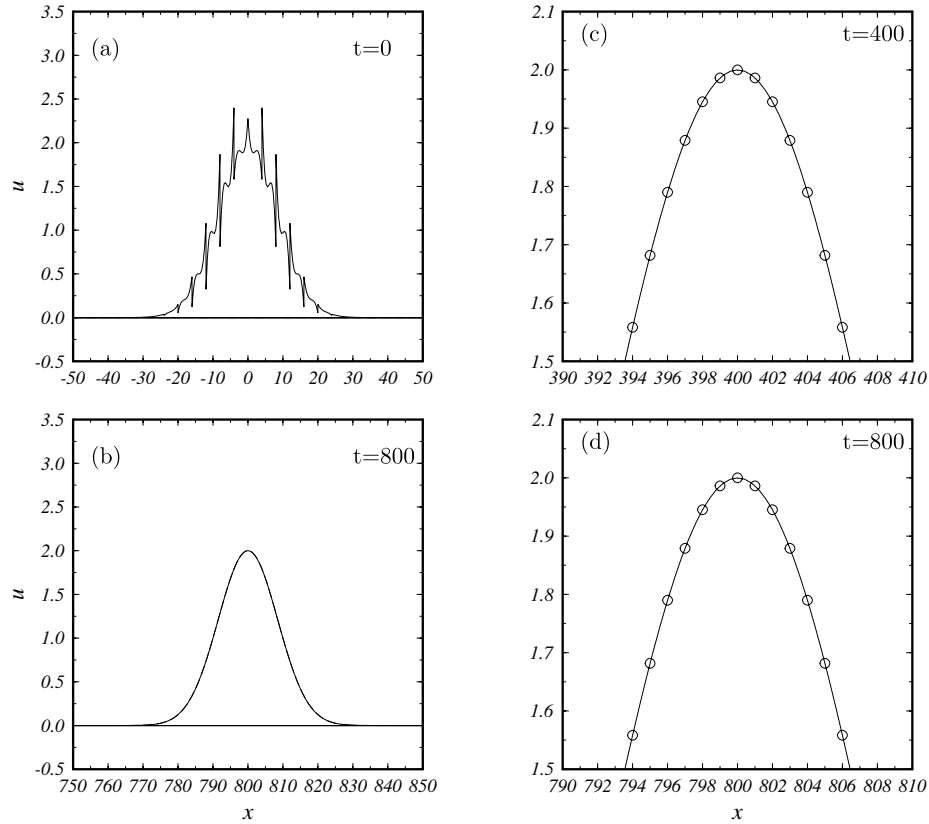
Figure 4: Numerical results of case II, $\alpha = 4.6$. (a) initial condition by projection process (7); (b) numerical solution at $t = 800$; (c) and (d) comparison with exact solution (without the oscillation part) at $t = 400$ and 800 respectively.

Case II, $\alpha = 4.6$

For the second case of $\alpha = 4.6$, the projected initial condition is shown in Figure 4(a). We note that, unlike grid-based finite difference methods, the initial condition is not "aliased" with a lower wavenumber, because the projection process (7) "sees" the initial condition as a "continuous" function.

Figure 4(b) shows the solution at $t = 800$ and Figures 4(c) and 4(d) show the numerical and exact (without the oscillation part) solutions. Again, the high oscillations in the initial condition are damped out and, at the same time, the mean profile if accurately preserved.

PERFECTLY MATCHED LAYER FOR A NONUNIFORM MEAN FLOW

In Problem 3, nonreflecting boundary conditions are needed at the inflow and outflow boundaries of the channel Couette flow. In our computation, Perfectly Matched Layer (PML) will be used as absorbing boundary conditions so that out-going waves are attenuated with minimal reflection (Figure 5). We will discuss the construction of a stable PML equation for a non-uniform mean flow and present the numerical results.

The linearized Euler equation with a non-uniform mean flow is

$$\frac{\partial \mathbf{u}}{\partial t} + \mathbf{A}\frac{\partial \mathbf{u}}{\partial x} + \mathbf{B}\frac{\partial \mathbf{u}}{\partial y} + \mathbf{C}\mathbf{u} = 0 \tag{8}$$
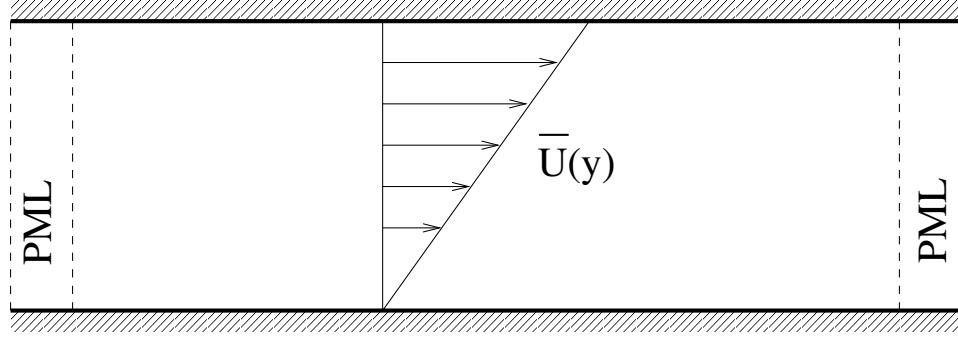
Figure 5: Schematic of Couette flow with PML absorbing boundary condition

where

$$\mathbf{u} = \begin{pmatrix} \rho \\ u \\ v \\ p \end{pmatrix}, \quad \mathbf{A} = \begin{pmatrix} \bar{U} & 1 & 0 & 0 \\ 0 & \bar{U} & 0 & 1 \\ 0 & 0 & \bar{U} & 0 \\ 0 & 1 & 0 & \bar{U} \end{pmatrix}, \quad \mathbf{B} = \begin{pmatrix} 0 & 0 & 1 & 0 \\ 0 & 0 & 0 & 0 \\ 0 & 0 & 0 & 1 \\ 0 & 0 & 1 & 0 \end{pmatrix}, \quad \mathbf{C} = \begin{pmatrix} 0 & 0 & 0 & 0 \\ 0 & 0 & \frac{d\bar{U}}{dy} & 0 \\ 0 & 0 & 0 & 0 \\ 0 & 0 & 0 & 0 \end{pmatrix}$$

For the subsonic case, the mean flow is given by $\bar{U}(y) = 0.9y$ in a physical domain of $(x, y) \in [-2, 2] \times [0, 1]$. The mean density has been assumed to be constant. Solid wall boundary conditions are applied at $y = 0, 1$.

The Perfectly Matched Layer (PML) technique can be viewed as a complex change of variables when the governing equation is written in the frequency domain[6, 4, 21, 9]. For the present case, since only vertical absorbing layers are needed for non-reflecting boundary conditions, the derivation of the PML equation for (8) would involve a complex change of variable for x as follows,

$$x \to x + \frac{i}{\omega} \int_{x_0}^{x} \sigma_x dx \tag{9}$$

where σ_x is an arbitrary positive function of x and x_0 is the location of the interface between the Euler and PML domains.

However, in order to avoid generating instability waves in the PML equation, it has been found necessary to apply a *proper* space-time coordinate transformation to the Euler equation before applying the PML complex change of variable (9)[9]. Such a space-time transformation is important because any wave of the Euler equation having opposite signs in its phase and group velocities will result in instability of the PML equation[18, 9, 2]. That is, the phase and group velocities have to be consistent and have the same sign in order to maintain the stability of the PML equation. In a recent paper[2], this necessary condition for stable PML equation was stated mathematically as

$$\frac{\omega}{k} \frac{d\omega}{dk} \geq 0 \tag{10}$$

where k is the wavenumber in the x direction. The purpose of the space-time transformation is to ensure that in the transformed space-time coordinates, all waves have consistent phase and group velocities and satisfy condition (10). For the Euler equation with a *uniform* mean flow, the proper space-time transformation was found to be

$$\bar{x} = x, \quad \bar{t} = t + \beta x, \text{ with } \beta = \frac{\bar{U}_0}{1 - \bar{U}_0^2} \tag{11}$$

where $\bar{U}_0$ is the mean flow Mach number[9]. The corresponding transformation in the frequency-wavenumber space is

$$\bar{k} = k + \beta\omega, \quad \bar{\omega} = \omega. \tag{12}$$

It was shown in [9] that, in the transformed coordinates, all linear waves associated with the Euler equation of a uniform mean flow $\bar{U}_0$ have their phase and group velocities in the same direction. The importance of the transformation (11) and the particular choice for β have been confirmed independently in recent works in [2, 7, 8].

Now to construct the PML equation for Euler equation (8) with a *nonuniform* mean flow, let's first examine the *physical* waves associated with (8) and their dispersion relations. For this purpose, a dispersive wave analysis of (8) will be carried out. Specifically, we let

$$\mathbf{u} = \hat{\mathbf{u}}(y)e^{i(kx-\omega t)}$$

in Euler equation (8) and get

$$-i\omega\hat{\mathbf{u}} + ik\mathbf{A}\hat{\mathbf{u}} + \mathbf{B}\frac{d\hat{\mathbf{u}}}{dy} + \mathbf{C}\hat{\mathbf{u}} = 0. \tag{13}$$

Together with the homogeneous boundary conditions at $y = \pm 1$, (13) forms an eigenvalue problem for ω for any given value of k. The eigensolutions are called normal modes in the theory of hydrodynamic stability analysis[5]. This eigenvalue problem has been solved numerically by a spectral collocation method using Chebyshev polynomials[16]. It yields a complete spectrum of the waves supported by (13).

Figure 6 shows the dispersion relation diagram of all the normal modes of (13), i.e., real part of ω v.s. k. The imaginary part of ω is found to be zero for all modes, indicating that the Couette flow does not have physical instability wave. In the dispersion diagram, we see two families of waves. One family has phase speed between $U_{min} = 0$ and $U_{max} = 0.9$, shown between dashed lines in the $\omega_r - k$ diagram. These are "vortical" modes that convect with the mean flow. They are non-dispersive waves, i.e., $\omega/k = constant$[22]. For these waves, condition (10) is satisfied. The other family of modes are "acoustic" modes[19, 17]. A closer examination of the acoustic modes indicates that they have a phase speed supersonic relative to part of the mean flow. They are dispersive waves.

Figure 6 indicates that the acoustic modes do not always have consistent phase and group velocities. A triangle on the acoustic modes denotes the location where the group velocity is zero. As we can see, for the acoustic modes in the upper left and lower right quarters in Figure 6 that lie between the triangle and the vertical axis, their phase velocity (ω_r/k) is negative but their group velocity ($d\omega_r/dk$) is positive. As we have explained earlier, applying the PML complex change of variable (9) to the Euler equation (8) without the a proper space-time coordinate transformation will result in these waves being amplified and becoming unstable modes.

Therefore, we would seek a proper space-time transformation so that condition (10) is satisfied in the transformed coordinates.

Remarkably, the locations of points of zero group velocity on the dispersion diagram (Triangles in Figure 6) appear to lie nearly on a straight line! Inspection of points of zero group velocity shows a line of $\omega_r = ck_x$ where the slope of the line is approximately $c = -1.85$. Considering (12), this suggests a space-time coordinate transformation of the form (11) with the value for β determined by

$$\beta = -\frac{1}{c}. \tag{14}$$

This gives $\beta = 0.54$ or equivalently a value of $\bar{U}_0 = 0.437$ in (11).
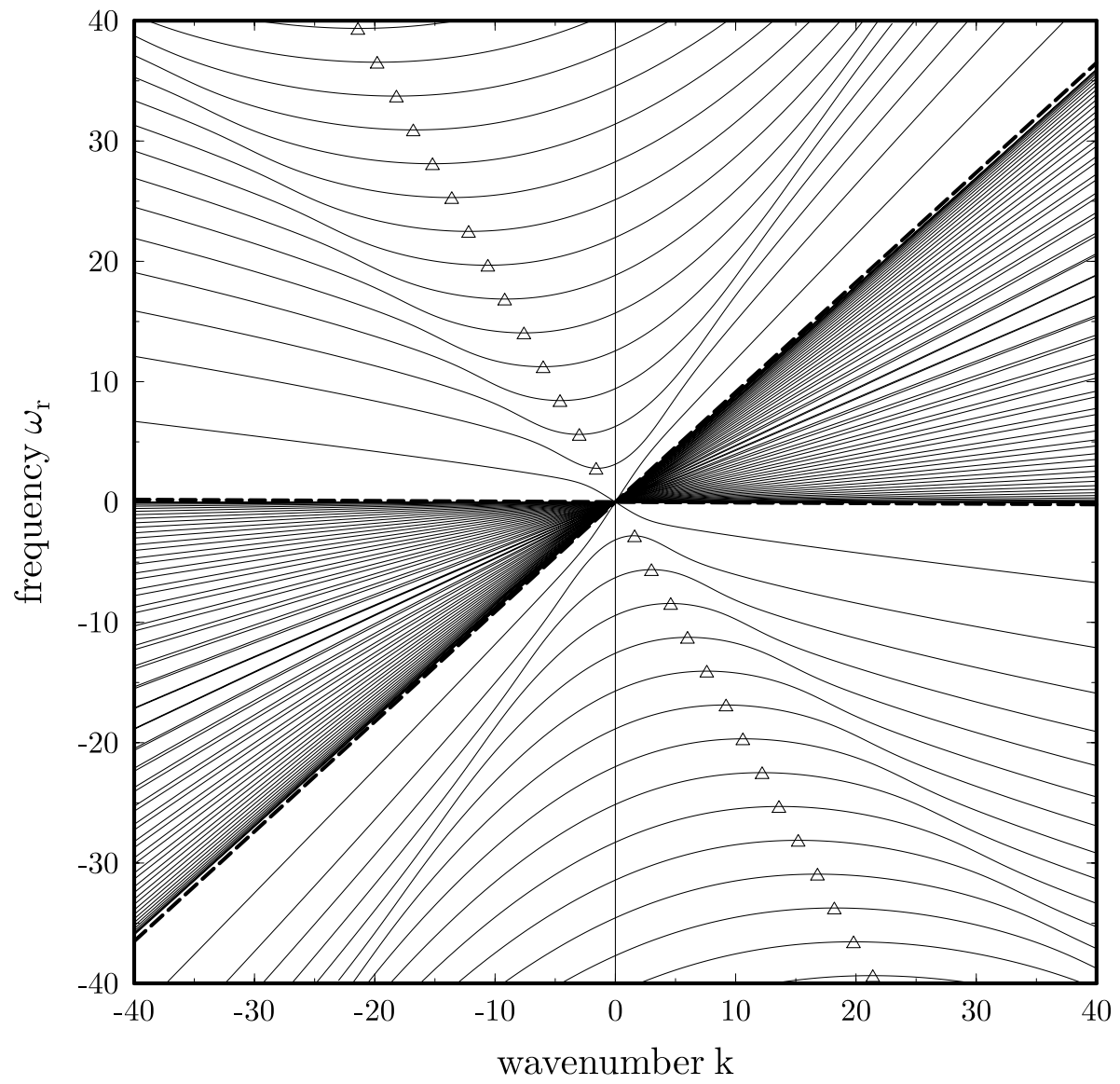
Figure 6: Dispersion relation diagram of physical wave. Triangles denote the points of zero group velocity.
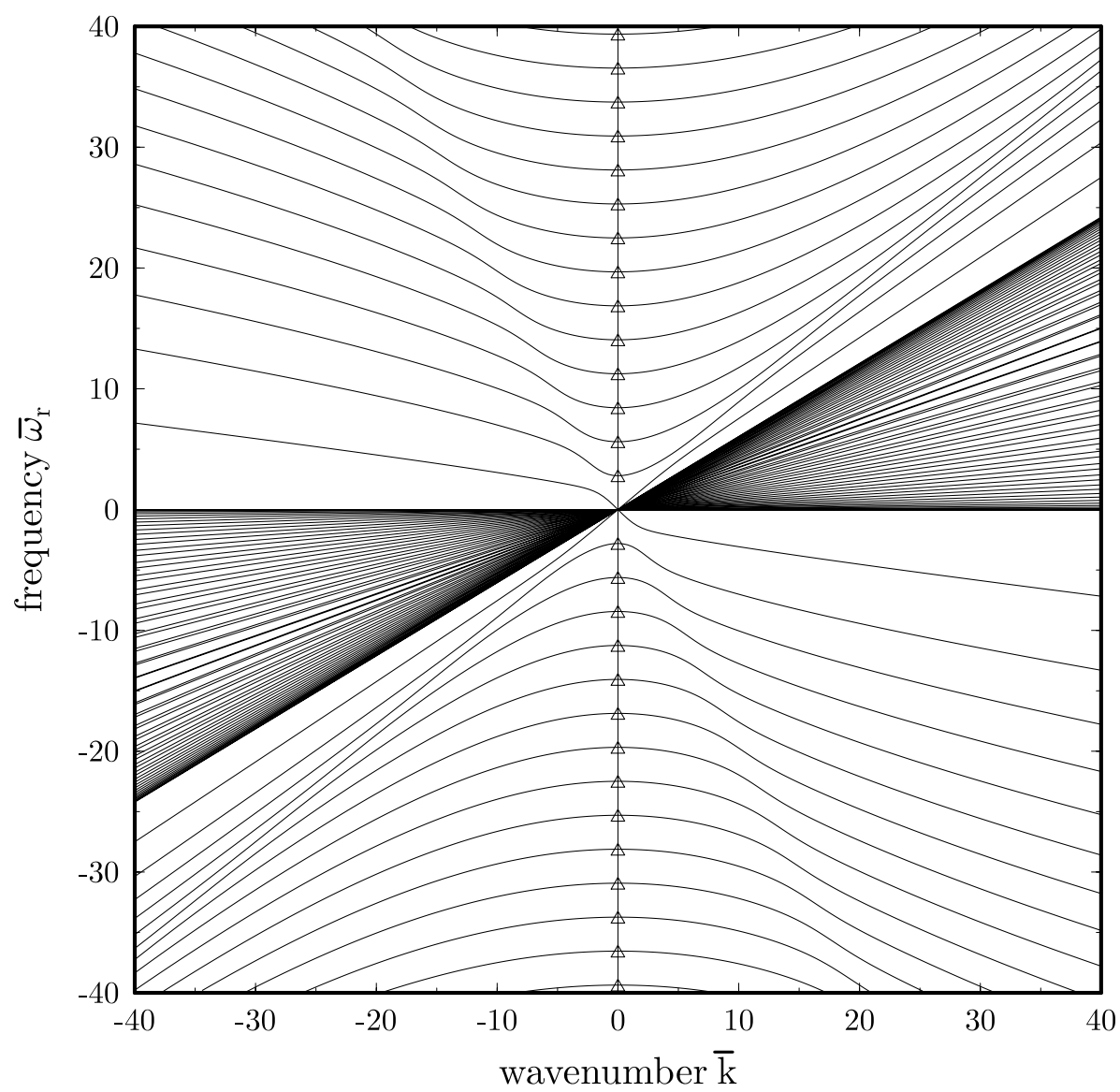
Figure 7: Dispersion relation diagram after applying the space-time transformation.

In Figure 7, we show the dispersion relation diagram in frequency-wavenumber space of the transformed coordinates. Indeed, we see that the phase and group velocities of all waves are consistent and the necessary condition (10) is now satisfied by all wave modes.

Once the value for β is chosen, the derivation of PML equation is similar to that of a uniform mean flow given in [9]. After the space-time transformation (11), the Euler equation in the frequency domain becomes

$$-i\bar{\omega}(\mathbf{I}+\beta\mathbf{A})\tilde{\mathbf{u}} + \mathbf{A}\frac{\partial\tilde{\mathbf{u}}}{\partial\bar{x}} + \mathbf{B}\frac{\partial\tilde{\mathbf{u}}}{\partial\bar{y}} + \mathbf{C}\tilde{\mathbf{u}} = 0.$$

By a complex change of variable of the form (9) for $\bar{x}$, we get the following PML equation in the frequency domain,

$$-i\bar{\omega}(\mathbf{I}+\beta\mathbf{A})\tilde{\mathbf{u}} + \mathbf{A}\frac{1}{1+\frac{i\sigma_x}{\bar{\omega}}}\frac{\partial\tilde{\mathbf{u}}}{\partial\bar{x}} + \mathbf{B}\frac{\partial\tilde{\mathbf{u}}}{\partial\bar{y}} + \mathbf{C}\tilde{\mathbf{u}} = 0.$$

Multiplying $1+\frac{i\sigma_x}{\bar{\omega}}$, we get

$$(-i\bar{\omega}+\sigma_x)(\mathbf{I}+\beta\mathbf{A})\tilde{\mathbf{u}} + \mathbf{A}\frac{\partial\tilde{\mathbf{u}}}{\partial\bar{x}} + (1+\frac{i\sigma_x}{\omega})\mathbf{B}\frac{\partial\tilde{\mathbf{u}}}{\partial\bar{y}} + (1+\frac{i\sigma_x}{\omega})\mathbf{C}\tilde{\mathbf{u}} = 0.$$

This can be readily re-written in the original physical time domain as follows

$$\frac{\partial\mathbf{u}}{\partial t} + \mathbf{A}\frac{\partial\mathbf{u}}{\partial x} + \mathbf{B}\frac{\partial\mathbf{u}}{\partial y} + \sigma_x\mathbf{B}\frac{\partial\mathbf{q}}{\partial y} + \mathbf{C}(\mathbf{u}+\sigma_x\mathbf{q}) + \sigma_x\mathbf{u} + \sigma_x\beta\mathbf{A}\mathbf{u} = 0 \qquad (15)$$

where

$$\frac{\partial\mathbf{q}}{\partial t} = \mathbf{u}. \qquad (16)$$

Here, $\mathbf{q}$ is an auxiliary variable vector. It is only needed inside the PML domain[9]. We note that this version of PML is almost identical to that given in [9] for the uniform mean flow, except for the term involving the $\mathbf{C}$ matrix. The value for β given by (14) is crucial for the stability of (15)-(16).

It is important to note that the fact that points of zero group velocity on the dispersion relation diagram fall on a line is not accidental. The same has been found in other types of subsonic mean flow velocity profiles, including mixing layers, jets and wakes[11]. In most cases, the value for β is found to be close to that given by (11) when $\bar{U}_0$ is taken to be the average of $\bar{U}(y)$. Therefore, PML equations (15)-(16) can be applied to a broad class of nonuniform mean flows. More examples will be presented in [11].

Numerical results

A computational domain of $[-2.15625, 2.15625] \times [0, 1]$ is discretized by a uniform grid of 553×129 points with $\Delta x = \Delta y = 1/128$ and 20 grid points in PML domains at the inflow and outflow. The spatial derivatives are approximated by the 7-point DRP scheme[20] and the time integration is carried out by the optimized 5- and 6-stage combined low-dissipation and low-dispersion Runge-Kutta scheme (LDDRK5-6[14]). A 10-th order filter has also been applied to limit the oscillations from the thin density wave in the problem.

The absorption coefficient in the PML domain varies with x as follows,

$$\sigma_x = \frac{4}{\Delta x}\left|\frac{x-x_0}{D}\right|^2$$
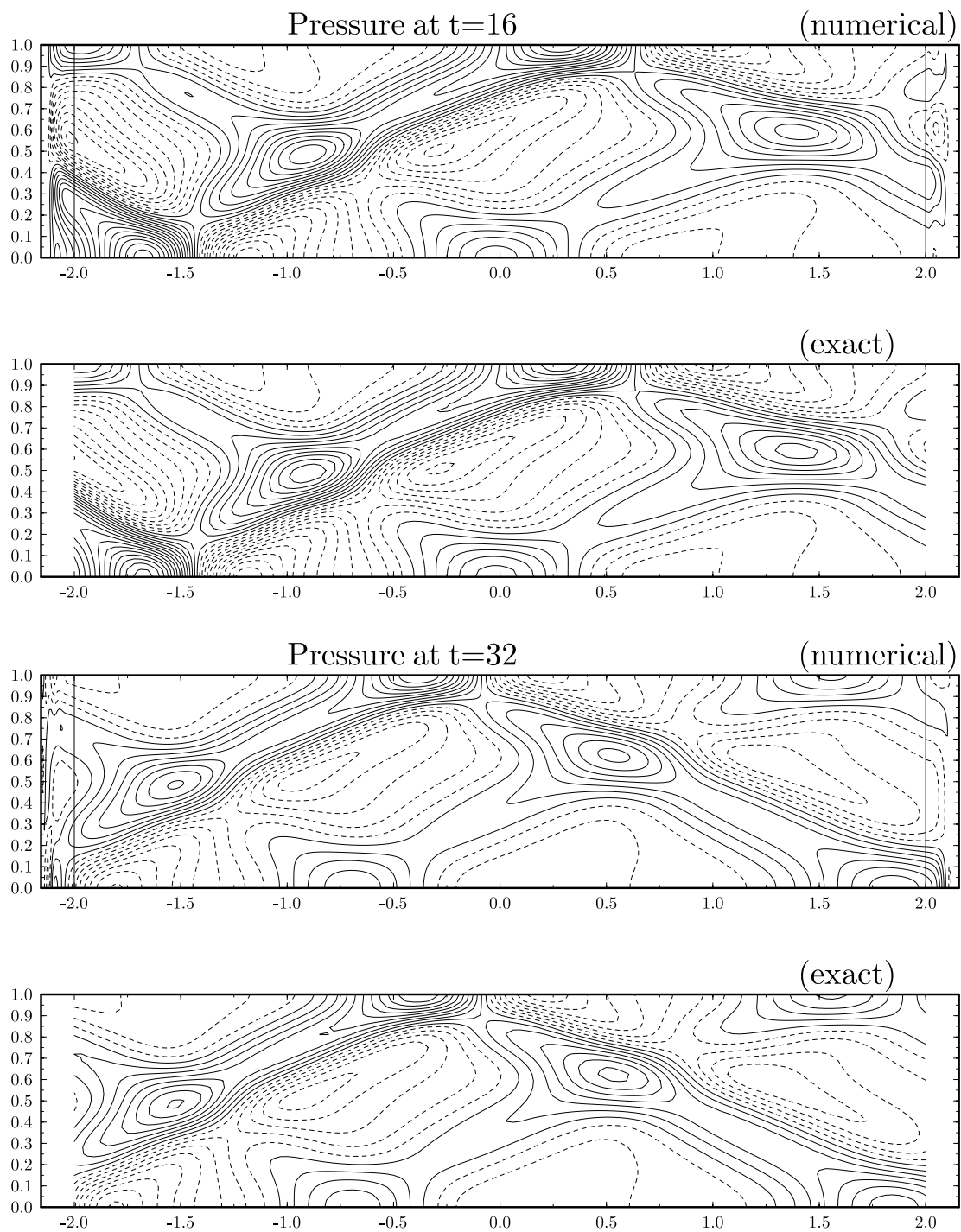
Figure 8: Pressure contours at $t = 16$ and 32.
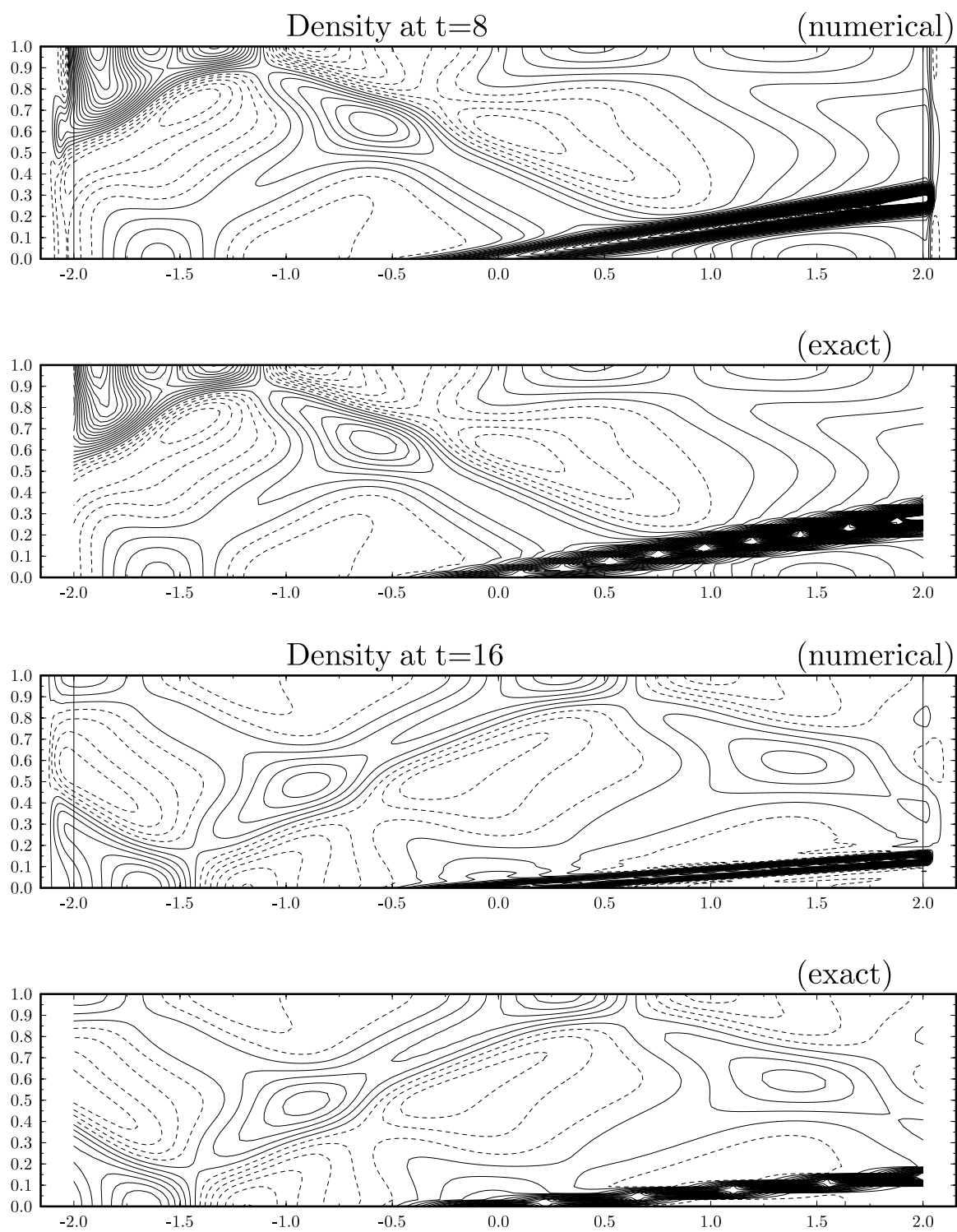
Figure 9: Density contours at $t = 8$ and 16.

where x_0 denotes the interface of the Euler and PML domains and D is the width of the PML domain, i.e., $D = 20\Delta x$ for the cases reported here.

A grid stretching inside the PML will also improve the effectiveness of the PML because the total absorption rate depends directly on the width of the PML domain[10]. On the other hand, we do not need the solutions inside the PML to be very accurate. The grid stretching is equivalent to modifying the x derivative term of the PML equation as

$$\frac{\partial}{\partial x} \rightarrow \frac{1}{\alpha(x)} \frac{\partial}{\partial x}$$

where $\alpha(x) \geq 1$ is a smooth function[10]. We have used the following expression for $\alpha(x)$ in our calculations,

$$\alpha(x) = 1 + 2 \left| \frac{x - x_0}{D} \right|^2 .$$

Figure 8 shows the pressure contours of the numerical and exact solutions at $t = 16$ and 32. The numerical solution decays exponentially inside the PML domain with very little reflection. Even with only 20 grid points in the PML domain, the agreements on contours between the numerical and exact solutions are excellent. Figure 9 shows the density contours at $t = 8$ and 16. The absorption of the density pulse by the PML domain is clearly shown. We note that the initial density pulse is stretched thin by the shear mean flow and becomes less well resolved by the 7-point finite difference scheme at $t = 16$ and beyond. Although there are some oscillations near the density wave, the overall contours compare well with the exact solution.

In Figure 10, the relative errors between the numerical and exact solutions are plotted as a function of time. The errors are computed as specified in the workshop problem, namely,

$$E_p = \frac{\|p - p_{exact}\|_2}{\|p_{exact}\|_2}, \qquad E_\rho = \frac{\|\rho - \rho_{exact}\|_2}{\|\rho_{exact}\|_2} \tag{17}$$

for pressure E_p and density E_ρ. The error in pressure is less than 5% even with only 20 grid points in the PML domain. Since the L2 norm is carried out throughout the entire computational domain, The errors given by (17) actually include the numerical errors due to the boundary condition as well as the numerical discretization of the Euler equation. The larger error in the density is not due to the boundary condition, but reflects the fact that the thin density wave is not well resolved by the 7-point finite difference scheme used.

To further assess the error due to the boundary condition alone, we show in Figure 11 the error in density obtained by comparing the numerical solution with a *reference* solution which is computed using the same numerical scheme but a larger computational domain so it is not affected by the boundary condition. The relative error in density is now less than 1% up to $t = 64$. It is further reduced to 0.2% when 30 grid points are used in the PML domain. To reduce computing time, the grid spacing is larger in this calculation, with $\Delta x = \Delta y = 1/32$.

TRANSONIC COUETTE FLOW

For the case of transonic Couette flow of $U(y) = 1.2y$, it becomes infeasible to use a space-time transformation of the form (11). The dispersion relations of all physical waves for this problem are plotted in Figure 12. There are now two points of zero group velocity for each acoustic mode. This is due to the fact that part of the mean flow is now supersonic. Therefore, a coordinate transformation of the form (11) will not be effective.

Since the mean flow is supersonic only in a narrow region of $5/6 \leq y \leq 1$, we have experimented with a "transition" zone over which the mean flow is modified gradually from supersonic to subsonic, and then
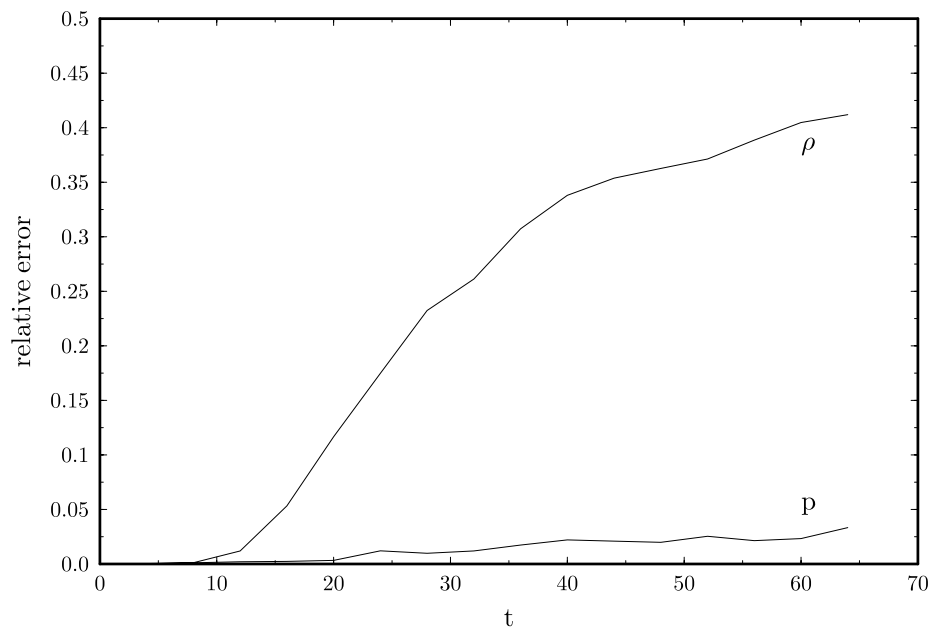
Figure 10: L2 norm of errors in pressure and density compared with the exact solution as defined in (17).
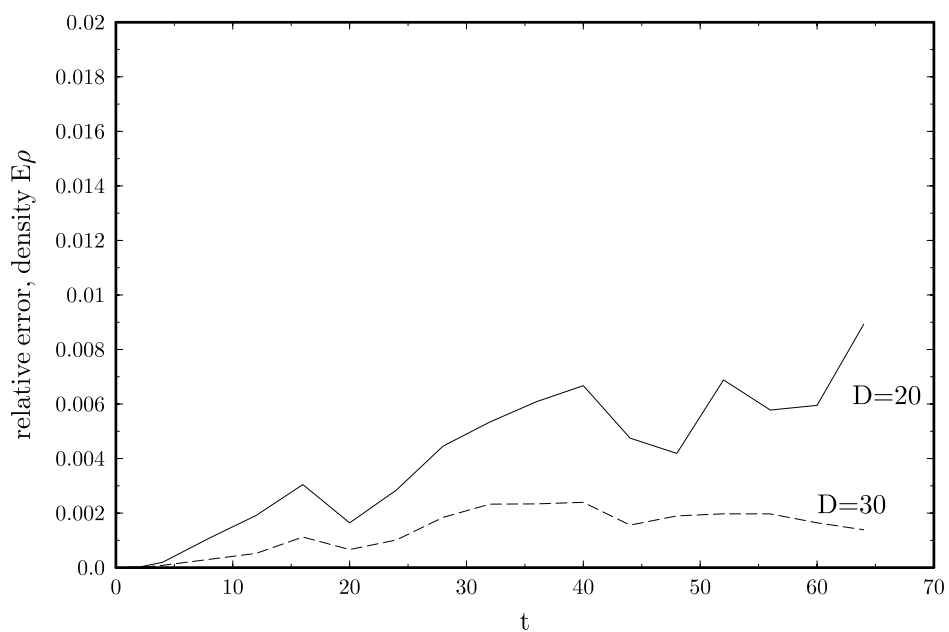
Figure 11: L2 norm of errors in density compared with reference solution. D indicates the number of grid points in side the PML domain.
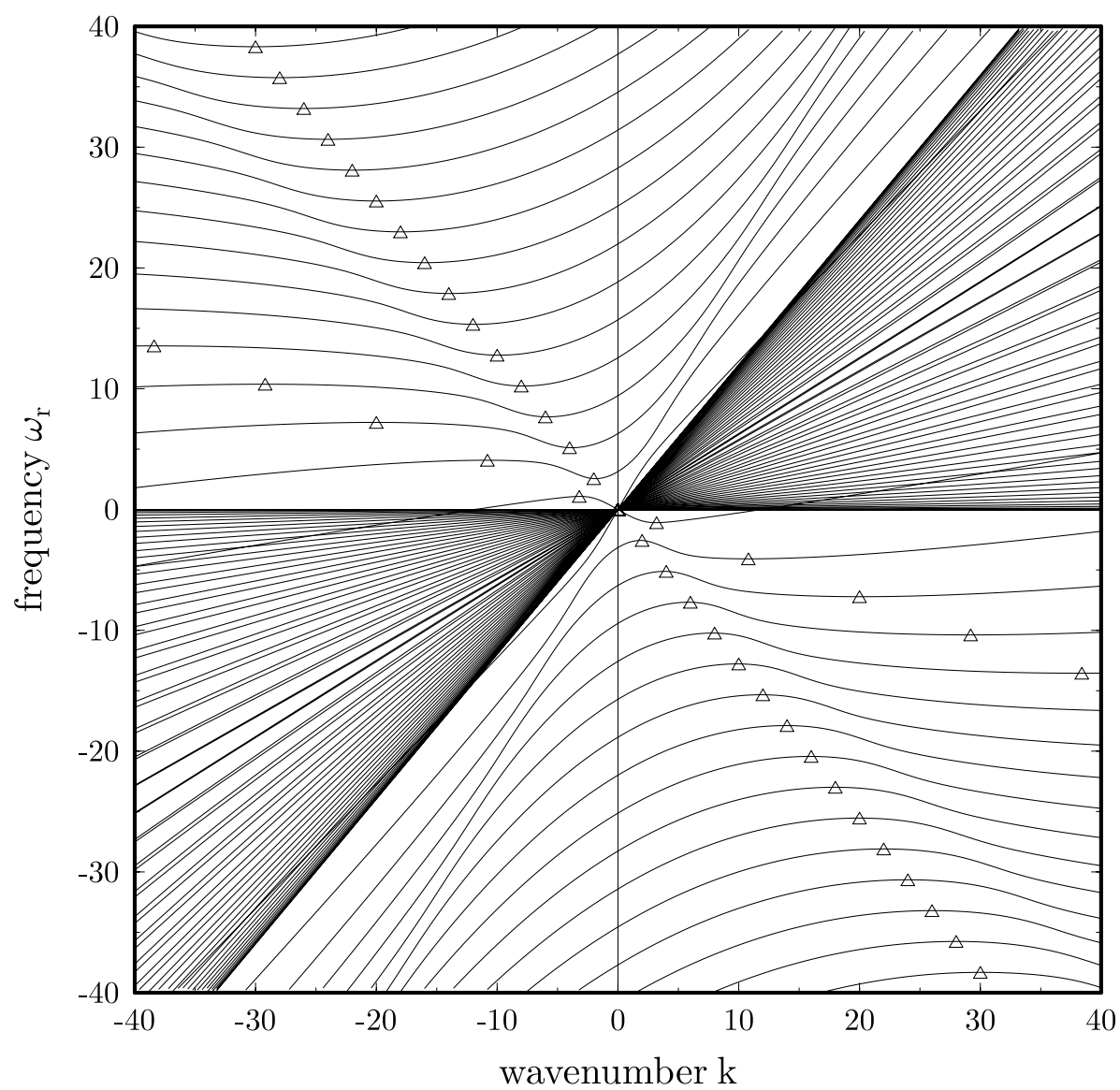
Figure 12: Dispersion diagram of the transonic flow. Triangles denote the points of zero group velocity.
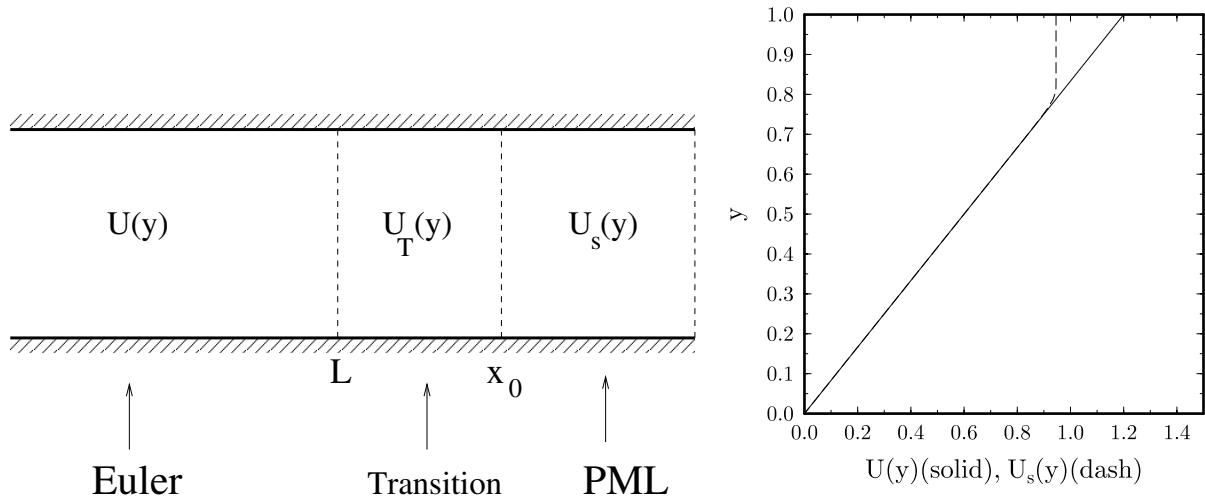
Figure 13: Left: a schematic showing a transition region from supersonic mean flow $U(y)$ to a subsonic mean flow $U_s(y)$; Right: mean velocity for $U(y)$, solid, and $U_s(y)$, dashed.

PML is applied to the subsonic mean flow, as shown in Figure 13. The result is not as good as in the previous case of subsonic flow, but it could be a practical solution as we will demonstrate below.

The subsonic mean velocity is given by

$$U_s(y) = \begin{cases} 1.2y(1 - e^{-(0.9-y)/0.025}) & y < 0.8122 \\ 0.9456 & y \geq 0.8122 \end{cases}$$

In the transition zone, the mean flow is morphed gradually from $U(y)$ at $x = L$ to $U_s(y)$ at $x = x_0$,

$$U_T(y) = (1 - \xi^2)U(y) + \xi^2 U_s(y), \text{ where } \xi = \frac{x - L}{x_0 - L}.$$

Figure 14 shows the pressure contours at $t = 16$ and $t = 32$, together with the exact solutions. In this computation, we have used a uniform grid of $\Delta x = \Delta y = 1/64$. The mean velocity transition zone has 20 grid points, with $L = 2.0$ and $x_0 = 2.3125$. The PML domain has 20 grid points as well. Due to a relatively short span of the PML zone, there are visible reflected waves from the end of the PML zone. However, inside the physical domain, the agreements on the contours between the numerical and exact solutions are generally good. Of course the solution can be further improved by using more grid points in the transition and PML zones.

CONCLUSIONS

Numerical solutions to problems 1 and 3 in Category 1 have been presented. The calculation and analysis for Problem 1 show that the built-in dissipation mechanism of the discontinuous Galerkin method affects only the unresolved high frequency oscillations and leaves the resolved waves intact. For the Perfectly Matched Layer nonreflecting boundary condition, we have shown that it is possible to derive stable PML equation for the linearized Euler equation with a nonuniform mean flow based on a dispersive wave analysis of the physical wave system. The parameter in the PML equation is intimately linked to the dispersion relations of linear waves of the Euler equation. The PML shown in this paper is applicable to a broad class of nonuniform mean flows. Its extension to fully nonlinear Euler equation will be presented in a future work.
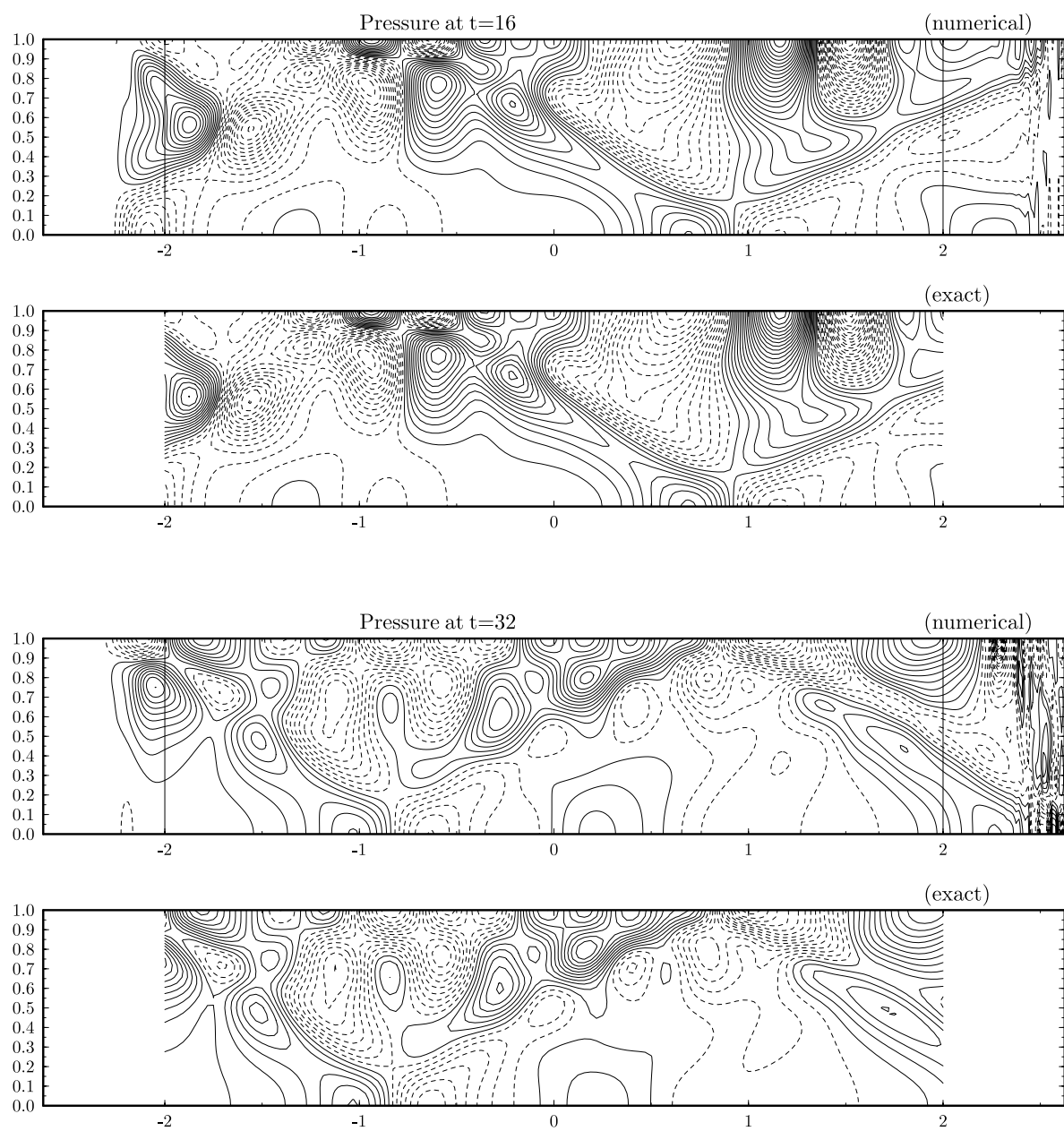
Figure 14: Pressure contours at $t = 16$ and 32 for the transonic mean flow.

References

[1] H. Atkins and C.-W. Shu, Quadrature-free implementation of discontinuous Galerkin methods for hyperbolic equations, *AIAA Journal*, Vol.36, 775-782, 1998.

[2] E. Becache, S. Fauqueux and P. Joly, Stability of perfectly matched layers, group velocities and anisotropic waves, *Journal of Computational Physics*, Vol. 188, 399-433, 2003.

[3] B. Cockburn and C.-W. Shu, The Runge-Kutta discontinuous Galerkin method for the conservation Laws V, *Journal of Computational Physics*, Vol. 141, 199-224, 1998.

[4] F. Collino and P. Monk, The perfectly matched layer in curvilinear coordinates, *SIAM J. Sci, Comp*, Vol. 19, No. 6, P. 2016, 1998.

[5] P. G. Drazin and W. H. Reid, *Hydrodynamic stability*, Cambridge University Press, 1981.

[6] S. D. Gedney, An anisotropic perfectly matched layer-absorbing medium for the truncation of FDTD lattices, *IEEE Trans. Antennas Propagation*, Vol. 44, P. 1630, 1996.

[7] T. Hagstrom and I. Nazarov, Absorbing layers and radiation boundary conditions for jet flow simulations, AIAA paper 2002-2606, 2002.

[8] T. Hagstrom and I. Nazarov, Perfectly matched layers and radiation boundary conditions for shear flow calculations, AIAA paper 2003-3298, 2003.

[9] F. Q. Hu, A stable,Perfectly Matched Layer for linearized Euler equations in unsplit physical variables, Journal of Computational Physics, Vol. 173, 455-480, 2001.

[10] F. Q. Hu, Absorbing boundary conditions (a review), to appear in *International Journal of Computational Fluid Dynamics*, 2004.

[11] F. Q. Hu, On using Perfectly Matched Layer for the Euler equations with a non-uniform mean flow, AIAA paper for the 10-th AIAA/CEAS Aeroacoustics Conference, 2004.

[12] F. Q. Hu and H. L. Atkins, Eigensolution analysis of discontinuous Galerkin method. Part I, One space dimension, *Journal of Computational Physics*,Vol. 182, 516-545, 2002.

[13] F. Q. Hu and H. L. Atkins, Two-dimensional wave analysis of the discontinuous Galerkin method with non-uniform grids and boundary conditions, AIAA-paper 2002-2514, 2002.

[14] F. Q. Hu, M. Y. Hussaini and J. L. Manthey, Low dissipation and low dispersion Runge-Kutta schemes for computational acoustics, *Journal of Computational Physics*, Vol. 124, 177-191, 1996.

[15] F. Q. Hu, M. Y. Hussaini and P. Rasetarinera, An analysis of the discontinuous Galerkin method for wave propagation problems, *Journal of Computational Physis*c, Vol. 151, 921-946, 1999.

[16] F. Q. Hu and C. K. W. Tam, Parametric instability of supersonic shear layers induced by periodic Mach wave, *Physics of Fluids A*, Vol. 6, No. 3, 1645-1656, 1991.

[17] L. M. Mack, On the inviscid acoustic-mode instability of supersonic shear flows, *Theoretical and Computational Fluid Dynamics*, Vol. 2, 97-123, 1990.

[18] C. K. W. Tam, L. Auriault and F. Cambulli, Perfectly Matched Layer as an absorbing boundary condition for the linearized Euler equations in open and ducted domains, *Journal of Computational Physics*, **144**, 213-234, 1998.

[19] C. K. W. Tam and F. Q. Hu, On the three families of instability waves of high-speed jets, *Journal of Fluid Mechanics*, Vol. 201, 447-483, 1989.

[20] C. K. W. Tam and J. C. Webb, Dispersion-relation-preserving finite difference schemes for computational acoustics, *Journal of Computational Physics*, Vol. 107, 262-281, 1993.

[21] E. Turkel and A. Yefet, Absorbing PML boundary layers for wave-like equations, *Applied Numerical Mathematics*, Vol. 27, 533-557, 1998.

[22] G. B. Witham, *Linear and nonlinear waves*, Willey, 1978.

Solutions of Category 1 Problems Using High-Order Difference Methods and Perfectly Matched Layers

Thomas Hagstrom[1] and Igor Nazarov
Dept. of Mathematics and Statistics
The University of New Mexico, Albuquerque, NM 87131
email: hagstrom@math.unm.edu, FAX: (505) 277-5505.

ABSTRACT

We present solutions to the three category 1 benchmark problems: the test of the dispersion characteristics of our difference methods, the scattering of a plane wave off an interface, and the propagation of a pulse through an artificial boundary for a skewed uniform flow and for subsonic Couette flow.

Our base numerical method is the combination of maximal order central differences in space with standard fourth order Runge-Kutta methods in time. Near boundaries we add additional mesh points to stabilize the one-sided differencing, which allows us to stably implement methods of orders in the twenties with nonoverlapping multiple domains. For problem 1 we also test Hermite difference methods. These use staggered two-point stencils and time-march via Taylor series with the order increased by carrying derivative data. For the Hermite methods no special treatments of the boundaries are required. For each type of discretization we consider various orders.

To truncate the domain we use a multi-parameter family of reflectionless sponge layers or PMLs. We study the accuracy and stability of the solutions as a function of the layer width and parameters, and the robustness of the parameter choices as the problems change.

PROBLEM 1

Standard Difference Methods

For these experiments we use the standard, order-$2q$ central difference approximations to approximate $u_x(x_k)$ using $u(x_{k+j})$, $j = -q, \ldots, q$. In time we use the standard 4-stage, 4th-order Runge-Kutta method. As we were mainly interested in studying the spatial differencing to high-order we used a small time-step, $\Delta t = 10^{-3}$, that is $800,000$ time steps.

To use high-order difference methods near boundaries one must introduce one-sided formulas which can adversely effect both the stability and the accuracy. Our technique for stabilizing one-sided differencing is to add a small number of additional mesh points near the boundaries in combination with the

Order, $2q$	No. of additional pts.	Location of additional pts.
8	1	$0.2h$
16	2	$0.1h$, $0.53h$
22	3	$0.1h$, $0.43h$, $1.76h$

Table 1: Meshes for stabilized one-sided differencing. h is the interior mesh width and the additional points near a left boundary of $x = 0$ are shown.

maximal order one-sided approximations computed using the first (last) $2q + 1$ function values. (See, e.g., [3].) The number of additional points required depends on the method order. Their location has been optimized by a simple numerical search. Here we consider three choices for the additional points in conjunction with methods of different order: a mesh with one additional point for 8th order; two additional points for 16th order; and three additional points for 22nd order. The details are given in Table 1. Note that we have not constructed boundary stabilizations for methods of order higher than 22. It should be emphasized that we do *not* pay a stability penalty for the small cells introduced by this technique. We also note that the first mesh has one extra point in the first regular cell, the second has two extra points in the first regular cell, while the third has two points in the first regular cell and one in the second.

To minimize the effects of the domain boundaries we compute on a very large domain, $-80 \leq x \leq 880$. We consider two cases; in the first the extra points are only used near -80 and 880, and do not interact much with the solution. In the second case we break the region into 10 subdomains. We use one-sided differencing near each subdomain boundary, and the additional points are put at the right and left boundaries of each subdomain. As the wave propagates across these subdomain boundaries the accuracy and stability of the boundary treatment is tested. We also tried some even higher order methods, $2q = 30$ and $2q = 40$. For these we have no stable one-sided boundary treatment and so we simply imposed periodic boundary conditions.

On the prescribed mesh, the 8th order method leaves behind an obvious tail due to numerical dispersion. As the order is increased this tail is still visible, but is located closer to the primary wave. Only at 30th order is this error small. We see some differences in the structure of the tail between the single domain and multidomain cases, but no appreciable differences in the error levels.

The relative l_2-errors at $t = 800$ are between 40% and 50% for the 8th and 16th order methods, between 30% and 35% for the 22nd order method, from 6% to 7% for the 30th order method, and below 1% for the 40th order method. Due to aliasing effects, there was not much difference between $\alpha = 1.7$ and $\alpha = 4.6$. For the second class of methods we test this is not the case.

On the following pages we plot the computed solution together with the exact solution for orders 22 and 30.
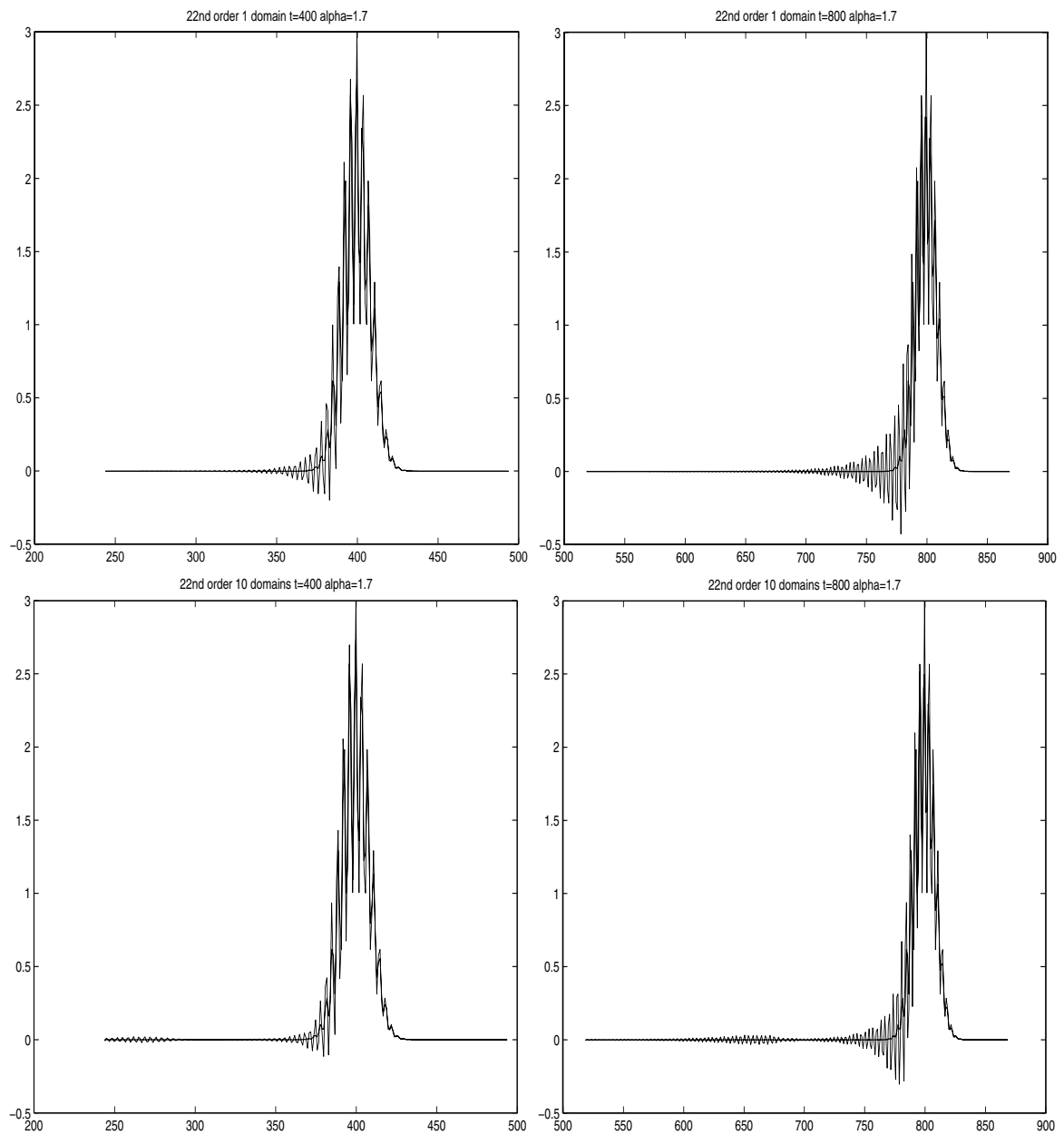
Figure 1: 22nd order solutions, $\alpha = 1.7$.
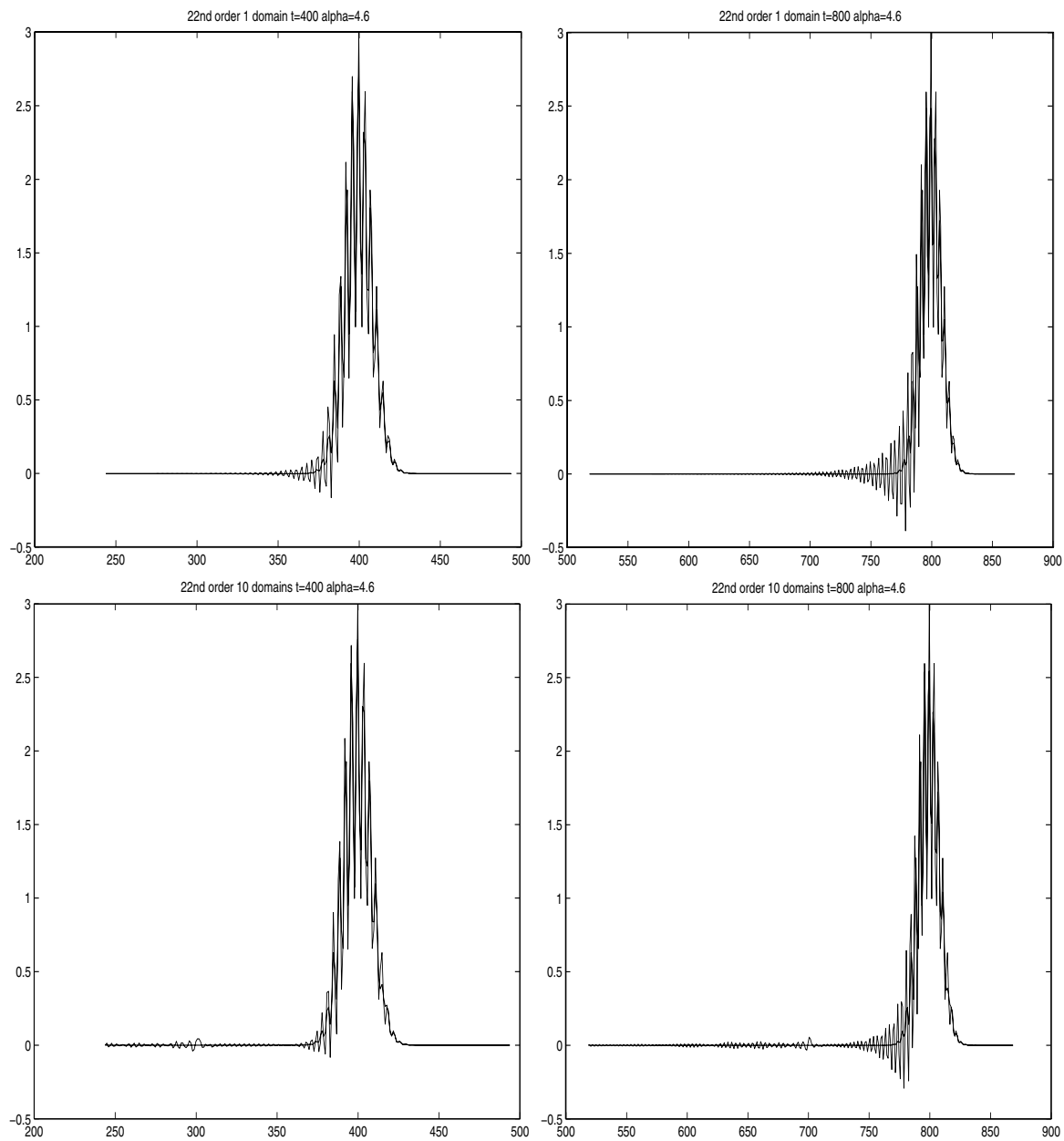
Figure 2: 22nd order solutions, $\alpha = 4.6$.
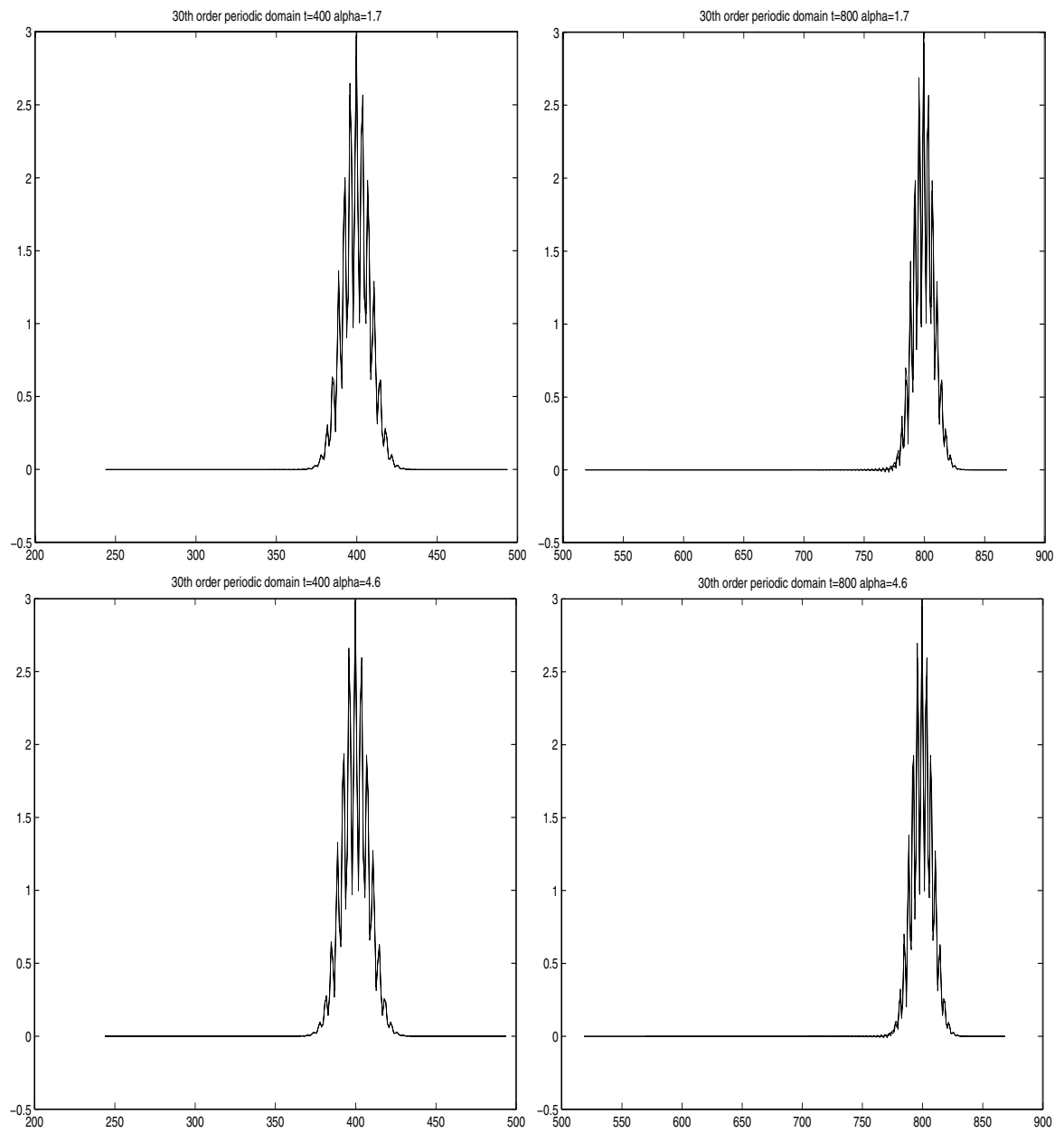
Figure 3: 30th order solutions, $\alpha = 1.7$ and 4.6.

Hermite Methods

The second class of methods we used are the Hermite-Taylor methods. These evolve derivative as well as function data on a staggered grid using Hermite interpolation and temporal Taylor series [1, 2]. We always use a two point stencil. Then if we carry derivatives up through order m, the method order, in space and time, is $2m + 1$. An advantage of this approach is that no special treatment near boundaries is required. We note that in contrast with the central difference schemes tested earlier, the Hermite-Taylor methods are primarily dissipative, thought not in the usual norms. Thus the effects of underresolution do not manifest themselves as dispersive tails, but rather as incorrect amplitudes. Generally, these amplitudes are smaller than those of the exact solution, though in the limit of gross underesolution they can be bigger.

We tested methods with $m = 3, 7, 15, 23$, that is of order $7, 15, 31, 47$. In some sense, the Hermite methods have an unfair advantage for the problem as stated, as they use many more degrees-of-freedom per gridpoint than a simple difference method. As a result, the higher order Hermite methods with $dx = 1$ provide many digits of accuracy, so that further increases in m become pointless. Thus we have also included results with much larger values of dx. Here we interpolate results back onto the prescribed grid for purposes of comparison. We cannot, in general, take $dx = m$, so that we are using more degrees-of-freedom than the difference methods. However, we are able to take huge time steps. We generally used a CFL number of about 1/2. Thus, for example, when $dx = 20$, our coarsest mesh, we took $dt > 8$. This makes the codes run very fast.

We summarize the results in the following table. Note that, unlike what we observed for the difference methods, the larger value of α required larger values of m or a smaller value of dx, as the use of derivative data eliminates the aliasing effect.

Finally, we plot some results on the coarser grids from the table along with the exact solution for $m = 3$ and $m = 23$. The dissipative rather than dispersive character of the error is obvious.

PROBLEM 2

Set-up and Methods

The solution to the problem is periodic in t with period:

$$T = \frac{2\pi}{\omega}, \tag{1}$$

and periodic in x with period:

$$X = \frac{T}{\sin \theta}. \tag{2}$$

We solve the equations for the scattered fields in fluids 1,2 on the regions D_1, D_2:

$$D_1 = (0, X) \times (0, X), \quad D_2 = (0, X) \times (-X, 0). \tag{3}$$
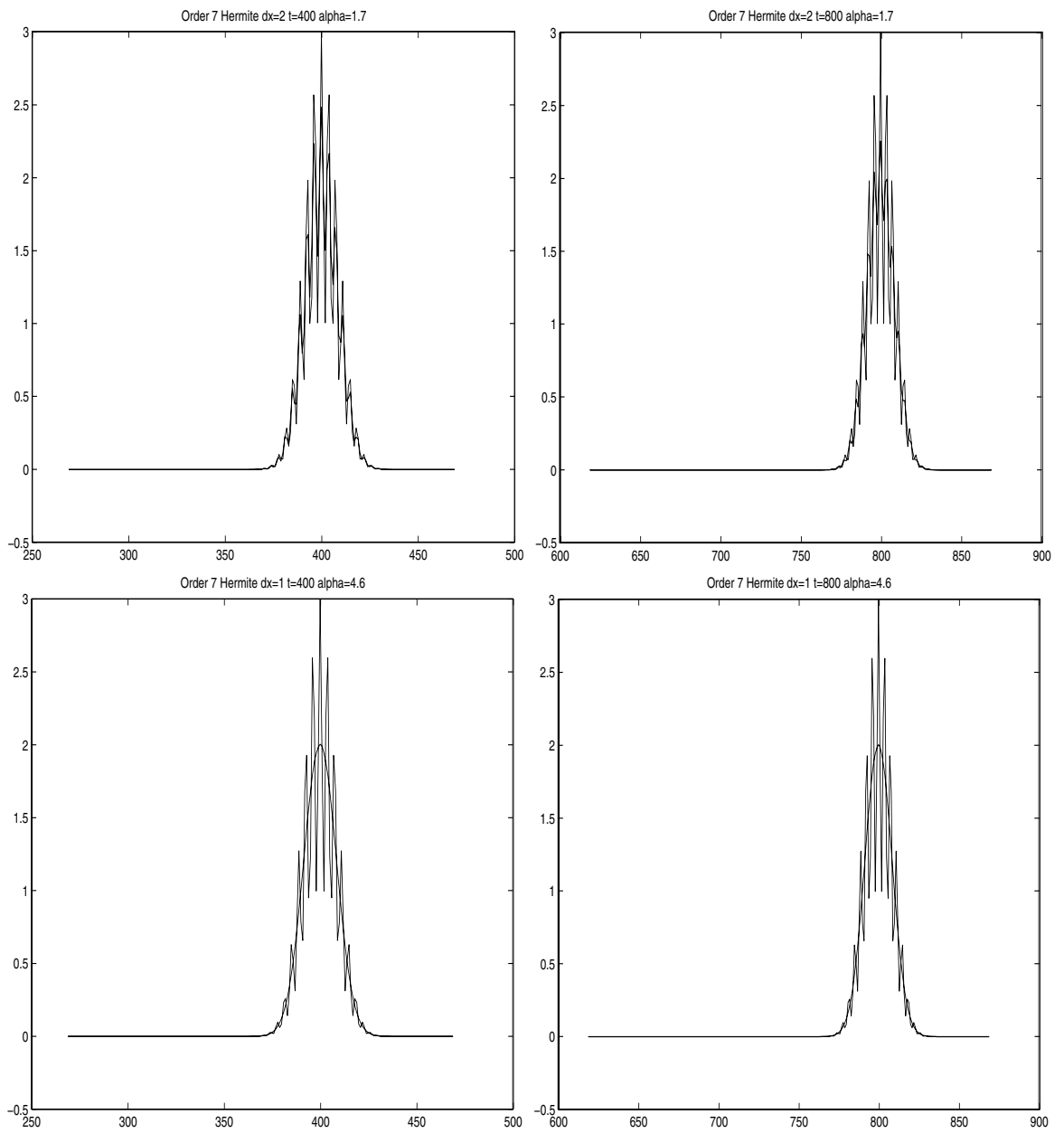
Figure 4: 7th order Hermite solutions.
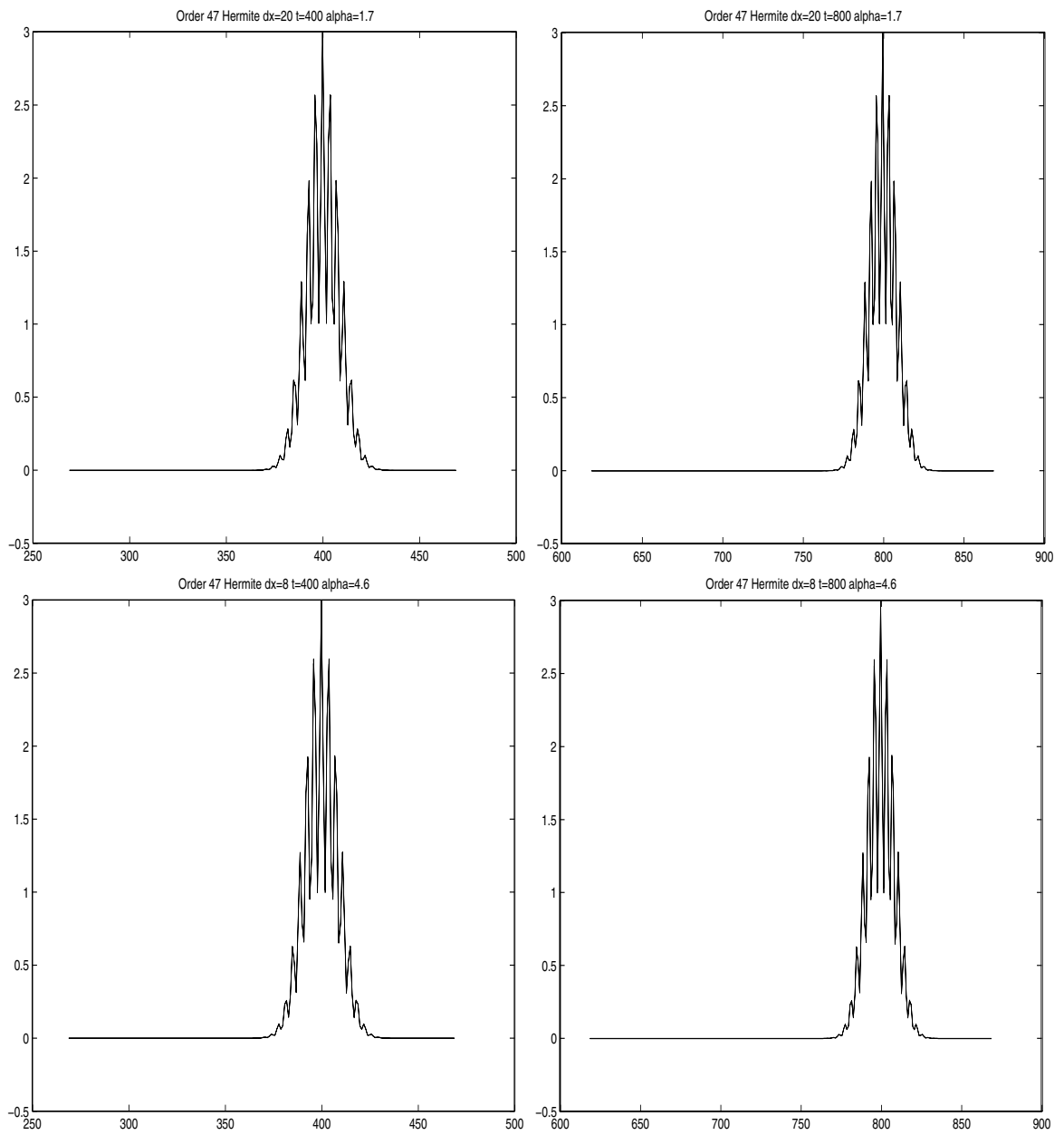
Figure 5: 47th order Hermite solutions.

m	dx	α	Rel. err. $t = 800$
3	1	1.7	5×10^{-3}
3	2	1.7	3×10^{-1}
3	1	4.6	3×10^{-1}
7	1	1.7	2×10^{-11}
7	5	1.7	4×10^{-2}
7	1	4.6	9×10^{-6}
7	2	4.6	2×10^{-1}
15	10	1.7	4×10^{-5}
15	14	1.7	7×10^{-2}
15	4	4.6	2×10^{-4}
15	5	4.6	4×10^{-2}
23	16	1.7	2×10^{-6}
23	20	1.7	2×10^{-3}
23	6	4.6	1×10^{-6}
23	8	4.6	1×10^{-2}

Table 2: Relative errors for the Hermite-Taylor methods - various orders and meshes.

We impose periodic boundary conditions in x, that is for any variable w in each region:

$$w(x + X, y, t) = w(x, y, t). \tag{4}$$

The interface conditions at $y = 0$ are the continuity of p and v for the total fields. Thus for the scattered fields we impose:

$$p_1 + \cos\left(\omega(\sin\theta \cdot x + t)\right) = p_2, \tag{5}$$

$$v_1 - \cos\theta\cos\left(\omega(\sin\theta \cdot x + t)\right) = v_2. \tag{6}$$

At the top and bottom of the domains we attach a reflectionless sponge layer or PML [7, 8, 5, 6, 4]. These occupy the regions S_j:

$$S_1 = (0, X) \times (X, 2X), \quad S_2 = (0, X) \times (-X, -2X). \tag{7}$$

Within the layers we solve a modified system with two additional variables. It is a special case of the system with 8 additional variables used for Problem 3. It will be described in more detail when that problem is discussed.

For the experiments shown we used 22nd order difference approximations. In x this was the standard central difference formula, as the solution can be extended outside the mesh using periodicity. In y, on the other hand, we use the stabilized one-sided difference methods described above. Accounting for the extra points near the interfaces, the meshes in D_1 and D_2 were 20×26. These are sufficient for providing excellent accuracy - errors below 1% in each domain. Note that the method requires a 23 point stencil, so we are at the limit

θ	$\frac{\|p_{1,\text{comp}} - p_{1,\text{exact}}\|}{\|p_{1,\text{exact}}\|}$	$\frac{\|p_{2,\text{comp}} - p_{2,\text{exact}}\|}{\|p_{2,\text{exact}}\|}$	No. of periods	CPU time (min:sec)
$\frac{\pi}{9}$	$7.7(-5)$	$4.3(-3)$	1062	$8:13$
$\frac{13\pi}{36}$	$8.8(-4)$	$8.8(-3)$	182	$3:33$

Table 3: Summary of Results: Problem 2

of the coarsest mesh we can use. We also used 16th and 8th order methods on grids of the same interior width, with two stabilizing points for the 16th order method and 1 for the 8th. The results with the 16th order method were nearly as accurate, while those with order 8 were less so.

In time we use the standard 4-stage, 4th-order Runge-Kutta method. The time step was:

$$\Delta t = \begin{cases} \frac{T}{40}, & \theta = \frac{\pi}{9}, \\ \frac{T}{100}, & \theta = \frac{13\pi}{36}. \end{cases} \tag{8}$$

(The smaller time step in the second case is associated with the smaller spatial grid.) The code was run until the solution became nearly periodic. Precisely, we ran until the sum of the relative change in the pressures in each region was smaller than a tolerance of 10^{-5} over a period, T.

The absorbing layer widths were also chosen to be X, so that each layer contained 20×26 points. Again, we had to have at least 23 points to contain a single stencil width. The other parameters were:

$$\sigma_{\max} = 20\omega, \quad \eta = \frac{1}{6X}, \quad \delta = \frac{1}{2}. \tag{9}$$

Results

We measured the relative l_2-error in the scattered fields in each case, using the exact solution to compute it. The final results are summarized in Table 3.

Clearly the results are accurate, particularly in domain 1 where the errors are less than .01% in the first case and .1% in the second. Note that many fewer periods were required to achieve convergence in the second case. The timing results were obtained on an AMD Athlon XP 2200, 1800mHz, 1.56gb of ram. The code was compiled using the Portland Group f77 compiler at optimization level 3.

Lastly we plot contours of the full and scattered fields. Note the scattered fields are discontinuous, which caused some problems for the contour plotter, as did the coarseness of our mesh. In fact, the "wiggles" in some of the contours are due purely to the contouring routine. Clearly there are no visible distortions at the abosrbing layer interfaces.
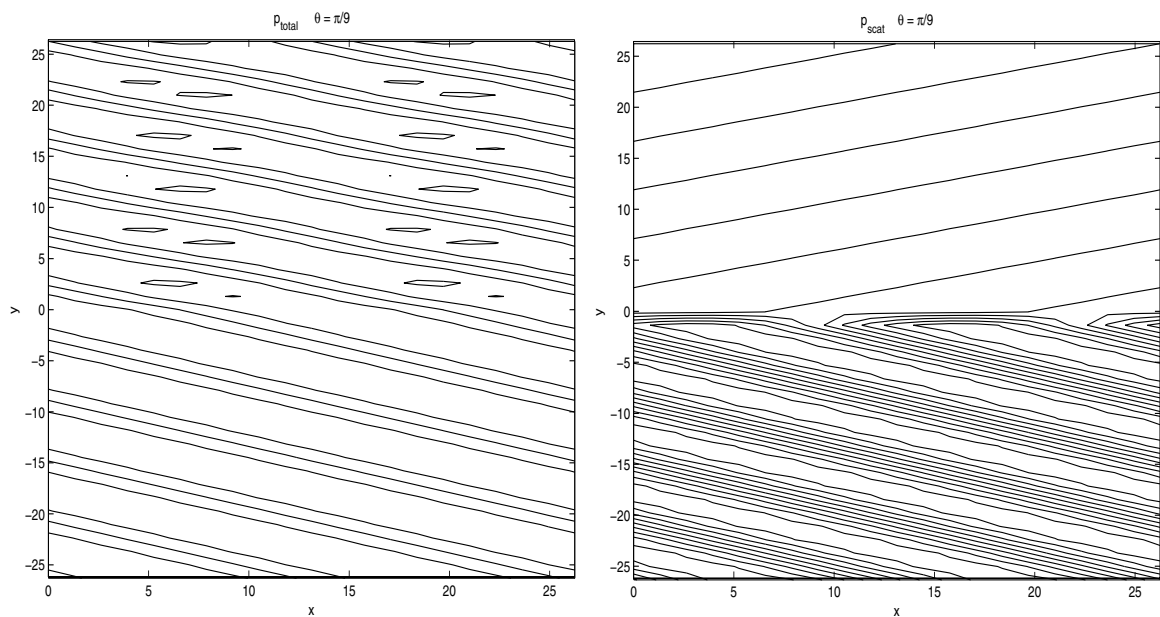
Figure 6: Full and scattered fields, $\theta = \frac{\pi}{9}$.
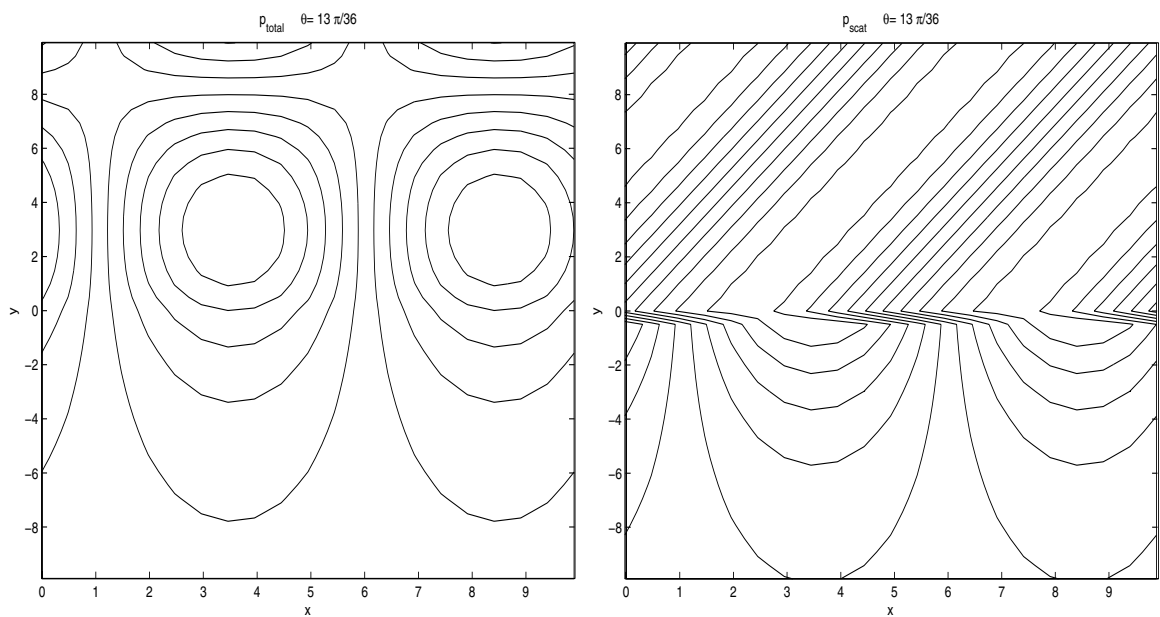
Figure 7: Full and scattered fields, $\theta = \frac{13\pi}{36}$.

PROBLEM 3

Methods

For the experiments shown we used the 8th order difference method with $\Delta x = \Delta y = \frac{1}{128}$, with one-sided differencing stabilized as described above. In time we used a 4th order 4-stage Runge-Kutta method with various time steps as indicated on the tables.

We attached reflectionless sponge layers at inflow and outflow. The layer equations are given by [4, 6]:

$$\frac{\partial \rho}{\partial t} \quad +U(y)\left(\frac{\partial \rho}{\partial x} + \sigma\mu\rho + \psi_{1,\rho} + \psi_{2,\rho}\right) \tag{10}$$
$$+\frac{\partial u}{\partial x} + \sigma\mu u + \psi_{1,u} + \psi_{2,u} + \frac{\partial v}{\partial y} \quad = 0,$$

$$\frac{\partial u}{\partial t} \quad +U(y)\left(\frac{\partial u}{\partial x} + \sigma\mu u + \psi_{1,u} + \psi_{2,u}\right) \tag{11}$$
$$+U'(y)v + \frac{\partial p}{\partial x} + \sigma\mu p + \psi_{1,p} + \psi_{2,p} \quad = 0,$$

$$\frac{\partial v}{\partial t} + U(y)\left(\frac{\partial v}{\partial x} + \sigma\mu v + \psi_{1,v} + \psi_{2,v}\right) + \frac{\partial p}{\partial y} = 0, \tag{12}$$

$$\frac{\partial p}{\partial t} \quad +U(y)\left(\frac{\partial p}{\partial x} + \sigma\mu p + \psi_{1,p} + \psi_{2,p}\right) \tag{13}$$
$$+\frac{\partial u}{\partial x} + \sigma\mu u + \psi_{1,u} + \psi_{2,u} + \frac{\partial v}{\partial y} \quad = 0,$$

and for $s = \rho, u, v, p$:

$$\frac{\partial \psi_{1,s}}{\partial t} + (\alpha + \sigma)\psi_{1,s} + \sigma\left(\frac{\partial s}{\partial x} + \sigma\mu s + \psi_{2,s}\right) = 0, \tag{14}$$

$$\frac{\partial \psi_{2,s}}{\partial t} + \alpha\psi_{2,s} + \sigma\mu\alpha s = 0. \tag{15}$$

Note that these equations generalize those used for Problem 2. We emphasize that the interface, $x = L$, is nonreflecting for *any* choice of α, μ and σ. The difficulty is to choose them so that all waves are damped. For linearizations about a uniform flow we have shown that the unique choice $\mu = U/(1 - U^2)$ achieves absorption for all waves of all families. (Cross flow is also allowed in this case. It is simply necessary to replace the time derivatives by tangential material derivatives.) Here we use $\sigma_{\max} \tanh\gamma(x - x_L)$ as our absorption profile and use characteristic matching across the layer interface.

t	Part 1. $L = 0.5$, $dt = 1/1500$			
	u	v	p	ρ
1.0	$3.2 \cdot 10^{-10}$	$8.0 \cdot 10^{-10}$	$7.1 \cdot 10^{-10}$	$2.2 \cdot 10^{-10}$
2.0	$3.1 \cdot 10^{-10}$	$7.4 \cdot 10^{-10}$	$1.1 \cdot 10^{-9}$	$1.9 \cdot 10^{-10}$
3.0	$4.8 \cdot 10^{-8}$	$3.9 \cdot 10^{-8}$	$1.5 \cdot 10^{-7}$	$2.0 \cdot 10^{-8}$
4.0	$4.3 \cdot 10^{-7}$	$4.6 \cdot 10^{-7}$	$1.6 \cdot 10^{-6}$	$1.8 \cdot 10^{-7}$
8.0	$2.2 \cdot 10^{-4}$	$2.0 \cdot 10^{-4}$	$4.1 \cdot 10^{-4}$	$4.1 \cdot 10^{-4}$
12.0	$4.0 \cdot 10^{-3}$	$6.5 \cdot 10^{-3}$	$2.2 \cdot 10^{-3}$	$2.2 \cdot 10^{-3}$
16.0	$1.3 \cdot 10^{-2}$	$1.1 \cdot 10^{-2}$	$2.0 \cdot 10^{-2}$	$2.0 \cdot 10^{-2}$
20.0	$2.1 \cdot 10^{-2}$	$3.9 \cdot 10^{-2}$	$3.1 \cdot 10^{-2}$	$3.1 \cdot 10^{-2}$
24.0	$4.8 \cdot 10^{-2}$	$6.2 \cdot 10^{-2}$	$5.4 \cdot 10^{-2}$	$5.4 \cdot 10^{-2}$
28.0	$7.4 \cdot 10^{-2}$	$7.6 \cdot 10^{-2}$	$9.0 \cdot 10^{-2}$	$9.0 \cdot 10^{-2}$
32.0	$8.7 \cdot 10^{-2}$	$1.2 \cdot 10^{-1}$	$1.0 \cdot 10^{-1}$	$1.0 \cdot 10^{-1}$
36.0	$1.3 \cdot 10^{-1}$	$1.4 \cdot 10^{-1}$	$1.4 \cdot 10^{-1}$	$1.4 \cdot 10^{-1}$
40.0	$1.6 \cdot 10^{-1}$	$1.7 \cdot 10^{-1}$	$1.7 \cdot 10^{-1}$	$1.7 \cdot 10^{-1}$
44.0	$1.8 \cdot 10^{-1}$	$2.1 \cdot 10^{-1}$	$1.9 \cdot 10^{-1}$	$1.9 \cdot 10^{-1}$
48.0	$2.2 \cdot 10^{-1}$	$2.3 \cdot 10^{-1}$	$2.3 \cdot 10^{-1}$	$2.3 \cdot 10^{-1}$
52.0	$2.5 \cdot 10^{-1}$	$2.7 \cdot 10^{-1}$	$2.7 \cdot 10^{-1}$	$2.7 \cdot 10^{-1}$
56.0	$2.8 \cdot 10^{-1}$	$3.0 \cdot 10^{-1}$	$3.0 \cdot 10^{-1}$	$3.0 \cdot 10^{-1}$

Results

We get good results with width 1-1.5 layers for Parts 1 and 2, and some accuracy for $L = 0.5$. Layer parameters $\sigma_{max} = 20.0$ and $\gamma = 4.0$ were used. For Part 1 (constant coefficient case), optimal parameters are $\mu = m_x/(1 - m_x^2) = .4/(1 - .4^2)$. For Part 2, different values of α and μ were tried. The best case has been found to be $\mu = .5$, $\alpha = .5$. There is little difference between the performance of the methods for Parts 1 and 2.

For Part 3 (transonic problem) our results are much worse. For stability we need to shut off the layer parameters in the supersonic region which leads to a loss of accuracy. We show no results in this case.

References

[1] J. Goodrich. Accurate finite difference algorithms. In V. Venkatakrishnan, M. Salas, and S. Chakravarthy, editors, *Barriers and Challenges in Computational Fluid Dynamics*, pages 43–61, Dordrecht, 1998. Kluwer Academic Publishers.

[2] J. Goodrich, J. Lorenz, and T. Hagstrom. Hermite methods for hyperbolic initial-boundary value problems. In preparation.

[3] T. Hagstrom. Experiments with stable, high-order difference approximations to hyperbolic initial-boundary value problems. In A. Bermudez, D. Gomez,

t	Part 1. $L = 1.0$, $dt = 1/1000$			
	u	v	p	ρ
1.0	$2.2 \cdot 10^{-9}$	$5.6 \cdot 10^{-9}$	$4.9 \cdot 10^{-9}$	$1.5 \cdot 10^{-9}$
2.0	$9.8 \cdot 10^{-10}$	$5.0 \cdot 10^{-9}$	$6.2 \cdot 10^{-9}$	$1.0 \cdot 10^{-9}$
3.0	$9.0 \cdot 10^{-10}$	$4.3 \cdot 10^{-9}$	$6.5 \cdot 10^{-9}$	$8.8 \cdot 10^{-10}$
4.0	$1.2 \cdot 10^{-9}$	$6.0 \cdot 10^{-9}$	$9.0 \cdot 10^{-9}$	$1.0 \cdot 10^{-9}$
8.0	$1.8 \cdot 10^{-8}$	$2.3 \cdot 10^{-8}$	$2.2 \cdot 10^{-8}$	$2.2 \cdot 10^{-8}$
12.0	$3.8 \cdot 10^{-8}$	$3.7 \cdot 10^{-8}$	$4.0 \cdot 10^{-8}$	$4.0 \cdot 10^{-8}$
16.0	$1.3 \cdot 10^{-6}$	$1.2 \cdot 10^{-6}$	$1.5 \cdot 10^{-6}$	$1.5 \cdot 10^{-6}$
20.0	$3.0 \cdot 10^{-5}$	$2.9 \cdot 10^{-5}$	$2.3 \cdot 10^{-5}$	$2.3 \cdot 10^{-5}$
24.0	$1.9 \cdot 10^{-4}$	$1.6 \cdot 10^{-4}$	$1.8 \cdot 10^{-4}$	$1.8 \cdot 10^{-4}$
28.0	$5.1 \cdot 10^{-4}$	$4.1 \cdot 10^{-4}$	$6.9 \cdot 10^{-4}$	$6.9 \cdot 10^{-4}$
32.0	$1.0 \cdot 10^{-3}$	$1.4 \cdot 10^{-3}$	$1.5 \cdot 10^{-3}$	$1.5 \cdot 10^{-3}$
36.0	$2.2 \cdot 10^{-3}$	$3.6 \cdot 10^{-3}$	$2.1 \cdot 10^{-3}$	$2.1 \cdot 10^{-3}$
40.0	$5.0 \cdot 10^{-3}$	$5.7 \cdot 10^{-3}$	$4.7 \cdot 10^{-3}$	$4.7 \cdot 10^{-3}$
44.0	$8.3 \cdot 10^{-3}$	$6.2 \cdot 10^{-3}$	$9.5 \cdot 10^{-3}$	$9.5 \cdot 10^{-3}$
48.0	$9.2 \cdot 10^{-3}$	$1.2 \cdot 10^{-2}$	$1.1 \cdot 10^{-2}$	$1.1 \cdot 10^{-2}$
52.0	$1.3 \cdot 10^{-2}$	$1.9 \cdot 10^{-2}$	$1.3 \cdot 10^{-2}$	$1.3 \cdot 10^{-2}$
56.0	$2.3 \cdot 10^{-2}$	$1.9 \cdot 10^{-2}$	$2.4 \cdot 10^{-2}$	$2.4 \cdot 10^{-2}$
60.0	$2.5 \cdot 10^{-2}$	$2.6 \cdot 10^{-2}$	$2.8 \cdot 10^{-2}$	$2.8 \cdot 10^{-2}$
64.0	$2.7 \cdot 10^{-2}$	$4.0 \cdot 10^{-2}$	$2.8 \cdot 10^{-2}$	$2.8 \cdot 10^{-2}$

t	Part 1. $L = 1.5$, $dt = 1/2000$			
	u	v	p	ρ
1	$2.1 \cdot 10^{-15}$	$3.7 \cdot 10^{-15}$	$2.9 \cdot 10^{-15}$	$2.2 \cdot 10^{-15}$
2	$4.6 \cdot 10^{-15}$	$7.1 \cdot 10^{-15}$	$1.0 \cdot 10^{-14}$	$5.0 \cdot 10^{-15}$
3	$5.8 \cdot 10^{-15}$	$9.5 \cdot 10^{-15}$	$1.5 \cdot 10^{-14}$	$6.8 \cdot 10^{-15}$
4	$6.7 \cdot 10^{-15}$	$1.3 \cdot 10^{-14}$	$1.9 \cdot 10^{-14}$	$8.4 \cdot 10^{-15}$
8	$6.9 \cdot 10^{-14}$	$2.9 \cdot 10^{-14}$	$2.9 \cdot 10^{-14}$	$8.7 \cdot 10^{-14}$
12	$1.7 \cdot 10^{-13}$	$4.8 \cdot 10^{-14}$	$8.8 \cdot 10^{-14}$	$1.5 \cdot 10^{-13}$
16	$4.4 \cdot 10^{-12}$	$3.6 \cdot 10^{-12}$	$2.1 \cdot 10^{-12}$	$2.1 \cdot 10^{-12}$
20	$4.6 \cdot 10^{-10}$	$6.9 \cdot 10^{-10}$	$4.8 \cdot 10^{-10}$	$4.8 \cdot 10^{-10}$
24	$1.4 \cdot 10^{-8}$	$9.8 \cdot 10^{-9}$	$2.6 \cdot 10^{-8}$	$2.6 \cdot 10^{-8}$
28	$2.1 \cdot 10^{-7}$	$2.5 \cdot 10^{-7}$	$2.3 \cdot 10^{-7}$	$2.3 \cdot 10^{-7}$
32	$1.0 \cdot 10^{-6}$	$1.8 \cdot 10^{-6}$	$1.7 \cdot 10^{-6}$	$1.7 \cdot 10^{-6}$
36	$6.1 \cdot 10^{-6}$	$5.9 \cdot 10^{-6}$	$1.1 \cdot 10^{-5}$	$1.1 \cdot 10^{-5}$
40	$2.0 \cdot 10^{-5}$	$2.9 \cdot 10^{-5}$	$3.0 \cdot 10^{-5}$	$3.0 \cdot 10^{-5}$
44	$5.1 \cdot 10^{-5}$	$9.5 \cdot 10^{-5}$	$6.4 \cdot 10^{-5}$	$6.4 \cdot 10^{-5}$
48	$1.6 \cdot 10^{-4}$	$2.2 \cdot 10^{-4}$	$1.3 \cdot 10^{-4}$	$1.3 \cdot 10^{-4}$
52	$3.7 \cdot 10^{-4}$	$4.1 \cdot 10^{-4}$	$3.1 \cdot 10^{-4}$	$3.1 \cdot 10^{-4}$
56	$7.0 \cdot 10^{-4}$	$5.0 \cdot 10^{-4}$	$7.2 \cdot 10^{-4}$	$7.2 \cdot 10^{-4}$
60	$9.0 \cdot 10^{-4}$	$8.3 \cdot 10^{-4}$	$1.1 \cdot 10^{-3}$	$1.1 \cdot 10^{-3}$
64	$1.1 \cdot 10^{-3}$	$1.8 \cdot 10^{-3}$	$1.2 \cdot 10^{-3}$	$1.2 \cdot 10^{-3}$

t	Part 2. $L = 0.5$, $dt = 1/1500$			
	u	v	p	ρ
1.0	$1.1 \cdot 10^{-9}$	$1.0 \cdot 10^{-8}$	$9.8 \cdot 10^{-9}$	$3.2 \cdot 10^{-9}$
2.0	$9.2 \cdot 10^{-7}$	$8.8 \cdot 10^{-7}$	$1.5 \cdot 10^{-6}$	$4.7 \cdot 10^{-7}$
3.0	$2.3 \cdot 10^{-6}$	$5.2 \cdot 10^{-6}$	$5.5 \cdot 10^{-6}$	$1.6 \cdot 10^{-6}$
4.0	$7.5 \cdot 10^{-6}$	$2.6 \cdot 10^{-5}$	$2.5 \cdot 10^{-5}$	$7.0 \cdot 10^{-6}$
8.0	$2.0 \cdot 10^{-4}$	$1.0 \cdot 10^{-3}$	$1.1 \cdot 10^{-3}$	$4.3 \cdot 10^{-4}$
12.0	$5.3 \cdot 10^{-3}$	$7.5 \cdot 10^{-3}$	$1.1 \cdot 10^{-2}$	$5.5 \cdot 10^{-3}$
16.0	$1.8 \cdot 10^{-2}$	$3.0 \cdot 10^{-2}$	$2.5 \cdot 10^{-2}$	$1.5 \cdot 10^{-2}$
20.0	$3.7 \cdot 10^{-2}$	$5.4 \cdot 10^{-2}$	$4.8 \cdot 10^{-2}$	$3.2 \cdot 10^{-2}$
24.0	$6.8 \cdot 10^{-2}$	$7.6 \cdot 10^{-2}$	$8.0 \cdot 10^{-2}$	$5.4 \cdot 10^{-2}$
28.0	$9.4 \cdot 10^{-2}$	$1.1 \cdot 10^{-1}$	$1.1 \cdot 10^{-1}$	$7.5 \cdot 10^{-2}$
32.0	$1.5 \cdot 10^{-1}$	$1.5 \cdot 10^{-1}$	$1.4 \cdot 10^{-1}$	$9.5 \cdot 10^{-2}$
36.0	$2.1 \cdot 10^{-1}$	$1.9 \cdot 10^{-1}$	$1.8 \cdot 10^{-1}$	$1.3 \cdot 10^{-1}$
40.0	$2.6 \cdot 10^{-1}$	$2.3 \cdot 10^{-1}$	$2.3 \cdot 10^{-1}$	$1.7 \cdot 10^{-1}$
44.0	$3.1 \cdot 10^{-1}$	$2.5 \cdot 10^{-1}$	$2.7 \cdot 10^{-1}$	$1.9 \cdot 10^{-1}$
48.0	$3.0 \cdot 10^{-1}$	$2.7 \cdot 10^{-1}$	$2.9 \cdot 10^{-1}$	$2.0 \cdot 10^{-1}$
52.0	$2.9 \cdot 10^{-1}$	$3.0 \cdot 10^{-1}$	$3.0 \cdot 10^{-1}$	$2.1 \cdot 10^{-1}$
56.0	$3.0 \cdot 10^{-1}$	$3.6 \cdot 10^{-1}$	$3.2 \cdot 10^{-1}$	$2.3 \cdot 10^{-1}$
60.0	$4.0 \cdot 10^{-1}$	$3.8 \cdot 10^{-1}$	$3.6 \cdot 10^{-1}$	$2.5 \cdot 10^{-1}$
64.0	$5.4 \cdot 10^{-1}$	$3.9 \cdot 10^{-1}$	$4.2 \cdot 10^{-1}$	$2.8 \cdot 10^{-1}$

t	Part 2. $L = 1.0$			
	u	v	p	ρ
1	$7.3 \cdot 10^{-10}$	$6.9 \cdot 10^{-9}$	$6.5 \cdot 10^{-9}$	$2.2 \cdot 10^{-9}$
2	$4.7 \cdot 10^{-10}$	$1.1 \cdot 10^{-8}$	$1.1 \cdot 10^{-8}$	$3.6 \cdot 10^{-9}$
3	$5.4 \cdot 10^{-10}$	$1.2 \cdot 10^{-8}$	$1.4 \cdot 10^{-8}$	$4.1 \cdot 10^{-9}$
4	$7.7 \cdot 10^{-10}$	$1.8 \cdot 10^{-8}$	$1.7 \cdot 10^{-8}$	$4.8 \cdot 10^{-9}$
8	$7.6 \cdot 10^{-9}$	$3.1 \cdot 10^{-8}$	$2.2 \cdot 10^{-8}$	$8.7 \cdot 10^{-9}$
12	$3.8 \cdot 10^{-7}$	$8.3 \cdot 10^{-7}$	$7.1 \cdot 10^{-7}$	$3.7 \cdot 10^{-7}$
16	$6.7 \cdot 10^{-6}$	$1.4 \cdot 10^{-5}$	$1.2 \cdot 10^{-5}$	$7.5 \cdot 10^{-6}$
20	$4.7 \cdot 10^{-5}$	$6.4 \cdot 10^{-5}$	$9.1 \cdot 10^{-5}$	$6.1 \cdot 10^{-5}$
24	$2.0 \cdot 10^{-4}$	$2.8 \cdot 10^{-4}$	$2.6 \cdot 10^{-4}$	$1.7 \cdot 10^{-4}$
28	$6.5 \cdot 10^{-4}$	$8.7 \cdot 10^{-4}$	$6.6 \cdot 10^{-4}$	$4.7 \cdot 10^{-4}$
32	$1.6 \cdot 10^{-3}$	$2.0 \cdot 10^{-3}$	$1.7 \cdot 10^{-3}$	$1.2 \cdot 10^{-3}$
36	$3.1 \cdot 10^{-3}$	$3.4 \cdot 10^{-3}$	$3.7 \cdot 10^{-3}$	$2.6 \cdot 10^{-3}$
40	$4.8 \cdot 10^{-3}$	$5.1 \cdot 10^{-3}$	$6.1 \cdot 10^{-3}$	$4.6 \cdot 10^{-3}$
44	$7.0 \cdot 10^{-3}$	$8.0 \cdot 10^{-3}$	$8.0 \cdot 10^{-3}$	$5.7 \cdot 10^{-3}$
48	$1.0 \cdot 10^{-2}$	$1.1 \cdot 10^{-2}$	$1.1 \cdot 10^{-2}$	$7.6 \cdot 10^{-3}$
52	$1.7 \cdot 10^{-2}$	$1.7 \cdot 10^{-2}$	$1.6 \cdot 10^{-2}$	$1.1 \cdot 10^{-2}$
56	$2.2 \cdot 10^{-2}$	$2.3 \cdot 10^{-2}$	$2.2 \cdot 10^{-2}$	$1.5 \cdot 10^{-2}$
60	$2.7 \cdot 10^{-2}$	$2.9 \cdot 10^{-2}$	$2.7 \cdot 10^{-2}$	$1.9 \cdot 10^{-2}$
64	$3.3 \cdot 10^{-2}$	$3.3 \cdot 10^{-2}$	$3.3 \cdot 10^{-2}$	$2.2 \cdot 10^{-2}$

t	Part 2. $L = 1.5$			
	u	v	p	ρ
1	$7.3 \cdot 10^{-10}$	$6.9 \cdot 10^{-9}$	$6.5 \cdot 10^{-9}$	$2.2 \cdot 10^{-9}$
2	$4.7 \cdot 10^{-10}$	$1.1 \cdot 10^{-8}$	$1.1 \cdot 10^{-8}$	$3.6 \cdot 10^{-9}$
3	$5.4 \cdot 10^{-10}$	$1.2 \cdot 10^{-8}$	$1.4 \cdot 10^{-8}$	$4.1 \cdot 10^{-9}$
4	$7.7 \cdot 10^{-10}$	$1.8 \cdot 10^{-8}$	$1.7 \cdot 10^{-8}$	$4.8 \cdot 10^{-9}$
8	$1.7 \cdot 10^{-9}$	$2.1 \cdot 10^{-8}$	$1.5 \cdot 10^{-8}$	$6.0 \cdot 10^{-9}$
12	$5.2 \cdot 10^{-9}$	$1.6 \cdot 10^{-8}$	$1.4 \cdot 10^{-8}$	$7.2 \cdot 10^{-9}$
16	$8.0 \cdot 10^{-9}$	$1.8 \cdot 10^{-8}$	$1.6 \cdot 10^{-8}$	$1.0 \cdot 10^{-8}$
20	$1.1 \cdot 10^{-8}$	$2.1 \cdot 10^{-8}$	$1.9 \cdot 10^{-8}$	$1.3 \cdot 10^{-8}$
24	$9.1 \cdot 10^{-8}$	$1.2 \cdot 10^{-7}$	$1.2 \cdot 10^{-7}$	$7.8 \cdot 10^{-8}$
28	$8.4 \cdot 10^{-7}$	$9.8 \cdot 10^{-7}$	$1.2 \cdot 10^{-6}$	$8.4 \cdot 10^{-7}$
32	$4.7 \cdot 10^{-6}$	$5.8 \cdot 10^{-6}$	$5.7 \cdot 10^{-6}$	$3.9 \cdot 10^{-6}$
36	$1.3 \cdot 10^{-5}$	$1.8 \cdot 10^{-5}$	$1.8 \cdot 10^{-5}$	$1.3 \cdot 10^{-5}$
40	$2.6 \cdot 10^{-5}$	$4.2 \cdot 10^{-5}$	$4.0 \cdot 10^{-5}$	$3.0 \cdot 10^{-5}$
44	$6.9 \cdot 10^{-5}$	$7.4 \cdot 10^{-5}$	$9.2 \cdot 10^{-5}$	$6.5 \cdot 10^{-5}$
48	$1.9 \cdot 10^{-4}$	$1.6 \cdot 10^{-4}$	$2.0 \cdot 10^{-4}$	$1.4 \cdot 10^{-4}$
52	$3.2 \cdot 10^{-4}$	$3.9 \cdot 10^{-4}$	$3.4 \cdot 10^{-4}$	$2.4 \cdot 10^{-4}$
56	$4.7 \cdot 10^{-4}$	$6.3 \cdot 10^{-4}$	$5.6 \cdot 10^{-4}$	$4.0 \cdot 10^{-4}$
60	$7.5 \cdot 10^{-4}$	$8.7 \cdot 10^{-4}$	$8.9 \cdot 10^{-4}$	$6.2 \cdot 10^{-4}$
64	$1.1 \cdot 10^{-3}$	$1.3 \cdot 10^{-3}$	$1.1 \cdot 10^{-3}$	$7.3 \cdot 10^{-4}$

C. Hazard, P. Joly, and J. Roberts, editors, *Proceedings of the Fifth International Conference on Mathematical and Numerical Aspects of Wave Propagation Phenomena*. SIAM, 2000.

[4] T. Hagstrom. A new construction of perfectly matched layers for hyperbolic systems with applications to the linearized Euler equations. In G. Cohen, E. Heikkola, P. Joly, and P. Neittaanmäki, editors, *Mathematical and Numerical Aspects of Wave Propagation Phenomena*, pages 125–129, Berlin, 2003. Springer.

[5] T. Hagstrom and I. Nazarov. Absorbing layers and radiation boundary conditions for jet flow simulations. Technical Report AIAA 2002-2606, AIAA, 2002.

[6] T. Hagstrom and I. Nazarov. Perfectly matched layers and radiation boundary conditions for shear flow calculations. Technical Report 2003-3298, AIAA, 2003.

[7] F. Hu. On absorbing boundary conditions for linearized Euler equations by a perfectly matched layer. *J. Comput. Phys.*, 129:201–219, 1996.

[8] F. Hu. A stable, perfectly matched layer for linearized Euler equations in unsplit physical variables. *J. Comput. Phys.*, 173:455–480, 2001.

COMPUTATION OF THE ALIASING AND THE INTERFACE TRANSMISSION BENCHMARK PROBLEMS BY THE DISPERSION-RELATION-PRESERVING SCHEME

Christopher K.W. Tam[†] and Hongbin Ju
Department of Mathematics
Florida State University
Tallahassee, FL 32306-4510, USA

ABSTRACT

The aliasing and the interface transmission benchmark problems are computed by the Dispersion-Relation-Preserving (DRP) scheme. The spatial resolution as well as possible wave propagation error of the DRP scheme can be quantified in wave number space. This allows the choice of a minimum size computation stencil that will provide accurate numerical solutions to these problems. The interface transmission problem involves a surface of discontinuity. Numerical treatment of boundary conditions at such a discontinuity is not well established in Computational Fluid Dynamics (CFD) and Computational Aeroacoustics (CAA). Here a ghost point method is introduced to impose the interface boundary conditions. Furthermore, the problem involves wave propagation in an infinitely large two-dimensional domain. Special consideration is required to perform the computation in a finite domain.

THE ALIASING PROBLEM

Two important features are to be noted in this problem. First is that the initial condition consists of a high wave number component. Computation of waves with high wave numbers often incurs large numerical dispersion error. Second is that in the second case of the benchmark problem, the wave number α in the initial condition is very large. In fact, $\alpha \Delta x$ is larger than π. Such wave with wave length less than two mesh spacings (Nyquist limit) will be under-resolved. They will alias as waves with a wave number equal to $(\alpha \Delta x - 2\pi)$. Thus for $\alpha \Delta x = 4.6$ the aliased wave number is -1.683. This is very similar in magnitude as the wave number in case 1 ($\alpha \Delta x = 1.7$). Because the magnitude of the wave numbers are very close to each other, the same mesh design may be used to compute the solution of both problems.

The mathematical theory of the Dispersion-Relation-Preserving (DRP) finite difference scheme (ref. 1) provides a quantitative analysis of the derivative approximation error and dispersion error in wave number space. Theoretical analysis indicates that to be able to resolve waves with a wave number of $\alpha \Delta x = 1.7$, a large finite difference stencil is necessary. For a 15-point stencil DRP scheme optimized over $\alpha \Delta x = 0$ to 1.8, the stencil coefficients are (see ref. 2).

$$
\begin{aligned}
a_0 &= 0.0 \qquad\qquad\quad a_{-j} = -a_j \\
a_1 &= 0.9194250111034304505927772885 \\
a_2 &= -0.3558295992683526875566764240l \\
a_3 &= 0.1525150160840649246910492867\!9 \\
a_4 &= -0.0594630408297157726668285968\!99 \\
a_5 &= 0.0190107527095082986598491679\!88 \\
a_6 &= -0.0043808649297336481851137000\!907 \\
a_7 &= 0.0005389612186862338465969295\!5878
\end{aligned}
$$

Figure 1 is a plot of the dependence of the wave number of the finite difference scheme, $\overline{\alpha}\Delta x$, on the exact wave number $\alpha \Delta x$. At $\alpha \Delta x = 1.7$, the relative error of the 15-point stencil DRP finite difference approximation is given by $(|\overline{\alpha}\Delta x - \alpha \Delta x|/\alpha \Delta x) = 0.2478 \times 10^{-4}$. Within the range $|\alpha \Delta x| \lesssim 1.7$, the maximum error is 0.411×10^{-4}. This error is negligibly small.

[†] Corresponding author. Email: tam@math.fsu.edu, Phone: 850-644-2455, Fax: 850-644-4053
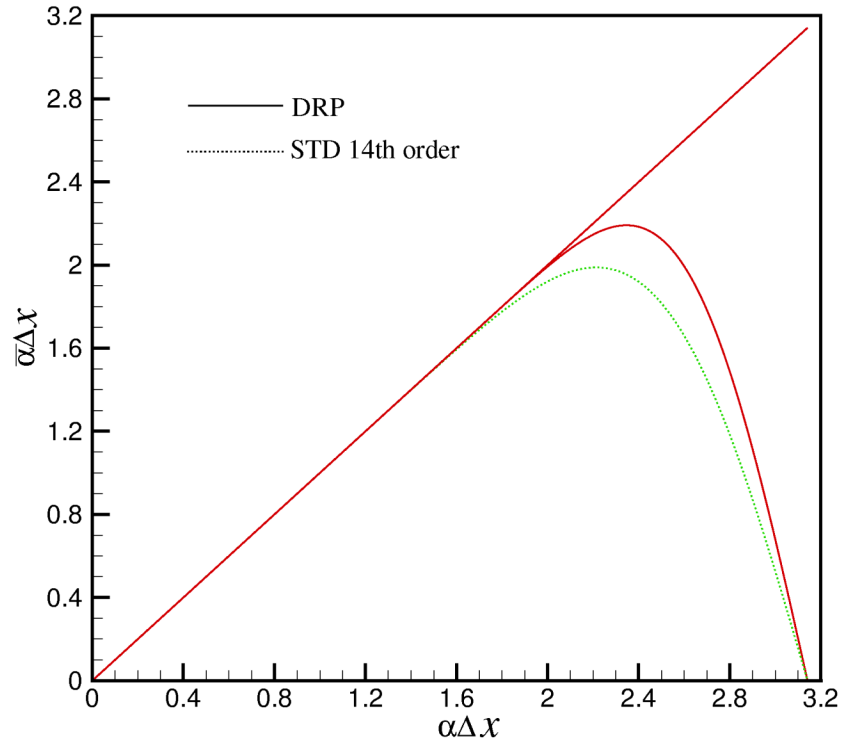
Figure 1. $\bar{\alpha}\Delta x$ versus $\alpha\Delta x$ for the 15-point stencil DRP scheme (optimized over $\alpha\Delta x =0$ to 1.8) and the standard 14th-order central difference scheme.
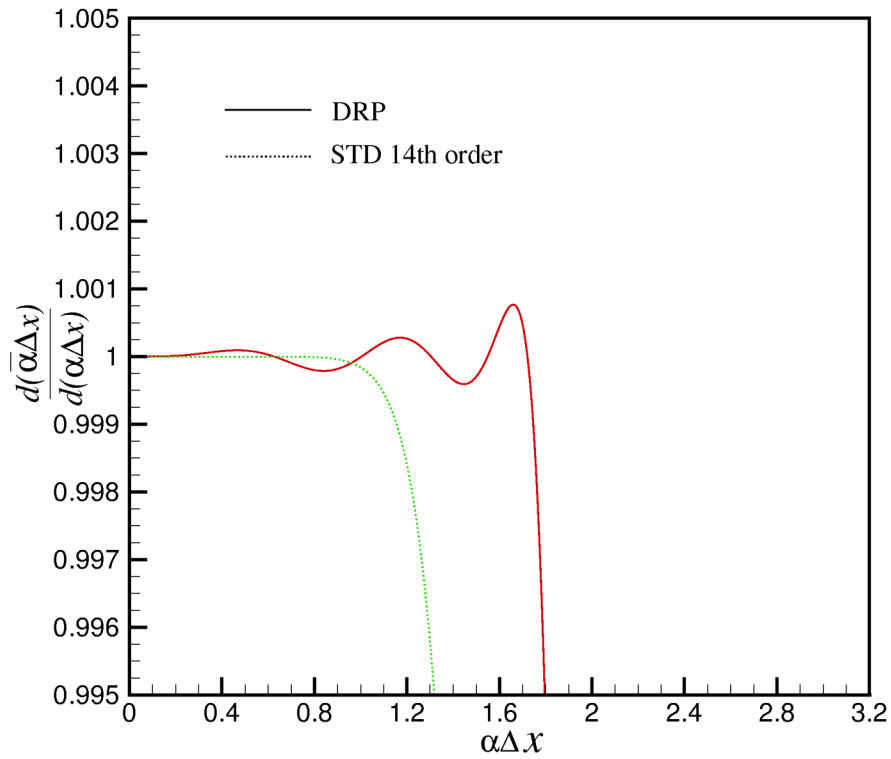
Figure 2. $d(\bar{\alpha}\Delta x)/d(\alpha\Delta x)$ versus $\alpha\Delta x$ for the 15-point stencil DRP scheme (optimized over $\alpha\Delta x =0$ to 1.8) and the standard 14th-order central difference scheme.

Another major source of error in numerical wave propagation is dispersive error. This is related to the dispersive nature of the group velocity of discretized approximation. It can be shown (see ref. 2) that if time computation is done exactly, the group velocity for the convective wave equation is proportional to $d\overline{\alpha}/d\alpha$ or the slope of the curve in Fig. 1. When $d\overline{\alpha}/d\alpha$ is equal to unity the group velocity of the DRP scheme would be equal to the exact wave speed. The $d\overline{\alpha}/d\alpha$ curve is plotted in Fig. 2. For waves with $|\alpha\Delta x| \leq 1.7$, the maximum difference between $d\overline{\alpha}/d\alpha$ and 1.0 occurs at $\alpha\Delta x = 1.66$ where $d\overline{\alpha}/d\alpha = 1.000768$. That is to say, for a wave packet propagation over 1000 mesh points, the wave component with $\alpha\Delta x = 1.66$ would propagate faster than the main wave packet. When the main wave packet reaches the 1000th mesh point, the $\alpha\Delta x = 1.66$ wave component would be ahead of it by 0.768 mesh spacing. This is less than 1 mesh spacing, so dispersion error cannot be detected. However, the initial condition is not of a single wave number. Because of the finite width of the Gaussian function, there are some wave components with $\alpha\Delta x > 1.7$. Figure 2 indicates that there is a rapid decrease in group velocity for these wave components. Thus they would propagate behind the main wave packet forming trailing waves.

The discrete form of the convective wave equation using the 15-point stencil DRP scheme is,

$$K_\ell^{(n)} = -\frac{1}{\Delta x} \sum_{j=-7}^{7} a_j u_{\ell+j}^{(n)}$$

$$u_\ell^{(n+1)} = u_\ell^{(n)} + \Delta t \sum_{j=0}^{3} b_j K_\ell^{(n-j)}$$

(1)

where superscript n is the time level and subscript ℓ is the spatial index. The time discretization coefficients b_j's can be found in reference 1.
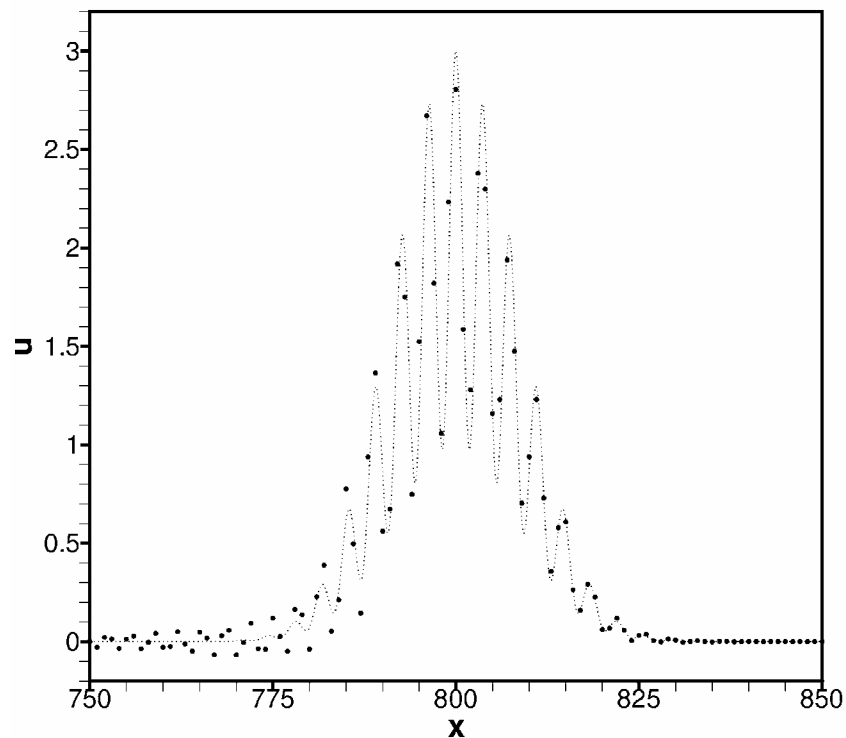
Figure 3. Comparison between computed and analytical solutions at $t = 800$ for $\alpha = 1.7$.
•, computed solution; · · · · · · · ·, analytical solution.

Figure 3 shows the computed waveform at $t = 800$ for $\Delta x = 1.0$ and $\alpha = 1.7$ using the 15-point stencil DRP scheme. Shown in this figure also is the exact analytical solution. Figure 4 shows the same information except that the computed values of the waveform are joined by straight lines. Except for the presence of small amplitude trailing waves, as anticipated, there is excellent agreement between the computed and the exact solution. To eliminate the weak trailing waves, the use of a larger stencil DRP scheme would be necessary.
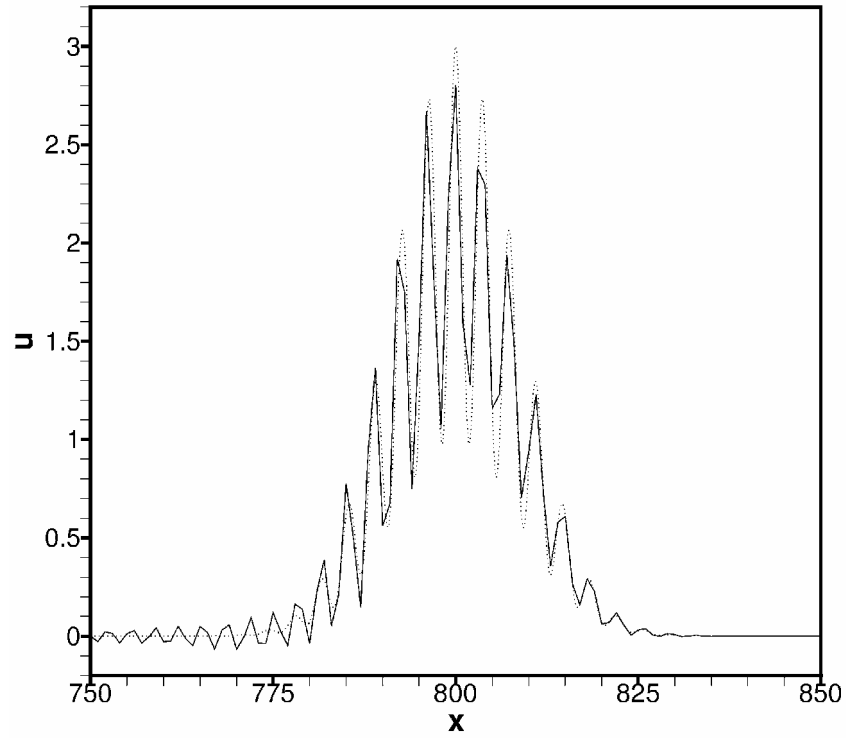
Figure 4. Comparison between computed and analytical solutions at $t = 800$ for $\alpha = 1.7$.
————, computed solution; $\cdots\cdots\cdots$, analytical solution.
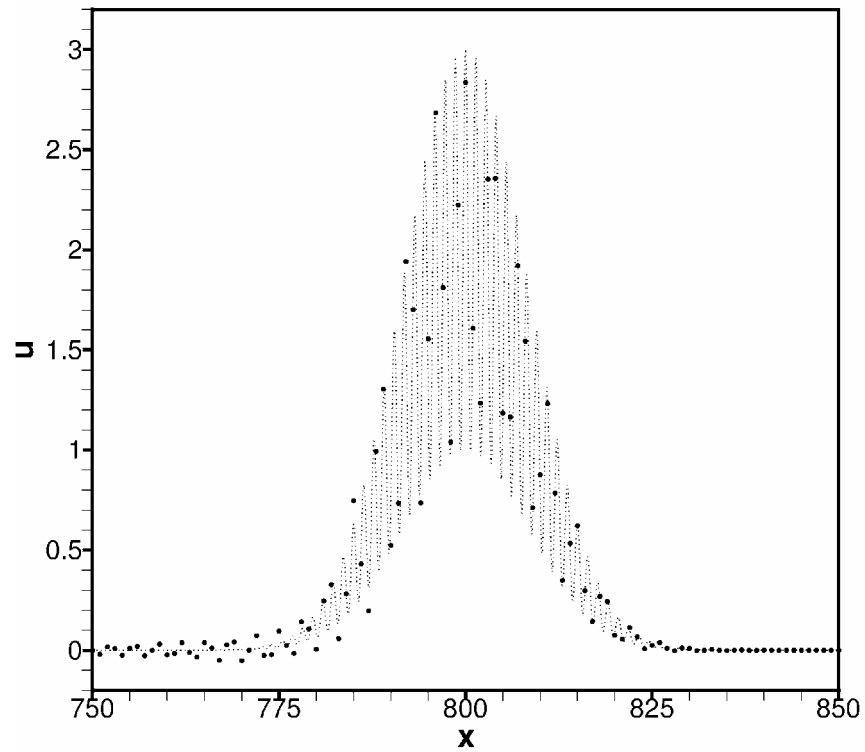
Figure 5. Comparison between computed and analytical solutions at $t = 800$ for $\alpha = 4.6$.
•, computed solution; $\cdots\cdots\cdots$, analytical solution.
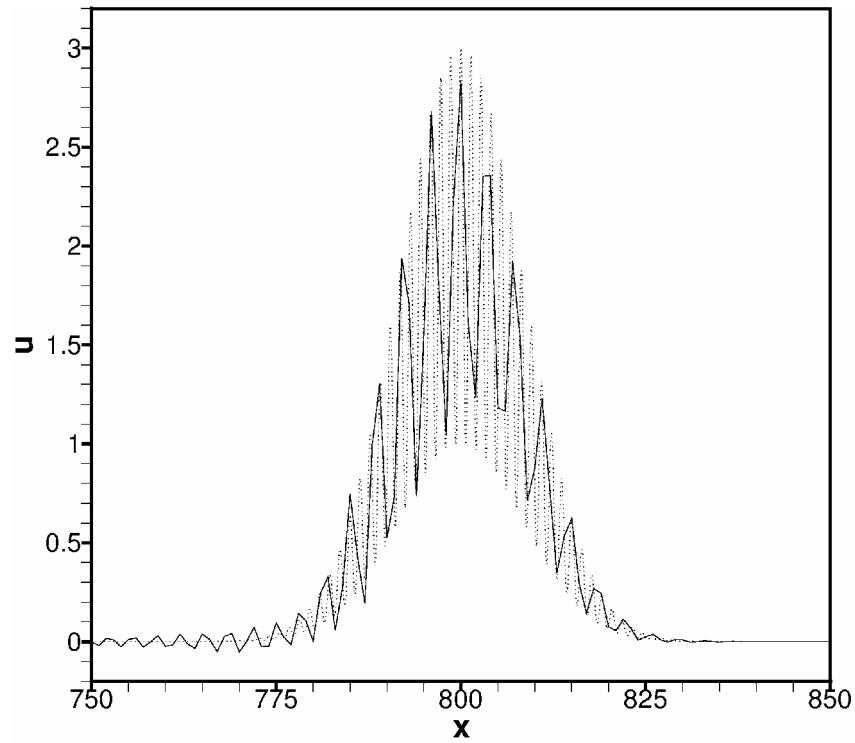
Figure 6. Comparison between computed and analytical solutions at $t = 800$ for $\alpha = 4.6$.
————, computed solution; $\cdots\cdots\cdots$, analytical solution.
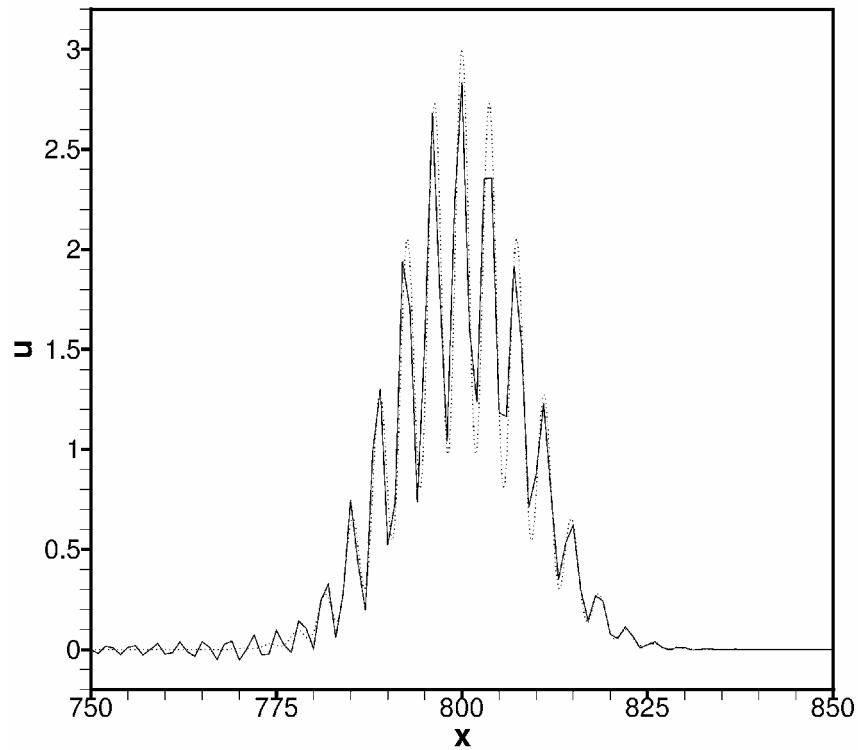
Figure 7. Comparison between computed and exact aliased solutions at $t = 800$ for $\alpha = 4.6$.
————, computed solution; $\cdots\cdots\cdots$, exact aliased solution.

Figure 5 shows the computed results at $t = 800$ for the case $\alpha = 4.6$. Shown in this figure also is the exact analytical solution. The computed values (in dots) fall right on the exact solution except for the trailing waves. Figure 6 shows the computed waveform with the computed values joined by straight lines. The computed waveform appears to differ significantly from the exact analytical solution. However, this is because aliasing has not been considered. Because $\alpha \Delta x$ is larger than π, the initial condition is aliased to a wave with wave number equal to $(\alpha \Delta x - 2\pi)$. The aliased wave number is -1.683. Thus effectively the initial condition for case 2 is

$$u(x,0) = \left[2 + \cos(1.683x)\right] \exp\left[-(\ln 2)\left(\frac{x}{10}\right)^2\right] \tag{2}$$

Figure 7 shows a comparison of the computed waveform and the exact solution using the aliased initial condition of (2). It is easily seen, other than in the trailing wave region, the agreement between computed and exact solution is very good. At this point, we would like to point out that the 15-point stencil used here is probably the smallest size stencil that can produce fairly accurate numerical solution for this problem. Most other schemes would require a much larger stencil to achieve comparable degree of accuracy.

INTERFACE TRANSMISSION PROBLEM

The DRP scheme is used to solve this problem computationally. Two special characteristics of this problem require careful consideration before computation can be performed. First, the incident, the reflected and the transmitted waves all occupy a half infinite domain. The immediate task is to choose a finite computation domain capable of simulating the infinite domain problem. Second, the problem is distinguished by the presence of an interface at which discontinuity occurs. The kinematic and dynamic boundary conditions assure that the pressure and velocity component in the y-direction are continuous across the interface. However, the y-derivatives of these quantities are discontinuous.

Choice of computation domain

We divide the computation domain into two parts as shown in Fig. 8. The top half is for waves in fluid 1. The bottom half is for waves in fluid 2. In the top half computation domain, the 7-point stencil DRP scheme is used to solve the governing linearized Euler equations.

$$\frac{\partial \mathbf{U}_1}{\partial t} + \frac{\partial \mathbf{F}_1}{\partial x} + \frac{\partial \mathbf{G}_1}{\partial y} = 0 \tag{3}$$

where

$$\mathbf{U}_1 = \begin{bmatrix} u_1 \\ v_1 \\ p_1 \end{bmatrix}, \qquad \mathbf{F}_1 = \begin{bmatrix} p_1 \\ 0 \\ u_1 \end{bmatrix}, \qquad \mathbf{G}_1 = \begin{bmatrix} 0 \\ p_1 \\ v_1 \end{bmatrix} \tag{4}$$

In the bottom half computation domain, the following linearized Euler equations are solved,

$$\frac{\partial \mathbf{U}_2}{\partial t} + \frac{\partial \mathbf{F}_2}{\partial x} + \frac{\partial \mathbf{G}_2}{\partial y} = 0 \tag{5}$$

where

$$\mathbf{U}_2 = \begin{bmatrix} u_2 \\ v_2 \\ p_2 \end{bmatrix}, \qquad \mathbf{F}_2 = \begin{bmatrix} \frac{1}{\alpha} p_2 \\ 0 \\ \lambda u_2 \end{bmatrix}, \qquad \mathbf{G}_2 = \begin{bmatrix} 0 \\ \frac{1}{\alpha} p_2 \\ \lambda v_2 \end{bmatrix} \tag{6}$$

The choice of the width of the computation domain is extremely important. We note that the x-dependence of the reflected wave as well as that of the transmitted wave must be the same as that of the incident wave. This

suggests that if the width is chosen to be equal to an integral number of the horizontal wave length of the incident wave, then the problem is periodic in the x-direction. This then allows the imposition of periodic boundary condition on the left and right boundary of the computation domain. Based on the incident wave frequency ω and angle of incidence θ, the horizontal wave length, λ_x, of the entire wave system is,

$$\lambda_x = \frac{2\pi}{\omega \sin\theta} \tag{7}$$

we will use a computation domain of $5\lambda_x$ by $5\lambda_x$ in both fluid region 1 and 2.
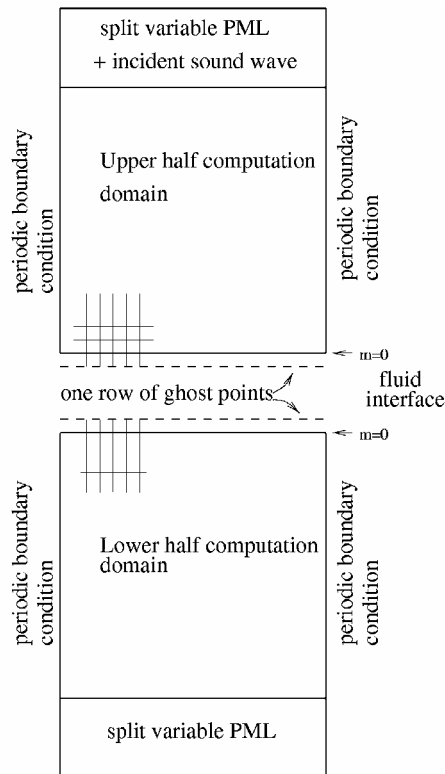
Figure 8. Computation domain and boundary treatment.

Boundary conditions and ghost point method

Proper boundary conditions are required in this problem to allow the total absorption or the smooth exit of outgoing waves. At the same time, the boundary condition on the top of the computation domain must generate the incident wave prescribed in the benchmark problem. In this work, a perfectly matched layer (PML) (see ref. 3) is installed at the bottom of the lower half computation domain. This PML serves to absorb all the outgoing transmitted wave without reflection. It has been shown in reference 4 that in the absence of a mean flow such a layer is computationally stable. A similar PML is also used on the top of the upper half computation domain. To introduce the incident wave into the computation, the following steps are taken. In the computation, only the reflected wave is calculated by the PML equations. The acoustic wave variables are taken as the sum of the reflected wave (computed by the PML equations) and the incident wave that is given. In this way, the variables of the acoustic waves are calculated. Below the PML, the wave variables (incident plus reflected waves) are calculated by solving equation (3). Stencils extending into the PML from the upper half computation domain require input of the combined values of the incident and reflected waves. They are found by adding the incident wave to the computed values of the reflected wave as mentioned above. Stencils extending from the PML into the computation domain below require values of the reflected wave alone. They are found by subtracting the known incident wave from the computed solution of (3). This technique has been used successfully in the past (see refs. 5 to 6).

The final task needed to complete the computation model is the development of a way to enforce the interface boundary conditions. These boundary conditions are

$$y = 0 \qquad\qquad p_1(x,0,t) = p_2(x,0,t) \tag{8}$$

$$v_1(x,0,t) = v_2(x,0,t) \tag{9}$$

For convenience, we will use ℓ and m to be the mesh indices in the x and y direction, respectively. $m = 0$ is the interface of the two fluids. To enforce interface boundary condition (8) and (9), we will use the ghost point method. The present method is a variant of the ghost point method of reference 7 developed for enforcing solid wall boundary conditions. Since there are two boundary conditions to enforce, two rows of ghost points are added. One row is added to the bottom of the top half computation domain. This is the $m = -1$ row of the upper half computation domain. Similarly, a row is added on the top of the lower half computation domain as shown in Fig. 8. This is the $m = 1$ row of the bottom half computation domain.

A study of equations (3) and (5) reveals that there are two possible choices of ghost values. The first choice is $(p_1)_{\ell,-1}^{(n)}$ and $(v_2)_{\ell,1}^{(n)}$. The alternative is $(v_1)_{\ell,-1}^{(n)}$ and $(p_2)_{\ell,1}^{(n)}$. We have implemented both choices and found almost identical numerical results. Here we will discuss only the first choice. The implementation of the second choice is similar.
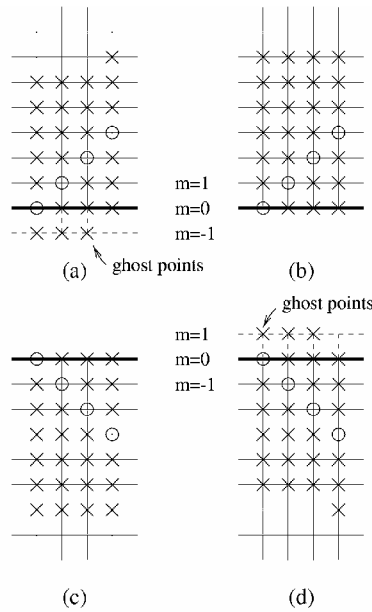
Figure 9. Backward difference stencils used near fluid interface ($m = 0$). Stencil for (a) $\frac{\partial p_1}{\partial y}$, (b) $\frac{\partial v_1}{\partial y}$, (c) $\frac{\partial p_2}{\partial y}$, and (d) $\frac{\partial v_2}{\partial y}$.

In the interior of the computation domain a 7-point central difference quotient is used in the DRP scheme to approximate the y-derivatives. However, as the fluid interface is approached, central finite difference approximation cannot be implemented. To approximate the y-derivatives, backward finite difference approximations are used. Figure 9 shows the backward difference stencils for the four derivatives $(\partial p_1)/(\partial y)$, $(\partial v_1)/(\partial y)$, $(\partial p_2)/(\partial y)$ and $(\partial v_2)/(\partial y)$. The stencils for $(\partial p_1)/(\partial y)$ extends downward to the row of ghost points at $m = -1$. The stencils for $(\partial v_2)/(\partial y)$ extends upward to the row of ghost values at $m = 1$. The two rows of ghost values $(p_1)_{\ell,-1}^{(n)}$ and $(v_2)_{\ell,1}^{(n)}$ are to be chosen so that interface conditions (8) and (9) are satisfied at the completion of updating all the variables to the next time level.

Now by differentiating (8) and (9) with respect to t, we obtain,

$$\frac{\partial p_1(x,0,t)}{\partial t} = \frac{\partial p_2(x,0,t)}{\partial t} \tag{10}$$

$$\frac{\partial v_1(x,0,t)}{\partial t} = \frac{\partial v_2(x,0,t)}{\partial t} \tag{11}$$

On replacing the time derivatives in (10) and (11) by the second and third equation of (3) and (5), the following equivalent interface boundary conditions may be derived.

$$y = 0 \qquad \frac{\partial u_1}{\partial x} + \frac{\partial v_1}{\partial y} = \lambda \left(\frac{\partial u_2}{\partial x} + \frac{\partial v_2}{\partial y} \right) \tag{12}$$

$$\frac{\partial p_1(x,0,t)}{\partial y} = \frac{1}{\alpha} \frac{\partial p_2(x,0,t)}{\partial y} \tag{13}$$

The discretized form of (13) using the backward difference stencils of Fig. 9 leads to,

$$\sum_{j=-1}^{5} a_j^{15} (p_1)_{\ell,j}^{(n)} = \frac{1}{\alpha} \sum_{j=-6}^{0} a_j^{60} (p_2)_{\ell,j}^{(n)} \tag{14}$$

On solving for the ghost value $(p_1)_{\ell,-1}^{(n)}$, it is easy to determine from (14),

$$(p_1)_{\ell,-1}^{(n)} = \frac{1}{a_{-1}^{15}} \left[\frac{1}{\alpha} \sum_{j=-6}^{0} a_j^{60} (p_2)_{\ell,j}^{(n)} - \sum_{j=0}^{5} a_j^{15} (p_1)_{\ell,j}^{(n)} \right] \tag{15}$$

(15) is the formula to use for calculating the ghost value $(p_1)_{\ell,-1}^{(n)}$ after all the variables in the computation domain have been updated to time level n.

The discretized form of (12) using the backward difference stencils of Fig. 9 leads to,

$$\frac{1}{\Delta x} \sum_{j=-3}^{3} a_j (u_1)_{\ell+j,0}^{(n)} + \frac{1}{\Delta y} \sum_{j=0}^{6} a_j^{06} (v_1)_{\ell,j}^{(n)} = \frac{\lambda}{\Delta x} \sum_{j=-3}^{3} a_j (u_2)_{\ell+j,0}^{(n)} + \frac{\lambda}{\Delta y} \sum_{j=-5}^{1} a_j^{51} (v_2)_{\ell,j}^{(n)} \tag{16}$$

By solving (16) for the ghost value $(v_2)_{\ell,1}^{(n)}$, it is straightforward to find

$$(v_2)_{\ell,1}^{(n)} = \frac{1}{a_1^{51}} \left[-\sum_{j=-5}^{0} a_j^{51} (v_2)_{\ell,j}^{(n)} + \frac{1}{\lambda} \sum_{j=0}^{6} a_j^{06} (v_1)_{\ell,j}^{(n)} + \frac{1}{\lambda} \frac{\Delta y}{\Delta x} \sum_{j=-3}^{3} a_j (u_1)_{\ell+j,0}^{(n)} - \frac{\Delta y}{\Delta x} \sum_{j=-3}^{3} a_j (u_2)_{\ell+j,0}^{(n)} \right] \tag{17}$$

Again (17) is used to find $(v_2)_{\ell,1}^{(n)}$ after all the variables in the computation domain have been updated to the time level n.

<div align="center">

Comparison with exact solution

</div>

Case 1, $\theta = 20$ degrees

Figure 10a shows the computed zero pressure contour map. In the upper half plane, the pressure is the sum of the incident and the reflected wave. In the lower half plane, it is that of the transmitted wave. In the computation, a mesh size of $\Delta x = \Delta y = (\lambda_x / 30)$ was used (λ_x is the horizontal wave length). Plotted in this figure also is the exact solution in dotted lines. The difference between the numerical and the exact solution is very small. So it cannot easily be detected.

At $20°$ incident angle, most of the incident wave are transmitted through the fluid interface. As a result, the intensity of the reflected wave is very small. In Fig. 10b, the upper half plane shows the computed and the exact zero pressure contours of the reflected wave. Near the interface, the computed zero pressure contours are not straight, contrary to the exact solution. There are spurious wiggles in the wave front. These wiggles diminish as the reflected wave propagate away from the fluid interface.

In an effort to determine the origin of the spurious wiggles of the zero pressure contours of the reflected wave, the computation was repeated using twice the mesh resolution. Figure 11 shows the computed and the exact zero pressure contours calculated on a mesh with $\Delta x = \Delta y = (\lambda_x / 60)$. Figure 11b clearly shows that the amplitudes of the wiggles are much reduced. The computation was further repeated using $\Delta x = \Delta y = (\lambda_x / 120)$. The computed result shows almost free of wiggles. Although the mesh size reduction exercise strongly suggests that the wiggles are related to the mesh size resolution, yet we are still puzzled by their existence. In the first computation with $\Delta x = \Delta y = (\lambda_x / 30)$, the resolution in the y-direction is $(\lambda_y / \Delta_y) = 9.64$. The 7-point stencil DRP scheme is known to be able to resolve waves using 7 to 8 mesh points per wavelength. Thus the 7-point stencil DRP scheme meets the resolution requirement. For this reason, we are surprised to find the wiggles. For the same reason, we are not convinced that the wiggles are the result of inadequate mesh resolution. We are still in search of a more convincing explanation.

(a)   (b)
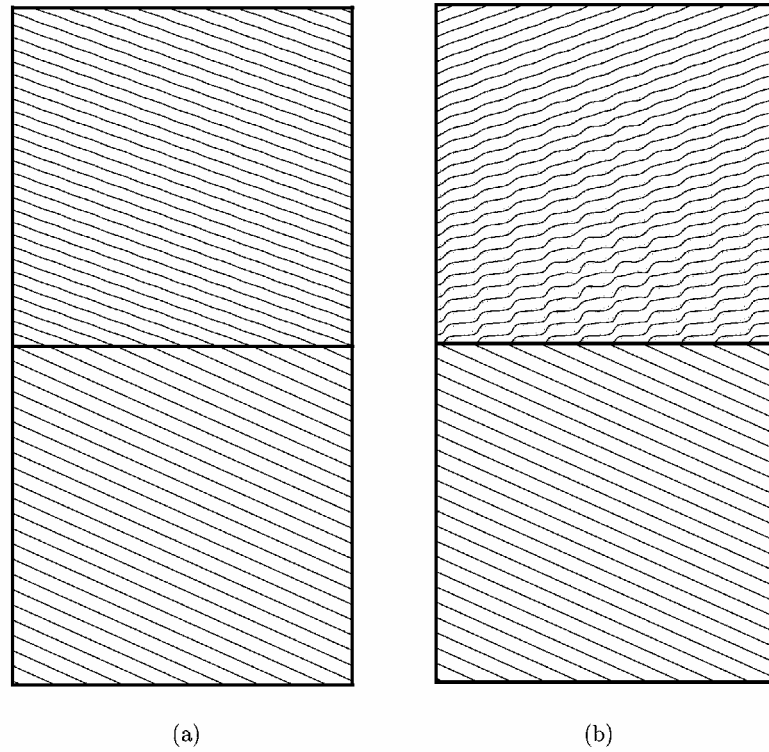
Figure 10. Zero pressure contours. Incident angle 20^0. $\Delta x = \Delta y = \lambda_x/30$. Upper half plane: (a) incident plus reflected waves; (b) reflected wave only. Lower half plane: transmitted wave. ————, computed solution, $\cdots\cdots$, exact solution.

(a)   (b)
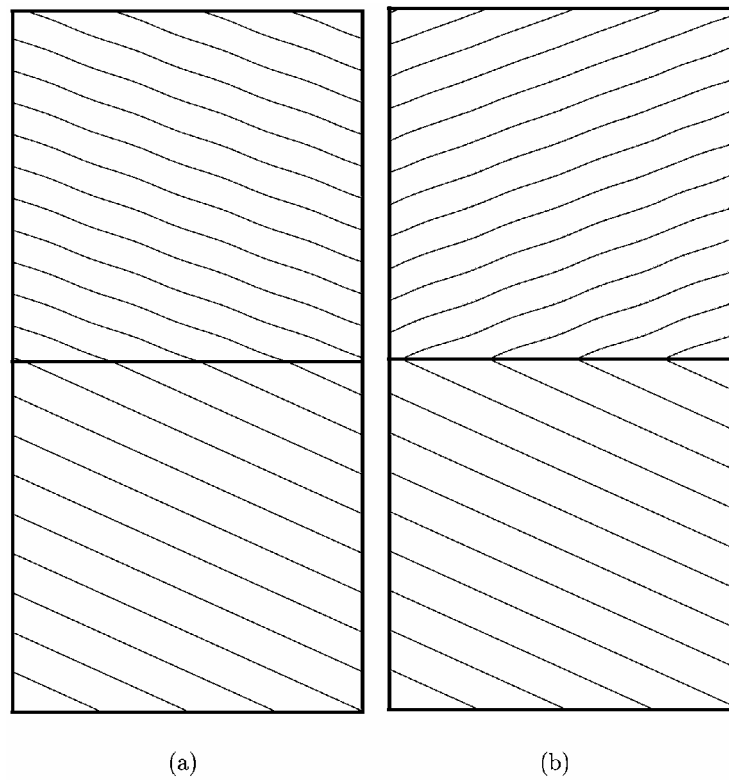
Figure 11. Same as Figure 10. $\Delta x = \Delta y = \lambda_x/60$. Scale enlarged.

Case 1, θ = 65 degrees

At 65 degrees angle of incidence total reflection of the incident wave takes place at the fluid interface. The upper half of Fig. 12a shows the computed pressure contours at the beginning of a cycle. Since the incident waves are totally reflected, the amplitude of the reflected wave is equal to that of the incident wave. As a consequence, the pressure contours form a symmetric pattern with respect to an axis parallel to the y-direction.

(a)   (b)
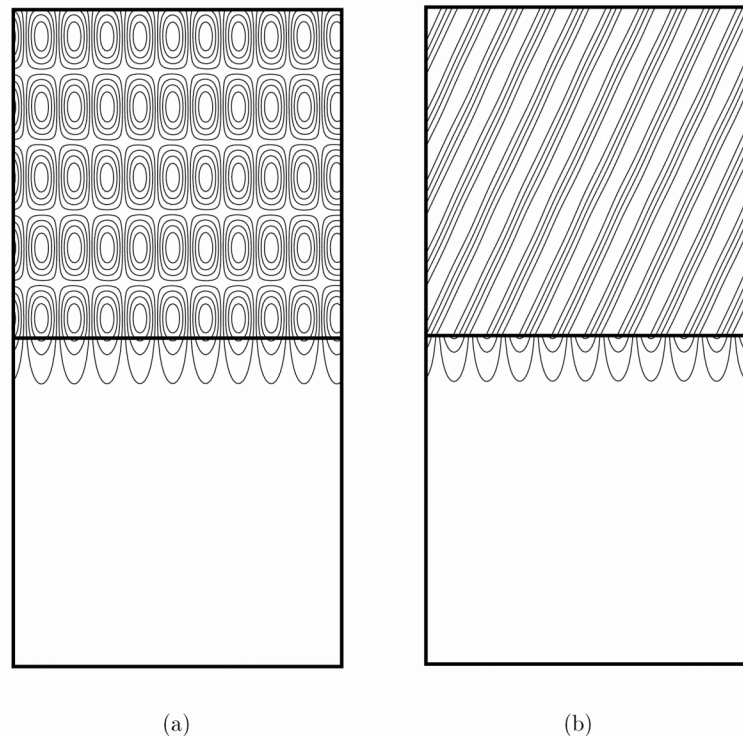
Figure 12. Pressure contours, contour levels from -2 to 2 with increments of 0.4444. Incident angle 65^0. $\Delta x = \Delta y = \lambda_x/30$. Upper half plane: (a) incident plus reflected waves; (b) reflected wave only. Lower half plane: transmitted wave. ————, computed solution, ········, exact solution.

In the lower half plane, the amplitude of the transmitted wave decreases exponentially with distance from the fluid interface. This results in a pressure contour pattern as shown in Fig. 12. Figure 12b shows the pressure contours of the reflected wave. Also shown in all these figures is the exact solution in dotted lines. Because the computed results are in good agreement with exact solution, the dotted lines cannot be easily identified.

REFERENCES

1. Tam, C.K.W.; Webb, J.C.: Dispersion-Relation-Preserving Finite Difference Scheme for Computational Acoustics. J. Comput. Phys., vol. 107, 1993, 262–281.

2. Tam, C.K.W.: Computational Aeroacoustics: An Overview of Computational Challenges and Applications. International J. Comput. Fluid Dyn. (to appear 2004).

3. Hu, F.Q.: On Absorbing Boundary Conditions for Linearized Euler Equations by a Perfectly Matched Layer. J. Comput. Phys., vol. 129, 1996, 201–219.

4. Tam, C.K.W.; Auriault, L.; Cambuli, F.: Perfectly Matched Layer as an Absorbing Boundary Condition for the Linearized Euler Equations in Open and Ducted Domain. J. Comput. Phys., vol. 144, 1998, 213–234.

5. Tam, C.K.W., et al.: A Computational and Experimental Study of Slit Resonators. AIAA Paper 2003-3310 (to appear in the J. of Sound and Vib.).

6. Tam, C.K.W.: Advances in Numerical Boundary Conditions for Computational Aeroacoustics. J. Comput. Acoustics, vol. 6, 1998, 377–402.

7. Tam, C.K.W.; Dong, Z.: Wall Boundary Conditions for High-Order Finite Difference Schemes in Computational Aeroacoustics. Theor. Comput. Fluid Dyn., vol. 6, 1994, 303–322.

DISCONTINUOUS GALERKIN METHOD FOR COMPUTATIONAL AEROACOUSTICS

Cheolwan Kim and Jang Yeon Lee
Korea Aerospace Research Institute
45 Eoeun-dong, Youseong-Gu, Daejeon, 305–333 Korea
E-mail: cwkim@kari.re.kr Tel: 82–42–860–2691 Fax: 82–42–860–2604

ABSTRACT

Discontinuous Galerkin method is a time-discrete higher-order compact scheme and its solution is accurate. It is also automatic methodology to raise the solution accuracy to any level. One-dimensional (1–D) convection solution shows its excellent accuracy. The original multidimensional version is very expensive. An alternative is suggested in this summary by combining 1–D staggered with an implicit mesh arrangement. This alternative is also accurate and less expensive but more research is required to expand its application to complex geometry and three-dimensional (3–D) problems.

1. INTRODUCTION

There are mainly three approaches in developing the higher-order method. One approach is based on the ideas of Lax and Wendroff (ref. 1). The solution is written as a Taylor series in time and the time derivatives are replaced by spatial derivatives from the governing equations. A more popular approach is a multistage-time-integration method. This method entirely separate the reconstruction stage from the evolution stage, thus are simple to program for complicated systems. The most popular reconstruction method is Tam's dispersion relation preserving (DRP) scheme (ref. 2). The third approach is to store and update more solution information at each cell. Therefore, solution and its moments are updated with a system of equations relaxed by higher-order test functions. One of these methods is the point implicit discontinuous Galerkin method. Initiated and developed by Lowrie (ref. 3), they adopted staggered-type mesh arrangement to separate incoming and outgoing wave surfaces. It is accurate and compact, but expensive and difficult to program for complicated geometry. In this paper, therefore, a less expensive approach is suggested and tested for some examples.

2. TIME-DISCRETE DISCONTINUOUS GALERKIN METHOD

Any hyperbolic equations can be simply written as

$$\partial_t U + \vec{\nabla} \bullet \overline{f} = 0 \tag{1}$$

where U is the vector of conservation variables and $\vec{\nabla} \equiv \left(\partial_{x_1}, ..., \partial_{x_d} \right)$, $\overline{f} = \left(\overline{f_1}, ..., \overline{f_d} \right)$

A simpler form is

$$\vec{\nabla} \bullet \overline{f} = 0 \tag{2}$$

where $\vec{\nabla} \equiv \left(\partial_{x_1}, ..., \partial_{x_d}, \partial_t \right)$ and $\overline{f} = \left(\overline{f_1}, ..., \overline{f_d}, U \right)$. Now U is considered as the flux in time and the weak form of equation (2) for each element is

$$\oint_{\Omega_e} \overline{f} \bullet \vec{n}_e \, dS - \int_{\Omega_e} \vec{\nabla}\phi \bullet \overline{f} \, dV = 0 \tag{3}$$

where $n_e = (n_{e,x_1}, ..., n_{e,x_d}, n_{e,t})$ is the outward boundary unit normal, and $\phi = \phi(\vec{x})$ is a suitable test function. Taking $\phi(\vec{x}) = 1$ simplifies equation (3) to the finite-volume approach $\oint_{\Omega_e} \overline{f} \cdot \vec{n}_e \, dS = 0$. However, the difference between the discontinuous Galerkin method and the finite-volume method is the approach to achieve higher accuracy. Finite-volume methods obtain greater accuracy by using higher-order differencing, while the discontinuous Galerkin method updates additional moments of the governing partial-differential equation.

The discontinuous Galerkin method adopts a staggered mesh arrangement separating incoming and outgoing wave surfaces. Therefore, equation (3) is written as

$$\oint_{\Omega_{e,in}} \phi \, \overline{f} \cdot \vec{n}_e \, dS + \oint_{\Omega_{e,out}} \phi \, \overline{f} \cdot \vec{n}_e \, dS - \int_{\Omega_e} \overline{\nabla}\phi \cdot \overline{f} \, dV = 0 \tag{4}$$

To get an algebraic system, the flux function is differentiated by the solution variable, $\overline{f} = \overline{\overline{A}} \cdot U$. Therefore, the governing equation is

$$\oint_{\Omega_{e,in}} \phi \, \overline{f} \cdot \vec{n}_e \, dS + \oint_{\Omega_{e,out}} \phi \, \overline{\overline{A}} U \cdot \vec{n}_e \, dS - \int_{\Omega_e} \overline{\nabla}\phi \cdot \overline{\overline{A}} U \, dV = 0 \tag{5}$$

The solution is a linear combination of the test functions, $U = \sum_j c_j \cdot \phi_j$ and $\overline{\overline{A}}$ is a constant matrix for a linear system of governing equations. Therefore, for a test function, ϕ_i, equation (5) is written as

$$\left[\int_{\Omega_e} \overline{\nabla}\phi_i \cdot \overline{\overline{A}} \phi_j \, dV - \oint_{\Omega_{e,out}} \phi_i \phi_j \, \overline{\overline{A}} \cdot \vec{n}_e \, dS \right] c_j = \oint_{\Omega_{e,in}} \phi \, \overline{f} \cdot \vec{n}_e \, dS \tag{6}$$

2.1 One-dimensional hyperbolic equations

To apply this idea to 1–D hyperbolic system, a staggered mesh arrangement, shown in figure 1, is prepared.
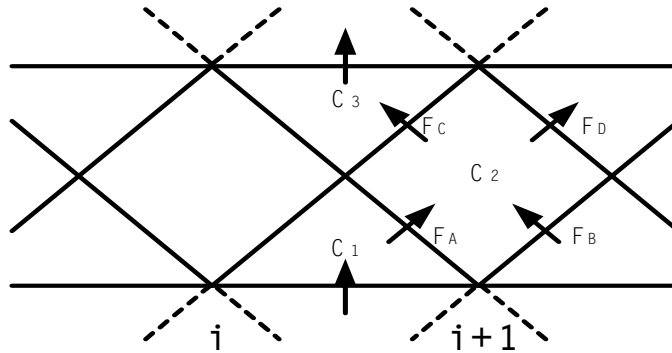
Figure 1.—Staggered mesh arrangement for 1–D discontinuous Galerkin method.

A cell (C_2) has four surrounding faces (F_A, F_B, F_C, and F_D). Every wave comes into the cell through two faces, F_A and F_B, and exits through F_C and F_D with Courant condition. Courant condition is

$$\frac{\max\limits_{i,j} | \lambda_j | \Delta t}{\Delta x} < 1$$

where λ_j is local average of the jth eigenvalue in i'th cell. Therefore, the information required to update a cell is from the previous step and independent from the neighboring cells at the same step. This method is point-implicit.

2.2 Two-dimensional (2–D) hyperbolic equations

The 2–D staggered mesh arrangement is more complicated than 1–D arrangement. It consists of eight pyramid and tetrahedron steps. Figure 2 shows this mesh arrangement to update a half time step (between n and n+1/2 time step). This arrangement is very expensive and difficult to apply to a complex geometry.

(a) Step 1: Pyramid covering x,y mesh cell   (b) Step 2: Tetrahedron filling x-axis valley

(c) Step 3: Tetrahedron filling y-axis valley   (d) Inverted pyramid
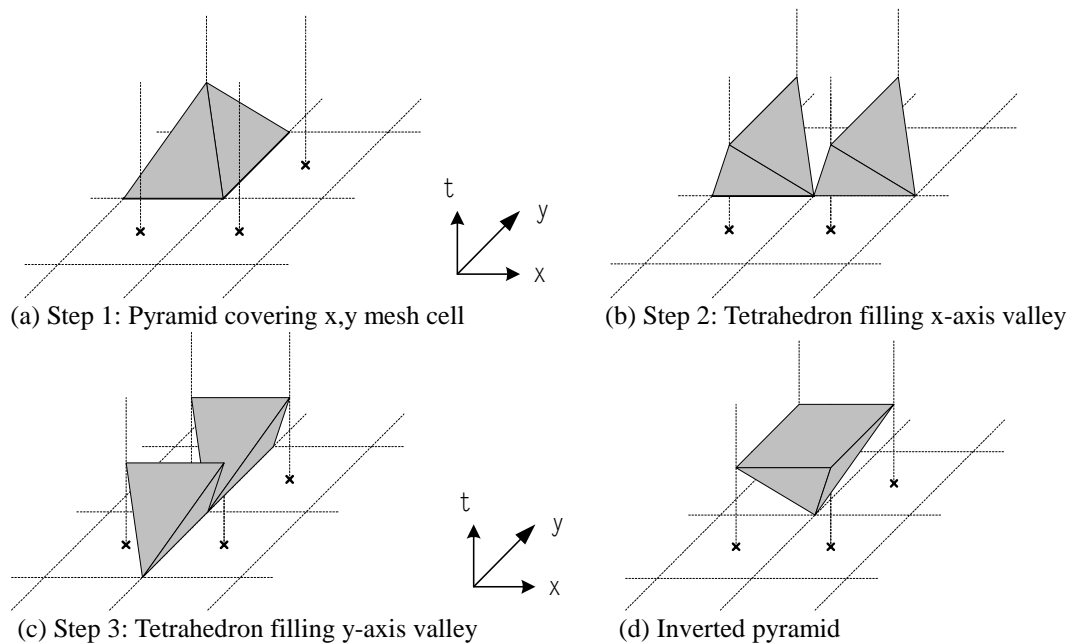
Figure 2.—A 2–D point implicit mesh arrangement.

As an alternative, a line-implicit mesh arrangement is suggested as shown in figure 3. Along a space direction (x-coordinate), Riemann face (line-implicit) is deployed and a staggered mesh is arranged along the other direction. Therefore, a two-step solution update completes a time step.

(a) Starting mesh pentahedron   (b) Step 1: Hexahedron centered at n+1/2 time step   (c) Hexahedron centered at n+1 time step
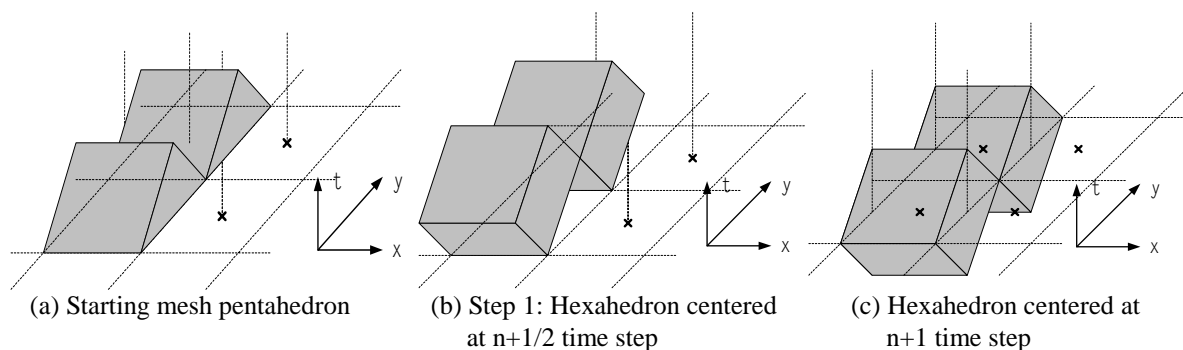
Figure 3.—A 2–D line-implicit mesh arrangement.

3. BENCHMARK PROBLEM SIMULATION

3.1 One-dimensional convection wave problem

The given problem for 1–D convection is

$$\frac{\partial u}{\partial t} + \frac{\partial u}{\partial x} = 0$$

and the initial value is

$$t = 0, \quad u = \left[2 + \cos(\alpha x)\right] \exp\left[-\ln 2(x/10)^2\right],$$

$$\Delta x = 1.0, \ \alpha = 1.7 \text{ and } 4.6$$

Figure 4 shows the simulation result at t = 400 and 800 when α = 1.7 and ν = 0.5. Figures 4(a) and (c) show the solutions at cell center and figures 4(b) and (d) present the reconstructed solutions. The symbols, +, x, and o present the results with first, second, and third test functions, respectively. The first-order test function dissipates the oscillating part of the initial value distribution and shows smooth Gaussian distribution. However, the third-order result preserves the initial distribution well. The discontinuous Galerkin method with a third-order test function shows good accuracy to update the high-frequency initial value. The choice of ν = 0.5 does not make any dispersion errors even at *t* = 800 (1600 iteration) and the result with ν = 0.8 is shown in figure 5. The result with ν = 0.8 shows lagging dispersion property and its error is E = 0.18 percent.
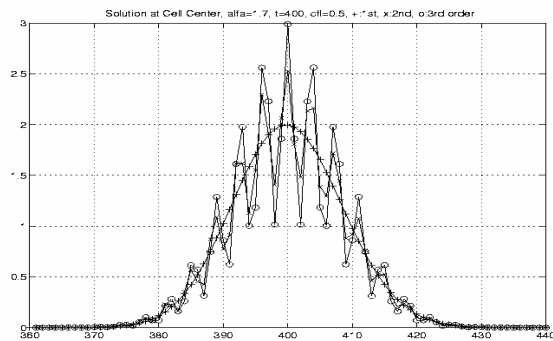
(a) Solution at cell center, t = 400, ν = 0.5
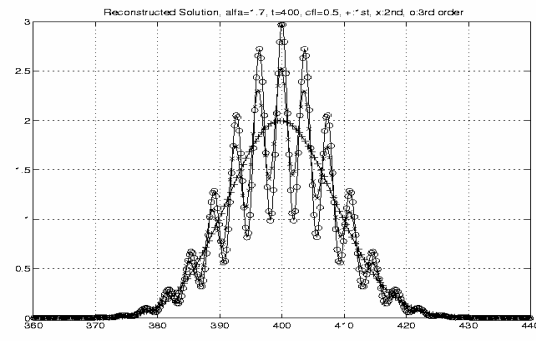
(b) Reconstructed solution, t = 400, ν = 0.5
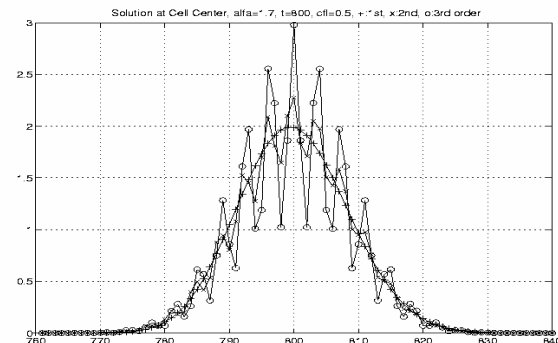
(c) Solution at cell center, t = 800, ν = 0.5
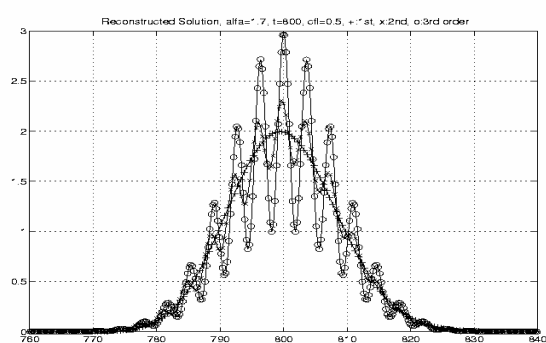
(d) Reconstructed solution, t = 800, ν = 0.5

Figure 4.—The 1–D convection wave simulation results, α = 1.7 and ν = 0.5.
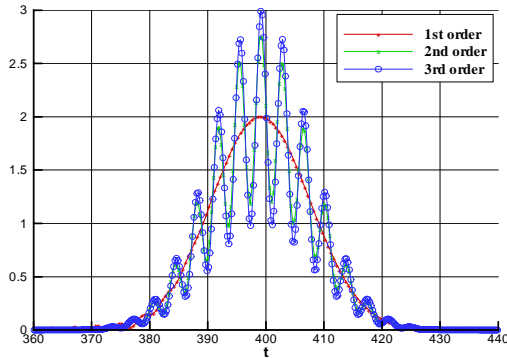
(a) Reconstructed solution, t = 400, ν = 0.8
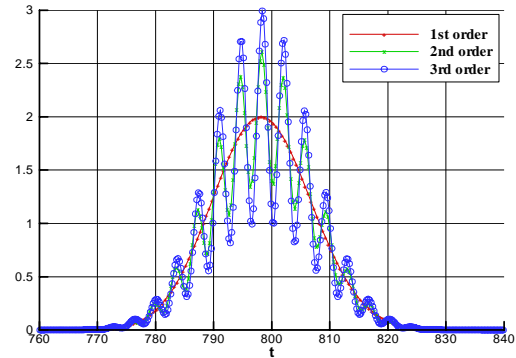
(b) Reconstructed solution, t = 800, ν = 0.8

Figure 5.—One-dimensional convection wave simulation results, α = 1.7 and ν = 0.8.

Figure 6 compares three simulation results with different test functions. The symbols, +, x, and o present the results with third, fourth, and fifth test functions, respectively. Figures 4(a) and (c) show the solutions at cell center and figures (b) and (d) present the reconstructed solutions. The given grid size is too coarse ($\Delta x = 1.0$) to figure the oscillating portion of the initial value distribution. Third- and fourth-order test function results show severe dissipation and only the fifth-order solution preserves the initial value profile very well. The dissipation error of the fifth-order solution is estimated as E = 0.006 percent.
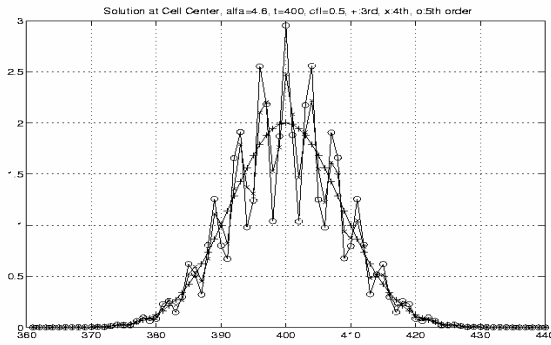
(a) Solution at cell center, t = 400, ν = 0.5
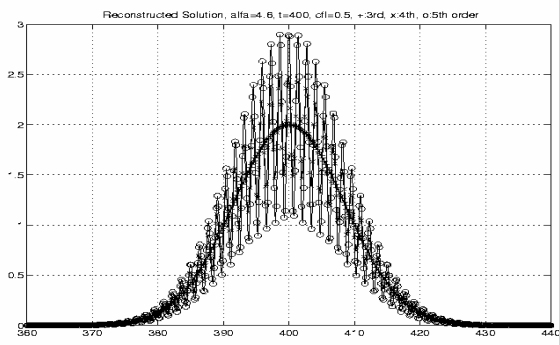
(b) Reconstructed solution, t = 400, ν = 0.5
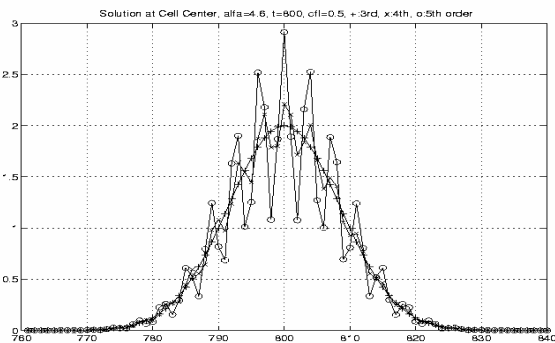
(c) Solution at cell center, t = 800, ν = 0.5
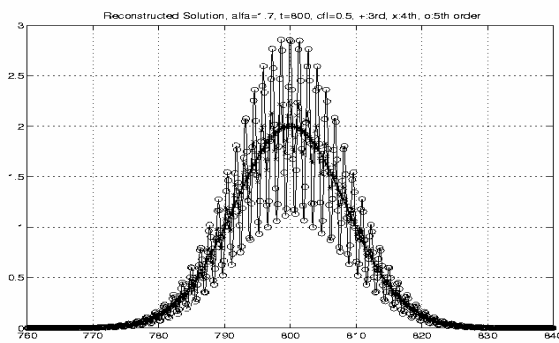
(d) Reconstructed solution, t = 800, ν = 0.5

Figure 6.—One-dimensional convection wave simulation results, α = 4.6 and ν = 0.5.

3.2 Two-dimensional initial value problem

The test case for 2–D initial value problem was presented at the Second Computational Aeroacoustics Workshop on Benchmark Problems (ref. 4). The geometry is shown in figure 7. The governing equations are 2–D linear Euler equations in cylindrical coordinate. The computational domain is $0.5 \leq r \leq 10.0$, $0° \leq \theta \leq 180°$ and the initial values are

$$u(x, y, t) = 0.0 \qquad v(x, y, t) = 0.0$$

$$p(x, y, t) = \exp\left\{ -\frac{\ln 2}{0.2^2}\left[(x - 4.0)^2 + y^2 \right] \right\}$$
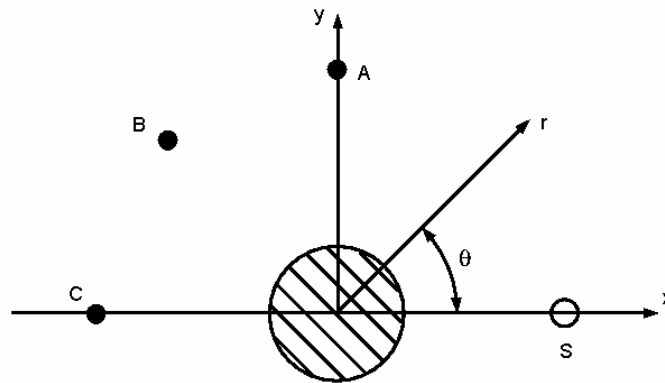
Figure 7.—Geometry for 2–D initial value problem.

As time evolves, pressure pulse propagates outward and is reflected from the cylinder wall. Pressure value is measured at three points: $A(r = 5, \theta = 90°)$, $B(r = 5, \theta = 135°)$, and $C(r = 5, \theta = 180°)$. Measuring time is from $t = 5$ to $t = 10$. Measured pressure values are compared with analytic ones. Figures 8 and 9 present contour plots of the results at $t = 2, 4, 6,$ and 8, according to the third-order test functions with $\Delta r = 0.36$ and 0.21. In early time, the wave front propagates outward(Fig.8&9 a) and is reflected from the cylinder while most of the pressure pulse propagates outside (figs. 8(a) and 9(a)). At later time (figs. 8(c) and (d) and 9(c) and (d)), the reflected wave follow the main pulse and there is a continuous front around the cylinder.

Time histories of pressure at points (A, B, and C) are shown in figure 10. The numerical results are presented for various grid sizes ($\Delta r = 0.36, 0.29, 0.21,$ and 0.16) and the analytic solution is expressed by a solid line. The numerical result on the coarsest grid ($\Delta r = 0.36$) produce noticeable deviation at peak values but the numerical result with $\Delta r = 0.16$ demonstrates good agreement with the analytic solution. For example, the errors of the first peak values at A, B, and C are 1.8 percent (point A), 0.92 percent (point B), and 0.43 percent (point C).

3. CONCLUSION

Discontinuous Galerkin method is excellent in preserving the accuracy of the solution. It is easy to control the accuracy locally. However, it is difficult to apply this method to complex geometry and 3–D problems. For future development of this method, more research should be focused on using complex geometry applications.
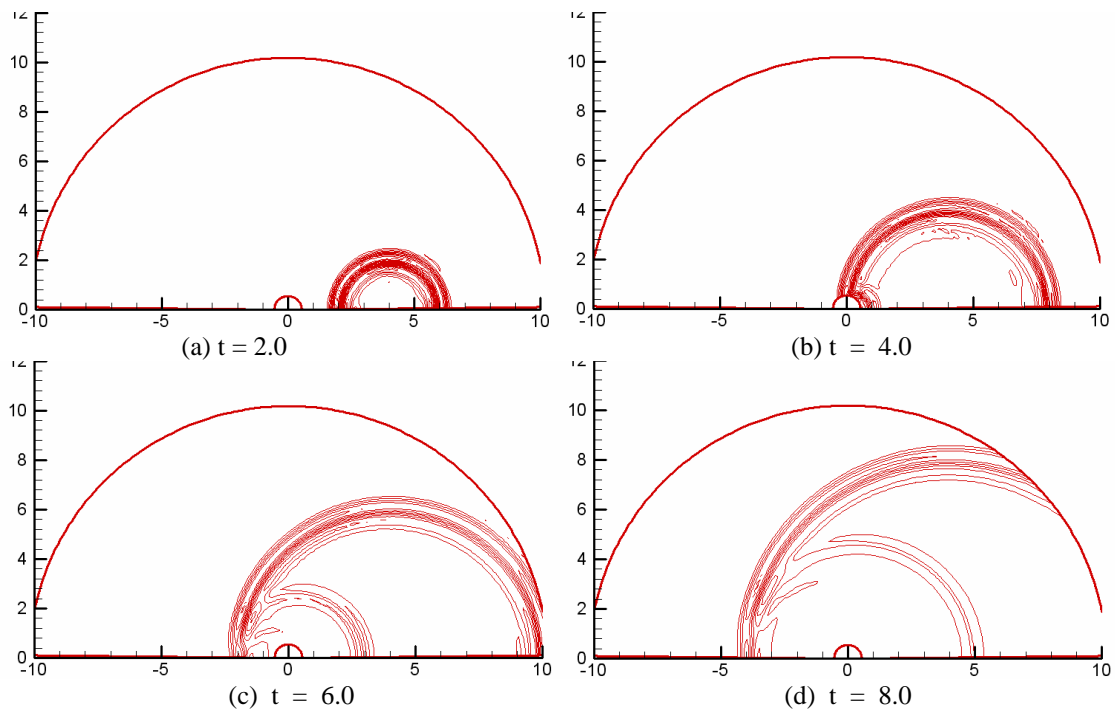
Figure 8.—Solution contour with third-order test function, $\Delta r = 0.36$, $\Delta t = 0.04$, and mesh size = 36×27.
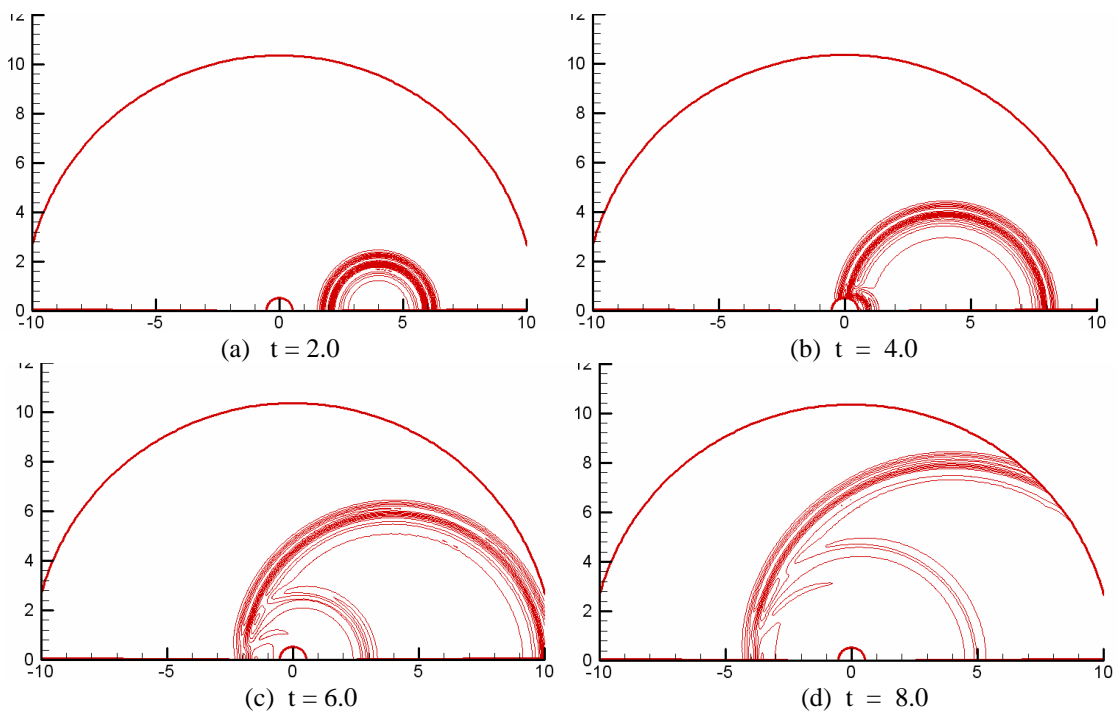
Figure 9.—Solution contour with third-order test function, $\Delta r = 0.21$, $\Delta t = 0.0278$, and mesh size = 56×45.
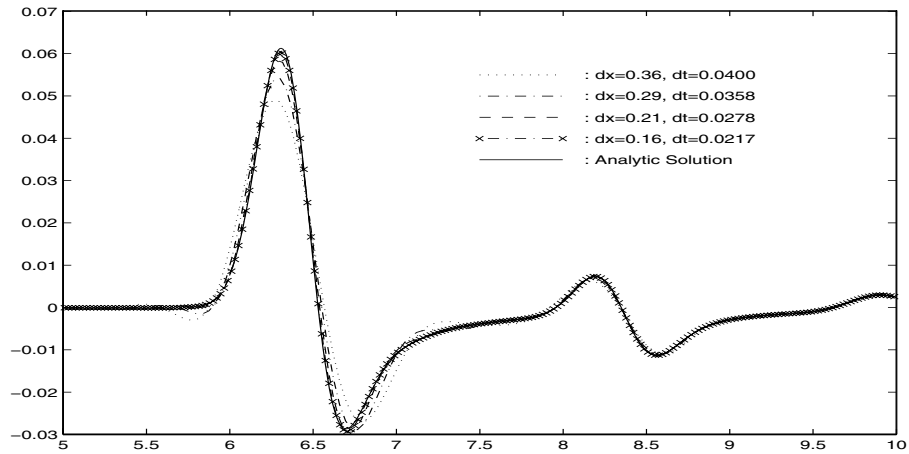
(a) Pressure history at point A
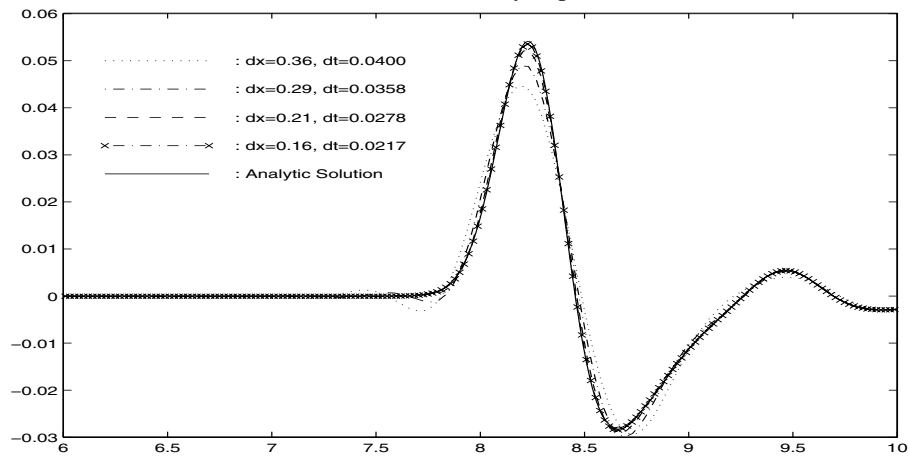
(b) Pressure history at point B
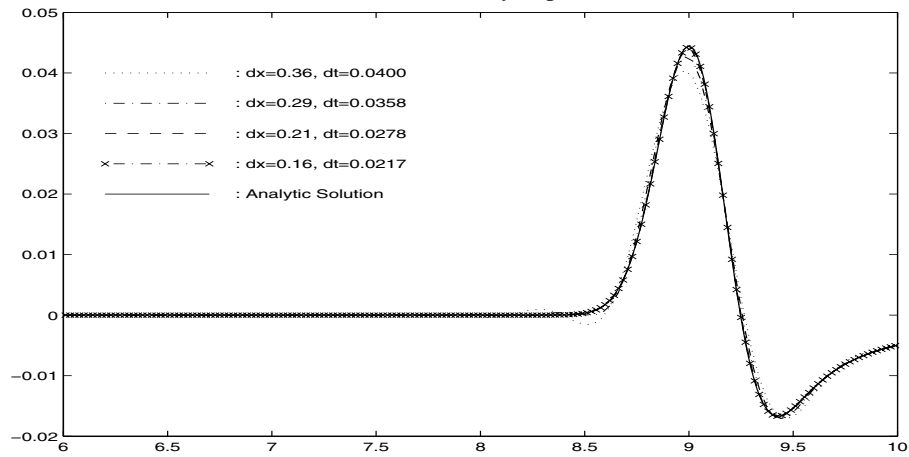
(c) Pressure history at point C

Figure 10.—Pressure histories of the third-order test function at points A, B, and C:
$5 \leq t \leq 10$, $\Delta r = 0.36$, 0.29, 0.21, and 016.

REFERENCES

1. Lax, P.D.; and Wendroff, B.: Difference Schemes for Hyperbolic Equations With High Order Accuracy. *Communications in Pure and Applied Mathematics*, 17, 1962.

2. Tam, C.K.W.; and Webb, J.C.: Dispersion-Relation Preserving Finite Difference Schemes for Computational Acoustics. Journal of Computational Physics, vol. 107, pp. 262–281, 1992.

3. Lowrie, R.B.: Compact Higher-Order Numerical Methods for Hyperbolic Conservation Laws. Ph.D. Thesis, University of Michigan, 1996.

4. Tam, C.K.W.; and Hardin, J.C. eds.: *Second Computational Aeroacoustics (CAA) Workshop on Benchmark Problems*. NASA Conference Paper–3352, 1997.

APPLICATION OF OPTIMIZED EXPLICIT SCHEMES
TO CATEGORY 1, PROBLEM 1

Christophe Bogey, Julien Berland and Christophe Bailly
Laboratoire de Mécanique des Fluides et d'Acoustique
UMR CNRS 5509, Ecole Centrale de Lyon
36 av. Guy de Collongue, 69134 Ecully, France
http://acoustique.ec-lyon.fr

ABSTRACT

This paper describes the application of optimized explicit schemes to the category 1, problem 1 of the Fourth CAA Workshop. The schemes used, *i.e.* finite differences, low-storage Runge-Kutta algorithm and selective filters removing grid-to-grid oscillations, were designed to be low dissipative and low dispersive for wave numbers up to about $k\Delta x = \pi/2$ corresponding to four point per wavelength. Their ability to compute long-range propagation of high-frequency disturbances is illustrated by the numerical solutions of the problem.

INTRODUCTION

In computational aeroacoustics (CAA), it is recognized that the propagation of sound waves in far-field requires integration with minimal dissipation and dispersion, as reminded in reference 1. This can not be done with the schemes generally used in computational fluid dynamics, which led to the developement of schemes with properties optimized for CAA problems. These schemes were used in direct computations of the aerodynamic noise from the unsteady compressible Navier-Stokes equations, for instance to study jet noise in reference 2. The use of accurate schemes is also of great importance for the flow simulation itself to correctly describe the turbulent field, especially in Large Eddy Simulations where the scales larger than the grid spacing are intended to be calculated.

To perform reliable simulation of turbulent flows and of their radiated sound fields, explicit schemes were therefore designed in reference 3 by minimizing their dissipation and dispersion for a large range of wave numbers, typically up to four points per wavelength (PPW). Finite-differences and selective filters removing grid-to-grid oscillations, using 9, 11 and 13-point stencils, and 5-stage and 6-stage low-storage Runge-Kutta algorithms were proposed. They have recently been used for LES of jets or cavity flows as illustrated in references 4 and 5.

In the present paper, the aliasing problem of the 4th CAA workshop is solved using these optimized schemes. The 13-point finite-differences and the 6-stage Runge-Kutta algorithm are used for spatial discretization and time integration. Solutions obtained without filtering, or using the standard 6th-order filter or the 13-point optimized filter, are presented and discussed. The motivation is to illustrate the accuracy of the different numerical methods, particularly for computing high-frequency waves. The paper is organized as follows: first the properties of the numerical schemes used are provided, second the formulation of the aliasing problem is briefly reminded, and finally the numerical solutions of the problem are shown.

NUMERICAL SCHEMES

Finite-difference scheme

The explicit centrered 13-point finite-difference scheme used in the present work was developed following the way proposed by Tam & Webb in reference 6, by minimizing its dispersion up to the wave number $k\Delta x \leq 3\pi/5 \simeq 1.9$ (*i.e.* 3.4 PPW). The difference between the exact wave number and the effective wave number provided by this scheme, $k^\star\Delta x = 2\sum_{j=1}^{6} a_j \sin\left(jk\Delta x\right)$ where a_j are the scheme coefficients given in reference 3, is shown in figure 1. It is found to be negligible for wave numbers well above $k\Delta x = \pi/2$ as requested. The criterium $|k^\star\Delta x - k\Delta x|/\pi \leq 2 \times 10^{-4}$ is here used to define the waves accurately resolved. One can thus associate to the present scheme an accuracy limit of $k_{max}\Delta x \simeq 1.8$ (3.4 PPW).
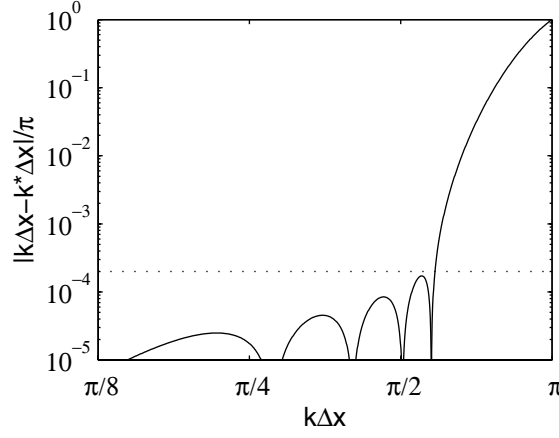
Figure 1: Dispersion error provided by the 13-point optimized finite-difference scheme. ⋯⋯⋯ accuracy criterium.

Low-storage Runge-Kutta algorithm

The time integration is performed using a low-storage 6-step Runge-Kutta algorithm optimized in the Fourier space, following the idea developed by Hu *et al.* in reference 7. The dissipation and dispersion provided by the algorithm have been minimized for angular frequencies up to $\omega\Delta t = \pi/2$ while demanding stability for high values of CFL numbers. The dissipation and dispersion errors per time step Δt calculated from the amplification factor $G_{RK}\left(\omega\Delta t\right) = \hat{u}^{n+1}/\hat{u}^n = 1 + \sum_{j=1}^{6} \gamma_j \left(i\omega\Delta t\right)^j$ are presented in figure 2 (see in reference 3 for the coefficients γ_j). As expected they are very small for a large range of angular frequencies. Considering that the dissipation and the dispersion are negligible, respectively, for $1 - |G_{RK}| \leq 2 \times 10^{-4}$ and for $|\omega^\star\Delta t - \omega\Delta t|/\pi \leq 2 \times 10^{-4}$, the accuracy limits in amplitude and in phase are observed to be $\omega_{max}^{ampl}\Delta t = 1.80$ and $\omega_{max}^{phase}\Delta t = 1.42$. These correspond, using a time step based on a CFL number of 0.8, to $k_{max}^{ampl}\Delta x \simeq 2.5$ (2.5 PPW) and to $k_{max}^{phase}\Delta x \simeq 1.8$ (3.6 PPW) in terms of wave numbers.

Selective filters

In simulations using finite-differences, filtering must usually be applied to remove grid-to-grid oscillations which might lead to numerical instabilities as reminded in reference 8. Filtering are generally selective in the sense that they do not significantly damp the well-resolved large scales. Two explicit filters are tested

(a)   (b)
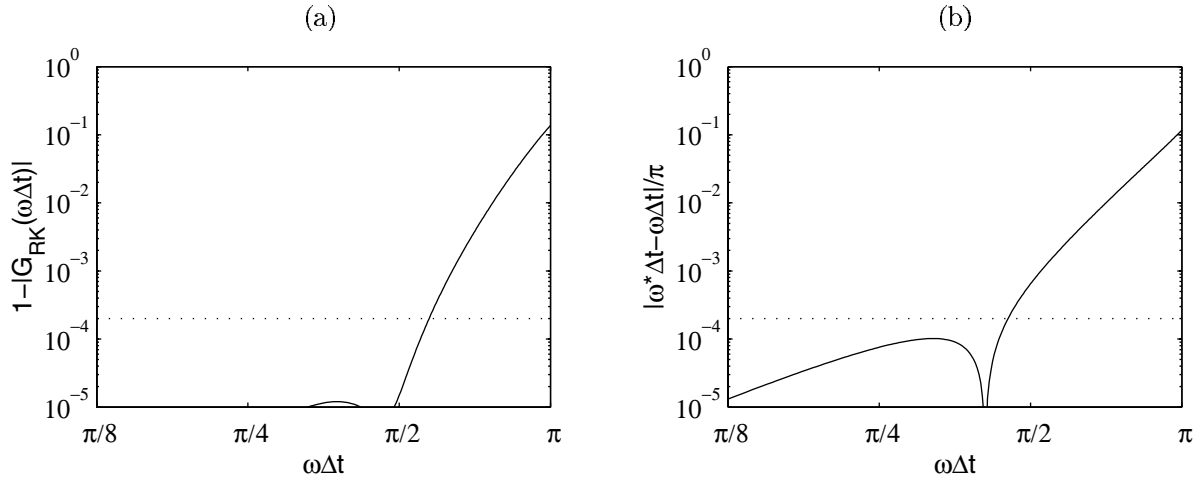
Figure 2: (a) Dissipation, and (b) dispersion error provided by the 6-step optimized Runge-Kutta algorithm per time step. $\cdots\cdots$ accuracy criteria.

in the present work: the standard 6th-order filter and the optimized 13-point stencil filter developed in reference 3. They are applied to variable u every time step to provide $u^f = u - \sigma_d D_k(u)$ with σ_d taken arbitrarily as 0.2 and $D_u(u_i) = \sum_{j=-6}^{6} d_j u_{i+j}$. The damping function of the filter is then $D_k(k\Delta x) = d_0 + \sum_{j=1}^{N} 2d_j \cos(jk\Delta x)$. It is presented in figure 3 for the two filters. The damping is less important for short waves using the 13-point filter as expected since its coefficients d_j were chosen to minimize dissipation for $k\Delta x \leq \pi/2$ (4 PPW).

(a)   (b)
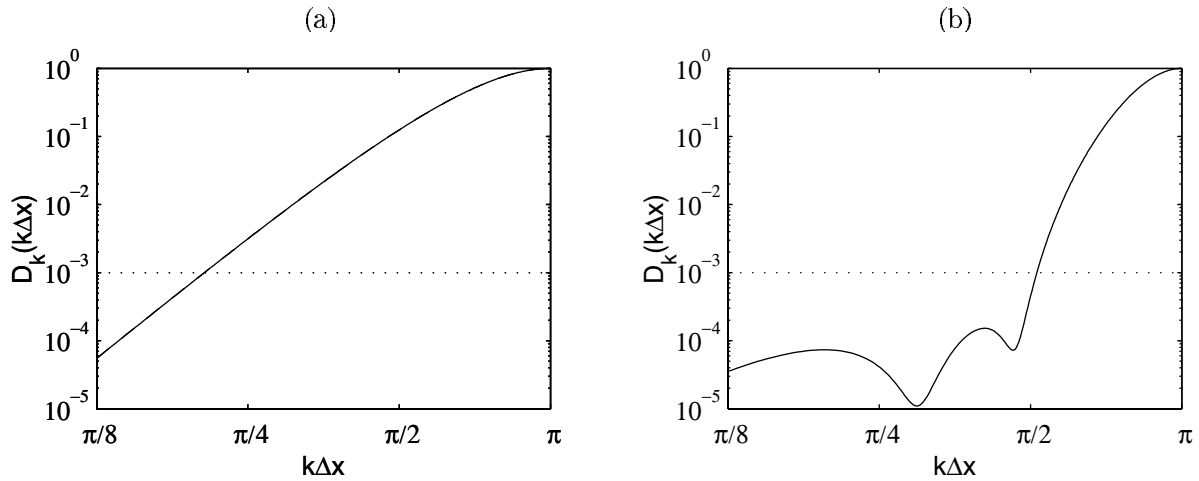
Figure 3: Damping functions of: (a) the standard 6th-order filter, and (b) the optimized 13-point filter. $\cdots\cdots$ accuracy criterium.

Accuracy limits are also determined, using the criterium $\sigma_d D_k(k\Delta x) \leq 2 \times 10^{-4}$ corresponding to $D_k \leq 10^{-3}$ with $\sigma_d = 0.2$. The highest wave numbers not dissipated are thus $k_{max}\Delta x = 0.64$ (9.8 PPW) for the standard 6th-order filter and $k_{max}\Delta x = 1.6$ (3.9 PPW) for the optimized 13-point filter. The propagation of short waves is clearly possible using the 13-point filter, while the 6th-order filter is able to take into account only very low frequencies.

CATEGORIE 1, PROBLEM 1

Formulation

This problem proposes to compute the solution of the wave equation

$$\frac{\partial u}{\partial t} + \frac{\partial u}{\partial x} = 0 \tag{1}$$

on a uniform mesh grid with $\Delta x = 1$ and the following initial conditions

$$u = [2 + \cos(kx)] \exp\left[-(\ln 2)\left(\frac{x}{10}\right)^2\right] \tag{2}$$

Two cases are to be considered:

(i) $k = 1.7$

(ii) $k = 4.6$

and the solutions are to be given at $t = 400$ and $t = 800$.

The initial disturbances are presented continuously in figure 4(a) and figure 5(a) for the two cases. As shown by spectra of figures 4(b) and 5(b), they are well resolved by the imposed grid in case (i) with 3.7 PPW, but they are unresolved in case (ii) with only 1.4 PPW. In this case, the wave number $k = 4.6$ will be aliased back into the resolved range to become $2\pi - 4.6 \simeq 1.7$. Thus solving case (ii) will be equivalent to solving case (i). Only solutions of case (i) will therefore be now presented.
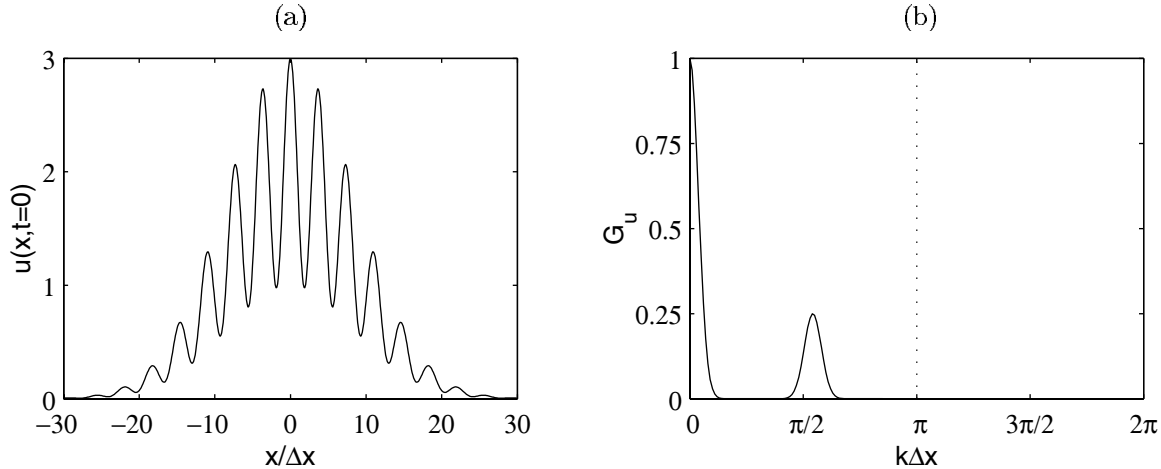
Figure 4: Case (i) with $k = 1.7$: (a) initial disturbances and, (b) their normalized spectral content. $\cdots\cdots$ maximum wave number supported by the grid

To later discuss of the numerical solutions, the spectral content of the initial conditions of case (i) is displayed in figure 6 with the maximum wave numbers resolved by the finite-differences, by the two filterings, and by the Runge-Kutta algorithm for a CFL number of 0.8.
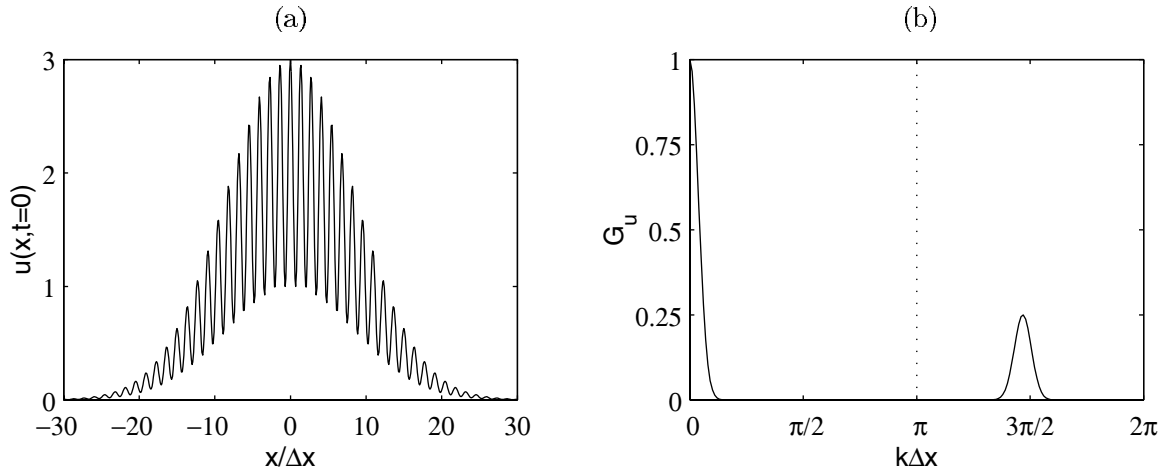
Figure 5: Case (ii) with $k = 4.6$: (a) initial disturbances and, (b) their normalized spectral content. ······· maximum wave number supported by the grid
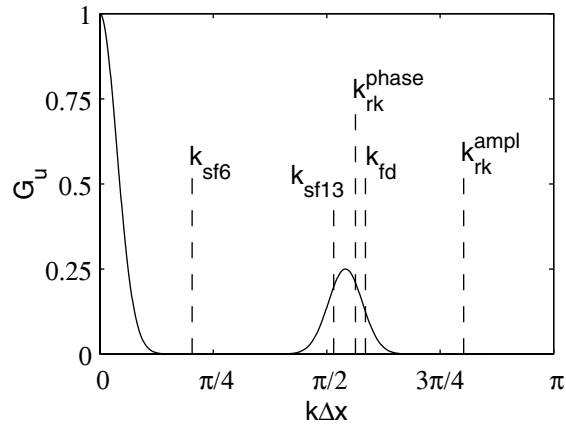
Figure 6: Normalized spectral content of the initial disturbances of problem (i), with the maximum wave numbers resolved by: the 13-point optimized finite-differences k_{fd}, the 6th-order standard filtering k_{sf6}, the 13-point optimized filtering k_{sf13}, the optimized Runge-Kutta algorithm in amplitude k_{rk}^{ampl} and in phase k_{rk}^{phase}.

Numerical solutions of case (i)

Solutions without filtering

First case (i) is resolved without filtering to only study the errors resulting from the spatial derivation and from time integration. The solutions at $t = 800$ thus obtained with CFL numbers of 0.05 and 0.8 are shown in figures 7(a) and (b), respectively.

The solution calculated with CFL = 0.05 is in fairly good agreement with the exact solution. No dissipation is observed but, as expected considering the accuracy limit k_{fd} in figure 6, a part of the high-frequency components of the wave is distorded.

In the solution calculated with CFL = 0.8, dispersion is still more visible. These errors in phase result both from the finite-differences and from the Runge-Kutta algorithm, whose accuracy limits k_{fd} and k_{rk}^{phase} are very close. It should be also noted that the high-frequency components are not dissipated by the time integration with the present CFL number of 0.8 corresponding to values usually chosen in simulations, which is remarkable in itself.
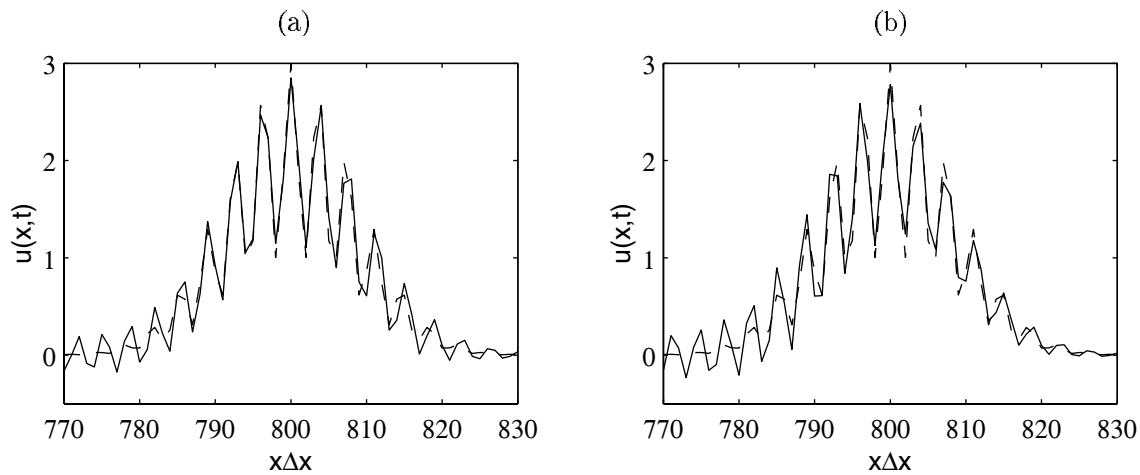
Figure 7: Solutions at $t = 800$: ———— numerical solutions without filtering using, (a), CFL = 0.05, and (b), CFL = 0.8; − − − exact solution.

Solutions with filtering

Case (i) is now resolved as in figure 7(b) using CFL = 0.8, but with the filtering. The solution obtained at $t = 800$ using the standard 6th-order filter is displayed in figure 8(a). The high-frequency components of the initial disturbances have been dissipated by the filtering. It only remains the low-frequency components corresponding to the initial Gaussian pulse, as shown in the figure. The removing of the high-frequency part of the problem disturbances is well visible in the spectrum of figure 8(b).

The solution of the problem at $t = 800$ obtained using the optimized 13-point filter is presented in figure 9(a). Compared to the exact solution, it is clearly dissipated by not significantly distorded. This results from the position of the maximum wave number affected by the filtering with respect to these of the accuracy limits of the finite-differences and of the Runge-Kutta algorithm. As supported in figure 7, the wave numbers not properly calculated by the two latter schemes are dissipated by the filtering. Thus the numerical solution contains only a part of the high-frequency components of the exact solution as demonstrated in figure 9(b), but the resolved part is properly calculated. This illustrates the attention we must pay when choosing the different schemes used in a numerical algorithm: one must ensure that their

(a)   (b)
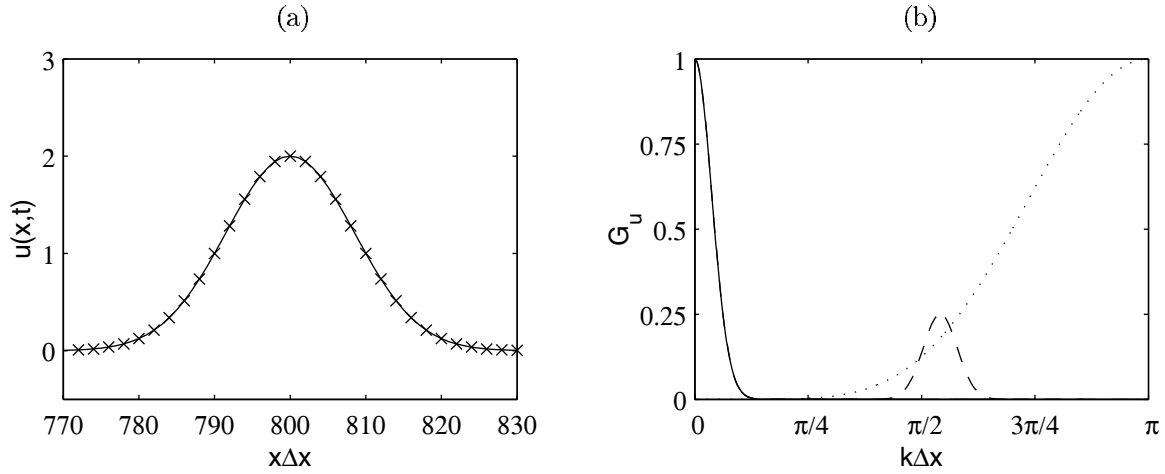
Figure 8: (a) Solutions at $t = 800$: ———— numerical solution with the 6th-order standard filtering using CFL $= 0.8$ and $\sigma_d = 0.2$; $\times$ solution corresponding to the Gaussian pulse alone. (b) Normalized spectral contents of the ———— numerical and $- - -$ exact solutions at $t = 800$; $\cdots\cdots$ damping function of the 6th-order filter.

respective limits of accuracy are similar and that the distorted waves are filtered out.

(a)   (b)
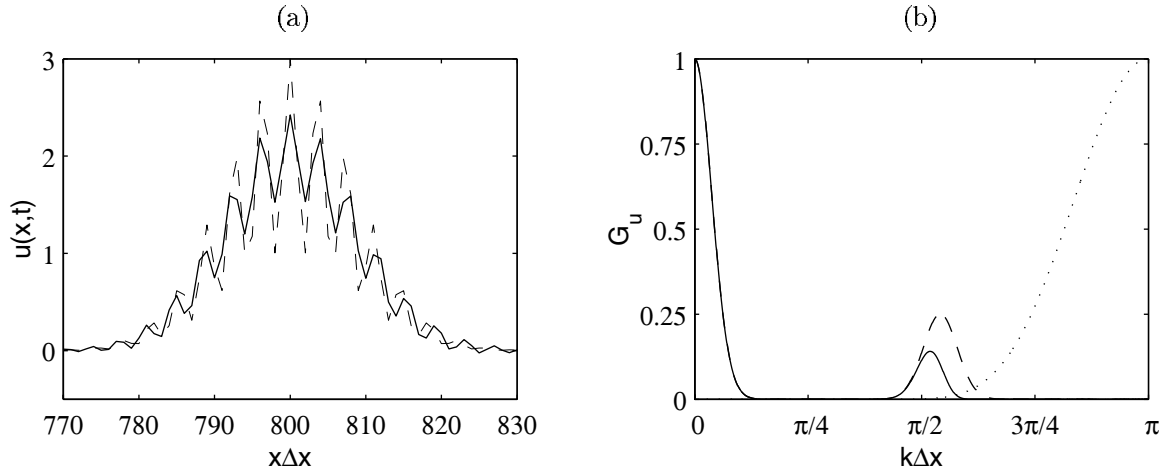
Figure 9: (a) Solutions at $t = 800$: ———— numerical solution with the 13-point optimized filtering using CFL $= 0.8$ and $\sigma_d = 0.2$; $- - -$ exact solution. (b) Normalized spectral contents of the ———— numerical and $- - -$ exact solutions at $t = 800$; $\cdots\cdots$ damping function of the 13-point filter.

REFERENCES

1. Tam, C.K.W: Computational aeroacoustics: issues and methods. AIAA Journal, vol.33, no.10, 1995, 1788-1796.

2. Bogey, C.; Bailly, C.; and Juvé, D.: Noise investigation of a high subsonic, moderate Reynolds number jet using a compressible LES. Theoret. Comput. Fluid Dynamics, vol.16, no.4, 2003, 273-297.

3. Bogey, C.; and Bailly, C.: A family of low dispersive and low dissipative explicit schemes for flow and noise computations. To appear in J. Comput. Phys., 2004. See also AIAA Paper 2002-2509.

4. Bogey, C.; and Bailly, C.: Direct computation of the sound radiated by a high Reynolds number, subsonic round jet. Proceedings of the CEAS Workshop From CFD to CAA, Nov. 2002, Athens, Greece. See also AIAA Papers 2003-3170 and 2003-3557.

5. Gloerfelt, X.; Bogey, C.; Bailly, C.; and Juvé, D.: Aerodynamic noise induced by laminar and turbulent boundary layers over rectangular cavities. AIAA Paper 2002-2476. See also AIAA Paper 2003-3234.

6. Tam, C.K.W.; and Webb, J.C.: Dispersion-relation-preserving finite difference schemes for computational acoustics. J. Comput. Phys., vol.107, 1993, 262-281.

7. Hu, F.Q.; Hussaini, M.Y.; and Manthey, J.L.: Low-dissipation and low-dispersion Runge-Kutta schemes for computational acoustics. J. Comput. Phys., vol.124, 1996, 177-191.

8. Tam, C.K.W.; Webb, J.C.; and Dong, Z.: A study of the short wave components in computational acoustics. J. Comput. Acoustics, vol.1, no.1, 1993, 1-30.

SOLUTION OF CATEGORY 1, PROBLEM 1, BY A SEMI-CHARACTERISTICS METHOD

Johan B.H.M. Schulten[*]
Acustica Nova, Hunzestraat 6, 8303 LK Emmeloord, The Netherlands
E-mail: johan.schulten@planet.nl

ABSTRACT

In the present paper a method based on characteristics is applied to the one-dimensional propagation of a tone burst. The method is called a semi-characteristics method and differs from the pure characteristics method by the adoption of a fixed grid in space. In general this means that for every time step the dependent variables have to be interpolated from the fixed grid values. Although this interpolation requires an additional computational effort, the advantage is that considerably more complex problems can be addressed than is possible with the pure characteristics method.

Essentially, the method of characteristics is the modeling of sound propagation and the method can yield exact results in the limit of planar waves and a uniform background. Under the ideal conditions of the present benchmark problem, the semi-characteristics method and the pure characteristics method become effectively identical. As a result the analytical solution of the benchmark problem is recovered with machine precision. Moreover this can be achieved with an arbitrary large time step, which implies a high computational efficiency. Compared to other CAA methods the most outstanding property however is the absence of any effect of the waveform on the accuracy of the results.

INTRODUCTION

Already in the early days of CFD several schemes based on characteristics in multi-dimensions were developed. In reference 1 Holt reviews the methods proposed in the 50's of the last century. Also in more recent times occasionally methods based on characteristics were published (refs. 2-4). Possibly because of the necessity of shock fitting instead of shock-capturing these methods have never become very popular in the CFD world.

Around 1990 computational power had grown strong enough to consider direct computational simulation of sound propagation problems. However, standard CFD methods appeared to have a notoriously poor performance (large numerical dissipation) for sound propagation and special, high order finite difference CAA methods were developed (refs. 5,6) to overcome this problem.

By nature the method of characteristics is particularly suitable for sound propagation and an attempt to apply this method in CAA was made by Thomas and Roe (ref. 7) in 1993. Although, they successfully computed some model problems, the staggered mesh arrangement they need does not look very inviting, apparently.

In its pure form, the method of characteristics yields the values of the characteristic variables at discrete points in space-time. In general these points are found as part of the solution by tracking the 'wave particle' positions convected by the flow. In reference 8 this pure form of the method was successfully applied to a number of test examples for computational aeroacoustics (CAA) from the 1st CAA Workshop on Benchmark Problems (ref. 9). The pure characteristics method works very efficiently and accurately for a single wave system in a uniform background flow.

Serious topological difficulties arise for more general problems in which the wave particle trajectories may become very complex. This difficulty is similar to that of pure Lagrangian fluid dynamics in which the same set of material fluid particles is followed all the time. In the semi-Lagrangian method (refs. 10,11) this problem is avoided by interpolating the solution to a fixed grid for every time step. This way out can be readily transferred to the method of characteristics to obtain the present 'semi-characteristics' method, which incorporates the semi-Lagrangian method as well. In the semi-characteristics method the required values of the characteristic variables at 'departure

---

[*] Research Scientist.

level' are interpolated from the fixed grid at every time step. It may be clear that this interpolation is a possible source of numerical dissipation or dispersion and therefore a matter of concern.

Fortunately, some of the favorable properties of the method of characteristics are conserved in the semi-characteristics method. One of the most striking properties is the absence of a CFL limit, i.e. a maximum time step, for numerical stability. In principle this property allows huge time steps. Indeed in the present one-dimensional benchmark problem a CFL number of 200 has been used. Actually, identical results are obtained for any other integer CFL number. As a matter of fact, in one-dimensional problems there is no significant difference between the pure characteristics method and the semi-characteristics method. However, it is to be noted that in multi-dimensional problems the time step magnitude may directly affect the accuracy of the solution because of possible cross-wave interactions. As a result much smaller time steps have to be taken in general.

THEORY

Multi-Dimensional Analysis

The starting point of the present analysis is the system of Euler equations for an inviscid, compressible flow. These equations can be written as:

continuity equation

$$\frac{\partial \rho}{\partial t} + \mathbf{v}\bullet\nabla\rho + \rho\nabla\bullet\mathbf{v} = 0 \tag{1}$$

momentum equation

$$\frac{\partial \mathbf{v}}{\partial t} + (\mathbf{v}\bullet\nabla)\mathbf{v} + \frac{\nabla p}{\rho} = \mathbf{0} \tag{2}$$

and energy equation

$$\frac{\partial p}{\partial t} + \mathbf{v}\bullet\nabla p + \gamma p\nabla\bullet\mathbf{v} = 0 \tag{3}$$

In the above equations the following, conventional notation has been adopted:

$\mathbf{v}$ = velocity, p = pressure, t = time, ρ = density, and γ = adiabatic index (ratio of specific heats at constant pressure and constant volume).

It is convenient to introduce the entropy S:

$$S = \ln\frac{p}{\rho^{\gamma}} \tag{4}$$

and to substitute the law for an ideal gas:

$$p = \frac{\rho c^2}{\gamma} \tag{5}$$

into equations (1) - (3) to eliminate p and ρ in favor of S and c (the local speed of sound).

Then linear combination of the continuity equation and the energy equation to eliminate $\nabla\bullet\mathbf{v}$ yields the entropy equation:

$$\frac{\partial S}{\partial t} + \mathbf{v}\bullet\nabla S = 0 \tag{6}$$

The next step is the transformation of the flow equations to the Lagrangian coordinate system, i.e. a system that moves with the flow. In such a system $d\mathbf{x}/dt = \mathbf{v}$. Hence, the convective time derivative ($\partial/\partial t + \mathbf{v}\bullet\nabla$) in the Euler system transforms into a pure time derivative $\partial/\partial t$ in the Lagrangian system. As a result we obtain the transformed

momentum equation

$$\left[\frac{\partial \mathbf{v}}{\partial t} + c\nabla\left(\frac{2c}{\gamma - 1}\right) = \frac{c^2 \nabla S}{\gamma(\gamma - 1)}\right]_{d\mathbf{x}/dt = \mathbf{v}} \tag{7}$$

energy equation

$$\left[\frac{\partial}{\partial t}\left(\frac{2c}{\gamma - 1}\right) + c\nabla\bullet\mathbf{v} = 0\right]_{d\mathbf{x}/dt = \mathbf{v}} \tag{8}$$

and entropy equation

$$\left[\frac{\partial S}{\partial t} = 0\right]_{d\mathbf{x}/dt = \mathbf{v}} \tag{9}$$

The Lagrangian equations (7) - (9) look more simple than the Euler equations (1) - (3) but it is to be noted that the Lagrangian equations are only valid when the path of a fluid particle is followed. This requires knowledge of the local velocity, which is, in general, a part of the solution. As a result, the solution of the Lagrangian equations is more intricate.

A problem arises if one tries to track an initially well-ordered set of particles over a longer period of time. Especially when vortices are present the particle paths are subject to a roll-up mechanism and tend to become very tortuous. The resulting discrete data points in space-time form a cumbersome basis to solve the equations.

In the semi-Lagrangian method (ref. 3) this difficulty is avoided by interpolating the solution to a fixed grid at every time step. In the present method this semi-Lagrangian practice is included. The price to be paid is of course the additional effort of the interpolation.

Next, we will construct linear combinations of the momentum and energy equations such that the equations in characteristic form appear. Because the momentum equation Eq. (7) is a vector equation each of its components is combined with the scalar energy equation Eq. (8). Here we adopt a Cartesian coordinate system, the orientation of which can still be chosen freely. Because the extension from two to three dimensions is trivial, we restrict ourselves in this paper to two-dimensional space.

In Cartesian coordinates the momentum equation in *x*-direction is given by:

$$\left[\frac{\partial v_x}{\partial t} + c\frac{\partial}{\partial x}\left(\frac{2c}{\gamma - 1}\right) = \frac{c^2}{\gamma(\gamma - 1)}\frac{\partial S}{\partial x}\right]_{d\mathbf{x}/dt = \mathbf{v}} \tag{10}$$

and in *y*-direction by:

$$\left[\frac{\partial v_y}{\partial t} + c\frac{\partial}{\partial y}\left(\frac{2c}{\gamma - 1}\right) = \frac{c^2}{\gamma(\gamma - 1)}\frac{\partial S}{\partial y}\right]_{d\mathbf{x}/dt = \mathbf{v}} \tag{11}$$

Similarly, the Cartesian version of the energy equation Eq.(8) becomes:

$$\left[\frac{\partial}{\partial t}\left(\frac{2c}{\gamma - 1}\right) + c\left(\frac{\partial v_x}{\partial x} + \frac{\partial v_y}{\partial y}\right) = 0\right]_{d\mathbf{x}/dt = \mathbf{v}} \tag{12}$$

Now, addition of Eqs. (10) and (12) yields:

$$\left[\frac{\partial}{\partial t}\left(v_x + \frac{2c}{\gamma - 1}\right) + c\frac{\partial}{\partial x}\left(v_x + \frac{2c}{\gamma - 1}\right) = -c\frac{\partial v_y}{\partial y} + \frac{c^2}{\gamma(\gamma - 1)}\frac{\partial S}{\partial x}\right]_{d\mathbf{x}/dt = \mathbf{v}} \tag{13}$$

Clearly, along the characteristic $dx/dt = c$ in the Lagrangian system the equation can be written as:

$$\left[\frac{d(v_x + \dfrac{2c}{\gamma - 1})}{dt} = \frac{c^2}{\gamma(\gamma - 1)} \frac{\partial S}{\partial x} - c\frac{\partial v_y}{\partial y} \right]_{d\mathbf{x}/dt = \mathbf{v} + c\mathbf{i}_x} \tag{14}$$

Note that Eq. (14) has the form of a simple ordinary differential equation: the first derivative in time of the characteristic variable equals a function of time. This is because the space coordinates are coupled to time through the direction of the characteristic. Eq.(14) describes a convected wave advancing in *x*-direction. The change of its amplitude is governed by the right hand side of the equation. Also note that the non-linearity of this equation is only present in the right hand side.

Quite similarly by subtraction of Eq. (12) from Eq. (10) the equation for the receding wave is obtained:

$$\left[\frac{d(v_x - \dfrac{2c}{\gamma - 1})}{dt} = \frac{c^2}{\gamma(\gamma - 1)} \frac{\partial S}{\partial x} + c\frac{\partial v_y}{\partial y} \right]_{d\mathbf{x}/dt = \mathbf{v} - c\mathbf{i}_x} \tag{15}$$

Eqs. (14) and (15) are called the bi-characteristic equations in *x*-direction. Note that for a constant v_y and a constant entropy *S,* Riemann's celebrated equations for one-dimensional, nonlinear gas dynamics are recovered.

The equations for the waves in *y*-direction are found analogously by addition and subtraction of Eq. (11) and Eq.(12).

The characteristics along which the bi-characteristics equations have to be integrated in time are presented in figure 1. The convective characteristic along which the entropy equation [Eq.(9))] has to be integrated forms the axis of a cone which is the locus of all possible characteristics passing through a certain point in space-time (the apex).
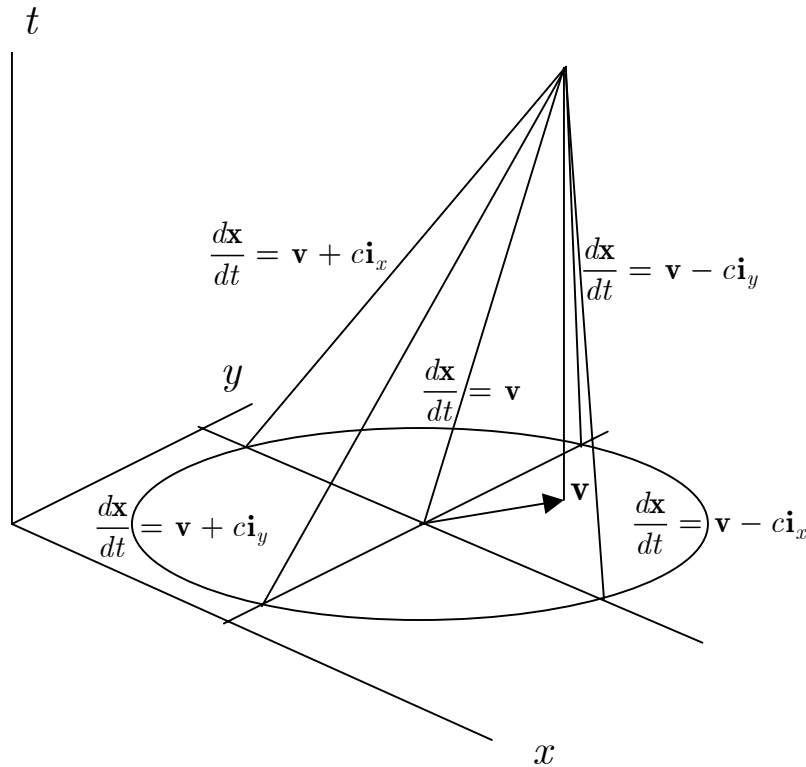
Figure 1. Characteristics in two-dimensional space-time

In total we now have five equations to be integrated in time. Since there are only four primitive variables (c, v_x, v_y, S), there is some redundancy. Indeed, c can be evaluated either from the bi-characteristic variables in x- or from those in y-direction. Averaging the two evaluations would lead to numerical instability, if the data at the new time level were not computed iteratively. This iteration is also required to compute the right hand sides of the bi-characteristic equations accurately. Numerically, time integration is performed by a standard 4th order Runge-Kutta method.

Although interpolation is an important issue in the semi-characteristics method, we will not discuss it here because it plays no role in the present benchmark problem.

Application to the Present Problem

The present problem concerns the numerical solution of the following equation

$$\frac{\partial u}{\partial t} + \frac{\partial u}{\partial x} = 0 \tag{16}$$

for given initial conditions. To see the relation with the flow equations we rewrite Eqs. (10) and (12) for a homentropic, one-dimensional flow linearized about a uniform background as follows:

$$\frac{\partial u}{\partial t} + \frac{\partial}{\partial x}\left(\frac{2c}{\gamma - 1}\right) = 0 \tag{17}$$

and

$$\frac{\partial}{\partial t}\left(\frac{2c}{\gamma - 1}\right) + \frac{\partial u}{\partial x} = 0 \tag{18}$$

where u and c now are the dimensionless perturbations of velocity and speed of sound respectively. Because the mean flow is zero, the Lagrangian and Eulerian formulation are identical in this case.

The bi-characteristic equations resulting from Eqs. (17) and (18) are:

$$\left[\frac{d\left(u + \dfrac{2c}{\gamma - 1}\right)}{dt} = 0\right]_{dx/dt = 1} \tag{19}$$

and

$$\left[\frac{d\left(u - \dfrac{2c}{\gamma - 1}\right)}{dt} = 0\right]_{dx/dt = -1} \tag{20}$$

The global initial condition

$$t = 0: \quad u(x) = \frac{2c(x)}{\gamma - 1} \tag{21}$$

guarantees zero amplitude of the receding wave for all time and as a result the initial condition remains valid for all times. Substitution of Eq.(21) in either Eq. (17) or (18) then recovers Eq.(16). Note that Eq. (21) does not specify anything about the waveform itself. So it is applicable to any shape of the wave.

Numerical integration in time of Eqs. (19) and (20) turns out to be just a triviality because of the zero right hand sides of the equations and the fixed characteristics $dx/dt = \pm 1$.

NUMERICAL RESULTS

In the present problem the specific initial condition is given by a 'tone burst':

$$t = 0: \quad u = \left[2 + \cos(\alpha x)\right] \exp\left[-\ln 2 (x/10)^2\right] \tag{22}$$

with a uniform discretization of $\Delta x = 1$.

Two values of the wave number α are considered: $\alpha = 1.7$ (3.7 points per wavelength) and $\alpha = 4.6$ (1.4 points per wavelength). For testing purposes the number of points per wavelength has been chosen deliberately (far) too low for a good resolution of the original signal.

As can be observed in figures 2 and 3 the semi-characteristics method perfectly mimics the analytical solution of this one-dimensional advection problem. A CFL number of 200 was used in the computation, but identical results are obtained for any other integer CFL number. An integer CFL number means that the interpolation is idle and does not introduce a significant numerical error. This is confirmed in figure 4 which shows that the numerical error is of the order of the machine accuracy.

CONCLUDING REMARKS

The present benchmark problem clearly illustrates the outstanding performance of the method of semi-characteristics in simulating the propagation of sound numerically.

In one space dimension with uniform background, there is effectively no difference between the pure characteristics and the semi-characteristics method. Both yield perfect results for certain discrete points in space-time.

Unlike the behavior of most other CAA methods, this perfect simulation does not depend on the wave shape. The propagation of very irregular signals, like the high frequency case in the present problem, is simulated with the same degree of perfection as smooth waves.

For a homentropic flow in one space dimension very large time steps are possible because there is no CFL-limit for numerical stability. In non-homentropic flow and in multi-dimensions the time step is limited by accuracy requirements. Large time steps can still be taken in regions with almost planar wave fronts and small entropy gradients, such as occur in atmospheric acoustics.

In the present semi-characteristics method some of the pitfalls of the pure characteristics method have been avoided. At the same time the main advantages of the pure characteristics method for aeroacoustics computations have been preserved.

REFERENCES

1. Holt, M., "Numerical Methods in Fluid Dynamics", Springer-Verlag, Berlin, 2nd Ed., 1984, pp.90-113.
2. Marcum, D.L., Hoffman, J.D., "Calculation of Three-Dimensional Flowfields by the Unsteady Method of Characteristics", AIAA Journal, Vol.23, No.10, Oct. 1985, pp. 1497-1505.
3. Parpia, H., Kentzer, C.P., Williams, M.H., "Multidimensional Time Dependent Method of Characteristics", Computers & Fluids, Vol.16, No.1, 1988, pp. 105-117.
4. Dadone, A., Moretti, G., "Fast Euler Solver for Transonic Airfoils Part I: Theory", AIAA Journal, Vol.26, No.4, April 1988, pp. 409-416.
5. Tam, C.K.W., "Computational Aeroacoustics: Issues and Methods", AIAA Journal, Vol. 33, No.10, Oct. 1995, pp. 1788-1796.
6. Lele, S.K, "Computational Aeroacoustics: A Review", AIAA Paper 97-0018, Jan. 1997
7. Thomas, J.P., Roe, P.L.," Development of Non-Dissipative Numerical Schemes for Computational Aeroacoustics", AIAA Paper 93-3382-CP, Proc. AIAA Comp. Fluid Dyn. Conf., July 1993, pp. 906-916.
8. Schulten, J.B.H.M., "On the Use of Characteristics in Computational Aeroacoustics", AIAA Paper 2002-2584, June 2002.
9. Hardin, J.C. et al., "ICASE/LaRC Workshop Benchmark Problems in Computational Aeroacoustics (CAA)", NASA Conference Publication 3300, May 1995.
10. Boyd, J.P., Chebyshev and Fourier Spectral Methods, Dover Publications Inc., 2nd Ed., 2000, Ch.14.
11. Margolin, L., Introduction to "Arbitrary Lagrangian-Eulerian Computing Method for All Flow Speeds", J. Comp. Phys., 135 (1997), pp. 198-202.
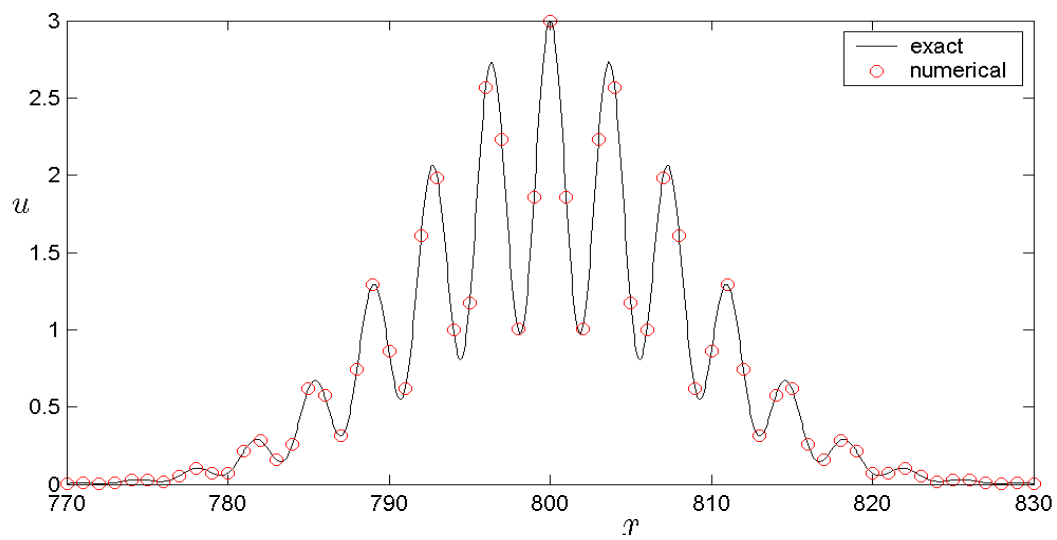
Figure 2. t = 800, α = 1.7
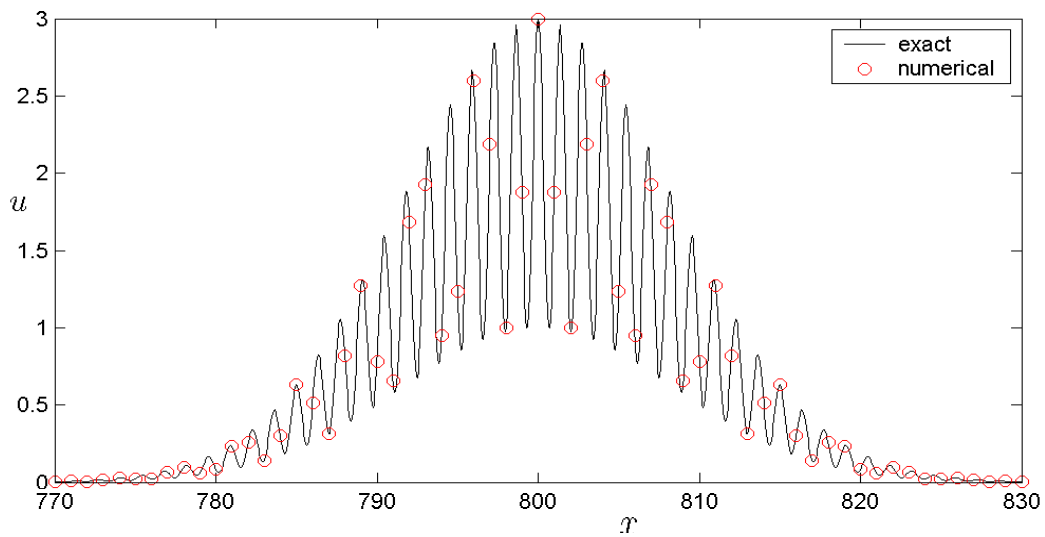
Figure 3. *t* = 800, *α* = 4.6
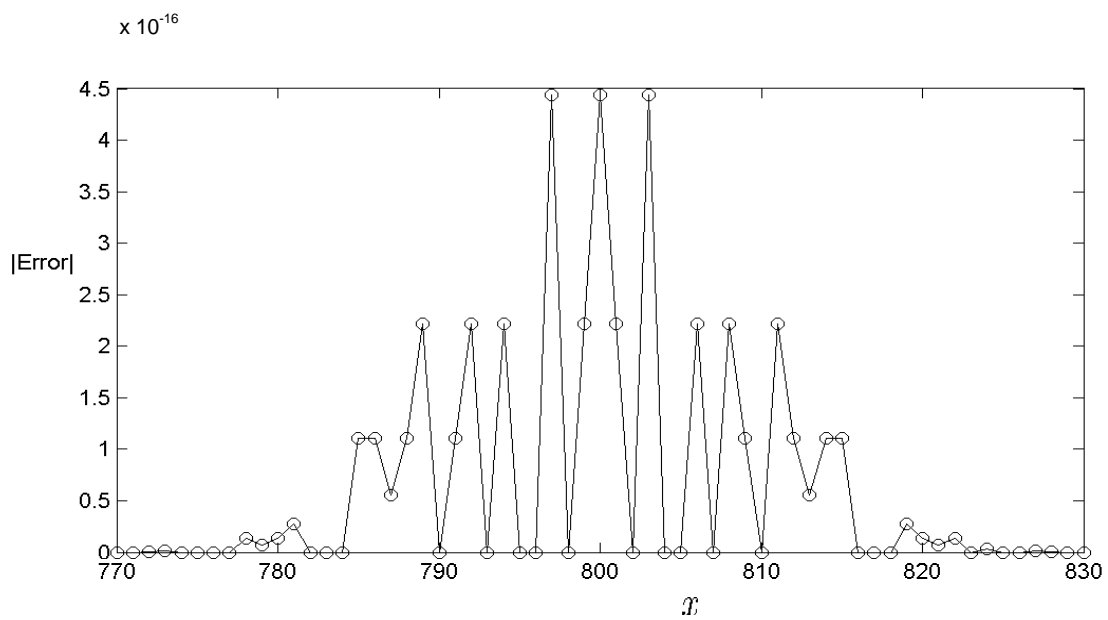
Figure 4. **Absolute numerical error for** $t = 800$, $\alpha = 4.6$

fastADER : An Arbitrary High Order Scheme for Linear Acoustics

T. Schwartzkopff, C.–D. Munz

Institute for Aero– and Gasdynamics, Stuttgart University
Pfaffenwaldring 21, 70550 Stuttgart, Germany
schwartzkopff@iag.uni-stuttgart.de
phone:+49-711-685-3444

Abstract

For the solution of aeroacoustical problems, it is necessary to use high order schemes to resolve the wave propagation accurately over long distances . Sixth order Finite–Difference schemes are used commonly in space, although the discretization method for time integration is often a fourth order accurate Runge Kutta type integration and thus the overall scheme remain fourth order. The *fast*ADER approach is not suffering from the order restriction of the Runge-Kutta schemes, the so called Butcher barrier. The schemes have uniform, arbitrary order in space and time. The schemes can be implemented highly efficiently if the following conditions are fulfilled: globally linearized hyperbolic PDE's discretized on Cartesian grids. The CPU time grows quadratically with the order while no extra memory is needed. In the paper a von Neumann stability test, amplitude and phase error diagrams as well as numerical convergence rates are included thus giving a good overview of the method.

1   Introduction

Finite-difference schemes are very popular in the aeroacoustic community. They are easy to implement and high spatial order can be achieved easily. For time integration a Runge-Kutta type scheme is used commonly. Runge-Kutta integration schemes of an order higher than four get more and more ineffective because the number of stages needed grows not longer linear but exponentially. A combination of a spatial discretization of order higher than four with Runge-Kutta fourth order time integration remains at fourth order overall accuracy.

In this paper the fastADER scheme is presented. It is a reformulation of the ADER approach of Toro et. al. [6] for linearized equations. The ADER approach is a Finite-Volume scheme and is in general conservative, thus no energy/mass is generated or destroyed. The big advantage of this approach is, that spatial and temporal discretization may have the same arbitrary order of accuracy. The fastADER formulation is a reformulation of the ADER approach, in such a way that the kernel of the schemes becomes only a sum over matrix-vector multiplications, which can be optimized highly efficiently. However, if properties of a Finite-Volume scheme are needed, such as the use of Riemann problem solutions in the presence of strong gradients, it can be switched back to the original formulation without any problems.

The properties of these schemes with regard to CAA applications are analyzed. The first issue is the stability limit. The nice property, that the stability increases if the order of the scheme is increased, is shown. Next the wave propagation properties are investigated and compared to the classical DRP-O4 / Runge-Kutta-O4 scheme of Tam [5]. The next paragraph show the effectiveness of the *fast*ADER implementation. The computational cost grows quadratically with the order while no extra memory is needed. Again a Finite-Difference O6 / Runge-Kutta O4 scheme is compared against the proposed scheme. It turns out that, e. g. the *fast*ADER O14 schemes needs the same CPU time, but only 40% of the memory. In the last paragraph the numerical convergence rates are observed for the 6th and 14th order scheme. Finally some conclusions are drawn.

2 The *fast*ADER Scheme

A brief review of the ADER approach is given in this section. More details can be found in [2, 3, 4, 6]. The aim is to find a numerical solution for a system of linear hyperbolic PDE's of the form

$$\underline{U}_t + \underline{\underline{A}}\, \underline{U}_x + \underline{\underline{B}}\, \underline{U}_y = 0, \quad \underline{U} = \underline{U}(x,y,t) \quad \text{and} \quad \underline{U}(x,y,0) = \underline{U}^0(x,y). \tag{1}$$

For the evolution in time a Finite-Volume discretization is applied and equation (1) is integrated in space and time:

$$\overline{\underline{U}}_{ij}^{n+1} = \overline{\underline{U}}_{ij}^{n} - \frac{\Delta t}{|I_{ij}|} \left[\hat{\underline{F}}_{i+\frac{1}{2},j} - \hat{\underline{F}}_{i-\frac{1}{2},j} + \hat{\underline{G}}_{i,j+\frac{1}{2}} - \hat{\underline{G}}_{i,j-\frac{1}{2}} \right]. \tag{2}$$

The state $\overline{\underline{U}}_{ij}^{n}$ and the flux $\hat{\underline{F}}_{i+\frac{1}{2},j}$ are defined as follows:

$$\overline{\underline{U}}_{ij}^{n} = \int_{x_{i-\frac{1}{2}}}^{x_{i+\frac{1}{2}}} \int_{y_{j-\frac{1}{2}}}^{y_{j+\frac{1}{2}}} \underline{U}(\xi, \eta, t^n)\, d\xi d\eta \tag{3}$$

$$\hat{\underline{F}}_{i+\frac{1}{2},j} = \int_{y_{j-\frac{1}{2}}}^{y_{j+\frac{1}{2}}} \frac{1}{\Delta t} \int_{t^n}^{t^{n+1}} \underline{\underline{A}}\, \underline{U}(x_{i+\frac{1}{2}}, \eta, \tau)\, d\eta d\tau \tag{4}$$

The integrals of (4) must be solved numerically. For the solution of the spatial integral a standard Gaussian integration method is used. The number of Gaussian integration points is N_G and the weight of each integration point λ is ω_λ. The second integral gives the mean value in time of the flux. This integral is solved by the ADER approach and is written as

$$\hat{\underline{F}}_{i+\frac{1}{2},j} = \frac{\Delta y}{2} \sum_{\lambda=1}^{N_G} \omega_\lambda \underline{\underline{A}}\, \underline{U}^{ADER}(x_{i+\frac{1}{2}}, \eta_\lambda). \tag{5}$$

What remains is the determination of $\underline{U}^{ADER}$. First a Taylor series in time is used. In this expansion time derivatives are needed, which are numerically not available, if only one time step is stored. If the Lax-Wendroff (or Cauchy-Kowalewskaja) procedure is applied, the time derivatives are replaced by spatial derivatives using equation (1). This equation can then be integrated explicitly:

$$\underline{U}^{ADER} = \frac{1}{\Delta t} \int_{t^n}^{t^{n+1}} \underline{U}(\tau)d\tau \tag{6}$$

$$= \frac{1}{\Delta t} \int_{t^n}^{t^{n+1}} \sum_{k=0}^{\mathcal{O}-1} \frac{\tau^k}{k!} \frac{\partial^k \underline{U}(t^n)}{\partial t^k} d\tau \tag{7}$$

$$= \frac{1}{\Delta t} \int_{t^n}^{t^{n+1}} \sum_{k=0}^{\mathcal{O}-1} \frac{\tau^k}{k!} (-1)^k \left(\underline{\underline{A}}\frac{1}{\partial x} + \underline{\underline{B}}\frac{1}{\partial y} \right)^k \partial^k \underline{U}(t^n)d\tau \tag{8}$$

$$= \sum_{k=0}^{\mathcal{O}-1} \frac{(-\Delta t)^k}{(k+1)!} \left(\underline{\underline{A}}\frac{1}{\partial x} + \underline{\underline{B}}\frac{1}{\partial y} \right)^k \partial^k \underline{U}(t^n) \tag{9}$$

To obtain the spatial derivatives of $\underline{U}$ a Lagrangian interpolation method is used, which projects the integral mean values (3) to the state or derivative at the desired location. Details can be found in [4]. This reconstruction process leads to a summation over a two dimensional stencil with $(\mathcal{O}+1) \times \mathcal{O}$ points, where each point has its specific weight $C_{ii,jj,\lambda}^{m,l}$ depending on the position ii, jj in the stencil, the desired derivative

$\partial^{m+l}/(\partial x^m \partial y^l)$ and the Gaussian integration point. The numerical Flux (5) is then given by:

$$\hat{\underline{F}}_{i+\frac{1}{2},j} = \frac{\Delta y}{2} \sum_{\lambda=1}^{N_G} \omega_\lambda \underline{\underline{A}} \sum_{k=0}^{\mathcal{O}-1} \frac{(-\Delta t)^k}{(k+1)!} \left[\sum_{m=k}^{0} \underline{\underline{M}}(\underline{\underline{A}},\underline{\underline{B}},k,m) \left(\sum_{ii=-\mathcal{O}/2+1}^{\mathcal{O}/2} \sum_{jj=-\mathcal{O}/2}^{\mathcal{O}/2} C_{ii,jj,\lambda}^{m,k-m} \underline{U}_{i+ii,j+jj} \right) \right] \quad (10)$$

$$\underline{\underline{M}} = \underline{\underline{M}}(\underline{\underline{A}},\underline{\underline{B}},k,m) = \sum_{I_{m,k}} \prod_{r=1}^{k} (\underline{\underline{A}}^{p_r} \cdot \underline{\underline{B}}^{q_r}), \quad (11)$$

$$I_{m,k} := \left\{ \left((p_r, q_r) \right)_{r=1}^{k} : p_r, q_r \in \{0,1\}, p_r + q_r = 1, \sum_{r=1}^{k} p_r = m, \sum_{r=1}^{k} q_r = k - m \right\}. \quad (12)$$

If the Jaccobians $\underline{\underline{A}},\underline{\underline{B}}$, the mesh size $\Delta x, \Delta y$ and the time step Δt are assumed to be constant[1], equation (10) is equivalent to

$$\hat{\underline{F}}_{i+\frac{1}{2},j} = \sum_{ii=-\mathcal{O}/2+1}^{\mathcal{O}/2} \sum_{jj=-\mathcal{O}/2}^{\mathcal{O}/2} \left[\sum_{k=0}^{\mathcal{O}-1} \frac{(-\Delta t)^k}{(k+1)!} \left(\frac{\Delta y}{2} \sum_{\lambda=1}^{N_G} \omega_\lambda \underline{\underline{A}}\, \underline{\underline{M}}(\underline{\underline{A}},\underline{\underline{B}},k,m) C_{ii,jj,\lambda}^{m,k-m} \right) \right] \underline{U}_{i+ii,j+jj} \quad (13)$$

$$= \underline{\underline{C}}^{\star} \underline{U}_{i+ii,j+jj} \quad (14)$$

Finally all discrete fluxes of the form (14) are inserted into the Finite-Volume discretization (2) and the constants are again gather in a new constant $\underline{\underline{C}}^{\star\star}$ to obtain

$$\overline{U}_{ij}^{n+1} = \overline{U}_{ij}^{n} - \left[\sum_{ii=-\mathcal{O}/2}^{\mathcal{O}/2} \sum_{jj=-\mathcal{O}/2}^{\mathcal{O}/2} \underline{\underline{C}}_{ii,jj}^{\star\star} \underline{U}_{i+ii,j+jj} \right]. \quad (15)$$

This scheme has some nice properties:

- It is a true one-step scheme.

- No extra memory is needed. Only the old and the new time steps have to be stored.

- The scheme is of uniform order $\mathcal{O}$ in space and time.

- The resulting kernel can be optimized highly efficiently.

- All information about the modeled equation and the discretization is included in the coefficients $\underline{\underline{C}}_{ii,jj}^{\star\star}$, which have to be calculated only once before the time integration starts.

The algorithm described here applies for all even order schemes. A similar algorithm can be deduced for odd order schemes. Here Riemann solutions at the cell interfaces have to be solved, but the resulting scheme is again of the form (15). For aeroacoustical calculation the even order schemes are of more interest than the odd order schemes that have more inherent dissipation. In contrast they are more preferable, if strong gradients occur in the solution.

3 Stability

An important issue of numerical schemes is the stability. A numerical von Neumann stability analysis has been made. The results are plotted in figure 1. It can be seen, that the stability region increases while the order of the scheme is increased. The limit stability region for the high order schemes is $CFL_x = CFL_y = 1$ with $CFL_{\{x/y\}} = (\{u/v\} \Delta t)/\{\Delta x, \Delta y\}$. As a reference the stability region of the DRP-04/RK-O4 scheme has been included in the figure.

---

[1]This condition can be easily given up. A recalculation for different time steps is very cheap.
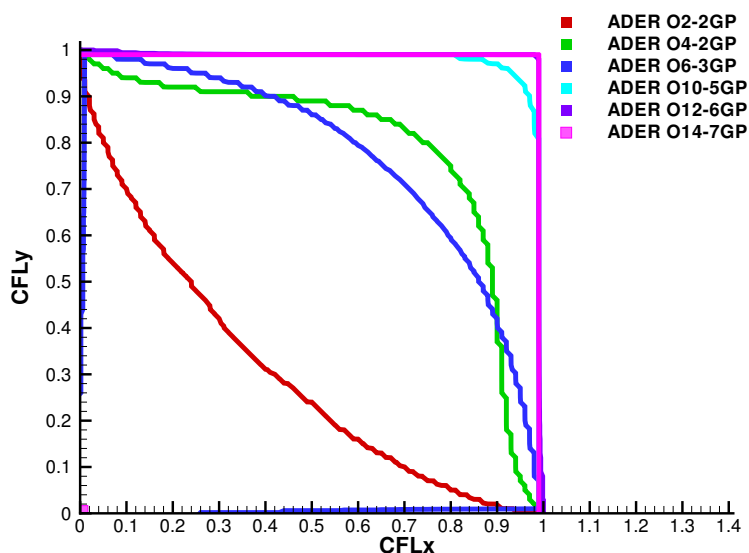
Figure 1: Von Neumann stability of odd order ADER schemes and DRP-RK scheme

4 Wave Propagation Properties

Next the wave propagation properties of the ADER approach are analyzed. The amplitude and phase errors are plotted in figure 2 as function of the resolution of the waves, given in *Points Per Wavelength*(PPW). The results are obtained in two different ways: First an analytical solution has been calculated, using the method of differential approximation and second a numerical solution is also included. The comparison of
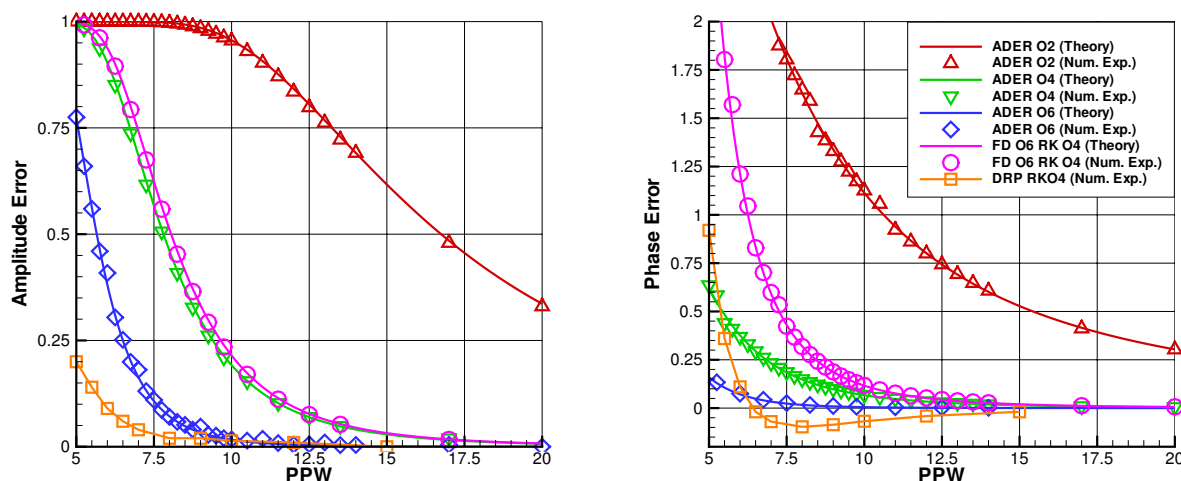
Figure 2: Amplitude and phase errors over the resolution of the wave in *Points Per Wavelength*(PPW)

the analytical solution with the numerical solution shows excellent agreement. A remarkable feature of the ADER schemes is the inherent damping of waves which are transported with the wrong wave speed. In the region where the phase error starts to be non-zero an amplitude error can already be found. This means that wave with non-zero phase error are damped. This feature is normally build into other schemes by

'artificial damping'. For comparison purpose the results from a standard finite-difference solution of order O6 with standard Runge-Kutta O4 time integration as well as the DRP-04 scheme with the same Runge-Kutta scheme has been included. One can clearly see that the DRP schemes produces wave which are too fast (negative phase error) and that these waves are not damped. Furthermore the standard finite-difference scheme of 6th order produces very bad solutions.

5 Computational Effort

Any numerical scheme, nevertheless how good it is, must have CPU costs which are comparable with that of the existing standard schemes. For the *fast*ADER scheme the computational cost can be estimated easily. The number of points included in the stencil grows quadratically with the desired order($N_P = (k+1) \times (k+1)$). As the scheme is always one single step in time, the CPU effort grows also quadratically[2]. The kernel of the scheme is only a sum over matrix-vector multiplications. Thus the total number of additions and multiplications is:

$$
\begin{aligned}
Nr_{Mul} &= [(k+1) \times (k+1)] \times [NrVar \times NrVar] & (16)\\
Nr_{Add} &= [(k+1) \times (k+1)] \times [NrVar \times (NrVar-1) + 1] & (17)
\end{aligned}
$$

In figure 3 the theoretical prediction is compared to numerical results, obtained on Pentium III 1GHz
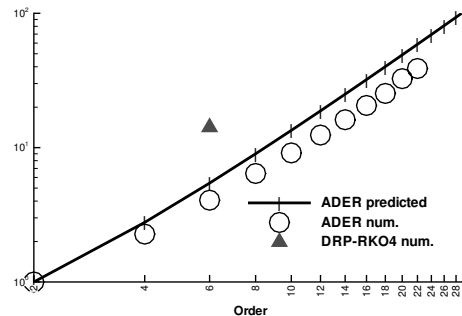
Figure 3: Comparison of predicted and real computational cost

System with 133MHz memory bus speed. It is obvious that the numerical results are even better than the prediction. A reason might be, that the compiler has optimized the kernel very efficiently, thus leading to a better performance. As a reference the DRP-O4 scheme with a standard Runge-Kutta O4 time integration has been included. It is plotted as a 6th order scheme, because it uses an 7point stencil (like a FD-O6) scheme. Comparing it with *fast*ADER -O6 scheme one can clearly see, that it is much slower. If an iso-cpu-time line is drawn, one finds that the DRP scheme is comparable to the 14th order *fast*ADER scheme. Furthermore one should notice, that no extra memory is needed for the *fast*ADER scheme, while the Runge-Kutta steps have to be stored separately.

6 Numerical Convergence Rate

In this section the numerical convergence rate is analyzed, using the *Aliasing* problem of Category 1 Problem 1. A theoretically analysis of the order of the schemes in space and time for one space dimension is given in [4].
The initial condition is given in the problem statement. For the spatial discretization the domain $[-50,..,50]$ is covered by NI cells. Periodic boundary conditions are used and the solution is taken after 10 periods. In table 1 the errors as well as the convergence rates for the 6th and 14th order ADER scheme are given. For fine grids the designed order of accuracy is reached very well, only for the 6th order scheme on coarse grid

---
[2]Note: We do not take into account, that higher CFL numbers can be used if the order is increased.

NI	ADER $\mathcal{O}6$				ADER $\mathcal{O}14$			
	L_∞	$\mathcal{O}_{L_\infty}$	L_1	$\mathcal{O}_{L_1}$	L_∞	$\mathcal{O}_{L_\infty}$	L_1	$\mathcal{O}_{L_1}$
100	8.6943E-01	–	1.3558E-01	–	4.9741E-01	–	7.9494E-02	–
150	7.7776E-01	0.3	1.1117E-01	0.5	8.3206E-03	10.1	1.1811E-03	10.4
200	2.5446E-01	3.9	3.6487E-02	3.9	2.0899E-04	11.2	2.9575E-05	11.4
250	7.8395E-02	5.3	1.0956E-02	5.4	1.0601E-05	13.4	1.5116E-06	13.3
300	2.7849E-02	5.7	3.8464E-03	5.7	9.0928E-07	13.5	1.2772E-07	13.6
350	1.1279E-02	5.9	1.5640E-03	5.8	1.0858E-07	13.8	1.5596E-08	13.6
400	5.2071E-03	5.8	7.1022E-04	5.9	1.7641E-08	13.6	2.4820E-09	13.8

Table 1: Numerical convergence rates for a 6th and 14th order ADER scheme.

grids one can find a stagnation. This is because the high frequency waves are in a range where they cannot be resolved, while the low frequency Gaussian pulse is already well-resolved (see also figure 2). In figure 4 the solution for the orders 6,12,16 and 24 are plotted for three different grids $NI = \{100, 150, 200\}$. The
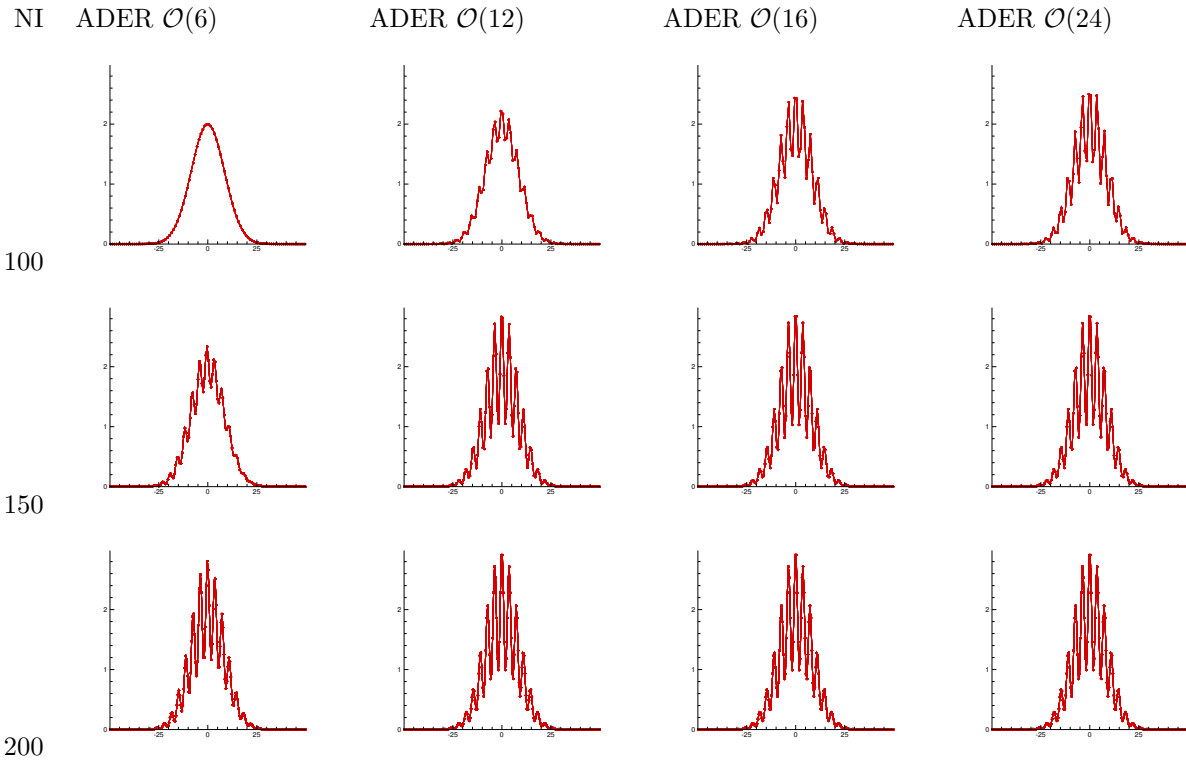
Figure 4: Comparison of Category 1, Problem 1 for different grids and different numerical orders

results indicate, that there is a real benefit to go to higher orders.

7 Complex Example

The requirements for the *fast*ADER scheme are restrictive: The grid has to be a cartesian grid with constant Δx and Δy. For aeroacoustical calculations in the compressible regime, our philosophy is to use a heterogenous domain decomposition [1]. The whole domain Ω is partitioned into small, non-overlapping sub-domains Ω_i. Each sub-domain is adapted to the local requirements: nonlinear/linear equations, structured/unstructured grid. Interface conditions ensure that the solution can get from one domain to another with only small errors. In each domain an explicit time stepping is used with the highest possible CFL
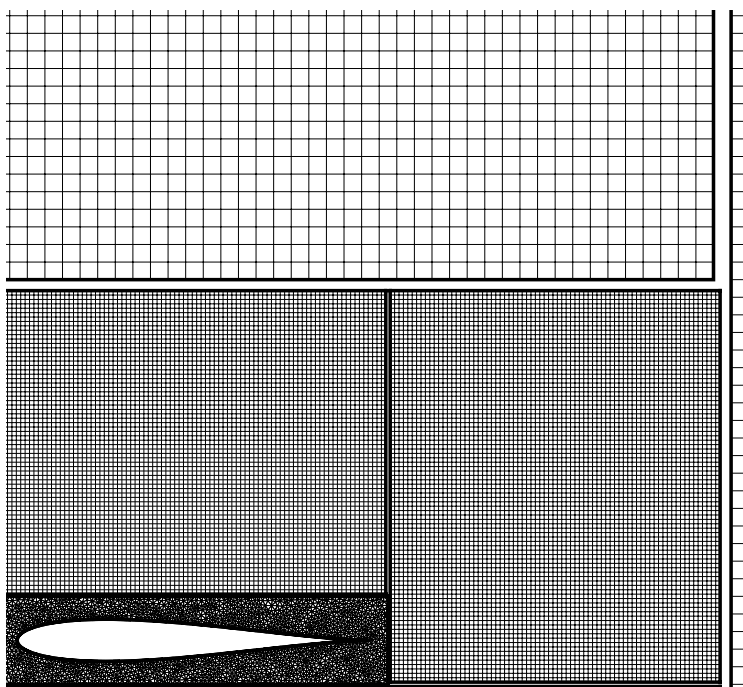
Figure 5: Grids used for the heterogenous domain decomposition of the profile in gust problem, solved on 1 unstructured Euler, 4 structured Euler and 4 structured linearized Euler domains

number thus leading to different time steps in each Ω_i. An example of such a domain decomposition is given in figure 5 and 6.

8   Conclusion

In this paper the *fast*ADER approach for CAA applications is analyzed. It has been demonstrated that the wave propagation properties are very good (Because waves transported with the wrong speed are automatically damped). The kernel of the scheme can be implemented highly efficiently with almost no extra memory needed compared to a first order, explicit time integration. For the 6th and 14th order scheme numerical convergence rates are shown. They are in good agreement with the designed order of accuracy.
If the assumptions of linearized equations, equidistant, cartesian meshes are met, than the *fast*ADER approach is a very good choice because it is 1.) is really high order (in space and in time), 2.) very fast due to a compact kernel where only sums of matrix-vector multiplications must be evaluated, 3.) needs no extra memory because it is explicit, one-step in time and 4.) has good wave propagation properties. The coupling with classical Finite-Volume solvers can be done easily because the ADER approach itself is a Finite-Volume approach and the *fast*ADER scheme is a reformulation only and thus does not neglect anything. This is especially important, if the solution contains strong gradients such as shocks.
In this paper only even order schemes were discussed. The procedure for odd order schemes is slightly more complicated but results in the same form. In this case the coefficients contain a Riemann-solution which means that in each characteristic variable a upwind stencil is used. Therefore these schemes are well suited for solutions with discontinuities were they do not generate large spurious oscillations.
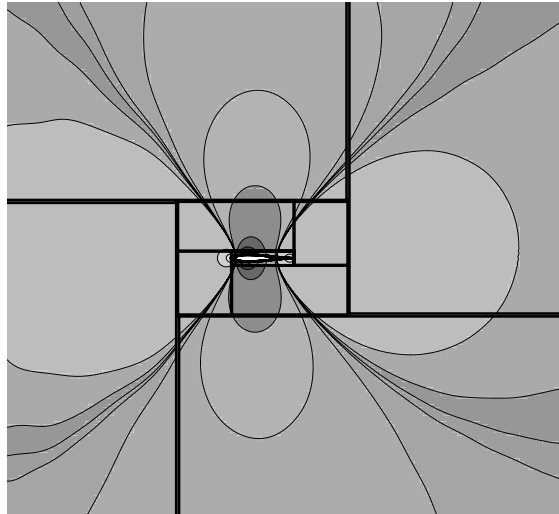
Figure 6: Profile in gust problem, solved on 1 unstructured Euler, 4 structured Euler and 4 structured linearized Euler domains

References

[1] T. Schwartzkopff and C.–D. Munz. Direct simulation of aeroacoustics. In W.L. Wendland and M. Efendiev, editors, *Analysis and Simulation of Multifield Problems*, volume 12 of *Lecture Notes in applied and computational Mechanics*, pages 337–342. Springer, 2003.

[2] T. Schwartzkopff, C.–D. Munz, E.F. Toro, and R.C. Millington. The ADER approach in 2d. In T. Sonar, editor, *Discrete Modelling and Discrete Algorithms on Continuum Mechanics*, pages 207–216, Berlin, 2001. Logos Verlag.

[3] T. Schwartzkopff, C.-D. Munz, and E.F. Toro. ADER: A high order approach for linear hyperbolic systems in 2d. *Journal of Scientific Computing*, 17(1-4):231–240, 2002.

[4] T. Schwartzkopff and M. Dumbser C.-D. Munz. Fast high order ader schemes for linear hyperbolic equations and their numerical dissipation and dispersion. Technical Report 2003/35, Preprint series of SFB404, Stuttgart University, 2003.

[5] C.K.W. Tam. Numerical methods in computational aeroacoustics. *Von Karman Institute for Fluid Dynamics*, Lecture Series 1996-04, Applied Aero-Acoutistics: Prediction methods, 1996.

[6] E.F. Toro, R.C. Millington, and T. Schwartzkopff. The basics of the ADER approach in 1–d,2–d and 3–d. In *Proceedings of ECCOMAS CFD*, September 2001. Preprint.

HIGH ORDER AND HIGH RESOLUTION METHODS
FOR A MODEL CAA PROBLEM

John W. Goodrich
NASA Glenn Research Center; Cleveland, OH 44135, USA
(216)433-5922; John.Goodrich@NASA.gov

ABSTRACT

The initial value problem for the first order linear wave equation in one space dimension is treated for two cases with specified initial data and grid, and data from solutions at $t = 400$ and $t = 800$ are presented, as prescribed for Problem 1 in Category 1. Results are shown from computations with a sequence of recently developed high order and high resolution methods which combine Hermite interpolation, Cauchy-Kowaleskya recursion for time derivatives, and Taylor series time advancement [3, 4, 5]. These methods have the same order of accuracy in time as in space. Results are shown from methods that range from third to nineteenth order. The stated problems with the prescribed coarse grid can be simulated with errors that are at the level of machine accuracy if the method is sufficiently high order. In addition, the growth of the maximum absolute error out to $t = 100,000$ is given for simulations with the stated problem data.

PROBLEM STATEMENT

The initial value problem is for the first order linear wave equation in one space dimension,

$$\frac{\partial u}{\partial t} + \frac{\partial u}{\partial x} = 0, \tag{1}$$

with initial data

$$u(x,0) = (2 + \cos[\alpha x]) \exp[-\ln[2](\frac{x}{10})^2]. \tag{2}$$

The two cases that are required are with $\alpha = 1.7$ and $\alpha = 4.6$, with solution data at $t = 400$ and $t = 800$. A uniform grid is supposed is to be used, with mesh size $\triangle x = 1$. Any method that captures the physical dynamics for this problem should be able to produce machine accuracy for time step size $\triangle t = \triangle x$, since this choice simply propagates the solution along the characteristic from one grid point to the next over one time step. The computations that are shown here use $\triangle t = \frac{1}{2}\triangle x$, so that the grid data is not simply propagated from one point to the next.

SOLUTION METHOD

Results are presented from a sequence of recently developed high order and high resolution methods which combine Hermite interpolation, Cauchy-Kowaleskya recursion for time derivatives, and Taylor series time advancement [3, 4, 5]. These methods can be thought of in a variaety of ways. Consider an expansion of the solution in both space and time about the grid point (x_i, t_j), with

$$u_{i,j}(x,t) = u(x - x_i, t - t_j) = \sum_{a,b=0}^{\infty} \frac{1}{a!b!} u_{a,b} x^a t^b \tag{3}$$

in local coordinates, where the grid index (i, j) has been suppressed in the series expansion on the right. If this expansion is a solution of the governing equation, then the expansion coefficients must satisfy

$$u_{a,b+1} + u_{a+1,b} = 0, \quad \text{or} \quad u_{a,b+1} = -u_{a+1,b}, \tag{4}$$

which reflects the recursion

$$\frac{\partial^{a+b+1} u}{\partial x^a \partial t^{b+1}} = -\frac{\partial^{a+b+1} u}{\partial x^{a+1} \partial t^b} \tag{5}$$

from the governing equation. Consequently, the solution for the model problem can be written in the form

$$u_{i,j}(x,t) = \sum_{\alpha=0}^{\infty} \frac{1}{\alpha!} u_\alpha (x - t)^\alpha, \tag{6}$$

which is just the method of characteristics. Note that

$$u_{i,j}(x,0) = \sum_{\alpha=0}^{\infty} \frac{1}{\alpha!} u_\alpha x^\alpha \tag{7}$$

is an expansion in space of the known solution at the current time, and that

$$u_{i,j}(0,t) = \sum_{\alpha=0}^{\infty} \frac{1}{\alpha!} u_\alpha (-t)^\alpha \tag{8}$$

is an expansion of the solution in time at the stencil center. These two local expansions in space and in time are connected by the recursion relations that are derived from the governing equations. The spatial expansion is just initial data on a noncharacteristic surface that is to be propagated by the governing equations, and the recursion relations are just the Cauchy-Kowaleskya recursions [2] from the governing equations. The key to applying this method to more complex systems is to obtain the recursion relationship for the local expansion coefficients from the governing equations, just as above in this particularly simple case.

Particular realisations of this method truncate the local expansion to a given order for spatial interpolation, and then the expansion in time is used to advance the solution to the same order at the stencil center. We use Hermite spatial interpolation with two point stencils on a staggered grid system. Two uniform Cartesian grids are used, where each is offset from the other by half a grid step. At each grid point at the current time level t_j we keep data for the dependant variable and all of the spatial derivatives up to order m, or numerically computed approximations for

$$\{\frac{\partial^k u}{\partial x^k} : k = 0, \ldots, m\}. \tag{9}$$

On a two point stencil this provides data for an interpolant that is of order $2m+1$, with consistant estimates at the stencil center for the derivatives of u up to order $2m+1$. In local coordinates about the center of the two point stencil $\frac{1}{2}(x_j + x_{j+1}) = x_{j+\frac{1}{2}}$ we have

$$u_{i,j}(x,0) \approx \sum_{\alpha=0}^{2m+1} \frac{1}{\alpha!} u_\alpha x^\alpha, \quad \text{where} \quad u_\alpha \approx \frac{\partial^\alpha u}{\partial x^\alpha}(x_i, t_j). \tag{10}$$

The time derivatives for the solution and for its spatial derivatives up to order m are obtained from the space derivatives by the Cauchy-Kowaleskya recursion relationships for the governing equation. For the workshop problem,

$$\frac{\partial^{\alpha+\beta} u}{\partial x^\alpha \partial t^\beta}(x_i, t_j) = (-1)^\beta \frac{\partial^{\alpha+\beta} u}{\partial x^{\alpha+\beta}}(x_i, t_j) \approx (-1)^\beta u_{\alpha+\beta}. \tag{11}$$

The local expansion in time can now be used to produce a Taylor series time expansion for the solution and its first m derivatives. In the case of the simple workshop problem, the time expansions are just

$$\frac{\partial^k u_{i,j}}{\partial x^k}(0, \triangle t) \approx \sum_{\alpha=0}^{2m+1-k} \frac{1}{\alpha!} u_{\alpha+k}(-\triangle t)^\alpha, \tag{12}$$

for $k = 0, 1, \ldots, m$. Note that a derivative of order k is advanced in time only to order $2m+1-k$, but that the solution itself ($k=0$) is advanced to order $2m+1$. Since the expansion center is halfway between two grid points on one of the two staggered grids, the time advanced solution data is provided for a grid point on the other offset grid. For these computations Taylor series time advance is with $\triangle t = \frac{1}{2}\triangle x$. Further details are in [3, 4, 5].

A summary of the algorithm realisations that are used for the workshop calculations is presented in Table 1. The first column on the left presents the method name. The second column gives the order m of the derivatives that are kept at each grid point, with derivative order $m = 1, 3, 5, 7, 9$. The third column gives the order $2m+1$ of the method, from 3rd to 19th, in both space and time. The fourth column gives the FLOP count for the number of multiplications that are required for each grid point for each time step. The higher order methods are clearly more complex, the number of FLOPS per grid point per time step for the 19th order c2o9 method is 26.5 times the count for the 3rd order c2o1 method. On a fixed grid the higher order methods will always be more expensive to use. However, if it

method	derivative order	method order	FLOPS/g.p/t.s.
c2o1	1	3	26
c2o3	3	7	108
c2o5	5	11	246
c2o7	7	15	440
c2o9	9	19	690

Table 1: Summary of Methods Used for Workshop Results

is necessary to stay below a fixed level of error, and if grid refinement and coarsening can be done, then the higher order methods will be able to produce a required accuracy with significantly coarser grids and fewer time steps than the lower order methods. The result is that the total FLOP count to reach a required level of accuracy for an entire simulation is significantly lower with high order methods than with lower order methods. In general, computational efficiency increases with order (see [5] for more details).

Because of their structure, these high-order high-resolution methods can be called Hermite/Cauchy-Kowaleskya/Taylor (HCKT) methods. Because of their development from local series expansions interrelated by the recursion relationships for the governing equations, they have also been called Modified Expansion Solution Approximation (MESA) methods [1]. HCKT methods are stable for $CFL \leq 1$, [8]. These methods can be of very high order accuracy, with very high resolution, and the high order methods are typically very computationally efficient, requiring orders of magnitude less total FLOPS to obtain a predetermined error level when compared to standard methods such as compact differencing with Runge-Kutta (see [5]). We have successfully used this approach with the linearized Euler, heat, Klein-Gordon, Burgers and Navier-Stokes Equations. In all cases the systems can be written with only first order time derivatives. For linear constant coefficient systems in Cartesian coordinates, the HCKT methods can have exact propagators in time even in multiple space dimensions. In the case of hyperbolic systems, if the propagation in time is exact, so that the dynamic evolution of the local initial data is correct, then information is correctly propagated along characteristic surfaces. In this sense, these methods can be viewed as a correct generalization to multiple space dimensions of the method of characteristics in one space dimension. The HCKT methods have been used succesfully with high order accuracy at both radiation [9, 7, 10] and surface [6] boundaries. The HCKT methods have also been used on randomized grids with no loss of accuracy and efficiency.

SUMMARY OF ERROR DATA FOR THE WORKSHOP COMPUTATIONS

method	order	$\alpha = 1.7$		$\alpha = 4.6$	
		$t = 400$	$t = 800$	$t = 400$	$t = 800$
c2o1	3	1.00	1.01	1.00	1.01
c2o3	7	7.12×10^{-3}	1.42×10^{-2}	9.96×10^{-1}	9.96×10^{-1}
c2o5	11	2.35×10^{-7}	4.69×10^{-7}	2.82×10^{-2}	5.56×10^{-2}
c2o7	15	3.26×10^{-12}	6.73×10^{-12}	8.39×10^{-6}	1.68×10^{-5}
c2o9	19	1.20×10^{-12}	1.73×10^{-12}	1.49×10^{-9}	2.97×10^{-9}

Table 2: Maximum Absolute Error for Workshop Problems From All Methods

The maximum absolute error for the workshop computations is presented in Table 2. Recall that all of these computations are with $\triangle x = 1$ and $\triangle t = \frac{1}{2}$. The numerical domain is for $-1000 \leq x \leq 1000$. The first column presents the method name for the data in each row. The second column gives the order of the method in both space and time. The third through sixth columns give maximum absolute errors in the solution u: columns three and four with $\alpha = 1.7$, and columns five and six with $\alpha = 4.6$; while columns three and five give the error at $t = 400$, and columns four and six at $t = 800$. To the scale of a solution plot, the errors are invisible if they are $O[10^{-3}]$. For this error tolerance, the seventh order c2o3 method provides an adequate solution for $\alpha = 1.7$, but the eleventh order c2o5 method is still not quite powerful enough for $\alpha = 4.6$. Note that for $\alpha = 1.7$, the fifteenth and nineteenth order methods produce errors that are in the machine roundoff range. For $\alpha = 4.6$, the ninteenth order c2o9 method

produces errors that are $O[10^{-9}]$. Clearly, powerful methods that are high order and high resolution can produce accurate solutions for this problem.

ADDITIONAL COMPUTATIONS ON A PERIODIC DOMAIN

The maximum absolute error at $t = 800$ as a function of grid size with $\alpha = 1.7$ is presented in Table 3, and with $\alpha = 4.6$ in Table 4. This data is from computations on the domain $-100 \leq x \leq 100$ with periodic boundary conditions. A periodic domain was chosen to avoid the need for a very large grid that would arise if the domain $-1000 \leq x \leq 1000$ were to be used with a small mesh size. The data in these Tables does not confirm the order of accuracy of the fifteenth and nineteenth order methods, because both methods produce very small errors on the coarsest grid that has been used ($\triangle x = 1$). The other methods have their orders of accuracy confirmed by this data.

$1/\triangle x$	c2o1	c2o3	c2o5	c2o7	c2o9
1	$1.01 \times 10^{+0}$	1.42×10^{-2}	4.69×10^{-7}	6.73×10^{-12}	1.73×10^{-12}
2	9.98×10^{-1}	1.25×10^{-4}	2.19×10^{-10}	1.01×10^{-12}	
4	5.80×10^{-1}	1.00×10^{-6}	2.97×10^{-13}		
8	1.07×10^{-1}	7.89×10^{-9}	3.46×10^{-13}		
16	1.41×10^{-2}	6.17×10^{-11}			
32	1.77×10^{-3}	7.21×10^{-13}			
64	2.22×10^{-4}				

Table 3: Maximum Absolute Error by Grid Density at $t = 800$ for $\alpha = 1.7$ With Each Method

$1/\triangle x$	c2o1	c2o3	c2o5	c2o7	c2o9
1	$1.01 \times 10^{+0}$	9.96×10^{-1}	5.56×10^{-2}	1.68×10^{-5}	7.48×10^{-10}
2	$1.00 \times 10^{+0}$	2.29×10^{-1}	2.85×10^{-5}	8.95×10^{-10}	
4	$1.00 \times 10^{+0}$	2.43×10^{-3}	1.29×10^{-8}	2.52×10^{-12}	
8	9.97×10^{-1}	2.00×10^{-5}	6.03×10^{-12}		
16	5.21×10^{-2}	1.58×10^{-7}			
32	8.85×10^{-2}	1.24×10^{-9}			
64	1.15×10^{-2}	9.72×10^{-12}			

Table 4: Maximum Absolute Error by Grid Density at $t = 800$ for $\alpha = 4.6$ With Each Method

$1/\triangle x$	c2o1	c2o3	c2o5	c2o7	c2o9
1	1.66×10^{7}	6.91×10^{7}	1.57×10^{8}	2.82×10^{8}	4.42×10^{8}
2	6.66×10^{7}	2.76×10^{8}	6.30×10^{8}	1.13×10^{9}	
4	2.66×10^{8}	1.11×10^{9}	2.52×10^{9}	4.51×10^{9}	
8	1.06×10^{9}	4.42×10^{9}	1.01×10^{10}		
16	4.26×10^{9}	1.77×10^{10}			
32	1.70×10^{10}	7.08×10^{10}			
64	6.82×10^{10}	2.83×10^{11}			

Table 5: Total FLOPS required to compute to $t = 800$ by Grid Density With Each Method

Tabel 5 presents the total FLOPS required to do the computations that are summarised in Tables 3 and 4, by grid size for each method. Recall that there are two half time steps per full time step, and the coarsest grid has 200 grid points, so that the total FLOPS to compute a solution on the coarsest grid out to $t = 800$ is $200 \times 2 \times 1600 \times F$, where F is the FLOP counts per grid point per time step from Table 1 for each method. The grid ratio is kept at $\triangle t = \frac{1}{2}\triangle x$ for all computations. The Total FLOP counts can be used with the data in Table 4 to make some useful comparisons. Note that an error of $O[10^{-2}]$ is obtained by the c2o1 and c2o5 methods with grid densities of $1/\triangle x = 16$ and 1,

respectively. Table 5 shows that the third order method requires approximately 27 times more computational effort than the ninth order method. Similarly, an error of $O[10^{-5}]$ is obtained by the c2o3 and c2o7 methods with grid densities of $1/\triangle x = 8$ and 1, respectively. Table 5 shows that the seventh order method requires approximately 16 times more computational effort than the eleventh order method. Finally, an error of $O[10^{-10}]$ is obtained by the c2o3 and c2o7 methods with grid densities of $1/\triangle x = 32$ and 2, respectively. Table 5 shows that the seventh order method requires approximately 63 times more computational effort than the eleventh order method. This data clearly shows a trend of greater efficiency for higher order methods, irrespective of the error level. We may also look at the level of accuracy produced by the different methods with a similar computational effort. Table 5 shows that four of the five methods have a total FLOP count entry that is $O[10^9]$. The c2o1, c2o3, c2o5, and c2o7 methods exert this effort with the grids $1/\triangle x = 8$, 4, 4, and 2, respectively, with corresponding errors that are $O[1]$, $O[10^{-3}]$, $O[10^{-8}]$ and $O[10^{-10}]$, respectively. This crude comparison shows a truly startling range of accuracy for the same computational effort, from errors that are the size of the solution itself to close to the machine roundoff level, for methods from third to fifteenth order accurate in both space and time. If a fuller range of grid resolutions were used, both finer grids for the low order methods and coarser grids for the high order methods, then a more systematic study of computational efficiency could be done, as in [5]. Nevertheless, it is clear from even this limited data that the higher order methods reach a given error limit more efficiently than lower order methods, and that a given level of effort produces much more accurate results with higher order methods than with lower order methods.

t	$\alpha = 0$	$\alpha = 2$	$\alpha = 4$	$\alpha = 6$	$\alpha = 8$	$\alpha = 10$
1×10^3	1.69×10^{-12}	2.61×10^{-12}	2.44×10^{-10}	6.15×10^{-7}	1.16×10^{-4}	6.39×10^{-3}
1×10^4	9.64×10^{-12}	9.95×10^{-12}	2.44×10^{-9}	6.13×10^{-6}	1.14×10^{-3}	5.36×10^{-2}
2×10^4	1.06×10^{-11}	1.30×10^{-11}	4.86×10^{-9}	1.23×10^{-5}	2.28×10^{-3}	1.03×10^{-1}
3×10^4	1.40×10^{-11}	1.42×10^{-11}	7.29×10^{-9}	1.84×10^{-5}	3.41×10^{-3}	1.51×10^{-1}
4×10^4	1.97×10^{-11}	1.34×10^{-11}	9.72×10^{-9}	2.45×10^{-5}	4.55×10^{-3}	1.96×10^{-1}
5×10^4	2.66×10^{-11}	1.76×10^{-11}	1.21×10^{-8}	3.06×10^{-5}	5.68×10^{-3}	2.38×10^{-1}
6×10^4	3.31×10^{-11}	1.93×10^{-11}	1.46×10^{-8}	3.68×10^{-5}	6.82×10^{-3}	2.78×10^{-1}
7×10^4	2.42×10^{-11}	1.70×10^{-11}	1.70×10^{-8}	4.29×10^{-5}	7.95×10^{-3}	3.17×10^{-1}
8×10^4	2.83×10^{-11}	2.88×10^{-11}	1.94×10^{-8}	4.90×10^{-5}	9.08×10^{-3}	3.53×10^{-1}
9×10^4	3.22×10^{-11}	2.54×10^{-11}	2.19×10^{-8}	5.51×10^{-5}	1.02×10^{-2}	3.87×10^{-1}
1×10^5	3.37×10^{-11}	2.92×10^{-11}	2.43×10^{-8}	6.13×10^{-5}	1.13×10^{-2}	4.20×10^{-1}

Table 6: Maximum Absolute Error Over Time for Variaous α With $\triangle x = 1$ for the c2o9 Method.

Table 6 presents maximum absolute error date for computations with the nineteenth order c2o9 method. These computations are all on the domain $-100 \le x \le 100$ with periodic boundaries, and on the coarsest grid with $\triangle x = 1$ and $\triangle t = \frac{1}{2}$. The compuatations are for a range of α from 0 to 10. Note that the computations run out to $t = 100,000$, or 125 time further than for the workshop problem. The data shown is for the absolute maximum cumulative errors for times from $t = 1000$ to $t = 100,000$. Note that the errors for $\alpha = 0$ and $\alpha = 2$ are very close, starting in the machine roundoff range at $t = 1000$, and increasing very slowly out to the final time $t = 100,000$. The errors for the other four values of α increase much more rapidly, by the same order as the increase in time from the first to last entry. These computations give a more complete sample of the accuracy of the nineteenth order c2o9 method. Note that for $\alpha \le 4$, the error growth can be projected to later times, and suggest the possibility of a scarcely visible error that is $O[10^{-3}]$ at $t = O[10^{10}]$. This data shows that these high order and high resolution methods can be used to accurately propagate relatively small scale data over large distances or long times, or for computations where there is a large difference between the scale of the problem as a whole and the scale of the smallest information that must be resolved and accurately propagated.

CONCLUSIONS

New high order and high resolution methods have been applied to a benchmark problem for the fourth CAA workshop. These HCKT of MESA methods combine Hermite differencing with high order derivative data on two point stencils, Cauchy-Kowaleskaya recursion for computing time derivatives from space derivatives, and high order Taylor series time advancement between staggered grids. These methods all have the same order of accuracy in space and in time. Methods from third to nineteenth order were used to produce the results in this paper. The sample

computations show that errors down to the machine roundoff level can be obtained by a sufficiently accurate HCKT method even on a coarse grid such as has been specified for the workshop problem. Data from additional computations show that the more accurate methods can reach a stated error limit with much greater computational efficiency than lower order methods, or that they can maintain a much lower error for a given level of computational effort than lower order methods. Sample calculations show that the higher order methods can produce very accurate results for extremely long times.

References

[1] Rodger W. Dyson, John W. Goodrich, "A Very High Order, Adaptable MESA Implementation for Aeroacoustic Computations," NASA/TM-2000-209944, April, 2000.

[2] Paul R. Garabedian, *Partial Differential Equations,* Wiley, New York, 1964.

[3] John W. Goodrich, "High accuracy finite difference algorithms for computational acoustics," AIAA 97-1584, 3rd AIAA/CEAS Aeroacoustics Conference, Atlanta, GA, May 12-14, 1997.

[4] John W. Goodrich, "Accurate finite difference algorithms," in V. Venkatakrishnan, M. Salas, and S. Chakravarthy, editors, *Barriers and Challenges in Computational Fluid Dynamics*, Kluwer Academic, Dordrecht, 1998.

[5] John W. Goodrich, "A Comparison of Numerical Methods for Computational Acoustics," AIAA 99-1943, 5th AIAA/CEAS Aeroacoustics Conference, Bellevue, WA, May 10-12, 1999.

[6] John W. Goodrich, "High order wall boundary conditions for scattering from a cylinder," these proceedings.

[7] John W. Goodrich, Tom Hagstrom, "High Order Implementations of Accurate Boundary Conditions," AIAA 99-1942, 5th AIAA/CEAS Aeroacoustics Conference, Bellevue, WA, May 10-12, 1999.

[8] J. W. Goodrich, T. Hagstrom, J. Lorenz, "Hermite methods for hyperbolic initial-boundary value problems," to be submitted.

[9] Tom Hagstrom, John Goodrich, "Experiments with approximate radiation boundary conditions for computational aeroacoustics," *Appl. Numer. Math.,* **27**(1998), pp. 385-402.

[10] Tom Hagstrom, John Goodrich, "Accurate Radiation Boundary Conditions for the Linearized Euler Equations in Cartesian Domains," *SIAM J. Sci. Comput.,* **24**No. 3 (1998), pp. 770-795.

DEMONSTRATION OF ULTRA HI-FI (UHF) METHODS

Rodger W. Dyson
NASA Glenn Research Center
21000 Brookpark Road
Cleveland, OH 44135
Rodger.W.Dyson@nasa.gov
216-433-3918 (FAX)
216-433-9083 (VOICE)

ABSTRACT

Computational aero-acoustics (CAA) requires efficient, high-resolution simulation tools. Most current techniques utilize finite-difference approaches because high order accuracy is considered too difficult or expensive to achieve with finite volume or finite element methods. However, a novel finite volume approach (Ultra HI-FI or UHF) which utilizes Hermite fluxes is presented which can achieve both arbitrary accuracy and fidelity in space and time. The technique can be applied to unstructured grids with some loss of fidelity or with multi-block structured grids for maximum efficiency and resolution. In either paradigm, it is possible to resolve ultra-short waves (<2 PPW). This is demonstrated here by solving the 4th CAA workshop Category 1 Problem 1.

INTRODUCTION

Simulating sound generation, propagation, and reflection is notoriously demanding because of the wide range of scales. For the past decade many of the successful CAA applications have been based upon finite difference methodologies because it was not clear how to achieve high numerical resolution and efficiency with finite volume and finite element approaches. Commercial computational fluid dynamics developers long ago settled on finite volume approaches for steady calculations because shocks and complex geometry are more naturally dealt with (ref. 1). Unfortunately, the low resolution and efficiency of CFD required new approaches – hence, the development of finite-difference based schemes with wide and/or Padé stencils (refs. 2 to 3). In (ref. 3) and later (ref. 4) the advantage of a staggered grid was demonstrated and it was suggested finite volume techniques could naturally utilize this property. The development of higher order finite volume and finite element schemes has quietly progressed (refs. 4 to 11).   And more recently, very high order finite volume approaches have been developed (refs. 12 to 14).   These recent developments demonstrate the feasibility and value of high order, low dissipation, low dispersion finite volume formulations. Unfortunately, none of these approaches can achieve both arbitrary accuracy and fidelity in both space and time for nonlinear aeroacoustic flows in complex geometries. As shown in Figure 1, conventional techniques require about 6 points per wavelength (PPW) for reasonable resolution and a lack of resolution directly affects the overall efficiency (ref. 15). This can make a significant difference in the tractability of simulating complex engineering devices.
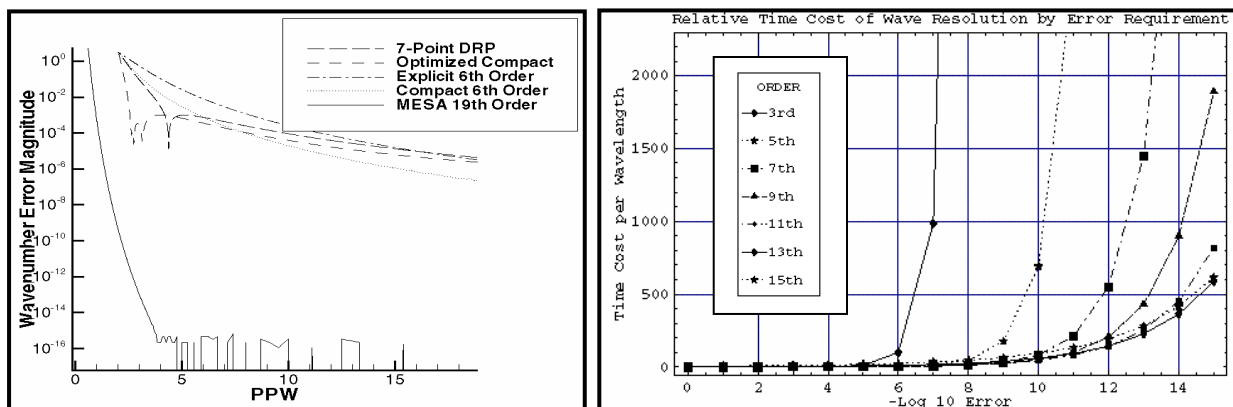
Figure 1 – Resolution and Efficiency Comparison

The desire to pursue a high resolution finite volume approach in turbo-machinery aero-acoustics is in part driven by the need to simulate the following:

- Mild shocks near transonic blade tips
- Sharp blade leading edges with steep flow gradients
- Sharp blade trailing edges to properly account for the Kutta condition
- Vortical, entropic, and acoustic wave propagation over approximately 10 wavelengths

It is also due in part by the need to maintain the following properties:

- Flow conservation in difficult areas such as blade leading edge and trailing edge (see Figure 2)
- Isotropic shock and wave speed everywhere in the machinery
- Nonlinear effects of blade curvature and active control surfaces
- Isentropic (for inviscid flows) flow along solid boundaries

Finite difference approaches have the following impediments to meeting the above needs:

- Structured, Overset, or Cartesian grids are either difficult to apply to complex geometries or grid singularities, as shown in Figure 3, occur as in the case of multi-block structured solvers
- Determining derivatives with wide stencils or compact schemes are undefined at shocks resulting in instabilities, shock smearing, etc.
- Corners pose difficulties (i.e. are multiply defined at wall/inflow and nonreflecting conditions require special treatment there)
- Spatial filtering/damping requires one-sided derivatives at boundaries which effectively changes the dispersion relations
- First order grid singularity noise sources arise from both multi-block curvilinear grids and sharp edged complex geometry

These considerations are addressed by using Ultra Hermite Integration, Flux, and Interpolation (Ultra HI-FI or UHF) methods. The term "Ultra" refers to the most salient characteristic of these methods which is they can resolve _**ultra-short**_ waves (<2 PPW) (ref. 16). This level of fidelity was first achieved with a finite difference Hermite-Taylor approach (ref. 17). In a similar vein, UHF methods use Cauchy-Kowalewski-Taylor time advance, and the spatial derivatives of the cell averages are carried on the grid; And Hermite fluxes are calculated and used to conservatively time advance all derivatives of the cell averages (ref. 6). This can be formulated with unstructured grids with upwinding (ref. 6); It can also be formulated in a centered staggered grid as by Chang/Van Leer (refs. 18 to 20). But the most efficient formulation is structured multi-block curvilinear because the geometry is implicitly represented to higher fidelity as higher derivatives of the metric terms are naturally included from differentiating the strong conservation of the governing equations. For example, the variation of the coordinate transformation first derivatives (metric term, η_x) near a typical leading edge is show in figure 4.
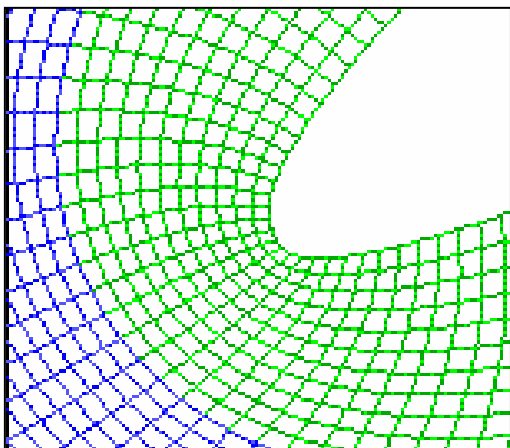
Figure 2 – Flux Conservation
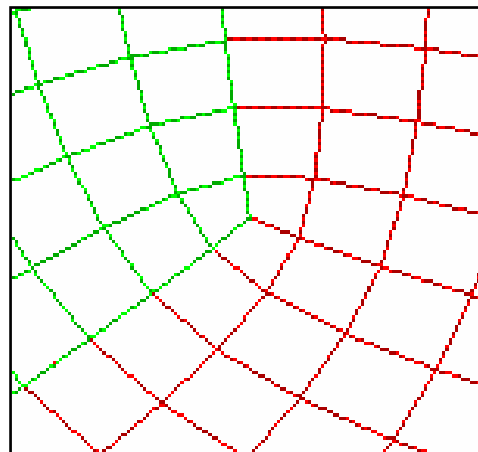
Figure 3 --Grid Singularities
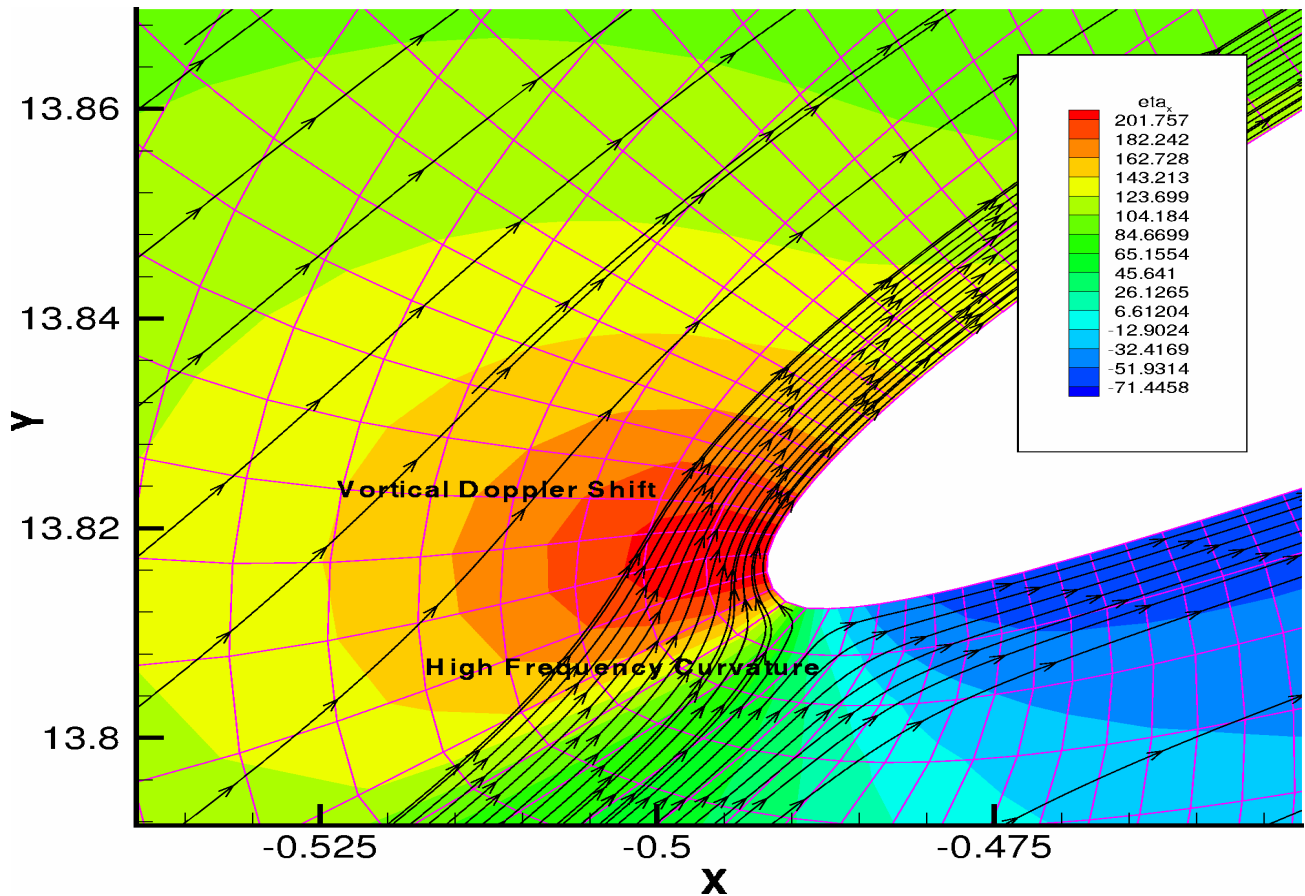
Figure 4 -- Spatial variation of curvilinear metric terms

NUMERICAL APPROACH
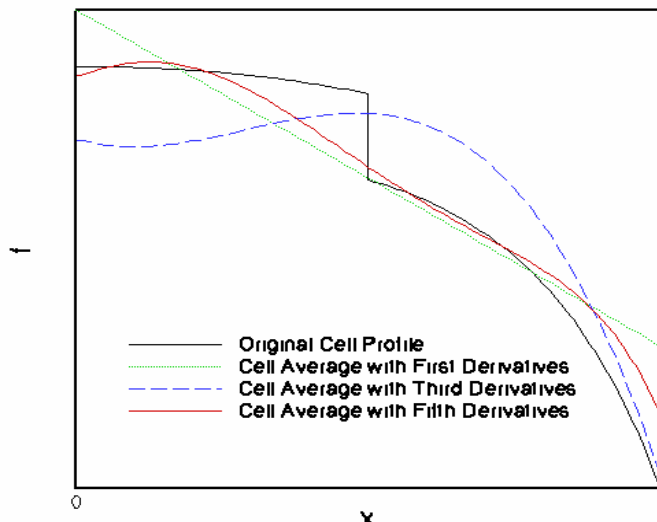
Figure 5 - Reconstruction of Shock

The key idea is to include spatial derivatives of the cell averages on the grid (ref. 6) which as shown in Figure 5 provide better shock fidelity as more derivative information is used in the reconstruction. The spatial derivative of the cell average is still defined at shocks which addresses the common criticism of high order finite difference methods. For the one-dimensional advection equation:

$$u_t + u_x = 0 \qquad (1)$$

the following cell averages are stored on the grid:

$$\bar{u} = \left(\frac{1}{\Delta x}\right)\int u\, dx \qquad \bar{u}_x = \left(\frac{1}{\Delta x}\right)\int u_x\, dx \qquad (2)$$

$$\bar{u}_{xx} = \left(\frac{1}{\Delta x}\right)\int u_{xx}\, dx \qquad \bar{u}_{xxx} = \left(\frac{1}{\Delta x}\right)\int u_{xxx}\, dx$$

More derivatives can be added as well to provide the fidelity and efficiency as shown in Figure 1.

The integral form of the governing equations (eq. 1) may be repeatedly differentiated:

$$\int u_t dV + \int u_x dV = \overline{u}_t \Delta x + u(j+1) - u(j) = 0$$

$$\int u_{tx} dV + \int u_{xx} dV = \overline{u}_{tx} \Delta x + u_x(j+1) - u_x(j) = 0$$

$$\int u_{txx} dV + \int u_{xxx} dV = \overline{u}_{txx} \Delta x + u_{xx}(j+1) - u_{xx}(j) = 0 \tag{3}$$

$$\int u_{txxx} dV + \int u_{xxxx} dV = \overline{u}_{txxx} \Delta x + u_{xxx}(j+1) - u_{xxx}(j) = 0$$

For this simple case the flux is simply the conserved variable, u. We need to reconstruct the sampled or un-averaged variables from the known averaged variables to calculate the flux at J=0 and J=1 in Figure 6.
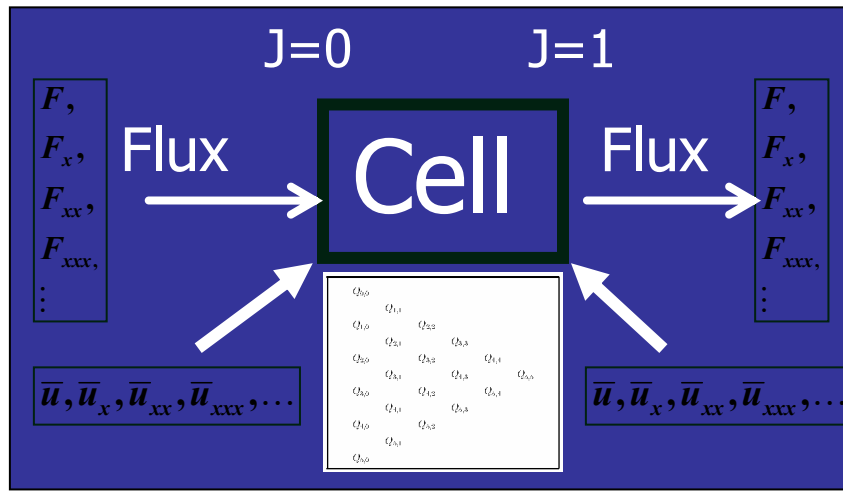
Figure 6- Basic Cell

This reconstruction can be accomplished in two ways, either by reconstruction via the primitive function (RP) (ref. 21) or by using constraints (ref. 22). For the structured curvilinear staggered UHF method one would use two cells for the reconstruction with the following constraints:

$$u(\xi) = \sum_{i=0}^{2s+1} a_i \xi^i,$$

$$\frac{1}{\Delta x} \int_{-\Delta x/2}^{\Delta x/2} \frac{\partial^m u(\xi)}{\partial x^m} d\xi = \frac{\partial^m \overline{u}_j}{\partial x^m},$$

$$\frac{1}{\Delta x} \int_{\Delta x/2}^{3\Delta x/2} \frac{\partial^m u(\xi)}{\partial x^m} d\xi = \frac{\partial^m \overline{u}_j}{\partial x^m} \tag{4}$$

with m=0 up to s.

For very high order UHF methods this process is intractable because current computer algebra techniques cannot symbolically invert large matrices and in those cases the RP approach using Hermite divided differences is more practical.

After calculating the fluxes with (eq. 4), the first time derivatives of the cell average spatial derivatives are found with (eq. 3). Next, the Cauchy-Kowalewski procedure can be applied as follows since from (eq. 1) we have:

$$\overline{u}_t = \overline{u}_t, \overline{u}_{tt} = -\overline{u}_{xt}, \overline{u}_{ttt} = \overline{u}_{xxt}$$

$$\overline{u}_{xt} = \overline{u}_{xt}, \overline{u}_{xtt} = -\overline{u}_{xxt}, \overline{u}_{xttt} = \overline{u}_{xxxt}$$

$$\overline{u}_{xxt} = \overline{u}_{xxt}, \overline{u}_{xxtt} = -\overline{u}_{xxxt}, \overline{u}_{xxttt} = \overline{u}_{xxxxt}$$

(5)

This procedure can by performed efficiently with unrolled recursion (ref. 15). At this point we can time advance the cell average data with a simple Taylor series in time:

$$\overline{u}^{n+1} = \overline{u}^n + \sum_{k=1}^{order}\left(\frac{1}{k!}\right)\frac{\partial^k \overline{u}^n}{\partial t^k}(\Delta t)^k$$

$$\overline{u}_x^{n+1} = \overline{u}_x^n + \sum_{k=1}^{order}\left(\frac{1}{k!}\right)\frac{\partial^k \overline{u}_x^n}{\partial t^k}(\Delta t)^k$$

(6)

$$\overline{u}_{xx}^{n+1} = \overline{u}_{xx}^n + \sum_{k=1}^{order}\left(\frac{1}{k!}\right)\frac{\partial^k \overline{u}_{xx}^n}{\partial t^k}(\Delta t)^k$$

$$\overline{u}_{xxx}^{n+1} = \overline{u}_{xxx}^n + \sum_{k=1}^{order}\left(\frac{1}{k!}\right)\frac{\partial^k \overline{u}_{xxx}^n}{\partial t^k}(\Delta t)^k$$

The cell average data, $\boxed{\overline{u}^n,(\overline{u}^n)_x,(\overline{u}^n)_{xx},(\overline{u}^n)_{xxx},\cdots}$, at the J=1/2 location in Figure 6 is simply interpolated using Hermite divided differences (ref. 15). Or, if the single cell unstructured UHF is used (ref. 6) then this information is already present.

After this process the following cell averaged data, $\boxed{\overline{u}^{n+1},(\overline{u}^{n+1})_x,(\overline{u}^{n+1})_{xx},(\overline{u}^{n+1})_{xxx},\cdots}$, is known at J=1/2 in Figure 6. The process just described is repeated at the next time level resulting in a staggered, centered UHF method. If an unstaggered single cell reconstruction is used as in (ref. 6), then an upwinding dissipation term should be included for stability.

RESULTS

The advection equation (1) is solved using the centered, staggered UHF procedure just described with the following initial condition:

$$u(t=0) = [2+\cos(\alpha x)]\exp[-(\ln 2)(x/10)^2] \quad (7)$$

The results at time = 800 are shown for α=1.7, α=4.6, and α=20 in figs. 7 to 9. Notice that Figures 8 and 9 show ultra-short wave resolution with at least 7 digits of accuracy.
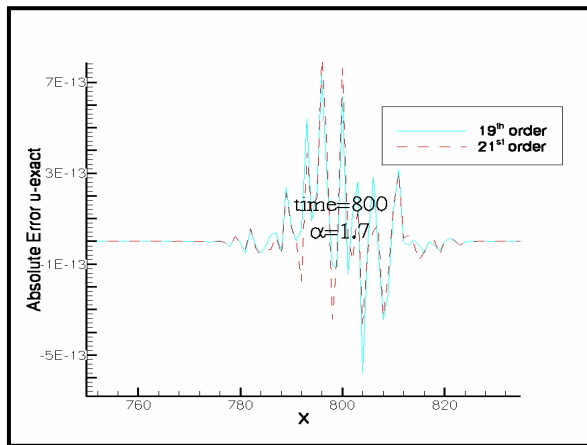
Figure 7 -- 3.69 PPW
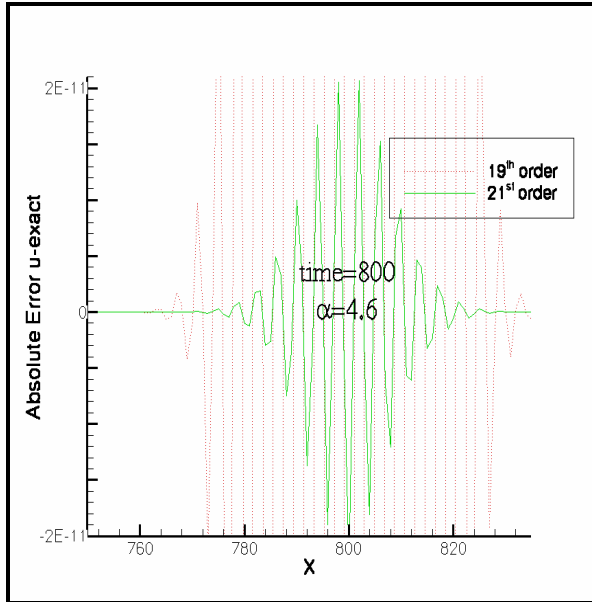
Figure 8 – 1.36 PPW
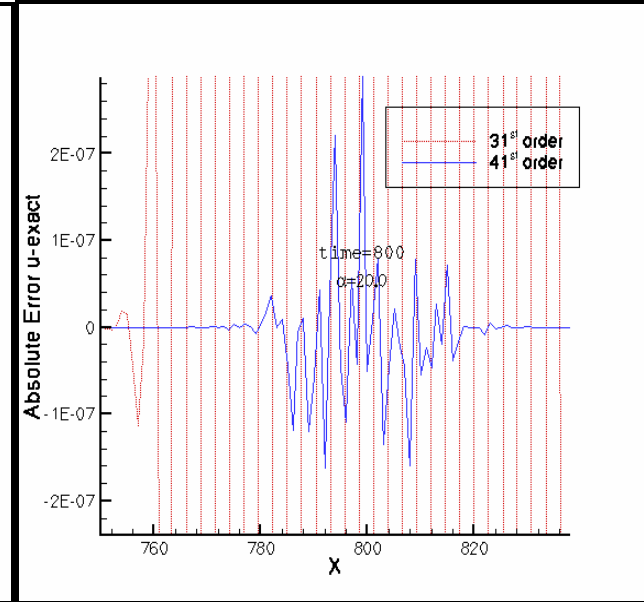
Figure 9 -- .314 PPW

This performance can be better understood by examining the UHF method's amplification factor as a function of wavenumber. Performing the usual Fourier linear modal analysis, assume a harmonic solution of the form in (1):

$$u(x,t) = Ae^{ik(x-t)} \tag{8}$$

$$g_{exact} = \left| \frac{u^{n+1}}{u^n} \right| = 1 \quad (g_{exact})_x = \left| \frac{u_x^{n+1}}{u_x^n} \right| = 1 \quad (g_{exact})_{xx} = \left| \frac{u_{xx}^{n+1}}{u_{xx}^n} \right| = 1 \tag{9}$$

We can immediately conclude that not only should the amplitude of all the waves remain unchanged, but that the amplitudes of the spatial derivatives of the waves should not change. By performing this analysis for $k>\pi$, we find that UHF methods are indeed resolving the ultra-short waves as shown in Figure 10. Notice the addition of 3 more spatial derivatives clearly improves the fidelity beyond $k>2\pi$.
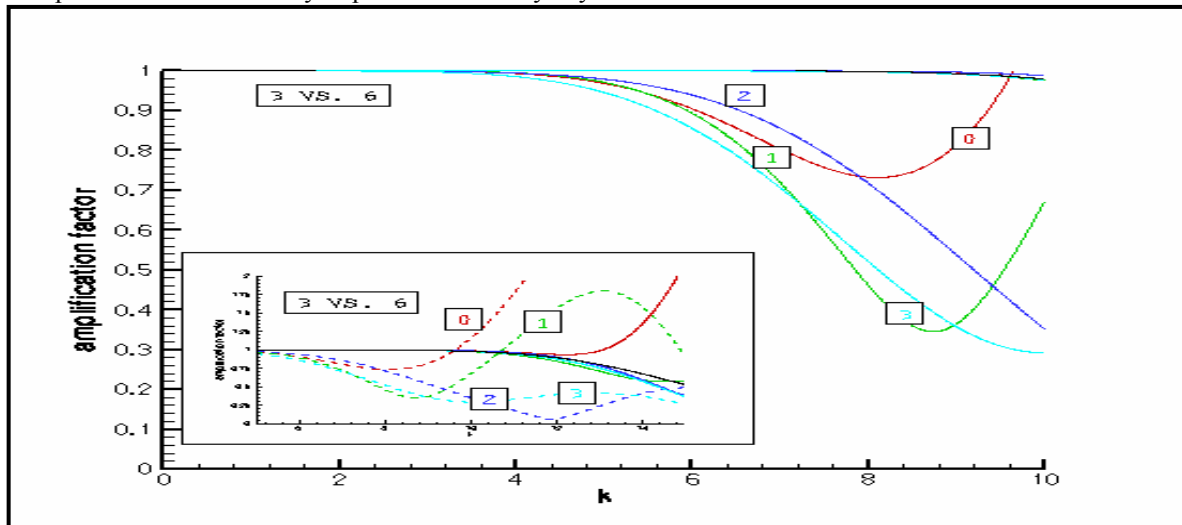
Figure 10 -- Fidelity Comparison of 3 and 6 spatial derivatives of the cell averages on the grid
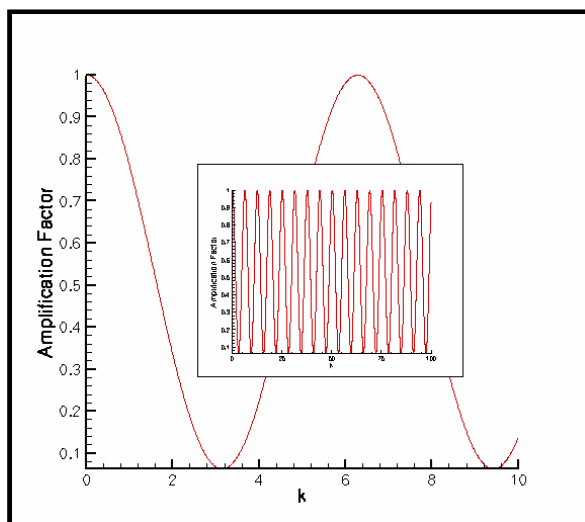
Figure 11 – No derivatives repeats
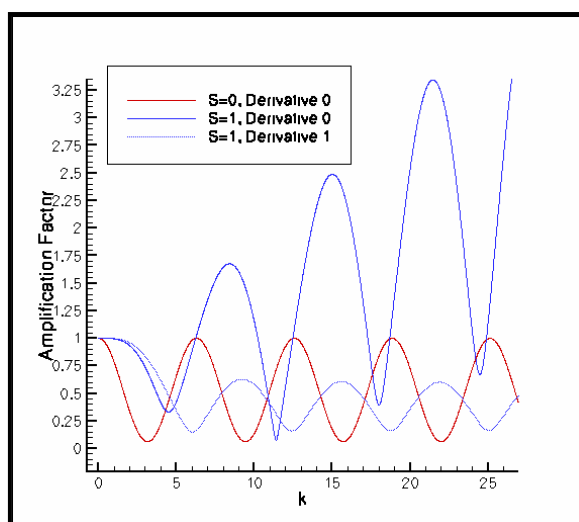
Figure 12 – Single derivative comparison

In Figure 11 we can see that the amplification factor merely repeats itself every **k**=π which is another way of observing ultra-short aliased waves are indistinguishable on the grid. Notice in Figure 12 that adding just one derivative to the calculation results in significant growth of the extremely short waves but in practice the method is stable because of the interaction of the damped spatial derivatives with the undamped portion of the ultra-short wave solution variables.

CONCLUSION

Much remains to be explored but it is clear that the ultra-short wave resolution implies significant efficiencies are attainable while keeping the desirable properties of finite volume formulations. New ultra-wave filters will need to be developed to fully utilize this level of fidelity (ref. 23). A discussion of boundary conditions is beyond the scope of the paper but the interested reader may find (ref. 24) helpful. The extension to Euler equations is laid out in (ref. 6) for unstructured single cell reconstruction and a demonstration of the multiblock structured two-cell reconstruction is being prepared. Space limitations preclude explaining more.

ACKNOWLEDGEMENTS

REFERENCES

1. Blazek, J.; Computational Fluid Dynamics: Principles and Applications. Elsevier, New York, 2001
2. Tam, C.K.W, Webb, J.C.: Dispersion-Relation-Preserving Finite-Difference Schemes for Computational Acoustics, J. Comp. Phys., Vol. 107, No. 2, 1993, pp. 262-281
3. Lele, S.K. : Compact Finite Difference Schemes with Spectral-like Resolution, J. Comp. Physics, Vol. 103, 1992, pp. 16-42
4. Nagarajan, S., Lele, S.K., Ferziger, J.H.: A robust high-order compact method for large eddy simulation, J. Comp. Physics, Vol. 191, 2003, pp. 392-419
5. Shu, C.: High-order Finite Difference and Finite Volume WENO Schemes and Discontinuous Galerkin Methods for CFD, Int. J. CFD, Vol. 17, No. 2, 2003, pp. 107-118
6. Agarwal, R. K., and Halt, D.W. : A Compact High-order Unstructured Grids Method for the Solution of Euler equations, Int. J. for Num. Meth. In Fluids, Vol. 31, 1999, pp.121-147
7. Wang, G. and Sankar, L.N. : Prediction of Rotorcraft noise with a low-dispersion finite Volume Scheme", Vol. 38, No. 3, March 2000
8. Hernandez, J.A. : High-order finite volume schemes for the advection-diffusion equation, Int. J. Num. Meth. Eng., Vol. 53, 2002, pp. 1211-1234
9. Rezgui, A., Cinnella, P., Lerat, A. : Third-order accurate Finite Volume Schemes for Euler Computations on Curvilinear Meshes, Computers & Fluids, Vol. 30, 2001, pp. 875-901
10. Nance, D.V., Viswanathan, K., Sankar, L.N.: Low-dispersion Finite Volume Scheme for Aeroacoustic Applications, AIAA J., Vol. 35, No. 2, Feb. 1997
11. Gaitonde, D., Shang, J.S.: High-order finite-volume schemes in wave propagation phenomena, AIAA Paper 96-2335, Plasmadynamics and Lasers Conference, June 17-20, 1996
12. Wang, Z.J. : Spectral (finite) volume method for conservation laws on unstructured grids: basic formulation, J. Comput. Phys., Vol. 178, No. 210, 2002
13. Wang, Z.J., Liu, Y. : Spectral (finite) volume method for conservation laws on unstructured grids II: extension to two-dimensional scalar equation, J. Comput. Phys., Vol. 179, 2002, pp. 665-697
14. Schwartzkopff, T., Munz, C.:Fast ADER: An Arbitrary High Order Scheme for Linear Acoustics, 4th CAA Workshop, OAI, Cleveland, OH, Oct. 2003
15. Dyson, R.W.: Technique for Very High Order Nonlinear Simulation and Validation, J. Comp. Acoustics, Vol. 10, No. 2, 2002, pp. 211-229
16. Tam, C.K.W. : Numerical Methods in Computational Aeroacoustics Short Course, Breckenridge, Colorado, June 15-16, 2002
17. Dyson, R.W. and Goodrich, J.W.: Automated Approach to Very High-Order Aeroacoustic Computations, AIAA J., Vol. 39, No. 3, 2001, pp. 396-406
18. Chang, S.-C.: The Method of Space-Time Conservation Element and Solution Element – A New Approach for Solving the Navier-Stokes and Euler equations, J. Comp. Physics, Vol. 119, 1995, pp. 295-324
19. Van Leer, B.:Towards the Ultimate Conservative Difference Scheme IV. A New Approach to Numerical Convection, J. Comp. Physics, Vol. 23, 1977, pp. 276-299
20. Huynh, H.T.: Analysis and Improvement of Upwind and Centered Schemes on Quadrilateral and Triangular Meshes, AIAA Paper 2003-3541, 16th AIAA Computational Fluid Dynamics Conference, June 23-26, 2003
21. Collela, P. and Woodward, P.R.: The Piecewise Parabolic Method (PPM) for Gas-Dynamical Simulations, J. Comp. Phys., Vol. 54, 1984, pp. 174-201
22. Lomax, H.; Pulliam, T.H., Zingg, D.W.: Fundamentals of Computational Fluid Dynamics, Springer-Verlag, 2001
23. Zhou, Y.C., Wei, G.W.: High resolution conjugate filters for the simulation of flow, J. Comp. Phys., Vol. 189, 2003, pp. 159-179
24. Dyson, R.W.; Hixon, R.: Towards Arbitrary Accuracy Inviscid Surface Boundary Conditions, AIAA-2002-2438, NASA-TM-2002/211583, 2002

B-SPLINE COLLOCATION

Jonathan B. Freund

Department of Theoretical and Applied Mechanics
University of Illinois at Urbana-Champaign
Urbana, IL 62801
(217) 244-7729, FAX: (217) 244-5707
Email: jbfreund@uiuc.edu

The simple advection equation, $u_t + u_x = 0$, is solved with initial condition

$$u(x,t) = (2 + \cos \alpha x) \exp\left[-\log 2 \left(\frac{x}{10}\right)^2\right] \tag{1}$$

using fourth-order Runge–Kutta time advancement and a B-spline collocation method for numerical evaluation of the spatial derivatives. The principal objective is demonstrate the B-spline method and point out certain attractive features it has.

B-splines, where the "B" stands for nothing grander than "basis", offer in a sense maximum continuity with minimal support. Support here is quantified by the number of discrete intervals they span. Thus, the 0th order B-spline is a simple box function

$$B_j^0(x) = \begin{cases} 1 & \text{if } t_{j-1} < x < t_j \\ \frac{1}{2} & \text{if } x = t_{j-1} \text{ or } t_j \\ 0 & \text{otherwise} \qquad j = 1, \ldots, N_k, \end{cases} \tag{2}$$

spanning only two t_j's, which are the user selected 'knots' that define the intervals of support. One of most attractive properties of the splines is the complete flexibility they give the user in selecting knot locations. The order d of the spline indicates the order of derivative through which is continuous. Order k B-splines are constructed from order $k-1$ B-splines recursively by

$$B_j^k(x) = \frac{x - t_{j-k-1}}{t_{j-1} - t_{j-k-1}} B_{j-1}^{k-1}(x) + \frac{t_j - x}{t_j - t_{j-k}} B_j^{k-1}(x), \qquad j = 1, \ldots, N_k + k. \tag{3}$$

This is analogous to a convolution operation: each B-spline function is the convolution of a one order lower B-spline with the box function. For uniformly spaced knots, this analogy is exact. Figure 1 shows order 1 and 3 B-splines for uniformly spaced knots in a domain $x \in [0, 10]$.
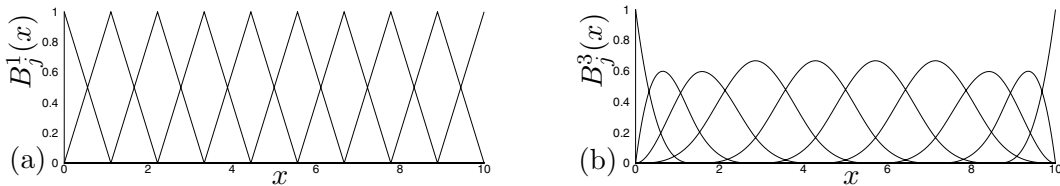
Figure 1: B-splines for uniformly distributed knots, with "end" knots placed at $x = 0, L$: (a) first order; (b) third order.

Continuous functions can be represented in terms of their d^{th}-order B-spline coefficients as

$$u(x_i) \approx \tilde{u}(x_i) = \sum_{j=1}^{N_x} \alpha_j B_j^d(x_i) \qquad i = 1, \ldots, N_x, \tag{4}$$

where x_i are the $N_x = N_k + d$ user specified collocation points. Given a distribution of knots, there remains some flexibility in selecting these points. Here we take them to be at the maximum of their respective $B_j^d(x)$ within $x \in [0, L]$. Since the B-splines have compact support, (4) is in effect a banded-matrix equation that can be solved for α_j's in terms of $\tilde{u}(x_i)$'s to compute the coefficients in the expansion. The B-spline order is one less than the bandwidth, so, for example, a second-order spline requires inversion of a tri-diagonal system to compute the coefficients.

The procedure for computing an mth-order derivative[1] follows from (4):

$$\left. \frac{d^m u}{dx^m} \right|_{x_i} = \sum_{j=1}^{N_x} \alpha_j \frac{d^m B_j^d}{dx^m}, \tag{5}$$

where

$$\frac{d^m B_j^d}{dx^m} = \sum_{l=j-m}^{j} \beta_{jl}^m B_l^{k-m}(x) \tag{6}$$

with coefficients determined recursively using properties of B-splines as[2]

$$\beta_{jl}^{m+1} = (k-1) \frac{\beta_{j(l+1)}^m - \beta_{jl}^m}{t_l - t_{l-k+m}}. \tag{7}$$

Hence the procedure for computing a derivative is effectively the solution of a banded-matrix system for the coefficients (4) and then a banded-matrix/vector multiplication (5). In practice, all the needed values of the B-splines and their derivatives can be pre-computed. Assuming flexible routines are used for the matrix operations, such as those readily available in the LAPACK and the BLAS libraries, a single input parameter d can change the order of the method without necessitating any changes to the code. Computation of any order of derivatives $m \leq d$ is simple. The dispersion properties are comparable to those of standard explicit and compact finite difference formulations, as shown in figure 2.
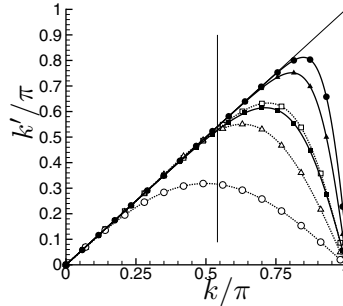
Figure 2: Modified wave number k' for wave number k: ○ second-order central; △ DRP;[3] □ sixth-order compact finite different;[4] ■ fourth-order B-spline; ▴ eighth-order B-Spline; and ● twelfth-order B-spline.
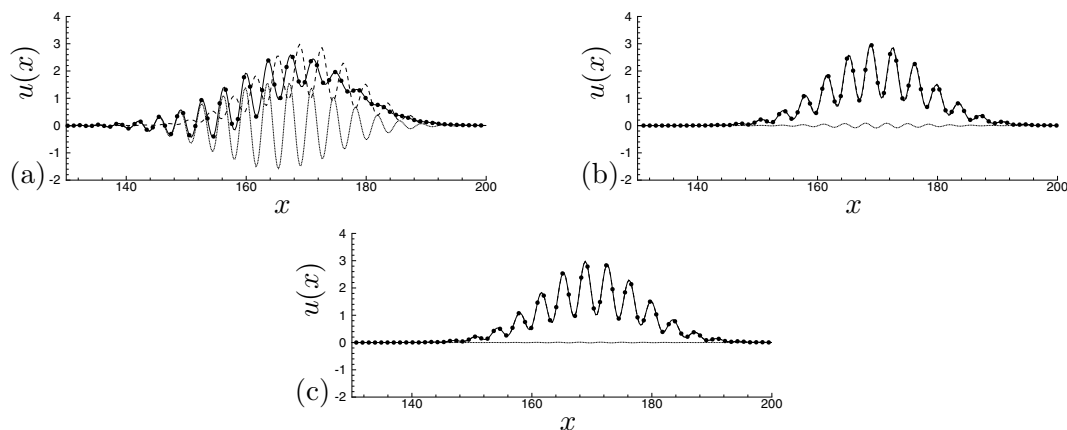
Figure 3: (a) Fourth-, (b) eighth-, and (c) twelfth-order solutions: ● numerical, - - - - exact, and
········ error. For the numerical solution the ——— line is the B-spline interpolant; the ● are the
values at the collocation points.

Figure 3 show the solution of the problem with $\alpha = 1.7$ for 4th, 8th and 12th order B-spline interpolants. Clearly the resolution increases substantially with order, as anticipated by wavenumber analysis of the effective derivative stencils.[1] However, such high-orders are rarely useful in practice. The computational price of for their extreme accuracy for the well resolved components is typically unnecessary. Clearly schemes designed to better match the modified wave number behavior, particularly at $\alpha = 1.7$ in this case, with some sacrifice of accuracy at lower wave numbers would be more efficient and probably more practical in most situations. Some notable features of B-splines that might find use in aeroacoustic simulations might be the stronger conservation properties of Galerkin formulations[1] and their potential to provide embedded mesh algorithms in which interpolation is exactly consistent with the derivative scheme.[5]

References

[1] W. Y. Kwok, R. D. Moser and J. Jiménez, "A critical evaluation of the resolution properties of B-spline and compact finite difference methods," J. Comp. Phys. **174**, 510 (2001).

[2] C. de Boor, *A Practical Guide to Splines* (Springer-Verlag, New York) (1978).

[3] C. K. W. Tam and J. C. Webb, "Dispersion-relation-preserving finite difference schemes for computational acoustics," J. Comp. Phys. **107**, 262 (Aug 1993).

[4] S. K. Lele, "Compact finite difference schemes with spectral-like resolution," J. Comp. Phys. **103**, 16 (1992).

[5] K. Shariff and R. D. Moser, "Two-dimensional mesh embedding for b-spline methods," J. Comp. Phys. **145**, 471 (1998).

Solution Comparisons

Christopher K.W. Tam
Department of Mathematics
Florida State University
Tallahassee, FL 32306-4510, USA
tam@math.fsu.edu

Category 1, Problem 1

Comparison with Exact Solution
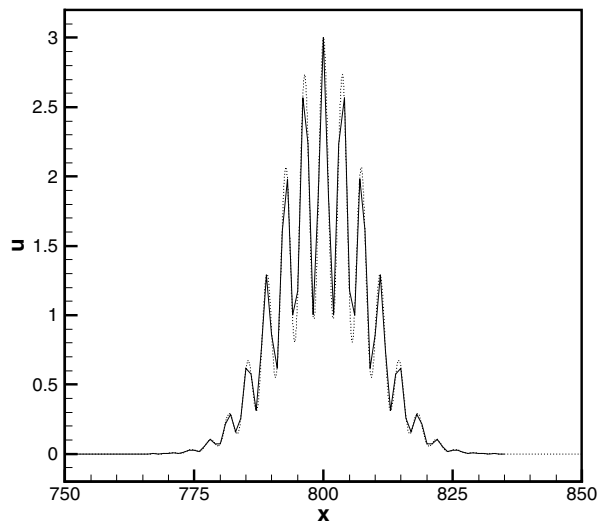
$t = 800, \alpha = 1.7$, ———, solution by Dyson,
$\cdots$, analytical solution.
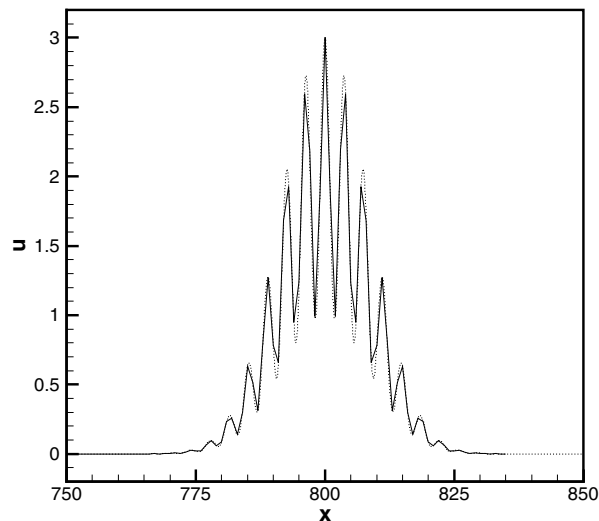
$t = 800$, ———, solution by Dyson, $\alpha = 4.6$;
$\cdots$, analytical solution, $\alpha = 4.6 - 2\pi$.

$t = 400, \alpha = 1.7$, ———, solution by Edgar,
6th order unfiltered method, $\cdots$,
analytical solution.

$t = 800, \alpha = 1.7$, ———, solution by Edgar,
6th order unfiltered method, $\cdots$,
analytical solution.

$t = 400, \alpha = 4.6$, ———, solution by Edgar,
6th order unfiltered method, $\cdots$,
analytical solution.

$t = 800, \alpha = 4.6$, ———, solution by Edgar,
6th order unfiltered method, $\cdots$,
analytical solution.

$t = 400, \alpha = 1.7$, ———, solution by Edgar,
6th order filtered method, $\cdots$, analytical
solution.

$t = 800, \alpha = 1.7$, ———, solution by Edgar,
6th order filtered method, $\cdots$, analytical
solution.

$t = 400, \alpha = 4.6$, ——, solution by Edgar, 6th order filtered method, $\cdot\cdot\cdot\cdot$, analytical solution.

$t = 800, \alpha = 4.6$, ——, solution by Edgar, 6th order filtered method, $\cdot\cdot\cdot\cdot$, analytical solution.

$t = 400, \alpha = 1.7$, ——, solution by Hu, $\cdot\cdot\cdot\cdot$, analytical solution.

$t = 800, \alpha = 1.7$, ——, solution by Hu, $\cdot\cdot\cdot\cdot$, analytical solution.

$t = 400, \alpha = 4.6,$ ———, solution by Hu,
$\cdots\cdots$, analytical solution.

$t = 800, \alpha = 4.6,$ ———, solution by Hu,
$\cdots\cdots$, analytical solution.

$t = 400, \alpha = 1.7,$ ———, solution by
Hagstrom, 40th order standard difference
method, $\cdots\cdots$, analytical solution.

$t = 800, \alpha = 1.7,$ ———, solution by
Hagstrom, 40th order standard difference
method, $\cdots\cdots$, analytical solution.

$t = 400$, ——, solution by Hagstrom, $\alpha = 4.6$, 40th order standard difference method, · · · ·, analytical solution, $\alpha = 4.6 - 2\pi$.

$t = 800$, ——, solution by Hagstrom, $\alpha = 4.6$, 40th order standard difference method, · · · ·, analytical solution, $\alpha = 4.6 - 2\pi$.

$t = 800, \alpha = 1.7$, ——, solution by Hagstrom, 47th order Hermite method, · · · ·, analytical solution.
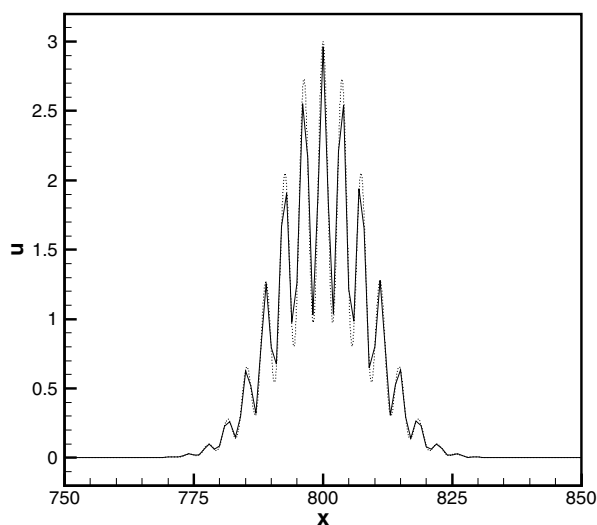
$t = 800$, ——, solution by Hagstrom, $\alpha = 4.6$, 47th order Hermite method, · · · ·, analytical solution, $\alpha = 4.6 - 2\pi$.

$t = 400, \alpha = 1.7$, ———, solution by Kim, 2nd order method, $\cdots$, analytical solution.

$t = 800, \alpha = 1.7$, ———, solution by Kim, 2nd order method, $\cdots$, analytical solution.
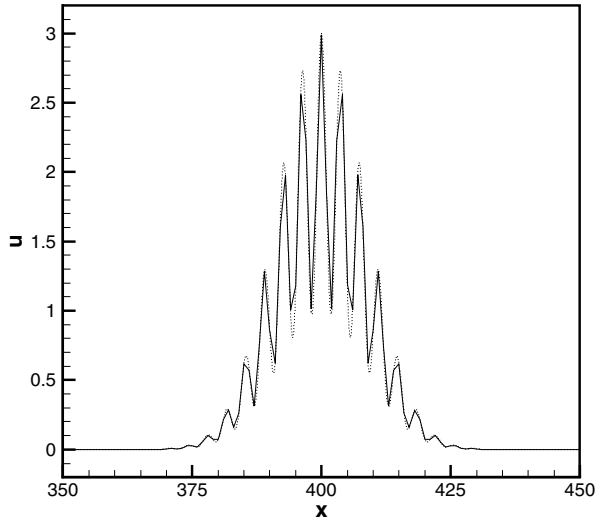
$t = 400, \alpha = 1.7$, ———, solution by Kim, 3rd order method, $\cdots$, analytical solution.
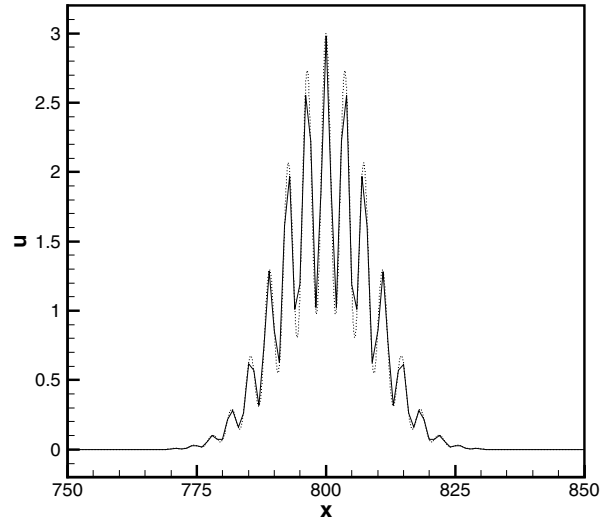
$t = 800, \alpha = 1.7$, ———, solution by Kim, 3rd order method, $\cdots$, analytical solution.
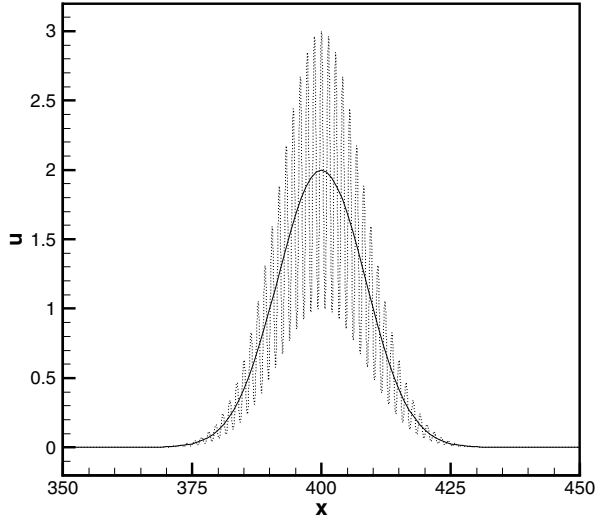
$t = 400, \alpha = 4.6,$ ——, solution by Kim, 3rd order method, $\cdots$, analytical solution.
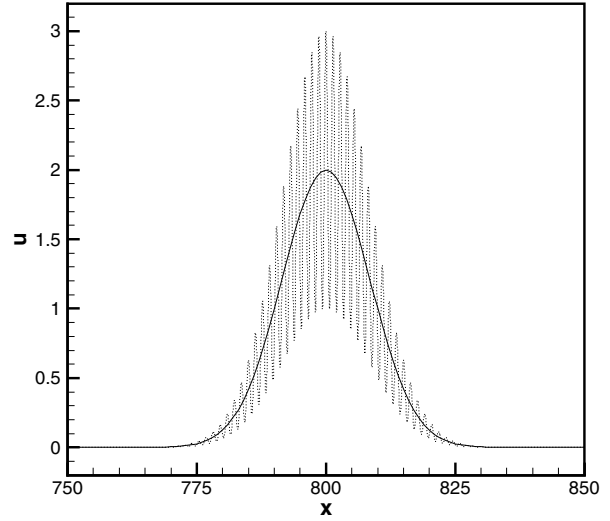
$t = 800, \alpha = 4.6,$ ——, solution by Kim, 3rd order method, $\cdots$, analytical solution.

$t = 400, \alpha = 4.6,$ ——, solution by Kim, $\alpha = 4.6$, 5th order method, $\cdots$, analytical solution, $\alpha = 4.6 - 2\pi.$

$t = 800, \alpha = 4.6,$ ——, solution by Kim, $\alpha = 4.6$, 5th order method, $\cdots$, analytical solution, $\alpha = 4.6 - 2\pi.$

$t = 400, \alpha = 1.7,$ ———, solution by Schulten, $\cdots$, analytical solution.

$t = 800, \alpha = 1.7,$ ———, solution by Schulten, $\cdots$, analytical solution.

$t = 400,$ ———, solution by Schulten, $\alpha = 4.6,$ $\cdots$, analytical solution, $\alpha = 4.6 - 2\pi.$

$t = 800,$ ———, solution by Schulten, $\alpha = 4.6,$ $\cdots$, analytical solution, $\alpha = 4.6 - 2\pi.$

$t = 400, \alpha = 1.7,$ ——, solution by
Schwartzkopff, 6th order method, $\cdots$,
analytical solution.

$t = 800, \alpha = 1.7,$ ——, solution by
Schwartzkopff, 6th order method, $\cdots$,
analytical solution.

$t = 400,$ ——, solution by Schwartzkopff,
6th order method, $\alpha = 4.6,$ $\cdots$,
analytical solution, $\alpha = 4.6 - 2\pi.$

$t = 800,$ ——, solution by Schwartzkopff,
6th order method, $\alpha = 4.6,$ $\cdots$,
analytical solution, $\alpha = 4.6 - 2\pi.$

$t = 400, \alpha = 1.7,$ ——, solution by
Schwartzkopff, 24th order method, $\cdots$,
analytical solution.

$t = 800, \alpha = 1.7,$ ——, solution by
Schwartzkopff, 24th order method, $\cdots$,
analytical solution.

$t = 400,$ ——, solution by Schwartzkopff,
24th order method, $\alpha = 4.6,$ $\cdots$,
analytical solution, $\alpha = 4.6 - 2\pi.$

$t = 800,$ ——, solution by Schwartzkopff,
24th order method, $\alpha = 4.6,$ $\cdots$,
analytical solution, $\alpha = 4.6 - 2\pi.$

$t = 400, \alpha = 1.7,$ ———, solution by Goodrich, $\cdots$, analytical solution.

$t = 800, \alpha = 1.7,$ ———, solution by Goodrich, $\cdots$, analytical solution.

$t = 400,$ ———, solution by Goodrich, $\alpha = 4.6, \cdots$, analytical solution, $\alpha = 4.6 - 2\pi.$

$t = 800,$ ———, solution by Goodrich, $\alpha = 4.6, \cdots$, analytical solution, $\alpha = 4.6 - 2\pi.$
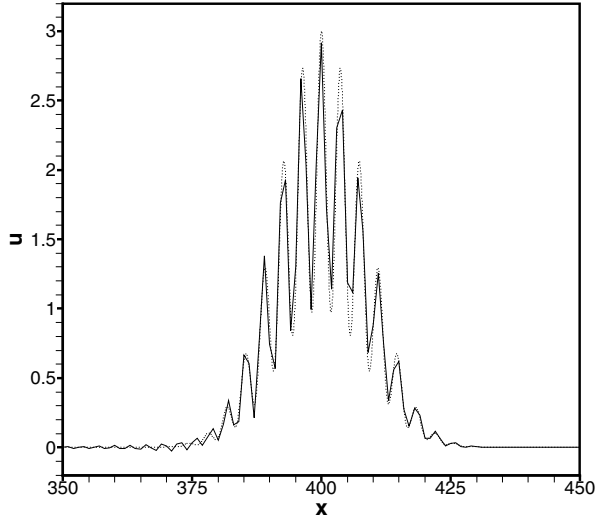
$t = 400, \alpha = 1.7,$ ——, solution by Tam
and Ju, $\cdots$, analytical solution.
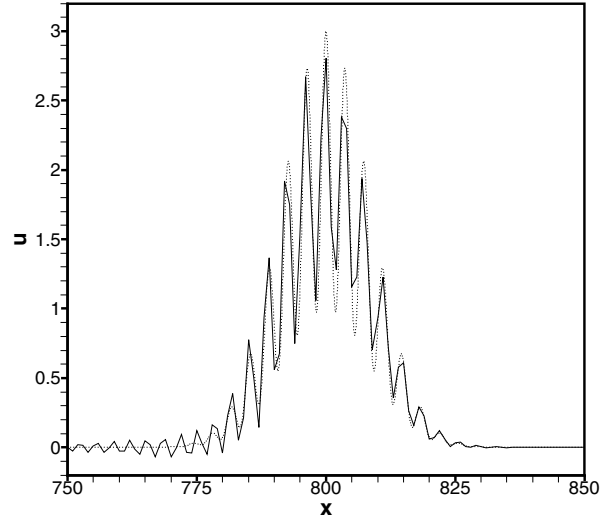
$t = 800, \alpha = 1.7,$ ——, solution by Tam
and Ju, $\cdots$, analytical solution.
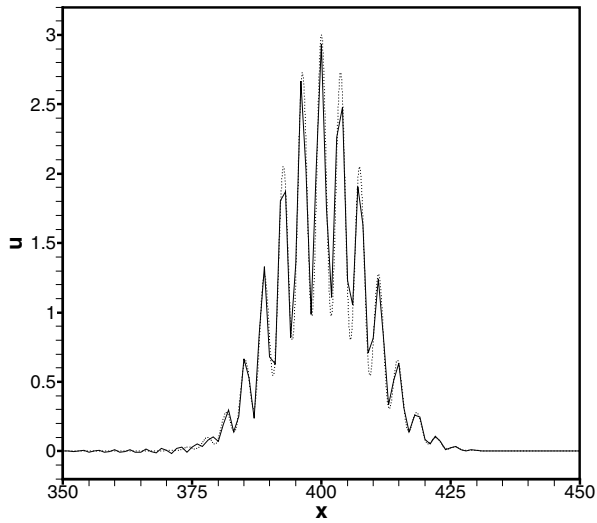
$t = 400,$ ——, solution by Tam and Ju,
$\alpha = 4.6,$ $\cdots$, analytical solution,
$\alpha = 4.6 - 2\pi.$
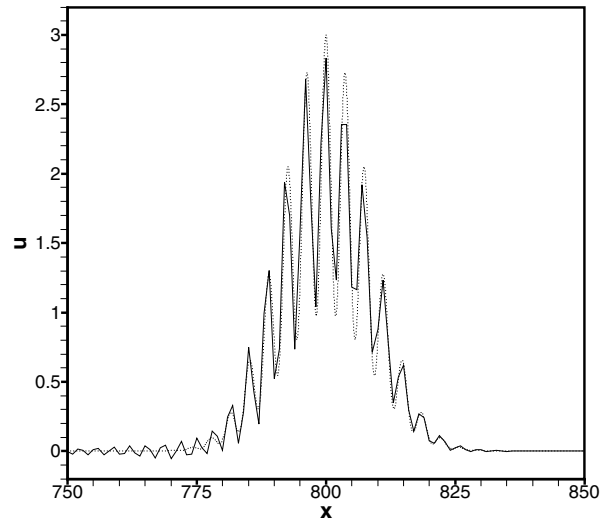
$t = 800,$ ——, solution by Tam and Ju,
$\alpha = 4.6,$ $\cdots$, analytical solution,
$\alpha = 4.6 - 2\pi.$
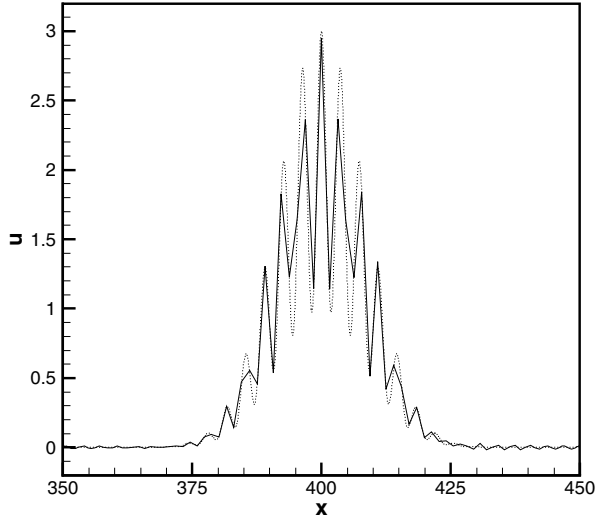
$t = 400, \alpha = 1.7,$ ———, solution by Wang, $\cdots\cdots$, analytical solution.
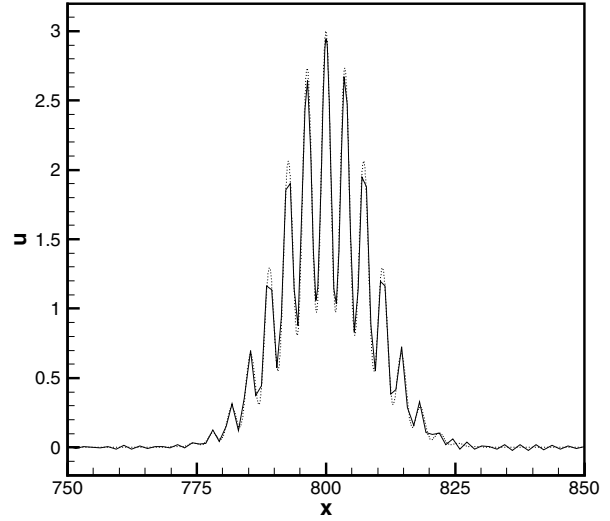
$t = 800, \alpha = 1.7,$ ———, solution by Wang, $\cdots\cdots$, analytical solution.
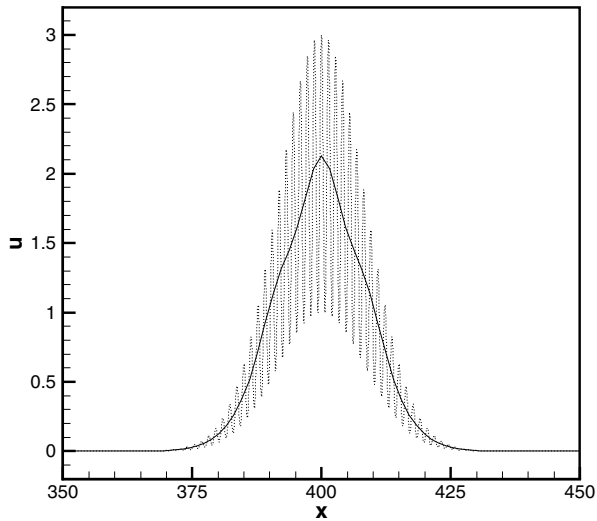
$t = 400, \alpha = 4.6,$ ———, solution by Wang, $\cdots\cdots$, analytical solution.

$t = 800, \alpha = 4.6,$ ———, solution by Wang, $\cdots\cdots$, analytical solution.

Christopher K.W. Tam
Department of Mathematics
Florida State University
Tallahassee, FL 32306-4510, USA
tam@math.fsu.edu
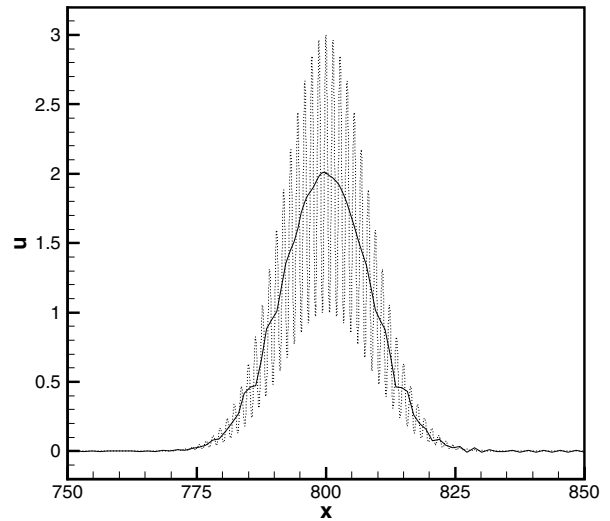
Category 1, Problem 2

Comparison with Exact Solution

Full pressure contour $(p = 0)$, incident wave angle 20^0. ——, calculated solution by Hagstrom; $\cdots$, analytical solution.

Scattered pressure contour $(p = 0)$, incident wave angle 20^0. ——, calculated solution by Hagstrom; $\cdots$, analytical solution.

Full pressure contours, incident wave angle 65^0. Pressure levels from -2 to 2 with increment 0.4444. ——, calculated solution by Hagstrom; $\cdots$, analytical solution.

Full pressure contours, incident wave angle 65^0. Pressure levels from -2 to 2 with increment 0.4444. ——, calculated solution by Hagstrom; $\cdots$, analytical solution.

Full pressure contour ($p = 0$), incident wave angle 20^0, $\Delta x = \Delta y = \lambda_x/120$.
——, calculated solution by Tam and Ju;
· · · ·, analytical solution.

Scattered pressure contour ($p = 0$), incident wave angle 20^0, $\Delta x = \Delta y = \lambda_x/120$.
——, calculated solution by Tam and Ju;
· · · ·, analytical solution.

Full pressure contours, incident wave angle 65^0, $\Delta x = \Delta y = \lambda_x/30$. Pressure levels from -2 to 2 with increment 0.4444.
——, calculated solution by Tam and Ju;
· · · ·, analytical solution.

Full pressure contours, incident wave angle 65^0, $\Delta x = \Delta y = \lambda_x/30$. Pressure levels from -2 to 2 with increment 0.4444.
——, calculated solution by Tam and Ju;
· · · ·, analytical solution.

Summary of Solutions to Category 1, Problem 3

Thomas Hagstrom[1]
Dept. of Mathematics and Statistics
The University of New Mexico, Albuquerque, NM 87131
email: hagstrom@math.unm.edu, FAX: (505) 277-5505.

The goal of this problem was to provide a detailed study of the accuracy of boundary treatments with a range of incidence angles including shear and a sonic point.

There are three parts. In each we solve the linearized Euler equations on a prescibed domain: $(-2, 2) \times (0, 1)$ with initial conditions consisting of a pressure dipole, entropy and vorticity disturbances. Here $x_1 = \pm 2$ are the artificial boundaries, the speed of sound is scaled to 1, and we solve up to $t = 64$.

The solvers were asked to provide to provide l_2 relative errors computed on a 129×33 mesh at 18 time stations ranging from 1 to 64. We note that these problems present a very stringent test of the boundary treatments, as at later times waves are incident on the artificial boundaries at increasingly skew angles. We also note that in many settings it might be more appropriate to measure the errors relative to the size of the initial disturbance, rather than against the solution remaining in the computational domain. Then the $O(100\%)$ late time relative errors reported below by some solvers are $O(1\% - 20\%)$, which may be acceptable.

PART 1

Solutions were provided by Colonius, Edgar and Visbal, and Hagstrom and Nazarov. Edgar and Visbal used a 70-point damping layer with exponential stretching and filtering. From their presentation, their results had good accuracy, which was not reflected in the error data they provided. Therefore, I suspect that the error calculations themselves are faulty, and haven't included them in the graphs below. Colonius provided results for a wide variety of domain truncation methods; the "supergrid" damping layers with 16, 32, 64 and 128 points, normal characteristic boundary conditions, and Padé conditions of degrees $(0, 0)$, $(4, 4)$, and $(8, 8)$. Finally, Hagstrom and Nazarov use a Perfectly Matched Layer with widths $L = 1$ and $L = 1.5$. Thus the number of points in the layers is the same as the number of points used to discretize a cross-section when $L = 1$ and half again as many when $L = 1.5$. For the fine mesh calculations shown these are 128 and 192 respectively, though they would be fewer with a coarser mesh.

Errors in the u variable are shown in Figures 1-2. In the interests of space we only show u errors for all examples: errors in other variables are typically similar. Here we present both semilogarithmic and untransformed plots. Clearly, the
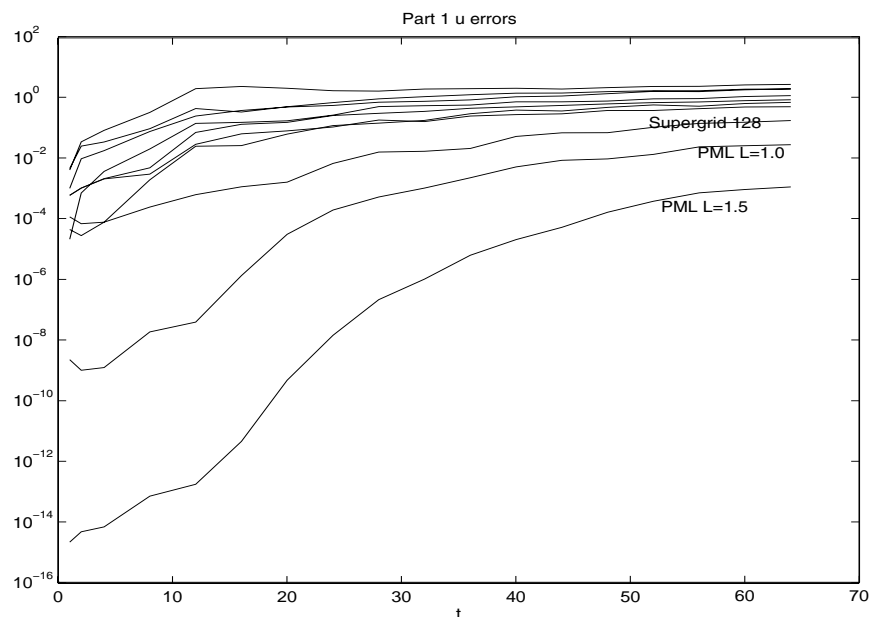
Figure 1: Relative u errors for Part 1.

PML results are more accurate, many orders of magnitude so at early times. However, they are also more expensive. Their extreme early time superiority is probably attributable both to the perfect matching property and to the fact that the Hagstrom-Nazarov simulations are better resolved. All methods are evidently convergent with increasing order or layer width. We also note that the size of the solution has decreased by a factor of about 70 from $t = 1$ to $t = 64$ so that the errors relative to the initial solution are all fairly small.

PART 2

Solutions were provided by Colonius, Hu, and Hagstrom and Nazarov. Colonius used 16-128 point supergrid layers, Hu used a 20-point PML, and Hagstrom and Nazarov used PMLs of widths $L = 0.5$, $L = 1.0$, and $L = 1.5$. A semilogarithmic plot of the relative u errors is shown in Figure 3. Again the PMLs provide the most accurate results, particularly for early times, though it is again unclear to what extent this is determined by the layer properties and to what extent it is determined by the resolution of the interior solvers. The Hu PML, which is mathematically identical to the one used by Hagstrom and Nazarov but which employs entirely different parameters, is the clear winner in this case from the point of view of combined accuracy and efficiency. We finally note that Hagstrom and Nazarov are for $L = 1.0$ and $L = 1.5$ using the same method and grid as was used to generate the exact solution, which minimizes their discretization error. However, at later times the error due to domain truncation is
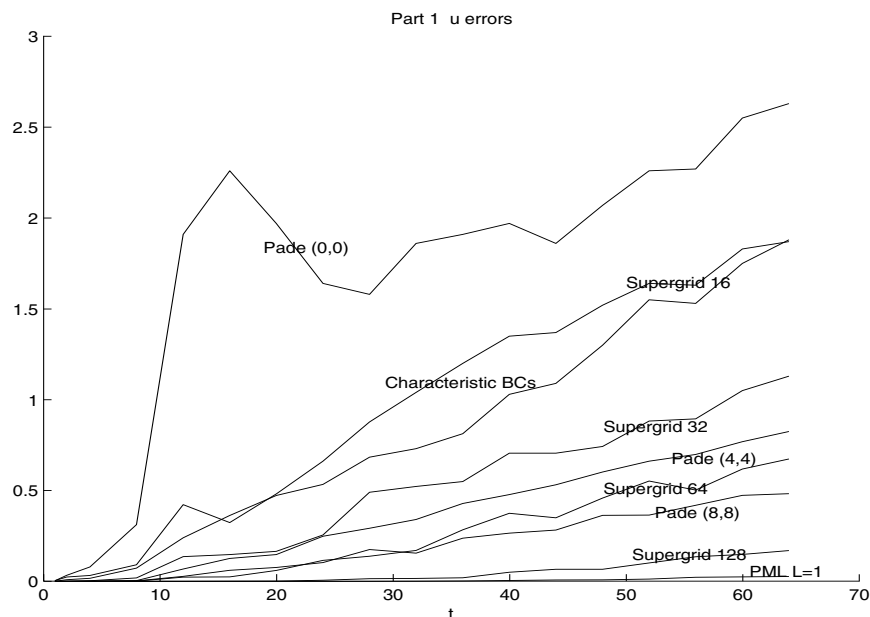
Figure 2: Relative u errors for Part 1.

dominant. Finally we note that in this case the decay of u from $t = 1$ to $t = 64$ is about a factor of 30.

PART 3

Only Colonius with the supergrid layer was able to provide solutions in this case. Stable PML formulations for a transonic flow are as yet unknown. The results are plotted in Figure 4, and are similar to the previous cases at late time. Here the decay of the solution is less pronounced, a factor of about 7 from $t = 1$ to $t = 64$.

CONCLUSIONS

The goal of these problems is not to definitively order various methods, but to provide a testbed where the accuracy of any domain truncation technique as a function of its complexity can be rigorously assessed. Nonetheless, we can make a few general comments.

- The PML provided the best results when it was usable - that is in Parts 1 and 2. However, no acceptable PML results were obtained for the transonic case.

- The supergrid method, though requiring more points than the PML in Parts 1 and 2, performed well and comparably in all three cases.
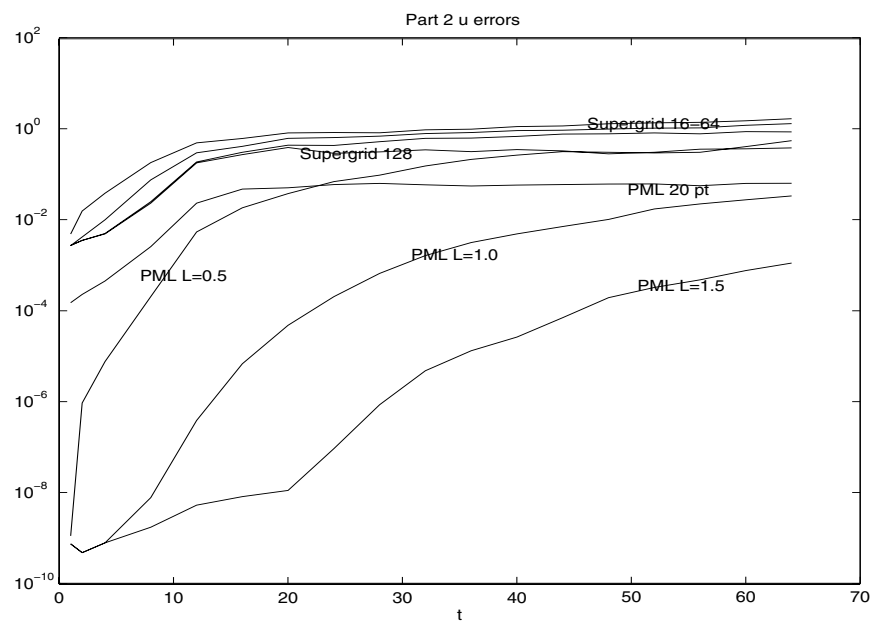
Figure 3: Relative u errors for Part 2.
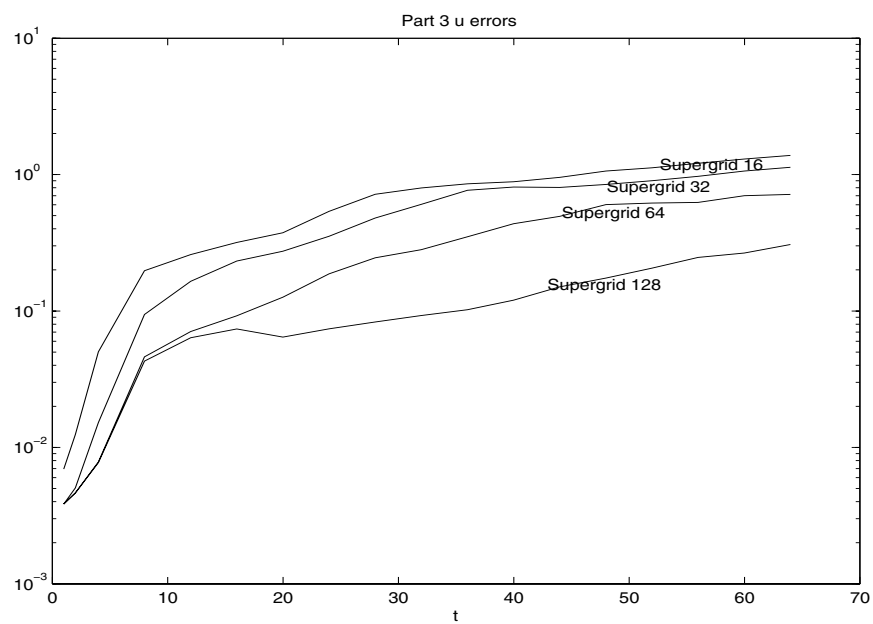
Figure 4: Relative u errors for Part 3.

COMPARISON WITH ANALYTIC SOLUTION

CATEGORY 2 – COMPLEX GEOMETRY

Miguel R. Visbal
Air Force Research Laboratory, WPAFB OH 45433
miguel.visbal@wpafb.af.mil

CASE 1 – TWO-CYLINDER SCATTERING PROBLEM
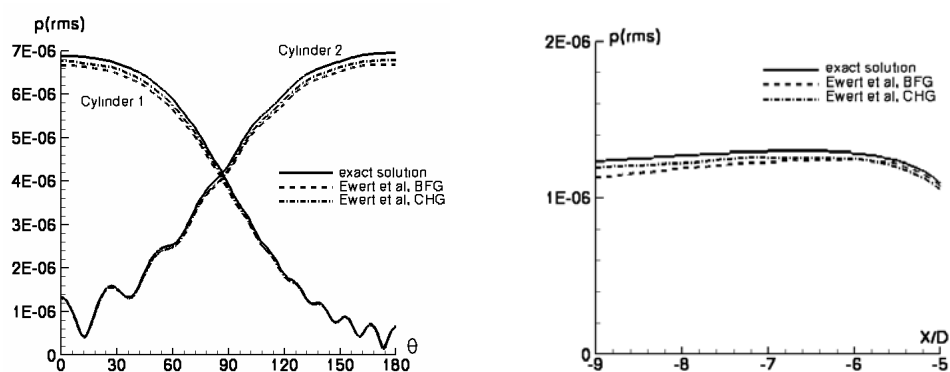
R. EWERT, J. YIN and J. DELFS
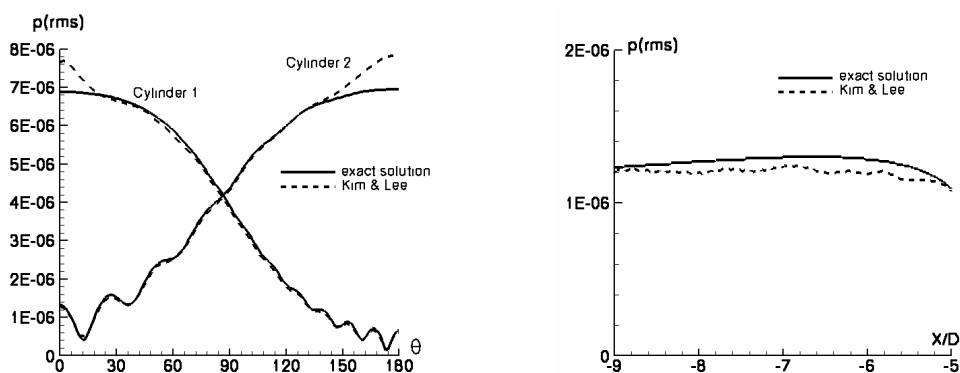
J. KIM and D. LEE
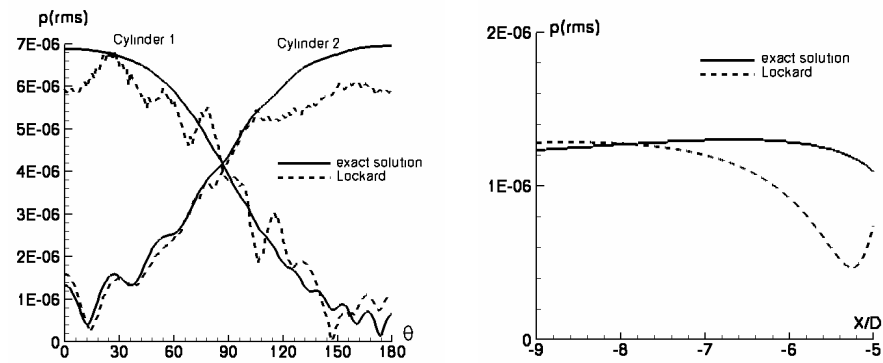
D. LOCKARD
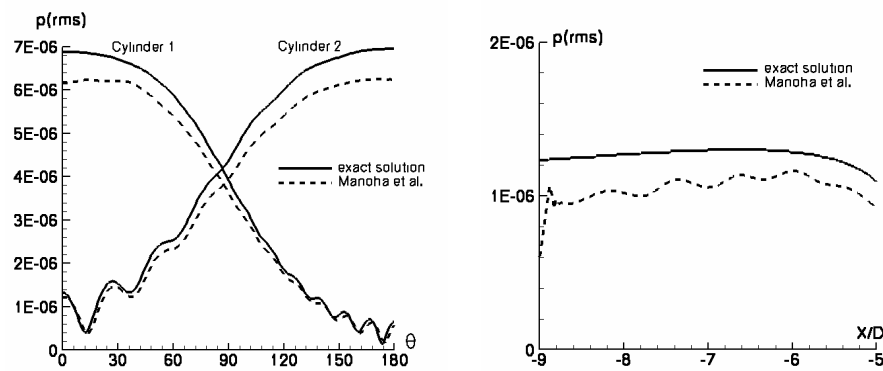
E. MANOHA, S. REDONNET, R. GUENANFF and M. TERRACOL
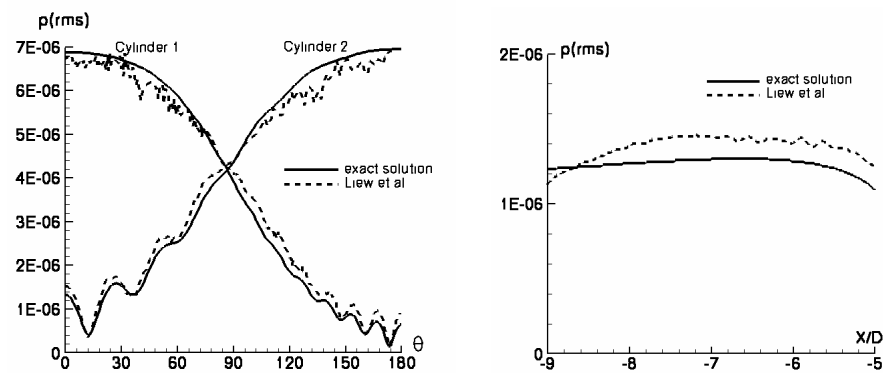
Y-P LIEW, S. BOLURIAAN and P. MORRIS
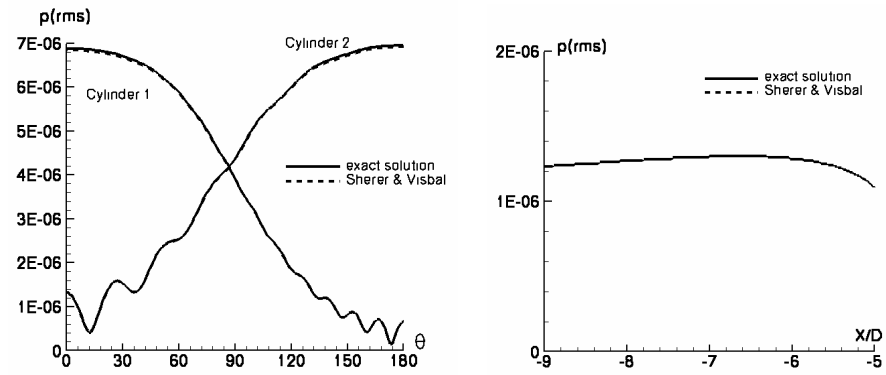
S. SHERER and M. VISBAL
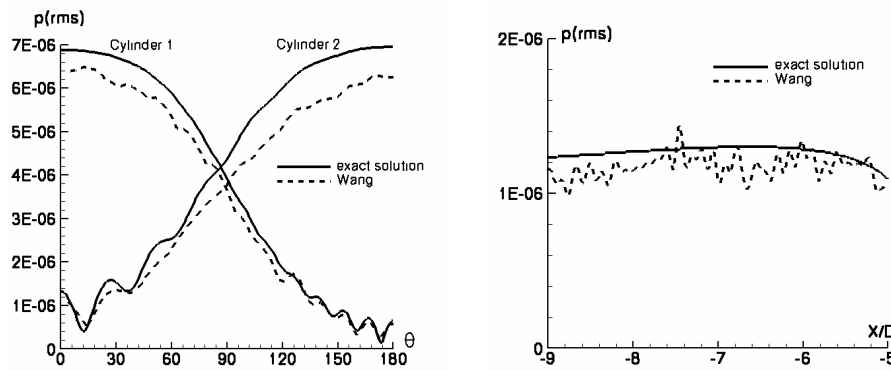
Z.J. WANG

CASE 2 – THREE-CYLINDER SCATTERING PROBLEM
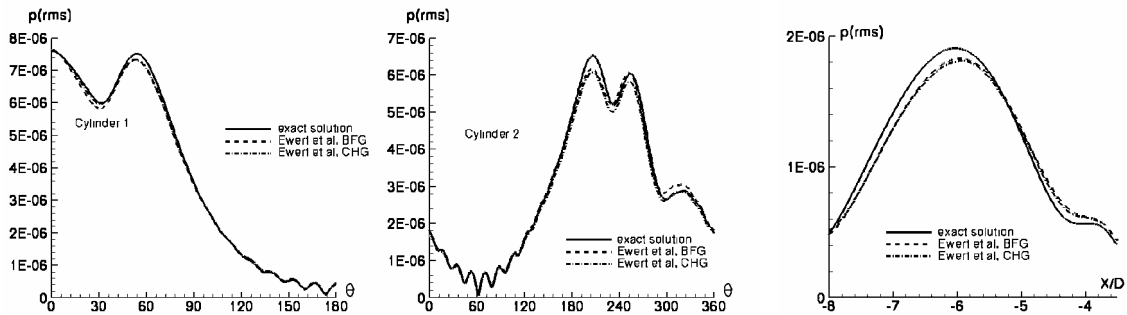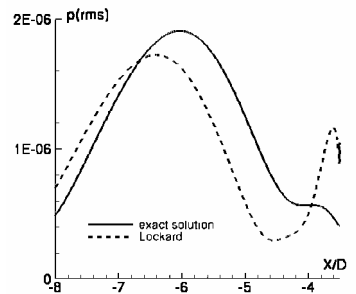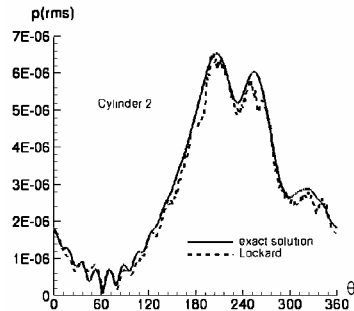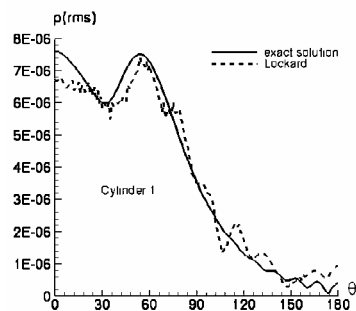
R. EWERT, J. YIN and J. DELFS

D. LOCKARD
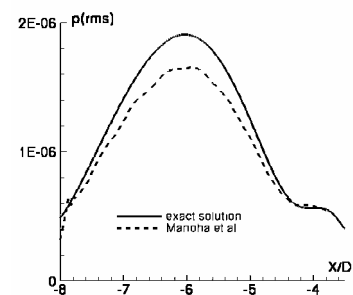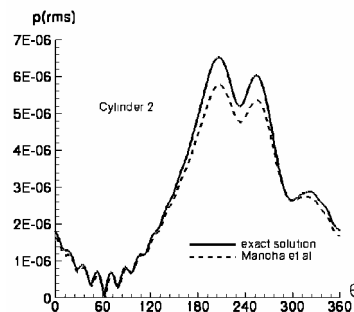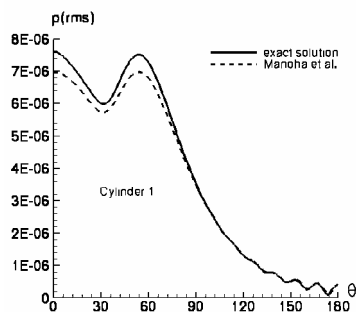
E. MANOHA, S. REDONNET, R. GUENANFF and M. TERRACOL
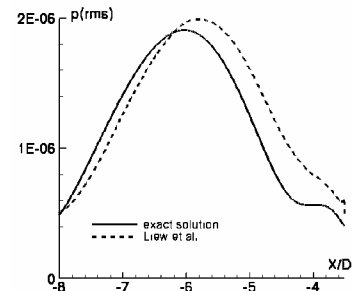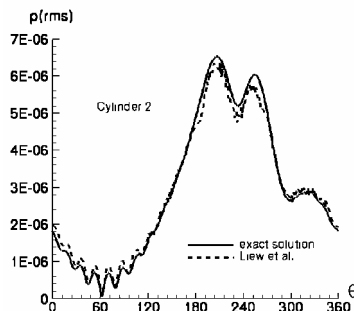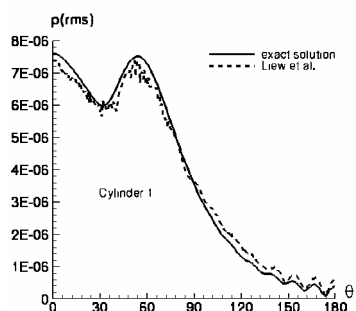
Y-P LIEW, S. BOLURIAAN and P. MORRIS
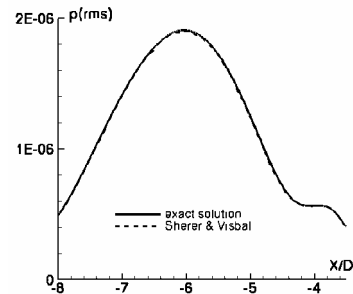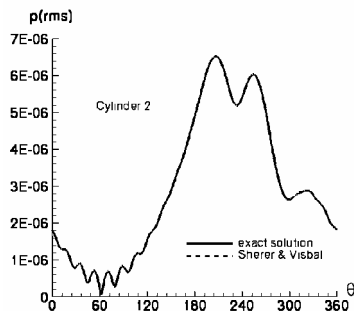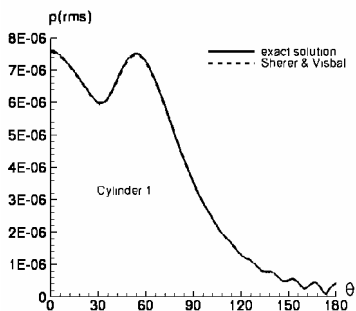
S. SHERER and M. VISBAL

CATEGORY 3, PROBLEM 1

Comparison of solutions - Wang et al

James R. Scott
National Aeronautics and Space Administration
Glenn Research Center
Cleveland, Ohio 44135
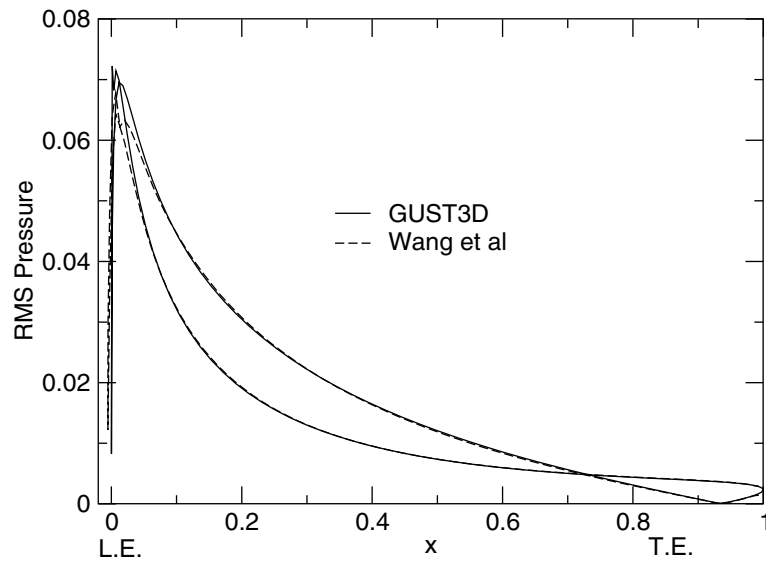
Figure 1   Comparison of RMS pressure on airfoil surface,
Case 1, k1=k2=0.1
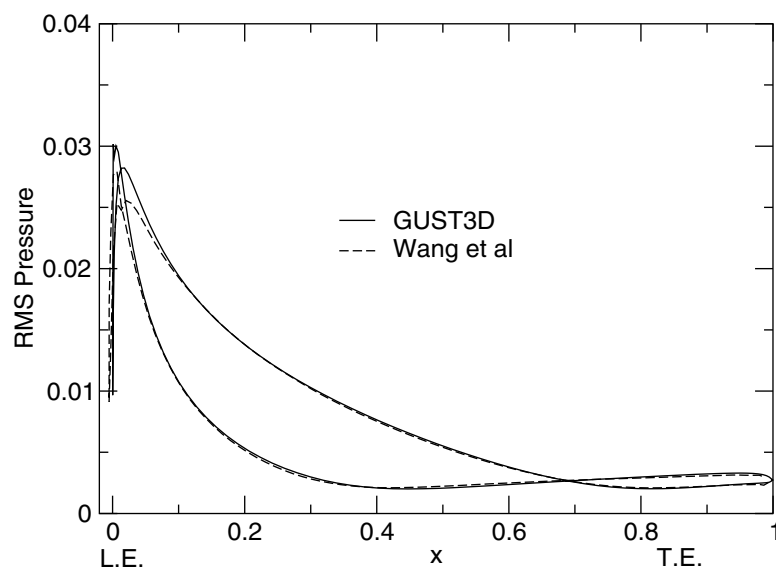
Figure 2   Comparison of RMS pressure on airfoil surface,
Case 1, k1=k2=1.0
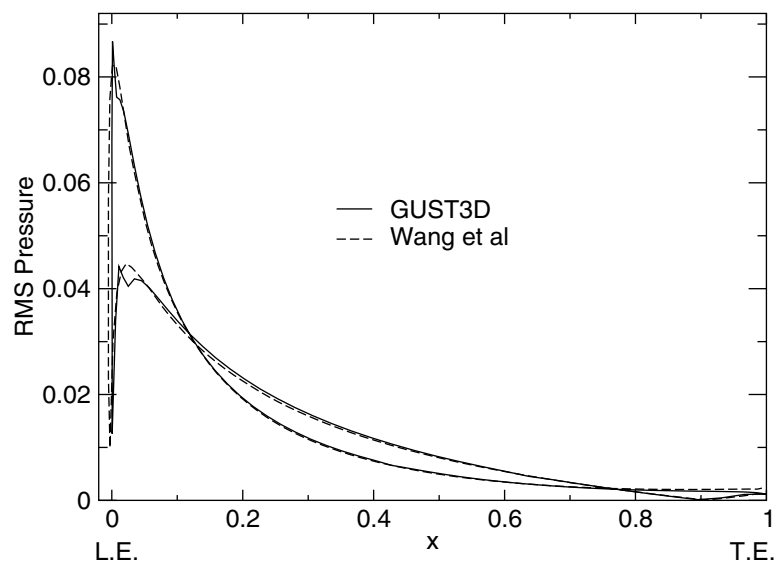
Figure 3   Comparison of RMS pressure on airfoil surface,
Case 2, k1=k2=0.1
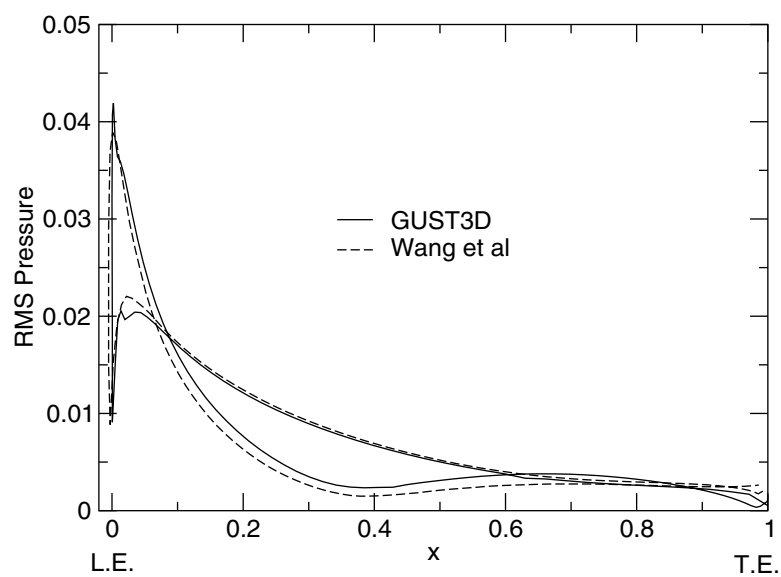
Figure 4   Comparison of RMS pressure on airfoil surface,
Case 2, k1=k2=1.0
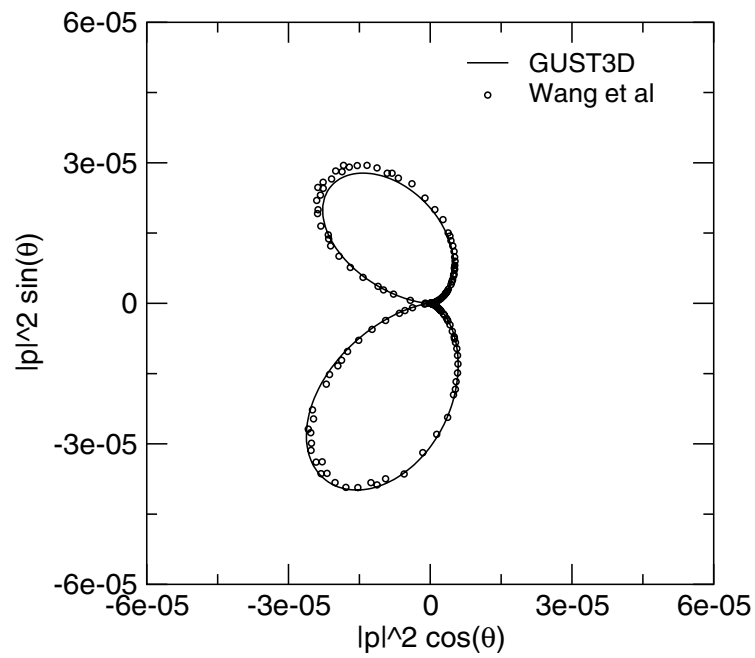
Figure 5.a   Comparison of acoustic intensity on circle R = 1 C,
                    Case 1, k1 = k2 = 0.1.
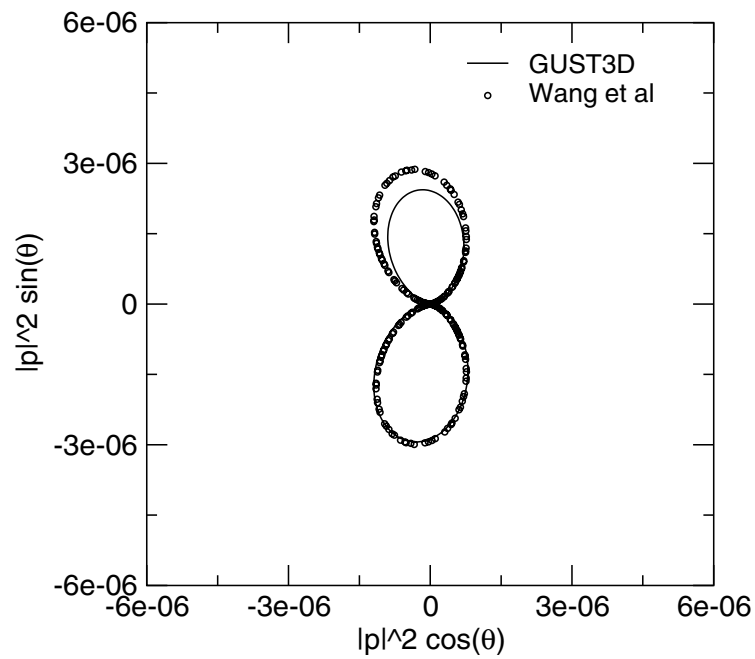
Figure 5.b   Comparison of acoustic intensity on circle R = 4 C,
                    Case 1, k1 = k2 = 0.1.
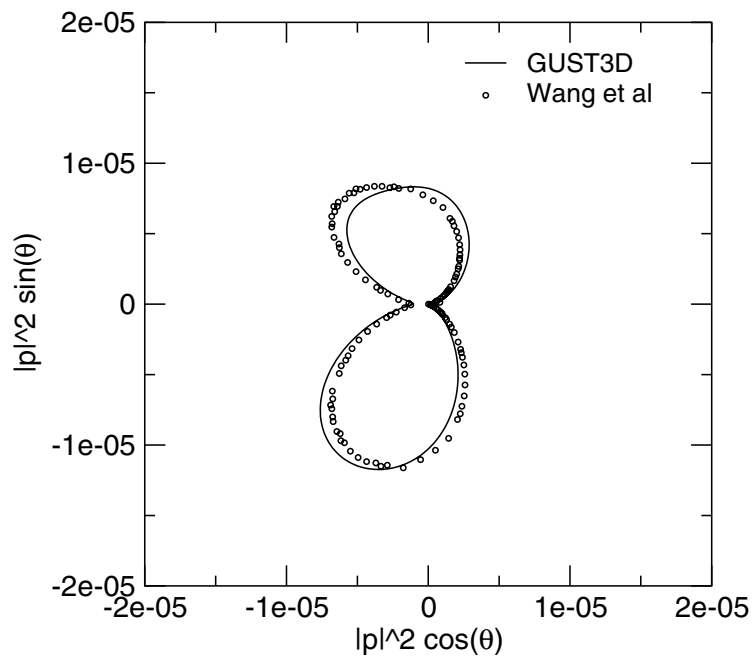
Figure 6.a   Comparison of acoustic intensity on circle R = 1 C,
              Case 1, k1 = k2 = 1.0.
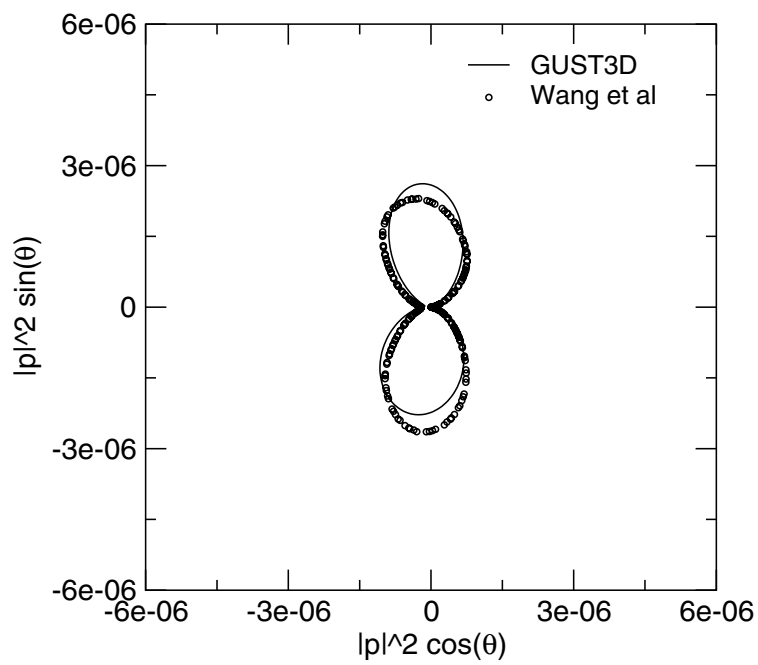
Figure 6.b   Comparison of acoustic intensity on circle R = 4 C,
              Case 1, k1 = k2 = 1.0.
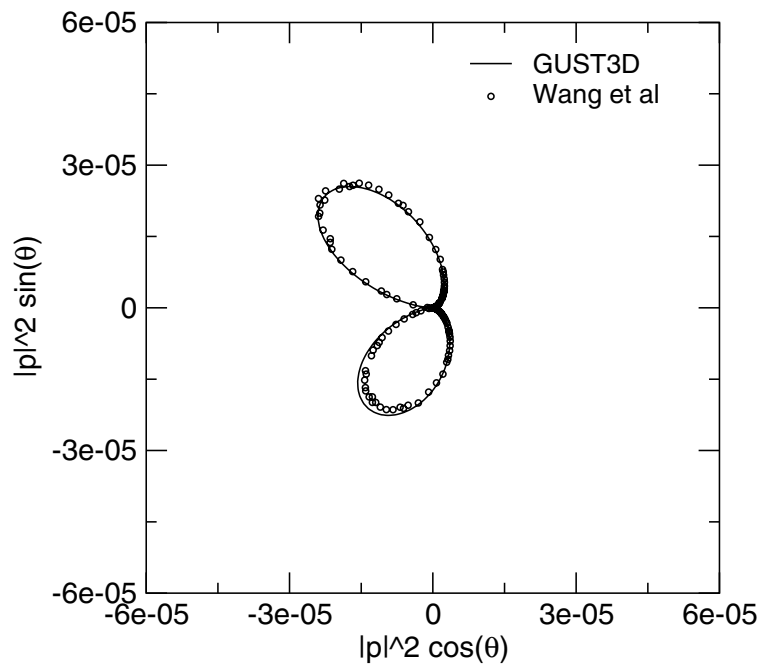
Figure 7.a   Comparison of acoustic intensity on circle R = 1 C,
              Case 2, k1 = k2 = 0.1.
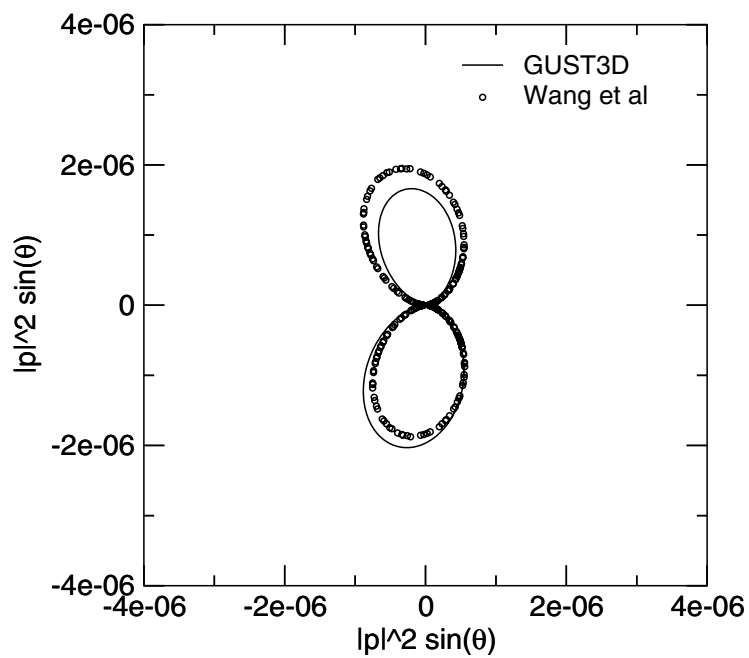
Figure 7.b   Comparison of acoustic intensity on circle R = 4 C,
              Case 2, k1 = k2 = 0.1.
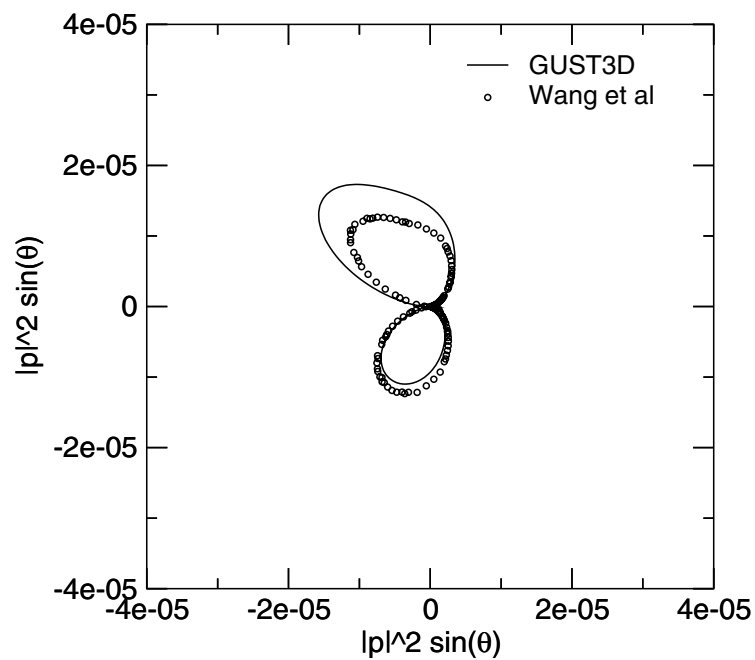
Figure 8.a   Comparison of acoustic intensity on circle R = 1 C,
                Case 2, k1 = k2 = 1.0.

Figure 8.b   Comparison of acoustic intensity on circle R = 4 C,
                Case 2, k1 = k2 = 1.0.

Figure 1   Comparison of RMS pressure on airfoil surface,
Case 1, k1=k2=1.0

Figure 2   Comparison of RMS pressure on airfoil surface,
Case 1, k1=k2=2.0
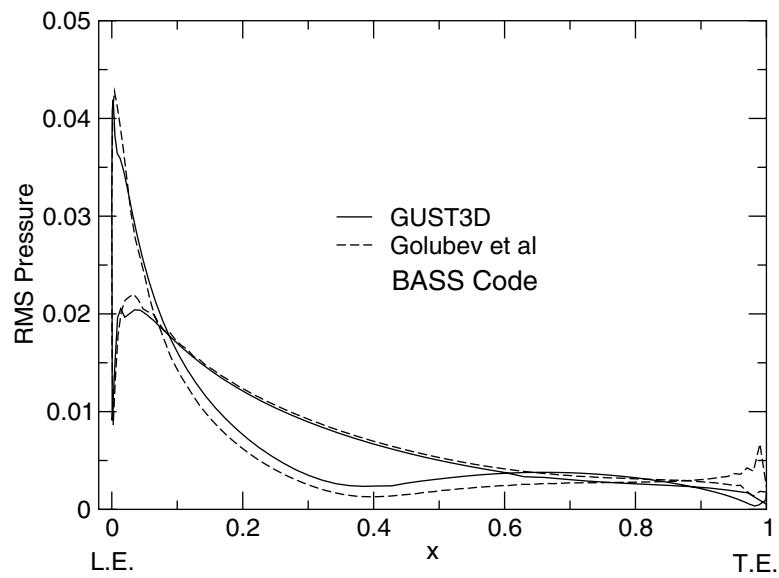
Figure 3   Comparison of RMS pressure on airfoil surface,
Case 2, k1=k2=1.0
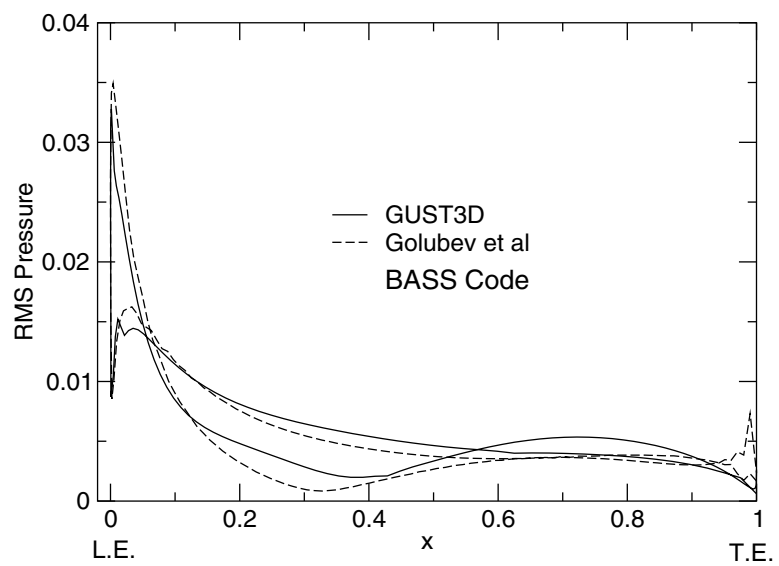
Figure 4   Comparison of RMS pressure on airfoil surface,
Case 2, k1=k2=2.0
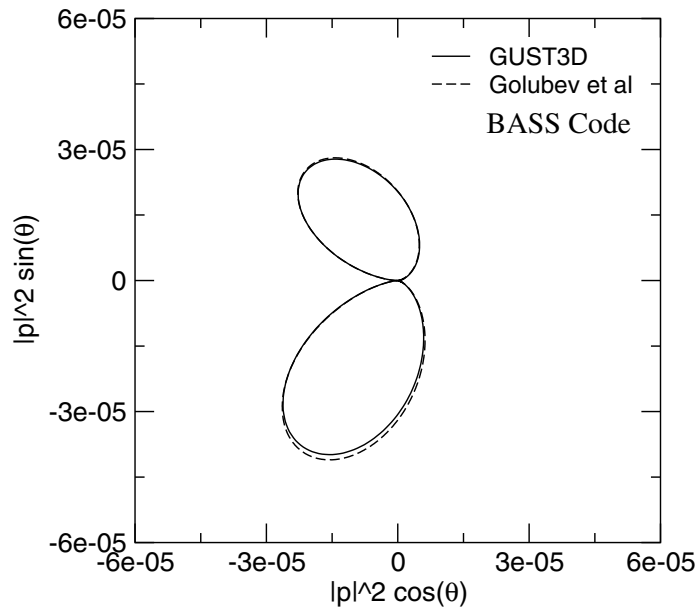
Figure 5.a   Comparison of acoustic intensity on circle R = 1 C,
              Case 1, k1 = k2 = 0.1
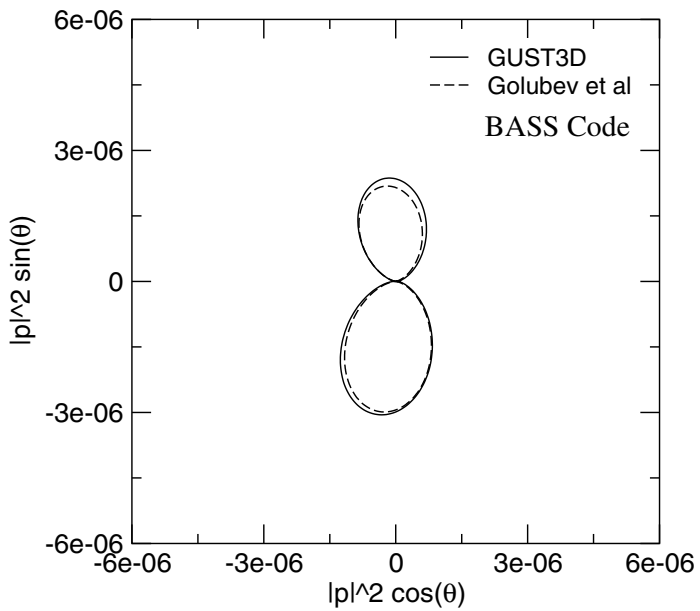
Figure 5.b   Comparison of acoustic intensity on circle R = 4 C,
              Case 1, k1 = k2 = 0.1
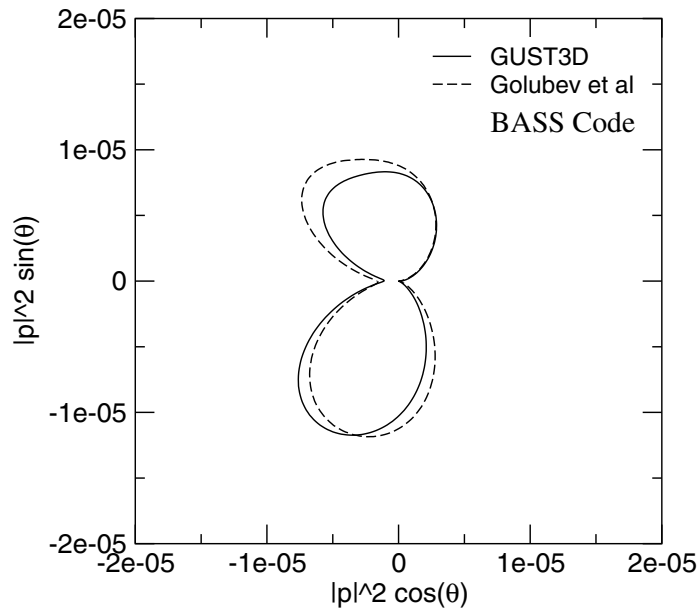
Figure 6.a   Comparison of acoustic intensity on circle R = 1 C,
Case 1, k1 = k2 = 1.0
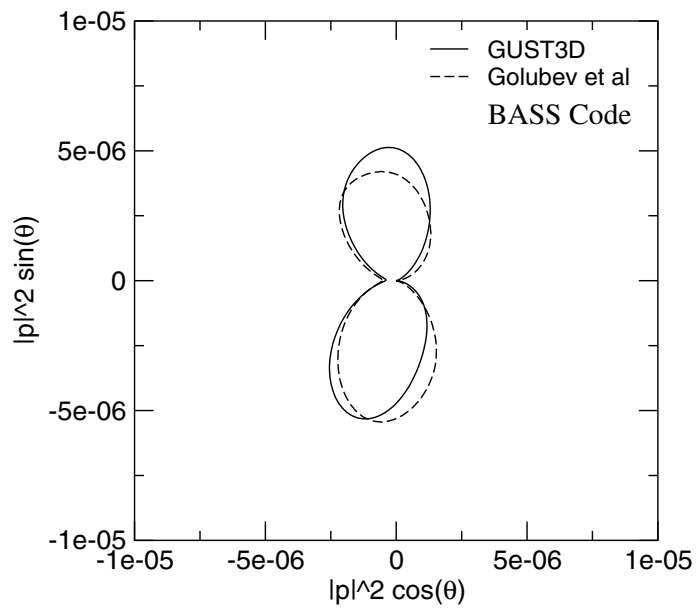
Figure 6.b   Comparison of acoustic intensity on circle R = 2 C,
Case 1, k1 = k2 = 1.0
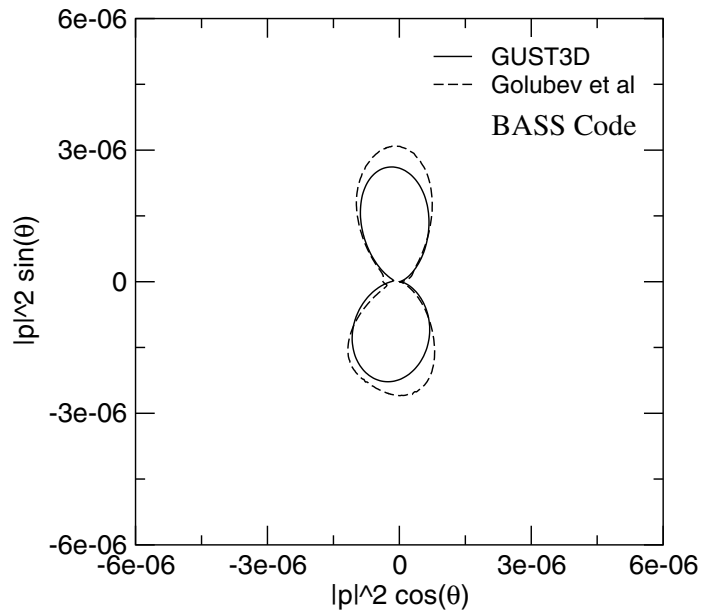
Figure 6.c   Comparison of acoustic intensity on circle R = 4 C,
              Case 1, k1 = k2 = 1.0
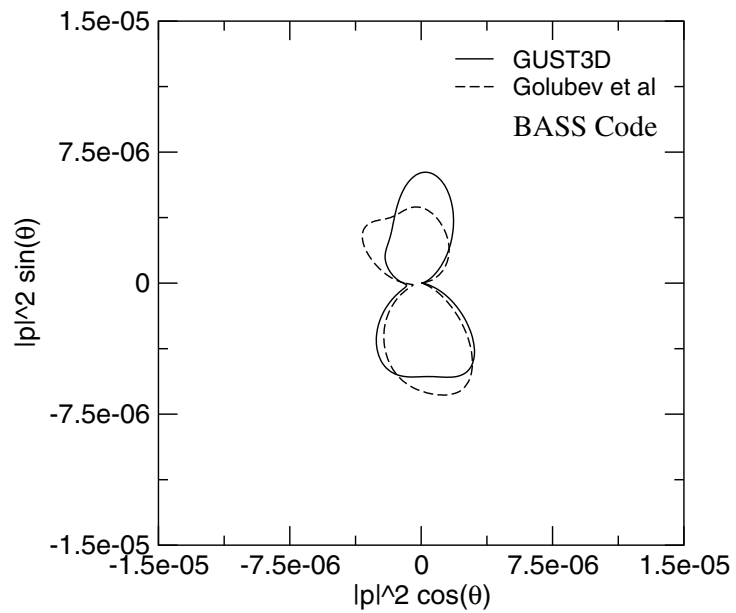
Figure 7.a   Comparison of acoustic intensity on circle R = 1 C,
              Case 1, k1 = k2 = 2.0
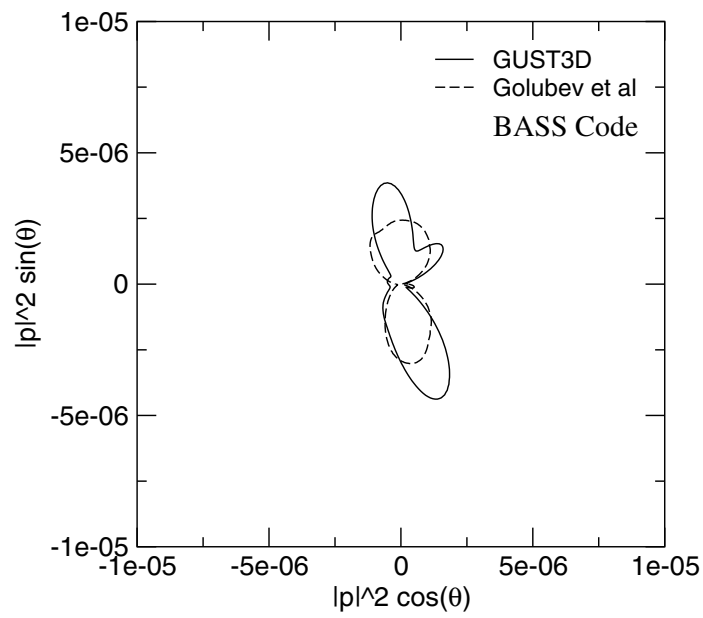
Figure 7.b   Comparison of acoustic intensity on circle R = 2 C,
Case 1, k1 = k2 = 2.0
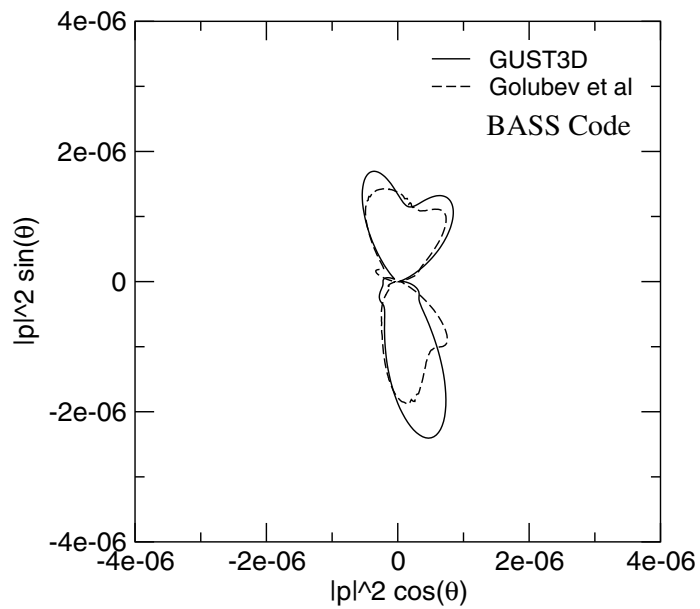
Figure 7.c   Comparison of acoustic intensity on circle R = 4 C,
Case 1, k1 = k2 = 2.0
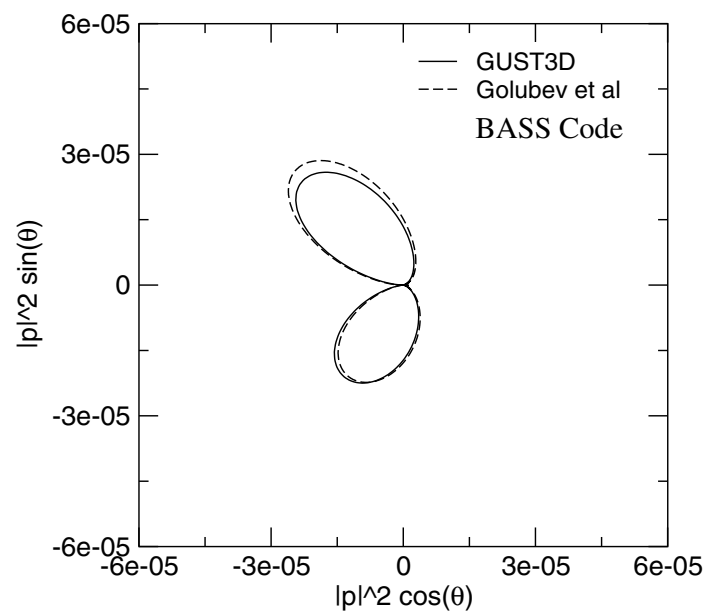
Figure 8.a   Comparison of acoustic intensity on circle R = 1 C,
              Case 2, k1 = k2 = 0.1
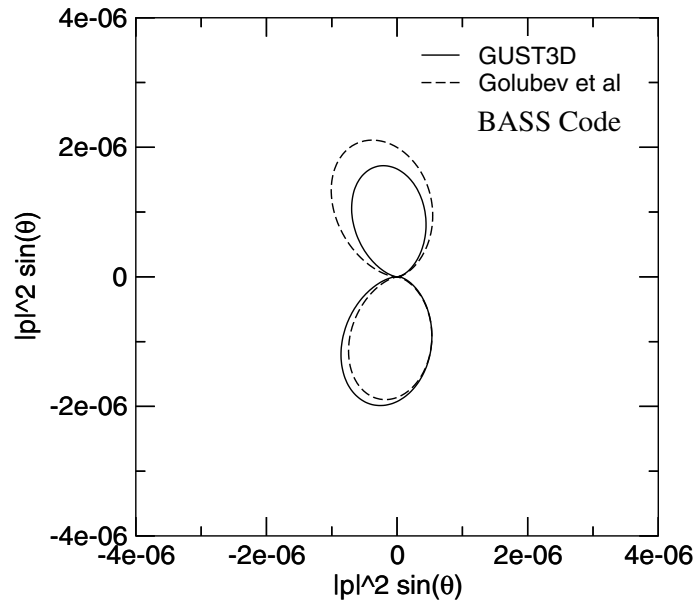
Figure 8.b   Comparison of acoustic intensity on circle R = 4 C,
              Case 2, k1 = k2 = 0.1
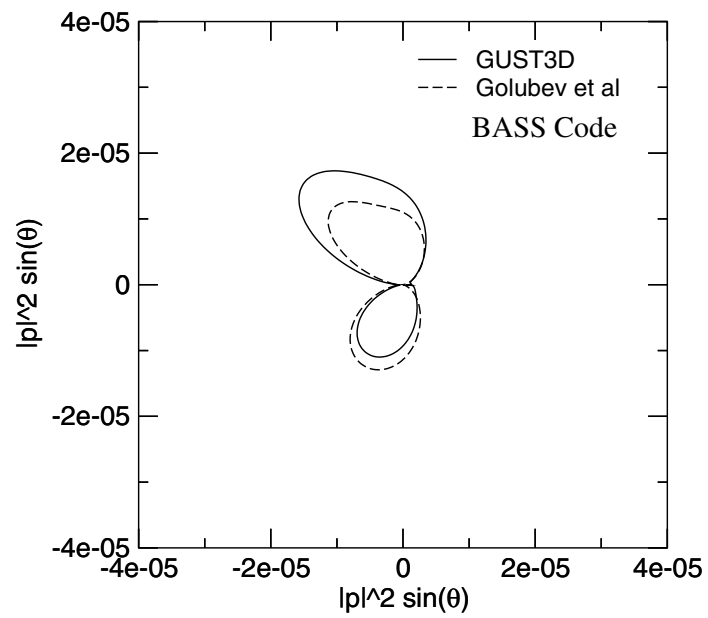
Figure 9.a   Comparison of acoustic intensity on circle R = 1 C,
Case 2, k1 = k2 = 1.0
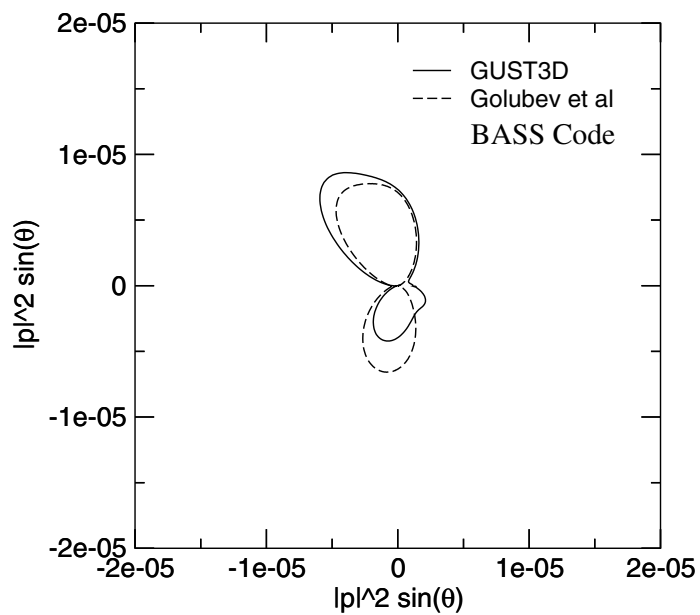
Figure 9.b   Comparison of acoustic intensity on circle R = 2 C,
Case 2, k1 = k2 = 1.0
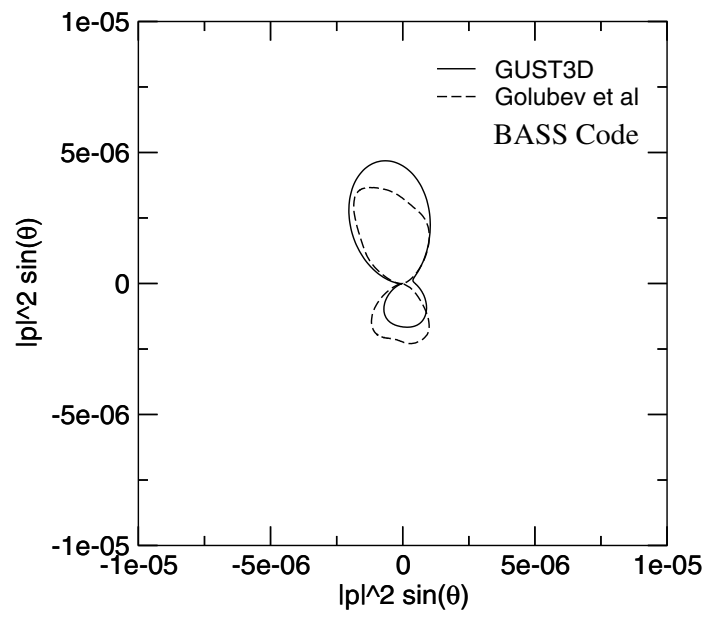
Figure 9.c   Comparison of acoustic intensity on circle R = 4 C,
Case 2, k1 = k2 = 1.0

Figure 1   Comparison of RMS pressure on airfoil surface,
Case 2, k1=k2=0.1

Figure 2   Comparison of RMS pressure on airfoil surface,
Case 2, k1=k2=1.0

Figure 3.a   Comparison of acoustic intensity on circle R = 1 C,
Case 2, k1 = k2 = 0.1
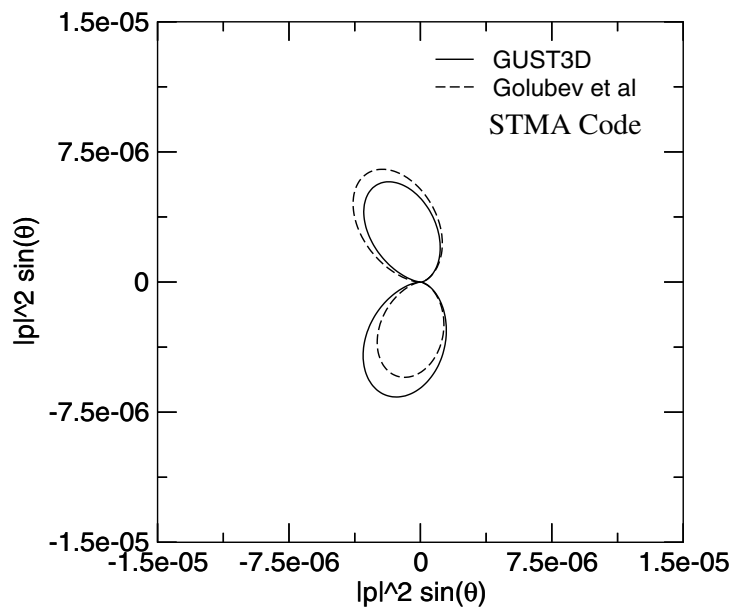
Figure 3.b   Comparison of acoustic intensity on circle R = 2 C,
Case 2, k1 = k2 = 0.1
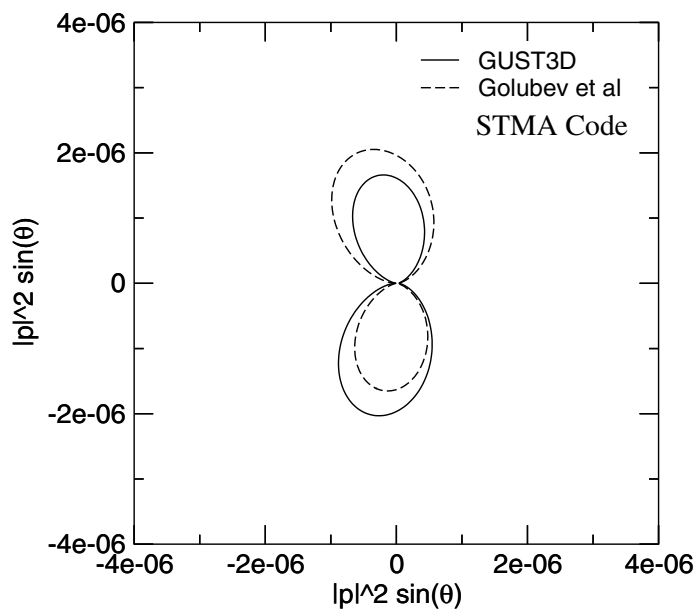
Figure 3.c   Comparison of acoustic intensity on circle R = 4 C,
            Case 2, k1 = k2 = 0.1.
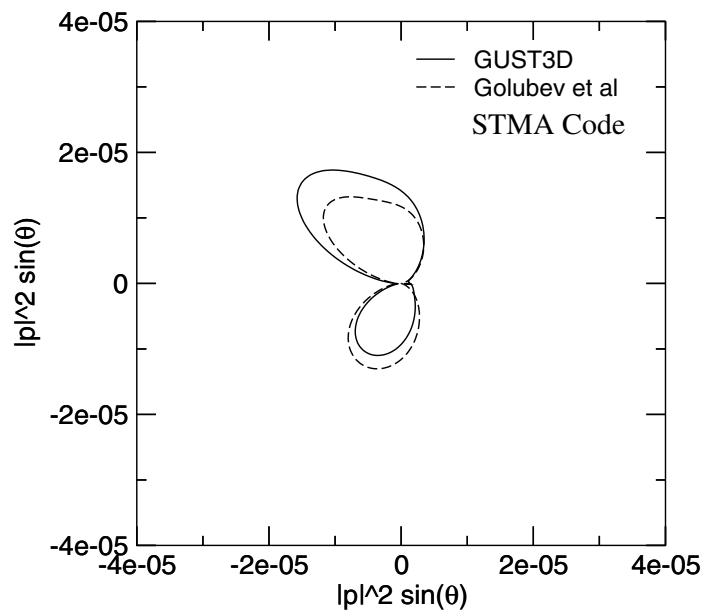
Figure 4.a   Comparison of acoustic intensity on circle R = 1 C,
            Case 2, k1 = k2 = 1.0
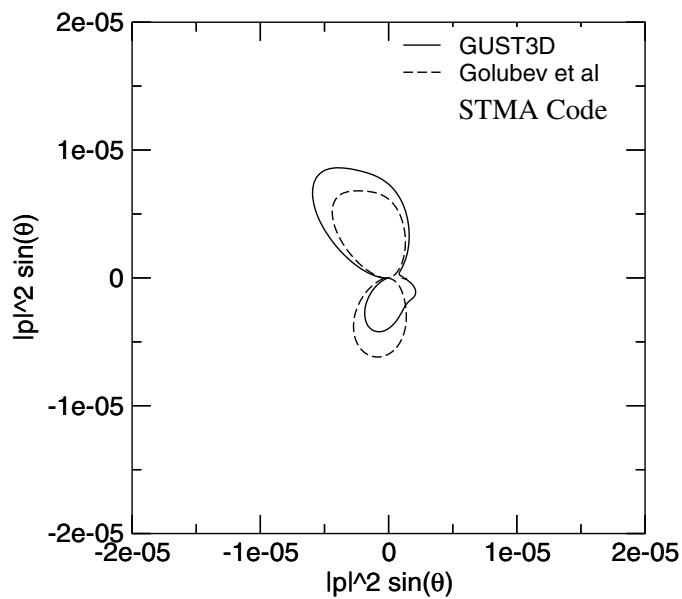
Figure 4.b   Comparison of acoustic intensity on circle R = 2 C,
Case 2, k1 = k2 = 1.0
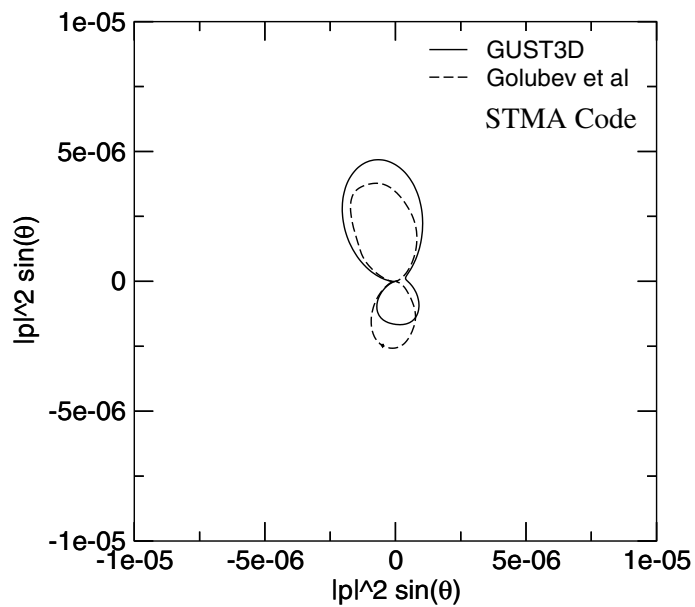
Figure 4.c   Comparison of acoustic intensity on circle R = 4 C,
Case 2, k1 = k2 = 1.0

COMPARISONS OF THE SOLUTIONS FOR
THE CATEGORY 3—PROBLEM 2: CASCADE–GUST INTERACTION

Edmane Envia
National Aeronautics and Space Administration
Glenn Research Center
Cleveland, Ohio 44135

Six different solutions were submitted for this benchmark problem. These were obtained using a variety of methods that can be conveniently categorized in two main groups, a nonlinear time-domain group and a linearized frequency-domain group. The first includes solutions submitted by (1) Hixon, (2) Nallasamy et. al, (3) Shieh et. al, and (4) Wang et. al, and the second includes solutions submitted by (5) Coupland and (6) Serrano et. al. Methods (1) and (2) use sixth order compact differencing schemes and the rest are essentially second order in space. With the exception of the solution submitted by Shieh et. al, all are individually discussed in great detail in the workshop proceedings. Comparisons of the submitted solutions with the benchmark solution are presented below. Due to differences in the level of solution detail provided to the author by the participants, the comparisons do not always include results from all submissions.

It should be noted at the outset that, since the benchmark solution itself was numerically computed, the comparisons are somewhat subjective. In order to provide maximum latitude for the participants of the workshop, no restrictions were placed on the type of method that could be used to solve the problem. Neither was there were any stipulations to use a particular grid topology or grid density. Therefore, without a detailed study of the critical features of the computed solutions, it is not possible to make concrete statements about the relative merits of one method over another. Such a study is beyond the scope of the current exercise, especially since complete flowfield details were not provided to the author by all participants. Instead a package, containing the information about the benchmark solution (both the steady and unsteady parts of it), is included on the proceedings' CD should the authors who submitted solutions for this problem wish to examine in detail the benchmark solution and compare their results to it.

The computed sound pressure levels (SPL) on the vane surface are presented in Figures 1 through 6. While there is some variation in the results, the agreement for the first two harmonic levels is quite good. The computed levels for the third harmonic show larger scatter probably as a result of differences in grid resolution among other factors. Another general observation is that the levels computed by the two high-order codes tend to be slightly higher than the ones calculated by the second order codes.

Figures 7 thought 12 summarize the comparisons at the inflow and outflow planes. Here the agreement is not as good as that for the vane surface pressure results. The discrepancy may be related to the different implementations of the non-reflecting boundary conditions in these codes. Also, the perturbation levels at the inflow and outflow boundaries are at least one order of magnitude smaller the vane surface pressures making them more difficult to capture accurately. Here once again, the two high-order codes predict somewhat higher pressure levels.

In Figure 13, a comparison is shown between the computed results at $x = 0.00$ for frequency 2ω. This is a repeat of some of earlier results but is presented to accommodate the solution by submitted by Shieh et. al who had supplied only a limited set of results and, as a result, could not be included in the previous Figures.

Finally, the acoustic mode levels at the each of the three frequencies are shown at the inflow and outflow planes in Figures 14 through 16. All submitted solutions show the same mix of modes, but the there are noticeable differences in the associated levels. Obviously these differences are related to those observed in Figures 7 through 12. Taken together these results suggest that the acoustic pressure levels on the vane are better captured than the radiated field. Among possible reasons for the discrepancies in the radiated levels are difference in the way different schemes handle the propagation of disturbances, and, of course, differences in the implementation of the non-reflecting boundary conditions.

It should be noted that this was the first attempt at solving a non-trivial cascade response problem for realistic frequencies of engineering interest. As a result, the comparisons should be viewed as encouraging in spite the differences, and the results of this study should serve as a stimulus to further investigate the similarity and differences between the various methods.
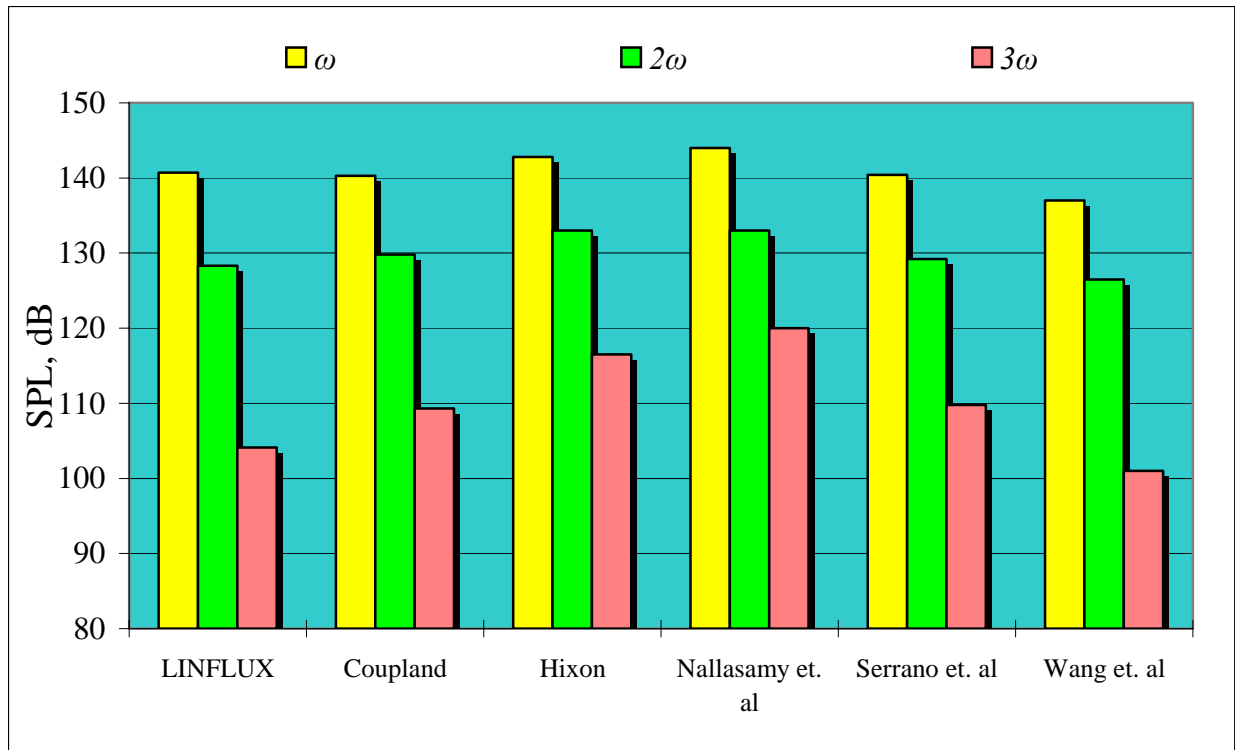
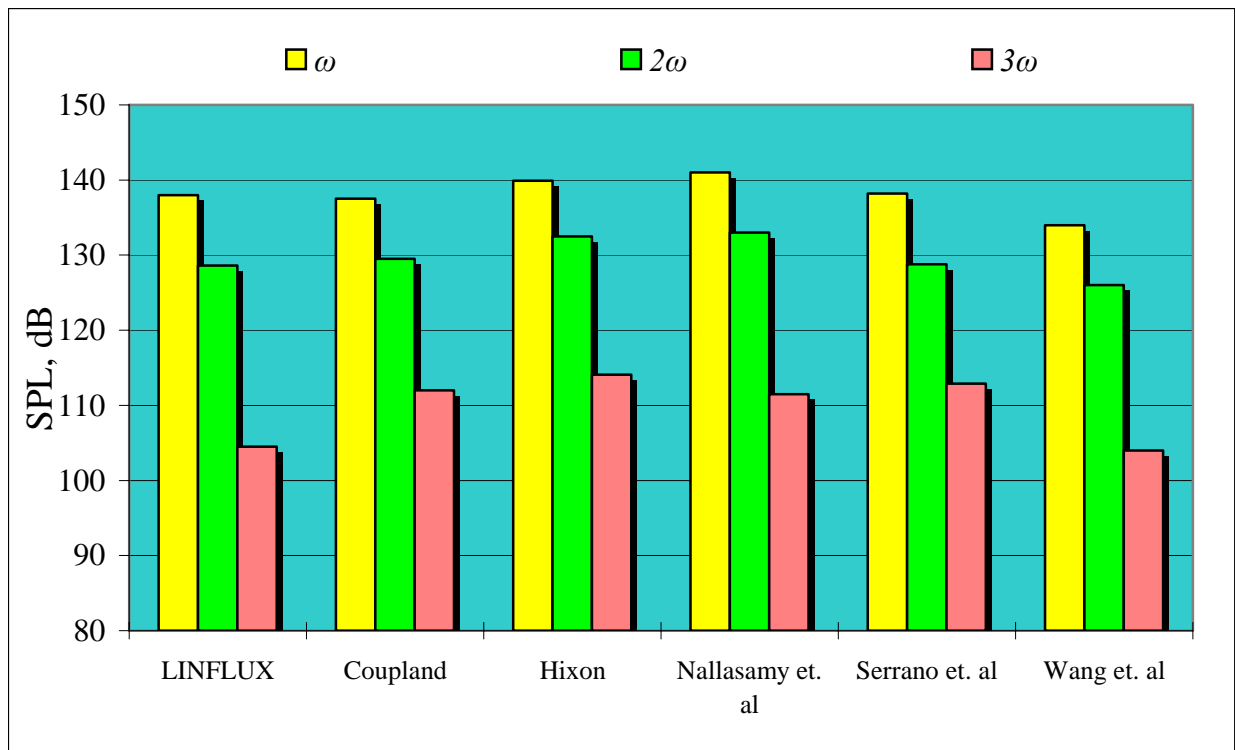**Figure 1. Comparison of computed sound pressure levels on the suction side of the vane at x/c = -0.25.**

Figure 2. Comparison of computed sound pressure levels on the pressure side of the vane at x/c = -0.25.
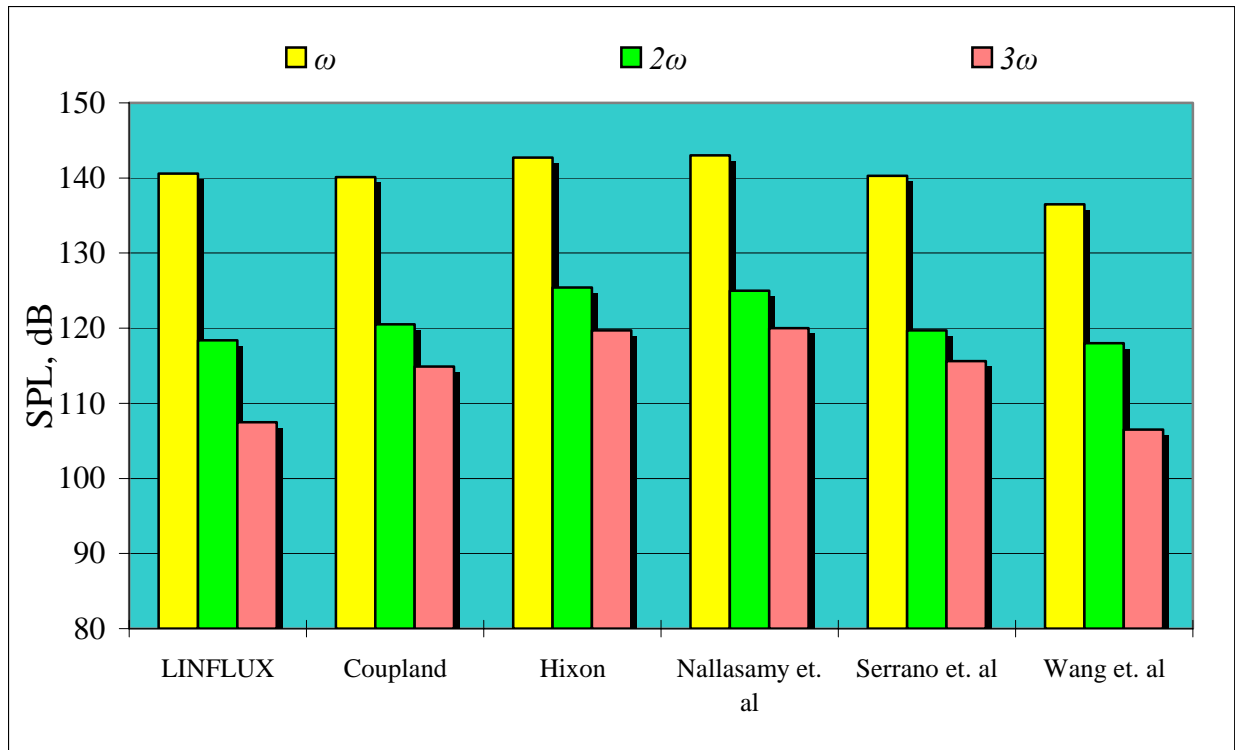
Figure 3. Comparison of computed sound pressure levels on the suction side of the vane at *x*/*c* = 0.00.
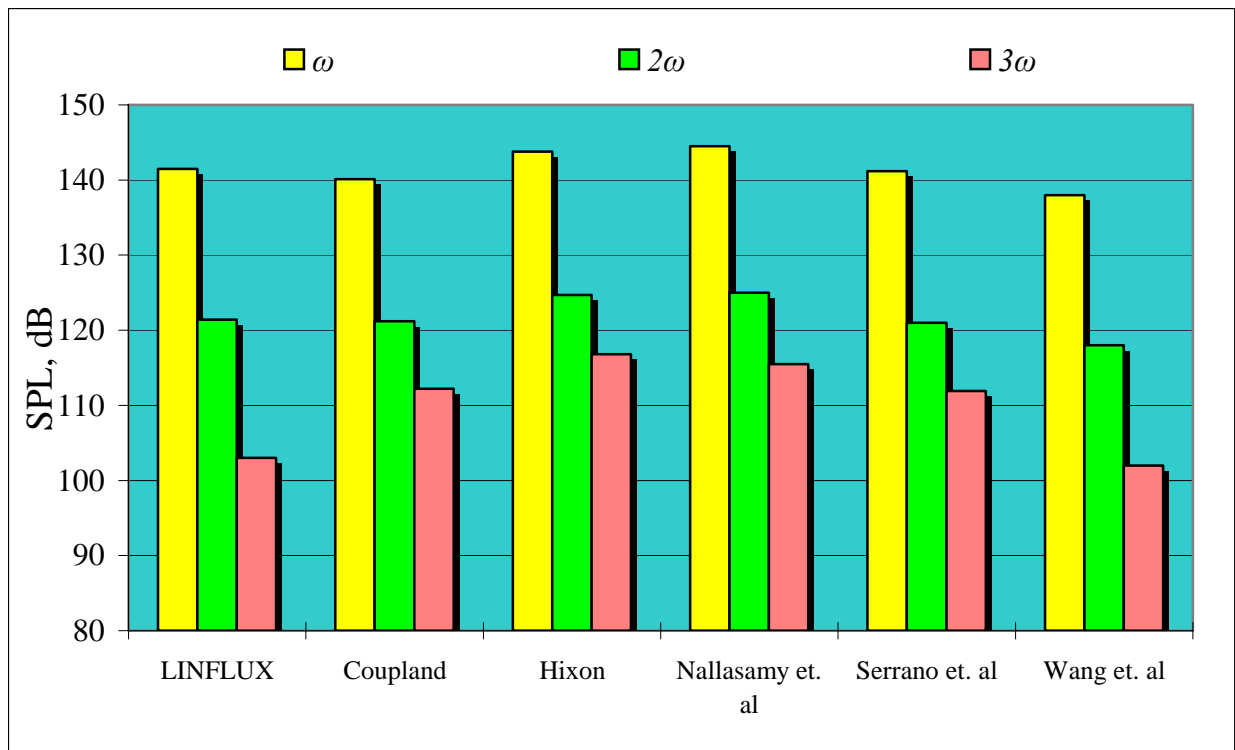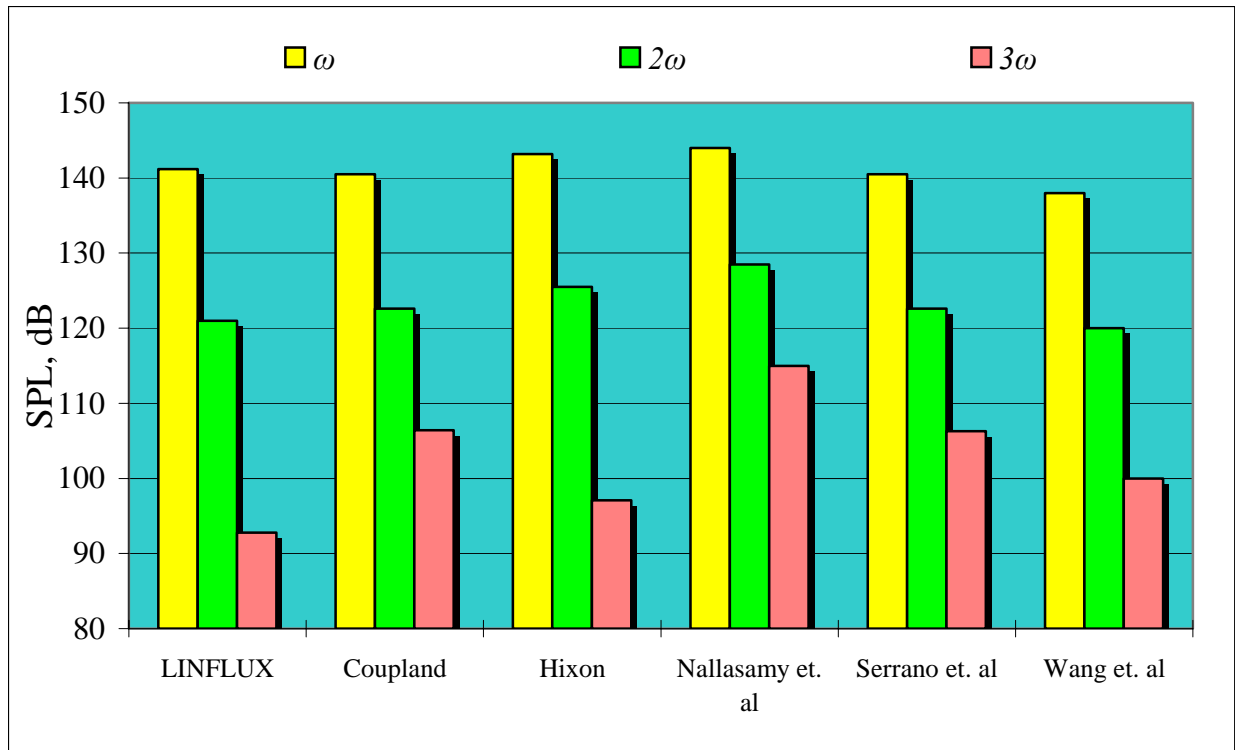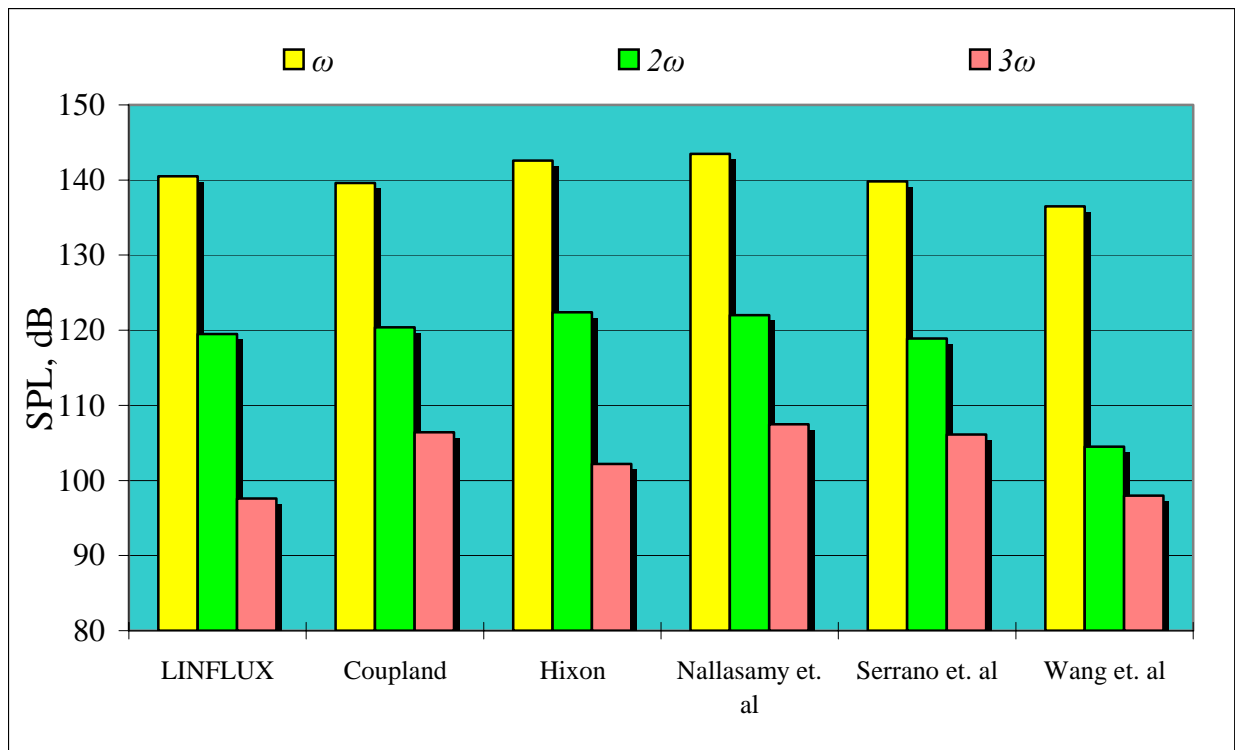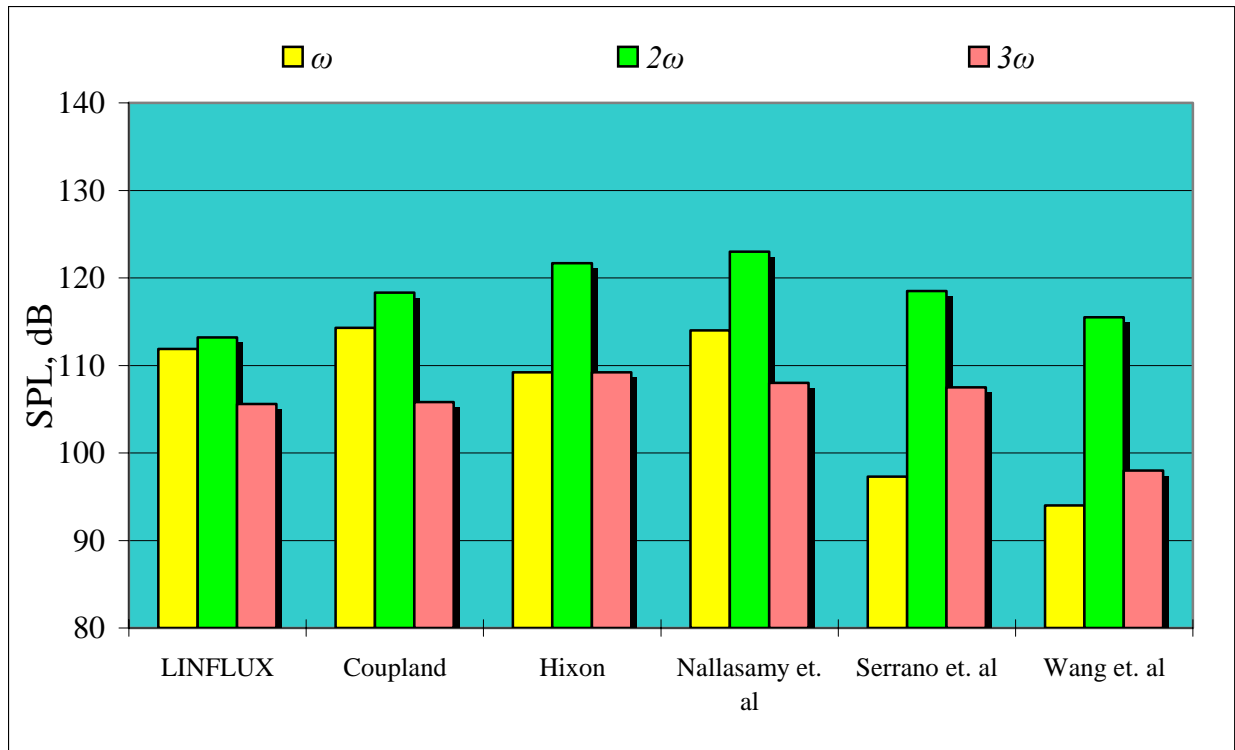

Figure 4. Comparison of computed sound pressure levels on the pressure side of the vane at *x*/*c* = 0.00.

Figure 5. Comparison of computed sound pressure levels on the suction side of the vane at $x/c = +0.25$.

Figure 6. Comparison of computed sound pressure levels on the pressure side of the vane at $x/c = +0.25$.

Figure 7. Comparison of computed sound pressure levels at the inflow plane at y/*c* = -0.3.
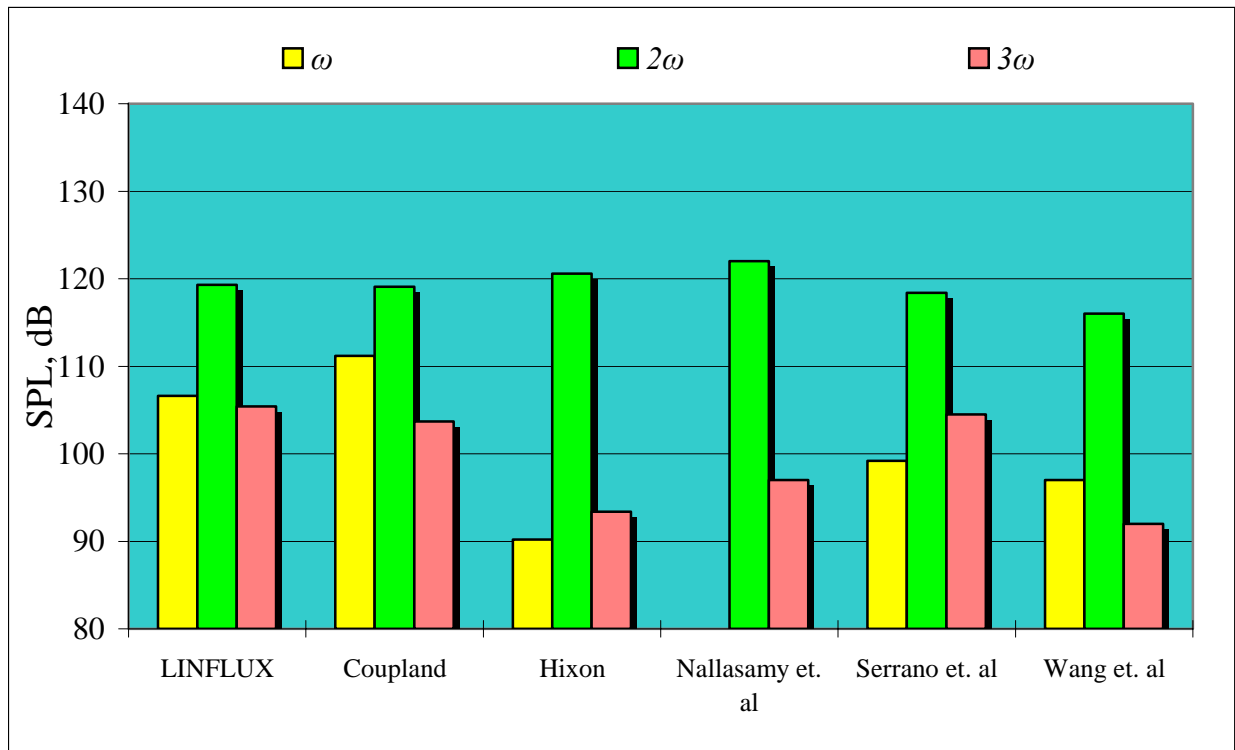
Figure 8. Comparison of computed sound pressure levels at the inflow plane at y/*c* = 0.0.
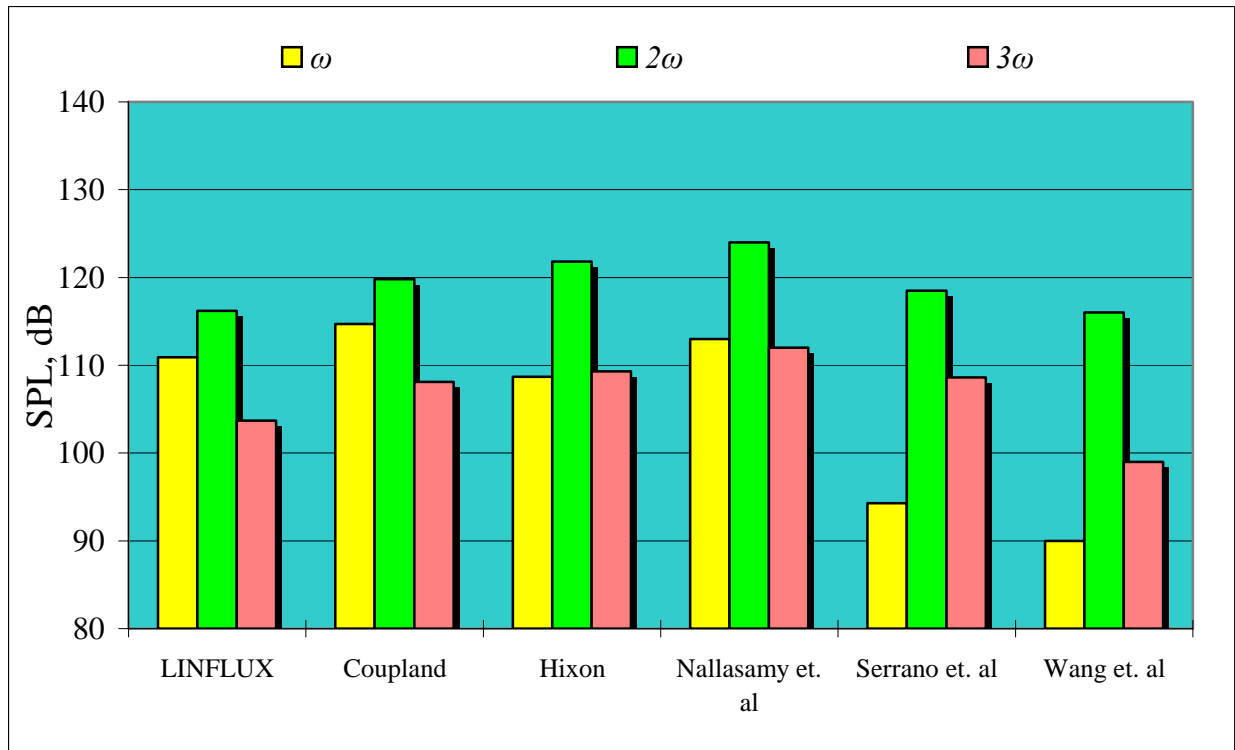
Figure 9. Comparison of computed sound pressure levels at the inflow plane at y/*c* = +0.3.
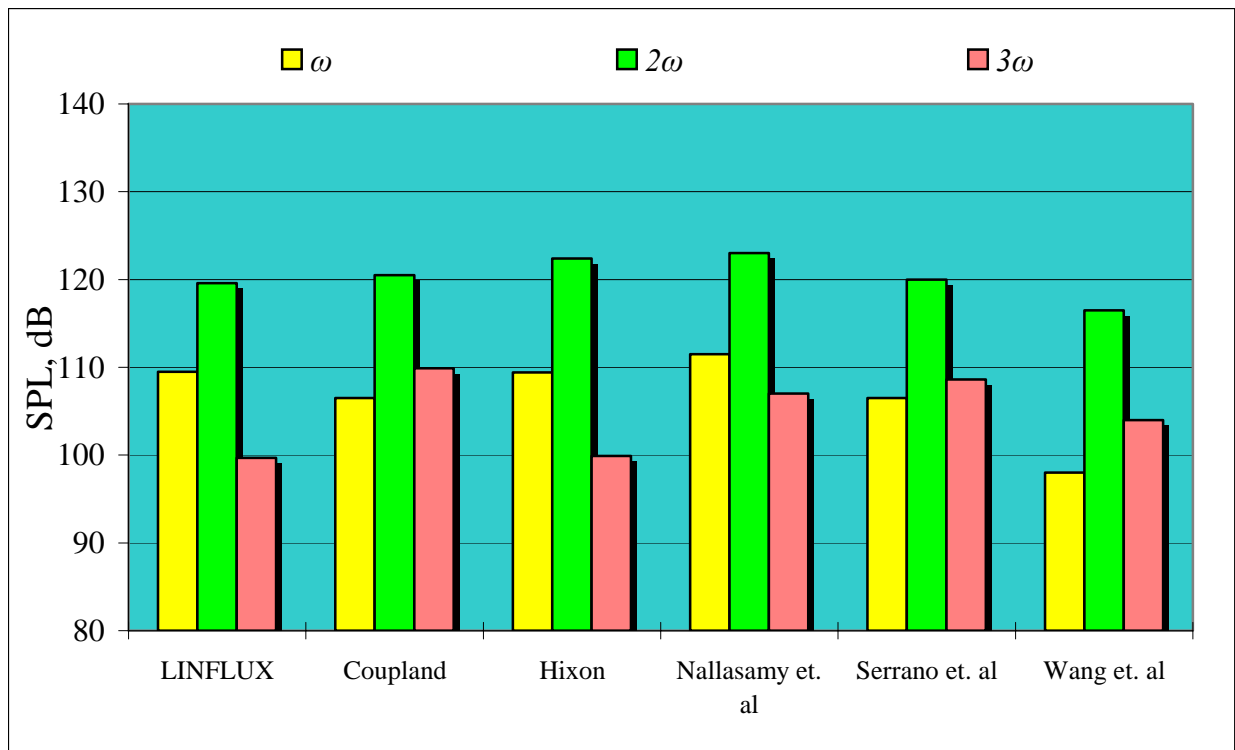
Figure 10. Comparison of computed sound pressure levels at the outflow plane at y/*c* = -0.3.
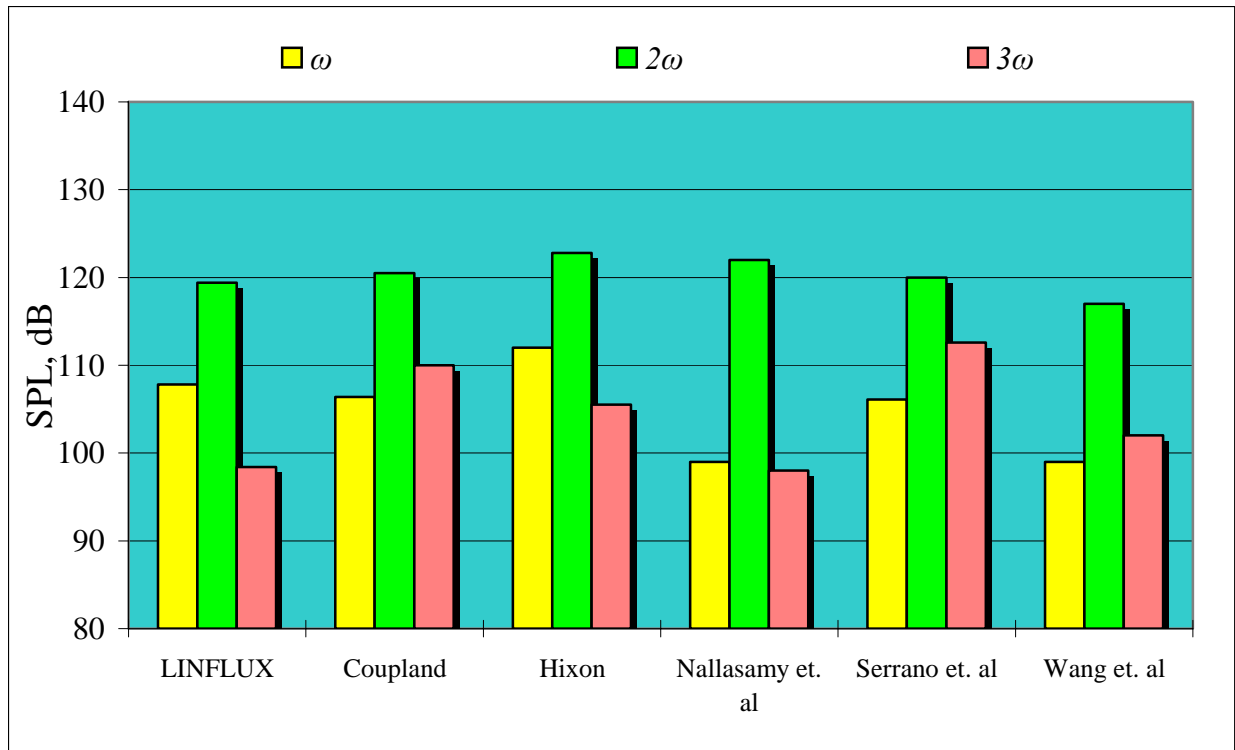
Figure 11. Comparison of computed sound pressure levels at the outflow plane at y/*c* = 0.0.
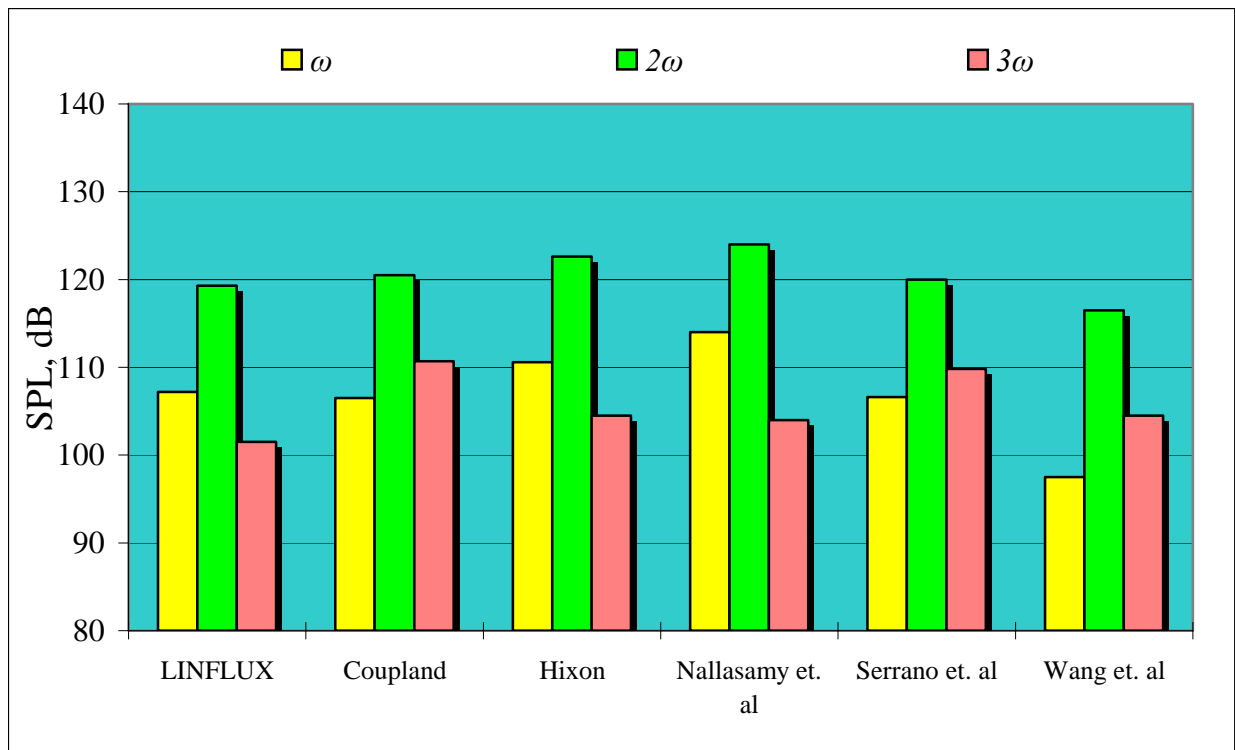
Figure 12. Comparison of computed sound pressure levels at the outflow plane at y/*c* = +0.3.
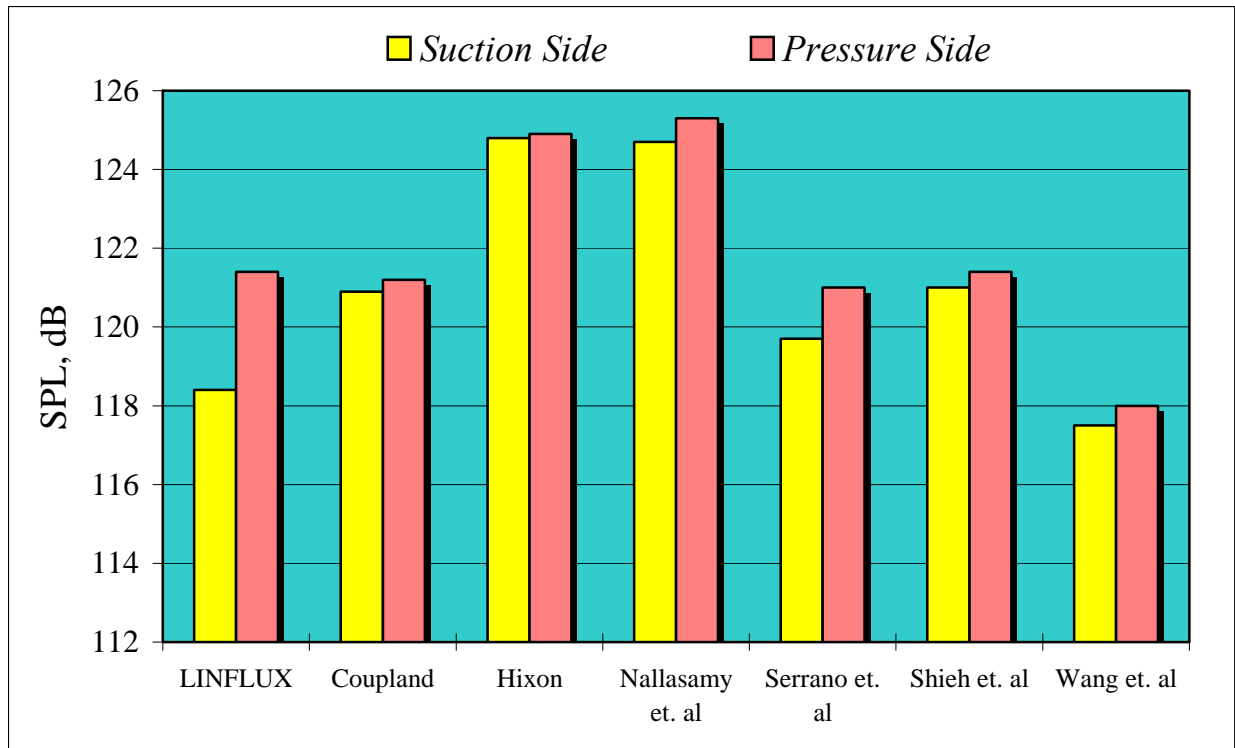
Figure 13. Comparison of computed sound pressure levels on the vane surface at $x/c = 0$ for frequency 2ω. (This chart includes results from Shieh et. al submission.)
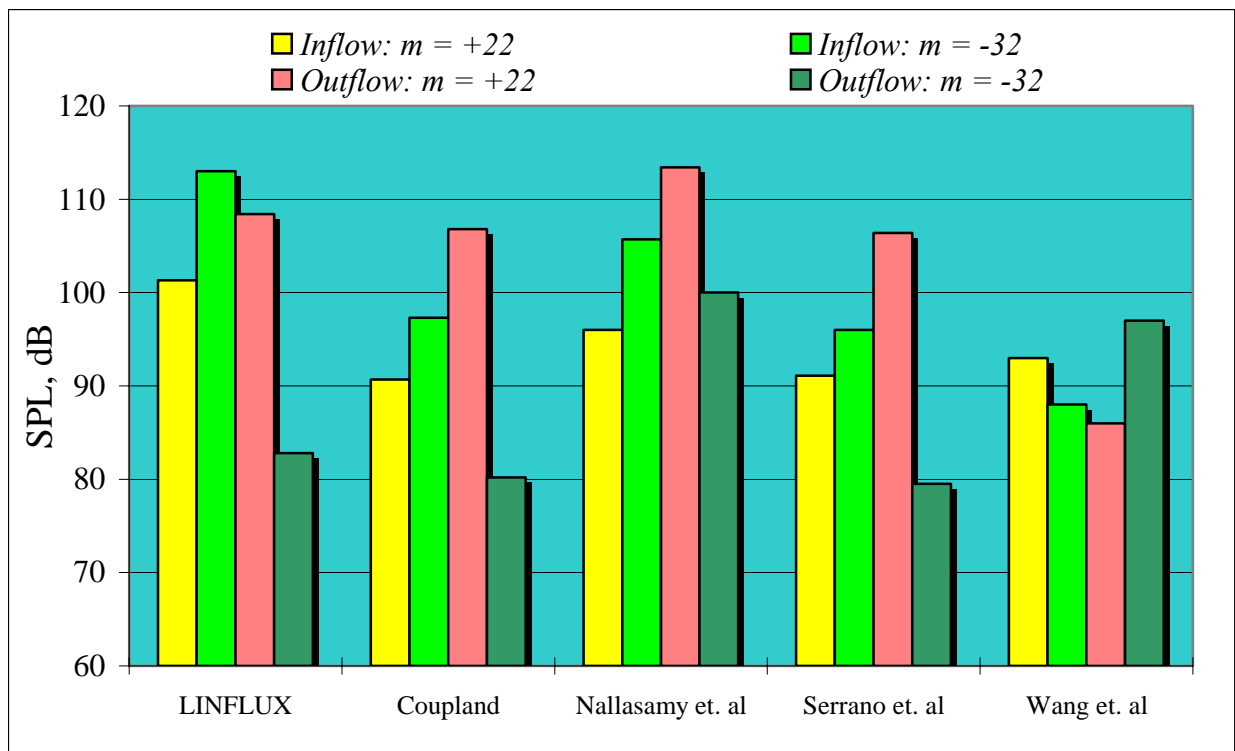
Figure 14. Comparison of computed sound pressure levels at the inflow and outflow planes at frequency ω.
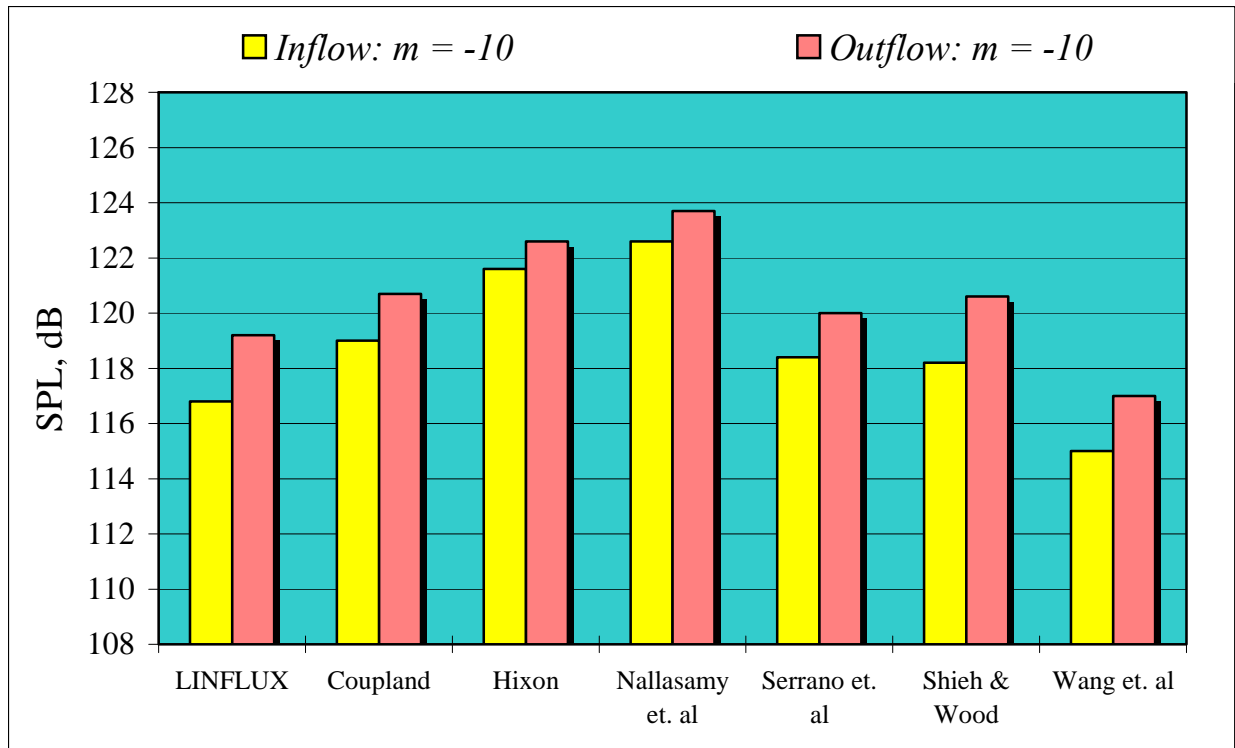
Figure 15. Comparison of computed sound pressure level at the inflow and outflow planes at frequency 2ω.
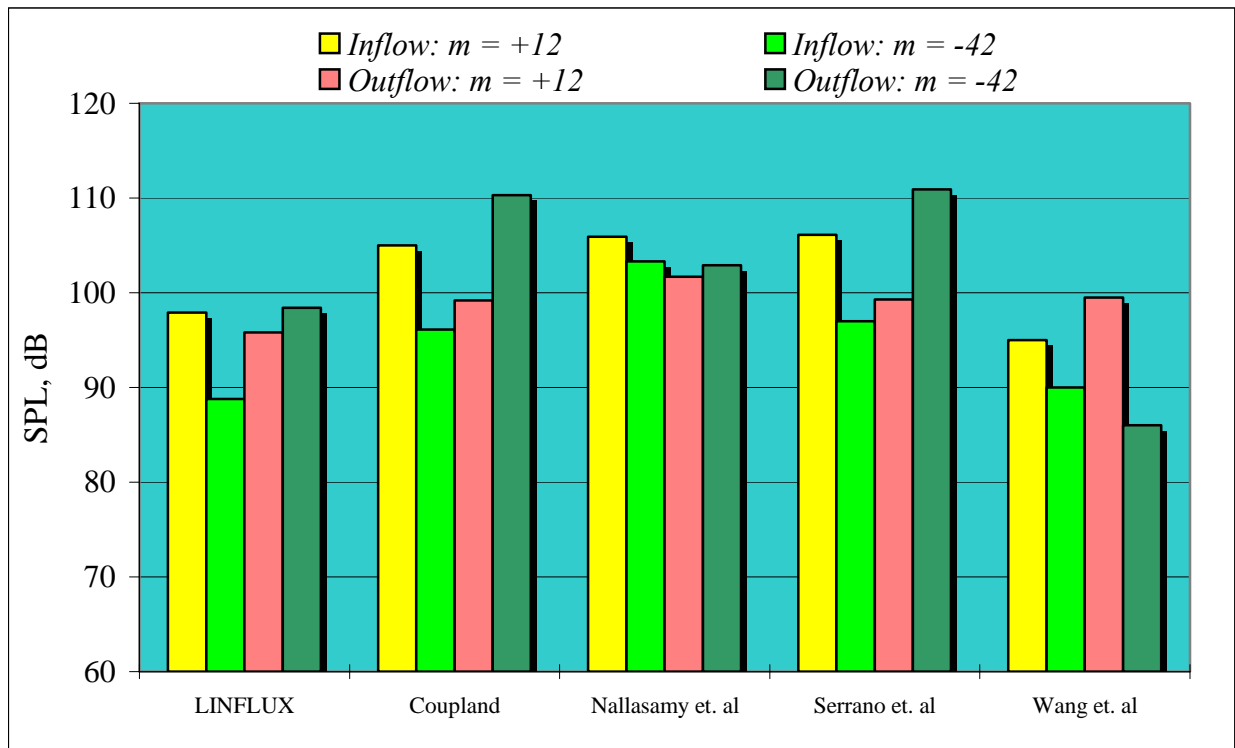
Figure 16. Comparison of computed sound pressure level at the inflow and outflow planes at frequency 3ω.

COMPARISONS: CATEGORY 4

Philip J. Morris and Anurag Agarwal
Department of Aerospace Engineering
The Pennsylvania State University
University Park, PA 16802, USA

COMPARISONS

Table 1 lists the computational resources used in the various submitted numerical solutions. In the following figures, the numerical solutions are compared with the analytical solution along three different lines: $y = 15$ (Fig. (1)), $y = 50$ (Fig. (2)), $x = 100$ (Fig. (3)).

	Hardware	CPU time	Grid Size	Memory	Scheme
Agarwal and Morris	Intel 1.5 GHz	57 min	440 x 300	2.6 GB	Frequency domain
Berland et al.	NEC SX-5	4.2 min	601×301	112 MB	Time domain
Li et al.	Intel 2.4 GHz	6.8 hours	521×124	34 MB	Time domain
Zheng et al.	Athlon 1.5 GHz	15 hours	400×75	10 MB	Time domain

Table 1: Numerical schemes and system requirements
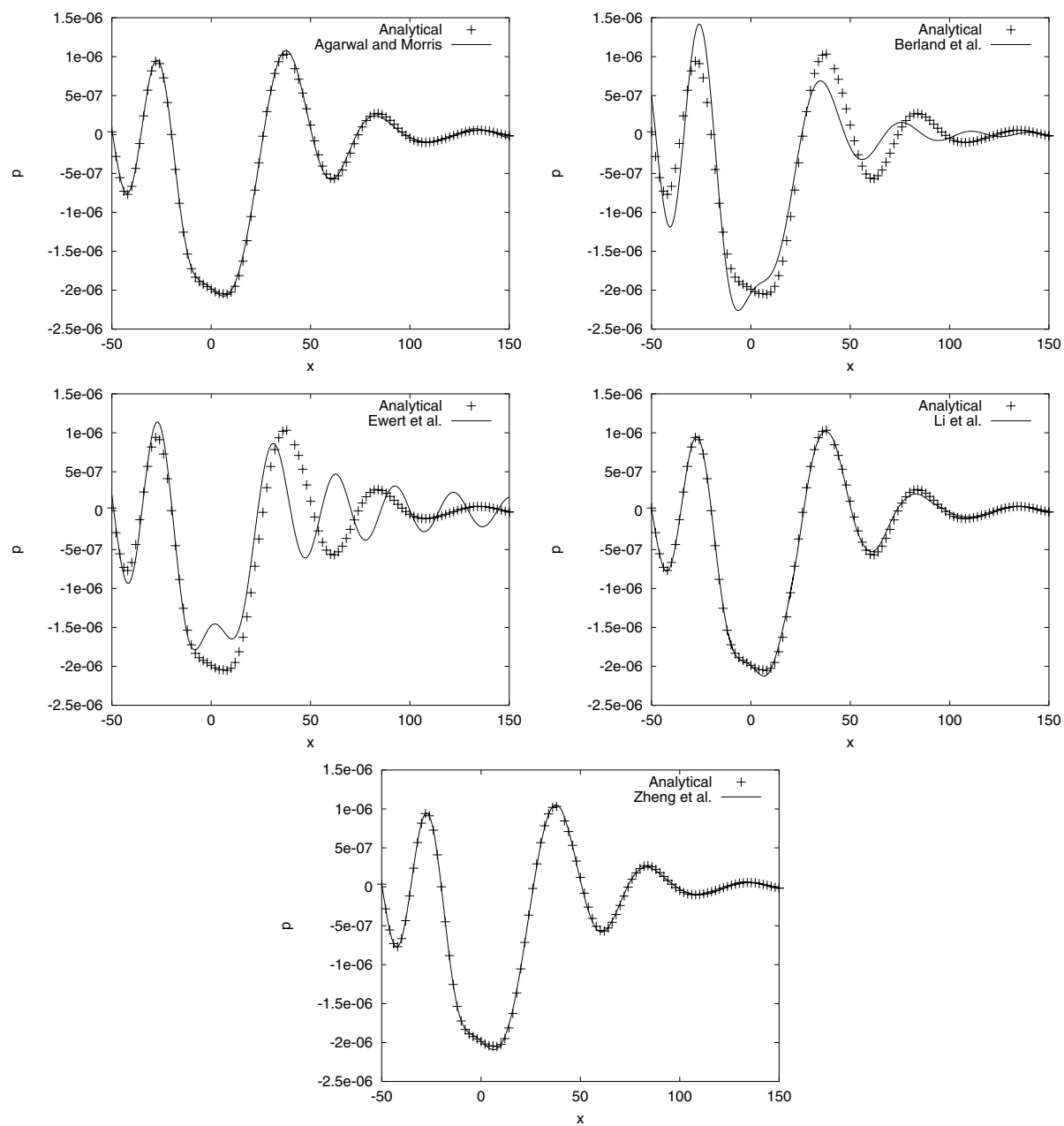
Figure 1: Instantaneous pressure field at the start of a cycle at y=15
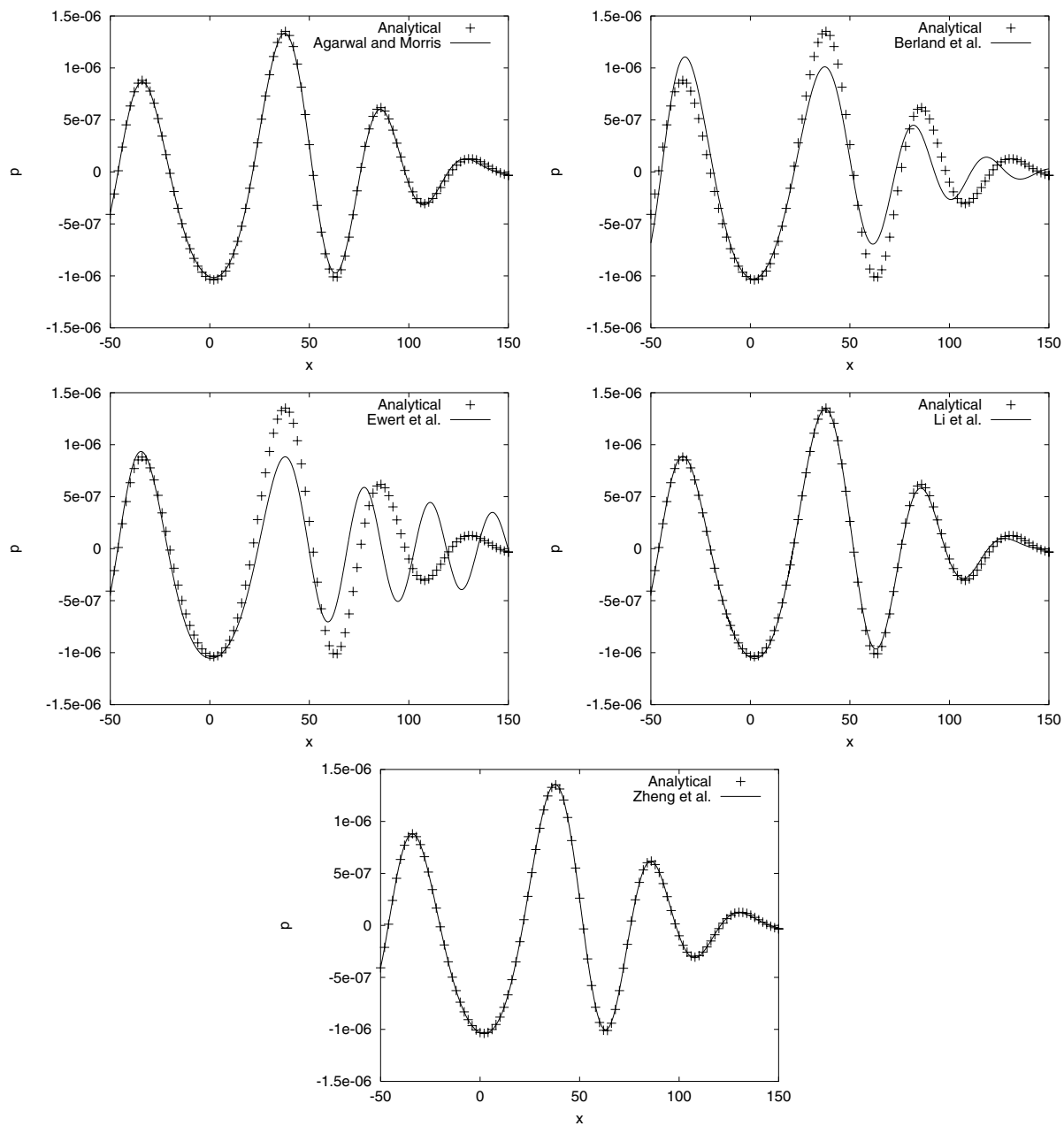
Figure 2: Instantaneous pressure field at the start of a cycle at y=50
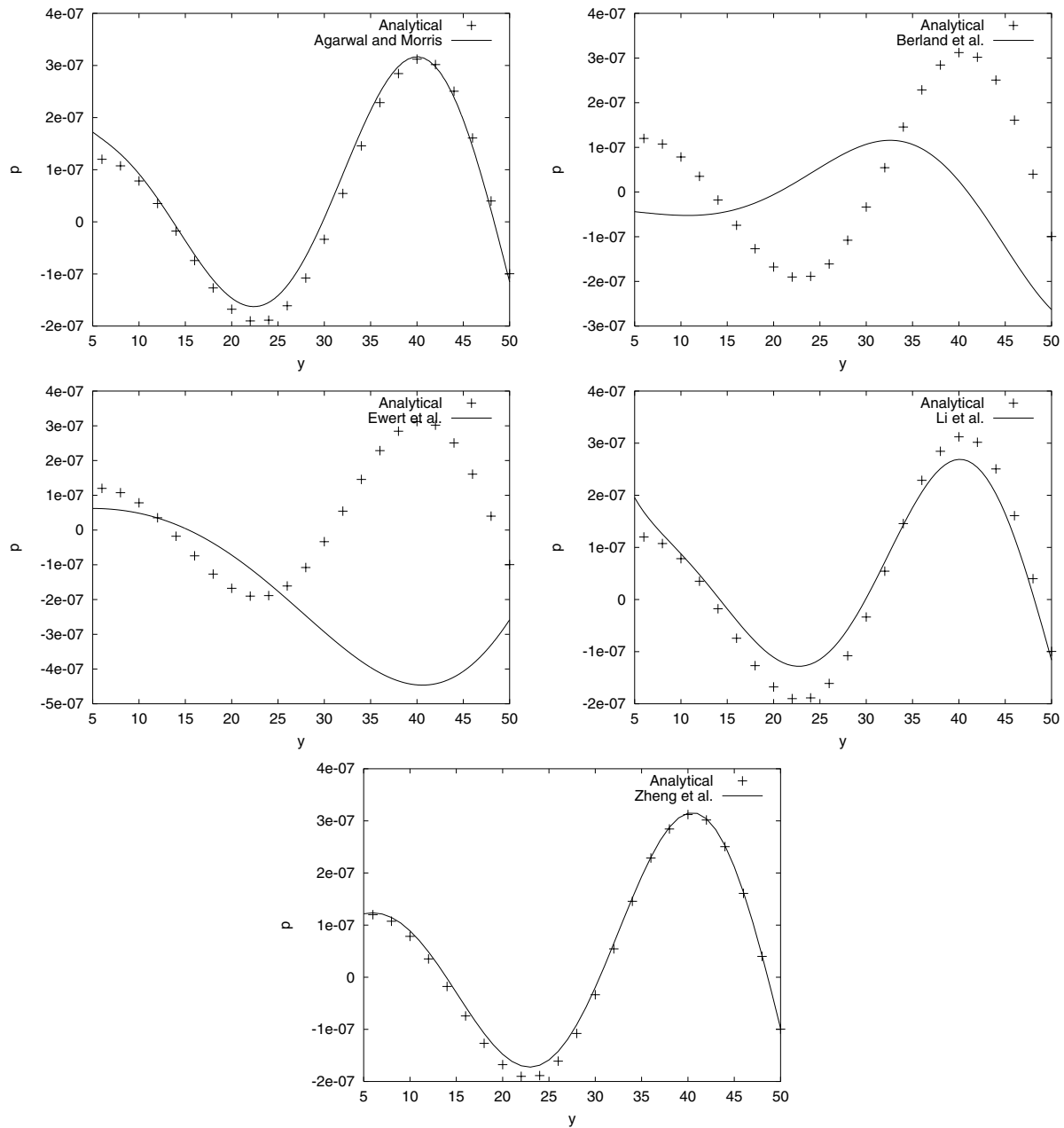
Figure 3: Instantaneous pressure field at the start of a cycle at x=100

SOLUTION COMPARISONS FOR CATEGORY 4, PROBLEM 2

Matthew F. Barone
Sandia National Laboratories

Sanjiva K. Lele
Stanford University
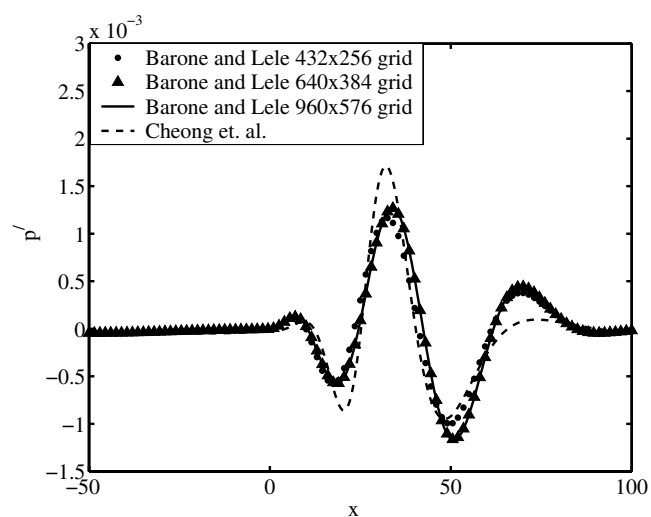
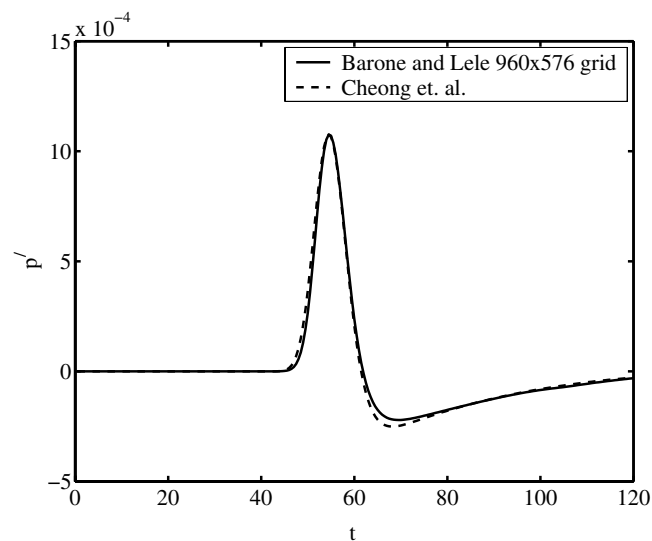**Figure 1: Pressure disturbance along the line y = −3 at t = 200 for problem 1 (acoustic pulse).**

Figure 2: Acoustic pulse signal at (x, y) = (−30, −1) for problem 1 (acoustic pulse).
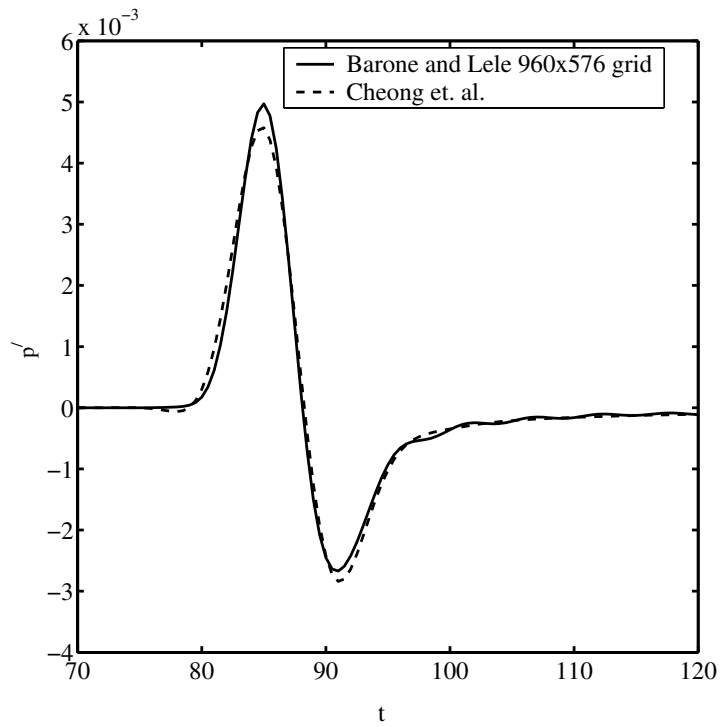
Figure 3: Acoustic pulse signal at $(\mathbf{x}, \mathbf{y}) = (\mathbf{50}, \mathbf{50})$ for problem 1 (acoustic pulse).
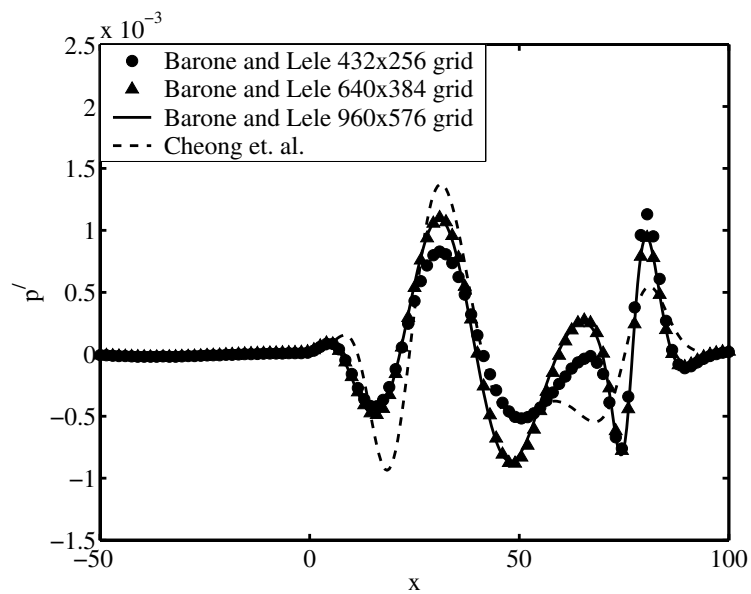
Figure 4: Pressure disturbance along the line $\mathbf{y} = -\mathbf{3}$ at $\mathbf{t} = \mathbf{200}$ for problem 2 (vortex passage).
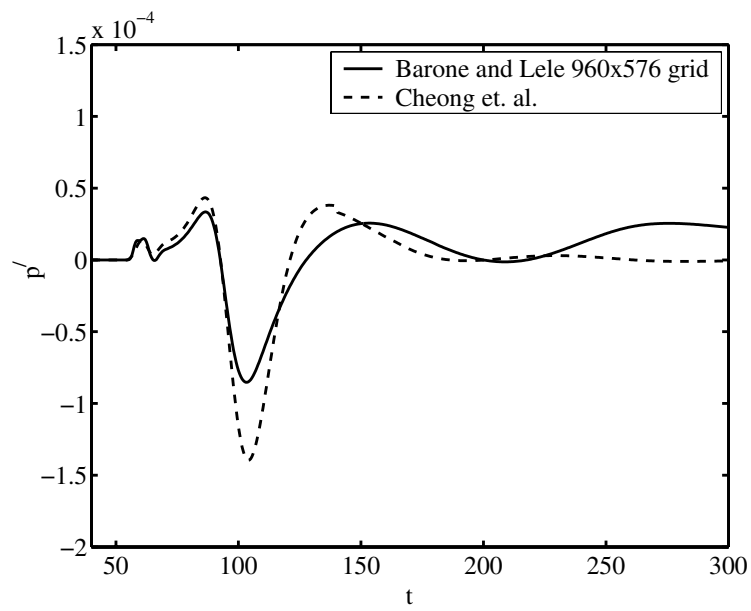
Figure 5: Acoustic pulse signal at $(\mathbf{x}, \mathbf{y}) = (-\mathbf{30}, -\mathbf{1})$ for problem 2 (vortex passage).
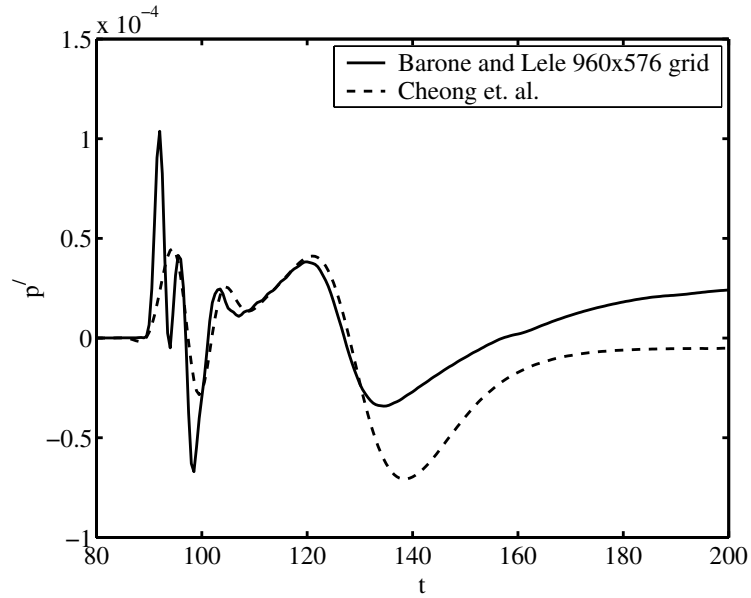
Figure 6: Acoustic pulse signal at $(\mathbf{x}, \mathbf{y}) = (\mathbf{50}, \mathbf{50})$ for problem 2 (vortex passage).
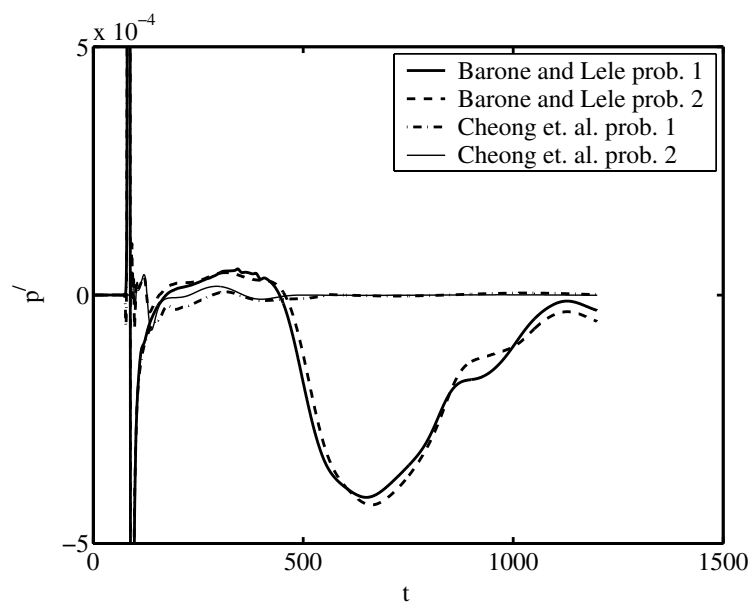
Figure 7: Long time pressure disturbance signal at $(x, y) = (50, 50)$ for both problem 1 and problem 2.

SOLUTION COMPARISON: CATEGORY 5, PROBLEM 1

Soogab Lee[†] and Cheolung Cheong[∗]

School of Mechanical and Aerospace Engineering
Seoul National University
Seoul 151-742, Korea

Aeolian tones from flow over cylinders are known to be significant with airframe and power plant noise (tubular heat exchanger, power transmission lines and chimneys). The purpose of this benchmark problem is to test the ability of a CFD/CAA code to accurately and effectively predict sound generation by viscous flows over a blunt body and sound propagation through interactions with solid wall and moving flows.

Unfortunately, no exact solution is available for this category; thus, numerical solutions from each contributor are carefully compared with. Figure 1 shows the comparison of calculated strouhal numbers of vortex shedding with experimental data. There is small discrepancy between the calculated data. It is also observed (not shown here) that the calculated fluctuating forces exerted on the cylinders show some differences between the contributors. These differences also make the variant directivities of acoustic pressure, which is shown in Figs. 2 and 3. Therefore, only for the comparison of acoustic computation, the directivities are normalized by $S_t \cdot C_{L,RMS}^2$ to which the mean square value of the acoustic pressure is theoretically known to be proportional in far field. The normalized directivities are shown in Figs. 4 and 5.
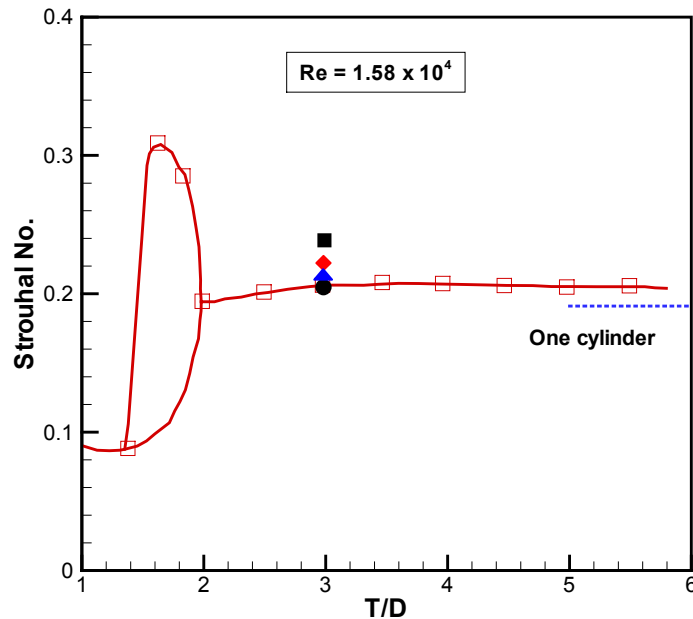

Figure 1. Comparison of the strouhal number of vortex shedding.
(●:Cheong, Ryu & Lee, ▲:Guénanff et al., ◆:Lockard,■:Loh & Jorgenson
and □: experimental data from Kia et al. ,1980)

[†] Professor, School of Mechanical and Aerospace Engineering, Seoul National University
  Address: Seoul National University, Shinrim-Dong, Gwanak-Gu, Seoul 151-742, Korea
  E-mail: solee@plaza.snu.ac.kr
  Tel: 82-2-880-7384
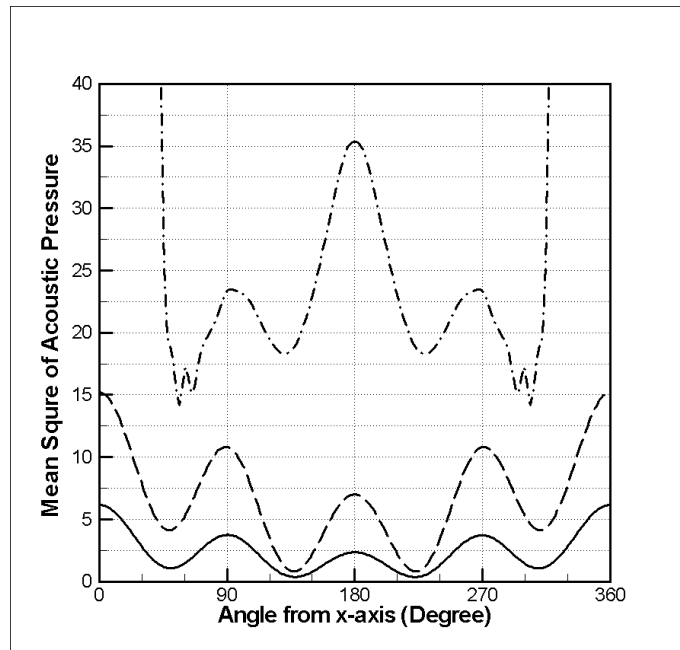 Fax: 88-2-875-4360
[∗] BK21 Post Doctor, accu99@snu.ac.kr

Figure 2. Comparison of Calculated Mean Square Acoustic Pressure on the *R = 10D*.

(————:Cheong, Ryu & Lee, — · — · — · —:Guénanff et al. and — — — —:Lockard)
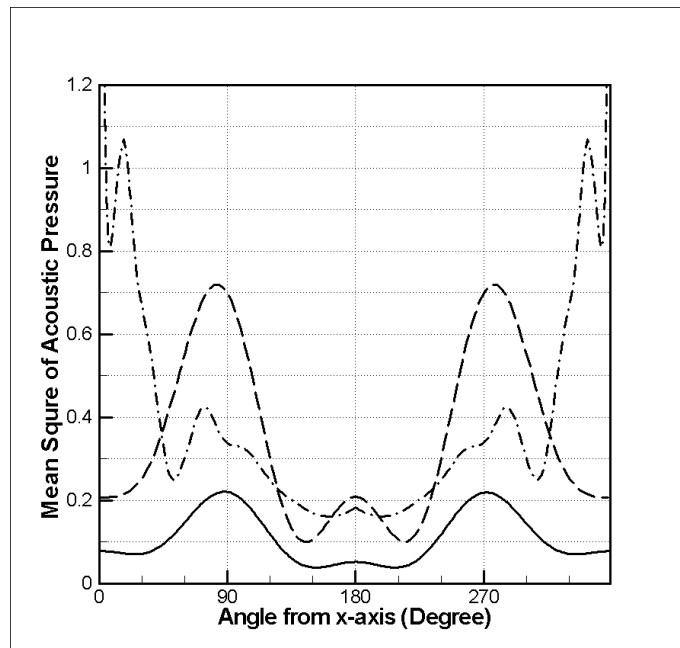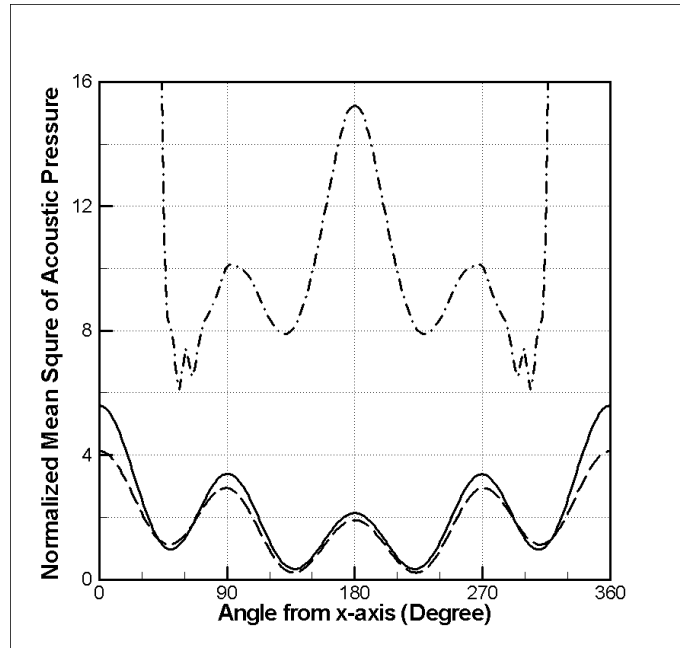

Figure 3. Comparison of Calculated Mean Square Acoustic Pressure on the *R = 100D*.

(————:Cheong, Ryu & Lee, — · — · — · —:Guénanff et al. and — — — —:Lockard)

Figure 4. Comparison of Mean Square Acoustic Pressure, Normalized by $S_t \cdot C^2_{L,RMS}$, on the **R = 10D**.

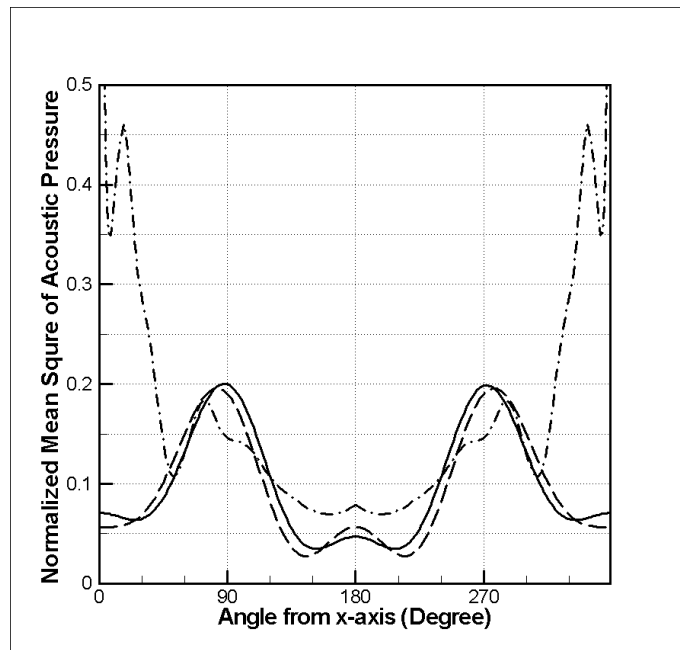(———:Cheong, Ryu & Lee, — · — · — · —:Guénanff et al. and — — — —:Lockard)

Figure 5. Comparison of Normalized Mean Square Acoustic Pressure, Normalized by $S_t \cdot C^2_{L,RMS}$, on the **R = 100D**.

(———:Cheong, Ryu & Lee, — · — · — · —:Guénanff et al. and — — — —:Lockard)

REPORT DOCUMENTATION PAGE

1. AGENCY USE ONLY (*Leave blank*)	2. REPORT DATE September 2004	3. REPORT TYPE AND DATES COVERED Conference Publication

4. TITLE AND SUBTITLE

Fourth Computational Aeroacoustics (CAA) Workshop on Benchmark Problems

6. AUTHOR(S)

Milo D. Dahl, editor

5. FUNDING NUMBERS

WBS–22–781–30–09

7. PERFORMING ORGANIZATION NAME(S) AND ADDRESS(ES)

National Aeronautics and Space Administration
John H. Glenn Research Center at Lewis Field
Cleveland, Ohio 44135–3191

8. PERFORMING ORGANIZATION REPORT NUMBER

E–14393

9. SPONSORING/MONITORING AGENCY NAME(S) AND ADDRESS(ES)

National Aeronautics and Space Administration
Washington, DC 20546–0001

10. SPONSORING/MONITORING AGENCY REPORT NUMBER

NASA CP—2004-212954

11. SUPPLEMENTARY NOTES

Proceedings from the Fourth Computational Aeroacoustics (CAA) Workshop on Benchmark Problems cosponsored by the Ohio Aerospace Institute, AeroAcoustics Research Consortium, and NASA Glenn Research Center, Brook Park, Ohio, October 20–22, 2003. These proceedings are available on CD–ROM in the PDF document format. In addition, the CD–ROM contains information related to all five categories of the benchmark problems including the numerical results from the calculations of the analytical and numerical solutions and the experimental data. See the README file in the CD–ROM directory entitled "caawksp4data" for further details. Responsible person, Milo D. Dahl, organization code 5940, 216–433–3578.

12a. DISTRIBUTION/AVAILABILITY STATEMENT

Unclassified - Unlimited
Subject Category: 71   Distribution: Nonstandard

Available electronically at http://gltrs.grc.nasa.gov

This publication is available from the NASA Center for AeroSpace Information, 301–621–0390.

12b. DISTRIBUTION CODE

13. ABSTRACT *(Maximum 200 words)*

The proceedings of the Fourth Computational Aeroacoustics (CAA) Workshop on Benchmark Problems cosponsored by the Ohio Aerospace Institute, AeroAcoustics Research Consortium, and the NASA Glenn Research Center are the subject of this report. As in previous workshops, the problems in this workshop were devised to gauge the technological advancement of computational techniques relevant to CAA. These proceedings show the technical progress achieved from the basic challenges to accurate CAA calculations to the solution of CAA problems of increasing complexity and difficulty. Problems were solved in five categories. In three of the five categories, exact solutions were available for comparison to CAA results. A fourth category representing the sound generation by interacting with a gust, a problem relevant to fan noise, had approximate analytical or completely numerical solutions. The fifth category problems had sound generation in a viscous flow. In this case, the CAA results were compared to experimental data.

14. SUBJECT TERMS

Aeroacoustics; Numerical methods; Wave propagation; Sound sources;
Acoustic boundary conditions

15. NUMBER OF PAGES

495

16. PRICE CODE

17. SECURITY CLASSIFICATION OF REPORT Unclassified	18. SECURITY CLASSIFICATION OF THIS PAGE Unclassified	19. SECURITY CLASSIFICATION OF ABSTRACT Unclassified	20. LIMITATION OF ABSTRACT